

ARO 34543.1-ms-CF



MATERIALS
RESEARCH
SOCIETY

SYMPOSIUM PROCEEDINGS

Volume 378

Defect and Impurity Engineered Semiconductors and Devices

EDITORS:

S. Ashok

J. Chevallier

I. Akasaki

N.M. Johnson

B.L. Soporì

DISTRIBUTION STATEMENT 1

Approved for public release
Distribution Unlimited

Public reporting burden for this collection of information is estimated to average 1 hour per response, including the time for reviewing instructions, searching existing data sources, gathering and maintaining the data needed, and completing and reviewing the collection of information. Send comment regarding this burden estimate or any other aspect of this collection of information, including suggestions for reducing this burden, to Washington Headquarters Services, Directorate for Information Operations and Reports, 1215 Jefferson Davis Highway, Suite 1204, Arlington, VA 22202-4302, and to the Office of Management and Budget, Paperwork Reduction Project (0704-0188), Washington, DC 20503.

1. AGENCY USE ONLY (Leave blank)		2. REPORT DATE June 1996	3. REPORT TYPE AND DATES COVERED Final 1 Apr 95 - 31 Mar 96
4. TITLE AND SUBTITLE Materials Research Society Symposium Proceedings, Vol 378. Defect and Impurity Engineered Semiconductors and Devices		5. FUNDING NUMBERS DAAH04-95-1-0150	
6. AUTHOR(S) John B. Ballance (principal investigator)			
7. PERFORMING ORGANIZATION NAME(S) AND ADDRESS(ES) Materials Research Society Pittsburgh, PA 15237		8. PERFORMING ORGANIZATION REPORT NUMBER	
9. SPONSORING / MONITORING AGENCY NAME(S) AND ADDRESS(ES) U.S. Army Research Office P.O. Box 12211 Research Triangle Park, NC 27709-2211		10. SPONSORING / MONITORING AGENCY REPORT NUMBER ARO 34543.1-MS-CF	
11. SUPPLEMENTARY NOTES The views, opinions and/or findings contained in this report are those of the author(s) and should not be construed as an official Department of the Army position, policy or decision, unless so designated by other documentation.			
12a. DISTRIBUTION / AVAILABILITY STATEMENT Approved for public release; distribution unlimited		12 b. DISTRIBUTION CODE	
13. ABSTRACT (Maximum 200 words) This volume results from a symposium held at the 1995 MRS Spring Meeting, April 17-21, in San Francisco. The symposium, bearing the title of this volume, followed upon a highly successful earlier symposium entitled "Defect Engineering in Semiconductor Growth, Processing and Device Technology," held at the 1992 MRS Spring Meeting. The intent of the present symposium was to go beyond defect control and explore deliberate introduction and manipulation of defects and impurities in order to engineer some desired properties in semiconductor materials and devices. The response from the academic and industrial research communities was overwhelming, with over 280 abstracts submitted from around the world. The theme of defect engineering has clearly come of age.			
14. SUBJECT TERMS		15. NUMBER OF PAGES 1054	16. PRICE CODE
17. SECURITY CLASSIFICATION OR REPORT UNCLASSIFIED	18. SECURITY CLASSIFICATION OF THIS PAGE UNCLASSIFIED	19. SECURITY CLASSIFICATION OF ABSTRACT UNCLASSIFIED	20. LIMITATION OF ABSTRACT UL

**Defect and Impurity Engineered
Semiconductors and Devices**

**MATERIALS RESEARCH SOCIETY
SYMPOSIUM PROCEEDINGS VOLUME 378**

Defect and Impurity Engineered Semiconductors and Devices

Symposium held April 17-21, 1995, San Francisco, California, U.S.A.

EDITORS:

S. Ashok

*The Pennsylvania State University
University Park, Pennsylvania, U.S.A.*

J. Chevallier

*CNRS
Meudon, France*

I. Akasaki

*Meijo University
Nagoya, Japan*

N.M. Johnson

*Xerox Palo Alto Research Center
Palo Alto, California, U.S.A.*

B.L. Sopori

*National Renewable Energy Laboratory
Golden, Colorado, U.S.A.*



PITTSBURGH, PENNSYLVANIA

19960812 024

DTIC QUALITY INSPECTED 1

This work was supported in part by the Army Research Office under Grant Number DAAH04-95-1-0150. The views, opinions, and/or findings contained in this report are those of the author(s) and should not be construed as an official Department of the Army position, policy, or decision, unless so designated by other documentation.

Single article reprints from this publication are available through
University Microfilms Inc., 300 North Zeeb Road, Ann Arbor, Michigan 48106

CODEN: MRSPDH

Copyright 1995 by Materials Research Society.
All rights reserved.

This book has been registered with Copyright Clearance Center, Inc. For further information, please contact the Copyright Clearance Center, Salem, Massachusetts.

Published by:

Materials Research Society
9800 McKnight Road
Pittsburgh, Pennsylvania 15237
Telephone (412) 367-3003
Fax (412) 367-4373
Homepage <http://www.mrs.org/>

Library of Congress Cataloging in Publication Data

Defect and impurity engineered semiconductors and devices (Symp. B) :
symposium held April 17-21, 1995, San Francisco, California, U.S.A. / editors,
S. Ashok, J. Chevallier, I. Akasaki, N.M. Johnson, B.L. Sopor.
p. cm.-(Materials Research Society symposium proceedings,
0272-9172 ; vol. 378)
Includes bibliographical references and index.
ISBN 1-55899-281-2 (alk. paper)
1. Semiconductors. 2. Semiconductors-Defects. 3. Semiconductors-Impurity
distribution. I. Ashok, S. II. Chevallier, J. III. Akasaki, I. IV. Johnson, N.M.
V. Sopor, B.L. VI. Series: Materials Research Society symposium proceedings ;
v. 378.

TK7871.85.D453 1995
621.3815'2-dc20

95-22910
CIP

Manufactured in the United States of America

CONTENTS

Preface	xix
Acknowledgments	xxi
Materials Research Society Symposium Proceedings	xxii

PART I: PLENARY REVIEW

*Order and Disorder in Semiconductors	3
<i>Hans J. Queisser</i>	

PART II: GROWN-IN DEFECTS IN BULK CRYSTALS

Surfaces and Crystal Defects of Silicon	17
<i>P. Wagner, M. Brohl, D. Gräf, and U. Lambert</i>	
The Formation of Defects Degrading Gate Oxide Integrity During CZ-Si Crystal Growth	23
<i>Y. Tsumori, K. Nakai, T. Iwasaki, H. Haga, K. Kojima, and T. Nakashizu</i>	
Analysis of Dislocation Networks and Electronic Properties of Dendritic Web Silicon	29
<i>S.L. Morelhão, D.L. Meier, G.T. Neugebauer, B.B. Bathey, and S. Mahajan</i>	
On the Recombination Activity of Oxygen Precipitation Related Lattice Defects in Silicon	35
<i>J. Vanhellemont, A. Kaniava, M. Libezny, E. Simoen, G. Kissinger, E. Gaubas, C. Claeys, and P. Clauws</i>	
Characterization of Growth Defects in CdZnTe Single Crystals by Synchrotron White Beam X-ray Topography	41
<i>H. Chung, B. Raghathamachar, J. Wu, M. Dudley, D.J. Larson, Jr., and D.C. Gillies</i>	
Large Persistent Photochromic Effect Due to DX Centers in AISb Doped with Selenium	47
<i>P. Becla, A.G. Witt, J. Lagowski, and W. Walukiewicz</i>	
Control of Oxygen Content in Heavily Sb-Doped CZ Si Crystal by Adjusting Ambient Pressure	53
<i>Koji Izunome, Xinming Huang, Shinji Togawa, Kazutaka Terashima, and Shigeyuki Kimura</i>	
Photodiffractive Characterization of Growth-Defects in GaAs	59
<i>K. Jarašiusas, M. Sudzius, A. Kaniava, and J. Vaitkus</i>	

*Invited Paper

Influence of Electric Field and Temperature on Magnetic Field Induced Prolonged Changes of Electric Parameters of Silicon Systems	65
<i>Vladimir M. Maslovsky</i>	
Electrical and Structural Properties of MeV Si⁺ Ion Implantation in Silicon	71
<i>Aditya Agarwal, S. Kovesnikov, K. Christensen, and G.A. Rozgonyi</i>	
Investigation of Resistivity Distributions in CdTe Crystals by Time Dependent Charge Measurements (TDCM)	77
<i>C. Eiche, W. Joerger, M. Fiederle, R. Schwarz, M. Salk, D.G. Ebling, and K.W. Benz</i>	
Scanning Tunneling Microscopy Studies of GaAs_{1-x}P_x Single Crystals	83
<i>X. Liu, E.R. Weber, D.F. Ogletree, M. Salmeron, and T. Slupinski</i>	
Study of Oxygen Diffusion and Clustering in Silicon Using an Empirical Interatomic Potential	89
<i>Z. Jiang and R.A. Brown</i>	
Computation of the Onset of Point Defect Aggregation in Crystalline Silicon Using an Empirical Interatomic Potential	95
<i>T. Sinno and R.A. Brown</i>	
Numerical Simulation of Point Defect Distributions in a Growing Czochralski Silicon Crystal in Response to an Abrupt Change in the Growth Conditions	101
<i>W. Wijaranakula, Q.S. Zhang, K. Takano, and H. Yamagishi</i>	
Deviation from Stoichiometry and Lattice Properties of Semiconducting SnTe Phase	107
<i>E.I. Rogacheva, G.V. Gorne, and O.N. Nashchekina</i>	

PART III: GROWN-IN DEFECTS IN THIN FILMS

Low Energy Ion Implantation of As During Si-MBE	115
<i>E.J.H. Collart, D.J. Gravesteijn, E.G.C. Lathouwers, and W.J. Kersten</i>	
Nucleation and Growth of Defects in SOI Materials	121
<i>G.C.M. Silvestre, R.A. Moore, and B.J. Kennedy</i>	
Extraction of Elastic Parameters of Heavily Boron-Doped Silicon Layer by Elimination of Misfit Dislocations	129
<i>Ho-Jun Lee, Chul-Hi Han, and Choong-Ki Kim</i>	
Efficient Nonradiative Recombination Centers in MBE-Grown Si and SiGe/Si Heterostructures	135
<i>W.M. Chen, I.A. Buyanova, A. Henry, W.-X. Ni, G.V. Hansson, and B. Monemar</i>	

Defect-Engineered Graded $\text{Ge}_x\text{Si}_{1-x}$ Buffers on Si (001) with Extreme Low Threading Dislocation Density	141
<i>G. Kissinger, T. Morgenstern, G. Morgenstern, H.B. Erzgräber, and H. Richter</i>	
DLTS Study on Annealed Low-Temperature GaAs Layers with An n-(LT)-n Structure Grown by MBE	147
<i>Tsai-Cheng Lin, Hiromasa T. Kaibe, and Tsugunori Okumura</i>	
Deep Impurities in AlGaAs Grown by MOCVD Using Different Hydrogen and Nitrogen as Carrier Gases	153
<i>J.C. Chen, Z.C. Huang, Bing Yang, H.K. Chen, and K.J. Lee</i>	
Atomic Structure of Deep Level Defects in Dimethylaluminum Methoxide-Doped GaAs	159
<i>Y. Park and M. Skowronski</i>	
Intentional Defect Incorporation in Metalorganic Vapor Phase Epitaxy Indium Gallium Arsenide by Oxygen Doping	165
<i>J.W. Huang and T.F. Kuech</i>	
The Ultrafast Carrier Dynamics in Semiconductors: The Role of Defects	171
<i>P.M. Fauchet, G.W. Wicks, Y. Kostoulas, A.I. Lobad, and K.B. Ucer</i>	
Dependence of Sheet Hole Concentrations on Growth Kinetics of a Carbon Doped Electron Beam Heated Graphite Source in GaAs and $\text{Al}_{0.3}\text{Ga}_{0.7}\text{As}$ Films Grown by Solid Source MBE	177
<i>D.L. Sato, F.J. Szalkowski, and H.P. Lee</i>	
Point Defect Supersaturation During Zinc Diffusion into InP	183
<i>D. Wittorf, W. Jäger, A. Rucki, K. Urban, H.-G. Hettwer, N.A. Stolwijk, and H. Mehrer</i>	
Low Deep Impurity $\text{In}_x\text{Ga}_{1-x}\text{P}$ Grown by Metalorganic Chemical Vapor Deposition	189
<i>Z.C. Huang, Bing Yang, H.K. Chen, and J.C. Chen</i>	
Very Low Deep Level $\text{Al}_x\text{Ga}_{1-x}\text{As}$ ($x=0.22$) Layer Grown by Metalorganic Chemical Vapor Deposition	195
<i>Z.C. Huang, Bing Yang, H.K. Chen, and J.C. Chen</i>	
Low-Temperature, Solid-Phase Epitaxial Growth of Amorphized, Non-Stoichiometric GaAs	201
<i>K.B. Belay, D.L. Llewellyn, and M.C. Ridgway</i>	
Magnetic Circular Dichroism of Low-Temperature-Grown $\text{Al}_x\text{Ga}_{1-x}\text{As}$	207
<i>A. Prasad, X. Liu, P. Stallinga, E.R. Weber, A.K. Verma, and J.S. Smith</i>	
Spectroscopic Ellipsometric Characterization of Low Temperature GaAs	213
<i>X. Gao, P.G. Snyder, P.W. Yu, Y.Q. Zhang, and Z.F. Peng</i>	

Optical Absorptions and EL2-Like Defects in Low Temperature Grown Molecular-Beam-Epitaxial GaAs	219
<i>S.K. So, M.H. Chan, and K.T. Chan</i>	
Investigation of Free Exciton Properties in GaAs Epitaxial Layer	225
<i>Wu Fengmei, Shi Yi, Martin Parenteau, Anouar Jorio, Zheng Youdou, and Cosmo Carlone</i>	
Uniformity of Arsenic Dimer and Tetramer Fluxes from a Valved Arsenic Cracking Source in MBE	231
<i>George A. Patterson, James S.C. Chang, and Forrest G. Kellert</i>	
*Dopant-Defect Interactions in II-VI Semiconductors Studied by PAC	237
<i>Thomas Wichert</i>	
Growth and Characterization of the Binary Defect Alloy Cu_{2-x}Se and the Relation to II-VI/I-III-VI Heterojunction Formation	249
<i>Art J. Nelson, K. Sinha, and John Moreland</i>	
Nonstoichiometric Defects in Semiconductor SnTe Thin Films	255
<i>O.N. Nashchekina, E.I. Rogacheva, L.P. Shpakovskaya, V.I. Pinegin, and A.I. Fedorenko</i>	

PART IV: GETTERING AND RELATED PHENOMENA

*Transition-Metal Impurity Luminescence in GaAs and its Application to Material Characterization	263
<i>T. Nishino</i>	
Transient Diffusion and Gettering of Au and Cu to Cavities in Si	273
<i>J. Wong-Leung, J.S. Williams, and E. Nygren</i>	
Minority Carrier Diffusion Length Improvement in Czochralski Silicon by Aluminum Gettering	279
<i>Subhash M. Joshi, Ulrich M. Gösele, and Teh Y. Tan</i>	
Impurity Gettering in MBE Grown Silicon	285
<i>A. Nylandsted Larsen, P. Kringhøj, J. Lundsgaard Hansen, and S.Yu. Shiryayev</i>	
Lateral Diffusion and Capture of Iron in P-Type Silicon	291
<i>Kevin L. Beaman, Aditya Agarwal, Sergei V. Kovesnikov, and George A. Rozgonyi</i>	
Phosphorus and Aluminum Gettering of Gold in Silicon: Simulation and Optimization Considerations	297
<i>R. Gafiteanu, U. Gösele, and T.Y. Tan</i>	

*Invited Paper

A Study of Gettering Efficiency and Stability in Czochralski Silicon	303
<i>Scott A. McHugo, E.R. Weber, M. Mizuno, and F.G. Kirscht</i>	
Gettering of Interstitial Iron in P/P+ Epitaxial Silicon Wafers	309
<i>W. Wijaranakula, X. Gao, K. Curtis, and H. Haddad</i>	
Characterization of the Damage on the Back Side of Silicon Wafers	315
<i>S.E. Lindo, K.M. Matney, and M.S. Goorsky</i>	
Mechanism of Iron Gettering by Polycrystalline Silicon Film in P-Type Czochralski (CZ) Silicon	321
<i>Kamal K. Mishra</i>	
External Gettering Comparison and Structural Characterization of Single and Polycrystalline Silicon	327
<i>Henry Hieslmair, Scott McHugo, and Eicke Weber</i>	
Effect of P-Doping Level-POCl₃ Diffused or Spin-On Deposited-On the Gettering Efficiency of Polycrystalline Silicon After RTA or CTA	333
<i>M. Loghmarti, K. Mahfoud, J.C. Muller, D. Sayah, and P. Siffert</i>	

PART V: HYDROGEN INTERACTION WITH SEMICONDUCTORS

*Spectroscopy of Transition-Metal-Hydrogen Complexes in Silicon	341
<i>Michael Stavola, S.J. Uffring, M.J. Evans, P.M. Williams, and G.D. Watkins</i>	
Coupling of Electronic and Structural Properties of Hydrogen in Crystalline Silicon	353
<i>Wolfgang Cszaszar and Arthur L. Endrös</i>	
Low-Temperature Diffusivity of Hydrogen in Different Silicon Substrates	359
<i>Xiaojun Deng and Bhushan L. Soporì</i>	
ECR Hydrogen Plasma Treatment of Si: Defect Activation Under Thermal Anneal	365
<i>C.W. Nam and S. Ashok</i>	
Hydrogen and Lithium Passivation of Gold in Silicon: A Comparative Study	371
<i>E.Ö. Sveinbjörnsson, S. Kristjánsson, O. Engström, and H.P. Gislason</i>	

*Invited Paper

Electron Spin Resonance Evidence for a Localized EP (E'δ-Like) Defect Structure	377
<i>John F. Conley, Jr. and P.M. Lenahan</i>	
*Hydrogen-Induced Metastability of Polycrystalline Silicon	381
<i>N.H. Nickel</i>	
Analysis of Hydrogen Passivation Mechanisms in Poly-Si TFT's by Employing R.F. Plasma	393
<i>K.Y. Choi, Y.S. Kim, H.S. Choi, B.S. Bae, and M.K. Han</i>	
Hydrogenation of Multicrystalline Si-Materials for Solar Cells: Discrimination Between Effects in the Intra-Grain and Grain Boundary Regions	399
<i>J. Poortmans, M. Rosmeulen, A. Kaniava, J. Vanhellemont, H. Elgamel, and J. Nijs</i>	
Enhanced Hydrogenation Due to Ultrasound Treatment in Polycrystalline Silicon: New Approach to Thin Film Defect Engineering	405
<i>S. Ostapenko, W. Henley, S. Karimpanakkel, L. Jastrzebski, and J. Lagowski</i>	
Hydrogen Passivation of Defects in Electron Irradiated Polycrystalline Silicon Solar Cells	411
<i>R.R. Bilyalov and B.M. Abdurakhmanov</i>	
Interaction of Atomic Hydrogen with Chalcogens in GaAs	417
<i>J. Vetterhöffer and J. Weber</i>	
Hydrogen Passivation of Shallow Dopants in Indium Doped Bulk CdTe	423
<i>Suma Gurumurthy, A.K. Sreedhar, H.L. Bhat, B. Sundershesu, R.K. Bagai, and Vikram Kumar</i>	
Plasma-Induced Electron Traps in n-InP	429
<i>Yoshifumi Sakamoto, Takashi Sugino, Koichiro Matsuda, and Junji Shirafuji</i>	
Hydrogen Diffusion in n-GaAs:Si Under Hydrostatic Pressure	435
<i>B. Machayekhi, J. Chevallier, B. Theys, J.M. Besson, G. Weill, and G. Syfosse</i>	
Native Defects in Low Temperature GaAs and the Effect of Hydrogenation	441
<i>R.E. Fritchard, S.A. McQuaid, R.C. Newman, J. Mäkinen, H.J. von Bardeleben, and M. Missous</i>	

*Invited Paper

Hydrogen-Related Electron Traps in GaAs and Their Relation to Crystal Stoichiometry	447
<i>Tatsuyuki Shinagawa and Tsugunori Okumura</i>	

Hydrogen Passivation of Shallow Dopants in InP Studied by Photoluminescence Spectroscopy	453
<i>Sathya Balasubramanian and Vikram Kumar</i>	

Hydrogen-Induced Passivation of Deep Traps in n-GaAs:Si Grown on LT-GaAs	459
<i>E.C. Paloura, A. Ginoudi, B. Theys, J. Chevallier, C.B. Lioutas, J. Kalomiros, M. Lagadas, and Z. Hatzopoulos</i>	

PART VI: DEFECT ISSUES IN WIDEGAP SEMICONDUCTORS

*Theory of Defects in Wide-Band-Gap Semiconductors	467
<i>Chris G. Van de Walle and Jörg Neugebauer</i>	

The Role of Impurities in Hydride Vapor Phase Epitaxially Grown Gallium Nitride	479
<i>R.J. Molnar, K.B. Nichols, B. Maki, E.R. Brown, and I. Melngailis</i>	

High Resistivity InAlN by Nitrogen or Oxygen Implantation	485
<i>J.C. Zolper, S.J. Pearton, C.R. Abernathy, and C.B. Vartuli</i>	

Deep Level Defects in GaN Characterized by Capacitance Transient Spectroscopies	491
<i>W. Götz, N.M. Johnson, R.A. Street, H. Amano, and I. Akasaki</i>	

Hydrogen Diffusion and Passivation in InGaAlN Alloys	497
<i>S.J. Pearton, C.R. Abernathy, J.D. MacKenzie, C.B. Vartuli, R.G. Wilson, J.M. Zavada, and R.J. Shul</i>	

Atomic Hydrogen in GaN	503
<i>Jörg Neugebauer and Chris G. Van de Walle</i>	

Photoluminescence Studies of GaN and AlGaIn Layers Under Hydrostatic Pressure	509
<i>C. Wetzel, W. Walukiewicz, E.E. Haller, H. Amano, and I. Akasaki</i>	

Photoconductivity as a Function of Temperature in MOCVD Grown Gallium Nitride Films	515
<i>C.H. Qiu, W. Melton, and J.I. Pankove</i>	

Time Resolved Photoluminescence Spectroscopy on GaN Epitaxial Layers	521
<i>B.K. Meyer, D. Volm, C. Wetzel, L. Eckey, J.-Ch. Holst, P. Maxim, R. Heitz, A. Hoffmann, I. Broser, E.N. Mokhov, P.G. Baranov, C. Qiu, and J.I. Pankove</i>	

*Invited Paper

Defect Studies in n-Type GaN Grown by Molecular Beam Epitaxy	527
<i>W. Götz, D.B. Oberman, and J.S. Harris, Jr.</i>	
The Effects of Sintering on the Microstructure and the Luminescent Characteristics of Polycrystalline ZnS	533
<i>R. Matthew Adams, Peter Mascher, and Adrian H. Kitai</i>	
Study of Deep Levels by Admittance Spectroscopy in High Resistivity P-Type 6H-SiC Single Crystals	539
<i>A.O. Ewwaraye, S.R. Smith, and W.C. Mitchell</i>	

PART VII: DEFECT CHARACTERIZATION

*Local Vibrational Mode (LVM) Spectroscopy of Semiconductors	547
<i>Eugene E. Haller</i>	
*Silicon Delta Doping in GaAs: An Ongoing Enigma	567
<i>R.C. Newman, M.J. Ashwin, J. Wagner, M.R. Fahy, L. Hart, S.N. Holmes, and C. Roberts</i>	
Applications of Scanning Defect Mapping System for Semiconductor Characterization	579
<i>Kevin F. Carr, N. Carlson, P. Weitzman, B.L. Sopori, C. Marshall, and L. Allen</i>	
Characterization of Fast Diffusing Charged Defects in Semiconductors	585
<i>T. Helser, A. Zamouche, and A. Mesli</i>	
Noncontact Photoconductivity Amplitude Technique to Characterize Polishing- and Slicing-Induced Residual Damage in Si Wafers	591
<i>Y. Ogita, M. Nakano, and H. Masumura</i>	
Non-Destructive Method for Simultaneous Mapping of Diffusion Length and Surface Recombination Velocity	597
<i>Hans-Christoph Ostendorf and Arthur L. Endrös</i>	
Investigation of Recombination Parameters in Ion Implanted Layer-Substrate Si Structures	603
<i>E. Gaubas, K. Jarasiunas, A. Kaniava, and J. Vaitkus</i>	
Peculiarities of Determination of Recombination Parameters at Moderate and High Excitation Levels in Silicon Wafers	609
<i>E. Gaubas and A. Kaniava</i>	

*Invited Paper

Application of Elastic Mid-IR-Laser-Light Scattering for Non-Destructive Inspection in Microelectronics	615
<i>Victor P. Kalinushkin, Vladimir A. Yuryev, Oleg V. Astafiev, Alexander N. Buzynin, and Nikolay I. Bletsan</i>	

**PART VIII: ION IMPLANTATION AND
PROCESS-INDUCED DEFECTS**

Activation of Implanted Phosphorus Ions into Silicon by Followed Hydrogen Ion Implantations	623
<i>Y. Hasebe, H. Ohshima, T. Hattori, A. Usami, and Y. Tokuda</i>	

Photoluminescence of Extended Defects in Silicon-on- Insulator Formed by Implantation of Oxygen	629
<i>Y.H. Qian, J.H. Evans, L.F. Giles, A. Nejim, and P.L.F. Hemment</i>	

Type II Dislocation Loops and Their Effect on Strain in Ion Implanted Silicon as Studied by High Resolution X-ray Diffraction	635
<i>R.H. Thompson, Jr., V. Krishnamoorthy, J. Liu, and K.S. Jones</i>	

Contactless Evaluation of the Surface Recombination Property of Silicon with an Ion-Implanted Layer	641
<i>Akira Usami, Takanori Makino, Hideaki Yoshida, and Etsuro Morita</i>	

Ultrasound Defect Engineering of Transition Metals Via Metal-Acceptor Pairs in Silicon	647
<i>Ronald E. Bell II, Serguei Ostapenko, and Jacek Lagowski</i>	

Inversion of Conductivity in p-Si After Ion Treatment	653
<i>Alexander N. Buzynin, Albert E. Lukyanov, Vyacheslav V. Osiko, and Vladimir V. Voronkov</i>	

Surface-Oriented Oxygen Mass Transport During Implantation	659
<i>A.B. Danilin, L.A. Charnyi, A.W. Nemirovski, and V.V. Saraikin</i>	

Observation of Vacancy-Oxygen Complexes in Silicon Implanted with Substoichiometric Doses of Oxygen Ions	665
<i>A.I. Belogorokhov, L.A. Charnyi, A.B. Danilin, and A.W. Nemirovski</i>	

X-ray Topography of Strain Fields Induced by 100 MeV Ti⁷⁺ Ion Irradiated Si(100)	671
<i>B.B. Sharma, S.R. Gupta, R.K. Sharma, V. Kumar, U. Tiwari, P. Sen, and G.K. Mehta</i>	

Relation Between Structure and Carrier Lifetime in As-Implanted GaAs	677
<i>Z. Lillental-Weber, W. Swider, H. Kagluchi, A. Claverie, H.H. Wang, and J.F. Whitaker</i>	

The Influence of Non-Stoichiometry on the Electrical Activation of n-Type Dopants in InP	683
<i>M.C. Ridgway, C.M. Johnson, and P. Kringhøj</i>	
Ellipsometric Monitoring of Defects Induced by Electron Cyclotron Resonance Etching of GaAs	689
<i>P.G. Snyder, N.J. Ianno, B. Wigert, S. Pittal, B. Johs, and J.A. Woollam</i>	
Electron-Beam-Induced Transformation of Defects in Proton-Implanted CdS Single Crystals	695
<i>V.B. Mityukhlyev</i>	

PART IX: DEFECTS IN DEVICES

*Defects and Future Silicon Technology	703
<i>J. Palm and L.C. Kimerling</i>	
*Probing Metal Defects in CCD Image Sensors	713
<i>William C. McColgin, J.P. Lavine, and C.V. Stancampiano</i>	
Crystallographic Defect Related Degradation in High Density Memory Devices	725
<i>S.S. Kim and W. Wijaranakula</i>	
Improvement of PIN Photodiodes on the SOI Layer by Rapid Thermal Annealing	731
<i>Yoshimaro Fujii, Akira Usami, Katsuhiko Fujiyoshi, Hideaki Yoshida, and Masaya Ichimura</i>	
Characterization of MOS Devices Fabricated on Carbon Implanted Silicon Substrates	737
<i>Ibrahim Ban, Mehmet C. Öztürk, Kim Christensen, and Dennis M. Maher</i>	
The Role of the Si-SiO₂ (CVD) Interface in Degradation Effects for High-Speed Bipolar Transistors	743
<i>J.-Q. Lü, S. Schöttl, E. Stefanov, F. Koch, R. Mahnkopf, and H. Klose</i>	
Influence of Dislocations on the I-V Characteristics of Silicon Solar Cells	749
<i>Robert Murphy, Bhushan L. Sopori, and Doug Rose</i>	
Effects of Light on the Resonant Tunneling in Silicon Quantum Dot Diode	757
<i>Chen Ding and Raphael Tsu</i>	

*Invited Paper

A Model for the Frequency Dependence of Charge Pumping Current in Polycrystalline Silicon Thin Film Transistor	761
<i>Ga-Won Lee, Jung-Yeal Lee, Deuk-Sung Choi, Sung-Hoi Hur, Choong-Ki Kim, and Chul-Hi Han</i>	
Analysis and Control of the Performance-Limiting Defects in HEM-Grown Silicon for Solar Cells	767
<i>Chandra P. Khattak, Frederick Schmid, Michael Cudzinovic, Martha Symko, and Bhushan L. Sopori</i>	
Resolving Degradation Mechanism in Carbon and Beryllium Doped HBT's Using Pulsed Mode Current Stress	777
<i>Y.C. Chou, G.P. Li, C.S. Wu, Peter Chu, C.K. Pao, and T.C. Cisco</i>	
Degradation of InGaAs High Electron Mobility Transistors: The Role of Channel Composition and Thickness	783
<i>Marjohn Meshkinpour, Mark S. Goorsky, Dwight C. Streit, Thomas R. Block, and Mike Wojtowicz</i>	
Improved Performance of MESFET Devices with L.T. GaAs Buffer Layers	789
<i>M. Lagadas, Z. Hatzopoulos, F. Karadima, G. Konstantinidis, N. Kornilios, C. Papavasiliou, and A. Christou</i>	
Defects and Impurities in Mercuric Iodide Processing	795
<i>J.M. Van Scyoc, R.B. James, T.E. Schlesinger, and T.S. Gilbert</i>	
Room Temperature Infrared Electroluminescence from Thin-Film Polycrystalline Chalcopyrite Cu(In,Ga)Se₂-Based Diodes	803
<i>Miguel A. Contreras, John Webb, Andrew Tennant, and Rommel Noufi</i>	

PART X: INTERFACES, QUANTUM WELLS AND SUPERLATTICES

*Electronic Properties of Ideal and Interface-Modified Metal-Semiconductor Contacts	811
<i>Winfried Mönch</i>	
Effect of RF Power on the Characteristic Parameters of W/n-GaAs Schottky Contacts Fabricated by RF Sputtering	823
<i>A. Singh, G. Aroca, and L. Velásquez</i>	
High Temperature I-V and C-V Characteristics of a Al/n-GaAs/In Schottky Barrier Type Device	829
<i>A. Singh and N. Marcano</i>	

*Invited Paper

Temperature Dependence of Metal-Semiconductor Contacts on 6H-SiC	835
<i>S.R. Smith, A.O. Evwaraye, and W.C. Mitchel</i>	
Surface Morphology Investigation of Au and Pt Electroless Contact on ZnCdTe Crystal by Atomic Force Microscopy	841
<i>Zhiyu Hu, Zhihua Hu, K.T. Chen, M.A. George, A. Burger, and W.E. Collins</i>	
Metastable Defect at Si-SiO₂ Interfaces	851
<i>Z. Jing, G. Lucovsky, and J.L. Whitten</i>	
Comparative Study of Experimental Techniques for Boron Profiling at Poly-Si/SiO₂ Interface	857
<i>M. Furttsch, J. Bevk, J. Bude, S.W. Downey, K.S. Krisch, N. Moriya, P.J. Silverman, and H.S. Luftman</i>	
Atomic Structure of the Interfaces Between Silicon Directly Bonded Wafers	863
<i>M. Benamara, A. Rocher, A. Laporte, G. Sarabayrouse, L. Lescouzères, A. PeyreLavigne, M. Fnaiech, and A. Claverie</i>	
Direct Wafer Bonding of Preamorphized Silicon Wafers	869
<i>A. Laporte, G. Sarabayrouse, M. Benamara, A. Claverie, A. Rocher, L. Lescouzères, and A. PeyreLavigne</i>	
Effect of Fermi Level Pinning at the Surface During OMVPE Growth	875
<i>R.M. Cohen, C.Y. Chen, W.M. Li, D.S. Simons, and P.H. Chi</i>	
Radiative Recombination Processes in Boron Modulation-Doped SiGe Quantum Wells	881
<i>I.A. Buyanova, W.M. Chen, A. Henry, W.X. Ni, G.V. Hansson, and B. Monemar</i>	
Introduction of Radiative Isoelectronic Complexes During Molecular Beam Epitaxial Growth of Si and Si_{1-x}Ge_x/Si Superlattices	887
<i>Karen L. Moore, Oliver King, Dennis G. Hall, Joze Bevk, and Matthias Furttsch</i>	
A Systematic Study of the Structural and Luminescence Properties of P-Type Porous Silicon	893
<i>H. Yoon and M.S. Goorsky</i>	
Space Charge Layers at the Porous Silicon Surface	899
<i>S.Z. Weisz, J. Avalos, M. Gomez, A. Many, Y. Goldstein, and E. Savir</i>	
Reversible and Irreversible Light-Induced Change of Photoluminescence in Porous Silicon	905
<i>Suk-Ho Choi and Byoung-Hun Mun</i>	

**PART XI: DEFECT PROPERTIES, REACTION,
ACTIVATION AND PASSIVATION**

*Chemistry of Point Defect in Silicon and its Applications in Semiconductor Technology	913
<i>S. Pizzini, S. Binetti, and M. Acciarri</i>	
*Bistability of Defects in Semiconductors	929
<i>Masashi Mizuta</i>	
Interaction Between EL5 and EL6 in Bulk GaAs	935
<i>Hiroyuki Shiraki, Yutaka Tokuda, and Koichi Sassa</i>	
The Kinetics of Capture and Emission of Discrete DX Related Centers in Silicon Doped AlGaAs Using Time Analyzed Transient Spectroscopy	941
<i>Sandeep Agarwal and Y.N. Mohapatra</i>	
DX-Like Centers in IV-VI	947
<i>Dmitriy R. Khokhlov</i>	
Low Temperature Anneal of the Divacancy in P-Type Silicon	953
<i>M.-A. Trauwaert, J. Vanhellemont, H.E. Maes, A.-M. Van Bavel, G. Langouche, A. Stesmans, and P. Clauws</i>	
Are the Models of the Triply Charged Gallium Vacancy and Doubly Charged Gallium Interstitial Alive or Dead?	959
<i>R.M. Cohen, C.Y. Chen, W.M. Li, D.S. Simons, and P.H. Chi</i>	
Some Peculiarities During Creation and Destruction of the Native Defects with the Negative Correlation Energy in Semiconductors	965
<i>Semyon D. Savransky</i>	
Classical and Rapid Thermal Process Effects on Oxygen and Carbon Precipitation in Silicon	971
<i>K. Mahfoud, M. Loghmarti, J.C. Muller, and P. Siffert</i>	
Studies of Defects in ZnO by Positron Annihilation	977
<i>Werner Puff, Sebastian Brunner, Peter Mascher, and Adam G. Balogh</i>	
Defect Reaction and Electrical Properties of Iron in n-Type Silicon	983
<i>Hajime Kitagawa and Shuji Tanaka</i>	
Modification of Recombination Activity of Dislocations in Si and SiGe by Contamination and Hydrogenation	989
<i>M. Kittler, W. Seifert, and V. Higgs</i>	

*Invited Paper

Recombination at Oxidation Induced Stacking Faults in Silicon	995
<i>J.A. Davidson, J.H. Evans, M. Vandini, and A.R. Peaker</i>	
Surface Passivation and the Ultrafast Optical Response of Low-Temperature-Grown GaAs	1001
<i>H.H. Wang, J.F. Whitaker, K. Al-Hemyari, and S.L. Williamson</i>	
Passivation Studies on AlGaAs Surfaces Suitable for High Power Laser Development	1007
<i>C. Edirisinghe, H.E. Ruda, I. Koutzarov, Q. Liu, L. Jedral, M.G. Boudreau, M. Boumerzoug, J. Brown, P. Mascher, A. Moore, and R. Henderson</i>	
Passivation of InGaAs/GaAs Vertical-Cavity Surface-Emitting Lasers by Amorphous GaAs Deposition	1013
<i>Hyo-Hoon Park, Byueng-Su Yoo, Min Soo Park, Jaejin Lee, Hae Gwon Lee, El-Hang Lee, Jae-Heon Shin, and Yong Hee Lee</i>	
Sulfidization in Alcoholic Solutions: A New Surface Passivation Method for GaAs	1019
<i>Vasily N. Bessolov, Andrew F. Ivankov, Elena V. Konenkova, and Mikhail V. Lebedev</i>	
Effects of Additive Elements on Electrical Properties of Tantalum Oxide Films	1025
<i>Hisayoshi Fujikawa and Yasunori Taga</i>	
Phase Separation of $\text{Si}_{1-x}\text{Ge}_x$ Alloys	1031
<i>Eunja Kim and Young Hee Lee</i>	
Incorporation of Hydrogen in SiO_2 and Si_3N_4 Thin Films Deposited by ECR-CVD	1037
<i>J. Brown, M. Boudreau, M. Boumerzoug, P. Mascher, T.E. Jackman, S.Y. Tong, and H. Haugen</i>	
Author Index	1043
Subject Index	1049

PREFACE

This volume results from a symposium held at the 1995 MRS Spring Meeting, April 17-21, in San Francisco. The symposium, bearing the title of this volume, followed upon a highly successful earlier symposium entitled "Defect Engineering in Semiconductor Growth, Processing and Device Technology," held at the 1992 MRS Spring Meeting. The intent of the present symposium was to go beyond defect control and explore deliberate introduction and manipulation of defects and impurities in order to engineer some desired properties in semiconductor materials and devices. The response from the academic and industrial research communities was overwhelming, with over 280 abstracts submitted from around the world. The theme of defect engineering has clearly come of age.

The organization of this proceedings volume closely follows the topics around which the sessions were built. After a broad plenary introduction by Professor Hans Queisser on "Order and Disorder in Semiconductors," the papers are grouped around ten distinct topics covering materials, processing and devices. The papers on grown-in defects in bulk crystals deal with overviews of intrinsic and impurity-related defects, their influence on electrical, optical and mechanical properties, as well as the use of impurities to arrest certain types of defects during growth and defects to control growth. In the case of epitaxial films, additional issues concerning stoichiometry and defects caused by plasmas and electron/ion irradiation are included. In view of the emerging interest in widegap semiconductors like GaN and SiC for blue light emitting devices and high-temperature electronics, a special session was devoted to this important topic.

Defect reaction processes pertaining to impurity gettering, precipitation and hydrogen passivation are specific examples of defect engineering that improve the electronic quality of the material. A large part of the symposium was devoted to these issues. A number of invited and contributed papers also dealt with characterization techniques needed to study and to identify these defects in materials and device structures.

The scope of defect and impurity engineering is far-ranging as exemplified by superlattice disordering phenomena, interface passivation and application of ion implantation, plasma treatment and rapid thermal processing for creating/activating/suppressing trap levels. All of these topics are addressed in this volume.

The symposium extended over the entire five days of the MRS meeting, with ten oral and two evening poster sessions. There were in all 17 invited talks, 75 contributed oral presentations and 130 posters. All the papers were peer-reviewed at the conference and revised as necessary. We are most grateful to the referees who often had to forego their evenings in San Francisco in order to perform this vital task in a timely manner. The quality of conference proceedings critically depends on this voluntary endeavor, in addition to the care exercised by the authors. Within the limitations of the publication deadline, every effort was made to minimize errors, but the reader is urged to bear with the inevitable shortcomings in the spirit of the symposium title!

S. Ashok
J. Chevallier
I. Akasaki
N.M. Johnson
B.L. Soporì

June 1995

ACKNOWLEDGMENTS

We would like to acknowledge the support received from the following sponsors:

Army Research Office
Balzers
DGA-DRET-DS France
Eastman Kodak
Fujitsu
Hughes Research Labs
Jobin-Yvon
Matsushita Electric
MEMC Electronic Materials
National Renewable Energy Laboratory
NEC
Nippondenso Company
Photowatt International
Riber
Shin-Etsu Handotai
Sumitomo Electric Industries
Toyota Central R & D
Wacker Chemitronic
Xerox Corporation

MATERIALS RESEARCH SOCIETY SYMPOSIUM PROCEEDINGS

- Volume 352—Materials Issues in Art and Archaeology IV, P.B. Vandiver, J.R. Druzik, J.L. Galvan Madrid, I.C. Freestone, G.S. Wheeler, 1995, ISBN: 1-55899-252-9
- Volume 353—Scientific Basis for Nuclear Waste Management XVIII, T. Murakami, R.C. Ewing, 1995, ISBN: 1-55899-253-7
- Volume 354—Beam-Solid Interactions for Materials Synthesis and Characterization, D.E. Luzzi, T.F. Heinz, M. Iwaki, D.C. Jacobson, 1995, ISBN: 1-55899-255-3
- Volume 355—Evolution of Thin-Film and Surface Structure and Morphology, B.G. Demczyk, E.D. Williams, E. Garfunkel, B.M. Clemens, J.E. Cuomo, 1995, ISBN: 1-55899-256-1
- Volume 356—Thin Films: Stresses and Mechanical Properties V, S.P. Baker, P. Børgesen, P.H. Townsend, C.A. Ross, C.A. Volkert, 1995, ISBN: 1-55899-257-X
- Volume 357—Structure and Properties of Interfaces in Ceramics, D.A. Bonnell, U. Chowdhry, M. Rühle, 1995, ISBN: 1-55899-258-8
- Volume 358—Microcrystalline and Nanocrystalline Semiconductors, R.W. Collins, C.C. Tsai, M. Hirose, F. Koch, L. Brus, 1995, ISBN: 1-55899-259-6
- Volume 359—Science and Technology of Fullerene Materials, P. Bernier, D.S. Bethune, L.Y. Chiang, T.W. Ebbesen, R.M. Metzger, J.W. Mintmire, 1995, ISBN: 1-55899-260-X
- Volume 360—Materials for Smart Systems, E.P. George, S. Takahashi, S. Trolier-McKinstry, K. Uchino, M. Wun-Fogle, 1995, ISBN: 1-55899-261-8
- Volume 361—Ferroelectric Thin Films IV, S.B. Desu, B.A. Tuttle, R. Ramesh, T. Shiosaki, 1995, ISBN: 1-55899-262-6
- Volume 362—Grain-Size and Mechanical Properties—Fundamentals and Applications, N.J. Grant, R.W. Armstrong, M.A. Otonari, T.N. Baker, K. Ishizaki, 1995, ISBN: 1-55899-263-4
- Volume 363—Chemical Vapor Deposition of Refractory Metals and Ceramics III, W.Y. Lee, B.M. Gallois, M.A. Pickering, 1995, ISBN: 1-55899-264-2
- Volume 364—High-Temperature Ordered Intermetallic Alloys VI, J. Horton, I. Baker, S. Hanada, R.D. Noebe, D. Schwartz, 1995, ISBN: 1-55899-265-0
- Volume 365—Ceramic Matrix Composites—Advanced High-Temperature Structural Materials, R.A. Lowden, J.R. Hellmann, M.K. Ferber, S.G. DiPietro, K.K. Chawla, 1995, ISBN: 1-55899-266-9
- Volume 366—Dynamics in Small Confining Systems II, J.M. Drake, S.M. Troian, J. Klafter, R. Kopelman, 1995, ISBN: 1-55899-267-7
- Volume 367—Fractal Aspects of Materials, F. Family, B. Sapoval, P. Meakin, R. Wool, 1995, ISBN: 1-55899-268-5
- Volume 368—Synthesis and Properties of Advanced Catalytic Materials, E. Iglesia, P. Lednor, D. Nagaki, L. Thompson, 1995, ISBN: 1-55899-270-7
- Volume 369—Solid State Ionics IV, G-A. Nazri, J-M. Tarascon, M. Schreiber, 1995, ISBN: 1-55899-271-5
- Volume 370—Microstructure of Cement Based Systems/Bonding and Interfaces in Cementitious Materials, S. Diamond, S. Mindess, F.P. Glasser, L.W. Roberts, J.P. Skalny, L.D. Wakeley, 1995, ISBN: 1-55899-272-3
- Volume 371—Advances in Porous Materials, S. Komarneni, D.M. Smith, J.S. Beck, 1995, ISBN: 1-55899-273-1
- Volume 372—Hollow and Solid Spheres and Microspheres—Science and Technology Associated with their Fabrication and Application, M. Berg, T. Bernat, D.L. Wilcox, Sr., J.K. Cochran, Jr., D. Kellerman, 1995, ISBN: 1-55899-274-X
- Volume 373—Microstructure of Irradiated Materials, I.M. Robertson, L.E. Rehn, S.J. Zinkle, W.J. Pythian, 1995, ISBN: 1-55899-275-8

MATERIALS RESEARCH SOCIETY SYMPOSIUM PROCEEDINGS

- Volume 374—Materials for Optical Limiting, R. Crane, K. Lewis, E.V. Stryland, M. Khoshnevisan, 1995, ISBN: 1-55899-276-6
- Volume 375—Applications of Synchrotron Radiation Techniques to Materials Science II, L.J. Terminello, N.D. Shinn, G.E. Ice, K.L. D'Amico, D.L. Perry, 1995, ISBN: 1-55899-277-4
- Volume 376—Neutron Scattering in Materials Science II, D.A. Neumann, T.P. Russell, B.J. Wuensch, 1995, ISBN: 1-55899-278-2
- Volume 377—Amorphous Silicon Technology—1995, M. Hack, E.A. Schiff, M. Powell, A. Matsuda, A. Madan, 1995, ISBN: 1-55899-280-4
- Volume 378—Defect- and Impurity-Engineered Semiconductors and Devices, S. Ashok, J. Chevallier, I. Akasaki, N.M. Johnson, B.L. Soporì, 1995, ISBN: 1-55899-281-2
- Volume 379—Strained Layer Epitaxy—Materials, Processing, and Device Applications, J. Bean, E. Fitzgerald, J. Hoyt, K-Y. Cheng, 1995, ISBN: 1-55899-282-0
- Volume 380—Materials—Fabrication and Patterning at the Nanoscale, C.R.K. Marrian, K. Kash, F. Cerrina, M. Lagally, 1995, ISBN: 1-55899-283-9
- Volume 381—Low-Dielectric Constant Materials—Synthesis and Applications in Microelectronics, T-M. Lu, S.P. Murarka, T.S. Kuan, C.H. Ting, 1995, ISBN: 1-55899-284-7
- Volume 382—Structure and Properties of Multilayered Thin Films, T.D. Nguyen, B.M. Lairson, B.M. Clemens, K. Sato, S-C. Shin, 1995, ISBN: 1-55899-285-5
- Volume 383—Mechanical Behavior of Diamond and Other Forms of Carbon, M.D. Drory, M.S. Donley, D. Bogy, J.E. Field, 1995, ISBN: 1-55899-286-3
- Volume 384—Magnetic Ultrathin Films, Multilayers and Surfaces, A. Fert, H. Fujimori, G. Guntherodt, B. Heinrich, W.F. Egelhoff, Jr., E.E. Marinero, R.L. White, 1995, ISBN: 1-55899-287-1
- Volume 385—Polymer/Inorganic Interfaces II, L. Drzal, N.A. Peppas, R.L. Opila, C. Schutte, 1995, ISBN: 1-55899-288-X
- Volume 386—Ultraclean Semiconductor Processing Technology and Surface Chemical Cleaning and Passivation, M. Liehr, M. Hirose, M. Heyns, H. Parks, 1995, ISBN: 1-55899-289-8
- Volume 387—Rapid Thermal and Integrated Processing IV, J.C. Sturm, J.C. Gelpy, S.R.J. Brueck, A. Kermani, J.L. Regolini, 1995, ISBN: 1-55899-290-1
- Volume 388—Film Synthesis and Growth Using Energetic Beams, H.A. Atwater, J.T. Dickinson, D.H. Lowndes, A. Polman, 1995, ISBN: 1-55899-291-X
- Volume 389—Modeling and Simulation of Thin-Film Processing, C.A. Volkert, R.J. Kee, D.J. Srolovitz, M.J. Fluss, 1995, ISBN: 1-55899-292-8
- Volume 390—Electronic Packaging Materials Science VIII, R.C. Sundahl, K.A. Jackson, K-N. Tu, P. Børgesen, 1995, ISBN: 1-55899-293-6
- Volume 391—Materials Reliability in Microelectronics V, A.S. Oates, K. Gadepally, R. Rosenberg, W.F. Filter, L. Greer, 1995, ISBN: 1-55899-294-4
- Volume 392—Thin Films for Integrated Optics Applications, B.W. Wessels, D.M. Walba, 1995, ISBN: 1-55899-295-2
- Volume 393—Materials for Electrochemical Energy Storage and Conversion—Batteries, Capacitors and Fuel Cells, D.H. Doughty, B. Vyas, J.R. Huff, T. Takamura, 1995, ISBN: 1-55899-296-0
- Volume 394—Polymers in Medicine and Pharmacy, A.G. Mikos, K.W. Leong, M.L. Radomsky, J.A. Tamada, M.J. Yaszemski, 1995, ISBN: 1-55899-297-9

Prior Materials Research Society Symposium Proceedings available by contacting Materials Research Society

Part I
Plenary Review

ORDER AND DISORDER IN SEMICONDUCTORS

HANS J. QUEISSER

Max-Planck-Institut für Festkörperforschung, Heisenbergst. 1, D-70569 Stuttgart, Germany

ABSTRACT

The astounding success of microelectronics rests on a simple materials principle : creating a highly purified and perfected , spatially ordered semiconductor matrix , whose electrical and optical properties may be selectively adjusted by local substitutions of host atoms by dopant atoms. This unique materials utilization differs remarkably from all earlier technologies , because the controlled , almost imperceptibly small disorder by doping (rather than the ordered host) dominates the relevant properties ! Defect control is thus a major concern for semiconductor technology. Homogeneity is an absolute necessity for this strategy, but only a few of the semiconductors can be made so homogeneous as to suppress the strong deleterious effects of inhomogeneity. Recent advances are summarized : atomic resolution of defect analyses, multiatom reactions and hope for applications, contactless measurements, gettering as well as detailed theory of simulations. The emergence of novel quantum devices, with both reduced dimensions and reduced dimensionalities heralds a paradigm change, since the quantizing small geometries exert stronger influences than defects do; nevertheless, materials perfection and interface control remain prerequisites for these structures.

INTRODUCTION

The pervasive impetus of modern semiconductor technology has become an accepted fact. Scientific mastering of materials and processes has increased tremendously within a rather short time frame. Technological control has been derived from this scientific base, and an industry with more than \$ 100 billions worth of silicon devices per annum- in 1994- and still almost incredibly high growth rates of production and applications is an economic reality as well as a matter of international industrial policy. The materials aspect of using perfected single crystals and applying local doping-control provide the basis of this unusual success. Earlier usage of materials differed remarkably. Bronze or steel are used for their specific bulk properties, the shaping and connecting of pieces is at the heart of iron-age or bronze-age technologies. Integration inside a regular spatial array of a host crystal is the semiconductor principle. The "Royal Road" to modern microelectronics consists in initially procuring a perfected single-crystal host, then locally establishing electrical and optical properties inside the host by specific replacements of host atoms by foreign "dopants". The somewhat disparaging expression of *defect* as a generic term for all deviations from the host perfection does not really convey the power of this "doping doctrine" for semiconducting materials. The early pioneers of germanium and silicon, however, placed great emphasis on the experimental verification that *n*-type and *p*-type doping by elements of the adjacent columns in the periodic table were accompanied by changes in the lattice parameter : atomic substitution of the host atoms as the guiding principle ! [1,2]

This keynote speech shall attempt to offer a few recent examples of ongoing research to illustrate the power of defect utilization and the degree of sophistication that has been achieved .

A warning is further uttered here, since this principle of doping by replacement can only be safely practiced for well-controlled, homogeneous materials - of which we still have only few semiconductors. Uncritical transfer of this principle to inhomogeneous materials does not guarantee success. Inhomogeneous materials derive many of their electronic properties *not* from the substituted point-defects but from the capricious details of the inhomogeneity itself. A similar situation arises in the current quests for novel quantum devices, where geometry plays an overriding role in establishing energy levels, densities of electronic states, or other electronic properties, thus diminishing the influence of substituents. Dimension-controlled quantum device structures, however, also command highly perfected base materials !

Dopant atoms, their interactions with native defects and their diffusion properties are exemplified first. Multiatomic defects, presently of vivid interest, and their stabilities are touched upon next. The topic of gettering, still of irreplaceable technical significance, is mentioned subsequently. The themes of inhomogeneity and quantum structures conclude this article.

CURRENT RESEARCH TOPICS

Dopants, Their Interactions and Diffusion

The diffusion of a simple trivalent acceptor or pentavalent donor in a silicon host still constitutes an essential element of device processing for bipolar and even for unipolar devices. An amazing degree of empirical knowledge rules these processes until today, because the atomistic details of diffusion -even for these simplest substitute atoms - are in reality very complex. A multitude of dopant-interactions with native defects, especially vacancies and interstitialcies, govern the diffusion processes and thus determine the technologically so vital properties, such as depth of a junction, space charge widths, or channel properties. Diffusion of the donor phosphorous near an interface SiO_2 / Si provides a good example. The solubility of P in the oxide is lower than in silicon itself, therefore one expects a pile-up of P atoms in the Si near an interface to the oxide, well known from the pioneering work by Grove [3]. Yet, no really satisfying model simulation with reliable, predictive power was available for a long time. Lau and his colleagues [4] at the Siemens Laboratories then proposed a new model, which included a third phase, sandwiched in between oxide and elemental silicon. This hypothetical interface phase was assumed to provide ample amounts of sites for phosphorous atoms; such P atoms are then assumed to become electrically inactive, which is an easily acceptable proposition since the direct substitution inside a regular lattice no longer prevails. Lau *et al.* then proceeded to simulate diffusion conditions with a set of rate equations and found good agreement with experimental data. One single curve was presented to fit data for different P concentrations, a variety of temperatures and diffusion ambients, including inert anneals.[4] Diffusion process technology was thus satisfactorily explained with the appropriate parameters inserted, all based upon the *ad hoc* assumption of an intermediate phase.

Experimental verification of the postulated intermediate region was difficult because of the different forms of incorporated P. A chemical analysis, such as by secondary-ion-mass-spectroscopy, gives the total amount of phosphorous atoms. The electrically active, substitutional atoms, however, are the ones determining device characteristics; their amount may be almost one order of magnitude lower than the total. Nicollian and Chatterjee [5] have just recently provided such proof, thus explained the almost paradoxically appearing observation of

an increasing P concentration from the interface toward the silicon interior. Figure 1 shows the results obtained in the fit with the model; the profile parameters are adjusted toward best fit, also a diffusion length ($0.95\mu\text{m}$) is a result of such fit. This recent example of work pertaining to a seemingly very simple phenomenon, on which much of modern device technology has to rely, demonstrates first the inherent complexity and secondly the methodology of high-resolution characterization combined with detailed mathematical simulation in a multi-parameter space.

Impurities at Internal Interfaces

Evidence for such a novel intermediate phase with special properties has very recently [6] been obtained in a rather different experiment. Grain-boundaries were investigated in silicon crystals with the oxygen content typical for crucible-grown Si material, as is utilized in modern MOS-technology. The precipitation of this deliberately introduced foreign atom is a very important part of the gettering technology to remove unwanted impurity atoms. Very-high-resolution transmission electron microscopy revealed beautiful examples of amorphous Si-O phases, nucleated directly at the grain boundary. The border between precipitate and host matrix was always found to be a well-defined crystallographic (111)-type plane. However, Gatts *et al.* [6] attempted an analysis of yet higher resolution by means of neural-pattern-recognition methods for the obtained electron-energy-loss spectra. The result of this novel type of nonsubjective analysis by neural-network-technique was an existence proof for a new phase of a different chemical environment, again as sandwiched between crystalline Si and amorphous oxide.

This recent example of modern transmission electron microscopy in conjunction with refined mathematical analysis and simulation furnishes impressive proof for the power of present-day tools and the degree of sophistication: resolution and image-handling!

Another piece of evidence arose from Ref. [6], which corroborated very old results of my own [7], regarding grain boundaries, their structure and electrical properties. A naive model views a

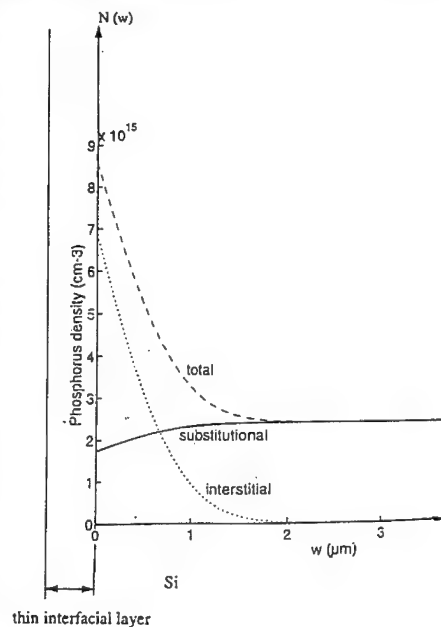


Fig. 1 Profiles of various species of P dopants in silicon near an oxide interface, see Refs. [4, 5]

grain boundary as a regular array of individual dislocations, which in turn supply electrically active sites -due to dangling bonds- along the dislocation line. A grain boundary (and even one single dislocation) should therefore be a strong electronic perturbation as a recombination, possibly even a doping, site. This simple picture is, fortunately for device technology, incorrect. It is much more the combined effect of boundary plus its impurity atmosphere, which affects the electronic properties. Measurements of the photovoltage arising at grain boundaries showed that the sign and the magnitude of such photo-signals could be massively altered by heat treatments, which are known to cause different phases of the oxygen impurities in Si. This old

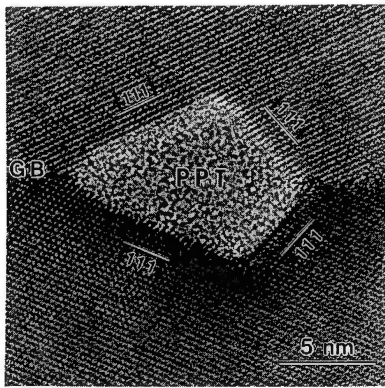


Fig.2 Electron micrograph of grain boundary in Si with oxide precipitate. Ref.[6]

proposition of 1962 [7] was a strong deviation from the simple reductionist tenet of ascribing electronic behavior exclusively to point-like defects in the semiconductor lattice. Dislocations are defects contributing intensely to formation of many types of inhomogeneities. Remarkable efforts were exerted very early in semiconductor history to completely eliminate dislocations-for rather different reasons-in silicon, thus establishing a very homogeneous base material of ever increasing wafer diameter, soon to reach 300 mm !

Dopants and Native Defects

The elementary step for a diffusing impurity or dopant is the jump to a new site, which may be a substitutional or an interstitial site. Availability of vacancies or of interstitials therefore quite strongly affect jump probabilities. Any local nonequilibrium of these native defects thus severely affects the diffusion constant. This dependence plus the varieties of diffusion mechanisms greatly complicated the quantitative understanding of diffusion, even until today. Earliest evidence, for example in the growth kinetics of oxidation-induced stacking faults [8,9] or the very puzzling and disturbing phenomenon of the *emitter push effect*, harmful for small base widths in bipolar devices, indicated already that changes in the native defect densities had very serious consequences. This situation has been greatly improved during the last decade; we now have much better insights. For example, at least a semi-quantitative knowledge exists about the excess of interstitials being generated by oxidation of a surface, as compared to a nitridation. Technologies are being developed to not merely control dopant quantities, but also to get native defects under control. [10]. Such control is -once again-most urgently needed around the gates and channels of MOS silicon devices. Control of geometry and dopant is a strict necessity. A judicious choice of mixing of oxides and nitrides has been shown [10] to offer just the desired amounts of native defects to achieve specific channel conditions. Such advances indicate the sophistication reached in coupling control of vacancies and interstitials with those of the dopants themselves. A stacking fault grows and shrinks with fluxes of vacancies and interstitials, therefore one can actually utilize [11] such stacking faults as (almost quantitative) detectors for native defects ! Lateral and vertical distributions of Si interstitials have been monitored in this fashion in wafer-bonded samples; the interstitials were injected by dry oxidation.

Another example involves the non-doping group IV-element carbon and its influence on the diffusion of the common substitutional acceptor boron in silicon. Stolk and colleagues [12] incorporated C into B-doped Si and implanted Si excess self-interstitials by ion beam techniques. Carbon was shown to completely suppress the interstitialcy-enhanced boron diffusion; the substitutional carbon hence traps and deactivates the interstitials in crystalline Si. The diffusion processes thus become more scientifically scrutinized, which is an absolute necessity for today's submicron device design lengths. Dopant impurity diffusion processes must be meticulously controlled, which includes guiding of the native host-defects, too.

Limits of the Doping Doctrine

The elemental semiconductors and their substitutional dopants, such as B or P, represent an unusually favorable case. Within wide ranges, both *n*-type and *p*-type doping are here possible. In almost all other cases for host and guest atoms, the situation is not nearly as auspicious. Rare earth atoms, for example, are very difficult to incorporate into silicon or gallium arsenide [13]. Their valence mismatch reduces their solubility; electrical pumping of the efficient luminescence is not easily feasible; the active f-shell is well screened by outer electrons. A marriage of the rare-earth doped luminescing oxides with the convenient semiconductors remains a predicament.

A similar difficulty arises for the more ionic semiconductors of the type $A^{\text{II}} - B^{\text{VI}}$, whose larger bandgaps and stronger tendencies for radiative recombination are most attractive for optoelectronic applications. Doping is, however, exceedingly more difficult than for the elements. This deplorable situation is still not understood, even less so is it under technological control. [14] There is possibly not one single, dominant physical or chemical reason for this dopability problem. Self-compensation is one assumption; the crystal lowers its total energy under a doping attempt by creating native defects, which are much more strongly charged in these ionic compounds than in Si or Ge. This self-compensation brings the Fermi level back to a position closer to the middle of the forbidden gap. This plausible principle does not, however, apply generally. In other examples, it seems to be just the low solubility which makes doping almost impossible. [15]. The remarkable progress in lasers based on Zn-containing $A^{\text{II}} - B^{\text{VI}}$ materials is founded on rather clever ways of circumventing these basic problems. [16] Not surprising is the prediction that our central theme "order-disorder in semiconductors" will be attacked very strongly for these compounds in the near future. It will, however, be interesting to see how far the analogs and patterns of the elemental semiconductors will carry us. There exist strong differences: high-dislocation-densities, for example, are quite common in light-emitting diodes, based on gallium nitride. [17] Densities exceeding 10^{20} cm^{-2} were found to be common in GaN, yet all minority-carrier properties were much less affected than in Si, GaP or related materials! In this compound GaN, therefore, nonradiative recombination is much less enhanced by dislocations, possibly because of the more ionic nature of the bonding [17] or, maybe, because of different tendencies of precipitation around dislocation cores?

Compensation by inadvertent presence of the opposite type of dopant is a serious and often conveniently ignored problem. [18]. For most technical applications, however, compensation is not a serious problem, although it represents a degradation of crystalline perfection by incorporating too many impurity atoms per desired function. Minority carriers will therefore suffer a reduction of their lifetimes. The most noticeable effect of compensating impurities, say donors in a *p*-type crystal, is the rather sharp reduction of the mobility μ at low enough temperatures,

where scattering at ionized impurities [19] is the dominating mechanism for the mobility. In Si, this regime is almost impossible to reach for device conditions, whereas for GaAs and related compounds, compensation is more influential. All these considerations show the unusually favorable physics and chemistry for silicon with its precious facility for doping. The integrity of the oxide SiO_2 and the dopabilities make Si the preferred semiconductor material.

Multiatomic Centers

A semiconductor crystal represents a solvent, in which multitudes of chemical reactions may occur, very similar to the well-known paradigms in aqueous solution. Defects with opposing charges, for example, may associate and dissociate akin to a salt in water. One of the best known examples for Si are the pairs of iron atoms with all the acceptors, such as FeGa. The reaction kinetics can be determined, energies of dissociation are measurable [20], just as in the familiar textbook knowledge concerning charged ions dissolved in water.

By far the most intensely studied biatomic centers in Si were recently those containing hydrogen as one of the partners.[21] Defects can easily be neutralized, thus rendered passive by the admixing of hydrogen. One recent example for these investigations is the work by Cheng and Stavola [22]. They studied the reorientation of BH and BD complexes and found evidence for a

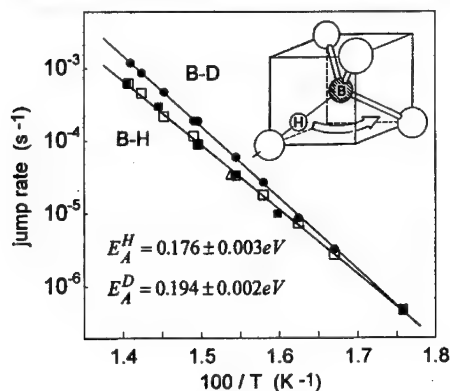


Fig.3 Tunnel rates of H and D in pairs with boron, from Ref. [22]

thermally assisted tunneling. Figure 3 gives a result. The jump rates are plotted for the tunneling between two different bond-centered sites, as indicated by the arrow in the inset. These centers were initially oriented by the application of mechanical stress and then allowed to relax. Tunneling was inferred from the non-Arrhenius behavior. Notice from the figure that the deuterated sample is the one with quicker rates, at least for the temperatures shown! Bonding and release make diffusion of H in Si and in other semiconductors a difficult problem and a highly complicated affair. Hydrogen is, however, ubiquitous, not only in wet chemical processes. [42]

Multiatomic centers are in many cases multistable defects, such as indicated by Fig.3. They may assume different positions, for example with respect to hydrogen relative to the boron atom. One could imagine bistable centers, where the two possible configurations are more distinctly different from each other as in the BH case, for example via a difference in the interatomic distance. Such centers with strongly differing arrangements offer some hope for a utilization in memory storage. The two configurations might represent a one and a zero, they might be switched by externally applied signals and might be susceptible to read-out. Such an application would yield a very small and -hopefully- simple means of data storage in Si. However, the difficulties seem formidable. At present, observable bistability is limited to low temperatures, and the addressing seems problematical for optical access, let alone for an electrical input and

output. This topic of atomic-size data storage is, however, such a fascinating proposition that more effort and research seem probable for the future.

The Indispensable Art of Gettering

Vacuum tubes had to rely on *gettering* the residual gases by means of a pill of a reactive metal to bind oxygen and nitrogen. This practical act out of desperation has been carried over to standard silicon device technology. Inadvertent and unavoidable metallic impurities must somehow be eliminated from the (relatively small) regions of active device relevance and ought to be firmly fixed in some passive region. No *hard p-n* junction, i.e. one with a sharp reverse I-V curve, was feasible, at least in the earlier history of bipolar devices, without such a gettering step, which removed the metallic generation centers from the junction's space charge layer.[23] Metallic impurities, often from the furnaces or implantation equipment, are still very difficult - and expensive - to remove by any other technique than by some gettering. The sinks for these metal atoms can be manifold: glassy surface layers, dislocations or even more robust, cruelly introduced lattice damage on the wafer-backside,[24] and -most importantly- the convenient oxide precipitates. Such gettering seems to apply quite universally for most metallic impurities [25]. The local change in the metal-solubility must be sufficient to capture the yield-diminishing culprit, and the diffusivity of the metal must suffice in order to reach the sink. These conditions can usually be met quite easily, and the needed process step can in most cases be inserted into the device processing sequence without great problems. Still, the details of the gettering kinetics and the interactions, especially with the native defects, are quite complex. Gettering is in principle a reversible process[26]; care must be taken to avoid re-dissolution. The smaller dimensions of future Si devices will here require more of a scientific basis; supportive research will be needed. Such research will, however, have to be based on a very close interaction between researchers in fundamental materials science and device production-line practitioners.

Pernicious Inhomogeneities

The powerful dogma of point-defects inducing semiconductor properties relies on a uniform, homogeneous crystal base. As soon as inhomogeneity of any sort creeps into the matrix, our principles begin to fail. Compensation by minority dopants or the deleterious, ill-defined influence of dislocations or two-dimensional defects, such as stacking faults or boundaries, even surfaces, have already been mentioned here. The basic theory of inhomogeneous materials and a discussion on their foundations upon quantum theory and thermodynamics have been outlined by Pantelides [27]. Detailed mathematical treatment of transport and other electronic properties in inhomogeneous semiconductors has been given by Pistoulet and his students [28]. The situation is demonstrated to quickly become intractable; general conclusions are very difficult to be formulated. Inhomogeneities have one major deleterious consequence: local potential fluctuations haphazardly arise! Transport is therefore randomly affected, which is a serious competition against the willful, designed external potentials, such as on a field-effect gate, to control electronic current flow. The function of a device, especially one of small geometric dimensions, is lost. The concept of doping as the source of electronic behavior breaks down.

One particularly forceful example of this breakdown is established by the maverick phenomenon of *persistent conductivity*. Many semiconductor samples of questionable homogeneity and ill-defined doping display a persisting conductivity *after* a photoconductivity-inducing illumina-

tion has been switched off.[29] Such a sample appears to have some sort of barrier against recombination, thus artificially prolonged lifetimes [30]. Such effects have long been known and have been associated -in most cases- with a lack of homogeneity.[29] For example, in a semiconductor with clusters of radiation-induced defects, space charges arise, as indicated schematically in Fig. 4.[28-31]. Upon illumination, one type of carriers is trapped at these radiation-induced defects, the other type is mobile to conduct current, which prevails even after illumination ceases. The cluster thus separates localized from delocalized carriers, very much like a gate. Any potential fluctuation fulfills this function, just like a junction does in a solar cell, separating electrons from holes. Persistence had therefore initially been taken as evidence for all kinds of non-uniformities [31].

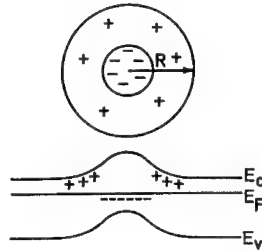


Fig. 4. Schematic of a carrier-separating fluctuation, Refs. [30,31]

This generally accepted, but not much recognized viewpoint underwent a complete change with the detection of specific multiatomic centers in the compound semiconductors, especially gallium arsenide. The so-called DX-center, a donor with a then unknown second partner was interpreted [32] as being bistable and being the source of the excess electrons persisting after illumination. The doping-doctrine was here successful once again. Atomic-size defects were linked to an unusual conduction property: the liberated electrons are unable to recombine with their source defects since they cannot overcome a configurational barrier at low temperatures. Individual defects in an orderly semiconductor had now found another significant property, aside from doping or lifetime-dominating recombination. This success in GaAs was swiftly carried over to many other materials, which were of much lesser homogeneity than GaAs. Suddenly, any observation of persistent photoconductivity was ennobled as an indicator of a most interesting defect, usually associated with strong lattice-interactions, rather than being an embarrassing stigma of inhomogeneity[30] Yet, the fact remains that any type of potential fluctuation will generate persistence under quite general experimental conditions. Our own work on GaAs epitaxial layers of high perfection has demonstrated this principle of spatial carrier separation [33-35], with one type of carriers trapped, the other being free to carry a current. The accumulation of carriers is quantitatively explained with this idea [34]. A specially made GaAs sample with two differing trap densities demonstrates two different slopes in a curve of current *versus* photon dose, which is a rather convincing proof [30,35]. see Fig. 5 We always warn against too easily interpreting such persistence phenomena with some multistable, special defect. The first, rather prosaic and admittedly discomfiting duty has to be a thorough check against potential fluctuations. Let me reiterate the message that the doping doctrine must be based on homogeneity !

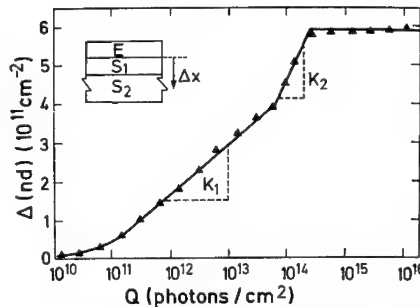


Fig. 5 Dose-dependence of persistence in a two-layer trap configuration Ref. [35]

Any deviation from the pristine concept of simple doping in an elemental semiconductor will cause problems. The step from an element to a compound semiconductor, or yet to one of those nice, useful compound alloys will complicate matters by opening many avenues toward inhomogeneities, such as being caused by alloy fluctuations, by doping clustering, by occupancy changes of amphoteric dopants (atoms acting as donors or acceptors, depending what type of atom they substitute). The more ionic the material, the greater will in general be the danger, because of the stronger local potential change per deviation from lattice ideality. The *antisite defect*, arising from a simple interchange of, say, the cationic partner with its anionic counterpart, is a serious imbalance in a compound, but does not exist -by definition- in an elemental semiconductor.

Materials Principles for Quantum Devices

Semiconductor technology with its masterful craftsmanship in lithography, etching, contact-forming and other artistry has opened broad avenues of novel device physics based upon the very foundations of quantum mechanics. Schrödinger's concepts of the quantized energies of an electron incarcerated in a small potential box have been beautifully demonstrated by many experiments in semiconductors with fine dimensional control. The concept of heterojunctions has been the essential idea of producing definite carrier-confining regions inside a crystal host.

The new regime of quantum-wells, quantum wires, and dots [36] really differs from the conventional, semiclassically tractable semiconductor device technology. It is now the reduced dimension (small size, comparable to wave function extents) as well as the reduced dimensionalities (1-dimensional, e.g. in a quantum-wire) which control the properties and the device operation. The materials parameters begin to fade into oblivion; size dominates over matter. Such important device parameters, as the carrier mobility for example, also lose their significance, because much of the transport is now ballistic in nature. The small dimensions enable the electrons to permeate the essential paths without ever encountering a scattering event, hence no longer being adequately described by the concept of mobility. Materials tend to become very similar to each other, it is more and more just the fundamental constants -such as Planck's h or the electronic charge e - which govern the elementary electronic processes

This new principle, with the crystal lattice merely becoming a miniature vessel for quantized particles, apparently slackens the previously so stringent demands upon the electronic materials. Yet, this appearance is not really correct. The essential semiconductor principle of initially securing a highly perfected host lattice still remains! Certain demands upon the perfection of the materials even seem to increase. For example, the validity and reproducibility of any device based upon quantum wells rest very heavily on the uniformity of such wells, especially the constancy of the width of the quantum well, which is sandwiched in between two barrier layers of a related material with a higher bandgap. Even small deviations, of the order of just one lattice parameter, now cause grave deviations - which certainly was not noticeable in our standard semiconductors of today. One of the most serious defects is therefore now the step in an interface plane. The quest for atomically flat surfaces and interfaces [37] will hence become a more serious task for scientists and engineers, who will have to concentrate on the elementary facts of growing a solid crystal out of a vapor- or liquid-phase. In general, however, the high standards of first securing a chemically and physically perfected matrix will *not* be lowered. [38]

The mesoscopic regime, intermediate between current technology and pure quantum-control

poses an even more difficult technological requirement. In this transition regime, the merciful statistical averaging -important in today's transistors - no longer prevails. On the other hand, the rigidity and constancy of the quantum regime is not yet reached. However, all fluctuations, such as by a random distribution of charged defects and their random, fluctuating charge state strongly influence all transport properties, say in a typical field-effect channel [39]. The resulting fluctuations appear like noise, yet they are often reproducible and deterministic. Any reliable mode of operation for devices in this difficult mesoscopic regime hence would require a very tight control of all charged impurities, among other tight tolerances. Defects thus are not simply overruled, they assume a different role, maybe altogether a much more difficult one.

CONCLUSIONS

Defects are the spices in an otherwise bland materials perfection. They provide the elements of electronic behavior, they enable us to precisely locate the electronic action, they allow us to make exceedingly small functional spaces within the lattice. Defects seem to be an ever growing family of individuals, the more demanding the specifications and thus the more precise the observations become for all those many possible deviations from strict translational symmetry.[40]

This review could only present some exemplary cases. Most of these cases were quoted for the most important material, silicon. This prototype material represents the leading ideal for all those other, more specialized competing semiconductor materials. Silicon will also, I am convinced, baptize our present era of modern information technology. I tried to convince the somewhat reluctant, conservative and timid European society that we are leaving the iron age, just as we had overcome the stone age, the bronze age - and that the world is entering the new age of silicon, where integration of functions into atomic rasters replaces the assembly of bulk parts. [41] I attempted to strengthen my case by counting the number of research papers on this unique material silicon -exponentially, frighteningly, indefatigably increasing - and matching those numbers against others, for iron or for water. Simon Sze joined me in this drumming for support and understanding. The more information we have gathered, the more further details we want to obtain and understand. A recent MRS laureate, David Eaglesham [43], has taken the courage to ask the otherwise usually avoided question of what we do *not* know about this so meticulously investigated stuff. He points out that much is still left to be done, and almost all of his points refer to better knowledge concerning defects ! This fact is, of course, not surprising since the ideal lattice is like the vacuum in modern field theory physics: you know it, thereafter you renormalize it away. Remain the excitations of this vacuum state that are the objects of interest and usage. Order in the clean, regular lattice is the prerequisite, disorder is the useful element of creation.

Several years ago, much fanfare and future were proclaimed for the supposedly so much simpler and by far cheaper amorphous semiconductors. Just an easy evaporation was deemed necessary for providing the materials, no crystal-pulling, no sawing, no polishing were required. Yet, the breakthrough did not occur; at most for some large-area applications is there usage for the non-crystalline semiconductors. The cost for procuring a highly perfected single-crystal material is high in absolute numbers, but represents an insignificant portion of the cost of making those densely configured, sophisticated circuits. Device miniaturisation and single-crystal matrix, this dopable spatial array, are inseparably linked to each other.

ACKNOWLEDGMENTS

I thank many colleagues and friends for suggestions, literature and advice. Special gratitude is due to Elisabeth Bauser, Jörg Weber, Jürgen Werner, Werner Frank, Gerd Düscher, and Manfred Rühle here at the Max-Planck-Institutes in Stuttgart, where growing of perfect crystals is as much a challenge as is the gentle introduction and keen observation of all kinds of defects. I acknowledge gratefully the invitation for this keynote address in San Francisco, *The City*, so close to where I learned my trade in silicon in an apricot barn in Mountain View, and where we dared to hope in the early Sixties that our Santa Clara Valley would sometime be called after that unique element from the fourth column of the periodic table - and the hope materialized! I was so fortunate to experience the birth and growth of a new era, and I want to express my sincere gratitude to the many friends, especially in the United States, with whom I had the privilege to share the adventurous voyage along this road of materials science.

REFERENCES

1. W.Shockley, Electrons and Holes in Semiconductors, (van Nostrand, Princeton, 1950), still a remarkable source, see esp. Chapter 1
2. B.G.Cohen, Sol.St.Electron. **10**,33 (1967), also: G.L.Pearson and J.Bardeen, Phys.Rev. **75**, 865 (1949), proof of substitutional position of the dominant dopants
3. A.Grove, O.Leistiko, and C.T.Sah, J.Appl.Phys. **35**, 2695 (1964)
4. L. Lau, L.Mader, C.Mazure, C.Werner, and M.Orlowski, Appl.Phys. **A49**, 671, (1989)
5. Edward H.Nicollian and Ajay Chatterjee, J.Electrochem.Soc. **141**, 3580 (1994)
6. C.Gatts, G.Düscher, H.Müllejans, and M.Rühle (private commun., to be publ. 1995)
7. H.J.Queisser, J.Phys.Soc.Jpn. **18**, Suppl. III, 142 (1963)
8. H.J.Queisser, R.H.Finch, and J.Washburn, J.Appl.Phys. **33**, 1536 (1962). This collaboration between UC Berkeley and Shockley Transistor Corp. identified the oxidation-induced stacking faults by the very first transmission electron microscopy on Si defects
9. For a review, see H.J.Queisser, in Defects in Semiconductors II, S.Mahajan and J.W.Corbett, editors, MRS Symposia, Vol. **14**, p.323 (1983)
10. P.G.Y. Tsui *et al.*, Paper 19.5.1 at Int.Electron Dev.Conf. San Francisco, 1995, (to be published)
11. D.Tsoukalas and C.Tsamis, Appl. Phys. Lett. **66**, 971 (1995)
12. P.A.Stolk, D.J.Eaglesham, H.-J. Gossmann, and J.M.Poate, Appl.Phys. Lett. **66**, 1370 (1995)
13. C.Delerue and M.Lannoo, Mat.Sci. Forum **143-147**, 699 (1994)
14. H.Kukimoto, Mat.Sci.Forum **143-147**, 385 (1994)
15. T.A.Kennedy, E.R.Glaser, B.N.Murdin, C.R.Pidgeon, K.A.Prior, and B.C. Cavenett, Appl.Phys. Lett. **65**, 1112 (1994)
16. S.Tomiya, E.Morita, M.Ukita, S.Itoh, K.Nakano, and A.Ishibashi, Appl. Phys. Lett. **66**, 1208 (1995)
17. S.D.Lester, F.A.Ponce, M.G.Crawford, and D.A.Steigerwald, Appl. Phys. Lett. **66**, 1249 (1995)
18. H.J.Queisser, in Proc.Int.Conf. Phys.Techn.Compensated Semicond. (Madras, 1985), B. Gopalam, editor, p.1

19. D.C.Chattopadhyay and H.J.Queisser, *Revs.Mod.Phys.* **53**, 745 (1981)
20. K.Graff and H.Pieper, *J.Electrochem.Soc.* **128**, 669 (1981) and Ref.[25],Ch.44.1
21. M.Stutzmann and T.L.Estle, editors, Hydrogen in Semiconductors, (Elsevier, Amsterdam 1991)
22. Y.M.Cheng and M.Stavola, *Phys. Rev.Lett.* **73**, 3419 (1994)
23. A.Goetzberger and W.Shockley, *J.Appl. Phys.* **31**, 1821 (1960), also Ref.[25]
24. D.M.Lee and G.A.Rozgonyi, *Appl.Phys. Lett.* **65**, 350 (1994)
25. K. Graff, Metallic Impurities in Silicon-Device Fabrication, (Springer, Heidelberg, New York, 1995) This recent book lists the most important metallic impurities in Si, gives numerical parameters for these impurities and offers recipes for etches and means of defect observations.
26. E.Ö.Sveinbjörnsson, O.Engström, and U.Södervall, *J.Appl.Phys.* **73**, 7311 (1993)
27. S.T.Pantelides, *J.Appl.Phys.* **75**, 3264 (1994)
28. B.Pistoulet, F.M.Roche, and S.Abdalla, *Phys. Rev.* **B 30**, 5987 (1984)
29. M.K.Sheinkman and Y.Ya. Shik, *Fiz. Tekh.Poluprovodn.* **10**, 209 (1976)
30. H.J.Queisser, *Annu.Reviews Mater.Sci.* **22**, 1 (1992)
31. B.L.Gregory, *Appl. Phys. Lett.* **16**, 67 (1970)
32. D.V.Lang, R.A.Logan, and M.Jaros, *Phys.Rev.* **B19**, 1015 (1979)
33. H.J.Queisser, *Phys. Rev.Lett.* **54**, 234 (1985), also Refs.[29,30]
34. H.J.Queisser and D.E.Theodorou, *Phys.Rev.Lett.* **43**, 401 (1979); for a very recent application towards measuring metal-insulator transitions, see: M. Smith, J.Y. Lin, and H.X.Jiang, *Phys.Rev.* **B51**, 4132 (1995)
35. D.E.Theodorou, H.J.Queisser, and E.Bauser, *Appl. Phys. Lett.* **41**, 628 (1982)
36. W.P.Kirk and M.A.Reed, Nanostructures and Mesoscopic Systems, (Academic, New York, 1992)
37. E.Bauser, Atomic Mechanisms in Semiconductor Liquid Phase Epitaxy, ch.20 in Handbook of Crystal Growth, D.T.J.Hurle, editor (Elsevier, Amsterdam, 1994)
38. A recent example of a team effort toward optimizing InGaAs/GaAs epitaxy, see: A.Höpner, B.Rechenberg, H.Seitz, H.Procop, K.Scheerschmidt, and H.J. Queisser, submitted to *phys.stat.sol.* (1995)
39. K.S.Ralls, W. J. Skocpol, L.D.Jackel, R.E.Howard, L.A.Fetter, R.W.Epworth, and D.M.Tennant, *Phys. Rev. Lett.* **52**, 228 (1984)
40. H. Rauh, Wacker's Atlas for Characterization of Defects in Silicon (Wacker-Chemitronic Co., Burghausen, Germany, undated). This atlas describes the categories of defects, all important preferential etches and gives pictorial examples of defect photomicrographs.
41. H.J.Queisser, Kristallene Krisen (Piper, Munich, 1985), English version: The Conquest of the Microchip (Harvard Univ.Press, Cambridge, MA, 1988)
42. A very recent review describes the ubiquity of H on and in Si : G.J.Pietsch, *Appl.Phys. A* **60**, 347 (1995)
43. David J. Eaglesham, *MRS Bulletin XIX*, (12), 59 (December 1994). Acceptance speech for the MRS Outstanding Young Investigator Award at the 1994 MRS Spring Meeting : „*What We Still Don't Know About Silicon*“

Part II
Grown-In Defects in Bulk Crystals

SURFACES AND CRYSTAL DEFECTS OF SILICON

P. WAGNER, M. BROHL, D. GRÄF, U. LAMBERT
Wacker-Chemitronic GmbH
P.O.Box 1140, D-84479 Burghausen, Germany

ABSTRACT

Bulk crystal defects are accessible for investigation when silicon crystals are sliced and the defects occur close to or at the surface of wafers. Such near-surface defects can then be delineated by modifying some processes used for preparing clean, polished wafers. The delineated defects usually occur as pits the shape of which depends on the delineation process used. The different shapes of the pits has consequences for their detection by light scattering techniques (laser scanners or surface inspection systems). The density of the such generated surface defects is related to the defect density in the crystal bulk and is influenced by the growth parameters. These surface defects therefore provide a means for studying and for characterizing the bulk defect density.

INTRODUCTION

Monocrystalline silicon of ultra-high purity used for manufacturing semiconductor devices still contains extrinsic and intrinsic defects. The main extrinsic defects are oxygen and dopant elements which are intentionally introduced in the Si crystal during its growth with concentrations of 10^{12} to 10^{19} cm⁻³ (dopants) and $5\text{--}10 \times 10^{17}$ cm⁻³ (oxygen, Czochralski Si). Unintentional contaminations are present in the crystal bulk with concentrations $\leq 10^{16}$ cm⁻³ (carbon) or $\leq 10^{12}$ cm⁻³ (metals) /1/. The knowledge about extrinsic defects and contaminants in bulk Si has increased considerably during the past ten to twenty years.

The quantitative knowledge about intrinsic defects is much less comprehensive as compared to the extrinsic defects, however their consequences can be at least as detrimental as e.g. Fe-contamination. Si self-interstitials (I) and vacancies (V) present at high concentrations during the growth of the crystal at or close to the growth interface between crystal and melt are frozen in the crystal bulk during cooling. Agglomerations of such defects are thought to be the origin e.g. of swirls /1, 2/ or D-defects /3/, also called Flow-Pattern Defects (FPD), which occur after Secco etching.

Other defects thought to be related to vacancy clusters are the so-called Crystal Originated Particles (COP) /4/ occurring at the surface of polished Si wafers. These COP are identified by Scanning Surface Inspection Systems (SSIS), sensitive techniques developed during the past ten years to detect surface flaws on polished or epitaxial silicon wafers. These techniques allow to localize small surface defects fast and with a lateral accuracy of about 100 μ m. The results of investigations of such surface flaws, called LPD (Light Point Defects) or LLS (Localized Light Scatterers) in a generic way, or specifically COP, are reported in the present paper.

DELINEATION OF DEFECTS

The range of concentration from 10^{12} to 10^{18} cm⁻³ in the bulk corresponds to a density of about 10^5 to 10^{11} cm⁻² on a surface assuming a 1 nm thick layer to represent the surface. On the other hand, surface defect densities of $\ll 1$ cm⁻² can easily be detected by SSIS /5/ provided the scattering cross section of such defects is > 0.1 μ m LSE (Latex Sphere Equivalent) /6/. Assuming again a layer thickness of 1 nm this corresponds then to a bulk defect density of only $< 10^7$ cm⁻³, corresponding to 0.2×10^{-3} ppt.

Only sufficiently large bulk defects localized close to the surface are detected by present surface inspection equipments without additional preparation. Smaller defects have to be delineated appropriately which can be performed in many different ways [7]. In the present paper results are reported which were obtained with p-type silicon wafers either by softly etching with a SC1 solution

($\text{NH}_4\text{OH}:\text{H}_2\text{O}_2$: water 1:1:5, several hours at 85 °C) or by appropriately modified polishing with a caustic slurry (chemomechanical polishing CMP). The SC1 solution does not increase the surface roughness significantly, so that surface inspection equipment can be used for detecting the delineated defects. A 100-150 nm thick layer is removed by etching with the given conditions. A defect density of 1 cm^{-2} therefore corresponds to a bulk defect density of 10^5 cm^{-3} assuming that the etching process accumulates the residues of the defects at the surface. The defects delineated by SC1 treatment or polishing are called COP [4].

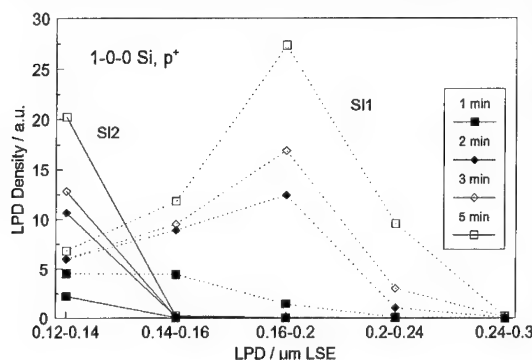


Fig. 1: LPD-size distribution as measured with two different surface inspection equipments

LIGHT SCATTERING AND ATOMIC FORCE MICROSCOPY OF COP

The surface inspection techniques mentioned above are based on scanning the surface of a wafer with a well focused laser beam. The slowly varying components of the signal - scattered light observed in dark field mode - then correspond to variations of the surface roughness whereas the high frequency, localized components of the signal indicate localized surface flaws. The scattered light, or more precisely the diffracted light, contains information about the Fourier transform of the surface profile or surface topography [8]. Therefore the solid angle of collection optics of the surface inspection equipments together with the incident angle of the laser beam and its wavelength define the spatial wavelength range covered by the tool. Extended flaws (or long spatial wavelengths) scatter (diffract) light only in a narrow cone around the specularly reflected laser beam whereas small flaws scatter in a wide solid angle. The scattering cross section - total as well as differential - of the surface flaws certainly also depends on the complex refractive index of the flaw as is outlined for particles in the Rayleigh-Gans or Mie theories [e.g. 9].

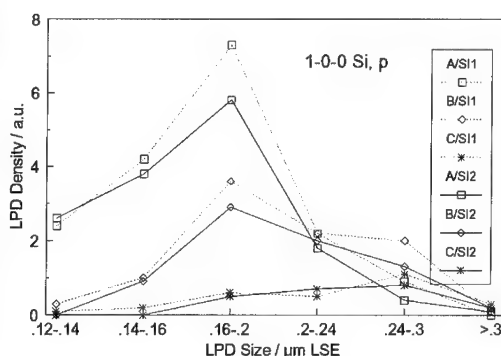


Fig. 2: LPD-size distribution for three different ingots A, B and C after SC1-treatment as measured with surface inspection equipments SI1 and SI2. Cooling rate $A > B > C$.

The influence of the shape of the surface flaws or the solid angle of the detection optics, respectively, is demonstrated by comparing the LPD distribution of a silicon wafer polished with modified CMP as measured by two different surface inspection equipments SI1 and SI2 (Fig. 1). Both equipments are calibrated with polystyrene latex (PSL) spheres of well defined sizes but they respond quite differently to the delineated crystal defects (COP). Less difference between both SSIS is observed when wafers are investigated where the COP were delineated by SC1 treatment (Fig. 2). The origin of this different behavior of the SSIS is the shape of the COP in both cases (Fig. 3). The shape of COP delineated by polishing corresponds to a shallow, extended etch pit with smooth edges. The COP after SC1 treatment are narrow, deep, well defined etch pits. The Fourier transform of their profile, corresponding to their diffraction pattern, is significantly different as well as the amount of light collected by the different SSIS (Fig. 4), as is expected according to the theory of diffraction of light /e.g.10/. Delineating by polishing therefore does not provide reliable information about the size distribution of COP.

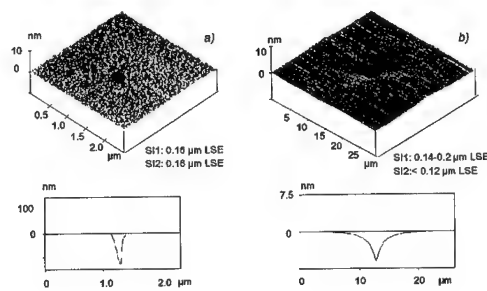


Fig. 3: AFM scans of COP delineated by SC1-treatment (a) or modified polishing (b). Displayed are also the cross sections of both COP as well as the sizes as reported by the surface inspection equipments SI1 and SI2.

The volume of the COP in Fig. 3b corresponds approximately to the volume of a sphere with a diameter of 180 nm. (A Si sphere with this volume contains $\approx 1.4 \cdot 10^8$ Si atoms.) The reported size was 160 nm LSE by both equipments. This defect - etch pit, missing silicon atoms - therefore

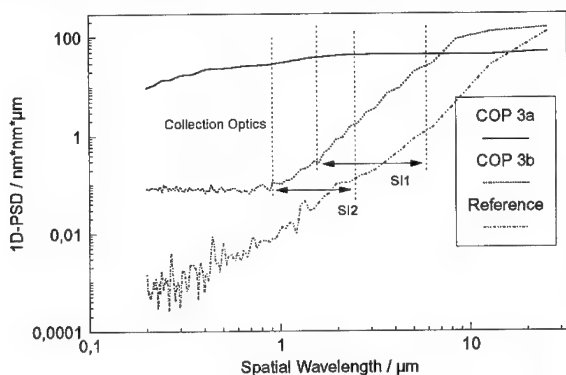


Fig. 4: One-dimensional Power Spectral Density (Fourier transform squared) curves of the profiles displayed in Fig. 3 and a reference curve of a polished surface. The spatial wavelength ranges collected by the surface inspection equipments SI1 and SI2 are indicated.

scatters light like a PSL sphere with a diameter of 160 nm. The volume of the COP of Fig. 3a on the other hand corresponds to the volume of a sphere with a diameter of about 600 nm and it is reported to have a size corresponding to a PSL of 140-200 nm or < 120 nm, respectively, by the different equipments. The lateral dimensions of COP a) allow to assume that it scatters light like a small particle (Rayleigh approximation) which is confirmed by the same effective size being reported by both SSIS. COP b) with lateral dimensions larger than the laser wavelength diffracts light like an extended defect (Mie

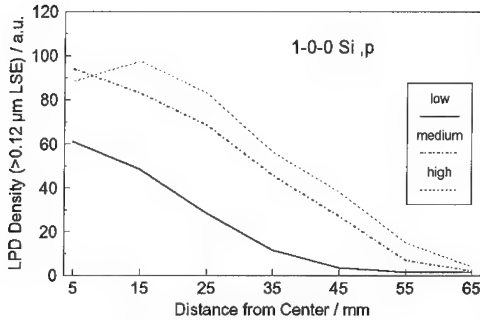


Fig. 5: Radial COP distribution for three different ingots pulled with low, medium and high pulling rate, respectively.

approximation in the case of particles, or diffraction by a slit). Therefore, care has to be taken when interpreting the sizes of COP as reported by SSIS.

COP a) with a volume of $2.9 \cdot 10^6 \text{ nm}^3$ (corresponding to a sphere with a diameter of 180 nm) scatters light like a PSL with a slightly smaller volume and not like a Si particle with the same volume. A Si particle is expected to scatter light by a factor of about 8-10 more than a PSL sphere of the same size due to the differences in the respective refractive indices. This is an indication that small etch pits might scatter light less efficiently than Si particles of the same volume.

CRYSTAL DEFECTS

Crystal growth conditions are known to influence the radial and axial COP distribution of a Si ingot severely [11, 12]. Regions with a surplus of vacancies or with Si self-interstitials occur in the ingot depending on pulling speed and the thermal gradient at the growth interface according to [13]. The diameter of the V-rich part along the center of the ingot increases with increasing pulling speed provided the thermal gradient remains unchanged. No V-rich region is generated when the pulling speed is sufficiently low, no or very few COP are delineated in this case.

The density of COP increases in parallel with the pulling rate. An example for the radial variation of COP density of ingots grown with three different pulling rates is displayed in Fig. 5. COP appear in the V-rich region of the ingot after a delineating treatment and their density is related to the density of D-defects. Their origin therefore is usually assumed to be related to V-clusters similarly like the D-defects [3]. The size distribution of COP can also be controlled by adjusting the cooling rate of the ingot after solidification. Slow cooling rates result in larger COP, fast cooling rates in smaller COP, with the total

volume of the COP estimated to be approximately constant [11] (Fig. 2) for similar pulling rates.

Another example for the influence of thermal history on the generation of COP are wafers which were annealed at high temperatures (around 1200 °C) for sufficiently long periods [14]. Such

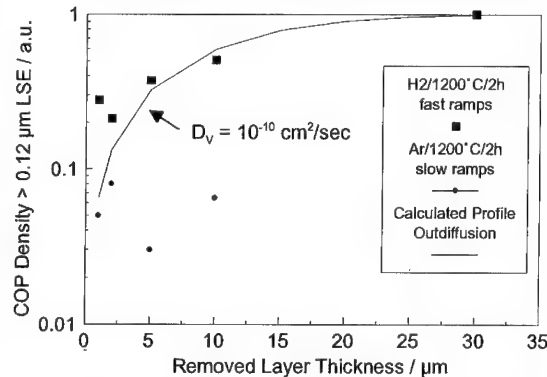


Fig. 6: COP density as a function of the by polishing removed layer. Diffusion profile was calculated neglecting temperature ramps of the annealing process.

wafers display again a very low LPD and COP density. The depth of the defect free zone depends on the annealing time and temperature. Defect free zones as deeper than 15 μm can be obtained as is demonstrated by removing successive layers by polishing (Fig. 6). A diffusion coefficient for vacancies of approximately $1 \cdot 10^{-10} \text{ cm}^2 \text{ sec}^{-1}$ at 1200°C can be estimated using this profile. This is a lower limit as any activation energies required for dissolving the V-clusters as well as temperature ramps are neglected. The Ar-annealed wafers in Fig. 6 were processed with

slow ramps. Therefore the ramping times cannot be neglected anymore and contribute a significant outdiffusion which is difficult to estimate. The value given above for the diffusion coefficient of V at 1200°C is at the lower end of the range of V-diffusion coefficients /15/.

Delineated COP by themselves do not degrade the GOI-yield /16/ (Gate Oxide Integrity /17/). There is a correlation, however, between the COP density as a measure for the density of bulk defects being the origin of COP and the GOI-yield or GOI-defect density /11, 18/ for p-type Si (Fig. 7).

Very few crystal defects occur in epitaxial silicon wafers. Correspondingly, only very few COP can be delineated. However, what does occur if an epitaxial layer is grown on a surface where the COP have been delineated by an SC1 treatment? Astonishingly enough, the surface is largely improved by depositing an epitaxial layer of a thickness of about 5 μm (Fig. 8). The epitaxial process either really makes the COP etch pits shrink or the scattering cross section of the etch pits diminishing by e.g. smoothing the edges.

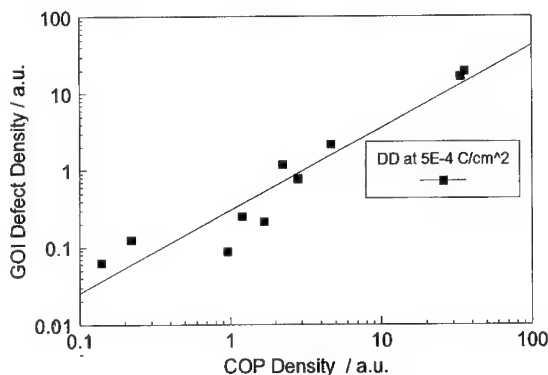


Fig. 7: GOI defect density as a function of COP density for annealed and epitaxial wafers.

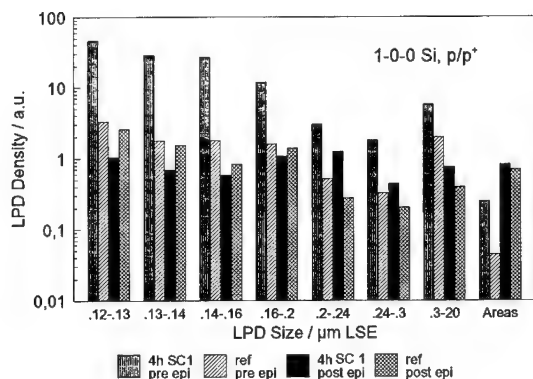


Fig. 8: Average LPD density (4 wafers) before and after epi-deposition for wafer on which the COP were delineated by SC1-treatment. The results of non-delineated reference wafers are also shown.

SUMMARY

Delineated bulk defects at the surface of Si wafers with lateral dimensions comparable to the laser light wavelength diffract the light according to the Fourier transform of their shape. Therefore different surface inspection tools with differing collection optics collect different amounts of the diffracted light and report different scattering cross section or effective sizes of the LPD, respectively. Defects small as compared to the laser wavelength scatter light like small particles and the various equipments report similar sizes. Reliable information about COP therefore can be obtained only after delineating them by soft etching.

The COP density was found to be correlated to the density and spatial distribution of FPD indicating that both defects may have the same origin and are presumably V-clusters. Both occur mainly in the vacancy rich region of the ingot. The thermal history during growth influences the density of COP significantly as well as thermal treatments after growth. Epitaxial deposition of Si reduces the scattering cross section of COP considerably thus contributing to the superior performance of epitaxial wafers.

ACKNOWLEDGMENTS

Help and support obtained by H. Piontek, A. Luger, H.A. Gerber, G. Valouch is highly appreciated. This work was supported by the Federal Department of Research and Technology of Germany under contract number M2793. The authors alone are responsible for the contents.

REFERENCES

1. W. Zulehner, B. Neuer, G. Rau, in Ullmann's Encyclopedia of Industrial Chemistry, Vol. A23, (VCH Publishers, Weinheim, 1993), p.721.
2. A.J.R. de Kock, Philips Research Reports Suppl. No. 1, (1973).
3. R.J. Roksnoer, M.M.B. von den Boom, J. Cryst. Growth **30**, 117 (1975).
4. J. Ryuta, E. Morita, T. Tanaka, Y. Shimanuki, Jpn. J. Appl. Phys. **31**, L1947 (1990).
5. E.F. Steigmeier, H. Auderset, Appl. Phys. **A50**, 531 (1990).
6. SEMI Document 1942.
7. D.C. Miller, G.A. Rozgonyi, in Handbook on Semiconductors, Vol.3, (North-Holland, Amsterdam, 1980), T.S. Moss, S.P. Keller, Eds., p. 217.
8. J.C. Stover, Optical Scattering, Measurement and Analysis, (McGraw-Hill, N.Y., 1990), R.E. Fisher, W.J. Smith, Eds.
9. H.C. van de Hulst, Light Scattering by Small Particles, (Dover, N.Y., 1981).
10. S.G. Lipson, H. Lipson, Optical Physics, (Cambridge University Press, Cambridge, 1969).
11. M. Brohl, D. Gräf, P. Wagner, U. Lambert, H.A. Gerber, H. Piontek, in ECS Fall Meeting 1994, Vol. 94-2, p. 619.
12. W. von Ammon, A. Ehlert, U. Lambert, D. Gräf, M. Brohl, P. Wagner, in Semiconductor Silicon / 1994, (The Electrochemical Society, Inc., Penningon, NJ, 1994), H.R. Huff, W. Bergholz, K. Sumino, Eds., p. 136.
13. V.V. Voronkov, J. Cryst. Growth **59**, 625 (1982).
14. D. Gräf, U. Lambert, M. Brohl, A. Ehlert, R. Wahlich, W. v. Ammon, P. Wagner, in ECS Fall Meeting 1994, Vol. 94-2, p. 640.
15. H. Bracht, N.A. Stolwijk, H. Mehrer, in Semiconductor Silicon / 1994, (The Electrochemical Society, Inc., Penningon, NJ, 1994), H.R. Huff, W. Bergholz, K. Sumino, Eds., p. 593.
16. E. Morita, H. Okuda, F. Inoue, Semiconductor International, July 1994, 156.
17. D.R. Wolters, J.J. van den Schoot, Philips J. Res. **40**, 115 (1985).
18. H. Yamagishi, I. Fusegawa, N. Fujimaki, M. Katayama, Semicond. Sci. Technol. **7**, A135 (1992).

THE FORMATION OF DEFECTS DEGRADING GATE OXIDE INTEGRITY DURING CZ-SI CRYSTAL GROWTH

Y. TSUMORI*, K. NAKAI*, T. IWASAKI*, H. HAGA*, K. KOJIMA**
AND T. NAKASHIZU**

*Nippon Steel Corp., Electronics Research Labs., Shimata, Hikari, Yamaguchi 743, Japan

**NSC Electron Corp., Shimata, Hikari, Yamaguchi 743, Japan

ABSTRACT

The formation of grown-in defects degrading the gate oxide integrity (GOI) has been studied. The growth-halting experiments were carried out to investigate the temperature ranges at which the formation of the defects was promoted or suppressed. GOI is improved in the crystal regions slowly cooled above 1330°C and between 1060°C and 1100°C. It is degraded in the crystal regions held below 1060°C. In the peripheral of the crystals, those temperature ranges are about 30°C lower. The defects are formed and grown below 1060°C in the center part of the crystal. The defect density is decreased with cooling time between 1060°C and 1100°C. These phenomena are considered to be closely related with reactions of intrinsic point defects, that is, the pair annihilation or the aggregation. The temperatures at which the pair annihilation and the aggregation of the point defects occur are dependent upon the supersaturation of the point defects.

INTRODUCTION

The Gate oxide integrity (GOI) becomes very important with increase of LSI integration. As cleaning technology in device manufacturing process has been developed, the degradation of GOI caused by grown-in defects formed in Cz-Si crystals has attracted special interest recently [1]. Tachimori *et al.* reported the influence of growth rate on GOI [2]. They showed that GOI depends on the radius of the ring zone where oxidation induced stacking faults are anomalously formed (OSF-ring)[3]. The inside region of the OSF-ring exhibits poor GOI compared to the outside region [2,4]. Recently, grown-in microdefects inside the OSF-ring have been studied in relation with GOI [5-12]. The nature of the defects degrading GOI has been reported by many authors to be oxygen precipitates created by the interaction between vacancies and oxygen [9], agglomerated vacancies coexisting with interstitially dissolved oxygen [10,11] or vacancy related voids [12]. On the other hand, the temperature and mechanism of the defect formation during the crystal growth have not been sufficiently clarified yet. For the defect behavior inside the OSF-ring, it was only reported that the density decreases and the size increases in the crystals grown at slow cooling rate in the temperature range from 1150°C to 1000°C [9]. Therefore, it is still difficult to control the defects during the crystal growth for GOI improvement.

The purpose of this study is to understand the formation mechanism of the defects degrading GOI in CZ-Si crystal growth process. We will show the nucleation and growth temperature range of them and discuss the formation kinetics.

EXPERIMENTAL

The growth-halting experiments were carried out to find the formation temperature range of the grown-in defects degrading GOI. Varying the halting time, five Cz-Si crystals were grown, which were 135 mm in diameter, 450 mm in body length, doped with phosphorus and had interstitial oxygen concentration of $9.5 \times 10^{17} \text{ cm}^{-3}$ (JEIDA standard). The pulling rate was 1.0 mm/min from the shoulder to 230 mm in length. Then it was suddenly changed to 0.2 mm/min, held for 7 min, 15 min, 30 min, 60 min or 100 min, and raised rapidly and maintained at 1.0 mm/min to the tail end. Figure 1 shows the cooling condition in the crystal position of 10 mm, 50 mm, 100 mm, 150 mm, 200 mm and 250 mm of the crystal halted for 60 min. The crystal position in this

paper represents the distance from the crystal-melt interface at the start of growth-halting. The temperature distribution of a growing crystal had been preliminarily measured by setting thermocouples in the center of the crystal.

To examine GOI characteristics, the crystals halted for 7 min, 15 min, 30 min and 60 min were sliced horizontally and polished into mirror wafers. MOS capacitors were fabricated on the wafers with a polycrystalline silicon gate with area 20mm^2 . Gate oxide films with thickness 25.0nm were thermally grown in dry oxygen at 1000°C . The breakdown field was measured by ramping-voltage method and determined from the applied voltage that induced the leakage current density of $1 \times 10^{-6} \text{ A/cm}^2$. The GOI yield and the average breakdown field were calculated from the number of the capacitors with the fields over 7.5 MV/cm and from the measured values of the capacitors with fields under 7.5 MV/cm respectively. The density per unit area of the defects worsening GOI is calculated from the breakdown frequency by assuming the Poisson distribution [13].

For the crystallographic investigation, the rectangle specimens were sliced and polished along the growing axis from the crystals halted for 7 min and 100 min. The distribution and density of the defects in the specimens were examined by X-ray topography and Wright's etching [14] after 2-step annealing at 800°C for 4 hours and at 1000°C for 16 hours in nitrogen. The distribution of oxygen concentration was measured by FT-IR with the conversion factor of $3.03 \times 10^{17} \text{ cm}^{-2}$ before and after the 2-step annealing.

High temperature annealing experiments were also carried out to study the thermal stability of the defects. Small samples of $20 \text{ mm} \times 10 \text{ mm} \times 2 \text{ mm}$ in dimensions were cut from the center of the crystal halted for 100 min. They were annealed at the temperatures between 1150°C and 1350°C for 2 hours in helium, and then cooled slowly down to 600°C at the rate of 4°C/min . Then, they were annealed at 800°C and 1000°C for 4 hours and 16 hours respectively in nitrogen to observe easily the defects remaining after the high temperature annealing. The density of the defects was measured after the Wright's etching.

RESULTS

The dielectric breakdown field was measured by separating the measurement area into two parts, the center and the peripheral part, which were within a circle with its radius of 35 mm and out of it. Figure 2(a) shows the GOI characteristics in the center part of the crystal halted for 60 min as a function of the crystal position with references for the crystal without halting. Figure 2(b) shows change in the density of the defect degrading GOI in the center part, calculated from the breakdown frequency at applied field of 4, 5 and 6 MV/cm and the GOI yield. These results show the GOI is significantly affected by cooling condition during crystal growth.

According to the breakdown characteristics, the influence of the growth halting can be classified into four regions. Region-A, the crystal positions between 0 and 25 mm , is slowly cooled above 1330°C and shows excellent GOI. Region-B, the positions between 25 mm and 120 mm , is slowly cooled in the temperature range between 1330°C and 1100°C and shows normal GOI, i.e., not affected by the growth-halting. Region-C, the positions between 120 mm and 140 mm , is slowly cooled in the range between 1100°C and 1060°C and shows good GOI. Region-D, the positions between 140 mm and 230 mm , is slowly cooled below 1060°C and shows poor GOI. The calculated density of the defects worsening the GOI in Region-C is about one fourth of that in Region-B. The total defect density in Region-D is almost the same as that in Region-B; however, there are more defects that destroy the gate oxides at lower applied fields in Region-D. And those defects are formed with higher density at higher temperature (especially 1060°C to 1000°C) in the

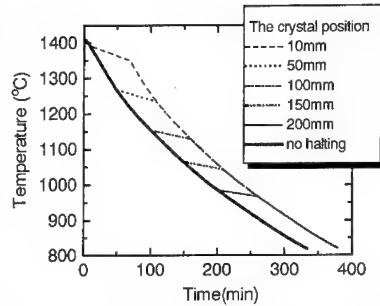


Figure 1. The cooling condition in the crystal positions of 10 mm, 50 mm, 100 mm, 150mm, 200mm and 250mm in the case of 60min growth-halting.

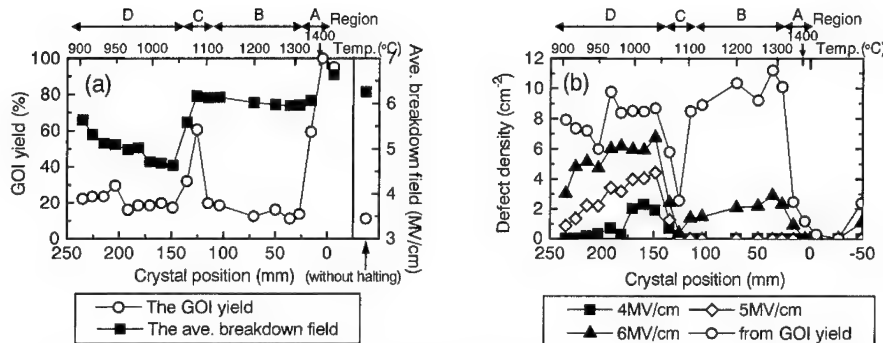


Figure 2 (a). The GOI characteristics in the center part of the crystals with halting for 60min and without halting. (b) The density of defects degrading GOI calculated from the breakdown frequency in the center part of the crystal halted for 60min.

region.

Figure 3 shows the influence of the halting time on the GOI yield in Region-A and Region-C and the average breakdown field in Region-D. The GOI yield is remarkably improved between 15 min and 30 min in Region-A. On the contrary, it is proportionally increased with the halting time in Region-C. These results show Region-A and Region-C differ from each other in the mechanism of GOI improvement. The average breakdown field in Region-D becomes lower with the halting time, indicating that harmful defects for GOI grow during halting in this region.

Figure 4 shows the radial difference in the GOI yield and the average breakdown field of the crystal halted for 60 min. In the peripheral part, the temperature regions are 30°C lower, where GOI is improved (Region-A and C) and is deteriorated (Region-D). This result shows that the change of the GOI is not determined directly by the temperature where the crystals are slowly cooled.

Figure 5(a) and (b) show X-ray topographs of the crystals halted for 7 min and 100 min respectively after the 2-step annealing. Figure 6 shows the distribution of the interstitial oxygen concentration along the center axis of the above crystals before and after the annealing. In Region-A, the OSF-ring (two dark bands in Figure 5) shrinks with the halting time. It shrinks out in the crystal halted for 100 min, which leads to low oxygen precipitation corresponding to low reduction of the solute oxygen shown in Figure 6. Anomalous high amount of oxygen

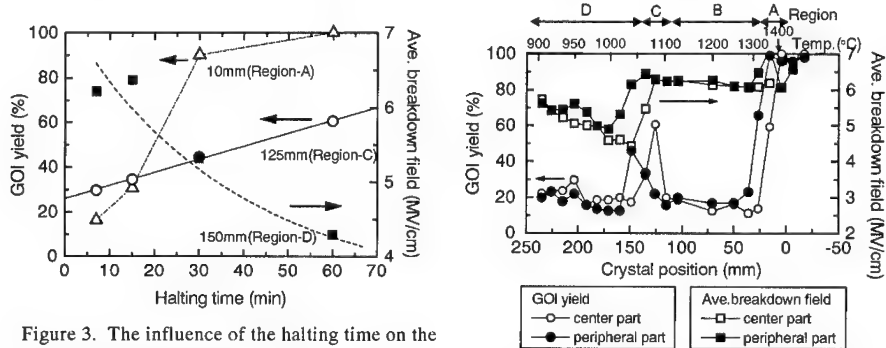


Figure 3. The influence of the halting time on the GOI yield and the average breakdown field in the center part of the crystals.

Figure 4. The radial difference in the GOI yield and the average breakdown field of the crystal halted for 60 min.

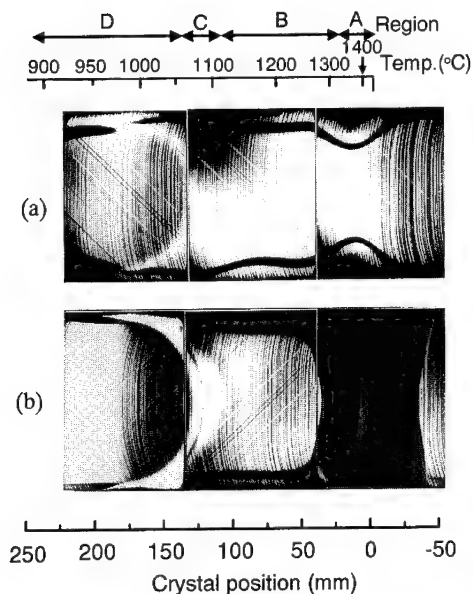


Figure 5. The X-ray topographies of the crystals halted for (a) 7 min and (b) 100 min after the 2-step annealing. The dark bands are the OSF-ring.

precipitation is observed in Region-C, which is seen as a strongly bright band in the X-ray topographies of Figure 5. It is noted that the position of the bright band (highly precipitated region) is independent of the halting time. In the temperature range around 1060°C to 1000°C, the precipitation is remarkably decreased with the halting time, which is clearly noticed as the contrast difference in the X-ray topograph (b).

As shown in Figure 3, Region-A exhibits excellent GOI as the halting time is longer and the OSF-ring shrinks. In other words, the outside region of the OSF-ring has excellent GOI property and Region-A becomes all outside region of the OSF-ring with sufficient holding time. On the other hand, Region-C is improved and shows good GOI although the region is inside the OSF-ring. Interestingly, the region coincides with the position of the anomalous oxygen precipitation (AOP). On the contrary, the crystal positions (around 150 mm) that exhibit the poorest GOI in Region-D coincide with the precipitation-retarded region. These results show GOI is independent of the oxygen precipitation after the 2-step annealing. The defects degrading GOI may be some specific precipitates.

Figure 7 shows the density of the residual defects after the high temperature annealing of the specimens cut from the position of 90 mm, 128 mm and 153 mm of the crystal halted for 100 min. At the position of 128 mm, where the GOI is superior, the density of the residual defects is the highest after annealing below 1250°C. However, it goes least after annealing above 1300°C. On the contrary, in the crystal position of 153 mm, where the GOI is inferior,

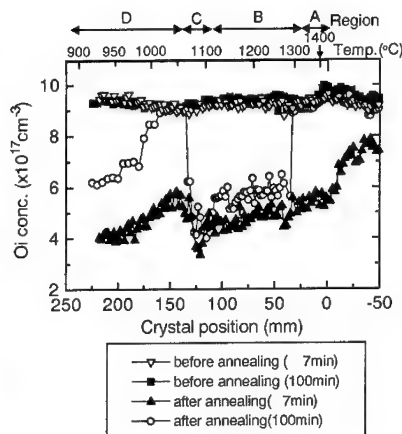


Figure 6. The distribution of the interstitial oxygen concentration along the center axis of the crystals halted for 7 min and 100 min before and after the 2-step annealing.

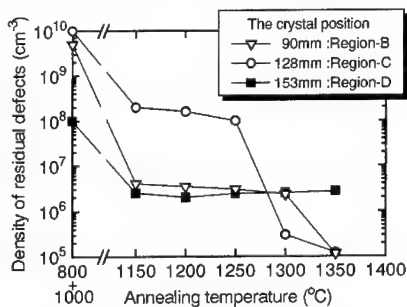


Figure 7. The density of the residual defects after the temperature annealing in the crystal position of 90 mm, 128 mm and 153 mm of the crystal halted for 100 min.

the density is the highest after annealing at 1350°C.

The thermal stability of the defects has a close correlation with GOI. Some stable defects remaining after annealing above 1300°C worsen GOI. Defects in Region-C exist in large quantity, but most of them dissolve easily by annealing above 1300°C. They may be small so that they do not degrade GOI. Defects in Region-D exist in small quantity, but some of them remain after the high temperature annealing. Those defects may be large and/or quite stable as some secondary defects are, and they cause the gate oxide destruction at lower applied field.

DISCUSSION

The defects affecting GOI exhibit the same number density in Region-B and in Region-D, although the defects are much harmful to GOI in Region-D. It seems as if the defects nucleated in Range-B and grew in Range-D, where Range-A, B, C and D are the temperature ranges in which Region-A, B, C and D are held respectively. However, this possibility is rejected by the fact that there exist few defects in Region-C. If the nucleation of the defects occurred in Range-B, there should have existed the nuclei in Region-C because the nucleation would occur in no relation to the pulling rate change (growth halting) and the crystal positions in Region-C pass Range-B before the halting starts. The nuclei should have grown due to high oxygen diffusivity at such high temperatures and should have not decomposed because Range-C is lower than Range-B. However, the fact is different, so that it is natural to consider the growth halting in Region-B gives any noticeable influence neither to GOI nor to oxygen precipitation characteristics.

It should be considered that the defects affecting GOI are formed in Range-D and that halting in Range-C has some effect to suppress the nucleation of the defects. Actually, the position passed slowly from Range-C to Range-D gives good GOI yield and low density of the harmful defects, as shown in Figure 8. In addition, this fact was confirmed by the crystal-thermal-history simulating annealing experiment, which clearly showed thermally stable defects are not produced by holding at 1050°C (Range-C) and successive at 1000°C (Range-D) during crystal cooling from 1380°C [15]. As for oxygen precipitation by the 2-step annealing, it is retarded in Region-D by the formation of the defects affecting GOI and promoted in Region-C by the suppression of them. The nuclei of AOP in Region-C should be formed at the temperatures lower than 900°C (around 700°C) since they are more unstable and have much higher density than the defects affecting GOI.

The above phenomena are considered to be closely related with reactions of intrinsic point defects, vacancies and/or self-interstitials. We assume that vacancies would be the dominant point defect that forms the harmful defects to GOI. The point defects are introduced accompanying the crystal solidification process. The diffusion above 1300°C determines the macroscopic density-distribution of them and the position of the OSF-ring according to the model by Habu *et. al.* [16]. The density of the point defects cannot change significantly and the degree of supersaturation increases in Range-B, because the diffusion constants are so small that point defects cannot diffuse out to surface and the pair annihilation hardly occurs on account of the entropy barrier proposed by Gosele [17]. The pair annihilation takes place in Range-C where the supersaturation (or free energy difference) increases enough to surpass the barrier. If the point defects annihilate sufficiently in Range-C, the defects affecting GOI cannot nucleate in Range-D; while if the annihilation is insufficient, the supersaturated vacancies will aggregate to form the nuclei of the defects. Accordingly, the formation of the defects affecting GOI depends on the supersaturation of vacancies in Range-D, which is controlled by the holding time in

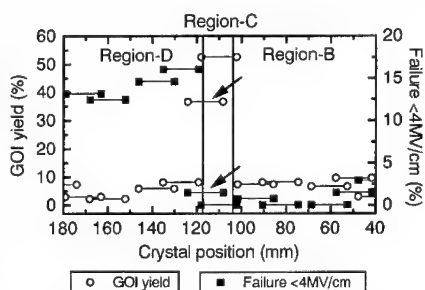


Figure 8. The GOI yield and the breakdown frequency at the applied field of 4MV/cm in other halting experiment. The sample with arrows is passed slowly from Range-C to Range-D

Range-C. A large amount of vacancy aggregation in Range-D suppresses the formation of nuclei for oxygen precipitation in the lower temperature range due to lack of supersaturation of vacancies. On the other hand, if the pair annihilation in Range-C occurs sufficiently to prevent residual vacancies from aggregating in Range-D, they become supersaturated in the lower temperature range and produce numerous nuclei of micro oxygen precipitates (AOP). As is obvious from above discussion, the temperature at which the pair annihilation and the aggregation occur is dependent upon the supersaturation of the point defects. In the peripheral parts of the crystals, the point defect concentration decreases due to out-diffusion to the surface and the degree of supersaturation becomes lower than that in the center parts, so that the pair annihilation and the aggregation will occur at lower temperatures. This explains the concave configuration of Region-C and D.

In the crystal parts of Region-A, the point defect density is very low enough to suppress the defect formation in Region-D, which leads excellent GOI and low precipitate density after the 2-step annealing.

CONCLUSIONS

The influence of crystal cooling condition during the growth on the defect formation harmful to GOI was investigated. The crystal positions slowly cooled in the temperature range over 1330°C increase the area of outside region of the OSF-ring and exhibit excellent GOI. In other positions characterized mostly as inside region of the OSF-ring, GOI is improved between 1060°C and 1100°C, the defects degrading GOI are formed and grown below 1060°C. These phenomena are considered to be closely related with reactions of intrinsic point defects, that is, the pair annihilation or the aggregation. The temperatures at which the pair annihilation and the aggregation of the point defects occur are dependent upon the supersaturation of the point defects.

REFERENCES

1. K. Yamabe and K. Taniguchi, IEEE Trans. Electron Devices, **ED-32** 423 (1985)
2. M. Tachimori, T. Sakon and T. Kaneko, 7th Kessho Kogaku Symp. of Jpn. Soc. Appl. Phys., ISAP Catalog No. AP902217, 27 (1990) in Japanese
3. M. Hasebe, Y. Takeoka, S. Shinoyama and S. Naito, in *Proc. Int. Conf. Defect Control in Semiconductors*, Yokohama, 1989, ed. K. Sumino (North-Holland, Amsterdam, 1990) pp.157
4. T. Yamauchi, Y. Tsumori, T. Nakashizu, H. Esaka, S. Takao and S. Shinoyama, Jpn. J. Appl. Phys. **31** L439 (1992)
5. H. Yamagishi, I. Fusegawa, N. Fujimaki and M. Katayama in *Proc. Symp. Advanced Science and Technology of Silicon Materials*, Kona, Hawaii 1991 (Japan Society for the Promotion of Science 145th Committee, Tokyo, 1991) pp.83
6. J. Ryuta, E. Morita, T. Tanaka and Y. Shimanuki, Jpn. J. Appl. Phys. **29** L1947 (1990)
7. J. Ryuta, E. Morita, T. Tanaka and Y. Shimanuki, Jpn. J. Appl. Phys. **31** L293 (1990)
8. S. Sadamitsu, S. Umeno, Y. Koike, M. Hourai, S. Sumita and T. Shigematsu, Jpn. J. Appl. Phys. **32** 3675 (1993)
9. M. Hourai, T. Nagashima, E. Kajita and S. Miki in *Semiconductor Silicon 1994*, edited by H.R. Huff, W. Bergholz, K. Sumino (The Electrochem. Soc., Pennington, NJ, 1994) pp.156
10. T. Abe in *Proc. of Progress in Semiconductor Fabrication*, Technical Conference at SEMICON Europe 1993, SEMI Europe, Brussels (1993)
11. W.v. Ammom, A. Ehler, U. Lambert, D. Graf, M. Bohl and P. Wagner in *Semiconductor Silicon 1994*, edited by H.R. Huff, W. Bergholz, K. Sumino (The Electrochem. Soc., Pennington, NJ, 1994) pp.136
12. J.-G. Park, H. Kirk, K.-C. Cho, H.-K. Lee, C.-S. Lee and G. A. Rozgonyi in *Semiconductor Silicon 1994*, edited by H.R. Huff, W. Bergholz, K. Sumino (The Electrochem. Soc., Pennington, NJ, 1994) pp.370
13. C.M. Osburn and D.W. Ormond, J. Electrochem. Soc. **119** 591 (1972)
14. M.W. Jenkins, J. Electrochem. Soc. **124** 757 (1977)
15. T. Iwasaki, Y. Tsumori, K. Nakai, H. Haga, K. Kojima and T. Nakashizu in *Semiconductor Silicon 1994*, edited by H.R. Huff, W. Bergholz, K. Sumino (The Electrochem. Soc., Pennington, NJ, 1994) pp.744
16. R. Habu, I. Yunoki, T. Saito and A. Tomiura, Jpn. J. Appl. Phys. **32** 1740 (1993)
17. W. Frank, U. Gosele, H. Mehrer and A. Seeger, in *DIFFUSION IN CRYSTALLINE SOLIDS*, edited by G.E. Murch and A.S. Nowick (ACADEMIC PRESS INC., 1984) pp.63-142

ANALYSIS OF DISLOCATION NETWORKS AND ELECTRONIC PROPERTIES OF DENDRITIC WEB SILICON

S.L. Morelhão^{*}, D.L. Meier[†], G.T. Neugebauer[†],
B.B. Bathey[†], and S. Mahajan^{*}

^{*}Dept. of MS&E, Carnegie Mellon University, Pittsburgh PA 15213, USA

[†]EBARA Solar, Inc., Large PA 15025, USA

ABSTRACT

During the growth of dendritic web silicon, an ideal material for fabrication of high efficiency solar cells, a thin ribbon of silicon single crystal is obtained. Due to thermal stresses characteristic in this growth process, dislocations and residual stresses are observed in most ribbons. In this study, transmission X-ray topography was used for analyzing dislocation networks in as-grown web silicon. We were able to correlate minority carrier diffusion length with the configuration of the networks that are strongly affected by twin planes lying midway across the web thickness. Analysis of the networks is also useful in providing information regarding regions of high stress levels associated with a given growth environment.

INTRODUCTION

The dendritic web growth technique has brought to the industrial world an elegant method for growing very thin ribbons of silicon single crystal. Its rectangular shape and its as-grown mirror-like surfaces (which eliminates the need for sawing and polishing) make it nearly ideal for manufacturing solar cells at low cost [1]. This fact has attracted the industrial interest for using web silicon as a basic material for the fabrication of efficient solar cells.

In the last decade, studies to increase the web output rate, minimize raw material cost and raise solar cell conversion efficiency as high as possible have been performed [2-6]. One of the most important issues is to control the thermal environment of the growth system. In general, numerical calculations involving finite elements are used to estimate the temperature profile in the growth system. Thermal stress modeling in a two-dimensional ribbon, assuming constant width and free-edges, is then used to find the stress levels associated with a given temperature profile [2,3,4]. Optimization of important parameters such as radiative heat transfer, susceptor shape, radiation shields, and others furnace components was possible with the above procedure. For instance, it has been shown that stress levels would increase with sample width and that changes in the melt level have a strong influence on thermal condition near the solid/melt interface. The need for melt replenishment during long growth periods is one important conclusion of these studies [3]. However, even in optimized systems, substantial thermal stresses remain throughout the growth region and their presence is manifested by generation of dislocations and ribbon buckling. Thermal stress modeling in a tridimensional ribbon (accounting for ribbon thickness) is necessary to understand buckling [4].

Actually, the thermal environment as well as the behavior of the material in such a complex growth process can be quite different from the idealized ones assumed in the calculations. The dislocation network observed across the web [7] reflects the material behavior for thermal stresses prevailing during growth. Therefore, analysis of dislocation networks can provide crucial information in order to optimize the growth conditions. Moreover, dangling bonds present along dislocation cores can lead to reduction in minority carrier diffusion length (MCDL) [8] and result in low photovoltaic efficiencies. In this work, transmission X-ray topography was used to analyze dislocation networks in dendritic web silicon. Drastic changes in the network configurations, their correlation with MCDL and factors affecting these changes are discussed here.

SYNOPSIS OF GROWTH PROCESS

The growth process is described briefly, and additional details can be found elsewhere [3,4]. When a fine silicon dendrite seed is inserted into a supercooled (below its melting temperature) silicon liquid, it grows laterally due to its crystallography (and thermal environment) and forms a button. By pulling the seed upward at a uniform rate, two dendrites, one from each end, grow from the button. As the dendrites emerge from the melt, a thin liquid silicon film, supported between them by surface tension forces, crystallize in a thin silicon web with a thickness of about 100 microns. Features of the process as well as the web crystallography are illustrated in Fig. 1. The presence of $\{111\}$ twin planes (parallel to the web surface) provides reentrant corners for dendritic growth but they do not appear to be essential for growth of the web itself [1]. Secondary effects due to the presence of twins is another issue and it is discussed later on in the paper.

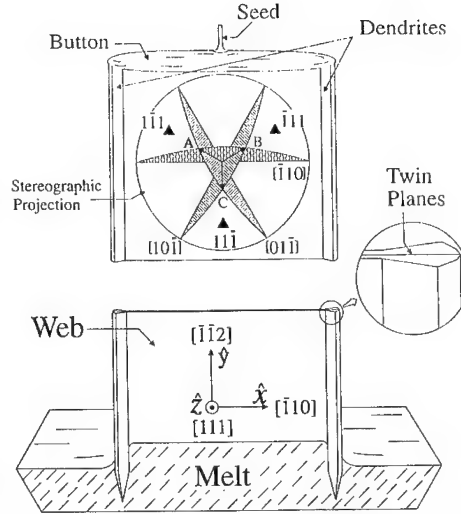


Fig. 1: Schematic depiction of dendritic web silicon growth. The stereographic projection of the slip systems $[101], [110](\bar{1}\bar{1}1)$, $[011], [110](1\bar{1}1)$ and $[101], [011](11\bar{1})$ are also illustrated. The A, B and C arrows stand for $[101]$, $[011]$ and $[110]$ slip directions, respectively.

EXPERIMENTAL DETAILS

A standard topographic Lang camera and a X-ray generator with Mo target were used to perform transmission topography measurements (Lang topography [9]). The X-ray beam was collimated in the incident plane (horizontal plane) to about three minutes of arc. The vertical beam size and the horizontal maximum scan range limit the size of the analyzed area to 18 mm by 26 mm, respectively. Exposure times of 3 hours per scanned centimeter were used for $\{220\}$ reflections, against 4 hours for $\{224\}$ reflections. Diffracted intensities were registered on high resolution nuclear plates. All dislocations with lattice strain field over a range larger than 1 micron can be observed with this technique. Of course, dislocations presenting Burgers vector (\mathbf{b}) perpendicular to the diffraction vector are invisible for such reflection. The measurements of minority carrier diffusion length were performed by surface photovoltage (SPV) technique [10].

RESULTS AND DISCUSSION

1 - DISLOCATION NETWORKS

In silicon crystals slip occurs on close-packed $\{111\}$ planes, with $\frac{a}{2}\langle 1\bar{1}0 \rangle$ Burgers vectors. This can be verified from the X-ray topographs shown in Fig. 2. These are images from the same area of the web taken using four different reflections. The visibility criterion for a dislocation allows a complete identification of all dislocations and dislocation interactions in this area. The observed contrast behavior is consistent with slip activity on $[011]$, $[110](1\bar{1}1)$ and $[110]$, $[101](\bar{1}\bar{1}1)$ systems, and it is also consistent with occurrence of interactions type $\frac{a}{2}\langle 110 \rangle + \frac{a}{2}\langle 011 \rangle = 3 \times \frac{a}{6}\langle 121 \rangle$. In this type of attractive interaction, the dislocations are dissociated into Shockley partials and the node is formed by subsequent rearrangement of the

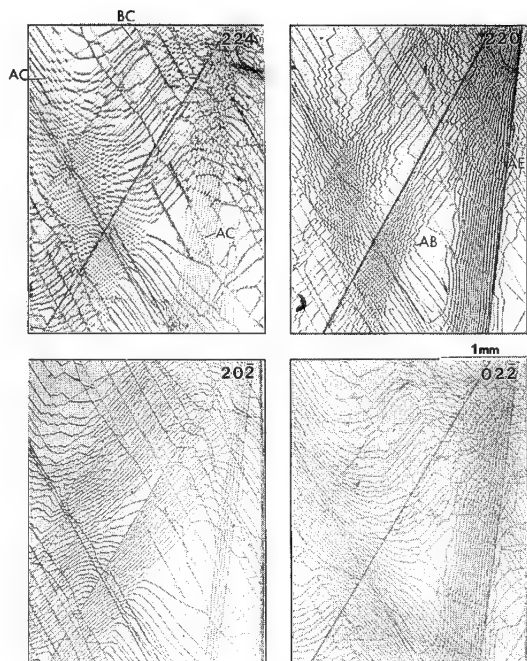


Fig. 2: Dislocation networks in dendritic web silicon obtained by transmission X-ray topography. They correspond to the same network imaged by four different reflections. The sample is 37 mm wide, 98 μm thick and 2.3 meters from the button. The analyzed area is at 10 mm from the nearest dendrite. A characterization of all dislocations lines and interactions observed in these topographs is presented in Fig. 3.

partials [11]. It had been observed in metals and alloys of low stacking-fault energy, but it is observed here for the first time in silicon. Furthermore, the occurrence only of this type of interactions indicates that the \mathbf{b} vector of these lines has the same sign. Another kind of dislocation is also visible. Few dislocations have $\mathbf{b} = \frac{a}{2} \langle \bar{1}10 \rangle$ and they are edge in character since their lines lie on the (111) plane along the $[\bar{1}\bar{1}2]$ direction. Interactions between mixed and edge dislocations have also been shown in Fig. 2, and an analysis concerning the visibility of all observed interactions is presented in

Fig. 3. Dislocation lines due to slip on $[101]$, $[011]$ ($11\bar{1}$) system are not visible in the imaged area (Fig. 2) but they occur, although in a relatively small number. They are short lines in the $[\bar{1}10]$ direction before cross slip to the inclined systems, as observed in the topography L of sample A13 in Fig. 4.

The configuration of the network, specifically in this case, is basically generated by interactions between two sets of long lines running across the web along $[01\bar{1}]$ and $[10\bar{1}]$ directions, which respectively correspond to the intersections of the $(\bar{1}11)$ and $(1\bar{1}1)$ slip planes with the (111) web surface. A curious fact is the length of the lines in comparison with the small web thickness. In such a thin crystal, a dislocation line can glide on its slip plane only for few microns before reaching the surface and being eliminated. However, the web is not a single crystal since an odd number of twin planes, located in a few micron ($\sim 5\mu\text{m}$) thick layer, divides the back and front sides of the web into two crystals with mirror symmetry. Dislocations cannot pass across a crystallographic twin plane with symmetric stress applied, and it was already observed in web crystals as a concentration of dislocations near the twin planes [6,7]. Then, the long lines can be understood as dislocations lying at the intersection of their slip planes with the twin (111) planes. In other words, the long lines observed in the topographs are dislocations moved towards the twins and blocked there, which explain why their Burgers vectors have the same sign. It does not apply to the edge dislocation or to any other dislocation with the \mathbf{b} vector parallel with the twins.

In general, dislocation networks in web silicon are formed by the above mentioned slip systems, although their configuration can be quite different depending on the temperature where they are generated. Two distinct situations may occur. When dislocations are formed at high temperature region near the growth front, they can climb out of their slip planes and long wavy light lines appear (as shown in Fig. 2). Light lines are an indication of little residual stress in the dislocation cores. On the other hand, high stress levels at lower temperature region (throughout and above the lid) can deform the ribbon or, when deformation does not occur, residual stress sometimes remains and it makes dislocation lines darker, not well defined, and the visibility

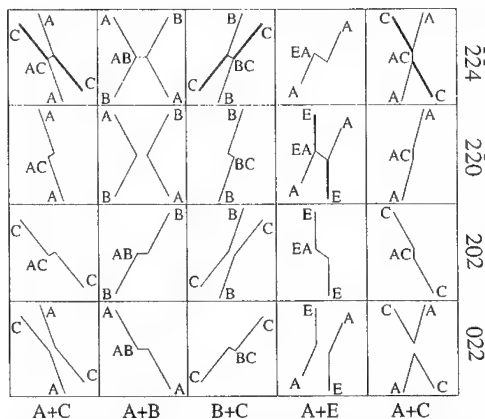


Fig. 3: Image contrast of dislocation interactions in dendritic web silicon for $\bar{2}\bar{2}4$, $2\bar{2}0$, $20\bar{2}$ and $02\bar{2}$ reflections. Dislocation lines with Burgers vector $\mathbf{b}_A = a/2[101]$, $\mathbf{b}_B = a/2[011]$, $\mathbf{b}_C = a/2[110]$, $\mathbf{b}_E = a/2[\bar{1}10]$ are labeled as A, B, C and E, respectively. In Fig. 2, the observed interactions among these lines are labeled AB: $\mathbf{b}_A + \mathbf{b}_B = 3a/6[112]$, AC: $\mathbf{b}_A + \mathbf{b}_C = 3a/6[211]$, BC: $\mathbf{b}_B + \mathbf{b}_C = 3a/6[121]$ and AE: $\mathbf{b}_A + \mathbf{b}_E = \mathbf{b}_B$.

criterion for a dislocation does not apply satisfactorily. Also, when the temperature is not enough for climbing, the Peierls stress is low along $[1\bar{1}0]$, $[10\bar{1}]$ and $[01\bar{1}]$ directions, and dark lines exactly following these directions can be generated (few of them are visible in Fig. 2). Experimentally, all these types of dislocation lines, and other types to be discussed next, have been observed. Sometimes they are superimposed in the same area, in different positions across the web width, or completely isolated. Since networks are variable in their configuration, modification in electrical and mechanical properties of this material should have some correlation with these variations.

2 - DISLOCATION NETWORKS AND MINORITY CARRIER DIFFUSION LENGTH

Three different webs samples, A01, A02 and A13, were imaged by X-ray transmission topography using the $2\bar{2}0$ reflection. Their networks in a $2.8 \times 3.6 \text{ mm}^2$ area at the center and at the midway between the center and each dendrite are shown in Fig. 4. Minority carrier diffusion lengths (MCDL) from SPV measurements performed at the center of these samples are also shown. As expected, the MCDL decreases as the number and the darkness of the dislocation lines increases. In the case of sample A13, with the lowest diffusion length ($2\mu\text{m}$), the dislocation network from a deformed web can be analyzed. By measuring deviation in the angle for the $2\bar{2}0$ reflection as a function of x (Fig. 1) position this deformation can be quantified, and it is shown in Fig. 5. The sample is flat on the left, where few dislocations are present (topography L). As the deformation increases, the blackness of the network does the same due to increases in the dislocation density and in the levels of residual stress. Also, the diffraction condition cannot be kept for any width x intervals and then, only narrow bands are imaged in the topographs from the center (C) and from the right (R). Ribbon deformation has been observed for others ribbon growth techniques where the principal cause was reported to be thermal stress generated by curvature of the vertical temperature profile [2]. In fact, when high stress levels occur in a non-plastic flow region (low temperature) it can deform the web and increase residual stresses.

Improvement in the diffusion length is observed in sample A02. The network is basically formed by long wavy dislocation lines barely following slip directions, and distributed in an average number of 100 lines/ mm^2 (or dislocation density of $10^5/\text{cm}^2$). At both side areas an interesting accumulation of dislocations is visible. They are moving from inclined to transverse $[1\bar{1}0]$ directions and vice-versa, as in a cross slip process. It indicates modification in the stress levels near the web-dendrite boundary. However, the most important features are those broad lines at the center area, running along the growth direction. They are grown-in dislocation, and should occur when a stress induced dislocation climbs towards the melt due to the high temperature and stress levels near the growth front. A large number of grown-in dislocation have edge character (as the edge dislocation in Fig. 2), but not exclusively. They concentrate at the center area where the transverse (x -direction) stress has it highest value [2,3]. The growth front is also a region where

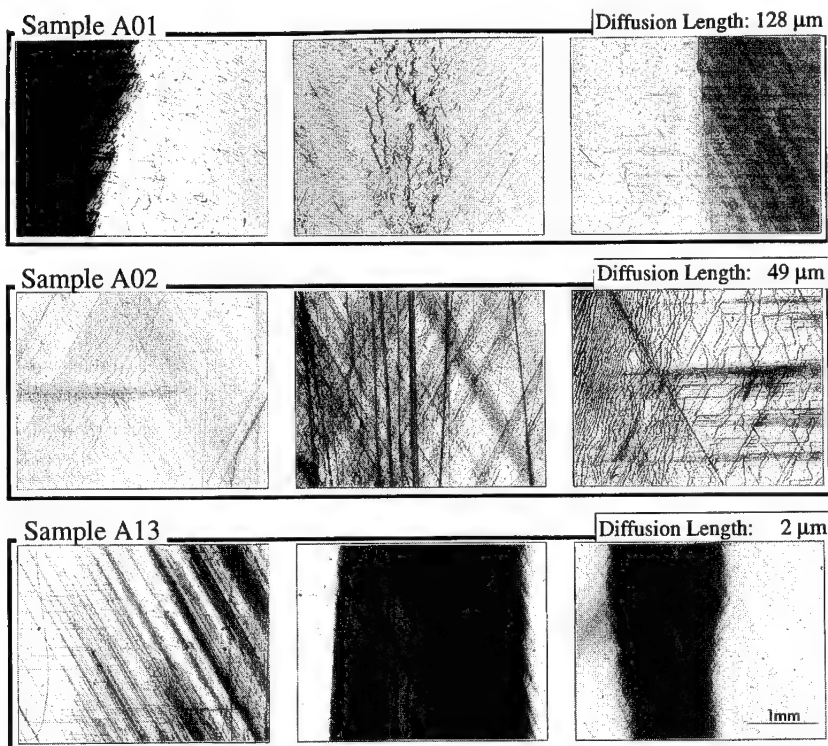


Fig. 4: Dislocation networks in dendritic web silicon obtained by transmission X-ray topography using $2\bar{2}0$ reflection. The networks in a 10 mm^2 area at the center (C) and in between the center and both left (L) and right (R) dendrites are shown. For Sample A13 the exactly position of these areas are indicated in Fig. 5.

oxygen in the melt (from a slowly-dissolving fused silica crucible) are introduced into the solid silicon. Furthermore, dislocations decorated with SiO_x impurity precipitates have been identified as the primarily defect that presently limits the MCDL in web solar cells [6,7]. Then considering the above two facts, dislocations generated near the melt-solid interface and mainly the grown-in dislocations can easily be decorated with silicon oxide precipitates, and be responsible for low MCDL in flat (not deformed) webs.

Finally let us discuss the network of sample A01 where a large area of the web, about 18 mm^2 wide, presents a very uncommon type of network. It has the highest MCDL ($128\text{ }\mu\text{m}$) in spite of its relatively high average number of dislocation lines of 80 lines/mm^2 . However in the case

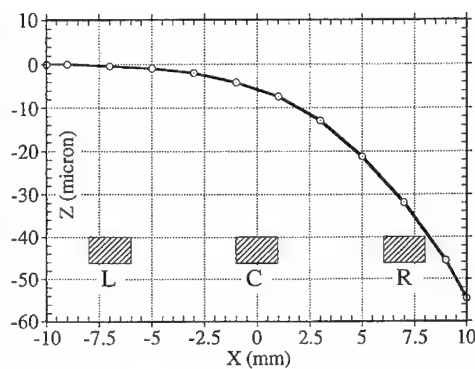


Fig. 5: Shape of a deformed web (sample A13) in cross section view, obtained by measuring deviations in the angular position for the $2\bar{2}0$ reflection as a function of x .

of this sample, since the lines are very short and the dislocation density is low ($8 \times 10^3/\text{cm}^2$), the enormous volume of dislocation-free material justifies the high diffusion length of minority carriers. This type of short lines, with length comparable to the web thickness, are exactly as the lines should be in such a thin single crystal, i.e., their occurrence could be easily understood if no twins were present across the web thickness. Using a microscope we analyzed the cross section cleaved normal to $[11\bar{2}]$ growth direction. It was observed that twins are absent in the center area. The heavily twinned region is about $3\text{ }\mu\text{m}$ thick, it is well centered in the dendrites and from there it continuously gets closer to one web surface until leaves the web near the same position where the abrupt changes in the network are observed in the L and R area. In the portion of these areas where the twins are still in the web, the dislocations are dark and not well defined indicating that some residual stress is stored in the lattice. These results show clearly the effects of the twins on the dislocation networks: they block the movement of dislocations which makes the material harder. Consequently the strain becomes smaller and the level of residual stress increases. The conditions that can lead to web crystals with twins out of the cross section center, or even leaving the web, are unknown. Speculation have been made [5] that the twins position could be varied by moving the ribbon back and forth during growth. Webs without any twins also have been found after ribbon buckling but it is not the case here, since sample A01 is flat.

CONCLUSIONS

In n-type ($\sim 20\text{ }\Omega\text{-cm}$) web crystals, the minority carrier diffusion length is well-correlated with dislocation density, which makes the control of networks a fundamental task in order to produce dendritic web silicon solar cells of high conversion efficiency. Twin boundaries (usually located midway between both surfaces of a web crystal) severely impede slip movement, thereby causing dislocations to be pushed up against the boundaries and giving rise to exceedingly long dislocation cores (~ 100 times the thickness). It increases the need for maintaining low levels of thermal stress during growth. A combination of thermal stress modeling with X-ray topography measurements is a powerful procedure to improve web crystal quality, since the analysis of the shape of the dislocation cores is useful in determining the temperature at which the dislocations were introduced in the growth process.

ACKNOWLEDGMENTS

The authors gratefully acknowledge R.H. Herlocher for making SPV measurements at the Center for Electronic Materials and Processing at the Pennsylvania State University, and also acknowledge the partial financial support provided by CNPq, Brazil.

REFERENCES

- [1] R.G. Seidensticker, J. of Crystal Growth **39**, 6 (1977).
- [2] R.W. Gurtler, J. of Crystal Growth **50**, 69 (1980).
- [3] R.G. Seidensticker and R.H. Hopkins, J. of Crystal Growth **50**, 221 (1980).
- [4] R.H. Hopkins and R.G. Seidensticker, J. of Crystal Growth **65**, 307 (1983).
- [5] D.L. Barrett, E.H. Myers, D.R. Hamilton and A.I. Bennett, J. Electrochem. Soc.: Solid State Science **118** (6), 952 (June 1971).
- [6] D.L. Meier, R.H. Ropkins and R.B. Campbell, J. Propulsion **4** (6), 586 (1988).
- [7] K. Joardar, C.O. Jung, S. Wang, D.K. Schoder, S.J. Krause, G.H. Schwuttke and D.L. Meier, IEEE Transactions on Electron Devices **35**(7), 911 (1988).
- [8] A. Baghdali, R.W. Gurtler, R.N. Legge, R.J. Ellis and B.L. Sopori, in: Conf. record 13th IEEE Photovoltaic Specialists Conf. 363 (IEEE, New York, 1978).
- [9] A.R. Lang, Acta Cryst. **12**, 249 (1959).
- [10] A.M. Goodman, J. Appl. Phys. **32**, 2550 (1961).
- [11] S. Mahajan, Metallurgical Transactions **6A**, 1877 (1975).

ON THE RECOMBINATION ACTIVITY OF OXYGEN PRECIPITATION RELATED LATTICE DEFECTS IN SILICON

J. VANHELLEMONT*, A. KANIAVA***, M. LIBEZYNY*, E. SIMOEN*, G.
KISSINGER***, E. GAUBAS**, C. CLAEYS* AND P. CLAUWS****

*IMEC, Kapeldreef 75, B-3001 Leuven, Belgium

**Vilnius University, Sauletekio 10, 2054 Vilnius, Lithuania

***Institute of Semiconductor Physics, D-15204 Frankfurt (Oder), Germany

****University of Gent, Krijgslaan 271 S1, B-9000 Gent, Belgium

ABSTRACT

The recombination activity of oxygen precipitation related lattice defects in p- and n-type silicon is studied with photoluminescence (PL) and microwave absorption (MWA) techniques. A direct correlation is observed between the amount of precipitated oxygen and the extended defect density on one hand and the minority carrier lifetime and PL activity on the other hand. The PL analyses show as dominant features in the spectra the D1 and D2 lines. The relative amplitude of the D-lines in the different samples is investigated as a function of the oxygen content, defect density and excitation level. The results are correlated with those of complementary techniques and are interrelated on the basis of Shockley-Read-Hall (SRH) theory.

INTRODUCTION

It has been known already for more than thirty years that the amount and the state of oxygen in Czochralski grown and heat treated silicon have an important impact on the electrical properties of the material both with respect to carrier lifetime and mobility. The behaviour of oxygen in silicon during thermal treatments has therefore been studied extensively with an armada of chemical, structural and electrical characterisation tools. References hereon can be found in a recent review paper¹. Despite this huge effort it is still not clear what is really causing the strong reduction of carrier lifetime after heat treatments of oxygen-rich silicon: are it the silicon oxide precipitates and more in particular their interface with the silicon matrix or are it the extended defects, i.e. dislocation loops and stacking faults often surrounding the precipitates which are the lifetime killers? To complicate further the picture, many of the early experiments have probably not been performed under the cleanest conditions leading to the unintentional introduction of metals, extremely efficient lifetime killers, during the heat treatments.

In the present paper results are presented on the recombination activity of oxygen precipitation related extended defects studied by photoluminescence and carrier lifetime measurements. These results are part of a more extended study involving also structural and chemical characterisation as well as the study of diode characteristics and low frequency noise spectroscopy²⁻⁴.

EXPERIMENTAL

n⁺p diodes are fabricated on p-type Czochralski-grown wafers with interstitial oxygen contents ranging from $7 \times 10^{17} \text{ cm}^{-3}$ to $11 \times 10^{17} \text{ cm}^{-3}$. Before the diode processing different thermal pre-treatments are performed. A set of n-type Cz silicon substrates with similar oxygen contents received the same thermal treatments as used in the diode process but no diodes were fabricated on these substrates. A detailed description of the diode process can be found elsewhere⁴. In a second

experiment the impact of the defect type on the recombination activity is evaluated by performing different one and two step anneals on wafers with different oxygen contents as listed in Table I.

After removal of the diode structures by etching and mechanical polishing, the minority carrier lifetime under moderate injection conditions ($\approx 5 \times 10^{15}$ carriers cm^{-3}) is determined using MWA measurements. A pulsed Nd:YAG laser is used to create excess carriers. The effective carrier lifetime is derived from a least squares fit of the asymptotic part of the excess carrier decay.

PL analyses are performed to assess the defect related radiative recombination. A Bio-Rad instrument is used, based on a Fourier transform spectrometer equipped with a liquid nitrogen cooled Ge detector. PL spectra are recorded at 4K using an Ar^+ -ion laser as excitation source.

The interstitial oxygen concentration before and after processing is determined from the absorption at room temperature of the 1106 cm^{-1} band, using a calibration factor of $3.14 \times 10^{17} \text{ cm}^{-3}/\text{cm}^{-1}$. FTIR is performed with a Bruker IFS 66v equipped with cooled MCT-detector.

The TEM analyses are performed on the Jeol 1250 microscope of the university of Antwerp (UCA) with an electron acceleration voltage of 1000 kV. Extended defect densities (N_{LST}) in the substrate are determined by infrared laser scattering tomography (LST) using a MILSA IRHQ-2 instrument of RATOC with a Nd-YAG laser of 1070 nm wavelength.

OBSERVATIONS AND DISCUSSION

TEM reveals typical oxygen precipitation related defects after the full diode process: SiO_x precipitates with or without prismatic punching systems or Frank type stacking faults with densities depending on the initial oxygen content and pretreatment. In the two step annealed samples the density of one of these defect types is intentionally enhanced.

Laser scattering tomography is a more suitable technique to determine the extended defect densities than TEM as it allows to cover easily a density range from 10^6 to a few times 10^{10} cm^{-3} which is usual the range of silicon oxide precipitate densities in silicon⁵. Typical examples of observation are shown in Fig. 1 for a high oxygen content wafer after a full diode process. At higher magnification LST allows also to identify stacking faults and prismatic punching systems⁶. Some prismatic punching systems are also visible in Fig. 1 (right) after an internal gettering pretreatment before the diode process.

The results of the effective lifetime measurements are summarised in Fig. 2 as a function of N_{LST} . A clear linear correlation between the inverse MWA carrier lifetime and N_{LST} is observed for samples which received the same thermal treatments. The lifetime can however be strongly different for wafers with the same N_{LST} (and amount of precipitated oxygen) but a different thermal history. This suggests that not the SiO_x precipitates (which are mainly observed by LST) but the type (stacking fault or dislocation) and density of extended defects determine the carrier lifetime. Choosing the appropriate pretreatment allows to have a large density of precipitates without having also a high dislocation density. This is illustrated by the point jumping out of the other measurements in Fig. 2. TEM inspection and preferential etching revealed a 10 times lower density of large stacking faults in that sample than in the samples with a comparable N_{LST} .

Table I: Experimental matrix for the one and two step anneals. A = 800°C in N_2 for 24h. B = A + 1100°C in O_2 for 3 h. C = 1050°C in O_2 for 20h + A.

Label	Initial O_i ($\times 10^{17} \text{ cm}^{-3}$)	Anneal	Final O_i ($\times 10^{17} \text{ cm}^{-3}$)	τ_{eff} (μs)	Precipitates ($\times 10^9 \text{ cm}^{-3}$)	SF density ($\times 10^9 \text{ cm}^{-3}$)	N_{LST} ($\times 10^{10} \text{ cm}^{-3}$)
c1	8.8	A	8.5	31	8.4	no	0.065
c6	10.5	A	10.4	25	8.1	no	< 0.01
c5	10.7	B	3.2	0.6	8.0	3.8	> 18
c11	8.8	B	7.2	16	9.9	0.25	17
c2	10.6	C	9.5	7	0.49	0.0082	0.8
c12	10.9	C	6.0	0.4	5.6	0.049	7.4

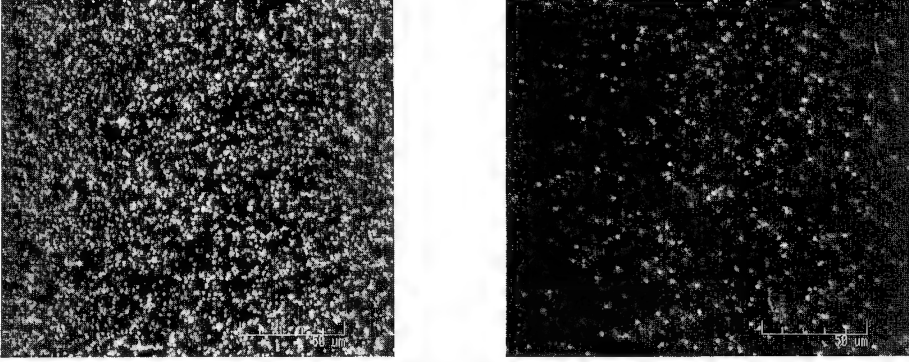


Fig. 1: LST image illustrating the defect densities which can be observed after a full diode process. The probed layer thickness is about 5 μm . Images are shown for a n-type high oxygen content wafer with (right) and without (left) internal gettering treatment before the diode process. The initial oxygen content is about 10^{18} cm^{-3} .

As the wafers are relatively thin and the surfaces were not passivated, the effective carrier lifetime determined from the asymptotic part of the carrier decay is strongly affected by surface recombination. Without surface passivation, the surface recombination lifetime is of the order of 10 μs . For that reason only for the samples with much smaller τ_{eff} , the surface recombination is negligible and the effective lifetime can be assumed to be equal to the bulk carrier lifetime.

The SRH lifetime is injection level dependent and $\tau_{\text{SRH}} \approx \tau_r$ for low level injection. τ_r is the microscopic lifetime of minority carriers which is inversely proportional to the concentration of recombination centres N_t and their capture cross-section σ , with in the first order approximation

$$\tau_{\text{SRH}} \approx \frac{1}{\sigma v_{\text{th}} N_t} . \quad (1)$$

v_{th} ($\approx 10^7 \text{ cm s}^{-1}$) is the thermal velocity of the carriers.

In the p-type substrates with high initial oxygen content, DLTS reveals an electron (minority) trap near to mid-gap with a position in the bandgap of $E_c - 0.43 \text{ eV}$ and an estimated capture cross-section σ_n at 240 K of 10^{-14} cm^2 . Chan et al. reported an electron (minority) trap with similar trap parameters and density after a diode process on p-type Cz silicon⁷. An electron (majority) trap with the same position in the bandgap was recently also reported in n-type Cz silicon by Kim et al⁸. DLTS analyses performed on the n-type substrates in the present study, both after a full diode process and after the double step anneal revealed a majority carrier trap level at $E_c - 0.37 \text{ eV}$ ($\pm 0.03 \text{ eV}$) and at $E_c - 0.40 \text{ eV}$ ($\pm 0.01 \text{ eV}$), respectively, in good agreement with the results on the p-type substrates. The trap density is $6.5 \times 10^{11} \text{ cm}^{-3}$ and $1.2 \times 10^{12} \text{ cm}^{-3}$, respectively.

For the high oxygen content wafers after diode processing $\tau_r \approx 0.75 \mu\text{s}$. Assuming that a trap at $E_c - 0.4 \text{ eV}$ with a trap density of about 10^{12} cm^{-3} is responsible for the carrier lifetime, one can calculate $\sigma \approx 10^{-13} \text{ cm}^2$ at room temperature, in fair agreement with $\sigma \approx 10^{-14} \text{ cm}^2$ at 240K obtained from a standard Arrhenius analysis of the DLTS results⁴.

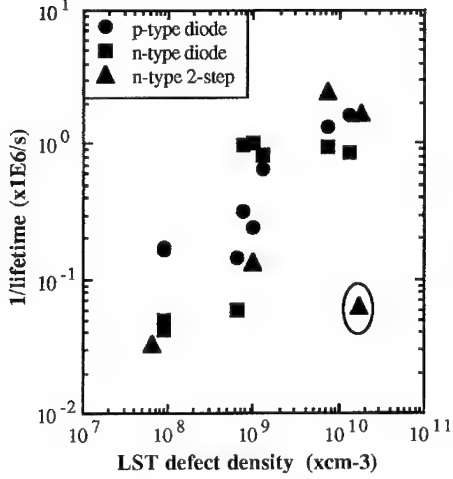


Fig. 2: Inverse carrier lifetime determined with MWA as a function of N_{LST} . For substrates containing similar extended defects, a linear correlation is observed. The sample with much less dislocations per precipitate jumps out.

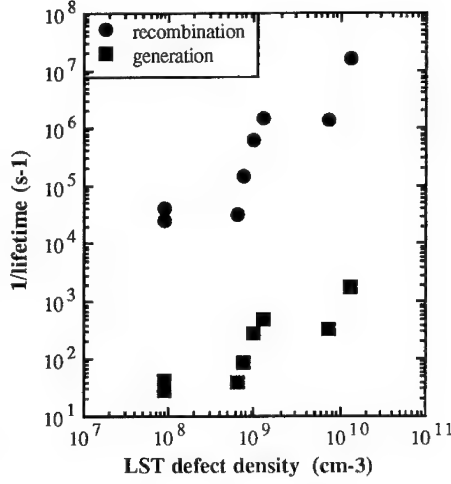


Fig. 3: Inverse τ_g and τ_r determined from diode characteristics on p-type Si substrates as a function of N_{LST} .

From the I/V characteristics of the diodes, information can be obtained on the generation and recombination lifetimes. The generation lifetime τ_g can in principle be calculated from the generation current density J_g which is derived from the reverse current density J_R (obtained after subtraction of the perimeter component). The recombination lifetime τ_r is calculated from the forward current density of the conventional diodes extrapolated to zero bias and corrected for perimeter effects and diode ideality³. Fig. 3 shows the inverse (= proportional to the trap density) generation and recombination lifetimes, τ_g and τ_r , respectively, calculated from the diode characteristics as a function of N_{LST} .

In the presence of trapping centres the generation and recombination lifetime are connected by the relationship

$$\tau_g \approx \tau_r \exp\left(\frac{|E_T - E_i|}{kT}\right) \quad (2)$$

E_T is the energy level of the trapping centre, E_i is the intrinsic level. From the ratio of τ_g and τ_r one can thus estimate E_T . For the diodes where there is a clear decrease of the lifetime one obtains $E_T \approx E_i \pm 0.16\text{eV}$ or $E_c - 0.4\text{eV}$ and $E_v + 0.4\text{eV}$ as possible positions in good agreement with the DLTS results.

Chan et al⁷ used a power law relation to fit generation lifetime τ_g values with trap density N_t

$$N_t = A\tau_g^{-n} \quad (3)$$

With $n \approx 1$, $N_t \approx 10^{12} \text{ cm}^{-3}$ and τ_g between $30 \mu\text{s}$ and $500 \mu\text{s}$, observed for high oxygen content wafer with and without internal gettering before the diode process, one obtains A between 3×10^7 and $5 \times 10^8 \text{ s cm}^{-3}$, in good agreement with reported values which range from 2 to $4.5 \times 10^8 \text{ s cm}^{-3}$.

As illustrated in Fig. 4, PL analyses reveal in the samples with medium and high oxygen content, as most prominent features the well known D1 and D2 lines at 807 and 874 meV , respectively⁴. The origin of the D bands in silicon is believed to be either linked with impurity-related optical transitions near the dislocation core or to be an intrinsic property of the dislocation. In the last case, the position of the PL lines might be correlated with the edge component b_e of the Burgers vector of the dislocations and one can write in first order approximation⁹

$$E_{PL} = E_g - A \left(\frac{b_e}{a} \right)^2. \quad (4)$$

a is the lattice constant of silicon and A a constant which is related to the deformation potential and the effective carrier mass.

The present study suggests a strong correlation between the D2 line ($E_{PL} = 874 \text{ meV}$) and the presence of Frank type SF's with $\left(\frac{b_e}{a} \right)^2 = \frac{1}{3}$. D1 ($E_{PL} = 807 \text{ meV}$) might correspond with 90° dislocations ($\left(\frac{b_e}{a} \right)^2 = \frac{1}{2}$), the dominant type in prismatic punching systems. Substitution in equation (4) leads to $A \approx 0.4$ and $E_g \approx 1.01 \text{ eV}$.

The D1 and D2 energies are also in good agreement with the $E_T \approx E_c - 0.4 \text{ eV}$ level which is observed with DLTS. A rough approximation of the energy level of the radiative recombination center is indeed given by $E_g - E_{PL} \approx 0.36 \text{ eV}$.

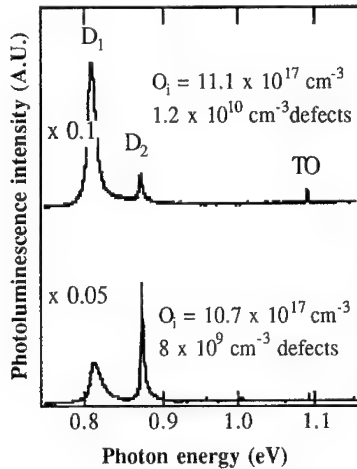


Fig. 4: PL spectra obtained on substrates containing different defects. For the upper spectrum (p-Si) prismatic punching systems dominate while in the lower one (n-Si), the dominant extended defects are Frank SF's.

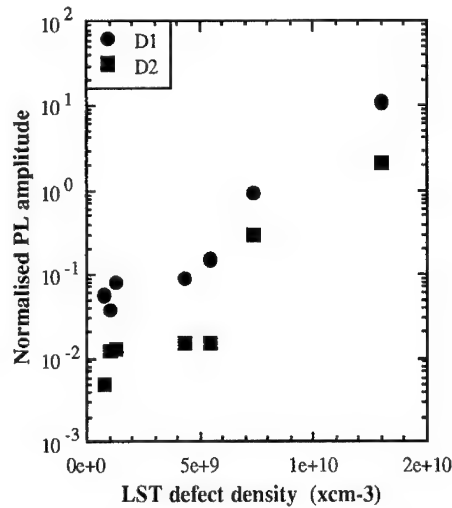


Fig. 5: D1 and D2 amplitudes normalised with respect to the Si free exciton versus N_{LST} .

A quantitative correlation between the observed D1 and D2 line intensities and the defect densities is not straightforward as illustrated in Fig. 5 and more detailed investigations of the PL intensity as a function of the level of excitation are required¹⁰. A simple model can be assumed in which one recombination centre and non-radiative processes for excitons are active¹¹. An example of a fit of the measured PL intensity as a function of the excitation power is given in Fig. 6.

The PL results in correlation with the DLTS and TEM observations thus suggest that D1 and D2 are connected with the dislocation complexes surrounding the silicon oxide precipitates and that they might be associated with two electron traps at about $E_c - 0.2$ and $E_c - 0.4$ eV.

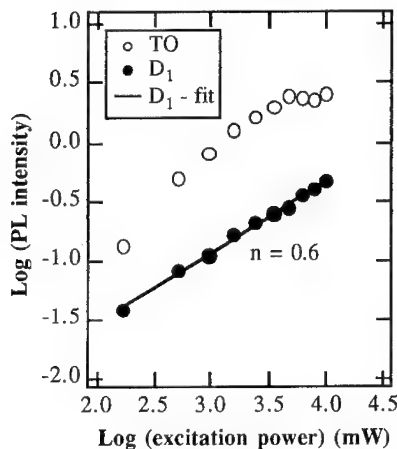


Fig. 6: Dependence of the PL intensity at 4.2 K on the excitation power for the same sample as in Fig. 1a.

CONCLUSIONS

It is shown that the change of electrical substrate properties due to oxygen precipitation is related with the formation of dislocations and stacking faults. Both the observed carrier recombination at room temperature and the exciton recombination observed at 4.2 K are related with a recombination center at $E_c - 0.4$ eV which is connected with the presence of extended defects. The same center is active both in p- and n-type silicon in agreement with other reports in literature. The obtained results can be correlated with diode characteristics based on straightforward application of SRH theory.

ACKNOWLEDGEMENT

Part of this work was performed with financial support from the National Science Foundation (NFWO project 4.0007.93) and within ESTEC Contract 8615/90/NL/PM(SC).

REFERENCES

1. H. Bender and J. Vanhellemont, "Oxygen in Silicon", in Handbook on Semiconductors, ed. T.S. Moss, Vol. 3, ed. S. Mahajan, Elsevier Science B.V., pp. 1637-1753 (1994)
2. E. Simoen, G. Bosman, J. Vanhellemont and C. Claeys, Appl.Phys.Lett., May 1995.
3. J. Vanhellemont, E. Simoen and C. Claeys, Appl.Phys.Lett, May 1995.
4. J. Vanhellemont, E. Simoen, A. Kaniava, M. Libezny and C. Claeys, J. Appl. Phys., June 1995.
5. K. Moriya, K. Hirai, K. Kashima and S. Takasu, J. Appl. Phys. **66**, 5267 (1989).
6. G. Kissinger, J. Vanhellemont, C. Claeys and H. Richter, submitted for publication in J. Crystal Growth.
7. S.S. Chan, C.J. Varker, J.D. Whitfield and R.W. Carpenter, Mat. Res. Soc. Symp. Proc. Vol. **46**, 281 (1985).
8. H.S. Kim, E.K. Kim and S.K. Min, J. Appl. Phys. **69**, 6979 (1991).
9. Y. Lelikov, Y. Rebane, S. Ruvimov, D. Tarhin, A. Sitnikova and Y. Shreter, Materials Science Forum Vol. **83-87**, 1321 (1992).
10. M. Libezny, A. Kaniava, G. Kissinger and J. Vanhellemont, to be presented at "Analytical Techniques for Semiconductor Materials and Process Characterization II" (ALTECH '95), and to be published in The Electrochem.Soc. Proc. Vol. (1995).
11. H. Erzgräber and K. Schmalz, submitted for publication in Appl.Phys.Lett..

CHARACTERIZATION OF GROWTH DEFECTS IN CdZnTe SINGLE CRYSTALS BY SYNCHROTRON WHITE BEAM X-RAY TOPOGRAPHY.

H. Chung*, B. Raghothamachar*, J. Wu*, M. Dudley*, D. J. Larson, Jr.**, and D. C. Gillies***

* Dept. of Materials Science & Engineering, SUNY at Stony Brook, NY 11794-2275.

** Northrop Grumman Research & Development, Bethpage, NY 11714.

***NASA, Marshall Space Flight Center, Huntsville, AL 35812.

ABSTRACT

Synchrotron white beam X-ray topography has been used to characterize structural defects in microgravity grown CdZnTe single crystals. Defects such as dislocations, slip bands, 180° rotation twins, precipitates and subgrain boundaries are observed but their density is much lower than those in crystals grown under normal gravity. The observed results also indicate that the defect structures of the as grown crystals are strongly influenced by cooling rates. X-ray transmission topographs recorded from regions grown at different cooling rates show that the dislocation density in rapidly cooled regions is higher than that in slowly cooled regions. The formation of dislocations is presumably attributed to the thermal stress caused by accelerated cooling rates, which is greater than the critical resolved shear stress. As the cooling rate is accelerated, the magnitude of thermal stress is increased and more dislocations are formed to relieve the accumulated lattice strain. In addition, if the cooling rates are increased further, the accentuated thermal stresses can give rise to more pronounced deformation processes, comprising the formation of dislocation slip bands, as confirmed by the extensive slip bands revealed by the X-ray reflection topographs.

INTRODUCTION

CdZnTe, a technologically important II-VI compound semiconductor, is the leading candidate material for use as substrates for the growth of HgCdTe epitaxial layers because its infrared transparency allows backside illumination of HgCdTe infrared detector arrays. By varying the Zn content, lattice matching with any HgCdTe alloy composition can be achieved. The overall performance, uniformity and operability of HgCdTe infrared focal plane arrays are affected by the presence of defects such as dislocations especially in the form of subgrain boundaries, twins, etc. originating mainly, from material growth [1]. These defects produce substantial amounts of dark current that limits device performance [2]. Such defects that affect device performance are known to propagate into the HgCdTe layers from the underlying CdZnTe substrate during epitaxial growth [3]. Hence, it is imperative to improve the structural perfection of the CdZnTe substrates. Single crystal substrates are usually obtained from bulk crystals grown by melt growth techniques. The defect structures in such crystals are highly sensitive to growth conditions. For example, dislocations can multiply by slip and subgrain boundaries are formed by gliding and climbing of dislocations under the influence of thermal gradient induced stresses[4]. Twinning can occur through growth accidents resulting from fluctuations in the growth rate at the liquid-solid interface[7]. Post solidification cooling rate is also an important parameter in reducing the density of slip defects [8]. Thus, growth of a low defect density crystal involves the consideration and control of numerous factors that may or may not be independent of each other.

In this study, Synchrotron White Beam X-ray Topography (SWBXT)[5,6] has been utilized to characterize growth defects in Bridgman grown CdZnTe single crystals. Defects in the as-grown boules are characterized and the correlation between the observed defects and the growth conditions used is discussed.

EXPERIMENTAL

Two boules (labeled GCRC-1 and GCRC-2) were grown in the Crystal Growth Furnace(CGF) on space shuttle flight USML-1 using the seeded Bridgman-Stockbarger method of crystal growth. The details of the growth technique are explained elsewhere [9]. The surface of the GCRC-1 boule was initially thoroughly examined by reflection topography in the as-grown condition. The crystal was then oriented and sliced such that the wafer surfaces were parallel to the (111) plane closest to the growth axis of the crystal. Selected sliced wafers from different regions of the boule were studied by the grazing Bragg reflection geometry. From the boule GCRC-2, one of the sliced wafers (also with surface parallel to (111) plane) was thinned down to a thickness of 180 μ m for transmission topography studies.

SWBXT experiments were carried out at the Stony Brook Synchrotron Topography Station, Beamline X-19C, at the National Synchrotron Light Source(NSLS), Brookhaven National Laboratory. In this study, a specific Bragg reflection geometry has been developed to fully utilize the broad wavelength range of the synchrotron source as well as to minimize the effects of harmonic contamination. Using this reflection geometry, high quality multiple topographic images covering a wide range of X-ray penetration depths (0.5~10.3 μ m) and diffraction rocking curve widths (0.7~17 arc seconds) can be obtained in a single exposure. To prevent possible surface deterioration of the crystals due to prolonged exposure to radiation, the higher wavelength components of the synchrotron source, which are easily absorbed, were selectively removed by employing a filter consisting of a few hundred micrometers of aluminum. All images were recorded on 8" \times 10" Kodak SR5 high resolution X-ray film.

RESULTS

Transmission topographs recorded from different regions of a wafer sliced from GCRC-2 are shown in figures 1(a) and (b). The cooling rate was not constant but varied (accelerated) down the length of the boule. The former topograph recorded from a region cooled with a relatively low post solidification cooling rate shows a very low dislocation density, with individual dislocations (**D**), capable of being resolved. Other features such as the singular dark spots are characterized as Te precipitates (**P**). The straight lines lying parallel to the $[\bar{1}10]$ directions are characterized as lamellar 180° rotation twins (**T**) about the $[11\bar{1}]$ plane normal. Figure 1(b) shows a topograph recorded from a more rapidly cooled region of the same sample. It is obvious that this region exhibits a relatively higher dislocation density in addition to the presence of Te precipitates. The variation in the dislocation density with cooling rate clearly indicates that the cooling rate could be an important factor in determining the overall growth dislocation density.

Figures 2 and 3 show reflection topographs recorded from the as-grown GCRC-1 boule and the sliced wafers #4(3(a)) and #7(3(b)) respectively. Defect structures studied in these topographs are characterized as follows:

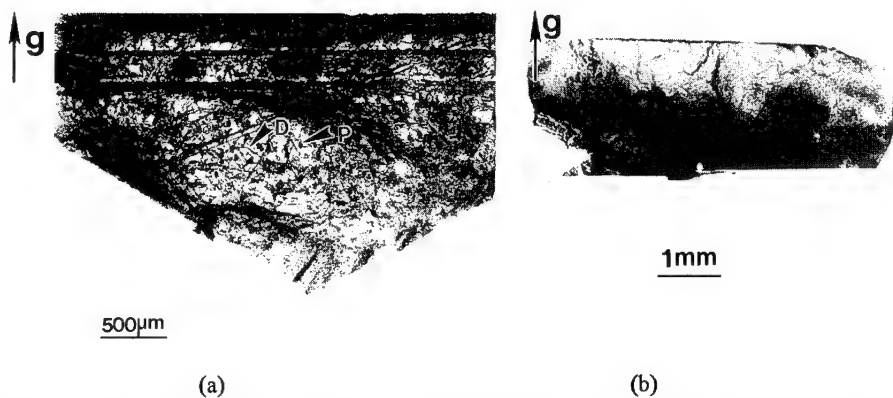


Figure 1. Transmission topographs ($g = \bar{1}\bar{1}3$, $\lambda = 0.42\text{\AA}$) recorded from different regions of a wafer sliced from GCRC-2: (a) from a slowly cooled region of the boule showing individual dislocations (D) and precipitates (P) and (b) from a rapidly cooled region of the boule.

Slip bands

In GCRC-1, the surface of the boule shows extensive slip band networks in regions that were in partial or full contact with the ampoule. Figure 2 shows slip band networks observed from different regions on the outer surface. To investigate slip band configurations in the interior of the boule, one wafer (#4) sliced from this boule is imaged as shown in figure 3(a). Two sets of slip bands (S_1 and S_2) initiated from the peripheral regions and extended into the interior of the wafer. By analyzing projected directions in different reflections, the slip bands (S_1 and S_2) can be

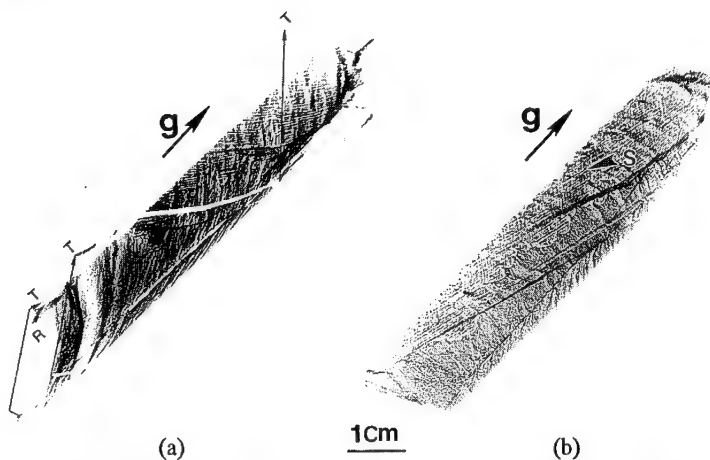


Figure 2. Reflection topographs recorded from the outer surface of GCRC-1 showing twins (T) and slip bands (S)

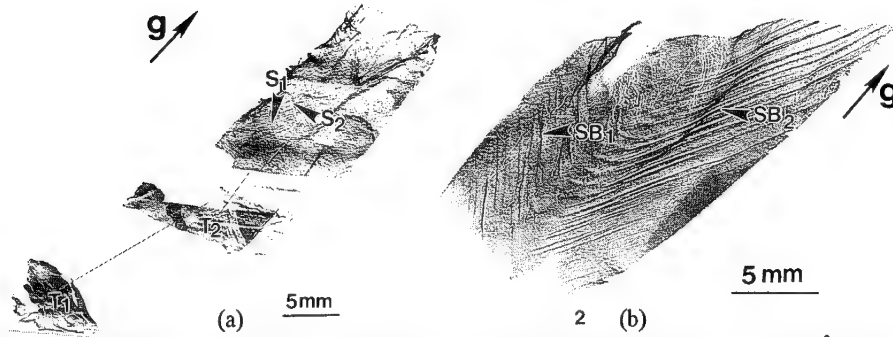


Figure 3. Reflection topographs recorded from (a) CdZnTe wafer #4 ($g=133$, $\lambda=0.98\text{\AA}$) and (b) CdZnTe wafer #7 ($g=044$, $\lambda=0.76\text{\AA}$) showing slip bands (S), twins (T) and subgrain boundaries (SB). Both wafers are sliced from GCRC-1.

characterized as belonging to the $[10\bar{1}]/(\bar{1}11)$ and $[0\bar{1}1]/(1\bar{1}1)$ slip systems respectively. The peripheral regions show localized orientation contrast (A_1) associated with distortion, which suggests high degrees of stress concentrated in this region due to wall contact and some of the slip bands appear to have been generated from the distorted region and propagated into the interior. In addition, thermal stresses generated by radial temperature gradients during crystal growth and cooling processes can also induce slip. Slip bands generated during post growth cooling have been observed in ZnTe crystals [10].

Subgrain boundaries

Figure 3(b) is a reflection topograph recorded from wafer #7 showing the extensive subgrain boundaries. It is worth noting that two sets of long and straight subgrain boundaries (SB_1 and SB_2) parallel to the $[\bar{1}10]$ and $[0\bar{1}1]$ directions, respectively, are observed. The overlapping or separation of the images is attributed to the different senses of tilt between neighboring subgrains. The tilt angles, which can be estimated from $\Delta\theta=X/2d$, where X is the image width of subgrain boundaries and d is the specimen-film distance, is determined to be of the order of 60~70 arc seconds. Numerous subgrain boundaries generated near the ampoule wall and propagating into the interior of the wafer as shown in Figure 3(b) suggest that the subgrain boundaries could be formed due to a combination of stresses associated with constrained growth and thermal stresses induced by rapid cooling.

Twins

Two twins, T_1 and T_2 , revealed by orientation contrast, are observed as shown in Figure 3(a). One of the twins (T_1) appears to have nucleated from the shoulder region of the boule where a bubble is present. This indicates that the nucleation of the twin occurred during growth due to disturbance at the growth interface. Detailed analyses of diffraction patterns recorded from these twinned regions reveal that the twins, T_1 and T_2 , are of 180° rotation type about $[\bar{1}11]$ and $[111]$ plane normals, respectively. The twinned regions do not show extensive slip bands similar to those observed in the matrix, which indicates that twinning processes may occur before the generation

of slip bands and the twin boundaries act as barriers for these slip dislocations. This phenomenon has also been observed in the growth of InP[12] and ZnTe crystals[10].

Precipitates

Te precipitates are observed clearly as singular dark spots in the transmission topographs shown in figure 1. The retrograde solubility of Te in solid CdZnTe [11] results in the supersaturation of Te that precipitates during cooling. The size and density of Te precipitates is strongly influenced by the cooling rate. Faster cooling rates result in higher density of Te precipitates due to spontaneous nucleation at various sites and smaller precipitate size because of insufficient time for the Te to diffuse and coalesce. This nature of precipitate distribution is observed in the transmission topographs shown in figure 1.

DISCUSSION

Solid solution strengthening of CdTe by doping with Zn is expected to reduce dislocation density by providing barriers to dislocation motion during post solidification cooling [4]. However, as a result of the high cooling rates employed due to time constraints imposed by the space flight schedule, the thermal stresses generated therefrom appear to have exceeded the yield strength of the material resulting in the formation of extensive deformation microstructures in some regions. Dislocations originating from sources such as dislocations propagating from the seed, dislocation loops formed by condensation of point defects during cool down and dislocations formed to accommodate surface strains due to contact with the ampoule wall can be multiplied under the influence of thermal stresses induced by rapid cooling. This is observed in the transmission topographs recorded from GCRC-2 (figure 1), in which dislocation density increases with cooling rate. Moreover, if cooling rates are increased further, the accentuated thermal stresses can give rise to more pronounced deformation processes, comprising the formation of dislocation slip bands as observed in GCRC-1. The dislocations can also realign to form energetically preferred configurations by the process of dislocation polygonization involving dislocation movement by gliding and climbing to form tilt subgrain boundaries [11]. Supersaturated vacancies and thermal stresses induced by rapid cooling can facilitate dislocation climbing and gliding during polygonization. This indicates that the formation of extensive subgrain boundaries may also arise from effects associated with rapid cooling. Observations, therefore, suggest that post solidification cooling strongly influences the final defect microstructure in the as-grown crystals.

CdZnTe like many other crystals with zinc blende structure is prone to twinning. During melt growth, nucleation of a growth twin has been observed to occur at a perturbation of the growth interface such as sudden changes in diameter or growth rate [7]. In GCRC-1, the nucleation of a twin at the shoulder of the boule is observed, which appears to be consistent with earlier observations. The uneven distribution of slip bands in the matrix and twinned region indicates that the twin boundary acts as a barrier to slip.

CONCLUSIONS

Defects in CdZnTe crystals grown by the Bridgman Stockbarger method in microgravity have been studied by SWBXT techniques. The reflection geometry used proved to be extremely useful

in non-destructively characterizing the defect microstructures and distributions in the crystals. Defects such as dislocations, subgrain boundaries, twins and precipitates were observed. Thermal gradient induced stresses associated with accelerated cooling rates as well as constrained growth due to contact with the ampoule wall can be attributed to the formation of extensive slip bands observed in GCRC-1. Moreover, the formation of extensive subgrain boundaries may also be a result due to rapid cooling. These observations strongly suggest that modification of the cooling rate has a significant effect on the final crystalline perfection of such materials. A growth twin (T_1) is nucleated near the shoulder region where sudden change in diameter causes perturbations in the growth interface. It is also observed that the twin boundary acts as a barrier to the propagation of slip dislocations. The variation in the density and size of Te precipitates in regions with different cooling rates is also observed.

ACKNOWLEDGMENTS

Work supported by NASA Marshall Space Flight Center under contracts NAS8-38147, NAG8-891, NCC8-53 and NCC8-48, and the Universities Space Research Association under contract 3536-03. Topography was carried out at the Stony Brook Synchrotron Topography Facility, beamline X-19C, at the National Synchrotron Light Source, at Brookhaven National Laboratory, which is supported by the Department of Energy.

REFERENCES

- [1] S.M. Johnson, D.R. Rhiger, J.P. Rosbeck, J.M. Peterson, S.M. Taylor, M.E. Boyd, J. Vac. Sci. Technol. **B10**, 1499 (1992).
- [2] R.S. List, J. Electron. Mater. **22**, 1017 (1993).
- [3] D.J. Larson Jr., R.P. Silberstein, D. Di Marzio, F.C. Carlson, D. Gillies, G. Long, M. Dudley, J. Wu, Semiconductor Sci. & Technol. **8**, 911 (1993).
- [4] R. S. Rai, S. Mahajan, D.J. Michel, H. H. Smith, S. McDevitt, C.J. Johnson, Mater. Sci. & Eng. **B10**, 219 (1991).
- [5] M. Dudley in *Applications of Synchrotron Radiation Techniques to Materials Science*, edited by D.L. Perry, R.L. Stockbauer, N.D. Shinn, K.L. D'Amico, and L.J. Terminello, (Mater. Res. Soc. Symp. Proc. **307**, Pittsburgh, PA 1993), pp. 213-224.
- [6] M. Dudley in, *Encyclopedia of Advanced Materials*, **4**, edited by D. Bloor, R.J. Brook, M.C. Flemings and S. Mahajan (Pergamon, 1994), p. 2950.
- [7] A.W. Vere, S. Cole, D.J. Williams, J. Electron. Mater. **12**, 551 (1983).
- [8] L.G. Casagrande, D. DiMarzio, M.B. Lee, D.J. Larson Jr., M. Dudley, T. Fanning, J. Cryst. Growth **128**, 576 (1993).
- [9] D.J. Larson Jr., J.I.D. Alexander, D. Gillies, F.M. Carlson, J. Wu, D. Black in *Joint Launch + One Year Science Review of USML-1 and USMP-1 with the Microgravity Measurement Group*, edited by N. Ramachandran, D.O. Frazier, S.L. Lehoczky, C.R. Baugher, (NASA Conference Publication **3272**, Huntsville, AL 1993), p. 129.
- [10] W. Zhou, M. Dudley, J. Wu, C.H. Su, M.P. Volz, D.C. Gillies, F.R. Szofran, S.L. Lehoczky, Mater. Sci. & Eng. **B27**, 143 (1994).
- [11] K. Durose, G.J. Russell, J. Cryst. Growth **86**, 471 (1988).
- [12] S. Tohno and A. Katsui, J. Cryst. Growth, **74**, 362 (1986).

LARGE PERSISTENT PHOTOCHROMIC EFFECT DUE TO DX CENTERS IN ALSB DOPED WITH SELENIUM

P. BECLA*, A. G. WITT*, J. LAGOWSKI** AND W. WALUKIEWICZ***

* Massachusetts Institute of Technology, Department of Materials Science, Cambridge, MA 02139

** University of South Florida, Center for Microelectronics Research, Tampa, FL 33620

*** Lawrence Berkeley Laboratory, Materials Sciences Division, Berkeley, CA 94720

ABSTRACT

A large photochromic effect has been observed in bulk AlSb crystals doped with Se. Illumination with the light of energy higher than 1 eV leads to an increase of the absorption coefficient in the spectral range 0.1 eV to 1.6 eV. The enhanced absorption is persistent at the temperatures below about 100 K. The effect is a manifestation of a DX-like bistability of Se donors. The illumination transfers the electrons from the DX center to a metastable hydrogenic level. The increased absorption with peaks around 0.2 eV and 0.5 eV is due to photoionization from the donor level to X_1 and X_3 minima of the conduction band

INTRODUCTION

The DX centers are highly localized impurity related defects. They were observed in a number of III-V and II-VI semiconductors¹⁻⁴. Their interesting and unique properties attracted a considerable attention in recent years. Besides very extensive studies of the basic properties of the defects it has been suggested and practically demonstrated^{5,6} that the persistent photoconductivity effect associated with DX centers could be utilized for optical memory devices. One of the most remarkable properties of the DX centers is their bistable behavior. It has been shown² that intentionally introduced donors can act as substitutional effective mass shallow dopants or, under specific circumstances, they can undergo a structural relaxation forming highly localized defect centers. $Al_xGa_{1-x}As$ alloys were among the most extensively studied materials systems. Although much less effort was directed towards other semiconductors there is a clear evidence for DX defects in GaAsP, InGaP, InGaAlP and AlGaSb alloys³.

In this paper we present the results of our studies of Se DX center in AlSb. We show that this impurity exhibits some unusual and unique properties different from the properties of donor impurities in other III-V compounds.

EXPERIMENTAL

The AlSb crystals were grown by the Czochralski technique from a selenium doped melt. The growth was carried out under Ar pressure of 4 atm. using an initially non-stoichiometric melt enriched with Sb to 0.515 atom fraction. Undoped AlSb crystals always show p-type conductivity. A series of crystals were grown with different concentration of Se added to the melt. The Se doping produces n-type material with the room temperature electron concentration as high as $3 \times 10^{17} \text{ cm}^{-3}$.

Temperature dependence of the resistivity for two samples with different Se concentration is shown in Fig. 1. The resistivity is increasing rapidly with decreasing temperature. The activation energy of about 180 meV has been determined from the slope at high temperatures. A change of the slope is observed for the temperatures lower than 120 K. Illumination of the samples with white light at the low temperatures resulted in a reduction of the resistivity which persisted after the light has been switched off. The saturation value of the persistent

photoconductivity (PPC) at 77 K corresponded to an increase of the electron concentration to about 10^{13} cm^{-3} . The PPC effect starts to decrease for temperature higher than 100 K and disappears at about 125K. The persistent effects are typical manifestation of the bistable behavior of DX centers and were routinely observed in other compound semiconductors³. The value of the PPC is relatively small, much smaller than PPC observed in the direct gap AlGaAs alloys. It is however quite typical for the indirect gap materials with a large binding energy of the effective mass donors.

Much more pronounced and interesting effects are found in the photoinduced absorption spectrum. As is seen in Fig. 2 a very small infrared absorption is observed in the sample cooled in the dark. Illumination with white light dramatically increases the absorption in the spectral range 0.1 eV to 1.6 eV. The absorption spectrum consists of two broad maxima at 0.2 eV and 0.5

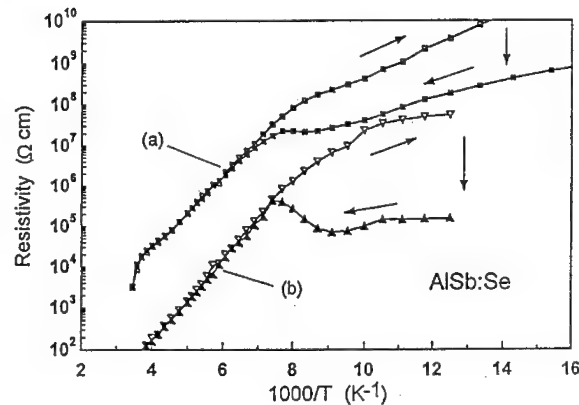


Fig. 1 Resistivity vs. temperature in two AlSb samples with different Se concentrations. The open squares represent cooling in the dark while the full squares represent the heating cycle after illumination at 77K. The difference between those two curves is a measure of the persistent photoconductivity.

eV and the absorption coefficient exceeds 50 cm^{-1} in the whole spectral range. This photochromic effect is much larger than that observed in AlGaAs alloys⁷. The absorption remains low for $h\nu < 0.1 \text{ eV}$. This is in agreement with electrical measurements which show a very small free carrier concentration at this low temperature. The photoinduced absorption is persistent at the temperatures below 100 K but it quickly vanishes at higher temperatures.

The excitation spectrum of the persistent optical absorption is shown in Fig. 3. The spectrum has been normalized to a constant photon flux. It was determined at 77 K from the initial slope of the photo-induced change in the absorption coefficient, $(d\Delta\alpha/dt)|_{t=0}$, measured point by point starting with the sample cooled in the dark after a complete thermal recovery of the low absorption state.

The excitation spectrum, with the threshold energy of about 1 eV is very similar to the photoionization cross section for the ground DX state involving large lattice relaxation in

AlGaAs³. The estimated value of the optical cross-section, σ_0 , is about 10^{-18} cm^2 for $h\nu = 1.3 \text{ eV}$. This agrees very well with typical values reported for the DX centers in other materials³.

The very large persistent optical absorption caused non-exponential excitation transients and long tails due to a decrease of the photon flux available for excitation. To alleviate this problem and to satisfy the requirement $\Delta\alpha d < 1$ the transient measurements were performed on a thin sample, $d = 0.2 \text{ mm}$ with lower Se concentration $n_{300} = 2 \times 10^{16} \text{ cm}^{-3}$. The results in the insert of Fig. 3 prove a single exponential character of the excitation process. Thus, the photoinduced transfer from low to high absorption states is governed by the first order rate equation and the time constant $\tau = (\Phi\sigma_{\text{eff}})^{-1}$, where Φ is the photon flux incident on the sample and σ_{eff} is the effective optical cross section for the white light illumination.

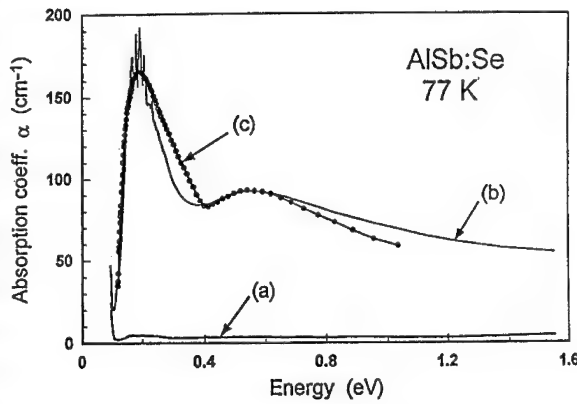


Fig. 2 Optical absorption in AlSb:Se at 77K. Absorption spectrum of the sample cooled in the dark (a) and after 15s illumination with a halogen light (b). The curve represents the calculated absorption coefficient.

DISCUSSION

The observed effects can be understood in terms of the DX-like bistability of Se donors in AlSb. A configuration-coordinate diagram for a donor impurity which can undergo a structural transformation into a DX-like state is shown in Fig. 4. The DX-like configuration is the ground state for the donor system. The DX level is located at the energy, E_{DX} , below the conduction band minimum. Lowering of the energy of the DX center is a result of the lattice relaxation around the Se impurity. The metastable, hydrogenic-like state of a substitutional donor is located at E_D below the lowest conduction band minimum X_1 . In AlSb, the closest higher minimum of the same symmetry, X_3 , is separated from X_1 by the energy, δ .

The two slopes of the resistivity vs. inverse temperature curve shown in Fig. 1 represent the thermal activation from the DX level and from the hydrogenic donor, D. When an AlSb:Se sample is cooled in the dark, most of the electrons freeze-out onto the DX level with only a small fraction being trapped on the metastable hydrogenic donor level. Therefore the high temperature slope of about 180 meV in Fig. 1 represents the binding energy of the DX center. Illumination with a photon energy higher than the threshold value of $h\nu_{th} = 1$ eV transfers the electrons from the DX centers to the conduction band. At low temperatures, these electrons are then trapped at the donor level, E_D . The increased occupancy of E_D leads to a higher absorption due to the photoionization transitions from E_D to X_1 to X_3 minima in the conduction band.

Curve c in Fig. 2 represents the calculated photoionization cross-section for the transition from the donor level to X_1 and X_3 minima of the conduction band. The best fit was obtained with $E_D = E(X_1) - 110$ meV and the separation between the minima $\delta = E(X_3) - E(X_1) = 290$ meV. Our value for the binding energy of Se donors is lower than 146 meV previously determined from the absorption spectra of lightly doped AlSb [8]. The value of δ is in a good agreement with the conduction band splitting as determined from intra subband infrared absorption ⁹.

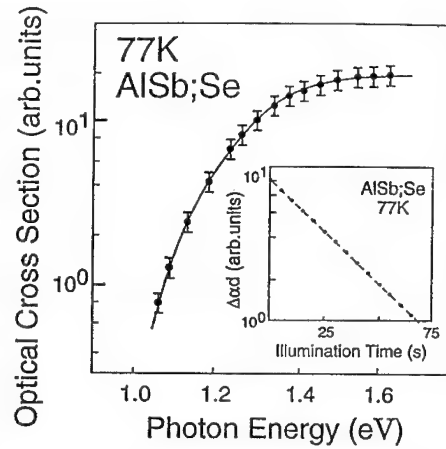


Fig. 3 The spectral dependence of the optical cross-section for the excitation of the persistent absorption. The insert shows the excitation kinetics of the absorption under white light illumination. All measurements were done at 77K.

The large persistent photochromic effect offers a possibility of using AlSb:Se for photodiffractive applications ¹⁰. As is seen in Fig. 2 one can produce an absorption grating with the modulation amplitude of the absorption coefficient $\Delta\alpha > 50 \text{ cm}^{-1}$. The diffraction efficiency of the absorption gratings is given by ¹¹,

$$\eta = \exp(-\alpha d)(\Delta\alpha L_{\text{int}}/4\cos\theta)^2 \quad (1)$$

where the interaction length $L_{\text{int}} = (1 - \exp(-\alpha d))/\alpha$, d is the thickness of the sample, θ is the half-angle between intersecting laser beams and α is the absorption coefficient.

For $\Delta\alpha = \alpha = 50 \text{ cm}^{-1}$ and the sample thickness of $2 \times 10^{-2} \text{ cm}$ the photodiffractive efficiency of about 0.9 % is expected. These expectations have been recently confirmed by a Purdue group where a diffraction efficiency of about 1% has been observed using the four-wave-mixing technique ¹². The result can be compared with previous reports of photodiffractive effect in GaAs:Cr and InP:Fe where 1 to 2 orders lower diffraction efficiencies were observed ¹⁰. Since both the sample thickness and the absorption coefficient can be independently controlled in the bulk AlSb it should be possible to optimize the parameters to achieve the theoretical efficiency limit of 6 % ¹².

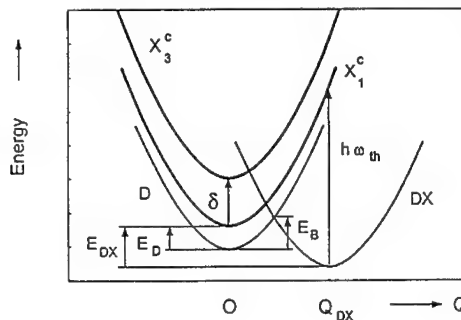


Fig. 4 Schematic representation of the configuration coordinate diagram describing the metastable behavior of the Se donors in AlSb

CONCLUSIONS

We have found that Se doped AlSb exhibits a very large photoinduced, persistent absorption. The absorption results from the photoionization of electrons from the metastable hydrogenic Se donor to the conduction band and is induced by optical transfer of electrons from the DX center to the hydrogenic Se donor. Because of the characteristic conduction band structure with two closely lying minima the absorption extends over a very broad spectral range from 0.1 eV to 1.6 eV. The persistent photo-induced absorption in AlSb:Se is the largest photochromic effect observed in any of III-V semiconductors. This effect could potentially find applications in photodiffractive devices.

ACKNOWLEDGMENTS

This work was supported by US DOE, Lawrence Livermore Laboratory, contract No B28.357 (MIT), US Army Research Office (USF) and the Director, Office of Energy Research, Office of Basic Energy Sciences, Materials Sciences Division of US Department of Energy under contract No. DE03-76SF00098 (LBL)

REFERENCES

1. D. V. Lang and R. A. Logan, Phys. Rev. Lett. **39**, 635 (1977).
2. D. J. Chadi and K. J. Chang, Phys. Rev. Lett. **B40**, 873 (1989).
3. P. M. Mooney, J. Appl. Phys. **67**, R1 (1990).
4. B. C. Burkey, R. P. Khosla, J. R. Fischer and D. L. Losee, J. Appl. Phys., **47**, 1095 (1976).
5. D. D. Nolte, D. H. Olson and A. M. Glass, Phys. Rev. **B40**, 10650 (1989).
6. R. A. Linke, T. Thio, J. D. Chadi and G. E. Devlin, Appl. Phys. Lett. **65**, 16 (1994).
7. J. E. Dmochowski, J. M. Langer, J. Raczynska and W. Jantsch, Phys. Rev. **B38**, 3276 (1988).
8. B. T. Ahlburn and A. K. Ramdas, Phys Rev. **167**, 717 (1968).
9. W. J. Turner and W. E. Reese, Phys. Rev. **117**, 1003 (1960).
10. D. D. Nolte and A. M. Glass, Opt. and Quantum Elect. **22**, S47 (1990).
11. H. Kogelnik, Bell Syst. Techn. J. **48**, 2909 (1969).
12. J. McKenna, D. D. Nolte, P. Becla, and W. Walukiewicz (to be published).

Control of Oxygen Content in Heavily Sb-Doped CZ Si Crystal by Adjusting Ambient Pressure

Koji IZUNOME, Xinming HUANG, Shiniji TOGAWA, Kazutaka TERASHIMA, and Shigeyuki KIMURA

Kimura Metamelt Project, ERATO, JRDC, 5-9-9 Tokodai, Tsukuba 300-26

Abstract

In Czochralski-grown (CZ) silicon single crystals, antimony (Sb) doping decreases the oxygen concentration by enhancing oxygen evaporation from the melt surface. In this study, Ar ambient pressures of around 100 Torr over the silicon melt were found to suppress evaporation of oxide species. To clarify the effect of the growth chamber ambient pressure on oxygen concentration, heavily Sb-doped CZ silicon crystals were grown under Ar pressures of 30, 60, and 100 Torr. Increasing Ar pressure increases the oxygen and Sb concentrations at the melt surface. The oxygen concentration under an Ar pressure of 100 Torr was 1.2 times higher than under 30 Torr when the solidified fractions are 0.5 or larger. The oxygen evaporation rate is controllable by gas phase transport of Sb_2O at high Ar pressures.

1. Introduction

Sb doping decreases the oxygen concentration in CZ silicon single crystal [1], seriously affecting device performance when utilized. To discover the reasons for oxygen reduction in heavily Sb-doped CZ silicon crystal, the influence of Sb on the dissolution rate of the silica crucible and oxygen solubility in the melt have been investigated, and the results showed that crucible dissolution rate and oxygen solubility increased with increasing Sb concentration in the melt [2, 3]. Meanwhile, the oxygen segregation coefficient in growth of Sb-doped silicon crystal has been investigated by the normal freezing method, and it was found to be nearly unity when the Sb concentration was less than 0.5 atom % [4] and reduced slightly with higher doping levels. The oxygen evaporation has also been measured when Sb was added, and it was found that the oxygen concentration in heavily Sb-doped CZ Si crystals was reduced due to increased oxygen evaporation [5]. Analysis of the evaporated species showed that evaporation of Sb_2O and SiO significantly increased oxygen loss from the Si melt [6], clearly being the main reason for oxygen reduction in Sb-doped CZ silicon crystals. It has been suggested that the atmospheric pressure of the background gas over the Si melt may be adjusted to control the evaporation of oxide species from the silicon melt [7]. However, no report has been presented on the effect of ambient pressure on the oxygen and Sb concentrations in silicon crystals.

The purpose of the present paper was to investigate the effect of growth chamber pressure on

the surface oxygen concentration of heavily Sb-doped silicon melt and the quality of crystals obtained. The effect of Ar pressure on the oxygen and Sb evaporation from the melt is discussed with respect to the evaporation mechanism.

2. Experimental

CZ silicon crystals (100 mm diameter, 700-900 mm length) were grown along the $\langle 100 \rangle$ direction under Ar pressures of 30 and 100 Torr in a conventional pulling apparatus. The Ar pressures were adjusted by controlling the Ar-gas flow rate (10-50 l/min) in the growth chamber. All the crystals were grown from the same initial 25 kg silicon charge containing 0.14 atom % Sb (99.9999 %) in a silica crucible. Growth was carried out under the same growth conditions : a pull rate of 1.0 mm/min, a crucible rotation speed of 10 rpm, and a seed rotation speed of 20 rpm. The polycrystalline starting material was melted completely and maintained in the molten state for 2 hours before the crystals were pulled.

The wafers for the evaluations were prepared to slices of 0.7-mm in thickness. Wafers for measurement were taken on the basis of one for each value of solidified fraction. Resistivity was measured by the four-point probe method. After Sb concentration evaluation, 6 mm x 12 mm chips were cut from the central regions of the wafers. Using 4 pieces (about 0.4 g) from each wafer, oxygen concentration was evaluated by Gas Fusion Analysis (GFA) .

Surface oxygen and Sb concentrations of the quenched melts under different Ar ambient pressures were measured by SIMS. The preparation of samples for SIMS was as follows : To preserve the condition of the melt during crystal growth, heater power was suddenly turned off and the remaining charge allowed to solidify and cool for 30 minutes. The solidified melt was 50 mm thick with no cracks in its surface region. Specimens were cut from the top surface at a radial distance of 100 mm from the center of the crucible with a diamond saw. Specimens were shaped into slices of 10 mm x 10 mm within a thickness of 2 mm. In SIMS measurement (IMS-3f/4f, CAMECA) , the primary ion beam species was Cs^+ and a 100 μm x 100 μm area was measured.

3. Results and Discussion

The variations of the oxygen concentrations in the growth direction in Sb-doped silicon crystals grown under different Ar pressures are shown in Fig. 1. Oxygen concentration decreases with increase in solidified fraction due to the enhancement of oxide evaporation from the melt surface with increasing Sb concentration. The oxygen concentration under an Ar pressure of 100 Torr is 1.2 times as large as that under 30 Torr when solidified fractions are 0.5 or larger. Thus, oxygen concentrations in the crystals are clearly controllable by adjusting the chamber Ar pressure. The depth profile of oxygen from the solidified melt surface under Ar pressures of 30 and 100 Torr shown in Fig.2 clearly indicates that the ambient pressure also affects oxygen concentration

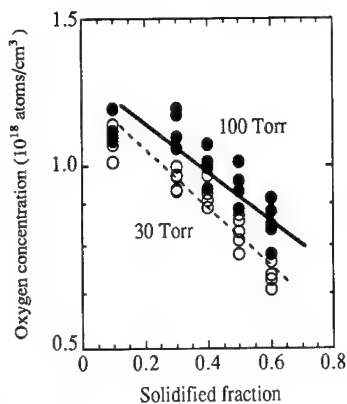


Fig. 1 Variation of the oxygen content along the growth direction under 30 and 100 Torr.

concentration at the melt surface. The oxygen concentration has a typical diffusion profile and decreases near the surface. Increase in Ar pressure increases the oxygen concentration in the melt surface. Thus, it is clear that the oxygen concentration profile reflects the oxygen distribution in the melt immediately before quenching. The surface concentration of oxygen is between 10^{16} atoms/cm³ and 10^{17} atoms/cm³. The depth profiles of Sb atoms from the solidified melt surface are shown in Fig. 3 for Ar pressures of 30 and 100 Torr. The profile of Sb concentration for the Ar pressure of 30 Torr shows the diffusion profile as in the case of the oxygen concentration profile as shown in Fig. 3. The diffusion profile of Sb under an Ar pressure of 100 Torr is flat and the Sb concentration at the surface under 100 Torr is 7.5 times greater than that under 30 Torr, indicating that the Sb evaporation mechanism at the melt surface changes between Ar pressures 30 and 100 Torr and that the increased chamber Ar atmospheric pressure suppresses evaporation of Sb and Sb oxide from the Sb-doped silicon melt. The absence of any surface depletion of the Sb concentration in the melt for an Ar pressure of 100 Torr indicates that transport in the gas phase has become rate limiting.

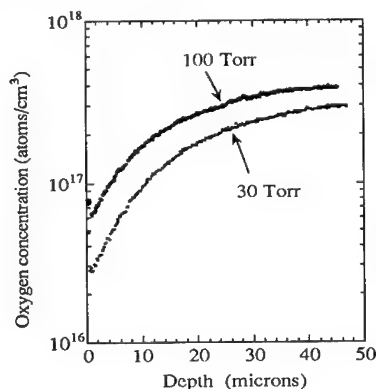


Fig. 2 Oxygen content profiles for the solidified melt under 30 and 100 Torr.

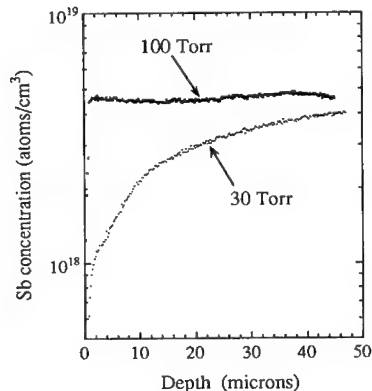


Fig. 3 Antimony content profiles for the solidified melt under 30 and 100 Torr.

Heavily Sb-doped CZ-Si crystals have been found to contain much less oxygen than those more lightly doped. The evaporation of SiO and Sb₂O from the Sb-doped silicon melt was investigated in an effort to explain the oxygen reduction. Evaporation of SiO from the silicon

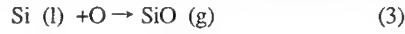
melt consists of three processes, namely, transport of the oxygen-bearing species in the melt to the melt surface, chemical reaction at the melt-ambient interface, and gas-phase transport away from the melt. The first and third processes are regulated by oxygen diffusion. In one dimensional analysis based on Nernst's formula [8], oxygen fluxes through unit area in the bulk melt (n_1) and in the Ar ambient (n_2) are expressed by oxygen concentrations C_m in the former and C_a in the latter as shown below ;

$$n_1 = k_1 (C_m - C_m^i) \quad (1)$$

$$n_2 = k_2 (C_a^i - C_a) \quad (2)$$

where the oxygen transport coefficients in the melt and in the Ar ambient are k_1 and k_2 , and the superscript i indicates the values at the interface.

The chemical reaction at the melt-ambient interface can be written as



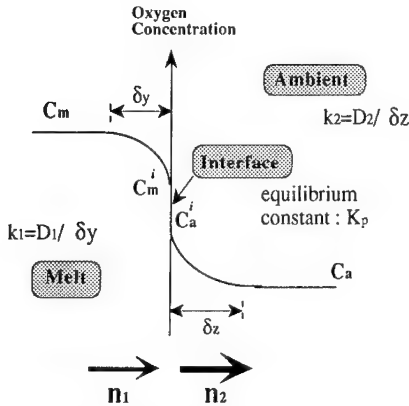
where O represents the dissolved oxygen in silicon melts [9]. We have assumed that the oxygen flux is close to the equilibrium value which is subject to the following constant :

$$\frac{C_a^i}{C_m^i} = K_c \quad (4)$$

where K_c is the equilibrium constant for the reaction in eq. (3).

Each oxygen flux is equal under the chemically steady state, i.e., $n_1 = n_2 = n$. Under such a state, oxygen flux n is rearranged using eqs. (1) and (2) by eliminating the interfacial oxygen concentrations C_m^i and C_a^i

$$n = \frac{C_m - C_a/K_c}{\frac{1}{k_1} + \frac{1}{K_c k_2}} \quad (5)$$



In eq. (5), we find that the oxygen transport rate depends on the terms of $1/k_1$ and $1/K_c k_2$, the so-called rate resistance. It is obvious that the oxygen transport rate mainly depends on the maximum resistance. We have estimated the rate resistance using eq. (5) and the previously reported data in the literature. As for the evaporation of SiO, one may have the values $1/k_1 = 10$ s/cm and $1/K_c k_2 = 250$ s/cm (under 100 Torr) on the basis of following equations [8,9] :

Fig. 4 Oxygen evaporation model near the Si melt surface.

$$\frac{1}{k_1} = \frac{\delta_y}{D_1} \quad (6)$$

$$\frac{1}{K_c k_2} = \frac{C_m^i \delta_z}{C_a^i D_2} \quad (7)$$

where D_1 is the oxygen diffusivity in the silicon melt at the melting temperature, D_2 the oxygen diffusivity in Ar ambient, δ_y the average boundary layer thickness of the diffusion layer in the melt along the surface, δ_z the average thickness of the diffusion boundary layer along the melt surface [3, 8, 10-12]. Details are given in Table 1.

It is assumed that the chemical reaction at the melt/ambient interface occurs at the melting temperature (1414 °C) and SiO evaporated from the melt surface is an ideal gas. Thus, under Ar pressure of 100 Torr one may have the value $C_a^i = 2.4 \times 10^{13}$ atoms/cm³ [5,9], and C_m^i is obtained as 6×10^{16} atoms/cm³ as shown in Fig. 2. The transport of oxygen-bearing species in the boundary layer on the ambient side has a larger resistance value than that on the melt side. The oxygen concentration of the melt surface depends on the ambient pressure as shown in Fig. 2. Thus, the transport of oxygen-bearing species in the boundary layer on the ambient side is found to be the rate-limiting process in the oxygen evaporation at the silicon melt surface. In other words, oxide evaporation from the melt surface determines the oxygen concentration at the melt surface and is practically independent of the oxygen partial pressure under Ar ambient in the growth chamber.

Table I Physical parameters used in the oxygen transport model.

Diffusion coefficient of oxygen in silicon melt at the melting temperature, D_1	$5 \times 10^{-4} \text{ cm}^2/\text{sec}$ ^{a)}
Diffusion coefficient of oxygen in Ar ambient, D_2	$3 \text{ cm}^2/\text{sec}$ ^{b)}
Boundary layer thickness along the silica crucible, δ_x	$2.0 \times 10^{-2} \text{ cm}$ ^{b)}
Boundary layer thickness below the melt surface, δ_y	$1.0 \times 10^{-2} \text{ cm}$ ^{b)}
Boundary layer thickness over the melt surface, δ_z	0.3 cm ^{b)}

a) Ref. 10, b) Ref. 8 and 9

4. Conclusion

In CZ Si crystal, Sb doping decreases the oxygen concentration due to the enhancement of oxygen evaporation. To minimize the evaporation of oxide species from the silicon melt, the atmospheric pressure of the background gas over the Si melt was increased. The effect of atmospheric pressure in a growth chamber on oxygen concentration in a grown crystal was clarified when heavily Sb-doped CZ Si crystals were grown in Ar pressures of 30 and 100 Torr.

The oxygen and Sb concentrations of the melt surface were found to increase with Ar ambient pressure. The oxygen concentration under an Ar pressure of 100 Torr was 1.2 times that under 30 Torr when the solidified fractions were 0.5 or larger. The oxygen evaporation rate is controllable by gas phase transport of Sb_2O at high Ar pressures.

References

- [1] K. G. Barraclough, R. W. Series, D. S. Kemp and G. J. Rae, VII Int. Conf. Crystal growth, Stuttgart, F. R. Germany, ICCG-7, Sept., (1983) SY 4/3.
- [2] X. Huang, K. Terashima, H. Sasaki, E. Tokizaki and S. Kimura, Jpn. J. Appl. Phys. 32 (1993) 3671.
- [3] X. Huang, K. Terashima, H. Sasaki, E. Tokizaki, Y. Anzai and S. Kimura, Jpn. J. Appl. Phys. 33 (1993) 1717.
- [4] X. Huang, K. Terashima, K. Izunome and S. Kimura, in print to J. Crystal Growth.
- [5] X. Huang, K. Terashima, E. Tokizaki, H. Sasaki and S. Kimura, Jpn. J. Appl. Phys. 33 (1994) 3305.
- [6] H. Harada, T. Itoh, N. Ozawa and T. Abe : VLSI Science and Technology 1985, eds. W. N. Bullis and S. Byoydo (Electrochem. Soc., Pennington, 1985) Softbound Proc. Series, PV 85-5, p. 526.
- [7] X. Huang, K. Terashima, K. Izunome and S. Kimura, Jpn. J. Appl. Phys. 33 (1994) L902.
- [8] H. Hirata and K. Hoshikawa, J. Japan Assoc. Crystal Growth, 15 (1988) 207.
- [9] K. Hoshikawa, H. Hirata, H. Nakanishi and K. Ikuta, Semiconductor Silicon 1981, eds. H. R. Huff, R. J. Kriegler, and Y. Takeishi (Electrochem. Soc., Pennington, 1981) p. 101.
- [10] H. Kodaera, Jpn. J. Appl. Phys. 2 (1963) 212.
- [11] W. Kaiser and J. Breslin, J. Appl. Phys. 29 (1958) 1292.
- [12] C. Wagner, J. Appl. Phys. 29 (1958) 1295.

PHOTODIFFRACTIVE CHARACTERIZATION OF GROWTH-DEFECTS IN GaAs

K.JARASIUNAS, M.SUDZIUS, A.KANIAVA, and J.VAITKUS
Institute of Material Science and Applied Research, Vilnius University,
Saulėtekio ave 9, bld.3, 2054 Vilnius, Lithuania

INTRODUCTION

The transient grating technique has been developed over the years and several reviews have been written concerning the subject [1,2]. The present paper will focus on its advantages for studies of main native defect in semiconducting GaAs crystals, namely, of EL2, which plays a crucial role in semi-insulating properties and optical absorption below band-gap, photorefractivity, metastability, etc. We will consider the role of EL2 in optical nonlinearities and its contribution to carrier transport in subnanosecond time domain. Nonlinear character of TG technique allows to get deeper insight into spatial distribution of growth defects (EL2 and dislocations) in the wafers and perform their nondestructive monitoring. Different experimental techniques, as DFWM in nano- and picosecond time domain, light self-diffraction, and set of differently grown GaAs crystals enabled us to show applicability of this technique for basic research and nondestructive determination of parameters, defect distribution, reveal fast transients of optical nonlinearities. The photorefractive nonlinearity at 300K is shown being dependent on dislocation density due to local strain fields around charged dislocations. Moreover, transient quenching of EL2 by short laser pulses and enhancement of low-temperature photorefractive nonlinearity is demonstrated.

1.EXPERIMENTAL TECHNIQUES AND SAMPLES

We have studied optical nonlinearities in GaAs by using Q-switched and mode-locked YAG lasers ($\lambda=1.06\mu\text{m}$, duration of laser pulses $\tau_L=12\text{ ns}$ or 28 ps , correspondingly) for the resonant excitation into EL2 absorption band. Degenerate four wave mixing (DFWM) scheme for Bragg-gratings and light self-diffraction regime on thin gratings were used to study peculiarities of light absorption and diffraction on free carrier (FC) and on photorefractive (PR) gratings, varying their period Λ (from 2 to $40\mu\text{m}$), sample temperature (in the range from 80 to 300 K), and excitation density (up to 50 mJ/cm^2).

Transient gratings have been studied in differently grown and oriented samples of GaAs: in semi-insulating (SI) undoped crystal D1 (cut in a typical photorefractive way, i.e. with faces along crystallographic directions $[110]$, $[-110]$, and $[001]$), in commercial SI (001)-grown LEC wafers MT10 (In-alloyed) and IC1 (undoped), and in heavily Si doped wafer IC2. This set allowed to vary dislocation density from $N_D \approx 10^5\text{ cm}^{-2}$ in D1 to $2 \cdot 10^3\text{ cm}^{-2}$ in IC2 [3]. The experimental configurations are shown on Fig.1a,b. The measured incident energy I_0 , transmitted I_T and self-diffracted or diffracted probe beam intensities I_1 are time-integrated values over the duration of laser pulse.

Optical illumination of GaAs at $1.06\mu\text{m}$ (i.e. in the spectral region $E_g/2 < \hbar\omega < E_g$) leads to the changes of its refractive index via FC and PR nonlinearities. The corresponding nonlinearities are described by Drude-Lorentz model or by linear electro-optic effect [1,2]

$$\Delta n_{\text{FC}} = -(\epsilon/2n\omega^2\epsilon)(\Delta N/m_e + \Delta P/m_p) \quad (1)$$

$$\Delta n_{\text{PR}} = -n^3 r_{\text{eff}} E_{\text{SC}}/2 \quad (2)$$

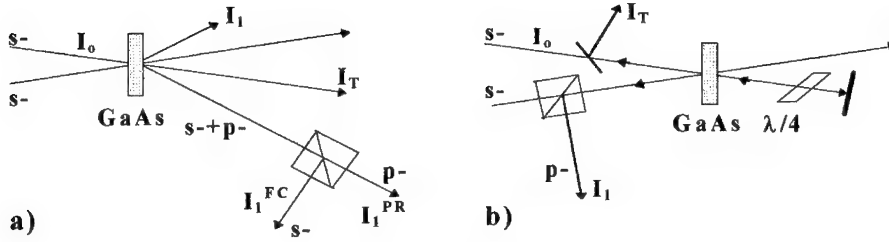


Fig 1. Experimental set-ups: self-diffraction scheme (a) and DFWM for ns-pulses (b)

where $\Delta N, \Delta P$ are nonequilibrium carrier concentrations, $m_{e,p}$ are their effective masses, ω is the laser frequency, $\epsilon_i [R.Kg]$ e_d is the effective electro-optic coefficient, E_{sc} is light-induced space charge field, R is electro-optic tensor, $e_{i,d}$ are the polarization vectors of incident and diffracted waves. The instantaneous values of $\Delta N, \Delta P$ follow from the solution of continuity equations for electrons, holes, ionized EL2 densities, and Poisson's equation for E_{sc} [4]. The changes of refractive index lead to simple relationship with the diffraction efficiencies of gratings in the first diffraction order $\eta_1 = I_1 / I_T = [(\pi/\lambda)\Delta n]^2 \leq 1\%$ the measured signals I_T and I_1 . Contribution of PR grating from the FC one was separated by monitoring the polarization states of probe and diffracted beams [5]. For ns-duration pulses, transmitted beam was retroreflected to probe PR grating; in addition it's polarization was rotated to probe FC grating. For ps duration pulses, we used conventional time resolved DFWM scheme with delayed probe beam [3]. In geometry of light self-diffraction, the coexisting orthogonally polarized diffracted components were separated by Glan prism and measured simultaneously.

2.ROLE OF DEFECTS IN CARRIER AND SPACE-CHARGE FIELD EVOLUTION

Numerical analysis of carrier and space charge field dynamics was performed by solving the set of coupled differential equations [6] and revealed number of excitation dependent effects. At low excitations, electron generation from deep traps dominates until the concentration $N_e = (2-3) \cdot 10^{15} \text{ cm}^{-3}$, close to initial density of neutral EL2 ($N_{EL2}(t=0) = 5 \cdot 10^{15} \text{ cm}^{-3}$), is reached. Hole concentration N_p is by order of magnitude less than N_e . Electron diffusive transport creates electric field E_{sc1} between ionized EL2 and electrons with its fast build-up time $\tau_{sc}^{(1)} \approx (\Lambda/2 D_e)^2$ and decay by dielectric relaxation time $\tau_{sc}^{(2)} \approx \tau_{di} (1 + \tau_R / \tau_{sc}) \gg \tau_L$ [7].

At higher excitations, two-step transitions through EL2 are efficient, thus hole generation rate approaches the electron one. New component of E_{sc2} - a Dember field between electrons and holes - overlaps with the previous one. Both PR and FC grating decay by ambipolar diffusion of carriers with $\tau_{sc} = \tau_a = (\Lambda/2 D_a)^2$ with $D_a = (kT/e)(N+P)/(N/\mu + P/\mu)$. Carrier recombination also may contribute to grating decay according to general relationship $1/\tau_e \approx 1/\tau_R + 1/\tau_a$.

The most interesting feature in dynamics of FC nonlinearity is a feed-back effect of light-created field E_{sc} on carrier transport, which is evident in compensation of grating diffusive decay by carrier drift. The other feature is a transport of holes, which leads to shift of hole spatial modulation by half-period of the grating (with respect to the initial light-induced modulation of holes) and to screening of the negative charge of electrons, transferred by diffusion to the grating minima. Both those peculiarities are efficiently contributing to carrier transport at moderate excitations, when deep trap assisted carrier generation dominates.

3. EXPERIMENTAL STUDIES

3.1. Nondestructive mapping of growth defects in GaAs wafers

In SI GaAs crystals the distribution of EL2 is usually revealed via optical absorption at $1.1\mu\text{m}$. A simple way to enhance the sensitivity is to use transformation of absorptive index variations to those of refractive index (see eq.1), and then amplify the latter distribution by nonlinear light diffraction technique. Indeed, investigations of light absorption and diffraction in GaAs wafers have shown much higher sensitivity of light diffraction to EL2 distribution [8,9]. This follows due to superlinear character of TG technique (as follows from relationship $\eta \sim \Delta n^2$) and, from the other hand, due to measurements of diffracted beam in dark far field of diffraction.

In addition to carrier generation efficiency, the grating erasure time was found varying across the SI wafers (e.g. from 1 ns in low-defect area to 2 ns in high defect area [8]). This feature correlates well with the distribution of dislocation density [10], and the observed variations of carrier lifetime were attributed to band-gap modulation by charged dislocations and carrier separation by the potential relief [8]. Our measurements confirmed that diffracted light intensity correlates well with the dislocation density, which was revealed by the selective etching. In this way, the applicability of this nondestructive technique for monitoring of growth defects distribution in GaAs was demonstrated and instrument D-SCAN assembled to implement this technique [11].

The recent studies revealed one more mechanism which allows the further increase of TG technique sensitivity for monitoring the defect distribution. The idea is based on role of light-induced internal space-charge field feed-back on carrier transport. At short pulse excitations, decay of coexisting gratings is coupled and varies with excitation power and time. In Fig.2 decay of FC grating in areas with different EL2 density is given. The higher is EL2 density, the stronger is E_{SC1} , which opposes the initial fast diffusive decay. In the area with lower EL2 density, nearly bipolar plasma and E_{SC2} are created. At high excitation levels, two step and two-photon absorption dominate over trap-assisted one and lead to bipolar carrier transport.

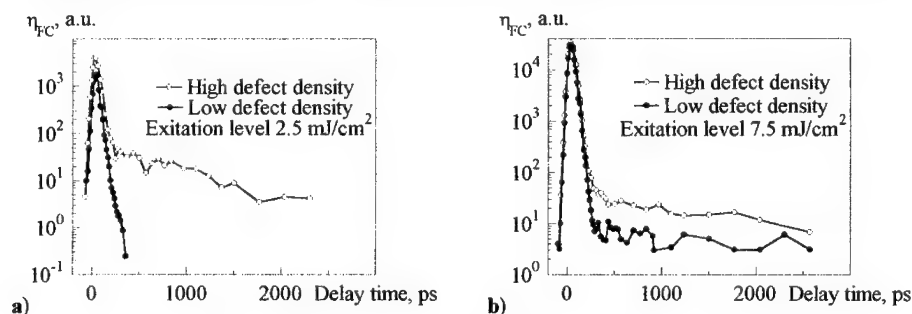


Fig. 2. Free carrier grating decay in LEC-grown GaAs crystals.

3.2. Dislocation-initiated PR-effect

The anisotropic feature of PR nonlinearity is well known [12] and predicts rotation of probe beam polarization in photorefractive cut crystals, if the orientation of grating vector K_g is parallel to the axis (110). For orientation $K_g \parallel [001]$ or in commercial GaAs substrates oriented perpendicular to the (001) axis, theory predicts zero effect, i.e. $r_{eff} = 0$. Nevertheless, a

strong diffracted signal with rotated polarization was recently observed in LEC-grown SI GaAs in forbidden geometry $K_g // [001]$ [13]. This unexpected signal was attributed to long-range distortions of the lattice due to internal strain and electric fields around charged dislocations [14]. The further studies have been carried out in commercial GaAs substrates (samples MT10, ICI1, ICI2) with different dislocation densities. The measurements of diffracted beam intensities on FC and PR gratings (I_{FC} and I_{PR} , correspondingly) by using DFWM scheme and grating period $\Lambda = 2 \mu\text{m}$ allowed us to determine the ratio of those signals $S = I_{PR}/I_{FC}$. The ratio was found dependent on dislocation density and varied from 2.5 % in non-photorefractive geometry of sample D1 down to 0.3 % in heavily doped GaAs. Square root of the ratio S shows a linear dependence of r_{eff} vs. dislocation density [4]. This correlation strongly supports the hypothesis that dislocations are responsible for PR effect in non-photorefractive geometry of LEC-grown GaAs crystals.

3.3. Low-T PR effect

The metastability of deep native donor EL2 may essentially modify the photorefractive nonlinearity. The effect of EL2 optical quenching [15] introduces a novel mechanism for photorefractivity at low-temperatures [16] and opens novel possibilities for nonlinear optical studies of EL2.

The previous studies of this novel effect have been performed in GaAs in quasi-equilibrium conditions, i.e. by using low-power CW sources [16,17]. We extended those studies in nanosecond time domain, where the PR nonlinearity coexists with the free carrier one. The temperature dependencies of light diffraction on FC and PR gratings and sample transmittivity have been measured during the cooling of GaAs samples down to 80 K and then during their slow heating up to room 300 K. The nonlinearities and linear optical properties were found dependent on grating period, sample characteristics, and revealed novel peculiarities in light diffraction and transmittivity.

A. Free carrier gratings. During the cooling of the sample D1 (Fig.3), we observed the decrease of FC diffraction efficiency η . The calculated dependence $\eta(T)$ (dashed curve), using the continuity equation for carriers and temperature-dependent carrier mobility, correlates well with the decrease of η down to 150 K. The faster decrease of η at $T < 150$ than expected from diffusive decay is probably related to changes in carrier generation processes: the transfer of EL2 from normal to metastable state lowers the defect-assisted generation rate. The similar features of decreasing η with absorption bleaching at $T < 130$ K were found in sample MT10 as well (Fig.4,5). The high density of charged dislocations, acting as scattering centers, leads to the weak dependence of mobility vs. T in this sample. In addition, this regime is not so sensitive to carrier diffusion due to large grating period. During the heating

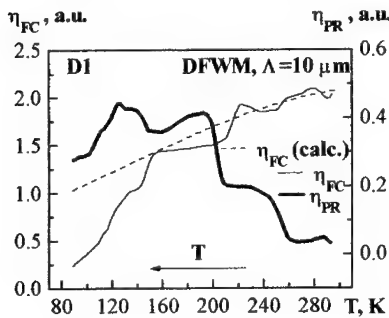


Fig. 3

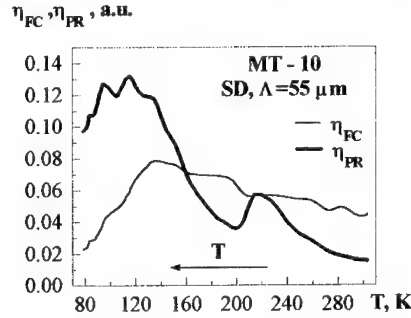


Fig. 4

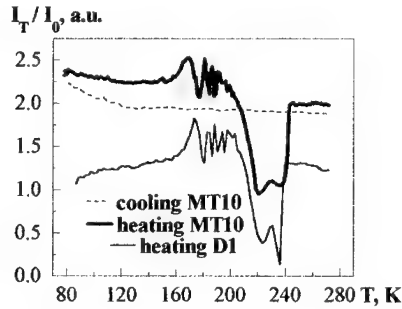


Fig. 5

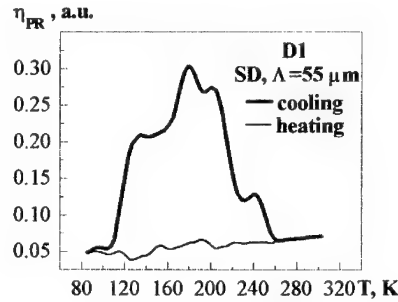


Fig. 6

of the samples, we observed the monotonous increase of η due to thermal recovery of EL2 state. The fine structure seen in $\eta(T)$ (Fig. 3,4) shows certain correlation with trap filling characteristic temperatures [18], and this analysis will be presented elsewhere.

We found novel features in transmittivity of the GaAs during the heating process: an increased absorption in the narrow temperature range 200-240 K, both in D1 and MT10 samples (Fig.5). It's worth to note that this the dip was not found during the cooling of the samples. In addition, this strong increase of absorption (it corresponds to $\Delta\alpha \approx 4-6 \text{ cm}^{-1}$) was not followed by higher diffraction efficiency. This indicates that the origin of light absorption at 200-240 K has non-photoactive nature and may be attributed to intracenter transitions assisting in the reconstruction of normal EL2 state. The further studies are in progress.

B. Photorefractive gratings. The essential increase of photorefractive grating efficiency η_{PR} (more than by order of magnitude) was observed during the cooling of sample D1 (Fig.3,4), in contrary to decrease of η_{FC} in this temperature range. This indicates that the mechanism responsible for the enhancement of photorefractive effect is different from Demmer field. This mechanism is supposed to be related with optical EL2 quenching, but starts to play role at $T < 250 \text{ K}$, i.e. much earlier than the typical $\text{EL2}^0 \Rightarrow \text{EL2}^*$ transitions at 130 K. When the grating period increased from 10 to 55 μm , the effect of enhanced η_{PR} was not so strong neither in D1 nor in MT10 samples. We found the enhancement being proportional to inverse grating period. We managed to observe light selfdiffraction on thin PR grating for the first time, and the efficiency of PR grating was higher than that from FC grating.

During the heating we observed the reverse behaviour in $\eta_{PR}(T)$ dependence than during the cooling, if the EL2 donors were not completely bleached. In the case of full transfer of deep donors to metastable states, the η_{PR} value was as low as that observed at 300 K (Fig.6).

We performed modelling of EL2 concentration and dynamics in neutral, ionized, and metastable states at different temperatures. In addition to the continuity and Poisson equations, we modified the rate equation for EL2 by adding the term of metastable EL2* generation and decay:

$$dN^*/dt = s_n^* I (N - N^+ - N^*) - (r^* + s_r^* I) N^* \quad (3)$$

here s_r^* stands for cross-section of the transfer from EL2^0 to EL2^* state [15], while recovery of EL2^0 is induced thermally with a rate r^* and optically with cross-section s_r^* .

Numerical solution using the parameters s_n^* , r^* , and s_r^* , given in [17], have shown that EL2^* concentration may reach considerable values, e.g. ratio $M = \text{EL2}^* / \text{EL2}^0$ equals to 0.42 at 100K and $M=0.07$ at 300 K for experimentally used excitation power density $10^{25} \text{ cm}^{-2} \text{ s}^{-1}$ and $\tau_c = 10 \text{ ns}$. The lifetime of metastable state varies with temperature from 0.4 ns at 300K to 18

ns at 200K due to decreasing role of thermal recovery from EL2 state. This evaluation may explain the observed decrease of PR grating efficiency at lower temperatures ($T < 120$ K) and longer exposures. Thus the process of optical transfer to metastable state via excited state and thermal recovery to $EL2^0$ at higher temperatures (250-150K) can be assumed as a *transient* EL2 quenching by short pulse excitation. It may introduce the local decompensation and to increase the internal electric field, leading to observed enhancement of PR-effect.

CONCLUSIONS

This review has focused on the use of transient grating applications for studies of native donor EL2 properties in bulk GaAs. The coexisting free carrier and photorefractive optical nonlinearities related to EL2 density are analyzed experimentally at short pulse excitation. The high sensitivity of free carrier TG technique for nondestructive mapping of EL2 and dislocation distribution is demonstrated. The dislocation-density dependent PR effect in (001)-cut GaAs samples was studied and attributed to long-range distortions of the lattice due to internal strain and electric fields around charged dislocations. EL2 quenching by short pulses at $1.06\ \mu\text{m}$ was realized for the first time and led to strong enhancement of low temperature PR effect. The existence of low-T PR effect in allowed and forbidden photorefractive orientations confirms the model of dislocation-dependent PR effect in non-photorefractive cut GaAs crystals.

The research described in this publication was made possible in part by long-term Grant No.LA9000 from the International Science Foundation.

REFERENCES

- 1 H.Eichler, P.Gunter, D.Pohl, Light Induced Dynamic Gratings (Springer Verlag, Berlin-Heidelberg, 1986).
2. R.K.Jain, M.B.Klein, in Optical Phase Conjugation, (ed. R.A.Fisher, N.Y.Acad.Press, 1983), p.307.
3. K.Jarasiunas, J.Vaitkus, P.Delaye, and G.Roosen, Optics Lett. **19**, 1946 (1994).
4. A.L.Smirl, G.C.Valley, K.M.Bohnert, T.F.Bogges, IEEE J.Quant.Electr. QE-**24**, 289 (1988).
5. W.A.Schroeder, T.S.Stark, M.D.Dawson, T.F.Bogges, A.L.Smirl, and G.C.Valley, Optics Lett. **16**, 159 (1991).
6. Ph.Delaye, L.Bastiene, K.Jarasiunas, and G.Roosen, SPIE, **2097**, 474-482 (1993).
7. M.B.Klein, Optics Letters **9**, 350 (1984).
8. J.Vaitkus, E.Gaubas, K.Jarasiunas, and M.Petrauskas, Semicond.Sci.Technol. **7**, A131 (1992).
9. R.B.Bylsma, D.H.Olson, and A.M.Glass, Appl. Phys. Lett. **52**(13), 1083 (1988).
10. S.Miyazawa, Progr. Crystal Growth and Charact. **23**, 23-71 (1991)
11. K. Jarasiunas, Development and Application of Nondestructive Techniques for Control of Semiconducting Wafers, Structures, and Technological Processes. Report, Vilnius u-ty, 1994.
12. J.C.Fabre, J.M.C.Jonathan, and G.Roosen, Optics Commun. **65**, 257 (1988).
13. K.Jarasiunas, P.Delaye, and G.Roosen, Phys. Stat. Sol. (b) **175**, 445 (1993).
14. A.R.Hutson and L.R.Walker, J. Appl. Phys. **50**, 6247 (1979).
15. G. Vincent, D.Bois, A.Chantre, J. Appl. Phys. **53**, 3643 (1982).
16. D.D.Nolte, D.H.Olson, and A.M.Glass, Phys. Rev. B **40**, 10650 (1989).
17. P.Delaye and B.Sugg, Phys. Rev.B **50**, 16973 (1994).
18. R.Kiliulis, V.Rinkevicius, J.Storasta, and J.Vaitkus, Phys. Stat. Sol. (a), **127**, 415 (1991).

INFLUENCE OF ELECTRIC FIELD AND TEMPERATURE ON MAGNETIC FIELD INDUCED PROLONGED CHANGES OF ELECTRIC PARAMETERS OF SILICON SYSTEMS.

VLADIMIR M. MASLOVSKY. Zelenograd Research Institute of Physical Problems.
Moscow 103460. Russia.

ABSTRACT

Magnetic field induced prolonged changes (MFIPC) of electric parameters of semiconductor systems is the phenomenon that has been recently established experimentally. In this work it is investigated for the first time the influence of electric field and temperature on duration of MFIPC of carrier generation lifetime in Si subsurface region and the influence of temperature on MFIPC of the MOS structure leakage voltage. The value of determined mobility of generated defects corresponds to the diffusion coefficient of vacancy -impurity complexes. These investigations of MFIPC of microstructure confirm that non-equilibrium defects reactions are limited by diffusion (in the absence of external electric field). It is shown that the corresponding diffusion coefficient is about $10^{-13} \text{ cm}^2\text{s}^{-1}$ and the magnitude of diffusion activation energy determined from these investigations is in the range 0.45-0.5 eV. This value is nearly the same as the diffusion coefficient of vacancy-impurity complex.

INTRODUCTION

This paper presents the new experimental results concerning the physics of the magnetic field induced prolonged changes (MFIPC) phenomenon that has been recently established experimentally [1-3]. MOS structure capacitance-voltage characteristics and histograms of MOS-structure transient capacitance relaxation times τ , flat-band voltage V_{fb} , leakage voltage V_l (positive voltage on Al-electrode at which the 10 nA tunnel current flows through dielectric [4]) were measured. It was registered MFIPC of τ histograms in MOS structures after PMFT with magnetic field magnitude 0.1-0.2 MA/m. It was observed that the value of τ corresponding to the peak value on histogram was decreasing during 7 days after pulsed magnetic field treatment (PMFT). The significant acceleration MFIPC of τ by electric field allows to determine the mobility of charged defects. Such a great decrease of τ was probably due to abnormal generation of carriers in depletion regions of the semiconductor with microdefects decorated by fast-diffusing impurities. That result demonstrated the possibility of impurity-defect complexes reconstruction in Cz - Si induced by PMFT.

EXPERIMENTAL RESULTS

To study processes induced by short-term PMFT effects in MOS-structures the test structures were used. These structures were formed by dioxide layer formed by the thermal oxidation in dry oxygen at 1050° C of phosphorus-dopes Si(100) substrates with 20 Ohm×cm resistivity. Dioxide thickness d was 40 nm and Al-electrode area was $S=1 \text{ mm}^2$. These structures were under the influence of some

PMFT pulses with amplitude of $H = 0.1\text{--}0.3 \text{ MA/m}$, $0.02\text{--}0.05 \text{ ms}$ duration, and pulse frequency 10 Hz . The PMFT duration was about 1 min . It was detected that there were no appreciable variations of the parameters just after short-term treatment (less than 10 s).

The measurement of MOS-structure transient capacitance relaxation times τ up to and after PMFT were carried out. It appeared, that the main peak on the histogram τ after effect PMFT displaces in the party of smaller values, that corresponds to the increase of carriers generation current in the Si subsurface area (in 8 days significance τ , appropriate to a peak on the histogram has decreased in 5-7 times (Fig. 1).)

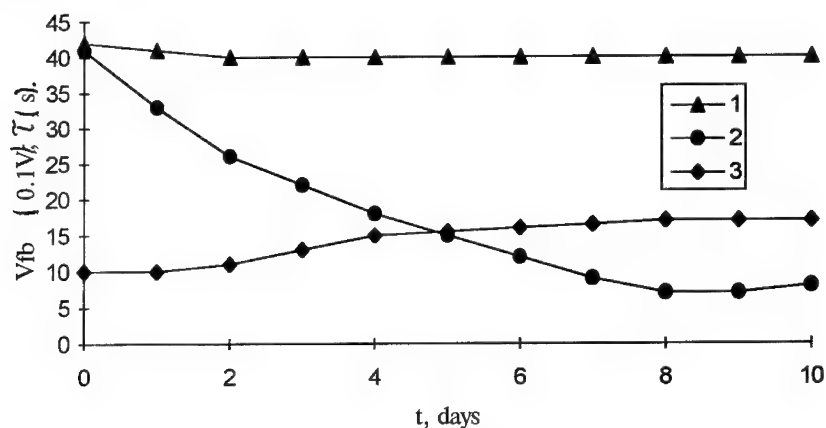


Fig. 1. The temporal dependencies of a position of a main peak on histogram τ and U_{fb} up to and after PMFT: (1) - τ before, (2) - τ after, (3) - U_{fb} after.

Using the rectangular pulsed depleted voltage of the same value U , the missing of τ is connected to carrier generation lifetime τ_g by the following: $\tau \sim \tau_g \sqrt{n}$, where n is the bulk free electron concentration [3] and the decrease of τ_g is due to the monotonous increase of generation centers concentration in the Si subsurface region. The PMFT of MOS structures alongside with the reduction τ results also in a increase of density of a built - in dielectric charge, registered as a shift of a flat band voltage to the negative area (Fig. 1.). High-frequency C-V characteristics were shifted on an axis of voltage without the change of the form. We shall note, that the change of density of a built - in dielectric charge is registered later then τ changes.

The conclusion about a initiating role of defect reactions in volume of the subsurface area was confirmed by the influence of a electrical field in the silicon on rate of MFIPC of τ . The electric field in Si depleted region considerably accelerates MFIPC of defect structure in Si subsurface region. The changes of τ has been registered in the regime when the time interval between the measurements τ and, accordingly, between repeated voltage application was essentially less then τ . That results in considerably more fast and non-monotonous change of time τ (Fig. 2) in

comparison with long-term changes, shown on Fig.1.

Such repeated voltage applications before PMFT did not result in the appreciable changes of τ . effect confirms a opportunity of defect migration in a silicon, as the strong electrical field in depleted region accelerates the migration of generated defects. Thus, the influence of a electrical field in the subsurface area of a semiconductor is displayed in the more fast change τ in comparison with absence of long-term effect of fields. The results (Fig. 2) permit to evaluate the mobility of defects induced by PMFT.

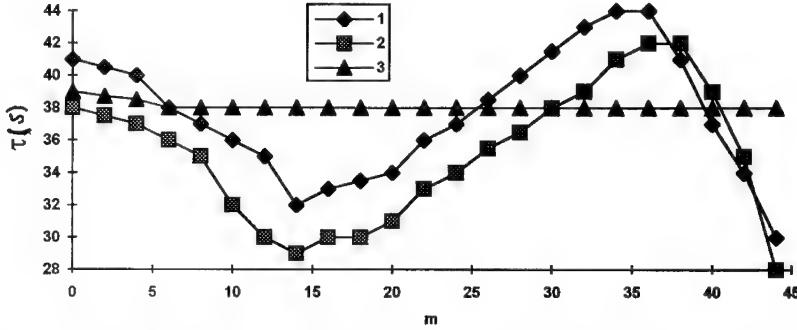


Fig. 2 Typical dependencies τ on the numbers m of depleted voltage ($U=5$ V) pulses after the PMFT: (1) - structure № 1, (2) - structure № 2, (3) - structure № 1 before PMFT.

From the continuity equation we have the following relations:

$$\mu E_m N = \frac{d(WN)}{dt}, \quad (1)$$

where μ and N are the mobility and concentration of charged defect, $E_m = 4\pi q n W / \epsilon$ is maximal electric field in depleted region, W is the maximal depleted region depth (related to applied voltage) and ϵ is the Si dielectric constant. As far as electric field results in considerably more rapidly τ decrease in comparison of one on Fig 1, where it determined only by diffusion of defect, we have found possible to neglect a diffusion current. As it follows from [3]:

$$\frac{\delta N}{N_i} = - \frac{\delta \tau}{\tau_i}, \quad (2)$$

where N_i and τ_i are the initial value of N and τ . Substituting (2) in expression (1) and integrating with respect to the time we obtain

$$\mu \int_0^{t_x} E_m dt = \frac{W \Delta \tau}{\tau_i}, \quad (3)$$

where $t_x = m\tau_i$ is the characteristic time, at which change of a τ is equal to some $\Delta \tau$. This expression describe the region of quasi - monotonous increase of τ in Fig 2. As W in accordance to [3] is the linear function of time in the processes of MOS structure capacitance relaxation, from expression (3) it follows:

$$\mu = \frac{W\varepsilon}{(W + W_0)2\pi q n \tau_i} \alpha \quad (4)$$

where $\alpha = \frac{1}{\tau_i} \frac{\partial \tau}{\partial m}$. In accordance with experimental results (Fig 2) $\alpha \cong 0.015$

(the middle region on Fig 2) and value of $\mu = 3-5 \times 10^{-12} \text{ cm}^2/(\text{V}\cdot\text{s})$. This value with in a good agreement with the diffusion coefficient established in [4] because

$$D = \frac{\mu k T}{q} \approx 10^{-13} \text{ cm}^2 / \text{s} \quad (T \text{ is the temperature}).$$

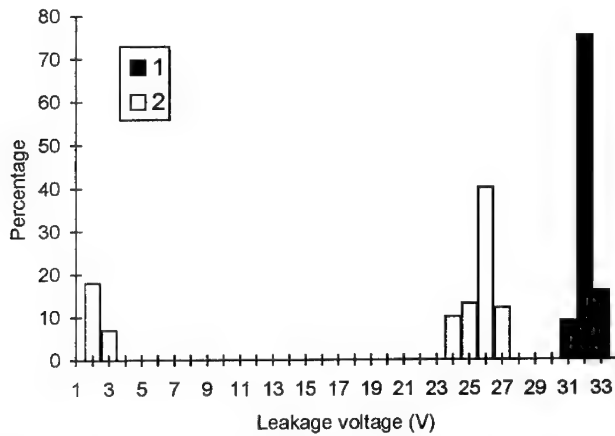


Fig.3. V_I histograms. Shaded - before, unshaded - in 6 days after PMFT (spec. №1).

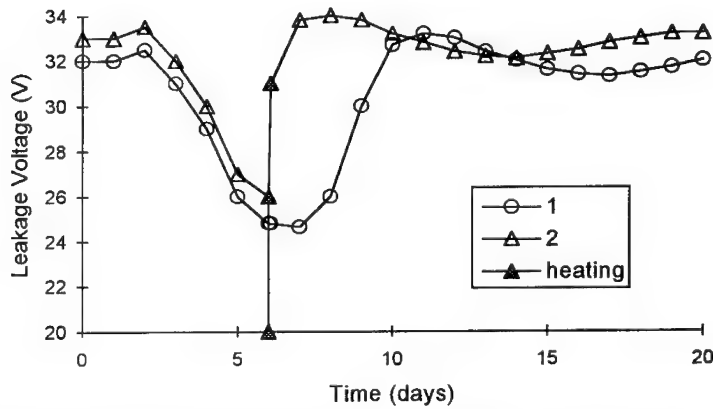


Fig.4. Variation of major peak position in V_I histograms after the end of PMFT: (1)

- for specimen № 1, (2) - for the specimen № 2 heated at time $t=t_0$

The subsequent V_I histogram registration reveals oscillatory (periodical variation in time with increasing period) changes of the major histogram V_I peak position corresponding to defect-free structures (Fig. 3) in accordance with the wafer warping. Fig. 4 shows the time dependence of $V_I(t)$ for two test specimens where curve 2 differs from the curve 1 by heating the specimen №2 for 1.5 hours starting in 6 days. The changes of V_I appeared only some days after PMFT owing to the gettering the defects at Si-SiO₂ surface.

DISCUSSION

These observed oscillations is probably connected with the reaction of strained bonds near Si-SiO₂ interface with non-equilibrium fast-diffusing impurity and intrinsic point defects, gettering by interface. Such reaction may results in appearance of charged centers in dielectric (for example E' centers). The similar oscillations of non-equilibrium defects in Si during ion implantation and ionizing radiation were described in [5]. The local quasi-chemical reactions may be the source of non-equilibrium defects in both cases. These reactions are induced by PMFT that results in the decay of impurity-defect complexes in Si subsurface region. In accordance with [1, 3] the model of the decay of the impurity-defect complexes is connected with increasing of the filling of the excited triplet states of the defects during relaxation of the electron-nuclear spin system polarization after the termination of PMFT. This results in the shift of the reaction of the defects forming defect complex to the direction of its decay because the triplet state is the dissociation state [6]. The observed auto-oscillatory character of Si-SiO₂ system parameters changes is similar to that for auto-wave processes in solid state systems with diffusion (appearance of diffusion instability) [5].

The degradation of MOS-structure electric parameters was caused by high concentrations of fast diffusion impurities and intrinsic defects. The estimated prolonged processes are in agreement with the idea about the defect structure evolution due to the decay of impurity-defect complexes [1-3], accompanied by a generation of fast diffusing impurity and intrinsic defects. These defects diffuse through the crystal and are captured by strained bonds. That results in a creation of generation centers. The migration defects were also getterred at the Si-SiO₂ interface, resulting in V_I decrease due to the positive built-in dielectric charge increase. When the bond is broken single species (H, fast diffusing atoms and vacancies) diffuse through the crystal and are captured by strained interface bonds (similar to impurity gettering at high temperature). The example of such decay metastable complexes are the complexes of oxygen, carbon, with transition metals and intrinsic defects. One of the defects, appearing after PMFT, is the generation center - COVV-complex (Carbon - Oxygen - Vacancy - Vacancy) [3], which formed by interaction of paramagnetic A-centers with carbon. The generation of such centers or the famous E-centers is the reason of generation lifetime decrease due to PMFT.

The time $\tau_r \approx 3-5 \times 10^5$ s of the maximum change V_I is determine by the linear size of fluctuation of defect concentration and the diffusion coefficient. In accordance with the results of [5] the characteristic linear size of fluctuation of non-equilibrium defects density in Si subsurface region is about 1 μ m. Using the diffusion

coefficient D , established in this work, we determined the linear size of fluctuation of defect concentration $l_r = \sqrt{D\tau_r} \approx 2\mu\text{m}$, that is an good agreement with the results of [5]. We try to estimate of diffusion activation energy E_d by heating the test specimen №2 up to 363 K for 1.5 hours. The temporal dependence of V_I is similar to for specimen №1 but shifted in 3 days approximately (Fig. 4). This allow to determine that the activation energy E_d in the following dependence of $\tau_r \approx \exp(E_d/kT)$ lies in the 0.45-0.5 eV range. It seems to as that these values of E_d and D characterize the migration of vacancies-impurity complexes (vacancy - fast diffusing atoms) in Si or positive-charged vacancy. That is in a good agreement with the registration of A - centers [2] in Si subsurface region after PMFT.

CONCLUSIONS

Thus, it was shown that PMFT can induce in thermodynamically non-equilibrium and non-magnetic silicon systems irreversible prolonged microstructures changes due to the impurity - defect complexes evolution in semiconductor subsurface layer.

Changes of carrier generation lifetime and dielectric leakage current could be observed for some days after shot-term PMFT at room temperature. Parameters changes is related to the metastable impurity-defect complexes decay and the following interaction of decay products.

The oscillatory character of the leakage voltage changes is connected with the changes in the build-in dielectric charge density near Si-SiO₂ interface and is due to the appearance of diffusion instability in the Si subsurface region induced by PMFT.

REFERENCES

1. V.M. Maslovsky, S.N. Postnikov, in *Proceedings of IV International Scientific-technical Seminar On Nontraditional Technologies*, Botevgrad 1989 (in Russian) (Sofia-Gorky) 5-14, (1989).
2. M.N. Levin, V.M. Maslovsky, *Defect-Interface Interactions* (Mater. Res. Soc. Proc. **319**, Pittsburgh 1994).
3. Maslovsky V.M., Klimov Y.A., Samsonov N.S., Simanovich E.V, *Fizika i tehnika poluprovodnikov*, **28** , № 5, 772-777, (1994)
4. V.M. Maslovsky, J.O. Lichmanov, N.S. Samsonov. *Physics Letters A*. **197**, 253-256 (1995).
5. J.W. Corbett, I.V. Verner and N.N. Gerasimenko, *Chaos and Stability In Defect Processes in Semiconductors*, (Trans Tech Publication, Switzerland 1992).
6. Ya. B. Zeldovich, A.L. Buchachenko, E.L. Frankevich, *Uspekhi fizicheskikh nauk* (in Russian) **155**, 3-45 (1988).

ELECTRICAL AND STRUCTURAL PROPERTIES OF MeV Si⁺ ION IMPLANTATION IN SILICON

ADITYA AGARWAL, S. KOVESHNIKOV, K. CHRISTENSEN AND G. A. ROZGONYI
Department of Materials Science and Engineering
North Carolina State University, Raleigh NC 27605, USA

ABSTRACT

The electrical properties of residual MeV ion implantation damage in Si after annealing from 600 to 1100°C for 1 hour have been investigated using Deep Level Transient Spectroscopy, Capacitance-Voltage, and Current-Voltage measurements. These data have been correlated with structural defects imaged by Transmission Electron Microscopy. It is shown that at least 4 deep levels are associated with the buried layer of extended defects after annealing at 800, 900, 1000 and 1100°C. Additionally, for the wafer annealed at 800°C at least 5 more deep level centers are present in the device layer above the buried defects.

INTRODUCTION

Ion implantation at MeV energies is being integrated into the device manufacturing process at a rapid pace. The process offers immediate advantages such as vertical well modulation, latch-up protection, device structure isolation, reduced temperature processing, and proximity gettering^{1,2}. The immediate advantages come hand in hand with a concern about how far the implant dose can be increased and how low an annealing temperature can be tolerated. Currently, 950°C annealing of a 2.0 MeV, $3 \times 10^{13} \text{ cm}^{-2}$ P⁺ implant produces acceptable device leakage; however, there have been reports that even after annealing at 1000°C for 1 hour the leakage current in a depletion region shallower than the implantation R_p will increase¹.

MeV implantation also offers an opportunity to achieve gettering of impurities from the active device region by placing secondary defect gettering sites within microns of the surface. Such a near surface gettering scheme, called proximity gettering³, has been validated by several investigators^{1,3,4} in samples heavily contaminated with impurities at concentrations in excess of 10^{17} cm^{-3} introduced at temperatures above 900°C. Since the techniques used to show gettering, namely SIMS or Auger, have a relatively low sensitivity, 10^{15} or 10^{17} cm^{-3} , respectively, gettering in the low impurity concentration regime applicable to the device manufacturing standards called for by the 1994 National Technology Roadmap for Semiconductors,⁵ or for low temperature (below 900°C) processes, has not yet been adequately confirmed. We have started such an investigation using more sensitive space charge-probe type electrical characterization techniques, such as Deep Level Transient Spectroscopy (DLTS). We report here the results of the first phase of this study--the electrical and structural characterization of both the near surface device region and the secondary defect gettering zone located at the implantation damage peak for 2.0 MeV Si⁺ implanted to a dose of $1 \times 10^{15} \text{ cm}^{-2}$, and then annealed from 600 to 1100°C. Additionally, diode characteristics of Schottky barrier contacts made on the as implanted and the annealed samples have been used as a measure of the overall device quality. A knowledge of the electrical behavior of the implantation damage prior to contamination will be utilized as a baseline for understanding gettering and the long term stability of the defect impurity complexes formed. Some preliminary results from Cu contaminated samples have been included in the last section of the paper illustrating how sensitive electrical measurements may be required to measure impurity/ extended defect interactions.

EXPERIMENTAL

N-type substrates with a $2-5 \Omega\text{-cm}$ resistivity were implanted at room temperature with Si^+ ions at 2.0 MeV to the dose of $1 \times 10^{15} \text{ cm}^{-2}$. Pieces of the wafers were subsequently annealed at 600, 800, 900, 1000 and 1100°C for 1 hour in a nitrogen ambient. After annealing, all the samples, annealed and as-implanted, were put through an RCA clean, and a 10 sec buffered oxide etch (BOE) to remove any oxides. Pieces of the samples were then cut for preparation into TEM foils and for electrical characterization. The remainder of the annealed wafer pieces were saved for further impurity contamination and gettering studies. For electrical characterization Schottky diodes, 1 mm in diameter, were fabricated simultaneously on all samples by evaporation of a 100 nm thick layer of Au. Current-Voltage (I-V) measurements were made on all diodes to check for rectifying behavior, and Capacitance-Voltage (C-V) measurements provided donor concentration vs. depth profiles on those samples showing rectifying behavior. DLTS measurements were made using a liquid helium insert type of cold stage and a lock-in amplifier to extract the signal. Our system has a sensitivity of $\Delta C/C = 10^{-5}$. Arrhenius plot data for determination of the trap activation energy was obtained by varying the time constant from 20 ms to 1.6 sec. All spectra presented in this paper were recorded using a 20ms time constant and the deep levels are referred to by their peak temperature corresponding to the same time constant. Depth dependent deep level concentration profiles were obtained by both a variation of the filling pulse with a constant reverse bias, and by varying the reverse bias and the filling pulse together. The width of the lambda layer was taken into account in determination of the depth dependent trap concentration profiles. The depth dependent DLTS results were correlated with the structural defects observed by XTEM.

RESULTS AND DISCUSSION

Implantation of Si^+ at 2.0 MeV results in a layer of buried damage centered approximately $1.7 \mu\text{m}$ below the surface. The damage is visible by XTEM as two bands of strain related dark contrast in the as-implanted sample, and as a buried layer of extended defects in the annealed samples, see Fig. 1. High resolution imaging of the as implanted sample (not presented here) showed the buried damage to consist of amorphous pockets within a crystalline lattice. The extended defects in the annealed samples are more clearly visible in the (g-2g), dark field images see Fig. 2, which shows interstitial dislocation loops expected to be lying along the 111 planes. The density and size of the dislocation loops, as well as the width of the dislocated layer, vary with the annealing temperature; the average loop size increasing from 20-30 nm for 800°C to 40-50 nm for 900°C and 100-150 nm for 1000°C, while the width of the defected region decreases from about $0.5 \mu\text{m}$ for 800°C to almost $0.3 \mu\text{m}$ for 1000°C.



Fig. 1. XTEM images before and after annealing for 1 hour at 800, 900 and 1000°C, from left to right, respectively, of Si (100) implanted with 2.0 MeV Si^+ to a dose of $1 \times 10^{15} \text{ cm}^{-2}$.



Fig. 2. Dark Field ($g_{400} \cdot 2g_{400}$) images showing dislocation loops after annealing at (left) 800°C, (middle) 900°C and (right) 1000°C.

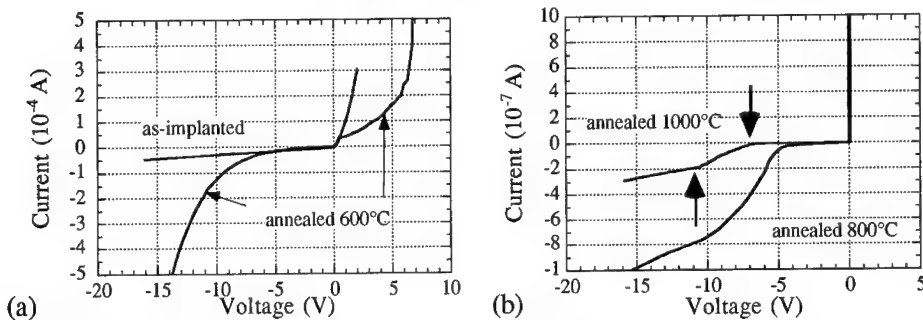


Fig. 3. I-V characteristics of Au Schottky barrier diodes on samples (a) as-implanted and annealed at 600°C, and (b) annealed at 800 and 1000°C.

Current-Voltage Characteristics

Typical I-V profiles of the diodes fabricated on the as-implanted samples and those annealed at 600, 800, and 1000°C are shown in Figs. 3a and b. Diodes on both as-implanted and 600°C samples failed to show good, or any, rectifying behavior, see Fig. 3a, precluding both C-V and DLTS measurements. The poor diode behavior in the as-implanted sample is presumed to be due to the primary implantation defects while the 600°C sample is even softer due to the beginning of formation of extended defects. For the 800 and 1000°C samples, the rectifying properties and leakage current improved with temperature, see Fig. 3b. In the sample annealed at 1000°C the conductivity suddenly increases when the expanding space charge region comes into contact with the buried layer of damage, and decreases when it moves beyond the damage, see arrows at -7 and -11V. For the sample annealed at 800°C the increase in conductivity begins at a lower reverse bias. There is a good correlation between the reverse bias (and hence, the depletion width) at which the increase in conductivity begins and then drops off, to the depth at which deep level centers are found by DLTS, as discussed below.

Ionized Donor Concentration from Capacitance-Voltage Measurements

C-V measurements were made on all samples except those with very high leakage current (as-implanted and 600°C annealed) and ionized donor concentrations were extracted. The concentration was found to be about $2 \times 10^{15} \text{ cm}^{-3}$, as expected from the starting material specifications, except in the region of the implantation damage peak where some modulation in the

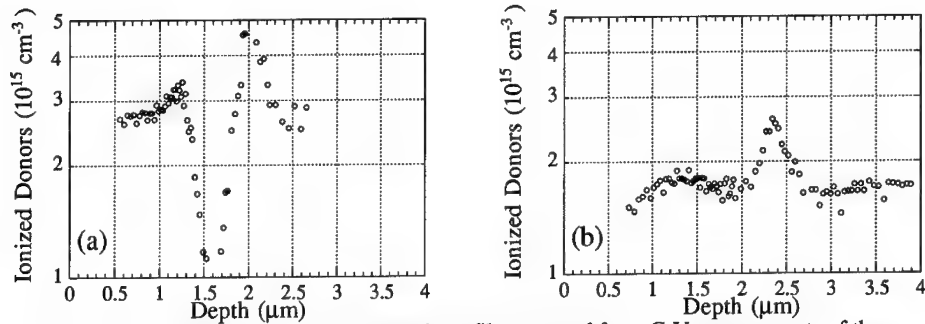


Fig. 4. Ionized donor concentration depth profile extracted from C-V measurements of the (a) 800°C, and (b) 1000°C samples.

ionized donor concentration was observed. All of the samples showed an increase in the ionized donor concentration at depths corresponding roughly to the top and bottom interfaces of the buried extended defect layer and a decrease in the region within the layer, see Figs. 4a and b. The 900 and 1100°C samples showed similar ionized donor localization behavior, but a general trend of less rearrangement with increasing annealing temperature was observed. Similar increases in the donor concentration related to MeV implantation, referred to as the dopant effect, have been previously observed in carbon implanted wafers, see Skorupa, et al.⁴, and the references therein; however, they reported that no dopant increase was observed in Si implanted wafers, as measured by spreading resistance measurements.

Deep Level Transient Spectroscopy

DLTS measurements were performed on samples annealed at 800, 900, 1000 and 1100°C. All the samples measured showed electrical activity arising from the buried layer of extended defects, while the 800°C sample additionally showed electrical activity in the region above, referred to as the device layer. The DLTS results are presented beginning with the 1000°C annealed sample, followed by 900 and 1100°C, and finally 800°C.

1000°C Annealing

The DLTS spectra corresponding to the 1000°C sample are shown in Fig 5a. The spectrum reveals 5 peaks. The most prominent peak at 211K, contains a shoulder at 170K. Two smaller peaks are located at approximately 135 and 100K, and finally a peak below 70K which is unresolvable due to carrier freezeout.

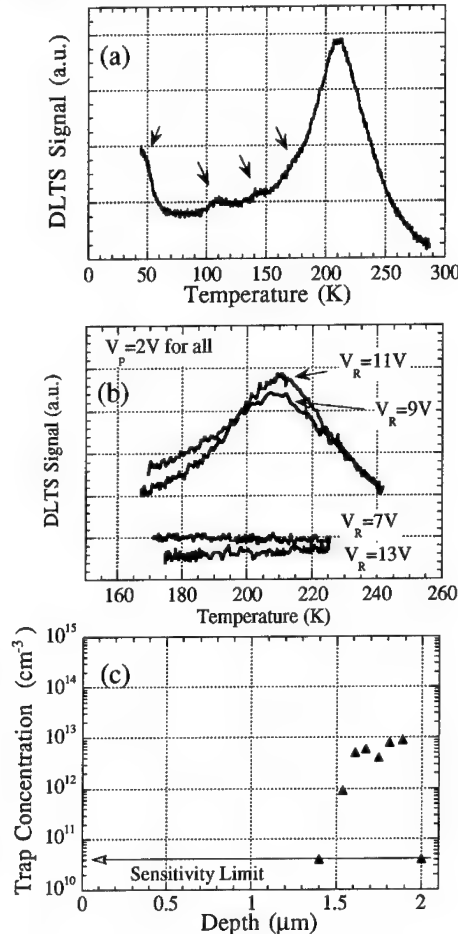


Fig. 5 (a), (b) DLTS spectra, and (c) Trap concentration vs. depth for 1000°C sample.

The activation energy for the 211K peak was found to be $E_C-0.44$ eV. The depth dependence of the DLTS spectrum was measured using the two methods described in the experimental section. Spectra obtained from the constant filling pulse method are presented in Fig. 5b, while trap concentrations derived from the constant reverse bias method are given in Fig. 5c. Results from the two methods are in agreement and establish that the electrical activity in the 1000°C annealed sample originates from the region of the extended defects only, note the flat scans in Fig. 5b for $V_R=7$ and 13V, corresponding to sampling volumes located above and below the defect layer. The average trap density was $5 \times 10^{12} \text{ cm}^{-3}$. Using the constant reverse bias method, the heights of the 100 and 135K peaks were found to change in the same proportion as the $E_C-0.44$ eV peak at 211K, indicating the possibility of the same defect center being responsible for all three.

1100 and 900°C Annealing

The DLTS spectra for the samples annealed at 1100 and 900°C were qualitatively the same as for the sample annealed at 1000°C and are not shown here. The deep level centers located at $E_C-0.44$ eV were found in all samples, with a trap concentration decreasing from $1 \times 10^{13} \text{ cm}^{-3}$ in the 900°C to $1 \times 10^{12} \text{ cm}^{-3}$ in the 1100°C annealed samples. No deep level activity was observed at depths shallower or deeper than the buried layer of extended defects.

800°C Annealing

Depth dependent DLTS spectra of the electrical activity in the 800°C sample are presented in Figs. 6a, b and c. The spectra corresponding to the defected layer look significantly different than the 900 and 1000°C samples, but closer inspection indicates that some of the same defect centers may be present. The spectrum corresponding to a filling pulse of 3V shown in Fig. 6b shows two well resolved peaks at 211K and 250K which begin to merge into one at $V_p=4$ and 5V. The peak at 211K was found to have an activation energy of $E_C-0.44$ eV and must originate from the same defect center responsible for the $E_C-0.44$ eV peak in the 1000°C sample, shown earlier in Fig. 5a. Further comparison of the 1000 and 800°C spectra, Fig. 5a and Fig. 6a ($V_p=5$ V), respectively, indicates the possibility of the 211K peak in the 1000°C sample containing a shoulder on the high temperature side, which may correspond to the 250K peak in the 800°C sample. We are unable to resolve these peaks at this time without the capability of pulse width variation in our DLTS system. The spectra corresponding to higher filling pulses of 6, 7, and 8V in Fig. 5b show saturation of the peak height at $V_p=7$ V, indicating once again confinement of the defects responsible for the 211K and 253K traps to the buried defected layer. A peculiar reduction in the DLTS signal appears in the spectra corresponding to $V_p=5, 6$ and 7V located at about 195K, Fig. 5b, which can not be explained at this time. The reduction is not seen in spectra

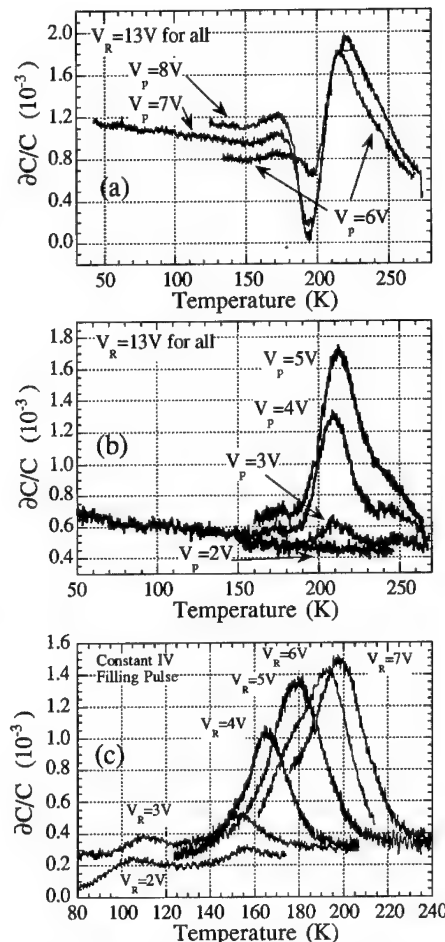


Fig. 6. DLTS spectra for 800°C sample with (a) constant $V_R=13$ V and $V_p=6, 7$ and 8V, (b) $V_R=13$ V and $V_p=2, 3, 4, 5$, and 6V, and (c) constant V_p with $V_R=2, 3, 4, 5, 6$, and 7V.

obtained at time constants longer than 20 ms. Investigation of the region above the defect layer using the constant filling pulse method indicated the presence of deep level centers, see Fig. 6c. The same region showed no electrical activity in samples annealed at temperatures above 900°C. At least 5 distinct traps can be seen in the various spectra: at 110K and 155K ($V_R=3V$), 165K ($V_R=4V$) 180K ($V_R=5V$) and 198K ($V_R=7V$). Due to the influence of neighboring defects, it is difficult to exactly determine activation energies for these defects but they have been estimated, with a relatively large error of $\pm 0.03eV$, to be $E_C-0.21$ (110K), $E_C-0.35$ (155K), $E_C-0.37$ (165K), $E_C-0.33$ (180K), and $E_C-0.38$ (198K).

Low Temperature Contamination with Cu

The 1000°C annealed sample containing the buried extended defect layer was contaminated by evaporating Cu onto the backside and then annealing for 1 hr at 500°C. The goal was to getter the small amount of copper which would be introduced at this temperature ($\sqrt{Dt} = 1.6$ mm for Cu in Si at 500°C). While XTEM failed to reveal any differences between the contaminated and uncontaminated samples in the defect layer, DLTS measurements revealed a slight 10% decrease in the concentration of the $E_C-0.44$ traps associated with the buried defects. XTEM did however reveal the presence of CuSi precipitates approximately 50nm large on the top surface of the contaminated sample, consistent with SIMS findings which showed a four orders of magnitude increase in the Cu signal above the 10^{15} cm^{-3} background level in the top 100nm. SIMS did not show any other increases in the Cu signal at lower depths corresponding to the defect layer. While it is probable that an insufficient vacuum in the sealed ampule allowed the Cu to contaminate the surface directly, some Cu should still have decorated the buried defects which both TEM and SIMS were unable to detect. It is unclear at this time whether the small decrease in the concentration of deep levels revealed by DLTS measurements is due to decoration by Cu or simply because of the additional annealing of the defects at 500°C.

SUMMARY

We have shown that empirically derived damage annealing cycles are adequate in controlling the residual electrical activity of MeV implantation. Our findings show that the electrical activity in the region above the secondary defects anneals out at some temperature between 800 and 900°C. We find that even after disappearance of the deep level activity in the near surface region following a 900°C anneal the nature of the deep level centers continues to evolve with higher annealing temperatures. While it is uncertain at this time whether the deep levels in the 800°C sample result from implantation damage interaction with intrinsic defects, or with unintentionally implanted impurities, it has been shown that higher temperature treatments result in adequate annealing of this damage. The preliminary results from a Cu gettering experiment demonstrated the inability of TEM and SIMS to measure gettering of the small amount of metallic impurities which may be introduced during processing.

ACKNOWLEDGMENTS

The authors wish to thank Dr. Dennis Maher, also at NC State, for valuable scientific discussion, and Ted McIntyre and Bob Simonton of Eaton Corporation for providing wafers and mega-electron-volt ion implantation services. Overall financial support for this work has been provided by the Semiconductor Research Corporation (SRC).

REFERENCES

- ¹K. Tsukamoto, T. Kuroi, S. Komori, and Y. Akasaka, Sol. St. Tech, June 1992.
- ²J. O. Borland and R. Koelsch, Solid State Tech., Dec. 1993.
- ³H. Wong, N.W. Cheung, P.K. Chu, J. Liu and J.W. Mayer, Appl. Phys. Lett **52** (12), 1023 (1988).
- ⁴W. Skorupa, R. Körgler, K. Schmalz, P. Gaworzewski, G. Morgenstern, and H. Syhre, Nucl. Instr. Meth. B **74**, 70 (1993).
- ⁵1994 National Technology Roadmap for Semiconductor Processing, SIA, San Jose, California.

INVESTIGATION OF RESISTIVITY DISTRIBUTIONS IN CDTE CRYSTALS BY TIME DEPENDENT CHARGE MEASUREMENTS (TDCM)

C. EICHE, W. JOERGER, M. FIEDERLE*, R. SCHWARZ, M. SALK, D. G. EBLING* AND
K.W. BENZ Kristallographisches Institut, University of Freiburg, Freiburg, Germany
*Freiburger Materialforschungszentrum (FMF), University of Freiburg, Freiburg, Germany

ABSTRACT

Spatially resolved resistivity measurements of CdTe crystals doped with Titanium (Ti) and Vanadium (V) were performed. From the temperature dependence of the resistivity the spatial variation of the thermal activation energy was deduced. Variations in axial as well as radial direction were observed and qualitatively explained by a combined segregation and compensation model. It is based on the deep donor levels of Ti and V at 0.95 eV below the conduction band.

INTRODUCTION

Semiinsulating II-VI semiconductors have a wide range of applications, e.g. x- and γ -ray detectors. The high resistivity is usually achieved by the compensation of excess carriers with a deep level. The deep level can either be an intrinsic defect or dopants (e.g. Vanadium (V) or Titanium (Ti)). Especially transition metal doped CdTe has gained increased interest in the last years. Photorefractive energy transfer at 1.5 μm has been reported [1] in these materials. Because of the segregation of the dopants and the residual impurities the compensation and in consequence the resistivity are usually not homogeneously distributed in the grown crystal. Nondestructive and spatially resolved measurements are therefore required to investigate these variations.

Time Dependent Charge Measurement (TDCM) [2] is a method to measure the resistivity contact free. The method can easily be extended to include temperature dependent measurements, which can provide information on the thermal activation energy of the charge carriers.

This paper reports on the investigation of CdTe crystals doped with Ti and V. Different growth techniques namely a vertical Bridgman method and a sublimation growth technique were applied. Details of the growth experiments are summarized in the following section. After that, results obtained with TDCM will be presented. They will be discussed qualitatively using a combined segregation and compensation model.

EXPERIMENTAL RESULTS

Growth experiments

Ti and V doped crystals were grown from the melt in pBN ampoules by the vertical Bridgman technique using a standard configuration. The growth temperature was set to 1130 °C. The crystals were grown with a growth velocity of 10 mm/d. Crystals with a length of about 20 cm

and a diameter of up to 15 mm were obtained.

The Sublimation Travelling Heater Method [3],[4] was used to grow crystals from the vapor phase. The transport rate was increased by reducing the height of the vapor zone to 6 mm in contrast to 10 mm in the original setup. At the growth temperature of 1050 °C a pulling rate of 1 mm/d was applied. Ti and V was not transported through the vapor phase at lower temperatures. The crystals had a length between 10 and 20 mm and a diameter of 15 mm. Fused silica ampoules could be used in the vapor phase growth experiments in contrast to the melt growth, where they were attacked.

The dopants were added to the synthesis in a concentration of about $5 \cdot 10^{19} \text{ cm}^{-3}$. Slices perpendicular and parallel to the growth axis were cut from the grown crystal rods. The samples with a thickness of approximately 1 mm were lapped and mechanically polished with diamond paste down to 1 μm .

Time Dependent Charge Measurement

TDCM is based on the capacitive relaxation of the sample in a capacitor arrangement [2]. It allows for the non-destructive measurement of the resistivity between $1 \cdot 10^6$ and $2 \cdot 10^{10} \Omega\text{m}$ with a resolution of $0.5 \times 0.5 \text{ mm}^2$. Temperature dependent measurements were performed using a hot chuck. The temperature can be set between 295 K and 340 K with an accuracy of 0.1 K. The thermal activation energy of the charge carriers can be obtained from temperature dependent measurements.

The resistivity of the Bridgman grown CdTe:Ti crystals was below $10^6 \Omega\text{m}$ in the first grown part of the crystal (solidified fraction $g < 0.3$). A strong increase in the resistivity was observed in the following section of the crystal ($0.3 < g < 0.7$). The resistivity distribution of a slice cut perpendicular to the growth axis at $g=0.4$ is given in Fig.1. The resistivity is increasing from the middle of the crystal towards the edge in an axial symmetric way. The distribution of the activation energy is qualitatively the same (Fig.2).

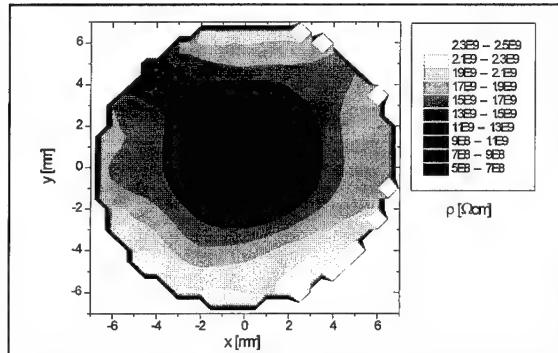


Fig.1: Resistivity distribution at $T=296 \text{ K}$ of a CdTe:Ti slice cut perpendicular to the growth direction at $g=0.4$ of a Bridgman grown crystal.

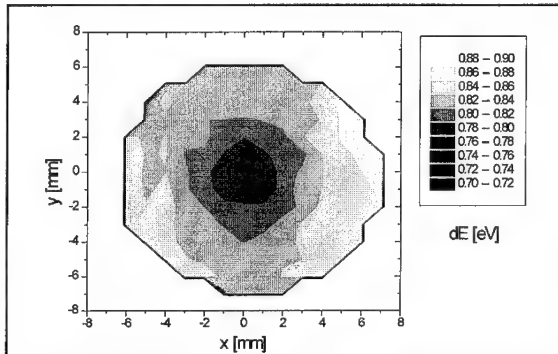


Fig.2: Distribution of the activation energy in the CdTe:Ti slice shown in Fig.1.

In the last part of the crystal ($g > 0.7$) the maximum resistivity of about $2 \cdot 10^9 \Omega\text{cm}$ remained nearly constant in axial direction. Radial variations were less pronounced. The activation energy of 0.85 eV was constant in axial and radial direction within the experimental error of about 10%.

In the case of V doped crystals the resistivity was already above $10^8 \Omega\text{cm}$ at the beginning of the grown crystals. The resistivity was increasing towards the end of the crystal reaching a maximum value of $1.3 \cdot 10^{10} \Omega\text{cm}$. In the last quarter of the crystals radial variations were within 10%. For $g < 0.6$ radial resistivity changes were greater than 20%. A similar radial distribution pattern as in CdTe:Ti crystals was observed.

In contrast to the Bridgman grown crystals the resistivity of the vapor phase grown crystals was already above $10^9 \Omega\text{cm}$ in the first part of the CdTe:Ti crystals (Fig.3). The resistivity was increasing nearly linearly towards the end of the crystal followed by a sharp decrease. The activation energy distribution resembled the resistivity distribution (Fig.4). Radial changes were less pronounced than in the case of the samples grown by the Bridgman method and mainly due to edge effects.

In V doped crystals the resistivity was $1.3 \cdot 10^{10} \Omega\text{cm}$ throughout the crystals varying less than 10%. A small decrease was observed towards the ampoule walls and in the last two millimeters.

Low resistivity seed crystals were used for the growth experiments. After the growth it was found that not clear transition from seed to grown crystal can be observed in the resistivity and activation energy distribution. The diffusion of dopants into the seed crystal during the creation of the vapor zone, which took several hours, is therefore fast enough to change the resistivity by orders of magnitude.

The conductivity of the samples was n-type with mobilities of about $500\text{--}600 \text{ cm}^2/\text{Vs}$ independent of the growth technique. Resistivity changes are therefore mainly caused by variations of the electron concentration.

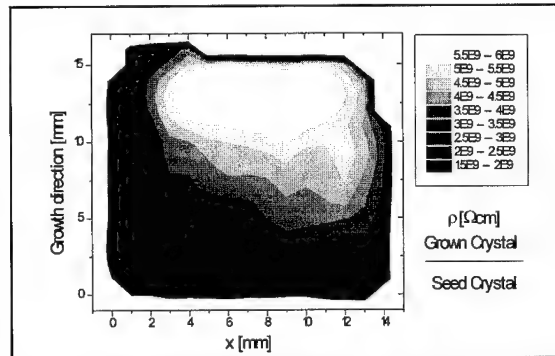


Fig.3: Axial resistivity distribution of a CdTe:Ti crystal grown from the vapor phase. The transition from seed to grown crystal is indicated.

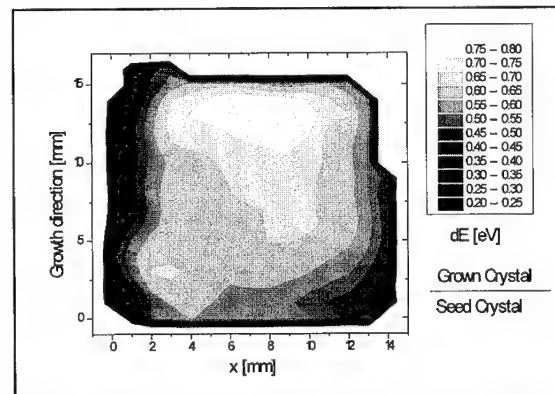


Fig.4: Axial activation energy distribution of a CdTe:Ti crystal grown from the vapor phase.

DISCUSSION OF THE EXPERIMENTAL RESULTS

Deep donor levels with an activation energy of about 0.95 eV are caused by the Ti and V doping [5],[6]. The acceptor surplus due to native defects and residual impurities in undoped CdTe is compensated by these deep levels. In consequence the Fermi level is pinned near the middle of the bandgap and semiinsulating material is obtained. The resistivity distribution can be described by a combined segregation and compensation model. The axial dopant profile can be calculated using Pfann's equation [7] in the case of the Bridgman growth. For the vapor phase growth Tiller's formula [8] has to be taken into account. These two formulas with the appropriate input can be used to calculate axial dopant profiles. After that the electron and hole concentrations and the resistivity can be calculated by an extension of the Johnson model [9]. The details of this procedure are published elsewhere [10].

The compensation is changing during the crystal growth process. Since in highly compensated semiconductors the concentrations of both electrons and holes are of the same order of magnitude the temperature dependence of the resistivity has to be calculated directly from

$$\rho = \frac{1}{q(\mu_e n + \mu_h p)} \quad (1)$$

(n/p : electron/hole concentration, μ_e/μ_h : electron/hole mobility, q : elementary charge). The measured resistivity and activation energy are then a strong function of the surplus of the deep donor N_{DD} over the difference between acceptors N_A and donors N_D (Fig.5). In these simulations an acceptor surplus of $1 \times 10^{14} \text{ cm}^{-3}$ is assumed to account for the p-type conductivity of the undoped samples. An additional donor level at about 0.4 eV below the conduction band has to be considered to obtain a good agreement between the experimentally observed n-type conductivity and the thermal activation energy distributions. In PICTS measurements a deep level with similar activation energy was found [5].

The qualitative behavior of the resistivity and the activation energy distribution can be reproduced by simulations for both growth techniques (Fig.6 for STHM grown crystals, [5] for Bridgman crystals). If this additional donor level is not taken into account, especially the activation energy distribution would differ significantly from the experiment.

The sharp decrease of the resistivity during the last few millimeters in the vapor phase grown crystal is due to a continued growth during the cooling down process. But as mentioned

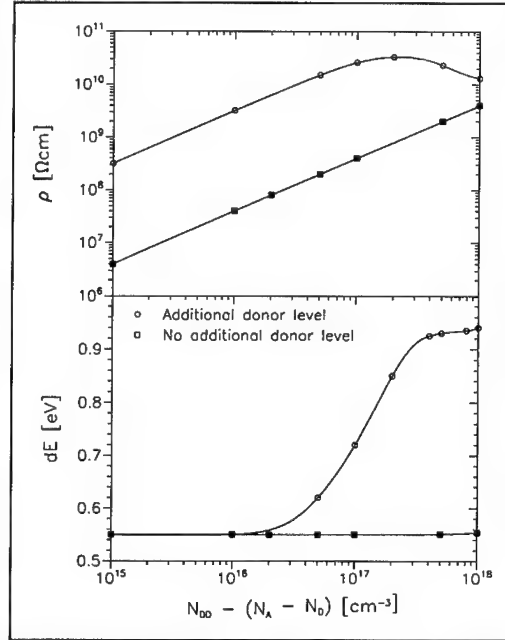


Fig.5: Resistivity and activation energy calculated from temperature dependent simulations as a function of the deep donor surplus.

above, Ti is only transported at temperatures above 1000 °C whereas the usual growth temperature in STHM is 850 °C. Therefore, during the first hours of the slow cooling ramp CdTe is still growing but less Ti is incorporated, which results in a lower resistivity. This assumption is supported by the decrease in the observed activation energy, which indicates a lower degree of compensation.

In both growth techniques the dopant concentration in the initial part of the grown crystal is given by $c_0 k_0$, where c_0 is the dopant concentration in the source material and k_0 the segregation coefficient. If the difference between shallow donors and acceptors is the same in both source materials, the initial resistivity should be the same. This is not observed in all our experiments although equal source materials were used. This result can be explained by the purification effect of the vapor phase growth technique because certain impurities do not sublime and stay in the remaining source material. By this, the excess acceptor concentration is reduced. In V doped crystals a similar dependency on the growth technique is obtained using the same dopant concentration.

It can be shown [5] that the strong axial variation of the resistivity in the Bridgman crystals is caused by a small segregation coefficient of Ti. Because of the convex phase boundary in Bridgman grown crystals radial variations in the resistivity are mainly due to the curvature of the phase boundary. The solidification is taking place in the center of the ampoule, which is the colder than the edge, first. Therefore, the incorporated dopant concentration and consequently the resistivity are lower. Because of the steep increase in resistivity in the transition region the radial variations can be very strong as seen in Fig.3. In the last part of the crystal, where not axial increase is observed, the radial variation is reduced. The phase boundary can be looked on during the vapor phase growth process. A nearly flat phase boundary is established by this growth technique. In consequence radial variations because of a strong axial resistivity increase are diminished.

In Bridgman crystals the resistivity should reach a maximum value of greater than $10^{10} \Omega\text{cm}$ [5]. There is always one point in the crystal where the resistivity will be intrinsic independent of the difference between shallow donors and acceptors. This can only be reproduced in V doped crystals. Using Ti as a dopant the maximum resistivity was always below $10^{10} \Omega\text{cm}$. A limited maximum solubility of Ti in CdTe can be responsible. The highest dopant concentration is obtained in the last part of the crystal. In CdTe:Ti this concentration is not

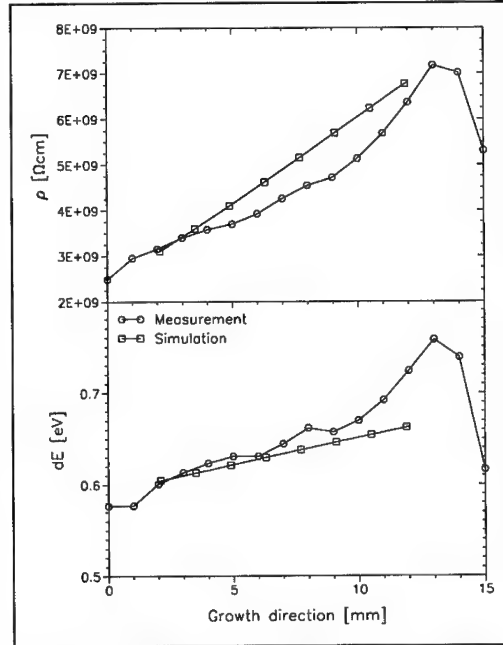


Fig.6: Comparison of simulated and measured axial resistivity and activation energy profiles in the case of vapor phase grown CdTe:Ti crystals. The first two millimeters of the measured data belong to the seed crystal.

high enough for a complete compensation.

CONCLUSION

The resistivity and the activation energy distributions of CdTe:Ti and CdTe:V crystals grown from the melt and the vapor phase were investigated. The qualitative behavior was described by a combined segregation and compensation model based on the assumption that the compensation is achieved by a deep donor level 0.95 eV below the conduction band. Good agreement between measured and simulated activation energy distributions could only be obtained, if an additional donor level is taken into account. Whether this level is due to the transition metal doping needs further investigations. It was shown that with V doping a higher resistivity and a more homogeneous distribution can be achieved. In the case of Ti doping a limited incorporation of the dopant into CdTe results in a lower maximum resistivity.

REFERENCES

1. A. Partovi, J. Millerd, E.M. Garmire, M. Ziari, W.H. Steier, S.B. Trivedi and M.B. Klein, *Appl. Phys. Lett.* **57**, 846 (1990).
2. R. Stibal, J. Windscheif and W. Jantz, *Semicond. Sci. Technol.* **6**, 995 (1991).
3. R. Triboulet, *Rev. Phys. Appl.* **12**, 123 (1977).
4. R. Schwarz, W. Joerger, C. Eiche, M. Fiederle and K.W. Benz, *J. Cryst. Growth* **146**, 92 (1995).
5. C. Eiche, W. Joerger, M. Fiederle, D. Ebling, R. Schwarz and K.W. Benz, *Opt. Mater.* **4**, 214 (1995).
6. G. Bremond, A. Zerrai, G. Marrakchi, A. Aoudia, Y. Marfaing, R. Triboulet, M.C. Busch, J.M. Koebbel, M. Hage-Ali, P. Siffert and J.Y. Moisan, *Opt. Mater.* **4**, 146 (1995).
7. W. G. Pfann, in *Zone Melting* (John Wiley, New York, 1966).
8. W. A. Tiller, K. A. Jackson, J. W. Rutter and B. Chalmers, *Acta Metall.* **1**, 428 (1953).
9. E.J. Johnson, J.A. Kafalas and R.W. Davies, *J. Appl. Phys.* **54**, 204 (1982).
10. C. Eiche, W. Joerger, M. Fiederle, D. Ebling, R. Schwarz and K.W. Benz, *J. Cryst. Growth* **146**, 98 (1995).

SCANNING TUNNELING MICROSCOPY STUDIES OF GaAs_{1-x}P_x SINGLE CRYSTALS

X. LIU, E. R. WEBER

*Department of Materials Science and Mineral Engineering, University of California,
Berkeley, CA 94720*

D. F. OGLETREE, M. SALMERON

Materials Science Division, Lawrence Berkeley Laboratory, Berkeley, CA 94720

T. SLUPINSKI

Institute of Experimental Physics, Warsaw University, Hoza 69, 00-681 Warsaw, Poland

ABSTRACT

We report cross-sectional scanning tunneling microscopy studies of GaAsP single crystals grown by the Liquid Encapsulated Czochralski technique. We show that the two group-V elements can be clearly distinguished, which is attributed to the difference in energies of surface dangling bond states of As and P. Our atomic scale imaging results show alloy composition in agreement with spectroscopic studies. They also provide valuable information about atomic scale alloy fluctuations and clustering effects.

INTRODUCTION

There is an increasing demand for substrates in alloy semiconductor electronics. Single crystals of bulk semiconductor alloys may remove the limitations of lattice matching with simple compounds. They offer a continuously variable lattice parameter, and so are potentially useful as substrates for strain-free epitaxy of semiconductors. However, it is a difficult task to produce these bulk alloy crystals due to phase diagrams with separated liquidus and solidus lines.¹ Segregation of components and related transport problems in the melt close to the growth interface easily lead to non-homogeneous growth. Nevertheless, a number of efforts have been undertaken to grow ternary alloys from the melt, such as InGaSb,² GaInAs,^{3,4} InSbBi,⁵ and InGaP.⁶

Recently, the Liquid Encapsulated Czochralski (LEC) technique has also been successfully used to grow bulk crystals of GaAsP with P composition up to 15 at. %.⁷ Small diameter (1-2.5 cm) crystals with longitudinal composition gradients were obtained. Characterization of these crystals by macroscopic techniques, such as photoluminescence (PL) and X-ray diffraction indicates good quality single crystals, but with the presence of composition fluctuation of about 1 at. %.⁷ In this work, we study these single crystals of GaAsP by scanning tunneling microscopy (STM). The ability of STM to distinguish As and P atoms allows us to investigate the alloy distribution at the atomic scale.

EXPERIMENTAL

GaAs_{1-x}P_x crystals were grown by a LEC 2-inch crystal growth apparatus (Galaxy Mark III, LPA Industrie, France). Rotation of the crystal (30 rpm) and the crucible (10-20 rpm) in opposite directions was employed to achieve better mixing of the melt. Small GaP or InP crystals were

used as a source of phosphorus. The initial charge of 0.6 - 1 kg was composed of elemental As and Ga and 1-5 molar percent of GaP or InP and a few ppm of Te. An As-rich melt was prepared for the growth with As/Ga = 1.06. The growth temperature was increased with the P concentration, at a rate of $dT/dx \sim 150^\circ\text{C}$ for small x . The axial gradient of the temperature close to the growth interface was 50°C/cm . The growth rate was 3.5 -6 mm/hr.

Cross-sectional STM studies of the $\text{GaAs}_{1-x}\text{P}_x$ crystals were performed in an ultrahigh-vacuum (UHV) chamber with a base pressure of 8×10^{-11} Torr.⁸ The STM was designed similarly to that developed by Frohn *et al.*⁹ Special modifications were made for cross-sectional studies, and the sample was cleaved in the UHV chamber to expose the clean (110) surface. The STM tip can be electronically translated on the sample surface over a distance of millimeters with nanometer resolution. This enables us to study the statistics over a large sample area and to focus on any specific features of interest. The images were obtained in a constant current mode, and electrochemically etched Pt-Rh tips were used.

RESULTS AND DISCUSSION

Fig. 1 shows filled-state STM images of the (110) surfaces of two $\text{GaAs}_{1-x}\text{P}_x$ crystals. Two images are shown for samples with a P composition of 2.1% (left) and 9.5% (right), respectively.

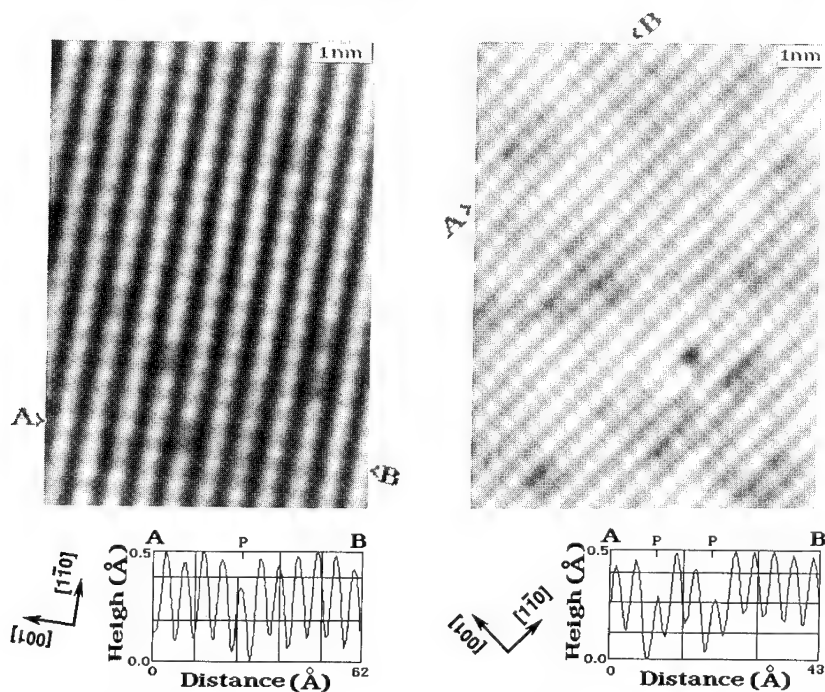


Fig. 1 Filled-state STM images taken at -2 V sample bias of GaAsP with P of 2.1% (left) and 9.5% (right). The P atoms appear darker than As atoms, and have a corrugation $\sim 1/2$ that of As atoms. This is more clearly observed in the amplitude profile along the A-B line cuts of each of the images.

For these filled-state images, the observed atomic structure is associated with the group V sublattice of the material. Both images show a unit-cell structure similar to that of the GaAs (110) surface. However, in contrast to GaAs, a very inhomogeneous distribution of corrugation amplitude is observed in the images. Some atomic maxima clearly appear darker. This may be more easily observed in the amplitude profiles along the A-B line cuts in both images.

The fluctuation of the corrugation amplitude is not a consequence of tip instability. Similar inhomogeneous corrugations are obtained for different tips. In addition, for a number of samples studied, including those shown in Fig. 1, the density of the darker maxima increases for samples with higher P composition. This leads us to the conclusion that in the images of group-V sublattice of GaAsP in Fig. 1, the darker maxima are associated with P atoms and the brighter ones associated with As atoms.

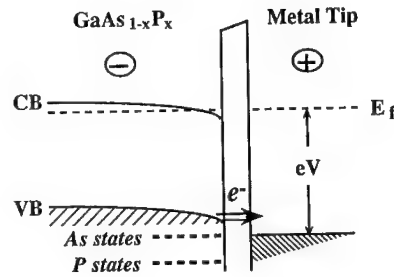
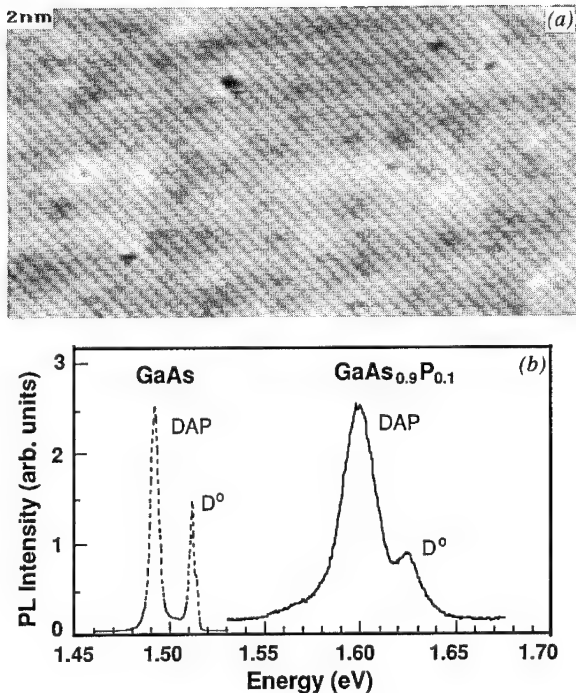


Fig. 2 Schematic energy band diagram illustrating the electron tunneling process at negative sample bias. The surface dangling bond states of As and P are illustrated as dashed lines. The states associated with P are expected to have a lower energy, resulting in a reduced tunneling current for P and the darker appearance of P in STM images.



The observed variation in the corrugation amplitude of the As and P atoms can be generally understood in terms of electron tunneling from dangling bond states of different energies associated with the As and P surface atoms. A similar mechanism has been employed to interpret the amplitude variation in the image of group-III sublattice in quantum-well structures containing layers of AlGaAs¹⁰ or InGaAs.¹¹

Fig. 3 (a) A typical STM image of GaAsP crystals at a sample bias of -2.5 V showing a random distribution of P, and (b) the PL spectrum of the same sample showing donor-bound exciton (D^0) and donor-acceptor-pair recombination (DAP). The P composition determined from the STM image and PL spectrum is 7% and 9.5%, respectively, indicating the presence of local composition fluctuations.

For most III-V semiconductors, it is commonly believed that a charge transfer and surface buckling occurs upon cleavage of the (110) surface.¹² This results in surface dangling bond states of both group-III and group-V elements being pushed out of the energy gap E_g , with the dangling bonds of group-III element unoccupied and group-V occupied. In semiconductor alloys, such as GaAsP, surface relaxation and charge transfer are expected between the group III and group-V elements, similar to that of binary compounds. However, since the Ga-P bond is more ionic than the Ga-As bond, the dangling bond states associated with P atoms are expected to be pushed to lower energies in the valence band than those associated with As atoms (see Fig. 2). Hence for the same tunneling bias, the tunneling current associated with the P will be smaller, and P atoms will appear darker in the image than As atoms.

While the simple model in Fig. 2 can qualitatively interpret the contrast between As and P atoms in GaAsP, the model predicts that the pure electronic effect should have a strong bias dependence. The relative corrugation amplitude of As and P should decrease with increasing bias voltage, and should diminish at high bias voltages. Experimentally, however, it is observed that the relative corrugation amplitude of these two elements have a very weak bias dependence, e. g. almost unchanged as the bias increases from -2.5 to -3.5 V. The bias-independent corrugation is not expected from the model in Fig. 2, unless the surface dangling bond states are much broader in energy than a few eV. An alternative interpretation is that the corrugation results from the difference in vertical positions of the As and P atoms. The topographic position difference will give rise to the bias-independent corrugation. Different surface relaxation associated with the As and P atoms can result in the difference in the vertical positions of these two elements.¹³ However, such an effect is expected to be very small, not sufficient to account for the observed relative corrugation of As and P of a few tenths of an angstrom. A better explanation should probably take into account the contributions of both topographic and electronic effects. The corrugation is thus due to topography enhanced electronic effects. Further studies are needed to fully understand these observations.

The ability of STM to distinguish two group V elements in GaAsP allows us to study the alloy composition distribution at the atomic scale. Fig. 3a shows a typical large-scale image of the

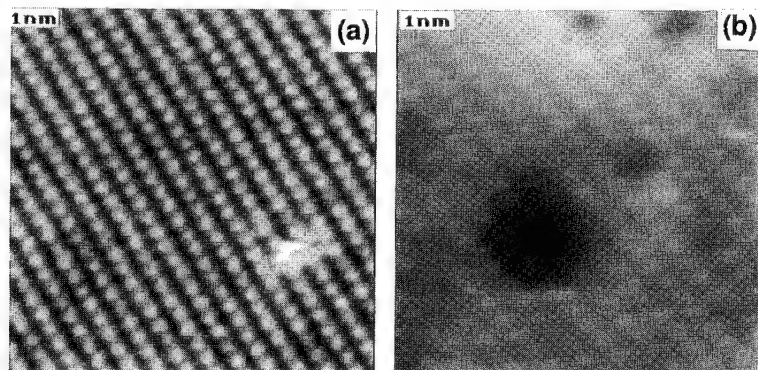


Fig. 4 Filled-state STM images of a GaAsP sample that show local segregation of components at the atomic scale. (a) a region of the sample that is depleted of P, and (b) a region that shows clustering of P of about 14 atoms.

GaAs_{0.9}P_{0.1} sample. The distribution of P in the material appears fairly random. By counting the number of darker maxima in the image, the local composition of P is determined to be 7%. In Fig. 3b, the PL spectrum of the same sample is shown, together with the reference sample of GaAs. The P composition can also be determined from the PL spectrum. Assuming $dE_g/dx = 11.7 \text{ meV/1 at.}\%$,¹⁴ the P composition is found to be 10% for the sample in Fig. 3.

It thus appears that there is a discrepancy between the microscopic and macroscopic P composition determined by STM and PL, respectively. The PL spectrum of GaAs_{0.9}P_{0.1} is very similar to that of GaAs. Both of them exhibit a PL peak due to the donor bound exciton recombination and the donor-acceptor pair recombination. However, the PL peak of the GaAs_{0.9}P_{0.1} sample is much broader than that of GaAs. Similar line broadening are also observed in X-ray rocking curve measurements.⁷ The full width at half maximum of the PL emission in Fig. 3b indicates a fluctuation of P composition of $\pm 1\%$. In addition, a tail on the lower energies of the PL emission is clearly observed in Fig. 3b. An estimation from the tail emission show that the P composition in the measured sample area ($\sim 10 \mu\text{m}$, the diameter of the focused laser beam) can be as low as 5%. The local P composition of 7% determined by STM is thus within the composition range measured by macroscopic measurements.

The typical random distribution of P observed for the bulk sample as shown in Fig. 3a is in strong contrast to the dominating alloy clustering in thin strained layers of InGaAs/GaAs.¹⁰ This observation is consistent with the previous suggestion that the preferential clustering of pairs of In atoms along the molecular beam epitaxial growth direction in InGaAs/GaAs is associated with the strain present in the thin film growth.

Although a significant fluctuation of P composition is sometimes observed, the density of P clusters is very low in the bulk GaAsP sample studied. Fig. 4a shows a region in the sample where no fluctuation of corrugation amplitude is observed in the imaged area (It is not clear what give rise to the white maxima observed in the imaged). This is thus an area depleted of P atoms. Fig. 4b, on the other hand, shows a typical image with a large fluctuation of the corrugation. The image shows a depression of about 14 atoms. This depression is associated with a cluster of P atoms. The most frequently observed cluster of P in the sample studied contains 10-20 P atoms, and there are only about 2 clusters observed out of ~ 50 imaged regions. These observations indicate that although no clear indication of the segregation of components is observed in macroscopic measurements, local segregation is present at the atomic scale.

SUMMARY

We have shown that cross-sectional STM is a unique tool to study semiconductor alloys at the atomic scale. For GaAs_{1-x}P_x single crystals studied, STM can clearly distinguish As and P atoms. This is attributed to the energy difference of surface dangling bond states of these two elements. Using STM, we have been able to determine local alloy compositions, and reveal atomic scale alloy fluctuation, clustering effects, etc. which are difficult to investigate using normal macroscopic characterization techniques.

ACKNOWLEDGEMENTS

We thank Dr. J. F. Zheng for fruitful discussions. This project was supported by the Director, Office of Energy Research, Office of Basic Energy Science, Materials Science Division, U. S. Department of Energy under contract No. DE-AC03-76SF00098.

REFERENCES

- [1] M. B. Panish, M. Ilegems, *Progress in Solid State Chemistry* **7**, 75 (1972).
- [2] A. Tanaka, A. Watanabe, M. Kimura, T. Sukegawa, *J. Cryst. Growth* **135**, 269 (1994).
- [3] H.-J. Sell, *J. Cryst. Growth* **107**, 396 (1991).
- [4] K. Nakajima, T. Kusunoki, C. Takenaka, *J. Cryst. Growth* **113**, 485 (1991).
- [5] T. Ozawa, Y. Hayakawa, M. Kumagawa, *J. Cryst. Growth* **109**, 212 (1991).
- [6] G. Bischofink, K. W. Benz, *J. Cryst. Growth* **97**, 245 (1989).
- [7] T. Slupinski, J. Przybytek, A. Wysmolek, M. Leszczynski, A. Babinski, J. Borysiuk, A. Kurpiewski, A. Barcz, and R. Stepniewski, *Proc. Semi-Insulating III-V Materials* (Warsaw, 1994), in press.
- [8] J. F. Zheng, X. Liu, N. Newman, E. R. Weber, D. F. Ogletree, and M. Salmeron, *Phys. Rev. Lett.* **72**, 1490 (1994).
- [9] J. Frohn, J. F. Wolf, K. H. Besocke, and N. Teske, *Rev. Sci. Instrum.* **60**, 1200 (1989).
- [10] M. B. Johnson, U. Maier, H.-P. Meier, and H. W. M. Salemink, *Appl. Phys. Lett.* **63**, 1273 (1993).
- [11] J. F. Zheng, J. D. Walker, M. B. Salmeron, and E. R. Weber, *Phys. Rev. Lett.* **72**, 2414 (1994).
- [12] A. R. Lubinsky, C. B. Duke, B. W. Lee, and P. Mark, *Phys. Rev. Lett.* **36**, 1058 (1976).
- [13] C. B. Duke, C. Mailhot, A. Paton, D. J. Chadi, and A. Kahn, *J. Vac. Sci. Technol.* **B 3**, 1087 (1985).
- [14] R. J. Nelson, N. Holonyak, W. O. Groves, *Phys. Rev.* **B 13**, 5415 (1976).

STUDY OF OXYGEN DIFFUSION AND CLUSTERING IN SILICON USING AN EMPIRICAL INTERATOMIC POTENTIAL

Z. JIANG AND R. A. BROWN

Department of Chemical Engineering, Massachusetts Institute of Technology, Cambridge,
MA 02139

ABSTRACT

The diffusion path and diffusivity of oxygen in crystalline silicon are computed using an empirical interatomic potential which was recently developed [1] for modelling the interactions between oxygen and silicon atoms. The diffusion path is determined by constrained energy minimization, and the diffusivity is computed using jump rate theory. The calculated diffusivity $D=0.025 \exp(-2.43\text{eV}/k_B T) \text{ cm}^2/\text{sec}$ is in excellent agreement with experimental data. The same interatomic potential also is used to study the formation of small clusters of oxygen atoms in silicon. The structures of these clusters are found by NPT molecular dynamics simulations, and their free energies are calculated by thermodynamic integration. These free energies are used to predict the temperature dependence of the equilibrium partitioning of oxygen atoms into clusters of different sizes. The calculations show that, for given total oxygen concentration, most oxygen atoms are in clusters at temperature below 1300K, and that the average cluster size increases with decreasing temperature. These results are in qualitative agreement with the effects of thermal annealing on oxygen precipitation in silicon crystals.

INTRODUCTION

Silicon crystals grown by Czochralski processes contain oxygen as an impurity with a concentration as high as 50 ppm. The oxygen is introduced into the crystal during solidification from the melt because of the dissolution of the quartz crucible used in the Czochralski puller [2,3]. Single oxygen atoms exist in silicon as interstitials that occupy the puckered bond-center sites that bridge two neighboring silicon atoms along the $\langle 111 \rangle$ direction [4]. Because the solubility of oxygen in silicon decreases with decreasing temperature, crystal cooling and thermal annealing leads to the precipitation of oxygen clusters that range in size from several nanometers to tens of micrometers. Small clusters of silicon and oxygen containing up to 20 oxygen atoms are electrically active and are referred to as thermal donors. Larger oxygen precipitates, believed to be microphases of silica, play important roles in the internal gettering of metallic impurities in the industrial processing of silicon. Oxygen precipitations also have been found to affect the gate oxide integrity (GOI) characteristics of MOS devices [5].

The oxygen precipitation processes are controlled by the thermodynamics of oxygen clusters and the kinetics of oxygen transport. While there have been many experimental studies of thermal donors, the structural and thermodynamic properties of oxygen clusters remain poorly understood. Experimental measurement [4-11] of the diffusivity of oxygen in silicon, either based on oxygen transport or relaxation of stress-induced-infrared-dichroism method has received much more attention. Although these experiments were performed in different and limited temperature ranges, most data from these experiments can be consistently fit to a single expression of the form $D=0.13 \exp(-2.53\text{eV}/k_B T) \text{ cm}^2/\text{sec}$, as pointed out by Mikkelsen [12], who obtained this expression by fitting to data from six independent experiments. This expression is generally believed to be the intrinsic diffusion constant involving oxygen jumping from a bond-center site to one of the six nearest bond-center sites.

Theoretical investigation of oxygen diffusion and oxygen clusters in silicon is difficult because of the large diffusion barrier and the complicated nature of the mixed bonding between oxygen and silicon atoms. Several researchers [13-17] have attempted to calculate the energy barrier of oxygen diffusion and the structures of small oxygen clusters using local den-

sity functional theories or self-consistent cluster calculations. These efforts have yielded diffusion barriers ranging from 1.2eV to 2.5eV. All these calculations assume that the saddle point configuration for diffusion is in a (110) plane and at the midway between the two bond-center sites. No calculations of the prefactor of the diffusion constant have been reported. A variety of stable and metastable structures of small oxygen clusters containing up to three oxygen atoms also have been reported [13-17].

We have studied oxygen diffusivity and oxygen clusters in silicon using an empirical potential that has recently been developed for oxygen-silicon interactions [1]. The diffusion path and diffusion barrier are determined [18] by a series of energy minimization calculations performed with the constraint of a constant cone angle θ between the O-Si bond and the axis connecting the two silicon atoms bonded to the oxygen atom in the initial equilibrium configuration; the angle θ is shown in Fig. 1. The diffusivity is calculated using jump rate theory [19,20]. The structures of small oxygen clusters are found by NPT molecular dynamics simulations using the same interatomic potential. The free energies of these clusters are calculated by thermodynamic integration and used to predict the temperature dependence of the equilibrium partitioning of oxygen atoms into clusters of different sizes.

In the remainder of this paper, we first present our computational methods, followed by a summary of the results of our calculations of oxygen diffusivity in silicon, which have been reported in an earlier publication [18]. The results of the calculations of small oxygen clusters and oxygen partitioning into these clusters are then described.

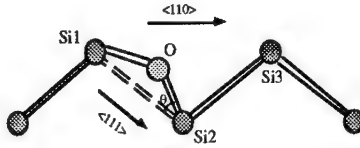


FIG. 1. Schematic diagram showing the constraint angle θ .

COMPUTATIONAL METHODS

Empirical interatomic potential

The empirical interatomic potential for the OSi system is constructed [1] using the Stillinger-Weber (SW) silicon potential [21] and the silica potential of van Beest *et al.* [22]. Three important new components are introduced to describe the charge-transfer and mixed bonding between oxygen and silicon atoms. These ingredients include (a) a charge transfer function, (b) a bond-softening function, and (c) an ionization energy. The parameters are fitted to the structure, vibrational frequency, and formation energy of an oxygen interstitial in silicon. The formulation of this composite interatomic potential, the parameter values, and the details of the construction and parameter fitting process are reported in [1], where the potential is also used to study the structural, energetic and vibrational properties of interstitial-oxygen and vacancy-oxygen clusters, yielding results in good agreement with available experiments on vacancy-oxygen structure.

Constrained energy minimization and jump rate theory

The diffusion path and the diffusion energy barrier are determined from a series of energy minimization calculations which are performed with the constraint of a constant cone angle θ , as shown in Fig. 1. This constraint allows the oxygen atom to move out of the (110) plane, and only reduces one degree of freedom of the system. The constraint is implemented using the augmented Lagrangian method [23] in which the generalized energy function

$$E_c(\{\mathbf{r}_i\}, \lambda) = E(\{\mathbf{r}_i\}) + \lambda g(\mathbf{r}_{20}, \mathbf{r}_{21}) + \frac{1}{2} w g^2(\mathbf{r}_{20}, \mathbf{r}_{21}) \quad (1)$$

is minimized by the steepest descent method. In Eq.(1), $E(\{r_i\})$ is the energy of the unconstrained system, λ is the Lagrangian multiplier,

$$g(r_{20}, r_{21}) = \frac{r_{20} \cdot r_{21}}{r_{20} r_{21}} - \cos \theta \quad (2)$$

is the constraint function, where r_{20} is the vector from Si2 to O and r_{21} is the vector from Si2 to Si1, as shown in Fig.1. The value of θ is increased gradually from 0 and the converged configuration for each θ is used as the initial configuration for the steepest-descent minimization at the next larger value of θ .

The diffusion constant is given by the jump rate theory [19,20] as an Arrhenius expression $D = D_0 \exp(-\Delta E/k_B T)$, where ΔE is the diffusion energy barrier, and the prefactor D_0 is determined by $D_0 = g l^2 \nu / (2d)$, where d the dimensionality of space, l is the elementary jump length, and g is the number of equivalent diffusion paths [19]. Because each bond-center site has six nearest neighbors and six fold degeneracy [4,19,24], $g=36$. The attempt frequency ν is given by [20]

$$\nu = \left(\prod_{i=1}^{3n} \nu_i^e \right) / \left(\prod_{i=1}^{3n-1} \nu_i^s \right) \quad (3)$$

where $\{\nu_i^e\}$ are $3n$ frequencies of the n -atom system in the equilibrium state, and $\{\nu_i^s\}$ are the $3n-1$ frequencies of the system at the saddle point configuration along the diffusion path. The frequencies $\{\nu_i^e\}$ and $\{\nu_i^s\}$ are calculated by direct diagonalization of the Hessian matrix of the system at the equilibrium and saddle point configurations, respectively.

NPT molecular dynamics and thermodynamic integration

The equilibrium structures of oxygen clusters are determined by NPT molecular dynamics simulations with zero pressure. The algorithm of Andersen [25] is used to keep the pressure constant and the integration of the equations of motion is performed numerically using the fifth-order predictor-corrector method [26]. Constant temperature is achieved by scaling the momentum. Simulations are performed with a time step of 0.1536 fs. The simulation cell has periodic boundaries and contains 216 silicon atoms and N oxygen atoms.

The free energy $G(T)$ is calculated using thermodynamic integration, i.e.,

$$G(T) = T \left(\frac{G_0}{T_0} - \int_{T_0}^T \frac{H(T)}{T^2} dT \right) \quad (4)$$

where G_0 is the free energy calculated using the harmonic approximation [1,27] at a reference temperature $T_0 = 500K$, and $H(T)$ is the enthalpy of the system, as computed by molecular dynamics simulations at temperature T .

RESULTS

Oxygen diffusion path and diffusivity

The computed energy of the system with one oxygen atom is shown in Fig. 2 as a function of θ . The saddle point configuration, with an energy barrier of $\Delta E = 2.43$ eV, is found to occur

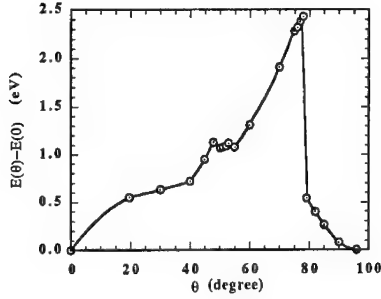


FIG. 2. The computed energy as a function of θ for the system with one oxygen atom. The saddle point configuration occurs at $\theta=78^\circ$.

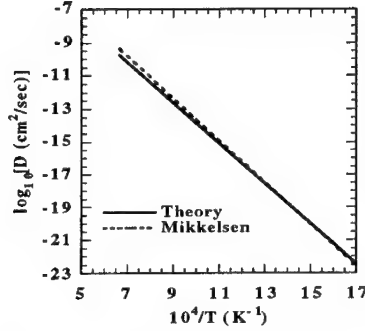


FIG. 3. Comparison of the calculated expression for the oxygen diffusivity with Mikkelsen's best fit to experimental data[10].

at $\theta=78^\circ$. The diffusing oxygen atom reaches the top of the energy barrier at a point beyond the midpoint between the two bond-center sites, which corresponds to $\theta=55^\circ$. Atomic configurations [18] show that the diffusion path is primarily in the (110) plane. In the diffusion process, only the three silicon atoms involved in the O-Si bonds are significantly displaced from their lattice positions. As the oxygen atom moves from the original equilibrium site, one of the Si-O bonds is stretched, but is not broken until the oxygen moves through the saddle point at $\theta=78^\circ$. Beyond the saddle point, the stretched bond is broken and a new Si-O bond is formed with a silicon atom in the other $\langle 111 \rangle$ direction, thus forming a new bridging configuration for the oxygen. This oxygen migration process is consistent with the numerical experiments of kicked oxygen performed by Needels *et al.* [13].

The jump frequency is computed from Eq.(3) to be $\nu=11.5\text{THz}$. In the equilibrium state, the distance between two nearest neighbor bond-center sites is $l=1.91\text{\AA}$. The diffusivity is predicted as

$$D = 0.025 \exp(-2.43\text{eV}/k_B T) \text{ cm}^2/\text{sec} \quad (5)$$

This calculated result is plotted in Fig. 3 together with Mikkelsen's best fit [12] to six sets of independent experimental data, $D=0.13 \exp(-2.53\text{eV}/k_B T) \text{ cm}^2/\text{sec}$. The agreement is excellent although the prefactors and energy barriers are different. The difference is well within range of experimental error in the data. Indeed, Newman *et al.* [11] reported an Arrhenius fit of the form $D=0.02 \exp(-2.42\text{eV}/k_B T) \text{ cm}^2/\text{sec}$ to data from an experiment relating to the kinetics of oxygen precipitation. His expression is virtually the same as our calculated result.

Oxygen clusters and partitions

The structures of the O_N ($N=2, 3, 4$) clusters are obtained as shown in Fig. 4. The O_2 and O_3 clusters are both in a (110) plane. They are similar to those found by Needels *et al.* [13], but the two oxygen atoms in O_2 are not bonded to a common silicon atom. The O_4 cluster has a tetrahedral structure. The formation energies per oxygen atoms are 0.47eV , 0.80eV and 0.13eV for $N=2, 3$ and 4 , respectively. Because the formation energy for single oxygen interstitial O_1 is 1.06eV [1], the O_2 structure has a binding energy of 1.18eV . The O_3 structure has an energy 0.28eV higher than the energy of an (O_1+O_2) configuration, it is therefore only metastable. The O_4 cluster is stable with respect to both the $4O_1$ and $2O_2$ configurations.

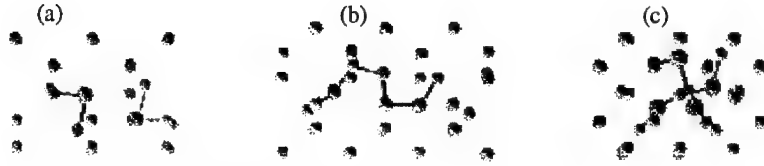


FIG. 4. The structures of small oxygen clusters: (a) O_2 viewed at the $[110]$ direction; (b) O_3 viewed at the $[110]$ direction; (c) O_4 viewed at the $[100]$ direction. The oxygen atoms are slightly larger, and connected by two bonds.

The free energies of O_1 , O_2 , and O_4 are calculated using the thermodynamic integration, Eq.(4). The results are shown in Fig. 5. Assuming that the total concentration of oxygen is 20 ppm and that oxygen only exists in the forms of either O_1 , O_2 , or O_4 , we have calculated the equilibrium partitioning of oxygen atoms. Fig. 6 displays the fractions of oxygen atoms in the forms of O_1 , O_2 and O_4 as a function of temperature. As temperature decreases, more and more oxygen atoms are partitioned into larger clusters. Below 1300K, less than 3% of oxygen atoms exist in the form of single interstitials. This is consistent with the experimental finding that pre-heating at a temperature higher than 1000C^o is effective in dissolving oxygen clusters and generating single oxygen interstitials [28].

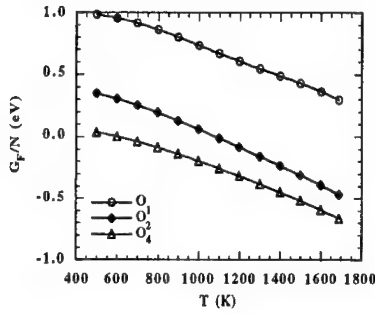


FIG. 5. The formation free energy per oxygen atom for oxygen clusters of size 1, 2 and 4.

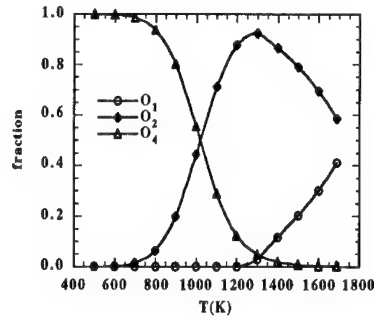


FIG. 6. The fraction of oxygen atoms in the form of O_1 , O_2 , and O_4 for a given total concentration of oxygen of 20ppm.

CONCLUDING REMARKS

We have presented theoretical calculations of oxygen diffusion and oxygen clustering in crystalline silicon using an empirical potential constructed to describe the complicated charge-transfer and bond-formation processes between silicon and oxygen atoms. We found the oxygen jumps from a bond-center site to another bond-center site along a path in the (110) plane. Because the oxygen atom has to break a Si-O bond before it is able to form a new bridging configuration with the other silicon atom, the saddle point is predicted to be farther than the midpoint between the two bond-center sites. The diffusion coefficient predicted using this saddle point configuration and jump rate theory is in excellent agreement with experiments. We also found that the O_3 zigzag structure along a $[110]$ direction is energetically unstable with

respect to the (O_1+O_2) configuration, which suggests that clusters of even number of oxygen atoms are favored in equilibrium. This is particularly interesting in the context of proposed possible role of O_2 in the thermal donor formation processes [29]. Our calculations of oxygen equilibrium partitioning into clusters of different sizes show that, for a given oxygen concentration, most oxygen atoms are partitioned into clusters at temperature below 1300K, and that the average cluster size increases with decreasing temperature. These results are in agreement with the general effects of thermal annealing on oxygen precipitation in silicon crystals.

ACKNOWLEDGMENT

We thank MEMC Corporation, Sematech, Shin-Etzu Handotai Company, and Wacker Chemitronic for financial support of this research.

REFERENCES

- [1] Z. Jiang and R. A. Brown, Chem. Eng. Sci. **49**, 2991 (1994).
- [2] W. Zulehner and D. Huber, in Crystals: Growth, Properties and Application **8**, edited by J. Grabmaier (Springer, New York, 1982).
- [3] R. A. Brown, AIChE Journal **34**, 881 (1988); T. A. Kinney and R. A. Brown, J. Crystal Growth **132**, 551 (1993).
- [4] J. W. Corbett, R. S. McDonald, and G. D. Watkins, J. Phys. Chem. Solids **25**, 873 (1964).
- [5] H. Yamagishi, I. Fusegawa, N. Fujimaki and M. Katayama, Sem. Sci. Tech. **7**, A135 (1992).
- [6] J. C. Mikkelsen, Jr., Appl. Phys. Lett. **40**, 336 (1982).
- [7] S. T. Lee and D. Nichols, Appl. Phys. Lett. **47**, 1001 (1985).
- [8] J. Gass, H. H. Muller, H. Stussi, and S. Schweitzer, J. Appl. Phys. **51**, 2030 (1980).
- [9] Y. Itoh and T. Nozaki, Jpn. J. Appl. Phys. **24**, 279 (1985).
- [10] M. Stavola, J. R. Patel, L. C. Kimerling, and P. E. Freeland, Appl. Phys. Lett. **42**, 73 (1983).
- [11] R. C. Newman, J. H. Tucker, and F. M. Livingston, J. Phys. C **16**, L151 (1983).
- [12] J. C. Mikkelsen, Jr., Mat. Res. Soc. Symp. Proc. **59**, 19 (1986).
- [13] M. Needels, J. D. Joannopoulos, Y. Bar-Yam, S. T. Pantelides, and R. H. Wolfe, Mat. Res. Soc. Symp. Proc. **209**, 103 (1991); Phys. Rev. B **43**, 4208 (1991).
- [14] A. Oshiyama and M. Saito, in Defect Control in Semiconductors, edited by K. Sumino (Elsevier Science Publishers, North-Holland, 1990).
- [15] M. Saito and A. Oshiyama, Phys. Rev. B **38**, 10711 (1988).
- [16] L. C. Snyder and J. W. Corbett, Mat. Res. Soc. Symp. Proc. **59**, 207 (1986); **104**, 179 (1988).
- [17] P. J. Kelly, Mat. Sci. Forum **38-41**, 269 (1989).
- [18] Z. Jiang and R. A. Brown, Phys. Rev. Lett. **74**, 2046 (1995).
- [19] C. Wert and C. Zener, Phys. Rev. **76**, 1169 (1949); K. Weiser, Phys. Rev. **126**, 1427 (1962).
- [20] G. H. Vineyard, J. Phys. Chem. Solids **3**, 121 (1957); J. H. Harding, Rep. Prog. Phys. **53**, 1403 (1990).
- [21] F. H. Stillinger and T. A. Weber, Phys. Rev. B **31**, 5262 (1985).
- [22] B. W. van Beest, G. J. Kramer, and R. A. van Santen, Phys. Rev. Lett. **64**, 1955 (1990).
- [23] D. M. Greig, Optimisation, (Longman, London, 1980).
- [24] C. Haas, J. Phys. Chem. Solids **15**, 108 (1960).
- [25] H. C. Andersen, J. Chem. Phys. **72**, 2384 (1980).
- [26] C. W. Gear, Numerical Initial Value Problems in Ordinary Differential Equations, (Prentice Hall, Englewood Cliffs, NJ, 1971).
- [27] D. A. McQuarrie, Statistical Mechanics, (Harper and Row, New York, 1976).
- [28] M. Ataka and T. Ogawa, J. Mater. Res. **8**, 2889 (1993).
- [29] U. Gosele and T. Y. Tan, Appl. Phys. A **28**, 79 (1982).

COMPUTATION OF THE ONSET OF POINT DEFECT AGGREGATION IN CRYSTALLINE SILICON USING AN EMPIRICAL INTERATOMIC POTENTIAL

T. SINNO AND R. A. BROWN

Department of Chemical Engineering, Massachusetts Institute of Technology
Cambridge, MA 02139

ABSTRACT

The Stillinger-Weber interatomic potential is used in molecular dynamics simulations to investigate the equilibrium, transport and aggregation properties of self-interstitials and vacancies in crystalline silicon at temperatures ranging from 500K to the melting point. The simulations predict equilibrium configurations of a $\langle 110 \rangle$ dumbbell for the single self-interstitial and an inwardly relaxed structure for the single vacancy. Both single-defect structures exhibit significant delocalization at high temperatures resulting in strongly temperature dependent entropies of formation, as suggested by diffusion experiments. Diffusion coefficients and mechanisms for the single defects are predicted as a function of temperature. The results for the single point defects are discussed in the context of the existing literature values. Aggregation of two point defects is investigated by the computation of binding energies and entropies for these structures. Interstitials exhibit significant aggregation driving forces across the entire temperature range under simulation conditions, while vacancies aggregate less readily.

INTRODUCTION

The transport and aggregation properties of intrinsic point defects in silicon play an essential role in determining the quality of single-crystal silicon in many aspects of the fabrication of microelectronic devices, [1,2]. In particular, the formation of microdefects during growth from the melt is becoming a more significant limitation as the size of such devices continues to decrease. Even though the detailed mechanisms responsible for the formation of microdefects are still poorly understood, there is ample evidence that the aggregation of intrinsic point defects and impurities is responsible for microdefect formation during growth and subsequent processing.

With this in mind, there have been many experimental studies aimed at measuring the equilibrium properties and diffusion coefficients of point defects in silicon; see references in [3] for a summary. Experimentally, both equilibrium and diffusion properties of point defects have to be measured indirectly, usually by fitting data for diffusion of interstitial or substitutional dopants to models for point defect facilitated transport; see the recent publications of Bracht et al. [4] and Döller et al. [5]. The results of these studies have generally been susceptible to large uncertainties due to simplified models and uncertainty in other parameters. These discrepancies have motivated the use of atomistic simulations based on empirical interatomic potentials [2,7-9] and first-principle electronic structure calculations [10,11] for estimating these properties.

This work reports the results of two investigations. The first deals with the configurations, energetics, and diffusivities of native point defects. The second investigation focuses on the formation thermodynamics of aggregates of two point defects. Both studies are

based on an internally consistent set of calculations using the Stillinger-Weber (SW) inter-atomic potential [12] at temperatures ranging from 500K to near the melting point (1683 K). Although the SW potential is imperfect in its predictions, it does give good agreement with experimental measurements of bulk physical properties, such as the lattice constant, cohesive energy, and crystal structure. Furthermore, it predicts a correct thermodynamic melting temperature [13] and formation energies for localized point defects that are in agreement with self-consistent-field, total energy calculations [6].

COMPUTATIONAL METHODS

All calculations are based on molecular dynamics simulations performed in both the (NVT) and (NPT) statistical ensembles employing 216 silicon atoms arranged in a perfect tetrahedral lattice. Constant temperature was maintained via velocity rescaling at each time step, while pressure was fixed using the piston method of Andersen [15]. Gibbs free energies of formation, $G^f(T)$, are computed by thermodynamic integration as

$$\left(\frac{G}{kT}\right)_2 - \left(\frac{G}{kT}\right)_1 = \int_{T_1}^{T_2} \left(\frac{H}{kT}\right) \frac{dT}{T}, \quad (1)$$

where the enthalpies are computed by (NPT) simulations at zero pressure. Thermodynamic integration provides a free energy *difference*; the reference free energy is computed at 500 K using the quasi-harmonic approximation (QHA) [16].

Diffusion coefficients were computed from the Einstein relationship employing long (NVT) molecular dynamics simulations. This direct approach is computationally feasible only at high temperature where point defect mobility is relatively large. The advantage of this method however, is that no assumption other than that of the potential's validity is necessary. Diffusivities at lower temperatures were extrapolated from an Arrhenius fit of the high temperature data.

The aggregation simulations were performed by introducing two defects of the same type into the simulation cell and allowing them to diffuse towards each other in a long (NPT) simulation. The simulation was terminated once a single cluster was formed and the system energy no longer changed with time. This equilibrium configuration was then used as a starting point for simulations at other temperatures, eliminating the need for long equilibration runs at each temperature. Binding energies were calculated as $E_{bind} \equiv 2 \times E_{single} - E_{cluster}$, where E_{single} is the energy of formation of a single defect and $E_{cluster}$ is the energy of a cluster.

RESULTS

The predicted equilibrium single point defect configurations are shown in Fig. 1. The silicon self-interstitial forms a dumbbell structure oriented along a $\langle 110 \rangle$ direction with a displaced lattice atom. Two other atoms in the same plane also are displaced from their lattice sites towards the dumbbell, forming a four atom ring. The $\langle 110 \rangle$ dumbbell configuration also was the lowest energy structure predicted by local density functional (LDF) calculations [11]. The predicted equilibrium structure for the vacancy consists of a vacant lattice site surrounded by atoms which are inwardly displaced, in agreement with electronic structure calculations [11,17]. Calculated values for the enthalpies and entropies of formation for isolated self-interstitials and vacancies are shown in Fig. 2a (insert).

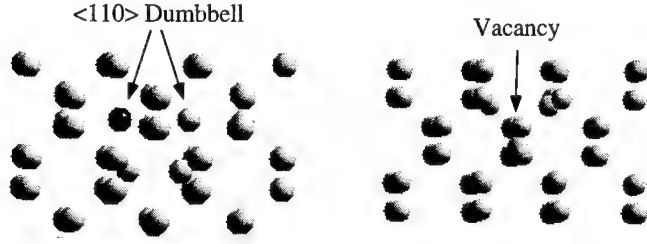


Figure 1: The equilibrium configurations of native point defects in silicon computed as (a) the $\langle 110 \rangle$ dumbbell for a self-interstitial and (b) an inwardly relaxed structure for a vacancy.

The enthalpies of formation for the isolated point defects are weakly temperature dependent, with values of $H_I^f = 3.5$ eV and $H_V^f = 2.5$ eV at 0 K for the self-interstitial and vacancy respectively. The corresponding values given by Blöchl et al. are 3.3 eV and 4.1 eV. The recent experimental measurements of Bracht et al. based on zinc diffusion, give these numbers as 3.18 eV and 2.0 eV. Thus, there is reasonable agreement between the SW potential, LDF calculations, and experimental measurements in the case of the interstitial but not for the vacancy. In both cases, the entropies of formation increase

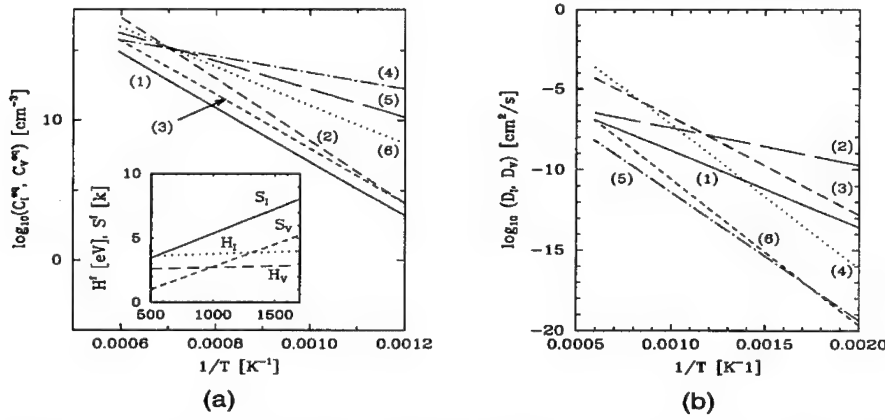


Figure 2: (a) Dependence of equilibrium concentrations on temperature of an isolated vacancy and self-interstitial: (1) C_I , this work; (2) C_I , [24]; (3) C_I , [23]; (4) C_V , [23]; (5) C_V , [24] (6) C_V , this work. Insert: Dependence of the formation enthalpy and entropy on temperature. (b) Dependence of diffusion coefficients on temperature for an isolated vacancy and self-interstitial: (1) D_I , this work; (2) D_V , this work; (3) D_I , [22]; (4) D_I , [4]; (5) D_I , [25] (6) D_V , [4].

monotonically with increasing temperature; S_I^f and S_V^f both change by about 4.5 k across the temperature range studied here. This significant increase is suggestive of increased delocalization of each point defect with increasing T , as has been verified by plotting the

displacement of each silicon atom from a lattice site as a function of distance from the defect [2]. Seeger and Chik [18] first discussed the possibility of point defect delocalization at high temperatures, and Seeger et al. [19] used this concept to interpret the self-diffusion data of Mayer et al. [20]. Their analysis yields an increase in S_f^f from $1.00 k$ at $T = 570 K$ to $6.11 k$ at $T = 1658 K$. Blöchl et al. estimated the entropy of formation of a self-interstitial to be constant at $6 k$. The delocalization of native point defects may play an important role in the mechanism for I-V recombination [2,21]. Maroudas and Brown [3] calculated values for H_f^f and H_v^f using Monte Carlo simulations in conjunction with the QHA. Their results are in good agreement with our calculations for temperatures up to $1100 K$. However, the QHA is a poor approximation at temperatures greater than $1000 K$ due to the increasingly anharmonic vibrations within the lattice, especially in the region close to the defect. A similar deviation was predicted by Ungar et al. [22], for calculations employing a Tersoff potential for silicon.

Our predictions for the equilibrium concentrations of point defects are shown in Fig. 2a as a function of temperature. The results of several experimental investigations [23-25] also are shown in Fig. 2a. For both point defects our results lie well within the bounds set by the other values. However, the very large scatter across the entire temperature range makes it difficult to meaningfully evaluate our results in the context of experimental predictions.

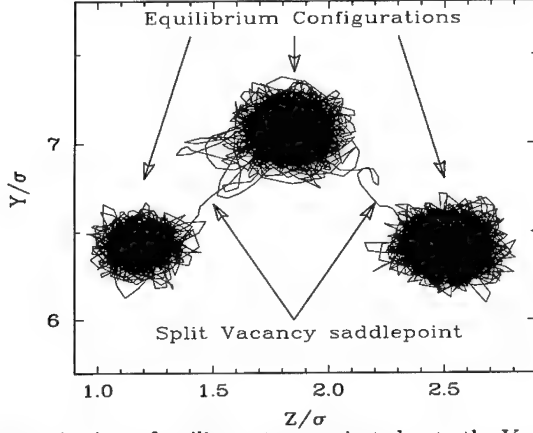


Figure 3: Trajectory in time of a silicon atom projected onto the Y and Z coordinate axes.

The temperature dependence of the diffusion coefficients of silicon vacancies and self-interstitials is shown in Fig. 2b along with experimental measurements [4,23,26]. Maroudas and Brown used jump rate theory along constrained diffusion paths to estimate the diffusivity of self-interstitials [14] and vacancies [3]. The interstitial calculation was based on assuming that the diffusion path connects two neighboring tetrahedral sites with the hexagonal site as the saddle point. This mechanism is probably incorrect given that the equilibrium configuration for the interstitial is the $\langle 110 \rangle$ dumbbell, and in fact there is significant disagreement between our estimate of the migration energy ($0.94 eV$), and the one predicted by Maroudas [14] ($1.74 eV$). The present results are in reasonable agreement with several experimental studies [4,23,26].

The prediction of vacancy diffusion from jump rate theory [3] was based on assuming that the split-vacancy configuration is the saddle point on the diffusion path and yielded

a migration energy of 0.43eV , while our results give the migration energy as 0.46eV . The excellent agreement suggests that the split vacancy is indeed the most probable path. This hypothesis is reinforced by examining the projection of the time trajectory of a silicon atom in a plane of the cubic coordinate system formed by the Y and Z coordinate directions as shown in Fig. 3.

An atomic jump from one equilibrium position to another is clearly visible, with the distance between two equilibrium positions being equal to one bond length. Accordingly, a vacancy has exchanged a lattice site with a neighboring atom by a direct diffusion path, in accord with the split-vacancy mechanism.

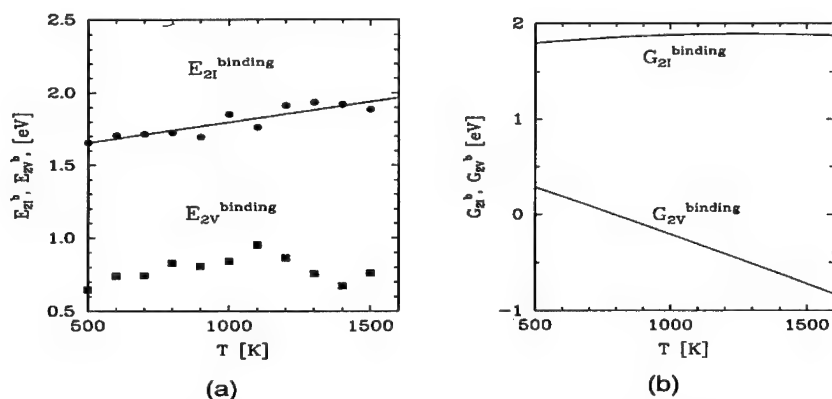


Figure 4: (a) Binding energies for the 2-interstitial and 2-vacancy clusters. (b) Binding free energies.

The temperature dependence of the binding energies and free energies of the two-defect clusters are shown in Figures 4a and 4b respectively. The interstitial cluster exhibits relatively high binding energies ($1.7 - 2.0\text{ eV}$) and free energies (1.8 eV). This implies that for the temperatures investigated there is a positive driving force for the aggregation of two interstitials. In the case of the vacancy however, the binding energy is significantly lower (0.7 eV) across the entire temperature range. The binding free energy is an inverse function of temperature and actually becomes negative for temperatures above 800 K. This suggests that vacancies will not tend to aggregate at elevated temperatures and that some other mechanism is required to facilitate their agglomeration.

CONCLUDING REMARKS

The atomistic simulations described here give an internally consistent set of computations for the equilibrium, diffusion and aggregation properties of native point defects in silicon over the range of temperatures that are important in the growth of silicon single crystals and the processing of microelectronic devices. The SW calculations suggest that for point defect formation at high temperatures, the material is dominated by vacancies, not self-interstitials. This picture is consistent with the dominant formation of D-defects or vacancy precipitates in floating zone silicon [1,4] and the rapid precipitation of oxygen in material grown by the Czochralski method, where vacancy addition to the precipitates is needed to

alleviate strain between SiO_2 and Si . The calculations of clusters of two defects suggest that the presence of impurity atoms such as oxygen are needed to promote the precipitation of vacancies. The validity of these simulation results must be tested by application in the analysis of diffusion results and in theories for predicting microdefect formation during crystal annealing at high temperatures.

We are grateful to MEMC Corporation, Shin Etsu Handotai Limited, Wacker Chemical and Sematech for support of this research.

REFERENCES

1. T. Abe in: VLSI Electronics: Microstructure Science, **12**, Eds. N. G. Einspruch and H. Huff (Academic Press, New York, 1985).
2. R.A. Brown, D. Maroudas, and T. Sinno, *J. Crystal Growth* **137**, 12 (1994).
3. D. Maroudas and R.A. Brown, *Phys. Rev. B* **47**, 15562 (1993).
4. H. Bracht, N. A. Stolwijk, and H. Mehrer in *Semiconductor Silicon 1994*, Eds. H. R. Huff, W. Bergholz, and K. Sumino, (Electrochemical Society, Pennington, 1994).
5. A. Döller, M. Seibt, and W. Schröter in *Semiconductor Silicon 1994*, Eds. H. R. Huff, W. Bergholz, and K. Sumino, (Electrochemical Society, 1994).
6. I.P. Batra, F.F. Abraham, and S. Ciraci, *Phys. Rev. B* **35**, 9552 (1987).
7. M.I. Baskes, J.S. Nelson, and A.F. Wright, *Phys. Rev. B* **40**, 6085 (1989).
8. P. J. Ungar, T. Takai, T. Halicioglu, and W. A. Tiller, *J. Vac. Sci. and Tech.*, **11**, 224, (1993).
9. S.T. Pantelides, A. Oshiyama, R. Car, and P.J. Kelly, *Phys. Rev. B* **30**, 2260 (1984).
10. Y. Bar-Yam and J.D. Joannopoulos, *Phys. Rev. B* **30**, 1844 (1984).
11. P.E. Blöchl, E. Smargiassi, R. Car, D.B. Laks, W. Andreoni, and S.T. Pantelides, *Phys. Rev. Lett.* **70**, 2435 (1993).
12. F.H. Stillinger and T.A. Weber, *Phys. Rev. B* **31**, 5262 (1985).
13. J.Q. Broughton and X.P. Li, *Phys. Rev. B* **35**, 9120 (1987).
14. D. Maroudas and R.A. Brown, *Appl. Phys. Letts.* **62**, 172 (1993).
15. M.P. Allen and D.J. Tildesley, *Computer Simulation of Liquids*. (Oxford University Press, Oxford, 1989).
16. J.F. Lutsko, D. Wolf, and S. Yip, *J. Chem. Phys.* **88**, 6525 (1988).
17. E.O. Kane, G.A. Baraff, and M. Schlüter, *Phys. Rev. B* **21**, 5662 (1980).
18. A. Seeger and K.P. Chik, *Phys. Status Solidi* **29**, 455 (1968).
19. A. Seeger, H. Föll and W. Frank, in: *Radiation Effects in Semiconductors 1975*, Eds. N.B. Urli and J.W. Corbett (1977).
20. H.J. Mayer, H. Mehrer and K. Maier, *ibid.*
21. U. Gösele, W. Frank, A. Seeger, *Solid State Commun.* **45**, 31 (1983).
22. P. J. Ungar, T. Halicioglu, and W. A. Tiller, *Phys. Rev. B* **50**, 7344 (1994).
23. F. F. Morehead, in: *Defects in Elec. Mater.*, Eds. M. Stavola, S. J. Pearton, G. Davies, *Mat. Res. Soc.*, Pittsburgh, (1988).
24. H. Zimmermann and H. Ryssel, *J. Electrochem. Soc.*, **139**, 256 (1992).
25. T. Y. Tan and U. Gösele, *Appl. Phys. A* **37**, 1, (1985).
26. P. B. Griffin and J. D. Plummer, *Int. Electron Device Meeting 1986*, p522, (1986).

NUMERICAL SIMULATION OF POINT DEFECT DISTRIBUTIONS IN A GROWING CZOCHRALSKI SILICON CRYSTAL IN RESPONSE TO AN ABRUPT CHANGE IN THE GROWTH CONDITIONS

W. WIJARANAKULA*, Q.S. ZHANG*, **, K. TAKANO***, AND H. YAMAGISHI***

*Shin-Etsu, SEH America, Inc., 4111 Northeast 112th Avenue, Vancouver, WA 98682, USA

**Department of Electrical and Computer Engineering, Oregon State University, Corvallis, OR 97331, USA

***Shin-Etsu Hondotai, Co., Ltd, Corporate Research and Development Center, Isobe 2-13-1, Annaka, Gunma, 379-01, Japan

ABSTRACT

Numerical simulation of point defect distributions in a growing Czochralski silicon crystal with an abrupt change in the crystal growth rate from 1.0 to 0.4 mm/min was performed. The result was fitted to the experimental data for the flow pattern defects obtained from a crystal grown under simulated conditions. From the simulation result, it was observed that the axial temperature distribution shifts slightly upwards as a result of the growth rate reduction. Based upon the argument that the flow pattern defects are of vacancy-type, it is proposed that the generation rate of the flow pattern defects during crystal growth can be described by the classical nucleation rate theory proposed by Becker [Proc.Phys.Soc., **52**, 71(1940)]. In addition, it is suggested that the vacancy concentration in the flow pattern defects depends upon the reaction time between the silicon interstitials and the flow pattern defects and thus the crystal growth rate.

INTRODUCTION

It is well recognized that the silicon matrix of a growing Czochralski silicon crystal is saturated with intrinsic point defects and interstitial oxygen atoms dissolved from the quartz crucible. The degree of point defect saturation and hence the type of crystal defects, whether silicon interstitials or vacancies, depends upon the radial and axial temperature gradients. Therefore, the crystal growth conditions play a significant role in defect generation during the Czochralski growth process. The effect of the crystal growth conditions such as the crystal growth rate on the formation of the flow pattern defects (FPD) and the crystal originated particles (COP) is well established [1-4]. Because the crystal originated defects affect the gate oxide integrity in metal-oxide-semiconductor (MOS) capacitors [1] and the refresh-time of high density dynamic random access memory (DRAM) devices [5], advanced crystal growth technology will play an essential role in silicon material development for future integrated circuit devices.

In this work, the temperature and point defect distributions in a growing Czochralski silicon crystal with an abrupt change in the crystal growth rate are numerically analyzed and compared with experimental data. The point defect aggregation mechanism in response to an abrupt change in the crystal growth conditions will be discussed.

SIMULATION METHODS

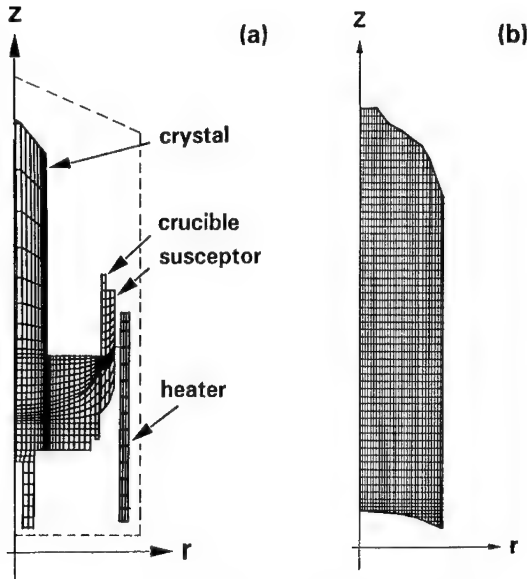


Figure 1: (a) Finite element mesh for the global temperature calculation and (b) Finite difference mesh for the point defect calculation.

In a dynamic point defect simulation, the temperatures on the surface of a growing crystal, as the boundary conditions, were obtained from a series of global temperature field calculations using the finite element model accounting for the radiative heat exchange between the crystal, furnace components, and the melt [6], shown in Figure 1a. In Figure 1b, a finite difference model used in the point defect simulation is illustrated. The model has an adjustable mesh size of $0.033r \times 0.067r$ where r is the radius of the crystal. A smaller mesh size was also employed in the solid and melt interface region where the melt interface changed in response to the

crystal growth rate Gr . In the dynamic simulation, the mesh density increases with increasing time. The rate at which the new meshes are added to the existing model is a function of Gr . In the present model, the transport equations for the point defects accounting for the pair annihilation can be expressed as

$$\frac{\partial C_v}{\partial t} = D_v \nabla^2 C_v + \frac{1}{\tau_v C_I^{eq}} (C_v^{eq} C_I^{eq} - C_v C_I) \quad (1a)$$

$$\frac{\partial C_I}{\partial t} = D_I \nabla^2 C_I + \frac{1}{\tau_I C_v^{eq}} (C_v^{eq} C_I^{eq} - C_v C_I) \quad (1b)$$

where C_v and C_I are the concentration of silicon interstitials and vacancies, respectively. D_v and D_I are the diffusivities of the corresponding point defects, respectively. In the above equations, the contribution of the diffusion fluxes driven by the thermal gradient to the point defect redistribution was not considered. The "up-hill" diffusion component, if there is any, is included in the first term of the equation. The second term is attributed to the pair recombination reaction where τ_v and τ_I are the lifetimes of corresponding point

defects. The method of estimating the point defect lifetime has been described in detail elsewhere [7]. C_v^{eq} and C_i^{eq} are the thermal equilibrium concentrations of the point defects. The diffusivities and equilibrium concentrations are taken from Ref.[7]

$$D_v = 257 \exp\left(-\frac{2.84 \text{ eV}}{k_B T}\right) \quad \text{and} \quad D_i = 0.335 \exp\left(-\frac{1.86 \text{ eV}}{k_B T}\right) \quad (2)$$

$$C_v^{eq} = 8.56 \times 10^{21} \exp\left(-\frac{1.56 \text{ eV}}{k_B T}\right) \quad \text{and} \quad C_i^{eq} = 2.18 \times 10^{26} \exp\left(-\frac{3.1 \text{ eV}}{k_B T}\right) \quad (3)$$

In this work, it is argued that a flow pattern defect consists of vacancies which are condensed into clusters during the crystal cooling period. The nucleation rate of the vacancy-type defects J_D was calculated based upon the classical nucleation rate theory in condensed systems proposed by Becker [8].

$$J_D = A \exp\left(-\frac{Q_v}{k_B T}\right) \exp\left(-\frac{16\pi V_D^2 \sigma_D^3}{3(k_B T)^3 [\ln(C_v / C_v^{eq})]^2}\right) \quad (4)$$

where A is a constant, Q_v is the activation energy for the diffusion of vacancies, equal to 2.84 eV [9], k_B is the Boltzman's constant, equal to 8.62×10^{-5} eV/K, and T is the absolute temperature. σ_D and V_D are the surface energy (eV/cm²) and the volume of the flow pattern defect containing a vacancy (cm³), respectively. Thus, the vacancy concentration in the flow pattern defect is $1/V_D$. In the above equation, A , σ_D and V_D are unknown.

In order to reduce the number of unknown parameters, several assumptions have been made. First, the maximum critical cluster size of the flow pattern defects must be smaller than 6 Å. The critical cluster size can be determined from the homogeneous precipitation theory expressed as [10]

$$r_c^* = \frac{2V_D \sigma_D}{k_B T \ln(C_v / C_v^{eq})} \quad (5)$$

In addition, it is assumed that σ_D is a first order approximation which is in the range between 0.62 and 1.4×10^{14} eV/cm² and can be expressed as a function of absolute temperature as

$$\sigma_D = \frac{1.05 \times 10^{17}}{T} - 1.86 \times 10^{13} \quad (6)$$

From the above equation, σ_D is equal to 3.4×10^{14} eV/cm² at room temperature. This value is equal to the surface energy of the reconstructed cavity σ_i resulting from vacancy precipitation estimated by Van Vechten [11], equal to 3.8×10^{14} eV/cm².

RESULTS AND DISCUSSION

Figure 2 shows the experimental data for the axial distribution of the FPD density obtained from a 150 mm-diameter crystal grown with an abrupt change in the growth rate. In the experiment, the top section of the crystal was grown at a rate of 1.0 mm/min. until the length of the crystal had reached 30 cm. The growth rate was then abruptly reduced to 0.4 mm/min. and maintained at this value until the crystal was tailed off.

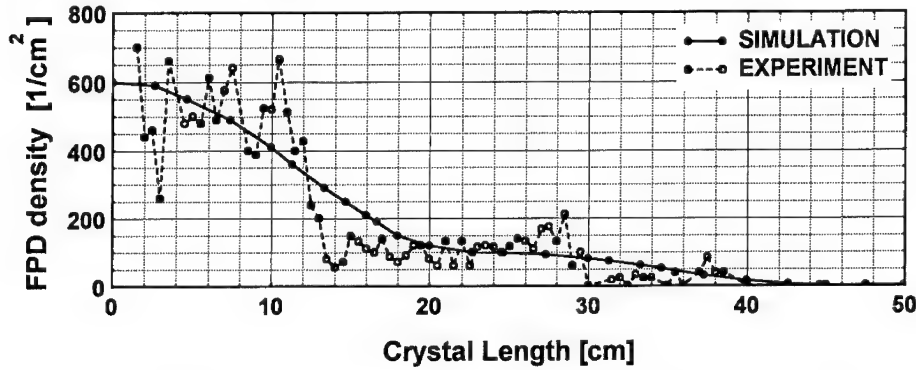


Figure 2: The axial distribution of the FPD density in a 150 mm-diameter crystal grown with an abrupt change in the growth rate.

The as-grown crystal was sliced along the axial position and then polished. The sliced and polished samples were etched in Secco etch for 30 min. without agitation to reveal the flow pattern defects [1]. The flow pattern defect density was determined under the optical microscope and then plotted as a function of crystal length. From the experimental data, it is apparent that an abrupt reduction in the crystal growth rate causes an abrupt decrease in the FPD density. It should be pointed out that a typical axial distribution of the FPD density in a 150 mm-diameter crystal is relatively uniform from the top to the bottom of the crystal, see for example Ref.[5].

The experimental data in Figure 2 were numerically fitted to Eqs. 1 to 6 using the finite difference model shown in Figure 1b. From the numerical fitting, A is 5.38×10^{10} defects/cm² sec. The volume of the flow pattern defect containing a vacancy V_D is 6.41×10^{-23} cm³ for $Gr = 1.0$ mm/min. and 8.9×10^{-23} cm³ for $Gr = 0.4$ mm/min. The result from the numerical analysis suggests that the vacancy concentration in the flow pattern defect decreases with decreasing crystal growth rate. In order to explain the dependence of the vacancy concentration in the flow pattern defect on the crystal growth rate, the effect of the crystal growth rate on the axial distributions for the temperature and vacancy saturation ratio, defined as C_V/C_V^s , is considered.

Figure 3 shows the simulation result of temperature distribution plotted as a function of the distance from the melt interface X_i before and after an abrupt change in the growth rate. It is observed that the axial temperature distribution shifts slightly upwards. In general, a decrease in the crystal growth rate causes an increase in the crystal diameter

which must be compensated by an increase in the melt temperature. As the result, the radiative heat exchange in the crystal growth chamber and hence the crystal temperature

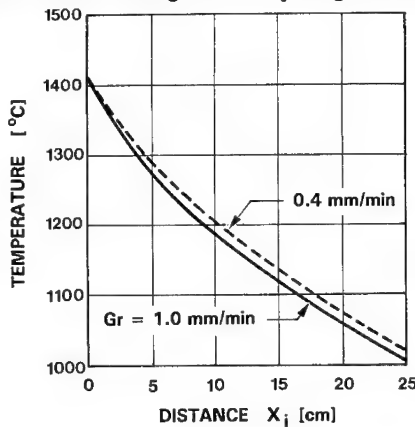


Figure 3: Axial temperature distribution.

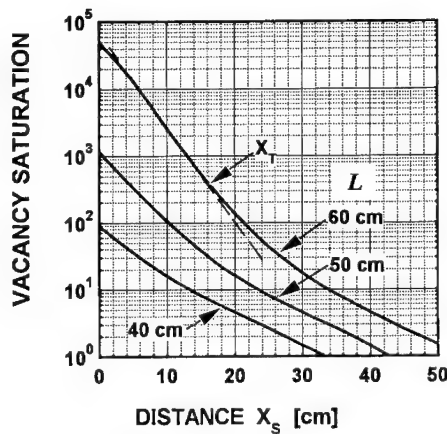


Figure 4: Axial vacancy saturation distribution.

between silicon interstitials and flow pattern defect could increase with decreasing crystal growth rate. Because the vacancy is considered to be the dominant point defect species in the pair annihilation reaction, a limited concentration of excess silicon interstitials will become available for the interaction between the flow pattern defect and the silicon interstitials. Form this argument, the interaction between the flow pattern defect and the silicon interstitials would result in a reduction in the vacancy concentration in the flow pattern defect and not to a complete dissolution of the flow pattern defect. Based upon this model, a slow growth rate Gr would lead to an increase in the volume of the flow pattern defect containing a vacancy V_D and a reduction in its generation rate J_D .

will increase. From the present analysis, a slight decrease in the temperature gradient near the melt interface resulting from a growth rate reduction was found not to be responsible for the drastic reduction in the FPD density shown in Figure 2. Figure 4 shows the axial distributions of the vacancy saturation ratio calculated as the function of the crystal length L and the distance from the crystal shoulder X_s . Although the axial vacancy saturation distributions appear to exhibit a transition from a high to low saturation gradient at X_T , it should be pointed out that such a vacancy distribution is related to crystal cooling conditions and not to an abrupt change in the crystal growth rate.

From the standard kinetic theory [12], the forward reaction rate constant for the diffusion limited process k_f is described as $k_f = 4 \pi r_R D_I \approx 4 \pi t_R D_I^2 / r_R$ where r_R could be the capture radius of the recombination reaction between silicon interstitials and a flow pattern defect and t_R is the reaction time. In the above expression, k_f can be increased only by increasing the reaction time because r_R is typically a small value. Therefore, it is suggested that the reaction time

SUMMARY

Numerical simulation of point defect distributions in a growing Czochralski silicon crystal with an abrupt change in the crystal growth rate from 1.0 to 0.4 mm/min was performed. The result from the global thermal simulation suggests that the axial temperature distribution shifts slightly upwards as a result of the growth rate reduction. Both the temperature and vacancy saturation gradients were found not to be responsible for an abrupt reduction in the flow pattern defect density. Based upon the result from the numerical fitting with the experimental data and the argument that the flow pattern defects are of vacancy-type, it is proposed that the generation rate of the flow pattern defects during crystal growth can be described by the classic nucleation rate theory proposed by Becker [8]. In addition, it is suggested that the vacancy concentration in the flow pattern defect depends upon the reaction time between the silicon interstitials and the flow pattern defect. With an increase in the reaction time and hence a decrease in the crystal growth rate, the model predicts a reduction in the generation rate of the flow pattern defects.

REFERENCES

1. H. Yamagishi, I. Fusegawa, N. Fujimaki, and M. Katayama, *Semicond.Sci.Technol.*, **7**, A135(1992).
2. J. Ryuta, E. Morita, T. Tanaka, and Y. Shimanuki, *Jpn.J.Appl.Phys.*, **31**, L293(1992).
3. H. Yamagishi, I. Fusegawa, K. Takano, E. Iino, N. Fujimaki, T. Ohta, and M. Sakurada, in *Semiconductor Silicon/1994*, edited by H.R. Huff, W. Bergholz, and K. Sumino, (The Electrochemical Society, Pennington, NJ, 1994) p.124-135,
4. K. Nakajima, J. Furukawa, H. Furuya, and T. Shingyouji, in *Semiconductor Silicon/1994*, edited by H.R. Huff, W. Bergholz, and K. Sumino, (The Electrochemical Society, Pennington, NJ, 1994) p.168-179.
5. S.S. Kim and W. Wijaranakula, *J.Electrochem.Soc.*, **141**, 1872(1994).
6. F. Dupret, P. Nicodème, Y. Ryckmans, P. Wouters and M.J. Crochet, *Int.J.Heat Mass Transfer*, **33**, 1849(1990).
7. W. Wijaranakula, *J.Electrochem.Soc.*, **140**, 3306(1993).
8. R. Becker, *Proc.Phys.Soc.*, **52**, 71(1940).
9. K. Wada and N. Inoue, in *Defects and Properties of Semiconductors: Defect Engineering*, edited by J. Chikawa, K. Sumino, and K. Wada (KTK Science Pub., Tokyo, 1987) pp.169-184.
10. R.E. Reed-Hill, *Physical Metallurgy Principles*, 2nd ed. (D. Van Nostrand Company, New York, 1973), p.368.
11. J.A. Van Vechten, *Phys.Rev. B.*, **17**, 3197(1978).
12. T.R. Waite, *J.Chem.Phys.*, **28**, 103(1958).

DEVIATION FROM STOICHIOMETRY AND LATTICE PROPERTIES OF SEMICONDUCTING SnTe PHASE

E.I.ROGACHEVA, G.V.GORNE and O.N.NASHCHEKINA
Polytechnical University, 21 Frunze St., 310002 Kharkov, Ukraine

ABSTRACT

The temperature dependences of lattice thermal conductivity λ_p in the range of 300-650 K were obtained for SnTe_{1+x} semiconducting phase with $x = 0-0.04$. It is established that the nonstoichiometric vacancies are centers of effective scattering of phonons. The scattering cross-section calculated from experimental data is in a good agreement with the theoretical calculations based on the Klemens theory. The linear change of thermal resistance with temperature is observed, which evidences the prevalence of three-phonon scattering processes. The additional thermal resistance grows as the concentration of cation vacancies increases.

INTRODUCTION

It is well known that all the semiconducting compounds are characterized by some degree of deviation from stoichiometry and have certain homogeneity regions (HR) which causes appearance of intrinsic defects whose concentration depends upon degree of deviation from stoichiometry.

The development of the perspective materials is closely connected with the investigation of influence of the native defects on their physical properties.

The object of the present investigation is semiconducting compound SnTe_{1+x} . It is known [1-3] that tin telluride has NaCl-type lattice and a wide (~ 1 at.%) one-sided homogeneity region (HR) located on the side of the Te excess (the peak in melting curves in Sn-Te system corresponds to $x=0.016$). The largest extent of HR ($x=0.004-0.035$) corresponds to 800-900 K; as temperature decreases, the HR narrows. Due to significant deviation from stoichiometry SnTe has a great amount of intrinsic defects, mainly cation vacancies and, consequently, high concentration of p-type charge carriers ($10^{20} - 10^{21} \text{ cm}^{-3}$) [1-4].

By the present time the influence of deviation from stoichiometry on unit cell parameter [1-4], microhardness [3-5], electrical conductivity, coefficient of thermo-e.m.f. [3,4], Mossbauer parameters [5] and coefficient of linear expansion [6] have been investigated.

The aim of the present work is to investigate the influence of deviation from stoichiometry on the lattice thermal conductivity of SnTe_{1+x} . Thermal conductivity λ of SnTe was studied in [7-8]. It was established in [7] that λ_p depends on both temperature and hole concentration. The authors of [7] pointed out that vacancies strongly scatter phonons. The authors of [8] who conducted measurements on pressed samples concluded that λ_p of SnTe practically is not dependent on non-stoichiometric vacancies concentration. Thus, the data presented in [7,8] are contradictory.

EXPERIMENTAL DETAILS

The measurements of λ and electrical conductivity were carried out in the temperature range 300-650K on the polycrystalline samples SnTe with $x=0-0.04$. Alloys were produced by fusing high-purity elements (99.999 at.% of the major component) in evacuated and sealed capsules at 1250 K. Then samples were annealed at 820 K during 200 hours. Thermal conductivity was measured on the cylinder-shaped specimens with diameter of 1.5 cm and height of 0.5 cm using the method of dynamical calorimeter in the regime of the monotonous heating. λ_p was determined by subtraction of electronic component λ_e calculated on the basis of Viedemann-Franz law from the measured λ . The Lorenz number was taken equal to $L = \frac{\pi^2}{3} \left(\frac{k_B}{e} \right)^2$, where k_B is Boltzmann factor.

RESULTS AND DISCUSSION.

In fig 1 and 2 the temperature dependences of λ, λ_e and thermal resistance $1/\lambda_p$ in the interval of 300-650 K as well as isotherms of these characteristics in Sn-Te system are given. The analysis of the temperature dependences of $1/\lambda_p$ shows that all the samples have the linear dependences of $1/\lambda_p$. The extrapolation of the straight lines down to the low temperature region ($T \rightarrow 0$) gives the vertical intercept $1/\lambda_p$ (fig. 1b). This value corresponds to additional thermal resistance caused by intrinsic defects. Thus

$$\frac{1}{\lambda_p} = AT + B, \quad (1)$$

where B is vertical intercept and A characterizes the slope of the straight lines. Values of A for the different lines are very close varying slightly within $\pm 3\%$; values of B increase as defect concentration characterized by x parameter grows (fig. 2b, $T = 0$).

It is known [9] that if the thermal resistance is caused by three-phonon scattering processes the Eucken law must hold:

$$\frac{1}{\lambda_p} = \frac{kT}{\theta_D^3}, \quad (2)$$

where k is the coefficient taking into account the degree of anharmonicity of crystal lattice oscillations and θ_D is Debye temperature.

The linear character of temperature dependences of $1/\lambda_p$ evidences that the thermal resistance caused by vacancies is not dependent on temperature and is determined only by scattering on defects. This result is in a good agreement with the theory: at the temperatures above the Debye temperature ($\theta_D = 130K$) thermal resistance arising due to defects must not depend on temperature [9].

Defect ordering, however, might lead to opposite effect. In case of ordering, concentration dependence of properties will be determined by simultaneous effect of two factors: increase in number of the centers of static and dynamic distortions of lattice caused by the growth of defect concentration and ordering processes. In [3 - 6] the assumption about vacancy superstructure

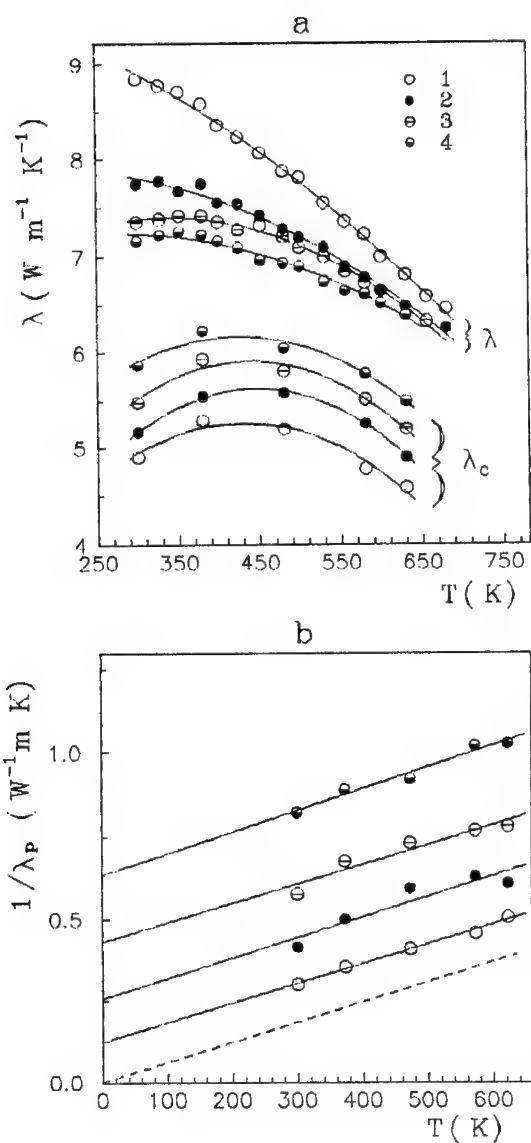


Fig. 1. Temperature dependences of total λ and electronic λ_e thermal conductivity (a), and thermal resistance $1/\lambda_p$ (b) of SnTe_{1+x} .
 $x = 0.008$ (1); 0.016 (2); 0.024 (3); 0.032 (4).

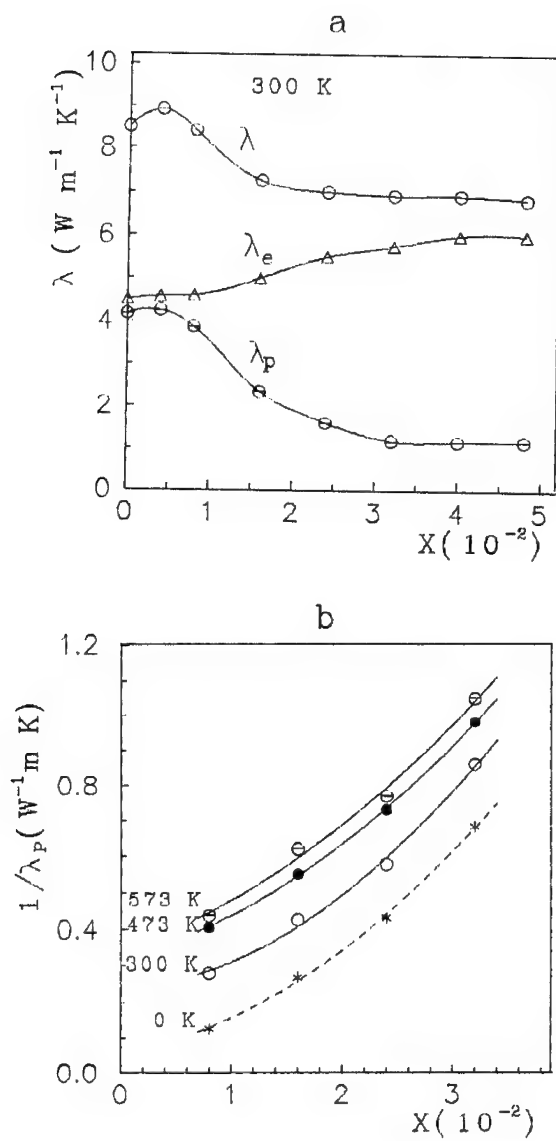


Fig.2. Isotherms of total λ , electronic λ_e , lattice λ_p thermal conductivity (a), and thermal resistance $1/\lambda_p$ (b).

formation at $x = 0,016$ was made. Slight change of k/θ_D^3 is another indirect evidence in favor of vacancies ordering.

The straight line drawn through the origin with the slope equal to the mean value of the slopes of the obtained straight lines (fig. 1) corresponds to the temperature dependence of thermal conductivity of hypothetical defectless crystal of SnTe. From the graphs in fig. 1 it follows that for the perfect SnTe $\lambda_p \cdot T$ is equal to (1650 ± 50) W/m. Theoretical calculation of $\lambda_p \cdot T$ of hypothetical SnTe without defects performed according to Julian [10]:

$$\lambda_p \cdot T = \frac{M_a \cdot a \cdot \theta_D^3}{T \cdot \gamma^2}, \quad (3)$$

where M_a is the average mass of an atom, a is the distance between atoms, γ is Gruneisen constant, gives the value of $\lambda_p \cdot T$ as 1620 W/m. In accordance with Keyes [11] $\lambda_p \cdot T = 1300$ W/m. Estimate made using Klemens theory [12] gives $\lambda_p \cdot T = 1300$ W/m. From the dependences of $1/\lambda_p$ on defect content one can estimate the additional resistance made by each defect and, consequently, the defect cross-section of phonon scattering σ . Value of σ can be estimated using Ioffe formula [13]:

$$\frac{\lambda}{\lambda_0} = 1 + \frac{N}{N_0} \cdot \Phi \cdot \frac{l_0}{a}, \quad (4)$$

where N is defect concentration ($N = (1,3-5,2) \cdot 10^{26} \text{ m}^{-3}$), N_0 is the number of atoms per volume unit of crystal ($N_0 = (3,2) \cdot 10^{28} \text{ m}^{-3}$), a is the distance between neighboring atoms, l_0 is mean free path of phonons in the material without impurities, Φ is multiplier in the expression of $\sigma = \Phi \cdot a^2$, where σ is cross section of scattering by impurities, λ and λ_0 are thermal conductivities of crystal lattice of the materials with and without defects respectively. The mean free path l_0 is determined from the Debye formula:

$$\lambda_0 = \frac{1}{3} C_v \cdot l_0 \cdot \bar{v}_g, \quad (5)$$

where C_v is heat capacity of volume unit and \bar{v}_g is mean group velocity. Assuming $\bar{v}_g = \sqrt{E/\rho} = 2550 \text{ m/s}$ (E is the Youngs' modulus, ρ is density) one obtains $\sigma \sim 2.5 a_0^2$ (a_0 is unit cell parameter, $a_0 = 2a$) and $\Phi = 10$. Thus, cross section of phonon scattering by vacancies is fairly large.

In conformity with the Klemens theory [13] phonon scattering on defects can be described by the contribution of three factors dependent on local change in density $\Delta M/M$, interatomic bond strength $\Delta G/G$ and elastic distortion of crystal caused by the difference in effective sizes of atom (ions) and substituting defect $\Delta R/R$. The cross section of scattering according to Klemens is

$$\sigma = \frac{v_0^2 \omega^4}{4\pi v^4} \left\{ \left(\frac{\Delta M}{M} \right)^2 + 2 \left[\frac{\Delta G}{G} - \frac{b}{\sqrt{5}} \cdot \gamma \cdot \frac{\Delta R}{R} \right]^2 \right\}, \quad (6)$$

where v_0 is volume occupied by one atom, ΔG is local change in elasticity modulus, ΔM is local change in mass, γ is Gruneisen constant, $b = 14.2$ [9]. Assuming $\omega = \omega_{\max} = \frac{k_B \theta_D}{\hbar}$, $\theta_D = 130$ K, $\gamma = 2$, $\Delta R/R = 0.13$, $v_0 = 31 \cdot 10^{-30} \text{ m}^3$, we get $\sigma_0 = 2,5a_0^2$, which coincides with the scattering cross section determined from the experimental data. Proximity of computed values of σ and experimental ones shows that despite the fact that ω is smaller than ω_{\max} and v is lower than v_{gr} both effects to all appearances compensate each other.

CONCLUSIONS

On the basis of analysis of the temperature (300-650K) and concentration ($x=0-0.04$) dependences of lattice thermal conductivity of SnTe_{1-x} it is concluded that the charged nonstoichiometric vacancies are the centers of effective scattering of phonons. The scattering cross-section calculated from experimental data ($\sigma = 2,5a_0^2$, where a_0 is unit cell parameter) is in a good agreement with the theoretical calculations based on the Klemens theory. In the investigated temperature range linear change of thermal resistance with T is observed which evidences the prevalence of three-phonon scattering processes. The additional thermal resistance grows as the concentration of cation vacancies increases.

REFERENCES

1. R.F.Brebrick, J.Phys. and Chem. Solids. **24**, 27 (1963); **32**, 551 (1971).
2. J.C.Lin, T.L.Ngai, A.Chang, Metallurgical Transactions . **A17**, 1241 (1986).
3. E.I.Rogacheva, G.V.Gorne, N.K.Zhigareva and A.B.Ivanova, Izv. AN SSSR. Ser. Neorgan. Materialy. **27**, 267 (1991).
4. E.I.Rogacheva, G.V.Gorne, S.A.Laptev, A.V.Arinkin, T.B.Vesene, Izv. AN SSSR. Ser. Neorgan. Materialy **22**, 41 (1986).
5. D.Baltrunas, S.Motiejunas and E.I.Rogacheva, Phys. Stat.Solidi (a). **97**, K131 (1986).
6. E.I.Rogacheva, N.A.Sinelnik, O.N.Nashchekina, V.P.Popov, T.A.Lobkovskya, Acta Physica Polonica A. **84**, 733 (1993).
7. D.H.Damon, J.Appl.Phys. **37**, 3181 (1966).
8. N.A.Erasova and V.I.Kaidanov. Fiz.Tekh.Poluprovodn. **2**, 34 (1968).
9. R.Berman, Thermal Conduction in Solids, (Clarendon Press, Oxford, 1976), p.74.
10. C.L.Julian, Phys. Rev. **137**, A128 (1965).
11. R.W.Keyes, Phys.Rev. **115**, 564 (1959).
12. P.G.Klemens, Phys.Rev. **118**, 507 (1960).
13. A.F.Ioffe, Dokl. AN SSSR. **97**, 821(1954).

Part III

Grown-In Defects in Thin Films

LOW ENERGY ION IMPLANTATION OF AS DURING SI-MBE.

E.J.H. Collart, D.J. Gravesteijn, E.G.C. Lathouwers, and W.J. Kersten. Philips Research Laboratories, Prof. Holstlaan 4, 5656 AA Eindhoven, The Netherlands.

ABSTRACT

As-doped Si layers were grown using Molecular Beam Epitaxy (MBE) together with simultaneous Low Energy Ion Implantation (LEII). The influence of growth conditions such as Si-substrate temperature, ion energy and ion dose was investigated using structural and electrical characterization techniques. Below the As solid solubility limit, well defined and 100 % electrically active As-doped layers were grown. Above solid solubility segregation occurred, with broadened profiles and less than 100 % activation.

INTRODUCTION

As both lateral and vertical dimensions of MOS and bipolar devices continue to shrink, there is a growing need for shallow implantations and very thin layer structures. In order to retain (or improve) at the same time the electrical device characteristics, higher doping levels are usually also required. This poses a challenge even to the most advanced growth techniques. MBE is a proven method to grow thin high-quality Si layers. However, during MBE growth, smearing of the dopant concentration due to segregation can destroy the desired doping profile. This limits, particularly for n-type doping (e.g. Sb or As), the capability to grow new device structures. Low energy implantation of dopant atoms can enhance the incorporation probability at MBE operating conditions to unity [1-5], and eliminate segregation.

EXPERIMENTAL

Details of the MBE system (Vacuum Generators V 80) have been reported elsewhere [6]. Recently, a research-type LEII system (High Voltage Engineering Europa B.V.) has been added. This system consists of two hot cathode Penning ion sources which can be operated simultaneously, at 30 kV extraction voltage. The switching time between the sources is <1 s, allowing one to grow very sharp and well defined doping profiles. To ensure minimal gas load for the MBE system during source operation the LEII is equipped with a five stage differential pumping vacuum system consisting of three 360 l/s turbomolecular pumps followed by two 1500 l/s cryopumps. During operation the ion beam is adjusted to the final implantation energy E by setting the total LEII system at a voltage of $(E/q - 30)$ kV. Before reaching the target, the 30 kV ions are decelerated in a multiple-electrode system. The unit is placed partly inside the MBE vessel and consists of an einzel lens to match the beam optics to the actual deceleration section, a multiple electrode system for deceleration of the ions and an electrostatic focusing and deflection system. Target currents were between 50 and 150 μ A for ion energies between 250 eV and 5 keV for $^{11}\text{B}^+$, $^{31}\text{P}^+$ and $^{75}\text{As}^+$. Stable ion

currents could routinely be obtained for long periods of time (> 60 min). Growth experiments were performed on 6 inch (100) Si-wafer substrates. Excellent uniformity over a 6" wafer was obtained: a 2000 Å Si layer was grown at 700°C and doped with 500 eV $^{11}\text{B}^+$ to a level of $2.10^{18} \text{ cm}^{-3}$. The sheet resistance was mapped over the wafer using a Prometrix OmniMap RS50. The mean R_{\square} was 1428 Ω/\square , in agreement with the grown layer, with a standard deviation of 4%.

Before epitaxial-Si growth all wafers received a 10 min, 900°C heat treatment in order to remove native oxide. For all experiments the growth rate was 3 Å/s with an implantation energy of 1 keV for $^{75}\text{As}^+$, except where indicated differently. Rutherford Backscattering Spectrometry (RBS) was used to determine implanted dose and layer thickness. Minimum yield values χ_{\min} were derived from the ratio between random and channelling yields. Secondary Ion Mass Spectrometry (SIMS) was employed to measure dose and depth profiles. The structural information from RBS and SIMS was correlated with electrical measurements such as sheet resistance R_{\square} and data obtained using the Hall effect. The latter gives Hall mobility μ and sheet concentration n_s of the carriers. A Hall factor of 1 was assumed.

RESULTS AND DISCUSSION

For certain applications, arsenic is attractive as an n-type dopant compared to Sb or P. It has a much higher solid solubility than Sb and, compared to P, As diffusion proceeds much slower with a smaller emitter-push effect on underlying B. The latter is relevant for bipolar device technology. For these devices, good control over concentration profiles is necessary. First results obtained with the Si-MBE/LEII combination are presented below.

Low Arsenic concentration.

Figure 1 shows a SIMS analysis of the following layer structure, grown at 720°C: a 2300 Å buffer layer of undoped Si, followed by a 2300 Å layer As-doped with an ion current corresponding to a doping level of $1.7 \cdot 10^{19} \text{ cm}^{-3}$ and capped by 600 Å undoped Si. Also shown is a second experiment with the same doping and growth conditions, but now a 600 Å As-doped amorphous Si layer was grown at room temperature. The incorporation probability γ is defined as the ratio of the ion dose (determined via a current integrator) to the final dose in the wafer (determined with RBS). For both conditions γ was unity and a well defined doping profile was obtained with comparable steepness of leading and trailing edge. RBS analysis yielded a $\chi_{\min}(\text{Si})$ of 2.6 %, and a $\chi_{\min}(\text{As})$ of 24 % for the layer grown at 720°C. The former value indicated high-quality epitaxial Si. The χ_{\min} for As should be treated with caution, since it is well known that RBS measurements with 2 MeV He^+ ions can displace substitutional As, depending on total He^+ dose delivered to the sample [7]. The minimum yield values for As can, however, be used as an upper bound for non-substitutional As. The sheet resistance, mobility and electron sheet concentration of the 2300 Å layer were 202 Ω/\square , 83 $\text{cm}^2\text{V}^{-1}\text{s}^{-1}$ and $3.7 \cdot 10^{14} \text{ cm}^{-2}$ respectively. This indicated a 100 % activation of the implanted layer with a bulk-like mobility.

Additional growth experiments at 560°C and 860°C are summarized in table I(a), I(b). The high dose ($>10^{14} \text{ cm}^{-2}$) determination was done with RBS. The lower doses

were too low to be reliably determined by RBS. For these, SIMS data were used. The As-concentrations listed in the tables are the peak concentrations from SIMS analysis. For the low dose results, the concentration was found constant over the layer for both temperatures. For the higher doses, the low temperature experiments showed segregation to the surface and a profile broadening when compared with the high temperature results. The mobility values listed between parentheses are bulk mobility values from [8]. The relative error for both the structural and electrical measurements is typically $\pm 10\%$.

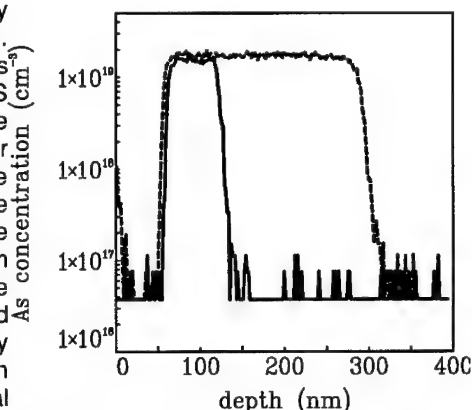


Figure 1: A 60 nm α -Si layer grown at RT and doped to a level of $1.7 \cdot 10^{19} \text{ cm}^{-3}$ and, under identical doping conditions, a 230 nm epitaxial Si layer grown at 720°C .

Table I(a): Electrical characteristics for different As concentrations at 560°C growth temperature. Listed are the sheet electron concentration n_s , the electron Hall mobility μ , and the sheet resistance R_\square .

[As] (cm^{-3})	As dose (cm^{-2})	n_s (cm^{-2})	μ ($\text{cm}^2\text{V}^{-1}\text{s}^{-1}$)	R_\square (Ω/\square)
$1 \cdot 10^{18}$	$5.4 \cdot 10^{12}$	$5.4 \cdot 10^{12}$	266 (290)	4328
$1.5 \cdot 10^{18}$	$8.1 \cdot 10^{12}$	$7.7 \cdot 10^{12}$	226 (250)	3527
$5 \cdot 10^{19}$	$3.5 \cdot 10^{14}$	$2.6 \cdot 10^{14}$	72 (70)	339
$1 \cdot 10^{20}$	$5.3 \cdot 10^{14}$	$4.6 \cdot 10^{14}$	63 (60)	216

Table I(b): same as I(a), but now at a growth temperature of 860°C .

[As] (cm^{-3})	As dose (cm^{-2})	n_s (cm^{-2})	μ ($\text{cm}^2\text{V}^{-1}\text{s}^{-1}$)	R_\square (Ω/\square)
$1 \cdot 10^{18}$	$5.2 \cdot 10^{12}$	$6.1 \cdot 10^{12}$	213 (290)	4837
$1.7 \cdot 10^{18}$	$8.4 \cdot 10^{12}$	$8.4 \cdot 10^{12}$	173 (215)	4296
$6 \cdot 10^{19}$	$2.7 \cdot 10^{14}$	$2.6 \cdot 10^{14}$	72 (70)	338
$7 \cdot 10^{19}$	$3.7 \cdot 10^{14}$	$4.1 \cdot 10^{14}$	68 (65)	223

At 560°C the γ was unity for the lower concentrations with a 100 % activation. For the higher concentrations there was segregation to the surface, implying a $\gamma < 1$, with an activation less than 100 %. Probably for the low temperature/high concentration set, the solid solubility limit was exceeded in agreement with [3] where

a limit of $1.10^{19} \text{ cm}^{-3}$ was reported at 460°C . Nevertheless, the electrical solubility ($\equiv n_0$) of $9.2 \cdot 10^{19} \text{ cm}^{-3}$ for the high dose reported here is much higher than the (extrapolated) values from [9]. For all concentrations bulk mobilities were found.

At 860°C γ was again unity for the lower concentrations with now mobilities lower than bulk mobilities. Within experimental error, a 100 % activation was found. For the higher concentrations there was no visible segregation. However, most likely segregation did take place but now all of the segregated As had evaporated. Evidence for this is presented in the next paragraph. The built-in As was 100% activated with bulk mobilities.

High As concentration.

In order to investigate the influence of the growth temperature on highly doped layers, the following structure was grown at three different temperatures: a 640 Å thick buffer layer of intrinsic Si, followed by a 640 Å arsenic doped layer and capped with a third 640 Å thick intrinsic Si layer. The growth temperatures were 560, 720 and 900°C . The growth rate was 0.3 Å/s with an intended As concentration of $1.8 \cdot 10^{21} \text{ cm}^{-3}$ (or a dose of $1.2 \cdot 10^{16} \text{ cm}^{-2}$). The SIMS analyses are shown in figure 2. Structural information from RBS has been compared to electrical measurements and are summarized in table II.

Except at 560°C , the γ was found to be much smaller than unity, with $\gamma=0.23$ at 720°C and $\gamma=0.18$ at 900°C . For all temperatures the As concentration was above the corresponding solid solubility of approximately $1.10^{20} \text{ cm}^{-3}$ at 720°C and $2.10^{20} \text{ cm}^{-3}$ [10] at 900°C . It can be seen that, while at 560°C the doping profile is very well defined, for 720°C and 900°C especially the profile is broadened. Possibly implantation damage, or a point-defect generating mechanism due to the high As concentration is responsible. At 560 and at 720°C some As had segregated to the surface, as could be concluded from RBS measurements. For the 560°C the amount was too small to allow a quantitative measurement, but at 720°C the As surface concentration was $2.7 \cdot 10^{14} \text{ cm}^{-2}$. This is too low to account for the lower As concentration in the ion-doped layer. Probably As has evaporated from the surface during growth. It is assumed that at most one monolayer of As can be present at the surface [11]. Then, with a monolayer of As (N_s^0) at the surface at the start of the capping layer growth a residence time τ of approximately 2000 s is calculated from $N_s^1/N_s^0 = \exp(-t/\tau) = 0.3$. At 900°C no segregated As could be detected. Presumably, at this temperature, the evaporation is fast enough to completely remove As segregated to the surface.

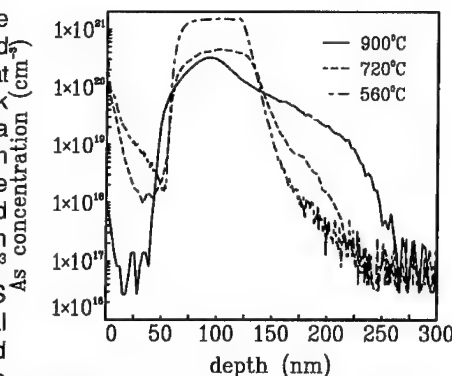


Figure 2 : For three different growth temperatures, a 64 nm thick layer doped with an ion current corresponding to a concentration of $1.8 \cdot 10^{21} \text{ cm}^{-3}$.

Table II: Structural and electrical characterization of identically doped layers at three different growth temperatures. The electrical characterization includes the electron sheet concentration n_e , the electron Hall mobility μ and the sheet concentration R_{\square} .

	560°C	720°C	900°C
[As] (cm ⁻³)	1.8 10 ²¹	4.2 10 ²⁰	3.3 10 ²⁰
[As] (cm ⁻²)	1.2 10 ¹⁶	2.7 10 ¹⁵	2.1 10 ¹⁵
$\chi_{\min}(\text{As})$ [%]	86	62	6
$\chi_{\min}(\text{Si})$ [%]	11	6.7	2.7
substitut[cm ⁻²]	1.8 10 ¹⁵	1.10 ¹⁵	2.10 ¹⁵
n_e [cm ⁻²]	4.5 10 ¹⁴	3.0 10 ¹⁴	1.2 10 ¹⁵
μ [cm ² /Vs]	16 (12)	28.4 (30)	27 (35)
R_{\square} [Ω]	203	237	55

As the growth temperature increases, the minimum yield χ_{\min} for Si decreases from 11 % to 2.7 %. The substitutional dose in the table is calculated via $100 \times [1 - \chi_{\min}(\text{As})] / [1 - \chi_{\min}(\text{Si})]$. The n_e values measured via the Hall effect are lower than the substitutional fraction, but increasing with higher temperature from 25 % at 560°C, to 30 % at 720°C and 60 % of the substitutional amount at 900°C. The latter two agree more or less with the electrical solubility from [9].

It appears that for an energy of 1 keV As is deposited too close to the growing surface to eliminate segregation. The following experiment gives further evidence of this. As-doped layers were grown at 720°C but with implantation energies of 1, 2 and 5 keV. The energy was changed from 5 keV to 2 keV and 1 keV during continuous growth of a Si layer. A buffer layer was grown between the implanted layers. As before, at 1 keV the maximum achievable concentration was 4.10²⁰ cm⁻³. However, at 2 and at 5 keV the intended concentration of 2.10²¹ cm⁻³ was build into the Si as can be seen from figure 3.

For these three energies the projected range R_p were calculated with the SUPREM-III simulation program, using a Monte Carlo calculation. This resulted in 45 Å, 60 Å and 100 Å for 1, 2 and 5 keV respectively. These numbers were verified by implanting As with these three energies into a Si-substrate at room temperature. Good agreement was found between simulation and experiment. (TRIM simulations gave values approximately 20 % lower). Going from 45 Å to 60 Å is sufficient, at 720°C, to trap all of

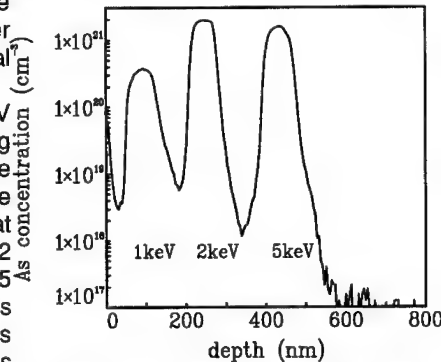


Figure 3: Concentration profile of three layers, As-doped with the same ion current but different ion energies, at $T_{\text{growth}}=720^\circ\text{C}$

the implanted As into the Si, with no loss due to segregation and subsequent evaporation.

CONCLUSIONS

A low energy ion implanter has been integrated with a Si-MBE set-up. The implanter proved to be compatible with MBE growth conditions. High currents could be obtained and uniformly scanned over 6" wafers. At all growth temperatures fully activated As-doped layers were grown. At higher concentrations ($>6.10^{19} \text{ cm}^{-3}$) segregation effects were observed, with considerable profile broadening, an incorporation probability <1 and activation less than 100%. By increasing the ion energy the incorporation probability could be improved.

ACKNOWLEDGMENTS

The authors would like to thank Rob de Kruif and Peer Zalm for the SIMS analyses, and Frank Hakken and Walter de Coster for RBS measurements.

REFERENCES

1. Y. Ota, J. Appl. Phys. **51**, 1102 (1980).
2. H. Sigiura, J. Appl. Phys. **51**, 2630 (1980).
3. M.W. Denhoff, D.C. Houghton, T.E. Jackman, M.L. Swanson, and N.R. Parikh, J Appl. Phys. **64**, 3938 (1988).
4. J.-E. Sundgren, J. Knall, W.-X. Ni, M.-A. Hasan, L.C. Markert, and J.E. Greene, Thin Solid Films **183**, 281 (1989).
5. N. Djebbar, J. Gutierrez, H. Charki, A. Vapaille, G. Prudon, and J.C. Dupy, Thin Solid Films **184**, 37 (1990).
6. A.A van Gorkum, G.F.A. van de Walle, R.A. van den Heuvel, D.J. Gravesteijn, and C.W. Frederiksz, Thin Solid Films **184**, 207 (1990).
7. J. Haskell, E. Rimini, and J.W. Mayer, J. Appl. Phys. **43**, 3425 (1972).
8. G.D. Masseti, M. Severi, and S. Solmi, IEEE Trans. Electron Devices **ED-30**, 764 (1983).
9. E. Guerrero, H. Pötzel, R. Tielert, M. Grasserbauer, and G. Stinger, J. Electrochem. Soc. **129**, 1826 (1982).
10. D. Nobili, A. Carabelas, G. Celotti, and S. Salmi, J. Electrochem. Soc. **130**, 922 (1983).
11. M. Kawabe, T. Ueda, and H. Takasugi, Jpn. J. Appl. Phys. **26**, L114 (1987).

Nucleation & Growth of Defects in SOI Materials

G. C. M. Silvestre, R. A. Moore & B. J. Kennedy
Department of Microelectronics and Electrical Engineering,
University of Dublin, Trinity College, Dublin 2, Ireland.

Abstract

To produce Silicon-On-Insulator (SOI) materials with thin Si overlayer, sacrificial oxidation is often used. This creates defects which have adverse effects on device performance. It has been observed that Stacking Faults (SFs) in thin Separation-by-IMplantation-of-OXYgen (SIMOX) or Bonded-and-Etched-back-SOI (BESOI) films of less than 600 Å, do not shrink as expected during neutral Ar anneals. Shrinkage of SFs in standard bulk substrates with different capping layers has been investigated to promote the understanding of the Si/SiO₂ interface effects on Si interstitial incorporation during anneals. The activation energy for growth and shrinkage of SOI samples thicker than 800 Å was found to be the same as bulk Si: 2.3 eV (growth) and 4.6 eV (shrinkage). Bulk silicon implanted with low doses of oxygen, permitted investigation of the nucleation sites of SFs in SIMOX where oxygen precipitates are believed to act as nuclei for SFs. A five step etch procedure was modified to reveal the defects in very thin SOI and an automatic defect counting system developed at T.C.D. permitted fast and reliable measurements of size and density of the defects. It appears that the two Frank partial dislocations that bound SFs, are pinned at the two Si/SiO₂ interfaces for both SIMOX and BESOI films thinner than 500 Å. In thicker SOI, the mechanisms for growth and shrinkage of SFs are the same as for bulk silicon.

1. Introduction

Silicon-On-Insulator (SOI) materials are acknowledged to be serious candidates as replacement substrates for high-performance, fully-depleted CMOS devices. The very thin Si overlayers required may be obtained by thermally oxidising Separation-by-IMplanted-OXYgen (SIMOX) materials and subsequently removing the grown oxide in HF. However, the implantation of a large oxygen dose during fabrication of SIMOX material, creates a large number of crystal imperfections in the silicon overlayer such as Stacking Faults (SFs) (density of the order of 10^4 cm^{-2}) or dislocations (density of at least $5 \times 10^5 \text{ cm}^{-2}$). Subsequent thermal oxidation leads to a growth of these defects as has been frequently observed in the past with bulk silicon [1]. Dislocations and SFs in silicon wafers are undesirable defects since they alter device performance [2]. In this study, the nucleation and the kinetics of the growth of defects in SOI materials have been studied through a set of experiments with SIMOX, Bonded-and-Etched-back-SOI (BESOI) materials and bulk silicon.

2. Experimental details

2.1. Defect delineation set-up

Figure 1 illustrates the five step preferential etching process modified to reveal the defects in thin SOI films [3]. Diluted Secco [4] is used to etch the Si film down to 100 Å (Figure 1b); 50% HF dissolves the buried oxide down to the bulk, at defect locations (Figure 1c); diluted Secco etch is used again to imprint defects into the bulk (Figure 1d); a 50% HF etch is used to etch away the oxide (Figure 1e); finally, a short Secco etch is used to clean the surface (Figure 1f). Using an automatic Defect Counting System (DCS) developed at TCD, the density of defects and length of SFs is determined very accurately in a fraction of the time needed for manual counting. A comparison between manual and automatic counting is made in Figure 2. Hardware for the DCS consisted of a high quality CCD camera mounted on top of an optical microscope and connected to a computer through a framegrabber. By means of signal processing techniques, it was possible to distinguish automatically between dislocations and SFs.

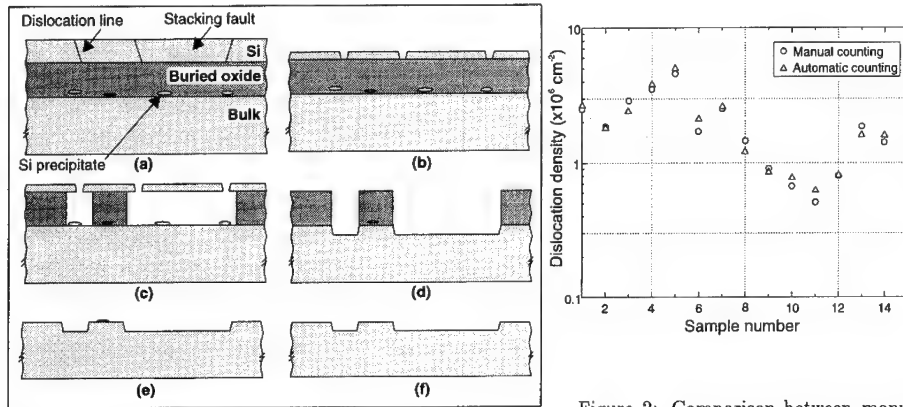


Figure 1: Preferential etching process for thin SOI

Figure 2: Comparison between manual and automatic counting of dislocations on various SIMOX wafers

2.2. Growth and shrinkage of SFs in SOI

SIMOX wafers, of [100] CZ p-type, from two batches (A and B) were fabricated using the standard LETI process as follows: single dose implantation of $1.8 \times 10^{18} \text{ O}^+ \text{ cm}^{-2}$ at 190 keV, with an implantation temperature in the range 550–650°C. This was followed by a high temperature anneal in Ar + 1% O₂ at 1320°C for 6 h resulting in a SIMOX material with a buried layer thickness of 4000 Å and a film thickness of 2000 Å [5]. Samples were subsequently thinned by dry oxidation (multi-step oxidation followed by removal of the oxide in buffered HF after each step). The 500 Å oxide layer from the last oxidation was kept on all samples. SIMOX samples of 15 different thicknesses ranging from 1600 Å to 300 Å were prepared (A1–A8 for lot A and B1–B7 for lot B). Table 1 summarises the details of the samples. The difference in SF length reported in Table 1 is due to different ambients (dry O₂ with and without TCE) and temperatures (1000°C and 1100°C) used for the oxidations. Dislocation and SF densities were lower for batch B than batch A. SIMOX samples were then annealed in Ar at 1100, 1120, 1150 and 1175°C to determine the activation energy (E_a) for shrinkage of SFs in thin SOI.

SIMOX	Si film thickness (Å)	SF characteristics		Dislocation density ($\times 10^6 \text{ cm}^{-2}$)	N_{SF} ($\times 10^{12} \text{ cm}^{-2}$)	N_{ox} ($\times 10^{17} \text{ cm}^{-2}$)	N_{SF}/N_{ox} ($\times 10^{-6}$)	E_a (eV)
		density ($\times 10^4 \text{ cm}^{-2}$)	length (μm)					
A1	1610	2.60	19.6	2.50	0.16	2.67	60.1	4.3
A2	1027	3.86	15.6	1.86	0.12	5.08	23.8	4.4
A3	982	3.88	8.7	2.90	6.47	5.31	12.2	4.3
A4	785	1.55	17.4	1.46	4.14	6.29	6.57	4.2
B1	720	1.08	24.4	0.91	3.71	6.62	5.60	4.9
B2	674	1.16	24.1	0.67	3.68	6.85	5.38	5.0
B3	622	1.29	24.1	0.51	3.78	7.11	5.32	4.6
A5	609	2.59	29.4	4.57	9.06	7.17	12.6	—
B4	590	1.01	24.0	0.80	2.79	7.27	3.85	4.3
B5	500	1.05	25.2	1.86	2.58	7.72	3.35	—
A6	496	3.45	8.4	1.71	2.81	7.74	3.63	—
B6	400	0.99	26.0	1.42	2.01	8.22	2.45	—
A7	386	2.59	18.0	2.53	3.51	8.29	4.24	—
A8	339	3.60	13.2	3.52	3.15	8.52	3.69	—
B7	300	1.03	26.4	0.97	1.59	8.72	1.83	—

Table 1: Characteristics of SIMOX samples

In a previous study, standard SIMOX wafers had been oxidised at various temperatures and oxidation times to study the SF growth kinetics, and an activation energy for growth was found to be 2.3 eV [3]. Finally, part of SIMOX wafer B1 was annealed in N_2 at 1150°C to provide a better understanding of point-defect annihilation in SOI films during neutral anneals.

A [100] p-type CZ BESOI wafer with an initial film thickness of $2\mu\text{m}$ was polished to reduce the thickness down to 2000 Å . Because of the poor uniformity of the initial Si overlayer, only a small region in the centre of the wafer was used. A boron implantation followed by low temperature annealing, similar to that used for bulk samples called IMPB1 and IMPB2, was carried out to provide nucleation sites for SFs. The BESOI wafer was divided in two, one half (sample BO1) was thinned down to 1500 Å and the other half (sample BO2) was thinned down to 500 Å by thermal oxidation resulting in SFs of $14.4\mu\text{m}$ for sample BO1 and $26.2\mu\text{m}$ for sample BO2. The two samples were then annealed in Ar under the same conditions as the SIMOX samples.

2.3. Effect of capping

Two [100] p-type CZ bulk wafers (IMPB1 and IMPB2) were implanted with a boron dose of 8×10^{13} at 80 keV to provide nucleation sites for SFs to grow. This was followed by a 30 min anneal in N_2 at 900°C . A 3 h oxidation at 1100°C in 100% O_2 was carried out to grow the SFs. On sample IMPB2, the thermal oxide was stripped off and a 2000 Å TEOS oxide was deposited instead. Four [100] p-type CZ grown bulk wafers (called IMPO1–IMPO4) were implanted with different low doses of oxygen at 110 keV. Implanted areas were restricted to 4 cm^2 to reduce the duration of implantation. The oxygen doses were chosen to be in the same range as that expected in the tail of the oxygen implantation for producing SIMOX. Samples were then annealed at 1050°C in Ar for 5 h and oxidised in 100% O_2 for 3 h at 1100°C . Table 2 summarises details on all bulk samples. Defects in bulk samples were revealed using the preferential Jenkins-Wright etch [6] for 2 min after removal of the oxide and measured with the DCS.

Sample	Implantation conditions			Anneal treatment			Dry oxidation		SF	
	type	dose (cm ⁻²)	energy (keV)	Gas	temp. (°C)	time (h)	temp. (°C)	time (h)	length (μm)	density (×10 ⁴ cm ⁻²)
IMPB1	B	8.0 × 10 ¹³	80	N ₂	900	0.5	1100	3	24.1	1.25
IMPB2	B	8.0 × 10 ¹³	80	N ₂	900	0.5	1100	3	24.1	1.31
IMPO1	O	5.0 × 10 ¹⁴	110	Ar	1000	5	1100	3	18.6	0.92
IMPO2	O	5.0 × 10 ¹⁵	110	Ar	1000	5	1100	3	18.6	5.46
IMPO3	O	5.0 × 10 ¹⁶	110	Ar	1000	5	1100	3	18.6	21.2
IMPO4	O	1.7 × 10 ¹⁷	110	Ar	1000	5	1100	3	18.6	20.2

Table 2: Characteristics of bulk Si samples

3. Results and discussions

3.1. Growth of defects

The activation energy for growth of SFs was found to be 2.3 eV, the same as for bulk silicon [7]. After an initial growth similar to that in bulk samples, the dislocation loop which surrounds the SF reaches the two Si/SiO₂ interfaces. Any further growth takes place laterally by moving the two Frank partial dislocations (Burgers vector $(1/3)\langle 111 \rangle$) which can be considered parallel. With this assumption, it is interesting to calculate the ratio between the number of Si atoms that have been consumed during the oxidation (N_{ox}) and the number of Si atoms incorporated in the SFs (N_{SF}), as suggested in reference [8]:

$$N_{SF} = N_0 D_{SF} \frac{L_{SF} t_{Si}}{\sin(55^\circ)} \quad (1)$$

where $N_0 = 1.6 \times 10^{15}$ Si/cm² is the number density of atoms in the {111} plane, D_{SF} the SF density, L_{SF} the SF mean length, t_{Si} the SOI film thickness and 55° the angle between the surface and the {111} plane. We shall assume a degree of incompleteness for the oxidation of about 10⁻³ as suggested by Hu [9]. From the results reported in Table 1, the ratio N_{SF}/N_{ox} of SIMOX samples is two to three orders of magnitude lower than the incompleteness of the oxidation. This indicates that some other very efficient sinks absorb or trap silicon interstitials (Si_I) during oxidation, possibly through a diffusion of SiO in the buried oxide via the reaction $\text{Si} + \text{SiO}_2 \rightarrow 2\text{SiO}$. SFs grow via a reaction-controlled mechanism by incorporation of Si_I through the partials which act like sinks [10].

The activation energy for SF shrinkage in SOI films thicker than 600 Å was found to be, on average, 4.6 eV and independent of the thickness of the layer. This is in good agreement with the bulk study (Figure 4) and other published results [11]. The value is also close to the activation energy for Si_I diffusion. During neutral anneals, SFs shrink by emission, from the two partials, of Si_I which diffuse away from the fault. However, in SIMOX layers thinner than 500 Å no shrinkage of SFs was observed. This was also verified on a BESOI sample (BO2). It is believed that in thin films, the two partial Frank dislocations that bound the SF are pinned to the interfaces and the energy required to move them using thermal annealing is too high.

During shrinkage, Si_I are emitted by the faults. The rate at which they are incorporated in the lattice determines the shrinkage rate of the faults. Figure 3 depicts SF length for SIMOX sample B1 after annealing at 1150°C in N₂. Because N₂ is not inert at this temperature, a reaction with the SIMOX overlayer took place and an oxide-nitride layer (Si_xO_yN_z) was formed. This layer acted as a barrier to the migration of Si_I and to their reincorporation at the surface. The exponential

behaviour observed in Figure 3 is directly related to the nitridation that has taken place at the top Si/SiO₂ interface.

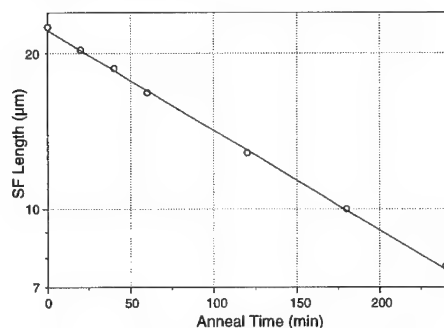


Figure 3: SF length for SIMOX sample B1 after anneal in N₂ at 1150 °C versus anneal time

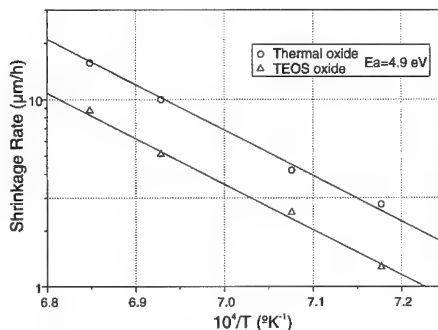


Figure 4: An Arrhenius plot of the shrinkage rate of SFs in bulk silicon IMPB1 and IMPB2

The importance of the top surface Si/SiO₂ interface in the absorption of the Si_I emitted by the SFs during shrinkage of SF in neutral ambients was also emphasised by the results obtained for the bulk samples IMPB1 and IMPB2 (Figure 4). The activation energy was found to be the same for both samples (4.9 eV). However, the shrinkage rates of the bulk sample, capped with TEOS oxide, were found to be a factor of 2 lower than that for the bulk sample capped with thermal oxide. The TEOS oxide silicon interface was not as good as the thermal one. The absorption mechanism of the excess of Si_I during neutral annealing was found to be extremely dependent on the quality of this interface.

3.2. Nucleation of defects

Infrared absorption measurements were carried out on bulk samples IMPO1–IMPO4 before and after anneal using Fourier Transform Infrared (FTIR) spectroscopy at room temperature, to provide an understanding of SF nucleation in SIMOX samples. A Perkin Elmer spectrometer with resolution of 4 cm⁻¹ was used in multiple scanning mode to collect the spectra with a good signal/noise ratio. In Figure 5, the absorption peak spectra of sample IMPO5 (before and after annealing) are given as examples.

The spectrum before annealing shows an absorption peak at 1106 cm⁻¹ corresponding to the oxygen interstitial mode (Si-O-Si bridges) in the Si substrate [12]. A successful Gaussian fit of the annealed spectrum showed a rise of the 1106 cm⁻¹ peak as well as the presence of two other peaks at 1080 cm⁻¹ and 970 cm⁻¹. The 1080 cm⁻¹ peak corresponds to the Si-O-Si stretching of the cyclotetrasiloxanes. This tends to show that oxygen atoms have been incorporated in large precipitates (SiO_x with $x > 5$). The small 970 cm⁻¹ peak was attributed to the Si-O-Ar stretching which is likely to be caused by the extended anneal in Ar (5 h). After the dry oxidation, samples IMPO1 to IMPO4 showed a large amount of SFs while a non-implanted test wafer which had not been annealed in Ar had no SFs. The SF density for samples implanted with a larger dose was found to be higher, as shown in Table 2. It is believed that high temperature anneals contribute to the precipitation of oxygen atoms remaining in the Si overlayer from the SIMOX implantation. These precipitates emit dislocation loops and SFs to release strain arising from their growth.

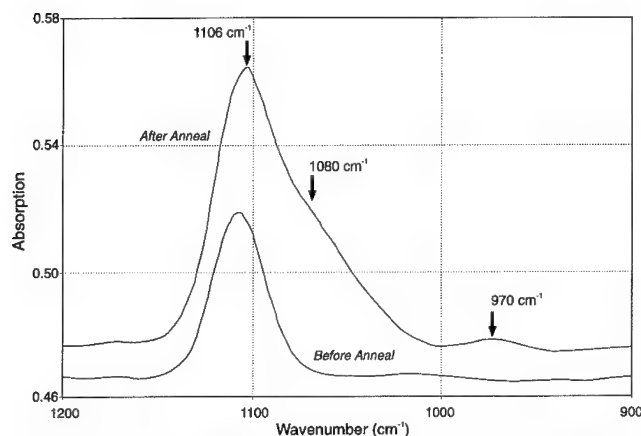


Figure 5: Infrared absorption peaks associated with Si-O-Si bridges in a low-dose, O-implanted silicon sample before and after anneal in Ar

4. Conclusions

The activation energies for growth and shrinkage of SFs in films thicker than 500 Å were found to be the same as for bulk silicon, 2.3 eV and 4.6 eV respectively. From this it was concluded that the same mechanisms were involved. Point defect absorption during neutral anneals was investigated through a study of bulk samples with different capping layers and a SIMOX sample annealed in N₂. It was found that the quality of the Si/SiO₂ interface was very important in the recombination of Si_i. Si_i are believed to combine with SiO₂ to form SiO which diffuse easily through the oxide. In very thin SOI films (thinner than 500 Å), it was not possible to shrink SFs. This was observed in BESOI material as well as SIMOX. SFs in very thin films are believed to be pinned at the two interfaces. This was attributed to an increase in the energy of the two partial dislocations bounding the SFs, and has consequences for device fabrication. High temperature oxidation should be avoided when films of less than 500 Å are required. Nucleation of SFs in SIMOX was investigated through a study of bulk silicon samples implanted with low doses of oxygen. It was shown that precipitation of implanted oxygen atoms took place during high temperature anneals leading to a high density of SFs. This would explain the presence of SFs in SIMOX films where a low dose of oxygen remains in the film after implantation. During the ramp down of the 1320°C Ar anneal, implanted oxygen atoms in the SIMOX overlayer precipitate, contributing to the emission of dislocation loops and the creation of SFs.

Acknowledgments

The authors would like to acknowledge Philips Research for funding this study. The University of Surrey, LETI/SOITEC and Queen's University Belfast are also acknowledged, respectively, for implanting bulk wafers with low oxygen dose, supplying standard SIMOX wafers, and polishing BESOI wafers. Prof. B.K.P. Scaife is gratefully acknowledged for his helpful suggestions.

References

- [1] R. Sanders and P.S. Dobson, *Phil. Mag.*, **20**, 881 (1969).
- [2] J.P. Colinge, *IEEE Electron Devices Lett.*, **9**, 91 (1988).
- [3] G.C.M. Silvestre, R.A. Moore, A. Garcia, and B. Aspar, *Proc. 1994 EMRS Spring Meet., 24-27 May, 1994, Strasbourg, France*, Elsevier Science, **50**, 24 (1995).
- [4] F. Secco d'Aragona, *J. Electrochem. Soc.*, **119**, 948 (1972).
- [5] J.M. Lamure, B. Biasse, C. Jaussaud, A.M. Papon, J.F. Papon, J.F. Michaud, F. Gusella, C. Pudda, A.M. Cartier, A. Soubie, and J. Margail, *Proc. 1990 IEEE SOS/SOI Technology Conf., 2-4 Oct., 1990, Key West, FL*, IEEE, NJ, 45 (1990).
- [6] M. Wright Jenkins, *J. Electrochem. Soc.*, **124**, 757, (1977).
- [7] S.P. Murarka and G. Quintana, *J. Appl. Phys.*, **48**, 46, (1977).
- [8] N. Guillemot, D. Tsoukalas, C. Tsamis, J. Margail, A.M. Papon, and J. Stoemenos, *J. Appl. Phys.*, **71**, 1713, (1992).
- [9] S.M. Hu, *J. Appl. Phys.*, **45**, 1567, (1974).
- [10] S.M. Hu, in *Defects in Semiconductors*, edited by J. Narayan and T.Y. Tan, (North-Holland, New-York, 1981), p. 55.
- [11] L. Claeys, J.G. Declerck, and J. van Overstraeten, *Appl. Phys. Lett.*, **35**, 797, (1979).
- [12] K. Licht and P. Reich, in *Literature Data for Infrared, Raman and N.M.R Spectra of Silicon, Germanium, Tin and Lead Organic Compounds*, Dent. Verlag. Wiss., Berlin, 1971.

EXTRACTION OF ELASTIC PARAMETERS OF HEAVILY BORON-DOPED SILICON LAYER BY ELIMINATION OF MISFIT DISLOCATIONS

HO-JUN LEE*, CHUL-HI HAN, AND CHOONG-KI KIM

Department of Electrical Engineering, Korea Advanced Institute of Science and Technology, Taejeon, Korea.

*also at Semiconductor R/D Laboratory of Hyundai Electronics Industries Co, Ltd, Ichon, Korea.

ABSTRACT

In this paper, various elastic parameters of heavily boron-doped silicon layer have been extracted by eliminating the misfit dislocations in the layer. The dislocation-free silicon membranes doped with the boron concentration of 1.3×10^{20} atoms/cm³ have been fabricated and the Young's modulus of 1.45×10^{12} dyn/cm² and residual tensile stress of 2.7×10^9 dyn/cm² have been extracted by blister method. From the Young's modulus and residual stress, the residual tensile strain of 1.34×10^{-3} , lattice constant of 5.424 Å, and misfit coefficient of 1.03×10^{-23} cm³/atom have been calculated. These parameters are very similar to those obtained from X-ray diffraction analysis and theory.

I. INTRODUCTION

Heavily boron doped (p^+) silicon layers are promising materials in ULSI because the junction leakage current of the electronic device fabricated on silicon wafer is drastically reduced by burying p^+ silicon layer under the surface of the wafer[1,2]. In addition, p^+ silicon layers have been widely used for the fabrication of various micro-mechanical structures due to its excellent etch-stop characteristics against ethylenediamine-pyrocatechol-water mixture(EPW)[3,4]. However, many misfit dislocations are frequently generated in p^+ silicon layers[5] and the elastic characteristics of the layers are screened by the dislocations. To accurately extract the elastic characteristics of a p^+ silicon layer, thus, the misfit dislocations must be eliminated or the density of the dislocation in the layer must be extracted. Recently, we formed misfit dislocation-free p^+ silicon layers[6], which makes extraction of the elastic characteristics of a p^+ silicon layer possible.

In this paper, we will fabricate misfit dislocation-free p^+ silicon membranes and will extract various elastic parameters of the membrane using blister method. It will be known that the extracted values are similar to those obtained from X-ray diffraction(XRD) analysis and theory.

II. SUPPRESSION OF MISFIT DISLOCATION

Misfit dislocations in p^+ silicon layer are generated by the tensile stress in the layer due to the substitutional boron atoms which are smaller than silicon atom[5]. In (001) silicon wafer, the

dislocations show the characteristics of edge dislocations of $[110]$ direction with (001) glide plane and Burgers' vector of $a/2[110]$ [7]. We found that the dislocations in the p^+ silicon layer formed by thermal boron diffusion process on well prepared silicon substrate are originated from the wafer edge and then propagate into the inner area of the wafer by the tensile stress in the layer[6]. Moreover, the dislocations could be suppressed in a p^+ silicon region by surrounding the p^+ region with an undoped region(protection region). This is because the dislocations from wafer edge cannot propagate across the protection region which is stress-free inherently. To suppress the misfit dislocations effectively, the masking material to form the protection region against boron diffusion must be chemical-vapor deposited oxide and the edges of the protection region must be aligned at $[110]$ direction. Large area of dislocation-free p^+ silicon region($2 \times 2 \text{ cm}^2$) doped with boron dose as high as $5.4 \times 10^{16} \text{ atoms/cm}^2$ can be obtained as reported in Ref.[6].

Figure 1 shows the defect-etched surface of the wafer after formation of the p^+ silicon layers. It can be seen that there is no misfit dislocation in the interior p^+ region which is surrounded by the protection region, while there are many misfit dislocations (dark lines) in the exterior p^+ region which is open to the wafer edge.

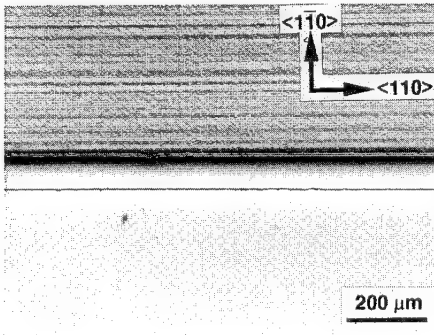


Figure 1. Photomicrograph of the defect-etched surface of the wafer after formation of the p^+ silicon layers. The defect-etching was performed in iodine etchant (125 ml glacial acetic acid, 100 ml HNO_3 (70%), 25 ml HF (49%), 2g I_2).

III. PREPARATION OF p^+ SILICON MEMBRANES

We fabricated two types of p^+ silicon membranes on (001) -orientation Czochralski silicon wafers using conventional substrate etching with EPW solution. One type is the dislocation-free membranes fabricated in the interior p^+ region and the other is the conventional membranes fabricated in the exterior p^+ region which contains many misfit dislocations. The area and thickness of both membranes were measured as $5 \text{ mm} \times 5 \text{ mm}$ and $1.5 \mu\text{m}$, respectively.

Figure 2 shows the boron doping profile of the wafer after formation of the p^+ layer. The etch-stopped surface of the membrane is indicated with the dashed line at the depth of $1.5 \mu\text{m}$ and the

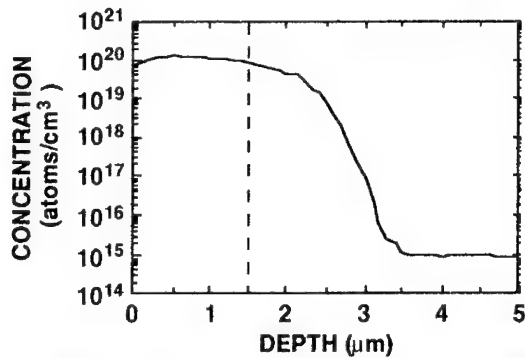


Figure 2. Measured boron doping profile of the wafer by spreading resistance profile analysis. The left region of the dashed line becomes the membrane.

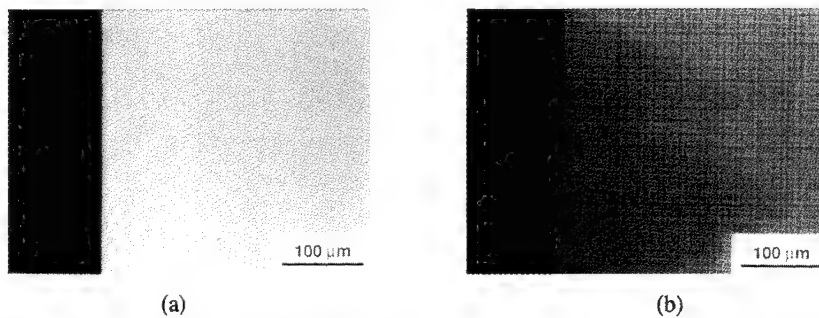


Figure 3. Photomicrographs of the fabricated membranes obtained by back-illuminated optical microscope. (a) is the dislocation-free membrane and (b) is the conventional membrane. The dark regions in the photomicrographs are surrounding bulk silicon.

boron concentration at the depth is about 7×10^{19} atoms/cm³ which is general boron concentration for the etch-stop in EPW solution. From the profile, the average boron concentration of the membranes was estimated as 1.3×10^{20} atoms/cm³ which will be treated as an important parameter throughout this study.

Figure 3 shows the photomicrographs of the fabricated membranes. There are many textile patterns in the conventional membrane but none in the dislocation-free membrane. These patterns are due to the large roughness of the etch-stopped surface originated from misfit dislocations.

IV. EXTRACTION OF ELASTIC PARAMETERS OF p⁺ SILICON LAYERS

Young's moduli and residual stresses

The fabricated membranes without pin holes, hillocks, and flaws were carefully selected by inspection with optical microscope and the selected twenty samples for each type of membrane were mechanically tested using blister method.

Figure 4 shows typical load-deflection curves of the membranes obtained by blister method. For the extraction of Young's moduli and residual stresses of the membranes, the measured curves were fitted to Tabata's model[8] for Poisson's ratio of silicon $\nu = 0.28$ [9]. The results from this analysis are like following: Average Young's moduli are 1.45×10^{12} dyn/cm² for both membranes; average residual stresses (tensile) are 2.7×10^9 dyn/cm² for the dislocation-free membrane and 9.3×10^8 dyn/cm² for the conventional membrane. It can be known that the residual tensile stress of p⁺ silicon membrane is decreased by the insertion of extra-half planes accompanying misfit dislocations.

Note that the extracted values are averaged for the depth and area of the membrane as well as for the twenty samples for each type, where the average boron concentration of the membrane is 1.3×10^{20} atoms/cm³.

Residual strains

The average residual strains of the membranes are directly calculated as $\epsilon_A = 1.34 \times 10^{-3}$ for the dislocation-free membrane and $\epsilon_B = 0.46 \times 10^{-3}$ for the conventional membrane by [10]

$$\epsilon = \sigma_0(1-\nu)/Y \quad (1)$$

where σ_0 and Y are the residual stress and Young's modulus of the membrane, respectively.

Lattice constants

In-plane lattice constant a_A of the dislocation-free membrane is the same as that of the substrate, thus, the lattice constant a_i of the strain-free p⁺ silicon membrane is calculated as 5.424 Å by [10]

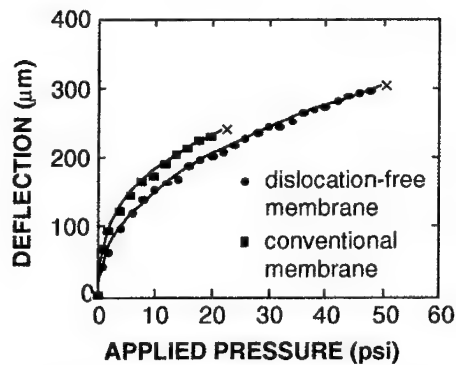


Figure 4. Measured load-deflection curves of the membranes using blister method.

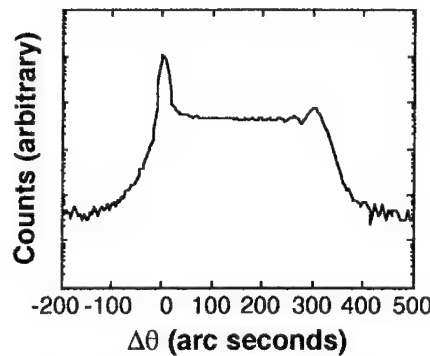


Figure 5. Measured X-ray rocking curve of the interior region.

$$\epsilon_A = (a_A - a_i)/a_i \quad (2)$$

where $a_A = 5.431 \text{ \AA}$. Similarly, in-plane lattice constant a_B of the conventional membrane is calculated as 5.426 \AA by replacing ϵ_A and a_A in Eq. (2) with ϵ_B and a_B , respectively.

Densities of misfit dislocation

The strain difference between the dislocation-free membrane and conventional membrane is caused by the insertion of the extra-half planes accompanying the misfit dislocations. Thus, the density of the extra-half plane or misfit dislocation across $\langle 110 \rangle$ or $\langle \bar{1}10 \rangle$ plane in the conventional membrane is calculated as $2.3 \times 10^4/\text{cm}$ by [11]

$$N = (\epsilon_A - \epsilon_B)/b \quad (3)$$

where the magnitude of Burgers' vector of the misfit dislocation in the p^+ silicon layer on (001) silicon wafer $b = 3.840 \text{ \AA}$ [12]. Also, the maximum density of misfit dislocation when the p^+ silicon membranes are stress-free can be calculated as $3.5 \times 10^4/\text{cm}$ by putting $\epsilon_B = 0$ in Eq. (3).

Misfit coefficient

Misfit coefficient β_o means the strain of a doped layer induced by one substitutional atom. Thus, the β_o of boron-doped layer is directly calculated as $1.03 \times 10^{-23} \text{ cm}^3/\text{atom}$ by

$$\beta_o = \epsilon_A/N_B \quad (4)$$

where the average boron concentration of the membrane $N_B = 1.3 \times 10^{20} \text{ atoms/cm}^3$.

The obtained β_o is very similar to the theoretical value of $1.15 \times 10^{-23} \text{ cm}^3/\text{atom}$ calculated from the volumetric model of [13]

$$\beta_o = \left[1 - \left(\frac{r_B}{r_{Si}} \right)^3 \right] N_{Si}^{-1} \quad (5)$$

where the density of silicon $N_{Si} = 5.0 \times 10^{22} \text{ atoms/cm}^3$, the radius of silicon atom $r_{Si} = 1.17 \text{ \AA}$, and the radius of boron atom $r_B = 0.88 \text{ \AA}$ [14].

XRD analysis

Figure 5 shows the (400) rocking curve for the interior p^+ region obtained by a double crystal X-ray diffractometer using $\text{CuK}\alpha_1$ radiation. The main peak (at $\Delta\theta = 0$) is due to the substrate and the satellite peak (at $\Delta\theta = 300$ arc seconds) due to the p^+ silicon layer. Using general elastic and XRD theory [10, 15], the peak separation of 300 arc seconds gives the strain of 1.35×10^{-3} of the p^+ silicon layer which is nearly the same as $\epsilon_A (= 1.34 \times 10^{-4})$ obtained by blister method.

V. CONCLUSION

By eliminating the misfit dislocations in the p^+ silicon layer, various elastic parameters of the layer similar to the theory have been extracted using blister method and XRD analysis. It is expected that the extracted elastic parameters can be utilized in various field, especially in the study on ULSI and micro-machining.

REFERENCES

1. J. W. Slotboom, M. J. J. Theunissen, and A. J. R. de Kock, *IEEE Electron Devices Lett.* **4**, 403 (1983).
2. G. A. Rozgonyi and R. R. Kola, in Defect Control in Semiconductors, edited by K. Sumino (Elsevier Science Publishers B. V, North-Holland, 1990), p. 579.
3. E. Bassous and E. F. Baran, *J. Electrochem. Soc.* **125**, 1321 (1978).
4. See, e.g., K. E. Petersen, A. Shartel, and N. Raley, *IEEE Trans. Electron Devices* **29**, 23 (1982).
5. H. J. Queisser, *J. Appl. Phys.* **32**, 1776 (1961).
6. H. J. Lee, Y. J. Jeon, C. H. Han, and C. K. Kim, *Appl. Phys. Lett.* **64**, 2955 (1994).
7. C. H. Schwuttke and H. J. Queisser, *J. Appl. Phys.* **33**, 1540 (1962).
8. O. Tabata, K. Kawahata, S. Sugiyama, and I. Igarashi, Micro Electro Mechanical Systems : An Investigation of Micro Structures, Sensors, Actuators, Mechanics, and Robots, IEEE, 152 (1989).
9. See, e.g., Properties of Silicon, edited by T. H. Ning and C. Hilsum (INSPEC, New York, 1988), p. 654.
10. W. R. Nix, *Metall. Trans. A*, **20A**, 2217 (1989).
11. E. A. Fitzgerald, *Materials Science Reports*, **7**, 87 (1991).
12. J. Washburn, G. Thomas, and H. J. Queisser, *J. Appl. Phys.* **35**, 1909 (1964).
13. S. Prussin, *J. Appl. Phys.* **32**, 1876 (1961).
14. H.-J. Herzog, L. Csepregi, and H. Seidel, *J. Electrochem. Soc.* **131**, 2969 (1984).
15. B. D. Cullity, Elements of X-Ray Diffraction, 2nd ed. (Addison Wesley, London, 1978), p. 351.

EFFICIENT NONRADIATIVE RECOMBINATION CENTERS IN MBE-GROWN Si AND SiGe/Si HETEROSTRUCTURES

W.M. Chen, I.A. Buyanova, A. Henry, W.-X. Ni, G.V. Hansson and B. Monemar
Department of Physics and Measurement Technology, Linköping University, S-581 83
Linköping, SWEDEN.

ABSTRACT

We carry out an investigation of grown-in nonradiative defects in Si and SiGe/Si heterostructures grown by molecular-beam-epitaxy (MBE). A number of such defects are observed by the optical detection of magnetic resonance (ODMR) technique, in samples with various structures and growth conditions. These defects are shown to provide efficient nonradiative shunt paths for carrier recombination, competing with and reducing radiative recombination processes. It is revealed that the dominant nonradiative defect is a low-symmetry vacancy-related complex, evident from a characteristic hyperfine structure due to ^{29}Si ligands (with nuclear spin $I=1/2$ and natural abundance of 4.67 %) connected to the dangling bonds. The introduction of these defects is believed to be largely due to a low surface adatom mobility during the low temperature growth. By varying the substrate bias during the MBE growth, it is shown that the formation of these nonradiative defects can be effectively enhanced by exposure to accelerated positive ions, presumably dominated by the Si^+ ions. Effects of hydrogenation on these defects are also studied.

INTRODUCTION

Optical and optoelectronic devices are among the most intriguing possibilities in applications of Si and SiGe/Si heterostructures, with the ultimate goal of integrating both optical and electronic devices based on the well-developed and mature Si technology. Recent rapid advances in modern epitaxial growth techniques have made feasible to achieve high quality SiGe/Si heterostructures, which exhibit well-resolved excitonic emissions near the band edge from materials grown by both MBE and rapid thermal chemical vapor deposition (RTCVD) [1, 2]. These successes have greatly stimulated a step-up in search for efficient Si-based light detectors and emitters. Much effort has been directed to improve the quantum efficiency of this indirect bandgap material system by exploring either bandgap engineering such as the zone-folding effects [3] or defect engineering by introducing light-emitting impurities such as Er in the materials [4]. Very little is known, however, about nonradiative centers. Among them are the lifetime limiting defects which are predominantly nonradiative in this indirect bandgap semiconductor system. These nonradiative centers provide efficient shunt paths for carrier recombination, competing with radiative recombination processes and thus reducing the light emitting efficiency of the material. These important nonradiative defects, which will to a large extent play a key role in determining the success of Si and SiGe/Si layered structures for potential applications in Si-based optoelectronics, have so far largely eluded from studies by various optical spectroscopies. This has resulted in a general lack of knowledge about the electronic and chemical structure of nonradiative defects in Si thin layers and SiGe/Si heterostructures.

The aim of this work is to carry out a detailed investigation of nonradiative defects in Si epilayers and SiGe/Si heterostructures grown by MBE. Both undoped and modulation doped structures, grown under various conditions by e.g. varying the substrate bias, have been studied. A number of nonradiative defects are observed, by the ODMR technique. These defects are shown to provide efficient channels for carrier recombination and, to a great degree, control the carrier lifetime.

The access to these nonradiative defects by ODMR is facilitated by competing carrier recombination processes between radiative and nonradiative defects as shown in Fig.1, where a magnetic-resonance enhanced recombination via nonradiative channels leads to a corresponding

COMPETING CARRIER RECOMBINATION PROCESSES

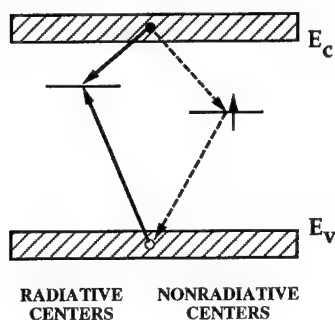


Fig.1 A schematic picture illustrating the competing carrier recombination processes between radiative and nonradiative channels.

reduced radiative recombination monitored by photoluminescence (PL) in the ODMR experiments [5]. This results in a decrease in PL intensity, or equivalently a negative ODMR signal. Previous ODMR studies in SiGe/Si structures have, to our knowledge, been mainly limited to radiative centers in SiGe/Si strained superlattices [6] where the observation of a dangling-bond-like negative ODMR signal was briefly mentioned [6].

EXPERIMENTAL

The samples studied in this work include both undoped and boron δ -doped thin Si epilayers and SiGe/Si heterostructures, grown on (100) Si substrate by MBE with a Balzers UMS 630 Si-MBE system. The undoped Si samples consist of a 1000 Å undoped Si buffer layer, followed by a 2000 Å undoped Si layer. The B-doped Si samples consist of a 1000 Å undoped Si buffer layer, followed by three periods of boron δ -doping spikes ($1 \times 10^{13} \text{ cm}^{-2}$) separated by 1000 Å undoped Si spaces. The growth temperature is typically $\sim 420^\circ\text{C}$, and the growth rate is 1-2 Å/sec. The undoped SiGe/Si quantum well (QW) structure studied in this work was grown at 620°C , with a 32 Å-wide $\text{Si}_{0.8}\text{Ge}_{0.2}$ QW. All the structures were finally capped by a 1000 Å undoped Si layer.

In the PL experiments, the samples were excited by the UV multilines (333.6 - 363.8 nm) or the 514.5 nm line of an Ar^+ laser. The resulting PL was first dispersed by a double grating monochromator and collected by a cooled Ge detector, and was then detected with lock-in techniques in phase with the modulation of the excitation laser light. The ODMR experiments were performed at the X-band (9.23 GHz) using a modified Bruker ER-200D ESR spectrometer, equipped with a TE_{011} microwave cavity with optical access in all directions. The PL emission from the samples under the illumination of the UV laser light was monitored by a cooled Ge detector. The ODMR signal was obtained by detecting a synchronous change in the PL with the field modulation of the magnetic field, corresponding to a change in the PL intensity with or without the applied microwave field. A derivative lineshape of the ODMR is observed in this case when the magnetic field is modulated on and off the spin resonance conditions.

RESULTS AND DISCUSSION

In Fig.2 we show the low temperature PL spectra obtained from the Si and SiGe/Si structures studied in this work. They typically consist of near bandgap sharp PL lines at an

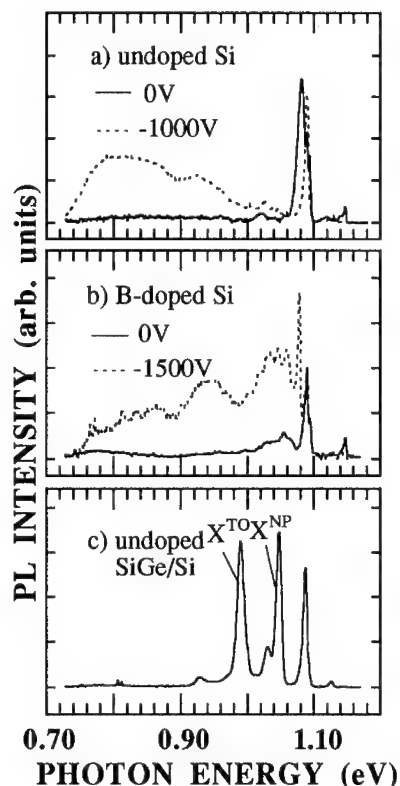


Fig.2 a) PL spectra obtained at 2K from the undoped Si epilayers grown with zero bias (solid curve) and negative bias (dashed curve). b) PL spectra obtained at 2K from the B-doped Si epilayers grown with zero bias (solid curve) and negative bias (dashed curve). c) PL spectrum obtained at 2K from undoped 32-Å $\text{Si}_{0.8}\text{Ge}_{0.2}/\text{Si}$ QW grown with zero bias. X^{NP} and X^{TO} denote the excitonic emissions from the QW.

energy higher than 1.08 eV and many broad, featureless PL bands at lower photon energy. The sharp line structure near the bandedge includes the free exciton, shallow bound excitons and sometimes electron-hole droplets. These PL emissions are mostly contributed by the substrates, and will therefore not be considered in this work. The broad bands, on the other hand, are known to originate from the MBE-layers. The presence of a specific type of the broad bands has been shown to be critically dependent on the growth conditions (e.g. the substrate bias) and the sample structures (e.g. B doping or alloy) [7]. Even within one specific sample, the broad bands over a wide spectral range (0.7-1.03 eV) have been shown to arise from at least two different defects. These broad PL bands are not related to the nonradiative defects studied in this work, as will be shown below, and will therefore not

be discussed further in the paper. A detailed study of these broad PL bands is described elsewhere [7].

By monitoring these broad PL bands over a wide spectral range, between 0.7 eV and 1.03 eV, ODMR spectra can clearly be observed as shown in Fig.3 for various samples studied. The negative ODMR signals correspond to a decrease in the PL intensity of various PL bands over the entire spectral range monitored under the spin resonance conditions. The fact that the ODMR can be detected via monitoring any broad PL band of different origin, together with the negative sign of the ODMR signal, has been taken as a signature that none of the radiative centers giving rise to the PL bands is directly involved in the spin resonance [5]. Rather, it has indicated that nonradiative defects of entirely different origin are responsible for the spin resonance. The competing processes in carrier recombination have in this case provided the link between the nonradiative defects participating in the spin resonance and the radiative ones giving rise to the broad PL bands. The spin-resonance-induced enhancement in carrier recombination via the nonradiative defects alters the overall recombination rate, if they are among the dominant recombination centers, leading to a corresponding and noticeable reduction in the radiative recombination monitored by the broad PL bands (see Fig.1).

There are a few remarkable features of the ODMR spectra which deserve attention. Firstly, stronger ODMR signals are observed from the samples grown with negative bias as compared to that grown with zero bias, easily seen from a much better signal-to-noise ratio of the curves b and d than that of the curve a and c in Fig.3. This observation can be attributed to

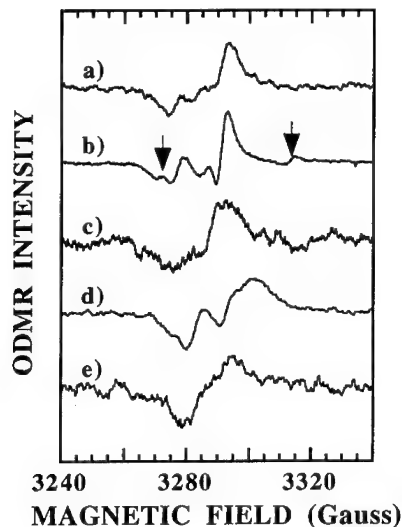


Fig.3 a)-b) The ODMR spectra obtained from the undoped Si epilayers grown with a) zero bias and b) negative bias (-1000 V), at a microwave frequency $f_{MW} = 9.2228$ GHz and $f_{MW} = 9.2232$ GHz, respectively. The ODMR signals related to the shallow P-donors are indicated by the arrows in curve b. c)-d) The ODMR spectra obtained from the B-doped Si epilayers grown with c) zero bias and d) negative bias (-1500 V), at a microwave frequency $f_{MW} = 9.2232$ GHz and $f_{MW} = 9.2292$ GHz, respectively. e) The ODMR spectrum obtained from the undoped 32-Å $\text{Si}_{0.8}\text{Ge}_{0.2}/\text{Si}$ QW grown with zero bias, at a microwave frequency $f_{MW} = 9.2366$ GHz.

stronger PL emissions monitored or/and an increased concentration of the nonradiative defects in the samples grown with negative bias. The appearance of the shallow P-donor ODMR in the undoped samples grown with negative bias (curve b in Fig.3), but not in the undoped samples grown with zero bias (curve a in Fig.3) though a similar P contamination is expected to occur, provides evidence that the concentration of the nonradiative defects is indeed higher in these samples. This is based on the facts that the participation of the shallow P-donors in carrier recombination is determined by the efficiency of charge transfer between the P-donors and the deep recombination centers [8]. The efficiency of the charge transfer is determined by the overlap of wavefunctions between the participating centers, which is a sensitive function of the concentration of the centers. An increase of the defect concentration in the samples grown with negative bias can be explained as being due to effects of ion bombardment. The results from the samples grown with positive bias resemble that from the samples grown with zero bias, suggesting that the positive ions such as Si^+ play a major role in the damage induced by ion bombardment.

Secondly, the ODMR signals are considerably broadened in the B-doped samples as compared to the undoped samples. The reason for this can be twofold, i.e. either different defects are created as a consequence of the B-doping or the same defects are perturbed by a distribution of a possible electric field and perhaps even a local strain field induced by the B-doping.

Thirdly, the ODMR spectrum obtained from the undoped SiGe/Si QW structures (curve e in Fig.3) resembles that from the undoped Si layers (curve a in Fig.3). In fact the intensity of this ODMR signal is stronger when the weak deeper broad PL background below 0.9 eV (Fig.2c) is detected as compared to the situation when the QW excitonic emissions (X^{NP} and X^{TO}) are monitored. This can be attributed to a more efficient recombination of the QW excitons or/and to the fact that the nonradiative defects inducing the ODMR signal are located in the Si layers of the structures. The presence of nonradiative defects even in the high-quality structures available demands that additional measures should be undertaken in order to bringing these nonradiative defects under control, leading to further improvements in the luminescence efficiency.

To obtain more detailed information on the electronic structure and chemical identity of the defects, we have carried out a careful angular dependence study of the ODMR signals. As an example, we show in Fig.4 the ODMR spectra from the undoped Si sample grown with negative bias when the external magnetic field is along three main crystallographic axes. The spectra contain three contributions. One of them, denoted as ^{31}P , is the ODMR related to the shallow P-

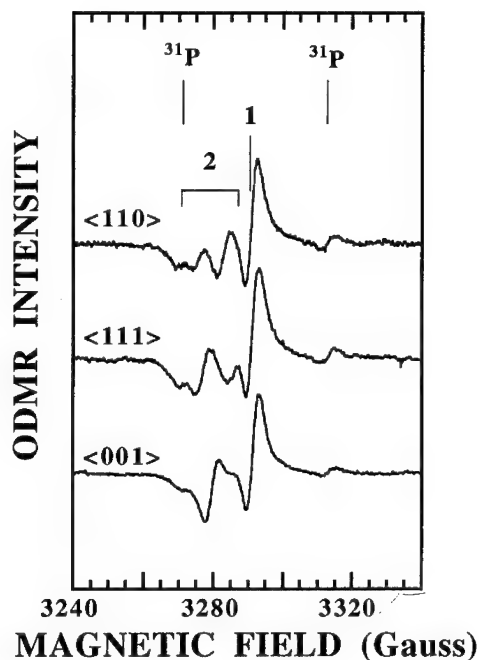


Fig.4 The ODMR spectra obtained from the undoped Si epilayers grown with negative bias (~ 1000 V), when the magnetic field is along three main crystallographic axes. Three types of defects are clearly seen.

donors, which participate in carrier recombination via a charge transfer process [8]. The doublet hyperfine structure from the ^{31}P atom (with nuclear spin $I=1/2$ and 100% natural abundance) is clearly resolved and is considered as an unambiguous proof of the P involvement. The presence of the P impurities in this materials is believed to be due to contamination by the stainless steel chamber during the growth. The background P concentration is in the order of 10^{15} – 10^{16} cm^{-3} , close to that required for an efficient charge transfer. The slightly anisotropic ODMR signal denoted as "1" in Fig.4 originates from a low-symmetry vacancy-related defect, evident from the characteristic hyperfine satellites from the ^{29}Si ligands ($I=1/2$ and natural abundance

of 4.67 %) connected to the dangling bonds. These satellites are observed over a larger magnetic-field range, not shown here. The apparently anisotropic ODMR signals marked as "2" in Fig.4 are due to another low-symmetry defect. No hyperfine structure which can lead to a positive identification of the defect can be observed, unfortunately. A detailed analysis of the full angular dependence of the ODMR signals from various samples is now in progress.

Effects of post-growth hydrogen treatments on these nonradiative defects have also been studied. It is shown that some of these defects can be passivated by hydrogen. There are, however, still some nonradiative defects remaining in the structures which can not be passivated. This observation is not surprising, though, since the hydrogenation of e.g. shallow acceptors in Si is known to be rather complete [9] whereas its effects on deep defects such as vacancy-related defects are incomplete [10].

The fact that these defects are readily present in samples grown without substrate bias (Fig.3a and 3c), thus without severe ion bombardment, is believed to be due to a low surface adatom mobility during the low temperature growth. The low temperature growth is, on the other hand, required to maintain a well-defined doping profile and to obtain a pseudomorphical growth of the strained SiGe/Si heterostructures.

SUMMARY

We have revealed nonradiative grown-in defects in MBE-grown Si and SiGe/Si, which play an important role in carrier recombination. These defects are shown to be deep level centers with a low symmetry, such as vacancy-related defects. In some circumstances shallow P impurities also provide efficient nonradiative shunt paths for carrier recombination when charge transfer is involved. The defects are introduced as the consequence of low temperature growth

or/and ion bombardment. Continuing efforts on a better understanding of physical properties and formation mechanisms of these defects will eventually lead to a control and ultimately elimination of these unwanted nonradiative defects and to a highly desired improvement in quantum efficiency of optoelectronic devices based on Si and SiGe.

REFERENCES

1. J.-P. Noël, N.L. Rowell, D.C. Houghton, A. Wang and D.D. Perovic, *Appl. Phys. Lett.* **61**, 690 (1992).
2. J.C. Sturm, H. Manohran, L.C. Lenchyshyn, M.L.W. Thewalt, N.L. Rowell, J.-P. Noël and D.C. Houghton, *Phys. Rev. Lett.* **66**, 1362 (1991).
3. K.B. Wong, M. Jaros, I. Morrison and J.P. Hagon, *Phys. Rev. Lett.* **60**, 2221 (1988).
4. J. Michel, F.Y.G. Ren, B. Zheng, D.C. Jacobson, J.M. Poate and L.C. Kimerling, *Mat. Sci. Forum* **143**, 707 (1994).
5. W.M. Chen and B. Monemar, *Appl. Phys.* **A53**, 130-135 (1991).
6. E. Glaser, J.M. Trombetta, T.A. Kennedy, S.M. Prokes, O.J. Glembocki, K.L. Wang and C.H. Chern, *Phys. Rev. Lett.* **65**, 1247 (1990); E. Glaser, T.A. Kennedy, D.J. Dodbey, P.E. Thompson, K.L. Wang and C.H. Chern, *Phys. Rev.* **B47**, 1305 (1993).
7. I.A. Buyanova, A. Henry, W.M. Chen, W.X. Ni, G.V. Hansson and B. Monemar, this proceedings.
8. W.M. Chen, B. Monemar, E. Janzén and J.L. Lindström, *Phys. Rev. Lett.* **67**, 1914 (1991).
9. For a review, see, e.g., S.M. Myers, M.I. Baskes, H.K. Birnbaum, J.W. Corbett, G.F. DeLeo, S.K. Estreicher, E.E. Haller, P. Jena, N.M. Johnson, R. Kirchheim, S.J. Pearton and M.J. Stavola, *Rev. Mod. Phys.* **64**, 559 (1992).
10. W.M. Chen, O.O. Awadelkarim, B. Monemar, J.L. Lindström and G.S. Oehrlein, *Phys. Rev. Lett.* **64**, 3042 (1990).

DEFECT-ENGINEERED GRADED $\text{Ge}_x\text{Si}_{1-x}$ BUFFERS ON Si (001) WITH EXTREME LOW THREADING DISLOCATION DENSITY

G. KISSINGER, T. MORGENSTERN, G. MORGENSTERN, H. B. ERZGRÄBER,
AND H. RICHTER
Institut für Halbleiterphysik Frankfurt (Oder) GmbH, Walter-Korsing-Str.2,
D-15230 Frankfurt (Oder), Germany

ABSTRACT

Stepwise equilibrated graded $\text{Ge}_x\text{Si}_{1-x}$ ($x \leq 0.2$) buffers with threading dislocation densities between 10^2 and 10^3 cm^{-2} on the whole area of 4 inch silicon wafers were grown and studied by transmission electron microscopy, defect etching, atomic force microscopy and photoluminescence spectroscopy.

INTRODUCTION

Strain-relaxed compositionally graded buffers provide a possibility to adjust the lattice constant of a Si or Ge substrate wafer to any value between these two elements thus forming a "virtual $\text{Ge}_x\text{Si}_{1-x}$ substrate". Such buffers have to be grown with steadily or step-wise increasing Ge concentration on Si-substrates or vice versa on Ge-substrates. The major problem of these totally relaxed heterostructures are threading dislocations arising from the lattice mismatch of 4.2% in the Si-Ge system because strained $\text{Ge}_x\text{Si}_{1-x}$ layers exceeding the x-dependent critical layer thickness relax their stress via formation of misfit dislocations. Their glissile threading parts intersecting the surface are detrimental to transport properties in modulation-doped structures¹. Usually, such buffers are some μm thick since the threading dislocation density is decreasing with decreasing compositional grading². In this way threading dislocation densities between 4.4×10^5 and $1.7 \times 10^6 \text{ cm}^{-2}$ have been obtained in totally relaxed alloy layers with 23 to 50% Ge³⁻⁶. However, threading dislocation densities in the order 10^4 cm^{-2} have been obtained with far steeper compositional grading using a modified Frank-Read source mechanism^{1,7-9}.

Until now all methods to grow unstrained $\text{Ge}_x\text{Si}_{1-x}$ buffers operate without adjustment of equilibrium conditions for stress relaxation. In this contribution a new stepwise equilibrated graded buffer on Si is presented with threading dislocation densities in the 10^2 to 10^3 cm^{-2} range. This buffer was grown stepwise with a layer by layer increasing Ge concentration. After each layer the growth process was stopped in order to achieve a nearly complete stress relaxation during an in-situ annealing¹⁰. This equilibration process requires an appropriate long annealing period¹¹ and temperatures $\geq 1000 \text{ }^\circ\text{C}$ in order to explore the drastically enhanced relaxation velocity in this temperature range assisted by interdiffusion

12,13. In this way each layer of the buffer was grown on a relaxed alloy layer. A more detailed description of the buffer concept is given in Ref. 14.

EXPERIMENTAL

The stepwise equilibrated graded buffers were grown on 4 inch p-type FZ (001) silicon wafers with a resistivity of 6-8 Ωcm using atmospheric pressure chemical vapour deposition (APCVD). The following layer sequence was deposited:

250nm $\text{Ge}_{0.05}\text{Si}_{0.95}$ + 100nm $\text{Ge}_{0.1}\text{Si}_{0.9}$ + 100nm $\text{Ge}_{0.15}\text{Si}_{0.85}$ + 150nm $\text{Ge}_{0.2}\text{Si}_{0.8}$.

Each and every layer deposition was followed by an in-situ annealing in hydrogen. Temperature and time of the equilibration annealings are given in Tab. 1. All

Tab. 1. Experimental conditions of the equilibration annealings

wafer number	annealing time (h)	temperature ($^{\circ}\text{C}$)
A	-	-
B	0.25	1050
C	0.50	1050
D	0.75	1050
E	1.00	1050
F	1.00	1095

buffers were capped with a 300 nm $\text{Ge}_{0.2}\text{Si}_{0.8}$ layer.

Transmission electron microscopy (TEM) was used to study the defects in the buffer layers. Profiles of the Ge concentration in the buffer were obtained by energy dispersive x-ray spectrometry (EDXS) at cross-sectional samples in the transmission electron microscop.

Owing to the extremely low defect density of threading dislocations in the buffers their density was counted by

interference phase contrast microscopy after etching the surface with a diluted Yang-etchant ¹⁵. These counts were performed every 5mm across the whole wafer diameter.

Atomic force microscopy (AFM) was used to examine the surface morphology. Photoluminescence (PL) spectra of the samples were taken at 4.2 K using the 488 nm line of a 6 W CW argon ion laser. The samples for the PL studies were choosen from the central parts of the wafers.

RESULTS AND DISCUSSION

Fig. 1 shows the defect density distribution across the whole wafer diameter. It is clearly visible that without equilibration annealings the threading dislocation density amounts to 10^6 cm^{-2} on the whole wafer area. The curves of wafers A-E demonstrate the time dependence of the effect of the equilibrating heat treatments at 1050 $^{\circ}\text{C}$ on the threading dislocation density. It becomes evident that extended periods of annealing are necessary to equilibrate the strained layers. During the first 15 min of annealing the dislocation nucleation at the wafer edge as well as heavy gliding are still in progress resulting in high densities of threading dislocations especially on the edge area. The high defect density in the central part

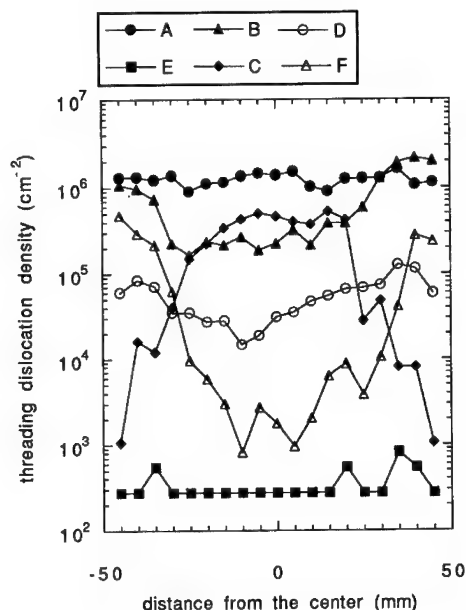


Fig. 1. Threading dislocation density in the cap layer on a stepwise equilibrated graded buffer in dependence on the distance from the wafer center for wafers A-F



Fig. 2. Cross-sectional TEM micrograph of a stepwise equilibrated graded buffer (wafer E)

grown layer almost free of threading dislocations exists.

The depth profile of the Ge concentration obtained by EDXS is given in Fig. 3. It bears a great resemblance to continuously graded buffers and confirms the smoothing of the step profile by interdiffusion.

of the wafer after 0.5 h of annealing indicates that meanwhile the nucleation at the edge was drastically decreased and many of the last nucleated slowly gliding dislocations have just reached the center of the wafer. Their further movement to the opposite edge is clearly seen in the curve of wafer D showing a decrease of the threading dislocation density and some higher values near the edge. Finally, the relaxation process seems to be almost finished after 1 h of annealing. This is the minimum period for equilibration annealings in order to reach really low densities of threading dislocations under these experimental conditions. Wafer F was annealed at 1095 °C also for 1h but its threading dislocation density is higher in the center and much higher on the edge region. This increased threading dislocation density results from dislocations formed in the silicon substrate due to thermal stress caused by the ring-shaped wafer rest of the heater.

They easily form glissile threading dislocations in the buffer. Therefore, the maximum temperature of the equilibration annealings is limited by this unintentional dislocation generation.

Fig. 2 shows a cross-sectional TEM micrograph of the dislocation network in the buffer. The misfit dislocations are arranged in different planes. They are connected via a lot of dislocations thus forming a spatial network that ends abruptly in a depth of about 460 nm below the surface. Above it a perfectly

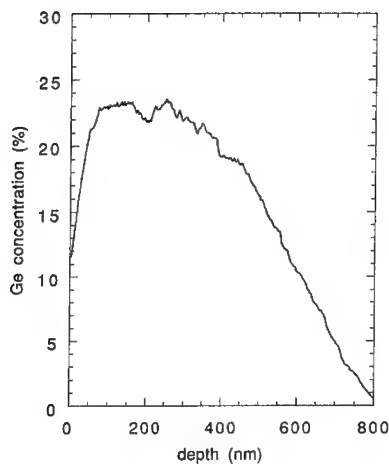


Fig. 3. Depth profile of the Ge concentration in the stepwise equilibrated graded buffer of wafer E obtained by EDXS

Regarding the Ge concentration in the cap layer determined by EDXS the measurement of the lattice constant perpendicular to the surface by x-ray diffractometry resulted in a relaxation degree of 100 %.

Buffers grown with equilibration annealings at such high temperatures possess a high thermal stability during further processing in comparison to buffers grown at lower temperatures.

Fig. 4 shows the photoluminescence spectra of the central parts of wafers A-F. They are arranged according to their threading dislocation density that decreases from top to bottom. It is evident from the right figure that the PL intensities of the D3 and D4 lines decrease with decreasing threading dislocation density. The PL spectrum of sample E with the lowest threading dislocation density of about $2 \times 10^2 \text{ cm}^{-2}$ possesses only a weak indication of the D3 line.

Additional measurements of the D-line intensities on the edge and the center of

wafers C and F with decreasing and increasing threading dislocation densities from center to edge, respectively, have confirmed the dependence of the D3 intensity on the threading dislocation density. These results obtained on different positions of the same wafer exclude that impurity/dislocation interactions are the main reason of the D-line modification as it could be possible in case of different impurity contamination¹⁶. Therefore, it is supposed that the D3 and D4 peaks are characteristic for the existence of threading dislocations in the $\text{Ge}_x\text{Si}_{1-x}$ buffer layers. These results correspond with the recently published observations in Ref. 17.

In sample A, grown without equilibration annealings, misfit dislocations are mainly formed in the region near the interface to the silicon substrate and extend also into the silicon substrate. The buffer layer as well as the cap layer are of low quality. Therefore, the electron hole pairs are rapidly lost in the defect rich layers via non-radiative recombination. As a result, the D1 and D2 lines of the deep lying misfit dislocations appear with low intensity and the spectra are dominated by a broad background luminescence.

Additionally, it is seen in Fig. 4 that for longer periods of equilibration annealing at 1050 °C not only the threading dislocation densities and the defect related broad background luminescence are reduced but also the D1 and D2 are found with increased intensity and very clear in the PL spectra. The D1/D2 lines of the samples E and F with the longest periods of equilibration annealing represent the misfit dislocation networks of about 450 and 700 nm thickness, respectively, as

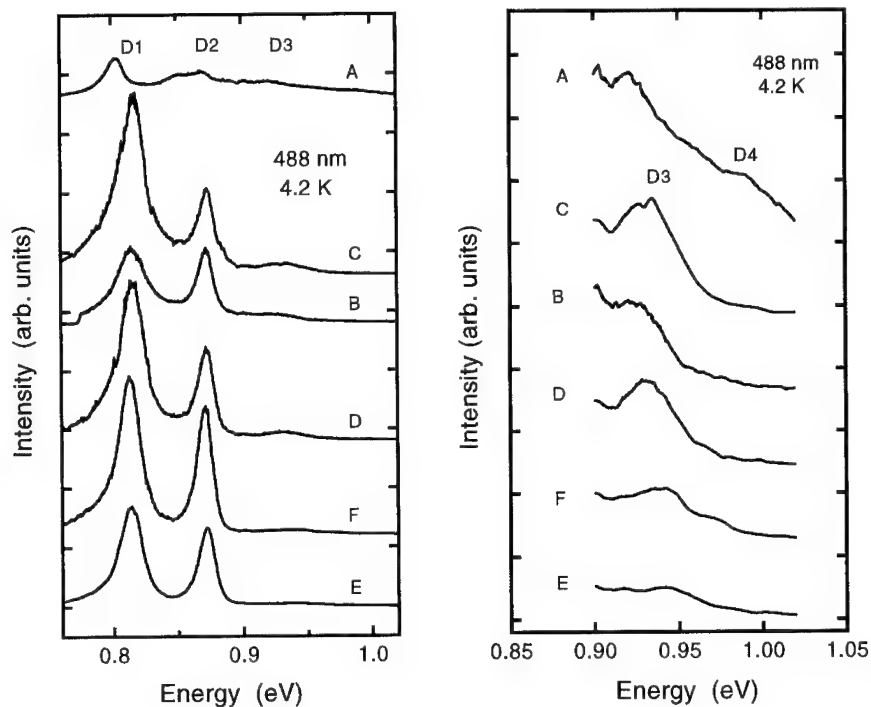


Fig. 4. PL spectra showing the dislocation related luminescence of wafers A-F (left side) with a higher magnification of the energy range from 0.9 to 1.02 eV (right side)

confirmed by TEM observations. These networks are located in the $\text{Ge}_x\text{Si}_{1-x}$ buffer layer below the 450 nm thick nearly defect-free $\text{Ge}_{0.2}\text{Si}_{0.8}$ surface region.

The absence of the characteristic excitonic recombination from the defect-poor cap layer of samples E and F is due to the low growth temperature of only 700 °C; near band-gap luminescence from APCVD grown $\text{Ge}_x\text{Si}_{1-x}$ layers was found to start at growth temperatures above 750 °C.

SUMMARY

It has been shown that equilibration annealings are an effective way to reduce the threading dislocation density in $\text{Ge}_x\text{Si}_{1-x}$ buffer layers down to 10^2 - 10^3 cm^{-2} on the whole area of 4 inch wafers. The threading dislocations were forced to glide out

during high-temperature in situ annealings between the Ge concentration steps. In this way relaxed buffer layers of high thermal stability are attainable. Photoluminescence studies confirm the results of threading dislocation density determination and show a clear dependence of the intensity of the D3 and D4 lines on the threading dislocation density. The results of the characterization of the buffer layers by defect etching, TEM, and photoluminescence agree well with each other.

ACKNOWLEDGEMENT

The authors wish to thank Dr. P. Zaumseil and G. Dominiak for the x-ray measurement, G. Kühnel for technical assistance during layer deposition and B. Knoll and G. Kotsch for sample preparation.

REFERENCES

1. K. Ismail, F. K. LeGoues, K. L. Saenger, M. Arafa, J. O. Chu, P. M. Mooney, and B. S. Meyerson, *Phys. Rev. Lett.* **73**, 3447 (1994).
2. C. G. Tuppen, C. J. Gibbings, and M. Hockley, *Mat. Res. Soc. Proc. Vol.* **220**, 187 (1991).
3. E. A. Fitzgerald, Y.-H. Xie, M. L. Green, D. Brasen, A. R. Kortan, J. Michel, Y.-J. Mii, and B. E. Weir, *Appl. Phys. Lett.* **59**, 811 (1991).
4. J. W. P. Hsu, E. A. Fitzgerald, Y. H. Xie, P. J. Silverman, and M. J. Cardillo, *Appl. Phys. Lett.* **61**, 1293 (1992).
5. Y. H. Xie, E. A. Fitzgerald, D. Monroe, P. J. Silverman, and G. P. Watson, *J. Appl. Phys.* **73**, 8364 (1993).
6. G. P. Watson, E. A. Fitzgerald, Y.-H. Xie, and D. Monroe, *J. Appl. Phys.* **75**, 263 (1994).
7. F. K. LeGoues, B. S. Meyerson, and J. F. Morar, *Phys. Rev. Lett.* **66**, 2903 (1991).
8. K. Ismail, B. S. Meyerson, and P. J. Wang, *Appl. Phys. Lett.* **58**, 2117 (1991).
9. F. K. LeGoues, B. S. Meyerson, J. F. Morar, and P. D. Kirchner, *J. Appl. Phys.* **71**, 4230 (1992).
10. G. Kissinger, T. Morgenstern, G. Morgenstern, and H. Richter, German Patent Application DE-P 44 38 380.0 (27.10.1994).
11. G. Kissinger, G. Morgenstern, and H. Richter, *J. Appl. Phys.* **75**, 4994 (1994).
12. P. Zaumseil, *phys. stat. sol. (a)* **140**, 421 (1993).
13. P. Zaumseil, U. Jagdhold, and D. Krüger, *J. Appl. Phys.* **76**, 2191 (1994).
14. G. Kissinger, T. Morgenstern, G. Morgenstern, and H. Richter, *Appl. Phys. Lett.* to appear 17 April (1995).
15. K. H. Yang, *J. Electrochem. Soc.* **131**, 1140 (1984).
16. W. Staiger, G. Pfeiffer, K. Weronek, A. Höpner, and J. Weber, *Mater. Sci. Forum*, **143-147**, 1571 (1994).
17. H. P. Tang, L. Vescan, C. Dieker, K. Schmidt, H. Lüth, and H. D. Li, *J. Cryst. Growth* **125**, 301 (1992).

DLTS STUDY ON ANNEALED LOW-TEMPERATURE GaAs LAYERS WITH AN N-I(LT)-N STRUCTURE GROWN BY MBE

TSAI-CHENG LIN, HIROMASA T. KAIBE AND TSUGUNORI OKUMURA
Department of Electronics and Information Eng., Tokyo Metropolitan University,
1-1 Minami-ohsawa, Hachiohji, Tokyo 192-03, Japan

ABSTRACT

Deep levels in the annealed low-temperature molecular beam epitaxial (LT-MBE) GaAs layer were successfully characterized by using the capacitance deep-level transient spectroscopy (C-DLTS) as well as photocapacitance quenching technique in combination with a unique sample structure. In this work, we have fabricated the samples by inserting the LT-GaAs layer into two n-type semi-conductive layers, like a sandwich (*n*-LT-*n* structure), grown at normal substrate temperatures. DLTS measurements have revealed that one electron trap dominates the annealed LT-MBE GaAs. The dominant electron trap was very similar to the so-called EL3 level. Moreover, we found the midgap level appeared upon 800-900°C RTA, although no midgap level was detected in the as-grown *n*-LT-*n* sample (annealed at 620°C) and confirmed with photoquenching measurements that it is the EL2 level.

INTRODUCTION

GaAs grown by molecular beam epitaxy (MBE) at substrate temperature as low as 200-300°C, have attracted much attention. As-grown LT-GaAs has been found to contain a number of arsenic antisite defects As_{Ga}, resulting from excess arsenic incorporated in the epitaxial layer during growth¹. These LT-GaAs layers, which become highly resistive after annealing around 600°C², have found several device applications such as semi-insulating buffer materials for metal-semiconductor field-effect transistor (MESFET) structures³ and as materials for ultrahigh-speed photoconductive switches and photodetectors because of its short carrier life-time⁴.

There are two proposed mechanisms by which the annealed LT layer becomes semi-insulating. The compensation model⁵ has emphasized that the deep-level defects could account for the semi-insulating behavior of the annealed LT-GaAs as in the case of bulk semi-insulating (S.I.) liquid encapsulated Czochralski (LEC) GaAs. The buried Schottky barrier model⁶ has proposed that the high resistivity can be understood in terms of the As precipitates acting as internal Schottky barriers with overlapping depletion regions. However, the mechanism for its semi-insulating property is not fully understood yet.

If a metal layer is brought into contact directly with a thin annealed LT-GaAs layer on top of the substrate, the depletion layer reaches through to the substrate because of the semi-insulating nature of the annealed LT-GaAs layer. Therefore, it is difficult to apply conventional capacitance deep-level transient spectroscopy (DLTS) technique to a simple structure with annealed LT-GaAs layers. In this work, we characterized deep levels in the annealed LT-MBE GaAs by using the capacitance DLTS technique in combination with a unique sample structure. We fabricated the samples by inserting the LT-GaAs layer between two n-type semi-conductive layers grown at normal substrate temperatures (*n*-LT-*n* sandwich structure)⁷. The metal Schottky contact is formed on the top n-GaAs layer. When the doping level of the top n-GaAs layer is appropriately selected, the edge of a depletion layer can reach the underlying LT-GaAs layer and cross it upon changing of the applied reverse-bias voltage. This structure, for the first time, made it possible to carry out capacitance DLTS measurements.

EXPERIMENTAL

The samples used in this work were grown in an ULVAC MBC-300 MBE system. The substrates were n^+ -type (001) GaAs, which were mounted on a molybdenum block using indium. The growth rate for all layers was 0.5 mm/h. Solid arsenic source was used and the beam equivalent ratio of As4 to Ga beams ($[V]/[III]$ ratio) was 15 as measured with an ionization gauge in the growth position. On the substrate, a $1\text{ }\mu\text{m}$ thick Si-doped ($1 \times 10^{16}\text{ cm}^{-3}$) GaAs buffer layer was grown at 620°C . Then, the As cell was left open while the substrate temperature was reduced to 250°C . At this temperature, the LT-GaAs epilayer was grown at various conditions. After growing the LT-GaAs layers, the substrate temperature was raised again to 620°C and another $1\text{ }\mu\text{m}$ thick Si-doped GaAs layer was grown (see Fig. 1). Therefore, the LT-GaAs layer experienced annealing for 2 hours at 620°C during the growth process of the top layer. As a reference sample, we also grew a $2\text{ }\mu\text{m}$ thick Si-doped (10^{16} cm^{-3}) GaAs layer at a normal substrate temperature of 620°C without inserting the LT-GaAs layer.

The samples were separated into several pieces and loaded into an infrared image furnace for RTA. The RTA process was performed under a hydrogen flow on the face-to-face capless condition and the annealed temperature was 900°C . The heating rate and the holding time at the highest temperature were set to 20K/sec and 5min, respectively. Then, the sample was cooled down as rapidly as possible.

Schottky diodes were fabricated by evaporating Al on the top of the n -GaAs layer through a metal mask. Standard current-voltage (I - V) and capacitance-voltage (C - V) measurements were carried out before DLTS measurements. Deep levels were detected by DLTS system with a YHP 4280A 1-MHz capacitance meter, which is computer automated with transient signals being digitally recorded for subsequent analysis. The voltages of a refilling pulse as well as a measuring bias were determined referring to the C - V data so that the edge of a depletion layer can cross over to the LT-GaAs region⁷. The capacitance difference signal was obtained by using the rectangle weighting function and the rate window was set to 400 ms for the purpose of spectrum comparison.

For photocapacitance quenching measurements, the light comes from a GaAs infrared (IR) light emitting diodes (1.32 eV, 5mW) and the photons are fed on top of the Al Schottky diode as nearly as possible. The experimental procedure consists in recording, after a long pulse of reverse bias which the edge of a depletion region can cross over the LT-GaAs layer, the transient of capacitance illumination at low temperature (77K).

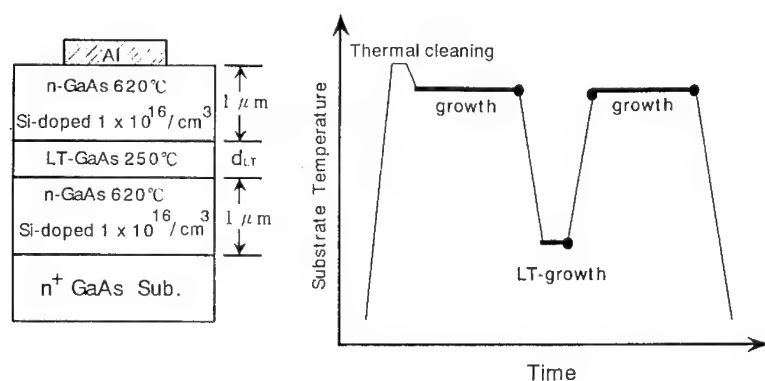


Fig. 1. Schematic cross section of the sample structure and time variation of the substrate temperature during the MBE growth.

RESULT AND DISCUSSION

Typical DLTS spectra of the LT-GaAs layers with various thicknesses are shown in Fig. 2. Negative peaks in the spectra are due to an electron-emission from deep levels. Three electron traps (labeled EAL1, EAL2 and EAL3) are observed in the n -LT- n sandwich sample, which contains a very thin LT-layer (1.3nm). When the thickness of LT-layer exceeds 6.5nm, the EAL2 level dominates the DLTS spectrum, and the signals of EAL1 and EAL3 relatively decreased and finally disappeared.

The Arrhenius plots for three electron traps (EAL1-EAL3) are shown in Fig. 3 and compared with various electron traps reported by Martin and Puechner^{8,9}. The values of the activation energy and capture cross section for the dominant level EAL2 are 0.55 eV and $5.8 \times 10^{-14} \text{cm}^2$, respectively. This result suggests that the EAL2 level is very similar to the EL3 level in the "signature" plot. Johnstone *et al.*¹⁰ reported a defect level (0.53-0.57 eV range) in an MIS structure with LT-layers as an insulator, which is possibly the same level as our EAL2.

We also grew the "growth interruption sample" (the same growth process applied to n -LT- n structure sample, but without growth of the LT-layer) to elucidate the influence of growth interruption. Figure 4 shows the DLTS spectra of the sample with the growth interrupted interface. Although the DLTS signal is small, we also detected the EAL3 level in the growth interruption sample. Puechner *et al.*⁹ have shown that there are three electron traps and several hole traps in their FET channel layers grown on LT-GaAs layers. From the signature plot, their electron traps (labeled P1, P2 and P3) in the FET channel are different from the EAL2 level in our annealed LT layers; EAL1 and EAL3 (detected in thick LT-layer of n -LT- n sandwich sample) could be the same as their P1 and P3 level, respectively. It might be speculated that EAL1 and EAL3 were formed due to the growth interruption at the interface(s) between the LT-GaAs and the normal layers.

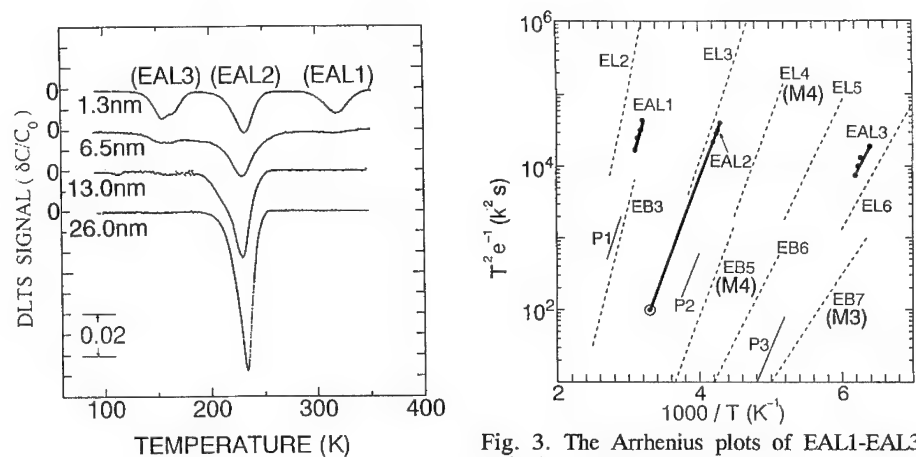


Fig. 2. Typical DLTS spectra of the n -LT- n sandwich sample with various thicknesses for LT-GaAs layer at an emission time constant of 400 ms. The thicknesses are 1.3, 6.5, 13 and 26 nm, respectively.

Fig. 3. The Arrhenius plots of EAL1-EAL3 and other reports: present work (DLTS results \bullet ; ICTS result at room temperature \odot), Martin⁸ (M3 and M4 are typical deep-levels observed in MBE material), Puechners⁹.

Figure 5 shows the as-grown (annealed at 620°C) *n*-LT(26nm)-*n* sandwich sample as well as the separated samples after RTA at 720, 810 and 900°C, respectively. Increasing the RTA temperature broadens the peak of EAL2 in the RTA samples more than in the "as-grown" state. No new level was detected in the 720°C RTA sample. However, it is interesting that we found a new peak which is seen around 350K, the EL2-like level, detected in the 810 and 900°C RTA samples.

Figure 6 shows a spectrum of the control sample (containing no inserted LT-GaAs layer) grown at normal temperature of 620°C before and after RTA at 900°C, respectively. The control GaAs layer as grown at normal temperature shows no signal within the detection limit of $5 \times 10^{12} \text{ cm}^{-3}$. On the other hand, beside an extremely small and broad signal at 100-200K, there is no significant midgap peak observed in 900°C RTA sample. It indicates that upon RTA the reference GaAs layer grown at normal temperature did not generated any debatable level. Therefore, the generation of midgap level was originated from the LT-layer.

The photoquenching effect is well recognized to be an important fingerprint of the EL2 level, which is explained by the transfer of all the EL2 levels from their normal state to an excited metastable state¹¹. Thus, we performed this technique to confirm the new generated midgap level as the EL2 defect. Figure 7 shows the photocapacitance transient signals after infrared (IR) light illumination at 77K. (a) the control reference sample RTA at 900°C. (b) *n*-LT(26nm)-*n* sandwich structure in the "as-grown" state (annealed at 620°C). (c) the *n*-LT(26nm)-*n* sample RTA at 900°C. The reference samples show no effect of photoquenching. Little or no capacitance quenching in the as-grown (annealed at 620°C) *n*-LT-*n* sandwich sample. However, IR light obviously causes quenching of photocapacitance in the sandwich sample RTA at 900°C, with a thermal recovery around 135K. Therefore, we are convinced that upon high temperature RTA the EL2 level is generated in LT-MBE GaAs layers.

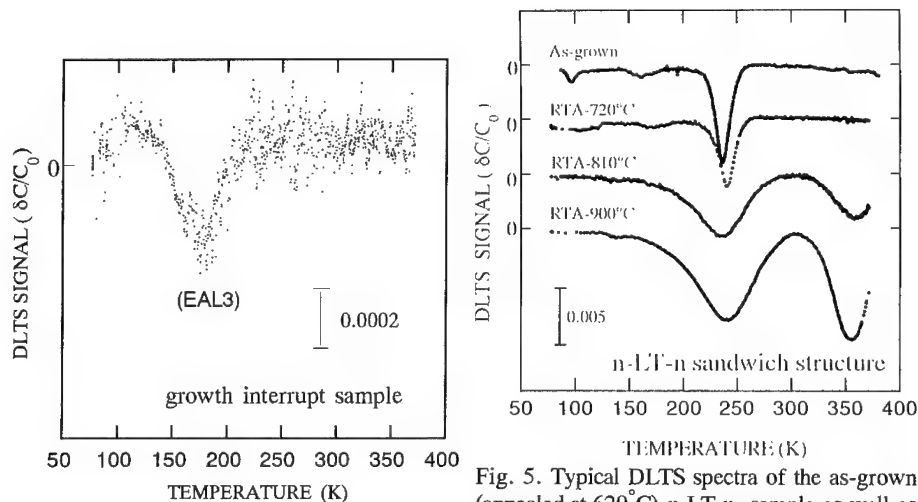


Fig. 4. Typical DLTS spectra of the sample with the growth interrupted interface.

Fig. 5. Typical DLTS spectra of the as-grown (annealed at 620°C) *n*-LT-*n* sample as well as the samples after RTA at 720, 810 and 900°C, respectively.

Fang *et al.*^{12,13} reported the LT-GaAs layer grown at 250°C and annealed (above 350°C) at various higher temperatures, all samples show IR quenching of photocurrent. Jäger¹⁴ observed the EL2-like defect levels in their annealed (600°C) p^+-LT-n^+ structure diodes verified by used photocurrent measurements. Fang and Look also found that the hopping conduction of the annealed LT-GaAs layer recovered at about 140K with a thermal activation energy of about 0.3eV. Their recover rate was very close to the EL2 observed in a recent study of bulk SI GaAs. They concluded that the dominant defect in LT-MBE GaAs layers is related to an arsenic antisite. However, based on some experimental results they argued that it is not the famous EL2^{13,15}.

Neither the EL3-like nor the EL2-like level was observed in our as-grown and 900°C RTA reference samples containing no inserted LT-GaAs layer. However, in those containing a 26nm thick layer of LT-GaAs layer (n -LT- n sandwich structure), as-grown (annealed at 620°C) and all RTA samples, the EL3-like level was detected. Since all the crystals in which the EL3 level was detected were grown in an As-rich condition, EL3 has been speculated to be a point defect or a point-defect/impurity complex⁸. Shen *et al.*¹⁶ suggested with their photoreflectance data that the pinning positions of the as-grown (unannealed) and annealed (600°C) samples are 0.47 eV and 0.65 eV, respectively, and the (0/+) donor level of the As antisite (As_{Ga}) in LT-GaAs locates at $E_c - 0.57$ eV. On the other hand, we found the appearance of EL2 level in 900°C RTA samples, which are generally believed to be the first donor levels of the As_{Ga} antisite defect¹⁷, but not in the "as-grown" (annealed at 620°C) state of n -LT- n sample. The generation of EL2 can be related to redissolving of some fraction of arsenic precipitates in the LT-GaAs layer upon high temperature annealing, although the size of precipitates became larger¹⁸. The relationship of electrical property (semi-insulating) and change in microstructure of LT-GaAs layers (EL3-like level became broader and generation of EL2) upon RTA requires further study.

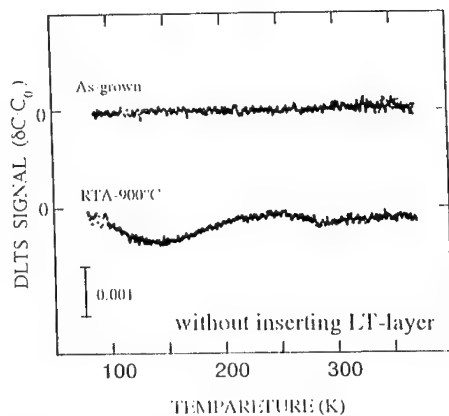


Fig. 6. Typical DLTS spectra of the reference sample (grown at normal temperature 620°C containing no inserted LT-GaAs layer) before and after RTA at 900°C.

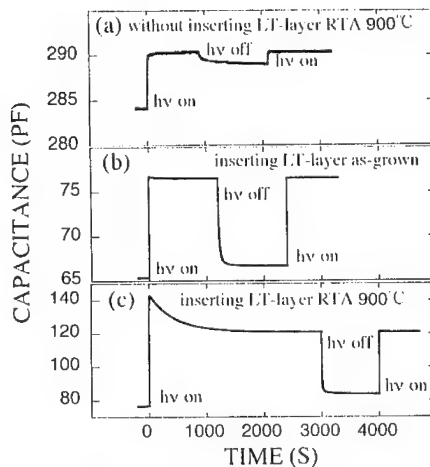


Fig. 7. The photocapacitance transient signals after infrared (IR) light illumination at 77K. (a) the reference sample RTA at 900°C. (b) as-grown (annealed at 620°C) sandwich sample. (c) the sandwich sample after RTA at 900°C.

CONCLUSIONS

Deep levels in the annealed LT-MBE GaAs have been characterized by using the capacitance DLTS technique in combination with a unique sample structure. We have fabricated the samples by inserting the LT-GaAs layer into two n-type semi-conductive layers, like a sandwich, grown at normal substrate temperatures. DLTS measurements have revealed that one electron trap dominates the annealed LT-MBE GaAs. The dominant electron trap was very similar to the so-called EL3 level. Moreover, we found the midgap level appeared upon 800-900°C RTA, although no midgap level was detected in the as-grown sample (annealed at 620°C) and confirmed with photoquenching measurements that it is the EL2 level.

ACKNOWLEDGMENT

The authors wish to thank S. Kuma and Y. Otoki of Hitachi Cable Co. for providing MBE-ready GaAs substrate.

REFERENCES

1. M. Kaminska, Z. Liliental-Weber, E. R. Weber, T. George, J.B Kortright, F. W. Smith, B. Y. Tsaur and A. R. Calawa, *Appl. Phys. Lett.* **54**, 1881 (1989).
2. Z. Liliental-Weber, W. Swider, K. M. Yu, J. Kortright, F. W. Smith and A. R. Calawa, *Appl. Phys. Lett.* **58**, 2153 (1991).
3. F. W. Smith, A. R. Calawa, C. L. Chen, M. J. Mantra and L. J. Mahoney, *IEEE Electron Device Lett.* **9**, 77 (1988).
4. F. W. Smith, H. Q. Le, V. Diadiuk, M. A. Hollis, A. R. Calawa, S. Gupta, M. Frankel, D. R. Dykaar, G. A. Mourou and T. Y. Hsiang, *Appl. Phys. Lett.* **54**, 890 (1989).
5. D. C. Look, D. C. Walters, M. Mier, C. E. Stutz and S. K. Brierly, *Appl. Phys. Lett.* **60**, 2900 (1992).
6. A. C. Warren, J. M. Woodall, J. L. Freeouf, D. Grischkowsky, D. T. McInturff, M. R. Melloch and N. Otsuka, *Appl. Phys. Lett.* **57**, 1331 (1990); and references therein.
7. T.-C. Lin, H. T. Kaibe and T. Okumura, *Jpn. J. Appl. Phys.* **33**, L1651 (1994).
8. G. M. Martin, A. Mitonneau and A. Mircea, *Electron. Lett.* **13**, 191 (1977).
9. R. A. Puechner, D. A. Johnson, K. T. Shiralagi, D. S. Gerber, R. Droopad and G. N. Maracas, *J. Cryst. Growth* **111**, 43 (1991).
10. D. K. Johnstone, C. E. Stutz and K. R. Evans, *Bull. Am. Phys. Soc.* **37**, 251 (1992).
11. G. Vincent, D. Bois and A. Chantre, *J. Appl. Phys.* **53**, 3643 (1982).
12. Z.-Q. Fang and D. C. Look, *Appl. Phys. Lett.* **61**, 1438 (1992).
13. Z.-Q. Fang and D. C. Look, *J. Electron. Mater.* **22**, 1429 (1993).
14. N. D. Jäger, A. K. Verma, P. Dreszer, N. Newman, Z. Liliental-Weber, M. Van Schilfgaarde and E. R. Weber, *J. Electron. Mater.* **22**, 1499 (1993).
15. D. C. Look, Z.-Q. Fang, J. R. Sizelove and C. E. Stutz, *Phys. Rev. Lett.* **70**, 465 (1993).
16. H. Shen, F. C. Rong, R. Lux, J. Pamulapati, M. Taysing-Lara, M. Dutta, E. H. Poindexter, L. Calderon and Y. Lu, *Appl. Phys. Lett.* **61**, 1585 (1992).
17. D. J. Chadi and K. J. Chang, *Phys. Rev. Lett.* **60**, 2187 (1988).
18. A. C. Warren, J. M. Woodall, P. D. Kirchner, X. Yin, F. Pollak, M. R. Melloch, N. Otsuka and K. Mahalingam, *Phys. Rev.* **B46**, 4617 (1991).

DEEP IMPURITIES IN AlGaAs GROWN BY MOCVD USING DIFFERENT HYDROGEN AND NITROGEN AS CARRIER GASES

J. C. CHEN, Z.C. Huang, Bing Yang, H.K. Chen and K. J. Lee,
Department of Electrical Engineering, Univ. of Maryland Baltimore County, Baltimore, MD 21228

ABSTRACT

A study was carried out to characterize the deep impurities in $\text{Al}_x\text{Ga}_{1-x}\text{As}$ grown by metal-organic chemical vapor deposition (MOCVD) using different carrier gases. Since $\text{Al}_x\text{Ga}_{1-x}\text{As}$ is very sensitive to any impurities, especially moisture and oxygen, in the growth process, the concentration of impurities in $\text{Al}_x\text{Ga}_{1-x}\text{As}$ can serve as a measure of the purity of carrier gases. The undoped AlGaAs layers grown by using H_2 have n-type background concentrations from 3×10^{15} to $10 \times 10^{15}/\text{cc}$. The concentrations of oxygen-related traps ($E_c - 0.53$ and 0.7 eV) are $0.2 - 9 \times 10^{13}$ and $3.4 - 5 \times 10^{14}/\text{cc}$ for Pd- and Li-purified H_2 , respectively. Low-temperature photoluminescence (PL) measurements show better PL efficiency in samples grown by using Pd-purified H_2 . $\text{Al}_x\text{Ga}_{1-x}\text{As}$ grown by using N_2 is p-type ($p \sim 6 \times 10^{16}/\text{cc}$) with an oxygen-related trap and two hole traps. The concentration of oxygen-related trap is more than one order of magnitude higher than that of AlGaAs using Pd-purified H_2 . The memory effect due to impurities from carrier gas left in source materials is also studied.

1. INTRODUCTION

The carrier gas used in the chemical vapor deposition (CVD) process is an important factor in affecting the purity of grown materials. Several manufacturers of commercial gas purification devices (for hydrogen or nitrogen) claim that they can produce hydrogen or nitrogen with impurities (mainly moisture or oxygen) concentrations less than 1 ppm (one part per million) or even 1 ppb (one part per billion). However most moisture or oxygen sensors are not very sensitive in such a low concentration level. Therefore the purity of carrier gas purified by different methods is difficult to be evaluated accordingly.

On the other hand, the AlGaAs epilayer is very sensitive to the purity of source materials used in the metal-organic chemical vapor deposition (MOCVD) process. Kisker et al. have shown that as little as 1 ppm of oxygen in the AlGaAs growth process resulted in extremely high, greater than 10^{19} cm^{-3} , oxygen concentrations in the AlGaAs epilayer [1]. Several studies also demonstrated the deleterious effect of oxygen incorporation on the photoluminescence (PL) efficiency of AlGaAs [2]. It is, therefore, reasonable to evaluate the purity of carrier gases by examining the impurities in AlGaAs grown under the same conditions except using different carrier gases.

In this study, we have systematically investigated the deep level impurities and optical properties of $\text{Al}_{0.2}\text{Ga}_{0.8}\text{As}$ which was grown by MOCVD using vaporized N_2 and different H_2 purified by Pd-cell and by Li-based purifiers as the carrier gases.

2. EXPERIMENTAL PROCEDURES

The $\text{Al}_x\text{Ga}_{1-x}\text{As}$ layers used in this study were grown in a conventional, horizontally configured, atmospheric pressure MOCVD reactor which has been routinely producing device-quality materials such as mobility of GaAs $> 100,000 \text{ cm}^2/\text{Vs}$ at 77K, and optoelectronic devices, e.g. laser diodes and photodetectors. The column III precursors were trimethylaluminum (TMAI) and trimethylgallium (TMGa). The column V precursor was pure arsine. No getters were used to purify any sources in this study. The materials were grown at 730°C with precursor V/III ratio of 40, and a growth rate of $4.0 \mu\text{m/hr}$. N_2 (vaporized from liquid N_2) or H_2 (purified by a Pd-cell, a product of Johnson Matthey, or by a Nanochem L-300 H_2 purifier, a product of Semi-Gas System, Inc.) were used as the carrier gas. According to

the manufactures' specifications, the impurity concentration in H_2 purified by Pd-cell or by Nanochem purifier will be less than 10 ppb. The Nanochem purifier consists of a Li-based organometallic polymer. The crude H_2 (prepurified grade, 99.99% pure) was purchased from Matheson Inc. A 2- μm -thick undoped $\text{Al}_{0.2}\text{Ga}_{0.8}\text{As}$ layer, unless otherwise noted, was grown on n+-GaAs (10^{18} cm^{-3}) substrates. The total carrier flow in this experiment is around 10 l/m.

Due to our MOCVD reactor is not load-locked and not located in a cleanroom, the interaction between the internal surfaces of the reactor and the laboratory ambient, i.e. humidity, can be different at different time, e.g. summer and winter. In addition, the purity of source materials may slightly change with time according to some studies [3]. In order to overcome those problems, we have carried out the calibration run using Pd-purified H_2 as a reference (we called it standard run) before the different purifier or gas was used. This approach, therefore, will give a reliable comparison of material quality.

The free carrier concentration was measured by capacitance-voltage (C-V) measurements. The composition of Al and Ga was determined by photoluminescence (PL) and by double crystal x-ray rocking curve measurements. The composition calculation was based on the DCC software provided by Bede Scientific Instruments Ltd. Surface morphology was studied with a Nomarski interference microscope. Low-temperature PL was employed to characterize the optical properties of material. The PL set-up includes an Ar⁺-ion laser (using the 514.5 nm line), a Spex monochromator, a liquid N₂-cooled Ge detector and a Si CCD array detectors. To quantitatively measure the deep impurities in $\text{Al}_{0.2}\text{Ga}_{0.8}\text{As}$, deep level transient spectroscopy (DLTS) was employed to characterize the $\text{Al}_{0.2}\text{Ga}_{0.8}\text{As}$ layer. Schottky contacts, 700 μm in diameter, were made by evaporating Au through a metal mask onto the AlGaAs surface immediately after etching in a freshly prepared $\text{H}_2\text{SO}_4\text{:H}_2\text{O}_2\text{:H}_2\text{O}$ (2:1:10) solution for 15 seconds. Ohmic contacts were made by evaporating AuGe/Au on the n+-GaAs substrate, and alloying in a forming gas (95% N₂ + 5% H₂) atmosphere at 420 °C for 2 minutes. Our DLTS setup was made by Sula Technologies, and consists of DLTS and a double-correlator DLTS (DDLTS). The temperature scan range was from 30 to 380 K. Data was taken automatically by a computer through a high speed analog-digital converter board.

3. RESULTS AND DISCUSSIONS

All samples show excellent surface morphology no matter what kind of carrier gases were used. The C-V results show that the undoped AlGaAs layers grown by H_2 always have n-type background concentrations from 3×10^{15} to $10 \times 10^{15}/\text{cc}$. The typical DLTS spectrum for an undoped- $\text{Al}_{0.2}\text{Ga}_{0.8}\text{As}$ layer of a standard run, which has a carrier concentration of $5.0 \times 10^{15}\text{ cm}^{-3}$, is shown in Fig.1. Three main deep electron traps, E1, E2 and E3, were observed with activation energies of 0.70, 0.53 and 0.30 eV, respectively. These traps are commonly observed in MOCVD-grown AlGaAs layers [4, 5]. The 0.53 (E2) and 0.70 eV (E1) traps were associated with oxygen-related impurities which may come from source materials, reactor, carrier gas or their combinations. The 0.30 eV trap (E3) has been attributed to Ge contamination in source material and not related to carrier gas [4]. Therefore, the very low concentration ($\sim 10^{13}/\text{cc}$) of this E3 trap in our undoped-AlGaAs indicates that our source materials are in general purer than those reported by other groups which have E3 density around $10^{14}/\text{cc}$ [4]. This assured us that a clean base line was established for this experiment. A shallow electron trap E4 was also observed with an activation energy of 0.08 eV, which could be a shallow impurity level.

The concentrations of oxygen-related traps (E_c-0.53 and 0.7 eV) are $0.2\text{--}9 \times 10^{13}$ and $3.4\text{--}5 \times 10^{14}/\text{cc}$ for Pd- and Li-purified H_2 , respectively. The deep impurity density of AlGaAs grown using Pd-purified H_2 is consistently lower than that of AlGaAs using Li-based purifier. In addition, the lifetime of Pd-cell is also longer than that of Li-based purifier. For example, the Pd-cell used in this experiment has been used for more than three years in our lab., however the Li-based purifier became saturated after 10 cylinders of H_2 (volume $\sim 213\text{ ft}^3/\text{cylinder}$, 99.99% pure) were used.

Figure 2 shows the DLTS spectrum. AlGaAs grown by N₂ (without using any getter) is

p-type (background concentration, $p \sim 6 \times 10^{16}/\text{cc}$) with an oxygen-related trap and two hole traps. The concentration of oxygen-related trap is more than one order of magnitude higher than that of

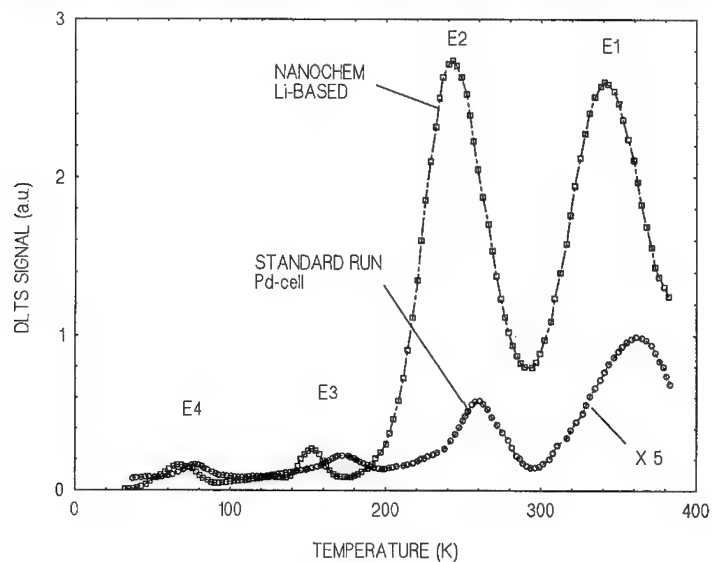


Fig. 1. DLTS spectra of $\text{Al}_{0.2}\text{Ga}_{0.8}\text{As}$ using H_2 as a carrier

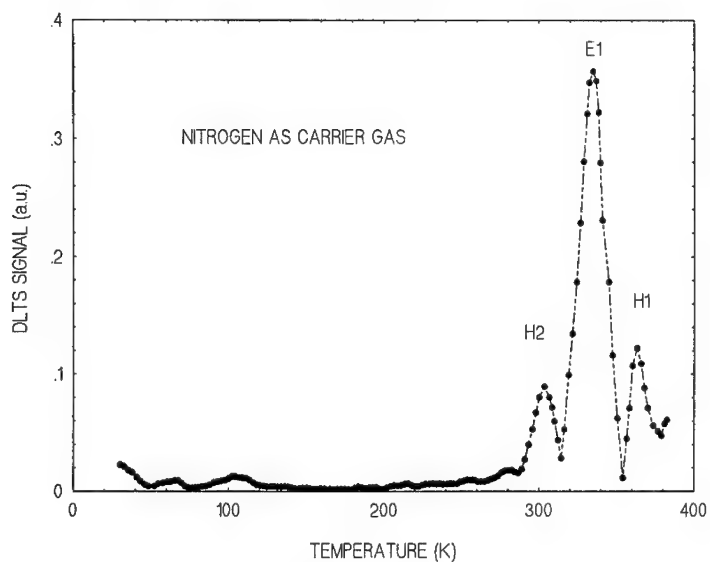


Figure 2, DLTS spectrum of $\text{Al}_{0.2}\text{Ga}_{0.8}\text{As}$ using N_2 as a carrier

Table 1. Deep impurity concentrations in AlGaAs using different carrier gases

H ₂ purifier or nitrogen	Sample #	E1: oxygen-related trap density (1/cc)
H ₂ (Pd cell)	OM368	6.6X10 ¹³
H ₂ (Pd cell)	OM374	8X10 ¹³
H ₂ (Pd cell)	OM377	9X10 ¹³
H ₂ (Li-based)	OM384	3.4X10 ¹⁴
H ₂ (Li-based)	OM404	5X10 ¹⁴
H ₂ (Pd cell)	OM480	2X10 ¹²
N ₂	OM481	1.8X10 ¹⁴
H ₂ (Pd cell)	OM482	3X10 ¹²

AlGaAs using Pd-purified H₂. The deep impurity concentrations of different AlGaAs are listed in Table 1. The memory effect due to impurities left in the reactor and/or other source materials is also studied. As can be seen from table 1, the E1 trap densities of standard runs 480 and 482 are 2x10¹² and 3x10¹²/cc, respectively. The difference is very small. This suggests that the memory effect of impure carrier gas in source materials may be negligible as long as the residence time in source is not very long. However the long-term memory effect is unknown at present.

Figure 3 shows the low-temperature (15K) photoluminescence spectra of three samples using Pd- and Li-purified H₂ and N₂ as the carrier. The samples using H₂ have similar PL spectra. The intensity of the near band edge peak ($\lambda \sim 698$ nm) is stronger if a Pd-purified H₂ is

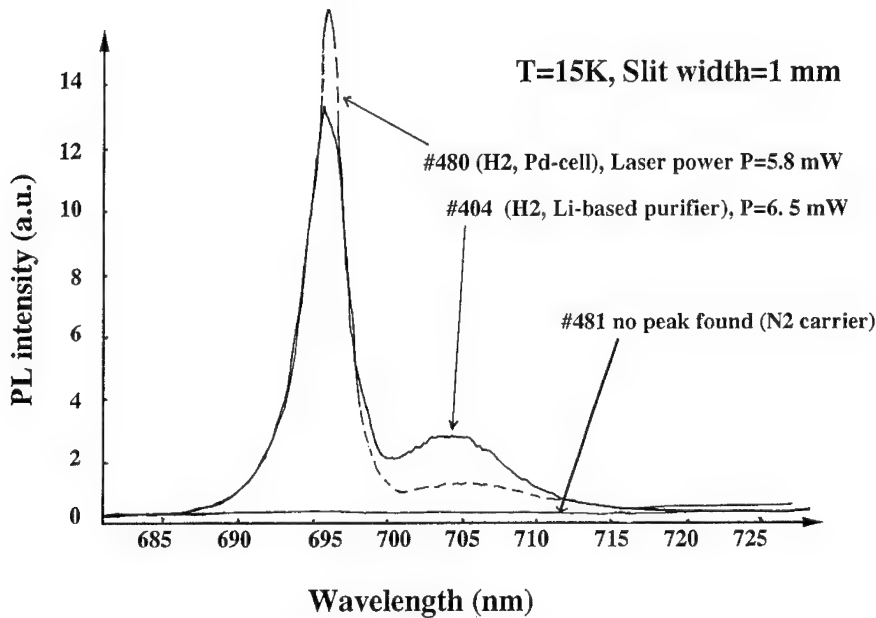


Figure 3, PL spectra of Al_{0.2}Ga_{0.8}As

used. It indicates that Pd-purified H_2 is purer than H_2 purified by Li-based purifier. This result is also in good agreement with the DLTS results. On the other hand, no near band edge peak can be detected in sample using N_2 . However, a strong peak, shown in Fig. 4, located at the longer wavelength ($\lambda \sim 1063$ nm) was observed for the first time in AlGaAs samples. It suggests that some unknown impurities were introduced when N_2 was used. The radiative nature of this deep level is interesting and not being reported. A study is underway to understand its origin.

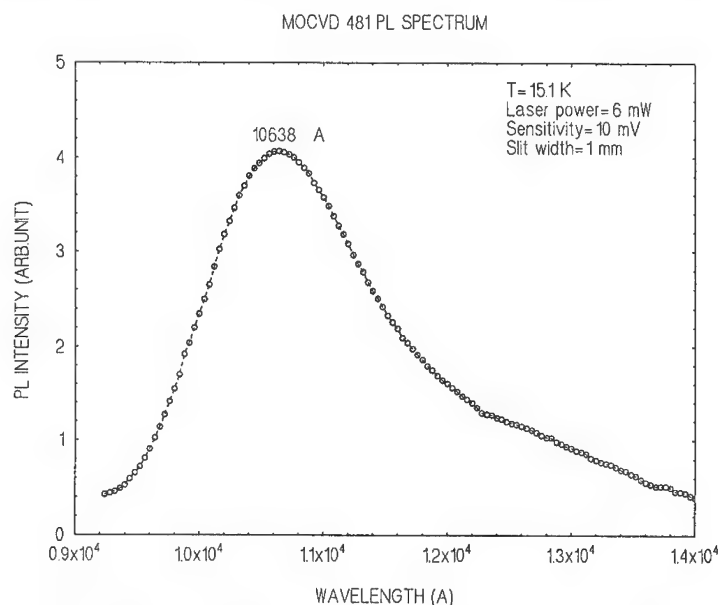


Figure 4, PL spectrum of $Al_{0.2}Ga_{0.8}As$ using N_2 as a carrier

4. SUMMARY

We have carried out a study to evaluate the purity of different gases commonly used in the semiconductor process. By measuring the deep impurity density in AlGaAs grown by MOCVD, we found that the lowest oxygen-related impurity was $2 \times 10^{12}/cc$ by using Pd-purified H_2 as a carrier. AlGaAs with poor optical quality and high impurity density was obtained when N_2 was used as a carrier.

5. REFERENCES

- [1] G.B. Stringfellow, *Organometallic Vapor-Phase Epitaxy: Theory and Practice*, p.298-300 (Academic, Boston, MA 1989).
- [2] M.J.Tsai et al, Jour. of Electronic Material, **13**, 437 (1984).
- [3] H. Terao and H. Sunakawa, J. Cryst. Growth, **68**, 157 (1984).
- [4] R.T. Green and W.-I. Lee, J. Electron. Mater., **20**, 583 (1991).
- [5] P.K. Bhattacharya, S. Subramanian, and M. J. Ludowise, J. Appl. Phys, **55**, 3664 (1984).

ATOMIC STRUCTURE OF DEEP LEVEL DEFECTS IN DIMETHYLALUMINUM METHOXIDE-DOPED GAAS

Y. PARK AND M. SKOWRONSKI

Department of Materials Science and Engineering, Carnegie Mellon University, Pittsburgh, PA 15213

ABSTRACTS

GaAs epilayers doped with dimethylaluminum methoxide (DMAIMO), an alkoxide bearing a pre-formed Al-O molecule, have been investigated using local vibrational mode (LVM) absorption and deep level transient spectroscopy measurements. LVM measurements indicated that oxygen and aluminum atoms are incorporated into GaAs layer as a complex and remain bound in the volume of the crystal. Electron traps with activation energies of 0.74 and 0.93 eV below the conduction band are main deep level defects responsible for the electrical and optical properties of the layers. Interpretation of the relationship between trap concentration and growth conditions led to the conclusion that the 0.93 and 0.74 eV traps have the atomic structures in which oxygen atom is bonded to one (AlO) and two aluminum atoms (Al_2O), respectively.

INTRODUCTION

Doping of GaAs with alkoxides bearing a pre-formed Al-O molecule has been investigated as a promising doping scheme to increase oxygen concentration in GaAs.[1-5] The basic idea of this new doping scheme is to introduce oxygen into a layer in a form of Al-O using the strong bond between aluminum and oxygen. Since oxygen is known to form deep level traps in GaAs,[6,7] the new doping scheme could find several applications in the growth of GaAs buffer layer and in the fabrication of ultrafast photoconductive detectors; dimethylaluminum methoxide (DMAIMO) doping of GaAs was observed to compensate shallow donors[1] and to quench near band edge luminescence.[4] Several electron traps have been reported in alkoxide-doped GaAs at 0.28, 0.44, 0.54, 0.71, 0.83, and 0.95 eV below the conduction band.[1,2,8,9] However, little is known about the atomic structure of those traps.

In this study, we will address the atomic structure of the deep level defects induced by DMAIMO doping of GaAs based on the relationship between defect concentration and incorporation mechanism of the Al-O molecule. Also, this study could give an insight into the atomic structure of oxygen-related defects in AlGaAs; since DMAIMO doping results in both aluminum and oxygen incorporation into a layer, the DMAIMO-doped GaAs can be considered as $\text{Al}_x\text{Ga}_{1-x}\text{As}$ with very small aluminum content. Although there is a large number of studies on oxygen incorporation into AlGaAs and resultant deep level defects,[10-13] their atomic structures are still in question. Precise control of aluminum and oxygen concentrations in a layer using DMAIMO is expected to give more reliable experimental data to approach this question.

EXPERIMENTAL PROCEDURE

GaAs epilayers were grown by atmospheric pressure organometallic vapor phase epitaxy (OMVPE) with a horizontal reactor heated by infrared radiation. Substrates were (100) undoped semi-insulating GaAs wafers misoriented 2° toward $[1\ 10]$. Substrates were used as-received without cleaning or etching. The oxide layer on the surface was removed by a thermal desorption at 750°C for 10 minutes in the arsenic overpressure prior to growth. Trimethylgallium (TMG) and tertiarybutylarsine (TBA) were employed as starting compounds for the growth of GaAs in a flow of palladium-purified H_2 carrier gas. The TBA and TMG mole fractions in a carrier gas flow of 4000 sccm were 5.6×10^{-4} and 5×10^{-5} , respectively. Typically, these conditions correspond to a growth rate of $1.5\ \mu\text{m/h}$ at 600°C .

Local vibrational mode (LVM) absorption measurements have been performed in the $300\text{--}1500\ \text{cm}^{-1}$ range with a resolution of $0.1\ \text{cm}^{-1}$ using a Bomem DA3 Fourier Transform Infrared spectrometer. For LVM absorption measurement, GaAs epilayers with a thickness of about $1.5\ \mu\text{m}$ were heavily doped with DMAIMO in the temperature range from 475 to 600°C . The samples were mounted on the cold finger of a cryostat cooled by a continuous flow of liquid helium.

Deep level transient spectroscopy (DLTS) measurements were performed over the temperature range from $100\text{--}450\ \text{K}$ with a Polaron DL 4600 system. GaAs epilayers were co-doped with DMAIMO and diethyltellurium to provide background free electron concentration for DLTS studies. Schottky diodes for DLTS measurements were fabricated by a thermal evaporation of gold in vacuum of 1×10^{-6} Torr. The reverse bias and filling voltages were -2.5 and $1.0\ \text{V}$, respectively.

RESULTS AND DISCUSSION

Since both aluminum and oxygen produce high frequency localized vibrations in GaAs, LVM spectroscopy is a powerful tool for investigation of the atomic structure of DMAIMO doping-induced defects in GaAs. It is well-known that oxygen atom produces LVM lines at 730 , $715\ \text{cm}^{-1}$ (at off-center substitutional arsenic site ($\text{Ga-O}_{\text{As}}\text{-Ga}$)), [14-16] and at $845\ \text{cm}^{-1}$ (at interstitial site bonding to Ga and As atoms). [14,17] An isolated substitutional aluminum atom in GaAs (Al_{Ga}) produces an LVM line at $361\ \text{cm}^{-1}$. [18] The LVM lines corresponding to the either form of isolated oxygen atom in GaAs were not detected in our DMAIMO-doped GaAs layers although the oxygen concentrations in the investigated samples were more than an order of magnitude above the detection limit; for example, the secondary ion mass spectroscopy measurement implies that the layer grown at 475°C contains $4 \times 10^{19}\ \text{cm}^{-3}$ oxygen concentration. The expected LVM sensitivity in epilayers with a $1\ \mu\text{m}$ thickness is about $10^{18}\ \text{cm}^{-3}$. The absence of LVM lines due to the isolated oxygen atoms indicates that most oxygen atoms in the layers exist in a

form of complex defect with other species. The fact that DMAIMO doping results in the incorporation of both aluminum and oxygen into a layer[3] suggests that aluminum is the most likely impurity bonding to oxygen. If this is true, the intensity of the 361 cm^{-1} LVM line corresponding to the substitutional Al_{Ga} in pure GaAs should be a function of growth conditions because the oxygen concentration and the ratio of oxygen and aluminum concentrations in the DMAIMO-doped layers depend strongly on growth conditions, specially growth temperature.[3]

Figure 1 shows a change of the 361 cm^{-1} LVM peak intensity versus growth temperature between 475 and 600°C . Since the layers have different thicknesses and different aluminum concentrations, the intensities of the peak were normalized to be obtained at the same number of aluminum atoms per area of the layers. As seen in Fig. 1, the 361 cm^{-1} LVM peak intensity decreases dramatically with decreasing growth temperature. This means that the concentration of the isolated Al_{Ga} decreases considerably at low growth temperatures. In other words, the number of Al-impurity complexes increases fast with decreasing growth temperature. Since the oxygen concentration increases exponentially with decreasing growth temperature,[3] oxygen is the most probable impurity bonded to aluminum. In layers grown at temperatures above 600°C , virtually all of aluminum atoms are expected to be present as isolated substitutional Al_{Ga} centers because the $[\text{O}]/[\text{Al}]$ ratio is much less than 1.[3] From Fig. 1, the isolated Al_{Ga} at 475°C is determined to account for less than 25% of the total number of aluminum atoms in the layer. Combination of the above results lead us to the conclusion that DMAIMO doping produces Al-O complex defects.

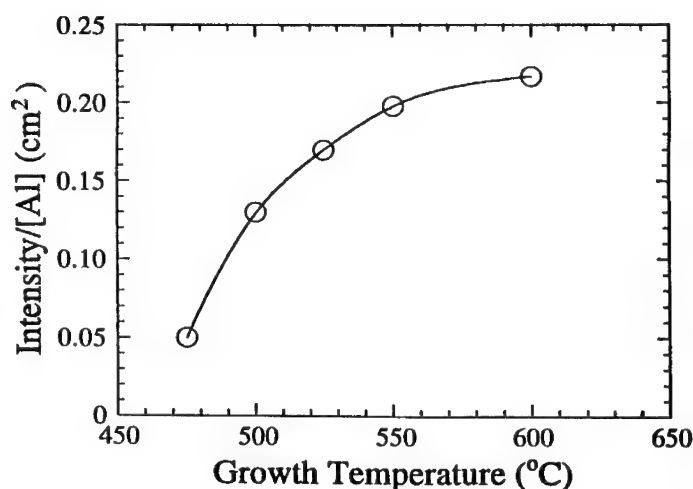


Fig. 1 Effect of growth temperature on the intensity of the 361 cm^{-1} local vibrational mode line due to the isolated Al_{Ga} in GaAs.

No new LVM absorption line has been observed in the investigated range. At this point there is no more information to explain the failure of observation of LVM lines due to the Al-O complex defects.

Figure 2 shows a typical DLTS spectrum of a DMAIMO-doped GaAs layer grown at 600°C. Seven electron traps with activation energies of 0.93, 0.74, 0.58, 0.40, 0.37, 0.30, and 0.25 eV below the conduction band were observed in the investigated temperature range. Some of these traps correspond to the traps with similar activation energies reported in DEAIEO-doped GaAs.[8] The trap with an activation energy of 0.58 eV (O_{OCS}) is the well-known off-center substitutional oxygen.[19] The defects present in highest concentrations are the OA1 ($E_a=0.93$ eV) and OA2 ($E_a=0.74$ eV) traps, and the above LVM measurements suggests that they are most likely the Al-O complex defects. Given a preference of oxygen atom being bonded to two atoms only (the off-center substitutional oxygen atom is also bonded to two atoms), the atomic configuration of the two complex defects should be the oxygen atom bonded to one (AlO) or two aluminum atoms (Al_2O).

As mentioned early, since the oxygen concentration and the ratio of oxygen and aluminum concentrations are dependent strongly on growth conditions, the relationship between the trap concentration and growth condition could give a clue to the atomic structure of the complex defects. The change of the OA1 and OA2 trap concentrations as a function of DMAIMO mole

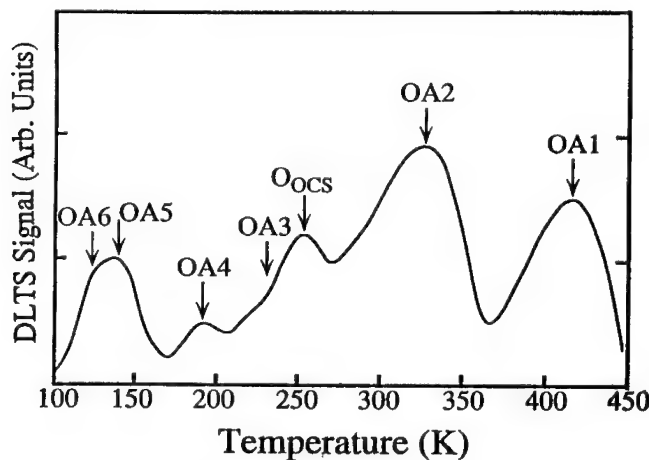


Fig. 2 A typical DLTS spectrum of a DMAIMO-doped GaAs at 600°C. DLTS signal is in log scale. Reverse-bias voltage was -2.5 V with a trap filling pulse of 1.0 V for 1 ms. The rate window was 10 s^{-1} .

fraction is shown in Fig. 3. As seen in Fig. 3, the OA1 trap concentration increases linearly with increasing DMAIMO mole fraction. On the other hand, the OA2 trap concentration shows different behavior; the ratio of OA1 and OA2 trap concentrations decreases by about a factor of three as DMAIMO mole fraction increases from 1.3×10^{-8} to 1.1×10^{-7} . In other words, with increasing DMAIMO mole fraction the OA2 trap concentration increases faster than that of the OA1 trap (i.e. superlinearly). The rates at which the trap concentrations change could be related to the incorporation mechanism of aluminum and oxygen. It has been observed that oxygen concentration at 600°C increases quadratically with increasing DMAIMO mole fraction.[3] This superlinear increase of oxygen concentration was attributed to the reaction of Al-O molecule with aluminum adatom on the growth surface, producing oxygen atom bonded to two aluminum atoms. The resultant stronger bonding of oxygen with two aluminum atoms could increase the possibility of oxygen incorporation into a layer. Also, it seems that the probability of such a reaction increases with increasing DMAIMO mole fraction, which is responsible for the superlinear increase of oxygen concentration. This incorporation mechanism implies that with increasing DMAIMO mole fraction the number of oxygen atom bonded to two aluminum atoms increases superlinearly. From the above argument we can draw the conclusion that the OA2 trap

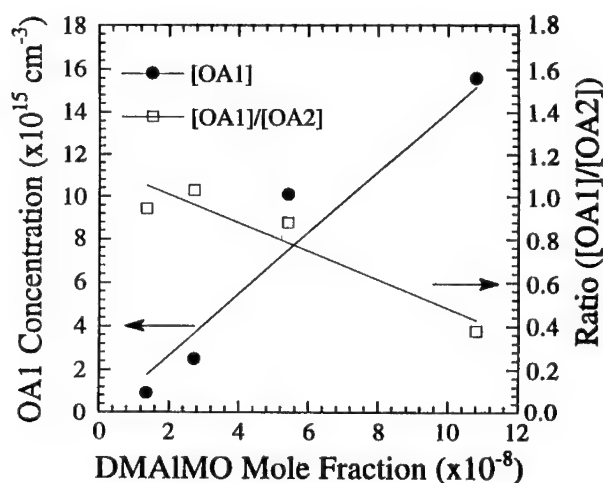


Fig. 3 Dependence of the OA1 and OA2 trap concentrations on DMAIMO mole fraction in the layer grown at 600°C . The OA2 trap concentrations are shown as the ratio of the OA1 trap to OA2 trap concentrations.

($E_a=0.74$ eV) has the atomic configuration of oxygen atom being bonded to two aluminum atoms (Al_2O); the OA1 trap ($E_a=0.93$ eV) is due to the configuration of oxygen atom being accompanied by only one aluminum atom (AlO). However, further study is necessary to have a direct spectroscopic evidence to determine the exact location of atoms and bonding arrangements.

SUMMARY

GaAs epilayers doped with DMAIMO during OMVPE has been investigated using LVM spectroscopy and DLTS. LVM absorption measurements proved that DMAIMO doping of GaAs produces Al-O complexes in the volume of the layers. Seven electron traps were observed in DMAIMO-doped GaAs at 0.93, 0.74, 0.58, 0.40, 0.37, 0.30, and 0.25 eV below the conduction band. Among the traps the 0.74 and 0.93 eV traps were main deep level defects responsible for the electrical and optical properties of DMAIMO-doped GaAs epilayers. Careful interpretation, based on the incorporation mechanism of Al-O molecule during the growth, of the relationship between trap concentration and growth condition led to the conclusion that the 0.93 and 0.74 eV traps have the atomic structures in which oxygen atom is bonded to one (AlO) and two aluminum atoms (Al_2O), respectively.

REFERENCES

1. M. S. Goorsky, T.F. Kuech, F. Cardone, P.M. Mooney, G.J. Scilla, and R.M. Potemski, *Appl. Phys. Lett.* **58**, 1979 (1991).
2. M. S. Goorsky, T. F. Kuech, P. M. Mooney, F. Cardonne, and R. M. Potemski, *Mat. Res. Soc. Symp.* **204**, 177 (1991).
3. Y. Park, M. Skowronski and T. M. Rosseel, *J. Crystal Growth* **137**, 442 (1994).
4. Y. Park and M. Skowronski, *J. Appl. Phys.* **75**, 2640 (1994).
5. J. W. Huang and T. F. Kuech, *Appl. Phys. Lett.* **65**, 604 (1994).
6. S. T. Neild, M. Skowronski and J. Lagowski, *Appl. Phys. Lett.* **58**, 859 (1991).
7. U. Kaufmann, E. Klausmann, J. Schneider and H. C. Alt, *Phys. Rev. B*, **43**, 12106 (1991).
8. J. W. Huang and T. F. Keuch, *Mater. Res. Soc. Symp.* **325**, 305 (1994).
9. Y. Park and M. Skowronski, *J. Appl. Phys.* **76**, 5813 (1994).
10. K. Akimoto, M. Kamada, K. Taira, M. Arai, and N. Watanabe, *J. Appl. Phys.* **59**, 2833 (1986).
11. P. K. Bhattacharya, T. Matsumoto and S. Subramanian, *J. Cryst. Growth* **68**, 301 (1984).
12. P. K. Bhattacharya, S. Subramanian and M. J. Ludowise, *J. Appl. Phys.* **55**, 3664 (1984).
13. R. H. Wallis, M. A. D. Forte-Poisson, M. Bonnet, G. Beuchet and J. P. Duchemin, *Inst. Phys. Conf. Ser.* **56**, 73 (1981).
14. J. Schneider, B. Dischler, H. Seelewind, P.M. Mooney, J. Lagowski, M. Matsui, D.R. Beard, and R.C. Newman, *Appl. Phys. Lett.* **54**, 1442 (1989).
15. C. Song, B. Pajot and F. Gendron, *J. Appl. Phys.* **67**, 7307 (1990).
16. H. C. Alt, *Appl. Phys. Lett.* **55**, 2736 (1989).
17. Z. L. Akkerman, L. A. Borisowa, A. F. Kravchenko, *Sov. Phys. Semicond.* **10**, 590 (1976).
18. O. G. Lorimer and W. G. Spitzer, *J. Appl. Phys.* **37**, 2509 (1966).
19. M. Skowronski, in *Deep Centers in Semiconductors*, 2nd ed., edited by S. Pantelides (Gordon and Breach, New York, 1992), p. 379.

INTENTIONAL DEFECT INCORPORATION IN METALORGANIC VAPOR PHASE EPITAXY INDIUM GALLIUM ARSENIDE BY OXYGEN DOPING

J. W. HUANG AND T. F. KUECH

Department of Chemical Engineering, University of Wisconsin, Madison, WI 53706

ABSTRACT

Intentional defect incorporation in metalorganic vapor phase epitaxy (MOVPE) $\text{In}_x\text{Ga}_{1-x}\text{As}$ was achieved by controlled oxygen doping using diethylaluminum ethoxide (DEALO). DEALO doping has led to the incorporation of Al and O, and the compensation of shallow Si donors in $\text{In}_x\text{Ga}_{1-x}\text{As}:\text{Si}$ with $0 \leq x \leq 0.25$. DLTS analysis on a series of $\text{In}_x\text{Ga}_{1-x}\text{As}:\text{Si}:\text{O}$ samples with $0 \leq x \leq 0.18$ showed that oxygen incorporation led to a set of deep levels, similar to those found in DEALO doped GaAs. The characteristic deep levels appear to remain at a relatively constant energy with respect to the valence band.

INTRODUCTION

High resistivity $\text{In}_{0.53}\text{Ga}_{0.47}\text{As}$ is of current interest for a variety of applications, such as $1.5 \mu\text{m}$ range photodetectors and device isolation in high speed signal processing. Nominally undoped epitaxial $\text{In}_{0.53}\text{Ga}_{0.47}\text{As}$ typically contains residual shallow impurities, rendering a net free electron concentration in excess of $1 \times 10^{15} \text{ cm}^{-3}$ [1]. The controlled introduction of transition metals has been used to incorporate deep levels for the compensation of these net shallow impurities. High resistivity $\text{In}_{0.53}\text{Ga}_{0.47}\text{As}$ has been grown using Fe [1]. The use of Cr, however, leads to the formation of a shallow donor-like center [2]. Transition elements generally exhibit a high thermal diffusion coefficient, and the resulting deep level concentrations may also be restricted due to solubility limit. We have considered the use of oxygen as an alternative route for the controlled formation of mid-gap states in $\text{In}_{0.53}\text{Ga}_{0.47}\text{As}$. Oxygen is known to be a common source of deep level centers in most semiconductors. Its presence in GaAs and especially $\text{Al}_x\text{Ga}_{1-x}\text{As}$ compensates shallow donors and reduces luminescence efficiency [3]. Recently, intentional oxygen incorporation into MOVPE GaAs with alkoxide precursors has been developed [4, 5], and has led to high quality GaAs with oxygen concentrations ranging from 10^{15} to 10^{20} cm^{-3} . The oxygen-related multiple deep levels within the GaAs bandgap [6] result in a room temperature resistivity greater than $5 \times 10^9 \Omega\text{-cm}$ [7] and sub-picosecond free carrier lifetime [8]. The major deep electron traps were determined to be at $\sim 0.75 \text{ eV}$ and $\sim 0.95 \text{ eV}$ below conduction band (E_c) [6]. Oxygen may therefore be a promising candidate for the formation of semi-insulating $\text{In}_{0.53}\text{Ga}_{0.47}\text{As}$.

We have extended the use of diethyl aluminum ethoxide (DEALO, $(\text{C}_2\text{H}_5)_2\text{AlOC}_2\text{H}_5$) [5] as a molecular dopant to intentionally co-introduce Al and O into MOVPE $\text{In}_x\text{Ga}_{1-x}\text{As}$. We have systematically grown a series of $\text{In}_x\text{Ga}_{1-x}\text{As}:\text{Si}:\text{O}$ samples with x at 0, 0.06, 0.12, 0.18, and 0.25 to follow the variation of electrical properties, as well as the deep level structure, as a function of In content. DEALO doping in $\text{In}_{0.53}\text{Ga}_{0.47}\text{As}$ was then performed. Similar approaches have been reported in the study of the intrinsic EL2 defect in nominally undoped $\text{In}_x\text{Ga}_{1-x}\text{As}$ grown by AsCl_3 vapor phase epitaxy process [9], MOVPE [10], and molecular beam epitaxy [11]. In general, the determination of the concentration and nature, as well as the control over such native defects are much more difficult than intentional doping. As a contrast,

the ability to manipulate the deep level impurity incorporation via DEALO doping in MOVPE process would provide us with a direct route for identifying the role of oxygen and its effects on the properties of $\text{In}_x\text{Ga}_{1-x}\text{As}$ as well as other compound semiconductors.

EXPERIMENTAL PROCEDURES

All samples were grown in a conventional horizontal low pressure (78 Torr) MOVPE reactor [5], using trimethyl gallium (TMGa), trimethyl indium (TMIn), and arsine (AsH_3). $\text{In}_x\text{Ga}_{1-x}\text{As}$ samples were grown on Si-doped n^+ (100) GaAs substrates with 2° off toward (110). Disilane (Si_2H_6) was employed for n-type Si doping, and DEALO was used for oxygen incorporation. The growth temperature was 600 °C and the V/III ratio was 40 to 60. A typical growth rate was 0.035 $\mu\text{m}/\text{min}$. A step-graded buffer layer was grown first before the thick $\text{In}_x\text{Ga}_{1-x}\text{As}$ layer (1 μm or more) to allow the growth of low dislocation density $\text{In}_x\text{Ga}_{1-x}\text{As}$ epilayers on GaAs. The growth details will be published elsewhere [12]. The In composition of the top thick $\text{In}_x\text{Ga}_{1-x}\text{As}$ layers was determined by electron microprobe analysis using GaAs and InAs wafers as standards. Measured In content was found to be very close (within 0.5% atomic composition) to the nominal value over the range of $0.06 \leq x \leq 0.53$.

The growth-property relationship was obtained by growing multilayer $\text{In}_x\text{Ga}_{1-x}\text{As}:\text{Si}:\text{O}$ samples with a growth sequence in which only the DEALO mole fraction was varied in a stepwise fashion. The growth temperature, V/III ratio, and Si_2H_6 mole fraction were kept constant throughout. Si doping together with oxygen is necessary to supply the background free carrier concentration for electrical measurements. The bottom and top layers of the samples were grown without DEALO and served as an internal standard in the same growth run. The physical concentration depth profiles of Al, O, and Si were obtained by secondary ion mass spectroscopy (SIMS). Electrical properties of these same samples were also studied by electrochemical capacitance-voltage (EC-V) profiling. Additional single layer ($\sim 1 \mu\text{m}$ thick) samples were grown on top of the grading layers for deep level transient spectroscopy (DLTS) measurements. Even with these grading layers, the possibilities of misfit dislocation-induced deep level states [13], acting as traps and affecting DLTS spectra, can not be completely ruled out. Therefore, complementary single layer $\text{In}_x\text{Ga}_{1-x}\text{As}:\text{Si}$ without DEALO were also grown as control samples. For DLTS measurements, back side Au/Ge/Ni/Ti/Au ohmic contacts were first alloyed to the n^+ GaAs substrates. Front side Au contacts were then deposited using a standard lithography and lift-off process. Due to the shrinkage of the $\text{In}_x\text{Ga}_{1-x}\text{As}$ bandgap at higher In content, the largest value of x was limited to 0.18 to ensure good rectifying behavior of the Au Schottky diode over the temperature range of investigation (77-410 K). Conventional DLTS scans were performed using double boxcar correlators [6].

RESULTS

Oxygen Incorporation Behavior in $\text{In}_x\text{Ga}_{1-x}\text{As}$

Multilayer samples of $\text{In}_x\text{Ga}_{1-x}\text{As}:\text{Si}:\text{O}$ were grown and studied with x at 0, 0.12, and 0.25. The $x = 0$ case would be the GaAs:Si:O material which we have previously reported [5]. The surface morphology on these lower In composition samples was specular. The use of a step graded buffer layer has, however, led to cross-hatching patterns, characteristic of dislocation

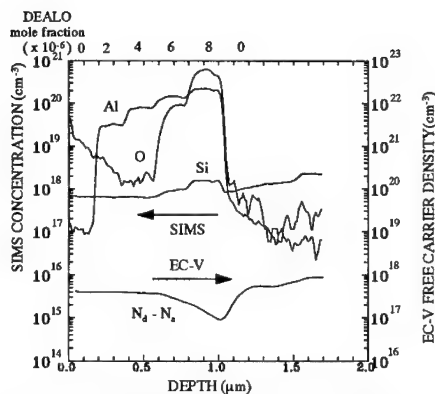


Fig. 1 The profiles of SIMS Al, O, and Si, and EC-V carrier concentration of an $\text{In}_{0.25}\text{Ga}_{0.75}\text{As:Si:O}$ multilayer sample grown at 600 °C and V/III ratio 60 with varying DEALO mole fractions.

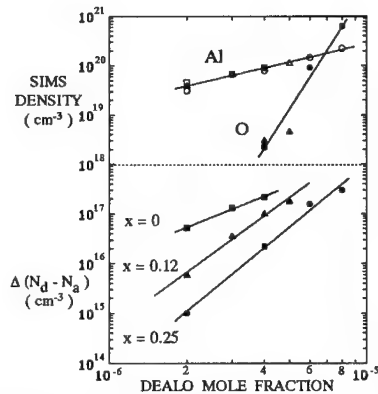


Fig. 2 The concentrations of Al and O and free carrier concentration reduction ($\Delta(N_d - N_a)$) as a function of DEALO mole fraction at different x in $\text{In}_x\text{Ga}_{1-x}\text{As:Si:O}$.

formation, on all our $\text{In}_x\text{Ga}_{1-x}\text{As}$ ($x > 0$) samples with smooth areas between the cross-hatching lines. Typical SIMS profiles of O, Al, and Si are shown in fig. 1 for $x = 0.25$. Stepwise increase of Al and O concentrations is noted as DEALO mole fraction was increased toward the substrate. SIMS detection limit for oxygen is $\sim 1 \times 10^{18} \text{ cm}^{-3}$, and the high oxygen densities in the surface layers were attributed to the contribution of particles present on the surface during SIMS profiling [14]. While Si_2H_6 mole fraction was kept constant throughout the growth of this sample, the Si profile in fig. 1 indicates that Si incorporation was slightly enhanced at higher DEALO mole fractions. The effect of DEALO mole fraction on the incorporation of O and Al into $\text{In}_x\text{Ga}_{1-x}\text{As:Si:O}$ is summarized in fig. 2. A linear dependence of the Al content on DEALO mole fraction is noted, independent of In composition, while the oxygen incorporation exhibits a highly non-linear power law relationship. Most of the oxygen densities in samples with $x = 0$ and 0.12 are beyond the SIMS detection limit. Oxygen content in fig. 2 is usually lower than that of Al, but exceeds that of Al at high DEALO mole fractions.

Similar multilayer growth approach was extended to $\text{In}_{0.53}\text{Ga}_{0.47}\text{As:Si:O}$. The surface of DEALO-doped $\text{In}_{0.53}\text{Ga}_{0.47}\text{As}$, however, was rough and textured which was visible to the naked eye as a surface haze. The rough surface has led to a smearing out, and subsequent degradation, in the depth resolution of the SIMS profiles [14], and only broad, non-abrupt profiles were obtained. Two additional 3 μm thick, single layer DEALO-doped $\text{In}_{0.53}\text{Ga}_{0.47}\text{As}$ samples were grown with low DEALO mole fraction at 1×10^{-6} and 2×10^{-6} . The surface was found to be partly hazy, indicating a non-uniform doping in $\text{In}_{0.53}\text{Ga}_{0.47}\text{As:O}$, and the size of the hazy area was also found to be increasing with DEALO mole fraction.

Electrical Properties of $\text{In}_x\text{Ga}_{1-x}\text{As:Si:O}$

Free electrons from Si donors in $\text{In}_x\text{Ga}_{1-x}\text{As}$ were found to be compensated due to DEALO doping. A comparison between SIMS and EC-V profiles in fig. 1 clearly correlates the

reduction of free carrier concentration ($\Delta n = n_{\text{no oxygen}} - n_{\text{with oxygen}}$) with the increase in oxygen content. For $\text{In}_x\text{Ga}_{1-x}\text{As}$ with $x = 0, 0.12$, and 0.25 , Si_2H_6 mole fractions in all samples were adjusted so that free carrier densities of the top $\text{In}_x\text{Ga}_{1-x}\text{As:Si}$ layers were all $\sim 3\text{--}4 \times 10^{17} \text{ cm}^{-3}$. A higher DEALO mole fraction was found to be required to produce a similar Δn , as illustrated in fig. 2, when x was increased. A non-linear power law dependence of Δn on DEALO mole fraction in all samples is also noted, indicating that the observed compensation is more related to oxygen than to Al. Given the Al contents, as shown in fig. 2 to be independent of x , and the available oxygen concentration data from SIMS analysis in fig. 2, the incorporation of oxygen from DEALO should also be independent of x . The change in the degree of compensation with In composition would then be related to the variation in the depth and concentration of the oxygen related deep levels.

EC-V profiling on a similar multilayer $\text{In}_{0.53}\text{Ga}_{0.47}\text{As:Si:O}$ sample with hazy surface morphology indicates that the layers doped with DEALO has a higher free carrier density than those of non-DEALO doped. One possible reason for this observation would be the enhanced Si incorporation due to DEALO doping as seen in the Si SIMS profile in fig. 1. Additionally, a change in oxygen deep level structure in the bandgap of $\text{In}_{0.53}\text{Ga}_{0.47}\text{As}$ could also be responsible. Hall measurements on the specular parts of the single layer DEALO-doped only $\text{In}_{0.53}\text{Ga}_{0.47}\text{As}$ samples have led to room temperature electron density $\sim 1 \times 10^{16} \text{ cm}^{-3}$, mobility $\sim 3000 \text{ cm}^2/\text{V sec}$, and resistivity $\sim 0.2 \Omega\text{-cm}$, similar to the results of undoped $\text{In}_{0.53}\text{Ga}_{0.47}\text{As}$. The resistivity on the hazy parts, however, was found to decrease by a factor ~ 10 .

Oxygen-related deep levels associated with the observed compensation in fig. 2 were investigated by performing DLTS analysis on a series of single layer $\text{In}_x\text{Ga}_{1-x}\text{As:Si:O}$ samples for x equal to 0, 0.06, 0.12, and 0.18. Complementary DLTS scans were also carried out on a series of no-oxygen doped $\text{In}_x\text{Ga}_{1-x}\text{As:Si}$ samples with the same x values and Si concentrations. No DLTS peak was detected over the temperature range of scan in these Si-doped control samples, indicating that the effects of dislocation or strain induced deep levels on the DLTS spectra are not significant in non-DEALO-doped $\text{In}_x\text{Ga}_{1-x}\text{As}$. The intrinsic EL2 defect with concentration $\leq 1.5 \times 10^{14} \text{ cm}^{-3}$ [10] is beyond our DLTS detection limit at the doping level $\sim 3 \times 10^{17} \text{ cm}^{-3}$. Features in DLTS spectra of $\text{In}_x\text{Ga}_{1-x}\text{As:Si:O}$ can thus be attributed exclusively to DEALO doping. Typical DLTS spectra are shown in fig. 3 with rate windows at 11.6 and 1162.8 sec^{-1} . Activation energies for peaks in fig. 3 were obtained through the standard Arrhenius plots [6]. Assuming negligible capture barrier heights, these activation energies are taken to be the energy differences between E_c and deep levels. All DLTS spectra in fig. 3 were adjusted to produce a comparable DLTS signal levels. The factors of adjustment, as labeled in fig. 3 and reflecting the difference in deep level concentrations, are found to be consistent with the differences in $\Delta(N_d - N_a)$ as shown in table I.

The DLTS spectrum of $x = 0$ (fig. 3 (a)) is essentially the same as what we have previously reported [6], with major deep levels at $E_c - 0.73$ (#2) and 0.93 (#1) eV along with some other minor levels at $E_c - 0.53$ (#3) and 0.31 eV. Similar multiple oxygen-related deep levels were also found to be present at $x = 0.06$, as shown in spectrum (b1) of fig. 3 with a major peak #2 at $E_c - 0.66$ eV and two other shoulder peaks (#3 at $E_c - 0.48$ eV, and #1 of which the exact energy level not resolved). A comparison between spectra (a) and (b1) indicates that, as the bandgap was decreased upon alloying with In, the general shape of the DLTS spectrum was essentially unchanged with #2 remaining as the major peak, but the emission energies (to E_c) of all deep levels were reduced. A similar trend was also observed in fig. 3 when x was increased to 0.12

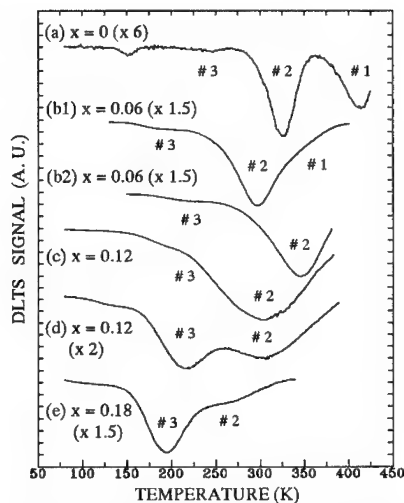


Fig. 3 DLTS spectra of $\text{In}_x\text{Ga}_{1-x}\text{As:Si:O}$ with $x =$ (a) 0, (b1) 0.06, (b2) 0.06, (c) 0.12, (d) 0.12, and (e) 0.18. Measurement conditions for (a) and (b1) are : reverse bias -1 V, pulse height 1 V, width 0.1 ms, period 500 ms, rate window 11.6 sec^{-1} . Measurement conditions for (b2), (c), (d) and (e) are : reverse bias -0.5 V, pulse height 0.5 V, width 0.1 ms, period 20 ms, rate window 1162.8 sec^{-1} .

Table I. $\text{In}_x\text{Ga}_{1-x}\text{As}$ DLTS samples in fig. 3. $N_d - N_a$ were determined by EC-V measurements and in the unit of $1 \times 10^{17} \text{ cm}^{-3}$.

x	$N_d - N_a$ (Si only)	DEALO mole fraction ($\times 10^{-6}$)	$N_d - N_a$ (Si/O)	$\Delta(N_d - N_a)$
(a) 0	1.0	0.75	0.6	0.4
(b) 0.06	3.5	3	2.0	1.5
(c) 0.12	3.0	5	0.5	2.5
(d) 0.12	3.0	4	1.8	1.2
(e) 0.18	4.1	5	2.4	1.7

(peak #2 and #3 at $E_c - 0.60$ and 0.46 eV) and 0.18 (peak #2 and #3 at $E_c - 0.54$ and 0.41 eV). The effect of oxygen doping level on deep level structure is also illustrated in fig. 3 where the DEALO mole fraction was varied in two otherwise identical $x = 0.12$ samples ((c) and (d) in table I). Two major peaks, #2 and #3, exhibit a shift in relative peak heights, and this shift is directly related to the change in DEALO doping level. This observation is very similar to the GaAs:Si:O case (fig. 3 (a)) where the height of peak #2 would be reduced relative to peak #1 at lower DEALO mole fraction [6]. The DLTS spectral comparison of $x = 0.12$ and $x = 0.18$ indicates that peak #3 dominated over peak #2 at $x = 0.18$.

DISCUSSION

The smooth shift in DLTS peak energy in fig. 3 suggests that the same set of defect configurations or charge states are responsible for the DLTS peaks in samples with different In content, similar to the case of EL2 defect in undoped $\text{In}_x\text{Ga}_{1-x}\text{As}$ [9, 10, 11]. We have therefore labeled the corresponding peaks accordingly in fig. 3. We have previously attributed the observed multiple peaks in GaAs:Si:O to the variations in local defect atomic configurations, specifically the number of Al nearest neighbors to oxygen [6]. A recent study [15] on intentional oxygen doping of GaAs using dimethylaluminum methoxide has reported similar DLTS spectra as in fig. 3 (a), and assigned peak #3 as an isolated off-center substitutional oxygen (Ga-O-Ga). The major traps, peaks #2 and #1, were attributed to complexes of Al and O involving two and one Al atom respectively. In both studies,

oxygen is incorporated through the Al-O molecular doping precursors. The weaker In-O bond (86 kcal/mole), when compared to the Al-O (121.3 kcal/mole) or Ga-O (91 kcal/mole) [16],

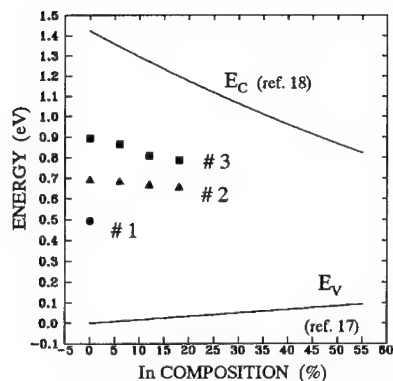


Fig. 4. Deep level structure evolution of $\text{In}_x\text{Ga}_{1-x}\text{As:Si:O}$ based on DLTS results. All energies referenced on GaAs E_v .

would indicate that the oxygen-related defect should still be dominated by the local configuration of Al-O bonds in DEALO-doped $\text{In}_x\text{Ga}_{1-x}\text{As}$.

Based on DLTS results of this study, InAs/GaAs valence band (E_v) offset at 0.17 eV [17], and the bandgap energy of $\text{In}_x\text{Ga}_{1-x}\text{As}$ at 300 K [18], the deep level evolution of $\text{In}_x\text{Ga}_{1-x}\text{As:Si:O}$ as x is increased is depicted in fig. 4 relative to E_v of GaAs. The deep levels #2 and #3 appear to remain relatively constant with respect to E_v , in contrast to the rapid decrease in E_c of $\text{In}_x\text{Ga}_{1-x}\text{As}$ with x . The relative invariance of the oxygen-induced deep level states with respect to E_v could have resulted in the reduced compensation in $\text{In}_x\text{Ga}_{1-x}\text{As}$ ($0 \leq x \leq 0.25$) with larger x , and the high electron concentration in $\text{In}_{0.53}\text{Ga}_{0.47}\text{As}$, as one or more of these deep levels become resonant with E_c .

CONCLUSION

The defect engineering in MOVPE $\text{In}_x\text{Ga}_{1-x}\text{As}$ by controlled oxygen doping using DEALO was studied. DEALO doping has led to the incorporation of Al and O, and the compensation of shallow Si donors in $\text{In}_x\text{Ga}_{1-x}\text{As:Si}$ with $0 \leq x \leq 0.25$. DLTS analysis on a series of $\text{In}_x\text{Ga}_{1-x}\text{As:Si:O}$ samples with $0 \leq x \leq 0.18$ showed that oxygen incorporation led to a set of deep levels, similar to those found in DEALO doped GaAs. The characteristic deep levels appear to remain at a relatively constant energy with respect to the valence band.

ACKNOWLEDGMENTS

The authors would like to thank Chingfu Lin for carrying out the electron microprobe analysis. Financial supports of this work are provided by Army Research Office, Naval Research Laboratory, and the National Science Foundation under DMR-9201558.

REFERENCES

1. A. R. Clawson, D. P. Mullin, and D. I. Elder, *J. Crystal Growth* **64**, 90 (1983).
2. M. V. Rao and P. K. Bhattacharya, *J. Appl. Phys.* **57**, 333 (1985).
3. Wallis, R. H., M-A di Forte Poisson, M. Bonnet, G. Beuchet and J-P Duchemin, *Inst. Phys. Conf. Ser.*, **56**, 73 (1981).
4. M.S. Goorsky, T.F. Kuech, F. Cardone, P.M. Mooney, G.J. Scilla, and R.M. Potemski, *Appl. Phys. Lett.* **58**, 1979 (1991).
5. J. W. Huang, D. F. Gaines, T. F. Kuech, R. M. Potemski, and F. Cardone, *J. Electron. Mater.* **23**, 659 (1994).
6. J. W. Huang and T. F. Kuech, *Appl. Phys. Lett.* **65**, 604 (1994).
7. J. W. Huang and T. F. Kuech, *J. Crystal Growth* **145**, 462 (1994).
8. M. Y. Frankel, J. W. Huang, and T. F. Kuech, *Appl. Phys. Lett.* **66**, 634 (1995).
9. A. Mircea, A. Mitonneau, J. Hallais, and M. Jaros, *Phys. Rev. B*, **16**, 3665 (1977).
10. R. V. Lang, J. D. Leslie, J. B. Webb, A. P. Roth, M. A. Sacilotti, and R. A. Masut, *Can. J. Phys.* **67**, 283 (1989).
11. A. C. Irvine and D. W. Palmer, *Phys. Rev. Lett.* **68**, 2168 (1992).
12. J. W. Huang, J. M. Ryan, K. L. Bray, and T. F. Kuech (unpublished).
13. A. Raisanen, L. J. Brillson, R. S. Goldman, K. L. Kavanagh, and H. Wieder, *J. Electron. Mater.* **23**, 929 (1994).
14. M. S. Denker (private communication).
15. Y. Park and M. Skowronski, *J. Appl. Phys.* **76**, 5813 (1994).
16. *CRC Handbook of Chemistry and Physics*, 65th ed. (CRC Press, Inc., Boca Raton, Florida, 1984).
17. S. P. Kowalczyk, W. J. Schaffer, E. A. Kraut and R. W. Grant, *J. Vac. Sci. Technol.* **20**, 705 (1982).
18. P. W. Yu, B. Jogai, T. J. Rogers, P. A. Martin, and J. M. Ballingall, *Appl. Phys. Lett.* **65**, 3263 (1994).

THE ULTRAFAST CARRIER DYNAMICS IN SEMICONDUCTORS: THE ROLE OF DEFECTS

P.M. Fauchet,^(a,b) G.W. Wicks,^(b) Y. Kostoulas,^(c) A.I. Lobad^(c) and K.B. Ucer^(a)
Laboratory for Laser Energetics, University of Rochester, Rochester NY 14623

ABSTRACT

The presence of point defects is expected to influence the properties of free carrier in semiconductors. We have used the techniques of ultrafast laser spectroscopy to characterize the dynamics of photoinjected carriers in several III-V semiconductors grown at low temperature. The initial scattering time and the lifetime of the carriers become very short at low growth temperatures. Results obtained with low-temperature grown III-Vs are compared to those obtained with III-Vs grown at normal temperatures and amorphous silicon.

INTRODUCTION

Many semiconductor optoelectronic devices such as photoconductive switches and photodetectors must operate in the multi-GHz regime. This requires a photoinjected carrier lifetime or trapping time of ~ 1 picosecond, which can be achieved by appropriate defect engineering. There are at least two important challenges. One is to identify the defects that not only produce such an ultrafast response time but also yield acceptable electrical properties and acceptable long-term stability. The second is to understand the detailed role of the defects and eventually manipulate them to achieve the desired functionality. We report some of the results of a large-scale study of the ultrafast carrier dynamics in semiconductors containing specific defects. Femtosecond time-resolved luminescence and photoinduced absorption measurements have been performed using several laser sources tunable from the ultraviolet to past $1.5 \mu\text{m}$. We present and discuss results obtained mostly on low-temperature (LT) grown III-V semiconductors, including GaAs, InGaAs, InP, and InGaP. Despite large differences in key properties such as the dark conductivity and position of the defect levels, the ultrafast optical response of these materials is surprisingly similar. In particular, we focus on the decrease of the carrier lifetime as the growth temperature decreases and the differences in the properties of free carriers between LT III-Vs and normally-grown III-Vs. Some qualitative similarities between the behavior of LT III-Vs and that of silicon samples containing a large number of defects, such as a-Si:H, $\mu\text{c-Si}$ and porous Si, are pointed out.

LOW-TEMPERATURE GROWN III-Vs.

For epitaxial growth of III-V semiconductors, the substrate temperature T_s is one of the most important parameters that control the growth mechanism and the quality of the layers. The standard growth temperature is near 600°C for GaAs and many other III-Vs. When T_s is lowered towards 200°C in GaAs, the layer remains crystalline but the mobility and carrier lifetime decrease substantially [1]. When T_s is around 200°C , the film contains approximately 1% excess arsenic and contains a large density of defects (mostly arsenic antisites, at the level of greater than 10^{19} cm^{-3}). After annealing above 600°C under an arsenic overpressure, the properties of LT GaAs are a dark resistivity of $10^6 \Omega\cdot\text{cm}$, a breakdown field of $5 \times 10^5 \text{ V}\cdot\text{cm}^{-1}$, a trap density of 10^{19} cm^{-3} , and a carrier lifetime below 1 ps. Annealed LT GaAs also contains arsenic clusters which may play a role in achieving these properties. Because of the short carrier lifetime, this material is attractive for devices where the response time must be in the picosecond time domain and at least one commercial device made of LT GaAs is available [2], for detection of ultrashort optical pulses having a photon energy above the bandgap of GaAs ($E_g = 1.4 \text{ eV}$).

It would be highly desirable to have other LT III-Vs. For example LT InGaAs lattice matched to InP could be used for high speed photodetectors that can detect $1.5 \mu\text{m}$ light, which is the wavelength of choice for long distance, high speed optical fiber communications. We have grown several LT III-Vs, including LT GaAs ($E_g = 1.4 \text{ eV}$), InP ($E_g = 1.3 \text{ eV}$), LT InGaP lattice matched to

GaAs ($E_g = 1.9$ eV), and LT InGaAs lattice matched to InP ($E_g = 0.73$ eV). Although, as we will demonstrate, the fast optical response of the four LT III-Vs are similar, many of their other properties are different. Both LT GaAs and InGaP [3] have a large dark resistivity, whereas LT InGaAs is n-type with a concentration of $\sim 10^{17}$ cm $^{-3}$ [4] and LT InP is n-type with a concentration well above 10^{18} cm $^{-3}$ [5]. The difference in residual carrier concentration results from the position of the defect levels. For example, in LT GaAs, the dominant defect is the arsenic antisite and it is located near the mid gap, whereas in LT InP, a phosphorus antisite related donor level appears to be degenerate with the conduction band. Note however that only LT GaAs has been studied extensively and that the precise assignment of defect levels in all other LT III-Vs remains unknown.

SAMPLES

The samples were grown by molecular beam epitaxy at temperatures between their respective normal growth temperatures and temperatures as low as $\sim 150^\circ\text{C}$. The LT GaAs films were grown under the standard LT growth conditions. A sacrificial AlGaAs layer was grown between the GaAs substrates and the LT GaAs films, and the LT GaAs films were separated from their substrate by the lift-off technique [6]. The $0.2\text{ }\mu\text{m}$ -thick LT InP films were grown at 200°C and 300°C [7]. A $0.5\text{ }\mu\text{m}$ $\text{In}_{0.53}\text{Ga}_{0.47}\text{As}$ sacrificial layer was grown between the InP substrates and the LT InP films, and the LT InP films were separated from their substrate by the same lift-off technique. The LT $\text{In}_{0.53}\text{Ga}_{0.47}\text{As}$ films were grown at various temperatures ranging from 600°C to 200°C . Because the InP substrate is transparent to InGaAs bandgap radiation, the LT InGaAs layers were not detached from their substrates. Some films were subjected to an annealing step at a modest temperature and other films were intentionally doped with Be. The film thickness varied from $< 1\text{ }\mu\text{m}$ to $> 3\text{ }\mu\text{m}$. The LT InGaP films were grown at 200°C and 300°C on GaAs wafers which were then selectively etched [8]. Part of the 200°C film was subjected to an annealing step at a modest temperature. The film thickness varied from $0.5\text{ }\mu\text{m}$ to $1\text{ }\mu\text{m}$. LT GaAs has been observed to become polycrystalline or even amorphous at film thicknesses of $0.2\text{ }\mu\text{m}$ to $2\text{ }\mu\text{m}$ depending on the growth conditions, as seen by electron microscopy, X-ray diffraction and electron diffraction [9]. All layers reported in this study were single crystalline. Figure 1 presents the Raman spectrum of a very thick LT GaAs grown with a small amount of P to make it lattice-matched to the GaAs substrate. The Raman spectrum is typical of a high-quality single-crystal with the (100) orientation.

EXPERIMENTS

Three femtosecond light sources were used in our experiments: a colliding-pulse mode-locked (CPM) dye laser, amplified by a copper vapor laser, an additive-pulse modelocked (APM) NaCl laser, amplified by a Nd:YAG laser, and a self-modelocked titanium sapphire (Ti:S) laser. The CPM laser produces 100 fs pulses, centered at 2 eV (620 nm), at a repetition rate of 100 MHz. After amplification at 8.5 kHz, the pulses can be used to produce a white light continuum from which 100 fs long pulses with a wavelength from 550 nm to 850 nm can be selected. The APM laser produces 200 fs pulses, tunable between $1.5\text{ }\mu\text{m}$ and $1.65\text{ }\mu\text{m}$, at a repetition rate of 76 MHz. After amplification at 1 kHz, the pulses can be used to produce a white light continuum from which 200 fs long pulses with a wavelength from the visible range to past $2\text{ }\mu\text{m}$ can be selected. The Ti:S laser produces sub-100 fs pulses, tunable between 800 nm and 880 nm, at a repetition rate of 85 MHz. These pulses are not amplified.

Our typical configuration is the pump-probe geometry. The pump, chosen to be above the bandgap of the LT III-V, injects electrons and holes in the conduction and valence bands respectively. The transient changes in optical properties induced by photoinjection, most notably the changes in transmission, are recorded as a function of time following photoinjection by monitoring the change in transmission of a probe beam. Since the pump and probe beams are generated from the same laser pulse, they are synchronized and thus the time delay between the pump and the probe is simply set by increasing the probe beam path. With the CPM and APM systems, the probe wavelength can be tuned independently of the pump wavelength, allowing simultaneous temporal and spectral spectroscopy. In all these experiments, the ultimate time resolution is set by the pulse duration. One additional series of experiments was performed in the time-resolved photoluminescence up-conversion arrangement. In this case, the luminescence emitted by the

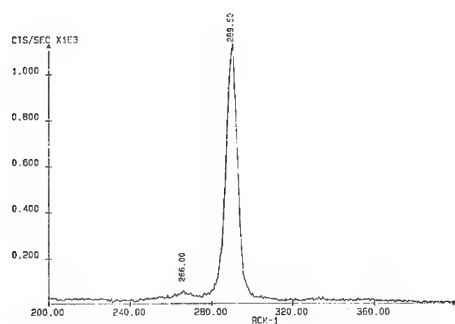


Figure 1
Raman spectrum of a 5 μm -thick LT GaAs that contains just enough P to make it lattice-matched to the GaAs substrate. The ratio between the LO and TO phonon intensities shows that the film maintains the (100) orientation of the substrate and is of high crystalline quality.

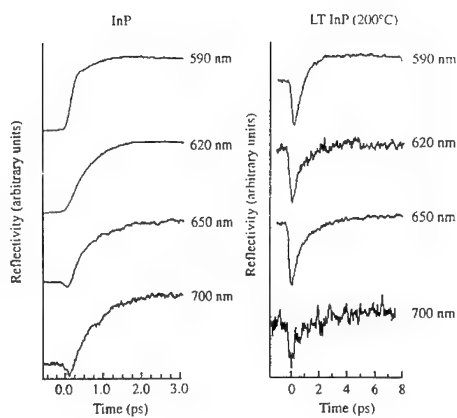


Figure 2
Transient reflectivity data obtained from NG InP and LT InP. The pump is at 620 nm (2 eV) and the probe wavelength varies. A spectral hole burning near $t=0$ ps is seen only in the NG InP.

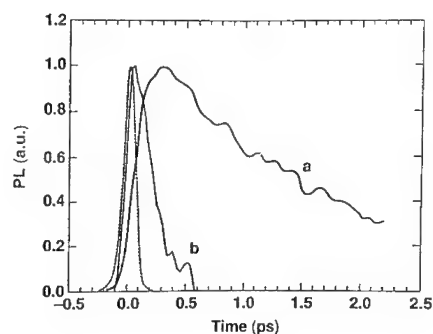


Figure 3
Transient luminescence data obtained from InP grown at (a) 300°C and (b) 200°C. The dashed line shows the pump pulse. For the 200°C sample, the rise time appears to be instantaneous and the decay is much faster.

recombination of electrons and holes following photoinjection with a 100 fs, 2-eV pulse is mixed in a nonlinear crystal with another part of the pump pulse that is appropriately delayed. As a result, the decay of the photoluminescence can be measured with 100 fs time resolution.

RESULTS

Figure 2 contrasts pump-probe reflectivity measurements performed on normally-grown (NG) and LT InP after photoinjection with a 2-eV pump [10]. In LT InP, all the traces are qualitatively similar, independent of the probe wavelength. In contrast, the response of the NG InP is probe wavelength dependent during the first 100-200 fs: at probe wavelengths longer than the pump wavelength, the reflectivity first decreases, whereas at probe wavelengths shorter than the pump wavelength the reflectivity increases immediately. As discussed in Ref. 10, the reflectivity traces of NG InP are typical of a short-lived hole burning, produced by the fact that it takes ~ 100 fs for the photoinjected carriers to leave the conduction and valence band states where they are produced. We call this time the dwell time. The lack of hole burning in LT InP seen in reflection (Fig. xx) and transmission (Ref. 7) suggests that the dwell time is much shorter than the pulse duration of 100 fs.

The results of the up-conversion luminescence measurements performed on LT InP and shown in Figure 3 support this conclusion [7]. The luminescence efficiency, measured at the peak of the spectrum near 880 nm, is lower by one order of magnitude in the 200°C sample because the incorporation of more phosphorus produces a larger density of point defects. The luminescence decays exponentially with a time constant of 0.5 ps for the 200°C sample and 1.6 ps for the 300°C sample. This time constants describe carrier trapping and not recombination, as can be seen from the pump-probe measurements [7]. The rise time of the bandgap luminescence is instantaneous, despite the fact that the carriers are injected high in the band. This indicates that a large number of electrons (holes) reach the bottom (top) of the conduction (valence) band within 100 fs or less. In NG III-Vs, the rise time of photoluminescence can be as long as 1 ps or more [11], because elastic scattering and inelastic scattering of carriers with phonons takes place on a time scale of 150 fs.

These results suggest that the presence of point defects not only reduces the free carrier lifetime but also strongly affects the properties of the carriers while they are in extended states. Because LT InP is n-type however it could be suggested that the extremely fast dwell time in fact results from electron-plasmon collisions, which have been demonstrated to lead to dwell times as short as 10 fs [12]. In order to check this hypothesis, femtosecond pump-probe experiments have been performed on other LT III-V. Figure 4 compares the photoinduced absorption measured near the bandgap of two LT GaAs samples after pumping at 2 eV. We observe that most of the photoinjected carriers reach the bottom of the band in a time that is ~ 100 fs in the 195°C sample and becomes comparable to what is seen in NG GaAs as the growth temperature increases. Thus, in LT GaAs, the presence of point defects decreases the dwell time to < 100 fs. Experiments performed on LT InGaP [8] and LT InGaAs lead to qualitatively similar conclusions.

One question that may be asked is what is the density of point defects necessary to have a strong influence on the properties of carriers in the extended states. It is difficult to answer this question accurately because the density and the nature of the point defects are not easy to establish. We have performed femtosecond optical experiments that answer a related question, namely what is the density of defects that can trap a carrier. Figure 5 shows pump-probe transmission data obtained with near bandgap excitation in LT InGaAs for different photoinjected carrier densities. At low injected carrier density, the carrier lifetime is short because of efficient trapping on a subpicosecond time scale. As the injected carrier density increases, the traps become saturated and the apparent carrier lifetime increases. From this measurement, we estimate that the "active" trap concentration is $> 5 \times 10^{18} \text{ cm}^{-3}$ in this LT InGaAs sample.

DISCUSSION

The fact that point defects have a strong influence on the properties of free carriers in III-V semiconductors is not surprising when one considers that the presence of a large density of traps has the same effect in silicon. In the past, we have conducted systematic measurements of the properties of photoinjected carriers in a-Si:H [13] and $\mu\text{-Si}$ [14], and recently we have extended these

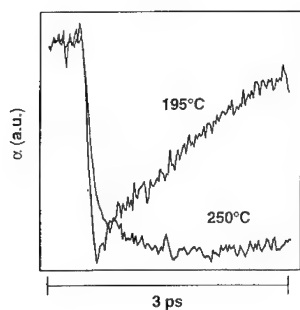


Figure 4

Comparison between the photoinduced changes in absorption measured at 890 nm, near the bandgap of LT GaAs grown at two temperatures. The rise time in the bleaching signal appears to be instantaneous for the 195°C sample, while it develops over ~ 1 ps for the 250°C sample GaAs.

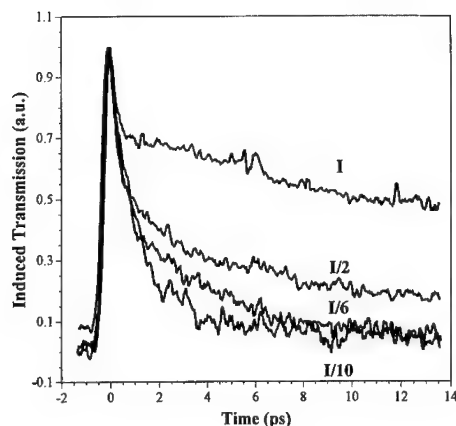


Figure 5

Transient transmission changes induced LT InGaAs for different pump intensities. The pump and the probe are 70 meV above the bandgap of NG InGaAs. The sample was Be doped and annealed at 450°C for 10 minutes. The photoinduced carrier density corresponding to the slowing down of the recovery produced by trap saturation is estimated to be $\sim 10^{19} \text{ cm}^{-3}$.

measurements to porous Si [15]. These three types of Si contain a large number of defects and exhibit a free carrier lifetime ranging from ~ 100 ps to < 1 ps. In a-Si:H, a material that contains $\sim 10^{19} \text{ cm}^{-3}$ bandtail states and $\sim 10^{16} \text{ cm}^{-3}$ midgap states, we have measured an initial scattering time of the order of 1 fs [16] and an energy relaxation rate approximately 10 times faster than in crystalline silicon [17]. These results are consistent with what has been presented in this paper: an ultrafast initial scattering time spreads the carrier distribution throughout the band and eliminates spectral hole burning, whereas an ultrafast energy relaxation time pushes the hot carriers toward the bottom of the band and leads to immediate near bandgap bleaching and luminescence. To go beyond a phenomenological interpretation of our results is beyond the scope of this paper, as this would require a detailed knowledge of the properties of the defects.

In conclusion, we have performed a systematic study of the femtosecond optical response of various LT III-V semiconductors and found many similarities among them, including a large influence of point defects on the properties of free carriers. A. Lobad and B. Ucer acknowledge financial support by the Frank Horton Fellowship program.

REFERENCES

- (a) also with the Department of Electrical Engineering
- (b) also with The Institute of Optics
- (c) also with the Department of Physics & Astronomy
- [1] *Low temperature (LT) GaAs and related materials*, G.L. Witt et al editors, Mat. Res. Soc. Symp. Proc. **241** (Pittsburgh, PA, 1992).
- [2] The photodetector is manufactured by Picometrix and commercialized by Newport Co.
- [3] D.C. Look, Y. He, J. Ramdani, N. El-Masry and S.M. Bedair, Appl. Phys. Lett. **63**, 1231 (1993).
- [4] B.C. Tousley, S.M. Mehta, A.I. Lobad, P.J. Rodney, P.M. Fauchet and P.Cooke, J. Electron. Mater. **22**, 1477 (1993).
- [5] P. Dreszer, W. M. Chen, D. Wasik, R. Leon, W. Walukiewicz, B. W. Liang, C. W. Tu and E. R. Weber, J. Electron. Mater. **22**, 1487, (1993).
- [6] T. Gong, W.L. Nighan, Jr. and P.M. Fauchet, Appl. Phys. Lett. **57**, 2713 (1990).
- [7] Y. Kostoulas, L.J. Waxer, I.A. Walmsley, G.W. Wicks and P.M. Fauchet, Appl. Phys. Lett. **66**, 1821 (1995).
- [8] Y. Kostoulas, K.B. Ucer, G.W. Wicks and P.M. Fauchet, submitted for publication.
- [9] A. Claverie, K.M. Yu, W. Swider, Z. Liliental-Weber, M. O'Keefe, R. Kilaas, J. Pamulapati and P.K. Bhattacharya, Appl. Phys. Lett. **60**, 989 (1992).
- [10] Y. Kostoulas, T. Gong, B.C. Tousley, G.W. Wicks, P. Cooke and P.M. Fauchet, in *Ultrafast Phenomena in Semiconductors*, edited by D.K. Ferry and H. van Driel (SPIE, Bellingham, WA, 1994), SPIE Proc. **2142**, p 100.
- [11] J. Shah, D. Deveaud, T.C. Damen, W.T. Tsang, A.C. Gossard and P. Lugli, Phys. Rev. Lett. **59**, 222 (1987).
- [12] T. Gong, P. Mertz, W.L. Nighan, Jr. and P.M. Fauchet, Appl. Phys. Lett. **59**, 712 (1991).
- [13] P. M. Fauchet, D. Hulin, R. Vanderhaghen, A. Mourchid and W. L. Nighan, Jr., J. Non-Cryst. Solids **141**, 76 (1992).
- [14] N. K. Bambha, W. L. Nighan, Jr., I. H. Campbell, P. M. Fauchet and N. M. Johnson, J. Appl. Phys. **63**, 2316 (1988).
- [15] P. M. Fauchet, Mat. Res. Soc. Symp. Proc. **358**, 525 (1995).
- [16] A. Mourchid, D. Hulin, C. Tanguy, R. Vanderhaghen, W. L. Nighan, Jr., K. Gzara and P. M. Fauchet, Solid State Commun. **74**, 1197 (1990).
- [17] D. Hulin, A. Mourchid, P. M. Fauchet, W. L. Nighan, Jr. and R. Vanderhaghen, J. Non-Cryst. S & **138**, 527 (1991).

**DEPENDENCE OF SHEET HOLE CONCENTRATIONS ON
GROWTH KINETICS OF A CARBON DOPED ELECTRON BEAM
HEATED GRAPHITE SOURCE IN GaAs AND $\text{Al}_{0.3}\text{Ga}_{0.7}\text{As}$ FILMS
GROWN BY SOLID SOURCE MBE**

D.L. SATO, F.J. SZALKOWSKI AND H.P. LEE

Department of Electrical and Computer Engineering, University of California, Irvine, CA
90715

ABSTRACT

A series of carbon delta- and uniformly- doped GaAs and $\text{Al}_{0.3}\text{Ga}_{0.7}\text{As}$ films have been grown by solid source Molecular Beam Epitaxy using an electron-beam heated graphite rod as the dopant source. In contrast to heated filament carbon sources, this electron-beam source produces atomic carbon C_1 , rather than C_3 as the predominant species. The purpose of these experiments was to compare measured sheet carrier concentration of delta-doped GaAs and $\text{Al}_{0.3}\text{Ga}_{0.7}\text{As}$ films under fixed growth conditions and with similar carbon beam fluxes using this electron-beam source. The films were characterized by Hall-effect measurements. The $\text{Al}_{0.3}\text{Ga}_{0.7}\text{As}$ films have consistently higher hole sheet carrier concentrations than GaAs films with similar carbon fluxes. Delta-doped $\text{Al}_{0.3}\text{Ga}_{0.7}\text{As}$ sheet carrier concentrations of up to $2.2 \times 10^{13} \text{ cm}^{-2}$ were measured, and thin uniformly-doped $\text{Al}_{0.3}\text{Ga}_{0.7}\text{As}$ carrier densities were measured up to $5.7 \times 10^{20} \text{ cm}^{-3}$. The uniformly doped $\text{Al}_{0.3}\text{Ga}_{0.7}\text{As}$ films appear to have higher atomic carbon activation than this delta-doped $\text{Al}_{0.3}\text{Ga}_{0.7}\text{As}$ films. These results can be possibly explained in terms of several concurrent processes involving C-C pairing, stronger Al-C bonding, and dopant surface segregation taking place on the growth surface of the delta-doped layer. Photoluminescence intensity measurements of uniformly-doped GaAs shows degradation at hole concentrations greater than 10^{18} cm^{-3} and bandgap contraction at hole densities greater than mid 10^{18} cm^{-3} .

INTRODUCTION

In recent years, carbon doping in GaAs and $\text{Al}_x\text{Ga}_{1-x}\text{As}$ has been increasingly studied as an attractive replacement to Be as a p-type dopant. Previous studies have used a resistively heated graphite filament in MBE^{1,2} or carbon containing gas molecules in MOMBE³, CBE⁴, and MOCVD⁵ as a p-type dopant source. In this study, a unique electron-beam heated, graphite rod source^{6,7}, where atomic carbon is the predominate species is used to delta- and uniformly- dope GaAs and $\text{Al}_{0.3}\text{Ga}_{0.7}\text{As}$. This allows the effects of atomic carbon deposition on the surface to be studied. It has previously been shown using carbon filament sources, that a higher value of x in $\text{Al}_x\text{Ga}_{1-x}\text{As}$ resulted in increased hole densities⁸. In this experiment, measured carbon delta-doped GaAs hole sheet carrier concentrations are compared with $\text{Al}_{0.3}\text{Ga}_{0.7}\text{As}$ using this particular carbon electron-beam source. Measured uniformly-doped $\text{Al}_{0.3}\text{Ga}_{0.7}\text{As}$ layer hole density is also converted to equivalent two-dimensional sheet carrier concentrations and are compared to delta-doped $\text{Al}_{0.3}\text{Ga}_{0.7}\text{As}$ layers formed by growth interruption. The uniformly-doped GaAs photoluminescence intensity is measured and the effective bandgap narrowing effect is calculated.

EXPERIMENTAL

The carbon-doped GaAs and $\text{Al}_{0.3}\text{Ga}_{0.7}\text{As}$ layers were grown on indium-free (100) semi-insulating GaAs substrates mounted in a standard III-V Varian GEN II MBE apparatus. A

graphite rod-fed e-beam source was mounted on a 4.5 inch diameter flange located below the III-V source flange and liquid nitrogen cryoshroud. This arrangement has been described elsewhere⁹. Figure 1 shows a schematic diagram of the MBE system used in this experiment.

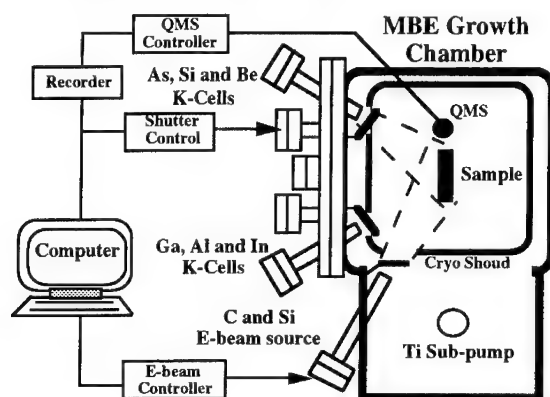


Figure 1. Schematic MBE system showing electron beam sources, III-V sources and computer arrangement.

The quadrupole mass spectrometer (QMS) has a line-of-sight to the graphite source and allows the carbon beam flux to be monitored during deposition of doped layers. The e-beam source acceleration voltage was maintained at 3.6KV while the deposition beam current was varied from 100mA to 170mA. Before epitaxial layers were deposited, the graphite rod was heated for five minutes at 5mA above the maximum deposition beam current to outgas contaminants. Figure 2 shows a typical QMS signal measured during the graphite outgassing process.

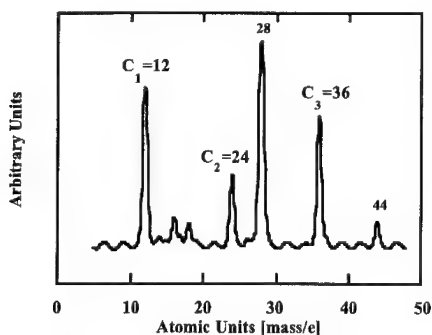


Figure 2. 64 averages of Quadrupole Mass Spectrometer (QMS) during an outgassing procedure of electron beam heated graphic rod is plotted versus atomic units.

The the dominate species is C₁ followed by C₃ and C₂. The system's titanium sublimation pump was used to reduce the background CO gas concentration (m/e = 28) before the growths. Figure 3

shows an Arrhenius plot of relative concentration for the three evaporated carbon species detected by the QMS.

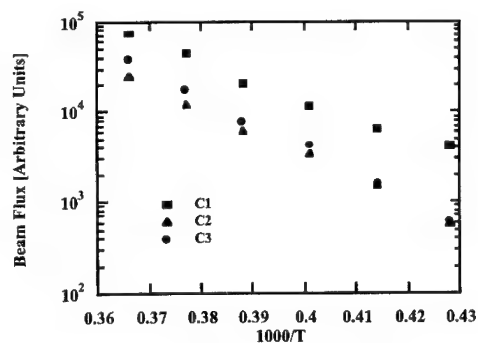


Figure 3. Arrhenius plot of carbon species (C1, C2, and C3) from electron-beam heated graphite rod.

The QMS intensities have been corrected for the contributions of fragmented background gases and for the species sensitivity factors¹⁰. Figure 3 also shows that the slope of the C₁ curve changes as the source temperature is raised, indicating a variation in the mechanism producing the species. This is in contrast to the C₂ and C₃ curves which are linear within experimental error. The most reasonable explanation for this is that a portion of the thermal C₂ and C₃ fluxes are cracked by the electron beam, and when these fluxes become significant with respect to the C₁ flux, the result is perceived as a change in the C₁ Heat of Sublimation. The carbon flux has been found to have a long decay time constant as the carbon source tip is consumed. To maintain carbon flux from growth to growth, the beam current was increased or the carbon rod was advanced. After advancing the graphite rod, outgassing and carbon flux calibration was necessary.

The growth temperature was maintained at 585°C and growth rates between 1.0µm/hr and 1.5 µm/hr were obtained. Figure 4 shows the four structures used in this experiment.

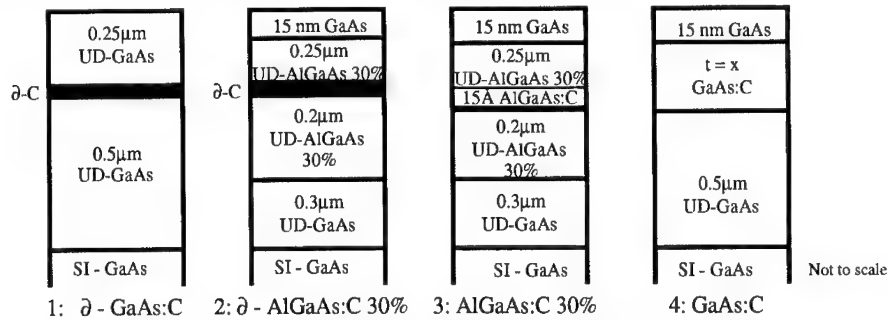


Figure 4. Four structures used in this experiment to study the unique electron beam heated graphite rod.

Four set of samples were grown with As_4 and $V/\text{III} > 15$. The first samples of delta-doped GaAs was grown on a $0.5\mu\text{m}$ undoped GaAs buffer layer. The delta doping was performed by terminating the Ga beam flux and depositing carbon for six seconds under an As_4 overpressure. After depositing the carbon, a $0.25\mu\text{m}$ GaAs cap layer was immediately grown. The second sample set of delta-doped $\text{Al}_{0.3}\text{Ga}_{0.7}\text{As}$ sample was grown on $0.3\mu\text{m}$ undoped GaAs buffers followed by $0.2\mu\text{m}$ undoped $\text{Al}_{0.3}\text{Ga}_{0.7}\text{As}$ layer. The delta-doping was performed by terminating the Ga and Al beam flux and depositing carbon for six seconds under As_4 overpressure. Again without any delay, both Ga and Al beam fluxes were resumed to grow a $0.25\mu\text{m}$ undoped $\text{Al}_{0.3}\text{Ga}_{0.7}\text{As}$ layer followed by a 15nm GaAs cap layer. A third sample set of thin uniformly doped $\text{Al}_{0.3}\text{Ga}_{0.7}\text{As}$ samples was grown with similar conditions to the second set except the Ga and Al beam fluxes were not terminated during the six second carbon deposition. A fourth sample set of thick uniformly-doped GaAs samples was grown on a $0.5\mu\text{m}$ undoped GaAs buffer with various thicknesses of uniformly doped layers followed by a 15nm undoped GaAs cap layer. All the samples were electrically characterized by Hall-Effect measurements. The Van der Pauw-Hall samples were prepared by cleaving the samples into 7 by 7 mm squares. Ohmic contacts were made by placing pure indium balls on each of the corners and alloying in 85% N_2 and 15% H_2 forming gas at 350°C for 50 seconds.

RESULTS

Figure 5 shows 300K Hall mobility vs. hole sheet carrier concentration for delta-doped GaAs, delta-doped $\text{Al}_{0.3}\text{Ga}_{0.7}\text{As}$, and thin uniformly-doped $\text{Al}_{0.3}\text{Ga}_{0.7}\text{As}$ samples (expressed in terms of two dimensional carrier density.)

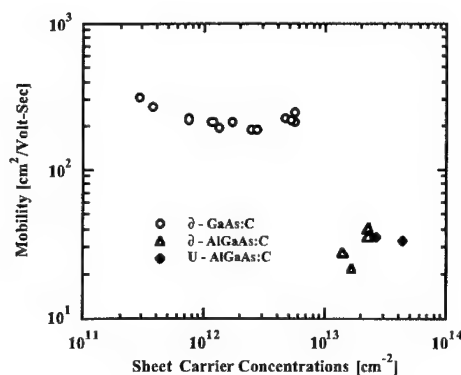


Figure 5. Room temperature mobility verses hole sheet carrier concentration for delta doped GaAs, $\text{Al}_{0.3}\text{Ga}_{0.7}\text{As}$ and thin uniformly doped $\text{Al}_{0.3}\text{Ga}_{0.7}\text{As}$ expressed in terms of two dimensional carrier density.

Delta-doped AlGaAs samples were found to have a larger sheet carrier concentrations than GaAs samples with similar carbon beam fluxes. A possible reason could be attributed to stronger Al-C bonding than Ga-C bond resulting in preferred carbon incorporation on As sites in $\text{Al}_{0.3}\text{Ga}_{0.7}\text{As}$.

¹¹. The thin, uniformly-doped $\text{Al}_{0.3}\text{Ga}_{0.7}\text{As}$ equivalent two dimensional (2D) carrier density is calculated by the following approximation:

$$\text{2D conc [cm}^{-2}\text{]} = (\text{uniform doping conc. [cm}^{-3}\text{]}) (\text{thickness [cm]})$$

The approximate two-dimensional carrier density of these uniformly-doped samples show higher sheet carrier concentrations than that obtained from the growth-interrupted, delta-doped $\text{Al}_{0.3}\text{Ga}_{0.7}\text{As}$ structures. This suggests that atomic carbon was constrained from forming non radiative recombination centers in $\text{Al}_{0.3}\text{Ga}_{0.7}\text{As}$ ¹². For delta-doped $\text{Al}_{0.3}\text{Ga}_{0.7}\text{As}$, energetic carbon was suspended on the epitaxial surface, thereby enhancing the probability of pairing. As growth was resumed, the buried carbon was inhibited from pairing¹³ and diffusing¹⁴. The surface morphology of the highest delta-doped $\text{Al}_{0.3}\text{Ga}_{0.7}\text{As}$ layer was degraded, and during the growth, a decrease in RHEED pattern intensity was observed. The RHEED intensity correlates well with surface morphology.

Figure 6 shows photoluminance intensity measurements versus hole carrier concentration of uniformly doped GaAs.

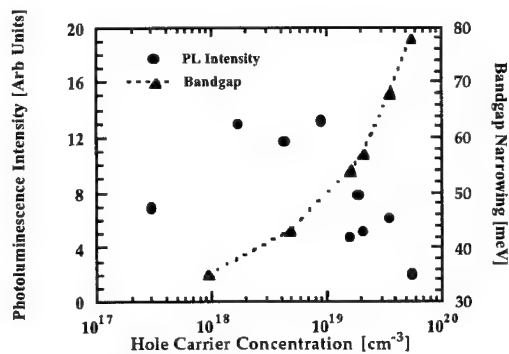


Figure 6. Photoluminance and bandgap narrow effect versus carrier density for uniformly doped GaAs.

The photoluminescence intensity decreases at hole densities $> 10^{18}\text{cm}^{-3}$. This is in good agreement with other carbon doping sources such as a filament¹⁵ evaporation. This drop is likely due to non-radiative recombination centers. Figure 6 also shows that the bandgap begins to narrow at hole concentrations above mid- 10^{18}cm^{-3} . The bandgap was determined by linear extrapolation of zero crossing of PL intensity on the lower energy side of the peak. The effective bandgap narrowing effect was calculated by subtracting the undoped GaAs energy band-gap from measured doped GaAs energy band gap. This is in good agreement with results from uniform doped GaAs using a filament source¹⁶. Good surface morphology was maintained in all uniform doped GaAs samples.

SUMMARY

Higher sheet carrier concentrations were achieved with delta-doped (up to $2.2 \times 10^{13}\text{ cm}^{-2}$) $\text{Al}_{0.3}\text{Ga}_{0.7}\text{As}$ samples than with (up to $5.6 \times 10^{12}\text{ cm}^{-2}$) delta-doped GaAs samples. The greater

hole sheet carrier concentration in $\text{Al}_{0.3}\text{Ga}_{0.7}\text{As}$ is likely due to higher carbon incorporation into As sites and reduced pairing as the result of stronger Al-C bonding as compared to Ga-C. Initial indications show that growth interruptions during delta-doping of $\text{Al}_{0.3}\text{Ga}_{0.7}\text{As}$ increased reactive carbon surface time and thereby increased the probability of pairing. Non-interrupted thin uniformly doped $\text{Al}_{0.3}\text{Ga}_{0.7}\text{As}$ appears to have a higher carbon incorporation efficiency relative to delta-doped $\text{Al}_{0.3}\text{Ga}_{0.7}\text{As}$. This was deduced by calculating the equivalent two dimensional carrier concentration from the measured three dimensional carrier concentration. Photoluminescence intensity measurements on uniformly doped GaAs was found to decrease at hole densities greater than 10^{18}cm^{-3} , and bandgap compression occurred at hole carrier concentrations exceeding mid- 10^{18}cm^{-3} range.

ACKNOWLEDGMENTS

This project is supported in part by Irvine Faculty Fellowship and Thermionics Laboratory through University of California MICRO program.

REFERENCES

- ¹ W.E. Hoke, P.J. Lemonias, D.G. Weir, H.T. Hendriks, and G.S. Jackson, J. Appl. Phys. 69, No. 1, 511 (1991).
- ² C. Giannini, A. Fischer, C. Lange, K. Ploog, and L. Tapfer, Appl. Phys. Lett. 61, No. 2, 183 (1992).
- ³ C.R. Abernathy, S.J. Pearton, R. Caruso, F. Ren, and J. Kovalchik, Appl. Phys. Lett. 55, No. 17, 1750 (1989).
- ⁴ J.L. Benchimol, F. Alexandre, N. Jourdan, A.M. Pougnet, R. Mellet, B. Sermage, F. Heliot and C. Dubon-Chevallier, J of Crystal Growth 127, 690 (1993).
- ⁵ G.E. Hofler and K.C. Hsieh, Appl. Phys. Lett. 61, No. 3, 327 (1992).
- ⁶ Thermionic Laboratory, Inc. (Model No. 1000-0010 R).
- ⁷ H.P. Lee, presented at the 1995 MRS Spring Meeting, Symposium C2.3, San Francisco, CA, 1995 (unpublished).
- ⁸ C. Giannini, O. Brandt, A. Fischer, K.H. Ploog and L. Tapfer, Journal of Crystal Growth 127, 724 (1993)
- ⁹ H.P. Lee, F.J. Szalkowski, D.L. Sato, X. Liu, E. Ranalli and T. George, J. Vac. Sci. Technol. B12, 1163 (1994).
- ¹⁰ UTI 100C Operation Manual (relative to N_2).
- ¹¹ C. Giannini, C. Gerardi, L. Tapfer, A. Fischer and K.H. Ploog, J. Appl. Phys. 74, No. 1, 77 (1993).
- ¹² H. Ito, O. Nakajima, and T. Ishibashi, Appl. Phys. Lett. 62, 2099 (1993).
- ¹³ D.L. Sato, F.J. Szalkowski, and H.P. Lee, Appl Phys. Lett. 66, No. 14, 1791 (1995).
- ¹⁴ C.R. Abernathy, S.J. Pearton, F. Ren, W.S. Hobson, T.R. Fullowan, A. Katz, and A.S. Jordan and J. Kovalchik, Journal of Crystal Growth 105 375 (1990).
- ¹⁵ J. Nagle, R.J. Malik, and D. Gershoni, J. of Crystal Growth 111, 264 (1991).
- ¹⁶ Z.H. Lu, M.C. Hanna, and A. Majerfeld, Appl Phys Lett, 64, No. 1, 89 (1994).

POINT DEFECT SUPERSATURATION DURING ZINC DIFFUSION INTO InP

D. WITTORF, W. JÄGER, A. RUCKI, K. URBAN, H.-G. HETTWER*,
N. A. STOLWIJK* AND H. MEHRER*

Forschungszentrum Jülich, Institut für Festkörperforschung, D-52425 Jülich, Germany

* Universität Münster, Institut für Metallforschung, D-48149 Münster, Germany

ABSTRACT

Formation of defects during Zn diffusion into undoped and Fe-doped InP single crystals at 700°C has been observed by transmission electron microscopy for various diffusion conditions. The observations are correlated with Zn concentration profiles obtained by electron microprobe measurements and secondary-ion mass spectrometry. The results allow the conclusion that indiffusing interstitial Zn can occupy In sublattice sites via a kick-out reaction. Under appropriate diffusion conditions supersaturations of In self-interstitial atoms result leading to defect formation. Observations in Fe-doped InP suggest that Zn also replaces Fe on In sublattice sites leading to redistribution and to precipitation of Fe.

INTRODUCTION

Little is known about the diffusion behaviour of dopants in InP which, beside GaAs, is the most important material used in optoelectronic communication technology. Zn atoms substituting In on In sublattice sites act as p-dopants in InP. It is generally accepted that diffusion of Zn in InP at high temperatures occurs via an interstitial-substitutional exchange mechanism¹⁻³ involving intrinsic point defects. From earlier analyses of the Zn concentration profiles obtained under various conditions of ampoule diffusion it has been concluded that Zn diffusion can be described by models based on a dissociative mechanism involving vacancies⁴. Previous investigations by transmission electron microscopy of InP single crystals after Zn diffusion showed that dislocations and precipitates are formed in the Zn-diffused crystal region⁵, and a model for defect formation based on a kick-out diffusion process has been recently suggested.⁶

In this paper we compare the results of a transmission electron microscopy investigation of defects formed in Zn-diffused InP crystals with Zn concentration profiles obtained by electron microprobe measurements and secondary-ion mass spectrometry on the same samples. Effects of diffusion source composition and InP substrate doping by Fe are shown.

EXPERIMENTAL TECHNIQUES

Zn was diffused into nominally undoped and semi-insulating Fe-doped ($C_{Fe}=1.2 \times 10^{17} \text{ cm}^{-3}$) LEC InP single crystals with a dislocation etch pit density of less than 10^5 cm^{-2} . Diffusion anneals were carried out in Ar-flushed and sealed quartz ampoules (ampoule volume $\sim 8 \text{ cm}^3$) at 700°C for 80 min or 900 min. Diffusion sources of pure Zn or of Zn and P in weight ratios of 5 : 1 (Zn^5P^1) or 1 : 1 (Zn^1P^1) with total Zn amounts ranging from 3 to 7 milligrams were used. After the diffusion anneals the ampoules were quenched to room

temperature in water. Depth profiles of the total Zn concentration were determined using electron microprobe (EMP) analysis⁷ (detection limit $5 \times 10^{18} \text{ cm}^{-3}$) and secondary ion mass spectrometry (SIMS, detection limit $5 \times 10^{16} \text{ cm}^{-3}$). SIMS analyses were performed on cross-section samples in a scanning mode (area $200 \times 200 \mu\text{m}^2$) using CsZn^+ secondary ions and calibrated using homogeneously Zn-doped InP. The depth profiles were obtained by integration of the signal across a window (lateral extension $10 \mu\text{m}$, depth extension $3 \mu\text{m}$). The defect structure in Zn-diffused InP wafers was investigated in cross-section samples by transmission electron microscopy (TEM) at 400 kV. Energy-dispersive X-ray (EDX) analyses of Zn- K_{α} , In- L_{α} , P- K_{α} , and Fe- K_{α} lines was used to determine the composition of precipitates.

RESULTS

High Zn concentrations at the surface (about 10^{20} cm^{-3}) are obtained after diffusion at 700°C into undoped and into Fe-doped InP using sources consisting of pure Zn and of Zn^5P^1 whereas lower surface concentrations (about 10^{19} cm^{-3}) are obtained for sources with higher weight fractions of P (Zn^1P^1). Figure 1 shows the Zn concentration depth profiles, C_{Zn} vs. x , obtained for Zn^5P^1 and Zn^1P^1 sources after a diffusion time of 80 min. Characteristic for diffusion with Zn^5P^1 sources is the plateau region extending from $20 \mu\text{m}$ to $50 \mu\text{m}$. Zn concentrations determined by EMP agree well with those determined by SIMS in the near-surface region. For Fe-doped InP substrates the penetration depth of Zn is higher, and the slope of $C_{\text{Zn}}(x)$ at the front is smoother. After diffusion with Zn^1P^1 sources much smaller penetration depths result. Diffusion of Zn for a duration of 900 min leads to deeper penetration depths for Fe-doped substrates compared to undoped ones. Connected with this a Zn concentration plateau appears in the front region extending to a depth of about $80 \mu\text{m}$, instead of $40 \mu\text{m}$ for undoped InP. The level of this Zn concentration plateau corresponds to that of the Fe concentration before diffusion ($\approx 10^{17} \text{ cm}^{-3}$).

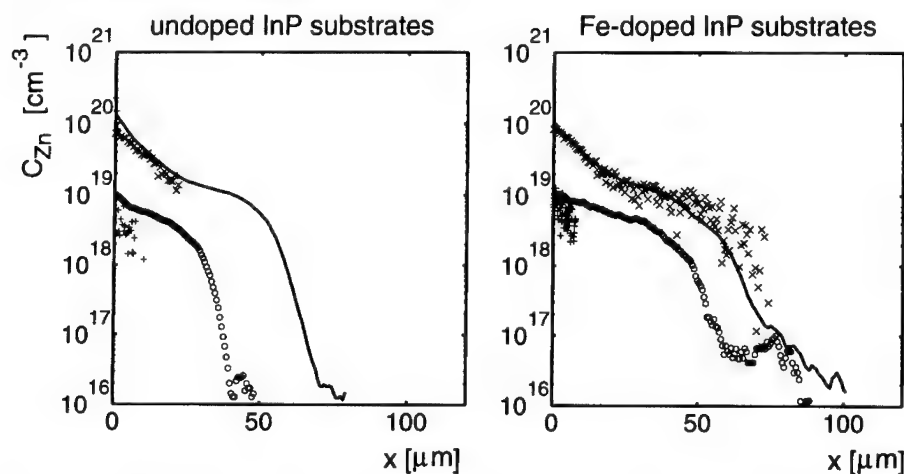


Figure 1 : Zn concentration profiles measured by EMP (x, +) and by SIMS (solid line, o) after diffusion at 700°C into undoped InP (left) and into Fe-doped InP (right). Also shown is the dependence of the diffusion source composition: Zn^5P^1 sources for 80 min (x, solid line) and Zn^1P^1 sources for 80 min (+) and for 900 min (o).

The TEM investigations show that for diffusion from strong Zn sources (Zn , Zn^{5}P^1) extended defects, such as agglomerates consisting of dislocation loops, dislocations and precipitates in voids, are formed in the Zn-diffused crystal regions of both undoped and Fe-doped InP, except for a near-surface region ($x < 10 \mu\text{m}$). Typical of this diffusion-induced defect structure is the inhomogeneous spatial arrangement of defect agglomerations and large planar arrays of precipitates. For all diffusion conditions the crystals are free of such defects in the undiffused crystal regions.

Figure 2a shows an example of an agglomerate of defects consisting of dislocations, a dislocation loop (arrow) and In precipitates inside voids which are depicted by a black dot contrast under the imaging conditions applied. From the center of such agglomerates large planar arrays of precipitates, frequently with $\{110\}$ habit planes and bounded by dislocations, extend into the crystal over large distances. Figure 2(b,c) shows an example of planar arrays of precipitates in an edge-on and an oblique projection view. Stereo tilt experiments reveal that occasionally loops are located close to the habit planes of such arrays. Additional observations in thick specimen areas indicate that the bounding dislocations of such arrays are frequently segments of large loops.

Contrast analyses of dislocation loops by means of the 'inside-outside' contrast method⁸ have shown their nature to be of interstitial type. Most of the loops are perfect with $\{110\}$ habit planes and a Burgers vector of $a/2 \langle 110 \rangle$ type. Only a few of the analyzed loops possess $\{111\}$ habit planes and a Burgers vector of $a/3 \langle 111 \rangle$ type. These results indicate that the loops are composed of layers containing In and P atoms at the stoichiometry of the crystal.

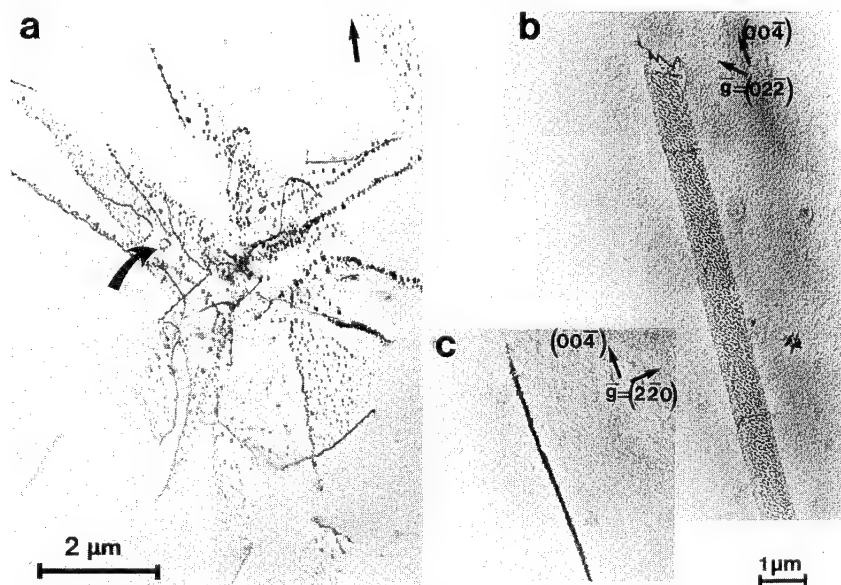


Figure 2: (a) Agglomerate of dislocations, a dislocation loop (arrow), and Indium precipitates in the diffusion front region. (b,c) Planar array of Indium precipitates and climbed dislocation segments on a $(1\bar{1}0)$ -plane shown (b) in projection (c) edge-on. Fe-doped InP, pure Zn source. TEM bright field micrographs, $g = \{220\}$.

Figure 3 shows examples of precipitates observed in undoped and in Fe-doped InP. The In precipitates (diameters typically between 20 nm and 50 nm) are connected with voids and are partly faceted (Fig. 3a). Under imaging conditions using imaging vectors $\mathbf{g} = \{111\}$ the precipitates show moiré fringe contrast indicating their crystalline nature. Lattice parameter values deduced from precipitate-related spots in the selected area electron diffraction patterns are compatible with those of crystalline In. The composition of the precipitates was analyzed by EDX and revealed in all cases significant enrichment in In with respect to the InP matrix. These results indicate that the precipitates consist of In which is liquid at the diffusion temperature of 700°C (melting temperature: 157°C) and crystallizes during rapid cooling to room temperature. Fig. 3c shows larger precipitates (diameters of up to 100 nm) observed in Fe-doped InP, together with small In precipitates and dislocations. EDX analyses revealed clearly the enrichment of Fe as well as P in these precipitates. Additional reflections observed in electron diffraction patterns from areas including such large precipitates are compatible with the presence of a FeP phase.

Diffusion with Zn^{10}P^1 sources does not lead to formation of defects in the bulk of the crystal, even for long diffusion times. Under such conditions large crystalline precipitates enriched in Zn and P (diameters $\leq 30 \mu\text{m}$) are observed at the surfaces of the diffusion samples.

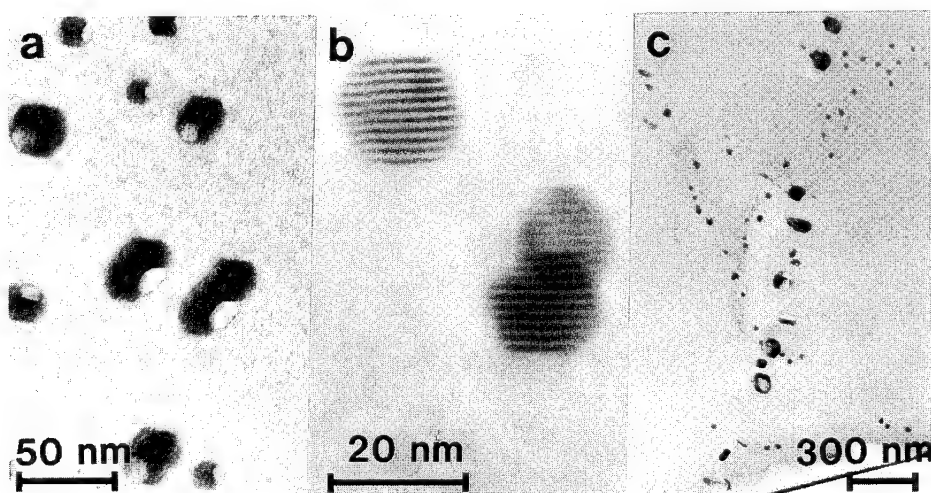


Figure 3: (a) Faceted In precipitates inside voids. Kinematical imaging conditions. (b) Moiré fringe contrast of In precipitates. Undoped InP substrate, Zn^{5}P^1 source. (c) Row of large (Fe, P)-rich precipitates. Fe-doped InP substrate, pure Zn source.

DISCUSSION

The experimental results show that Zn diffusion in InP and defect formation are clearly correlated with each other and are strongly dependent on the diffusion source composition

chosen. In the following discussion we suggest a mechanism for defect formation during Zn diffusion into InP and discuss the different phenomena observed in our experiments.

Under diffusion conditions with strong Zn sources (Zn , Zn^{5}P^1) defects are generated during Zn indiffusion into the InP bulk crystal. The formation of dislocation loops and In precipitates inside voids during Zn indiffusion can be described by a model which is based on a kick-out reaction substituting In matrix atoms by incorporation of Zn^6 . The resulting concentration of In interstitials can become supersaturated, and interstitial dislocation loops are formed. P interstitials are provided during loop growth by the emission of P vacancies which themselves aggregate and form voids containing In. Earlier TEM studies of Zn diffusion induced defects in GaAs have led to a similar model explaining the generation of interstitial dislocation loops and Ga precipitates inside voids⁹⁻¹¹.

From the observation of extended planar arrangements of In precipitates on $\{110\}$ planes bounded by dislocations we conclude that growth of dislocation loops and climb of dislocation segments occurs very effectively during Zn diffusion in InP thus bringing the point defect concentrations close to their local equilibrium values. Observation of further dislocation loop formation near a planar arrangement of precipitates suggest indeed that at a sufficient distance from climbing dislocations the local supersaturation of In interstitials can again become large enough to form new loops⁶. As observed here, point defects of both sublattices are involved in dislocation climb processes also for other III-V compound semiconductors^{12,13}.

The plateau regions observed for Zn^{5}P^1 sources (Fig. 1, $20\ \mu\text{m} \leq x \leq 50\ \mu\text{m}$) have their origin probably in the reduction of In self-interstitial concentrations by the presence of extended defects. As addressed above, the incorporation of Zn on In sublattice sites via the kick-out mechanism increases the In interstitial concentration. Effective annihilation of In interstitials at extended defects acting as sinks would therefore increase the number of Zn atoms becoming incorporated on substitutional sites thus leading to the observed plateau region.

Defect formation is suppressed in the near-surface region ($x < 10\ \mu\text{m}$) for diffusion with Zn or Zn^{5}P^1 sources and in the whole bulk crystal for Zn^1P^1 sources. The surface obviously acts as a sink for In self-interstitials, and therefore a supersaturation leading to defect generation does not build up in the near-surface region. For sources with a sufficient P fraction (Zn^1P^1) the formation of a Zn-rich surface precipitate phase obviously reduces the Zn partial pressures in the quartz ampoule. Zn diffusion under such conditions results in lower Zn concentrations (Fig. 1) and in In interstitial concentrations which are below the critical value for defect formation.

Effects of substrate doping with Fe are revealed by the diffusion-induced precipitation of Fe (Fig. 3) and by higher penetration depths under otherwise identical conditions. The formation of Fe-enriched precipitates indicate that Fe atoms on In sublattice sites are replaced and redistributed as mobile interstitial Fe atoms. We suggest as likely mechanism a kick-out reaction between indiffusing interstitial Zn and substitutional Fe atoms on In sublattice sites. This would explain also the Zn concentration plateau observed at depths between $60\ \mu\text{m}$ and $80\ \mu\text{m}$ at the level of the Fe doping concentration (Zn^1P^1 source, Fig. 1) which indicates an accelerated incorporation of Zn atoms into the In sublattice. Defects generated during Zn diffusion with Zn^{5}P^1 sources seem to prevent the formation of such a plateau (Fig. 1).

CONCLUSIONS

Zinc diffusion into InP performed at 700°C can lead to formation of extended defects under certain diffusion conditions. The defect formation results from supersaturation of the In

interstitials which are generated by the exchange of indiffusing interstitial Zn atoms with In via a kick-out reaction. The formation and growth of perfect interstitial-type dislocation loops leads to a generation of P vacancies which aggregate and form voids partly filled by In atoms. This pattern of defect formation as response to the incorporation of Zn into the crystalline lattice during diffusion is analogous to that occurring in GaAs⁹. These extended defects act as sinks for point defects thus leading to dislocation climb and precipitate formation and hence influence the point defect concentrations inside the crystal. Such influences manifest themselves in the plateau region of the Zn concentration profiles (Fig. 1, $20\ \mu\text{m} \leq x \leq 50\ \mu\text{m}$) caused by an increased effective Zn incorporation. In Fe-doped substrates formation of FeP precipitates and observation of higher Zn penetration depths provide evidence that interstitial-substitutional exchange also occurs between Zn and Fe on In sublattice sites via the kick-out mechanism. Sample surfaces appear to be effective as sinks for point defects thus suppressing formation of extended defects in near-surface crystal regions. For diffusion sources with sufficiently high weight fractions of P (Zn^{1}P^1) large precipitates, being enriched in Zn and P, form at the sample surfaces. The Zn partial pressure in the ampoule is presumably lowered to values below the critical value for defect formation, and the Zn diffused crystal regions remain free of defects. Accordingly, low Zn concentrations at the surface would result and a self-doping dependent Zn diffusivity would produce smaller penetration depths (Fig.1).

ACKNOWLEDGEMENTS

We thank H. Holzbrecher and U. Breuer (ZCH Forschungszentrum Jülich) for performing the SIMS analyses. Helpful discussions with U. Gösele and T.Y. Tan are gratefully acknowledged.

REFERENCES

1. B. Tuck and A. J. Hooper, *Phys. D: Appl. Phys.* **8**, 1806 (1975).
2. H. B. Serreze and H. S. Marek, *Appl. Phys. Lett.* **49**, 210 (1986).
3. G.J. van Gurp, T. van Dongen, G.M. Fontijn, J.M. Jakobs and D.L.A. Tjaden, *J. Appl. Phys.* **65**, 553 (1989).
4. B. Tuck, *Atomic Diffusion in III-V Semiconductors* (Adam Hilger, Bristol, 1988).
5. R. H. Dixon, W. Jäger, A. Rucki, K. Urban, H.-G. Hettwer, N. A. Stolwijk and H. Mehrer, *Inst. Phys. Conf. Ser.* **134**, 539 (1993).
6. D. Wittorf, A. Rucki, W. Jäger, R. H. Dixon, K. Urban, H.-G. Hettwer, N. Stolwijk and H. Mehrer, *J. Appl. Phys.* **74**, 2843 (1995).
7. H.-G. Hettwer, W. Lerch, B. Lentfort, N. A. Stolwijk and H. Mehrer, *Appl. Surf. Sci.* **50**, 470 (1991).
8. H. Föll and M. Wilkens, *phys. stat. sol. (a)* **31**, 519 (1975).
9. M. Luysberg, W. Jäger, K. Urban, M. Schänzer, N. Stolwijk and H. Mehrer, *Mat. Res. Soc. Symp. Vol.* **163**, 659 (1989) and *Mater. Sci. Eng.* **B13**, 137 (1992).
10. T.Y. Tan, U. Gösele and S. Yu, *Crit. Rev. Sol. St. Mater. Sci.* **17**, 47 (1991).
11. W. Jäger, A. Rucki, K. Urban, H.-G. Hettwer, N. Stolwijk, H. Mehrer and T.Y. Tan, *J. Appl. Phys.* **74**, 4409 (1993).
12. P.M. Petroff and L.C. Kimerling, *Appl. Phys. Lett.* **29**, 461 (1976).
13. B. P. R. Marioton, T. Y. Tan and U. Gösele, *Appl. Phys. Lett.* **54**, 849 (1989).

LOW DEEP IMPURITY $\text{In}_x\text{Ga}_{1-x}\text{P}$ GROWN BY METALORGANIC CHEMICAL VAPOR DEPOSITION

Z.C. HUANG, BING YANG, H.K. CHEN AND J.C. CHEN

Department of Electrical Engineering, University of Maryland Baltimore County, Baltimore, MD
21228

ABSTRACT

$\text{In}_x\text{Ga}_{1-x}\text{P}$ ($x=0.49$) layers lattice-matched to GaAs have been grown by metalorganic chemical vapor deposition (MOCVD). We did not observe any deep levels in the temperature range of 30-380K by deep level transient spectroscopy (DLTS) in undoped $\text{In}_{0.49}\text{Ga}_{0.51}\text{P}$ layers which have a background concentration of $3.1 \times 10^{15} \text{ cm}^{-3}$. The deep levels, if they exist, have a concentration of less than $5 \times 10^{11} \text{ cm}^{-3}$, which is the lowest deep level concentration found so far in $\text{In}_x\text{Ga}_{1-x}\text{P}$ materials. Moreover, lattice-mismatched $\text{In}_x\text{Ga}_{1-x}\text{P}/\text{GaAs}$ heterojunctions were deliberately grown by varying the In-composition ranging from 0.43 to 0.57. No deep levels were created in 1- μm -thick $\text{In}_x\text{Ga}_{1-x}\text{P}$ layers due to lattice mismatch when $0.469 < x < 0.532$. However, we have observed a shallow electron trap at $E_C - 60 \text{ meV}$ in $\text{In}_x\text{Ga}_{1-x}\text{P}$ layers with $x < 0.469$, and a deep electron trap located at $E_C - 0.85 \text{ eV}$ in the samples with $x > 0.532$. We suggest that the lattice-mismatch-induced-defects in $\text{In}_x\text{Ga}_{1-x}\text{P}$ are either electrically inactive or resided outside the bandgap when In content ranging from 0.469 to 0.532.

I. INTRODUCTION

$\text{In}_x\text{Ga}_{1-x}\text{P}$ lattice-matched to GaAs offers many potential advantages over $\text{Al}_x\text{Ga}_{1-x}\text{As}$ in laser diodes¹, light-emitting diodes² and heterojunction bipolar transistors³. These minority carrier devices require extremely low deep level concentration. Although it is claimed that the $\text{In}_x\text{Ga}_{1-x}\text{P}$, grown either by molecular beam epitaxy (MBE) or by metalorganic chemical vapor deposition (MOCVD), has fewer deep levels than $\text{Al}_x\text{Ga}_{1-x}\text{As}$ does, the reported deep level concentration was still high for the devices application. Paloura et al.⁴ and Feng et al.⁵ have reported that the deep level concentration in MOCVD-grown $\text{In}_{0.49}\text{Ga}_{0.51}\text{P}$ was in the order of 10^{14} and 10^{15} cm^{-3} , respectively. Huang et al.^{6,7} have measured the deep level concentration in MBE-grown $\text{In}_{0.49}\text{Ga}_{0.51}\text{P}$ to be in the range of 10^{15} - 10^{16} cm^{-3} . Defect concentrations were even higher in low-temperature-grown $\text{In}_{0.49}\text{Ga}_{0.51}\text{P}$ by MBE⁸. It is difficult to conclude from the previous reports which traps may be common to all $\text{In}_x\text{Ga}_{1-x}\text{P}$ and which arise only in MOCVD-grown $\text{In}_x\text{Ga}_{1-x}\text{P}$. Some traps vary in concentration with growth condition and others may be due to contamination in gas sources or reactors. Therefore, it is difficult to control the deep levels in $\text{In}_x\text{Ga}_{1-x}\text{P}$, especially in MOCVD-grown materials. In this paper, we report the growth of low defect density $\text{In}_x\text{Ga}_{1-x}\text{P}/\text{GaAs}$ heterojunctions by MOCVD. The deep level concentration was

found to be less than $5 \times 10^{11} \text{ cm}^{-3}$ measured by deep level transient spectroscopy (DLTS). We have also grown a series of $\text{In}_x\text{Ga}_{1-x}\text{P}/\text{GaAs}$ heterojunctions in which the In-composition was varied over a broad range from 0.43 to 0.57, corresponding to the in-plane lattice mismatch from -0.23 to +0.31%. We found that the lattice mismatch ranging from -0.125 to +0.224% ($0.469 < x < 0.532$) does not generate deep levels in $\text{In}_x\text{Ga}_{1-x}\text{P}$ epilayers.

II. EXPERIMENT AND SAMPLE PREPARATION

The $\text{In}_x\text{Ga}_{1-x}\text{P}$ layers were grown in a conventional, horizontally configured, atmospheric pressure MOCVD reactor which has been routinely producing device-quality materials, such as mobility of GaAs $> 100,000 \text{ cm}^2/\text{Vs}$ at 77K, and optoelectronic devices, such as laser diodes and photodetectors. Pd-cell purified H_2 was used as the carrier gas. The column III precursors were trimethylindium (TMIn) and trimethylgallium (TMGa). The column V precursor was pure phosphine. No getters were used to purify any sources in this study. The materials were grown at 650°C with precursor V/III ratio of 150, and a growth rate of $4.0 \text{ }\mu\text{m/hr}$. A $1\text{-}\mu\text{m}$ -thick nonintentionally doped $\text{In}_x\text{Ga}_{1-x}\text{P}$ layer was grown on $\text{n}^+\text{-GaAs}$ (100) substrate with its surface tilted 10° towards the nearest $\langle 110 \rangle$ direction. The free carrier concentration was found to be in the range of $3\text{-}9 \times 10^{15} \text{ cm}^{-3}$ by capacitance-voltage (C-V) measurements. The composition of Ga and In and the in-plane lattice mismatch were determined by double-crystal x-ray rocking curve measurements. Ohmic contacts were made by evaporating AuGe/Au to the $\text{n}^+\text{-GaAs}$ substrate, and alloyed in forming gas ($95\%\text{N}_2+5\%\text{H}_2$) atmosphere at 420°C for 2min. Schottky contacts, $700 \text{ }\mu\text{m}$ in diameter, were made by evaporating Au through a metal mask onto the InGaP surface immediately after etched in freshly prepared 1:5 HCl : H_2O solution for 10 seconds. Current-voltage characteristics were measured by a computer controlled Keithley 236 Source-Measure Unit. Our DLTS setup was manufactured by Sula Technologies.

Sample number	In content	Free carrier concentration $10^{15} \text{ (cm}^{-3}\text{)}$	Ec-60meV concentration $10^{14} \text{ (cm}^{-3}\text{)}$	Ec-0.85eV concentration $10^{13} \text{ (cm}^{-3}\text{)}$
302	0.430	6.7	6.2	—
461	0.452	7.4	1.0	—
455	0.469	4.3	0.36	—
454	0.479	5.8	—	—
456	0.490	3.1	—	—
459	0.502	4.2	—	—
438	0.532	5.7	—	2.4
439	0.556	8.4	—	8.0
299	0.572	7.3	—	7.4

Table I. Sample parameters and DLTS results

The temperature scan range was from 30 to 380K. Data were taken automatically by a computer through a high speed analog-digital converter board.

III. RESULTS AND DISCUSSION

A typical current-voltage characteristics recorded for three $n\text{-}n^+$ $\text{In}_x\text{Ga}_{1-x}\text{P}/\text{GaAs}$ diodes with $x=0.452$, 0.490 and 0.556 at room temperature are shown in Fig.1(a), (b) and (c), respectively. The lattice-matched diode, Fig.1(b), could be interpreted on the basis of a Schottky barrier thermionic emission mode. Diode ideality factors at low bias varied from 1.03 to 1.16. Forward current are limited by series resistance effects at higher bias. The ideality factors for the lattice-mismatched diodes, Fig.1(a) and (c), were from 1.30 to 1.38, indicating that other transport mechanism could be involved, such as interface recombination.

The samples used in this study and DLTS results are summarized in Table I. The typical DLTS spectra obtained from three $\text{In}_x\text{Ga}_{1-x}\text{P}$ samples were shown in Fig.2 (a), (b) and (c) with $x=0.452$, 0.490 and 0.556 , corresponding to the in-plane lattice mismatch of -0.18% , 0% , and 0.26% , respectively. No deep levels were observed in lattice-matched $\text{In}_{0.49}\text{Ga}_{0.51}\text{P}$ samples in the temperature range of 30-380K, as

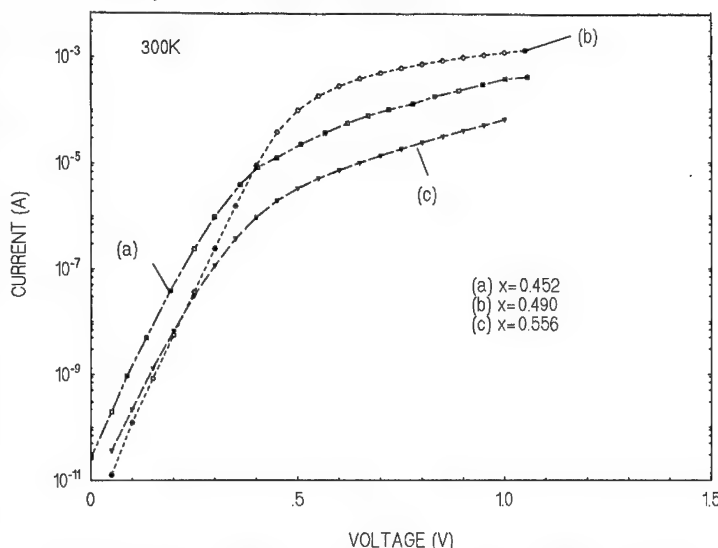


Figure 1. Current-voltage characteristics for $\text{In}_x\text{Ga}_{1-x}\text{P}/\text{GaAs}$ Schottky diodes with (a) $x=0.452$, (b) $x=0.490$, and (c) $x=0.556$.

shown in Fig.2(b). The deep levels, if exist, have concentration of less than $5 \times 10^{11} \text{ cm}^{-3}$, which is the detection limit of our DLTS system. By varying different measurement conditions such as the width and height of filling pulse, and the initial delay of time window, we did not observe any peaks from the DLTS measurement in $\text{In}_{0.49}\text{Ga}_{0.51}\text{P}$ samples. This is the lowest defect density in InGaP epilayer obtained so far by any growth methods. We also grew a GaAs buffer layer before the $\text{In}_{0.49}\text{Ga}_{0.51}\text{P}$ epilayer was grown, no additional traps were observed from these samples by DLTS measurement.

The stoichiometry of phosphorus seems to be very sensitive to the presence of the deep levels in InGaP materials. Huang et al.⁷ reported that the depress of phosphorus may cause a vacancy-related electron trap in their MBE-grown $\text{In}_{0.49}\text{Ga}_{0.51}\text{P}$. However, Lan et al.⁹ reported

very recently that the suppress of phosphorus may introduce a phosphorus interstitial-related deep trap in their liquid phase epitaxy-grown $\text{In}_{0.49}\text{Ga}_{0.51}\text{P}$, and they obtained a deep level free InGaP layer by optimizing the phosphorus vapor pressure. In our MOCVD growth, we obtained a deep level free InGaP under a very high III/V vapor pressure ratio, which

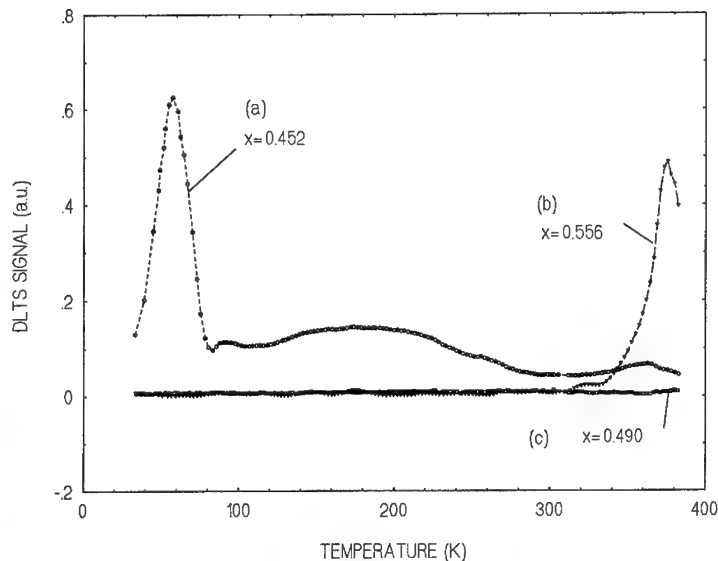


Figure 2. DLTS spectra for $\text{In}_x\text{Ga}_{1-x}\text{P}$ samples with (a) $x=0.452$, (b) $x=0.490$, and (c) $x=0.556$.

was above 200. A detailed study of the deep levels in InGaP under different III/V vapor pressure ratio is under investigation.

In order to investigate the effect of lattice mismatch on deep levels, we have varied the In-composition to introduce different lattice mismatch at the $\text{In}_x\text{Ga}_{1-x}\text{P}/\text{GaAs}$ interface. Nine samples were investigated for this purpose with x varying from 0.43 to 0.572. No deep levels were found in $\text{In}_x\text{Ga}_{1-x}\text{P}$ in the range of

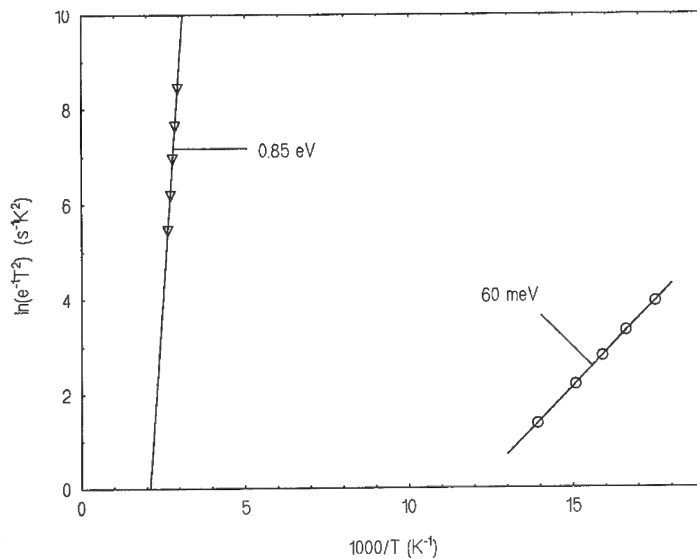


Figure 3. Variation of the emission rate with the inverse of temperature for 60meV trap and for 0.85 eV trap.

$0.469 < x < 0.532$, corresponding to in-plane lattice mismatch of -0.125 to $+0.224\%$. This is, to our knowledge, the first observation that the lattice mismatch has no effect in the generation of deep levels in $\text{In}_x\text{Ga}_{1-x}\text{P}/\text{GaAs}$ heterojunctions.

However, when In composition $x < 0.469$, a shallow electron trap in a concentration of 10^{14} cm^{-3} was observed in $\text{In}_x\text{Ga}_{1-x}\text{P}$ layers (Fig.2(a)) corresponding to an activation energy of 60 meV (Fig.3). We have found that further decrease of the In composition does not change its activation energy, but increases its concentration. In other words, the increase of In composition could eliminate this trap. When $x > 0.532$, a deep electron trap at $E_C - 0.85 \text{ eV}$ (Fig.3) appeared in $\text{In}_x\text{Ga}_{1-x}\text{P}$ as can be seen in Fig.2(c) for the sample with $x=0.556$, where E_C is the conduction band edge. Its concentration is about $8 \times 10^{13} \text{ cm}^{-3}$. The depth profiling of these two traps has been measured throughout the $\text{In}_x\text{Ga}_{1-x}\text{P}$ layer by double-correlator DLTS (DDLTS)¹⁰. The results are showing in Fig.4. The concentrations of these two electron traps have a uniform distribution in depth, indicating that they are not lattice-mismatch-induced deep levels, because for the partially relaxed interface, the lattice-mismatch-induced-defects would have higher concentration near the interface, as can be seen in the inset of Fig.4 for the 0.58 eV trap at $\text{GaInAs}/\text{GaAs}$ interface with similar lattice-mismatch (0.25%) (after ref.10). Thus these two electron traps must be a native defect in $\text{In}_x\text{Ga}_{1-x}\text{P}$ incorporation related to the In composition.

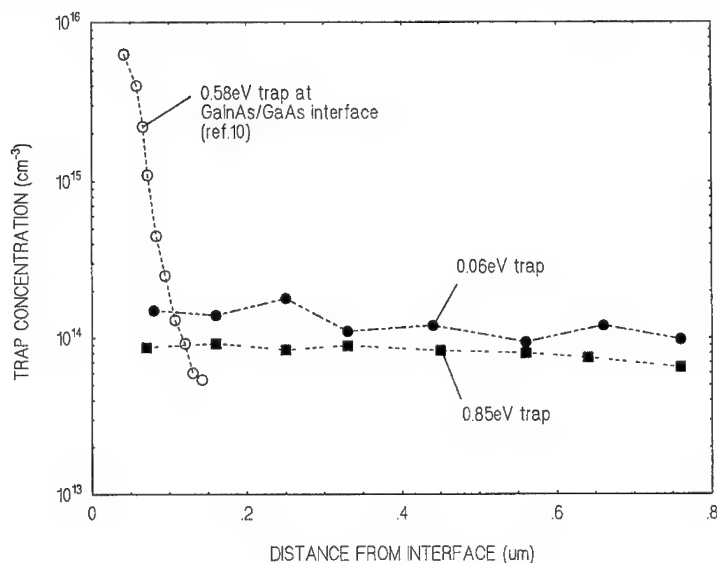


Figure 4. The depth profiles for 0.060 eV trap in the sample with $x=0.452$ (filled circle) and for 0.85 eV trap in the sample with $x=0.556$ (filled square). The inset is the depth distribution of 0.58 eV trap at $\text{GaInAs}/\text{GaAs}$ interface with in-plane mismatch of 0.25% (after ref.10).

In general, lattice mismatch can introduce dislocations and other defects in both side of the heterojunctions. Deep levels induced by the lattice mismatch in heterojunctions have been

reported by many authors¹⁰⁻¹². Zhu et al.¹³ have reported a lattice-mismatch-induced deep level at 0.57 eV in their liquid phase epitaxy-grown $\text{In}_x\text{Ga}_{1-x}\text{P}/\text{GaAs}$ heterojunctions. In contrast, our observation suggests that the defects induced by lattice-mismatch in MOCVD-grown $\text{In}_x\text{Ga}_{1-x}\text{P}/\text{GaAs}$ heterojunctions may not be electrically active, or the energy states created by lattice-mismatch-induced-defects are either pulled into the conduction or valence band of $\text{In}_x\text{Ga}_{1-x}\text{P}$, instead of residing in the band-gap region. It should be pointed out that the deep states near the midgap ($E_i \pm 0.1\text{eV}$) in $\text{In}_x\text{Ga}_{1-x}\text{P}$ can not be measured by our DLTS due to the difficulty in reaching very high temperature ($T=450^\circ\text{C}$). However, for our lattice-matched samples, no tendency of having a trap was observed during the DLTS measurement as we approached to the higher temperature.

IV. CONCLUSION

In conclusion, very low defect density $\text{In}_x\text{Ga}_{1-x}\text{P}$ layers have been grown by MOCVD with no detectable deep levels ($N_t < 5 \times 10^{11} \text{ cm}^{-3}$) observed with $0.469 < x < 0.532$. One shallow electron trap at 60 meV and one deep electron trap at 0.85 eV below the conduction band edge were observed in $\text{In}_x\text{Ga}_{1-x}\text{P}$ samples with $x < 0.469$ and $x > 0.532$, respectively. They were found not to be related with lattice mismatch. We suggest that, in $\text{In}_x\text{Ga}_{1-x}\text{P}$, the lattice-mismatch-induced defects, if they exist, are either electrically inactive, or located outside the band-gap.

This work was supported by Integrated Technology for Medicine, Silver Spring, MD (Dr. P. Skeath) through the Maryland Industrial Partnership (MIPS) Program.

REFERENCES

1. M.Ishikawa, Y.Ohba, H.Sugawara, M.Yamamoto and T.Nakanishi, Appl. Phys. Lett., **48**, 207 (1986)
2. L.J.Stinson, J.G.Yu, S.D.Lester, M.J.Peanasky and K.Park, Appl. Phys. Lett., **58**, 2012 (1991)
3. H.Kroemer, J. Vac. Sci. Technol. B, **1**, 126 (1983)
4. E.C.Paloura, A.Ginoudi, G.Kiriakidis, N.Frangis, F.Scholz, M.Moser, A.Christou, Appl. Phys. Lett., **60**, 2749 (1992)
5. S.L.Feng, J.C.Bourgoin, F.Omnes and M.Razeghi, Appl. Phys. Lett., **59**, 941 (1991)
6. Z.C.Huang and C.R.Wie, J. Appl. Phys., **75**, 989 (1994)
7. Z.C.Huang, C.R.Wie, J.A.Varriano, M.W.Koch and G.W.Wicks, J. Appl. Phys., **77**, 1587 (1995)
8. D.C.Look, Y.He, J.Ramdani, N.El-Masry and S.M.Bedair, Appl. Phys. Lett., **63**, 1231 (1993)
9. S.Lan, C.Q.Yang, D.L.Cui, W.J.Xu and H.D.Liu, Appl. Phys. Lett., **66**, 872 (1995)
10. Z.C.Huang, C.R.Wie, D.Johnstone, C.E.Stutz and K.R.Evans, J. Appl. Phys., **73**, 4362 (1993)
11. V.Krishnamoorthy, P.Ribas and R.M. Park, Appl. Phys. Lett., **58**, 2000 (1991)
12. W.J.Schaff and L.F.Eastman, E-MRS Meeting, June 1989, Vol. XVI, p.295
13. Q.S.Zhu and I.Akasaki, Semicond. Sci. and Technol., Vol. 7, 1441 (1992)

VERY LOW DEEP LEVEL $\text{Al}_x\text{Ga}_{1-x}\text{As}$ ($x=0.22$) LAYER GROWN BY METALORGANIC CHEMICAL VAPOR DEPOSITION

Z.C. HUANG, BING YANG, H.K. CHEN AND J.C. CHEN

Department of Electrical Engineering, University of Maryland Baltimore County, Baltimore, MD 21228

ABSTRACT

We have achieved deep-level-free $\text{Al}_{0.22}\text{Ga}_{0.78}\text{As}$ epitaxial layers using low selenium (Se)-doping ($8.4 \times 10^{16} \text{ cm}^{-3}$) grown by metalorganic chemical vapor deposition (MOCVD). Deep levels in various $\text{Al}_{0.22}\text{Ga}_{0.78}\text{As}$ layers grown on GaAs substrates were measured by deep level transient spectroscopy (DLTS). We have found that the commonly observed oxygen contamination-related deep levels at $E_C-0.53$ and 0.70 eV and germanium-related level at $E_C-0.30$ eV in MOCVD-grown $\text{Al}_{0.22}\text{Ga}_{0.78}\text{As}$ can be eliminated by low Se-doping. In addition, a deep hole level located at $E_V+0.65$ eV was found for the first time in highly Se-doped $\text{Al}_{0.22}\text{Ga}_{0.78}\text{As}$ epilayers. We suggest that low Se-doping ($<2 \times 10^{17} \text{ cm}^{-3}$) produces a passivation effect and then deactivates other deep levels in $\text{Al}_{0.22}\text{Ga}_{0.78}\text{As}$.

I. INTRODUCTION

$\text{Al}_x\text{Ga}_{1-x}\text{As}$ epitaxial layers are an integral part of many of the most advanced high speed and optoelectronic devices. Epitaxial growth technologies such as molecular beam epitaxy (MBE) and metalorganic chemical vapor deposition (MOCVD) have been the major methods used to produce high-quality $\text{Al}_x\text{Ga}_{1-x}\text{As}$ materials. For some device applications, this material system requires extremely low deep level density. However, n-type AlGaAs alloys exhibit several problems related to deep levels such as DX centers¹, oxygen and germanium contamination^{2,3}. It seems very difficult to avoid device degradation caused by deep levels, although a lot of effort has been expended in order to reduce these deep levels³⁻⁵.

In this paper, we demonstrate that low selenium (Se)-doping is very effective in reducing the concentration of deep levels, especially the oxygen contamination-related deep traps, which are commonly observed in MOCVD-grown $\text{Al}_x\text{Ga}_{1-x}\text{As}$ layers. By carefully controlling the doping conditions, a deep-level-free ($N_t < 10^{13} \text{ cm}^{-3}$) $\text{Al}_{0.22}\text{Ga}_{0.78}\text{As}$ epilayer was obtained with Se doping concentration of $8.4 \times 10^{16} \text{ cm}^{-3}$.

II. SAMPLE PREPARATION AND EXPERIMENT

The $\text{Al}_x\text{Ga}_{1-x}\text{As}$ layers used in this study were grown in a conventional, horizontally configured, atmospheric pressure MOCVD reactor which has been routinely producing device-quality materials. Pd-cell purified H_2 was used as the carrier gas. The column III precursors

were trimethylaluminum (TMAI) and trimethylgallium (TMGa). The column V precursor was pure arsine. H_2Se (100 ppm in ultra high-purity H_2) was used for Se-doping. No getters were used to purify any sources in this study. The materials were grown at 730°C with precursor V/III ratio of 40, and a growth rate of 4.0 um/hr . A 2-um-thick $\text{Al}_{0.22}\text{Ga}_{0.78}\text{As}$ (Se-doped or undoped) layer, unless otherwise noted, was grown on n^+ -GaAs (10^{18} cm^{-3}) substrates. The free carrier concentration was measured by capacitance-voltage (C-V) measurements. The composition of Al and Ga was determined by double crystal x-ray rocking curve measurements.

Schottky contacts, 700 um in diameter, were made by evaporating Au through a metal mask onto the AlGaAs surface immediately after etching in freshly prepared 2:1:1 $\text{H}_2\text{SO}_4\text{:H}_2\text{O}_2\text{:H}_2\text{O}$ solution for 15 seconds. Ohmic contacts were made by evaporating AuGe/Au on the n^+ -GaAs substrate, and alloyed in forming gas (95% N_2 +5% H_2) atmosphere at 420°C for 2 min. Our DLTS setup was made by Sula Technologies, and consists of DLTS and a double-correlator DLTS (DDLTS). Details for trap depth profiling are contained in Ref. 6. The temperature scan range was from 30 to 380 K. Data were taken automatically by a computer through a high speed analog-digital converter board.

III. RESULTS AND DISCUSSION

The DLTS spectrum for the undoped- $\text{Al}_{0.22}\text{Ga}_{0.78}\text{As}$ layer, which has a carrier concentration of $5.0 \times 10^{15} \text{ cm}^{-3}$, is shown in Fig. 1(a). Three main deep electron traps, E1, E2 and E3, were observed with activation energies of 0.70, 0.53 and 0.30 eV, and trap concentrations of $3.4 \times 10^{14} \text{ cm}^{-3}$, $3.6 \times 10^{14} \text{ cm}^{-3}$ and $3.8 \times 10^{13} \text{ cm}^{-3}$, respectively. These traps are commonly

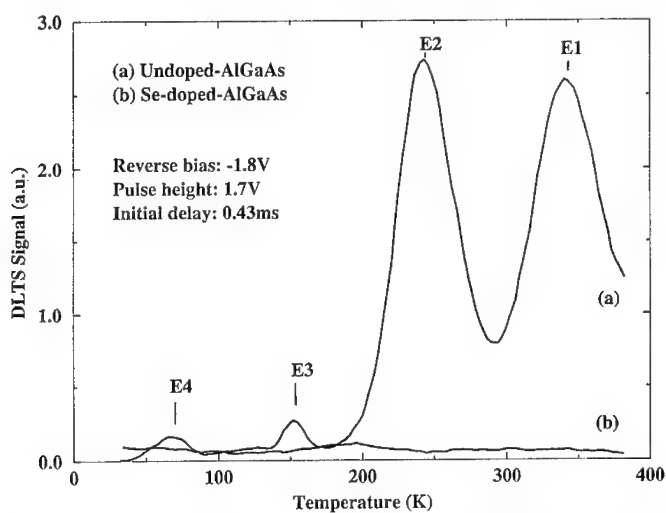


Figure 1. DLTS spectra for (a) undoped- $\text{Al}_{0.22}\text{Ga}_{0.78}\text{As}$ layer, showing three main electron traps at 0.70, 0.53 and 0.30 eV; (b) lightly Se-doped- $\text{Al}_{0.22}\text{Ga}_{0.78}\text{As}$ layer, showing no traps.

observed in MOCVD-grown AlGaAs layers^{7,8}. The 0.30 eV trap E3 has been attributed to Ge contamination in arsine³. The very low concentration of this trap in undoped-AlGaAs indicates that our arsine source (Megabit-grade, Solktronic Chemicals, Inc.) is very pure compared with that reported elsewhere³. The 0.53 and 0.70 eV traps were associated with oxygen. A shallow electron trap E4 was also observed with an activation energy of 0.08 eV, which could be a shallow impurity level.

Fig. 1(b) shows the DLTS spectrum for the lightly Se-doped $\text{Al}_{0.22}\text{Ga}_{0.78}\text{As}$ layer with a carrier concentration of $8.4 \times 10^{16} \text{ cm}^{-3}$ as obtained by C-V measurement. Under the detection limit (10^{13} cm^{-3}) of our DLTS system, no deep levels were observed up to 380K. Not only were the oxygen contamination-related traps E1 and E2 eliminated, but also the Ge-related trap E3 disappeared.

In order to confirm that the disappearance of deep levels is due to Se doping, we first grew a 200Å Se-doped ($5.0 \times 10^{17} \text{ cm}^{-3}$) $\text{Al}_{0.22}\text{Ga}_{0.78}\text{As}$ thin layer on a GaAs substrate, followed by a 2-μm-thick undoped- $\text{Al}_{0.22}\text{Ga}_{0.78}\text{As}$ layer. Because of the memory effect, one might expect residual Se impurity in the undoped AlGaAs layer although the source of H_2Se was shut off, and expect less Se near the surface region. The carrier concentration profile of this sample is shown in Fig. 2. An increased carrier concentration with distance away from the surface was observed due to the memory effect as expected. We used the DDLTS technique to probe the depth distri-

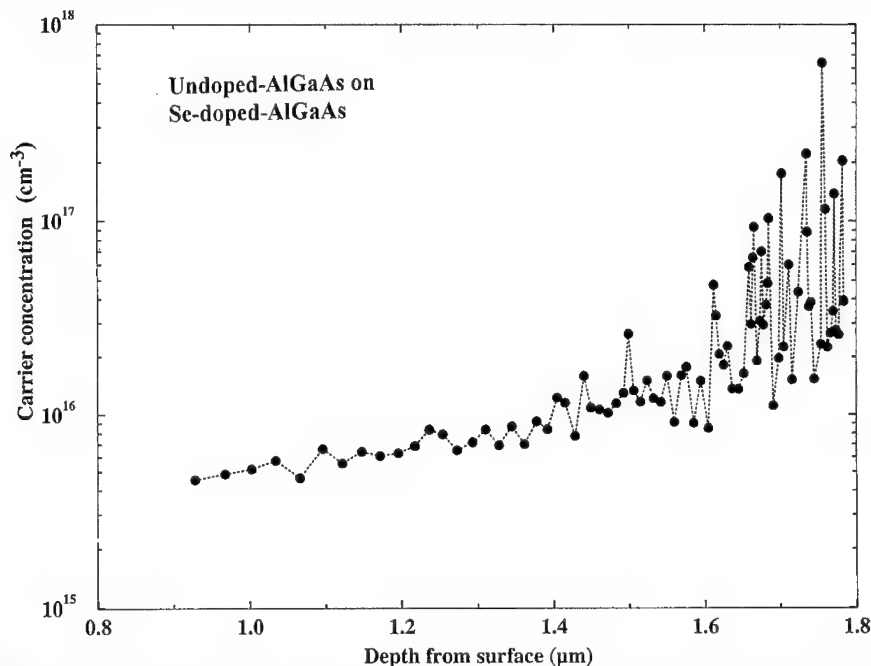


Figure 2. The distribution of carrier concentration in undoped- $\text{Al}_{0.22}\text{Ga}_{0.78}\text{As}$ sample grown on a 200Å-thick Se-doped $\text{Al}_{0.22}\text{Ga}_{0.78}\text{As}$ layer.

bution of trap concentrations in this sample. The results for traps E1, E2 and E3 are shown in Fig.3, which indeed shows that the electron traps E1, E2 and E3 have larger concentrations near the surface, which decrease with distance away from the surface. In order to eliminate the possible annealing effect during the alloying for small ohmic contacts, we also made Schottky contacts on the AlGaAs surface by evaporating two contacts with different sizes (30:1). Measurements on these diodes gave the same results. We believe that the reduction of these deep traps is due to the presence of the Se impurity.

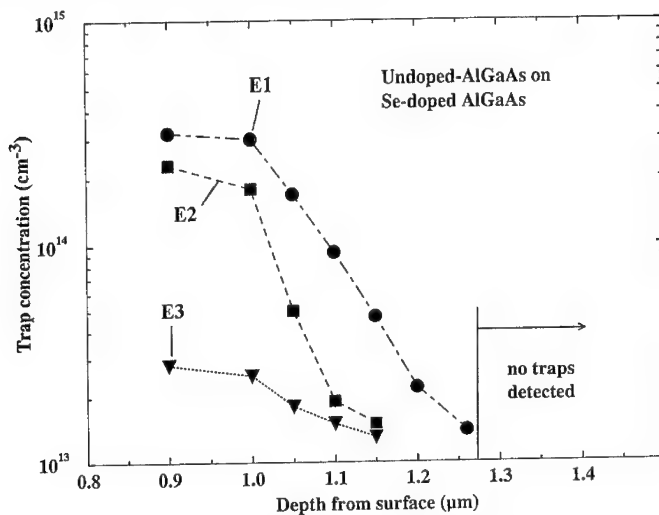


Figure 3. Depth profiles of main electron traps E1, E2 and E3 in undoped- $\text{Al}_{0.22}\text{Ga}_{0.78}\text{As}$ grown on Se-doped AlGaAs layer.

The reason that Se-doping can reduce the deep traps in $\text{Al}_{0.22}\text{Ga}_{0.78}\text{As}$ is not known at the present time. Reports on the effect of Se impurity in AlGaAs are controversial. Several authors^{9,10} have reported that Se can produce two deep electron levels at 0.24 and 0.29 eV below the conduction band edge in $\text{Al}_x\text{Ga}_{1-x}\text{As}$ with $x > 0.23$, which was not observed in this study, partly due to lower doping level and smaller Al composition of our samples. Ishikawa⁵ et al. reported that Se doping could reduce the DX center concentration compared to their MBE-grown Si-doped AlGaAs. It is also often found that the most useful n-type dopants, such as S and Se, do not become electrically active in AlGaAs¹¹. It is reasonable to consider, in our case, that the reduction of trap E1 and E2 could be due to the reduction of oxygen incorporation caused by Se-doping. However, we did not observe any change of oxygen concentration in our Se-doped and undoped-AlGaAs from secondary ion mass spectroscopy (SIMS) measurements and analysis (Fig.4). Moreover, when Se doping was greater than $2 \times 10^{17} \text{ cm}^{-3}$, a hole trap appeared. Fig.5. shows the hole trap observed by DLTS in a Se-doped $\text{Al}_{0.22}\text{Ga}_{0.78}\text{As}$ layer with a doping concentration of $5.0 \times 10^{17} \text{ cm}^{-3}$. By changing the reverse bias and/or pulse height, we did not observe any peak shift for this trap, indicating that this hole trap could be a bulk trap in AlGaAs, and related to Se. Its activation energy obtained from an Arrhenius plot was $E_V + 0.65 \text{ eV}$. This is the first time that a hole trap has been

observed in Se-doped AlGaAs. We found that Au on Se-doped $\text{Al}_{0.22}\text{Ga}_{0.78}\text{As}$ has a high barrier height (1.15eV), which enables this hole trap to be observed. A detailed study on this

Figure 4. SIMS data for the sample grown with Al content of 0.22, but with and without Se-doping. (0-4 μm Se-doped, 4-5 μm undoped AlGaAs)

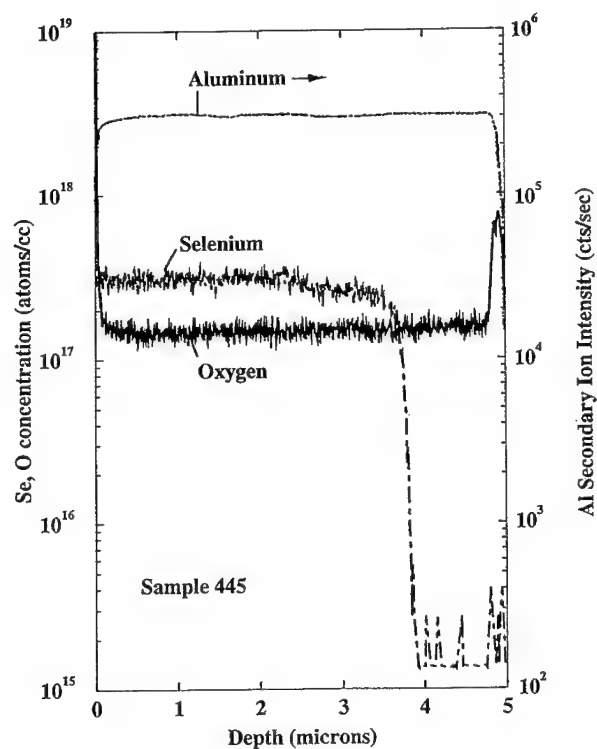
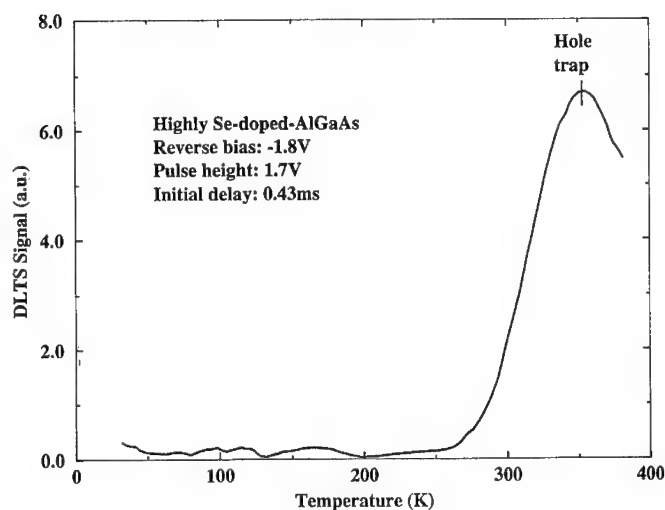


Figure 5. DLTS spectrum in highly Se-doped $\text{Al}_{0.22}\text{Ga}_{0.78}\text{As}$ sample. A strong hole trap at $E_V+0.65$ eV was observed.



hole trap will be reported elsewhere. In view of these results, we suggest that Se could produce a passivation effect in AlGaAs material when doping is less than $2 \times 10^{17} \text{ cm}^{-3}$, instead of reducing the actual incorporation of other impurities. This passivation effect renders other deep levels electrically inactive. The passivation effect by Se on GaAs surfaces has been reported by several authors^{12,13}. The underlying physics needs more study.

Finally, it should be stressed that the memory effect in an AlGaAs layer due to Se-doping could last up to 1 μm thick during the MOCVD growth, as can be seen in Fig.2 and 3, and the undoped-AlGaAs layer within the memory effect has a very low trap concentration. This gives us a hint that, for device applications, a deep-level-free AlGaAs layer with low carrier concentration can be achieved simply by growing it on a thin Se-doped buffer layer. The effect of Se-doping on $\text{Al}_x\text{Ga}_{1-x}\text{As}$ with higher Al composition ($x > 0.22$) will be published elsewhere.

IV. CONCLUSION

In conclusion, the deep levels in Se-doped and undoped- $\text{Al}_{0.22}\text{Ga}_{0.78}\text{As}$ epilayers have been investigated by DLTS measurements. Se was found to be effective to reduce the deep levels which are commonly observed in MOCVD-grown AlGaAs. A deep-level-free $\text{Al}_{0.22}\text{Ga}_{0.78}\text{As}$ layer was obtained by low Se-doping with concentration of $8.4 \times 10^{16} \text{ cm}^{-3}$. We suggest that Se can provide a passivation effect in AlGaAs when doping is less than $2 \times 10^{17} \text{ cm}^{-3}$, and electrically deactivate deep levels.

This work was supported by Integrated Technology for Medicine, Silver Spring, MD (Dr. P. Skeath) through the Maryland Industrial Partnerships (MIPS) Program. The authors would like to express their thanks to Dr. F. Johnson (Laboratory for Physical Science, Univ. of Maryland College Park) for assistance in SIMS measurements.

REFERENCES

1. D.V.Lang, R.A.Logan, and M.Jaros, *Phys. Rev. B* **19**, 1015 (1979)
2. P.K.Bhattacharya, S.Subramanian and M.J.Ludowise, *J. Appl. Phys.*, **55**, 3664 (1984)
3. R.T. Green and W.-I. Lee, *J. Electron. Mater.*, **20**, 583 (1991)
4. K.Kobayashi, M.Yamaga, I.Fujimoto and T.Suzuki, *Jpn. J. Appl. Phys.*, **28**, L1073 (1989)
5. T.Ishikawa, T.Maeda and K.Kondo, *Appl. Phys. Lett.*, **53**, 1926 (1988)
6. Z.C.Huang, C.R.Wie, D.K.Johnstone, C.E.Stutz and K.R.Evans, *J. Appl. Phys.*, **73**, 4362 (1993)
7. H.Terao and H.Sunakawa, *J. Cryst. Growth*, **68**, 157 (1984)
8. T.F.Keuch, E.Veuhoff, T.S.Kuan, V.Deline and R.Potemski, *J. Cryst. Growth*, **77**, 257 (1986)
9. E.G.Oh, M.C.Hanna, Z.H.Lu, D.M.Szmyd and A.Majerfield, *J. Appl. Phys.*, **74**, 1057 (1993)
10. O.Kumagai, H.Kawai, Y.Mori and K.Kaneko, *Appl. Phys. Lett.*, **45**, 1323 (1984)
11. A.K.Rai, R.S.Bhattacharya and P.P.Pronko, *Appl. Phys. Lett.*, **41**, 1086 (1982)
12. C.J.Sandroff, M.S.Hegde, L.A.Farrow, R.Bhat, J.P.Harbison and C.C.Chang, *Appl. Phys. Lett.*, **67**, 586 (1990)
13. J.Fan, H.Oigawa and Y.Nannichi, *Jpn. J. Appl. Phys.*, **27**, L2125 (1988)

LOW-TEMPERATURE, SOLID-PHASE EPITAXIAL GROWTH OF AMORPHIZED, NON-STOICHIOMETRIC GaAs

K.B. BELAY*, D.L. LLEWELLYN** AND M.C. RIDGWAY*

*Department of Electronic Materials Engineering, Australian National University, Canberra, Australia

**Electron Microscopy Unit, Research School of Biological Sciences, Australian National University, Canberra, Australia

ABSTRACT

Non-stoichiometric GaAs layers with semi-insulating properties can be produced by low-temperature molecular beam epitaxy or ion implantation. The latter is the subject of the present report wherein the solid-phase epitaxial growth of amorphized, non-stoichiometric GaAs layers has been investigated with time-resolved reflectivity, Rutherford backscattering spectrometry and transmission electron microscopy. GaAs substrates were implanted with Ga and/or As ions and annealed in air at a temperature of 260°C. The recrystallized material was composed of a thin, crystalline layer bordered by a thick, twinned layer. Non-stoichiometry results in a roughening of the amorphous/crystalline interface and the transformation from planar to non-planar regrowth. The onset of the transformation and the rate thereof can increase with an increase in non-stoichiometry. Non-stoichiometry can be achieved on a macroscopic scale via Ga *or* As implants or on a microscopic scale via Ga *and* As implants. The influence of the latter is greatest at low doses whilst the former dominates at high doses.

INTRODUCTION

The novel electrical and optical properties of non-stoichiometric GaAs yield unique device applications such as high-speed photodetectors and photoconductive switches [1]. Viable technologies for the fabrication of As-rich GaAs include both low-temperature molecular beam epitaxy [2] and ion implantation [3]. The latter typically involves As ion implantation at an energy and dose of 200 keV and 1×10^{16} /cm², respectively, with the substrate maintained at room temperature. Subsequent annealing at temperatures of ~600°C results in the solid-phase epitaxial growth (SPEG) of the implantation-induced amorphous layer and the formation of As precipitates and As_{Ga} anti-site defects. The resistivity of the resulting non-stoichiometric, epitaxial layer can exceed that of the underlying, semi-insulating substrate.

The potential technological applications of As-rich GaAs have renewed interest in the SPEG of amorphous GaAs. As previously observed by others [4], layers recrystallized at temperatures of 200-300°C are typically composed of a thin, single-crystal layer bordered by a thicker, heavily-twinned layer at lesser depths. For the present report, Ga and/or As ion implantation has been utilized to determine the influence of non-stoichiometry on the SPEG of amorphous GaAs. Ga *and* As implantation can yield non-stoichiometry on a microscopic scale as a result of the statistical nature of the ion stopping and recoiling processes. Alternatively, macroscopic non-stoichiometry can be achieved with Ga *or* As implantation and thus, as

demonstrated below, the relative influences of both microscopic and macroscopic non-stoichiometry can be differentiated.

EXPERIMENTAL

Semi-insulating GaAs wafers of (100) orientation were implanted with Ga and/or As ions at energies of 190 and 200 keV, respectively, to total doses of 3×10^{14} – 1×10^{16} /cm². At such energies, the two ions have comparable range and straggle and thus, macroscopic stoichiometry can be maintained in samples implanted with both ions to the same dose. During implantation, substrates were maintained at temperatures of $\sim 196^\circ\text{C}$ to ensure both the formation of a continuous amorphous layer extending to the surface and the minimization of the extent of disorder in the crystalline substrate in close proximity to the amorphous/crystalline (a/c) interface. Substrates were subsequently annealed in air at a temperature of 260°C and the recrystallization of the amorphous layer was monitored in-situ with time-resolved reflectivity (TRR) [4] utilizing HeNe laser irradiation at a wavelength of 633 nm. TRR results were correlated with both Rutherford backscattering spectrometry combined with channeling (RBS/C) measurements, performed with 2 MeV He ions and a scattering angle of 100° , and cross-sectional transmission electron microscopy (XTEM), using a 200 keV electron beam. For the latter, samples were prepared by ion-beam milling at a temperature of $\sim 196^\circ\text{C}$.

RESULTS AND DISCUSSION

Figure 1 shows TRR spectra of Ga- and As-implanted samples as a function of total ion dose. Though macroscopic stoichiometry has been maintained in such samples, an increase in non-planarity at the a/c interface is evident with an increase in total ion dose. (Note the reduction in amplitude of the TRR oscillations at annealing times of $< \sim 300$ sec.) Correlating TRR and RBS/C spectra (some of the latter are shown below), the average velocity of the a/c interface is insensitive to ion dose at depths of $> \sim 60$ nm while at lesser depths, a decrease in velocity is apparent with an increase in total ion dose. (Note the increase in time from minimum to maximum to minimum associated with the last TRR oscillation.)

Figures 2(a) and (b) show corresponding RBS/C spectra for the Ga- and As-implanted samples with total ion doses of 3×10^{14} and 1×10^{16} /cm², respectively. For both samples, the recrystallized layer is evidently composed of a thin, crystalline region and a thicker, twinned region (the latter at lesser depths) as consistent with the previously published reports cited above. The width of the amorphous layer increases with total ion dose, as anticipated. Furthermore, the relative fraction of twins increases and/or the volume of individual twins decreases with total ion dose as evidenced by the increase in backscattered ion yield over the extent of the twinned region in Fig. 2(b). Figs. 1 and 2 thus demonstrate that microscopic non-stoichiometry potentially influences both interfacial non-planarity and the extent and/or volume of twinned material. Implantation-induced voids and/or recoiled surface contaminants may also yield a similar trend but the relative contribution of such effects is considered insignificant in the present report.

The influence of macroscopic non-stoichiometry is apparent in Figure 3 which compares TRR spectra of Ga-, As- or Ga- and As-implanted samples to a total ion dose of 1×10^{16} /cm². On average, both the non-planarity and velocity of the a/c interface are greater in the macroscopically

non-stoichiometric samples. The nature of such effects is evident from the XTEM micrographs of Figure 4 which show the recrystallization of the Ga-implanted sample as a function of time. Recrystallization initially proceeds in a single-crystal manner followed by the onset of twinning as noted above. Thereafter, a rapid amorphous-to-crystalline transformation is apparent (note the protuberances at the twinned/amorphous interface) yielding the increase in interfacial non-planarity and velocity evident from the TRR spectra of Fig. 3. Excess Ga perturbs the SPEG of amorphous GaAs to a greater extent than excess As, potentially as a result of the molten nature of any Ga precipitates at temperatures of 260°C.

Figure 1. TRR spectra of Ga- and As-implanted GaAs as a function of total ion dose.

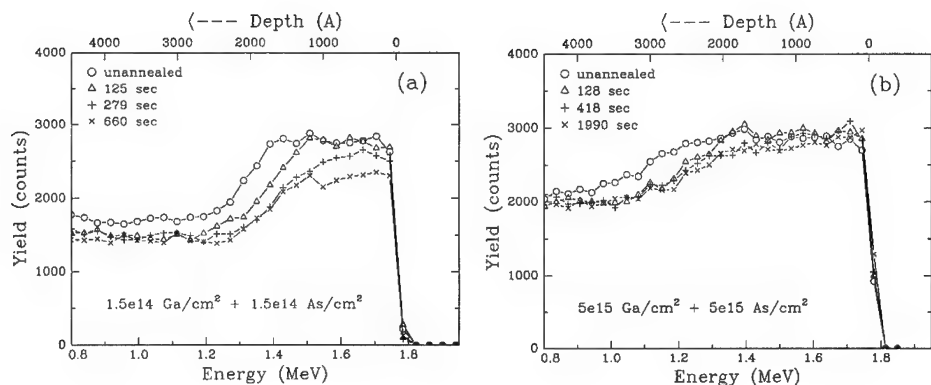
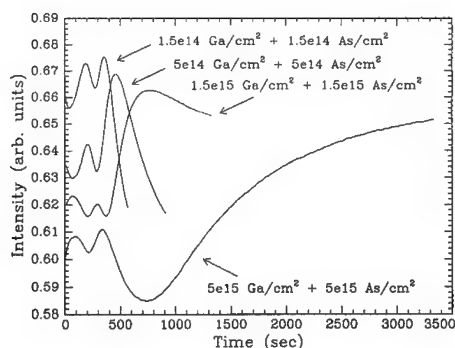
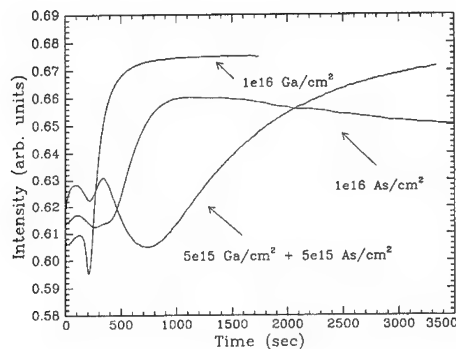


Figure 2. RBS/C spectra of Ga- and As-implanted GaAs for total ion doses of (a) 3×10^{14} and (b) $1 \times 10^{16} / \text{cm}^2$.

Figure 3. TRR spectra of Ga-, As- or Ga- and As-implanted GaAs as a function of total ion dose for a total ion dose of $1 \times 10^{16} / \text{cm}^2$



TRR and RBS/C measurements indicate the initial stages of recrystallization for both stoichiometric and non-stoichiometric samples are similar. Figures 5(a) and (b) show measurements of the depth and corresponding energy deposition in displacements (vacancies and replacements), respectively, for the original *a/c* interface and the onset of twinning as a function of total ion dose. Fig. 5(b) was derived from Fig. 5(a) with the aid of modified TRIM calculations [5]. From Fig. 5(a), it is evident that the width of the amorphous layer increases as total ion dose increases, as noted previously, and furthermore, that extent of twin-free recrystallization is typically ~ 30 nm. Note that both parameters are independent of the implanted ion species. From Fig. 5(b), the critical energy deposition in displacements required for amorphization at temperatures of $\sim 196^\circ\text{C}$ is $\sim 3 \times 10^{22} \text{ eV/cm}^3$ whilst that for the onset of twinning during SPEG at 260°C is $\sim 2 \times 10^{23} \text{ eV/cm}^3$. Both parameters are independent of total ion dose as anticipated. Given that microscopic non-stoichiometry is necessarily correlated with energy deposition in displacements, Fig. 5(b) demonstrates the onset of twinning during SPEG of GaAs is thus consistent with a critical level of microscopic non-stoichiometry. It is also evident from Fig. 5(b) that the macroscopic non-stoichiometry inherent in Ga- or As-implanted samples does not induce twinning.

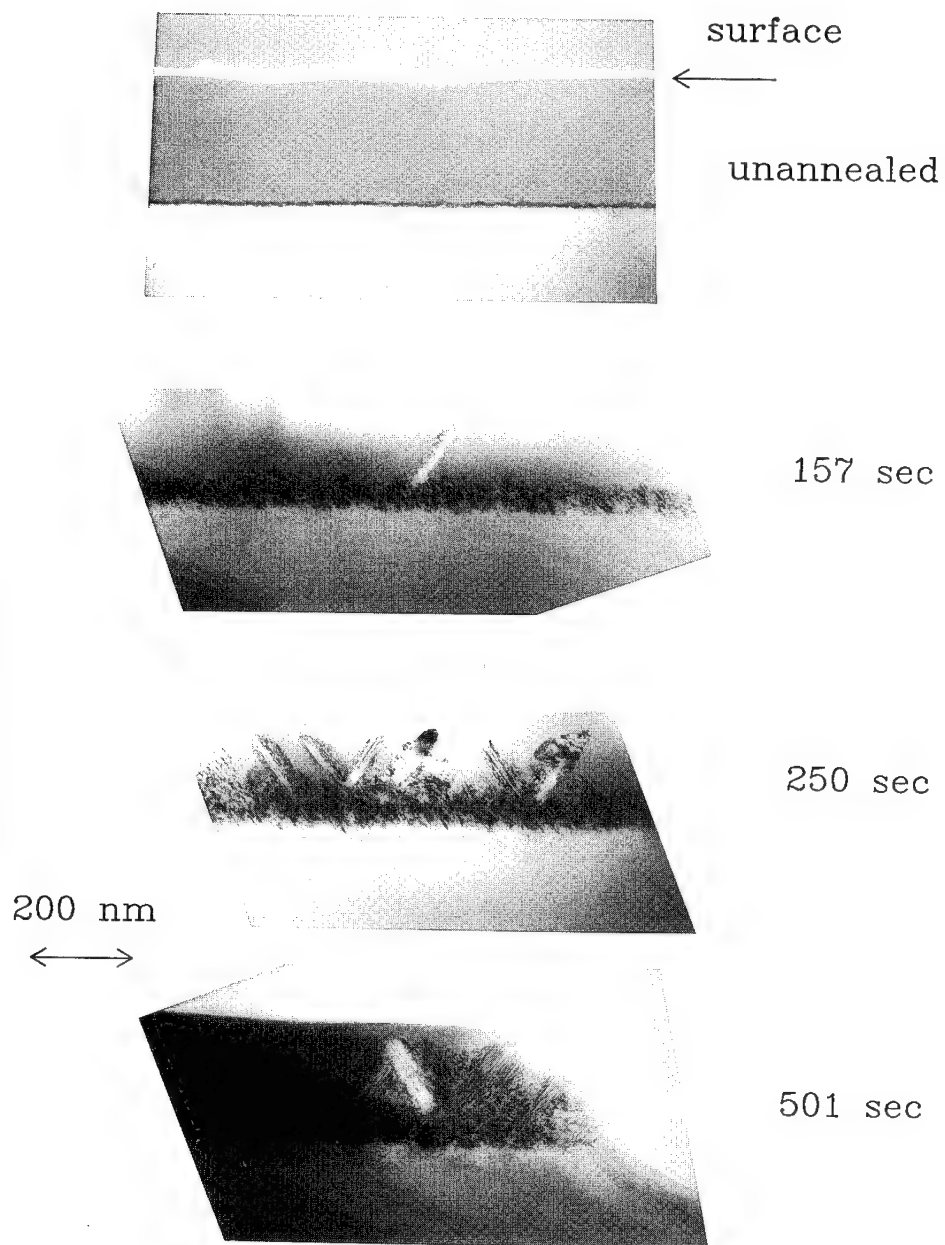


Figure 4. XTEM micrographs of Ga-implanted GaAs as a function of annealing time for an ion dose of $1 \times 10^{16} / \text{cm}^2$.

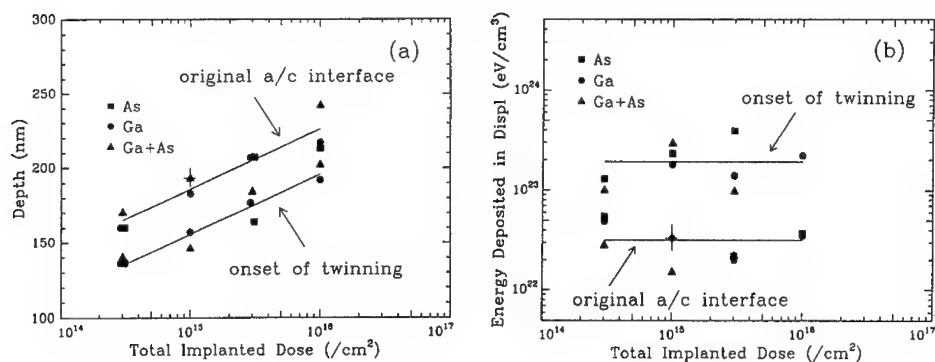


Figure 5. Plots of (a) the depth and (b) the corresponding energy deposition in displacements for the original a/c interface and the onset of twinning as a function of total ion dose.

CONCLUSIONS

Non-planarity of the a/c interface and twin formation during the SPEG of amorphous GaAs is consistent with the presence of microscopic non-stoichiometry. At high ion doses, macroscopic Ga-rich non-stoichiometry can induce a rapid, amorphous-to-crystalline transformation potentially mediated via molten Ga precipitates. Macroscopic As-rich non-stoichiometry has a lesser influence than that of excess Ga. Comparing microscopic and macroscopic non-stoichiometry, the relative influences of the former and latter are greatest at low and high ion doses, respectively.

REFERENCES

- [1] U.K. Mishra, *Mat. Sci. and Eng.* **B22** (1993) 72 and references therein.
- [2] G.L. Witt, *Mat. Sci. and Eng.* **B22** (1993) 9 and references therein.
- [3] A. Clavarie, F. Namavar, Z. Liliental-Weber, P. Dreszer and E.R. Weber, *Mat. Sci. and Eng.* **B22** (1993) 37.
- [4] G.L. Olson and J.A. Roth, *Handbook of Crystal Growth* **3** and references therein.
- [5] J.F. Ziegler, J.P. Biersack and U. Littmark, *The Stopping and Range of Ions in Matter* (Pergamon, Oxford, 1985).

MAGNETIC CIRCULAR DICHROISM OF LOW-TEMPERATURE-GROWN $\text{Al}_x\text{Ga}_{1-x}\text{As}$

A. PRASAD^a, X. LIU, P. STALLINGA, E. R. WEBER
*Department of Materials Science and Mineral Engineering, University of California,
Berkeley, CA 94720*

A. K. VERMA, J. S. SMITH
*Department of Electrical Engineering and Computer Science, University of California,
Berkeley, CA 94720*

ABSTRACT

We study magnetic circular dichroism of absorption (MCDA) of LT $\text{Al}_x\text{Ga}_{1-x}\text{As}$ as a function of aluminum content. The MCDA spectrum of LT $\text{Al}_x\text{Ga}_{1-x}\text{As}$ is distinctly different from the MCDA spectrum of LT GaAs, which has one paramagnetic and one diamagnetic peak at 0.95 eV and 1.18 eV, respectively. As the aluminum content increases, the spectrum of LT $\text{Al}_x\text{Ga}_{1-x}\text{As}$ is dominated by a diamagnetic peak similar to the 1.18 eV peak of the EL2⁰-like defects in LT GaAs. However, the peak shifts to higher energies as x increases. The photoquenching and temperature dependence of this peak indicates an association with the EL2 defect. The paramagnetic peak observed in LT GaAs also shifts to higher energies but faster and eventually merges with the diamagnetic peak as the Al content increases. The study of the MCDA spectrum of LT $\text{Al}_x\text{Ga}_{1-x}\text{As}$ as a function of aluminum content allows a better understanding of the MCDA phenomena of LT $\text{Al}_x\text{Ga}_{1-x}\text{As}$ and LT GaAs, as well as the EL2-related transitions in bulk semi-insulating GaAs.

INTRODUCTION

Low-temperature-grown (LT) III-V semiconductors, especially LT GaAs, in the recent years have generated extensive interest in both academia and industry. The high resistivity and short carrier lifetime of LT GaAs have led to its use in various devices such as GaAs MESFETs and fast photodetectors^{1,2}. This material has a high intrinsic defect concentration (As on a Ga site, As_{Ga}) which controls the material properties in both the as-grown³ and most likely even the annealed states⁴. Scientists are in pursuit of understanding this defect and its effects on the material properties. Recently LT AlGaAs has been shown to have an even higher resistivity⁵, and is being used in LT-GaAs/AlGaAs superlattices⁶. Electrical measurements indicate that the As antisite also might in this material play an important role⁷. To further the understanding of the influence of As_{Ga} on LT AlGaAs, and vice-versa, we study this defect as a function of Al content. This may increase our understanding of As_{Ga} in LT AlGaAs as well as in LT GaAs and bulk semi-insulating (SI) GaAs.

Magnetic circular dichroism of absorption (MCDA) is a good tool with which to obtain a fingerprint of the As antisite defect as well as determine its concentration. It is sensitive to paramagnetic defects. However, high concentrations of diamagnetic defects can also contribute to the signal. A contribution from only the paramagnetic As_{Ga}^+ is observed in bulk GaAs⁸ (Figure 1). This spectrum has the typical one negative (0.94 eV) and two positive bands (1.1 eV and 1.35 eV). In comparison, the MCDA of LT GaAs (Figure 1) has two negative peaks (0.94 eV and 1.18 eV). From previous studies^{4,9-11}, it

has been shown that the 0.94 eV peak is paramagnetic and that the 1.18 eV peak is mostly diamagnetic, as evidenced by the independence of the MCDA from the temperature. It has previously been suggested that this diamagnetic peak is related to the $A_1 \rightarrow T_2$ internal transition associated with the diamagnetic state of the As antisite, As_{Ga}^0 . Occurrence of the diamagnetic band in the MCDA is due to the high concentration of As_{Ga}^0 , $\sim 10^{20} \text{ cm}^{-3}$. Such a high concentration is present only in LT GaAs and As implanted GaAs. Similarly, LT $Al_xGa_{1-x}As$ should also have a high concentration of the antisite. Via MCDA we may determine the concentration of the antisite in this new material and how the Al content affects the incorporation and MCDA spectrum of As_{Ga} .

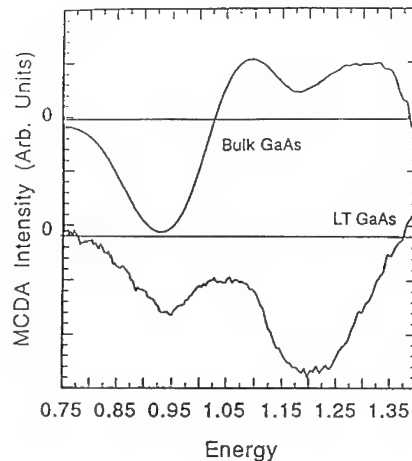


Figure 1: Typical MCDA spectra of As_{Ga} defects in bulk SI GaAs and LT GaAs grown at 210°C. The spectra are measured at $T=1.8 \text{ K}$ and $B=2 \text{ T}$.

EXPERIMENTAL

The LT $Al_xGa_{1-x}As$ samples studied here are fabricated using a Varian Modular Gen II MBE chamber. On an n^+ GaAs substrate, first a buffer layer ($\sim 0.1 \mu\text{m}$ at 600 °C) of n^+ GaAs is grown and then the $1.5 \mu\text{m}$ epilayer of interest is grown at the substrate temperature of 230°C. The Al contents studied are $x=0.0, 0.05, 0.1, 0.13, 0.16, 0.2$, and 0.3 . Substrates of n^+ doping are used to minimize the MCDA signal from the As antisites present in the GaAs substrate¹². However, the sample with $x=0.3$ is grown to a $1 \mu\text{m}$ thickness on a semi-insulating (SI) GaAs. To further reduce the substrate influence on the MCDA spectrum, the substrate is polished down to less than $100 \mu\text{m}$ and the remaining signal from the SI substrate is subtracted out by the computer.

For MCDA measurements the samples are placed in an optical cryostat at a temperature of 1.8K. The cryostat also houses a 6 T superconducting magnet, which is set to 2 T for MCDA. A 250W tungsten-halogen lamp is used as the light source. The generated photons which are dispersed by a grating monochromator are then polarized linearly. They then transverse through a long pass filter ($\lambda > 780 \text{ nm}$) and a quartz stress modulator operating at 42 kHz. The transmission of the alternating left and right circularly polarized light through the LT $Al_xGa_{1-x}As$ samples is collected by the liquid- N_2 -cooled Ge-detector and the difference is taken by the lock-in. The MCDA spectrum thus obtained is corrected for the system response by subtracting the MCDA signal at 0 T and then dividing by the transmission (the modulator is replaced by the chopper) of the system plus sample. Finally, to remove the substrate influence, the spectrum of the substrate is subtracted.

Photo-quenching studies are made as well to correlate the MCDA signal with the EL2 defect. First, spectra are collected with the sample cooled in the dark. Then the samples are exposed to white light illumination. After removing the light, new spectra are collected. If the spectra are associated with EL2 then the signal should decrease, implying that the illumination transformed the EL2 into its metastable state. To recover the full EL2 signal the sample has to be heated to above 140 K.

RESULTS

The MCDA spectra of LT $\text{Al}_x\text{Ga}_{1-x}\text{As}$ and LT GaAs are similar as seen in Figure 2. At low Al percentage the MCDA spectrum of LT $\text{Al}_x\text{Ga}_{1-x}\text{As}$ has the same features of two negative peaks. As the amount of Al increases the two peaks still exist but they start to shift to higher energies with the paramagnetic peak shifting faster than the diamagnetic peak. Eventually the paramagnetic peak merges into the diamagnetic peak (around $x=0.2$), but a definite shoulder at lower energies is visible. Even the shoulder disappears near $x=0.3$. For $x=0.3$ the only MCDA band observed is located at 1.35 eV.

Photo quenching studies indicate that these two peaks and eventually the one peak are associated with the EL2 defect. Unlike in LT GaAs¹¹, the peaks in LT $\text{Al}_x\text{Ga}_{1-x}\text{As}$ are quenchable to a greater extent, ~ 80-90%. Temperature dependent MCDA is performed on the $x=0.2$ and 0.3 samples. The samples are first cooled in the dark to 1.8 K and MCDA spectra are collected at different, increasing temperatures. Next, the samples are cooled down to 1.8 K again and then quenched with white light. MCDA spectra are

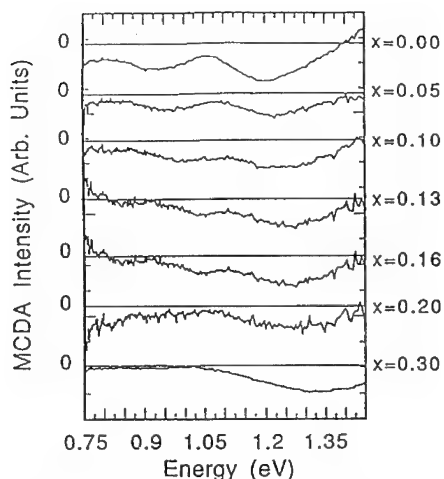


Figure 2: MCDA spectra of LT $\text{Al}_x\text{Ga}_{1-x}\text{As}$ as a function of increasing Al content. The two negative peaks shift to higher energies with increasing x . The paramagnetic band starting at 0.94 eV shifts faster than the diamagnetic band at 1.18 eV for $x=0.0$, and eventually only the one peak is observable.

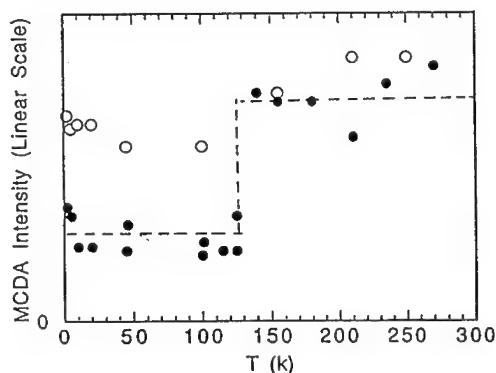


Figure 3: Recovery from photo quenching as a function of temperature for the 30% Al sample. Open circles are the MCDA signal of the unquenched sample while the filled circles represent the signal from the photo quenched sample.

collected for these samples at increasing temperatures as well. As seen from Figure 3, the original unquenched signal is fully recovered from the quenching process around 140 K, which is identical to the recovery process of quenched EL2 in bulk GaAs¹³.

DISCUSSION

As mentioned earlier, MCDA is a sensitive technique for studying paramagnetic defects. Previous studies on bulk GaAs have shown that the As_{Ga} defect in its paramagnetic form (As_{Ga}^+) has a signal composed of two derivative like bands⁸. When added together, the resulting spectrum has a negative peak at 0.94 eV and two positive peaks at 1.1 eV and 1.35 eV. However, studies done by Pillkuat et al.¹⁴ show that a diamagnetic peak associated with the As_{Ga} defect can also be detected by MCDA. A temperature scan enables one to distinguish between paramagnetic and diamagnetic contributions. The diamagnetic part is temperature independent, whereas the paramagnetic part decreases with temperature. Recently, a diamagnetic peak has also been observed in LT GaAs⁴.

Large quantities of As_{Ga} defects present in LT GaAs have been shown to control the properties of this material. The antisite defect has been shown to have high concentration in both neutral and positive charge states, $[\text{As}_{\text{Ga}}^0]=10^{20} \text{ cm}^{-3}$ and $[\text{As}_{\text{Ga}}^+]=5 \times 10^{18} \text{ cm}^{-3}$, respectively. Previous MCDA measurements⁴ show that the negative diamagnetic contribution at 1.18 eV is most likely related to the As_{Ga}^0 . The two positive peaks observed in bulk GaAs are overlapped with the diamagnetic band in LT GaAs. The strong intensity of the As_{Ga}^0 -related peak overshadows the positive peaks; therefore, only two negative MCDA bands are visible in LT GaAs. The two negative peaks are also observed in LT $\text{Al}_x\text{Ga}_{1-x}\text{As}$, though, they shift to higher energies as a function of increasing Al content. The paramagnetic band shifts faster than the diamagnetic band. The two MCDA peaks eventually merge into the one broad peak around $x=0.3$.

In the past, two models, the internal-transition model⁸ and the valence-band-transition model¹⁵, have been proposed to explain the MCDA spectrum of bulk SI GaAs. According to Meyer et al.⁸, in the internal transition model, the MCDA transitions of As_{Ga}^+ are intra-center from the A_1 ground state to the two T_2 excited states of the defect. This A_1 state is at 0.52 eV above the valence band, and the two T_2 states are 1.05 eV and 1.29 eV above the A_1 states and are resonant with the conduction band. Because the transitions are internal, they are not expected to be strongly affected by the change in bandgap that arises when Al is incorporated into the system as derived from pressure dependence studies done on EL2 in GaAs¹⁶.

The valence-band-transition model proposed by Kaufmann et al.¹⁵ postulates that the two MCDA transitions of bulk GaAs are the photoneutralization transitions $\text{As}_{\text{Ga}}^+ + h\nu \rightarrow \text{As}_{\text{Ga}}^0 + \text{hole}$ to the spin orbit splitting of the valence band. The transitions from the s-like ground state to p-like excited states are allowed by the dipole transition selection rules. These are satisfied in the valence band because of the band's p-like nature. The transitions are specifically to the heavy and light hole states of the Γ_8 valence band and the spin-orbit-split band. Thus, the hole transitions are from the ground As_{Ga}^+ defect to the excited valence band states. If this model is applied to the behavior of As_{Ga}^+ in LT $\text{Al}_x\text{Ga}_{1-x}\text{As}$, it would require the valence band to shift with the increasing Al content. Studies done by J. Menéndez et al. show that the valence band of $\text{Al}_x\text{Ga}_{1-x}\text{As}$ shifts with the Al composition^{17,18}.

From our results in LT $\text{Al}_x\text{Ga}_{1-x}\text{As}$ the large shift in energy of the paramagnetic MCDA band seems to be in good accord with the shifting valence band. The internal transition model cannot account for the large shift. Thus, this shift is in better agreement with the valence band model. A more detailed discussion will be presented in a forthcoming publication¹⁹. Also, the diamagnetic band in the MCDA spectra shifts slower than the paramagnetic band to higher energies with Al content, which is clearly indicated by the merging of the two spectra (Figure 2). The shift is still slightly larger than expected from the pressure dependence of the internal transition of EL2¹⁶. However, the deviation is not large enough to make a conclusive statement about this tentatively assigned transition, further studies are needed.

CONCLUSION

Our study of MCDA of LT $\text{Al}_x\text{Ga}_{1-x}\text{As}$ indicates a high concentration of As_{Ga} in the material. The energy shift of the MCDA transitions observed in LT $\text{Al}_x\text{Ga}_{1-x}\text{As}$ cannot be explained by ascribing the transitions to the internal T_2 states, however the shift is more consistent with the transitions to the valence band.

ACKNOWLEDGEMENTS

The authors thank Dr. B. K. Meyer for fruitful discussions. This work is supported by the Air Force Office of Scientific Research under grant F49620-95-1-0091. The use of experimental facilities at the Lawrence Berkeley Laboratory is supported by the U.S. Department of Energy under Contract DE-Ac03-76SF00098.

REFERENCES

- ^a Department of Chemistry, University of California, Berkeley, CA 94720.
1. F. W. Smith, A. R. Calawa, C. L. Chen, M. J. Manfra and L. J. Mahoney, IEEE Electron Device Lett. **9**, 77 (1988).
2. S. Gupta, J. F. Whitaker, S. L. Williamson, G. A., Mourou, L. Lester, K. C. Hwang, P. Ho, J. Mazurowski, and J. M. Ballingall, J. of Electronic Mats. **22** (12), 1449 (1993).
3. D. C. Look, D. C. Walters, M. O. Manasreh, J. R. Sizelove, C. E. Stutz, and K. R. Evans, Phys. Rev. B **42**, 3578 (1990).
4. X. Liu, A. Prasad, W. M. Chen, A. Kurpiewski, A. Stoschek, Z. Liliental-Weber, and E. R. Weber, Appl. Phys. Lett. **65** (23), 3002 (1994).
5. A. C. Campbell, G. E. Crook, T. J. Rogers, and B. G. Streetman, J. Vac. Sci. Technol. B **8**, 305 (1990).
6. K. Mahalingam, N. Otsuka, M. R. Melloch and J. M. Woodall, App. Phys. Lett. **60**, 3253 (1992).
7. A. K. Verma, J. Tu, J. Smith, H. Fujioka, and E. R. Weber, J. of Elec. Mater. **22** (12),

1417 (1993).

8. B. K. Meyer, J. M. Spaeth, and M. Scheffler, *Phys. Rev. Lett.* **52** (10), 851 (1984).
9. K. Krambrock, M. Linde, J. M. Spaeth, D. C. Look, D. Bliss, and W. Walukiewicz, *Semicond. Sci. Technol.* **7**, 1037 (1992).
10. F. C. Rong, L. Fotiadis, H. J. Sun, G. D. Watkins, M. A. Taysing-Lara, J. Flemish, W. and H. Chang, Low Temperature(LT) GaAs and Related Materials, edited by G. L. Witt, R. Calawa, U. Mishra, and E. Weber (*Mat. Res. Soc. Sym. Proc.* **241**, Pittsburgh, PA, 1992) pp. 75-80.
11. X. Liu, A. Prasad, W. M. Chen, and E. R. Weber, 22nd International Conference on the Physics of Semiconductors, edited by D. J. Lockwood (3, New Jersey, 1994) pp. 2427.
12. J. Lagowski, H. C. Gatos, J. M. Parsey, K. Wada, M. Kaminska, and W. Walukiewicz, *Appl. Phys. Lett.* **40**, 342 (1982).
13. G. Vincent and D. Bois, *Solid State Commun.* **27**, 431 (1978).
14. A. Pillukat and P. Ehrhart, *Appl. Phys. Lett.* **60** (22), 2794 (1992).
15. U. Kaufmann, and J. Windscheif, *Phys. Rev. B* **38** (14), 10060 (1988).
16. M. Baj and P. Dreszer, *Materials Science Forum* **38-41**, 101 (1989).
17. J. Menéndez, A. Pinczuk, D. J. Werder, J. P. Valladares, T. H. Chiu, and W. T. Tsang, *Solid State Communications* **61** (11), 703 (1987).
18. J. Menéndez, A. Pinczuk, D. J. Werder, A. C. Gossard, and J. H. English, *Phys. Rev. B* **33** (12), 8863 (1986).
19. A. Prasad, P. Stallnga, X. Liu, E. R. Weber, A. K. Verma, and J. S. Smith, to be published.

SPECTROSCOPIC ELLIPSOMETRIC CHARACTERIZATION OF LOW TEMPERATURE GaAs

X. GAO,* P. G. SNYDER,* P. W. YU,** Y. Q. ZHANG,*** AND Z. F. PENG***

*Center for Microelectronic and Optical Materials Research, and Dept. of Electrical Engineering, Univ. of Nebraska-Lincoln, Lincoln, NE 68588-0511

**WL/MLPO Bldg. 651, Wright Patterson AFB, OH 45433-7707

***Nanjing Electronic Devices Institute, Nanjing, 210016, P. R. China

ABSTRACT

Pseudodielectric functions of low temperature grown GaAs (LT GaAs) measured by spectroscopic ellipsometry are presented. The spectral range includes the E1 (2.92eV) and E1+ Δ 1 (3.13eV) critical point structure of GaAs. A Lorentz-oscillator model was used to fit the dielectric function of LT GaAs for samples with nominal growth temperatures (T_g) varying from 200°C to 580°C. For T_g of 200°C, 30% and 19% broadenings and -0.011eV and -0.007eV red shifts were found for the E1 and E1+ Δ 1 structures respectively, compared with normal GaAs. The red shift can be explained in terms of a strain effect in the LT layer. In annealed LT GaAs the broadening decreased significantly and no red shift was found.

INTRODUCTION

Since the discovery that low temperature MBE grown GaAs can be used as a buffer layer to reduce the "backgating" in GaAs MESFETs,^{1,2} much has been done to investigate its microstructural, electrical and optical properties. TEM and particle-induced x-ray emission studies provided the evidence of excess arsenic atoms in LT GaAs.^{3,4} After annealing at the normal grown temperature (550°C~600°C), these arsenic atoms precipitate and the material becomes semi-insulating. The result of double crystal x-ray diffraction shows that the lattice constant of 200°C grown LT GaAs is expanded by a factor of ~0.15%.^{5,6} Before and after annealing of 225°C grown, the mismatches are 0.133% and ~0.016% respectively.⁶ The lattice expansion in as-grown material is believed to be related to interstitial defects produced by excess arsenic atoms. The bandgap energy of LT GaAs is difficult to determine because it is not luminescent.¹

In this paper, room temperature pseudodielectric function spectra of MBE grown LT GaAs measured by spectroscopic ellipsometry (SE) are given as a function of growth temperature. Red shifting and broadening of the E1 and E1+ Δ 1 critical point structure were observed for T_g below 350°C in one set of samples. The origin of the red shifts will be discussed in terms of a strain effect in LT layer. Comparisons between as-grown and annealed LT GaAs samples are also presented.

EXPERIMENT

MBE grown LT GaAs samples were provided by Wright Labs (WL) and Nanjing Electronic Devices Institute (NEDI) of China. Seven samples from WL were as-grown LT GaAs with growth temperatures (T_g) varying from 200°C to 500°C every 50°C. Another one was grown at normal temperature (580°C). NEDI provided two samples grown at 200°C and 250°C and two annealed (at 550°C) samples with the same growth temperatures as well as a “normal” epilayer grown at 550°C. Both groups used a thermocouple to determine T_g . NEDI also estimated it by using the melting point of indium (156°C) at the surface of the molybdenum holder as a reference.

The characterizations were performed by variable angle spectroscopic ellipsometry (VASE). VASE measures the change in polarization state of a collimated polarized light beam reflected from the sample surface, over a range of wavelengths and at one or more angles of incidence. A rotating analyzer ellipsometer (from J. A. Woollam Co.) was used. The sample's complex reflection coefficients for light polarized in ‘p’, and ‘s’ directions (parallel and perpendicular to the plane of incidence, respectively) are given by R_p and R_s . Ellipsometric parameters ψ and Δ are related to these coefficients by $\rho \equiv \tan(\psi)e^{i\Delta} = R_p/R_s$. R_p and R_s are calculated using a standard technique from a model containing a substrate and the required number of layers with flat parallel interfaces. They also depend on the incident angle (ϕ) and the wavelength of the light beam which are known. With initial estimates for the unknown layer thickness and (or) optical constants, a set of ψ and Δ values are calculated for the wavelengths and angles of incidence. The biased estimator⁸ (weighted mean square difference between calculated and measured values) is then calculated, and the Levenberg-Marquardt algorithm is used to vary the model parameters so as to minimize the biased estimator.

The complex pseudodielectric function $\langle \epsilon \rangle$ of the measured material as a function of ψ and Δ is given by

$$\langle \epsilon \rangle = \langle \epsilon_1 \rangle + i \langle \epsilon_2 \rangle = \sin^2 \phi \left[1 + \tan^2 \phi \left(\frac{1 - \rho}{1 + \rho} \right)^2 \right] \quad (1)$$

We can also use a parametric model—Lorentz oscillator (LO)—to model the dielectric function ϵ for a layer with unknown optical constants. Here, the dielectric function is expressed as the sum of a set of Lorentz oscillators:

$$\epsilon = \epsilon_\infty + \sum_j \frac{Am_j}{(E_j^2 - E^2) - iE \cdot Br_j} \quad (2)$$

where $Am_j = 4\pi e^2 \hbar / m_j^*$, $Br_j = \hbar / \tau_j$, $E_j = \hbar \omega_j$, $E = \hbar \omega$. E_j is the center energy of each oscillator, with effective electron mass m_j^* and relaxation time τ_j . Am_j , Br_j are the amplitude and the broadening of each individual oscillator, and ϵ_∞ is a constant. Am_j , Br_j , E_j and ϵ_∞ are the parameters to be fitted.

RESULTS AND DISCUSSION

Figure 1 shows the second derivatives of measured $\langle\epsilon_2\rangle$ for the WL samples. Notice that there is no significant difference between samples with $T_g \geq 350^\circ\text{C}$. However, for T_g at or below 300°C , E1 and E1+ $\Delta 1$ are broadened and the positions of E1 and E1+ $\Delta 1$ are shifted to lower energy.

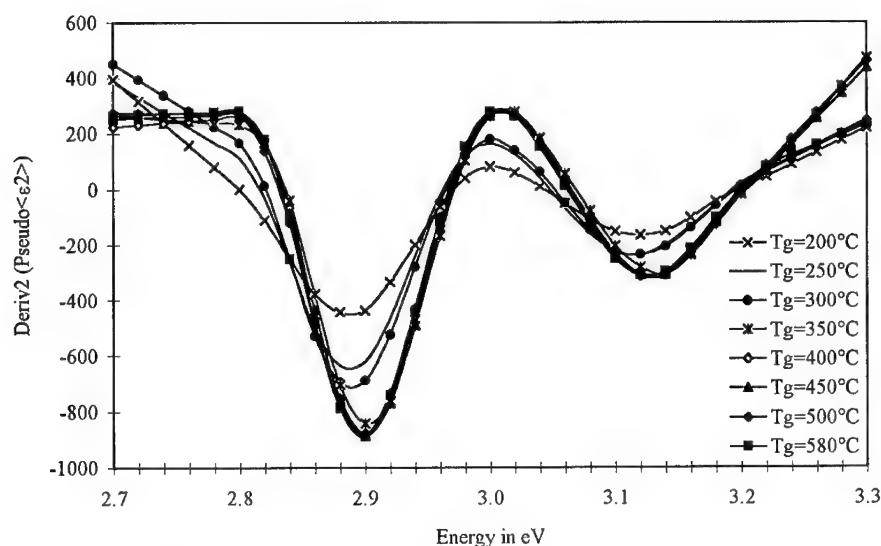


Figure 1. Second derivatives of $\langle\epsilon_2\rangle$ in E1 and E1+ $\Delta 1$ region for WL samples.

To quantify these effects, we need first to correct the measured pseudodielectric data for the native oxide layer. Oxide thicknesses were determined by modeling the LT GaAs layer (which is optically thick above the bandgap) as normal GaAs, with a native oxide layer on top. Published tabulated dielectric function data were used for GaAs⁹ and its oxide¹⁰. Fitting only the oxide thickness, good fits were obtained for samples with T_g from 350°C to 580°C . Poorer, but still acceptable fits were obtained for the 250°C and 300°C grown samples. The 200°C sample data could not be fitted in this way, so its oxide thickness was assumed to be the same as the 250°C grown sample. Oxide thickness, in the range of 2.6–3.1 nm for all samples, was kept fixed in the model thereafter. The GaAs tabulated ϵ data were then replaced with an LO model with seven oscillators.¹¹ All oscillator parameters were first fitted to the 580°C sample data from 2.0 eV–5.0 eV, producing a very good fit. For the remaining samples, ϵ_∞ and the A_m were kept fixed to their previous fitted values, while the E_j and B_j were fitted to the data over the same spectral range. Good fits were obtained in all cases. These LO parameters represent the dielectric functions of the LT GaAs, with the effects of the oxide overlayer mathematically removed. Figure 2 plots the center energies and the broadening parameters of the two oscillators representing the E1 and E1+ $\Delta 1$ critical points. It shows that broadening increases strongly as T_g

decreases below 350°C, with a corresponding weak red shift. Comparing 200° with the 580°C results, broadening increases 30% for E1 and 19% for E1+Δ1, with red shifts of -0.011eV for E1 and -0.007eV for E1+Δ1.

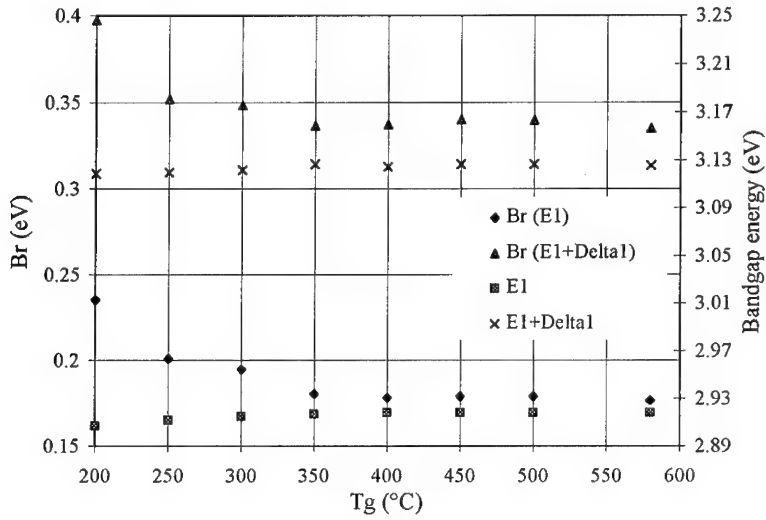


Figure 2. The broadening parameters and bandgap energies of the E1 and E1+Δ1 critical point structures obtained from Lorentz-oscillator models for the WL samples.

The red shift of the E1 and E1+Δ1 structure can be explained by an increased lattice constant in the LT layer. The strain dependence of E1 and E1+Δ1 can be expressed as:^{12,13}

$$\Delta E1 = \frac{\Delta 1}{2} + E_H - \frac{1}{2}[\Delta 1^2 + 4 E_S^2]^{\frac{1}{2}} \cong E_H - E_S^2/\Delta \quad (3)$$

$$\Delta(E1 + \Delta 1) = -\frac{\Delta 1}{2} + E_H + \frac{1}{2}[\Delta 1^2 + 4 E_S^2]^{\frac{1}{2}} \cong E_H + E_S^2/\Delta 1 \quad (4)$$

where $E_H = 2\xi_1(1 - \frac{c_{12}}{c_{11}})\sigma$, $E_S = \sqrt{\frac{2}{3}}D_3^3(1 + 2\frac{c_{12}}{c_{11}})\sigma$. σ is the biaxial strain, $(a - a_0)/a_0$. For GaAs at room temperature, $\xi_1 = -4.3\text{eV}$, $D_3 = 3.45\text{eV}$, and the adiabatic values of c_{11} and c_{12} are $11.88 \cdot 10^{11}\text{dyne/cm}^2$ and $5.38 \cdot 10^{11}\text{dyne/cm}^2$ respectively¹⁴. Taking the value 0.15% as the strain,^{5,6} we calculate $\Delta E1 \cong -0.011\text{eV}$ and $\Delta(E1 + \Delta 1) \cong -0.004\text{eV}$. Recall that the red shifts from the LO fit were -0.011eV and -0.007eV for E1 and E1+Δ1 respectively. The experimental ΔE1 is very close to the theoretical calculation and Δ(E1+Δ1) is smaller but still in the same order of magnitude. This calculation assumes a fully strained layer. Partial relaxation would

reduce E_s with little effect on E_H . In a fully relaxed layer, ΔE_1 and $\Delta(E_1+\Delta_1)$ would have the same value.

Strain in the as-grown LT layer is known to be due to the presence of excess arsenic. The strong correspondence between red shift and broadening seen in figure 2, for T_g below 350°C, indicates that the broadening may also be related to excess arsenic in the layer.

Figure 3 shows the second derivatives of measured $\langle \epsilon_2 \rangle$ for samples from NEDI in the E_1 and $E_1+\Delta_1$ region. The as-grown samples are much more broadened than the annealed samples. The data of the 250°C as-grown sample is also red shifted. An LO fit of it results in -0.014eV and -0.010eV for ΔE_1 and $\Delta(E_1+\Delta_1)$ respectively. The 200°C as-grown sample is so broadened that no structure can be resolved. Annealing is known to make the excess arsenic in as-grown LT layer precipitate into clusters,⁵ so the strain and broadening which are related to it decrease largely. We see hardly any bandgap shift for the annealed samples. The broadening of annealed sample with $T_g=250^\circ\text{C}$ is very close to the 550°C grown. The annealed 200°C grown regains part of the bandgap structure.

The greater broadening in the NEDI as-grown samples compared with the WL samples of the same nominal T_g , together with the larger red shift in the NEDI 250°C as-grown sample, implies that these samples had a higher concentration of excess arsenic. This in turn implies lower actual growth temperatures. Since T_g is notoriously difficult to measure at these low temperature,⁵ wide variations between nominal and actual growth temperatures are possible.

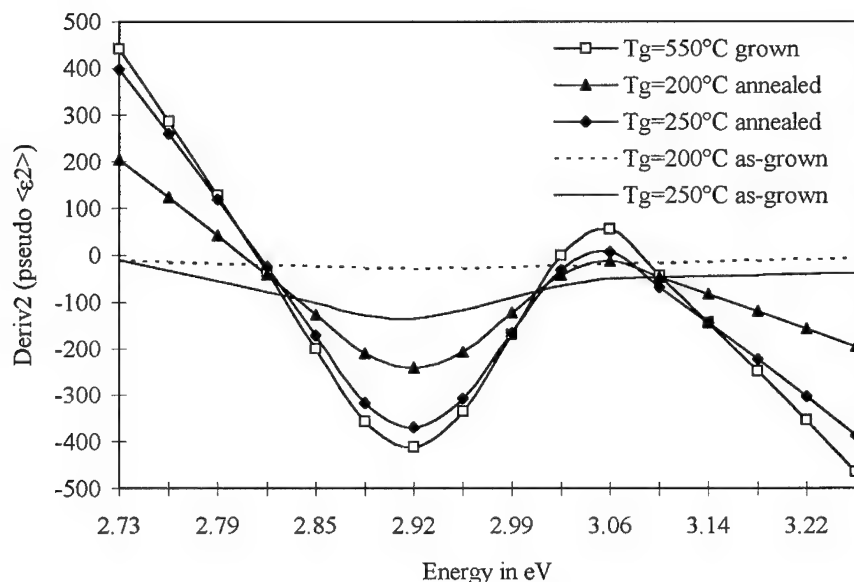


Figure 3. Second derivatives of $\langle \epsilon_2 \rangle$ in the E_1 and $E_1+\Delta_1$ region for NEDI samples.

CONCLUSION

The critical point structure of low temperature grown GaAs has been found to be much broader and slight red shifted compared with normal grown GaAs. We believe that we are the first to get the approximate E1 and E1+ Δ 1 values of LT GaAs. Both the red shifting and broadening appear to be related to the amount of excess arsenic in the as-grown material. Annealing removes or reduces both effects. The red shift is consistent with a theoretical calculation of strain effect in the LT layer.

References

1. F. W. Smith, A. R. Calawa, C.-L. Chen, M. J. Manfra, and L. J. Mahoney, *IEEE Electron Device Lett.* **9**, 77 (1988).
2. M. Kaminska, Z. Lilient-Weber, E. R. Weber, T. George, J. B. Kortright, F. W. Smith, B.-Y. Tsaar, and A. R. Calawa, *Appl. Phys. Lett.* **54**, 1881 (1989).
3. A. C. Warren, J. M. Woodall, J. L. Freeouf, D. Grischkowsky, D. T. McInturff, M. R. Melloch, and N. Otsuka, *Appl. Phys. Lett.* **57**, 1331 (1990).
4. K. M. Yu and Z. Lilient-Weber, *Appl. Phys. Lett.* **59**, 3267 (1991).
5. D. C. Look, *Thin Solid Films* **231**, 61 (1993).
6. R. J. Maty, M. R. Melloch, and J. M. Woodall, *Appl. Phys. Lett.* **60**, 2642 (1992).
7. R. M. A. Azzam and N. M. Bashara, *Ellipsometry and Polarized light*, (North-Holland, New York, 1977), Ch. 4.
8. G. E. Jellison, Jr., *Appl. Opt.* **30**, 3354 (1991).
9. E. Palik ed., *Handbook of Optical Constants of Solids*, (Academic, Orlando, 1985), Ch. 5.
10. S. Zollner, *Appl. Phys. Lett.* **63**, 2525 (1993).
11. M. Erman, J. B. Theeten, P. Chambon, S. M. Kelso, and D. E. Aspnes, *J. Appl. Phys.* **56**, 2664 (1984).
12. F. H. Pollak, in *Strained-Layer Superlattice: Physics, Semiconductors and Semimetals*, edited by T. P. Pearsall (Academic Press, 1990), P. 40.
13. C. M. Herzinger, P. G. Snyder, F. G. Celii, Y.-C. Kao, D. Chow, B. Johs, and J. A. Woollam, submitted for publication in *J. Appl. Phys.*
14. J. C. Brice, *Properties of Gallium Arsenide*, (The Institute of Electrical Engineering, London and New York 1990), P. 15.

OPTICAL ABSORPTIONS AND EL2-LIKE DEFECTS IN LOW TEMPERATURE GROWN MOLECULAR-BEAM-EPITAXIAL GaAs

S.K. SO*, M.H. CHAN*, AND K.T. CHAN**

*Department of Physics, Hong Kong Baptist University, 224 Waterloo Road, Kowloon, Hong Kong

**Department of Electronic Engineering, The Chinese University of Hong Kong, Shatin, Hong Kong

ABSTRACT:

The optical absorptions and the defect densities of GaAs grown by low temperature molecular-beam-epitaxy at growth temperatures between 200-580 °C were evaluated by photothermal deflection spectroscopy. The shapes of the absorption spectra exhibit EL2-like characteristics. Defect densities were found to be in the range of 10^{18} - 10^{19} cm⁻³. The PDS phase spectra were shown to be useful to differentiate the absorptions of the epilayer from those of the bulk.

1. Introduction

Epitaxial layers of GaAs grown by low temperature molecular-beam-epitaxy (LT-MBE) are recently shown to possess very useful properties for device fabrication. It is now generally believed that these special properties of LT-MBE GaAs are due to an excess amount of As present during epitaxial growth.¹ High concentration of point defects is found in LT-MBE GaAs and is thought to be associated with the excess As in forms of As antisites (As_{Ga}), As interstitials, As precipitates after annealing, or their complexes. An understanding of the nature of these defects will, therefore, provide useful insights for improving the performance of devices constructed from these materials.

Several techniques have been used to study the defects in LT-GaAs grown by MBE.²⁻¹² From optical absorption measurements,^{5,6} it was discovered that the shapes of the absorption spectra of LT-GaAs closely resemble those of intrinsic GaAs grown by liquid-encapsulated Czochralski (LEC) method. Since As antisite defects are present in both LT-MBE and LEC materials, defects in both cases should have very similar properties. The majority of defects in LEC grown GaAs are now generally accepted to be due to EL2 defects ($\sim\text{As}_{\text{Ga}}$), and therefore, it was proposed that defects in LT-GaAs are also EL2-like.^{5,6} Some of the key parameters for evaluating the EL2-like defect concentrations are the photo-ionization cross sections for neutral defects (σ_n) and positive defects (σ_p). For GaAs, the photo-ionization cross sections for both neutral and positive As antisites have been evaluated using photocapacitance measurements.^{13,14} In this study, we demonstrate that it is possible to use photothermal deflection spectroscopy (PDS), a very sensitive technique for measuring optical absorption, to evaluate defect densities in LT-GaAs using known photo-ionization cross sections for EL2 in GaAs.

2. Experimental

The GaAs MBE layers (1 μm thick) were grown on 100 Å thick buffer layer of AlAs using LEC GaAs as the substrate. The MBE layers were subsequently annealed at 620°C for 25 minutes in the MBE chamber under As-rich condition. The AlAs buffer layer has a relatively large bandgap

energy (2.2 eV) and can be considered to be optically transparent in this study. GaAs epilayers grown at different substrate temperatures (200-585°C) were investigated by PDS. The principle of operation of PDS is well documented.¹⁵ The measurements were carried out with a standard setup consisting of a 1kW Xe arc lamp and a 1/4 m grating monochromator as the pump beam which was modulated by a chopper before irradiating on the sample (Fig. 1). Carbon tetrachloride was used as a deflecting fluid. A HeNe laser was directed parallel to the layer surface as the probe laser. The photothermal deflection signal was detected by a quadrant cell. The output of the detector was fed into a lock-in amplifier for phase sensitive measurements.

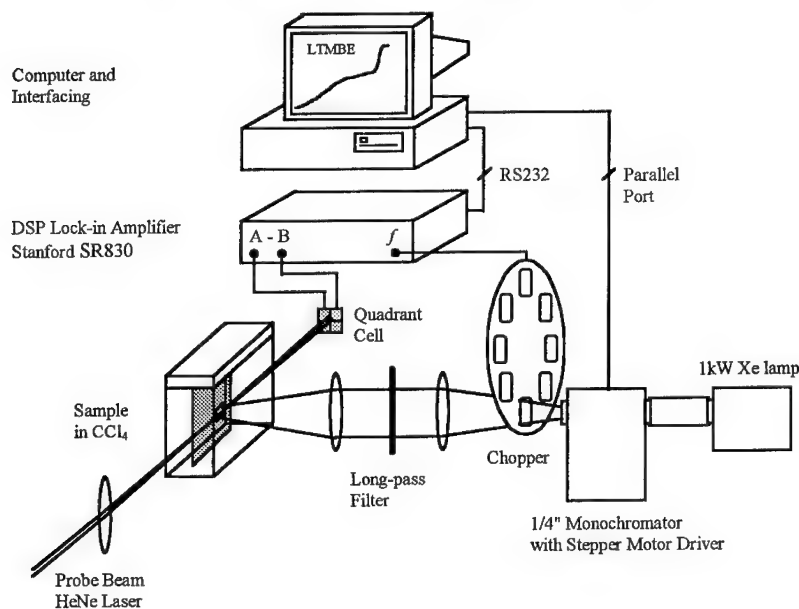


Fig. 1: Apparatus for photothermal deflection measurements of optical absorptions of low temperature grown MBE GaAs

In PDS experiments, the deflection angle (ϕ) can be shown to be proportional to the amount of heat released due to optical irradiation. In terms of the absorption coefficient (α) and the sample thickness (d), the deflection angle is given by

$$\phi = C \cdot P [1 - \exp(-\alpha d)] \quad (1)$$

where P is the power of the incident pump beam, and C is a constant relating to instrumental factors. In the case of small αd , $\phi \sim \alpha d$, and hence the deflection angle is a direct measure of the optical absorption. In the other extreme (large αd), $\phi \approx CP$ and the PDS signal saturates. In this case, the signal is a measure of the power spectrum of the incident pump beam and is independent of α . Such results have been obtained for a carbon film sample for the wavelength region shown in Fig. 2.

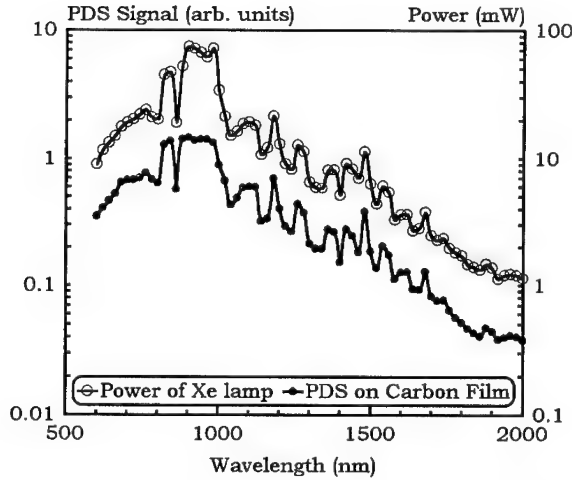


Fig. 2: Correlation of the pump beam power measured by power measurement and PDS on carbon film

3. Results and Discussions

Results of normalized PDS spectra on MBE grown GaAs are shown in Fig. 3. The spectra were calibrated by transmission measurements using a multilayer model.⁶ For LT-MBE layer (thickness d_l) on GaAs substrate (thickness d_s), the effective absorption coefficient α_{eff} is given by

$$\alpha_{\text{eff}}d = \alpha_l d_l + \alpha_s d_s \quad (2)$$

The subgap absorption, which correlates closely to the defect density, increases as the substrate temperature decreases at a fixed wavelength. The defect densities in the MBE layer, $[\text{As}_{\text{Ga}}]^0$ and $[\text{As}_{\text{Ga}}]^+$, can be calculated accurately with the known electron and hole photo-ionization cross sections, σ_n and σ_p respectively, according to the equation

$$\alpha(\lambda) = \sigma_n(\lambda)[\text{As}_{\text{Ga}}]^0 + \sigma_p(\lambda)[\text{As}_{\text{Ga}}]^+ \quad (3)$$

where $\alpha(\lambda)$ is the absorption coefficient at wavelength λ for the MBE layer. Since the shapes of the absorption spectra for both the MBE layers and the substrate are very similar, and As_{Ga} is involved in both cases,⁶ it can be assumed that the photo-ionization cross sections for the substrate can be used in (3) for evaluating the defect concentrations. In addition, PDS is known to be sensitive to the surface rather than the bulk.^{15,16} Hence, the absorption due to the GaAs epilayer is expected to be much larger than that of the substrate due to high defect density of the epilayer (about 10^{18} cm^{-3} for annealed LT-MBE GaAs grown at 200°C ^{1,5,6}). Therefore, the PDS signal should be dominated by the epilayer. Based on the assumptions above, the defect densities for the epilayers, $[\text{As}_{\text{Ga}}]^0$ and $[\text{As}_{\text{Ga}}]^+$, can be calculated from equation (3) using the measured absorptions at two different wavelengths. For LEC GaAs, the cross sections are $\sigma_n(1.1\mu\text{m}) = 9.07 \times 10^{-17}$, $\sigma_n(1.2\mu\text{m}) = 4.8 \times 10^{-17}$, $\sigma_p(1.1\mu\text{m}) = 3.2 \times 10^{-17}$, and

$\sigma_p(1.2\mu\text{m}) = 4.72 \times 10^{-17} \text{ cm}^2$.^{13,14} Results of the defect concentrations derived from these known values of absorption cross sections are shown in Table I. Total defect concentrations are in the range of 10^{18} to 10^{19} cm^{-3} . The total defect density calculated according to the above method appears to be abnormally high ($5.5 \times 10^{18} \text{ cm}^{-3}$) for the MBE layer grown at 585°C , in sharp contrast to reports that the MBE layer grown at $580\text{-}600^\circ\text{C}$ can produce $\sim 10^{13} \text{ cm}^{-3}$ shallow donor and acceptor concentrations.¹⁷

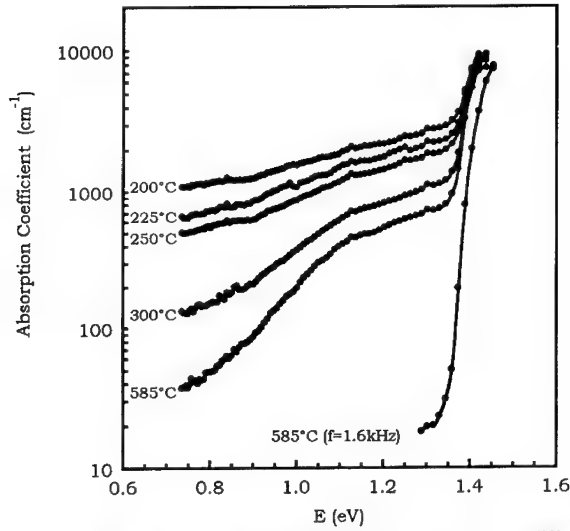


Fig. 3: The absorption spectra measured by PDS for MBE layers grown at different substrate temperatures. The chopping frequencies are 13 Hz unless indicated otherwise.

Table I: Summary of the EL2-like defect densities of annealed MBE layers grown at different substrate temperatures obtained from equation (3). The chopping frequency employed is 13 Hz.

Substrate Temperature (°C)	$[\text{As}_{\text{Ga}}]^0$ ($\times 10^{19} \text{ cm}^{-3}$)	$[\text{As}_{\text{Ga}}]^+$ ($\times 10^{19} \text{ cm}^{-3}$)	Total defect density $[\text{As}_{\text{Ga}}]^0 + [\text{As}_{\text{Ga}}]^+$ ($\times 10^{19} \text{ cm}^{-3}$)	$\frac{[\text{As}_{\text{Ga}}]^+}{[\text{As}_{\text{Ga}}]^0 + [\text{As}_{\text{Ga}}]^+}$
200	1.7 ± 0.1	1.8 ± 0.1	3.5 ± 0.2	0.51
225	1.4 ± 0.1	1.2 ± 0.1	2.6 ± 0.2	0.46
250	1.2 ± 0.1	0.81 ± 0.06	2.0 ± 0.2	0.40
300	0.72 ± 0.05	0.21 ± 0.02	0.93 ± 0.06	0.23

The apparent contradiction above can be explained by a careful consideration of the PDS phase spectra in Fig. 4. For the MBE layers grown at 200, 225, 250 and 300°C , as both the MBE layer and the bulk become more transparent (just below the gap energy), the effective center of absorption moves away from the surface and causes a sudden phase lag in the PDS signal. Below the bandgap energy, the phase lag becomes smaller for smaller photon energies because the center of absorption moves to the front surface where the absorption is dominated by the MBE layer. Similar phase motion has been observed previously by Zammit *et al.*^{18,19}

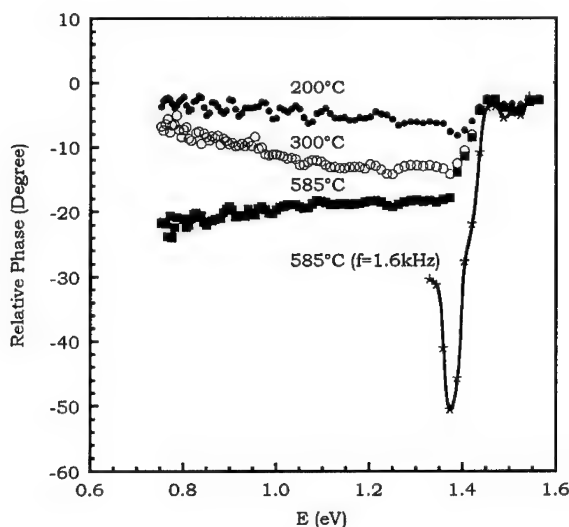


Fig. 4: The PDS phase spectra for MBE layers grown at different substrate temperatures (some of the phase spectra are not shown for clarity). The phase spectra were taken simultaneously with the PDS spectra shown in Fig. 3. The chopping frequencies are 13 Hz unless indicated otherwise

The PDS phase spectrum for the 585°C sample (obtained at a chopping frequency $f = 13$ Hz) also shows a similar phase shift just below the bandgap. However, the phase lag becomes larger for smaller photon energies, indicating that the effective center of absorption shifts gradually to the bulk and remains there. The phase spectrum in Fig. 4 ($f = 13$ Hz) suggests that the corresponding absorption spectrum for the 585°C sample ($f = 13$ Hz) in Fig. 3 is a measure of the average absorption of the entire sample rather than the MBE layer alone. Since the modulated heating from the pump beam is spread over a distance given by the thermal diffusion length (μ_T), the contribution to the PDS signal due to the MBE layer can be enhanced by reducing $\mu_T = (D/\pi f)^{1/2}$ where D is the thermal diffusivity ($0.003 \text{ cm}^2 \text{ s}^{-1}$ for GaAs). For $f = 13$ Hz, $\mu_T \approx 86 \text{ }\mu\text{m}$; the major contribution to the absorption is due to the substrate because MBE layer grown at 585°C is known to have relatively few defects and therefore should be essentially transparent below the bandgap. To support this argument, PDS was performed again for $f = 1.6$ kHz where $\mu_T \approx 8 \text{ }\mu\text{m}$. The measured absorption for the 585°C sample is significantly reduced (Fig. 3). Simultaneously, the PDS phase spectrum exhibits the characteristic phase motion where the phase lag increases sharply just below the bandgap followed by a smaller phase lag (Fig. 4). On the other hand, PDS measurements performed at $f = 1.6$ kHz on other MBE layers are similar to those obtained at $f = 13$ Hz. It is more desirable but difficult to reduce the thermal diffusion length to $1 \text{ }\mu\text{m}$ as a chopping frequency of 10^5 Hz is required.

The total defect concentration for the annealed MBE layer grown at 200°C is about an order of magnitude higher than the value ($3 \times 10^{18} \text{ cm}^{-3}$) observed by Look *et al* for both absorption and Hall-effect measurements.^{1,5,6,7} Also, the compensation ratio of deep acceptors $[\text{As}_{\text{Ga}}]^+$ to total defect density ($[\text{As}_{\text{Ga}}]^0 + [\text{As}_{\text{Ga}}]^+$) for the MBE layer grown at 200°C is about 0.5 (Table I)

whereas about 0.1 is observed by Look *et al.*^{6,7} The discrepancy may be attributed to different annealing conditions. In Look's study, post-growth-anneals on the LT-MBE GaAs were performed in a flowing inert gas. In our study, post-growth-anneals on the MBE GaAs at 620°C were performed in situ under arsenic overpressure.

4. Conclusion

PDS measurements have been used to evaluate the optical absorption and the defect densities of LT-MBE GaAs. The defect densities are in the range of 10^{18} - 10^{19} cm⁻³. Also, from the phase spectra were shown to be useful to separate the absorptions of the epilayer and the bulk.

Acknowledgment

Support of this research by the Research Grant Council under grant number RGC/93-94/12 (HKBC 107/93E) is gratefully acknowledged.

References

1. David C. Look, Thin Solid Films **231**, 61 (1993).
2. M. Kaminska, E. R. Weber, Z. Liliental-Weber, R. Leon, and Z. U. Rek, J. Vac. Sci. Technol. B **7**, 710 (1989).
3. H.-J. Sun, G. D. Watkins, F. C. Rong, L. Fotiadis, and E. H. Poindexter, Appl. Phys. Lett. **60**, 718 (1992).
4. K. Krambrock, M. Linde, J. M. Spaeth, D. C. Look, D. Bliss, and W. Walukiewicz, Semicond. Sci. Technol. **7**, 1037 (1992).
5. M. O. Manasreh, D. C. Look, K. R. Evans, and C. E. Stutz, Phys. Rev. B **41**, 10272 (1990).
6. D. C. Look, D. C. Walters, M. Mier, C. E. Stutz, and S. K. Brierley, Appl. Phys. Lett. **60**, 2900 (1992).
7. D. C. Look, D. C. Walters, M. O. Manasreh, J. R. Sizelove, C. E. Stutz, and K. R. Evans, Phys. Rev. B **42**, 3578 (1990).
8. D. C. Look, D. C. Walters, G. D. Robinson, J. R. Sizelove, M. G. Mier, and C. E. Stutz, J. Appl. Phys. **74**, 306 (1993).
9. I. Ohbu, M. Takahama, and K. Hiruma, Appl. Phys. Lett. **61**, 1679 (1992).
10. P. W. Yu, D. C. Reynolds, and C. E. Stutz, Appl. Phys. Lett. **61**, 1432 (1992).
11. C. E. C. Wood, J. Woodcock, and J. J. Harris, Inst. Phys. Conf. Ser. **45**, 29 (1979).
12. R. A. Stall, C. E. C. Wood, P. D. Kirchner, and L. F. Eastman, Electron. Lett. **16**, 171 (1980).
13. P. Silverbery, P. Omling, and L. Samuelson, Appl. Phys. Lett. **52**, 1689 (1988).
14. S. K. Brierley and D. S. Lehr, Appl. Phys. Lett. **55**, 2426 (1989).
15. W.B. Jackson, N.M. Amer, A.C. Boccara, and D. Fournier, Appl. Opt. **20**, 1333 (1981).
16. Andreas Mandelis, J. Appl. Phys. **54**, 3404 (1983).
17. H. Sakaki, in *III-V Semiconductor Materials and Devices*, (R. J. Malik ed., Amsterdam, North-Holland, 1989), p. 217.
18. U. Zammit, F. Gasparrini, M. Marinelli, R. Pizzoferrato, F. Scudieri, and S. Martellucci, J. Appl. Phys. **69**, 2577 (1991).
19. U. Zammit, M. Marinelli, and R. Pizzoferrato, J. Appl. Phys. **69**, 3286 (1991).

INVESTIGATION OF FREE EXCITON PROPERTIES IN GaAs EPITAXIAL LAYER

Wu Fengmei, Shi Yi, Martin Parenteau*, Anouar Jorio*, Zheng Youdou and Cosmo Carlone*

Department of Physics, Nanjing University, Nanjing 210008, P.R.China

**Département de Physique, Université de Sherbrooke, Sherbrooke J1K 2R1, Canada*

ABSTRACT

The transition energy, the binding energy, the intensity, the broadening and the lifetime of the free-exciton transitions in GaAs epitaxial layer have well been investigated using photoconductivity measurement which is analyzed in term of an improved fitting model. We have found that as the thickness is increased, the bind energy increases, but both the intensity of the high excitonic level and the lifetime of the excitons decrease. These effects are attributed mainly to imperfections located near the surface of the epitaxial layer.

Introduction

Excitons are elementary crystal excitation which are created by light absorption. Once created, the excitons interact with the crystal imperfections. Consequently, the exciton's properties such as its transition energy E_x , binding energy R_x , and lifetime τ depend on growth conditions, temperature, etc.. Photoconductivity (PC) has become well known and often used spectroscopic technique to study semiconductors [1-4]. This technique has the advantage of yielding information about the free-excitonic and the band to band transitions only in the epilayer. Through modelling of PC spectra, some parameters of these transitions can be obtained. The fit of experimental exciton peaks is often made with a simple Lorentzian or Gaussian function [5]. In order to get reliable and accurate values, improvements have to be made on PC spectrum modelling. The Lorentzian function is always used for homogeneous samples [6]. However, there are impurities, imperfections, and strains can be inhomogeneously distributed in semiconductors. In this case, the Lorentzian function can not fit very well the excitonic part of the experimental spectrum. Then, Gaussian broadening must be added to account for the inhomogeneity of the samples [5,6]. The resulting lineshape is called a Voigt profile. In this work, an improved model was used to analyze the free-exciton position, the binding energy, the intensity, and the lifetime from photoconductivity spectra of undoped MOCVD GaAs epilayers.

Experimental

Photoconductivity measurements have been performed on GaAs layers grown by metallorganic chemical vapor deposition (MOCVD) on semi-insulating GaAs substrate, at Université de Sherbrooke. They were unintentionally n-doped, the carrier concentration ranging from 1 to $2 \times 10^{15} \text{ cm}^{-3}$. The mobility of these epitaxial layers was $\mu = 34000 \text{ cm}^2/\text{V s}$. The PC spectra were taken with a 2 meter spectrometer. The light excitation was provided by a tungsten lamp with adjustable intensity, and chopped at a frequency chosen in the range of $f = 4$ to 300 Hz. Most of the PC spectra reported in this paper were measured with $f = 20 \text{ Hz}$ and at $T = 60 \text{ K}$, with the spectrometer slits at $500 \mu\text{m}$. For GaAs samples, the resistivity minimum is close to $T = 60\text{-}80 \text{ K}$, so the PC signal is stabler at these temperatures. For these measurements, the

samples were placed in a simple voltage divider, and the alternating signal ΔV was measured with standard lock-in amplification [7].

Analysis of photoconductivity spectra

The Fig. 1 shows a typical PC spectrum of sample 3 at $T = 60$ K, along with the model used to extract the physical parameters. All the PC spectra exhibit two main structures: the free exciton peak and the interband transition. The energy E_x of the excitonic transition can simply be obtained by the position of the $n = 1$ free-exciton peak of the spectrum. The broadening parameter Γ of this peak can also provide us with the exciton lifetime. To fit the PC curves and obtain the physical parameters, we can express the PC signal $\Delta V(\hbar\omega)$ as a function of the optical absorption coefficient $\alpha(\hbar\omega)$ [7]:

$$\Delta V(\hbar\omega) = A \times (1 - e^{-\alpha(\hbar\omega)d}) + B \quad (1)$$

where $A \propto V/\sigma$ (V is the source voltage for the divider and σ is the dark conductivity of the sample), d is the sample thickness, and the constant B accounts for an artificial offset of the lock-in signal, due to noise. The absorption coefficient $\alpha(\hbar\omega)$ is then expressed as a sum of the two processes, the excitonic and interband transitions:

$$\alpha(\hbar\omega) = \alpha_{exc}(\hbar\omega) + \alpha_{bb}(\hbar\omega) \quad (2)$$

The excitonic absorption $\alpha_{exc}(\hbar\omega)$ takes the form of a series of peaks, one for each excitonic level [8], while the interband transition $\alpha_{bb}(\hbar\omega)$ is nearly a step function. All these structures

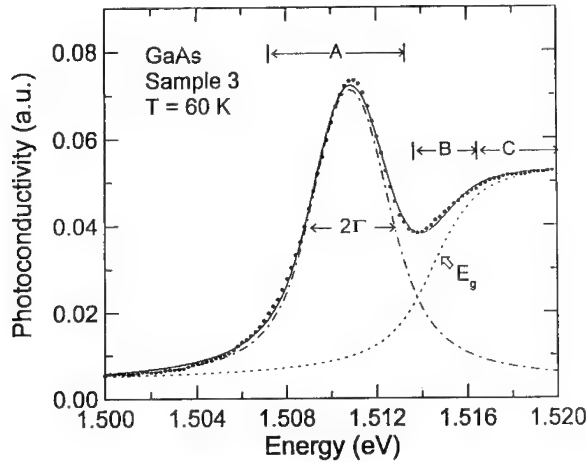


Fig. 1. Experimental photoconductivity spectrum of MOCVD GaAs epitaxial layer . . . and theoretical curve given by equation (1) (solid line). Excitonic --- and interband----- components of the theoretical model are shown separately. Three energy ranges are shown: A) the fundamental excitonic level($n=1$), B) the high excitonic bound states($n>1$), and C) the unbound excitonic states.

must be broadened to account for the finite lifetimes of the electronic levels involved [9]. We approximated the absorption coefficient for the band to band transition with a Heaviside step function of amplitude A_{bb} :

$$\alpha(\hbar\omega) = \begin{cases} A_{bb} & \text{for } \hbar\omega \geq E_g \\ 0 & \text{for } \hbar\omega < E_g \end{cases} \quad (3)$$

For the free-exciton, the absorption of m levels is given by:

$$\alpha_{exc}(\hbar\omega) = \sum_{n=1}^m \left(\frac{A_x}{n^3} \delta\left(\hbar\omega - E_g + \frac{R_x}{n^2}\right) \right) \quad (4)$$

where A_x is the intensity of the transition.

The broadening function is often chosen to be a Lorentzian [9,10] or Gaussian function. None of these simple functions fitted our data very well. Instead, the two kinds of broadening had to be combined in order to reproduce our experimental spectra. In fact, it is equivalent to consider a Gaussian distribution of Lorentzian peaks. The final absorption curve $\alpha(\hbar\omega)$ is then obtained by convoluting the expressions (3) and (4) with a Voigt profile. Fig. 1 shows that this theoretical model (solid line) fits the experimental spectra (dots) very well. For spectra taken at $T = 60$ K, the fit was better when only the first excitonic transition was considered. The situation at lower temperatures was different: as many as four excitonic levels ($m = 4$) had to be added to get the best fit.

Results and Discussions

The PC spectra for samples 1 to 4 at $T = 60$ K are shown in Fig. 2. The signal given by the

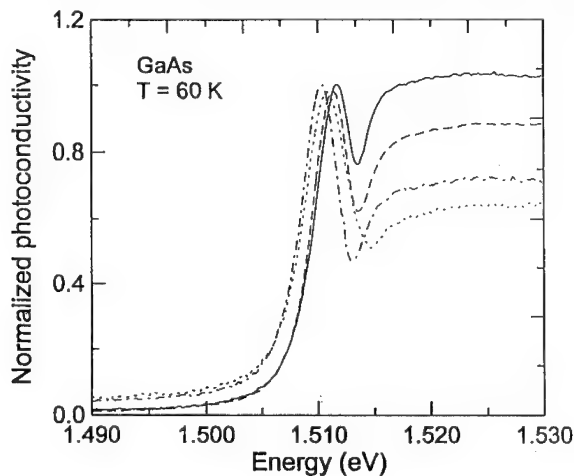


Fig. 2. Photoconductivity spectra of MOCVD GaAs epitaxial layers at $T=60$ K. Sample 1: —, sample 2: ---, sample 3: - · -, and sample 4: · · · · ·.

Table I. Exciton transition energy (E_x), binding energy (R_x), broadening parameter (Γ_L), lifetime (τ) and ratio of exciton and interband transition intensities (A_x/A_{bb}), obtained from the modelling of photoconductivity spectra.

Sample	Thickness (μm)	E_x (meV)	R_x (meV)	A_x/A_{bb} (a.u.)	Γ_L (meV)	τ (ps)
1	4.21	1511.49 ± 0.10	3.65 ± 0.37	0.0028 ± 0.0001	0.54 ± 0.20	0.609 ± 0.230
2	6.27	1510.94 ± 0.47	3.83 ± 0.11	0.0047 ± 0.0004	0.70 ± 0.22	0.470 ± 0.150
3	8.85	1510.60 ± 0.69	3.96 ± 0.12	0.0077 ± 0.0002	1.07 ± 0.28	0.307 ± 0.080
4	29.65	1510.67 ± 0.37	4.39 ± 0.14	0.0114 ± 0.0011	1.50 ± 0.36	0.219 ± 0.053

interband transitions has been normalized so as to show the relative change in the excitonic transition intensity. From Fig. 2, we can see a slight red-shift of the $n = 1$ free exciton transition (E_x) with increasing thickness. When the thickness reaches about $8 \mu\text{m}$, E_x approaches the value of bulk material. The values of the exciton transition energy E_x are listed in Table I. Most publications give the transition energies at low temperatures. To compare with our values at $T = 60 \text{ K}$, we must include the shift caused by temperature [11].

We can also see that the excitonic transition intensity increases relative to the interband transition as the layer thickness is increased. In Fig. 2, we did not consider the absolute PC intensity, because the signal depends on many factors that vary from one sample to another. However, the ratio between the excitonic and interband intensities could be used to compare different spectra. The values of A_x/A_{bb} are listed in Table I.

The $n = 1$ free-exciton binding energy R_x is the separation between the exciton energy E_x and the interband transition threshold E_g (Fig. 1). We have found that this binding energy increases with increasing thickness, as can be seen on Fig. 2 by the increasing separation between the excitonic peak and the band to band step. The values for R_x are listed in Table I. We have also observed that the free-exciton binding energy R_x in thinner undoped GaAs epilayers is lower than that in thicker one. For an epilayer about $8 \mu\text{m}$ thick, the value of R_x is equal to that of bulk GaAs. The binding energy R_x of the free-exciton in sample 3 at $T = 60 \text{ K}$ is $3.96 \pm 0.12 \text{ meV}$, which agree well with those reported in the literature [12].

The broadening parameter Γ_L and the lifetime τ obtained from the modelling of spectra are listed in Table I. The exciton lifetime is usually calculated from the Lorentz broadening parameter Γ_L with the help of the expression [9]:

$$\tau = \hbar / 2\Gamma_L \quad (5)$$

The lifetimes of free-excitons in our samples at $T = 60 \text{ K}$ are very short, about 0.21-0.61 ps. The values of Gaussian broadening Γ_G of samples 1 to 4 are in the range of 0.9-1.0 meV. This result shows that the inhomogeneity of the four samples are similar, and the Gaussian contribution is rather independent of thickness.

We measured the intensity of free excitons and interband transition as a function of the excitation power, as shown in Fig.3. We found that the intensity of $n = 1$ free- exciton increases as $P^{0.57}$ and the intensity of interband transition increase as $P^{0.56}$ in our investigation. Additionally, we observed the $n = 1$ free-exciton peak to shift slightly toward lower energies.

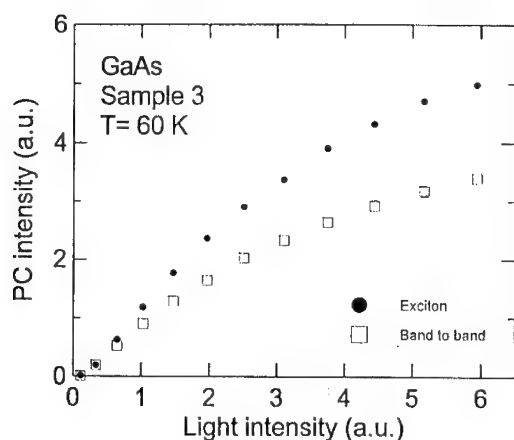


Fig. 3. Photoconductivity intensity of free exciton and band to band transitions as a function of excitation power, at $T = 60$ K, for MOCVD GaAs epitaxial layer.

As mentioned above, several main parameters of free-excitons vary with the thickness of MOCVD GaAs epilayer. One reason is the traps and the defects which are distributed throughout the interface between the epilayer and the semi-insulating substrate [13]. Another, there are surface electric field in the surface charge region (SCR), and band bending near the quasineutral bulk [14]. The influence of the surface and interface can cause the variations of the static dielectric constant ϵ and the reduced effective mass m^* . We know that $R_x \propto m^*/\epsilon^2$. Thus, a change in R_x can be attributed to either m^* or ϵ , or to both.

For the thicker samples in Fig.2, we see that the intensity of the unbound excitonic states (range C) decreases relative to the peak associated with the $n = 1$ free exciton. From the sharpness of the interband transition (range B), we can suppose that the intensity of excitonic of bound states $n = 2, 3, 4$, etc. also decreases relative to the state $n = 1$. Such a reduction of intensity has been observed for the high excitonic levels of Cu_2O , when this crystal is subjected to an electric field. Such perturbation of the excitons should also affect the lifetime of the first excitonic level.

Information on the lifetime is very useful in understanding the decay mechanism of excitons and the dependence of free-exciton lifetime on concentration of defects and impurities. In general, the measured lifetime will usually be much shorter due to trapping of the free-excitons by impurities and defects. In addition, these short lifetimes can also be attributed to the effect of the surface electric field [15]. The thicker epilayer contains more imperfections, some defects could have diffused from the bulk during its growth. As a result, the excitonic lifetime is reduced.

In some thicker samples, we observed $n = 1$ and 2 free-exciton states at $T = 21$ K. These peaks are separated by 3.2 meV. As this PC spectrum is related not only to the fundamental exciton state, the model must include many excitonic levels. We evaluated that the R_x was (4.08 ± 0.14) meV and the lifetime was (0.40 ± 0.04) ps for sample 3 at $T = 21$ K.

Conclusion

Using photoconductivity measurement which were analyzed in terms of an improved model, the transition energy, the intensity, the binding energy, the broadening and lifetime of the free-excitons have been investigated in undoped MOCVD GaAs epilayer. We have found that the intensity of the high excitonic levels ($n > 1$) decreases relative to the $n=1$ level for the thicker epilayers. We have also found that for these thick epilayers, the lifetime of excitons is shorter. We attribute these changes in the lifetime mostly to imperfections located near the surface of the epilayer. The binding energy of the excitons increases slightly as the epilayer thickness is increased and the $n = 1$ free-exciton peak shifts slightly towards lower energies. The raising of excitation power causes a red shift.

Acknowledgements

This work was supported by the National Research Council of Canada.

References

- [1] M. Parenteau, C. Carlone, and S. M. Khanna, J. Appl. Phys. **71**, 3747 (1992).
- [2] S. M. Khanna, C. Carlone, S. Hallé, M. Parenteau, A. Béliveau, C. Aktik, and J. W. Gerdes Jr., IEEE Trans. Nucl. Sci. **38**, 1145 (1991).
- [3] D. Bimberg and W. Schairer, Phys. Rev. Lett. **28**, 442 (1972).
- [4] D. D. Sell, S. E. Stokowski, R. Dingle, and J. V. DiLorenzo, Phys. Rev. **B7**, 4568 (1973).
- [5] H. B. Bebb and E. W. Williams, in: *Semiconductors and Semimetals*, edited by R. K. Willardson and A. C. Beer (Academic Press, New York, 1972), Vol. 8, p. 289.
- [6] O. Svelto, *Principles of Lasers* (Plenum Press, New York, 1989), p. 30.
- [7] S. M. Ryvkin, *Photoelectric effects in semiconductors* (Consultants Bureau, New York, 1964), p. 18.
- [8] K. Nakao, H. Kamimura, and Y. Nishina, Il Nuovo Cimento **LXIII B**, 45 (1969).
- [9] D. D. Sell and P. Lawaetz, Phys. Rev. Lett. **26**, 311 (1971).
- [10] J. Camassel, P. Merle, H. Mathieu, and A. Chevy, Phys. Rev. **B 17**, 4718 (1978).
- [11] Y. P. Varshni, Physica **34**, 149 (1967).
- [12] D. D. Sell, Phys. Rev. **B 6**, 3750 (1972).
- [13] R. S. Berg, N. Mavalvala, T. Steinberg, and F. W. Smith, J. Electron. Mater. **19**, 1323 (1990).
- [14] O. Yu. Borkovskaya, N. L. Dmitruk, V. G. Litovshenko, and O. I. Maeva, Phys. Stat. Sol. **A 84**, 285 (1984).
- [15] D. D. Sell, in: *Proceedings of the 11th International Conference on the Physics of Semiconductors*, edited by M. Miasek (Elsevier, Amsterdam, and PWN-Polish Scientific, Warsaw, 1972).

UNIFORMITY OF ARSENIC DIMER AND TETRAMER FLUXES FROM A VALVED ARSENIC CRACKING SOURCE IN MBE

GEORGE A. PATTERSON, JAMES S.C. CHANG, AND FORREST G. KELLERT
Hewlett-Packard Co., Microwave Technology Division, 1412 Fountain Grove Parkway,
Santa Rosa, California 95403

ABSTRACT

We have studied the uniformity of the arsenic flux from a commercially available valved arsenic cracker source for MBE. There are many epitaxial structures that require a uniform arsenic flux distribution for rotated epitaxial growth and, in the non-rotated case, for RHEED. For non-stoichiometric GaAs growth at low substrate temperatures, which results in arsenic precipitates being formed during the in-situ anneal process, a specific As/Ga ratio must be used to maintain high crystalline quality and to achieve the desired electrical properties. Also, in the growth of InGaAsP the As/P ratio is equally important for lattice match and quality device results. We report on the uniformity of amorphous arsenic (a-As) films condensed on the surface of 3" diameter sapphire wafers slightly below room temperature. Sapphire substrates were used in place of GaAs wafers to facilitate the use of x-ray fluorescence for the measurement of the arsenic film uniformity. Uniformity maps will be presented for rotated and non-rotated a-As depositions of As_2 and As_4 . Results indicate the uniformity of a-As, As_4 , films to have a standard deviation of $< 2.5\%$ across a 3" diameter substrate for the rotated case. Characteristics of the non-rotated case will be presented.

I. INTRODUCTION

The uniformity of arsenic flux becomes an increasingly important issue as more complex materials are being explored by MBE. For GaAs grown at low temperatures, researchers have demonstrated that the As_4/Ga ratio¹ is important to control. The V/III flux ratio needs also to be controlled during migration enhanced epitaxy (MEE)². For quaternary materials the precise control of composition places a very heavy burden on the uniformity of the group V fluxes.

Developments in molecular beam epitaxy (MBE) have led to the availability of arsenic valved cracking effusion cells³ equipped with two heating zones, a sublimator filled with an arsenic charge and a cracking tube. The heated cracking tube can provide thermal decomposition ("cracking") of the arsenic molecules from the tetrameric molecule, As_4 , to the dimeric molecule, As_2 . The valve is positioned at the end of the cracking tube nearest the growth position. While this design allows for rapid modulation of the incident arsenic flux, it increases the complexity of modeling the system.

In this work, we are concerned with the uniformity of the arsenic flux incident onto a 3" diameter sapphire substrate. We continue by assuming that both As_2 and As_4 molecules are adsorbed on cooled sapphire substrates. An appropriately low substrate temperature is required that allows a suitably high sticking coefficient for both As_2 and As_4 .

Foxon and Joyce⁴ have reported that, in the absence of a Ga adatom population, there is a near zero sticking coefficient of As_4 on {100} oriented GaAs substrates in the temperature range

of 300 to 450°K. It has also been shown that As₄ can be deposited⁵⁻⁷ at substrate temperatures $T_s < 273^\circ\text{K}$ and As₂ deposited^{8,9} at $T_s < 320^\circ\text{K}$ on GaAs substrates and on silicon substrates⁹. Panish⁹ reported that As₂ will adsorb onto non-reactive substrates at 77°K with near unity sticking coefficient. Of great importance, from both the theoretical and practical aspects, is the assumption that the temperature dependent As₄ and As₂ sticking coefficients tend not to influence the resulting uniformity of the deposited arsenic layers. A practical lower limit to the substrate temperature for the Varian MOD GEN II MBE system is, $T_s = -40^\circ\text{C}$. The sticking coefficient s in Eq. (1) is defined as the ratio of the number of atoms adhering to the surface to the number of atoms arriving there:

$$s = \frac{N_{adh}}{N_{tot}} \quad (1)$$

The result is that the physically adsorbed arsenic atoms, N_{adh} , embody the uniformity of the incident flux for a substrate at a uniform temperature, although not necessarily the total incident flux, N_{tot} .

II. EXPERIMENTAL

The MBE system used for this work was a Varian MOD GEN II equipped with a valved arsenic cracking source capable of producing As₄ and As₂ molecular beams. The valved arsenic cracking source was placed in the furnace port at the 10 o'clock position. The eight furnace ports of the MOD GEN II MBE system are tilted off axis from the wafer normal by $\theta = 33^\circ$. The source to substrate distance is, $d = 18.3$ cm. Fig. 1 depicts a schematic of the source to substrate geometry. To determine the uniformity of arsenic fluxes over the maximum possible area we chose 3" diameter sapphire wafers mounted in In-free substrate holders. The MBE system's cryopaneling was filled continuously with liquid nitrogen. The substrate, mount, and heated station were allowed to cool below room temperature overnight while facing the growth direction. The source shutter between the arsenic cracking zone valve and the substrate remained in the open position. During the deposition of As₄ the temperature of the cracking zone was maintained at $T_{cz} = 500^\circ\text{C}$ and for the As₂ deposition $T_{cz} = 900^\circ\text{C}$. A deposition (physisorption) of arsenic was conducted by allowing the flux of arsenic molecules to impinge onto the wafer surface for a 2 hour period. The substrate temperature, T_s , was determined by monitoring of the substrate thermocouple. The substrate temperature during deposition of the As₄ for use in determining uniformity was $T_s = -36^\circ\text{C}$ and for the As₂ deposition, $T_s = -6^\circ\text{C}$ as there is greater radiative substrate heating with $T_{cz} = 900^\circ\text{C}$. The beam equivalent pressure, P , for As₄ was set to $P_{As_4} = 1.4 \times 10^{-5}$ torr. The resulting cracker valve position was held constant for all the As₄ and As₂ depositions. The beam equivalent pressure for the As₂ depositions was recorded at $P_{As_2} = 6.4 \times 10^{-6}$ torr with $T_{cz} = 900^\circ\text{C}$.

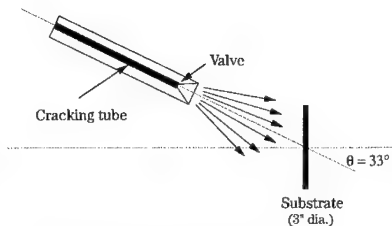


Fig. 1. Valved arsenic cracker schematic

III. RESULTS AND DISCUSSION

Arsenic Sticking Properties

The dependence of the physisorption of arsenic onto non-reactive sapphire substrates was investigated to determine the influence on subsequent uniformity analysis. As reported by Panish⁹, As₂ will adsorb onto non-reactive substrates at LN₂ temperatures with near unity sticking coefficient. For the MOD

GEN II MBE system it proved impractical to cool the substrate and it's holder to LN₂ temperatures. The practical limit for the In-free mount substrate holder was -40°C when the cracking zone was at 500°C and -10°C when it was at 900°C. The difference in the lower limits of substrate holder temperature is due to radiative heating of the substrate and wafer holder assembly from the arsenic cracking furnace. The sticking coefficient, *s* was calculated from the experimentally observed beam equivalent pressures, BEP and used to calculate the absolute flux, *J_x* using Eq¹⁰. (2), with the ionization efficiency relative to nitrogen, *I_x* calculated from Eq¹¹. (3).

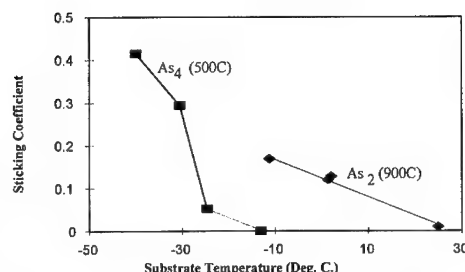


Figure 2. Arsenic sticking coefficient versus substrate temperature for *T_{cz}* = 500°C and *T_{cz}* = 900°C

$$J_x = 3.92 * 10^{20} * \frac{P_x}{I_x} \sqrt{\frac{T_x}{M_x}} \text{ [molecules cm}^{-2} \text{ sec}^{-1} \text{]} \quad (2)$$

$$I_x = \left(0.6 * \frac{\sum Z}{14} + 0.4 \right) \quad (3)$$

where *J_x* is the effusion flux in units of molecules per cm² per sec, *P_x* is the BEP in torr, *T_x* is the effusing flux temperature in Kelvin degrees, *M_x* is the molecular weight in grams per mole, and *Z* is the number of electrons per molecule. The *N_{tot}* was calculated for each case by multiplying *J_x* by the number of atoms per molecule. The *N_{adh}* values were calculated from weight differences of the substrates before and after arsenic depositions. The temperature dependent sticking coefficients calculated in the above manner for As₂ (900°C) and As₄ (500°C) is plotted in Fig. 2. For As₂, at the substrate temperature of -10°C, the influence on deposition uniformity is determined to be 4% per degree C and for As₄, at -30°C, is ~10% per degree C. From these observations, it is very important to maintain extremely uniform substrate temperatures during the depositions used for the analysis of flux uniformity.

Uniformity Analysis

The As₂ and As₄ films were subjected to x-ray fluorescence¹² measurements to determine the uniformity of the respective depositions. The background noise, bremsstrahlung, of the x-ray fluorescence system was subtracted from each measurement. The visual appearance of the As₂ films deposited onto sapphire substrates was similar to that reported by Panish⁸ for the

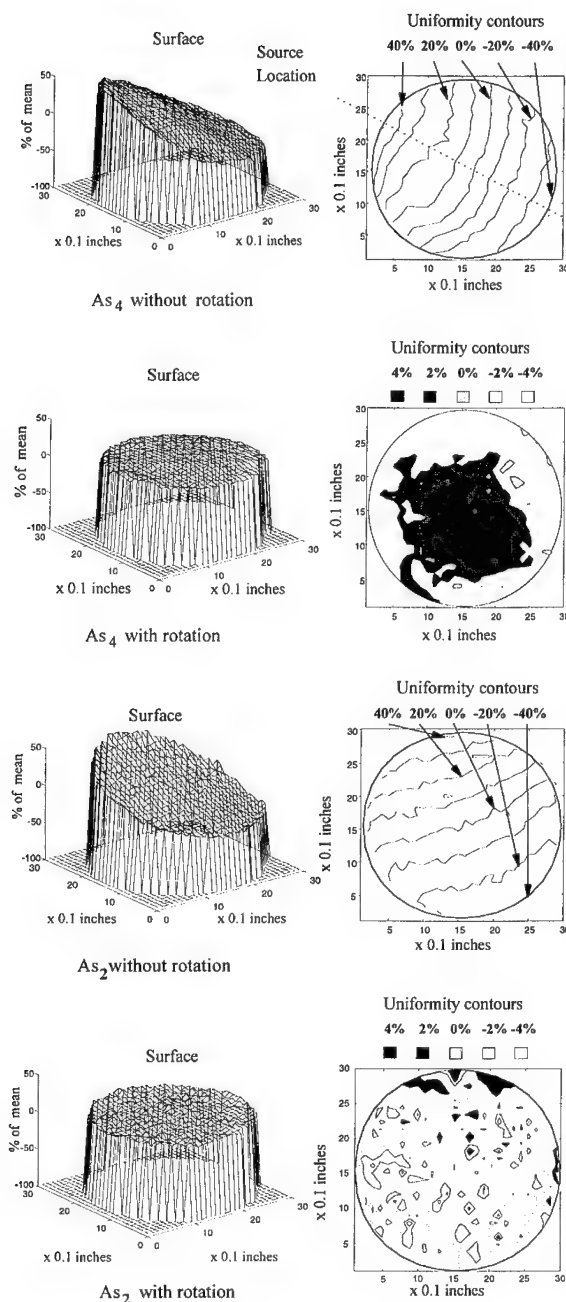


Figure 3. Arsenic surface and contour plots

deposition of As_2 onto GaAs substrates, as being metallic in appearance with a mirrored surface, while the deposition of As_4 resulted in films being light gray in appearance, but not at all mirrored. By SEM examination of the arsenic films, it was apparent that the As_2 surfaces were smooth when viewed at 2,000X while the As_4 surfaces were rough and exhibited a periodic surface structure. Analysis by x-ray fluorescence was used to determine the quantity of arsenic atoms that were present on the sapphire substrates per unit area. At each point on a 0.1" x 0.1" grid a beam of x-rays from a $Cu K_{\alpha}$ source was used to probe an area 0.5mm. x 0.5mm. for each substrate. Characteristic x-ray emissions from the $As K_{\alpha 1} L_{II}$ and $As K_{\alpha 2} L_{III}$ lines, a closely spaced doublet at 1.17987 and 1.17588 Å, were counted with no interference from those emitted by the sapphire (Al, O) substrate. Experimentally obtained surface and contour maps of the As_2 and As_4 films are plotted in Fig. 3 to represent the uniformity of the arsenic depositions. The x-ray counts data has been corrected for bremsstrahlung and normalized to the mean value to present the uniformity of the arsenic flux. The surface and contour maps of Fig. 3 represent both As_2 and As_4 depositions with and without rotation. The expected arsenic flux non-uniformity without rotation was calculated, using the computer model of Curless¹³ for conical effusion sources, to be -32% and +55% relative to the wafer's center. The flux being greatest at the edge of the wafer

nearest the arsenic valved cracker cell. The experimental data are found to be in reasonable agreement with this calculation. Also shown in Fig. 3 are the maps for As_2 and As_4 films that show dramatically improved uniformity from rotation. The data collected from x-ray measurements for both the As_2 and As_4 films are summarized in Table 1. These measurements

	Rotated		Not Rotated	
	As_2	As_4	As_2	As_4
$\sigma\%$	1.87	2.73		
Range (% of mean)			<div style="border: 1px solid black; padding: 2px; display: inline-block;"> +50.9 to -36.4 +57.3 to -40.4 </div>	

Table 1. Measured uniformity summary

contain both the uncertainty of the deposition uniformity and the x-ray system variance. The films of As_4 compared to the films of As_2 when either rotated or not rotated appear less uniform, which may be the result of a slight temperature variation across the substrates during the depositions. This suggests that the As_2 may be similarly influenced, but to a lesser degree, by substrate temperature non-uniformity. The x-ray fluorescence system uses a Geiger-Müller tube counter that exhibits measurement noise. In this case, for a single measurement repeated 100 times, the variance due to the x-ray fluorescence system is $\sigma^2 = 1.3\%$. The implication is that the measured arsenic film uniformity, corrected for the Geiger-Müller tube noise, but not for substrate temperature non-uniformity requires us to subtract the x-ray system variance from the measured variance of the arsenic depositions. The result of this difference of variances expressed as standard deviations becomes $1\sigma = 1.5\%$ for As_2 and $1\sigma = 2.5\%$ for As_4 , thus reported, represents an upper bound on the flux uniformity achievable from the valved arsenic cracker source.

IV. CONCLUSIONS

We have determined the uniformity of arsenic flux from a valved cracking source to be better than $1\sigma = 1.5\%$ across a 3" diameter substrate when rotated during deposition of As_2 . This uniformity should meet the needs of producing lattice matched InGaAsP quaternary compounds on 3" substrates. Our measurements of the arsenic flux uniformity show that there may be a slight decrease in uniformity when using an As_4 flux over that of the As_2 flux, although further study is indicated to determine the exact source of this difference, but it may only be an indication of poor substrate temperature control. In the case of no rotation, it can be seen that there is a large and predictable, spread in arsenic flux across the substrate with the average value near the substrate's geometric center. Should RHEED studies be conducted, care should be exercised to avoid errors due to this extreme non-uniformity during non-rotated growth.

V. ACKNOWLEDGMENT

The authors gratefully acknowledge Jon James for valued technical discussions and the use of the x-ray fluorescence measurement system.

VI. REFERENCES

1. S. O'Hagan and M. Missous, J. App. Phys, **75**, 7835 (1994).
2. Y. Horikochi, M. Kawashima, and H. Yamagushi, Jpn. J. Appl. Phys. **27**, 169 (1986).

-
3. "Valved Cracking Effusion Cell for Arsenic", Model 500V-As, EPI MBE Products Group, St. Paul, MN 55110
 4. C.T.Foxon and B.A. Joyce, Surface Science **50**, 434 (1975).
 5. S.P. Kowalczyk, D.L. Miller, and J.K. Waldrop, P.G. Newman, and R.W. Grant, J. Vac. Sci. Technol. **19**, 255 (1981).
 6. N.J. Kawai, T. Nakagawa, T. Kojima, K. Ohta, and M. Kawashima, Electron. Lett. **20**, 47 (1984).
 7. A. Kahn, J. Carelli, D.L. Miller, and S.P. Kowalczyk, J. Vac. Sci. Technol. **21**, 380 (1982).
 8. G.L. Price in Collected Papers of the International Symposium on MBE / CST 1982, Tokyo, 259
 9. M.B. Panish, J. Electrochem. Soc., **127**, 2729 (1980).
 10. Douglas M. Collins, Varian Corporate Research Memorandum, CMR-346, May 15, 1979
 11. T.A. Flaim and P.D. Ownby, J. Vac. Sci. Technol. **8**, 661 (1971).
 12. Fischerscope X-ray 1510 system, Fischer Technology, Inc., Windsor, CT 06095
 13. Jay A. Curless, J. Vac. Sci. Technol. **B3(2)**, 531 (1985).

DOPANT-DEFECT INTERACTIONS IN II-VI SEMICONDUCTORS STUDIED BY PAC

THOMAS WICHERT

Technische Physik, Universität des Saarlandes, 66041 Saarbrücken, Germany

ABSTRACT

The application of the perturbed $\gamma\gamma$ angular correlation technique (PAC) as an analytical tool for the characterisation of atomic defect configurations is discussed, using recent results on donor-acceptor pairs, which were observed in CdTe and other II-VI semiconductors by the radioactive donor ^{111}In . For bulk CdTe crystals and MOCVD grown CdTe films, the role of the cation vacancy, group I and group V elements is discussed.

INTRODUCTION

In order to solve the problems associated with the *p*- and *n*-type doping of II-VI semiconductors, information on the incorporation of the dopant atoms has to be obtained. The same element might act as a donor, an acceptor, or an electrically neutral species depending, on the lattice site, on which the dopant atoms are incorporated. Thereby, the dopant atom can be incorporated either on a substitutional cation or anion lattice site or at different interstitial sites. In addition, the presence of unwanted impurities and intrinsic defects, such as vacancies, self-interstitial atoms or anti-site defects, can compensate or passivate the introduced dopant atoms. There are numerous electrical and optical techniques which characterise the electrical and optical properties of the doped semiconductors. But, they do not yield detailed microscopic information about the involved extrinsic and intrinsic defects and, therefore, are not able to explain the absence of a *p*- or *n*-type conductivity. On the other hand, these techniques, such as electrical transport (like Hall), capacitance (DLTS), and optical (PL) measurements, are distinguished by their high sensitivities to defect concentrations well below 10^{16} cm^{-3} (fig. 1).

Experimental techniques that are able to perform a chemical identification of extrinsic or intrinsic defects, however, most often lack the needed sensitivities to defect concentrations in the order of 10^{16} cm^{-3} . These techniques, such as Raman scattering, infrared spectroscopy, extended X-ray absorption fine structure (EXAFS), Rutherford backscattering spectroscopy (RBS) including ion channeling, or nuclear magnetic resonance (NMR), allow routine investigations down to concentrations in the order of 10^{18} cm^{-3} (fig. 1). Besides secondary ion mass spectroscopy (SIMS), the electron spin resonance techniques, EPR and ENDOR, are important exceptions which detect concentrations around or below 10^{16} cm^{-3} if the defects form paramagnetic centres.

The application of radioactive isotopes, however, for the chemical identification of defects can improve the sensitivities of these techniques, like channeling or NMR, which, in this case, are called blocking and β -NMR, respectively (fig. 1). In addition, new techniques, such as the perturbed $\gamma\gamma$ angular correlation technique (PAC) and Mössbauer spectroscopy (MS), become available. They measure the local hyperfine interaction that is characteristic for a specific defect, similar to EPR and ENDOR, but without the restriction to the presence of paramagnetic centres. In the following, it will be shown what type of experimental information is obtained if the PAC technique is used for the characterisation of dopant-defect complexes in II-VI compounds.

It should be noted that the values in fig. 1 only present an overview of the sensitivities of different techniques and correspond to concentrations which should allow routine investigations

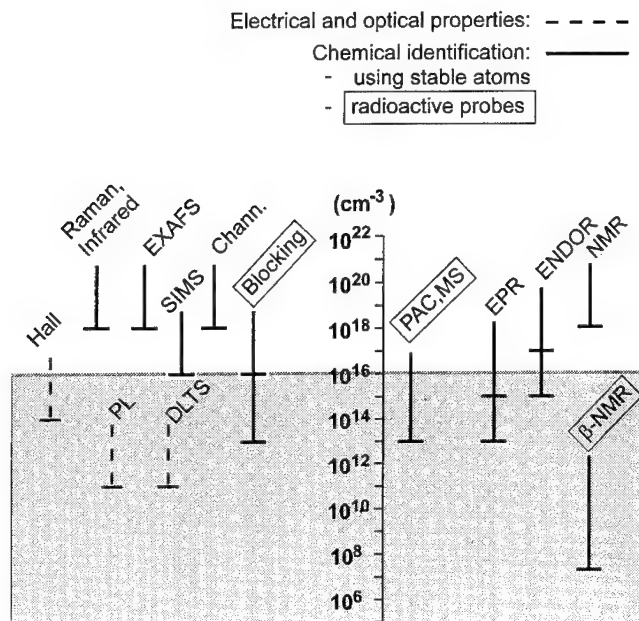


Fig. 1. Minimal defect concentrations which can be detected by various techniques in semiconductors. In case of EPR and ENDOR, the lower and higher bounds refer to the semiconductors Si and GaAs, respectively; in case of Blocking, the lower bound refers to the probe ^8Li .

of defects. For a more detailed discussion of the influence of parameters, such as chemical composition of the host material, the defects involved, sample thickness etc., as well as of the conditions for applying each technique, the reader has to be referred to other publications^{1,2,3}.

Furthermore, there were efforts to employ techniques, being originally applied to stable isotopes, in combination with radioactive probes, in order to improve the chemical selectivity of these techniques: For example, PL and EPR experiments were performed in the II-VI compounds ZnS and ZnO, respectively, using the radioactive isotope ^{65}Zn , which decays to ^{65}Cu with a half life of $T_{1/2} = 245$ days⁴. Lately, these types of experiments have been resumed, performing DLTS at Si doped with ^{195}Au (decaying to ^{195}Pt , $T_{1/2} = 183$ days)⁵ and at Si doped with ^{111}In (^{111}Cd , $T_{1/2} = 2.8$ days)⁶ as well as Hall⁷ and PL⁸ measurements at GaAs doped with ^{111}In .

PERTURBED $\gamma\gamma$ ANGULAR CORRELATION

Donor-Acceptor Pairing

For the investigation of defects in semiconductors, the PAC technique complements the more common electrical and optical techniques, supplying information on the chemical nature, composition and geometrical arrangement of defects on an atomic scale. The microscopic information about defects is obtained by measuring the local hyperfine interaction at the site of a radioactive probe atom. The defect of interest contributes a characteristic electric field gradient (efg) to this interaction, which is sensed by the nuclear electric quadrupole moment Q of the probe atom. It

has been shown that the technique is sensitive to all types of extrinsic and intrinsic defects if they give rise to a measurable efg at the site of the probe atom⁹. Since the strength of the efg falls off with r^{-3} , only defects within a distance r of typically a few Ångströms from the probe atom contribute to an observable efg. Therefore, the defect has to form a close pair with the probe atom. In semiconductors, close pairs are easily formed between an ionised donor (D^+) and an ionised acceptor (A^-) according to



yielding a thermally stable donor-acceptor pair (DAP). Here, the probe atom is either the D^+ or A^- and the oppositely charged defect in the formed DAP gives rise to a characteristic efg at the site of the probe atom and, thereby, is visible in a PAC experiment.

Using the radioactive isotope ^{111}In as a probe in II-VI semiconductors, which on a cation site acts as a donor, the following problems can be addressed: (i) Does a particular impurity, incorporated into a semiconductor, act as an acceptor? In this case, the impurity will form a DAP with the probe atom. (ii) Are there extrinsic or intrinsic defects in the material acting as acceptors? These defects will form DAP with the probe atom and can be identified via a characteristic efg. Since the formation and dissociation of the DAP is controlled by the sample temperature, information about the mobility of the defects involved and the stability of these pairs can also be obtained. The sensitivity to defects is high because the pair formation, driven by the Coulomb interaction, is very efficient.

It is obvious that for the investigation of donor-type defects a different type of probe atom is required that has to act as an acceptor in the respective semiconductor. At present, the radioactive donor atoms ^{111}In and ^{77}Br and the acceptor atom ^{79}Rb are available for PAC investigations in II-VI semiconductors. Finally, it should be noted that the radioactive probe itself gives direct information about the incorporation of the respective element as a donor or acceptor atom and about its interaction with other defects.

The Defect Specific Electric Field Gradient

The defect that is trapped at a radioactive probe atom, thereby forming a DAP, is detected

Electric Field Gradient Tensor

$$V_{ij} \sim \sum_q \frac{3q}{r^5} \begin{pmatrix} x^2 - \frac{r^2}{3} & xy & xz \\ xy & y^2 - \frac{r^2}{3} & yz \\ xz & yz & z^2 - \frac{r^2}{3} \end{pmatrix} \rightarrow \begin{pmatrix} V_{xx} & 0 & 0 \\ 0 & V_{yy} & 0 \\ 0 & 0 & V_{zz} \end{pmatrix}$$

$$\left. \begin{array}{l} \text{a) } V_{xx} + V_{yy} + V_{zz} = 0 \\ \text{b) } |V_{zz}| \geq |V_{yy}| \geq |V_{xx}| \\ \text{c) } \frac{(V_{xx} - V_{yy})}{V_{zz}} = \eta \end{array} \right\} \rightarrow \begin{array}{l} v_Q = \frac{eQV_{zz}}{h} \\ 0 \leq \eta \leq 1 \end{array}$$

Fig. 2. Correspondence between the components V_{ij} of the efg tensor and the parameters v_Q and η , used by PAC

through its efg produced at the site of the probe nucleus. This efg is the second spatial derivative of the electrostatic potential of the solid and is determined by both the positively charged nuclei of the lattice atoms and the negative charge distribution of the electrons. Its components, V_{ij} , form a 3x3 tensor, as shown in fig. 2, and in its principal-axis system the traceless efg tensor contains the three components V_{xx} , V_{yy} , and V_{zz} . These are usually expressed by the quadrupole coupling constant $v_Q = eQV_{zz}/h$, describing the strength of the EFG tensor, and the asymmetry parameter $\eta = (V_{xx} - V_{yy}) / V_{zz}$, describing the deviation of the tensor from axial symmetry. Fig. 3 depicts three lattice environments of the nuclear probe ^{111}In in a lattice with diamond structure: (a) No defects are

located in the immediate vicinity of the probe. The charge distribution about each lattice atom in a cubic lattice structure (diamond, zincblende) produces an efg tensor in which all three components of the tensor have to be identical, and, therefore, requires $V_{zz} = 0$. Thus, a radioactive probe atom on a substitutional lattice site is labelled by a zero efg. Unfortunately, this label is not unambiguous because there are certain interstitial sites, surrounded by a cubic charge distribution, and, therefore, for these probe atoms the efg vanishes, too. In contrast, in II-VI semiconductors with wurtzite structure (ZnS, CdS, CdSe) a substitutional dopant atom is characterised by a unique, non-zero efg, as was shown for the dopant ^{111}In in CdS¹⁰. (b) A single defect resides next to the probe atom. It gives rise to a non-zero EFG with $V_{zz} = 1/2 \cdot C_1$ and axial symmetry ($\eta = 0$) about a $\langle 111 \rangle$ lattice direction ($V_{zz} \parallel \langle 111 \rangle$). (c) In this case, the defect resides on a next-nearest neighbour site. The efg tensor again possesses axial symmetry but with $V_{zz} = 1/2 \cdot C_2$ and $V_{zz} \parallel \langle 110 \rangle$; because of the r^{-3} dependence C_2 will be significantly smaller than C_1 . It should be noted that theoretical calculations of the absolute values of a defect induced efg tensor still pose a problem. The components of the efg tensor given here are based on calculations within a simple point-charge model, which is not able to yield the absolute magnitude of the efg in a semiconductor. These calculations assume a charge q at a distance r from the probe atom within an unrelaxed host lattice. Without taking into account a possible relaxation of the electric charge distribution about the probe atom-defect complex, also the given values of the parameter η and the orientation of V_{zz} only represent an approximation.

Detection of the Electric Field Gradient

The energy shift induced by the efg at a nuclear state with the electric quadrupole moment Q , spin I , and z-component M is⁹

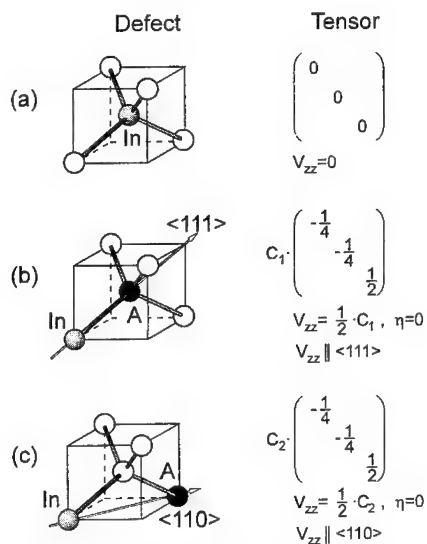


Fig. 3. Different lattice environments of the probe ^{111}In , including a defect A, along with their corresponding efg tensors.

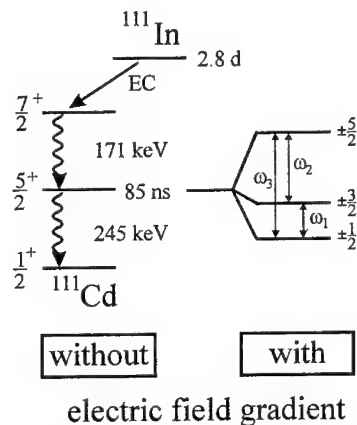


Fig. 4. Nuclear decay scheme of the radioactive probe $^{111}\text{In} / ^{111}\text{Cd}$ along with spin and parity of the nuclear states, the energies of the emitted $\gamma\gamma$ cascade and the half lives of the parent isotope and the isomeric state used for measuring the hyperfine interaction.

$$E(M) = \frac{3M^2 - I(I+1)}{4I(2I-1)} eQV_{zz} = \frac{3M^2 - I(I+1)}{4I(2I-1)} h\nu_Q \quad (2)$$

which holds for an axially symmetric efg ($\eta = 0$). Between two sublevels M and M' the energy difference ΔE becomes

$$\Delta E(M, M') = E(M) - E(M') = \frac{3|M^2 - M'^2|}{4I(2I-1)} h\nu_Q \quad (3)$$

In a "resonance" experiment, like ENDOR or MS, this energy difference is measured in order to obtain V_{zz} . In a "spin precession" experiment, like PAC or μ SR, the frequency $\omega = \Delta E/\hbar$ of the precession of the nuclear spin I is measured, which is effected by the efg.

For the determination of this spin precession frequency the orientation of the spin I at the time $t=0$ and at a later time $t>0$ has to be known. In a PAC experiment, a γ - γ cascade is used for this purpose, which in case of the probe ^{111}In is emitted after the β -decay (EC) into the excited $7/2^+$ -nuclear state of ^{111}Cd (fig. 4). The orientation of the spins at $t=0$ is prepared by detecting the γ -quanta belonging to the first transition, γ_1 , which leave behind nuclei with a preferred spin orientation. This preferred orientation or "alignment" of the nuclear spins I is connected to the intrinsic property of γ rays that their angular momentum vector is always oriented either parallel or antiparallel to their propagation direction. If an efg exists, the nuclear spins, which were aligned at the time t_{γ_1} of the detection of γ_1 , start to precess and at the same time the probability of detecting γ_2

becomes time dependent. At the time t_{γ_2} of the detection of γ_2 the nuclear spins are rotated through the angle $\omega \cdot (t_{\gamma_2} - t_{\gamma_1}) \equiv \omega \cdot t$. By measuring the elapsed time t and the change in the angular correlation, which depends on the angle $\omega \cdot t$, the frequency ω and thereby the energy difference ΔE is determined. Thus, for measuring the efg at the site of the probe nucleus the spin I and nuclear quadrupole moment Q of the intermediate state, populated by γ_1 , are of importance; in case of ^{111}Cd , they are $I = 5/2$ and $Q = 0.8$ b. Actually, the determination of ω requires the recording of a coincidence spectrum with typically 10^4 to 10^5 γ - γ coincidences.

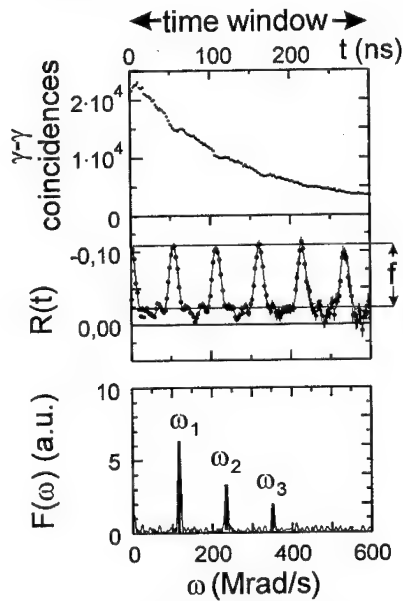


Fig. 5. Raw data of the coincidence spectrum along with the extracted PAC spectrum $R(t)$ and its Fourier transform $F(\omega)$.

Data Analysis and Experimental Set-up

The experimental set-up used for recording the γ - γ coincidences requires at least two γ detectors for analysing the emission time t_γ and energy of each γ -quantum, in order to qualify the recorded γ quantum as "start" or "stop" event and to measure the time difference. For the probe atom ^{111}In (see fig. 4) detectors 1 and 2 are tuned to the γ energies of 245 keV and

171 keV, respectively, and assuming a relative detector angle of 180° the coincidence probability reads

$$I(t) = I_0 e^{-t/\tau} (1 + R(t)) \quad \text{with} \quad R(t) = f \cdot \left(a_0 + \sum_{n=1}^3 a_n \cos \omega_n t \right) + (1 - f) \quad (4)$$

Thereby, $\tau = T_{1/2} / \ln 2$ is the lifetime of the intermediate state ($T_{1/2} = 84$ ns for ^{111}Cd), which determines the available "time window" for observing the nuclear spin precession, and the spin I determines the number of different frequencies ω_n , being three in the present case of $I = 5/2$. In fig. 5, a $\gamma\gamma$ coincidence spectrum is plotted along with the so called PAC spectrum $R(t)$, which is obtained by eliminating the exponential decay function. The Fourier transform $F(\omega)$ of the $R(t)$ time spectrum clearly shows the three spin precession frequencies ω_n . In order to improve the detection efficiency, usually four instead of two γ detectors are used so that 12 coincidence spectra are recorded simultaneously⁹.

With regard to the characterisation of a defect within a DAP, the PAC data in fig. 5 contain the following information: The asymmetry parameter η of the defect induced efg tensor, which is determined by the ratio ω_2/ω_1 . The strength V_{zz} of the efg, which is proportional to the fundamental frequency ω_1 , being $\omega_1 = (3\pi/10) \cdot v_Q$ for the case of axial symmetry ($\eta = 0$). The parameter f in eq. (4), which describes the fraction of probe atoms forming the DAP that is characterised by v_Q and η . Finally, the orientation of the efg tensor relative to the host lattice for a given orientation of the sample crystal relative to the γ detectors; this information is contained in the amplitudes a_n , which yield the orientation of V_{zz} in case of $\eta = 0$ (see fig. 3).

DONOR-ACCEPTOR PAIRING USING ^{111}In

In the past, PAC investigations of defects were performed predominantly in elemental⁹ and in III-V compound semiconductors¹¹ whereas the number of PAC experiments in II-VI semiconductors has been significantly smaller. Using the radioactive donor ^{111}In , a systematic investigation of six different Zn- and Cd-chalcogenides has been started, in order to study the formation of different DAP, and thereby the behaviour of acceptor-type defects, on an atomic scale^{10,12,13}. For illustrating the properties of the different DAP, in context of these semiconductors, particular emphasis will be put on CdTe, which was already the subject of earlier PAC experiments^{14,15,16}.

For CdTe crystals, doped with the donor probe ^{111}In , either by diffusion (1070 K, 30 min) or by implantation (350 keV, 293 K), the PAC spectra in fig. 6 (top to bottom) show the formation of DAP between the donor ^{111}In and the following acceptors: the cation vacancy (V_M) and the group V elements As and Sb¹⁷. In each case, the sharp frequency triplet visible in the Fourier transform spectra shows the unique labelling of the different DAP by their characteristic efg tensors, i.e. by the coupling constant v_Q and the asymmetry parameter η . For all DAP, the efg tensor is characterised by an η value close to zero and the v_Q values are 60 MHz in the first two spectra and 186 MHz and 154 MHz in the other two spectra. The first spectrum was measured after annealing CdTe under Te vapour, a procedure which is known to favour the incorporation of V_{Cd} defects¹⁸. The other three spectra were measured at CdTe doped with Li by diffusion (800 K, 30 min) and with As and Sb by implantation (60 and 300 keV followed by annealing at about 700 K). Compared with the efg of the trapped vacancy, the As and Sb atoms give rise to new efg tensors, whereas the treatment with Li atoms produces the same efg as the cation vacancy. The increase of the formation of $\text{In}_M\text{-V}_M$ pairs, which is directly visible through the increased

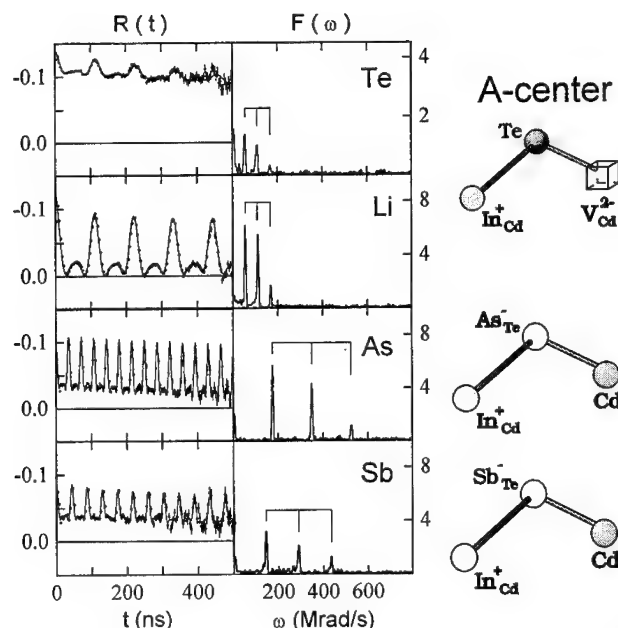


Fig. 6. Different donor-acceptor pairs in CdTe observed by the donor ^{111}In .

amplitudes of the involved frequencies in the PAC spectrum, demonstrates that the diffusion with Li increases the concentration of vacancies. At the same time, the absence of a new efg shows that Li atoms as acceptors are not available for trapping by the donor In under the used experimental conditions. In the following the different defects will be discussed in more detail.

The Cation Vacancy

Since both processes, annealing under Te and diffusion with Li, give rise to efg that have to be regarded as identical within the experimental accuracy of the PAC technique, the chemical identity of the trapped defect has to be carefully discussed. Unfortunately, the available theoretical calculations for defect induced efg do not allow a direct identification via the measured efg tensor.

The efg, collected in Table I, characterise DAP that in ZnS, CdS, ZnSe, CdSe, CdTe are easily, in ZnTe are hardly formed, if ^{111}In is diffused into these compounds at the presence of the respective chalcogen component. Also the strengths of the efg, characterising the In-defect pairs, are very similar so that it can be expected that in all compounds the same type of DAP is observed. For each compound, the strength of the efg is mainly determined by the respective chalcogen element of the host lattice, whereas the group II element, Zn or Cd, hardly affects the efg. In ZnSe, ZnTe, and CdTe, crystals with zincblende structure, the DAP are characterised by a single efg, while in CdS and CdSe, crystals with wurtzite structure, two different efg are observed. This result is easily understood because in the wurtzite lattices the same defect can form two DAP complexes, differing in their local arrangements and, therefore, giving rise to two different efg. In case of the ZnS crystal, the c/a ratio is close to $\sqrt{8/3}$, the ratio for an ideal hcp

Table IElectric field gradients of $\text{In}_\text{M}-\text{V}_\text{M}$ pairs measured at the site of the probe atom $^{111}\text{In} / ^{111}\text{Cd}$.

Compound	Lattice	ν_Q (MHz)	η	$V_{zz} \parallel \langle ijk \rangle$
ZnS	wurtzite	81.0(7)	0.16(2)	-
CdS	wurtzite	72.0(6)	0.35(5)	-
		79.0(5)	0.21(2)	-
ZnSe	zincblende	71.5(5)	0.05(2)	$\langle 111 \rangle$
CdSe	wurtzite	66.7(5)	0.32(5)	-
		71.2(5)	0.05(2)	-
ZnTe	zincblende	58.8(5)	0.08(2)	-
CdTe	zincblende	60.0(5)	0.09(2)	$\langle 111 \rangle$

structure; therefore, the difference between the two structurally non-equivalent DAP is very small and the difference between the resulting efg is too small to be experimentally resolved.

Also the growth and decrease of the fraction of the DAP upon alternately annealing under the vapour of the respective chalcogen and metal component, respectively, confirms the assignment of the efg in Table I to the same type of DAP and is to be expected if a V_M defect is involved. The identification of the trapped defect with a cation vacancy is in good agreement with the results of other microscopic techniques: With EPR, which has shown the formation of a DAP - the so called A-centre - between group III or group VII donors and the V_M defect in several II-VI semiconductors^{19,20}; with positron annihilation spectroscopy, which detected the vacancy specific positron lifetime in CdTe doped with In²¹; and with PAC, performed at ^{111}In implanted CdTe, in which the DAP characterised by $\nu_\text{Q} = 60$ MHz and $\eta = 0.19$ was assigned to an $\text{In}_\text{M}-\text{V}_\text{M}$ pair¹⁴. The measured $\langle 111 \rangle$ orientation of the efg tensor is in agreement with EPR data, which showed the unpaired spin of the V_M defect to be localised at the neighbouring chalcogen atom for this type of DAP¹⁹. But, as will be discussed below and described elsewhere²², different mechanisms for the creation of the cation vacancy do exist, which show the fundamental importance of this defect for the understanding of the doping problems in II-VI semiconductors.

Doping with Li and Ag

Like the formation of the $\text{In}_\text{M}-\text{V}_\text{M}$ pair itself, also its enhanced production upon diffusion with Li is a phenomenon that occurs in all II-VI semiconductors, which were investigated by PAC. Since the data in fig. 6 clearly show that the diffusion of Li produces a significantly larger fraction of the DAP characterised by $\nu_\text{Q} = 60$ MHz than the treatment under Te vapour, it would be tempting to interpret the DAP rather as an $\text{In}_\text{Cd}-\text{Li}_\text{Cd}$ than as an $\text{In}_\text{Cd}-\text{V}_\text{Cd}$ pair. Such an assignment, on the other hand, would require a strong contamination of the II-VI compounds with Li which, indeed, is reported to occur in these materials²³. The amount of the contamination has to be comparable to the concentration of probe atoms in order to explain the visibility of these DAP in samples that were not intentionally treated with Li. In order to pursue this possibility, CdS crystals were doped with 10^{18} In atoms cm^{-3} by diffusion with stable In in addition to the radioactive ^{111}In ²⁴. It was found that 50 % of the In atoms still form the respective DAP so that its explanation by an $\text{In}_\text{Cd}-\text{Li}_\text{Cd}$ pair would require a concentration of at least $5 \cdot 10^{17}$ Li atoms cm^{-3} , being much higher than the $5 \cdot 10^{15}$ Li atoms cm^{-3} , reported in the literature²³. Infrared absorption measurements at In doped CdTe, that was diffused with Li, report localised vibrational modes (LVM) of an $\text{In}_\text{Cd}-\text{V}_\text{Cd}-\text{Li}_\text{i}$ complex²⁵. Such a complex would be in agreement with the

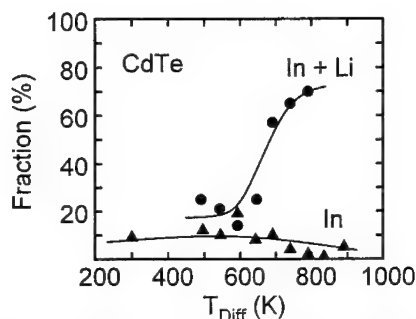


Fig. 7. Fraction of $\text{In}_{\text{Cd}}\text{-V}_{\text{Cd}}$ pairs as a function of the temperature, used for Li diffusion (circles). For comparison, the data of a reference crystal, heated without Li, are shown.

PAC results if the association of the interstitial Li_i to the $\text{In}_{\text{Cd}}\text{-V}_{\text{Cd}}$ pair would not alter the efg of the $\text{In}_{\text{Cd}}\text{-V}_{\text{Cd}}$ in a measurable way. And, the data also showed dominant LVM of $\text{In}_{\text{Cd}}\text{-Li}_{\text{Cd}}$ pairs, which were not observed by PAC.

In fig. 7, the step-like increase of the fraction of $\text{In}_{\text{Cd}}\text{-V}_{\text{Cd}}$ pairs and, thereby of the V_{Cd} concentration, is shown as a function of the temperature, used for Li diffusion. Also shown are PAC data of a CdTe reference sample, that was identically treated, only without Li. From detailed investigations in CdS and ZnSe, it can be concluded that under thermal equilibrium conditions the temperature of the steep increase around 650 K is mostly determined by the solubility of Li in the compound. At this temperature, the concentration of Li atoms

reaches the concentration of ^{111}In atoms, which is in the order of 10^{16} cm^{-3} .

In contrast to the diffusion experiment, a recent experiment in ZnSe revealed that implantation of Li along with an adequate annealing treatment did not effect an increase of the V_{Zn} concentration. Obviously, the respective doping procedure determines the microscopic incorporation of the dopant atoms in a decisive way. This phenomenon is also known for N in ZnSe²⁶.

Besides Li, also the diffusion of CdTe with Ag leads to the efg that is listed in Table I for the formation of the $\text{In}_{\text{Cd}}\text{-V}_{\text{Cd}}$ in CdTe²⁷. In principle, the formation of an $\text{In}_{\text{Cd}}\text{-Ag}_{\text{Cd}}$ could be expected, for Ag on a Cd lattice site forms an acceptor state. Since each procedure, however, the heat treatment under Te vapour, diffusion with either Li or Ag, produces the same efg in CdTe, an assignment of the DAP to an $\text{In}_{\text{Cd}}\text{-V}_{\text{Cd}}$ pair has to be favoured.

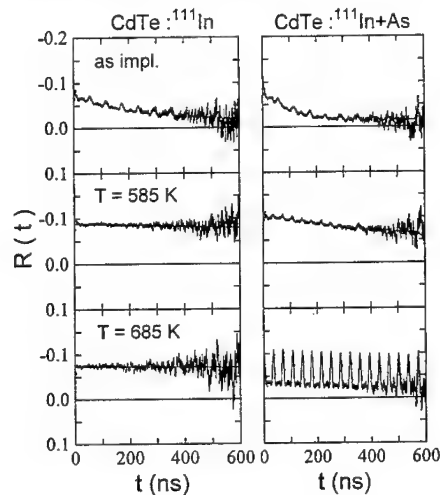


Fig. 8. Annealing sequence of PAC spectra measured at CdTe, which was implanted with ^{111}In and with ^{111}In and As at 295 K.

Doping with Group V Elements

In order to study the incorporation of group V elements as acceptors in CdTe, different crystals were implanted with the donor ^{111}In (350 keV) and subsequently co-implanted with a group V element. Fig. 8 compares the annealing of a crystal, which was co-implanted with $2 \cdot 10^{14} \text{ As cm}^{-2}$ (300 keV) and $5 \cdot 10^{12} \text{ As cm}^{-2}$ (60 keV), with that of a reference crystal, which was exclusively implanted with ^{111}In . In the as implanted state, in both PAC spectra an In-defect complex is visible that is characterised by $\nu_Q = 114 \text{ MHz}$ and $\eta = 0$. This complex was already observed in earlier PAC experiments immediately after implantation of ^{111}In at 295 K and was ascribed to an athermally formed $\text{In}_{\text{Cd}}\text{-V}_{\text{Te}}$ pair^{14,15}. In addition, the crystal implanted with As, weakly shows a second efg, characterised by $\nu_Q = 186 \text{ MHz}$ and $\eta = 0$. Upon annealing

under Cd vapour, the proposed $\text{In}_{\text{Cd}}\text{-V}_{\text{Te}}$ pair disappears and, above 600 K, the fraction of the second complex starts to grow until it finally reaches 58 % at 735 K.

Since the presence of the complex characterised by $\nu_Q = 114$ MHz and $\eta = 0$ does not depend on the co-implanted group V element - it is observable in each implanted CdTe crystal - an intrinsic, irradiation induced defect is most probably involved. The proposed V_{Te} defect should be a donor in CdTe and, therefore, should not form a DAP with the donor ^{111}In . This explains that the complex exclusively develops athermally during the irradiation process and exhibits a low thermal stability.

In contrast, the efg of the second complex depends on the co-implanted group V element, being characterised by $\nu_Q = 186$ MHz and $\nu_Q = 154$ MHz for the As and Sb co-implantation, respectively (see fig. 6). The formation is thermally activated and the complexes exhibit a high thermal stability. Obviously, they correspond to DAP and the formed pairs in fig. 8 are $\text{In}_{\text{Cd}}\text{-As}_{\text{Te}}$ pairs. Since the formation of a DAP requires the presence of an ionised acceptor, implanted As atoms must be incorporated as acceptors within CdTe after annealing at 685 K. This result is in good agreement with the reported electrical activation of As implanted into HgCdTe after annealing at 730 K²⁸. The identification of this complex with As_{Te} as a nearest neighbour to an In_{Cd} probe atom is also in agreement with the fact that the associated efg is significantly stronger than that of the next nearest neighbour pair $\text{In}_{\text{Cd}}\text{-V}_{\text{Cd}}$ (see fig. 6) and with the measured $\langle 111 \rangle$ orientation of V_{Zz} (see fig. 3, bottom).

DEFECTS IN CdTe LAYERS

The above discussed information on defects in bulk II-VI crystals is of importance for the characterisation of the technologically more relevant II-VI epi-layers. There are first results for

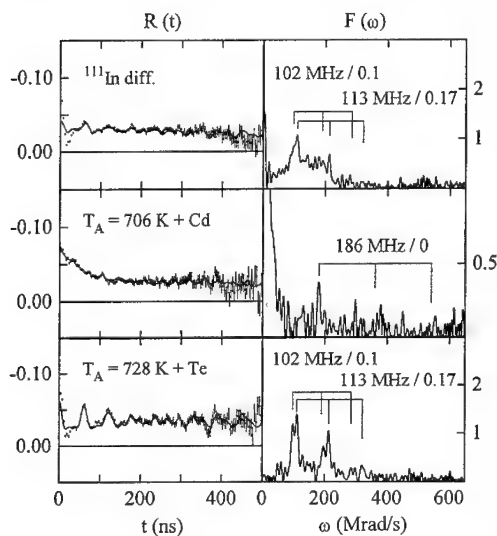


Fig. 9. Different In-defect complexes observed in CdTe epi-layers, diffused with ^{111}In and heated under Cd and Te vapour.

PAC experiments in CdTe layers grown on GaAs by MOCVD²⁹. The incorporation of the donor ^{111}In into these layers takes place either via diffusion, implantation, or by *in situ* doping during the MOCVD growth. The latter process uses trimethylindium as the In precursor, which is labelled with radioactive ^{111}In . The process is performed in a customised MOCVD reactor which is suited for work with radioactive isotopes. In this way, intrinsic defects and contaminants, introduced during the growth process can be controlled in addition to the incorporation of the dopant In itself.

First results, obtained from MOCVD grown CdTe layers doped with ^{111}In by diffusion, are shown in fig. 9. The first spectrum shows that diffusion of the CdTe layers with ^{111}In leads to the formation of two In-defect complexes, characterised by $\nu_Q = 102(1)$ MHz, $\eta = 0.10(5)$ and $\nu_Q = 113(1)$ MHz, $\eta = 0.17(5)$. They were not observed in the above shown PAC spectra for CdTe, but were also reported to occur in bulk CdTe

Table II
In-defect complexes observed in MOCVD grown CdTe layers, which were diffused with ^{111}In .

Complex	ν_Q (MHz)	η	Procedure
$\text{In}_{\text{Cd}}\text{-V}_{\text{Cd}}$	60(1)	0.09(5)	Li diffusion
In-defect	102(1)	0.10(5)	highly In doped
In-defect	113(1)	0.17(5)	highly In doped
$\text{In}_{\text{Cd}}\text{-As}_{\text{Te}}$	186(1)	0.00(5)	diffusion out of GaAs substrate

crystals¹⁵. Fig. 9 also shows that annealing the sample under Cd and Te vapour reduces and increases the fractions of these complexes, respectively. Their interpretation, however, has to await more detailed investigations. As already discussed in¹⁵, the formation of precipitates involving In atoms can be excluded based on the known values of the corresponding efg. It was proposed that a formation of In-defect complexes involving interstitials and/or anti-site atoms and possibly more than one In atom might cause these efg. In recent experiments, it has been shown that in bulk CdTe the same In-defect complexes are formed, if the crystals show up high concentration of In atoms around 10^{19} cm^{-3} . Under these conditions, also in CdS¹⁰ and in ZnTe new complexes were observed, which were characterised by efg that a similar to those in CdTe.

The second spectrum in fig. 9 shows the sensitivity of PAC to low concentrations of contaminants. The observed In-defect complex, characterised by $\nu_Q = 186 \text{ MHz}$ and $\eta = 0$, is already known to be caused by the presence of $\text{In}_{\text{Cd}}\text{-As}_{\text{Te}}$ pairs in CdTe. Obviously, As atoms from the GaAs substrate diffused into the CdTe layer and formed the passivating DAP with about 3 % of the In dopant atoms. The In-defect complexes observed by PAC in CdTe epi-layers after diffusion of ^{111}In are collected in Table II.

CONCLUSIONS

The experimental data have shown the limitations and advantages of the PAC technique for the study of defects in II-VI semiconductors. Due to the donor character of the most commonly used probe atom ^{111}In , data on the formation of DAP involving acceptor-like defects were presented. This limitation of the technique is removed with help of the PAC probe atoms ^{77}Br , ^{79}Rb , and ^{73}As , which represent additional donor and acceptor atoms besides the probe ^{111}In . These new dopants are provided by the ISOLDE facility at CERN³⁰. Accordingly, the potential for research on the electrical activation of dopant atoms in II-VI semiconductors using PAC will be considerably broadened. From a technological point of view, the PAC technique has proven itself as a sensitive tool for the characterisation of bulk material and epi-layers with respect to the presence of intrinsic and extrinsic defects. As discussed in the introductory part, the use of radioactive isotopes, in general, will enhance the efficiency of several analytical techniques in semiconductors.

It is a great pleasure to thank my co-workers in Saarbrücken and the members of the PAC group at the Universität Konstanz for their experimental help, many fruitful discussions, and their effort in preparing this manuscript. The financial support of the Deutsche Forschungsgemeinschaft and the Bundesministerium für Bildung und Forschung (contract 03-WI3SAA) is gratefully acknowledged.

REFERENCES

- 1) R.A. Stradling and P.C. Klipstein (eds.): *Growth and Characterisation of Semiconductors*, (Adam Hilger, Bristol, 1990).
- 2) L.C. Feldman and J.W. Mayer (eds.): *Fundamentals of Surface and Thin Film Analysis*, (North-Holland, New York, 1986).
- 3) G. Langouche (ed.): *Hyperfine Interactions of Defects in Semiconductors* (Elsevier, Amsterdam, 1992).
- 4) I. Broser and K.H. Franke, J. Phys. Chem. Solids **26**, 1013 (1965);
I. Broser and M. Schulz, Z. Physik **254**, 35 (1972).
- 5) J.W. Petersen and J. Nielsen, Mat. Sci. Forum **83-87**, 1103 (1992).
- 6) M. Lang, G. Pensl, M. Gebhard, N. Achtziger and M. Uhrmacher, Mat. Sci. Forum **83-87**, 1097 (1992).
- 7) R. Gwilliam, B.J. Sealy and R. Vianden, Nucl. Instrum. and Meth. **B63**, 106 (1992).
- 8) R. Magerle, T. Kerle, A. Burchard, M. Deicher, W. Pfeiffer, to be published.
- 9) Th. Wichert, N. Achtziger, H. Metzner and R. Sielemann in ref. 3, p. 77.
- 10) Th. Wichert, Th. Krings and H. Wolf, Physica B **185**, 297 (1993), and references therein.
- 11) M. Deicher, Nucl. Instrum. and Meth. **B63**, 189 (1992).
- 12) H. Wolf, Th. Krings, U. Ott, U. Hornauer and Th. Wichert, Mater. Sci. Forum **83-87**, 1259 (1992).
- 13) H. Wolf, U. Hornauer, R. Lermen, Y. Endalamaw, T. Filz, Th. Krings, St. Lauer, U. Ott, E. Singer, M. Tsige and Th. Wichert, Mat. Sci. Forum **143-147**, 391 (1994).
- 14) R. Kalish, M. Deicher and G. Schatz, J. Appl. Phys. **53**, 4793 (1982).
- 15) D. Wegner and E.A. Meyer, J. Phys.: Condens. Matter **1**, 5403 (1989).
- 16) J.W. Griffith, R. Lundquist, R. Platzter, J.A. Gardner, G. Karczewski and J. Furdyna, Mat. Sci. Forum **143-147**, 405 (1994).
- 17) H. Wolf, A. Burchard, M. Deicher, T. Filz, A. Jost, R. Magerle, V. Ostheimer, W. Pfeiffer and Th. Wichert, in *18th Int. Conf. on Defects in Semiconductors*, Sendai, Japan, 1995.
- 18) D.G. Thomas (ed.), *II-VI Semiconducting Compounds* (Benjamin, New York, 1967).
- 19) J. Schneider, Mat. Res. Soc. Symp. Proc. **46**, 13 (1985).
- 20) D.M. Hofmann, P. Omling, H.G. Grimmeiss, B.K. Meyer, K.W. Benz and D. Sinerius, Phys. Rev. B **45**, 6247 (1992).
- 21) C. Gély-Sykes, C. Corbel and R. Triboulet, Solid State Commun. **80**, 79 (1991).
- 22) H. Wolf, Th. Krings, P. Hautojärvi, U. Hornauer, R. Lermen, L. Liskay, T. Filz, St. Lauer, U. Ott, E. Singer and Th. Wichert, to be published.
- 23) C.H. Henry, K. Nassau and J.W. Shiever, Phys. Rev. B **4**, 2453 (1971).
- 24) H. Wolf, Th. Krings and Th. Wichert, Nucl. Instrum. and Meth. **B63**, 240 (1993).
- 25) R. Zielinska, A. Król and W. Nazarewicz, J. Phys. C: Solid State Phys. **17**, 5209 (1984).
- 26) H. Kukimoto, Mat. Sci. Forum **143-147**, 385 (1994).
- 27) M. Rüb, N. Achtziger, J. Meier, U. Reislöhner, P. Rudolph, M. Wienecke and W. Witthuhn, J. Cryst. Growth **138**, 285 (1994).
- 28) D.D. Edwall, L.O. Bubulac and E.R. Gertner, J. Vac. Sci. Technol. B **10**, 1423 (1992);
J.M. Arias, J.G. Pasko, M. Zandian, S.H. Shin, G.M. Williams, L.O. Bubulac, R.E. DeWames and W.E. Tennant, to be published.
- 29) T. Filz, J. Hamann, R. Müller, V. Ostheimer, H. Wolf and Th. Wichert, in *7th Int. Conf. on II-VI Compounds and Devices*, Edinburgh, Schottland, 1995.
- 30) H. Wolf, T. Filz, St. Lauer, A. Jost, V. Ostheimer, Th. Wichert, M. Deicher, R. Magerle, A. Burchard, D. Forkel-Wirth and H. Haas, in *10th Int. Conf. on Hyperfine Interactions*, Leuven, Belgium, 1995.

GROWTH AND CHARACTERIZATION OF THE BINARY DEFECT ALLOY Cu_{2-x}Se AND THE RELATION TO II-VI/I-III-VI HETEROJUNCTION FORMATION

ART J. NELSON*, K. SINHA* and JOHN MORELAND**

*National Renewable Energy Laboratory, 1617 Cole Blvd., Golden, CO 80401

**National Institute of Standards and Technology, Boulder, CO 80303

ABSTRACT

Synchrotron radiation soft x-ray photoemission spectroscopy was used to investigate the development of the electronic structure at the $\text{CdS}/\text{Cu}_{2-x}\text{Se}$ heterojunction interface. Cu_{2-x}Se layers were deposited on GaAs (100) by molecular beam epitaxy from Cu_2Se sources. Raman spectra reveal a strong peak at 270 cm^{-1} , indicative of the Cu_{2-x}Se phase. Atomic force microscopy reveals uniaxial growth in a preferred (100) orientation. CdS overlayers were then deposited in-situ, at room temperature, in steps on these epilayers. Photoemission measurements were acquired after each growth in order to observe changes in the valence band electronic structure as well as changes in the $\text{Se}3d$ and $\text{Cd}4d$ core lines. The results were used to correlate the interfacial chemistry with the electronic structure and to directly determine the $\text{CdS}/\text{Cu}_{2-x}\text{Se}$ and heterojunction valence band discontinuity and the consequent heterojunction band diagram. These results are compared to the valence band offset (ΔE_v) for the $\text{CdS}/\text{CuInSe}_2$ heterojunction interface.

INTRODUCTION

A better understanding of polycrystalline thin-film $\text{Cu}(\text{In,Ga})\text{Se}_2$ device operation has recently emerged based on the concept of a shallow buried junction between a Cu-poor n-type surface phase and the stoichiometric p-type bulk material.[1-4] Polycrystalline $\text{Cu}(\text{In,Ga})\text{Se}_2$ devices have demonstrated efficiencies exceeding 16% (total area)[5] based on an optimized n-type surface region which effectively reduces recombination at the $\text{CdS}/\text{Cu}(\text{In,Ga})\text{Se}_2$ heterojunction interface. Recently, epitaxial layers of this Cu-poor n-type surface phase have been isolated and characterized.[6] However, device grade polycrystalline $\text{Cu}(\text{In,Ga})\text{Se}_2$ thin-films may contain secondary binary phases at grain boundaries which can affect device performance. Experimental data on interfaces between CdS and these secondary phases and how they effect $\text{CdS}/\text{Cu}(\text{In,Ga})\text{Se}_2$ heterojunction formation are non-existent. Thus, a comprehensive experimental investigation addressing the electronic structure at these interfaces is needed.

This paper presents and discusses the results of an investigation on the in-situ growth of $\text{CdS}/\text{Cu}_{2-x}\text{Se}$ heterojunction and the consequent characterization of the electronic band structure by synchrotron radiation soft x-ray photoemission spectroscopy. Photoemission spectra were obtained before and after each growth in order to observe the development of the electronic structure at the heterojunction interface.

EXPERIMENTAL

The Cu_{2-x}Se films were deposited on GaAs (100) substrates by molecular beam epitaxy from a single liquid nitrogen shrouded boron nitride effusion cell containing Cu_2Se . The substrate temperature was 500°C for these depositions. The GaAs(100) wafer preparation included solvent cleaning and a standard $\text{NH}_3\text{OH}:\text{H}_2\text{O}_2:\text{H}_2\text{O}$ (2:1:10) etchant/oxidant followed

by annealing in vacuum to desorb the oxide. The films were typically 480 nm thick. Quantitative compositional analysis was performed with X-ray photoemission spectroscopy (XPS). X-ray diffractometry (XRD) and atomic force microscopy (AFM) were also used to characterize the crystalline orientation of the resulting binary films.

Raman spectra were measured at room temperature, in a near back-scattering geometry, in the 200 - 300 cm^{-1} range using the 514.5 nm emission line of an Ar ion laser. The incident laser power was kept below 200 mW and focused to a line on the sample to minimize local heating effects and photocreation of carriers. The scattered radiation was dispersed by 0.65 m triple spectrometer and detected by a liquid nitrogen cooled charge-coupled detector. The spectral resolution for the measurements was 2-3 cm^{-1} .

CdS overlayers were then deposited in-situ, at room temperature, in steps on these Cu_2Se epilayers. Deposition rates were monitored with a calibrated water cooled quartz crystal thickness monitor and showed the typical Arrhenius behavior (the deposition rate is linear versus the reciprocal of the absolute source temperature).

Photoemission experiments were performed on the Amoco 6-meter toroidal grating monochromator on the 1 GeV storage ring (Aladdin) at the University of Wisconsin Synchrotron Radiation Center. The photoemitted electrons were analyzed using a hemispherical sector analyzer with a total angular acceptance of 1.5° . Photoemission spectra were taken in an energy range $h\nu=40\text{--}100$ eV. The combined energy resolution of the monochromator and the analyzer was $\Delta E=0.2$ eV. All spectra were measured at normal emission with a photon angle of incidence of $\theta_c=45^\circ$ and were normalized to the measured restoring current from a 90% transmission Ni mesh.

RESULTS AND DISCUSSION

Results of the quantitative XPS compositional analysis reveal that the films grown from the binary Cu_2Se source are indeed representative of Cu_{2-x}Se ($E_g \approx 1.2$ eV).[7] Results of the XRD measurements for the Cu_{2-x}Se films confirm that the films are cubic (100) oriented layers and are complementary to the compositional data.

Figure 1 is an AFM image of the Cu_{2-x}Se layer showing what appears to be a uniaxial

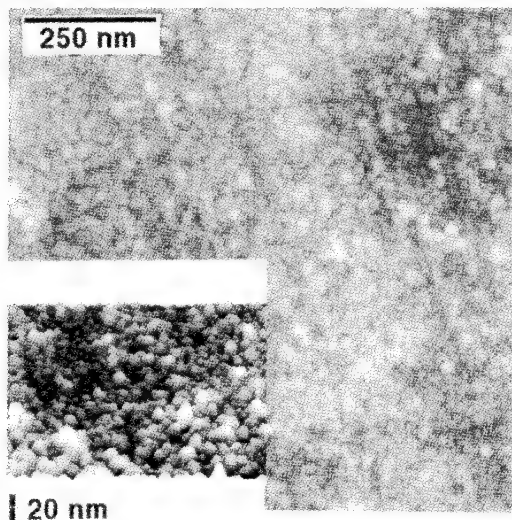


Figure 1. Atomic force micrograph for the epitaxial Cu_{2-x}Se film.

granular surface texture. The image was taken in air using tapping mode with an etched single crystal Si tip microcantilever. Tapping mode has the advantage of applying minimal frictional and vertical forces to the sample surface.[8] This reduces the amount of nanomilling that can occur on soft samples during contact mode AFM.

The grain size ranges from 10 to 20 nm in diameter. The maximum vertical range deviation for the image is 14 nm with an rms roughness of 1.4 nm and mean roughness of 0.991 nm. The deviation from a flat $1 \mu\text{m}^2$ surface area is 3.2%.

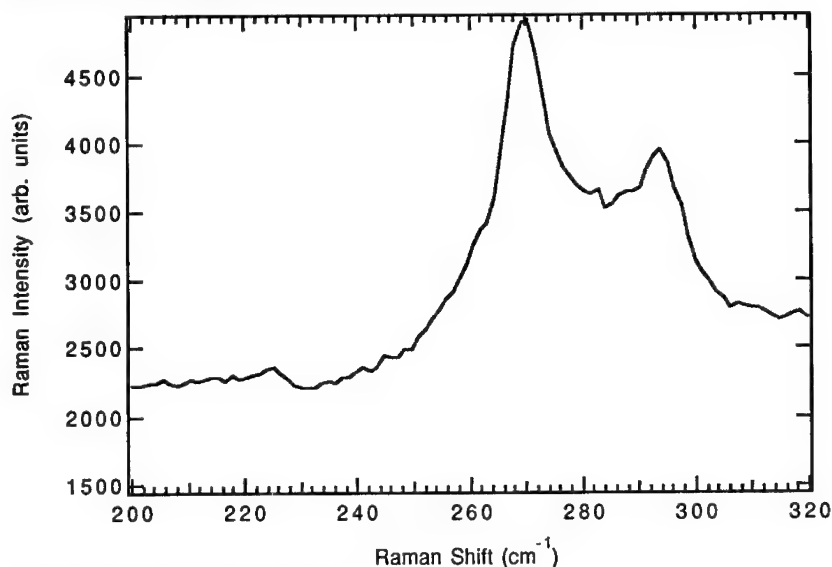


Figure 2. Raman spectrum for the Cu_{2-x}Se film.

The Raman spectra of the Cu_{2-x}Se film is presented in Figure 2. The peak close to 291 cm^{-1} arises from the light scattering from the LO phonons of the GaAs substrate. The stronger peak close to 270 cm^{-1} arises from the scattering from the vibrations corresponding to the Cu-Se bonds in the layer. [9] The presence of the peak at 270 cm^{-1} further complements the XPS, XRD and AFM measurements. Raman scattering peaks in the ordered vacancy compound CuIn_3Se_5 and in the chalcopyrite CuInSe_2 occur at 152 cm^{-1} and 175 cm^{-1} , respectively.[6,10,11]

In order to fully characterize the Cu_{2-x}Se films prior to CdS growth, normal emission valence-band (VB) spectra were acquired at several photon energies and are presented in Figure 3. The position of the VBM (E_v) is determined from the linear extrapolation of the leading edge of the spectrum. Although the precision of this technique can be quite good ($<0.1 \text{ eV}$), the accuracy is generally in the range of $\approx 0.2 \text{ eV}$. Additionally, the Fermi level position was determined from a clean Ta metal surface in contact with the sample. The position of the valence band maximum (E_v) for the Cu_{2-x}Se surface is approximately equivalent ($\pm 0.2 \text{ eV}$) to the Fermi energy (E_F) indicating a highly degenerate p-type surface. The upper valence band consists of a mixture of Se, p and Cu, d orbitals and appears as a two peak structure corresponding to the two branches of the Cu d bands. In addition, at the lower photon energies, the photoionization cross-sections for the Cu d states are much lower than the cross-sections for the Se p states and thus, the valence band is dominated by these p states. The observed emission above E_v

originates from the convolution of the lifetime broadened emission with the finite energy resolution of the electron analyzer and monochromator [12].

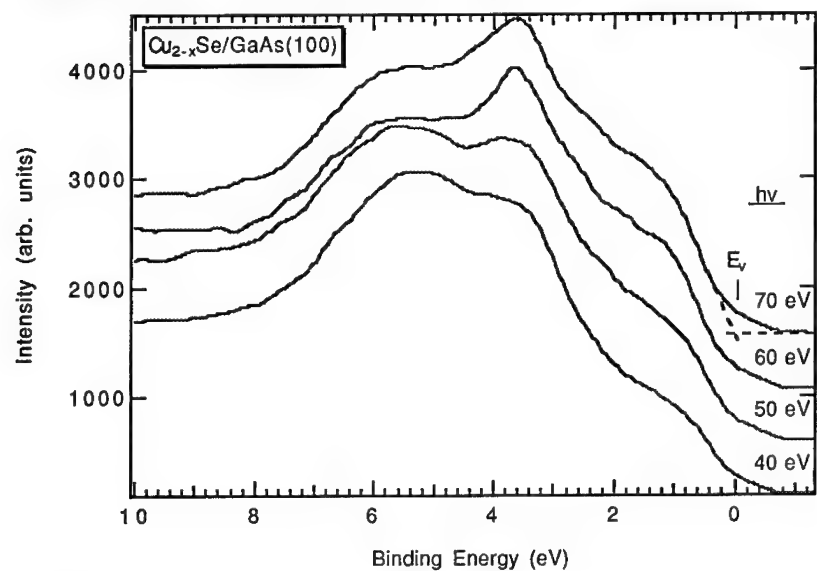


Figure 3. Normal emission valence-band spectra of Cu_{2-x}Se acquired in the energy range $h\nu = 40\text{--}70$ eV.

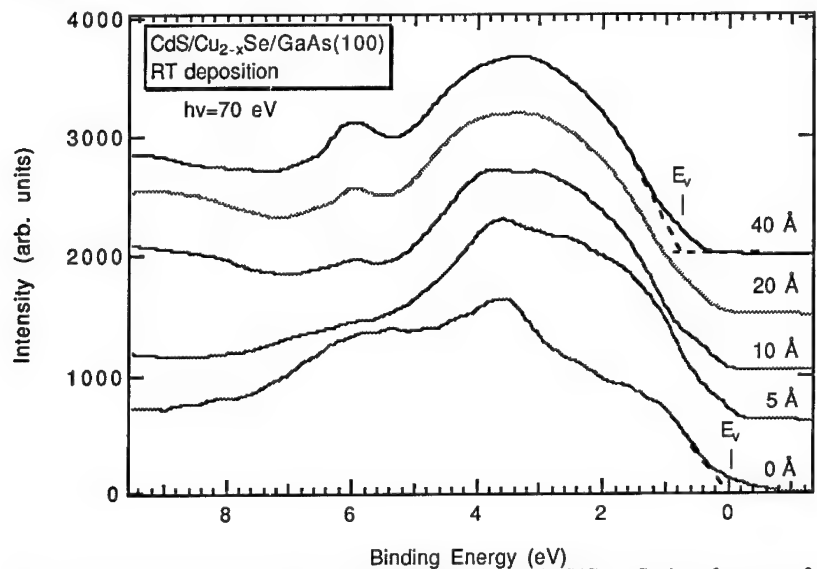


Figure 4. Normal emission valence-band spectra of the $\text{CdS}/\text{Cu}_{2-x}\text{Se}$ interface as a function of the effective CdS coverage.

Figure 4 shows the normal emission valence band spectra of the CdS/Cu_{2-x}Se interface as a function of the effective CdS coverage. For the Cu_{2-x}Se surface, $E_F - E_{vbm} = 0.0(\pm 0.2)$ eV while for the CdS covered surface we observe $E_F - E_{vbm} = 0.8$ eV. Since the film is p-type, the Cu_{2-x}Se bands are very nearly flat near the surface with minimal (<0.2 eV) band bending. No significant shift is observed in the dominant Cu *d* band features which indicates that the flat band condition remains in the Cu_{2-x}Se with CdS coverage. As additional CdS is deposited onto the Cu_{2-x}Se epilayer, the Cu_{2-x}Se valence band remains flat and the structure becomes dominated by the uppermost CdS bands. Hence, the valence band offset (E_v) given by the different positions of E_{vbm} in the clean and covered surface is 0.8 eV.

Combining all of the aforementioned results with $E_g(\text{Cu}_{2-x}\text{Se}) = 1.2$ eV and $E_g(\text{CdS}) = 2.42$ eV, one may determine the conduction band discontinuity ΔE_c to be 0.42 ± 0.20 eV for an abrupt CdS/p-Cu_{2-x}Se heterojunction. This discontinuity presents a significant barrier to electron flow through the CdS window layer and would partially explain the observed device performance.[13] These results are summarized schematically in Figure 5 for the region in the vicinity of the CdS/p-Cu_{2-x}Se interface. Bands may bend outside these interfacial regions on a length scale of $\approx 1000\text{\AA}$.

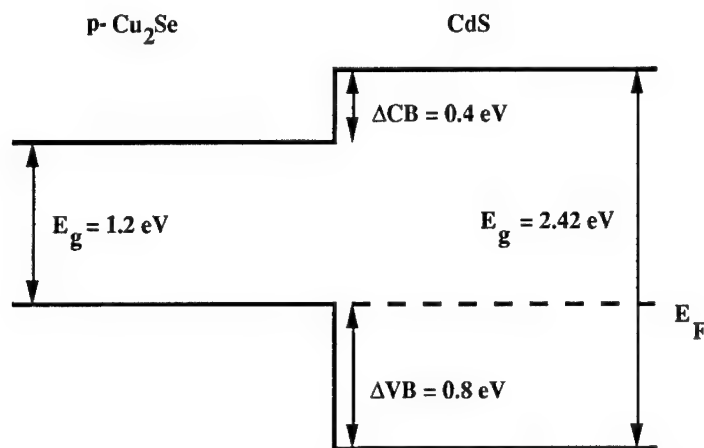


Figure 5. Schematic of the experimentally determined band lineup in the vicinity of the CdS/p-Cu_{2-x}Se heterojunction interface.

Applying the transitivity rule [14] to the CdS-CuInSe₂-Cu_{2-x}Se system, we can predict ΔE_v between Cu_{2-x}Se and CuInSe₂. Thus, using our previous result $\Delta E_v = 0.9$ eV for CdS/CuInSe₂ [15,16] and these new results, $\Delta E_v = 0.1$ eV for the Cu_{2-x}Se/CuInSe₂ junction which, based on the bandgaps of the two phases, indicates that $\Delta E_c = 0.1$ eV. These results are for an abrupt interface and neglect interdiffusion.

CONCLUSIONS

Cu_{2-x}Se films were deposited on GaAs(100) substrates. XPS, XRD, AFM and Raman measurements confirmed the composition and physical structure. Synchrotron radiation soft x-ray photoemission spectroscopy was used to characterize the electronic band structure of the binary defect semiconductor Cu_{2-x}Se and the consequent heterojunction band alignment with

CdS. High-resolution photoemission measurements for the Cu_{2-x}Se surface indicates a highly degenerate p-type surface. In addition, for the abrupt CdS/ Cu_{2-x}Se interface, we observe $\Delta E_v = 0.8 \pm 0.2$ eV and a conduction-band discontinuity $\Delta E_c = 0.42 \pm 0.20$ eV.

ACKNOWLEDGEMENTS

This work was supported by the U.S. Department of Energy under Contract No. DE-AC02-83CH10093. The Synchrotron Radiation Center is supported by the NSF under Grant No. DMR92-12658. The technical support of the SRC staff is also duly noted.

REFERENCES

1. J.R. Tuttle, M. Contreras, A. Tennant, A. Duda, J. Carapella, D. Albin, and R. Noufi, Proceedings of the 11th PV AR&D Review Meeting, Denver, CO, AIP Conference Proceedings No. 268, 186 (1992).
2. A.J. Nelson, J.R. Tuttle, R. Noufi, D. Rioux, and Hartmut Hochst, J. Appl. Phys. **74**, 5757 (1993).
3. D. Schmid, M. Ruckh, F. Grunwald, and H.W. Schock, J. Appl. Phys. **73**, 2902 (1993).
4. W.H. Schock, 10th European Photovoltaic Solar Energy Conference, Lisbon (1991) p.777.
5. A.M. Gabor, J.R. Tuttle, M.A. Contreras, D.S. Albin, R. Noufi, and A.M. Hermann, Appl. Phys. Lett. **65**, 198 (1994).
6. A.J. Nelson, M.H. Bode, G.S. Horner, K. Sinha and John Moreland in Compound Semiconductor Epitaxy, edited by C.W. Tu, L.A. Kolodziejski, and V.R. McCrary (Mater. Res. Soc. Proc. **340**, San Francisco, CA, 1994) pp. 599-603.
7. G.P. Sorokin, IZV. Vyssh. Ucheb. Zaved. Fizika No. 4, 140 (1965).
8. Q. Zhong, D. Innis, K. Kjoller, and V.B. Elings, Surf. Sci. Lett. **290**, L688 (1993).
9. Satoshi Yamanaka, Masayuki Tanda, Nobuyuki Nakada, Akira Yamada, Makoto Konagai, and Kiyoshi Takahashi, Jpn. J. Appl. Phys. **30**(3), 442 (1991).
10. H. Tanino, T. Maeda, H. Fujikake, H. Nakanishi, S. Endo, and T. Irie, Phys. Rev. **B45**, 13323 (1992).
11. C. Rincón and F.J. Ramírez, J. Appl. Phys. **72**, 4321 (1992).
12. H. Höchst, D.W. Niles, and I. Hernandez-Calderon, Phys. Rev. **B40**, 8370 (1989).
13. Wen S. Chen, J.M. Stewart and R.A. Mickelsen, Appl. Phys. Lett. **46**(11), 1095 (1985).
14. A.D. Katnani and G. Margaritondo, Phys. Rev. **B28**, 1944 (1983).
15. A.J. Nelson, D.W. Niles, C.R. Schwerdtfeger, Su-Huai Wei, A. Zunger, and Hartmut Hochst, Proceedings of the 5th International Conference on Electron Spectroscopy, Kiev, Ukraine, J. Electron Spectroscopy and Related Phenomena **64/65** (1994) 185.
16. T. Löher, W. Jaegermann, and C. Pettenkofer, J. Appl. Phys. **77**, 731 (1995).

NONSTOICHIOMETRIC DEFECTS IN SEMICONDUCTOR SnTe THIN FILMS

O.N.NASHCHEKINA, E.I.ROGACHEVA, L.P.SHPAKOVSKAYA, V.I.PINEGIN,
A.I.FEDORENKO

Polytechnical University, Department of Technical Physics
21 Frunze St., 310002 Kharkov, Ukraine

ABSTRACT

The mono- and polycrystalline films of the SnTe_{1+x} semiconducting phase with controlled content of nonstoichiometric defects (NSD) were grown by thermal evaporation and hot wall epitaxy methods from the charges of different composition. The concentration of NSD was determined using X-Ray diffraction method and the measurements of carrier density. The temperature dependences of electrical conductivity and Hall coefficient were obtained in the temperature range of 77 - 300 K. The best results were obtained for hot wall epitaxy method: the perfect monocrystalline films with NSD content corresponding to $x = 0.025$ and high mobility of charge carriers were grown.

INTRODUCTION

The investigation of structure and properties of SnTe semiconducting compound has been the subject of a great attention in recent years [1-3]. The special interest arises from the fact that SnTe and alloys based on it have potential for use in infrared detectors, lasers, and thermoelectric devices [2-4].

Among the interesting peculiarities of SnTe are the high concentrations ($10^{20} - 10^{21} \text{ cm}^{-3}$) of native defects (mainly cation vacancies) and p-type charge carriers whose presence is caused by the high degree of deviation from stoichiometry. SnTe_{1+x} is the phase of variable composition with wide (~ 1 at.%) homogeneity region (HR) located on the side of Te excess relatively to stoichiometric composition [5,6]. The maximum size of HR ($x = 0.004-0.03$) corresponds to $T = 800-900$ K. As temperature lowers the width of HR decreases and at 450 K equals 0.3 at.% ($x=0.01-0.02$) [6].

Since in bulk crystals of SnTe_{1+x} the concentration of nonstoichiometric defects (NSD) changes in a wide range and strongly affects the electrical and other physical properties, growing SnTe_{1+x} thin films with the controlled content of nonstoichiometric defects is a very important problem of semiconductor material science.

A number of publications is devoted to studying mono- and polycrystalline SnTe_{1+x} thin films [7-14]. The majority of authors sets as a goal growing films with low concentration and high mobility of charge carriers. That is why either stoichiometric SnTe or SnTe with Sn excess [10,13] was used as the charge. In [9] the evaporation from two sources - SnTe and Sn was performed. At the same time for certain purposes, such as studying SnTe energy band structure or interactions between nonstoichiometric defects, it is necessary to obtain films with concentrations of nonstoichiometric defects and p-type carriers in the whole range of their possible values.

The aim of the present work was to develop the methods of SnTe_{1+x} thin films growth with controlled content of NSD.

2. EXPERIMENTAL DETAILS

SnTe_{1+x} thin films were obtained from polycrystalline bulk crystals whose compositions are given in Table I.

TABLE I
The Compositions of Bulk Specimens Used for Preparation of SnTe_{1+x} Thin Films

NN	at % Te	x	NN	at % Te	x	NN	at % Te	x
1	50.0	0	4	50.6	0.024	7	51.2	0.049
2	50.2	0.008	5	50.8	0.032			
3	50.4	0.016	6	51.0	0.040			

The ingots used as the charges for evaporation were obtained by fusing Sn and Te of 99.9999% purity in quartz ampules evacuated down to 10^{-4} Pa at $T=1300$ K with subsequent homogenizing annealing at 820 K during 200 hours.

Two methods were used to prepare thin films. The first one was thermal evaporation in vacuum of 10^{-5} Pa. The films were obtained by deposition on substrates of polished glass or freshly cleaved surface of KCl crystals. The films grown on glass substrates had structure of textured polycrystals, the ones deposited on KCl were monocrystalline thin films with the [001] orientation. The temperature of substrates was varied in the range of 350-550 K. The rate of evaporation and film thickness were monitored by a quartz crystal-thickness monitor.

In the hot wall epitaxy method, the evaporating cell was made of quartz tube with diameter of 2.5 cm. Inside the tube was placed the reactor with charge. Two independent heaters provided the necessary temperature of the reactor and the walls of cylindric chamber. The temperature of substrate was maintained in the range of 520-550 K.

X-Ray investigations were performed using diffractometer DRON-2.0 in accordance with the scheme of one-crystal spectrometer in characteristic X-Rays of copper. The relative error of determination of unit cell parameter did not exceed $\Delta a/a = 2 \cdot 10^{-5}$. For monocrystalline thin films the unit cell parameters were determined from the positions of (804), (408) and (008) reflections. In case of polycrystalline films the values of unit cell parameter were determined from the positions of (800), (444) and (642) reflections. The measurements of Hall coefficient R_H and electrical conductivity σ were carried out using the method of direct current and constant magnetic field (up to 15 kOe) in the temperature range of 77-300 K. The carrier concentration was calculated as $p = 1/R_H \cdot e$, where e is electron charge. Hall mobility μ_H was calculated as $\mu_H = R_H \cdot \sigma$. To facilitate measurement of electrophysical characteristics, the film condensation was performed through the special mask with double-cross geometry.

RESULTS AND DISCUSSION

In fig. 1a,b the values of a and p for initial alloys annealed at 820 K during 200 hours are shown with light circles. As is seen from the figure, the boundaries of homogeneity region at this temperature correspond to $x=0.008-0.032$ which is in a good agreement with [6]. The values of unit cell parameter of the samples with high values of x after the annealing at 450 K shown with dark circles were taken from [6].

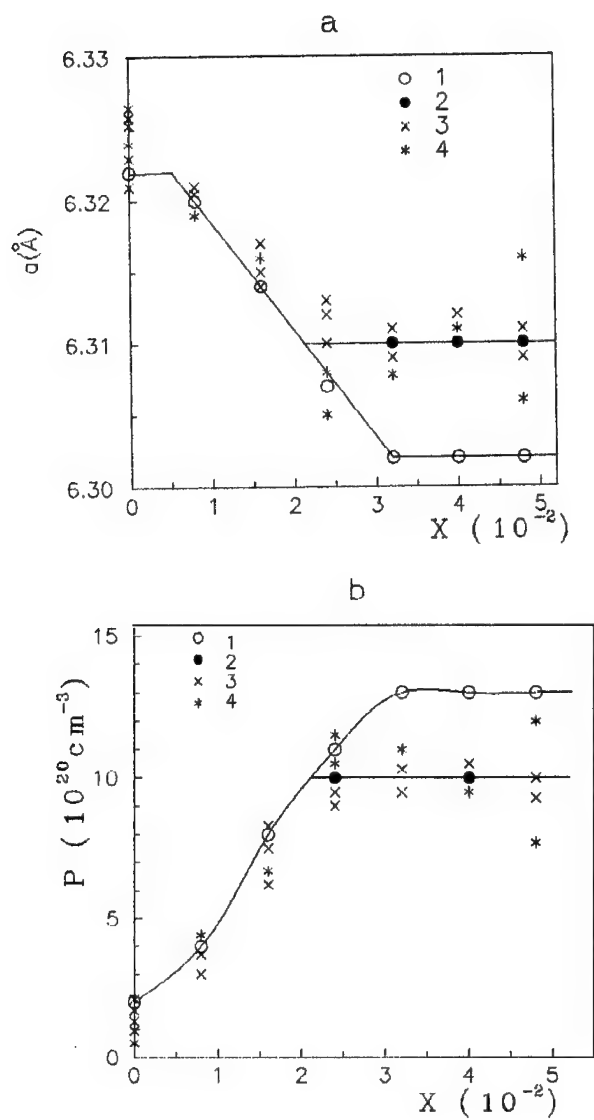


Fig.1. Dependence of the lattice constant (a) and charge carrier concentration (b) on the nonstoichiometry parameter X in SnTe_{1+x} phase; 1, 2 - bulk samples annealed at 820 K (1) and 450 K (2), 3, 4 - thin films received by thermal evaporation (3) and hot wall epitaxy method (4).

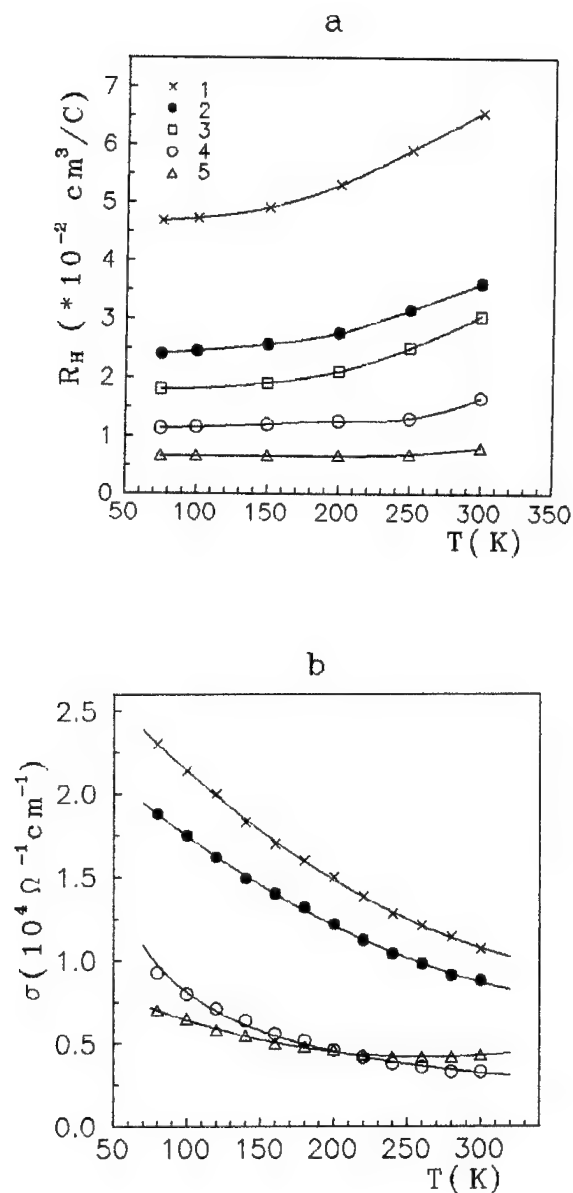


Fig.2. Temperature dependence of Hall coefficient R_H (a) and electrical conductivity σ (b) for SnTe_{1+x} thin films with different values of p_{300} : $0,96 \cdot 10^{20} \text{ cm}^{-3}$ (1); $1,7 \cdot 10^{20} \text{ cm}^{-3}$ (2), $2,1 \cdot 10^{20} \text{ cm}^{-3}$ (3), $4,1 \cdot 10^{20} \text{ cm}^{-3}$ (4), $8 \cdot 10^{20} \text{ cm}^{-3}$ (5).

The investigation of SnTe_{1+x} films obtained by thermal evaporation in vacuum showed the following. Monocrystalline films deposited on KCl substrates heated up to 550 K had high degree of perfection. Polycrystalline films grown on glass were also of a good quality which was confirmed by high values of carriers mobility μ_H . The carrier mobility values didn't differ significantly from those obtained for monocrystalline films.

The investigation showed that under the deposition on substrates with temperature $T_s = 550$ K one could obtain films with the carrier concentration $p_{300} = (0.5-4) \cdot 10^{20} \text{ cm}^{-3}$ and mobility $\mu_{H300} = (50-900) \text{ cm}^2 / \text{V} \cdot \text{s}$. The unit cell parameter changed in the range of $a = (6.326-6.32) \text{ \AA}$ which corresponded to the composition range of $x = 0-0.01$. The strong correlation between a , p and μ_H was observed. Regardless of charge composition the films with higher carrier concentration were not obtained. On the other hand there were obtained films with carrier concentrations down to $0.5 \cdot 10^{20} \text{ cm}^{-3}$, i.e. lower than in bulk crystals. The similar effect was observed for $T_s = 450$ K although the degree of film perfection was lower.

In thin films deposited on the substrates with $T_s = 400$ K the concentration of carriers was up to 10^{21} cm^{-3} which approximately corresponded to the composition with $x = 0.025$. Thus, as T_s reduces, the concentration range of phase existence broadens, though still remains narrower than in bulk crystals.

In fig. 1a,b the values of a and p for films obtained by thermal evaporation are shown with crosses. In the concentration range $x = 0.01 - 0.025$ the films with the values of a and p indicated in fig. 1 were grown on the substrates with $T_s = 400$ K.

As one can see from the fig. 1 there is a fairly good correspondence between the compositions of the films and the charges.

The films grown by the hot wall method (substrate temperature $T_s = 550$ K) had the highest degree of perfection. Judging by the values of a and p the compositions of thin films grown by hot wall epitaxy correspond to those of films obtained by thermal evaporation on substrates with $T_s = 400$ K.

Note that the range of compositions obtained in thin film state $x = 0 - 0.025$ approximately corresponds to the size of homogeneity region of SnTe_{1+x} at 450 K.

Our investigations showed that even evaporation of charge with significant excess of tellurium (x up to 0.05) did not allow to obtain thin films with $x > 0.025$.

The temperature dependences of σ and R_H in the range of 77 - 300 K obtained for several samples are shown in fig. 2. It is seen from fig. 2 that R_H practically doesn't change in the temperature range up to ~ 200 K; then it grows slightly with T . For the samples with high concentration of charge carriers, R_H virtually remains constant throughout the whole range of temperature which is typical for degenerated semiconductors. Increase in temperature leads to the drop in σ which is also common for degenerated semiconductors. Increase in x , i.e. increase in Te content at fixed temperature results in initial drop in σ (up to $x \sim 0.008$) following by its growth. It is consistent with the results of σ measurements for bulk samples with different contents of Te.

Minimum concentration of carriers obtained in thin films corresponds to $p = 0.5 \cdot 10^{20} \text{ cm}^{-3}$, maximum - to 10^{21} cm^{-3} .

Note that like in the reported works of other authors there were obtained films with minimum carriers concentration lower than in bulk crystals prepared using the conventional methods. To obtain such a low concentration of carriers in bulk crystals one should use special techniques similar to the ones used in [2, 3].

Thus, during deposition of thin films, states corresponding to lower degree of deviation from stoichiometry are realized. The values of unit cell parameter in the obtained films with the lowest concentration of carriers exceed the values of a for bulk specimens with the lowest charge carrier concentration.

It is necessary to note that the carrier mobility values obtained for the mono- and polycrystalline thin films condensed at the same T_s do not differ. For the polycrystalline films values of μ_H at 77 K practically coincide with μ_H values obtained in [9] for epitaxial thin films of SnTe.

CONCLUSIONS

Thus, the complex investigation of crystal structure and electrophysical properties of SnTe_{1+x} thin films obtained using different techniques was carried out with a view to develop the methods of growing thin films with controlled concentration of nonstoichiometric defects.

The best results were obtained for hot wall method: the perfect epitaxial films with nonstoichiometric defects contents corresponding to $x = 0 - 0,025$ at substrate temperature of 550 K were grown. Using the thermal evaporation method one can receive the mono- and polycrystalline films of the same compositions only at the substrate temperature equal to ~ 400 K.

As follows from the obtained data, the deposition of thin films results in shifting the boundaries of SnTe HR towards the smaller Te contents in comparison with bulk alloys. That is the evidence of change in thermodynamic equilibrium conditions in thin film state.

REFERENCES

1. J.C.Lin, T.L.Ngai, A.Chang, Metallurgical Transactions. **17A**, 1241 (1986)
2. Y.Ota, S.Rabii, J Non-metals. **1**, 117 (1973)
3. R.S.Allgaier and B.Houtson, J. Appl. Phys. **49**, 442 (1978)
4. T.C.Haman, Physics of IV-VI Compounds and Alloys, edited by S. Rabii (Gordon & Breach, London, 1971), p. 141
5. R.F.Brebrick, J.Phys. and Chem Solids. **24**, 27 (1963); **32**, 551 (1971)
6. E.I.Rogacheva, G.V.Gorne, N.K.Zhigareva and A.B.Ivanova, Izv.AN SSSR. Ser.Neorgan. Materialy. **27**, 267(1991).
7. E.G.Bylander, Mater. Sci. Engin. **1**, 190(1966).
8. J.N.Zemel, J.D.Jensen and R.B.Schoolar, Phys. Rev. **140**, A330(1965).
9. A.Nishiyama, J. Phys. Soc. Jap. **40**, 471(1976).
10. A.L.Dawar, P.C.Mathur, A.O.Mohammed and O.P.Taneja, Thin Solid Films. **82**, 273(1981).
11. S.Santhanam, B.K.Samantapay, and A.K.Chaudhri, J.Phys. **C15**, 2531(1982).
12. D.M.Freik, M.Galushchak, and V.L.Avgustimov, Inorg.Mater. **13**, 1382(1977).
13. N.Ganesan and V.Sivaramakrishnan, Phys. Stat. Sol.(a) **105**, 461(1988).
14. Yu.V.Sokolov, M.Oszwaldowski and H.Shveytser, Izv. AN SSSR, Ser. Neorgan. Mater. **27**, 152(1991).

Part IV

Gettering and Related Phenomena

TRANSITION-METAL IMPURITY LUMINESCENCE IN GaAs AND ITS APPLICATION TO MATERIAL CHARACTERIZATION

T. Nishino

Kobe University, Department of Electrical and Electronics Engineering,
Rokkoudai 1-1, Nada-ku, Kobe 657, Japan

ABSTRACT

A number of sharp characteristic luminescence lines has been observed for GaAs doped with 3d transition-metal impurities in the near-infrared region, the origin being attributed to the zero-phonon intracenter transitions between the energy levels of the metal ions split by the crystal field of the GaAs lattice. It is also known that these luminescence lines are very sensitive to the surrounding field of the transition-metal impurities. The luminescence of Cr-doped GaAs has been most extensively studied, the spectrum revealing a very sharp luminescence line at 0.839 eV. In this paper we review the results on the successful applications of this Cr-related luminescence line to characterization of in-depth profiles of arsenic vacancy in thermally annealed GaAs, local strain field in In-doped GaAs and interface stress at heterostructures grown on Cr-doped GaAs substrate.

INTRODUCTION

In GaAs crystal, a 3d transition-metal (TM) ion occupies in most cases the Ga site in the lattice and forms a deep acceptor center. The 3d TM deep acceptor is a multivalent impurity with many d-shell electrons in the center and also holes are bound in the d-shell of the acceptor rather than bound hydrogenically in a simple acceptor such as IV element atoms in GaAs. These 3d TM impurities in GaAs have been studied so far, together with those in GaP and InP, but the complete understanding of the electronic states has not yet been achieved [1]. This is essentially due to the fact that these deep acceptors are multivalent impurities with many d-shell electrons and form various kinds of complicated complexes involving other shallow impurities or defects.

A number of sharp photoluminescence (PL) lines have been observed for GaAs doped with 3d TM impurities in the near-infrared region, the origin being attributed to the zero-phonon intracenter transition between the energy levels of the metal ions split by the crystal field of the GaAs lattice. In most cases, these luminescence centers are not isolated impurity centers but complexes involving TM impurities and other shallow impurities or defects. These PL lines are also very sensitive to the surrounding field of the TM impurities.

In the recent few years, we have studied these characteristic PL lines in GaAs and demonstrated that the PL lines are very useful to characterize defects and local strain field in GaAs crystal. In particular, we have utilized the well-known Cr-related PL line which is easily observed with conventional Cr-doped semi-insulating GaAs wafers. In this paper we review the results on the successful applications of the Cr-related PL line observed at 0.839 eV to characterization of in-depth profiles of arsenic vacancy in thermally annealed GaAs, local strain field in In-doped GaAs and interface stress at some technologically important heterostructures grown on Cr-doped semi-insulating GaAs substrate.

LUMINESCENCE ASSOCIATED WITH Cr IMPURITY IN GaAs

A number of sharp characteristic PL lines has been so far observed for GaAs doped with 3d TM impurities in the near-infrared region. These PL lines are essentially due to the zero-phonon intracenter transitions between the energy levels of the 3d TM ions split by the crystal field of the GaAs lattice. For GaAs doped with Mn and Cu TM impurities, no sharp zero-phonon lines due to intracenter transitions are observed. These two 3d TM impurities easily form complicated complexes involving other impurities or defects in GaAs and they act as relatively shallow acceptors, different from other 3d TM impurities. Therefore, the luminescence associated with these two acceptors is similar to those due to radiative recombination in conventional band-to-acceptor transitions in semiconductors.

In Fig. 1 a typical PL spectrum taken at 4.2 K is shown, which was observed for GaAs doped with Cr impurities. The Cr-related PL lines in GaAs have been most extensively studied so far, the spectrum revealing a very sharp PL line at 0.839 eV, compared with the normal band edge PL lines, as shown in the figure. This 0.839 eV PL line in GaAs is essentially attributed to the zero-phonon intracenter transition between the crystal-field split 5E and 5T_2 levels of the Cr^{2+} center at a Ga site in GaAs crystal. But Zeeman spectroscopic data on this zero-phonon line revealed that the luminescence center has $[111] C_{3v}$ axial symmetry rather than T_d symmetry expected for an isolated Cr ion at a Ga site in GaAs [2], suggesting the contribution of another impurity or defect to the Cr-related center. Effects of uniaxial stress on these Cr-related PL lines were also studied in details to get knowledge about the origin of this luminescence center and it was demonstrated that the results are well interpreted by the hypothesis of a substitutional divalent Cr ion at a Ga site subjected to the perturbation of C_{3v} symmetry [3].

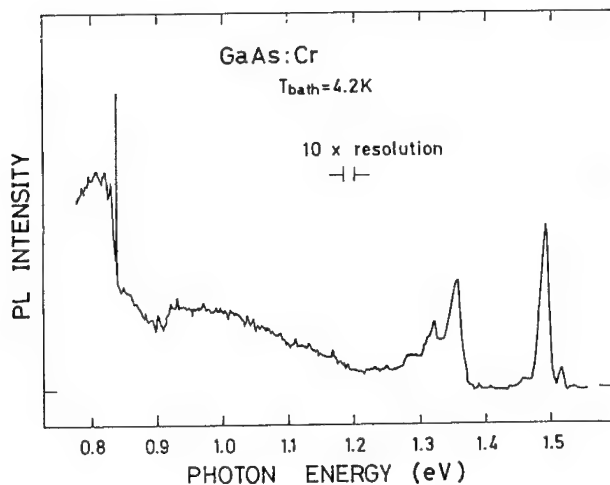


Fig. 1 Typical PL spectrum of Cr-doped semi-insulating GaAs crystal taken at 4.2 K.

The energy level scheme of an isolated Cr ion and a Cr- V_{As} complex in GaAs lattice is shown in Fig. 2. The 5D ground state of a free Cr^{2+} ion splits into two levels by the crystal field of the GaAs lattice, as mentioned above. This isolated Cr^{2+} ion in GaAs is subjected to perturbation by the presence of a V_{As} in its nearest neighbor. As a result, the 5E excited state of the isolated Cr ion which is embedded in the conduction band shifts downward and locates in the band gap, and the 5T_2 ground state splits into two levels by perturbation of V_{As} in the nearest neighbor of the Cr ion. The $^5E - ^5E$ transition shown in the figure is responsible for the 0.839 eV

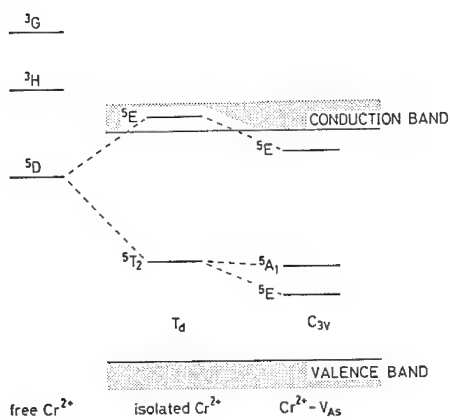


Fig. 2 Energy level scheme of a Cr atom in GaAs crystal.

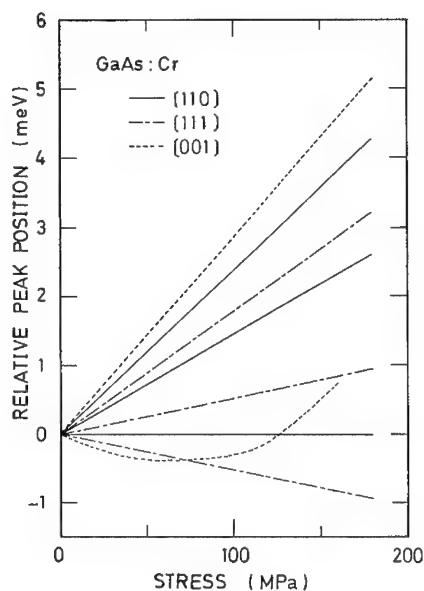


Fig. 3 Energy splitting of the Cr-V_{As} PL line at 0.839 eV unser uniaxial stress.

Cr-related PL line. It is noted here that this assignment to the luminescence center of the Cr- V_{As} complex with C_{3v} symmetry explains well previously reported experimental results on this Cr-related PL line observed with Cr-doped GaAs crystal.

As mentioned above, the experiment of the 0.839 eV PL line under uniaxial stresses revealed the C_{3v} symmetry of this luminescence center. This PL line is very sensitive to the local field of the luminescence center. Therefore, it is easily considered that the PL line changes drastically when other perturbations exist around the luminescence center. In Fig. 3 the feature of energy-level splitting under compressive uniaxial stress is shown in three different directions, which was calculated from data by Barrau et al. [3]. For example, the transition energy responsible for the Cr- V_{As} PL line under the [110] compressive uniaxial stress splits into three components. As a result, we can observe three luminescence lines, one in the same energy position at 0.839 eV and two in the higher energy side. These energy splittings under uniaxial stresses were experimentally observed with the use of GaAs:Cr wafers plastically deformed along the three principal crystallographic axes shown in the figure [6]. These experimental results of the 0.839 eV Cr-related PL line can be successfully applied to the characterization of local strain field in GaAs crystal and interface stress at some technologically important heterostructures grown on Cr-doped semi-insulating GaAs substrate, as will be shown later.

MATERIAL CHARACTERIZATION BY Cr-RELATED LUMINESCENCE

In-depth profiles of arsenic vacancy in GaAs

When GaAs crystals are annealed at high temperatures, a high density of lattice vacancies is created near the surface due to the evaporation of constituent atoms Ga and As from the GaAs crystal. As a result, the surface of thermally annealed GaAs becomes nonstoichiometric, which plays an important role in the device processing. It is thus important to characterize thermally annealed GaAs wafers. Moreover, it should be noted that there are no powerful characterization techniques for lattice vacancies in GaAs crystal. From these points of view, we have developed a new optical characterization technique for arsenic vacancy, V_{As} , in conventional Cr-doped semi-insulating GaAs substrate wafers, which utilizes in-depth profile measurements of the 0.839 eV Cr- V_{As} PL intensity.

We have performed a series of in-depth profile measurements for the Cr- V_{As} PL intensity in Cr-diffused GaAs and thermally annealed Cr-doped semi-insulating GaAs in order to get information on the diffusion coefficient and diffusion behaviors of V_{As} in GaAs crystal [7]. In Fig. 4 we show the Cr-related PL spectrum of GaAs:Te diffused with Cr at 1100 °C for 24 hrs under As pressure, together with that of the conventional Cr-doped semi-insulating GaAs. The upper PL spectrum was measured at the depth of 28.6 μm from the surface and showed a new Cr-Te PL line at 0.844 eV. The in-depth profiles of the PL intensities of both the Cr- V_{As} and Cr-Te lines in Cr-diffused GaAs were measured using a series of layer stripping by chemical etching. Figure 5 shows the typical in-depth profiles of these PL intensities which are normalized at the surface. These PL intensity profiles were analyzed by fitting to the well-known complimentary error function and we could estimate the diffusion coefficient of V_{As} in GaAs at 1100 °C to be $8 \times 10^{-12} \text{ cm}^2/\text{s}$, this value being comparable to the previously reported data.

The in-depth profiles of the Cr- V_{As} PL intensity in thermally annealed

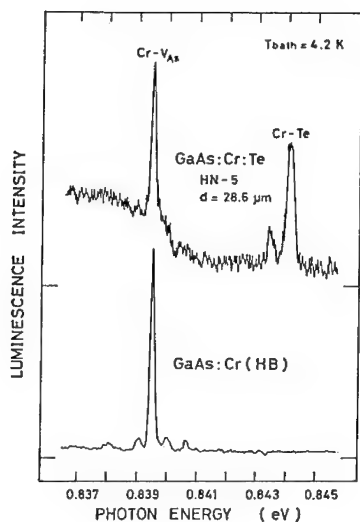


Fig. 4 Cr-related PL spectra Cr-diffused and Cr-doped GaAs wafers.

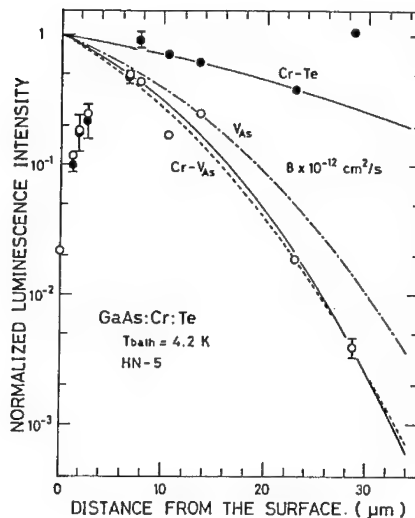


Fig. 5 In-depth profiles of V_{As} estimated from the Cr-related PL line.

semi-insulating GaAs:Cr wafers were also studied as a function of annealing temperature and time [8]. The thermal annealing of GaAs:Cr wafers at high temperatures was performed under the condition of excess As. Based upon the substitutional-interstitial-dissociative mechanism, we estimated the out-diffusion profiles of Cr atoms from GaAs:Cr wafers. It was found that the results show the main features of the measured in-depth profiles of the Cr- V_{As} PL intensity, which reveal sharp drops at the near-surface followed by a constant region in the interior GaAs bulk. Thus we can demonstrate that the behaviors of V_{As} in GaAs crystal are characterized by this new method using the well-known Cr-related PL line observed at 0.839 eV.

Local strain field in In-doped GaAs

In-doped semi-insulating GaAs grown by the LEC method is known as low dislocation density substrate for GaAs devices, because the addition of a few percent In to GaAs grown from the melt reduces the dislocation density by several orders of magnitude without degrading its high resistivity. We have investigated the Cr-related PL lines in this In-doped semi-insulating GaAs wafers [9,10]. Figure 6 shows Cr-related PL spectra of In-doped dislocation-free GaAs crystals. In GaAs doped with In and Cr we observed for the first time new Cr-related PL lines, though the normal Cr- V_{As} spectrum in GaAs:Cr exhibits the main PL line at 0.839 eV accompanied by the TA-phonon replicas in the low-energy side. It seems that the newly observed PL lines (A and B) at 0.8730 and 0.8564 eV are zero-phonon lines, because the half widths are almost same as that of the main Cr- V_{As}

line at 0.8395 eV and two other PL lines (assigned as the TA-phonon replicas) at 0.8645 and 0.846 eV are broader than these zero-phonon lines. These new Cr-related PL lines showed the same behaviors as the Cr-V_{As} PL line in the excitation-power and temperature dependences and also in the in-depth profiles of the PL intensities.

In In- and Cr-doped GaAs, it can be speculated that a new Cr-V_{As}-In complex is formed in the crystal, in which an In atom at a Ga site locates in the second-nearest neighbor of a Cr ion. Based upon this complex model, we analyzed PL data observed with GaAs co-doped with In and Cr, the results showing that the In-concentration dependence of the PL intensity ratio of A and Cr-V_{As} lines can be well explained by considering the occupation probability of In atoms in the equivalent second-nearest neighbor of a Cr ion in GaAs. The Cr atom in the Cr-V_{As}-In complex seems to suffer local strain field along the $[110]$ direction because the covalent radius of In atom is larger than that of Ga atom. This was confirmed by previously reported data for $[110]$ uniaxial stress effects on the Cr-V_{As} PL line, these data showing that two stress-induced PL lines appear in the high-energy side of the unshifted Cr-V_{As} line under compressive stress along $[110]$ direction, as shown in Fig. 3.

Figure 7 shows a comparison of the energy positions of these newly observed PL lines to the uniaxial stress dependence of the Cr-V_{As} PL line. These data suggest that the Cr atom in the second-nearest neighbor of an In atom in GaAs suffers a large compressive stress of 1.3 GPa. This result

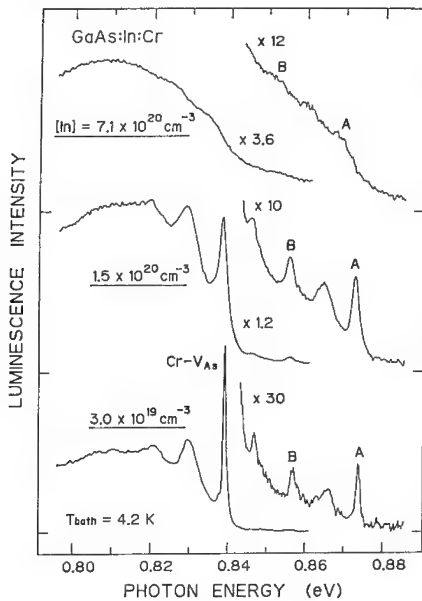


Fig. 6 In concentration dependence of the Cr-related PL spectra in GaAs codoped with In and Cr.

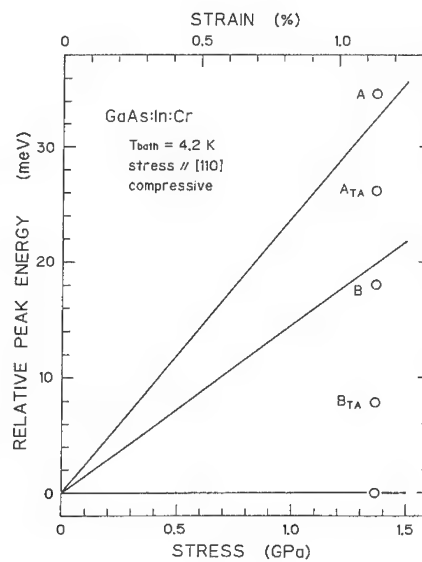


Fig. 7 Estimation of lattice strain induced by In-doping in GaAs by the Cr-related PL line.

also suggests that a local lattice distortion of about 1 % exists in the second-nearest neighbor of In atoms in GaAs, considering the Young modulus of GaAs. Thus, we could revealed the existence of a large local strain field around In atoms in In-doped semi-insulating GaAs crystals with the use of the Cr-related PL lines.

Interface stress at heterostructures grown on GaAs:Cr

With the use of the Cr-related PL line, we have also characterized the interface stress at some technologically important heterostructures grown on Cr-doped semi-insulating GaAs substrate [11,12].

Figure 8 show Cr-related PL spectra of GaAs:Cr in the 0.839 eV region for (100) and (111)B InGaPAs/GaAs heterostructures prepared by the LPE method with different lattice mismatch, together with the PL spectrum of a GaAs:Cr wafer. A peak shift of the main Cr-related PL line can be clearly seen in both heterostructures. Because of the lattice mismatching between InGaPAs and GaAs, the lattice of the InGaPAs epi-layer with larger lattice constant than GaAs is tetragonally deformed due to biaxial compressive stress and then the GaAs substrate suffers biaxial tensile stress. This biaxial tensile stress can be decomposed into compressive uniaxial stress and tensile hydrostatic pressure components with the same magnitude. These two stress components affect the energy levels of the Cr ion

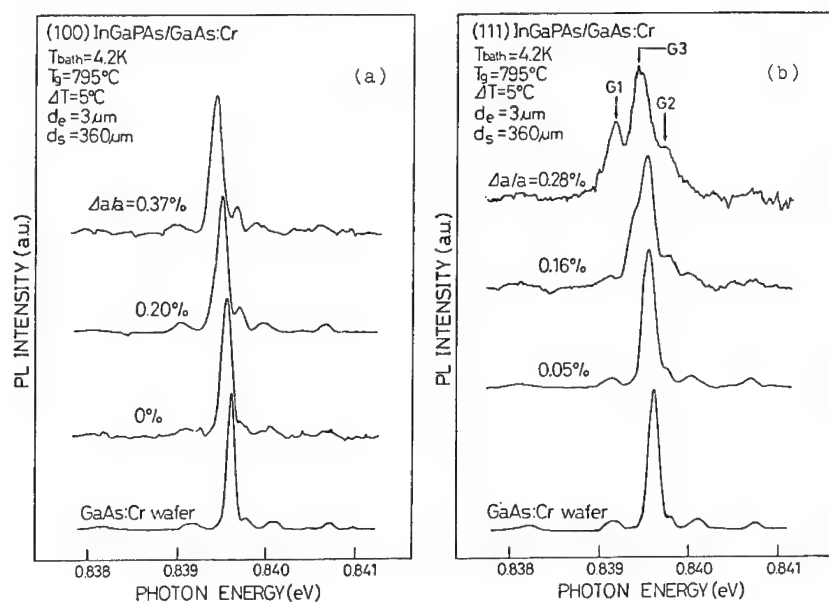


Fig. 8 Cr-related PL spectra from GaAs substrate of InGaPAs/GaAs heterostructures prepared by the LPE method with different lattice mismatching, where (a) and (b) correspond to sample grown on (100) and (111)B GaAs substrate, respectively.

responsible for the Cr- V_{As} PL line. These stress effects on the Cr-related PL line suggest that the PL line from GaAs:Cr substrate at (111)B InGaPAs/GaAs heterostructures shifts to lower-energy side by the tensile hydrostatic pressure component and splits into three PL lines by the compressive $[111]$ uniaxial stress component. These shift and splitting of the Cr-related PL line were clearly observed, as shown in Fig. 8(b). Similar results were also observed with (100) InGaPAs/GaAs heterostructures in which the splitting is not clearly seen, as shown in Fig. 8(a). The PL peak shift of 0.04 meV observed in samples with $\Delta a/a$ of 0 % is due to the lattice mismatch at 4.2 K caused by difference in thermal expansion of InGaPAs and GaAs during cooling down to 4.2 K from room temperature for PL measurements.

Using the uniaxial-stress data mentioned above and the previously reported hydrostatic pressure coefficient on the Cr-related PL line, we could estimate the magnitude of the interface stress at InGaPAs/GaAs heterostructures. The typical value was about 4 MPa for both heterostructure samples with large lattice mismatching. We also calculated the interface stress due to lattice mismatching between InGaPAs and GaAs at 4.2 K. The comparison between these experimental and calculated data shows that about the half of interface stress is relaxed by the formation of misfit dislocations at the heterointerfaces.

Figure 9 shows Cr-related PL spectra taken at the interface of the GaAs substrate of $ZnS_xSe_{1-x}/(100)GaAs:Cr$ heterostructures prepared by the OMVPE method, together with that of a GaAs:Cr wafer. It can be seen that all the Cr-related PL peak positions shift toward the higher-energy side and the PL line widths become broader than the normal Cr-related PL line in GaAs, independent of the composition of the ZnSSe epi-layers. Similar results were also obtained in the cases of ZnSe/GaAs:Cr and $ZnS_xSe_{1-x}/(111)GaAs:Cr$ heterostructures. It is noted that the direction of the PL peak shift does not change between both composition sides of the lattice-matching composition ($x=0.06$) in $ZnS_xSe_{1-x}/GaAs$ heterostructures. This means that the stress due to lattice mismatching between ZnSSe and GaAs does not dominate the heterointerface stress in this ZnSSe/GaAs system. The observed blue shifts of the Cr-related PL line suggest that the GaAs substrates suffer a compressive biaxial stress in all the composition range. For compositions of $x < 0.06$, the existence of such compressive biaxial stress at the surface of the GaAs substrates cannot be interpreted in terms of the interface stress due to lattice mismatching between ZnSSe alloys and GaAs substrate.

The magnitude of the interface stress on the GaAs substrate in these ZnSSe/GaAs heterostructures was also estimated, based upon the observed blue shifts of the main Cr-related PL line. The result is shown in Fig. 10 for $ZnS_xSe_{1-x}/(100)GaAs:Cr$ heterostructures. The estimated interface stresses are all compressive as mentioned above, and therefore cannot be understood by lattice-mismatch stress the magnitude of which was calculated as shown by a broken line in the figure. It was found that this compressive biaxial stress at ZnSSe/GaAs heterostructures is well explained by thermal stress due to the difference in the thermal expansion coefficients between ZnSSe epi-layer and GaAs substrate, which was induced during cooling down from the epitaxial growth temperature to 4.2 K for PL measurements. The magnitudes of such thermal stresses shown by dash-dotted lines were also calculated and compared to experimental data, the result showing good agreement.

Thus we have developed a new method to characterize the interface stress at semiconductor heterostructures by the Cr-related PL line in GaAs, and demonstrated that the interface stress at some technologically important

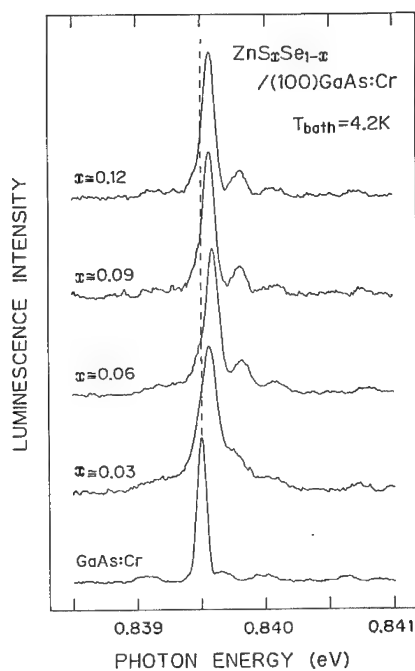


Fig. 9 Cr-related PL spectra of GaAs substrate of (100) $\text{ZnS}_x\text{Se}_{1-x}/\text{GaAs}$ heterostructures.

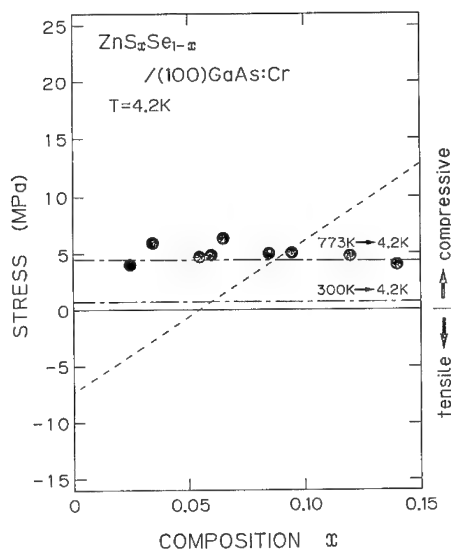


Fig. 10 Composition dependence of interface stress on GaAs substrate of $\text{ZnS}_x\text{Se}_{1-x}/\text{GaAs}$ heterostructures, in which broken and dash-dotted lines are calculated for lattice mismatch stress and thermal stress, respectively.

heterostructures grown on Cr-doped GaAs substrate can be characterized with high sensitivity. The detection limit of interface stress by this method was estimated to be about 0.5 MPa, small compared to the limits of other optical characterization methods.

SUMMARY

We have systematically investigated the photoluminescence due to a series of 3d transition-metal impurities forming deep acceptors in III-V compound semiconductors, especially in GaAs. The luminescence spectra exhibit some characteristic emission lines in the near-infrared region, which are very sensitive to local atomic arrangement and local strain field around the luminescence centers. With the use of these advantages, we have developed new characterization methods for defects such as arsenic vacancy in thermally annealed GaAs, local strain field in In-doped semi-insulating GaAs and interface stress at some technologically important heterostructures grown on Cr-doped semi-insulating GaAs.

This work was in part supported by a Scientific Research Grant-in-Aid, the Priority Area Research Program from the Ministry of Education, Science and Culture. The author would like to thank Y. Fujiwara, Y. Hamakawa, J. T. Hsu, Y. Kita, A. Kojima, M. Kondo, S. Shirakata and Y. Tonami for collaboration in a series of work summarized in this paper.

REFERENCES

1. A. Zunger, in *Solid State Physics*, edited by H. Ehrenreich and D. Turnbull (Academic Press, Orlando, 1986) vol. 39, pp. 276-464.
2. Ch. Uihlein and L. Eaves, *Phys. Rev. B* **26**, 4473 (1982).
3. J. Barrou, F. Voillot, M. Brousseau, J. C. Brabant and G. Poilblaud, *J. Phys. C: Solid State Phys.* **14**, 3447 (1982).
4. Y. Fujiwara, T. Nishino and Y. Hamakawa, *Jpn. J. Appl. Phys.* **21**, L727 (1982).
5. Y. Fujiwara, A. Kojima, T. Nishino and Y. Hamakawa, *J. Lumin.* **31&32**, 451 (1984).
6. Y. Fujiwara, T. Nishino and Y. Hamakawa, *Appl. Phys.* **A41**, 115 (1986).
7. T. Nishino, Y. Fujiwara, A. Kojima and Y. Hamakawa, in *Proc. Int. Symp. on Spectroscopic Characterization Techniques for Semiconductor Technology*, Boston, 1983 (SPIE Proc. **452**, Washington) pp. 2-8.
8. J. T. Hsu, T. Nishino and Y. Hamakawa, *Jpn. J. Appl. Phys.* **26**, 685 (1986).
9. Y. Fujiwara, Y. Kita, Y. Tonami, T. Nishino and Y. Hamakawa, *Appl. Phys. Lett.* **49**, 161 (1986).
10. T. Nishino, Y. Fujiwara and Y. Hamakawa, in *Proc. Int. Conf. on Physics of Semiconductors*, Stockholm, 1986, pp. 959-962.
11. T. Nishino, *IEEE J. Quantum Electron.* **25**, 1046 (1989).
12. T. Nishino, in *Proc. Int. Conf. on Thin Film Physics and Applications*, Shanghai, 1991 (SPIE Proc. **1519**, Washington) pp. 382-390.

TRANSIENT DIFFUSION AND GETTERING OF Au AND Cu TO CAVITIES IN Si

J. WONG-LEUNG, J. S. WILLIAMS AND E. NYGREN,

Department of Electronic Materials Engineering, Research of Physical Sciences and Engineering,
The Australian National University, Canberra, ACT 0200, Australia

ABSTRACT

This paper addresses the diffusion and gettering of Cu and Au to internal cavities in Si introduced by H-implantation. Rutherford backscattering and channeling and cross-sectional transmission electron microscopy are the main analysis methods used. During annealing at temperatures and times typical of low temperature device processing conditions, we observe a transient gettering regime in which implanted Au and Cu segregate to cavities leaving metal concentrations in the Si lattice well below the solubility level. Longer times and/or higher temperatures are required for equilibrium to be reached. These results may have important implications for developing optimum gettering strategies during thermal processing of device structures.

INTRODUCTION

Efficient gettering of metallic impurities away from active device regions has become an important area of research since very low metal concentrations ($\sim 10^{10} \text{ cm}^{-3}$) are detrimental for the operation of ultra-small devices. The gettering process is strongly dependent on the diffusion and solubility of the metallic impurity under study. Nanocavities in Si created by He implantation were first reported by Myers et al. [1] to provide excellent getter sites. We have previously shown [2-4] that a large proportion of implanted metallic impurities (Cu, Au and Ni) can be relocated to a sharp band of nanocavities introduced by H implantation. In this study, we have examined further details of the segregation process and progression to equilibrium conditions. Our results suggest that the initial gettering process is a transient non-equilibrium situation under our annealing conditions. Equilibration of the metallic impurities in terms of uniform solubility throughout the wafer may occur at appropriate higher annealing temperatures and/or longer times.

EXPERIMENTAL

100 keV H⁺ ions were implanted into n-type Cz Si wafers of (100) orientation to a fluence of $3 \times 10^{16} \text{ cm}^{-2}$ at room temperature. These samples were annealed at 850°C for 1 hr to drive the H out of the wafer leaving a band of faceted cavities at a depth of $\sim 1.0 \text{ } \mu\text{m}$. The annealing treatments in this study were carried out in an Ar ambient. The sample is further implanted with 95 keV Au⁺ ions to a fluence of $5 \times 10^{13} \text{ cm}^{-2}$ at room temperature. Similar Cz wafers were

implanted with both 50 keV H^- ions (depth of cavity band at $\sim 0.5 \mu m$) to a fluence of $3 \times 10^{16} cm^{-2}$ and 70 keV Cu^- ions to a fluence of $6 \times 10^{14} cm^{-2}$ at room temperature.

Similar H-induced cavities were introduced into Boron-doped Fz Si wafers of (100) orientation and polished both sides so that through-wafer diffusion and gettering experiments could be carried out without the complication of a rough back side of the wafer. Such wafers were similarly implanted with 100 keV H, pre-annealed at $850^\circ C$, then implanted with Au to a dose of $1 \times 10^{15} cm^{-2}$ on the same side of the wafer. Similar experiments were carried out on wafers implanted with 50 keV H and Cu to dose of $2.2 \times 10^{15} cm^{-2}$ to study the equilibration of Cu through the wafer.

All samples were annealed under different time/temperature conditions and Rutherford backscattering was used to study the details of gettering of Au and Cu to the cavities and subsequent equilibration throughout the wafer. Cross-sectional transmission electron microscopy (XTEM) was used to study the microstructure of the samples. It is important to note that the samples in this study were rapidly quenched following annealing at rates of about $100^\circ C s^{-1}$. This avoids appreciable relaxation induced gettering during the quench and allows segregation gettering at temperature to be examined.

RESULTS AND DISCUSSION

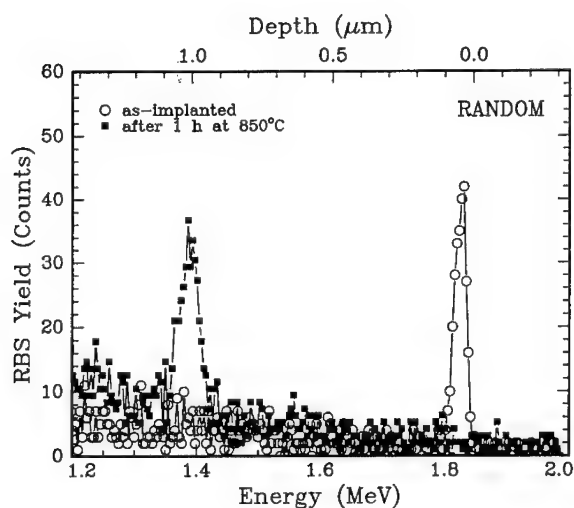


Fig. 1 RBS showing Au profiles in Si implanted with H (pre-annealed at $850^\circ C$) and $5 \times 10^{13} Au cm^{-2}$ and annealed at $850^\circ C$

Fig. 1 shows the random RBS spectrum for the sample implanted with a low dose of Au $5 \times 10^{13} cm^{-2}$. This result clearly indicates that most of the implanted Au diffuses to a band of nanocavities after a 1 hr anneal at $850^\circ C$. This amount of Au, if distributed throughout the bulk of the wafer corresponds to a concentration ($1.43 \times 10^{15} cm^{-3}$) which is below the solubility level of Au in Si at $850^\circ C$ ($2 \times 10^{15} cm^{-3}$) [5]. It is interesting to note that the Au first segregates to the

cavities without equilibration of Au throughout the wafer. For Au, which has a complex diffusion behaviour [6,7] and is known to require high temperatures and times to achieve equilibrium solubility, the 'lack' of solubility may not be surprising in this case. What is surprising is the very efficient relocation of Au from the implanted layer to the cavity layer at 850°C. To examine the behaviour of Au at cavities for very long annealing times and higher temperatures, the above sample was re-annealed for 25 hrs at 950°C. In this case, the Au left the cavities to presumably redistribute throughout the wafer up to the solubility limit, thus achieving thermal equilibrium. This data will be presented in more detail elsewhere [8].

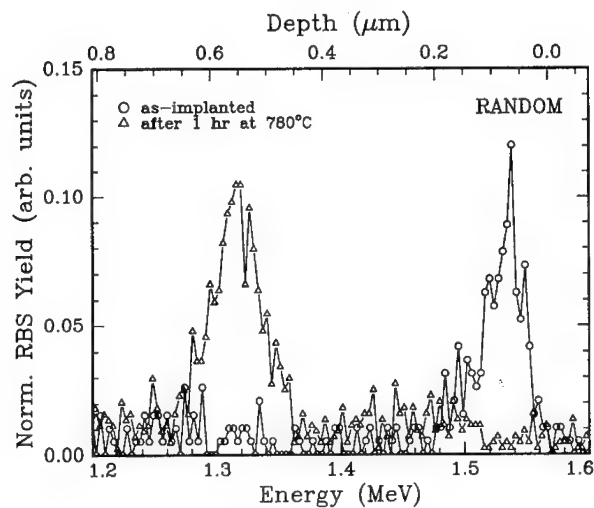


Fig. 2 RBS showing Cu profiles in Si implanted with both H and 6×10^{14} Cu cm⁻² and annealed at 780°C for 1 hr.

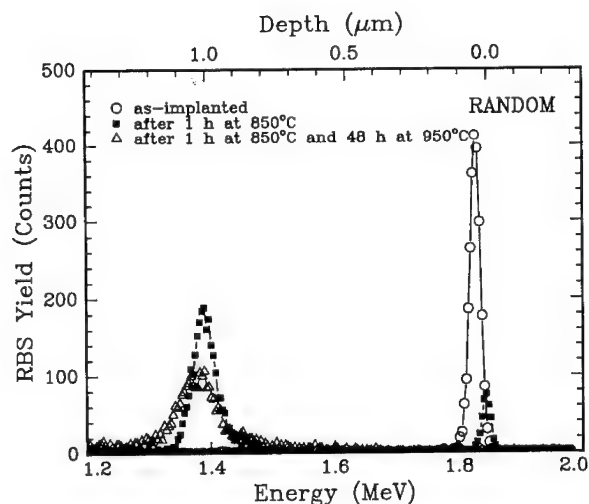


Fig. 3 RBS showing the evolution of Au profiles in Si wafers polished both sides and implanted on the same side with H (pre-annealed) and 1×10^{15} Au cm⁻² and subjected to different annealing treatments.

Similarly for Cu, when a sample implanted with 6×10^{14} Cu cm⁻² is annealed at 780°C for 1 hr. RBS analysis shows (see Fig. 2) that essentially all the implanted Cu segregates to the cavities. Again, this amount, if distributed throughout the wafer would correspond to a concentration (1.7×10^{16} cm⁻³) well below the solubility of Cu at 780°C (4.2×10^{16} cm⁻³) [9]. For such annealing treatment, the diffusion length of Cu in Si is much greater than the wafer thickness and hence the system should have achieved thermal equilibrium. We are convinced that our quench rate is fast enough to avoid significant relaxation gettering of Cu to the cavities and that the segregation of Cu to cavities occurs at temperature. Indeed, we have recently carried in-situ (hot) RBS measurements [10] which confirm that Cu accumulation to cavities occurs at temperature. Thus, our results for both Au and Cu suggest that the initial stage of annealing is the very efficient gettering of these metals to the cavities even when the total metal content is below the equilibrium solubility limit throughout the wafer.

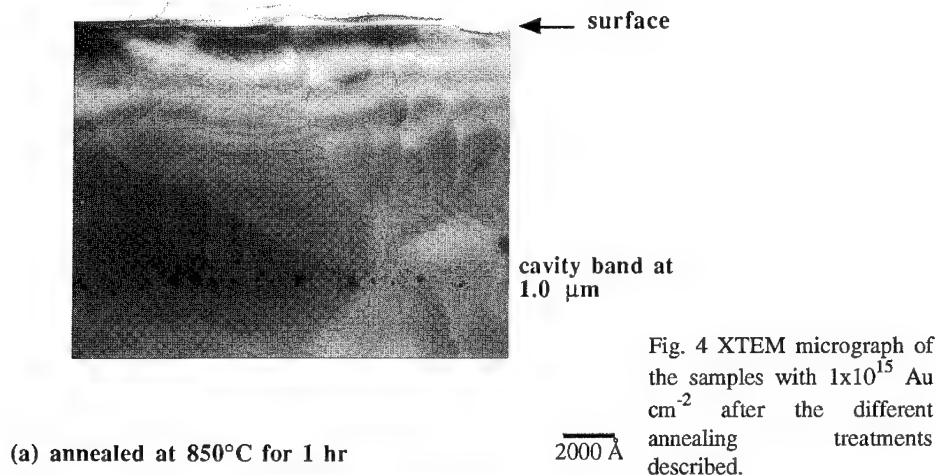
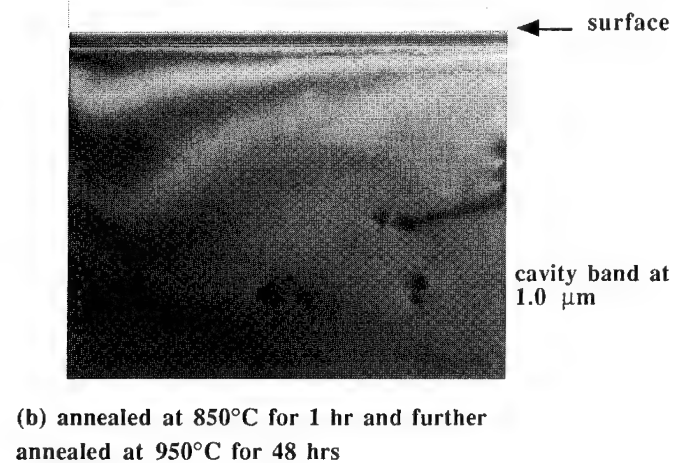


Fig. 4 XTEM micrograph of the samples with 1×10^{15} Au cm⁻² after the different annealing treatments described.



To examine the effect of higher concentrations of Au and Cu (where the amount of metals exceeds the solubility limit at the annealing temperature if distributed throughout the wafer), a further series of experiments was carried out on wafers polished on both sides. For a $1 \times 10^{15} \text{ cm}^{-2}$ Au implant annealed for 1 hr at 850°C , Fig. 3 shows that most of the implanted Au is found at the cavities with the remaining left at the surface. In this case, the amount of Au at the cavities exceeds the internal surface area of the cavities and bulk phase Au is observed [4]. Indeed, the XTEM micrograph in Fig. 4(a) indicates that some of the cavities are filled with Au. A further anneal at 950°C for 48 hrs appears to result in a dissolution of the Au at the cavities as shown in Fig. 3. It is interesting to note that the amount of Au missing, of distributed throughout the wafer, again corresponds to a concentration which is close to the solubility limit of Au in Si at 950°C . Indeed, our annealing conditions are consistent with conditions previously used to achieve equilibration of Au throughout Si wafers [6]. XTEM examination shows that the microstructure of the cavity region is slightly changed during the second anneal. The density of cavities is smaller but the Au filled cavities are larger in size. The latter presumably results from an Ostwald ripening process.

The above experiment was repeated for a high dose of Cu ($2.2 \times 10^{15} \text{ cm}^{-2}$). Briefly, after a 1 hr anneal at 780°C , most of the Cu relocates to the cavities while a residual amount of Cu remains at the surface. As we have previously indicated, bulk phase Cu is observed in this case at the cavities since the amount of Cu exceeds the internal cavity surface area. A further anneal at 780°C for 24 hrs is accompanied by a loss of Cu from the cavities. This loss is again equivalent to a concentration close to the solubility level of Cu at 780°C , and again indicates a slowness of the system to achieve thermal equilibrium. We do not at present understand this behaviour for Cu and we are undertaking further experiments to clarify the situation. However, what is clear is that our annealing treatments result in a transient non-equilibrium gettering of Au and Cu to cavities.

We believe that the behaviour can be characterised by a three step process :

- (i) Detrapping of metal from implanted damage where its concentration far exceeds substitutional solubility at the annealing temperature.
- (ii) Diffusion (presumably by interstitial motion) to preferred trapping or precipitation sites which are the internal cavity walls or free volume. This is the initial transient gettering phase.
- (iii) Possible equilibration at longer annealing times to achieve equilibrium solubility concentration throughout the wafer. Further discussion of these mechanisms will be presented elsewhere [8].

CONCLUSION

Our results clearly indicate that the accumulation of implanted metallic impurities to cavities can take place prior to equilibration of such impurities to the solubility level throughout the wafer. We therefore believe that the segregation of implanted metallic impurities to nanocavities introduced by H-implantation is a transient non-equilibrium situation, where the amount of metal in solution is well below the solubility limit in silicon at the annealing temperature. Such a gettering scheme may have significant advantages for future device processing.

REFERENCES

- [1] S. M. Myers, D. Follstaedt and D. M. Bishop, Mater. Res. Soc. Symp. Proc. Vol. 316., 33 (1994)
- [2] J. Wong-Leung, C. Ascheron, M. Petravic, R. G. Elliman and J. S. Williams, Appl. Phys. Lett., 66, 1231 (1995).
- [3] B. Mohadjeri, J. S. Williams and J. Wong-Leung, Appl. Phys. Lett., 66, 1889 (1995).
- [4] J. Wong-Leung, E. Nygren, J. S. Williams and D. J. Eaglesham, Appl. Phys. Lett., in press (1995).
- [5] N. A. Stolwijk, B. Schuster and J. Hoezl, Appl. Phys. (Germany), Vol 33, 133 (1984).
- [6] S. Coffa, N. Tavolo, F. Frisina, G. Ferla, S.U. Campisano, Nucl. Meth and Meth., B74, 47 (1993).
- [7] U. Gosèle, W. Frank and A. Seeger, Appl. Phys. 23, 361 (1980).
- [8] J. Wong-Leung, J. S. Williams, E. Nygren and D. J. Eaglesham, submitted to Phys. Rev. Lett.
- [9] E. R. Weber, Appl. Phys. A Vol. 30 no. 1, 1 (1983).
- [10] J. Wong-Leung, E. Nygren, J. S. Williams and D. J. Eaglesham, Mat. Res. Soc. Symp. Proc., in press (1995).

MINORITY CARRIER DIFFUSION LENGTH IMPROVEMENT IN CZOCHRALSKI SILICON BY ALUMINUM GETTERING

SUBHASH M. JOSHI*, ULRICH M. GÖSELE* ** AND TEH Y. TAN*

* Department of Mechanical Engineering and Materials Science, Duke University, Durham, NC 27708-0300

** Max-Planck-Institute of Microstructure Physics, Weinberg 2, D-06120 Halle/Saale, Germany

ABSTRACT

Gettering is widely used for fabricating integrated circuits using Si substrates, and has great potential for solar cell fabrications as well. Recently available solar cell efficiency studies have shown the benefits of the wafer backside Al, attributable to effects of gettering, a wafer backside field, and passivation of grain boundaries and dislocations. In this paper, we report experimental results which showed unambiguously that Czochralski Si wafer bulk minority carrier diffusion lengths can be significantly improved due to gettering of impurities by wafer backside Al, which also provided a protection from environmental contamination.

INTRODUCTION

Gettering of unwanted impurities away from the device active regions has already become an integral part of manufacturing integrated circuits (IC) using Czochralski (CZ) Si wafers. It is anticipated that gettering will also be used in the near future in Si solar cell fabrications for improving the cell efficiency. For IC fabrication, intrinsic or internal gettering (IG) is used, which utilizes oxygen precipitates and their associated defects in the CZ Si wafer bulk as gettering sites.^{1,2} Because of the bulk nature of IG sites, the scheme cannot be also used for solar cells, since they are bulk devices. Only some kind of extrinsic or external gettering (EG) schemes can be used for solar cells. The designations IG and EG indicate where the gettering sites or regions are created. The gettering of contaminants, usually transition metals, to the gettering region involves the metal dissolution (if existing in a precipitated form), the diffusion of metal atoms to and their being stabilized at the gettering sites.

Cost effective gettering schemes for solar cell applications can include P indiffusion gettering, Al gettering, and a combination of the two. Since both P and Al are used in the cells, it may only need a minimal effort to incorporate these schemes into a manufacturable cell fabrication process. The mechanism of P gettering is fairly well known.^{3,4} Aluminum can provide a gettering effect because the solubility of other metals in Al is very high, reaching 1 at% in the temperature range below the eutectic temperature of 577°C, and even higher above the eutectic temperature at which a liquid Al-Si alloy forms. In this liquid, the solubility of a typical metal can exceed 10 at%, i.e., on the order of $5 \times 10^{21} \text{ cm}^{-3}$. For example, Cu, Ni, Fe, Mn form eutectics with Al at temperatures ranging from 548°C for Cu to 658°C for Mn with solubilities in the eutectic liquid ranging from ~2% for Mn to ~18% for Cu.⁵ Since the solubility of metals in Si does not exceed $\sim 10^{17} \text{ cm}^{-3}$, the segregation coefficient of the metal between the liquid and Si is of the order of 10^4 , which provides a tremendously large driving force for the metal to segregate into the liquid. A first evidence of Al gettering is that reported by Thompson and Tu.⁶ At 540°C, for which Al is a solid, they found that a Si wafer backside Al layer can dissolve a tremendous amount of Cu diffused in from the Si wafer frontside. A number of reports on the beneficial effects of using Al or of using P and Al together for improving the performance of solar cells are available.⁷⁻¹² A beneficial effect due to gettering by Al was noticed.^{7,8} The main effect, however, appears to have been due to the cell back surface field¹³ produced by the p⁺-p junction resulting from a high concentration of Al

diffused into the cell back surface.^{7,8} For polycrystalline Si substrate solar cells, the benefits of Al also include the production of the p⁺-p junction around a grain boundary or a dislocation core⁹ due to fast Al pipe diffusion,¹⁴ and the catalytic effect of Al for producing atomic H which passivates grain boundaries and dislocations.¹⁰ Incorporating the beneficial effects of P and Al together with other design and processing optimizations, solar cell structures with very high efficiencies have been fabricated using polycrystalline Si substrates.^{11,12}

In this paper we report experimental results of a study of the role of Al as an effective getterer above the Al-Si eutectic temperature in improving the bulk Si minority carrier diffusion lengths. In these experiments, all the other roles that the Al layer may have played in previous studies using solar cell structures⁷⁻¹² are not involved. Furthermore, it is shown that Al can prevent the detrimental effects of environmental contamination from occurring.

EXPERIMENTAL

The present experiments involve measuring the minority carrier diffusion lengths of a Si wafer before and after an Al treatment using the ELYMAT (electrolytic mapping of transition metals) technique.¹⁵ The ELYMAT measurements yield maps of the minority carrier diffusion lengths across the wafer, presently operated with a lateral resolution of 2mmx2mm. In these experiments, we have used dislocation free single crystal CZ Si wafers, 4 inch in diameter, 500 μ m thick, p-type (doped by B) in the resistivity range of 1-20 Ω -cm. For as-received wafers, the minority carrier diffusion length maps were obtained from the ELYMAT measurement after a 5 min chemical etch using a HF:HNO₃:C₂H₄O₂=1:3:8 solution. This exposes a fresh Si surface possessing a very low leakage current when the electrolyte-Si junction is reverse biased, which is suitable for the ELYMAT measurement to be carried out. After the initial ELYMAT measurement, a 1 μ m thick Al (of a purity of 99.9999 at%) layer was evaporated onto half of each wafer, and the wafer was then annealed for 30 min in the temperature range of 600 to 750°C in dry N₂. After the anneal, the as-formed Al-Si alloy was stripped away using a HF:H₂O=1:50 solution, which was followed by a 15 min to 1 h chemical etch using the HF:HNO₃:C₂H₄O₂=1:3:8 solution. The carrier diffusion lengths of the wafer were then again mapped using ELYMAT. The second chemical etch mentioned above preferentially removes the p⁺ layers,¹⁶ under an over-etching condition incurred by the etching times employed. In addition, this etch also exposes a fresh p-type Si surface as it has a slight etching action on p-type Si too, though at a much lower rate than on p⁺ Si. In a few cases, following the carrier diffusion length mapping by ELYMAT after the first Al treatment, a second Al treatment was carried out.

RESULTS AND DISCUSSION

Figure 1 shows the results obtained from a Si wafer treated by Al once and annealed at 600°C for 30 min in a clean furnace. The left half of the wafer had no Al coverage, and the right half of the wafer had Al coverage on the backside. For the left half of the wafer (without Al), the minimum, maximum, and average carrier diffusion lengths were respectively 120, 155, and 136.6 μ m in the as-received state, while the respective quantities became 130, 167.5, and 146 μ m after the annealing. Thus, annealing in N₂ has a small beneficial effect of improving the carrier diffusion lengths, which seems to be a feature observed for the first time. For the right half of the wafer (with Al), the minimum, maximum, and average carrier diffusion lengths were respectively 130, 165, and 147.7 μ m in the as-received state, while the respective quantities became 167.5, 207.5, and 186 μ m after the annealing. Thus, the minority carrier diffusion length improvement on the Al covered half of the wafer is considerably larger. It will be discussed later that the beneficial effect of Al is due to gettering by the Al-Si liquid.

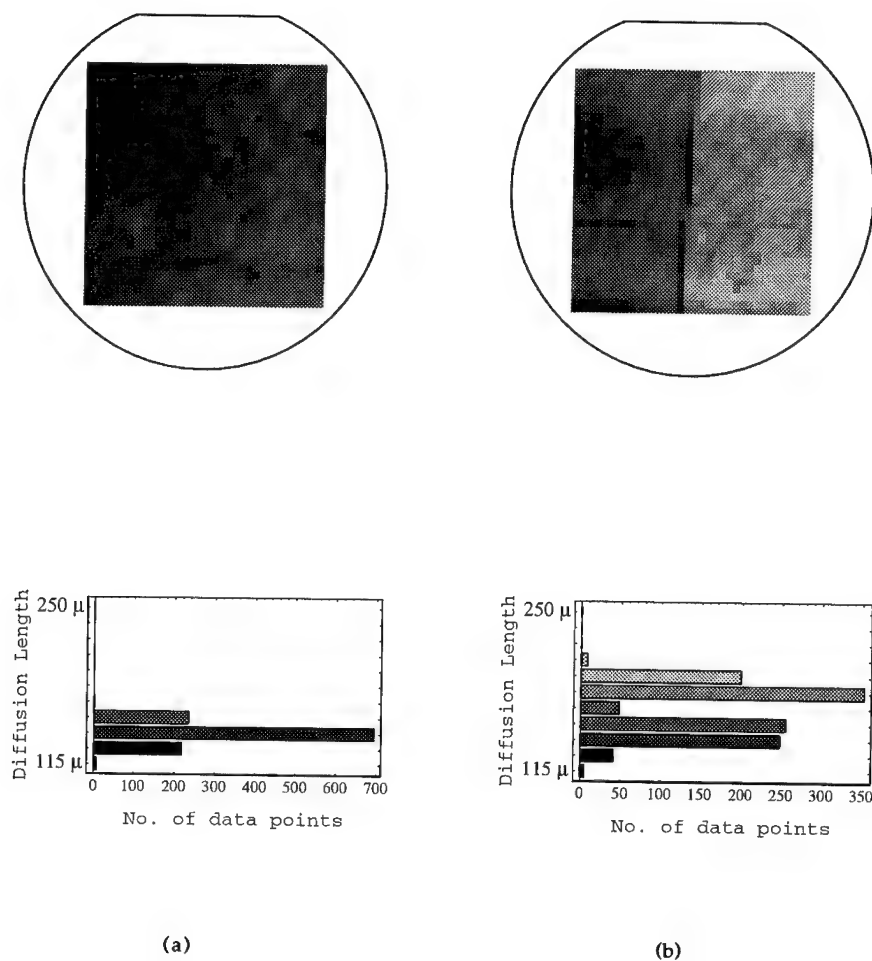


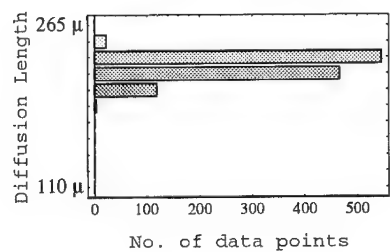
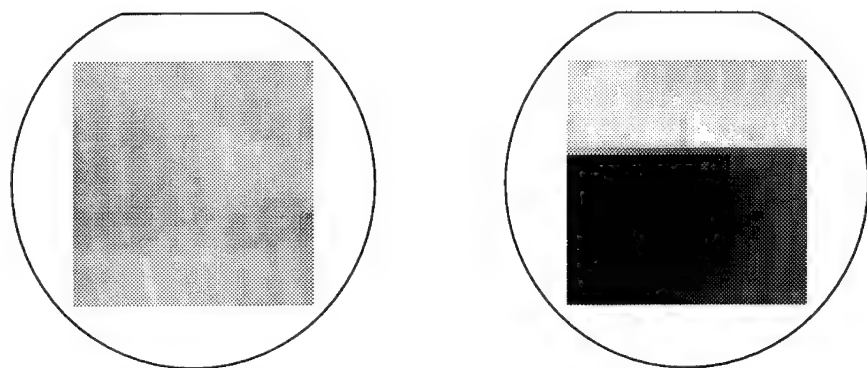
Fig. 1 Minority carrier (electron) diffusion length maps of a 4" Si wafer with and without an anneal in a clean furnace at 600°C, with accompanying histograms (in scales relating diffusion length values to gray levels) showing diffusion lengths vs. number of measurement points. The square shape of the maps is due to measurement tool limitations. (a) Unannealed; (b) Annealed, with the right and left halves of the wafer respectively with and without a backside Al layer. In the left half, the average diffusion length increased from 136.6 μm to 146 μm , while in the right half, the average diffusion length increased from 147.7 μm to 186 μm .

Figure 2 shows the results obtained from another Si wafer, treated by Al once and annealed at 750°C for 30 min in a contaminated furnace. The lower half of the wafer had no Al coverage, and the upper half of the wafer had Al coverage on the backside. For the lower half of the wafer (without Al), the minimum, maximum, and average carrier diffusion lengths were respectively 187.5, 247.5, and 222.7 μm in the as-received state, while the respective quantities became 110, 170, and 135 μm after the annealing. Thus, annealing in N_2 in a contaminated furnace has a significant effect of decreasing the carrier diffusion lengths. For the upper half of the wafer (with Al), the minimum, maximum, and average carrier diffusion lengths were respectively 202.5, 245, and 227.3 μm in the as-received state, while the respective quantities became 227.5, 265, and 251 μm after the annealing. Thus, the wafer backside Al has provided a substantial protection effect against environmental contaminations. In addition, the carrier diffusion lengths in the Al covered half have actually increased to some extent. As with the case shown in Fig. 1, this beneficial effect of Al should also be that due to gettering by the Al-Si liquid.

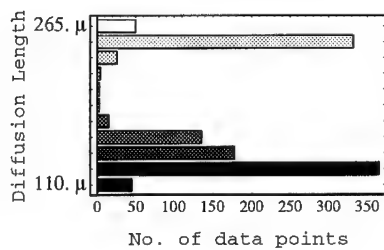
We believe that the present results are evidences of the effectiveness of gettering using a layer of the liquid Al-Si alloy. The technique should be useful in solar cell fabrications, and perhaps also useful in IC fabrication cases for which IG cannot be implemented, e.g., when using silicon on insulator (SOI) substrates. IG cannot be effectively implemented when using SOI substrates since the bulk of the silicon wafer cannot act as an effective gettering region for the SOI device layer due to the insulator layer between the two. In the present experiments, the other beneficial effects of Al, as reported in the literature,⁷⁻¹² do not exist. Since dislocation free single crystal CZ Si wafers have been used, there are no grain boundaries or dislocations. Thus, the observed beneficial effect of Al cannot be due to $\text{p}^+\text{-p}$ junction formation at grain boundaries or at dislocation cores or due to hydrogen passivation of these defects. In the present experiments, the effect cannot be due to a wafer backside field, because the Al indiffusion produced p^+ Si region has been completely etched away employing an over-etching scheme. The absence of a p^+ layer on the wafer backside is evidenced by successful measurements of the Si carrier diffusion lengths using the ELYMAT technique. The ELYMAT measurement relies on the Schottky-like characteristics of the Si-electrolyte junction when the freshly exposed Si surface is p-type¹⁵ whereas the characteristics are Ohmic when the Si is p^+ -type,¹⁷ giving rise to a very high reverse leakage current even when a fresh surface is exposed, which prevents the ELYMAT measurement from being carried out. The present results came from wafers for which, after the p^+ etching, the ELYMAT leakage currents are as low as those of the starting wafers.

In the present experiments, the nature and concentrations of the contaminants that have been getterted away from the Si bulk are unknown, which seems to be a weak point. On the other hand, this can also be viewed as a strong point in the sense that it corresponds to a real world device fabrication situation for which the starting Si material contaminant nature and concentrations are unknown. Furthermore, contaminants unintentionally introduced during device processing, e.g., those from the furnace, are certainly of an unknown nature and concentration. Owing to the low getterting temperature and short getterting time used, we believe that the getterted species are the fast moving interstitial metal atoms such as those of Fe, Ni, Cu, etc. Substitutionally dissolved metal atoms, e.g., Au, or precipitated metals could not have been significantly affected by the present getterting treatment.

For the wafers for which two Al getterting treatments were carried out, it was observed that the second getterting treatment gave a further improvement in the diffusion lengths over the first treatment.



(a)



(b)

Fig. 2 Minority carrier (electron) diffusion length maps (and the accompanying histograms showing diffusion lengths vs. number of measurement points) of a 4" Si wafer with and without an anneal in a contaminated furnace at 750°C. (a) Unannealed; (b) Annealed, with the upper and lower halves of the wafer respectively with and without a backside Al layer. In the lower half, the average diffusion length decreased from 222.7 μm to 135 μm , while in the upper half, the average diffusion length increased from 227.3 μm to 251 μm .

SUMMARY

In summary, we mention that a fairly large beneficial effect in improving Si minority carrier diffusion lengths has been observed using wafer backside Al deposition and annealing processes. The effect can be attributed to gettering of metallic impurities by the Al-Si liquid at annealing temperatures above the Al-Si eutectic temperature. The gettering process is also effective as a protection against environmental contamination.

ACKNOWLEDGMENT

This work is supported by National Renewable Energy Laboratory via subcontract XD-2-11004-1.

REFERENCES

1. T. Y. Tan, E. E. Gardner, and W. K. Tice, *Appl. Phys. Lett.* **30**, 175 (1977).
2. Semiconductor Silicon 1994, edited by H. R. Huff, W. Bergholz, and K. Sumino (The Electrochem. Soc., Pennington, NJ, 1994).
3. W. Schröter, M. Seibt, D. Gilles, Ch. 11 of Electronic Structure and Properties of Semiconductors, edited by W. Schröter, Vol. 4 of Materials Science and Technology: A Comprehensive Treatment, edited by R. W. Cahn, P. Haasen, and E. J. Kramer (VCH Publishers, New York, 1991), p. 576.
4. E. Ö. Sveinbjörnsson, O. Engström and U. Södervall, *J. Appl. Phys.* **73**, 7311 (1993).
5. compiled from Alloy Phase Diagrams, Vol. 3 of ASM Handbook, edited by H. Baker (ASM International, Metals Park, OH, 1992).
6. R. D. Thompson and K. N. Tu, *Appl. Phys. Lett.* **41**, 440 (1982).
7. T. M. Bruton, A. Mitchell, L. Teale, and J. Knobloch, Proc. 10th European Photovoltaic Solar Energy Conference (Kluwer Academic Publishers, Netherlands, 1991) pp. 667-669.
8. B. Hartiti, A. Slaoui, J. C. Muller, and P. Siffert, *Appl. Phys. Lett.* **63**, 1249 (1993).
9. R. Sundaresan, D. E. Burk, and J. G. Fossum, *J. Appl. Phys.* **55**, 1162 (1984).
10. R. Janssens, R. Mertens, and R. Van Overstraeten, Conference Record of the 15th IEEE Photovoltaic Specialists Conference (IEEE, New York, 1981) pp. 1322-1325.
11. S. Narayanan, S. R. Wenham, and M. A. Green, *IEEE Trans. Electron Dev.* **ED-37**, 382 (1990).
12. A. Rohatgi, P. Sana, and J. Salami, Proc. 11th European Photovoltaic Solar Energy Conference (Harwood Academic Publishers, Switzerland, 1992) pp. 159-163.
13. J. Mandelkorn and J. Lamneck, Jr., *J. Appl. Phys.* **44**, 4785 (1973).
14. J. C. M. Hwang, P. S. Ho, J. E. Lewis, and D. Campbell, *J. Appl. Phys.* **51**, 1576 (1980).
15. V. Lehmann and H. Föll, *J. Electrochem. Soc.* **135**, 2831 (1988).
16. Y. Sumitomo, T. Yasui, H. Nakatsuka, T. Ohashi, H. Tsutsumi, and H. Muraoka, *Electrochem. Soc. Spring Mtg.*, Abstract No. 25 (1972).
17. Y. Arita and T. Sunohara, *J. Electrochem. Soc.* **124**, 285 (1977).

IMPURITY GETTERING IN MBE GROWN SILICON

A.NYLANDSTED LARSEN, P.KRINGHØJ, J.LUNDGAARD HANSEN, AND
S.YU.SHIRYAEV

Institute of Physics and Astronomy, University of Aarhus, DK-8000 Aarhus C, Denmark

ABSTRACT

A MBE growth procedure of epitaxial silicon layers is demonstrated which includes a special designed buried strained compositionally graded $\text{Si}_{1-x}\text{Ge}_x$ layer. Upon thermal relaxation closed dislocation loops are formed in this $\text{Si}_{1-x}\text{Ge}_x$ layer without altering the structure of the Si top layer. This dislocated layer is shown to getter contaminants in the Si top layer reducing the concentration of deep levels in this layer to $\approx 1 \times 10^{12} \text{ cm}^{-3}$.

INTRODUCTION

Molecular beam epitaxial (MBE) growth of silicon is known to incorporate metallic contaminants in the epitaxial layers¹. There are many sources of these contaminants in a MBE-system, mainly heated areas such as sample heating elements, filaments, effusion cells, and e-guns. Even the most careful precautions have not been successful in reducing the concentration of unwanted contaminants below $\approx 1 \times 10^{14} \text{ cm}^{-3}$ in our MBE-system for a typical growth temperature of 550°C as deduced from deep level transient spectroscopy (DLTS). Similar contamination levels have been reported by other groups^{2,3}. There have been reports in the literature⁴ demonstrating that growth temperatures as high as 795°C are able to reduce this concentration to a level of $\approx 1 \times 10^{12} \text{ cm}^{-3}$; such high growth temperatures, however, are normally not suitable as they tend to reduce the dopant sticking coefficients resulting in a reduced range of doping levels. Instead it seems more appropriate to look for a suitable gettering scheme.

We have observed that in relaxed $\text{Si}_{1-x}\text{Ge}_x$ grown by the compositional grading technique, in which a high concentration of misfit dislocations are confined to the buried graded buffer layer, the concentration of deep levels in the top $\text{Si}_{1-x}\text{Ge}_x$ layer as determined by DLTS is reduced significantly compared to the case of Si-growth; we have ascribed this to a gettering effect of the misfit dislocations. A similar conclusion has been reached by Kissinger and Grimmeiss⁵ in a study of metallic impurity levels in $\text{Si}_{1-x}\text{Ge}_x$ grown by MBE. Salih et al.^{6,7} and Lee et al.⁸ have studied the effect of a buried dislocated layer on the performance of devices in chemical vapor deposited Si; they found an improvement in electrical parameters such as leakage current and minority-carrier lifetime which they could ascribe to metallic impurity gettering in the dislocated layer.

Considering the above-mentioned results we have designed a special MBE-growth procedure which includes a buried dislocated layer; this growth procedure is shown to be capable of reducing the concentration of deep levels to $\approx 1 \times 10^{12} \text{ cm}^{-3}$ while maintaining the large range of doping levels.

EXPERIMENTAL

The epitaxial layers were grown by MBE on 100 mm, (100) Si substrates in a VG80 system. The base and growth pressures were 5×10^{-11} and about 5×10^{-10} Torr, respectively. A growth rate of 5 \AA/s was maintained constant throughout all the growth procedure. A number of precautions were taken to reduce the contamination during growth e.g. a meander-shaped graphite heater was used as sample heater, the e-gun evaporators, collimator house and shutters were covered with Si, and a special sample holder with no gear inside the growth chamber was used.

Schottky diodes were made from the samples by deposition of Pd. DLTS measurements were performed using a commercial Semitrap instrument; all the samples were measured with the same voltage-settings corresponding to an investigated depth window of about $0.5 \mu\text{m}$ around a depth of $2 \mu\text{m}$. The trap concentration was determined from the measured capacities using the approximation $dC/C_0 \approx \frac{1}{2} N_T/N_0$ where N_T and N_0 are the trap concentration and doping concentration, respectively and dC/C_0 is the measured capacity normalised to the diode capacity.

RESULTS AND DISCUSSION

A layout of the MBE growth procedure is given in Fig.1. The critical layer for gettering is the $\text{Si}_{1-x}\text{Ge}_x$ bottleneck-layer in which the Ge content is gradually increased to 10% over $0.5 \mu\text{m}$ and then gradually reduced over $0.5 \mu\text{m}$ to 0%. Grown at 550°C this layer is fully strained with no misfit dislocations. Grown at 800°C , however, the layer relaxes during growth with the formation of misfit dislocations and with threading dislocations in the Si toplayer⁹. The strain conditions were investigated by x-ray analysis using the (400) Bragg reflection. An ideal agreement

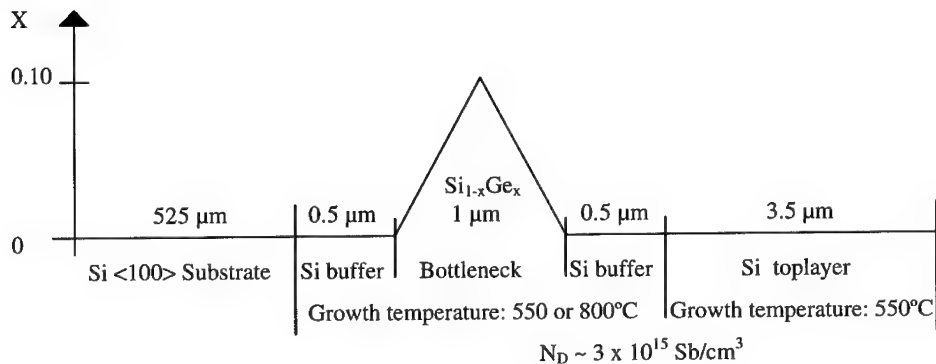


Fig.1 Layout of the MBE growth procedure

between measurements and simulation was obtained using the triangular Ge distribution discussed above in the simulations; the structural conditions were investigated by transmission electron microscopy (TEM). The strained bottleneck was subsequently relaxed by an in-situ annealing at 900°C for 15 min.; this relaxation produces misfit dislocations in the bottleneck layer without any threads in the Si toplayer. The reason for the lack of threads in the Si toplayer is believed to be the following: The misfit dislocations nucleate in the $\text{Si}_{1-x}\text{Ge}_x$ layer in the form of dislocation loops. In the case where the strain relaxation occurs after finishing the epitaxial growth, the upper and lower misfit segments of the loops are trapped in the bottleneck layer by misfit strain leaving no possibility for the threading segments to penetrate into the top layer. Thus, in this case the strain relief is achieved by closed dislocation loops confined to the bottleneck layer. On the other hand, during growth at high temperature (800°C) the dislocation loops nucleated in the layer with the positive Ge concentration gradient expand to the surface of the growing film producing in this way threading arms which remain in the Si top layer after finishing the growth of the whole structure. Another advantage of this bottleneck layer is that the Si toplayer is unstrained; this is due to the grading-down to 0% Ge. The in-situ annealing can be done at any time subsequent to the growth of the bottleneck e.g. before the growth of the Si toplayer or as in the present case after the growth of the Si toplayer. Cross-sectional TEM micrographs of the epitaxial layers before and after annealing are shown in Fig.2; the misfit dislocations appear after annealing and are confined to the two interfaces.

Samples with different combinations of growth parameters were made: with and without the bottleneck layer, the bottleneck grown at either 550 or 800°C, and with and without annealing.

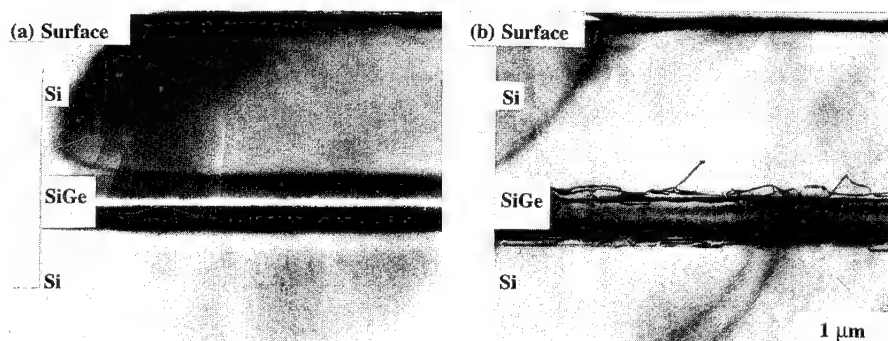


Fig. 2 Cross-sectional TEM micrographs of wafers with (a) strained SiGe bottleneck and (b) after 900°C annealing.

A series of DLTS spectra of the different samples are shown in Figs.3-5. The DLTS spectrum of a sample grown at 550°C without bottleneck and annealing consists of a multitude of peaks demonstrating the presence of many deep levels in the band gap of concentrations up to $\approx 1 \times 10^{14} \text{ cm}^{-3}$ (Fig.3a). This is in agreement with results published by other groups^{2,3}.

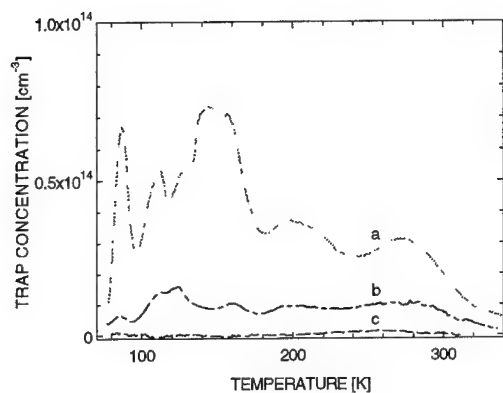


Fig.3 DLTS spectra of (a) as-grown wafer, (b) wafer with strained bottleneck, and (c) wafer with strained bottleneck relaxed after growth by annealing.

The introduction of a strained bottleneck reduces the deep trap concentration to $\approx 1 \times 10^{13} \text{ cm}^{-3}$; thus, the strained bottleneck alone acts as an efficient getter layer (Fig.3b). A further reduction is achieved as the result of the annealing in which case the layer relaxes with the formation of misfit dislocations as discussed above (Fig.3c). The effect of the bottleneck growth temperature is shown in Fig.4; only minor differences are observed and both bottlenecks reduce the trap concentration to $\approx 1 \times 10^{13} \text{ cm}^{-3}$.

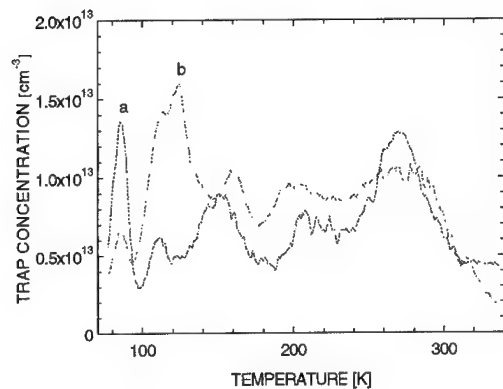


Fig.4 DLTS spectra of wafers with (a) strained bottleneck and (b) with bottleneck relaxed during growth.

This is a somewhat surprising result as dislocations are present in the bottleneck in the one case but not in the other and, consequently, a more efficient gettering would be expected in the case of a dislocated bottleneck; however, in this latter case threading dislocations also extend into the depth-region under investigation, and these threading dislocations will probably act as gettering centers thus increasing the observed trap concentration. A significant reduction in the trap concentration is achieved as a result of the combination of strained bottleneck and annealing (Fig.5a): the trap concentration is reduced to a level of $\approx 1 \times 10^{12} \text{ cm}^{-3}$ which is the lowest concentration we have achieved. A 900°C annealing of samples without the bottleneck layer is also found to reduce the trap concentration (Fig.5b). This is probably due to defect diffusion from the epitaxial layer into the Si substrate which from the ratio of the layer thicknesses is expected to result in a reduction of about two orders of magnitude in agreement with the observation.

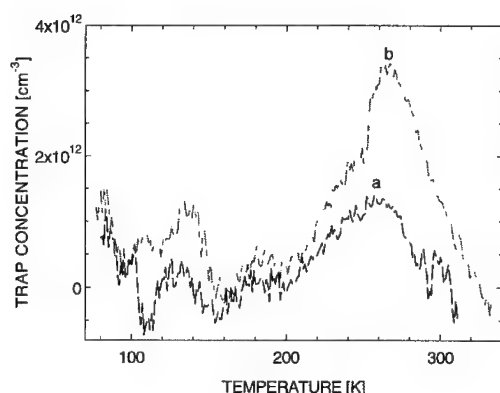


Fig.5 DLTS spectra of (a) a wafer with bottleneck which was relaxed after growth by annealing and (b) a wafer without bottleneck but exposed to the same annealing as wafer (a).

We have not made any effort to assign the observed peaks to any known defects. Traps observed by other groups have been assigned to metal decorated dislocations, vacancy related defects, and isolated metallic impurities; the fact that the defects observed in the present investigation can be gettered by dislocations indicate that they are probably not due to metal-decorated dislocations in the Si top layer; we presume, anyhow, that they are correlated to metallic contaminants.

CONCLUSION

It has been demonstrated that the high concentration of deep levels present in low temperature MBE grown silicon can be reduced by two order of magnitudes as a result of the inclusion of a special designed, buried, dislocated $\text{Si}_{1-x}\text{Ge}_x$ layer. In this layer the Ge content is first graded up to 10% then down to 0% resulting in the formation of closed loops of misfit dislocations without any threads in the Si toplayer; these dislocations act as gettering centers. The Si toplayer is grown unstrained and can be grown at low temperature thus without a reduction of the doping range.

ACKNOWLEDGEMENTS

This work was supported by the Danish Natural Science Research Council and the Danish National Research Foundation through the Aarhus Center of Advanced Physics (ACAP).

REFERENCES

- 1) see e.g. Ogden J.Marsh in Proc. of the Second Int.Symp. on Silicon Molecular Beam Epitaxy edited by J.C.Bean and L.J.Schowalter (The Electrochemical Society, Pennington, NJ) **88-8**, 333 (1988)
- 2) R.F.Houghton, G.Patel, W.Y.Leong, T.E.Whall, E.H.C.Parker, R.A.A.Kubiak, and R.Nayler, J.Cryst.Growth **81**, 326 (1987)
- 3) A.R.Peaker, E.C.Sidebotham, B.Hamilton, and M.Pawlik, *ibid* **1**, p.392
- 4) E.C.Sidebotham, A.R.Peaker, B.Hamilton, M.Hopkinson, R.Houghton, G.Patel, T.E.Whall, and E.H.C.Parker, *ibid* **1**, p.360
- 5) G.Kissinger and H.G.Grimmeiss, *phys.stat.sol. (a)* **145**, K5 (1994)
- 6) A.S.Salih, H.J.Kim, R.F.Davis, and G.A.Rozgonyi, *Appl.Phys.Lett.* **46**, 419 (1985)
- 7) A.S.Salih, Z.Radzimski, J.Honeycutt, and G.A.Rozgonyi, *Appl.Phys.Lett.* **50**, 1678 (1987)
- 8) D.M.Lee, J.B.Posthill, F.Shimura, and G.A.Rozgonyi, *Appl.Phys.Lett.* **53**, 370 (1988)
- 9) A.Nylandsted Larsen, J.Lundsgaard Hansen, R.Schou Jensen, S.Y.Shiryaev, P.Riis Østergaard, J.Hartung, G.Davies, F.Jensen, and J.Wulff Petersen, *Physica Scripta*, **T54**, 208 (1994)

LATERAL DIFFUSION AND CAPTURE OF IRON IN P-TYPE SILICON

KEVIN L. BEAMAN, ADITYA AGARWAL, SERGEI V. KOVESHNIKOV,
AND GEORGE A. ROZGONYI

Department of Materials Science and Engineering
North Carolina State University, Raleigh, NC

The lateral motion of iron impurities was observed and studied in p-type iron contaminated silicon. The lateral diffusion was induced by and then measured using Schottky diodes with a special interdigitated fingers design. Capture of the impurities was done by diffusing to laterally placed dislocation loops formed by a self aligned ion implantation. Lateral changes in Fe concentration were determined using capacitance-voltage and deep level transient spectroscopy.

To insure proper operation of today's ever-shrinking ULSI devices, transition metal contamination of active areas must be exceedingly low. Contamination by iron is of special concern, as it is inherent in many fabrication processes and severely degrades carrier lifetime. Traditional gettering techniques may not be sufficient to reduce the impurity concentration to acceptable levels, which are projected to be $\sim 10^{10} \text{ cm}^{-3}$ in the year 2000. For example, using the well-developed internal gettering (IG) procedures, based on relaxation of supersaturated impurities, a fundamental limitation exists due to the low solid solubility of the metal impurities in silicon. Thus, very low processing temperatures are required to achieve supersaturation of the impurity. Moreover, IG methods cannot be applied for SOI structures because of the isolation layer between the device active region and the bulk wafer. To overcome these limitations, a novel approach has been recently proposed [1] to place gettering sites adjacent to active areas, and use lateral diffusion to capture mobile impurities.

In p-type silicon, Fe is known to exist predominately as Fe^+B^- pairs [2]. In order to diffuse iron, the pairs must first be dissociated. This can be done by photoexcitation, minority carrier injection, or under thermal annealing at $\sim 200^\circ\text{C}$ followed by quenching. At lower temperatures, in the absence of external perturbation, pair re-association is the dominant process allowing the pairs to be reformed in a matter of hours, even at room temperature [1]. However, pair reassociation can be effectively suppressed within the space charge region (SCR) of reverse biased Schottky diodes or p/n junctions where Fe is in its neutral charge state, and hence no coulombic attraction occurs with B^- . Such a difference in pair formation rates within and beyond the SCR creates a concentration gradient of isolated Fe, which, in turn, provides a driving force for both in-depth and lateral Fe diffusion out of the SCR, see Fig. 1. If gettering sites are present in the area where the iron is diffused to, they will capture the iron, and prevent it from returning to the original area. The aim of the present work is to verify experimentally the ability to both laterally redistribute iron and capture it by implantation induced damage.

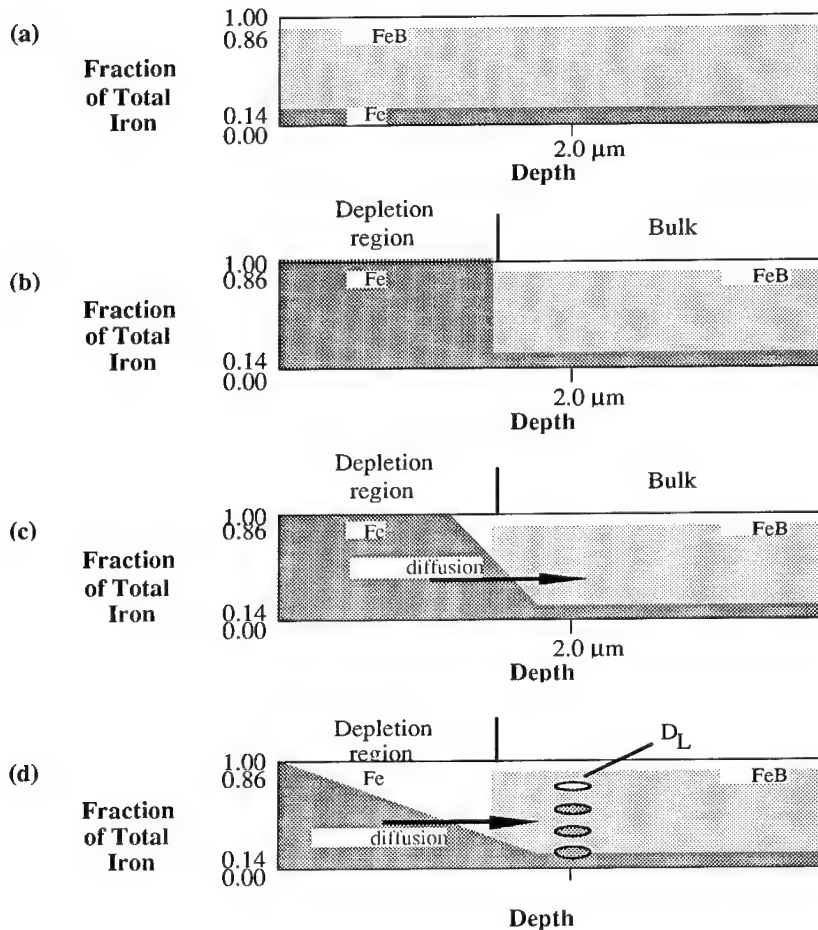


Figure 1 - Schematic representation of novel gettering process for Fe on dislocation loops created by MeV ion implantation in B-doped Si: (a) - at room temperature most of the Fe is tied up in Fe-B pairs, (b) - application of an electric field dissociates Fe-B pairs producing Fe_i which is confined within the space-charge region, (c) - the resulting concentration gradient causes the iron to diffuse out of the depletion region, and (d) - finally, the diffusing iron may be captured on gettering sites such as end-of range dislocation loops. The concept can be extended to a "lateral" or x-y diffusion and capture mode by using lower energy self-aligned implantation. [1]

To allow monitoring of the lateral component of Fe diffusion, an interdigitated fingers structure containing adjacent Schottky diodes was designed, see Fig. 2. Two types of test structures were used to enhance the lateral component of Fe diffusion. To investigate the capture process, the test structure contained only one Schottky diode, namely source, while the area of the probe diode was selectively implanted with 200 keV Si^+ ions. These structures were fabricated on boron-doped

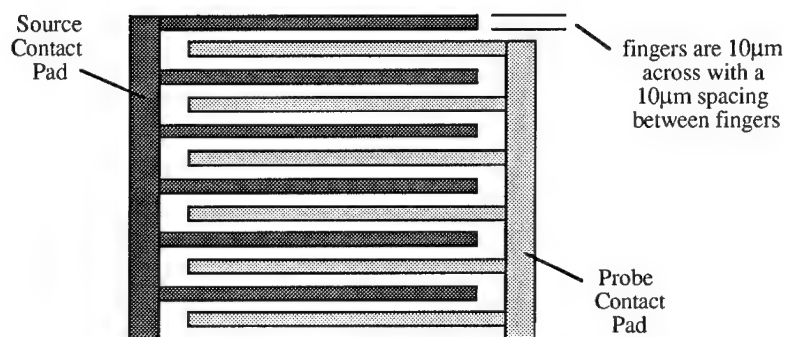
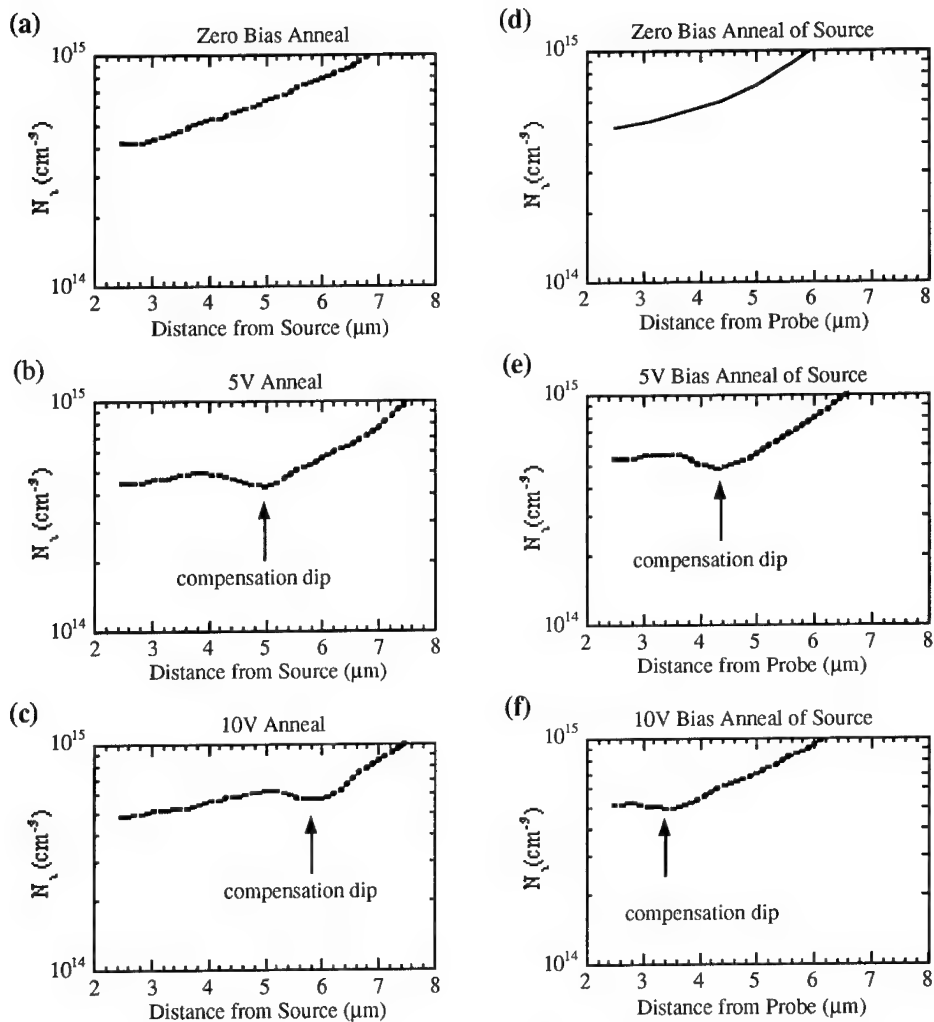


Figure 2 - Interdigitated Schottky diode structure with 136 fingers in each diode

(100) CZ silicon wafers with resistivities of $\sim 10\Omega\text{-cm}$ which were contaminated with iron to a concentration of $\sim 4 \times 10^{15} \text{ cm}^{-3}$ by dipping into a contaminated bath followed by a heat treatment. An RCA clean, followed by a BOE dip was performed to remove any contaminated surface oxides.

Schottky diodes were formed by evaporation of aluminum. Diffusion of Fe was monitored via changes in acceptor concentration using C-V carrier depth profiling, as well as in determining the Fe and Fe-B deep level traps using DLTS measurements. By applying a reverse bias to one of the Schottky diodes, which we call source, the iron was forced to diffuse out from the SCR. Bias annealing of the source diode was carried out at 120°C to dissociate the Fe^+B^- pairs, enhance lateral diffusion and inhibit pair re-association. The bias was varied from 0V to 15V, for 1 hour to 15 hours. Figure 3 presents the C-V profiles measured at room temperature for the source and companion diode, which served as a probe to measure changes in the concentration of free holes. Figure 4 is a time-dependent series of DLTS spectra for the probe fingers which tracked the Fej trap centered at 248K, corresponding to a trap at $E_v + 0.4\text{eV}$.

The C-V data in Fig. 3 provided doping versus depth profiles of the regions around both the source and probe diodes. After zero bias annealing, the diodes showed a sloped, free hole distribution profile as seen in Figs. 3a and 3d. After the source diode had been bias annealed at 393K for 1 hour at 5V reverse bias, the doping profiles showed two major changes. In the near surface region, an increase in the hole concentration is indicated, resulting from dissociation of the Fe^+B^- pairs. The width of the region with increased hole concentration is greater for the source diode, corresponding to the width of the space charge region during the bias annealing step. The second feature is a dip in both profiles. This results from a build-up of iron just outside the space-charge region of the source diode, where Fe^+B^- pairs reformed and compensated the hole concentration. As the bias voltage is increased to 10V for another hour, the dip moves farther away from the source and closer to the probe diode, for example, compare curves (e) and (f) in Fig. 3. This variation of the bias applied to the source diode during annealing is a procedure to enhance detectability of the lateral diffusion component. Detecting the dip with the probe diode, which was not bias annealed at 393K, is the confirming signature that iron has diffused laterally under the source bias annealing conditions imposed.



All annealing done at 393K for 1 hour

Figure 3 - Free acceptor concentration vs. distance from diodes. When Fe-B pairs are present, an acceptor is compensated. This causes a decrease in acceptor concentration in this region. After zero bias annealing there is a higher concentration of iron near the diode, in this case near the surface. This is shown by the sloped acceptor concentration profile, see a) and d). After 5V bias annealing a dip in the profile is observed in the area just outside the space charge region of the source diode. This represents a local increase in iron concentration, see b) and e). Measured after 10V bias annealing, a dip is observed in c) and f) which moves closer to the probe as the other dip moves farther from the source. This indicates lateral motion of the Fe rich zone.

The second set of experiments used DLTS to quantify the changing iron concentration. In this stage, the bias voltage remained constant at 10V, and the annealing time was increased. Unpaired iron exhibits a characteristic DLTS peak at ~250K, corresponding to a deep level at $E_V + 0.4\text{eV}$ [3], which increases as the Fe^+B^- pair dissociation process proceeds. It has been found previously that a 10V reverse bias applied at 393K for 20 minutes will dissociate essentially all the iron within the SCR with minimal diffusion away from this region [1]. Thus, before each DLTS measurement, a 293K, 20 minute dissociation was performed on the diode of interest. DLTS probe data were taken after annealing at 1 hour, again after 2 additional hours, then 3 additional hours, etc., up a total of 15 hours. Figure 4 presents the DLTS measurements for each annealing time. It can be seen that the iron concentration increased near the probe region with increasing duration of bias annealing, then reached a saturation point somewhere between 6 and 10 hours. After this, the iron concentration decreased. This decrease in iron concentration is a result of the concentration gradient in the z-direction as seen from the C-V curves. After annealing for many hours, the source region is depleted, and the probe region starts losing more iron to the bulk than is coming in laterally from the source. Using the equation $N_T = 2(\Delta C/C)N_A$, where N_T is trap concentration and N_A is acceptor concentration, we determined Fe_i concentrations ranging from $4.9 \times 10^{12} \text{ cm}^{-3}$ for one hour bias annealing, increasing to $7.7 \times 10^{12} \text{ cm}^{-3}$ for six hours bias annealing.

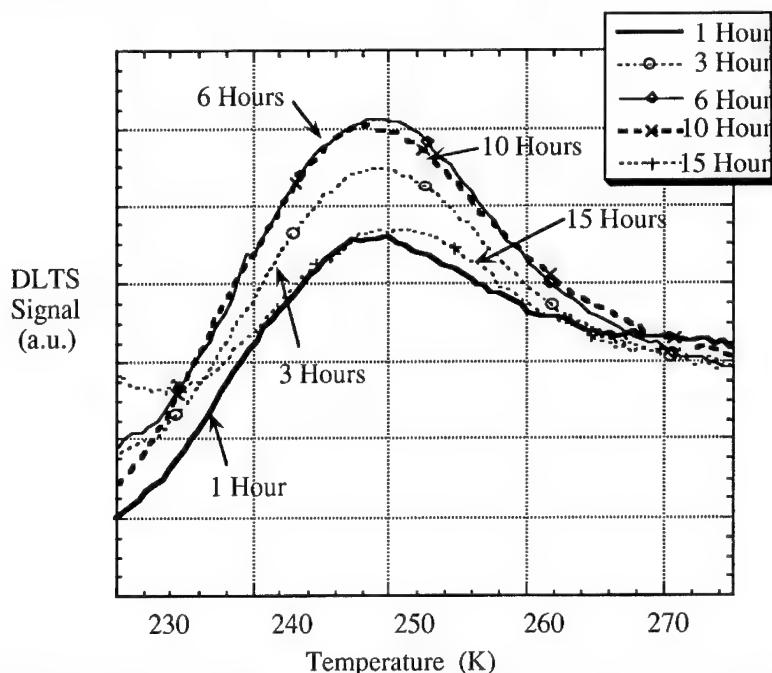


Figure 4 - The DLTS peak for Fe_i at ~250K. As the bias annealing time of the source diode increases, Fe_i concentration first rises then falls near the probe diode.

It was also observed that upon subsequent zero bias annealing at 393K for several hours, the iron concentration was again the same under the source and probe diodes, with profiles similar to those shown in Figs. 3 a) and d). This showed that the Fe-B pairs are not a stable gettering site. We then processed new diodes which consisted of only one pair of fingers. Ion implantation

of Si^+ was done at 200keV at a dose of 5×10^{14} . A thermal anneal of 950°C for one hour formed a layer of dislocation loops at the projected range [4], and also caused the concentration profile of iron to flatten out. The processing was such that the regions directly below the diodes were not implanted. DLTS studies then showed that with bias annealing, the Fe-B concentration again decreased near the source diode. However, further thermal annealing at 400K for 30 minutes did not cause the iron concentration to return to the original value, as it would have if no capture sites were present. Each bias anneal followed by thermal annealing resulted in an additional decrease in iron concentration near the diode of approximately 50%, see Fig. 5. This indicates that the iron was captured by these laterally placed dislocation loops.

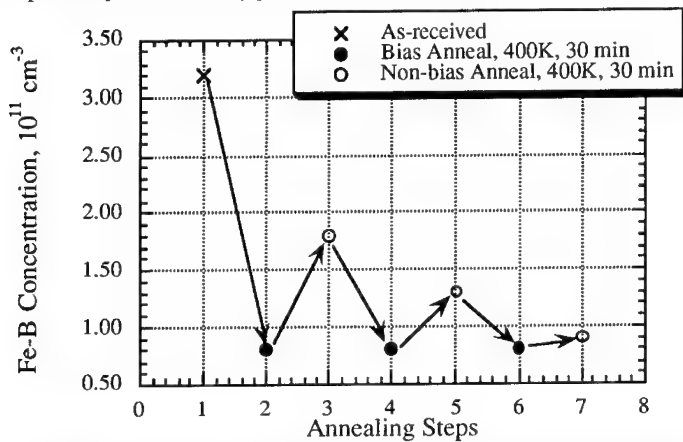


Figure 5 - Changing Fe-B concentration as a function of annealing steps as indicated. Concentration measured via DLTS.

We have shown, using two sensitive space charge probing techniques, that lateral diffusion can be used to getter iron impurities in p-type silicon. This finding holds particular promise for future gettering applications, particularly for SOI. It also lends itself very well for integration into Vertically Modulated Well (VMW) processing, where formation of gettering sites in close proximity to the active regions is achieved by MeV implantation. In the case of Fe-B pairing, the iron was gettering by a segregation-induced method. The nature of gettering by dislocation loops is not fully understood at this temperature and concentration. Further studies are underway to determine whether this is a segregation or relaxation induced mechanism.

Acknowledgments

We would like to thank the Semiconductor Research Corporation for supporting this work. Also, many thanks to Dr. Kamal Mishra for supplying contaminated wafers and to T. Eustis, E. Condon and J. O'Sullivan for their technical support.

References

- [1] G. A. Rozgonyi, S. Koveshnikov, and A. Agarwal, in *Semiconductor Silicon 1994*, ed. by H.R. Huff, W. Bergholz and K. Sumino (Electrochemical Society, 1994), p. 868.
- [2] E. Weber, *Appl. Phys. A*, **30**, 1-22 (1983)
- [3] K. Graff and H. Pieper, *J. Electrochem. Soc.*, **128**, No. 3, 669, (1981)
- [4] S.N. Hsu and L.J. Chen, *Nuc. Inst. and Methods in Phys. Research*, **B55**, p. 620, (1991)

PHOSPHORUS AND ALUMINUM GETTERING OF GOLD IN SILICON: SIMULATION AND OPTIMIZATION CONSIDERATIONS

R. GAFITEANU, U. GÖSELE AND T. Y. TAN

Department of Mechanical Engineering and Materials Science, Duke University, Durham, NC
27708-0300

ABSTRACT

Using the *diffusion-segregation equation*, modeling and simulations of gettering Au (a substitutional-interstitial species in Si) away from the Si bulk have been performed. Three *external* gettering schemes have been considered: wafer frontside P indiffusion gettering, wafer backside Al deposition gettering, and a combination of the two processes. Under the same processing conditions, it has been shown that P indiffusion gettering is faster than Al gettering, but P gettering has a lower gettering capacity and is less stable than Al gettering for longer gettering times. The combined P and Al gettering process is as fast as P gettering in reaching an optimum gettered state, and possesses the capacity and stability of the Al gettering process.

INTRODUCTION

To improve device fabrication yield, impurity gettering in Si by the *intrinsic* or *internal* gettering scheme [1] has already become an integral part of the IC processing technology. It is anticipated that the *external* gettering schemes will play the same role for solar cell processing in the near future. Because solar cells are bulk devices, intrinsic gettering is not suitable. The impurity gettering processes involve the diffusion of the species to, and their stabilization at the gettering sites. For the precipitated impurity cases, the additional process of impurity dissolution from the precipitates into the Si matrix needs to precede its diffusion to the gettering sites.

Improvement by external gettering schemes of the solar cell efficiency has been intensively studied and significant results have been obtained [2-5]. High concentration P indiffusion and Al backside deposition gettering schemes are used since they are compatible with the Si solar cell fabrication processes. In these gettering processes, based on *segregation-induced* gettering mechanism [6], the gettered impurity stabilization is due to the enhanced solubility of the impurity in the gettering regions. Experimental results showed that P and Al gettering, when performed simultaneously, exhibit a synergistic effect. Until now this effect has not been explained in a self-consistent manner. In previous simulations of the impurity gettering processes, only impurity diffusion have been treated quantitatively. With the use of the *diffusion-segregation equation* (DSE) [7-10], the impurity removal by a segregation process at the gettering sites can now be treated quantitatively. We have simulated P and Al gettering processes, performed separately and simultaneously, by considering both fast diffusers (interstitially dissolved impurities) and substitutional-interstitial impurities as the gettered species.

PHOSPHORUS INDIFFUSION GETTERING

Phosphorus indiffusion gettering has a twofold effect. First, it provides a high P concentration ($>10^{20} \text{ cm}^{-3}$) gettering layer at the Si surface, where impurities are attracted to and localized at. Secondly, it generates a high supersaturation of Si self-interstitials *I*, which promote, via the *kick-out* mechanism, substitutional impurity atoms onto interstitial sites where they possess a much higher diffusivity. Under this *I* supersaturation, the alternative substitutional-interstitial impurity atom changeover mechanism, the *Frank-Turnbull* mechanism (involving vacancies), should generally be unimportant. However, it cannot be ruled out completely, since it may play a role in regions where the *I* supersaturation is diminishing (e.g., close to the wafer surfaces). In the present work we consider only the kick-out mechanism as being operative, because most Au experimental results have been consistently explained using only the kick-out mechanism. Au is the model substitutional-interstitial impurity species considered in our simulations.

Phosphorus indiffusion has been modeled according to the approach of Orlowski [11], considering both neutral I and neutral V as vehicles for P diffusion. The mathematical treatment of the kick-out mechanism is based on a system of coupled nonlinear partial differential equations which takes into account the fact that the concentrations of the involved species may change with time either by diffusion or by the interstitial-substitutional exchanges [12]. The following system of equations has been solved numerically using the software package ZOMBIE [13]:

$$\frac{\partial C_P}{\partial t} = \frac{\partial}{\partial x} \left[\left(D_P f_I \frac{C_I}{C_I^{eq}} + D_P f_V \frac{C_V}{C_V^{eq}} \right) \frac{\partial C_P}{\partial x} + \frac{D_P C_P f_I}{C_I^{eq}} \frac{\partial C_I}{\partial x} + \frac{D_P C_P f_V}{C_V^{eq}} \frac{\partial C_V}{\partial x} \right], \quad (1)$$

$$\frac{\partial C_I}{\partial t} - \frac{\partial C_s}{\partial t} = \frac{\partial}{\partial x} \left[\left(D_I + D_P f_I \frac{C_P}{C_I^{eq}} \right) \frac{\partial C_I}{\partial x} + \frac{D_P C_I f_I}{C_I^{eq}} \frac{\partial C_P}{\partial x} \right], \quad (2)$$

$$\frac{\partial C_V}{\partial t} = \frac{\partial}{\partial x} \left[\left(D_V + D_P f_V \frac{C_P}{C_V^{eq}} \right) \frac{\partial C_V}{\partial x} + \frac{D_P C_V f_V}{C_V^{eq}} \frac{\partial C_P}{\partial x} \right], \quad (3)$$

$$\frac{\partial C_s}{\partial t} = k_b C_i^{eq} \left(\frac{C_i}{C_i^{eq}} - \frac{C_s}{C_s^{eq}} \frac{C_I}{C_I^{eq}} \right), \quad (4)$$

$$\frac{\partial C_i}{\partial t} + \frac{\partial C_s}{\partial t} = \frac{\partial}{\partial x} \left[D_i \frac{\partial C_i}{\partial x} - D_i C_i \frac{\partial \ln m_i}{\partial x} \right], \quad m_i(x) = \frac{C_i^{eq}(x)}{(C_i^{eq})^{int}}. \quad (5)$$

Here C_P , C_I , C_V , C_i , and C_s respectively represent the concentrations of P , I , V , Au_i and Au_s . The diffusivities of these species are denoted by D_P , D_I , D_V , and D_i respectively (the diffusion of Au_s via a direct site exchange mechanism was neglected, i.e. $D_s = 0$ is assumed, since this quantity is known to be much smaller than the other diffusivities); f_I is the fractional interstitialcy diffusion component for phosphorus, f_V is the corresponding fractional vacancy component ($f_I + f_V = 1$), k_b is the reaction rate for the changeover of an Au_i to become an Au_s , C_i^{eq} and C_s^{eq} denote the thermal equilibrium concentrations of Au_i and Au_s , whereas C_I^{eq} and C_V^{eq} denote the thermal equilibrium concentrations of Si self-interstitials and vacancies respectively.

The diffusion of Au_i is described by the diffusion-segregation equation (5), where m_i designates the segregation coefficient of Au_i . This is defined as the ratio between the actual equilibrium concentration of Au_i (which is dependent on the local doping conditions), and a conveniently chosen reference value, that under intrinsic conditions. An analogous definition holds for the segregation coefficient of Au_s . Considering that the overall kick-out mechanism reaction rate is independent of the doping conditions and that I are neutral, it is readily shown that both interstitial and substitutional Au have the same segregation coefficient, i.e. $m_i = m_s$. Considering only the Fermi-level and the ion-pairing effects in the *enhanced metal-solid solubility model* [14,15], m_s has the following explicit dependence on the P concentration C_P :

$$m_s(C_P) = \frac{C_{Au^0}^{eq} + C_{Au^{+*}}^{eq} + C_{Au^{+*}}^{eq} + C_{AuP}^{eq}}{C_{Au^0}^{eq}} = 1 + \alpha^- \left(\frac{n}{n_i} \right) + \alpha^+ \left(\frac{n}{n_i} \right)^{-1} + \alpha^- K_{pair} \left(\frac{n}{n_i} \right) C_P, \quad (6)$$

where α^- and α^+ are, in the dilute concentration approximation, given by [16]

$$\alpha^{\pm} = \frac{(C_{Au^{\pm*}})^{int}}{C_{Au^0}^{eq}} = \frac{\theta_{Au^{\pm*}}}{\theta_{Au^0}} \exp \left(\pm \frac{E_{Au^{\pm*}} - E_i}{k T} \right), \quad (7)$$

and n is given by the charge neutrality condition $n = 0.5 \left(C_P + \sqrt{C_P^2 + 4 n_i^2} \right)$. Here $\theta_{Au^{\pm*}}$ and θ_{Au^0} are spin degeneracy factors (considered subsequently equal to unity), $E_{Au^{\pm*}}$ represent the energy

levels of gold acceptors and donors (in our simulations the values of Ledebro and Wang[17] were used for these energy levels), E_i is the intrinsic Fermi level and n_i is the intrinsic carrier concentration. K_{pair} is the thermodynamic constant of the pairing reaction and is dependent only on temperature.

We used the most reliable data for the parameters so that the simulation results are consistent with other kinds of experimental results. For C_I^{eq} , C_V^{eq} , D_I , and D_V , we used the values estimated by Tan and Gösele [18]. For the temperatures of interest, we used $f_I = 0.9$. For the diffusivity of Au, we used data of Wilcox et al. [19], for C_s^{eq} we used the relationship given by Stolwijk et. al. [20], and assumed that C_i^{eq} is 1% of C_s^{eq} . For the diffusivity of P we used the expression implemented in SUPREM [21], and $k_p = 6 \times 10^{-4} \text{ s}^{-1}$. The initial and boundary conditions for solving this set of equations are as follows. At the onset of simulation, uniform concentrations have been assumed throughout the wafer for I, V, Au_i, and Au_s. In the case of P, a very shallow initial predeposited profile has been set which was then indiffused. For point defects, the wafer surfaces are assumed to be perfect sinks/sources, i.e., $C_I = C_I^{eq}$ and $C_V = C_V^{eq}$ hold at the wafer surfaces. To obtain a fair estimate of the pairing constant K_{pair} , we fitted the results of Sveinbjörnsson et al. [22]. The best fit obtained was for $K_{pair} = 10^{-18} \text{ cm}^3$, which was subsequently used in the simulations.

The P indiffusion Au gettering simulation was carried out using the model described above and the experimental conditions of Sveinbjörnsson et al. [22]. The case consists of a 400 mm thick Si wafer with an initial uniform Au concentration of $2.5 \times 10^{14} \text{ cm}^{-3}$, processed at 988°C. The conditions for P indiffusion simulation were the same as in [22]. Figure 1(a) shows the results for Au after 30 min and 2 h processing times, with the latter being the optimum time for gettering. Longer gettering times proved to be less effective because of the spreading and consequent flattening of the P profile which weakens the efficiency of stabilizing Au at the surface P layer.

ALUMINUM GETTERING

A wafer backside Al layer getters impurities from the bulk. In this scheme, an Al-Si liquid alloy forms above the eutectic temperature of 577°C. Since the solubilities of metallic impurities in the Al-Si liquid are several orders of magnitude higher than those in Si, the Al layer can be a very effective getter. The gettering efficiency will depend on whether the metallic impurities are fast diffusers (predominantly interstitially dissolved impurities) or slower diffusers (predominantly substitutionally dissolved impurities diffusing interstitially). For Au, we have simulated the case of a 0.4 μm thick Al layer deposited on the Si wafer backside. Au diffusivity in Al (D_{Au}^{Al}) was assumed to be one order of magnitude higher than that of Au_i in Si (D_i), and the segregation coefficient was inferred from the Al-Si phase diagram as $m_s = 8 \times 10^5$. All the other necessary parameters were kept the same as in the P indiffusion gettering simulations. The system of PDE's to be solved numerically includes 3 equations that describe diffusion of I, Au_i and Au_s in Si, and another one that describes diffusion of Au in Al. The boundary conditions between the Si and Al layer have been described elsewhere [10]. The results are plotted in Fig. 1(b). It is seen that for a 2 h (the optimum time for the P indiffusion case) gettering treatment, the removal of Au is not significant in the middle region of the wafer where the Au concentration is remaining practically at its initial value. However, for a 7 h gettering treatment, the Au concentration in the whole wafer have become uniformly low, and we have found that there is practically no further Au concentration change for still longer gettering times. This indicates that the Al gettering scheme leads to a steady state Si wafer Au concentration which needs ~7 h gettering time to attain. The results for fast diffuser gettering have been already reported in reference [10]. Those results showed that the gettering process is limited only by the impurities' diffusion coefficient and Al layer thickness, and is at least two orders of magnitude faster than that of gettering Au.

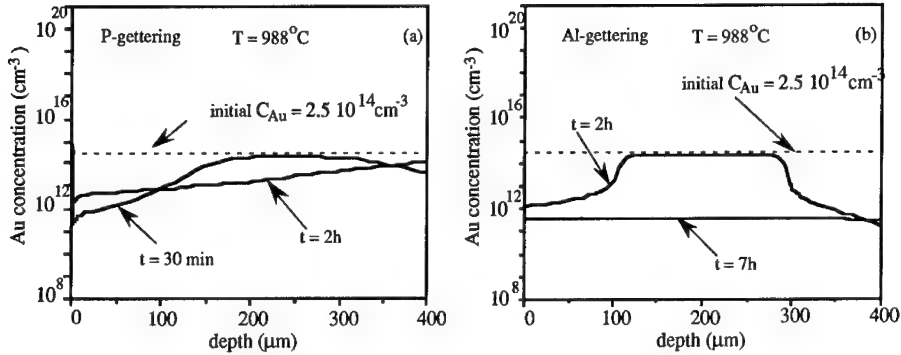


Fig. 1. (a) Au concentration after 30 min and 2 h of P indiffusion gettering from the left (front) surface; (b) Au concentration after 2 and 7 h of Al layer gettering at the right (back) surface. See text for details on the simulation method and conditions.

COMBINED PHOSPHORUS AND ALUMINUM GETTERING

In the *combined P and Al gettering* process, P is indiffused into Si from the wafer frontside while the wafer backside is covered by a predeposited Al layer. The other conditions used in the simulations are the same as for P indiffusion gettering and Al gettering performed separately. Figure 2(a) shows the simulated Au and P profiles for the gettering time of 2 h, which is optimal. Still longer gettering times turned out to be somewhat less effective. As already mentioned, this is due to the spreading and flattening out of the P profile which releases some of the already gettered Au back into the Si wafer when the processing time becomes too long. For the same gettering time, however, the deterioration of gettering effectiveness of the combined P and Al gettering scheme is much less severe than that of the P indiffusion gettering case, because now the P layer released Au is in turn gettered into the Al layer. For the combined P and Al gettering scheme, one can consider that a practical or quasi steady state of Au concentration value has been attained in the Si wafer after the 2 h gettering run, since for still longer gettering times the rate of Au concentration change is very small.

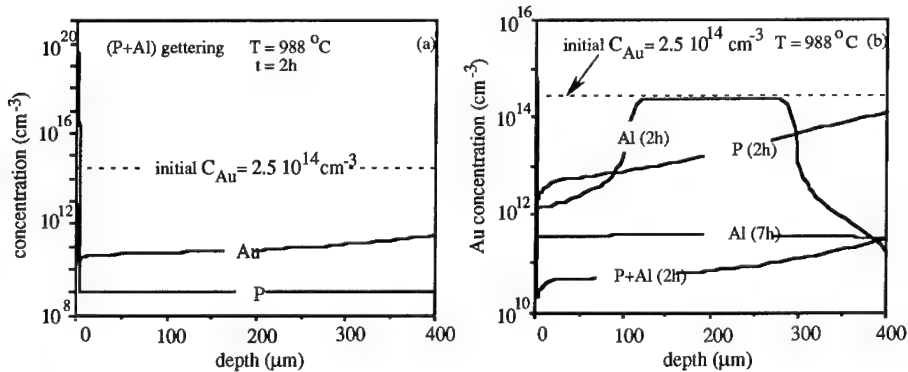


Fig. 2. (a) Au and P concentrations after 2 h of simultaneous P indiffusion gettering from the left (front) surface, and Al layer gettering at the right (back) surface; (b) Comparison between the three gettering techniques (P, Al, P+Al) for 2 h gettering times, and Al gettering for 7 h.

DISCUSSIONS

In both P and Al gettering schemes, gettering sites exist on only one side of a Si wafer and our simulation results showed that the gettering of Au is highly effective at both Si wafer surface regions but not in the bulk. The gettering of Au from the Si surface region neighboring the gettering region should be highly effective because of the short Au diffusion distance involved. The removal of Au from the wafer surface region opposite to the gettering layer location is found to be also highly effective. In fact, it is more effective than in the wafer interior regions located much closer to the gettering region. This situation arises because of the substitutional-interstitial nature of Au in Si. To be gettered, Au has to be in its high diffusivity state, i. e. as an interstitial. The promotion of substitutional Au atoms to interstitial sites is governed by I supply. In the process of kicking-out Au atoms onto interstitial sites, I are consumed and become undersaturated. Since wafer surfaces are assumed to be perfect point defect sources/sinks, in the two surface regions the consumed I have been rapidly replenished, leading to an unsuppressed rate of promoting substitutional Au atoms to the interstitial sites which are rapidly gettered away because of their high diffusivity. In the Si bulk, due to the need of I flowing in from the wafer surfaces and because of their low diffusivity, severe I undersaturation develops, leading to an insufficient promotion of substitutional Au atoms to the interstitial sites to be gettered. Our simulation results on the I profiles (not shown here) accompanying the gettered Au profiles, have indeed shown the severe I undersaturation in the Si wafer interior for shorter gettering time cases.

To compare the efficiencies of the three different gettering schemes in this study, we define the *gettering capacity* to be the maximum amount of Au that can be removed from the Si wafer, the *optimum gettering time constant* t_{og} to be the gettering process run time for reaching the gettering capacity, and the *gettering rate* to be the rate of removing Au from the Si wafer. Clearly, a superior gettering process will have a short t_{og} , a large gettering capacity, and a high gettering rate. To make this comparison, we show in Fig. 2(b) the simulation results of the 2 h processing time cases for all three gettering schemes, as well as that for the Al gettering case with a processing time of 7 h. For the P indiffusion gettering scheme, the optimum gettering time constant t_{og} is ~ 2 h. Still longer processing times are detrimental because of the spreading and consequent flattening of the P profile which leads to a substantial weakening of the capability of the P layer to stabilize the gettered Au. The P gettering capacity is the worst among all three schemes, whereas the gettering rate is reasonably high. For the Al gettering scheme, the optimum gettering time constant t_{og} is ~ 7 h, which indicates that this method has the lowest gettering rate. The gettering capacity of the Al gettering scheme is much larger than that of the P indiffusion gettering scheme. Furthermore, this gettering capacity is a steady state value which does not deteriorate for still longer processing times. For the combined P and Al gettering scheme, the optimum gettering time constant t_{og} is ~ 2 hours, which is just that of the P indiffusion gettering scheme. A comparison of the P (2h) and the Al (7h) curves with the P+Al (2h) curve shown in Fig. 2(b) readily shows that the gettering capacity of the combined P and Al gettering scheme is larger than that of the P indiffusion gettering scheme and that of the Al gettering scheme respectively by more than two orders of magnitude and by a few times. Furthermore, the gettering rate of this scheme is the highest among all three schemes. Thus, by all measures, the combined P and Al gettering scheme is the best. Apparently, when the P indiffusion and Al gettering schemes are combined, a synergistic effect exists for yielding the best result. This synergistic effect is, on the one hand, due to the supersaturation of I produced by P indiffusion which speeds up the gettering process by the Al layer, and on the other hand due to the very large and stable gettering capacity of the Al layer.

A most outstanding feature of these external gettering schemes is that the impurity concentration in the gettered Si regions attains a dynamic solubility value which can be lower than the corresponding impurity thermal equilibrium solubility value at the gettering temperature, because the steady state distribution of the impurity depends only on the solubility ratio or segregation coefficient of the impurity in the two regions, but not on the actual impurity concentration. Thus, the impurity concentration can be lowered by repeated application of the gettering schemes to values as low as desired. This should constitute a major advantage for applying these gettering schemes to solar cell fabrications.

CONCLUSION

Using the diffusion-segregation equation, we have modeled and simulated the process of getting Au away from the Si bulk. Au is a substitutional-interstitial species in Si, and the gettering processes of Au involve Si point defects. Three *external* gettering schemes have been considered: wafer frontside P indiffusion gettering, wafer backside Al deposition gettering, and the combined P and Al gettering. Under otherwise the same processing conditions, it has been shown that P indiffusion gettering is faster than Al gettering, but it has a lower gettering capacity and is less stable than Al gettering in long gettering time cases. The combined P and Al gettering process is as fast as P gettering in reaching an optimum gettering state, and possesses the capacity and stability of the Al gettering process. A most outstanding feature of these external gettering processes is that an impurity dynamic concentration value below its thermal equilibrium solubility can be obtained in the gettering Si region. It is possible to getter a specific impurity from Si to concentrations as low as desired by repeated application of an external gettering scheme.

ACKNOWLEDGMENT

This work has been supported by National Renewable Energy Laboratory via Subcontract XD-2-11004-1.

REFERENCES

1. T. Y. Tan, E. E. Gardner, and W. K. Tice, *Appl. Phys. Lett.* **30**, 175 (1977).
2. M. Pasquinelli, S. Martinuzzi, J. Y. Natoli, and F. Floret, in *Proceedings of the 22nd IEEE PV Specialists Conference*, Las Vegas, NV, 1991 (IEEE, New York, 1991), pp. 1035-1037.
3. M. Loghmarti, R. Stuck, J. C. Muller, D. Sayah, and P. Siffert, *Appl. Phys. Lett.* **62**, 979 (1993).
4. B. Hartiti, A. Slaoui, J. C. Muller, and P. Siffert, *Appl. Phys. Lett.* **63**, 1249 (1993).
5. P. Sana, A. Rohatgi, J. P. Kalejs, and R. O. Bell, *Appl. Phys. Lett.* **64**, 97 (1994).
6. W. Schröter, M. Seibt, D. Gilles, Ch. 11 of "Electronic Structure and Properties of Semiconductors", Vol. 4 of "Materials Science and Technology: A Comprehensive Treatment" eds. R. W. Cahn, P. Haasen, and E. J. Kramer, Vol. 4 ed. W. Schröter (1991), p. 576.
7. T. Y. Tan, R. Gafiteanu, H.-M. You, U. Gösele (1993), in *Proceedings of the National Renewable Energy Laboratory Third Workshop on Point Defects* (Vail, CO).
8. H.-M. You, U. Gösele, and T. Y. Tan, *J. Appl. Phys.* **74**, 2461 (1993).
9. R. Gafiteanu, H.-M. You, U. M. Gösele, and T. Y. Tan (1993), in *Interface control of Electrical, Chemical, and Mechanical Properties*, eds. S. P. Muraka, T. Omi, K. Rose, and T. Seidel. *Mater. Res. Soc. Proc.* 318 (Mater. Res. Soc., Pittsburgh, PA, 1994) p. 31.
10. T. Y. Tan, R. Gafiteanu, U. Gösele, in *Semiconductor Silicon 1994*, eds. H. R. Huff, W. Bergholz, and K. Sumino (The Electrochem. Soc., Pennington, PA, 1994) p. 920.
11. M. Orlowski, *Appl. Phys. Lett.* **53**, 1323 (1988).
12. U. Gösele, W. Frank, A. Seeger, *Appl. Phys.*, **23**, 361 (1980).
13. W. Jüngling, P. Pichler, S. Selberherr, E. Guerrero, and H. W. Pötzl, *IEEE Trans. Electron. Devices* **ED-32**, 156 (1985).
14. S. L. Chou and J. F. Gibbons, *J. Appl. Phys.* **46**, 1197 (1975).
15. J. S. Kang and D. K. Schroder, *J. Appl. Phys.* **65**, 2974 (1989).
16. W. Shockley and J. Last, *Phys. Rev.* **107**, 392 (1957).
17. L.-A. Ledebro and Zhan-Guo Wang, *Appl. Phys. Lett.* **42**, 680 (1983).
18. T. Y. Tan and U. Gösele, *Appl. Phys. A* **37**, 1 (1985).
19. W. R. Wilcox and T. J. LaChapelle, *J. Appl. Phys.* **35**, 240 (1964).
20. N. A. Stolwijk, B. Schuster, and J. Hölzl, *Appl. Phys. A* **33**, 133 (1984).
21. C. P. Ho, I. D. Plummer, S. E. Hansen and R. W. Dutton, *IEEE ED-30*, 1438 (1983).
22. E. Ö. Sveinbjörnsson, O. Engström and U. Södervall, *J. Appl. Phys.* **73**, 7311 (1993).

A STUDY OF GETTERING EFFICIENCY AND STABILITY IN CZOCHRALSKI SILICON

SCOTT A. MCHUGO*, E. R. WEBER*, M. MIZUNO** AND F.G. KIRSCHT***

*University of California, Department of Materials Science, Berkeley, CA 94720

**SEH Isobe R&D Center, Shin-Etsu Handotai Co., Ltd. 2-13-1 Isobe. Annaka-shi, Gunma 379-01, Japan

***Siltec Silicon, 1351 Tandem Avenue, Salem OR 97303, USA

ABSTRACT

Gettering efficiencies and stabilities of internal gettering sites for metallic impurities in high and low carbon doped silicon have been compared with ramped and standard two-step pre-annealing conditions. This study was intended to compare two proposed techniques to shorten the long low temperature nucleation step in the standard Hi-Lo-Hi internal gettering site formation treatment. Specifically, we compare the affect of carbon and a ramped annealing sequence on oxygen precipitate formation and gettering effectiveness. Our results show both techniques accelerate oxygen precipitation, however, only the low carbon ramped materials produced efficient and stable gettering sites. The high carbon materials did not with either annealing treatment. This disparity in performance is due to a difference in the oxygen precipitate's strain field. The precipitates in the low carbon material possessed a high strain field with strain-induced defects while in the high carbon material they were strain-free with no defects. These results indicate the strain stabilizes the gettered impurity such that the gettering rate is increased and stability is enhanced.

INTRODUCTION

Transition metals are the prevalent contaminants in silicon which severely degrade device performance by forming metal silicides and/or remaining dissolved in the silicon lattice. A standard Integrated Circuit industry technique for removal of these impurities is internal gettering which localizes impurities away from device areas[1]. This is accomplished by forming oxygen precipitates and related defects in the bulk of the material. These defects are generally created with a three-step heat treatment consisting of a wafer anneal above 1100°C for out-diffusion of oxygen in the near-surface region followed by a nucleation of oxygen precipitates at approximately 700°C and a third annealing at about 900-1000°C which serves to accelerate oxygen precipitate growth. Oxygen precipitates do not form in the near-surface region because a high supersaturation of oxygen is required to form precipitates. Therefore, a defect-free region or "denuded zone" is created in the device region while deep in the material's bulk, oxygen precipitates and their growth-related defects are formed and act as internal gettering sites for deleterious contaminants.

The mechanism of internal gettering for Fe has been proposed by Gilles et al [2], which is based on a disparity of impurity precipitation kinetics in the denuded zone and bulk. The precipitation driving force is a supersaturation of the impurity. The kinetics are limited by diffusion of the impurity to a precipitation site such as an oxygen precipitate or related defect. Therefore, a high density of oxygen precipitates and related defects are desired for efficient gettering. Generally a long low temperature pre-annealing is required to form a high density of oxygen precipitates greater than the critical radius of the high temperature precipitate growth

treatment which follows. The undesirably long process time is the primary disadvantage of this conventional two-step annealing.

In order to avoid this disadvantage a new low temperature pre-annealing procedure has been proposed [3,4] where the temperature is ramped at a definite rate during the low temperature pre-annealing period. This keeps a large fraction of oxygen precipitates above the critical radius and enables oxygen precipitates to form in large numbers after the high temperature growth stage. An alternative approach is to incorporate carbon into the silicon during crystal growth. The effect of carbon on the formation mechanism of oxygen precipitates and their related defects is still controversial [5,6]. Although carbon has been shown to promote oxygen precipitate growth [7,8], the mechanism for this enhancement is unknown. It has been suggested the volume expansion associated with SiO₂ precipitation leads to the injection of silicon self-interstitials, Si_i, into the matrix which can be described by a simplified reaction [9,10]. The generated Si_i may kick out the substitutional carbon atoms to form interstitial carbon, C_i, or form clusters of SiC. Additionally, formation of SiC leads to a volume contraction, opposite to SiO₂ formation, so this removal of Si_i and formation of SiC could enhance oxygen precipitation. An alternative explanation is that the carbon atom or group of carbon atoms act as a nucleation site for the oxygen, again enhancing the oxygen precipitation rate.

This study differentiates gettering efficiency and stability of high and low carbon concentration silicon with two-step and ramped pre-annealing conditions. We are analyzing two possible techniques, ramped annealing and carbon addition, in order to shorten the long process times of standard internal gettering site formation. The analysis was carried out by comparing the Fe concentration decay at low temperature annealing and the release of Fe from the gettering sites at elevated temperatures. We use Fe as a model impurity because it is one of the most common contaminants in the Integrated Circuit industry and it can be easily detected.

EXPERIMENTAL PROCEDURES

Phosphorous doped ($\approx 1 \times 10^{15}$ atoms/cm³) <100> Czochralski silicon with high and low carbon concentrations were studied. The high carbon material had 5.4×10^{17} atoms/cm³ of substitutional carbon concentration, [C_s], and the low carbon material possessed a [C_s] below the Fourier Transform Infrared Spectroscopy (FTIR) detection limit, 1×10^{16} atoms/cm³. Interstitial oxygen concentrations [O_i] of those materials were 8.5×10^{17} and 8.7×10^{17} atoms/cm³, respectively (ASTM 1983). Two samples, one high and one low carbon content sample, were annealed at 700°C for 48 hrs, and another pair of the samples were annealed at 700°C for 48 hrs followed by a ramped annealing from 750°C to 1000°C in increments of 50°C for 30 min each. We call the former case straight annealing and the latter case ramped annealing. After this pre-annealing, Fe was deposited on the sample surface. In-diffusion was performed in a vertical quartz tube furnace at 1050°C for 2 hrs in a nitrogen ambient. The annealings were terminated by immediate specimen quench into ethylene glycol which gives a quenching rate of about 1000 K/sec. Residual surface Fe was removed by mechanical polishing and chemical etching. Room temperature FTIR was used to measure [O_i] after each stage of the pre-annealing heat treatments. Low temperature (5K) FTIR measurements were used in the final stage of the heat treatments to determine [O_i]. This was required was to separate the O_i peak from neighboring precipitate-induced peaks, as in past studies [11]. The conversion constant of 6.7×10^{15} atoms/cm³ was determined by measuring [O_i] in a 400μm thick silicon sample at room temperature and 5K. Additionally, defect densities and structural characterization of oxygen precipitates, stacking faults and dislocation loops was performed with Transmission Electron

Microscope (TEM) and preferential etching studies. Interstitial Fe concentrations during gettering and after emission were determined by Electron Paramagnetic Resonance (EPR). The samples were annealed for various times at 256°C in a nitrogen ambient to trigger the internal gettering process. After confirmation that the remaining Fe concentration was below the EPR detection limit ($\approx 10^{13} \text{ cm}^{-3}$), an additional 45min annealing at 256°C was carried out to getter the remaining Fe. Heat treatments at 1050°C were performed to emitted the Fe from the gettering sites and compare each site's stability.

RESULTS & DISCUSSION

The results of the [Fe] decay during gettering are shown below in Figure 1.

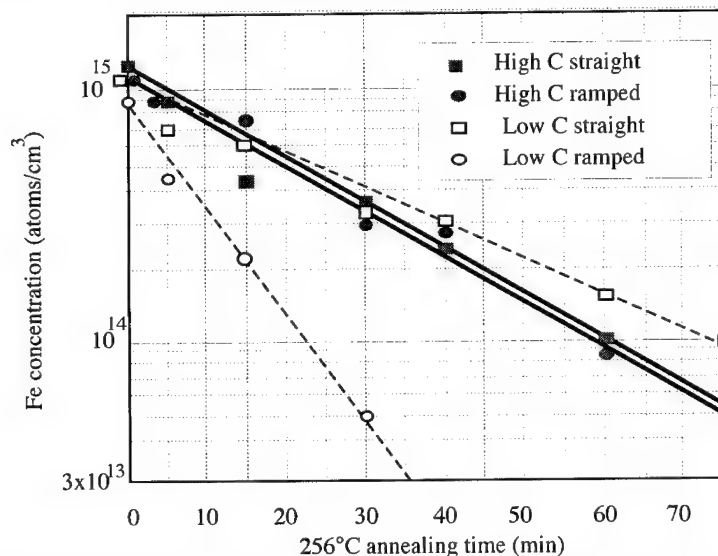


Figure 1: Fe gettering kinetics in CZ silicon of various carbon contents and annealing treatments.

The Fe precipitation kinetics are exponential as expected with the low carbon ramped sample having the highest gettering efficiency. In order to investigate reasons for the different gettering efficiencies, we inspected the microdefect densities in the material by polishing, preferential etching and optical microscopy following the heat treatments. It was seen that the low carbon ramped material had a significantly higher concentration of stacking faults and dislocation loops than any of the other materials suggesting these defects are the cause for high gettering efficiency, as would be expected. In order to quantitatively compare the gettering efficiencies amongst these samples, the time constants were found from:

$$[\text{Fe}] = [\text{Fe}]_0 \exp(-t/\tau) \quad (1)$$

with $[\text{Fe}]_0$ being the initial Fe concentration. This τ value was then used to calculate precipitate density*radius products, nr_0 . For Fe precipitates and oxygen precipitates with a straight pre-annealing sequence, the relation between the time constant and nr_0 can be expressed from Ham's

equation[12]:

$$nr_o = 1/4\pi D \tau \quad (2)$$

where D_{Fe} is the diffusion coefficient of iron = 4.34×10^{-10} cm²/sec at 256°C,[13] and D_{O_i} for oxygen = 3.01×10^{-11} cm²/sec at 1050°C,[14]. The oxygen precipitates with ramped pre-annealings use the relation [15]:

$$nr_o = (3/4\pi C_p) (D_{O_i}/r_o^2) \quad (3)$$

where C_p is the number of oxygen atoms in unit volume of SiO₂, 4.65×10^{22} atoms/cm³. TEM investigations of these samples showed the oxygen precipitates are near-spherical in shape, validating the assumption in equation (3). The changes of interstitial oxygen concentrations [O_i] during the various annealings are shown below in Figure 2.

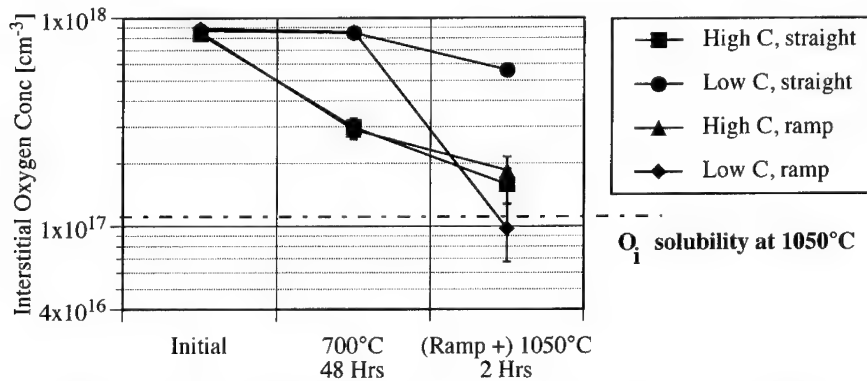


Figure 2: Oxygen precipitation for high and low carbon CZ with various anneals

The most striking fact from this figure is the rapid oxygen precipitation of both high carbon materials and the ramped low carbon material compared to the straight pre-annealing low carbon material. All three of these materials approximately reach the solubility limit of O_i in silicon after the 1050°C growth step [11]. This data along with that from figure 1 was used in equations (2) and (3) to compare nr_o products. The calculated results are summarized below in Table I.

TABLE I: Calculated nr_o values

		Straight annealing		Ramped annealing	
		Fe	Oxygen	Fe	Oxygen
High carbon	nr_o (cm ⁻²)	1.25×10^5	2.34×10^5	1.24×10^5	$2.2 \sim 5.5 \times 10^5$
Low carbon	nr_o (cm ⁻²)	1.00×10^5	1.52×10^5	2.96×10^5	$2.5 \sim 6.5 \times 10^5$

This shows a good correlation between nr_o products of Fe and oxygen precipitates for both low

and high carbon material. Additionally, this data shows the ramped-low carbon content silicon possesses approximately the same nr_o value as the high carbon material. However, the gettering efficiencies differ drastically. TEM analysis of low-carbon ramped annealed material showed oxygen precipitates with punched-out dislocation loops and evidence of large strain fields around the precipitates while both high carbon materials have virtually strain-free oxygen precipitates and no related defects. Therefore, as expected, carbon has an important role in relaxing the strain of oxygen precipitates and halting the formation of related defects. From these observations, we can conclude that the high strain field of the oxygen precipitates and/or defects created from this high strain field are the cause for the rapid gettering rate in low carbon material. Gilles et al.[2] have obtained a nr_o value of 3×10^5 after a 700°C , 64 hr straight pre-annealing with low carbon material. This is equal to the value obtained after our works much shorter ramped annealing sequence and clearly shows the advantages of ramped pre-annealings.

The results of re-emitted Fe concentrations after a 10 min annealing at 1050°C are shown below in Figure 3. In general, the high carbon material re-emitted Fe faster than low carbon material.

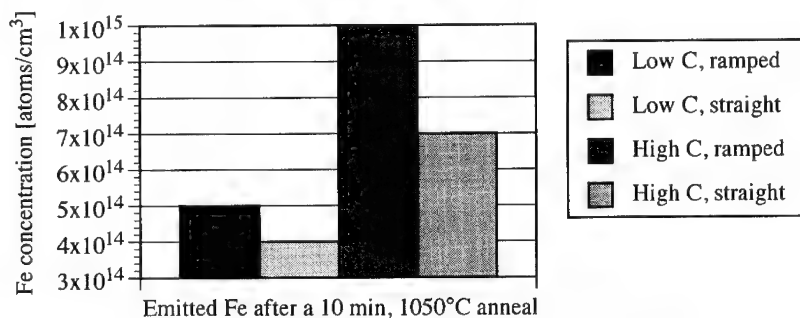


Figure 3: Emitted Fe concentrations for the various CZ materials

This reveals low carbon materials produce more stable gettering sites than high carbon materials even if the precipitation rate is slightly lower, as in the low carbon straight pre-annealing silicon.

We propose the following to explain the above gettering efficiency and stability results. The high efficiency and stability of low carbon silicon gettering can be ascribed to the high strain field around oxygen precipitates and its related defects which allows FeSi_2 to form at each of these sites. Essentially, the strain field of the precipitation site stabilizes the Fe precipitates. During Fe gettering, the strain field acts as a beacon for precipitation via reduction of the precipitation site's strain field. Conversely in Fe re-emission, the strain field of the precipitation site will increase with emitted Fe, thus increasing the system's free energy and retarding the Fe re-emission process. In the same manner, the low gettering efficiency and stability of high carbon silicon gettering sites is related to a low strain field associated with its oxygen precipitates. The ramped annealing sequence forms a high density of strained oxygen precipitates by slowly increasing the critical radius required for oxygen precipitate growth. This allows for a higher percentage of oxygen precipitate nuclei to survive the growth step and thus a high gettering efficiency while retaining gettering stability. This model is more completely described in [16]. The fact that the low carbon straight pre-annealing sample shows an even weaker gettering efficiency than the high carbon materials is deceiving. It is not due to weaker gettering sites in this material but rather because of a lower oxygen precipitate density, see Table I, and low dislocation loop and stacking fault densities as seen by TEM. From the Fe emission results we see the low carbon straight anneal material has more stable gettering sites than the high carbon material which delineates the difference between gettering site density effects and gettering "strength".

CONCLUSIONS

We have compared two proposed techniques for reduction of the lengthy low temperature nucleation step in the standard process of oxygen precipitate formation in CZ silicon. Specifically, increasing the material's carbon content and using a ramped annealing sequence. Both increase the oxygen precipitation rate but only the ramped annealing sequence provides efficient and stable gettering sites. A model is proposed which regards the oxygen precipitate's strain field as a key factor towards efficient and stable gettering.

REFERENCES

1. T.Y. Tan, E.E. Gardner and W.K. Tice, Appl. Phys. Lett. **30**, 175 (1977).
2. D. Gilles, S. Hahn and E.R. Weber, Phys. Rev. Lett. **64**, 196 (1990).
3. S. Kishino, T. Aoshima, A. Yoshinaka, H. Shimizu and M. Ono, Jpn. J. Appl. Phys. **23**, L9 (1984).
4. F.G. Kirscht, E.R. Weber and I. Babanskaya, Solid State Phenomena **19**, p. 137 (1991).
5. Q. Sun, K.H. Yao, J. Lagowski and H.C. Gatos, J. Appl. Phys. **67**, 1 (1990).
6. S. Gupta, S. Messoloras, J.R. Schneider, R.J. Stewart and W. Zulehner, Semiconductor Sci. Technology **7**, 6 (1992).
7. S. Hahn, M. Arst, K.N. Ritz, S. Shatas, H.J. Stein, Z.U. Rek and W.A. Tiller, J. Appl. Phys. **64**, 15 (1988).
8. H.L. Tsai, in *Semiconductor Silicon*, edited by H.R. Huff, T. Abe and B. Kolbesen (Electrochemical Society, Pennington, NJ, 1986), p. 790.
9. W.B. Rodgers, H.Z. Massoud, R.B. Fair, U. Gösele, T.Y. Tan and G.A. Rozgonyi, J. Appl. Phys. **65**, 4215 (1989).
10. P. Gaworzewski, E. Hild, F.G. Kirscht and L. Vecsernyes, Phys. Status Solidi (a) **85**, 133 (1984).
11. F.M. Livingstone, S. Messoloras, R.C. Newman, B.C. Pike, R.J. Stewart, M.J. Binns, W.P. Brown and J.G. Wilkes, J. Phys. C: Solid State Phys., **17**, 6253 (1984).
12. F.S. Ham, J. Phys. Chem. Solids **6**, 335 (1958).
13. E.R. Weber, Appl. Phys. **A30**, 1 (1983).
14. J.C. Mikkelsen, Jr., in *Oxygen, Carbon, Hydrogen, and Nitrogen in Crystalline Silicon*, edited by J.C. Mikkelsen, Jr., S.J. Peaton, J.W. Corbett and S.J. Pennycook (Materials Research Society, Pittsburgh, 1986), p. 19.
15. D. Gilles, E.R. Weber, S. Hahn, O.R. Monteiro and K. Cho, in "Semiconductor Silicon", edited by H.R. Huff, T. Abe and B. Kolbesen (Electrochemical Society, Pennington, NJ, 1990), p. 697.
16. S.A. McHugo, E.R. Weber, M. Mizuno and F.G. Kirscht, to be published in Appl. Phys. Lett., May 22, 1995

GETTERING OF INTERSTITIAL IRON IN P/P⁺ EPITAXIAL SILICON WAFERS

W. WIJARANAKULA*, X. GAO*, K. CURTIS*, AND H. HADDAD**

*Shin-Etsu, SEH America, Inc., 4111 NE 112th Avenue, Vancouver, Washington 98682

**Hewlett Packard Company, Northwest Integrated Circuits Division, 1020 Northeast Boulevard, Corvallis, Oregon 97330.

ABSTRACT

Gettering of interstitial iron in p/p⁺ epitaxial silicon wafers during an integrated circuit device simulation annealing was examined. The results from the deep level transient spectroscopy and optical microscope examination suggest no correlation between the interstitial iron concentration in the epitaxial layer and the bulk microdefect density. An electron microscopic analysis revealed that gettering of interstitial iron took place at an oxide polyhedral precipitate located at the center of a bulk stacking fault. By comparing the results of iron implanted to non-implanted samples, it is concluded that iron gettering occurs via a phase transformation of SiO₂ to an α FeSi₂ iron disilicide. In this study, it is suggested that gettering of iron atoms is fundamentally different from that of other transition metals where the silicide formation occurs predominantly along the Frank partial dislocations of the bulk stacking fault.

INTRODUCTION

Interstitial iron (Fe_i) atoms incorporated into the silicon lattice during silicon wafer and integrated circuit (IC) device manufacturing introduce energy levels in the bandgap and in turn reduce the retention time of charge-storage devices such as dynamic random access memory (DRAM). Iron disilicide precipitates occurring during high-temperature IC device manufacturing steps cause an increase in junction leakage of metal-oxide semiconductor (MOS) devices and degrade the gate oxide integrity [1-3]. Therefore, it is agreed that the iron concentration level in silicon must be reduced in order to lower junction leakage and increase the reliability of thin gate oxide in submicron-size IC devices. During the past few years, iron behavior and the gettering mechanism in lightly doped Czochralski silicon has been extensively examined [3-5].

It is well recognized that gettering of iron atoms via bulk microdefects requires a supersaturation of the iron concentration [5]. In p/p⁺ epitaxial silicon wafers used predominantly for the fabrication of advanced microprocessors and memory devices, the complexity of the iron gettering mechanism increases. One of the factors which contribute to the complexity of the iron gettering mechanism is a strong dependence of the solubility limit of interstitial iron atoms on the boron doping concentration resulting from the Fermi level effect [6]. Another factor is the influence of heavily doping with boron on the characteristics of crystallographic defects and thus the internal gettering sites. Thus far, neither the preferred gettering sites nor the gettering mechanism of interstitial iron atoms in silicon heavily doped with boron have been identified. The objective of this paper is to address this issue in more detail.

EXPERIMENTAL PROCEDURES

Samples were prepared from 150 mm-diameter Cz grown p⁺ epitaxial substrate wafers heavily doped with boron to the concentration of 3×10^{18} atoms/cm³. The oxygen concentration, as determined by gas fusion analysis (GFA) and calibrated using the coefficient of 2.45×10^{17} 1/cm², was 7.25×10^{17} atoms/cm³. A 10 μ m-thick epitaxial silicon layer lightly doped with boron to the concentration of 8×10^{14} atoms/cm³ was deposited in an Applied Materials AMT 7800 reactor operated at 1050°C. As-received epitaxial wafers were annealed at 750°C for 4h in nitrogen ambient to enhance oxygen precipitation which was followed by Fe implantation. Fe-ions were implanted at 180 keV with a dose of 1×10^{14} cm⁻² in a hybrid mode with the beam normal to the epitaxial surface. Following the implantation, a 2 min. drive-in was carried out in a rapid thermal processing (RTP) system at 1100°C. The CMOS device manufacturing was simulated using multiple annealing steps with a maximum temperature of 1100°C. Epitaxial wafers without nucleation annealing and those without Fe-implantation were included for comparison. The iron concentration in the epitaxial layer was monitored from the H(0.43 eV) peak in the deep level transient spectroscopy (DLTS) spectrum which is assigned to Fe_i defects. Prior to the DLTS measurements, the samples were annealed at 210°C for 3 min. and then quenched in water to dissociate Fe_i from the Fe-B pair. The bulk microdefects were examined under the optical microscope after preferential etching. The implantation damages in the epitaxial layer as well as the morphology of the bulk microdefects were examined using the TEM Philips 430 operated at an accelerating voltage of 300 kV. No implantation damages in the epitaxial layer were detected.

RESULTS AND DISCUSSION

Fig. 1 shows the typical DLTS spectra after a RTP step and device simulation annealing, respectively. The Fe_i concentration in samples after the RTP step is consistently at 2×10^{13} atoms/cm³. After annealing, the Fe_i concentration reduces by approximately one order of magnitude. A slight difference in the Fe_i concentration between samples with and without nucleation annealing in Fig. 1b should be considered as

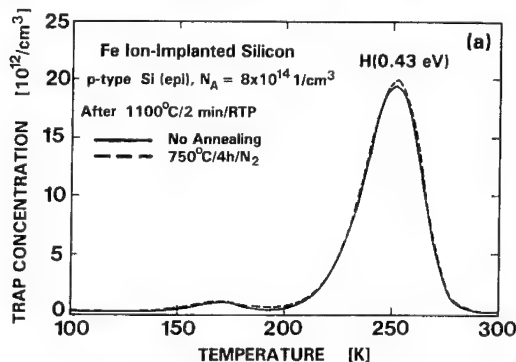


Figure 1a: DLTS spectra for Fe ion-implanted silicon after a RTP step.

insignificant, compared to a total reduction of the Fe_i concentration. Based upon the DLTS results, it is concluded that the nucleation anneal prior to the device simulation annealing does not have any effect on the iron gettering efficiency in the epitaxial silicon wafers.

Under the optical microscope, a bulk defect density on the order of $\sim 1 \times 10^6$ cm⁻², was

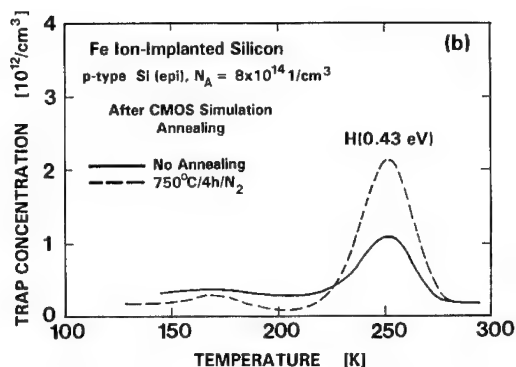


Figure 1b: DLTS spectra for Fe ion-implanted silicon after a CMOS simulation.

observed in epitaxial wafers receiving a nucleation annealing. The epitaxial wafers without nucleation annealing, on the other hand, contain a relatively low defect density, $\sim 2 \times 10^4 \text{ cm}^{-2}$. The above results suggest no correlation between the Fe concentration in the epitaxial layer and the bulk microdefect density in the substrate.

From the TEM analysis, the bulk microdefects are identified as oxide polyhedra and oxide precipitate platelets with punch-out dislocations. Bulk stacking

faults with an average diameter of $10 \mu\text{m}$ were also detected, but predominantly in the epitaxial wafers receiving a nucleation anneal. Figure 2 shows the TEM micrograph of an oxide polyhedron with facets along the $\{111\}$ and $\{100\}$ planes and an elongated punch-out dislocation loop bounded by $\langle 111 \rangle$ and $\langle 113 \rangle$ dislocation line segments. Oxide precipitate platelets detected in the substrate region have a square shape with edges along the $\langle 110 \rangle$ directions and are similar to those typically found in Cz silicon after annealing [7].

Generally, it is concluded that the bulk stacking faults observed in epitaxial wafers receiving a nucleation annealing are of $1/3 \langle 111 \rangle$ -type and generated via the Bardeen-

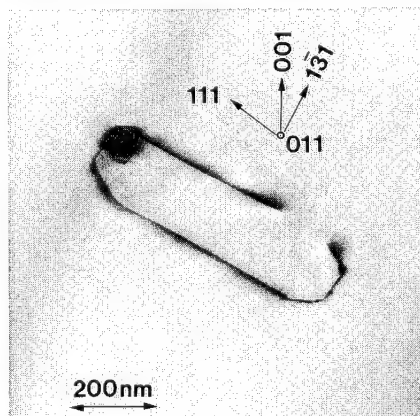


Figure 2: TEM micrograph of a polyhedral oxide precipitate with an elongated punch-out dislocation loop.

Herring mechanism as proposed by Wada et al [8]. Consider the fact that the punch-out dislocation at an oxide polyhedral precipitate shown in Fig.2 is bounded by $\langle 111 \rangle$ and $\langle 113 \rangle$ dislocation line segments while the dislocation loops generated at the oxide precipitate platelet are of $1/2 \langle 110 \rangle$ -type, the possibility of a bulk stacking fault to evolve from the dislocation loops generated at an oxide polyhedron is higher than that at an oxide precipitate platelet. It should be pointed out that the oxide polyhedra found here are nucleated at 1150°C or higher during the crystal growth process [9-10] and not during the CMOS simulation annealing.

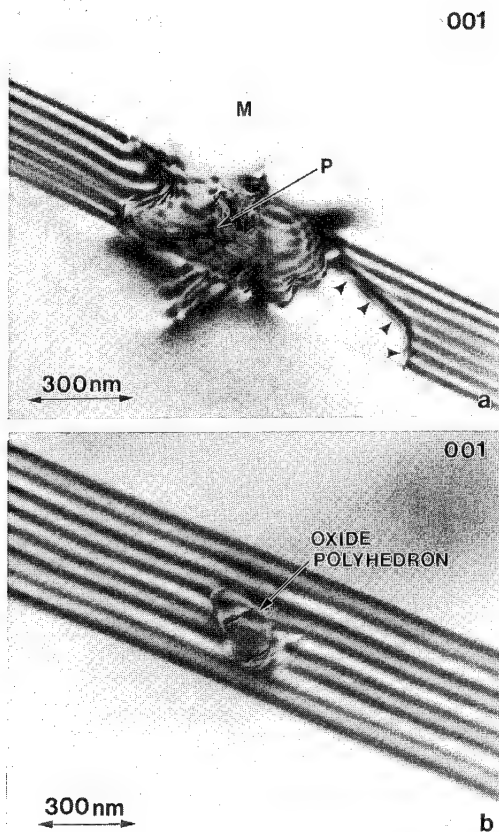
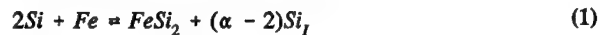


Figure 3: TEM micrograph of a bulk stacking fault segment containing a precipitate in samples (a) with and (b) without Fe-implantation.

Figures 3a and 3b show TEM micrographs of the center section of typical bulk stacking faults containing precipitates in samples with and without Fe implantation, respectively. In the Fe-implanted sample, the morphology of precipitate **P** exhibits no preferential orientations. The preliminary chemical analysis of the precipitate **P** using the energy dispersive x-ray spectrometer revealed no conclusive evidence that the precipitate **P** contains iron. In the vicinity near the precipitate **P**, a large portion of the Shockley partial of the stacking fault is missing. This observation suggests that a formation of precipitate **P** consumes silicon interstitials. In the sample without Fe implantation, the precipitate is characterized as an oxide polyhedron bounded by {111} and {100} planes. The results in Figure 3 suggest that the Fe contaminant could cause a transformation of an oxide polyhedron into precipitate **P**. From the above argument, the anomalous disappearance of a portion of the Shockley partial may be explained by considering a reaction leading

to the iron disilicide formation given by



where the subscript I is for silicon interstitials. α is the ratio between the molecular volume of iron disilicide $FeSi_2$ (25.23 \AA^3) [11] and silicon (20 \AA^3) and ≈ 1.26 . The above reaction indicates that the formation of silicon-rich iron disilicide consumes excess silicon interstitials. Therefore, during an iron disilicide precipitation, the necessary excess silicon interstitials must be taken from the Shockley partial. Based upon this model, the bulk stacking faults could be one of the most effective sites for iron gettering.

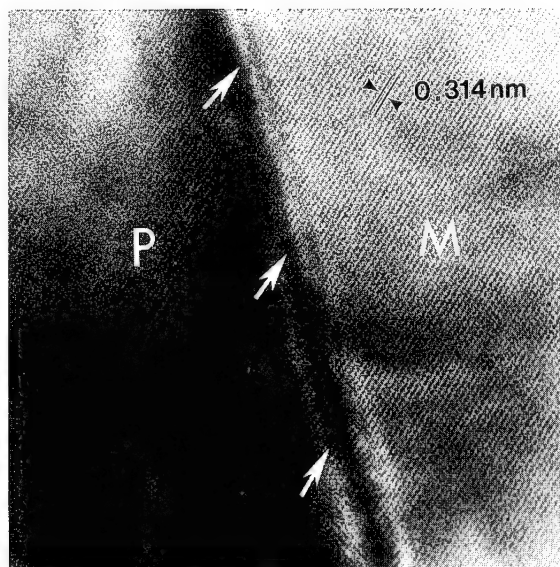


Figure 4: HREM image of the interface between precipitate P and silicon matrix M in the sample receiving an Fe-implantation.

Figure 4 shows a high magnification image of the interface region between the precipitate P and silicon matrix M in the Fe-implanted sample. From the figure, it may be seen that the interface is highly coherent, with only few misfit dislocations along the length of the interface. Consider the lattice parameters of tetragonal α FeSi₂, which are $a = b = 2.6901 \text{ \AA}$ and $c = 5.134 \text{ \AA}$ [11], iron disilicide will be the most probable precipitate which exhibits excellent matching to the silicon matrix. The result from the atomic resolution electron microscopy and other evidences in this work conclusively suggests that the precipitate P is iron disilicide.

SUMMARY

Gettering of interstitial iron in p/p⁺ epitaxial silicon wafers during an integrated circuit device simulation annealing was examined. The results from the deep level transient spectroscopy and optical microscope examination suggest no correlation between the interstitial iron concentration in the epitaxial layer and the bulk microdefect density. Although an electron microscopic analysis revealed evidence of internal gettering at an oxide polyhedral precipitate located at the center of the bulk stacking fault, such a gettering appears to have a small impact on the total Fe concentration in the epitaxial layer after annealing. From the present analysis, it is hypothesized that the observed reduction in the Fe concentration in the epitaxial layer after annealing could be attributed mainly to a migration of interstitial iron atoms from the epitaxial layer either to the wafer surface or the heavily doped region. By comparing the results from the iron implanted to the non-implanted samples, it is concluded that iron gettering at the bulk microdefects occurs via a phase transformation of SiO₂ to an α FeSi₂ iron disilicide. In this study, it is suggested that gettering of iron atoms is fundamentally different from that of other transition metals where the silicide formation occurs predominantly along the Frank partial dislocations of the bulk stacking fault [10, 12].

ACKNOWLEDGEMENTS

TEM works were performed at MCNC Microelectronics Center, Research Triangle Park, NC, AMER, Inc., Sunnyvale, CA, and Electron Microscopy Consortium, University of Washington, Seattle, WA.

REFERENCES

1. A. Ohsawa, K. Honda, R. Takizawa, T. Nakanishi, M. Aoki, and N. Toyokura, in Semiconductor Silicon 1990, edited by H.R. Huff, K.G. Barraclough and J. Chikawa (Electrochem.Soc.Proc., **90-7**, Pennington, NJ, 1990), pp.601-613.
2. W.B. Henley, L. Jastrzeski and N.F. Haddad, in Defect Engineering in Semiconductor Growth, Processing and Device Technology, edited by S. Askok, J. Chevallier, K. Sumino and E. Weber (Mater.Res.Soc.Proc., **262**, Pittsburgh, Pennsylvania, PA, 1992) pp.993-998.
3. P.W. Mertens, M. Meuris, H.F. Schmidt, S. Verhaverbeke, M.M. Heyns, P.Carr, D. Gräf, A. Schnegg, M. Kubota, K. Dillenbeck and R. de Blank, in Crystalline Defects and Contamination: Their Impact and Control in Device Manufacturing, edited by B.O. Kolbesen, P. Stallhofer, C. Claeys and F. Tardif, (Electrochem.Soc.Proc., **93-15**, Pennington, NJ, 1993), pp.87-102.
4. D. Gilles, E.R. Weber, S. Hahn, O.R. Monteiro and K. Cho, in Semiconductor Silicon 1990, edited by H.R. Huff, K.G. Barraclough and J. Chikawa (Electrochem.Soc.Proc., **90-7**, Pennington, NJ, 1990), p.697-708.
5. M. Aoki, A. Hara and A. Ohsawa, J.Appl.Phys., **72**, 895(1992).
6. D. Gilles, W. Schröter and W. Bergholz, Phys.Rev. B, **41**, 5770(1990).
7. W. Wijaranakula, J.Appl.Phys., **72**, 2713(1992).
8. K Wada, H. Takaoka, N. Inoue, and K. Kohra, Japan.J.Appl.Phys., **18**, 1929(1979).
9. M. Hasebe, Y. Takeoka, S. Shinoyana and S. Naito, in Defect Control in Semiconductors, edited by K. Sumino (North-Holland, Amsterdam, 1990), pp.157.
10. S.S. Kim and W. Wijaranakula, J.Electrochem.Soc., **142**, 553(1994).
11. M.-A. Nicolet and S.S. Lau, VLSI Electronics: Microstructural Sciences, (Academic Press, **6**, Boston, 1983) pp.329-464.
12. K. Ryoo, R. Drosd, and W. Wood, J.Appl.Phys., **63**, 4440(1988).

CHARACTERIZATION OF THE DAMAGE ON THE BACK SIDE OF SILICON WAFERS

S. E. LINDO, K. M. MATNEY, AND M. S. GOORSKY

University of California, Los Angeles, Department of Materials Science and Engineering, Los Angeles, CA 90095-1595

ABSTRACT

Gettering represents a standard procedure to remove harmful impurities from device active regions of a silicon wafer. An affordable technique for the creation of a defect free (denuded) zone is the introduction of gettering sites on the wafer back side via mechanical damage (i.e. lapping). However, optimizing the extrinsic gettering process requires a technique to quantify the extent of damage introduced through a typical back-side damaging step. Here, we present results from a study using triple axis x-ray diffraction. We characterized the level of damage present in wafers subjected to different lapping conditions. By comparing reciprocal space maps from samples that had undergone different lapping steps, we concluded that all the as-lapped samples showed similar levels of damage in terms of both strain variations and lattice tilts. However, the integrated diffuse scattering intensities decreased from medium to soft to double-soft lapping, which confirmed that the double soft lapping introduced the least damage. Typically, the damage step introduced a symmetrical distribution of both lattice strain and lattice tilts (mosaicity) in the surface layer. KOH etching was employed to determine the depth of the damaged layer. In all cases the as-lapped samples had integrated intensities two orders of magnitude greater than those of the etched samples. Analysis of the residual damage present in the lapped samples after chemical etching confirmed that the more aggressive lapping conditions introduced damage of greater depth.

INTRODUCTION

The presence of extended defects in device active regions is detrimental to electrical performance and could eventually lead to device failure [1,2]. Transition metal impurities are especially detrimental to performance, because they can behave as nuclei for the formation of stacking faults and precipitates near the wafer surface; they are also electrically active species that can interfere with device operational characteristics, as in the case of deep traps, lowering device yield [1].

Generally speaking, transition metal impurities are fast diffusing species that tend to gather near the surface region in perfectly crystalline materials. In order to avoid this unwanted migration of impurities to the device region, a gettering step can be implemented. Gettering is a mechanism that serves the purpose of removing these transition metals away from active regions of the devices [3]. Intrinsic gettering [4,5] refers to the collection of impurities within the bulk of the wafer, while extrinsic gettering [6,7] deals with the trapping of impurities at the wafer back side. In both cases a denuded zone is created (at the "device" side). In this study, we focused on

the extrinsic gettering process, for which a necessary condition is that the back side must be rich in extended defects [1].

In order to effectively implement the extrinsic gettering step, we must be able to quantify the extent and reproducibility of the damage initially present at the wafer's back side. This damage can be introduced by different techniques: local melting by laser irradiation, polysilicon deposition, ion implantation, phosphorus predeposition, or mechanical working (e.g. sandblasting, lapping) [1]. At present, the extent of the initial damage introduced by any one of these techniques has not been quantified. Double Crystal x-ray Diffraction (DCD) is typically considered a technique to assess crystalline damage. The diffuse scattering obtained in DCD is known to be related to crystal quality, however, it presents the problem that the angular range of acceptance of the detector is too wide to selectively identify the diffuse scattering source [8]. The triple axis technique (TAD), on the other hand, is known to correct for this major disadvantage and readily yield information regarding the source of diffuse scattering in terms of strains and mosaic tilt present in the sample [9]. This is achieved by the introduction of a third crystal (analyzer) in front of the detector in order to reduce the angular range of acceptance. TAD has been reported to be extremely sensitive to the detection of near surface damage in GaAs single crystals [10].

EXPERIMENTAL

Three sets of silicon wafers, p-type (6" diameter), of (100) orientation subjected to different lapping parameters (medium, soft and double-soft lapping) were examined. Each set consisted of three samples with the same lapping parameter: one in the as-lapped state, a second one after a chemical etching step was implemented (KOH- etched), and a third one etched under identical conditions for twice as long (double-etched). A Bede D³ diffractometer was used in its triple axis set-up as described by the schematic (Fig. 1). This apparatus has encoded direct drive sample and detector motion with better than 0.5 arcseconds precision; and a range of 2 to 10 arcseconds step sizes was used, depending upon the extent of diffuse scattering obtained from each individual sample. The x-ray beam incident on the sample was collimated and monochromated by a series of silicon conditioning crystals. The dimensions of this beam at the sample surface are 1mm x 1mm. In all cases, the beam was directed to a position near the center of the wafer.

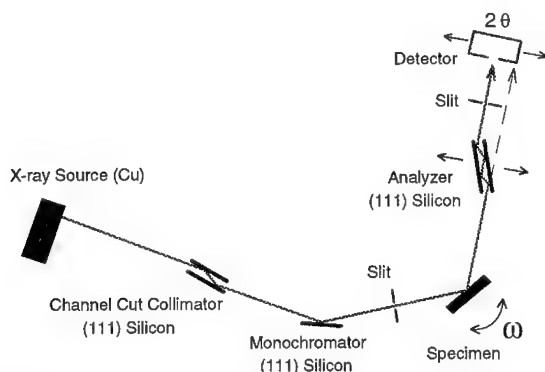
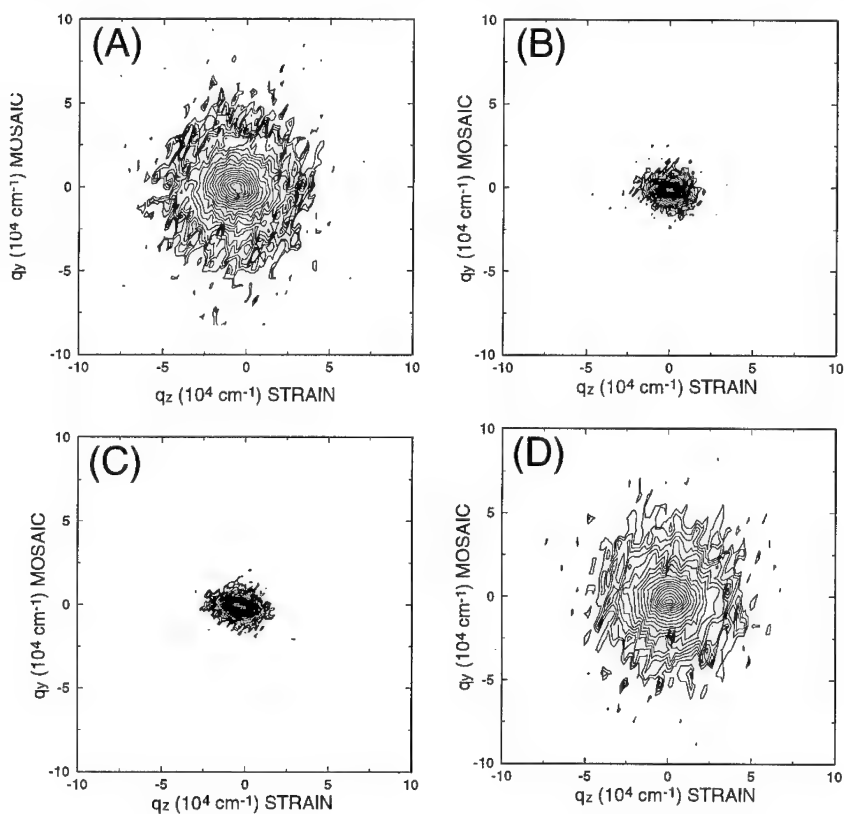


Fig. 1: Bede D3 diffractometer in triple axis mode

The third axis (analyzer) crystal, consisting of a channel cut (111) silicon single crystal allows for selective recording of intensities from the diffracted beam as to deconvolute the effects due to strain and mosaic tilt in the sample [9].

RESULTS AND DISCUSSION

The extent of the damage introduced by lapping the silicon wafers can be qualitatively analyzed by direct observation of the diffuse scattering spread generated in reciprocal space [9,10]. Figure 2 shows reciprocal space maps of the (004) reflections for the three sets of wafers mentioned in the experimental section. In these maps, q_z (along $\langle 001 \rangle$) is sensitive to interplanar spacing variations (strain); q_y is a measure of mosaic tilt about the $\langle 110 \rangle$ zone axis. The lines represent iso-intensity contours. These results illustrate that the lapping step for the different samples introduced a symmetrical distribution of lattice strain and lattice tilts (mosaicity).



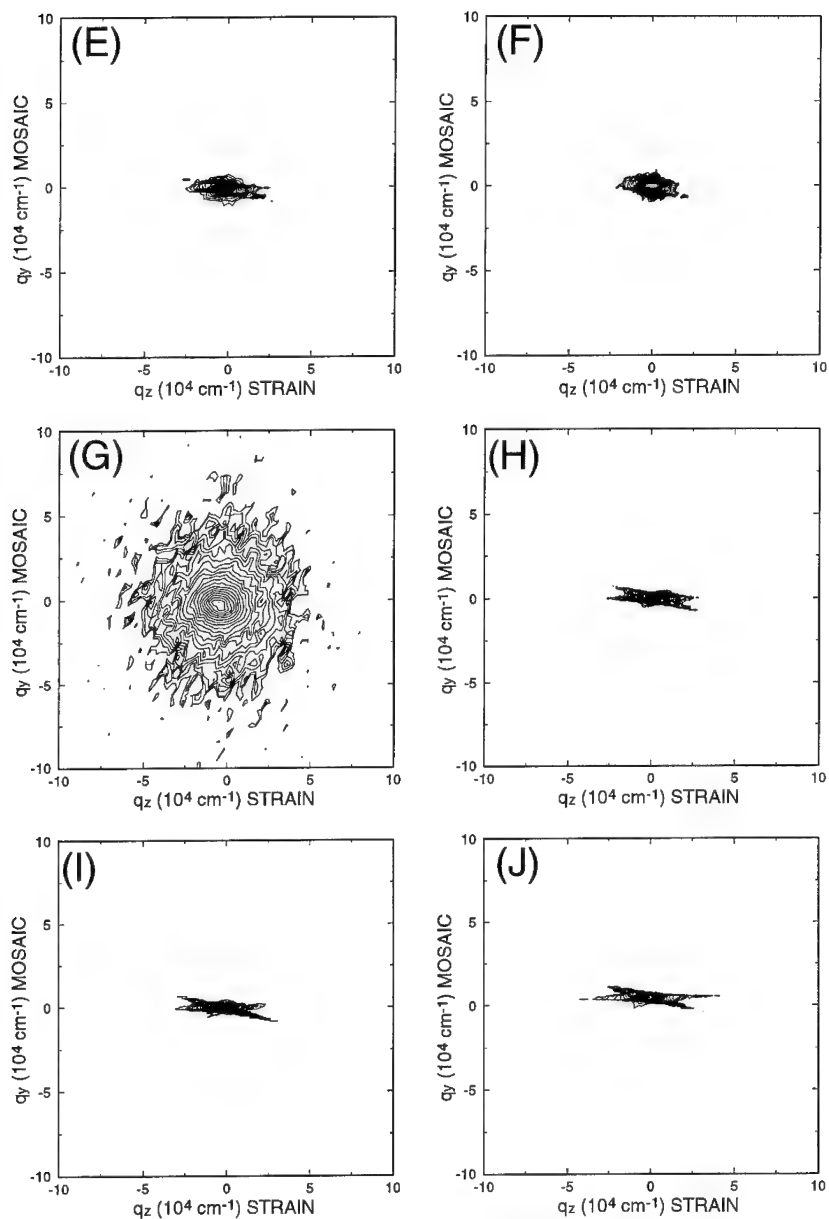


Fig. 2: Reciprocal space maps of silicon (004) reflections. **MEDIUM lapping:** A) as-lapped sample; B) single etched sample; C) double-etched sample. **SOFT lapping:** D) as-lapped; E) single etched; F) double etched. **DOUBLE SOFT lapping:** G) as-lapped; H) single etched; I) double etched; J) **Perfect crystal** (polished face).

From Fig. 2, it is also apparent that in all cases, some residual damage is still present after the first and second etching steps when compared to a perfectly crystalline sample (polished face of wafer). Since each etching step removes the same amount of damaged material, the amount of diffuse scattering present after an etching step can be correlated to the initial depth of the damaged layer. It follows from the extent of the spread in the reciprocal space after the etch step, that the medium lapping condition introduced the deepest damage, and the double-soft lapping created the most shallow damaged layer.

In the case of the as-lapped samples, the integrated intensities for the different lapping conditions decreased from medium to soft to double-soft lapping. From these results, it is apparent that the medium lapping condition introduced the most extensive damage. The soft and double-soft lapping conditions, introduced similar levels of damage (within experimental error).

In order to effectively compare results from the different sets of wafers and make variations in experimental conditions negligible, the integrated intensities were normalized by dividing the calculated value by the corresponding peak intensity to obtain the Integral Breadths (I.B.). The I. B. showed the exact same trends as the FWHM of the ω scans. We also compared the FWHM of the ω and $\theta/2\theta$ scans to verify the trends in crystalline quality. Figure 3 illustrates the results of this comparison.

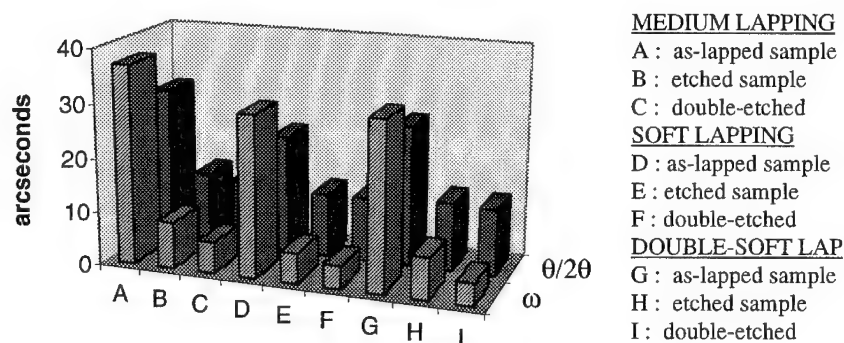


Fig. 3: Full Widths at Half Maximums (FWHM) of ω scans and $\theta/2\theta$ scans.

The trends shown in Fig. 3 confirm our qualitative analysis of the reciprocal space maps and show direct agreement between the numerical figures corresponding to I.B and those from FWHM of the central ω scans and $\theta/2\theta$ scans. From Fig. 3, we see that the medium lapping conditions introduced both greater strain variations and lattice tilt variations in the layers than the other two conditions. The soft and double-soft lapping conditions both introduced about the same level of strain and tilt. It is important to note that although the $\theta/2\theta$ FWHM appear to decrease after etching the samples, the values obtained are limited by the intrinsic resolution of the diffractometer (approximately 12 arcseconds) in this required space direction.

CONCLUSIONS

It has been shown that the triple axis x-ray diffraction (TAD) technique is extremely effective to characterize the damage present on the back side of the wafers. A decreasing trend in the spread of the reciprocal space maps (in terms of mosaicity and strain) was observed from the medium to the soft to the double-soft lapping condition. The most extensive damage was created by the medium lapping, while the level of damage introduced by the soft and double-soft lapping conditions appeared to be extremely similar (within experimental error).

In all cases, the second etching step seems to remove most of the damaged material initially present, although residual damage was still observed when compared to a polished substrate. The FWHM of the central ω and $\theta/2\theta$ scans confirmed this result.

The sample with the greatest extent of diffuse scattering present after etching corresponded to the medium lapping condition, which shows that more severe lapping introduces a damaged layer of greater depth. Similarly, the double soft lapping corresponded to the smallest damage depth.

ACKNOWLEDGMENT

We thank Pamela Flesher at Pacific Scientific for supplying the sets of wafers with different back side damage conditions.

REFERENCES

1. G. F. Cerofolini, L. Meda, Physical Chemistry of, in and on Silicon, (Springer-Verlag Publication, Berlin, New York, 1989).
2. C. Cane, M. Lozano, E. Cabruja, J. Esteve E. Gracia, F. Serra, and L. Fonseca, Defects of Silicon II, edited by W. M. Bullis, U. Gosele and F. Shimura (The Electrochemical Society, Inc., New Jersey, 1991) pp 643.
3. D. K. Sadana, Impurity Diffusion and Gettering in Silicon, edited by R.B. Chen, C. W. Pearce, and J. Washburn (Mat. Res. Soc. Proc., **36**, Pittsburgh, PA) pp. 245.
4. T. Y. Tan, E. E. Gardner and W. K. Tice, Appl. Phys. Lett., **30**, 175 (1977).
5. K. H. Yang, H. F. Kappert and G. Schwuttke, Phys. Stat. Sol. A, **50**, 221 (1978).
6. J. E. Lawrence, Trans. Metall. Soc. AIME **242**, 484 (1968).
7. K. H. Yang and G. H. Schwuttke, Phys. Stat. Sol. A, **58**, (1980).
8. P. F. Fewster, Appl. Surf. Sci., **50**, 9 (1991).
9. A. Iida and K. Kohra, Phys. Stat. Sol. (a), **51**, 533 (1979).
10. V. S. Wang and R. J. Matyi, J. Appl. Phys., **72**, 5158 (1992).

Mechanism of Iron Gettering by Polycrystalline Silicon film in p- Type Czochralski(CZ) Silicon

Kamal K. Mishra
MEMC Electronic Materials, Inc., 501 Pearl Drive,
St. Peters, Mo 63376

ABSTRACT

Iron gettering in p-type CZ silicon at 600C has been investigated using deep level transient spectroscopy(DLTS), and the surface photovoltage(SPV) method. A quantitative analysis of the gettering kinetics of iron using the polycrystalline silicon film is presented for the first time. Depth profiles of iron concentration indicated a sharp gradient in the Fe concentration near the polycrystalline silicon/substrate interface. Concurrent decrease in the minority carrier diffusion length was also observed in the same region. The majority of iron gettering from the bulk silicon was found to be associated with the enhancement of the internal gettering.

The presence of small oxygen precipitates/nuclei generated by prolonged heat treatment at 600C was found to prevent regeneration of FeB pairs at the room temperature. On the other hand, large precipitates formed at 1000C do not influence the diffusion or the recombination of Fe_i with B⁻ to form FeB pairs.

INTRODUCTION

Gettering by polysilicon film deposited onto the backside of silicon (PB) is frequently used in VLSI manufacturing¹⁻³. Although the beneficial effect of the polysilicon film in gettering the metallic impurities has been clearly demonstrated, the mechanism of gettering of metals specially relatively- slow diffusing iron is far from being understood. Several gettering mechanisms for iron in silicon by the polysilicon film has been proposed. It is believed that the grain boundaries in polysilicon film act as gettering sink³⁻⁴. Extended defects, such as dislocations and oxidation induced stacking faults(OISF) generated at the polysilicon/silicon interface were reported to be responsible for the gettering⁵⁻⁶. In addition, it has been proposed that the enhancement of the oxygen precipitation caused by the deposition of polysilicon provides additional gettering⁷⁻⁸.

The gettering efficiency of iron has been determined qualitatively using the haze test, the oxide integrity test, the generation(MOS- τ) lifetime, the recombination lifetime, and by measuring the concentration of iron in near the surface region using deep level transient spectroscopy(DLTS). Recently Hayamizu et al.⁹ studied the gettering of Fe in float zone silicon wafers. The time constant of iron removal by the backside film was found to be in good agreement with the diffusion coefficient of iron. However, no clear evidence for the segregation or precipitation of the iron in the backside has been reported. Gettering of iron by the polysilicon film takes place effectively only at low temperatures⁹⁻¹⁰. In this paper, a quantitative study of gettering of iron is presented. Time resolved measurements as well as depth profile measurements of iron distribution has been carried out using the SPV and DLTS to elucidate the mechanism of iron gettering.

EXPERIMENTAL PROCEDURE

The wafers used in this experiment were 150mm, p-type [100] material with resistivity of 4-6 ohm-cm with an initial oxygen concentration of 28-30ppma(old ASTM). Polysilicon layers were deposited on the back of the samples to a target thickness of 1.2 microns. Samples were doped with Fe and B during the crystal growth process. Samples were cleaned using an HF based cleaning recipe prior to a heat treatment. All the heat treatments were conducted in the oxygen ambient to reduce the in- diffusion of surface contaminants.

Iron concentrations in samples following the various gettering treatments were determined using the surface photovoltage(SPV) and the deep level transient spectroscopy(DLTS) methods. The SPV method of determining the minority carrier lifetime utilizes a very low level($p/p = 10^{-5}$) of excitation. The constant flux method used in this study is discussed in reference 11. Dissociation of Fe-B pairs was achieved by optical illumination using a 250 Watt-halogen lamp. The Fe concentration in the Si were determined by means of DLTS (BIO RAD Model DL 8000) in the single pulse mode. In this method the capacitance transient is digitized and the discrete Fourier coefficients are formed via numerical transformations. Data analysis to calculate the trap properties is carried out using Fourier coefficients¹². To determine the depth profile of iron, DLTS measurements were conducted after etching off various amounts of silicon chemically.

All the gettering experiments were conducted at 600C. The solubility of iron at this temperature is reported to be $< 1 \times 10^{10} \text{ cm}^{-3}$. The initial concentration of iron in the samples was $5 \times 10^{12} \text{ cm}^{-3}$.

RESULTS AND DISCUSSION

To demonstrate the gettering efficiency of samples with polysilicon film on the backside (PB), iron contaminated samples were heat treated at 600 C for various time intervals. All the samples were heat treated for 60 minutes at 1000C prior to the gettering experiments. Figure 1 compares the dependence of iron concentration on the annealing time in samples with polycrystalline film on the back (PB) and the reference sample without the PB surface. The bulk iron concentration was determined using the SPV method from the front side. The concentration of iron in the bulk silicon decreased by a factor of five in the PB samples. On the other hand, no reduction in the iron concentration was detected in the reference sample. These results unequivocally prove the advantageous effect of polycrystalline film in gettering the iron. Similar results were also reported by Hayamizu et al.⁹.

In order to determine the gettering sink for the iron, depth profiles for the concentration of iron were determined by step etching the samples. These samples were analyzed from both the front and the back side using the SPV and DLTS methods (Figures 1-3). The minority carrier diffusion length as a function of the thickness in a representative sample is presented in Figure 2. The sample underwent gettering treatment at 600C for 6hrs. The minority carrier diffusion length measurement were not limited by the thickness in these experiments. The minority carrier diffusion length measurements in these samples were made after the dissociation of FeB pairs; thus the recombination diffusion length was limited by the $\text{Fe}(\text{Ev} + 0.4\text{eV})$ defect (see below). The value of the diffusion length was found to be uniform with depth of approximately up to 550 microns from the front surface. A sharp decrease in the diffusion length from approximately 80

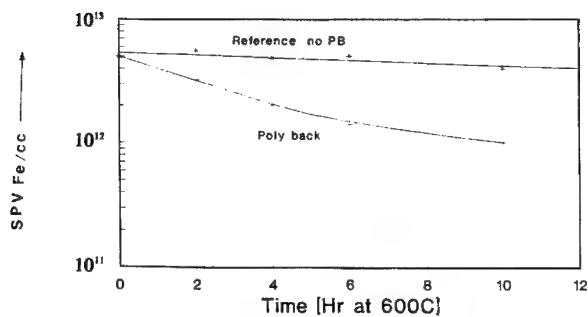


Figure 1. Effect of PB film on the bulk Fe concentration (SPV) after annealing at 600C.

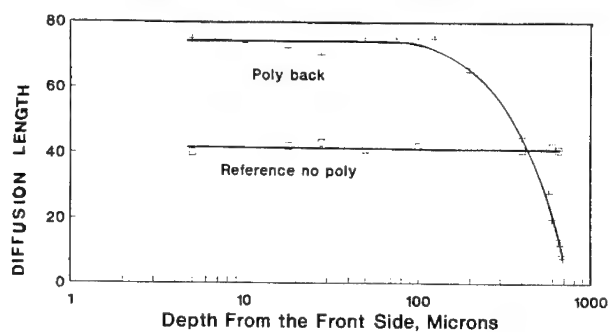


Figure 2. Depth profiles of the minority carrier diffusion length for samples heated at 600C for 6 hours.

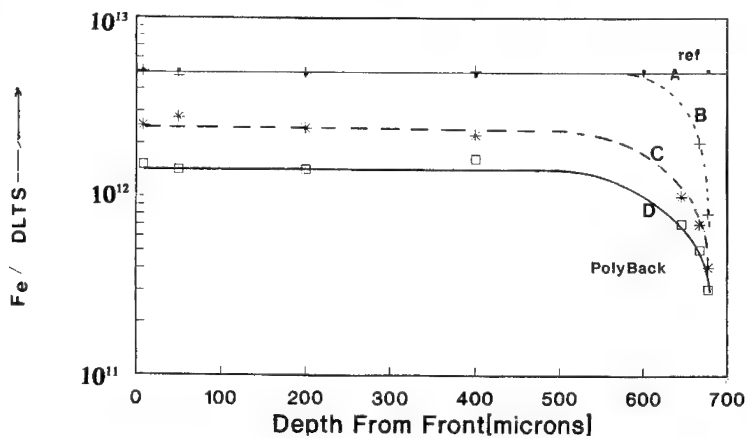


Figure 3. DLTS concentration profiles for Fe in samples heat treated at 600C for A. 0 hrs., B. 2 hrs., C. 4 hrs., and D. 6 hrs.

microns to a value of 9 microns is observed near the back surface region. The enhanced precipitation of SiO_2 near the PB surface has been reported. Since minority carrier diffusion length is sensitive to the oxygen precipitation even at early stages of nucleation, it is suggested that the drop in the diffusion length is caused by small oxygen precipitates formed by extended heat treatment at 600C rather than the iron impurity(see below).

Figure 3 shows concentration vs. depth profiles for iron after 0, 2, 4 and 6 hr at 600C. The initial concentration of iron in the samples was $5 \times 10^{12} \text{ cm}^{-3}$. The concentration of iron in the samples was found to be uniform with the depth except in the region near the back side. A sharp concentration gradient near the back side is observed, i.e., the concentration of iron decreases by a factor of 5-7 in the region. However, the minority carrier diffusion length was found to decrease in the same region (Figure 2) indicating that the defects other than iron is responsible for the degradation in the diffusion length. On increasing the gettering time at 600C, a systematic decrease in the iron concentration is observed over the entire thickness of the sample. It is interesting to note that these concentration profiles can not be described by a simple model of diffusion of iron to an infinite sink at the backside. A sharp concentration gradient for iron at the PB side confirms the diffusion of iron to the backside, at least, during the early stages. However, a parallel mechanism for the loss of iron from the bulk silicon must exist. The enhancement of the oxygen precipitation in the PB sample is reported^{7,8,13,14}. It is proposed here that the majority of iron gettering, under the present experimental conditions, is caused by the enhancement of the internal gettering. On the study of interaction between intrinsic and extrinsic gettering, Yang and Tan¹³ reported that the enhancement of oxygen precipitation in the external gettering sample was caused by the presence of dislocations and/or stress field. The enhancement of precipitation increased monotonically from the front side to the back side¹³.

A detailed study of interaction of iron with oxygen precipitates using the DLTS has revealed, for the first time, a specific phenomenon shown in Figure 4. The peaks at 53K and 220K in the DLTS spectra are attributed to the $\text{FeB}(0.1\text{eV})$ and $\text{Fe}_i(0.4\text{eV})$ defects, respectively. Majority of the iron was found to exist in the unpaired state ($\text{E}_v + 0.4\text{eV}$) near the backside surface whereas the majority of Fe recombined with B to form FeB pairs in the front side. The complete regeneration of FeB pairs could not be obtained in the former case even after annealing the samples at room temperatures for a period of over a month. The phenomenon of the irreversibility of FeB dissociation reaction is important for two reasons: it implies the presence of additional thermal reaction barrier height preventing the pairing reaction; and in some cases, it interferes with the quantitative determination of iron using the minority carrier diffusion length measurement(see below). It is postulated here that the stress associated with the formation of oxygen nuclei at low temperatures provide additional barrier. To test the hypothesis silicon samples with an initial oxygen concentration of 32 ppma were subjected to heat treatments at 1000C for 10 hours and 600C for 10 hours following a nucleation anneal cycle at 600C for 4 hours to generate large and small oxygen precipitates respectively. As reported in Figure 5, complete regeneration of FeB pairs was obtained in the presence of relatively large stress free precipitates. A broad peak in the temperature range of 100 to 180K in the sample heat treated at 1000C is due to the presence of oxygen-precipitation induced defects. On the other hand, the majority of iron is found to be present in the unpaired interstitial form in the samples heat treated at 600C. As expected no change in the minority carrier diffusion length in samples annealed at lower temperature was seen following the optical dissociation indicating the presence of Fe in the interstitial form. At present, the effect of such interaction on the diffusion and subsequent gettering of iron to the back surface is under investigation.

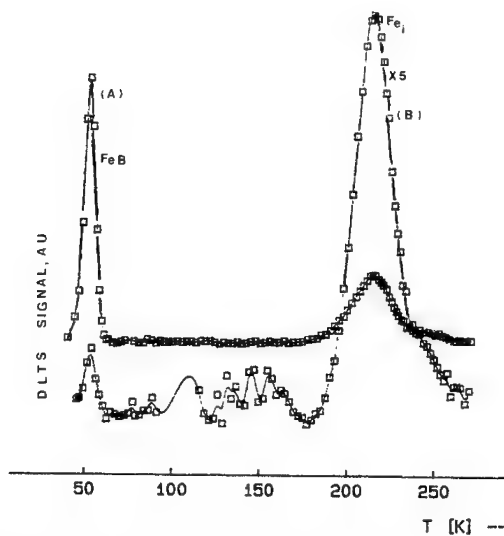


Figure 4. DLTS spectra of Fe doped sample after gettering in the a. front side, and the b. back side near the poly/single crystalline silicon interface.

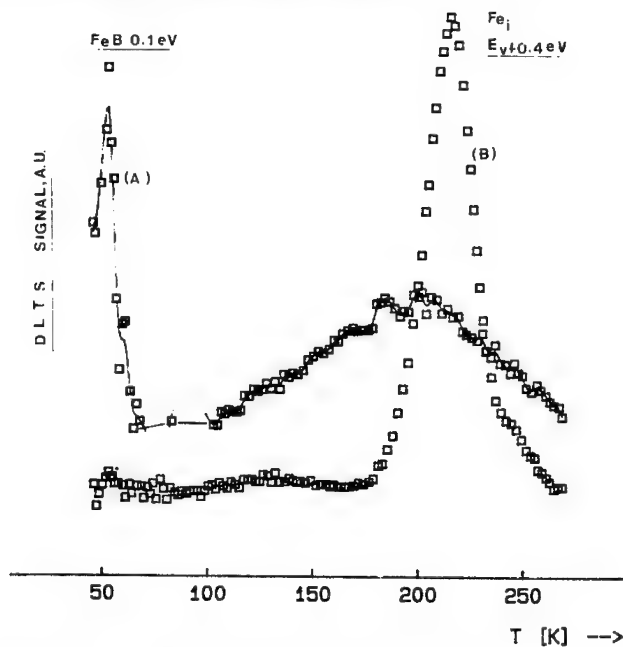


Figure 5. DLTS spectra of Fe containing sample in the presence of a. large precipitates b. small nuclei generated at 1000C and 600C, respectively.

SUMMARY AND CONCLUSIONS

The gettering of iron using the polysilicon film in p-type CZ Si has been studied by monitoring the distribution of iron using the SPV and DLTS techniques. The presence of polycrystalline film on the back surface enhances the gettering of iron at 600°C. A sharp gradient in the iron concentration near the poly/ single crystalline silicon interface observed suggests the diffusion of iron towards the backside. Time resolved study of concentration profiles of iron indicates the presence of a parallel gettering mechanism in the bulk silicon. It is suggested that the enhancement of internal gettering occurs in the PB samples.

This study has revealed that the regeneration of FeB pairs at the room temperature is hindered in the presence of oxygen nuclei/precipitates formed at low temperatures. Further studies are in progress to understand the effect of interaction between Fe and the precipitates on the diffusion and /or gettering of Fe.

ACKNOWLEDGEMENTS

The author would like to thank Lionel Kimerling, Jon Rossi, Harold Korb and D.M. Lee for valuable discussions in the course of this study.

REFERENCES

1. S. M. Hu, Method of Gettering Using Backside Polycrystalline Silicon, United States patent No 4053,335(1977)
2. D. E. Hill, in Defects in Silicon 1983, edited by W. M. Bullis and L. C. Kimerling(the Electrochemical Society, Pennington, N.J., 1983), p.433.
3. H. Yamanaka, H. Kaneko, Y. Haruta and Y. Iwamoto, Jpn. J. Appl. Phys. 32, L738 (1993).
4. J. Partanen, T. Tuomi, M. Tilli, S. Hahn and F. A. Ponce, J. Mater. Res. 4, 623 (1989).
5. G. Keefe- Fraundorf, D.E. Hill, and R.A Craven, in Proc. Conf.EMTAS'83, (Society of Manufacturing Engineers 1983) p. 131.
6. W. T. Stacy, M. C. Arst, K. N. Ritz, J. G. De Groot and M.H. Norcott, Solid State Technol.26, 423 (1983).
7. E. R. Weber and F. Kirscht , in Advanced Science and Technology of Silicon Materials edited by T. Ogawa, (The 145th Committee of JSPS, Kona, Hawaii, 1991) p.476.
8. D. C. Gupta, Solid State Technol. 26, 149 (1983).
9. Y. Hayamizu, S. Ushio and T. Takenaka in Defect Engineering in Semiconductor Growth, Processing and Device Technology, edited by S. Ashok, J. Chevallier, K. Sumino and E. Weber(MRS Proc. 262, Pittsburgh, PA, Vol. 262, 1992) p.1005.
- 10.R. B. M. Girish in Crystalline Defect and Contamination, edited by B. Kolbesen, P. Stallhofer, C. Claeys and F. Tardif (ECS Proc. 93-15, Pennington, N.J., 1983)p. 170.
- 11.J. Lagowski, P. Edelman, O. Milic, W. Henley, Semicond. Sci. Technol. 7A, 185-189(1992).
- 12.S. Weiss and R. Kassing, Solid State Electronics 31, 1733-1742 (198
- 13.K. H. Yang and T. Y. Tan in Impurity Diffusion and Gettering in Silicon, edited by R. B. Fair, C. W. Pearce and J. Washburn (MRS Proc. 36, Pittsburgh PA, 1985) 223.
- 14.J. Borland, *ibid*, 269.

External Gettering Comparison and Structural Characterization of Single and Polycrystalline Silicon

HENRY HIESLMAIR, SCOTT McHUGO AND EICKE WEBER
University of California- Berkeley, Department of Materials Science, Berkeley, CA 94720

ABSTRACT

Various silicon samples, both single and polycrystalline, were intentionally contaminated and externally gettered using phosphorus, aluminum and co- phosphorus/aluminum gettering. Gettering efficiencies were quantified via diffusion length improvements. Structural characterization was used to correlate defects with low gettering efficiencies. External gettering was found to be particularly effective at recovering diffusion length in large grain polycrystalline silicon and solar grade single crystal silicon despite Fe contamination and high defect densities. One of two explanations is possible, 1) the structural defects are initially undecorated and are completely gettered after Fe contamination, or 2) metal decoration on as-grown structural defects are structurally and/or chemically different from intentional Fe decoration.

INTRODUCTION

Many experimental investigations have been made of the gettering phenomena of phosphorous and aluminum layers in single and polycrystalline silicon materials[1, 2, 3, 4]. These have generally shown that single crystal materials and some high diffusion length regions in polycrystalline materials respond well to these external gettering treatments[3, 4]. In contrast, low diffusion length regions in polycrystalline materials, do not improve significantly from these external gettering processes. Recent results have further demonstrated that single crystalline silicon materials, with equivalent initial minority carrier diffusion lengths, are more responsive to these gettering treatments than polycrystalline silicon [3, 5].

Structural defects, such as swirl defects, oxygen precipitates, dislocations, etc., are thought to account for this disparity between high and low diffusion length regions by trapping impurities in their strain fields. Oxygen precipitates, for instance, are better internal getterers and do not re-emit metals into the bulk as easily when they have a high strain field associated with them[6]. Structural defects, so decorated, become highly active recombination centers, lowering the minority carrier diffusion length.

The theoretical nature of the gettering mechanisms have been studied and proposed by numerous researchers. The gettering action of the phosphorous doped layer is explained by W. Schröter and R. Kühnapfel [1], as a combination effect of Fermi-level enhanced solubility in the P layer, and a large silicon interstitial drift (or wind) toward an interstitial sink such as stacking faults. These interstitial are thought to also migrate toward a silicon interface near SiP particles, resulting in essentially an epitaxial growth which, if metals are present, leads to an epitaxial silicide growth. J.S Kang and D.K.Schroder [2] contend that all external gettering is an effect of differences in metal solubilities, without the Fermi-level effects. They propose a model with two rate-limiting steps: 1) below the optimum temperature where the gettering process is hindered by the release of impurities or the diffusion of impurities, and 2) above the optimum temperature where gettering is governed by the segregation model. The segregation phenomena is a result of differing energies of formations, ΔH , of the impurities in the bulk silicon and in the gettering layer.

In materials with a high number of structural defects, an external gettering process must therefore 1) release the impurities from the strain fields of the structural defects which hold them, 2) provide reasonable diffusion times to the gettering layers, and 3) provide a layer with orders of magnitude higher solubilities of the impurities than the bulk silicon or the local vicinities of the structural defects.

PROCEDURE

The samples used in this gettering study included EFG, cast ingot poly-silicon, magnetic Czochralski, and three types, labeled 'A', 'B', and 'C', of solar grade Czochralski silicon materials. Two of these materials, 'B' and 'C', are from the same vendor and differ by carbon content only. The samples labeled 'C' contain greater than 10^{17} carbon /cm³. All samples were first etched and then measured with SPV to determine initial minority carrier diffusion lengths. After depositing iron on the back sides, the samples were then annealed at 950°C for 40 minutes and quenched to room temperature in ethylene glycol. This quenches in iron at a concentration of 1.4×10^{14} /cm³ uniformly throughout the samples. The samples were then cleaned and etched to remove any silicide, and re-measured with SPV.

For samples to be gettered with an aluminum layer, 3.2 microns of Al (with 2% Si) are sputtered onto the backs of the samples. For the samples to be phosphorous gettered, a film of spin on glass is applied to the front side of the samples. The samples which are co-gettered have an aluminum layer on the back and a phosphorous layer on the front. All these samples were exposed to 1000°C for 15 minutes and then 850°C for 2 hours and 45 minutes for a total process time of three hours. The samples were then cleaned, etched and measured with SPV for the final minority diffusion length. Some samples were then polished and preferentially etched with a Schimmel [7] etch to observe dislocations and microdefects.

RESULTS AND DISCUSSION

Gettering Methods

The SPV results show that for all materials the diffusion length is between 9 and 15 microns after iron in-diffusion and quench. Furthermore, the 850°C gettering temperature would represent an equilibrium iron concentration of 10^{13} cm⁻³. The results of the gettering experiments are shown in Figures 1, 2 and 3. The graphs plot initial minority carrier diffusion lengths vs. final minority carrier diffusion lengths. The percent recoveries are indicated by the diagonal lines.

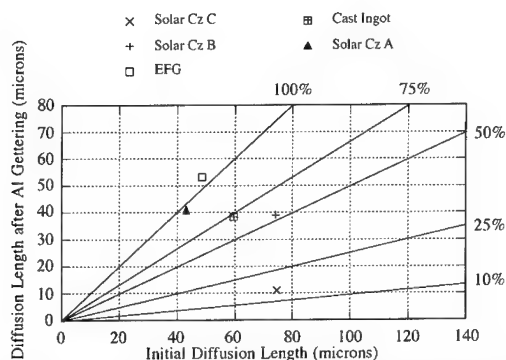


Figure 1: Initial minority diffusion length vs. final minority diffusion length after aluminum gettering. The diagonal lines represent percentage recoveries.

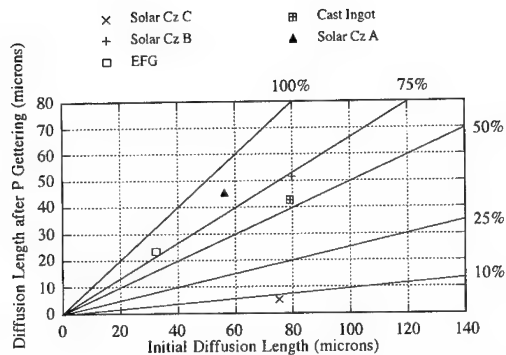


Figure 2: Initial minority diffusion length vs. final minority diffusion length after phosphorous gettering. The diagonal lines represent percentage recoveries.

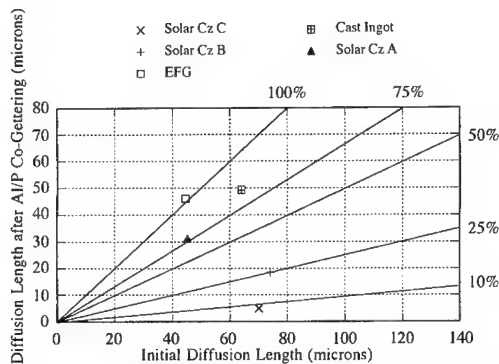


Figure 3: Initial minority diffusion length vs. final minority diffusion length after aluminum-phosphorous co-gettering. The diagonal lines represent percentage recoveries.

All three of the gettering treatments seem to be equivalent, with the aluminum and aluminum/phosphorous co-gettering yielding slightly better results for cast ingot and EFG materials. Results from the magnetic Czochralski are presented in Table I. This material responds very well to aluminum/phosphorous co-gettering and worst to aluminum gettering. The responses varied from 48% to 136%.

Table I: Magnetic Czochralski silicon material

	As Grown (μm)	After Gettering (μm)	Response
Al Gettering	420	202	48%
P Gettering	200	185	92%
Al/P Gettering	338	460	136%

Various structural defects are associated with each material and give rise to different behaviors. Each type of material is further discussed below.

EFG and Cast Ingot

Both of these materials are poly-crystalline with regions of low and high dislocation densities as shown in Figure 4. These dislocations could trap impurities during growth and

cooling. We expect that the intentional introduction of iron increases the amount of decoration of these defects. Yet the gettering responses are rather high, between 75% and 100%.

One of two explanations is possible for this. First, the as-grown dislocations have little or no metal decoration. The Fe in-diffusion then decorates the dislocations and the gettering process then re-absorbs the iron, leaving the dislocations clean again. Thus the clean dislocations alone are responsible for low initial diffusion lengths. This is unlikely since Higgs et al[8] has shown that clean dislocations have little or no recombination activity.

The other explanation is that the as-grown defects are already decorated and thus have an increased recombination activity. The in-diffusion of iron increases the amount of decoration, but this decoration is different from the as-grown decoration. In other words, the decoration which occurs during growth and cooling is structurally and/or chemically different from decoration taking place during intentional contamination. Upon gettering, most of the decoration from intentional contamination is re-absorbed from the dislocations, but the as-grown decoration is fixed and undisturbed.

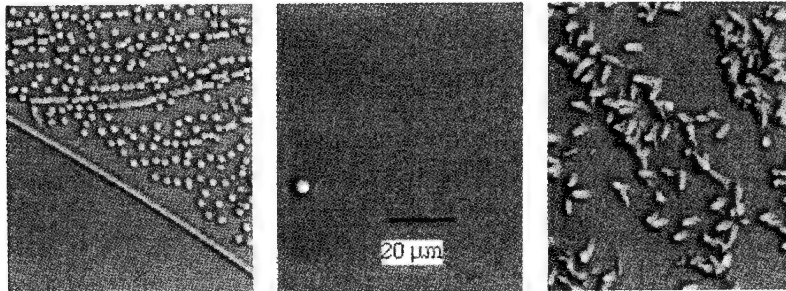


Figure 4: Cast ingot silicon material (left) and EFG regions of low (center) and high (right) dislocation densities after iron in-diffusion and gettering

Solar Grade Czochralski Silicon A, B, and C

All of these materials are grown with conventional Czochralski methods. Defects, i.e. oxygen precipitates, are found in the as-grown state as well as after iron in-diffusion and gettering. This can be seen in Figure 5. The A type material, and to a lesser extent, B type materials, behaved similarly as the cast ingot and EFG materials. Gettering response was also in the 75% to 100% range with the B materials performing slightly worse. The explanation for this relatively good response is similar to that of the cast ingot and EFG materials. Either the oxygen precipitates have no decoration in the as-grown state and are completely gettering after Fe contamination, or the as-grown decoration is qualitatively different from the intentional in-diffused Fe decoration.

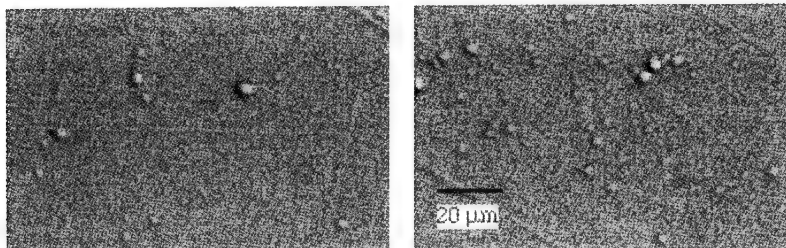


Figure 5: Solar grade Czochralski silicon 'A' before (left) and after (right) iron in-diffusion and gettering

The B and C solar grade Czochralski silicon materials gave us an opportunity to observe the influence of carbon on the gettering process since the C samples have a carbon concentration of $>10^{17} \text{ cm}^{-3}$. We had expected to see a greater number of structural defects in the high carbon materials since their recovery was so poor. Yet all Czochralski samples had approximately similar numbers of defects as shown in Figures 5 and 6. Therefore, carbon must be playing a different role. One possibility is that the carbon is binding the iron in iron-carbide precipitates which may not necessarily be seen in preferential etching. This may have serious implications for EFG materials which have high carbon and iron concentrations.

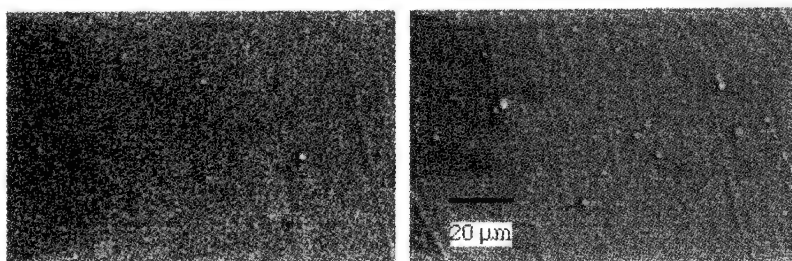


Figure 6: Solar grade Czochralski silicon 'B' (left) and 'C' with $>10^{17}$ carbon / cm^3 (right)

Magnetic Czochralski

These samples had a spectrum of recoveries from about 48% to 136%. This may at first seem surprising but it should be pointed out that the final minority carrier diffusion lengths (after gettering) were all well above 100 microns. These materials have thus improved from roughly 12 micron diffusion lengths after iron diffusion to between 185 to 460 microns. The maximum recovery was realized for the aluminum/phosphorous co-gettering. Furthermore, aluminum gettering was the poorest treatment which is in contrast to the polysilicon materials in which aluminum gettering performed slightly better than phosphorous gettering. The as-grown structural defects, possibly swirl defects, are distributed inhomogeneously and possibly may not be seen without metal decoration. A preferential etch reveals these structural defects in the aluminum-phosphorus gettering sample and is shown in Figure 7. Despite these defects, this material improved 136%. An as-grown sample was also etched and shown in Figure 7, but does not exhibit any structural defects either because there are none in this region of the wafer or the defects are not decorated.

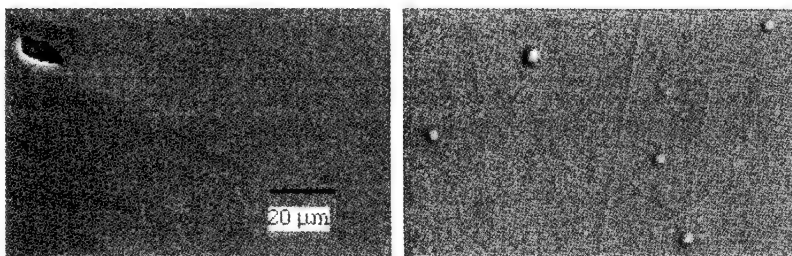


Figure 7: Magnetic Czochralski before (left) and after (right) iron in-diffusion and gettering

CONCLUSIONS

We have attempted to correlate gettering responses to microstructures in solar grade silicon materials. We have observed polysilicon materials with relatively high gettering recoveries of

between 75% and 100% and containing regions of both low and high defect densities. Solar grade Czochralski silicon materials showed similar responses. This is a result of either 1) complete gettering of intentionally decorated structural defects (dislocations, oxygen precipitates, etc.) which were completely undecorated in the as-grown state, or 2) the as-grown decoration on the structural defects being structurally and/or chemically different from the intentional Fe decoration which is removed by the gettering treatments. Since low diffusion length regions are associated with high structural defect densities, and since structural defects increase in recombination activity with metal decoration, the second explanation may be more plausible.

We had expected to find higher defect densities in the carbon Czochralski materials since these materials had extremely poor gettering responses. We have not seen significantly higher defect densities. This indicates that there are other interactions between carbon and intentional iron which do not respond to gettering. We have shown the decoration of defects in magnetic Czochralski silicon upon iron in-diffusion and gettering with a spectrum of gettering recoveries between 48% and 138%.

REFERENCES

1. W. Schröter and R. Kühnappel, Applied Physics Letters **56**, 2207 (1990)
2. J. S. Kang and D. K. Schroder, Journal of Applied Physics **65**, 2974 (1989)
3. J. Bailey, Scott A. McHugo, Henry Hieslmair, Eicke Weber, Jour. of Elec. Matls. submitted in Sept. 1994 as part of the July 1994 EMC conference, (1994)
4. J. Bailey, J.P. Kalejs, C. Keaveny, presented at First World Conference on Photovoltaic Energy Conversion, Dec 5-10, 1994
5. Scott A. McHugo, Jeff Bailey, Henry Hieslmair and Eicke R. Weber, presented at First World Conference on Photovoltaic Energy Conversion, Dec 5-10, 1994
6. S.A. McHugo, E.R. Weber, M. Mizuno and F.G. Kirscht, to be published in Appl. Phys. Lett., May 22, 1995
7. ASTM, in *ASTM Annual Book of Standards* p. 620
8. V. Higgs, E. C. Lightowers, C. E. Norman and P. Kightley, Proc. ICDS, Lehigh University, USA 1992, in print.

EFFECT OF P-DOPING LEVEL- POCl_3 DIFFUSED OR SPIN-ON DEPOSITED- ON THE GETTERING EFFICIENCY OF POLYCRYSTALLINE SILICON AFTER RTA OR CTA

M. LOGHMARTI*, K. MAHFOUD, J.C. MULLER, D. SAYAH* AND P. SIFFERT
Labo. PHASE (UPR du CNRS n°292), BP 20, F-67037 Strasbourg cedex France.

* Laboratoire de physique des matériaux. Rabat. Morocco.

ABSTRACT

Large grain polycrystalline silicon wafers have been subjected to post-thermal annealing after a POCl_3 pre-diffusion or after a phosphorus doped silica-film deposition ($10^{19}\text{P}/\text{cm}^3$ - $2.10^{21}\text{P}/\text{cm}^3$). The different doping levels are obtained by a dilution of the P-doped SOG ($2.10^{21}\text{at}/\text{cm}^3$) in a undoped SOG solution. For the first time we have achieved the maximum of the gettering efficiency after post-thermal annealing. The best combination of post thermal cycle parameters and doping level improves the minority carrier diffusion length of quite (300% to 400%) for POCl_3 pre-diffused samples and (200% to 275%) for spin-on P-doped (P-SOG) polycrystalline silicon.

Introduction

The minority carrier diffusion length is an important parameter which give information on n^+p polycrystalline silicon junction before and after each thermal treatment. Fabrication of acceptable solar cells from such material require processes that are tolerant or that can even improve poor materials.

Gettering refers to a process step that removes deleterious impurities from active regions of the device to less important regions. Typically, gettering requires several actions to occur. First, the unwanted impurity must be placed into solid solution in the silicon crystal. Next, it must be mobile. Finally a site must be provided that is in less important region of device as grain boundary in case of polycrystalline silicon. The gettering agent (P, Al, B...) must be present in gettering sites to capture the metallic impurities and others.

A well-known technique for gettering in silicon is Phosphorus diffusion [1-4]. Phosphorus concentration play an important role in the gettering efficiency. Experiments have shown that metal impurities migrate and trapped in heavily doped phosphorus layer.

In this paper we have studied the effect of doping level on gettering efficiency of polycrystalline silicon.

The n^+p junctions were realised firstly by POCl_3 diffusing and by phosphorus doped silica-film (Spin-on oxide glass SOG) deposition. The doping level was controlled by diffusing temperature and duration of POCl_3 pre-diffusion or by a dilution of phosphorus doped silica-film (P-SOG : $2.10^{21}\text{at}/\text{cm}^3$) by the undoped (SOG) solution. The phosphorus

surface concentration was varied from 10^{19} P/cm³ to 2.10^{21} P/cm³. A series of classical and rapid thermal annealing was performed on phosphorus doped polycrystalline silicon, in order to achieve the maximal gettering efficiency.

Experimental

Our study was carried out on 2.5×2.5 cm² P-type low quality polycrystalline silicon ($35 \mu\text{m} < L_n < 45 \mu\text{m}$) with thickness of about $340 \mu\text{m}$ and resistivity of $0.8 \Omega\text{cm}$. The n^+pn^+ structures were realised by two techniques: A first group of samples was initially bifacial pre-diffused using POCl₃ gas. The control of doping level is assured by the variation of pre-diffusing temperature from 800°C to 900°C and duration from 10 min to 30 min. A second group of samples was coated by 2000\AA thick phosphorus doped silica (SOG) films provided by Emulsitone Co (USA), (concentration 10^{19} P/cm³ to 2×10^{21} P/cm³) and deposited by the spin-on technique. The samples were prebacked for 15 min at 250°C using a hot plat.

The P-SOG structures were rapid thermal annealed (RTA) using furnace (F4V4 model of JIPELEC, Grenoble, France) which is characterised by "cold walls" ($< 250^\circ\text{C}$ for a wafer temperature processed at 1100°C).

The minority carrier diffusion length was determined with surface photovoltage technique (SPV) [5]. This technique presents many advantages, such as to be simple, fast (15 min), there is no need for permanent contacts and there is no complication arising from junction fabrication. The average bulk diffusion length has been studied before and after the post-thermal treatment on a great number of samples and for many positions of the probe in order to increase the statistic.

Results and discussion

Figure 1 shows the evolution of bulk minority carrier diffusion length L_n with classical annealing temperature (800°C - 1000°C) and annealing duration (1min-180 min), the POCl₃ pre-diffusing condition is $825^\circ\text{C}/20$ min. The classical (CTA) and rapid (RTA) thermal annealing conditions are presented in table 1. The detailed study of CTA optimising of gettering efficiency is described in previous work [6].

Table 1. Classical and rapid thermal conditions of post-annealing

	CTA	RTA
Heating rate	$10^\circ\text{C}/\text{min}$	$300^\circ\text{C}/\text{sec}$
Annealing temperature	800°C - 1000°C	850°C
Annealing duration	1mn-180 min	25sec
cooling rate	$2^\circ\text{C}/\text{min}$	$200^\circ\text{C}/\text{sec}$

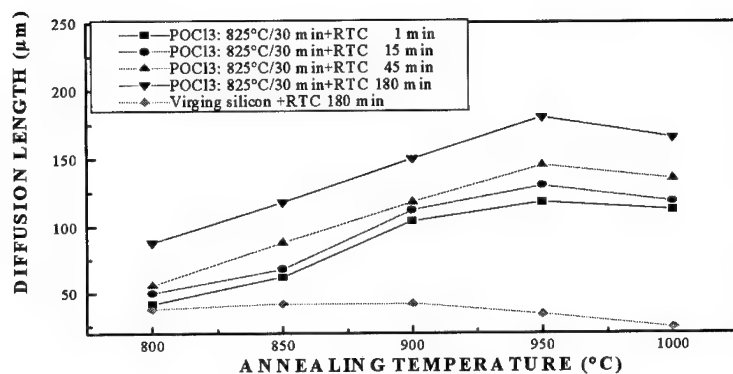


Figure 1: Effect of annealing temperature and duration on diffusion length of POC13 diffused polycrystalline silicon (Initial value of L_n : 40 μm)

The initial distribution of L_n value (L_n across the wafer) is ranged between 30 and 43 μm .

After CTA (Fig 1), the bulk minority carrier diffusion length of the undoped sample remains nearly constant around 43 μm for annealing temperature lower than 900°C. Towards higher annealing temperatures a slightly decrease of the minority carrier diffusion length is observed. This reduction is probably due to the activation of the residual metallic impurities, which degraded the volume of the grains or their boundaries. Nevertheless the gettering efficiency of phosphorus doping is clearly demonstrated by comparison to undoped samples.

For POC13 pre-diffusing samples there is a strong improvement of diffusion length. The gettering efficiency depends on the temperature and duration of annealing; the improvement percentage ($\Delta L_d/L_{d0}$) is of 20%, 100%, 200% and 350% respectively for annealing temperature and duration of 800°C/1min, 800°C/180 min, 950°C/1min and 950°C/180 min. The metallic impurities are highly mobile and diffuse long distances in the crystal at moderate temperatures. For example, Cu can diffuse about 600 μm in 1 min at 900 °C, and Fe 3000 μm in 30 min at 1000 °C. This is a reason why long annealing durations are required.

To explain this high gettering efficiency further, different mechanisms, presented in the literature, could be pointed out, i.e. the enhanced solubility of metallic impurities, which act as acceptors, and their enhanced pairing with phosphorus within the highly n^+ -doped layer [7,8]. The solubility of metallic impurities such as Au and Cu is increased with the doping concentration through enhanced metal-solid solubility by the position of the Fermi level and ion pairing. Compound formation between metal and phosphorus atoms also enhances the solubility of some metallic impurity as Au. It has been reported that a Au_2P_3 and Cu_2P_3 compound are observed in highly n^+ -doped silicon [9,10]. Ourmazd and Schroter [11] have found that NiSi_2 particles are closely associated with the SiP particles and are most frequently observed in regions containing a high density of SiP particles. They proposed that phosphorus causes SiP particles formation, which leads to a large emission of silicon interstitial, due to a volume expansion. The post-thermal annealing of heavy phosphorus doped polycrystalline silicon is required in order to make the segregation more efficient and to move metal impurities into the phosphorus doped n^+ -region. A maximum gettering

efficiency result from the association of higher generation of gettering sites and higher phosphorus concentration.

The common extrinsic gettering process by phosphorus diffusion is well documented [12,13]. Recently, Kang and Schroder [14] have proposed a gettering model which involves two-rates limiting steps: (1) the released diffusion of metallic impurities which determine the lower-temperature limit during gettering, and (2) the segregation model which governs the gettering above the optimum temperature. in our case, the critical temperature, which gives the highest gettering efficiency, range from 900°C and 950°C.

Fig2 shows the effect of CTA temperature (during 180min) for different samples pre-diffused at 800°C/10min, 850°C/10min, and 900°C/10min. The gettering efficiency increases with increasing of POCl₃ pre-diffusing temperature and reach 400% corresponding to an increasing of diffusion length from 40µm to 200µm. For temperature higher than 950 °C, the gettering efficiency decreases dramatically from 400% to less than 175%, perhaps higher annealing temperature around 1000°C induced structural defects which are not compensated by phosphorus gettering. For lower prediffused temperature, the phosphorus diffusion was not sufficiently heavy to produce a maximal gettering. Our results show that the optimal phosphorus concentration to obtain maximal gettering is about $7 \times 10^{20} \text{P/cm}^3$ corresponding to POCl₃ pre-diffusing conditions of 900°C/10min.

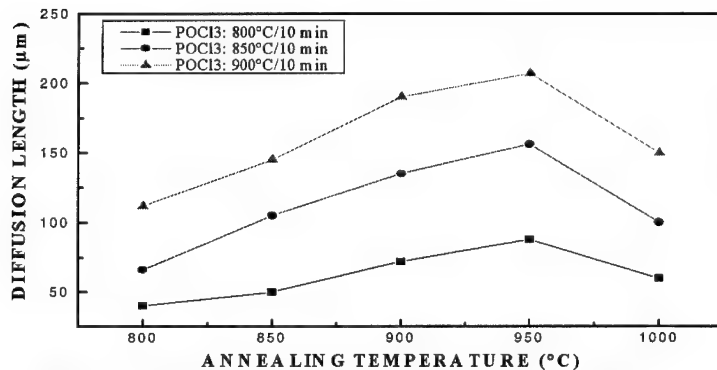


Figure 2: Effect of annealing temperature (180 min) on diffusion length for different POCl₃ diffusion temperature (Initial value of L_n : 40 µm)

The evolution of bulk diffusion length for P-SOG diffused samples is reported in Fig 3 as function of phosphorus doping level after CTA and RTA. Result shows that for RTA, there is a degradation of L_n when P-concentration is below 10^{20}at/cm^3 ; in this case, phosphorus concentration is not sufficiently important to produce gettering, so the most residual metallic impurities are not gettered, but activated by the quenching step. When P-concentration increases, gettering efficiency increases and reaches 100% (L_n : 40µm→80µm) for P-concentration of $2 \times 10^{21} \text{P/cm}^3$. For CTA treatment, there is no degradation of L_n for lower doping level, and the maximal gettering efficiency is of about 250% corresponding to doping

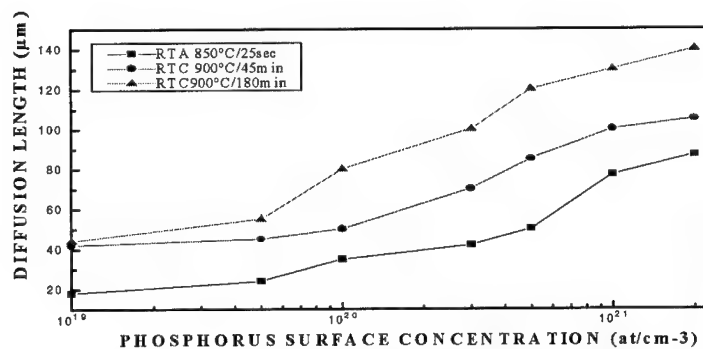


Figure 3: Effect of doping level on diffusion length of P-SOG/poly-Si at different doping level after RTA (850°C/25sec and CTA (900°C/45 min and 900°C/180 min) (initial value of L_n : 30 μm)

level of 2×10^{21} P/cm³ (SOG) and CTA condition of 900°C/180 min. This result is nearly comparable to result found for POCl₃ diffused sample (825°C/20 min) where phosphorus concentration is only of about 1.5×10^{20} at/cm³. The strong improvement of gettering efficiency was specify to use of this highly purified and highly phosphorus doped source (P-SOG/Si, POCl₃/Si), in this case, the solubility limit is reached so that precipitates are present to enhance the gettering effect.

Conclusion

These results confirm that rapid thermal gettering can be effective only for P-SOG concentration superior to 10^{20} at/cm³. The best choice of post-thermal annealing (CTA) and phosphorus concentration lead to 400% minority carrier diffusion length improvement for POCl₃ diffusing technique and 275% for P-SOG (2×10^{21} at/cm³) diffused samples.

We are able to transform bad and lower cost polycrystalline silicon substrates into ones, by gettering, comparable to good monocrystalline silicon in performance.

References

1. S. Wolf, R.N. Tauber, Silicon processing for VLSI Era, volume 1, Process Technology. Lattice press, Sunset Beach (California), (1986).
2. M. Loghmarti, R. Stuk, J.C. Muller, D. Sayah, P. Siffert. Appl. Phys. Lett. 62(9), 979 (1993).
3. G.F. Cerofolini, M.L. Polignano, H. Bender, C. Clays. Phy. Stat. Sol (a). 103, 643 (1987).
4. M.L. Polignano, G.F. Cerofolini, H. Bender, C. Clays, J. Reffle. Phy. Stat. Sol (a). 103, 307 (1987).

-
5. A.M. Goodman. J. Appl. Phys. 32, 2250 (1961).
 6. M. Loghmarti, K. Mahfoud, L. Ventura, J.C. Muller, D. Sayah, P. Siffert. To be published in J. Phys III.
 7. S.L. Chou and J.F. Gibbons, J. Appl. Phys. **46**, 1197 (1975)
 8. D. Lecrosnier, J. Paugam, G. Pelous, F. Richou and M. Salvi, J. Appl. Phys. **52**, 5090 (1981)
 9. W.R. Wilcox, T.J. Lachapelle and D.H. Forbes, J. Electrochem. Soc. **111**, 1377 (1964)
 10. E.D. Wolley and R. Stickler, J. Electrochem. Soc. **114**, 1287 (1967)
 11. A. Ourmazd and W. Schroter, Appl. Phys. Lett. **45**, 781 (1984)
 12. I. Perichaud, S. Martinuzzi. Twety second IEEE Photovoltaic Specialist conference, 877 (1991).
 13. M. Yoneta, Y. Kamiura, F. Hashimoto. J. Appl. Phys. 70 (3), 1295 (1991).
 14. J.S. Kang, D.K. Schroder. J. Appl. Phys. 65, 2974 (1989).

Part V

**Hydrogen Interaction with
Semiconductors**

SPECTROSCOPY OF TRANSITION-METAL-HYDROGEN COMPLEXES IN SILICON

MICHAEL STAVOLA, S.J. UFTRING, M.J. EVANS, P.M. WILLIAMS AND G.D. WATKINS
Department of Physics, Lehigh University, Bethlehem, Pennsylvania 18015

ABSTRACT

Transition-metal-hydrogen complexes have been introduced into bulk Si samples that contained Pt, Au, or Rh by the indiffusion of hydrogen at 1250°C from H₂ gas. The structure and electrical properties of a PtH₂ complex in Si have been studied by vibrational spectroscopy and electron paramagnetic resonance (EPR). The PtH₂ complex has been found to introduce two levels in the Si bandgap. There is one paramagnetic charge state for which EPR provides detailed structural information and two nonparamagnetic charge states. The hydrogen vibrations of all three charge states of PtH₂ have been assigned. In addition to the PtH₂ complex, the hydrogen vibrations of several additional complexes in Si samples that contain hydrogen and Pt, Au, or Rh have been identified.

INTRODUCTION

Hydrogen-passivated shallow impurities in semiconductors have been studied extensively in recent years and much progress has been made toward understanding the structures and properties of these defect complexes.¹⁻⁴ The hydrogen passivation of deep-level impurities⁵ has remained poorly understood because, in part, the application of structure-sensitive spectroscopic techniques has been difficult. For example, in pioneering studies of deep level passivation, the deep level transient spectroscopy (DLTS) features of deep level defects were shown to disappear following exposure to a hydrogen plasma.^{5,6} In recent work, new DLTS features have been assigned to Au-H complexes in Si samples containing Au that had received a wet chemical etch.^{7,8} Plasma exposure or etching introduces hydrogen into surface layers that are only a few microns thick. This does not lead to a sufficient number of hydrogenated deep centers to study by techniques like electron paramagnetic resonance (EPR) or vibrational spectroscopy because of the low solubility of typical deep level impurities.

There have been a few cases where hydrogen has been introduced into *bulk* samples, either during crystal growth or by annealing in H₂ at elevated temperature.⁹⁻¹⁵ For example, Kahn *et al.*¹⁶ have studied a CuH₂ complex in Ge. Shallow acceptors in Si can also be passivated by annealing in H₂ at high temperature and quenching to room temperature.^{14,15} Recently, the introduction of hydrogen into *bulk* Si has permitted samples to be fabricated with a sufficient number of hydrogenated transition metal impurities to be studied by EPR¹⁷⁻²¹ and infrared (IR) absorption^{17,18,21} spectroscopies. A PtH₂ center has been identified by EPR and the hydrogen vibrations of this defect have been assigned. Surprisingly, it was found that the Pt is not strictly passivated and that the PtH₂ center introduces two levels in the band gap.^{17,18,21}

In this paper we describe recent IR absorption and EPR results for a few transition-metal-hydrogen complexes in Si. The PtH₂ complex is understood best and is the focus of most of this paper. In addition to the PtH₂ center, the hydrogen vibrations of several complexes in Si samples that contain hydrogen and Pt, Au, or Rh have been identified. Results for these additional centers will be discussed briefly.

EXPERIMENTAL PROCEDURES

Samples for our experiments were prepared from both n- and p-type Si grown by the floating-zone method. The samples were doped with $[P] = 3 \times 10^{16} \text{ cm}^{-3}$ and $[B] = 2 \times 10^{15} \text{ cm}^{-3}$ for the n- and p-type samples, respectively. Transition metal impurities were introduced by diffusion in sealed quartz ampoules in a He ambient followed by a quench to room temperature in ethylene glycol. Diffusion times between 24 and 72 h were used. (Results for Pt, Au, and Rh are shown below.) To introduce H and/or D into the transition-metal-diffused Si, the samples were subsequently sealed in quartz ampoules with 0.66 atm of H_2 , D_2 , or mixtures of both, annealed at 1250°C for 30 min, and then cooled rapidly to room temperature by removal from the oven.

The Pt concentration in some samples was varied to help change the position of the Fermi level. From previous solubility data,^{22,23} diffusion temperatures of 975 and 1250°C were selected so as to produce samples with Pt concentrations of $4 \times 10^{15} \text{ cm}^{-3}$ and $1 \times 10^{17} \text{ cm}^{-3}$. In the following, these are referred to as the low-Pt and high-Pt samples. These Pt concentrations were chosen so that in the low-Pt, n-type samples, the Fermi level would be near the P level at $E_C - 0.045 \text{ eV}$. In the high-Pt samples the Fermi level position will be determined by the Pt impurity's deep levels,^{23,24} i.e., by the Pt acceptor level at $E_C - 0.23 \text{ eV}$ in n-type starting material and the Pt donor level at $E_V + 0.32 \text{ eV}$ in p-type starting material.

IR absorption measurements were made with a Bomem DA3.16 Fourier transform spectrometer that was equipped with a KBr beamsplitter and InSb and HgCdTe detectors. Most spectra were recorded with a resolution of 0.35 cm^{-1} . A $4.5 \mu\text{m}$ long-pass filter was inserted before the sample for some of our experiments. EPR measurements were performed on a 14 GHz balanced bolometer spectrometer, at 8.5 K in dispersion.

THE PARAMAGNETIC CHARGE STATE OF THE PtH_2 COMPLEX

In the hydrogenated high-Pt, n-type samples, the $S = 1/2$ EPR spectrum shown in Fig. 1 was observed.¹⁷⁻²⁰ This spectrum was assigned to a PtH_2 complex by the observation of hyperfine interactions with a single ^{195}Pt nucleus ($I = 1/2$, 33% abundant) and two equivalent hydrogen nuclei ($I = 1/2$, 100% abundant). The change in the hyperfine structure upon the substitution of D ($I = 1$) for H confirmed this assignment. The anisotropy of the g and ^{195}Pt hyperfine tensors

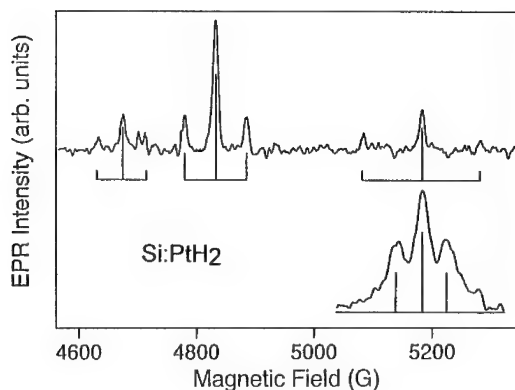
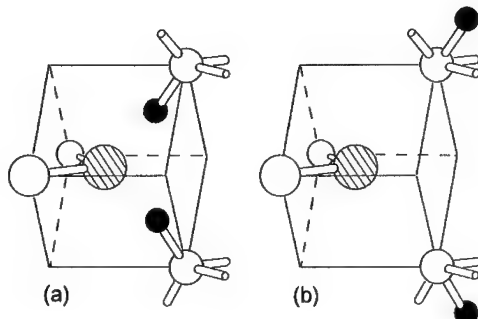


Figure 1. EPR spectrum assigned to the PtH_2 defect measured at $T = 8.5 \text{ K}$ by monitoring dispersion in adiabatic fast passage with $\mathbf{B} \parallel \langle 110 \rangle$. The spectrum in the inset was recorded at higher resolution for the center line in the spectrum above and shows a 1:2:1 intensity pattern characteristic of hyperfine interactions with two equivalent hydrogen atoms. (The magnetic field axis is expanded by a factor of 12)

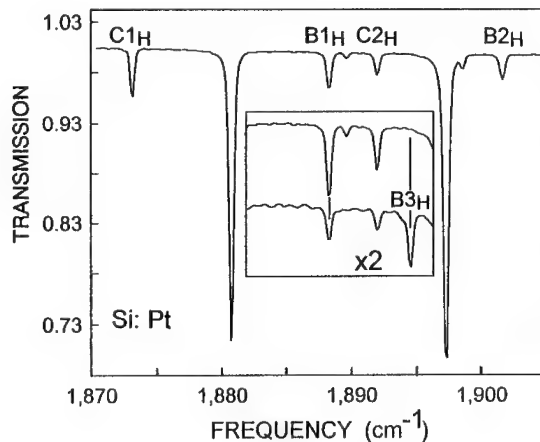
Figure 2. Tentative models for the PtH_2 complex in Si. The Pt atom is shown shaded. The H atoms are drawn black. In (a) the weak Si bonds are terminated by H atoms that point toward the Pt atom. In (b) the H atoms point away from the Pt atom. Although the Si atoms are drawn on their lattice sites, there may be substantial relaxations that are not shown.



showed that the center has C_{2v} symmetry and the model shown in Fig. 2(a) was tentatively proposed for the defect.¹⁷ The rationale for the model was that isolated substitutional Pt^- , which has been extensively studied by EPR,²⁵ also has C_{2v} symmetry, with the Pt atom displaced off-center toward two of its Si neighbors. The remaining Si bonds were therefore suggested to be terminated by hydrogen atoms, as shown, retaining the C_{2v} symmetry.

IR absorption spectra were measured for the same samples that were used in the EPR experiments and several new hydrogen stretching modes were observed.^{17,18,21} A spectrum is shown in Fig. 3. The vibrational bands $B1_H$, $B2_H$, $C1_H$, and $C2_H$ decay together upon subsequent annealing and are eliminated together by a 30 min anneal at 600°C . The PtH_2 EPR signal has very similar annealing behavior. In a variety of samples and under different measurement conditions, the lines $B1_H$ and $B2_H$ always appear with the same relative intensity. Further, when a high-Pt sample was annealed in a mixture of H_2 and D_2 , a new band, $B3_H$, appeared. (See the inset in Fig. 3). The band $B3_H$ was assigned to the hydrogen-stretching mode of the PtHD complex (in this case decoupled by the frequency difference between the H and D vibrations) and confirms that $B1_H$ and $B2_H$ are the vibrations of a center that contains two equivalent hydrogen atoms. Thus, the bands $B1_H$ and $B2_H$ were assigned²⁶ to the two weakly coupled hydrogen-stretching modes of the paramagnetic charge state of the PtH_2

Figure 3. Infrared absorption spectrum measured at 4.2 K for n-type Si that contains Pt and hydrogen. The inset shows vertical expansions of the vibrational bands of the PtH_2 (upper) and PtHD (lower) complexes.



	n-2	n-1	n
PtH ₂	1889.6 (A1 _H)	1888.2 (B1 _H)	1873.1 (C1 _H)
	1898.0 (A2 _H)	1901.6 (B2 _H)	1891.9 (C2 _H)
PtHD	1893.9 (A3 _H)	1894.6 (B3 _H)	1880.3 (C3 _H)
	1367.5 (A3 _D)	1366.9 (B3 _D)	1361.0 (C3 _D)
PtD ₂	1363.3 (A1 _D)	1362.5 (B1 _D)	1352.4 (C1 _D)
	-----	1370.7 (B2 _D)	1365.2 (C2 _D)

Table I. Infrared bands assigned to the three charge states of the PtH₂ complex in Si.²¹ The paramagnetic charge state, n-1, has vibrational bands labeled B. The two nonparamagnetic charge states, n-2 and n, have vibrational bands labeled A and C, respectively. Frequencies are given in cm⁻¹.

complex.^{17,18,21} There are also corresponding vibrational bands in the deuterium stretching region of the spectrum. Table I contains a list of the hydrogen and deuterium vibrational bands assigned to the PtH₂, PtD₂, and PtHD complexes. Corresponding bands are labeled similarly with subscripts that indicate whether the band is an H- or D-stretching vibration.

Uniaxial stress studies have also been performed for the hydrogen vibrational bands observed in the n-type, high-Pt samples.^{18,21} The stress splittings of the vibrational bands B1_H and B2_H are consistent with C_{2v} symmetry. These results also showed that the transition moment for band B2_H is along the C₂ principal axis of the center and for B1_H is along the perpendicular <110> principal axis that is in the plane that contains the two hydrogen atoms. Thus, B2_H was assigned to the symmetric hydrogen mode and B1_H was assigned to the antisymmetric mode. These results further confirm that these are the vibrations of the PtH₂ center observed by EPR.

As was noted when the model shown in Fig. 2(a) was first suggested,¹⁷ the positions of the hydrogen atoms are uncertain, the C_{2v} symmetry requiring only that the two hydrogens lie in one of the {110} planes, symmetrically above and below the other {110} plane. Recently, Jones and coworkers²⁷ have suggested the structure shown in Fig. 2(b) for the PtH₂ complex as an additional possibility based upon their calculations for a similar NiH₂ complex. To probe further the positions of the hydrogen atoms in the model, a careful analysis of the angular dependence of the hydrogen hyperfine interactions was performed.^{18,21} For defect orientations in which **B** is rotated in the {110} plane that contains the two hydrogen atoms (making the H atoms inequivalent) there is a partially resolved splitting of the central component of the EPR line. From an analysis of this splitting, the hydrogen hyperfine tensor was deduced. The hydrogen hyperfine tensor was found to be approximately axially symmetric about directions ±35° from the <001> C₂ axis of the complex. From the magnitude of the small anisotropy in the hydrogen hyperfine interaction a Pt-H distance of $r \approx 4.2$ Å was estimated.²¹ This is remarkably close to the expected Pt-H distance of roughly 4.05 Å in the model of Fig. 2(b), i.e., 2.35 Å, the Si-Si nearest neighbor distance, plus ~ 1.7 Å, a typical back-bond Si-H distance.^{28,29} The small anisotropy of the hydrogen hyperfine interactions therefore provides evidence that the PtH₂ complex has a configuration in which the hydrogen atoms are at a greater distance than in the model shown in Fig. 2(a). Further work will be required to definitively locate the H atoms in the complex.

NONPARAMAGNETIC CHARGE STATES OF THE PtH_2 COMPLEX

The new PtH_2 EPR spectrum was observed in the dark only when the Pt concentration was greater than the P concentration, i.e., when the Fermi level was lowered to the Pt acceptor level at $E_C - 0.23$ eV. For a lower Pt concentration, $[\text{Pt}] < [\text{P}]$, the PtH_2 resonance was only observed under illumination.¹⁷ These results indicate that PtH_2 is nonparamagnetic when the Fermi level is above a level it introduces in the gap between the P and Pt levels at $E_C - 0.045$ and $E_C - 0.23$ eV, respectively. In experiments in which the Fermi level position was controllably lowered from the P level by successive electron irradiations, the position of the level introduced by PtH_2 was refined further and found to be above $E_C - 0.1$ eV (ref. 17).

In addition to the level at $\sim E_C - 0.1$ eV for the PtH_2 center, a level closer to mid-gap has also been found.²¹ Therefore, there are three possible charge states of the complex, one of which is paramagnetic (discussed above) and two additional nonparamagnetic charge states. When the charge state of the PtH_2 center is changed, either by varying the Fermi level position or by photoionization, the vibrational frequencies are shifted due to the consequent changes of the defect's force constants.³⁰ Thus the additional charge states can be detected and studied by vibrational spectroscopy even though they are nonparamagnetic. In the following we will refer to the paramagnetic charge state as PtH_2^{n-1} . The more negative charge state that is populated when the Fermi level is above $\sim E_C - 0.1$ eV is then PtH_2^{n-2} . The more positive charge state that is populated when the Fermi level is deep in the gap is PtH_2^n . The frequencies of the vibrational modes associated with the different charge states are listed in Table I. In order for the paramagnetic charge state to contain an odd number of electrons, n should be either 0 or 2, which would make the complex a double acceptor or a double donor, respectively.

Effect of the Fermi level position on the vibrational spectrum

An energy level diagram is shown in Fig. 4 along with the spectra that are observed for different positions of the Fermi level.²¹ In Fig. 4(b) a spectrum is shown for an n-type, high-Pt sample in which the paramagnetic charge state PtH_2^{n-1} that was discussed in the previous section is occupied. In this case the Fermi level should be near the Pt acceptor level at $E_C - 0.23$ eV.

In Fig. 4(a), a spectrum measured at 4.2K is shown for an n-type, low-Pt sample annealed in H_2 (with the Fermi level above the level near $E_C - 0.1$ eV for PtH_2). New bands are observed in addition to bands B1_H and B2_H . (C1_H , C2_H are also present and are weak.) When the sample temperature is raised to near 40K, lines B1_H and B2_H disappear and line A1_H increases in intensity. This result suggests that A1_H is a hydrogen mode of the PtH_2 complex when it is in its more negative, nonparamagnetic charge state. Presumably band B1_H is present at low temperature because light from the spectrometer photoionizes the PtH_2 center and the photogenerated electrons are trapped by the partially compensated P donors at low temperature. At 40K, the P donor can be thermally ionized and it is no longer an effective trap for the photoionized electrons.

In Fig. 4(c), a spectrum is shown for a p-type sample into which Pt and H had been indiffused at 1250°C. In this case, $[\text{Pt}] > [\text{B}]$ and the Fermi level in the sample is expected to be near the Pt donor level at $E_V + 0.32$ eV. Only bands C1_H and C2_H appear along with the strong unassigned band at 1880.8 cm^{-1} . In a variety of samples prepared under different conditions, C1_H and C2_H always appear with the same relative intensity. These results suggest that there is another nonparamagnetic charge state, PtH_2^n , that is populated when the Fermi level is below an additional level $(n-1)/n$ which must be between the Pt acceptor level at $E_C - 0.23$ eV and the Pt

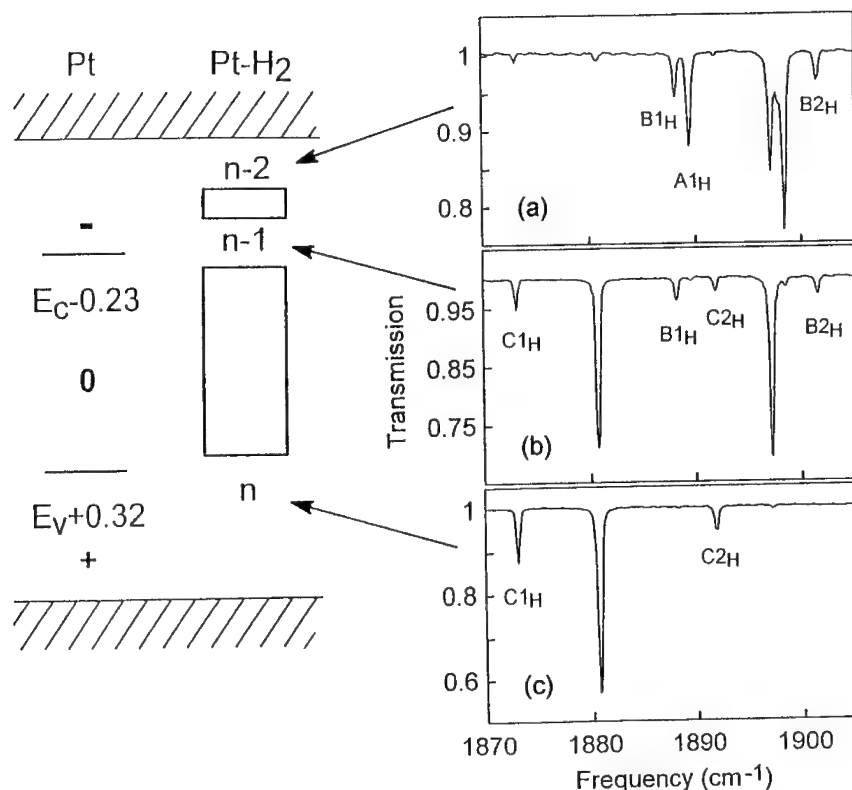


Figure 4. Energy level diagram that shows the levels of the Pt and PtH₂ defects. The open rectangles indicate that the (n-2)/(n-1) level of the PtH₂ complex is between $E_C - 0.045$ and $E_C - 0.1$ eV and that the (n-1)/n level is between $E_C - 0.23$ and $E_V + 0.32$ eV. The spectra shown in (a)-(c) are obtained when the Fermi level is near the energies in the gap that are indicated. For (a) and (b) the samples were n-type Si into which Pt had been diffused at 975°C and 1250°C, respectively. For (c) the sample was p-type Si into which Pt had been diffused at 1250°C.

donor level at $E_V + 0.32$ eV. (The range of possible energies for this level is shown in Fig. 4.) The bands C1_H and C2_H are assigned to the hydrogen modes of PtH₂ⁿ.

In addition to the hydrogen modes already discussed, the corresponding deuterium modes for the nonparamagnetic charge states of PtHD and PtD₂ have also been assigned.²¹ Their frequencies are listed in Table I.

Effect of illumination on the vibrational spectrum

Further support for the assignments discussed above comes from the effect of illumination on the populations of the different charge states.²¹ Filtering the spectrometer light provides a simple and convenient means to vary the illumination conditions and to identify charge-state-

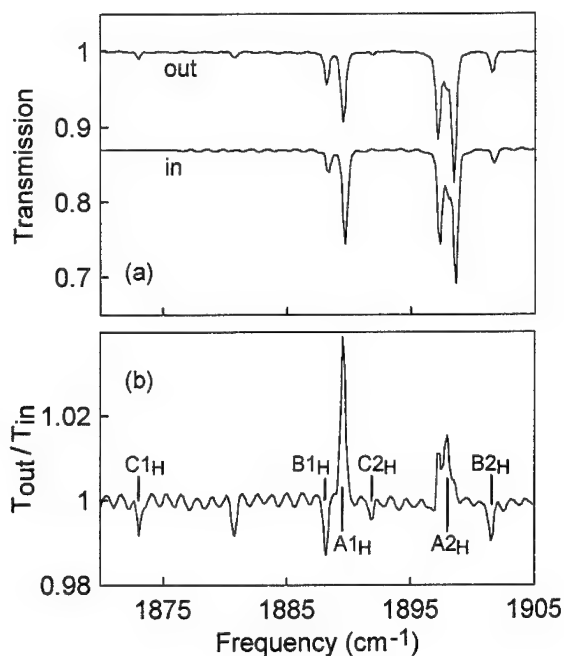
sensitive vibrational modes. In our experiments we have inserted a $4.5\text{ }\mu\text{m}$ ($\approx 2220\text{ cm}^{-1}$) long-pass filter before the sample to eliminate a portion of the spectrometer light (which is outside of our measurement range). Eliminating short wavelength light from the spectrometer causes the populations of the light-induced charge states to be reduced and for the populations of equilibrium charge states to be enhanced.

Spectra are shown in Fig. 5(a) for an n-type, low Pt sample (Fermi level above $E_C-0.1\text{ eV}$) that were measured with and without the $4.5\text{ }\mu\text{m}$ filter in place. The ratio of these spectra is shown in Fig. 5(b). The changes in the relative intensities of the vibrational bands are clearly seen. In Fig. 5(b), the downward going bands correspond to charge states that would not be populated in darkness, i.e., charge states whose population is reduced when the filter is inserted, and upward going bands correspond to charge states that are depopulated by the spectrometer illumination.

Two upward going bands, $A1_H$ and $A2_H$, are apparent in Fig. 5(b). In the section above, $A1_H$ was proposed to be a hydrogen mode of the charge state PtH_2^{n-2} . The light-induced intensity changes support this suggestion. $A2_H$ was tentatively assigned to the second hydrogen mode of PtH_2^{n-2} because of its behavior upon illumination.²¹ $A2_H$ appears only as a weak shoulder between two stronger unassigned bands in the spectra in Fig. 5(a) but is seen clearly as an upward going band in the ratio shown in Fig. 5(b). Bands $B1_H$ and $B2_H$ are downward going which suggests that they would not be present in the dark and that they appear at the expense of $A1_H$ and $A2_H$ when the Fermi level is above the PtH_2 level at $E_C-0.1\text{ eV}$.

The effect of spectrometer illumination on the populations of the different charge states provides further support for the assignment of lines $C1_H$ and $C2_H$ to a deeper charge state of PtH_2 (ref. 21). It is first noted that bands $C1_H$ and $C2_H$ were present in the spectra for the n-type samples with both high and low Pt concentrations [Figs. 4(a) and 4(b)] and that the deep

Figure 5. (a) Absorption spectra measured at 4.2 K with and without a $4.5\text{ }\mu\text{m}$ long-pass filter placed before the sample. The samples are n-type Si into which Pt was diffused at 975°C and that were subsequently annealed in H_2 . In (b) the ratio of the spectra in (a) is shown.



charge state we have proposed should not be populated in the dark for these samples. (The Fermi level is at or above the Pt acceptor level at $E_C - 0.23$ eV in both cases.) In the ratio of spectra measured with and without the 4.5 μm filter for the n-type, low-Pt sample shown in Fig. 5(b), $C1_H$ and $C2_H$ are observed as downward going bands which shows that they are due to an optically populated charge state in this case. Similar experiments performed for n-type, high-Pt samples also showed that bands $C1_H$ and $C2_H$ appear at the expense of $B1_H$ and $B2_H$ under illumination.²¹ These results explain why $C1_H$ and $C2_H$ appear in Figs. 4(a) and 4(b) and fully support the assignment of $C1_H$ and $C2_H$ to a more positive, nonparamagnetic charge state, PtH_2^n . Finally, the 4.5 μm filter had no observable effect on the spectrum shown in Fig. 4(c) for the p-type sample in which the Fermi level is low in the gap.²¹

To this point, the absolute charge state of the PtH_2 center has been left uncertain. The paramagnetic charge state must have an odd number of electrons so that either PtH_2^- or PtH_2^+ is being seen by EPR. The illumination-induced effects provide a clue to which of these charge states is seen. Under illumination at low temperature, one expects defects in the sample to tend toward their more neutral charge states because the capture radius for a Coulomb capture process is large. For example, donors are expected to have greater electron capture cross-sections than acceptors. In our experiments, the illumination of P-doped samples reduces the number of electrons trapped at the PtH_2^{n-2} center suggesting that the EPR active charge state is the acceptor PtH_2^- , i.e. $n=0$, and that photoionized electrons are preferentially trapped by the P donors. The illumination of B-doped samples (Fermi level near $E_V + 0.32$ eV) does not preferentially ionize PtH_2^n , which is also consistent with this being an acceptor center that can compete effectively with B for photoionized holes. These results suggest that the PtH_2 center is a double acceptor ($n = 0$ in Fig. 4 and in Table I) and that the charge states that are observed are PtH_2^{2-} , PtH_2^- (paramagnetic), and PtH_2^0 .

Our results show that the $(n-1)/n$ level is between the Pt acceptor and donor levels at $E_C - 0.23$ and $E_V + 0.32$ eV, respectively. The electron-electron correlation energy U for isolated transition metals in Si is typically $\sim 0.3 - 0.6$ eV (refs. 9 and 10). Hence we expect the $(n-1)/n$ level to be near mid-gap, i.e., roughly 0.5 eV below the $(n-2)/(n-1)$ level at $\approx E_C - 0.1$ eV.

OTHER TRANSITION-METAL-HYDROGEN RELATED VIBRATIONAL BANDS

Up to this point we have focused on spectra associated with a PtH_2 center about which much has been learned. There are several additional vibrational bands, about which much less is known, in samples containing Pt and H and also in samples containing H and Au or Rh.

Unassigned hydrogen modes in Si that contains Pt and H

There are a number of hydrogen-stretching bands observed in samples that contain Pt and H that have not been assigned.²¹ For example, there are the strong features at 1880.8 and 1897.2 cm^{-1} observed in the spectra shown in Figs. 3 and 4. The intensities of these bands are not well correlated to the bands assigned to the PtH_2 complex and are presumably associated with an additional complex (or complexes) that contains Pt and hydrogen. There are no additional new bands related to the 1880.8 and 1897.2 cm^{-1} bands in samples annealed in a mixture of H_2 and D_2 suggesting that each involves the vibration of a single hydrogen atom. Changes in the relative intensities of these bands upon a change in illumination conditions suggest that the 1880.8 and

1897.2 cm^{-1} bands are associated with different charge states of the same defect. Preliminary stress alignment results also support this conclusion.²¹

In the low-Pt, n-type sample, there is an unassigned band observed at 1898.6 cm^{-1} [Fig. 4(a)]. Additionally, for Pt-diffused samples that were rapidly quenched in ethylene glycol following the anneal in H_2 , several hydrogen-stretching bands were observed with higher frequencies than are shown in Fig. 3. Vibrational bands have been observed at 1905.9, 1914.2, 1918.0, 1922, 1924.7, 1930 and 1935.5 cm^{-1} . A representative spectrum that contains several of these bands is shown in Fig. 6(a). An anneal at 400°C eliminates these bands and shows that the complexes that give rise to them are less thermally stable than the PtH_2 complex.

Hydrogen modes in Si that contains Au or Rh and H

New hydrogen vibrational modes have been observed in n-type Si into which Au or Rh had been diffused followed by an annealing treatment in H_2 at 1250 °C. Spectra are shown in Figs. 6(b) and 6(c). The lines in the spectrum for the sample that contains Au and H are at 1813.3 and 1827.1 cm^{-1} . These bands have different intensities in different samples which indicates that they are not both hydrogen modes of the same center. The corresponding vibrational bands in a Au-diffused sample that was annealed in D_2 are at 1310.9 and 1319.4 cm^{-1} . Both bands are eliminated by a 30 min anneal at 400 °C. Pearton and Tavendale⁶ have reported a similar annealing stability for the hydrogen passivation of the Au acceptor level in n-type Si. The similar annealing stability suggests that these hydrogen modes might be related to the hydrogen passivation of isolated Au but more work will have to be done to establish such a connection.

The lines in the spectrum for the sample that contains Rh and H are at 1814.0, 1816.8, 1847.5 and 1860.8 cm^{-1} . The lines at 1847.5, and 1814 cm^{-1} are annealed away at 200 and above 500 °C, respectively. The lines at 1816.8 and 1860.6 cm^{-1} are annealed away at 350 °C.

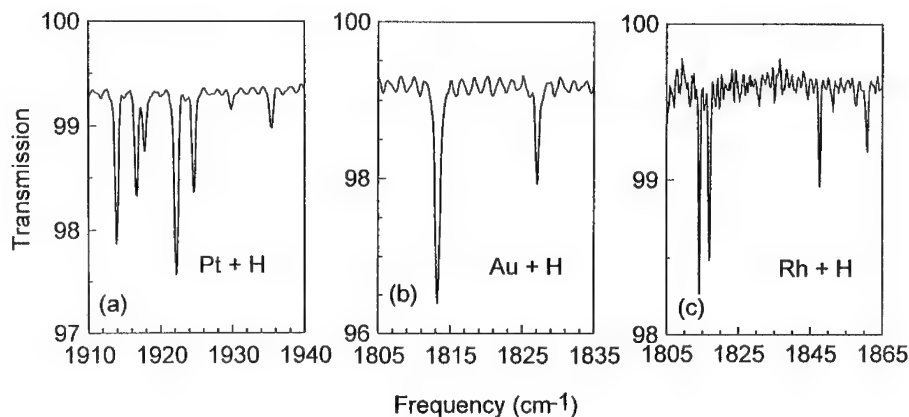


Figure 6. Absorption spectra measured at 4.2 K for n-type Si into which Pt (a), Au (b), or Rh (c) had been diffused at 1250°C. The samples were subsequently annealed in H_2 at 1250°C.

CONCLUSION

The ability to produce transition-metal-hydrogen complexes throughout bulk samples has allowed structure-sensitive spectroscopic techniques to be applied.¹⁷⁻²¹ The combination of EPR and IR absorption spectroscopies has provided detailed information about the microscopic structure and electrical characteristics of a PtH₂ complex in Si. The vibrational modes of other transition-metal-hydrogen centers have been observed and are the subject of continuing work in our laboratory.

The conventional wisdom⁵ had been that when hydrogen forms a complex with a transition metal impurity, the gap is swept clean of states. (Exceptions are provided by recent work in which DLTS peaks have been observed in Si that contained a transition metal impurity and hydrogen that had been introduced at low temperature.^{7,8}) For the PtH₂ center, it has been found that there are two levels, one near the conduction band¹⁷ and a second close to mid-gap.²¹ We note that it is possible to miss new levels that might be introduced following hydrogenation with DLTS measurements. For example one level introduced by PtH₂ might be too shallow to be detected by DLTS and the other too deep. This might explain why new features were not reported in previous work.³²

Of the three possible charge states for PtH₂, only one is paramagnetic. Both EPR and the stress-induced splittings of the hydrogen vibrational bands show that the PtH₂ complex has C_{2v} symmetry in its paramagnetic charge state.¹⁷⁻²¹ Vibrational spectroscopy is not limited to the paramagnetic charge states of defects and this has been exploited for the PtH₂ complex.²¹ The changes in the vibrational frequencies that occur when the charge state of the PtH₂ defect is changed, either by a shift of the Fermi level or by photoionization, help to locate the levels of the defect and have led to an assignment of the hydrogen vibrations of all three charge states. There are 3 pairs of hydrogen vibrational bands, one pair for each of the different charge states of the PtH₂ center. (There are also 3 pairs of bands for PtD₂ and 3 pairs of bands for PtHD.) It has been argued²¹ that the PtH₂ defect is a double acceptor and that the charge states that have been observed are PtH₂²⁻, PtH₂⁻ (paramagnetic), and PtH₂⁰.

The availability of data that provides structural information for transition-metal-hydrogen complexes should help to advance theory in this area. For example, it was previously suggested that for the PtH₂ complex, hydrogen atoms terminate two weak bonds that point toward the off-center Pt atom.¹⁷ Recent calculations by Jones *et al.*²⁷ have suggested alternative structures.

ACKNOWLEDGMENTS

We are grateful to R. Jones for communicating theoretical results to us prior to publication. The work performed by M.S., S.U. and M.E. was supported by the National Science Foundation under Grant No. DMR-9415404. The work by G.W. was supported by the U.S. Navy Office of Naval Research (Electronics and Solid State Sciences Program) under Contract No. N00014-90-J-1264.

REFERENCES

1. S.J. Pearton, J.W. Corbett, and M. Stavola, *Hydrogen in Crystalline Semiconductors* (Springer Verlag, Berlin, 1992).

2. *Hydrogen in Semiconductors*, edited by J.I. Pankove and N.M. Johnson (Academic, San Diego, 1991).
3. *Hydrogen in Semiconductors*, edited by M. Stutzmann and J. Chevallier (North Holland, Amsterdam, 1991).
4. *Hydrogen in Compound Semiconductors*, edited by S.J. Pearton (Trans Tech, Zürich, 1994).
5. Chapt. 3 in *Hydrogen in Crystalline Semiconductors* [Ref. (1)] or S.J. Pearton, *Hydrogen in Semiconductors* [Ref. (2)], Chapt. 5.
6. See, for example, S.J. Pearton and A.J. Tavendale, Phys. Rev. B **26**, 7105 (1982), and the references contained therein.
7. E.Ö. Sveinbjörnsson and O. Engström, Appl. Phys. Lett. **61**, 2323 (1992); Phys. Rev. B, to be published; and also in this volume.
8. E.Ö. Sveinbjörnsson, G.I. Andersson, and O. Engström, Phys. Rev. B **49**, 7801 (1994).
9. R.N. Hall, Inst. Phys. Conf. Ser. No. **23**, 190 (1975).
10. E.E. Haller, in *Hydrogen in Crystalline Semiconductors* [Ref. (1)], p. 351 or in *Hydrogen in Semiconductors* [Ref. (3)], p. 351.
11. G.R. Bai, M.W. Qi, L.M. Xie, and T.S. Shi, Solid State Commun **56**, 277 (1985).
12. K. Muro and A.J. Sievers, Phys. Rev. Lett. **57**, 897 (1986); R.E. Peale, K. Muro and A.J. Sievers, *Shallow Impurities in Semiconductors*, edited by G. Davies, (Trans Tech, Zürich, 1991), p. 141.
13. B. Clerjaud, D. Côte, and C. Naud, Phys. Rev. Lett. **58**, 1755 (1987); B. Clerjaud, F. Gendron, M. Krause, and W. Ulrici, Phys. Rev. Lett. **65**, 1800 (1990).
14. I.A. Veloarisoa, M. Stavola, D.M. Kozuch, R.E. Peale, and G.D. Watkins, Appl. Phys. Lett. **59**, 2121 (1991); Bull. Am. Phys. Soc. **36**, 945 (1991).
15. S.A. McQuaid, R.C. Newman, J.H. Tucker, E.C. Lightowlers, R.A.A. Kubiak, and M. Goulding, Appl. Phys. Lett. **58**, 2933 (1991).
16. J.M. Kahn, L.M. Falicov, and E.E. Haller, Phys. Rev. Lett. **57**, 2077 (1986).
17. P.M. Williams, G.D. Watkins, S. Uffring, and M. Stavola, Phys. Rev. Lett. **70**, 3816 (1993).
18. P.M. Williams, G.D. Watkins, S. Uffring, and M. Stavola, *Defects in Semiconductors 17*, edited by H. Heinrich and W. Jantsch (Trans Tech, Zürich, 1994), p. 891.
19. M. Höhne, U. Juda, Yu. V. Martynov, T. Gregorkiewicz, C.A.J. Ammerlaan, and L.S. Vlasenko, *Defects in Semiconductors 17*, edited by H. Heinrich and W. Jantsch (Trans Tech, Zürich, 1994), p. 1659.
20. M. Höhne, U. Juda, Yu. V. Martynov, T. Gregorkiewicz, C.A.J. Ammerlaan, and L.S. Vlasenko, Phys. Rev. B **49**, 13423 (1994).
21. S.J. Uffring, M. Stavola, P.M. Williams, and G.D. Watkins, Phys. Rev. B **51**, 9612 (1995).
22. K.P. Lisiak and A.G. Milnes, Solid State Electron. **18**, 533 (1975).
23. *Impurities and Defects in Group IV Elements and III-V Compounds, Vol. III/22b*, in the Landolt-Bornstein, New Series, edited by O. Madelung and M. Schulz (Springer, Berlin, 1989), p. 283.
24. H. Fechtinger, *Electronic Structure and Properties of Semiconductors*, edited by W. Schröter (VCH, Weinheim, 1991), p. 143.
25. F.G. Anderson, R.F. Milligan, and G.D. Watkins, Phys. Rev. B **45**, 3279 (1992).
26. The bands C1_H and C2_H behave very similarly to B1_H and B2_H in the high-Pt, n-type samples and, without further information, are also good candidates for the hydrogen-stretching modes of the paramagnetic charge state. Changes in the spectrum that occur as the Fermi level is varied or under illumination confirm the assignment of B1_H and B2_H.
27. R. Jones, A. Resende, S. Öberg, J. Goss, P.R. Briddon, unpublished and R. Jones, private communication.

-
28. S.B. Zhang and D.J. Chadi, Phys. Rev. B **41**, 3882 (1990).
 29. P.J.H. Denteneer, C.G. Van de Walle, and S.T. Pantelides, Phys. Rev. B **41**, 3885 (1990).
 30. R.C. Newman, *Infrared Studies of Crystal Defects* (Taylor and Francis, London, 1973). See, for example, the discussion of irradiation damage in silicon on p. 117 and the discussion of the oxygen-vacancy center that follows.
 31. The band $A2D^{n-2}$ has not been identified, presumably because it is obscured by a strong unassigned band in the spectrum.
 32. S.J. Pearton and E.E. Haller, J. Appl. Phys. **54**, 3613 (1983).

COUPLING OF ELECTRONIC AND STRUCTURAL PROPERTIES OF HYDROGEN IN CRYSTALLINE SILICON

WOLFGANG CSASZAR AND ARTHUR L. ENDRÖS

Siemens Corporate Research and Development, Otto-Hahn-Ring 6, D-81739 Munich, Germany

ABSTRACT

Theory has made great progress during recent years in calculating the fundamental properties of monatomic hydrogen in crystalline silicon. By applying the DLTS and DDLTS method we use the hydrogen-carbon complex which consists of an electronically inactive carbon atom on a substitutional lattice site and a hydrogen atom near the bond-center position to detect theoretically predicted properties of hydrogen in silicon. The results of two independent experiments show that there exists a coupling of the electronic and structural properties of monatomic hydrogen, as predicted by theory.

INTRODUCTION

During recent years the properties of hydrogen (H) in crystalline silicon have been extensively studied in both experimental and theoretical terms [1,2]. Nevertheless, only little *experimental* work has been done on *isolated* H [3-7]. This is mainly due to the fact that this species is less stable than molecular hydrogen (H_2), the diatomic hydrogen complex (H_2^+) or the hydrogen boron (HB) or hydrogen phosphorus (HP) complex [8,9] and is therefore invisible in experiments where the hydrogenation takes place at room temperature. In order to better understand the nature of H *diffusion* in Si more experimental investigations have to be carried out on isolated H and their results have to be compared with theoretical predictions. Theory [10] predicts that the *electronic* properties and the *structural* properties of isolated H interact with each other: (1) The position of its energy level depends on the configuration of H in the lattice. (2) The most favorable site is determined by the charge state of H, i.e., the position of the Fermi level in the Si crystal. Charge state reactions and site changes have also been observed for muonium, the hydrogen analogue, in Si [11].

In this work, we use the hydrogen-carbon (HC) complex [3,12,13] in c-Si which consists of an electronically inactive carbon (C) atom (isoelectronic to Si) on a substitutional lattice site and a H atom near the bond-center (BC) position between the C and the Si atom [14] to carry out two independent *experiments* whose results indicate that the electronic and structural properties of hydrogen in c-Si are coupled, as predicted by theory.

In silicon [3] as well as in ultra-pure germanium [15] the hydrogen acts as an "electronic activator" for the substitutional C atom. By comparing the positively charged HC center in Si (or more precisely the $\{C-H-Si\}^+$ complex) with isolated bond-center H^+ ($\{Si-H-Si\}^+$) the group IV element Si is replaced by the group IV element C, which has the same valence orbital configuration as Si, it is reasonable to expect that the HC complex reflects the principal electronic properties of BC hydrogen. This is strongly supported by the result of pseudopotential-density-functional calculations [16], which reveal that an HC complex has

an energy level that is identical to that of an H atom at the same atomic site but with an Si atom instead of the C atom at the substitutional lattice site. The increased stability of the HC center compared with isolated BC hydrogen is mainly due to the large amount of energy gained by capturing interstitial H and shortening the C-Si bond length [14]. The HC complex acts as a deep donor with a low electric field activation energy of about 0.16 eV below the edge of the conduction band [3]. This value agrees closely with the work of Holm et al. [5] who implanted H at low temperatures and found a similar level (0.16 eV) which they regard as (probably isolated) BC hydrogen.

EXPERIMENTS

Measurements

In our first experiment we investigate the field-dependence of the electron activation energy of the HC center by means of double-correlation deep level transient spectroscopy (DDLTS). Only thermal emission processes at a fairly constant electric field strength are studied, thus yielding exponential capacitance transients from which the emission time constants τ can be directly determined according to

$$C(t) - C_e = \Delta C e^{-t/\tau}, \quad (1)$$

where $C(t)$ is the capacitance of the DDLTS transient at time t and C_e is the capacitance at reverse bias applied in the equilibrium state. ΔC is the amplitude of the DDLTS transient. The average electric field strength \bar{F} is calculated from C - V measurements that are carried out at the corresponding DDLTS temperatures.

In the second experiment we study the annealing behavior of the HC center in the dark with short-circuited contacts as a function of the Fermi-level position. The annealing temperatures are 280 K and 310 K. After each annealing step the sample is cooled under reverse bias down to below ≈ 110 K before DLTS and/or DDLTS experiments are carried out to determine the HC concentration. Following this the sample is heated up under reverse bias to the annealing temperature and annealing takes place. Cooling and heating under reverse bias is necessary to ensure that HC complexes do not anneal during the temperature ramps [12].

Sample Preparation

The samples consist of Czochralski (CZ) and float-zone (FZ) grown Si crystals ([100]-oriented) which are doped with phosphorus and carbon ($\approx 4 \times 10^{17} \text{ cm}^{-3}$). In order to vary the *electric field* and the *Fermi level* in the observation volume, three different types of samples with different shallow dopant-concentrations are prepared: sample L with $[P] \approx 1 \times 10^{15} \text{ cm}^{-3}$, sample M with $[P] \approx 5 \times 10^{15} \text{ cm}^{-3}$ and sample H with $[P] \approx (5 - 6) \times 10^{16} \text{ cm}^{-3}$. The samples are hydrogenized by wet chemical etching at room temperature for 30 seconds in an acid consisting of $\text{HNO}_3:\text{HF}:\text{CH}_3\text{COOH}=5:1:1$. Following this, the polished front surfaces of all samples are supplied with Schottky barriers by evaporating Au onto a substrate at room temperature. In order to form the HC complex, the samples are subjected to a reverse-

bias annealing (RBA) treatment (-4 to -5 V, ≈ 320 K, several hours to days) [3,12]. The process of sample preparation is described in detail in reference 12.

RESULTS AND DISCUSSION

Position-dependent band-gap level of hydrogen

In order to obtain a detailed description of the field-dependence of the activation energy of the hydrogen-carbon complex, sample H is investigated on the basis of the DDLTS principle. It is found that the emission rates ($= 1 / \text{emission time constant}$), which are directly determined from Eq. (1), depend strongly on the electric field and that the field effect increases with decreasing temperature [17]. The activation energy of the HC complex at each electric field is then deduced from the slope of the Arrhenius plot according to the Shockley-Read-Hall statistics [18]. The results show (Fig. 1) that a strong linear correlation (0.998) exists between the activation energy E_A and the electric field F . By extrapolating the data to $F = 0$ we observe that the zero-field activation energy of the HC complex equals 185 meV ($\pm 5 \text{ meV}$).

As a first step we used the three-dimensional Poole-Frenkel model by Hartke [20] with a Coulomb defect potential to explain the field-dependence of the HC complex. Due to the microscopic nature of the Si screening during the emission process of the electron from the positively charged HC center we allow three different values for the permittivity ϵ_{Si} of silicon: $\epsilon_{Si} = 11.9$ (macroscopic value), $\epsilon_{Si} = 5$ and $\epsilon_{Si} = 3$. However, it can be seen in Fig. 1 that such a model bears little resemblance to our experimental results. The observed field-dependence ($\approx 31 \text{ meV} / 10^4 \text{ V cm}^{-1}$) is much stronger than that predicted by the model of Hartke ($\approx 6 \text{ meV} / 10^4 \text{ V cm}^{-1}$ for $\epsilon_{Si} = 11.9$). The strongest field-dependence reported in literature [21,22,23] was observed for defects where *phonon-assisted tunneling* played a dominant role in the emission process. However, it was shown previously [19] that neither

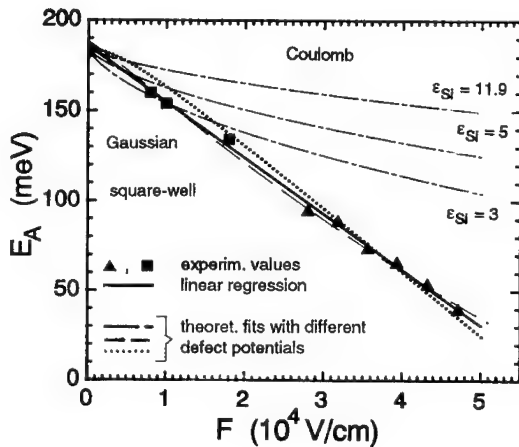


FIG. 1. Electric field-dependence (F) of the electron activation energy E_A of the HC complex in Si. Triangles and squares: experimental values measured by the DDLTS principle (triangles) and taken from reference 19 (squares). The solid line represents the computed linear regression between E_A and F : $E_A = -31 (\text{meV} / 10^4 \text{ V cm}^{-1}) \times F + 185 \text{ meV}$. Other curves: theoretical fits with the three-dimensional Poole-Frenkel model ($T = 70 \text{ K}$) using Coulomb potentials (dash-dotted lines), a square-well potential of radius 37.0 nm (dotted line), and a Gaussian potential with an amplitude of 185 meV and a characteristic width of 21.5 nm (dashed line).

phonon-assisted tunneling nor pure tunneling takes place in the process of electron emission from the HC center in the investigated range of temperature and electric field.

Since the Coulomb potential was found to be unsuitable for describing the experimental results, we tried to fit our data to Poole-Frenkel emission from other three-dimensional defect potentials, namely a square-well potential and a Gaussian potential. The best fits (Fig. 1) that could explain the experimental data are gained for a square-well potential with radius $r = 37$ nm and for a Gaussian potential with an amplitude $V_0 = 185$ meV and a characteristic width α of 21.5 nm. However, if we compare the range of our fit potentials (37 nm and 21.5 nm) with the lattice constant of Si (0.357 nm) we see that such long-range defect potentials may only be considered if we are dealing with large defects, i.e., defects involving typically more than ten lattice sites, but not with point defects as for a hydrogen atom (a single proton!) bound to C. We conclude that the standard theories used to describe the field-enhanced emission of charge carriers from deep levels, namely the Poole-Frenkel model and the quantum-mechanical tunneling model, cannot satisfactorily explain the experimental data.

The following model is proposed, in which the observed properties of the HC center are explained within the scope of the present theory of the behavior of hydrogen in Si. There is theoretical conformity that the charge state of H as well as its *energy level* are expected to depend on its lattice position in the Si crystal [10] although direct experimental evidence is still lacking. At zero electric field the equilibrium position of H^+ is near the BC site between an Si atom and a substitutional C atom. Due to the electric field in the space-charge layer of the samples, however, the position of H^+ is altered in line with the electric field strength. According to the calculations of Denteneer et al. [16] this is accompanied by a change of its electronic properties, i.e., the energetic position of the H^+/H^0 defect level in the Si band-gap is changed. Consequently, the strong field-dependence of the HC activation energy of ≈ 31 meV / 10^4 V cm $^{-1}$ is the sum of two effects: (1) a contribution of ≈ 6 meV / 10^4 V cm $^{-1}$, which is caused by the field-enhanced emission of electrons described by the Poole-Frenkel model with a Coulomb defect potential (assuming $\epsilon_{Si} = 11.9$) due to the ionized center being a proton, and (2) a *structural* term to the amount of ≈ 25 meV / 10^4 V cm $^{-1}$, which results from the position-dependent electronic properties of H.

Charge state-dependent stability of the hydrogen-carbon complex

The isothermal annealing kinetics at 280 and 310 K of the HC center is investigated at zero bias (short-circuit case) in the dark in the three differently doped samples L, M and H. It can be seen in Fig. 2 that the concentration N of the HC defect decreases exponentially as a function of annealing time t and can be fitted by $N(t) = N_0 \exp(-t/\tau_a)$ for each sample type, where N_0 is the initial HC concentration at $t = 0$ and τ_a is the annealing time constant.

Figures 2a and 2b demonstrate clearly that the annealing time constant τ_a , which is the reciprocal slope of the linear regressions, depends strongly on the dopant concentration of the samples, i.e., the position of the Fermi level. From the value E_F of the Fermi level the probability of occupation P_{HC^0} with an electron of either spin of the monovalent HC donor can be calculated for each annealing temperature T_a according to [24]

$$P_{HC^0} = \frac{N_{HC^0}}{N_{HC}} = \frac{1}{\frac{1}{2} \exp[(E_T - E_F)/(kT_a)] + 1} \quad (2)$$

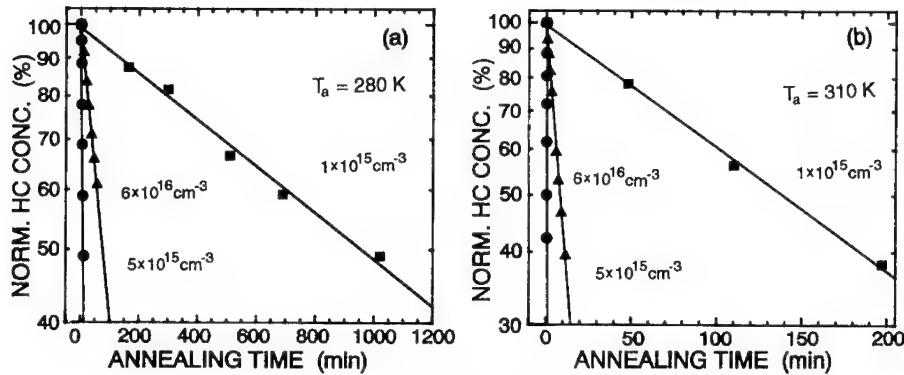


FIG. 2. Normalized HC concentration as a function of annealing time for three different dopant concentrations at (a) $T_a = 280\text{ K}$ and (b) $T_a = 310\text{ K}$. Squares: $[P] \approx 1 \times 10^{15}\text{ cm}^{-3}$. Triangles: $[P] \approx 5 \times 10^{15}\text{ cm}^{-3}$. Circles: $[P] \approx (5-6) \times 10^{16}\text{ cm}^{-3}$. Solid lines: first-order kinetics according to $N(t) = N_0 \exp(-t/\tau_a)$; symbols of the equation are explained in the text.

where N_{HC^0} is the concentration of the neutrally charged HC complexes, N_{HC} is the total concentration of HC centers, E_T is the energy level of the HC complex at zero electric field (185 meV, see above) and k is the Boltzmann constant. Table I shows unambiguously that the stability of the HC center depends considerably on the occupation probability $P(E)$ with electrons, i.e., the *charge state*. The HC complex is more stable when the value of P_{HC^0} is smaller, i.e., when a larger portion of the centers is in the *positive* charge state. This is confirmed by previous measurements [12] where it was shown that the HC donor in n-Si is only stable inside the space-charge region of a Schottky barrier where the trap level is *above* the Fermi level. When the center becomes neutrally charged and the temperature is high enough ($\approx 250\text{ K}$) the H dissociates from the substitutional C atom (immobile for temperatures around 300 K) and becomes part of a new configuration. Due to the fact that C is electronically inactive in Si the charge-state dependence of the annealing behavior of the HC defect should exclusively be a property of the H atom. There exists no Coulomb interaction between the carbon and the hydrogen atom when H is detached from C.

Table I: Annealing time constant τ_a of the HC complex as a function of the occupation probability P_{HC^0} for two different annealing temperatures T_a .

$T_a = 280\text{ K}$		$T_a = 310\text{ K}$	
P_{HC^0}	τ_a (min)	P_{HC^0}	τ_a (min)
0.15	1404	0.05	204
0.43	113	0.25	12.3
0.91	16.2	0.79	0.56

SUMMARY

In summary, we have carried out two different experiments which show that the *electronic* and *structural* properties of hydrogen are coupled, as predicted by theory. The first experiment reveals that the energy level of the H^+/H^0 donor state should change when hydrogen alters its lattice position in the Si crystal. Secondly, we demonstrate that the stability of the hydrogen species depends on its charge state. Hydrogen at (or near) the BC site is more stable in the positive charge state than in the neutral one. Both results are in perfect agreement with theory.

References

- [1] J.I. Pankove and N.M. Johnson, *H in Semiconductors*, Vol. 34 of SEMICONDUCTORS AND SEMIMETALLS (Academic Press, San Diego, 1991).
- [2] S.J. Pearton, J.W. Corbett, and M. Stavola, *H in Crystalline Semiconductors*, Springer Series in Materials Science 16 (Springer Verlag, Berlin Heidelberg, 1992).
- [3] A. Endrös, Phys. Rev. Lett. **63**, 70 (1989).
- [4] A.L. Endrös, W. Krühler and J. Grabmaier, Physica B **170**, 365 (1991).
- [5] B. Holm, K. Bonde Nielsen, and B. Bech Nielsen, Phys. Rev. Lett. **66**, 2360 (1991).
- [6] N.M. Johnson and C. Herring, Phys. Rev. B, **46**, 15554 (1992-I).
- [7] N.M. Johnson, C. Herring, and C.G. Van de Walle, Phys. Rev. Lett. **73**, 130 (1994).
- [8] K.J. Chang and D.J. Chadi, Phys. Rev. B **40**, 11644 (1989-I).
- [9] C.G. Van de Walle, Phys. Rev. B **49**, 4579 (1994-I).
- [10] C.G. Van de Walle, in reference 1, pp. 595-614, and references therein.
- [11] R.L. Lichti, K.H. Chow, T.L. Estle, B. Hitti, R.F. Kiefl, S.R. Kreitzman, and J.W. Schneider, Materials Science Forum **143-147**, 915 (1994).
- [12] A.L. Endrös, W. Krühler, and F. Koch, J. Appl. Phys. **72**, 2264 (1992).
- [13] M. Yoneta, Y. Kamiura, and F. Hashimoto, J. Appl. Phys. **70**, 1295 (1991).
- [14] Dj.M. Maric, P.F. Meier, and S.K. Estreicher, Phys. Rev. B **47**, 3620 (1993-I).
- [15] E.E. Haller, B. Joss, and L.M. Falicov, Phys. Rev. B **21**, 4729 (1980).
- [16] P.J. Denteneer, C.G. Van de Walle, and S.T. Pantelides, Phys. Rev. Lett. **62**, 1884 (1989).
- [17] W. Csaszar, diploma thesis, Technical University of Graz, 1992.
- [18] W. Shockley and W.T. Read Jr., Phys. Rev. **87**, 835 (1952).
- [19] W. Csaszar and A.L. Endrös, Phys. Rev. Lett. **73**, 312 (1994).
- [20] J.L. Hartke, J. Appl. Phys. **39**, 4871 (1968).
- [21] G. Vincent, A. Chantre, and D. Bois, J. Appl. Phys. **50**, 5484 (1979).
- [22] S. Makram-Ebeid, Appl. Phys. Lett. **37**, 464 (1980).
- [23] N.C. Halder and D.E. Barnes, J. Vac. Sci. Technol. B **10**, 94 (1992).
- [24] R.A. Smith, *Semiconductors* (Cambridge University Press, London, 1959), p. 87.

LOW-TEMPERATURE DIFFUSIVITY OF HYDROGEN IN DIFFERENT SILICON SUBSTRATES

XIAOJUN DENG* AND BHUSHAN L. SOPORI

National Renewable Energy Laboratory, 1617 Cole Boulevard, Golden, CO 80401

*Current address: Washington State University, Electronic Materials Laboratory, 100 Sprout Road, Richland, WA

ABSTRACT

The diffusivity of deuterium (D) at 250°C was determined in silicon samples grown by different techniques. It is found that the diffusivity increases with the growth speed, increase in carbon content and a decrease in oxygen concentration of the substrate. These growth conditions correlate well with the concentration of vacancy-type defects in the as-grown state. Hence, we conclude that a vacancy mechanism is responsible for low-temperature hydrogen diffusion in silicon. The highest diffusivity for hydrogen, calculated from these data, was found to be $3 \times 10^{-7} \text{ cm}^2/\text{s}$.

INTRODUCTION

It is now well known that hydrogen greatly influences the characteristics of a variety of silicon devices. It has been determined that observed improvements in the device performance due to treatments in hydrogen-containing ambients, such as forming gas (FG) or water vapor, involved unintentional introduction of hydrogen [1-3]. Such results have generated a great deal of interest in the use of hydrogen for passivation of interface and bulk defects. Recent understanding of the role of hydrogen passivation in silicon has led to the use of hydrogen treatments in the fabrication of a number of devices. Many of these treatments involve low process temperatures, typically <500 °C. Hence, there is considerable interest in studying properties of hydrogen that relate to its diffusion and passivation in silicon at temperatures below 500 °C. Our current work relates primarily to the bulk diffusion and passivation by hydrogen in silicon. Deep diffusion of hydrogen in Si is particularly important for solar cell processing because significant improvements in the solar cell performance require that hydrogen must diffuse (and passivate) the entire bulk of the device.

Diffusivity of hydrogen was determined first by Van Weirengen and Warmohltz (VWW) by measuring its permeation rate through a cylinder of silicon at temperatures above 900°C [4]. Their data for H diffusivity, D_h , fit the following expression:

$$D_h = 9.67 \times 10^{-3} \exp(E_a/kT) \text{ cm}^2/\text{sec} \dots \dots \dots (1)$$

where $E_a = -0.48 \text{ eV}$ is the activation energy, k is the Boltzmann's constant, and T is the temperature. These results agree well with the expected high diffusivity of hydrogen based on interstitial diffusion. An extrapolation of these data to lower temperatures gives the value of $D_h \approx 2.3 \times 10^{-7} \text{ cm}^2/\text{sec}$ for 250°C. However, experiments performed to measure diffusivity of hydrogen in silicon at lower temperatures do not produce consistent results and, in general, show diffusivity values considerably lower than calculated from equation 1. These experiments have shown that hydrogen diffusion is influenced by a number of factors. For example, the diffusivity is higher in a p-type vs. an n-type substrate, in higher resistivity material, and in float zone (FZ) vs. Czochralski (CZ) material [5, 6]. These variations in the diffusivity are reconciled by invoking trapping of hydrogen by impurities and defects present in

the material. This hypothesis leads to a general inference that the diffusivity of hydrogen in lower quality material should be lower than in typical FZ material. However, it has been observed that hydrogen can diffuse very rapidly in solar cells, fabricated on low quality material, to produce effective bulk passivation [7]. These deep diffusions are indirectly confirmed from solar cell analyses [8-10]. The objective of this work is to determine the properties of the substrates that influence the hydrogen diffusion.

EXPERIMENTAL

We have carried out deuterium diffusions in silicon substrates grown by different techniques. The materials selected for this work consisted of FZ, CZ, ribbon, and cast polycrystalline wafers. These samples were all p-type with resistivity of $\approx 1\Omega\text{-cm}$. Deuterium diffusions were done in a low-energy Kaufman ion source. The diffusivity was determined from **erfc** fit to the SIMS depth profiles. The choice of low-energy implantation was made because it allows high concentrations of D to be incorporated in the sample. This facilitates the measurement of deep profiles needed for diffusivity measurements.

Results:

Since our experiments are intended to determine the diffusivity from the diffusion profiles, it is necessary to establish the validity of such computation. It is particularly important to determine if the diffusivity is controlled by a single mechanism. It is therefore instructive to analyze a typical diffusion profile due to a low-energy implantation process. Figure 1 shows SIMS deuterium profiles in three samples taken from the same large-grain polycrystalline ribbon, deuterated at three different temperatures 150°C, 250°C, and 350°C. The samples were taken from the same grain to ensure the same material properties. The deuteration was performed at 1.5 K eV, with a beam current density of 0.6 mA/cm². The diffusion profiles were measured by a CAMECA system that can have a measurement sensitivity for D of about 10¹⁵/cm³.

The diffusion profiles show several features that are characteristic of the depth from the surface. These regions are labeled as I, II, and III in Fig. 1. The region I near the surface shows a profile that is typical of ion implantation damage. The damage depth can be predicted from a well-established energy dissipation model discussed in references [11, 12]. This process results in a peak in the D concentration that lies about 0.1 μm below the surface of the wafer. In region II, the D profile shows a rapid decrease in the concentration to a level that is close to the solubility of D in the wafer (as discussed later). The region III typifies diffusion from a D-rich surface that acts as a source of D. Analysis has shown that the depth of region I increases with an increase in the ion energy and depends only weakly on the temperature. TEM analysis has shown that this region contains a high density of dislocation loops and some stacking faults. Under these low energies, there is little or no amorphization of silicon but, in many cases, nucleation of "platelet" type of defects is observed. Such defects have highly crystallographic features and are found lying in (111) planes, with oblong axis along $\langle 112 \rangle$ or $\langle 110 \rangle$ directions. The platelets can, however, penetrate deeper into regions II and III. The region III reflects the bulk diffusion properties of D.

It is seen that the profile at 150°C has several kinks in region III indicative of trapping processes and involvement of several different diffusion mechanisms. At 250 °C and above there appears to be a single diffusion mechanism present. As discussed below, the diffusion profile in region III can be well fitted by a **erfc** profile, indicating a single diffusion mechanism.

It is thus clear that meaningful diffusivity values can be determined from the diffusion profiles fitted with the **erfc** profiles. Figure 2 shows diffusion profiles of deuterium in two cast

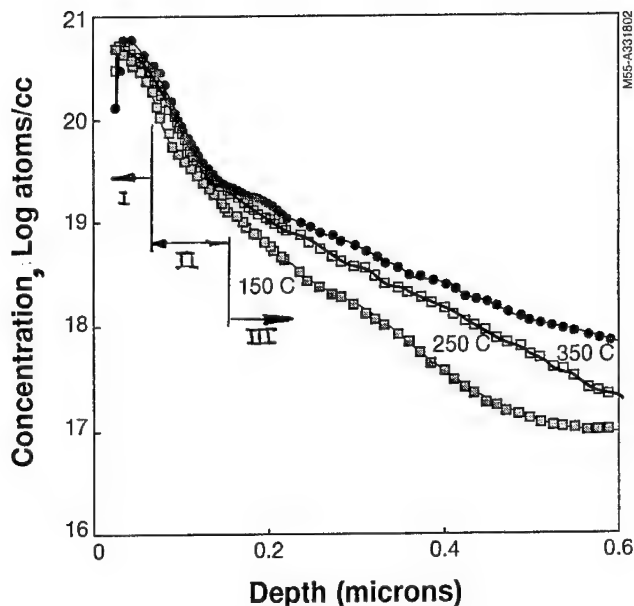


Figure 1. SIMS profiles of deuterium in p-type Si ribbon samples at three different temperatures. Deuteration was done by low-energy implantation

samples taken from the same ingot which differ only in the oxygen concentration. The data beyond the depth of $0.5 \mu\text{m}$ is fitted with an **erfc** profiles that yield the diffusivity values of 1.5×10^{-8} and 2.4×10^{-9} for the low and the high oxygen content samples, respectively. The corresponding values of D_h , obtained by multiplying D_d values by $(2)^{1/2}$ to correct for the effects of lower mass, are $2.1 \times 10^{-8} \text{ cm}^2/\text{sec}$. and $3.4 \times 10^{-9} \text{ cm}^2/\text{sec}$, respectively. Figure 2 also shows that if the fitted profiles are extrapolated to the surface region, they intercept the surface at a value of $10^{17}/\text{cm}^3$. This concentration is greatly lower than the actual concentration at the surface. We believe $10^{17}/\text{cm}^3$ represents the solubility of D if there was no surface damage i.e. the bulk solubility.

We have used this procedure to determine the diffusivity of D for a number of silicon materials grown by different techniques. Figure 3 shows the diffusivity of five different silicon materials of nearly the same resistivity. The major differences in these growth techniques are the growth rate, and the concentrations of oxygen and carbon in the material. In addition, the solar grade materials have higher impurity concentrations and higher defect densities. The sample RP-1 is a polycrystalline ribbon grown by laser recrystallization method. This sample has low impurity levels and was grown at $2.5\text{-cm}/\text{min}$. The other ribbon sample, RP-2, was polycrystalline silicon grown by the edge-defined film-fed growth (EFG) method from ASE Americas (previously Mobil Solar). The EFG technique utilizes a graphite die, inserted into

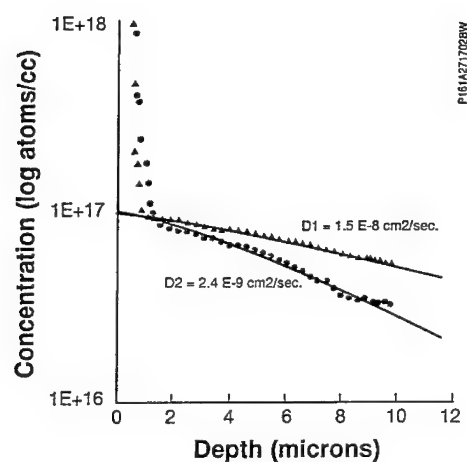


Figure 2. Deuterium profiles of high- (♦) and low-oxygen (●) samples. SIMS profiles are fitted with *erfc* profiles to obtain diffusivity values.

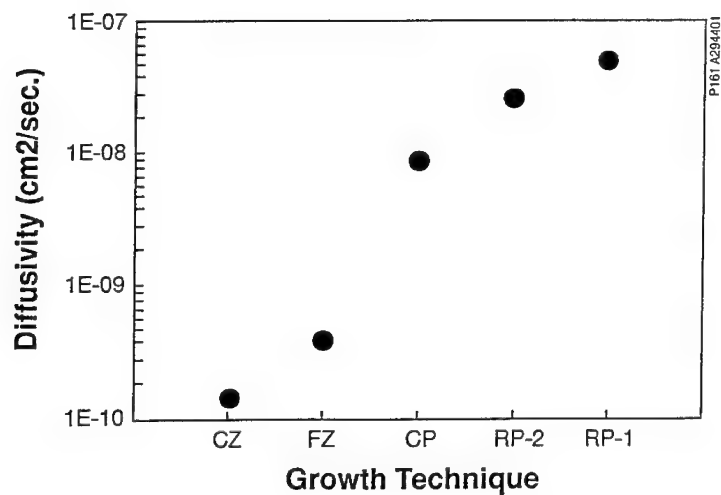


Figure 3. Diffusivity values obtained for materials grown by different methods.

the silicon melt, to shape the growth in the form of a nonagon. The growth rate for this sample was 1.5-cm/min. This material has a low concentration of oxygen and near-saturation levels of carbon. Hence, this ribbon sample is expected to have a vacancy concentration close to that of RP-1. The sample CP was polycrystalline silicon grown by a casting technique. In this technique, the melted silicon solidifies from the bottom toward the top of the ingot. The growth rate in a casting process is typically higher than that of the CZ and FZ processes but lower than ribbon growth techniques. The sample FZ and CZ were commercial single crystal wafers grown by standard processes.

DISCUSSION

From the experiments described above we have determined bulk solubility value for D, at 250°C to be $1 \times 10^{17}/\text{cm}^3$. Through experiments involving implantation (and diffusion) at different energies, we have found that the concentration of H or D at the surface increases with an increase in the ion energy. Hence, it is concluded that the solubility of H or D in silicon increases with an increase in the degree of damage. Such results have also been observed by other researchers, and has also been attributed to trapped H(D) at non-equilibrium defects produced by implantation damage [13]. Although the questions of solubility and trapping remain unresolved, it is clear that the bulk solubility value obtained by this procedure is free from trapping effects due to dopants because, at 250°C, the dopant related trapping is unlikely. Furthermore, the solubility value of $1 \times 10^{17}/\text{cm}^3$ is considerably higher than the boron concentration in our samples.

From the above results it is clear that the diffusivity depends on material parameters other than resistivity. It is seen that diffusivity increases with increase in growth rate, carbon concentration, and decreases with oxygen content. It is interesting that the same factors also influence the vacancy concentration in silicon. The vacancy concentration is expected to increase in the following monotonically increasing manner: CZ \rightarrow FZ \rightarrow CP \rightarrow RP-2 \rightarrow RP-1. It is therefore concluded that the diffusivity of hydrogen in as-grown silicon depends on the vacancy concentration. We have proposed that hydrogen forms a complex with a vacancy, and such a complex has a high diffusivity, close to that of a vacancy. Theoretical studies have shown H can interact with a neutral or negatively charged mono-vacancy, and that the energy associated with the vacancy assisted motion of a hydrogen atom is lower than that of the vacancy alone [14].

In order to verify that vacancy concentration in the as-grown substrates varies in the order mentioned above, we performed Positron Annihilation Spectroscopy on these samples. Although these results are not quantitative, the PAS has shown that qualitatively the increase in the concentration of the vacancy type of defects is in accordance with the above order [15]. It was also found that the defects in the solar cell materials are not mono-vacancy type but vacancy clusters [15]. The mobility of such clusters is not expected to be high. However, it is conceivable that at the processing temperatures such vacancy clusters will dissociate allowing hydrogen to be coupled to mono-vacancies. It is known that dissociation of vacancy clusters can occur at moderately low temperatures. Indeed this mechanism would explain why kinks in Figure 1 do not appear at or above 250°C. One would also expect that hydrogen-vacancy complex would not experience significant trapping.

It is interesting to note from Fig. 3 that the maximum hydrogen diffusivity value of $7 \times 10^{-8} \text{ cm}^2/\text{sec}$ at 250°C is slightly lower than obtainable from VWW data. This value is also lower than the expected diffusivity of vacancies. This result may suggest that coupling of hydrogen to vacancy lowers the diffusivity of vacancies but enhances diffusivity of hydrogen by minimizing trapping.

These conclusions are very important to solar cells in terms of identifying the materials that can respond favorably to impurity and defect passivation. Experimental results on solar cell passivation show that hydrogen introduced from the backside can produce passivation of the entire cell [16]. However, if the oxygen concentration is high (>20 ppma) very little or no passivation effect is observed. Likewise, rapidly grown ribbon cells exhibit a high degree of passivation.

The results of this work are only preliminary indications that the low-temperature diffusion involves vacancy participation. Further experiments are underway to determine diffusivity as a function of temperature for FZ material grown at different speeds, and in the presence of vacancy injection.

ACKNOWLEDGMENT

The authors would like to thank Robert Reedy and Sally Asher for SIMS analyses, and Profs. S. Ashok of Pennsylvania State university for ECR hydrogenation. They are very grateful to Prof. S. Estreicher and T. Tan for many valuable discussions. This work was supported by the U. S. Department of Energy under contract No. DE-AC02-83CH10093.

REFERENCES

1. C. T. Sah, J. Y. Chen, and J. J. T. Tzou, *J. Appl. Phys.*, **54**, 944(1983).
2. R. Gale, F. J. Feigl, C. W. Magee, and D. R. Young, *J. Appl. Phys.*, **54**, 6938 (1983).
3. C. H. Seager, R. A. Anderson, and J. K. G. Panitz, *J. Mater. Res.* **2** (1), 96, Jan. /Feb.(1987).
4. A. Van Wieringen and N. Warmholtz, *Physica*, **22**, 849(1956).
5. J. W. Corbett, J. L. Lindstrom, and S. J. Pearton, *MRS Proc.* **104**, 229(1988).
6. S. J. Pearton, J. W. Corbett, and M. Stavola, *Hydrogen in Crystalline Semiconductors*, Springer Verlag, 1992.
7. B. L. Sopori, K. Jones, and X. Deng, *Appl. Phys. Lett.* **21**, 5260 (1992).
8. I. Perichaud and S. Martinuzzi, *Proc. 22nd IEEE, PVSC*, 877 (1991).
9. J. C. Muller, Y. Ababou, A. Barhdadi, E. Courcelle, S. Unamuno, D. Salles, and P. Siffert, *Solar Cells*, **17**, 201 (1986).
10. B. L. Sopori, Symposium, Defect Engineering in Semiconductor Growth, Processing, and Device Technology, *MRS, Proc.* **262**, 407(1992).
11. J. Lindhard and M. Scharff, *Phys. Rev.* **124**, 128 (1961).
12. J. G. Gibbons, W. S. Johnson, and S. W. Mylroie, *Projected Range Statistics (Semiconductors and Related Material)*, John Wiley & Sons, Stroudsburg, Pennsylvania, 1975.
13. S. Ashok and K. Giewont, *Jap. J. Appl. Phys.*, **24**, L533(1985).
14. S. K. Estreicher, *Mater. Sci. Engr. Reports*, to be published.
15. B. L. Sopori, X. Deng, R. Reedy, S. Asher, and S. Sharma, to be published.
16. B. L. Sopori, *J. Appl. Phys.* **64**, 5264(1988).

ECR HYDROGEN PLASMA TREATMENT OF Si: DEFECT ACTIVATION UNDER THERMAL ANNEAL

C.W. Nam* and S. Ashok

Departments of Electrical Engineering & Engineering Science

Electronic Materials and Processing Research Laboratory

The Pennsylvania State University, University Park, PA 16802, USA

*Present address: Dept. of Elec. Engg., University of Ulsan, South Korea

ABSTRACT

Si wafers subject to short-time (4-12 min.), low-temperature atomic hydrogen cleaning in an electron cyclotron resonance (ECR) plasma system have been annealed subsequently in the temperature range 300-750 °C for 20 mins. While only a small broad peak is seen immediately after hydrogenation, several pronounced and distinct majority carrier trap levels show up in deep level transient spectroscopy (DLTS) measurements of subsequently fabricated Schottky diodes on samples annealed at 450 °C and above. The concentrations of these deep levels reach a maximum at anneal temperatures around 500 °C and drop substantially beyond 750 °C. This phenomenon appears to be unrelated to the presence of oxygen in Si and is of potential importance in silicon processing technology.

INTRODUCTION

The role of hydrogen in crystalline silicon is of considerable applied interest in Si technology due to its inevitable presence in several processing steps such as plasma etching and deposition as well as Si surface cleaning and passivation. A body of experimental results in recent years also attests to possible future applications of hydrogen; these include improvement of MOS (metal-oxide-semiconductor) gate oxide integrity with pre-oxidation high-temperature H₂ anneal,¹ passivation of ion bombardment damage at Si/SiO₂ interface with atomic hydrogen,² and suppression of oxygen precipitates in SIMOX (Separation by Ion Implant Oxidation) process with hydrogen implantation.³ The interaction of hydrogen with Si encompasses a variety of topics such as dopant-hydrogen complexes, passivation of defects, and hydrogen-induced defects.⁴

The behavior of non-dopant species in Si is also considerably influenced by the presence of hydrogen. An interesting finding concerns the enhancement of thermal donor (TD) formation in (Czochralski-grown or CZ) Si when the necessary thermal annealing step is done *in* a hydrogen plasma^{5,6}. This hydrogen-assisted TD formation has been studied by infrared (IR) and spreading resistance measurements. TDs are a consequence of oxygen present in CZ Si and usually arise from prolonged thermal anneal at around 400 °C. In continuation our study of the surface electrical properties of Si following low-temperature ECR H plasma cleaning,⁷ we have uncovered generation of pronounced deep level defects in both p-type and n-type Si when the

wafers were *subsequently* annealed at 450 °C and above for short durations (20 min.). The defect concentrations peak at an anneal temperature of around 500 °C and drop to negligible values above 750°C. While this temperature dependence is similar to that of thermal donors characteristic of CZ Si, our studies with CZ-Si of different oxygen concentrations suggest that the generation of these deep level defects is unrelated to the oxygen concentration in Si.

EXPERIMENTAL TECHNIQUE

The wafers used in this study were 6 inch diameter boron-doped p-type <100> Si and phosphorous-doped <100> Si, both CZ-grown with resistivity in the range 1-20 ohm-cm. The hydrogen plasma cleaning chamber is a downstream Varian ECR module operated at 2.45 GHz. The wafers were exposed to an H ECR plasma (2.5 mTorr pressure and 15 sccm H₂ flow) at a net microwave power of about 800 W for periods of 4, 8 and 12 mins. The temperature rise of the Si substrates was estimated to be below 200°C during the treatment.

The evolution and annihilation of defects following the ECR hydrogen plasma treatment was monitored by 20 min. isochronal anneal in N₂ of different sets of samples at temperatures over the range 300 -750 °C. After an HF drip to remove any native oxide, suitable Schottky (Au for n-Si and Al/Ti for p-Si) and ohmic contacts were deposited by thermal evaporation on all the chips.

RESULTS AND DISCUSSION

The current-voltage (I-V) and capacitance-voltage (C-V) characteristics of the devices reveal changes in Schottky barrier height for both n- and p-Si, and considerable dopant deactivation in p-Si due to the well-known B-H complex formation. Bias-temperature anneal of the latter devices also show the expected drift of hydrogen as H⁺ from the high electric field region near the interface to the lower field bulk region.

The DLTS measurements were carried out on the Schottky diodes using a BioRad system. The absence of DLTS signal for control samples (no H plasma or anneal) reveals defect concentrations below the detection limit ($< 10^{11} \text{ cm}^{-3}$). The samples exposed to the ECR H plasma displayed a single broad peak, with a bias dependence of the peak suggesting a shallow depth profile. We shall designate the electron and hole traps as E and H respectively, followed by numbers in parentheses specifying the location in energy (eV) from the conduction and valence band edges respectively. For a reverse bias of -2 V and filling pulse height of 0.5 V, the 4 min. exposed n-sample has a dominant (majority carrier) peak E(0.42) with a concn. of $\sim 1.6 \times 10^{12} \text{ cm}^{-3}$; the corresponding values for the p-sample are H(0.47) and $\sim 1.2 \times 10^{12} \text{ cm}^{-3}$ respectively. Since the low-energy H plasma could cause very little lattice damage, we attribute these levels to hydrogen-induced defects that are electrically active.

The H plasma cleaned (as well as control) samples were annealed for 20 min. in N_2 at temperatures varying from 300 to 750 °C. For the H plasma cleaned n-Si sample, there is only a slight broadening of the E(0.42) peak, with a slight reduction in concentration after the 400 °C anneal. However, after a 450 °C anneal four strong new peaks - E(0.25), E(0.36), E(0.53) and E(0.64) - begin to emerge. They are greatly accentuated at slightly higher anneal temperatures, and the dramatic change in the defect states of the 4 min. H plasma cleaned n-type Si samples before and after a 530°C-20 min. anneal is shown in Fig. 1. The E(0.42) H-related defect peak of the sample before the anneal is hardly visible on the scale of Fig. 1. On control samples that were annealed simultaneously with the H cleaned samples none of the above peaks were detected, thus confirming that these levels are a consequence of H in the Si and not due to any possible heavy metal contamination.

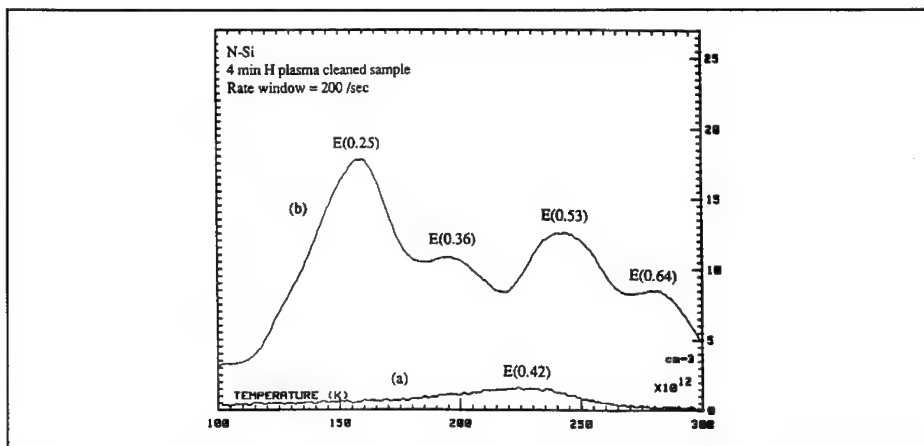


Figure 1 DLTS spectra of n-type Si sample exposed to ECR H plasma for 4 min. (a) before and (b) after annealing at 530 °C for 20 min. In the designation E(x), E denotes electron trap and x its location in eV below the conduction band edge of Si.

Fig. 2 shows the concentrations of the various peaks seen in H cleaned n-Si samples as a function of the anneal temperature. This pattern is rather similar to that of thermal donors (TD) well known to occur in oxygen-rich CZ-Si under long-term (20+ hours) anneal at ~ 400-450 °C and be annihilated at ~ 750 °C. While we are not aware of any reports of the above electron trap levels associated with thermal donors in n-type CZ Si, similarities with thermal donor behavior are evident. For instance, the trap concentrations reach their maxima at 500 °C, and decrease gradually at higher temperature. Further, under an extended anneal at 500 °C for 30 min., the concentrations of deep levels increase (not shown in figure) as expected for thermal donors. But as will be shown below, this appears to be a mere coincidence and the mechanisms of thermal donor enhancement by H plasma and deep level formation reported in this study are quite different.

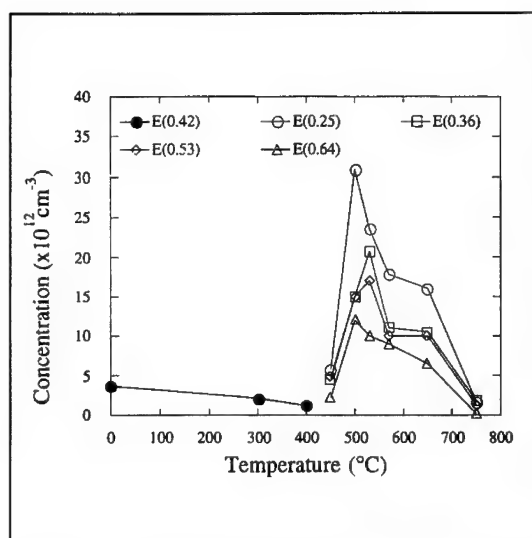


Figure 2 Annealing behavior of thermally induced defects for the 4 min. ECR H plasma cleaned n-Si samples. The anneal time is 20 min. at each temperature. In the designation E(x), E denotes electron trap and x its location in eV below the Si conduction band edge.

The formation of deep levels under thermal anneal of H plasma cleaned p-Si has also been seen in our study. As shown in Fig. 3, distinct peaks of pronounced magnitude [H(0.19), H(0.46) and H(0.56)] develop after the anneal. As in the case of n-Si, control p-Si samples subject to the same 500 °C - 20 min. anneal do not show any of these peaks. An earlier study of anneal *in* hydrogen plasma (300 °C - 3 hr.) has also revealed several hole traps ranging in energy from 0.07 to 0.49 eV⁸, and contrasts with the frequent passivation of defects - including the oxygen-related TD - by hydrogen plasma⁹. To reiterate, our samples had the H plasma exposure without any intentional heating of the wafers, and the annealing was done subsequently in an inert ambient.

It has been reported that thermal anneal of Si *in* a hydrogen plasma enhances oxygen diffusion

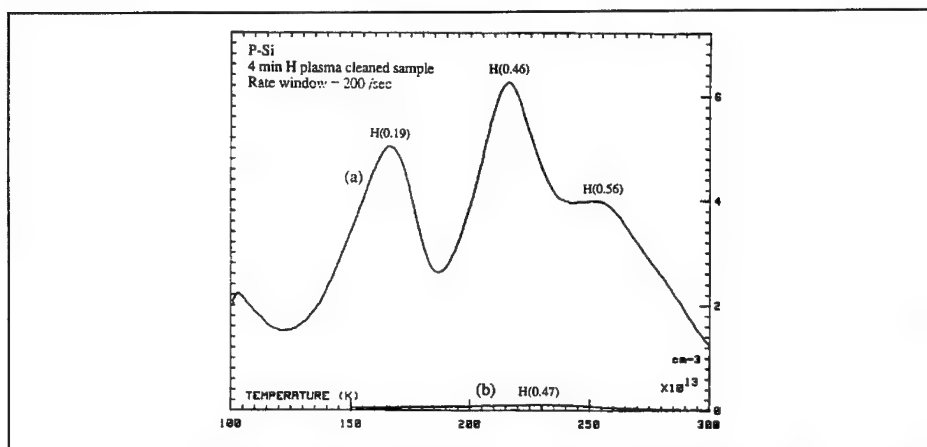


Figure 3 DLTS spectra of 4 min. H plasma treated p-Si (a) before and (b) after annealing at 500 °C for 20 min. In the designation H(x), H denotes electron trap and x its location in eV above the valence band edge of Si.

as well as TD formation, while anneal in molecular hydrogen does not.¹⁰ In addition, the TDs appear only after a minimum anneal time of ~2 hours in the hydrogen plasma at ~400 °C, suggesting a diffusion-limited process. It is hence rather surprising that a 4 min. ECR H plasma clean followed by a 450 °C anneal for a duration as short as 20 min. can give rise to such pronounced deep level defects in both n- and p-Si. Incidentally, we have also carried out parallel anneal experiments of ECR Ar plasma cleaned Si, and none of the above deep levels are detected in these samples. Thus the presence of these deep levels only in the H plasma treated samples precludes the possible involvement of Cu or Fe, which are known to create vacancies during cool-down and enhance TD formation.¹¹ Moreover, as the H plasma exposure time increases, the concentrations of the deep levels after anneal increase.

In order to verify any correlation between these post-H-plasma thermal anneal-induced deep level defects and enhanced thermal donor generation in H-plasma-treated Si, we ECR-hydrogenated magnetic CZ (MCZ) samples with lower oxygen concentration (5 ppma) along with conventional CZ samples (10-12 ppma). The deep level concentration in the MCZ samples turned out to be higher, thus precluding the role of oxygen in the defect activation process. In fact, we have observed development of the deep levels even in epitaxial Si films that incorporate minimal amounts of oxygen. Thus the deep level generation phenomenon reported here is unrelated to the enhanced thermal donor generation in H-plasma-treated Si, and has its origins elsewhere.

SUMMARY

In summary, we have observed strong distinctive DLTS peaks developing on ECR hydrogen plasma cleaned n- and p-Si after the samples have been annealed at 450 °C for durations as short as 20 min. On isochronal anneal, the concentrations of these levels monotonically reduce at temperatures above 500 °C, and reach negligible levels above 750 °C. The absence of correlation between these defects and the oxygen concentration in the Si rule out any relation to the recently reported hydrogen-enhanced thermal donor formation in Si. One possible speculation on the nature of this phenomenon is that these hydrogen-induced *latent defects* may be the consequence of Si microcavities arising from the high-fluence ECR hydrogen plasma. The defects are then electrically inactive immediately after the hydrogenation, due apparently to the (self-)passivation by H. Anneals at temperatures above 450 °C then activates these defects by the thermal release of passivating H-species.

ACKNOWLEDGMENTS

We would like to thank Drs. Wilman Tsai and Mary Day of Varian Research Center for carrying out the ECR plasma cleaning of the wafers. We also acknowledge the generous support of the Nam Foundation, Korea.

REFERENCES

1. N. Adachi, H. Nishikawa, Y. Komatsu, H. Hourai, M. Sano and T. Shigematsu, in Defect Engineering in Semiconductor Growth, Processing and Device Technology, edited by S. Ashok, J. Chevallier, K. Sumino and E. Weber (Mater. Res. Soc. Proc. **262**, Pittsburgh, 1992), p. 815.
2. S. Kar and S. Ashok, J. Appl. Phys. **73**, 2187 (1993).
3. B. Mizuno, M. Kubota, N. Nomura and M. Yamamoto, J. Appl. Phys. **62**, 2566 (1987).
4. N.M. Johnson, C. Doland, F. Ponce, J. Walker and G. Anderson, Physica B **170**, 3 (1991).
5. H.J. Stein and S. Hahn, Appl. Phys. Lett. **56**, 63 (1990).
6. R. Murray, A.R. Brown and R.C. Newman, Materials Science and Engineering **B4**, 299 (1989).
7. C.W. Nam, S. Ashok, W. Tsai and M.E. Day, J. Vac. Sci. Technol. B **5**, 3010 (1994).
8. J.M. Hwang, D.K. Schroder and W.J. Biter, J. Appl. Phys. **57**, 5275 (1985).
9. S.J. Pearton, A.M. Chantre, L.C. Kimmerling, K.D. Cummings and W.C. Dautremont-Smith in Oxygen, Carbon, Hydrogen and Nitrogen in Silicon, Edited by J.C. Mikkelsen, Jr. et al Mat. Res. Soc. Proc. **59**, Pittsburgh, 1986) p. 475.
10. R. Murray, Physica B **170**, 115 (1991).
11. R.C. Newman, A.K. Tipping and J.H. Tucker, J. Phys. C **18**, L 861 (1985).

HYDROGEN AND LITHIUM PASSIVATION OF GOLD IN SILICON : A COMPARATIVE STUDY

E.Ö. SVEINBJÖRNSSON*, S. KRISTJANSSON**, O. ENGSTRÖM*, and H.P. GISLASON**

*Department of Solid State Electronics, Chalmers University of Technology,
S-412 96 Göteborg, Sweden

**Science Institute, University of Iceland, Dunhaga 3, IS-107 Reykjavik, Iceland

ABSTRACT

We report studies of passivation of the gold center in silicon by hydrogen and lithium using deep level transient spectroscopy (DLTS), capacitance voltage (CV) profiling and secondary ion mass spectroscopy (SIMS). Both lithium and hydrogen are able to remove the electrical activity of the gold center from the silicon band gap but the passivation mechanisms are different. In the case of lithium the passivation is most likely due to a Coulomb attraction between lithium donors Li^+ and gold acceptors Au^- . No complex formation is observed between Li^+ and Au^0 . In contrast, hydrogen is able to passivate the gold center without the need of opposite charge states of the species involved. Two Au-H complexes are observed, one (G) electrically active, and another (PA) passive. Based on the annealing kinetics of these complexes we propose that the active complex is a Au-H pair and that the passive complex contains two H atoms (Au-H_2).

INTRODUCTION

The possible use of hydrogen to deactivate deep impurities in silicon has been investigated considerably in recent years¹. From technical point of view such a passivation technique is an alternative method to gettering², where the aim is to suppress the concentration of deep level metallic impurities in the active regions of devices. However, the thermal stability of the passivation is in general too low to be of practical use¹. Another drawback is that new deep levels related to hydrogen and the metal impurities are sometimes observed after hydrogenation³⁻⁶. The purpose of this work is to investigate whether lithium is able to electrically passivate transition metal impurities and if so, compare it with hydrogen passivation. This study is supported by recent investigations of Li-doped GaAs where it was demonstrated that both shallow and deep acceptors in GaAs are passivated by lithium^{7,8}. Lithium is a fast interstitial diffuser in silicon with high interstitial solubility⁹ and acts as a shallow donor at $E_c - 0.034 \text{ eV}$ ¹⁰. In this paper we report lithium passivation of gold acceptors in n-type silicon and compare the results with our new findings concerning hydrogen-gold complexes.

EXPERIMENTAL DETAILS

In the Au-H study presented here we used p-type silicon with resistivities between 1 and 70 Ωcm . The details of the gold doping procedure have been given elsewhere⁵. Atomic hydrogen was introduced into the surface layers of the wafers by means of wet chemical etching^{3,5}. Schottky contacts were formed by evaporation or sputtering of aluminum or titanium at room temperature and GaAl was used as an ohmic contact.

The starting material in the Li study was gold-doped FZ n-type silicon with resistivities between 8.5 and 11 Ωcm . After etching and cleaning the samples were covered with Li (99.9%) in mineral oil emulsion. The samples were then heat-treated in a diffusion furnace in open quartz boats using argon ambient. The usual procedure was a Li pre-deposition at 300-350°C for 10-30 minutes, after which excess Li was removed from the surface of the samples. Lithium was driven in using heat treatment between 250 and 350°C followed by rapid quenching in liquid nitrogen. Finally the samples were polished and etched and Al-Schottky diodes were fabricated. Two types of reference samples received the same heat treatment as the Au-Li co-doped specimens: 1) samples doped only with Au and 2) samples doped with Li alone. The gold acceptor concentration in the gold-doped reference samples did not change during the processing. DLTS revealed no deep levels in the lithium-doped reference samples.

RESULTS AND DISCUSSION

Lithium passivation of gold acceptors

SIMS analysis and CV profiling revealed that most of the lithium in the Au-Li co-doped samples was electrically active as shallow donors and the Li density was in most cases uniform throughout the samples¹¹. Figure 1 shows typical DLTS spectra of lithium-diffused gold doped samples after heat treatment at different temperatures. After Li diffusion at 300°C the sample was slowly cooled to 100°C and kept at this temperature for 12 hours. This resulted in active lithium donor concentration of $5 \times 10^{14} \text{ cm}^{-3}$. Thereafter the sample was polished and etched and divided into a number of $5 \times 5 \text{ mm}^2$ specimens, and each piece was then annealed at a specific temperature, as indicated in the figure, for 30 minutes followed by quenching in liquid nitrogen. After surface cleaning, several Schottky diodes were made from each specimen.

The peak at 270 K is due to the gold acceptor level³ with an activation energy $\Delta E = 0.54 \text{ eV}$ (including T^2 adjustment) and an electron capture cross section $\sigma_n = 1 \times 10^{-16} \text{ cm}^2$. The feature labeled L1 has $\Delta E = 0.41 \text{ eV}$ and $\sigma_n = 1.5 \times 10^{-17} \text{ cm}^2$. No temperature dependence of this capture cross section is observed within the temperature range 225-256 K. This new signal is not observed in either type of reference samples. The small peak labeled G1 ($\Delta E = 0.19 \text{ eV}$, $\sigma_n = 1 \times 10^{-17} \text{ cm}^2$) has been studied previously³ and arises from an acceptor level of a hydrogen-gold complex. G1 is only found in the surface region of the sample and is due to injection of hydrogen during wet chemical etching.

Reference samples doped with gold but no Li show DLTS spectra that are similar to spectrum f, corresponding to gold concentration of approximately $2 \times 10^{14} \text{ cm}^{-3}$. We notice that gold acceptors are reactivated with increasing annealing temperature while the L1 peak is strongest at 250°C. In addition, the reactivation and passivation of gold acceptors is reversible; the amount of active gold acceptors is only dependent upon the final heat treatment, as long as no out-diffusion of Li takes place. SIMS and CV analysis reveal that the lithium concentration within the samples usually remains constant during the annealing cycles. The passivation of gold is stable at room temperature; storage for several months had no effect on the DLTS spectra.

The above results suggest that the L1 trap is related to both gold and lithium. This is even more apparent when the dissociation of L1 is studied during reverse bias annealing (RBA). Figure 2 shows the concentration depth profiles of L1 and the Au acceptors before and after reverse bias annealing at 100°C for 30 minutes. At this temperature the dissociation and the formation of L1 are in equilibrium, as is clearly evident outside the depletion region. However, inside the space charge region there is a net dissociation of L1. This is probably due to the electric field within the space charge layer which rapidly drives the positively charged lithium towards the surface and results in a net dissociation of L1 and an equal increase in the Au signal. This demonstrates the participation of gold in L1 and suggests that L1 contains one Au atom. Au-Li co-doped samples without L1 traps do not show any change in the gold acceptor density after similar heat treatment.

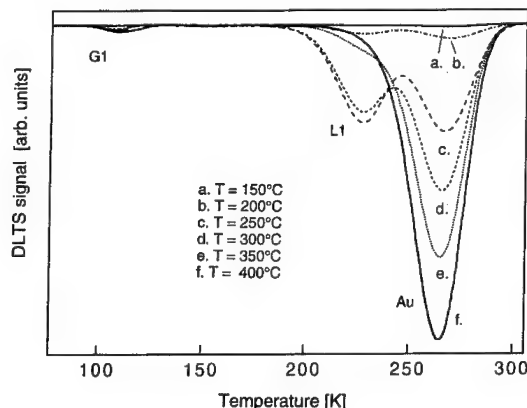


Figure 1. Reactivation of lithium passivated gold acceptors as a function of temperature. The samples were first heat-treated at 100°C for 12 hours and each sample was then annealed for 30 minutes at the temperature indicated. Gold acceptors are fully reactivated after annealing at 400°C for 30 minutes (sample f).

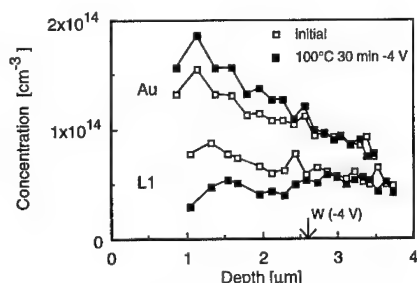


Figure 2. Depth profiles of L1 and active gold acceptors before and after reverse bias annealing at 100°C for 30 minutes using a bias of -4 V. The depletion layer edge W during the heat treatment is at approximately 2.6 μm.

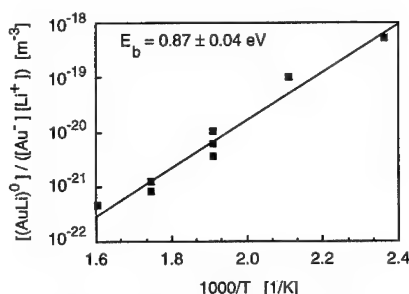


Figure 3. Estimation of the binding energy of Au-Li pairs.

The strong passivation of gold acceptors by lithium suggests that a long-range Coulomb interaction between mobile interstitial Li donors and immobile Au acceptors is responsible for the passivation. It is possible to describe the equilibrium concentration of such Au-Li pairs by the law of mass action¹²

$$[N_{(\text{Au}-\text{Li})^0}] / [N_{\text{Au}^-}] [N_{\text{Li}^+}] = (1/N_i) \exp [\Delta S/k] \exp [-\Delta H / kT]. \quad (1)$$

where $[N_{(\text{Au}-\text{Li})^0}]$ is the equilibrium concentration of neutral Au-Li pairs, $[N_{\text{Au}^-}]$ is the fraction of the negatively charged gold given by Fermi-Dirac statistics, $[N_{\text{Li}^+}]$ the lithium donor concentration, N_i is the number of possible sites for the pair, ΔH is binding enthalpy of the pair and ΔS is the entropy change. The concentration of Au-Li pairs is estimated by $[N_{(\text{Au}-\text{Li})^0}] = [N_{\text{Au},\text{t}}] - [N_{\text{Au}}] - [N_{\text{Li}}]$, i.e. both the remaining active gold density, $[N_{\text{Au}}]$, and the L1 concentration, $[N_{\text{Li}}]$, are subtracted from the initial gold concentration $[N_{\text{Au},\text{t}}] = 2 \times 10^{14} \text{ cm}^{-3}$. The phosphorus donor density was $5 \times 10^{14} \text{ cm}^{-3}$. The time needed to reach equilibrium was shorter than 30 minutes in the temperature range 150–400°C. We determined the binding energy of the Au-Li pair from the Arrhenius plot of equilibrium data. A least squares fit to the data in figure 3 gives a free binding energy $E_b = -\Delta H = 0.87 \pm 0.04 \text{ eV}$ and a prefactor of $3 \times 10^{-23} \pm 2 \times 10^{-23} \text{ cm}^3$. The prefactor is an estimate of $(1/N_i) \exp [\Delta S_0/k]$, where ΔS_0 is the temperature-independent part of the entropy. N_i is often¹² of the same order as the silicon lattice density $N_{\text{Si}} = 5 \times 10^{22} \text{ cm}^{-3}$. This suggests that the entropy term is small.

In general we observe that diffusions giving Li concentrations above $\approx 1 \times 10^{15} \text{ cm}^{-3}$ result in a decrease of the active gold acceptor concentration by more than two orders of magnitude, or below the detection limit of the DLTS system ($5 \times 10^{11} \text{ cm}^{-3}$). For lithium concentrations in the $1 \times 10^{14} - 1 \times 10^{15} \text{ cm}^{-3}$ range, L1 appears after lithium diffusion at the same time as a significant gold passivation occurs. From a series of experiments using different Li concentrations we observe that the portion of gold which is neutral at the annealing temperature ($\leq 200^\circ\text{C}$) is not passivated by lithium while virtually all negatively charged gold atoms are passivated¹¹. Hence, in order to strongly passivate the gold atoms the Fermi-level must be well above the gold acceptor level at the annealing temperature. This is also supported by our investigations of p-type samples co-doped with gold and lithium where no significant gold donor passivation is observed after Li diffusion.

It is possible that Li occupies different interstitial sites in the two Au-Li complexes, one resulting in passivation of gold acceptors and the other responsible for the L1 level. Altheld et al¹³ reported two separate gold-lithium centers, identified as an orthorhombic Au-Li pair and a trigonal Au-Li₃ complex by EPR and Double ENDOR studies. The Au-Li pair in their work is one possible candidate for the gold passivation observed in the present work. The Au-Li₃ complex has a single donor level within the band gap above $E_c - 0.4 \text{ eV}$ ¹³. It is possible that L1 is the donor level of this complex, although the electron capture cross section ($\sigma_n = 1.5 \times 10^{-17} \text{ cm}^2$) is smaller than expected for a single donor trap.

Hydrogen passivation of gold

Figure 4 summarizes the reactions that we have observed between gold and hydrogen¹⁴. Three deep levels G1, G2, G4 are observed after etching and we attribute them to the same Au-H complex. This complex is labeled G. Another Au-H complex PA (passive) has no deep levels in the band gap. In this paper we concentrate on the $G2 \Rightarrow PA$ transition and present data which suggests that PA contains a larger number of hydrogen atoms than the G complex.

In p-type Si we used reverse bias annealing to drive in atomic hydrogen from the surface layer into the bulk⁵. This is monitored by studying the active boron acceptor depth profiles from CV analysis before and after RBA. Figure 5 shows the corresponding depth profiles of active boron acceptors, gold donors and G2 before and after RBA at 120°C using -3 V bias for 10 minutes. The depletion layer edge during the RBA was at approximately 1.4 μm . We note the correlation between the trap profiles and the active boron profile. During the heat treatment B-H pairs dissociate and the released positively charged atomic hydrogen ions are driven towards the depletion layer edge where three processes occur: 1) new B-H pairs form, 2) the active gold donor density decreases and 3) the G2 concentration increases by roughly the same amount. We observed earlier that all these changes follow the depletion layer edge and that the profiles can be modulated by adjusting the reverse bias⁵. Furthermore, no significant changes of the trap profiles are observed if the samples are annealed under a reverse bias at lower temperatures where the B-H pairs are stable⁵. This demonstrates that the B-H pairs act as a source of hydrogen and the G2 trap is evidently hydrogen-related. No passivation of gold donors is observed at this temperature, i.e., the G2 concentration fully accounts for the decrease of the gold donor concentration. This is no longer true if the temperature is raised to 150°C as demonstrated below.

The annealing behavior of G2 at 150°C depends on the hydrogen concentration in the vicinity of the complex. G2 transforms only into the passive Au-H complex PA if free atomic hydrogen is available. Otherwise, G2 dissociates at a slow rate. This is demonstrated in figures 6 and 7.

Figure 6a) shows reactivation of boron acceptors during annealing at 150°C without bias. The sample was first annealed as in figure 5. Majority of the B-H complexes were dissociated after about 30 minutes annealing and no significant change was seen in the active boron acceptor density upon further annealing (not shown). A reference sample showed that the remaining B-H density after 60 minutes zero bias annealing at 150°C was $\approx 5 \times 10^{14} \text{ cm}^{-3}$ at depths between 1.1 and 1.6 μm . This means that atomic hydrogen is available at these depths during the heat treatment. This is where the DLTS data in Fig. 6b) was collected. During the first 10 minutes the G2 concentration increased while the gold donor concentration steadily decreased. Thereafter concentrations of both traps decreased. This was not accompanied by any new DLTS peaks; the gold involved was apparently passivated. We label the passive hydrogen-gold complex PA. It should be pointed out that PA could possibly have shallow level(s) within the band gap that are not accessible with DLTS. The gold donor density reached a constant value after about 30 minutes and remained unchanged during further annealing.

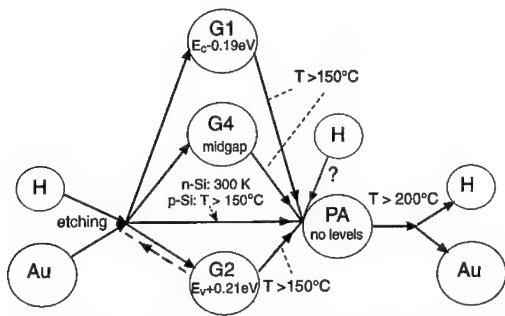


Figure 4. Schematic diagram of the reactions observed involving gold and hydrogen.

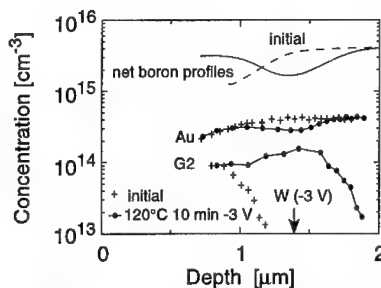


Figure 5. Depth profiles of active boron acceptors, gold donors and G2 before and after reverse bias annealing at 120°C.

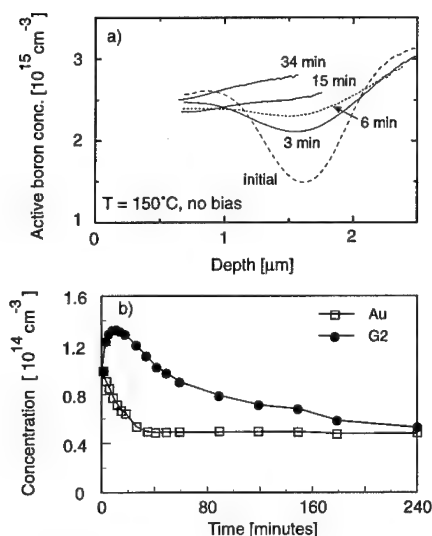


Figure 6. a) Dissociation of B-H complexes at 150°C . Most of the B-H pairs dissociated during the first 30 minutes. The B-H density thereafter remained more or less constant at a value of about $5 \times 10^{14} \text{ cm}^{-3}$, see text. b) Concentrations of G2 and gold donors at depths between 1.1 and $1.6 \mu\text{m}$ as functions of time at 150°C .

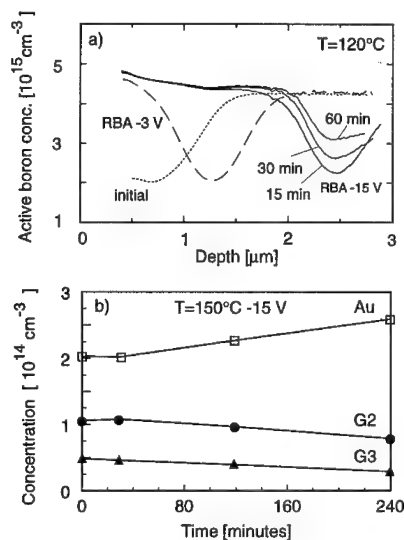


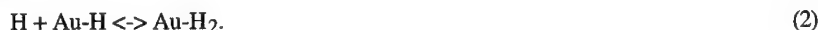
Figure 7. a) Active boron concentration during pre-annealing at 120°C . First, hydrogen was injected by RBA (-3 V) for 10 minutes to form G2 as in Fig. 5. Thereafter the sample was annealed using -15 V bias for 60 minutes to remove virtually all B-H complexes at depths between 0.9 and $1.4 \mu\text{m}$ where the deep level densities were estimated using DLTS. b) Concentrations of the deep centers during RBA (-15 V) at 150°C after pre-annealing as in a).

The annealing kinetics of G2 in the absence of free hydrogen are shown in figure 7b). In this case the region monitored with DLTS was made hydrogen free by proper pre-annealing as shown in figure 7a). The sample was first annealed at 120°C for 10 min. using -3 V bias to inject hydrogen and form G2 as in figure 5. Thereafter the sample was annealed at 120°C for 60 minutes using a reverse bias of -15 V . During this treatment hydrogen released from B-H pairs is driven towards the depletion layer edge at $\approx 2.5 \mu\text{m}$ where new B-H complexes are formed. This is detected after 15 minutes as a decrease in the active boron density in figure 7a). The concentrations of gold donors, G2 and G3 at depths between 0.9 and $1.4 \mu\text{m}$ did not change significantly during this heat treatment (not shown). G3 is a Au-H-related level⁵ but its annealing behavior differs from that of G1, G2 and G4¹⁴. Hence, it probably belongs to a different Au-H complex.

Figure 7 shows the changes in the densities of G2, G3 and gold donors during annealing at 150°C using a bias of -15 V after pre-annealing as in 7a). The annealing kinetics are completely different from those observed in figure 6b). As expected, no gold donor passivation is observed. In contrast, the gold donor concentration increases with annealing time. The increase of the gold donor density roughly equals the simultaneous decrease of the concentrations of both the G2 and G3 centers. Apparently, the G2 complexes dissociate at a slow rate during the annealing instead of transforming into passive Au-H complexes as in figure 6b). This suggests that additional hydrogen atoms are needed to transform G2 into PA complexes. In other words the passive Au-H complex (PA) seems to contain more hydrogen atoms than the G2 complex.

Furthermore, similar annealing kinetics are observed if no bias is applied to a sample during annealing at 150°C provided that virtually all B-H pairs in the region monitored with DLTS have been removed by pre-annealing at 120°C using a -15 V bias. This demonstrates that the reactions depend on the concentration of free hydrogen rather than the bias applied during annealing. We

tentatively assign G2 to Au-H and PA to Au-H₂ and suggest that G transforms to PA through the reaction



This reaction is a possible explanation for the absence of electrically active Au-H complexes in the previous studies of Pearton and Tavendale¹⁵. The hydrogen density in their samples was evidently much higher than in the current study and we expect the passive Au-H₂ complex to dominate in such a case.

The degree of the gold passivation seems to depend mostly on the interaction between hydrogen and the shallow dopants in the samples. In p-Si most of the incoming hydrogen immediately forms pairs with boron while in n-type samples only a fraction of the hydrogen forms pairs with phosphorus. This agrees with the observation that gold acceptors in n-Si are strongly passivated in the surface region after etching but gold donors in p-Si are not^{3,5}. Apparently, in p-Si, the hydrogen first has to be released from B-H pairs to a large extent to be able to form PA. This means that gold-doped silicon hydrogenated by annealing in H₂ ambient at very high temperatures should mainly contain the PA complex. This is in line with a similar study of Pt diffused silicon where a Pt-H₂ complex was identified after hydrogenation¹⁶.

CONCLUSIONS

We find that both hydrogen and lithium are able to passivate gold in silicon but we observe important differences. In the case of lithium we observe two different complexes between gold acceptors and lithium where one of them is most likely a passive Au-Li pair. The other complex has a deep level L1 in the band gap. Our results give no evidence for complex formation between neutral gold and lithium donors, i.e. Coulomb attraction between the species involved is apparently a prerequisite for complex formation. This together with the poor thermal stability of the passive Au-Li complexes severely limits the possible technical use of this method to passivate deep level impurities. In the case of hydrogen and gold we find that the elements form two separate complexes, the electrically active G and the passive PA. The complex G transforms irreversibly into PA during annealing and from the annealing kinetics we propose that the G complex is a Au-H pair while the passive complex is Au-H₂.

This work was financially supported by the Swedish National Board for Industrial and Technical Development (NUTEK), NorFA and the Icelandic Council of Science.

REFERENCES

1. S. J. Pearton, J. W. Corbett and M. Stavola, *Hydrogen in Crystalline Semiconductors* (Springer, Berlin-Heidelberg, 1992).
2. D. Gilles, in *Defect Engineering in Semiconductor Growth, Processing and Device Technology* edited by S. Ashok, J. Chevallier, K. Sumino, and E. Weber, Mater. Res. Soc. Symp. Proc. Vol. **262**, 917 (1992).
3. E. Ö. Sveinbjörnsson and O. Engström, in reference 2, p. 501.
4. T. Sadoh, H. Nakashima, and T. Tsurushima, J. Appl. Phys. **72**, 520 (1992).
5. E. Ö. Sveinbjörnsson, G. I. Andersson and O. Engström, Phys. Rev. B **49**, 7801 (1994).
6. T. Sadoh, M. Watanabe, H. Nakashima, and T. Tsurushima, J. Appl. Phys. **75**, 3978 (1994).
7. B. H. Yang, H. P. Gislason, and M. Linnarsson, Phys. Rev. B **48**, 12345 (1993).
8. T. Egilsson, H. P. Gislason, and B. H. Yang, Phys. Rev. B **50**, 1996 (1994).
9. E. M. Pell, Phys. Rev. **119**, 1222 (1960).
10. R. L. Aggarwal and A. K. Ramdas, Phys. Rev. **140**, A 1246 (1965).
11. E. Ö. Sveinbjörnsson, S. Kristjánsson and H. P. Gislason, J. Appl. Phys. **77** (7) (1995, in press).
12. H. Lemke, Physica Status Solidi (a) **76**, 223 (1983).
13. P. Alteheld, S. Greulich-Weber, J. -M. Spaeth, H. Overhof and M. Höhne, Mater. Sci. Forum **143-147**, 1173 (1994).
14. E. Ö. Sveinbjörnsson and O. Engström (unpublished).
15. S. J. Pearton and A. J. Tavendale, Phys. Rev. B **26**, 7105 (1982).
16. P. M. Williams, G. D. Watkins, S. Ufring, and M. Stavola, Phys. Rev. Lett. **70**, 3816 (1993).

ELECTRON SPIN RESONANCE EVIDENCE FOR A LOCALIZED EP (E' δ -LIKE) DEFECT STRUCTURE

JOHN F. CONLEY, JR. AND P.M. LENAHAN

The Pennsylvania State University, Department of Engineering Science and
Mechanics, University Park, PA 16802

ABSTRACT

We report the first observation of a hydrogen complexed EP (E' δ) center. Comparing EP/H and E' γ /H electron spin resonance spectra, we provide the first strong evidence that EP (E' δ) centers do not have a delocalized structure.

INTRODUCTION

Trapped holes dominate the electronic properties of amorphous thin film SiO₂. Trapped holes are also believed by some to participate in the formation of interface traps at the Si/SiO₂ boundary by interacting with H₂ to release a hydrogen species.^{1,2} This hydrogen species then travels to the interface where it creates defects. It has long been known that E' γ centers³⁻¹⁴ (an oxygen vacancy related defect consisting of an unpaired electron localized on a silicon backbonded to three oxygens) are important hole traps and it has been shown that there is a rough one to one correspondence between E' γ centers and trapped holes in the gate oxides of gamma irradiated MOS devices.³⁻⁵ E' γ centers also play an important role in hole trapping in separation by implanted oxygen (SIMOX) buried oxides.¹⁴ It was recently demonstrated that exposure to H₂ at room temperature results in the rapid transformation of E' γ centers into two H complexed defects.⁶ Since a buildup of interface traps occurred on the same time scale as the E' γ / H₂ reactions, it was concluded that E' γ center hole traps play an indirect role in interface trap formation.^{7,8}

Recently, a new type of E' center, which we provisionally term EP (for Provisional E'), has been reported in a variety of thin SiO₂ films.⁹⁻¹¹ EP (E' δ) defects (1) can participate in hole trapping in thermal oxides,^{9,11,15} (2) are responsible for approximately 20% of SIMOX E' centers,¹⁰ and (3) have been suggested as the defect responsible for border traps.¹² The center's electron spin resonance (ESR) spectra strongly resembles the E' δ spectra reported in bulk SiO₂ by Griscom and Friebele.¹³ Griscom and Friebele's proposed model for the E' δ consists of an unpaired electron delocalized over a cavity of Cl capped Si. While recent thin film experiments suggest that Cl is not involved,^{9,10,15} no strong evidence exists for the structure of the EP (E' δ) center in thin films. A thin film EP (E' δ) model has been proposed in

which the unpaired electron is delocalized over a silicon microcluster.¹⁰ This model has neither been confirmed nor proven wrong; EP structure remains unknown.

We demonstrate for the first time the conversion of EP centers into hydrogen complexed EP/H centers. (It had not previously been known whether EP defects would interact with H₂ at room temperature.) We compare EP/H₂ with E'_γ/H₂ reactions and find close similarities between the EP/H doublet spectra and the previously studied E'_γ/H 74G doublet ESR spectra. These similarities suggest that the structure of the EP center is similar to the structure of the E'_γ center and thus, contrary to a recent proposal,¹⁰ not delocalized. The EP/H₂ reaction occurs rapidly at room temperature, suggesting a possible role for EP centers in interface trap formation in some oxides.

EXPERIMENTAL DETAILS/RESULTS

Our study utilized "state of the art" SIMOX buried oxides since it is possible to preferentially generate quite high densities of either EP or E'_γ centers in these films.¹⁴ ESR measurements were performed at room temperature on an X-band spectrometer. H₂ exposures were performed at room temperature in forming gas (10% H₂, 90% N₂).

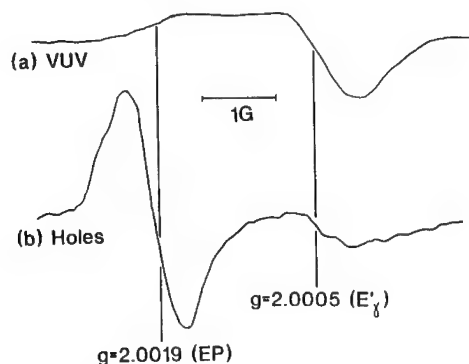


Fig. 1: ESR traces of SIMOX oxides after (a) 50 hours of VUV illumination without bias and (b) injection of approximately 5×10^{13} holes / cm².

Fig. 1 shows that extended exposure to vacuum ultraviolet (VUV) illumination ($hc/\lambda \leq 10.2$ eV) generates a very strong E'_γ signal (Fig. 1(a)) while very brief exposure to filtered VUV ($hc/\lambda = 10.2$ eV) with positive potential across the oxide generates a very strong EP signal (Fig. 1(b)).^{9,15} Substantial fractions of both of these E'_γ and EP centers are positively charged when paramagnetic.^{9,14}

Wider field ESR traces in Fig. 2 illustrate that room temperature H₂ exposure generates quite similar responses in the E'_γ and EP samples. In both cases, the H₂

exposure results in the conversion of E' centers into hydrogen complexed E' centers. Both conversion reactions take place in minutes and saturate within two hours at room temperature suggesting a role for both E' variants in the interface trap formation process. (The similar time scale also suggest a similar structure for E'_γ and EP centers.) Figure 2 illustrates the effects of the H₂ exposure after

approximately two hours. The strong center lines in Fig. 2 correspond to (a) $E'\gamma$ and (b) EP signals. The close side peaks in 2(a) are due to the so called 10.4 G $E'\gamma/H$ complex.¹⁶ Weak doublets appear separated by 74G about the $E'\gamma$ in 2(a) and separated by 78 G about the EP center in 2(b). (Since hydrogen doublets are split in two by the hydrogen hyperfine interaction and since spin densities are an order of magnitude lower than for standard E' signals, the hydrogen complexed defects are difficult to observe. ESR traces are thus shown after saturation of the E'/H reactions.) The $E'\gamma/H$ 74G doublet (an $E'\gamma$ center in which one of the backbonded oxygens is replaced by a hydrogen) has an effective $g = 2.0014$, very close to the value reported by Vitko.¹⁷ This effective g shift is somewhat greater than that predicted from the Breit-Rabi correction (if the E' electron wavefunction were otherwise unperturbed by the hydrogen). Vitko¹⁷ and Tsai and Griscom¹⁶ have noted that the 74G separation suggests about 15% localization on the hydrogen, consistent with very strong localization on a central silicon.

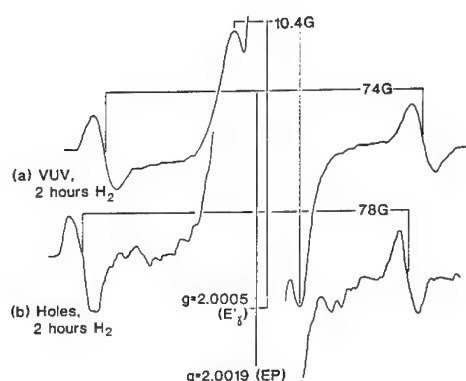


Fig. 2: Wide field ESR traces of the oxides from figure 1 after a subsequent two hour exposure to H_2 .

The EP/H 78G doublet has an effective $g=2.0036$, a shift again somewhat greater than one would expect from the Breit-Rabi correction but roughly comparable to that observed for the $E'\gamma/H$ doublet. The 78G splitting, consistent with the earlier suggestions of Vitko¹⁷ and Tsai and Griscom¹⁶ regarding the 74G doublet, suggests a nearly identical ~15% localization on the hydrogen. As in the case of the $E'\gamma/H$ 74G doublet, this suggests very strong localization of the unpaired electron on (presumably) one silicon atom.

DISCUSSION

The close similarity between the EP/H complex spectrum and the $E'\gamma/H$ complex spectrum combined with the similarity of the hydrogen reaction rates indicates similar defect structures. The close correspondence in doublet splitting suggests that, as in the $E'\gamma$ case, the EP unpaired electron is quite strongly localized on a single silicon atom. Strong localization on a single central silicon does not support the current delocalized silicon microcluster model of the EP ($E'\delta$) centers in thin films. An absolutely conclusive identification of the EP center awaits observation of the ^{29}Si doublet spectra.

Earlier studies have shown that a decrease in $E'\gamma$ density as a result of room temperature $E'\gamma/H$ reactions takes place on the same time scale (minutes) as a comparable increase in interface trap density. Since EP/H reactions also occur on this same time scale, they too may be involved in the post stress interface trap formation process.

CONCLUSIONS

We present the first substantial evidence that EP ($E'\delta$) do not have a highly delocalized unpaired electron. Our results suggest that EP centers are not silicon microclusters but are more closely related to conventional $E'\gamma$ centers. The fact that EP/ H_2 reactions take place at room temperature and on a time scale similar to $E'\gamma/H$ reactions suggests that EP centers may also play a role in interface trap formation in some oxides. Our results may also be of particular relevance to gate oxides since it has been suggested that EP ($E'\delta$) centers are border traps¹¹ and to SIMOX oxides where approximately 20% of E' are EP.¹²

REFERENCES

1. M.R. Shaneyfelt, J.R. Schwank, D.M. Fleetwood, P.S. Winokur, H.L. Hughes, and F.W. Sexton, IEEE Trans. Nuc. Sci. **37**, 1632 (1990).
2. R.A. Kohler, R.A. Kushner, and K.H. Lee, IEEE Trans. Nuc. Sci. **35**, 1492 (1988).
3. P.M. Lenahan and P.V. Dressendorfer, IEEE Trans. Nuc. Sci. **30**, 4602 (1983), J. Appl. Phys. **55**, 3495 (1984).
4. L. Lipkin, L. Rowan, A. Reisman, and C.K. Williams, J. Electrochem. Soc. **138**, 2050 (1991).
5. T. Takahashi, B.B. Triplett, K. Yokogawa, and T. Sugano, Appl. Phys. Lett. **51**, 1334 (1987).
6. J.F. Conley and P.M. Lenahan, Appl. Phys. Lett. **62**, 40 (1993).
7. J.F. Conley and P.M. Lenahan, Microelec. Engr. **22**, 215 (1993).
8. J.F. Conley, Jr. and P.M. Lenahan, IEEE Trans. Nuc. Sci. **40**, 1335 (1993).
9. J.F. Conley, Jr., P.M. Lenahan, H.L. Evans, R.K. Lowry, and T.J. Morthorst, J. Appl. Phys. **76**, 2872 (1994).
10. K. Vanheusden and A. Stesmans, J. Appl. Phys. **74**, 275 (1993).
11. W.L. Warren, M.R. Shaneyfelt, J.R. Schwank, D.M. Fleetwood, P.S. Winokur, R.A.B. Devine, W.P. Maszara, and J.B. McKitterick, IEEE Trans. Nuc. Sci. **40**, 1755 (1993).
12. W.L. Warren, M.R. Shaneyfelt, D.M. Fleetwood, J.R. Schwank, and P.S. Winokur, IEEE Trans. Nuc. Sci. **41**, 1817 (1994).
13. D.L. Griscom and E.J. Friebele, Phys. Rev. B. **34**, 7524 (1986).
14. J.F. Conley, Jr., P.M. Lenahan, and P. Roitman, proceedings INFOS '91, p. 259 (1991).
15. J.F. Conley, Jr., P.M. Lenahan, H.L. Evans, R.K. Lowry, and T.J. Morthorst, in Materials Reliability in Microelectronics IV, Vol. **138**, 1994 MRS Spring Meeting Proc., pp. 37-42 (1994).
16. J. Vitko, J. Appl. Phys. **49**, 5530 (1978).
17. T.E. Tsai and D.L. Griscom, J. Noncryst. Sol. **91**, 170 (1987).

HYDROGEN-INDUCED METASTABILITY OF POLYCRYSTALLINE SILICON

N. H. NICKEL

Xerox Palo Alto Research Center, 3333 Coyote Hill Road, Palo Alto, California 94304

ABSTRACT

The presence of H in polycrystalline silicon gives rise to new and hitherto unexpected phenomena. In this paper two of the most recent observations are reviewed: (i) Hydrogen-induced metastable changes of the dark conductivity due to the formation and dissociation of an electrically active H complex and (ii) the generation of acceptor states during prolonged exposure of poly-Si to monatomic H at elevated temperatures. The observed type conversion is clearly due to the diffusion of excess H from the plasma since it does not occur during exposure to other species such as oxygen.

1. INTRODUCTION

Since many years the optical, electrical, and structural properties of polycrystalline silicon (poly-Si) have been investigated. A great deal of interest was devoted to grain boundaries, one of the most common two dimensional extended defects in crystals. The electronic properties of poly-Si are mainly determined by the energy levels in the band gap which are introduced by grain-boundary defects. These defects which have been detected by electron-spin-resonance (ESR) and were identified as silicon dangling-bonds¹ have to be passivated to obtain device-grade poly-Si. Commonly, this is accomplished by exposing poly-Si to a hydrogen plasma at elevated temperatures. This results in a decrease of the defect density and thus improves the electrical properties of poly-Si films and devices, for example, by increasing the carrier mobilities, reducing leakage currents, and decreasing the threshold voltage in thin-film transistors.^{2,3} Hydrogen also decreases the concentration of strained Si-Si bonds at or near the grain boundaries, as indicated by a reduction of band-tail states in poly-Si after hydrogenation.⁴ Defect passivation is governed by diffusion kinetics. As a function of the passivation time, the dangling-bond density decreases to a residual value, which strongly depends on the hydrogenation temperature.⁵

Previously, there was no evidence of any deleterious aspects due to the presence of hydrogen in poly-Si. However, recent work demonstrate that hydrogen is directly involved in various unexpected phenomena such as a cooling-rate dependent change in the electrical dark conductivity⁶ and the light-induced defect generation.⁷ In the latter case, prolonged illumination of hydrogenated polycrystalline silicon (poly-Si:H) with white light causes the formation of additional Si dangling-bonds with defect states in the gap. The newly created defects are metastable as in hydrogenated amorphous silicon (*a*-Si:H) and an anneal at 160 °C completely restores the initial state. The existence of the light-induced defect creation in poly-Si:H is evidence that the disorder along grain boundaries is sufficient for metastability and the greater degree of disorder found in *a*-Si:H is not essential. However, unlike in *a*-Si:H the magnitude of the light-induced degradation decreases with repeated illumination and anneal cycles and is restored upon reexposure to monatomic hydrogen. The ability to rejuvenate the light-induced metastability simply by reexposure to monatomic H establishes the participation of hydrogen in the phenomenon.⁷

The cooling-rate dependent metastable change of the dc dark-conductivity, σ_D , in poly-Si:H is reviewed in section 3 of this paper. We demonstrate that the changes in the dark conductivity are due to the formation and dissociation of an electrically active hydrogen complex at the grain boundaries. The relaxation kinetics of the dark conductivity along with results obtained from first-principles calculations suggest that the electrically active center consists of a single H atom residing in a Si-Si bond-center site. Recently, this complex has been identified as a donor in crystalline silicon.⁸⁻¹⁰ In section 4 we demonstrate that H in poly-Si diffuses in the positive charge state and prolonged exposure of poly-Si thin films to monatomic hydrogen at elevated temperatures causes the generation of acceptor-like defects which produces conductivity type-conversion.

2. EXPERIMENTS

Undoped polycrystalline silicon films were prepared by three different methods using quartz wafers as substrates. A set of fine grain poly-Si films was deposited by low-pressure chemical vapor deposition at 625 °C to a thickness of 0.55 μm . Cross-sectional transmission electron microscopy revealed that the films were composed of columnar grains extending from the substrate to the sample surface with an average diameter of 15 nm. A second set of samples was prepared by solid state crystallization of undoped LPCVD amorphous silicon at 600 °C. Some specimens were doped by multiple phosphorous or boron implantations. Subsequently the dopants were activated in a 30 min furnace anneal at 900 °C. Solid-state crystallization produces material in which crystal grains with an average size of 150 nm are randomly distributed. A third set of poly-Si films was prepared by laser crystallization of undoped LPCVD amorphous silicon, 0.1 μm thick. By increasing the laser energy the grain size of the resulting poly-Si films was varied from 650 Å to 1.1 μm .

Prior to the passivation of grain-boundary defects the native oxide of the poly-Si films was removed with dilute HF to avoid a barrier for the incorporation of H. The poly-Si films were then hydrogenated through a sequence of 1-h exposures to monatomic H generated in an optically isolated remote plasma at 350 °C until the spin density was minimized.⁵ According to secondary ion mass spectrometry measurements the hydrogenation produces a nearly depth independent H concentration of $\approx 2 \times 10^{20} \text{ cm}^{-3}$. On top of unhydrogenated and completely passivated samples electrical contacts were deposited. To eliminate the influence of space-charge effects due to non-Ohmic contacts, coplanar and four-probe electrical contacts were deposited consisting of either n^+ -Si:H or phosphorous implants covered with a thin chrome layer, or a titanium-gold double layer. These contacts yielded linear I - V characteristics for applied voltages of $\pm 100 \text{ V}$. Dark conductivity and Hall-effect measurements were performed in vacuum or in nitrogen atmosphere to avoid the influence of surface adsorbates on the conductivity.¹¹

3. HYDROGEN-INDUCED CHANGES IN THE ELECTRICAL CONDUCTIVITY

The temperature dependence of the dark electrical conductivity of poly-Si films before and after defect passivation is represented by the open and solid circles in Fig. 1, respectively. At temperatures below 250 K the conductivity of unpassivated poly-Si exhibits a $T^{-1/4}$ behavior which is indicative for variable range hopping¹² while a simple exponential behavior is observed at $T > 250 \text{ K}$. Furthermore, the temperature dependence of the dark conductivity of unhydrogenated

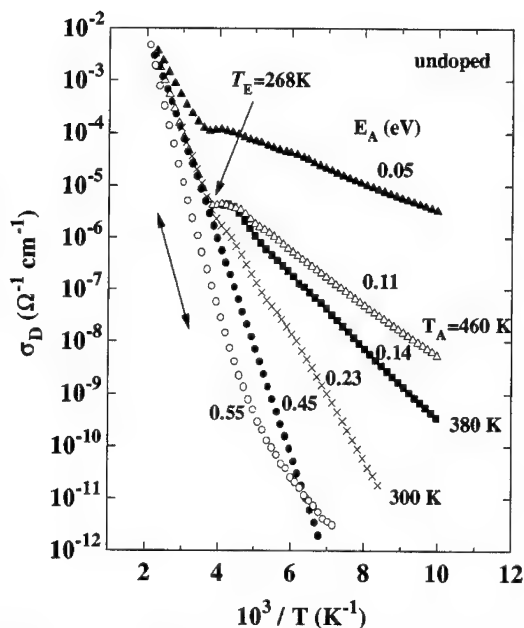


Figure 1: Arrhenius plot of the dark electrical conductivity σ_D , of unhydrogenated (open circles) and hydrogen passivated poly-Si. The full circles represent the relaxed state which is obtained after carefully cooling the specimen. The curves depicted by crosses, squares and open triangles are obtained after a 10 min anneal at the indicated temperatures T_A , and a subsequent rapid thermal quench with a cooling rate of 1.5 K s^{-1} . The solid triangles represent the dark conductivity after a rapid thermal quench from 460 K with a quenching rate of 3 K s^{-1} . σ_D was measured while the sample was heated with a rate of 0.1 K s^{-1} .

460 K. At $T_E = 268 \text{ K}$ the curves merge and the dark conductivity becomes independent of the thermal treatment.

In addition to the annealing temperature dependence of σ_D , poly-Si:H also exhibits a quenching-rate dependence of the dark conductivity. After an anneal at 460 K a hydrogenated poly-Si film was immersed into liquid nitrogen which increased the quenching rate to 3 K s^{-1} . The resulting temperature dependence of σ_D is represented by the full triangles in Fig. 1 and shows a striking increase of the dark conductivity by more than 8 orders of magnitude. The increase of σ_D above 268 K indicates that the heating rate (0.1 K s^{-1}) at which the measurements were performed is too high to allow for a complete relaxation of the quenched-in state during the measurement time. This is supported by the data plotted in Fig. 2. A poly-Si:H film was annealed at 460 K and subsequently quenched with a rate of $dT/dt = 1.5 \text{ K s}^{-1}$. Then the dark conductivity was measured while the sample was heated with heating rates ranging from 0.02 to 0.1 K s^{-1} . A decrease of the

poly-Si is independent of any thermal treatment prior to the measurement (open circles in Fig. 1). Passivation of grain-boundary defects results in a decrease of the activation energy from $E_A = 0.55 \text{ eV}$ to 0.45 eV which is accompanied by an increase of the dark conductivity at temperatures above 150 K. This is due to a decrease of the grain-boundary potentials caused by the passivation of Si dangling-bonds. Furthermore, the hydrogenated poly-Si sample exhibits simple activated behavior of σ_D in the entire temperature range. On the other hand, thermal treatment of hydrogen passivated poly-Si produces striking changes of the dark conductivity below 268 K. The dependence of the annealing temperature T_A on σ_D is illustrated by the crosses, squares, and open triangles. A hydrogen passivated poly-Si sample was annealed at the indicated temperatures for 10 min and subsequently thermally quenched with a cooling rate of $dT/dt = 1.5 \text{ K s}^{-1}$. Then the dark conductivity was measured while the specimen was heated with a rate of 0.1 K s^{-1} . With increasing T_A the dark conductivity increases below room temperature and all curves exhibit activated behavior according to $\sigma_D = \sigma_0 \exp(-E_A/kT)$ and E_A of the low-temperature branch decreases from 0.45 eV for the slow cooled sample to 0.11 eV for a thermal quench from

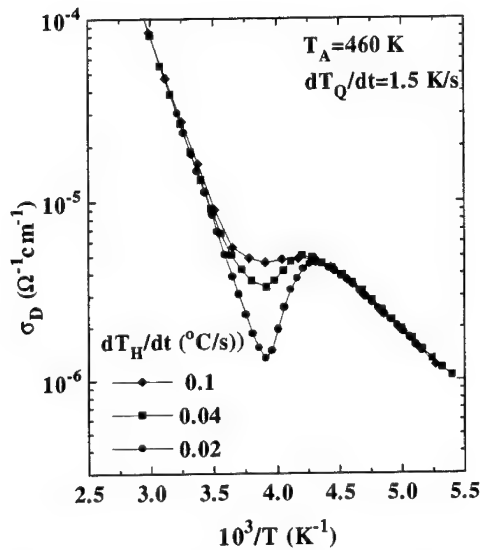


Figure 2: Heating rate dependence of the dark conductivity σ_D . The hydrogenated poly-Si film was rapidly quenched from 460 K with a rate of 1.5 Ks⁻¹.

The changes of the dark electrical-conductivity of both undoped and doped hydrogen passivated poly-Si are reversible. Annealing the specimens followed by a slow cool completely restores the temperature dependence of the relaxed state shown by the full circles in Fig. 1. The fact that the quenching-induced conductivity enhancement occurs only in H passivated poly-Si films is direct evidence that H participates in the phenomenon.

Important information on the microscopic mechanism responsible for the conductivity enhancement can be obtained from the relaxation kinetics. An undoped hydrogenated poly-Si sample was rapidly quenched from $T_A=460\text{K}$ by immersing the specimen in liquid N₂. Then the poly-Si film was heated to the desired measurement temperature at which the time dependence of the relaxation of the metastable state was recorded. The normalized conductivity transients are represented by the data points in Fig. 3. The relaxation curves of σ_D can be described quite reasonably by stretched exponential decays:

$$\frac{\sigma_D(0) - \sigma_D(t)}{\sigma_D(0) - \sigma_D(\infty)} = \frac{\Delta\sigma_D(t)}{\Delta\sigma_D(\infty)} \exp\left(-\left(\frac{t}{\tau}\right)^\beta\right) \quad (1)$$

Least-squares fits of Eq. (1) to the data are shown by the solid lines in Fig. 3. The fitting parameters are the dispersion parameter β which varies between 0.49 and 0.66 and the relaxation time constant τ . The temperature dependence of τ is shown in the inset of Fig. 3 and exhibits activated behavior with $E_a \approx 0.74$ eV and the preexponential factor is $\tau_0 \approx 8 \times 10^{-11}$ s. This indicates that the underlying microscopic mechanism is a first-order process.

It is important to note that the total hydrogen concentration in completely passivated polycrystalline silicon exceeds the concentration of preexisting Si dangling bonds by more than 2 orders of magnitude.⁵ Thus, most of the excess H must be accommodated in locations that do not

heating rate provides more time for the quenched-in state to relax. The conductivity begins to decay at approximately 210 K and passes through a minimum. The magnitude of the minimum strongly depends on the heating rate. These results are consistent with measurements of the relaxation kinetics which are presented in the next section.

A similar set of data was obtained by quenching phosphorous doped poly-Si films. However, the magnitude of the conductivity enhancement was somewhat smaller which most likely is due to a smaller grain-boundary volume since the average grain size in the phosphorous doped samples was 150 nm. With increasing phosphorous concentration the quenching-induced conductivity enhancement decreases and eventually disappears at a P concentration of 10^{18} cm^{-3} . This important result indicates that dopants do not participate in the quenching metastability.

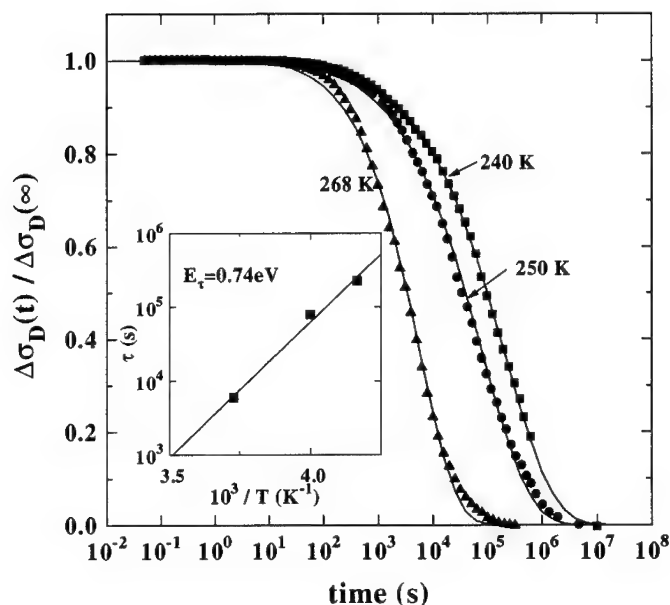


Figure 3: Normalized transient dark conductivity for various indicated temperatures. The solid curves represent least-squares fits to Eq. (1). The inset shows the temperature dependence of the relaxation time constant τ .

require the existence of dangling bonds either before or after hydrogenation. Possible configurations include the H_2^+ complex¹³ and hydrogen-induced platelets.¹⁴ During an anneal at T_A weakly bound excess hydrogen is released and migrates through the poly-Si lattice. Subsequent rapid cooling forces the sample into a non-equilibrium state in which the electrical conductivity is enhanced by more than 8 orders of magnitude (solid triangles in Fig. 1). This requires the formation of approximately 10^{15}-cm^{-3} electrically active H complexes in the grain-boundary region. An Arrhenius plot of the quenching-induced change of σ_D as a function of $1/T_A$ reveals that the formation of the electrically active H complex is thermally activated with $U_H \approx 0.35\text{ eV}$. According to the time and temperature dependence of the relaxation experiments, the microscopic process of the generation and dissociation of the electrically active H complex is first order. Hence, the quenching-induced metastability can be described in terms of a two level system. The energetically higher level corresponds to the metastable state and is associated with the H complex and the lower level corresponds to the relaxed state. This is sketched on the left hand side of Fig. 4. The total barrier height between the two levels is given by $E_{\text{total}} = E_{\tau} + U_H \approx 1.09\text{ eV}$.

According to the data the electrically active H complex has to be low enough in energy to dissociate below room temperature. The only H configuration which satisfies this requirement is an interstitial H atom which also is electrically active and has previously been identified as a donor state in crystalline silicon.^{8,9} However, in c-Si this H center is not stable above 100 K. On the other hand, poly-Si provides a simple mechanism which allows for H in a Si-Si bond center to be stable up to room temperature. At grain boundaries the bond length deviates from its intra-grain value. Previously it was reported that the bond distribution is asymmetric with stretched bonds

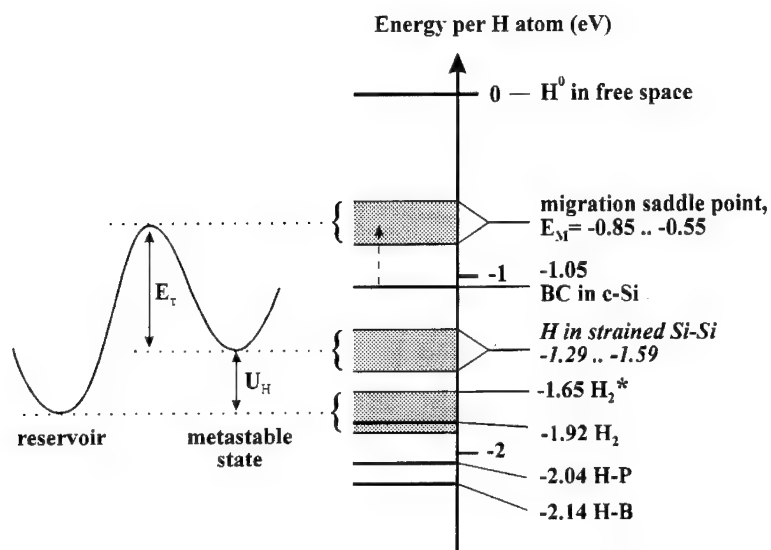


Figure 4: Calculated energies for various H configurations in silicon. The energy scale is the energy per H atom to form the various configurations. The zero of energy corresponds to a free hydrogen atom. The energy levels of the two level model for the formation and dissociation of the electrically active H complex are adjusted at the saddle point for H migration which lies 0.2-0.5 eV above the ground state for interstitial H at BC. The activation energy of the relaxation time constant is $E_r \approx 0.74$ eV and the formation energy of the H complex is $U_H \approx 0.35$ eV.

outnumbering compressed bonds and tensile stress results in bond-length distortions of up to 15 %.¹⁵ The energy necessary to insert a H atom in a Si-Si bond-center position strongly depends on the bond length. First-principles calculations reveal that an increase of the bond length of the initial Si-Si bond leads to a lower formation energy for the Si-H-Si configuration. An increase of the bond length due to tensile stress or bond angle distortion results in an energy gain of 0.4 eV per 0.1 Å bond distortion.¹⁶ Thus, disorder at grain boundaries can easily account for the stabilization of H in a bond-center site above 100 K.

The two-level model can be adjusted to a relative energy scale using the maximum of the barrier between metastable state and reservoir. This maximum represents the saddle point for H migration. In crystalline silicon the migration saddle point occurs 0.2 to 0.5 eV above the ground state of the H interstitial (E_M in Fig. 4). The lower number results from first-principles calculations¹⁰ and the higher value was obtained from high-temperature H diffusion experiments.¹⁷ Hence, the maximum of the two-level model is located at $E_M = -0.55$ to -0.85 eV with respect to the energy of a free H atom. The dissociation of the electrically active H complex occurs over a barrier of $E_r \approx 0.74$ eV which places the metastable state at -1.29 to -1.59 eV. This is 0.24 to 0.54 eV below the H interstitial site in c-Si. According to first-principles calculations this gain in energy translates into a bond distortion of 0.06 to 0.14 Å and is consistent with bond length distortions reported at grain boundaries in polycrystalline germanium.¹⁵ The formation energy of the metastable state was found to be $U_H \approx 0.35$ eV which places the reservoir, out of which H is released during the anneal prior to a thermal quench, to -1.65 to -2.09 eV. Possible H

configurations in this range are H_2^+ and H platelets (Fig. 4). Thus, the energies for the metastable state and hydrogen reservoir are consistent with the identification of bond-center hydrogen as the electrically active H complex responsible for the quenching metastability.

4. HYDROGEN-INDUCED ACCEPTOR GENERATION

Hydrogen at a Si-Si bond-center site is positively charged, because the proton is Coulombically attracted to the high negative charge density due to the valence electrons in the bond. The dissociation process of bond-centered H presented in the previous section (see Fig. 3) requires hydrogen atoms to migrate. This gives rise to an interesting question: What is the charged state of diffusing H in poly-Si? Commonly, information on H diffusion is obtained by exposing poly-Si to a hydrogen plasma at elevated temperatures and subsequently the depth distribution is measured with secondary-ion-mass spectrometry (SIMS). However, hydrogen depth profiles provide only limited information on the microscopic diffusion process. In this section we present results obtained from *in-situ* conductivity measurements during hydrogenation which illustrate that in undoped (intrinsic) poly-Si hydrogen diffuses as H^+ . Furthermore, we

demonstrate that the prolonged exposure of poly-Si to monatomic H causes the generation of acceptor-like defects. This occurs on a time scale of 10^4 s and results in conductivity type-conversion.

The samples investigated in this section were $0.1\ \mu\text{m}$ thick poly-Si films on quartz substrates. The electrical contacts consisted of a titanium-gold double layer in a square four-probe array. Prior to the *in-situ* conductivity measurements the native oxide of the poly-Si films was removed. Then the specimens were mounted in an optically isolated remote plasma system and a 8 nm thick oxide layer was grown by exposing the samples to monatomic oxygen. Then the specimens were exposed to monatomic H generated in the same reactor and the *in-situ* conductivity, σ_P , was measured as a function of the hydro-

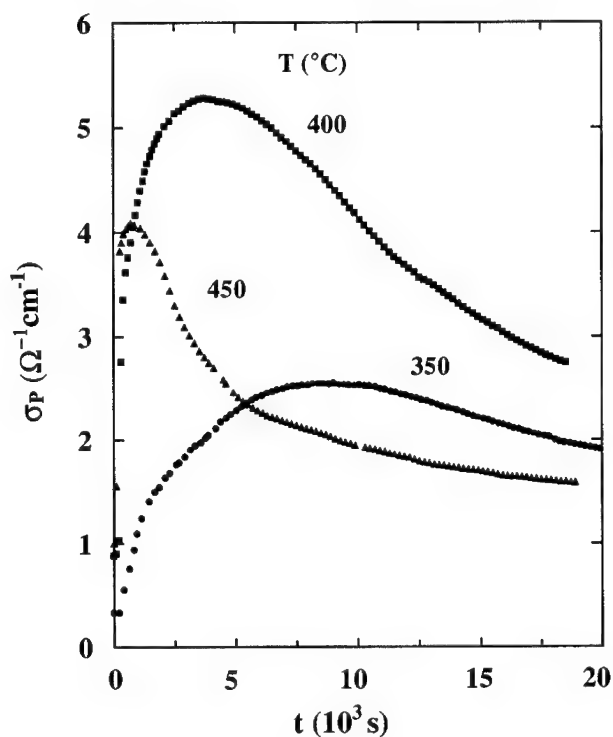


Figure 5: *In-situ* conductivity transients, σ_P , obtained on undoped poly-Si films during exposure to monatomic hydrogen at various indicated temperatures. The average grain-size is $1.5\ \mu\text{m}$.

generation time. *In-situ* conductivity transients for various temperatures are shown in Fig. 5. Immediately after the remote H plasma is ignited a steep increase of σ_p is observed and eventually after reaching a maximum the *in-situ* conductivity decays. The data shown in Fig. 5 could be due to a plasma-induced temperature change. This was carefully evaluated by exposing a poly-Si film to other species such as O. At substrate temperatures ranging from 350 to 450 °C plasma heating resulted in an increase of σ_p by less than 5 % with respect to the dark conductivity ($\sigma_p(t=0)$). On the other hand, fixed charge in the deposited oxide layer can cause a significant change of the *in-situ* conductivity. Fixed charge can be introduced during either the oxide deposition or the hydrogenation. However, removing the oxide layer of a poly-Si sample which was exposed to monatomic H for 8 h and re-measuring the conductivity resulted in a conductivity change by only 9% which is small compared to the observed conductivity enhancement during the hydrogenation. This indicates that the remote H plasma did not introduce a significant amount of fixed charge in the oxide layer.

With increasing hydrogenation temperature the time for σ_p to reach the maximum decreases. This is consistent with the temperature dependence of the effective diffusion coefficient.¹⁸ On the other hand, the H concentration decreases with increasing substrate temperature and therefore, the largest increase of the *in-situ* conductivity should be observed for the lowest temperature

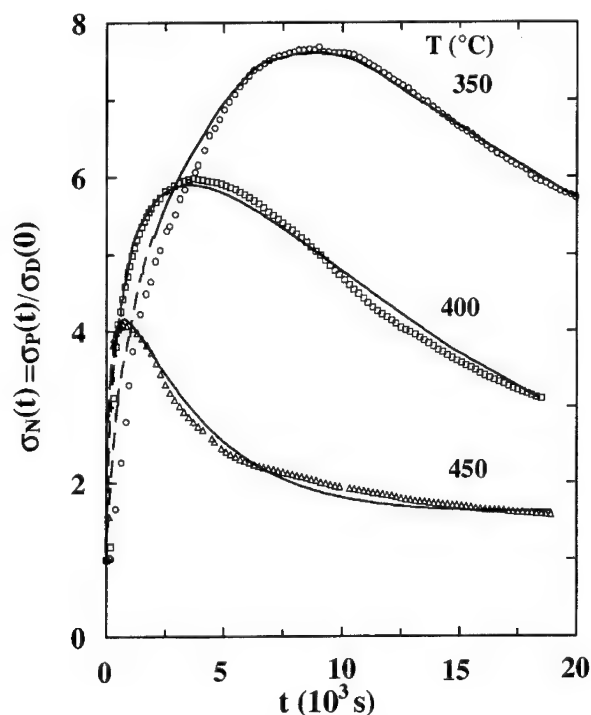


Figure 6: *In-situ* conductivity transients of Fig. 5 normalized to unity at $t=0$. The data are shown by the open symbols and the solid lines represent the calculated *in-situ* conductivity.

(350°C). To observe this behavior the temperature dependence of the dark conductivity [$\sigma_p(t=0)$] has to be taken into account. The *in-situ* conductivity transients normalized to unity at $t=0$ are plotted in Fig. 6. The largest increase of σ_p by a factor of 7.6 is observed at 350 °C. This corresponds to approximately 10^{17}-cm^{-3} additional carriers. The conductivity maximum is inversely proportional to the hydrogenation temperature and the grain size of the poly-Si films. Exposing samples to an attenuated H plasma revealed that the plasma-induced increase of σ_p is proportional to the concentration of monatomic H while the time to reach the maximum is inversely proportional to the H^0 concentration. *In-situ* conductivity transients as shown in Figs. 5 and 6 were only obtained when the poly-Si film was

exposed to a remote hydrogen plasma. An exposure to other species such as oxygen did not produce a conductivity enhancement. This is consistent with the idea that the conductivity enhancement is due to hydrogen introduced from the plasma which diffuses as H^+ .

When the hydrogen plasma is turned off, the *in-situ* conductivity decreases to a residual value with a time constant of 3 s at 350 °C. This is illustrated in Fig. 7. The residual value of σ_P is somewhat larger than the dark conductivity at $t=0$. This is due to the passivation of grain-boundary defects which lowers the potential barriers and therefore results in an increase of the dark conductivity (see open and solid circles in Fig. 1). The residual values of σ_P shown in Fig. 7 do not change significantly with increasing passivation time. The defect

concentration reaches a minimum during the first 2000 s⁵ and by the time the first decay is measured most of the spins are already passivated. Annealing H out of Si dangling bonds does not influence the decay measurement since the dehydrogenation rate of Si-H is negligible at temperatures below 500 °C.¹⁹ When the plasma is ignited again the *in-situ* conductivity increases faster than at the beginning of the experiment until σ_P approaches the value at which the H plasma was turned off. Most likely, this is due to the defect passivation and an increase of the H concentration prior to the decay measurement.

At longer hydrogenation times the *in-situ* conductivity decreases exponentially with time constants of 2.8×10^4 s and 2×10^3 s at 350 °C and 475 °C, respectively. However, a change in the H concentration cannot account for the decay. At the time σ_D reaches the maximum (Figs. 5 and 6) the carrier concentration due to H^+ diffusion ($H^0 \rightarrow H^+ + e^-$) is constant with time.

In order to illuminate the origin of the exponential decay of the *in-situ* conductivity the temperature dependence of dark conductivity and Hall-effect were measured before and after hydrogenation at 400 °C. Arrhenius plots of the dark conductivity, σ_D , are shown in Fig. 8. The results obtained from Hall-effect measurements are represented by the open symbols and the solid

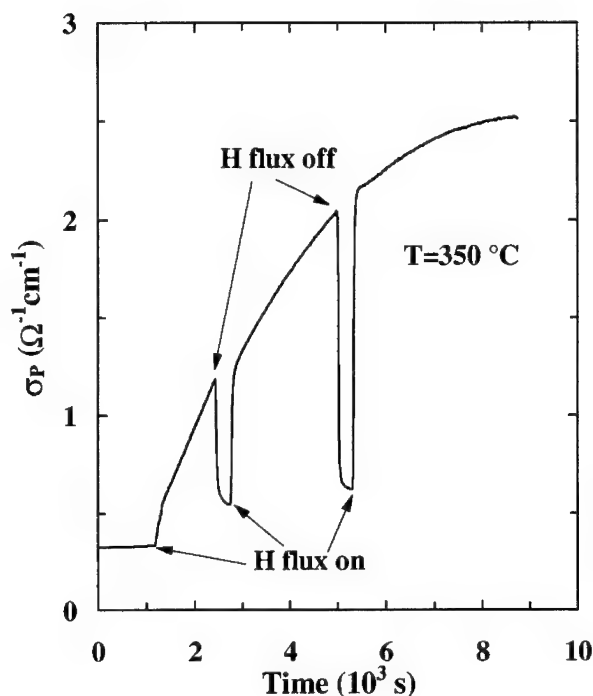


Figure 7: *In-situ* conductivity transient measured at 350 °C. When the H plasma is turned off σ_P decays to a residual value higher than the dark conductivity at $time=0$ with a time constant of 3 s. Igniting the plasma gives rise to conductivity enhancement.

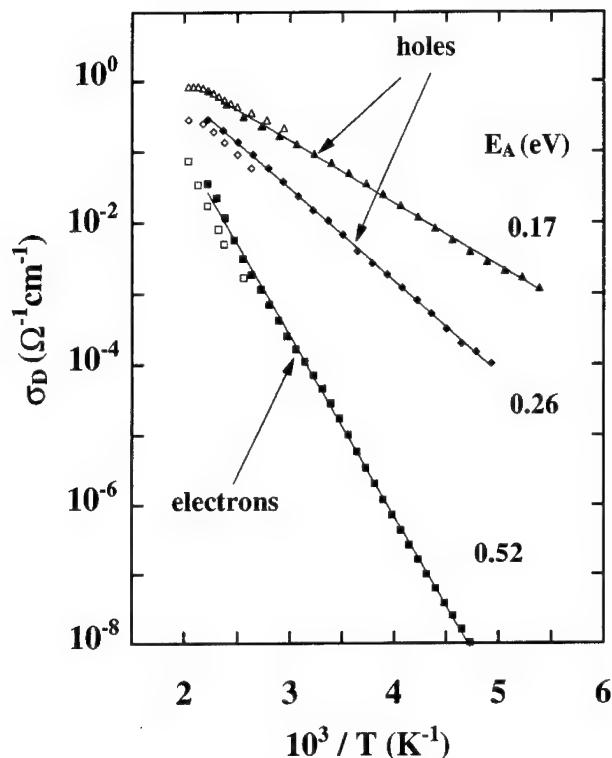


Figure 8: Temperature dependence of the dark conductivity of intrinsic poly-Si. The solid symbols were obtained with coplanar contacts and the open symbols represent Hall-effect data. The lines are least-squares fits to the data. The dark conductivity of the unhydrogenated poly-Si film is represented by the squares and the majority carriers are electrons. The diamonds and triangles were obtained after hydrogenation for 6×10^3 s and 3.5×10^4 s at 400 °C, respectively. In both cases Hall-effect measurements reveal that the majority carriers are holes.

exposures. Data shown by triangles in Fig. 8 were obtained after the *in-situ* conductivity reached steady state ($t = 3.5 \times 10^4$ s). The activation energy decreased to 0.17 eV and the hole mobility was found to be $\mu_H = 12.4$ cm²/Vs at 400 K. The time dependence of the activation energy and the hole mobility occur because the H-induced acceptor generation commences at the sample surface and with increasing exposure time the acceptor distribution approaches a homogeneous depth distribution. These results clearly demonstrate that prolonged exposure of poly-Si to monatomic hydrogen causes the generation of acceptor states which leads to electrical type-conversion. The acceptor concentration is determined by the H concentration and not limited by the number of sites, since the steady state value of the *in-situ* conductivity is temperature dependent.

symbols refer to measurements with a 2-contact configuration. The data are in good agreement in the temperature range where both techniques could be applied. Prior to the hydrogenation the dark conductivity is thermally activated with $E_A = 0.52$ eV and the majority carriers are electrons (squares in Fig. 8). At 400 K the electron mobility is $\mu_E \approx 1.9$ cm²/Vs which is characteristic of undoped poly-Si films with an average grain-size of 1.1 μm. Data represented by the diamonds were taken after a poly-Si film was exposed to monatomic H for 6000 s at 400 °C. Hydrogenation resulted in a noticeable increase of the dark conductivity which is accompanied by a decrease of the activation energy to $E_A = 0.26$ eV. The most striking result, however, is obtained from Hall-effect: After H exposure the majority carriers have changed from electrons to holes. This effect is even more pronounced after longer hydrogen

Three microscopic mechanisms are contributing to the *in-situ* conductivity: (a) The passivation of grain-boundary defects; (b) Monatomic H from the gas phase diffusing in the positive charge state H^+ and donating electrons, and (c) the creation of acceptor states. The first two mechanisms contribute to an increase of σ_p while mechanism (c) reduces the conductivity. Grain-boundary passivation occurs on a very short time scale of 500 to 2000 s at 450 and 350 °C, respectively, and enhances the conductivity by less than 15 %. Hence, the main contributions to σ_p are the diffusing monatomic H donors and the generation of acceptor states. With these two mechanisms the time dependence of σ_p can be calculated. As shown by the solid curves in Fig. 6 the calculated time dependence of σ_p is in good agreement with the data, supporting that H in poly-Si diffuses in the positive charge state and causes the formation of acceptor states.

5. SUMMARY

In summary, we have presented a cooling-rate dependent change of the dark conductivity in hydrogenated poly-Si. Annealing at 460 K followed by a rapid thermal quench produces an increase of the dark conductivity by more than 8 orders of magnitude below 268 K. The quenched-in conductivity is metastable and the relaxation is characterized by a stretched exponential behavior. The relaxation time-constant is thermally activated with 0.74 eV. The quenching metastability occurs only in hydrogen passivated poly-Si which clearly demonstrates that the effect is due to the formation and dissociation of an electrically active H complex. We propose bond-center hydrogen as the active H complex which is stabilized up to room temperature due to disorder at the grain boundaries. This explanation is consistent with experimental and theoretical studies of H in silicon. *In-situ* conductivity measurements reveal that prolonged exposure of poly-Si films to monatomic H at elevated temperatures causes electrical type-conversion, a new and hitherto unexpected phenomenon. The concentration of the H-induced acceptor states is limited by the H concentration and not by the number of sites. Model calculations of the time and temperature dependence of the *in-situ* conductivity are in good agreement with the data and support that hydrogen in undoped poly-Si diffuses in the positive charge state.

ACKNOWLEDGMENTS

The author is grateful to Chris G. Van de Walle for his contributions to and interest in the H-induced metastability, to G. Anderson for TEM analysis, to W. B. Jackson, N. M. Johnson, and R. A. Street for many stimulating discussions, and to J. Walker for technical support. This work was partially supported by NREL. The author also acknowledges support from the Alexander von Humboldt foundation, Federal Republic of Germany.

REFERENCES

- ¹ N. M. Johnson, D. K. Biegelsen, and M. D. Moyer, Appl. Phys. Lett. **40**, 882 (1982).
- ² A. Mimura, N. Konishi, K. Ono, J.-I. Ohwada, Y. Hosokawa, Y. A. Ono, T. Suzuki, K. Miyata, and H. Kawakami, IEEE Trans. Electron Devices **36**, 351 (1989).
- ³ T. J. Kamins and P. J. Marcoux, IEEE Electron Device Lett. **EDL-1**, 159 (1980).

- ⁴ W. B. Jackson, N. M. Johnson, and D. K. Biegelsen, *Appl. Phys. Lett.* **43**, 195 (1983).
- ⁵ N. H. Nickel, N. M. Johnson, and W. B. Jackson, *Appl. Phys. Lett.* **62**, 3285 (1993).
- ⁶ N. H. Nickel, N. M. Johnson, and C. G. Van de Walle, *Phys. Rev. Lett.* **72**, 3393 (1994).
- ⁷ N. H. Nickel, W. B. Jackson, and N. M. Johnson, *Phys. Rev. Lett.* **71**, 2733 (1993).
- ⁸ Y. V. Gorelkinskii and N. N. Nevinnii, *Sov. Tech. Phys. Lett.* **13**, 45 (1987).
- ⁹ B. Holm, K. Bonde Nielsen, and B. Bech Nielsen, *Phys. Rev. Lett.* **66**, 2360 (1991).
- ¹⁰ C. G. Van de Walle, P. J. H. Denteneer, Y. Bar-Yam, and S. T. Pantelides, *Phys. Rev. B* **39**, 10791 (1989).
- ¹¹ M. Tanielian, *Phil. Mag. B* **45**, 435 (1982).
- ¹² N. F. Mott, *J. Non-Cryst. Solids* **1**, 1 (1968).
- ¹³ K. J. Chang and D. J. Chadi, *Phys. Rev. Lett.* **62**, 937 (1989).
- ¹⁴ N. M. Johnson, F. A. Ponce, R. A. Street, and R. J. Nemanich, *Phys. Rev. B* **35**, 4166 (1987).
- ¹⁵ E. Tarnow, P. Dallot, P. D. Bristowe, J. D. Joannopoulos, G. P. Francis, and M. C. Payne, *Phys. Rev. B* **42**, 3644 (1990).
- ¹⁶ C. G. Van de Walle and N. H. Nickel, *Phys. Rev. B* **51**, 2636 (1995).
- ¹⁷ A. Van Wieringen and N. Warmoltz, *Physica (Utrecht)* **22**, 849 (1956).
- ¹⁸ N. H. Nickel, W. B. Jackson, and J. Walker, submitted for publication.
- ¹⁹ K. Zellama, P. Germain, S. Squelard, B. Bourdon, J. Fontenille, and R. Danielou, *Phys. Rev. B* **23**, 6648 (1981).

ANALYSIS OF HYDROGEN PASSIVATION MECHANISMS IN POLY-SI TFT's BY EMPLOYING R.F. PLASMA

K.Y. CHOI, Y.S. KIM*, H.S. CHOI, B.S. BAE**, and M.K. HAN

Department of Electrical Engineering, Seoul National University, Seoul 151-742, KOREA

* Department of Electrical Engineering, Myongji University, Kyonggi-do 449-728, KOREA

** Samsung Electronics Co., Kiheung, Yongin-Gun, Kyonggi-do 449-990, KOREA

ABSTRACT

The dominant pathways for hydrogen diffusion in poly-Si TFT's are identified by analyzing the hydrogenation effect on the various device geometries. It is observed that the gate poly-Si thickness and channel width didn't affect the hydrogenation. As the channel length was decreased down to 3 μm , threshold voltage was reduced and field effect mobility was increased significantly with hydrogenation time. In the thick gate oxide (2000 Å, 4000 Å) poly-Si TFT's, the device characteristics have been improved rapidly with hydrogenation time. The tail state density of thin gate oxide TFT wasn't change by hydrogenation while that of thick gate oxide TFT was significantly reduced. Our experimental results may support the model that hydrogen atoms diffuse into the bulk of the active channel layer through the gate oxide and passivate the grain boundary and intragranular defects limitedly by gate oxide area.

INTRODUCTION

Polycrystalline-silicon (poly-Si) thin film transistors (TFT's) have attracted much attention recently due to their large mobility.[1] However, in poly-Si TFT's, the relatively high trap densities located at grain boundaries and within grain exert a profound influence on the device characteristics and degrade carrier transport. It is well known that hydrogenation reduce the trap densities of poly-Si TFT's most effectively.[2,3] However, it has scarcely been reported that how the hydrogenation effects on poly-Si TFT's with various device geometry. We have previously reported that active layer thickness and channel length play an important role to control the hydrogenation effects on the device performance while the variation of gate poly-Si thickness and channel width do not control.[4]

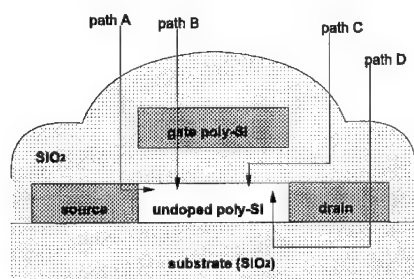


Fig. 1 Possible hydrogen diffusion pathways in top-gate poly-Si TFT's; a) through the S/D (path A), poly-Si gate (pathB), gate oxide (path C) and substrate oxide (path D)

The possible hydrogen diffusion pathways in poly-Si TFT's are shown in Fig. 1.[4,5,6] The hydrogen atoms which are generated by r.f. plasma, may diffuse into the active channel region through the source/drain (path A), poly-Si gate (path B), gate oxide (path C), or substrate oxide (path D). According to the previous paper[4,5], the path A and path C may be assumed as the dominant pathways while the path B and path D are negligible. However, the more evidences of practical device characteristics are needed to confirm the diffusion model.

In this paper, we have identified the dominant hydrogen pathway by analyzing the hydrogenation effects on the poly-Si TFT's with various gate oxide thickness (500 Å~ 4000 Å) and various channel length (3 μm ~ 20 μm) and analyzed the hydrogenation effects on trap state distribution within bandgap.

EXPERIMENTAL

The amorphous silicon (a-Si) for active layer, of which thickness was 1000 Å, was deposited by low-pressure chemical vapor deposition (LPCVD) at 550 °C. These a-Si films were crystallized by thermal annealing at 600 °C for 48 hrs in N_2 ambient. After definition of silicon island, the silicon dioxide film, of which thickness varied from 500 Å to 4000 Å, deposited by atmospheric-pressure chemical vapor deposition (APCVD) was used as a gate dielectric layer. The thickness of poly-Si gate, which was deposited in the amorphous phase by LPCVD at 550 °C and crystallized by thermal annealing at 600 °C, was 1000 Å. The polysilicon for gate and source/drain electrodes was heavily doped by self-aligned P^+ implantation at an energy of 30 KeV and dose of 5×10^{15} ions/ cm^2 . The implant was annealed at 600 °C for 12 hrs. A 7000 Å thick interlayer oxide film was deposited and defined. The devices were then sintered at 450 °C for 30 min in H_2 .

Plasma hydrogenation was performed with various periods. The hydrogen plasma treatment conditions were 300 °C and 0.5 Torr. the power density was 0.25 W/cm^2 at the frequency of 13.56 MHz. Other hydrogenation procedures are similar to earlier report.[4]

RESULT AND DISCUSSION

Fig. 2 shows the variation of device parameters with different hydrogenation time as a function of channel length for N-channel poly-Si TFT's. As the channel length of poly-Si TFT's, where the channel width was fixed at 20 μm , was decreased from 20 μm to 3 μm , threshold voltage reduced significantly with hydrogenation time as shown in Fig. 2(a). The increase of field effect mobility of short channel poly-Si TFT's was also much severer than that of long channel device as shown in Fig. 2(b). The effects of hydrogen passivation on short channel device is relatively significant compared with those on long channel device. The transfer characteristics (I_{ds} vs V_{g}) of poly-Si TFT's with $W/L = 20/10 \mu\text{m}/\mu\text{m}$ at $V_{\text{ds}} = 5 \text{ V}$ as a function of hydrogenation time was shown in Fig. 3. The hydrogen effects on the poly-Si TFT's with 4000 Å-thick gate oxide (Fig. 3(a)), were much more significant than those with 1000 Å-thick gate oxide (Fig. 3(b)). In case that the gate oxide thickness was 1000 Å, most of threshold voltage reduction due to hydrogenation were occurred within 60 min, while on-current ($V_{\text{g}} = 25 \text{ V}$) was increased gradually with hydrogenation time. On the other hand, in case of poly-Si TFT's with 4000 Å-thick gate oxide, the threshold voltage were reduced and on-current were increased predominantly within 60 min, above which the threshold voltage and on-current slowly saturated. In addition to these parameter shifts, the minimum leakage currents of 4000 Å-thick gate oxide device were reduced dramatically above 60 min, while those of 1000 Å-thick

gate oxide device were almost identical. It was well known that the threshold voltage was affected by the deep trap states near midgap, and the on current and minimum leakage current were dependent on the the tail trap states near band-tail.[7]

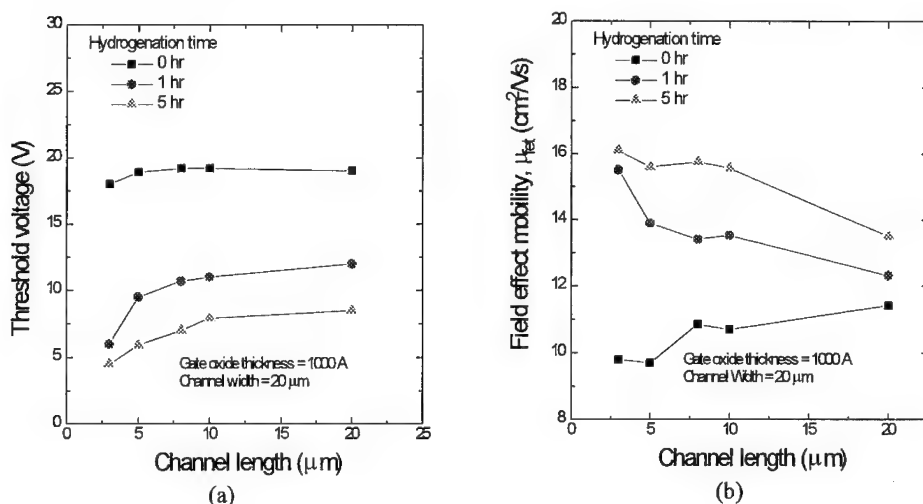


Fig. 2 Variation of device parameters as a function of channel length and different hydrogenation time for $W = 20 \mu\text{m}$, (a) threshold voltage shift, (b) field effect mobility increase

It was reported that as hydrogen atoms diffused to active poly-Si layer, the hydrogen atoms passivated the deep trap states located at grain boundary first, and then the tail trap states existed within the grain.[3] As a consequence, Fig. 3(a) may indicate that in thin gate oxide TFT's, most of the hydrogen atoms, which were transported to active poly-Si layer, passivate the deep trap states at grain boundary but scarcely passivate the intragranular defects within grain because the amount of hydrogen atoms transported to the active layer were limited by gate oxide area. However, in the thick gate oxide device, a large amount of hydrogen atoms could passivate the deep trap states located at grain boundary and the tail trap states within grain simultaneously because the sufficient amount of hydrogen atoms were provided through the gate oxide. The rapid reduction of leakage current in poly-Si TFT's, of which gate oxide thickness were 4000 Å, implied definitely that hydrogen atoms passivated the tail trap states as well as deep trap states.[3] On the contrary, in thick gate oxide poly-Si TFT's, the transferred hydrogen atoms within active poly-Si layer diffused out to gate oxide after 5 hrs because the hydrogen atoms provided through the gate oxide was limited to a small quantity. Fig. 4 shows the threshold voltage shift (ΔV_{th}) of the devices with different channel lengths as functions of hydrogenation time and gate oxide thickness. Except of 500 Å-thick gate oxide, the threshold voltage shift had saturated within 200 min regardless of gate oxide thickness and channel length, which means that the threshold voltage reduction was affected less significantly by the gate oxide thickness which is the pathway for hydrogen diffusion. In the case of 500 Å-thick gate oxide, the

threshold voltage shift of short channel poly-Si TFT's was greater than those of long channel devices.

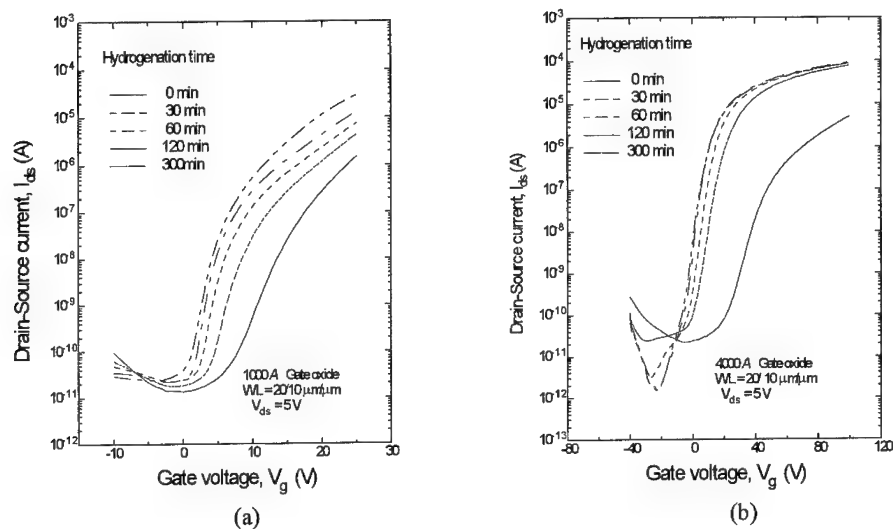


Fig. 3 Drain-source current vs gate voltage characteristics of thin gate oxide and thick gate oxide poly-Si TFT's with different hydrogenation time for $W/L = 20/10 \mu\text{m}/\mu\text{m}$, (a) gate oxide thickness = 1000 Å (b) gate oxide thickness = 4000 Å

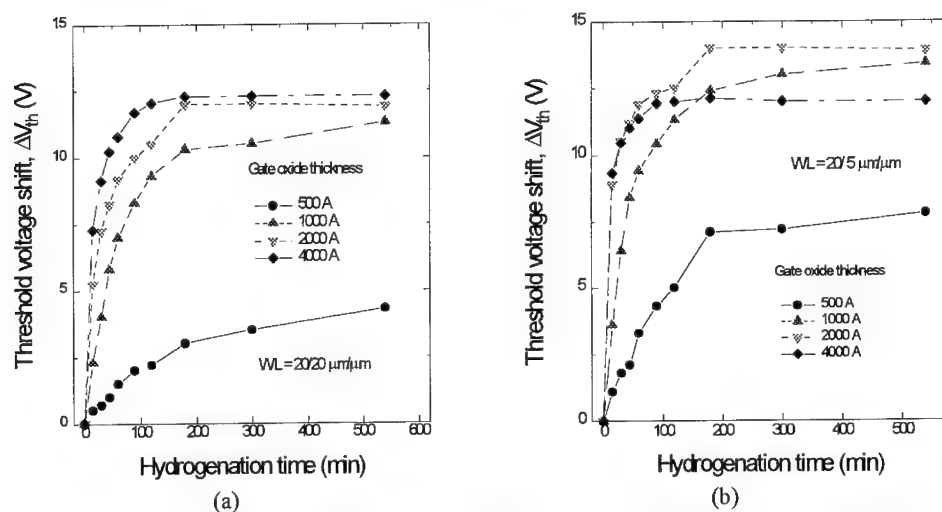


Fig. 4 Variation of threshold voltage shift as a function of hydrogenation time and gate oxide thickness for long and short channel poly-Si TFT's, (a) $W/L = 20/20 \mu\text{m}/\mu\text{m}$, (b) $W/L = 20/10 \mu\text{m}/\mu\text{m}$

Fig. 5 is the variation of normalized field effect mobility with different channel lengths as functions of hydrogenation time and gate oxide thickness. It can be seen in Fig. 5(a) that in the long channel devices, as the gate oxide thickness was increased from 500 Å to 4000 Å, the field effect mobility was increased significantly and rapidly. On the other hand, the field effect mobility of the thick gate oxide TFT's, of which thickness exceeded 1000 Å, had shown the rapid increase independently of the gate oxide thickness, whose tendency were similar to the threshold voltage reduction shown in Fig. 4. These results may be explained as follows; As can be seen the leakage current decrease of Fig. 3(b), the hydrogen atoms could diffuse to the long channel and passivate the whole defects including the grain boundary and intergranular defects just only through thick gate oxide. However, in the case of short channel devices, the hydrogen atoms could passivate the tail states, which affect the field effect mobility, through the thin gate oxide.

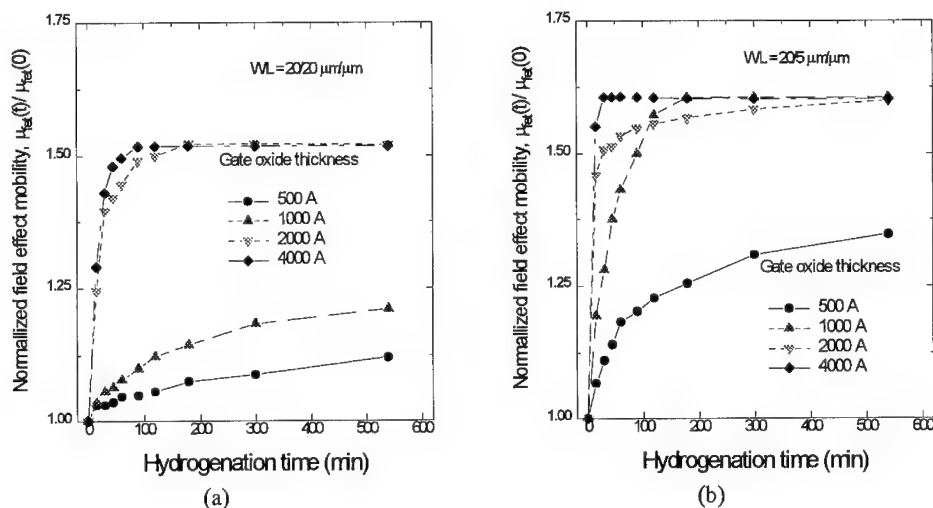


Fig. 5 Variation of normalized field effect mobility increment ($\mu_{\text{fet}}(t)/\mu_{\text{fet}}(0)$) as a function of hydrogenation time and gate oxide thickness for long and short channel poly-Si TFT's, (a) $W/L = 20/20 \mu\text{m}/\mu\text{m}$, (b) $W/L = 20/5 \mu\text{m}/\mu\text{m}$

Fig. 6 shows the trap states distribution within bandgap for thin (a) and thick (b) gate oxide devices as functions of hydrogenation time. In thin gate oxide, the deep states were reduced significantly while the tail states weren't changed as hydrogenation went on. In thick gate oxide, however, the most of deep and tail trap states reduction were occurred within 60 min simultaneously. It can be explained that the sufficient hydrogen quantity to passivate the grain boundary and intragranular defects simultaneously isn't diffused through the thin gate oxide that may be the dominant hydrogen diffusion path.

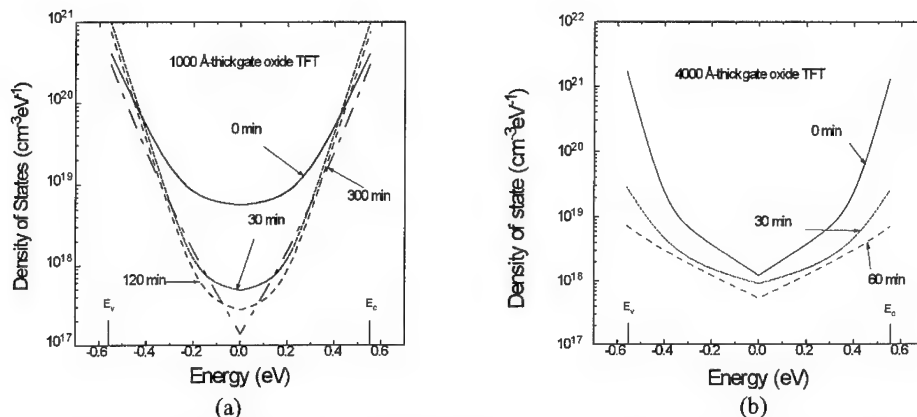


Fig. 6 Trap states distribution within bandgap for thin and thick gate oxide devices as functions of hydrogenation time (a) 1000Å (b) 4000Å

CONCLUSION

In this work, we have investigated the hydrogenation effects on poly-Si TFT's with various device structures. As the channel length was decreased from 20 μm to 3 μm , threshold voltage reduced and field effect mobility was increased significantly with hydrogenation time. In thick gate oxide devices, the threshold voltage reduction and field effect mobility increase took place predominantly within 60 min. In thin gate oxide devices, however, the field effect mobility and leakage current were changed monotonically to 540 min while the threshold voltage reduced significantly within 60 min. We have investigated that the hydrogenation couldn't reduce the tail trap states effectively in thin gate oxide TFT.

In summary, active channel length and gate oxide thickness play an important role to control the hydrogenation effects on the device performance. It may be considered that the limiting factor of hydrogenation of poly-Si TFT's may be the gate oxide thickness, especially for the reduction of tail trap states located within grain. As a consequence, it may be concluded that the limited amount of hydrogen atoms by the gate oxide path diffuses to the active poly-Si channel layer and couldn't reduce the tail trap states effectively in thin gate oxide TFT.

REFERENCE

1. A. Chiang, T.Y. Huang, I.-W. Wu and M. Zarzycki in Polysilicon Films and Interfaces, edited by C.Y. Wong, C.V. Thompson, and K.N. Tu (Mater. Res. Soc. Symp. Proc., **106**, Boston, MA, 1987) pp. 305-310
2. T.I. Kamins and P.J. Marcoux, IEEE Electron Device Lett, vol. EDL-1, p.159, 1980
3. I-Wei Wu *et al.*, IEEE Electron Device Letter, vol. 12, p.181, 1991
4. Y.S. Kim *et al.*, Jpn. J. Appl. Phys. vol. 33, p.649, 1994
5. W.B. Jackson *et al.*, Appl. Phys. Lett., **61** p.1670, 1992
6. U. Mimura *et al.*, J. Electrochem. Soc., **138**, p.3420, 1991
7. J.G. Fossum *et al.*, IEEE Trans. Electron Dev., ED-32 p.1878, 1985

HYDROGENATION OF MULTICRYSTALLINE SI-MATERIALS FOR SOLAR CELLS: DISCRIMINATION BETWEEN EFFECTS IN THE INTRA-GRAIN AND GRAIN BOUNDARY REGIONS

J. POORTMANS, M. ROSMEULEN, A. KANIAVA*, J. VANHELLEMONT, H. ELGAMEL, AND J. NIJS

IMEC, Kapeldreef, 75 B-3001 Belgium

*Vilnius University, Sauletekio 10, 2054 Vilnius, Lithuania

ABSTRACT

In this paper we describe the results of a study on the hydrogenation treatment of multicrystalline substrates by an RF-plasma with emphasis on discriminating between effects on the intra-grain material and grain boundary regions. For this purpose small mesa-type diodes were processed. Two types of multicrystalline material are being compared in this study. The main difference between these materials is their oxygen and metallic impurity content. The effects of the hydrogenation treatment were studied by means of I-V and DLTS-measurements. Finally, we will present data on small multicrystalline solar cells and the effect of hydrogenation on the main parameters of this device to illustrate the correlation and the differences between the measurements on small-scale diodes and the effects on the macroscopic device which is the solar cell.

INTRODUCTION

One of the possibilities to reduce the price of solar energy is to use low-cost Si substrates. A common feature of these low-cost casted materials is the presence of a large number of crystallographic defects. These can be present as intra-grain defects or grain boundaries. A lot of effort has been done in the past to give a detailed microscopic description of these defects,¹⁻³ however only with success in a few well-defined cases. Besides the structural characterisation, there is a strong need for understanding the effects of these crystallographic flaws on the electronic properties (mobility, recombination lifetime, trapping) of the material. These directly affect the output characteristics of solar cells, being processed in the multicrystalline substrates. In addition, in recent years one can see the emerging of new technological steps to improve the electronic properties of the multicrystalline substrates.

These techniques comprise both gettering and bulk passivation techniques. In the last category, hydrogenation is taking a key position.⁴⁻⁶ Although hydrogenation has received a lot of attention over the last years, there is still need for improved understanding and more specifically, one should try to link the results of microscopic studies to results reported on the level of solar cells. This paper tries to bridge the gap between these two worlds for the case of a specific comparison between two materials, being different in oxygen and impurity content.

The first material is a classically casted multicrystalline material (directional solidification) with relatively large oxygen content ($1 - 3 \cdot 10^{17} \text{ cm}^{-3}$) and large grains (a few mm's to 1 cm). The material is being manufactured by Eurosolare and is referred to as material A. The second material has been made by a new casting technique (electromagnetically casted material)⁷, which is being used by the Japanese company Susitomo Sitix. It will be called material B throughout the text. In the last method, the melt does not come in contact with the cooled crucible walls which results in a much lower level of oxygen ($\approx 10^{16} \text{ cm}^{-3}$) and metallic impurities in the material. On the other hand, the grain size in this material is substantially lower (smaller than 3 mm). The diodes processed on solar grade Czochralski substrates, which were included as a reference, will be indicated as material C.

EXPERIMENTAL

For the experiments p-type Si-material of 1 ohm-cm (350 micron) has been used. The substrates used are typical for a solar cell process. This means that the wafers are as-cut without any additional surface finish. In order to insure that the results are relevant for a real solar cell process (equal thermal budget), the diode process is nearly equal to the solar cell process for multicrystalline cells, developed at IMEC.⁸ The process consists of the following steps:

- Damage etch of the Si-substrates in a mixture of HNO₃, HF and CH₃COOH. This step is intended to remove about 10 micron of Si. This region contains the damage due to dicing the substrates from the block or ingot.
- Diffusion of a p⁺-region at the backside to insure a good back contact and which acts as a back-surface field
- Diffusion of the phosphorus-doped emitter at the front side by diffusion from a P-containing solid source to a sheet resistance of 20 ohms/square
- Hydrogenation from the front side in an RF-plasma. The hydrogenation was done at a temperature of 350°C, with a power of 11 W at a pressure of 1500 mTorr. The hydrogenation was done in pure hydrogen for a time of 180 min
- Short etch-back of the emitter to remove the plasma-damaged zone at the surface of the n⁺-emitter. The emitter after etch-back has a sheet resistance of 90-100 ohms/square.
- Evaporation of Al at the backside to realise the back contact
- Evaporation of Ti/Al (50nm/1000nm) at the front side to realise the front contact. By means of a photolithographical step, small diodes are defined at the front side. The mesa-diodes are isolated from each other by etching the Al in H₃PO₄, Ti in a mixture of NH₄OH, H₂O₂ and H₂. The Si is etched in a mixture of HNO₃, HF and H₂O.
- At the end of the process, the sidewalls of the mesa are passivated by a thin layer of a-Si:H, deposited at 200°C. This provides a very effective surface passivation, even better than thermal oxide and suppresses anomalous perimeter currents, which are not occurring in a solar cell (because of its much smaller perimeter to area ratio).

A schematic cross-section of the thus obtained devices is shown in Fig. 1.

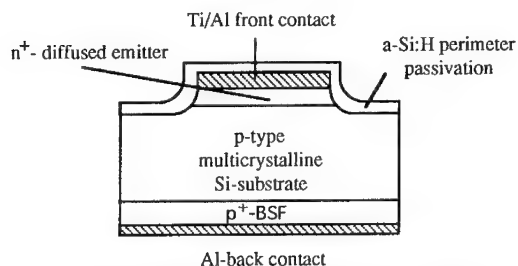


Fig. 1 Schematic cross-section of the mesa-diodes

One can see that the process is basically the same as for a solar cell with exception of the last step, which however is not believed to have a strong influence on the bulk of the device. The metal on top prevents the vertical diffusion of additional hydrogen into the device area and the temperature is too low to have appreciable lateral diffusion of hydrogen from the sidewalls. It was found in earlier devices without a-Si:H sidewall passivation that the

perimeter currents in such unpassivated devices were obscuring the actual effects of the bulk passivation by hydrogen.

EXPERIMENTAL RESULTS

1. I-V-characteristics of the mesa-diodes

The dark I-V-measurements were done on an HP4145B parameter analyser. Measurements were performed at room temperature. The measurement needles were put on the front contact. The a-Si:H layer on top of the front contact was thin enough to penetrate it easily when putting

the needle. Most device characteristics were measured in parts of the substrate where the regions look most shiny after the saw damage etch. In these parts the I-V characteristics are less influenced by the surface roughness of the wafers (which is substantial on these non-mirror like substrates). Since this study aims at finding out the bulk passivation effects of the hydrogenation treatment, this represents no fundamental problem.

In Fig. 2 a typical log(I)-V curve is shown for the GB-diodes made in material B

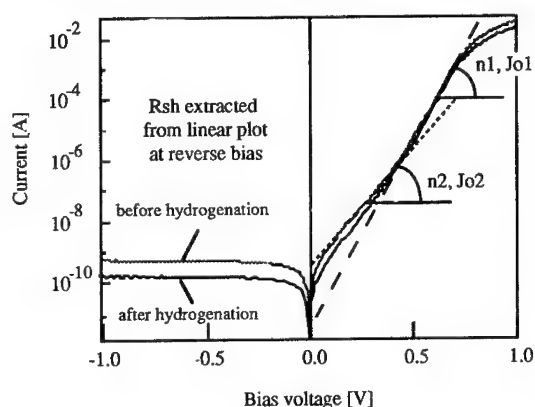


Fig. 2 : I-V-characteristic for material B after hydrogenation (diode with grain boundary)

(referred to as GB-diodes) or intra-grain diodes (referred to as IG-diodes) are shown in Table I as a function of hydrogenation. The geometrical average was taken for R_{sh} , J_{01} , J_{02} and J_{leak} . For n_1 and n_2 the arithmetic average was calculated.

		R_{sh} [ohm- μm^2]	J_{leak} [A/ μm^2]	J_{01} [A/ μm^2]	n_1 [mV/decade]	J_{02} [A/ μm^2]
A no hydrogen	IG	1e14	2e-14	1e-16	85	8e-15
	GB	2e13	6e-14	2e-16	88	2e-14
A hydrogenated	IG	3e15	2e-15	3e-18	70	9e-16
	GB	1e15	3e-15	4e-18	71	1e-15
B no hydrogen	IG	3e12	6e-13	2e-16	83	2e-14
	GB	2e13	2e-13	6e-17	82	2e-14
B hydrogenated	IG	2e15	1e-14	4e-17	79	4e-15
	GB	3e14	2e-14	4e-17	82	4e-15
C no hydrogen		3e14	1e-13	4e-15	95	2e-14
C hydrogenated		5e15	9e-16	4e-18	71	3e-16*

Table I : Overview of averaged values for ten diodes before and after hydrogenation

* no part with a slope of 120 mV/decade was found in the characteristics. The average slope in the region between 0.1 and 0.3 V is 94 mV/decade

This table deviates from the results reported in an earlier paper⁹ because of the more effective sidewall passivation by the a-Si:H deposition and different calculation of the averages.

From Table I one can deduce the following trends. In all cases, the hydrogenation leads to a substantial improvement of the reverse and forward characteristics. The leakage current is reduced by a factor of 10 (20) in the material A IG (GB)-diodes. For B the behaviour is different in the sense that in this case the improvement is most pronounced for the IG-diodes (reduction

by a factor of 60), while for the GB-diodes the reduction is only a factor of 10. One parallel is seen for material A and B: after hydrogenation the leakage currents in IG- and GB-diodes become comparable.

For the forward characteristics a comparable conclusion can be made: after hydrogenation the intercept current J_{01} becomes similar for IG- and GB-diodes both in material A and B. A detailed analysis however reveals a quite surprising result. Whereas the improvement in material A goes together with a substantial increase of the slope of the I-V-curve (n_1), the slope for material B remains more or less unaffected. This is very well illustrated by the scatter plots in Fig. 3a and b. For material C we observed a behaviour very similar to material A.

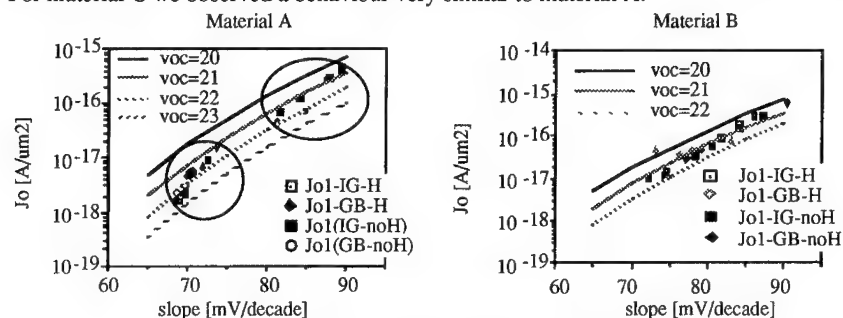


Fig. 3a and b: scatter plots revealing the effect of hydrogenation in J_{01} - n_1 -plot

Finally in Table I one can also see the evolution of the second diode current J_{02} as a function of material and treatment. The improvement is most pronounced for material A. The IG(GB)-diode improves by a factor of 10 (20) and, just as for the J_{01} , one sees that after hydrogenation the second diode saturation current is the same for the IG and GB-diodes. For material B the improvement is smaller (a factor of 5 for both GB- and IG-diodes). Again one can remark for material B the fact that before and after hydrogenation the J_{02} for IG- and GB-diodes are nearly equal.

The most surprising observation on the level of the I-V-characteristics is the drastic improvement of the diodes in material C. Although it is unclear what exactly the effect of a hydrogenation on a monocrystalline material would be, one must remark that material C behaves in most respects like material A, not only for the trends observed but also for the absolute values; the J_{01} and n_1 after hydrogenation can be seen to be nearly equal.

2. DLTS-measurements

Emphasis was on the study of minority carrier traps. Therefore, the junction capacitance was pulsed from -5V to 0.5V. In reference 9 we already reported in detail about the DLTS-measurements on material A. The basic features can be found in that publication. The main trends observed are the disappearance of the shallow minority carrier traps (especially in the GB-diodes) after hydrogenation, with a peak remaining around 230-250K.

For material B the situation is less clear (see Fig. 4). Before hydrogenation, one also sees a tendency, although less pronounced, towards a large tail at low temperatures in the DLTS-spectrum of GB-diodes, whereas for IG-diodes the spectrum has a clearer peak around 230K. The peak density of traps in the IG-diodes however is larger than in the GB-diodes (a factor of 3 in the shown spectra), which corresponds with the higher J_0 's, observed on material B before hydrogenation. After hydrogenation, the low-temperature tail disappears. The DLTS-spectra are having their peak between 230 and 250K, but also a tail at higher temperature remains. The last observation explains why the dark I-V-characteristics of the material B-diodes after hydrogenation are less good than for material A.

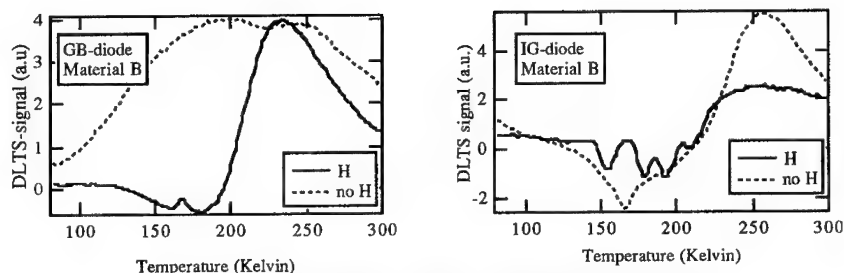


Fig. 4 DLTS-spectra before and after hydrogenation of material B

3. Results on the level of solar cells

Together with the diodes we also processed solar cells. The only difference with the process-flow outlined on page 2 is that after the evaporation of the back contact, the front side metallisation is done by evaporation of Ti/Pd/Ag (50nm/50nm/5µm) and lift-off. The results of I-V-measurements under AM1.5 illumination are shown in Table II. The cells were 4 cm² large.

Table II : I-V-measurements under AM1.5-illumination for solar cells of 2x2 cm²

Material	H-passivation	J _{sc} [mA/cm ²]	V _{oc} [mV]	FF [%]	Efficiency [%]
A	no	23	580	76.5	10.2
A	yes	23.7	586	76.8	10.7
B	no	21.7	567	76.9	9.5
B	yes	23.5	586	76.7	10.5

One can see that the hydrogenation leads to increased efficiencies both for material A and B. For material C, no cells were made for this comparison.

Concerning the discussion of these results and their relation with the small devices, it is interesting to return to Fig. 3. According to elementary diode-theory, one can write for the open-circuit voltage V_{oc} of a solar cell :

$$V_{oc} = n_1 \cdot \ln(J_{sc}/J_{01}) \quad (1)$$

The current which flows through the cell when short-circuited is denoted J_{sc}. Since the dark current in these devices is still determined by the properties of the base (and not by the emitter) and the effect of the hydrogenation is most pronounced on the level of J₀₁ (the J_{sc}-change is only in the order of a few percent), one can write the following expression :

$$V_{oc} = n_1(k - \ln(J_{01})) \quad (2)$$

Equation 2 indicates that the iso-V_{oc}-lines in a n₁-ln(J₀₁) graph will be shifted hyperbolic curves. In Fig. 3a and b such iso-V_{oc}-curves are included for v_{oc} = 20, 21, 22 and 23 where v_{oc} stands for the normalised open-circuit voltage (= qV_{oc}/kT). From these curves one can see that the improvement of v_{oc} after hydrogenation in material A and B should be less than kT/q, which is indeed found back in the solar cell results of B. For A the improvement in V_{oc} is smaller

DISCUSSION

The above results indicate a quite different behaviour of a multicrystalline Si-material with low oxygen content at one side and materials with an intermediate concentration of oxygen and impurities at the other side.

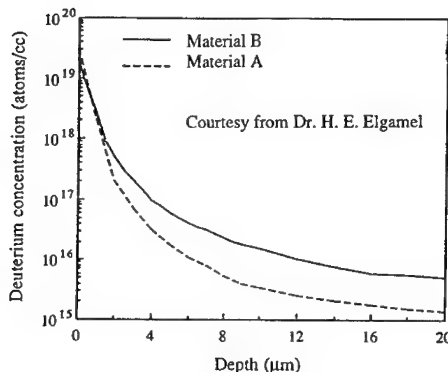


Fig. 5 : Deuterium SIMS-profile

In the SIMS-profile (fig. 5) of deuterium it is seen that the penetration is deeper in material B. Despite this difference, the improvement seems to be stronger in material A. One can clearly see that in a $\ln(J_0)$ -n-graph hydrogenation leads only to a reduction of J_0 for material B, while in the material A both n and J_0 are reduced. Such a behaviour can be explained qualitatively by realising that the defect level distribution in the two materials is basically different after hydrogenation. For the materials with intermediate oxygen content it was found that after hydrogenation the shallow states were removed and the only clear peaks remaining were mostly centred around $E_c - E_t = 0.45$ eV.⁹

For the material with low oxygen content the spectra revealed a rather broad band of states with a tail at higher temperature, which did not disappear after hydrogenation. The effect of the hydrogenation in this kind of materials is mainly a reduction of a broad band of states around midgap without fully eliminating them. In the dark I-V-characteristics the effect of the hydrogenation is however not fully revealed. When illuminating the sample, most of these remaining traps are filled because of the much higher minority carrier concentration existing in the bulk under these conditions. Therefore, the effect of the remaining traps is reduced when used under normal illumination conditions.

CONCLUSIONS

In this paper we report on the effects of hydrogenation on multicrystalline materials with different oxygen content. It was found that hydrogenation affects the characteristics in a quite different manner. It was seen that in the low-oxygen content material IG- and GB-diodes show similar characteristics before and after hydrogenation, whereas in the moderate-oxygen content material both types of diodes become only similar after hydrogenation. DLTS showed that after hydrogenation the remaining trap levels are centred around 230K. For the low-oxygen content material DLTS showed however a high-temperature tail which points to a subsisting trap density around midgap.

REFERENCES

1. A. Bourret and J. L. Rouviere, "Polycrystalline Semiconductors", edited by H. J. Möller, H. Strunk and J. Werner, Springer Proceedings in Physics, Vol. 35, p.8 (1989)
2. H. Möller, and H. Singer, "Grain Boundary Structure and Related Phenomena" Supplement to Transactions of Japan Institute of Metals, Vol. 27, p.987 (1986)
3. H. Möller, "Semiconductors for solar cells", edited by Artech House p.178 (1993)
4. K. D. Rasch, K. Roy, W. Schmidt and G. Wahl, Proceedings of the 4th European Photovoltaic Solar Energy Conference, Stresa, 919, (1982)
5. J. I. Hanoka, C. H. Seager, D. J. Sharp and J. K. G. Pantiz, Appl. Phys. Lett., vol. 42, 618 (1983)
6. H. E. Elgamel, M. Y. Ghannam, M. R. Murti, J. Nijs and R. Mertens, Appl. Phys. Lett., 18, 2171 (1993)
7. K. Kaneko, R. Kawamura, H. Mizumoto and T. Misawa, Proceedings of the 11th European Photovoltaic Solar Energy Conference, Montreux, p.1070 (1992)
8. H. E. Elgamel, Ph. D. dissertation at Katholieke Universiteit Leuven, p.116 (1994)
9. M. Rosmeulen, H. E. Elgamel, J. Poortmans, M. A. Trauwert, J. Vanhellemont, J. Nijs, to be published in the proceedings of the 1st World Conference on Photovoltaic Energy Conversion, December 1994 (1994)

ENHANCED HYDROGENATION DUE TO ULTRASOUND TREATMENT IN POLYCRYSTALLINE SILICON: NEW APPROACH TO THIN FILM DEFECT ENGINEERING

S. OSTAPENKO, W. HENLEY, S. KARIMPANAKKEL, L. JASTRZEBSKI and
J. LAGOWSKI

Center for Microelectronics Research, University of South Florida, 4202 Fowler Ave., Tampa,
FL 33620

ABSTRACT

We applied the ultrasound treatment (UST) to improve properties of poly-Si thin films on glass substrates for thin-film transistor applications. A strong decrease of the sheet resistivity in hydrogenated films subjected to UST was observed. UST improves the film homogeneity as monitored by spatially resolved surface photovoltage mapping. Studies of hydrogenated thin-film transistors demonstrated remarkable UST induced improvement in transistor characteristics, especially, a reduction of leakage current by as much as one order of magnitude. All these effects are explained in terms of UST enhanced hydrogenation of poly-Si film.

INTRODUCTION

Hydrogenation is a critical process for improving properties of polycrystalline silicon for thin-film transistors. Proper hydrogenation has been shown to passivate traps, reduce device leakage current, and improve drive current by increasing carrier mobility [1]. The degree of poly-Si hydrogenation is often inferred from time consuming analytical measurements or from end-of-line transistor parameter characteristics. Recently, we found that poly-Si hydrogenation can be also monitored in a quick, non-contact manner by surface photovoltage (SPV) measurement [2], which provides a convenient real-time feedback for process control. In this paper we present results on enhanced hydrogenation in poly-Si thin films on a glass substrate stimulated by the ultrasound treatment (UST). Ultrasound waves propagating through a semiconductor are known to produce lasting changes in recombination properties related to point and extended defects. As was found recently, UST applied to p-type Cz-Si [3,4] and solar-grade polycrystalline Si [5] caused significant changes in the dissociation-association kinetics of metal-acceptor pairs. These results support a growing evidence that by coupling the ultrasound vibrations to semiconductor materials, one can expect it to vary properties of point and extended defects not only in compound semiconductors, but also in silicon. Stimulated by UST, the processes of point defect generation by releasing them from traps as well as point defect gettering by sinks can be of particular importance for UST of polycrystalline silicon thin films. In this work an emphasis is given to UST in hydrogenated poly-Si films. The hydrogen passivation of dangling bonds at grain boundaries and at the surface is recognized as a key process improving film quality. The new approach to enhance the efficiency of hydrogenation in thin poly-Si films by ultrasound treatment is reported in this paper.

EXPERIMENTAL DETAILS

Semi-insulating as-grown Si films with thicknesses ranging from 0.35 to 0.55 μm were deposited at 625°C or 550°C on Corning 7059 glass substrates by low pressure chemical vapor deposition using SiH_4 pyrolysis. X-ray diffraction proved that 625°C films had a crystallite structure with (110) orientation, while the films deposited at 550°C were amorphous. Subsequent prolonged annealing (8 to 75h) of 550°C films under nitrogen flow at 550°C caused a gradual development of the crystallite structure oriented predominantly along (111) direction. The films were selectively hydrogenated using a pattern defined by an opening in an Al mask.

This enabled us to study the UST effect by comparing hydrogenated ("H") with non-hydrogenated ("non-H") areas on the same film. The hydrogenation was performed at 300°C in a plasma system operating at a 100ccm H₂ flow with 0.3Torr pressure and 200W radio frequency power for 1 to 3 hours.

The hydrogenation efficiency was monitored by measuring the sheet resistivity using the four-point-probe method. Complimentarily, the surface photovoltage (SPV) measurements were performed on the same films by utilizing the approach developed in Ref.2. According to the principles of SPV method, the surface potential can be modulated by photo-induced carriers, therefore, the magintude and phase of AC voltage is a sensitive measure of bulk and surface recombination properties of material. Using chopped optical excitation with 514nm Ar-laser line (light penetration of 0.3μm in poly-Si) and a lock-in response measurement technique, both the amplitude and the phase shift can be determined. The phase shift technique provides the information regarding recombination lifetime in the conditions of a strong trapping effect [2]. SPV measurements were performed with a modified Semiconductor Diagnostics CMSIII analysis system using an Ar -laser as photo-excitation source.

For UST experiments, ultrasonic vibrations were applied to the poly-Si sample through the glass substrate by external circular piezoceramic transducers of 1.5" or 2.9" diameter and 0.125" thickness as shown in Fig.1. The transducers were driven by a function generator and power amplifier adjusted to the resonance frequency of the radial or thickness vibrations. Each UST can be specified by the following parameters: ultrasound mode and frequency (25 to 650kHz); amplitude of acoustic strain generated by transducer, (typically, on the order of 10⁻⁵); temperature (20 to 120°C); and UST time (5 to 120min). The sample temperature during UST was measured in-situ by a remote infrared pyrometer, while the amplitude of acoustic vibrations generated into the sample was controlled by a miniature piezoelectric detector (Fig.1). UST induced changes in film properties and their post-UST relaxation were monitored by measuring poly-Si sheet resistivity and SPV signal.

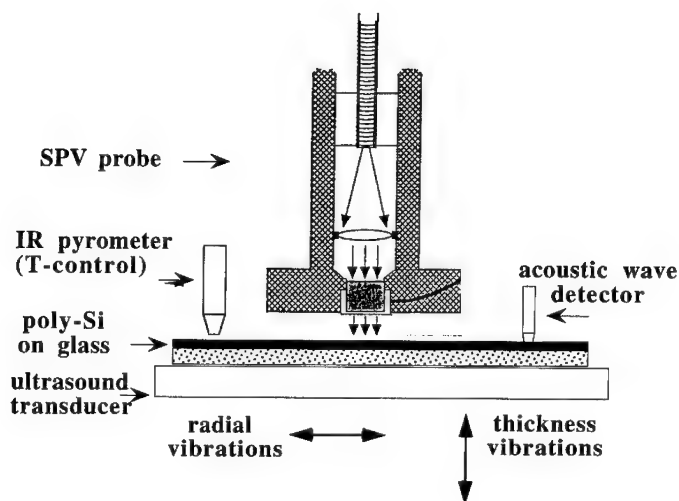


Fig.1 General scheme of ultrasound treatment in poly-Si thin films with SPV as diagnostic technique of hydrogenation.

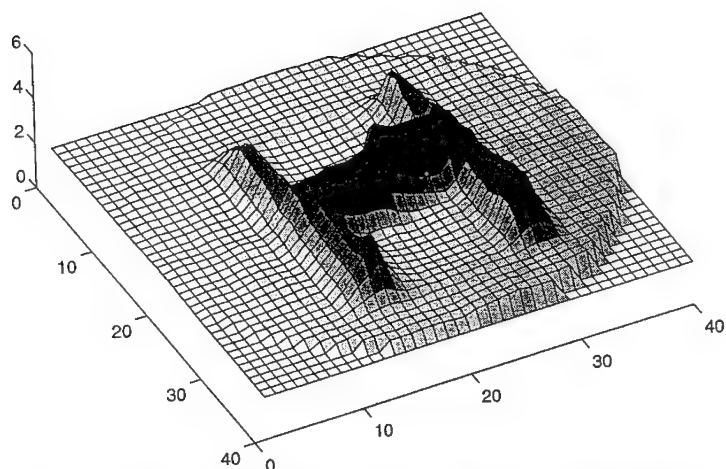


Fig.2 Surface photovoltage map of selectively hydrogenated poly-Si thin film on glass ("H"-character)

RESULTS

The surface photovoltage measurements show increased SPV signal magnitude in the hydrogenated areas compared to non-hydrogenated regions of the same sample. This is demonstrated in Fig. 2 by SPV map of a thin poly-Si film selectively plasma hydrogenated with a pattern of the letter "H". These results were published previously [2], and are consistent with the known role of hydrogenation in thin film poly-Si. The hydrogen passivates traps, thereby reducing minority carrier recombination and as a consequence changes the SPV amplitude and phase. The four point probe resistivity measurement on the same film have shown a resistivity drop by approximately 1 order of magnitude in the H-region compared to the non-H region. This is consistent with published data on hydrogenation effect on poly-Si film resistivity. In the present work, we used resistivity and SPV measurements as two independent techniques for monitoring the hydrogenation efficiency.

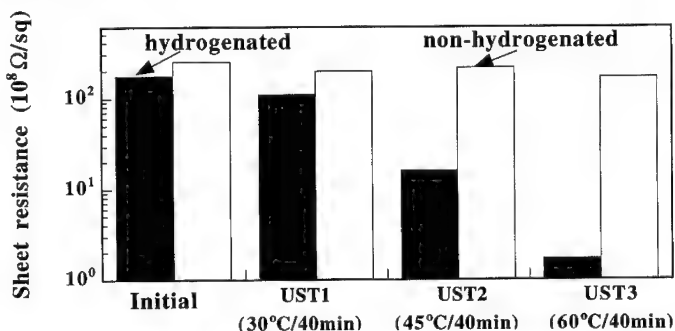


Fig.3 Effect of ultrasound treatment on hydrogenation efficiency in poly-Si for thin-film transistors application

The results of UST on sheet resistance of hydrogenated and non-hydrogenated samples are shown in Fig.3. The "H"-sample demonstrates a dramatic one to two orders of magnitude decrease in resistance after UST. In comparison, the same UST applied to "non-H" sample produced only 30 to 40% reduction of resistance. The UST effect is specified by a time constant of 25 min at 55°C. We notice, that this low temperature UST processing of poly-Si on glass can be specifically beneficial for thin-film transistor technology, where the temperature stability of the glass substrate is a critical parameter.

We have also observed that UST improves the homogeneity of hydrogenated poly-Si films. In Fig.4 a comparison is given between the resistivity of two different regions of the same plasma hydrogenated sample. It is obvious that UST stimulated two effects: (a) decreases the absolute value of film resistivity, and (b) it reduces differences between film regions. In the case presented in Fig.4, the resistivity ratio in the two regions was reduced from one order of magnitude before the UST to less than 10% after treatment. This result is confirmed by a 177-point SPV mapping (spatial resolution of 2mm) of 2 inch diameter poly-Si film subjected to a set of consecutive UST. As shown in the Table, the 177-point SPV signal standard deviation gradually decreased after UST by a factor of 2.5. Therefore, we conclude that the improvement of the film homogeneity after UST is documented by both resistivity and SPV measurements.

Table. Changes in standard deviation of 177-point SPVmap after UST in a poly-Si film.

State of poly-Si	Standard Deviation (%)	Average SPV Amplitude (mV)
Before UST	42	1.32
UST1 (30min/70°C)	28	1.21
UST2 (120min/100°C)	24	1.26
Relaxation (12h/20°C)	17	1.60

The transient character of UST effect and post-UST relaxation are of special concern in practical utilization of this treatment. The relaxation for 12h at room temperature to a new, but lower than initial value of resistance had been observed for "H" samples subjected to UST as shown in Fig.5. This relaxation process can be noticeably suppressed by cyclic UST-relaxation-UST procedure (Fig.5). This scheme enabled a permanent reduction of the sheet resistivity in hydrogenated poly-Si film by as much as one order of magnitude.

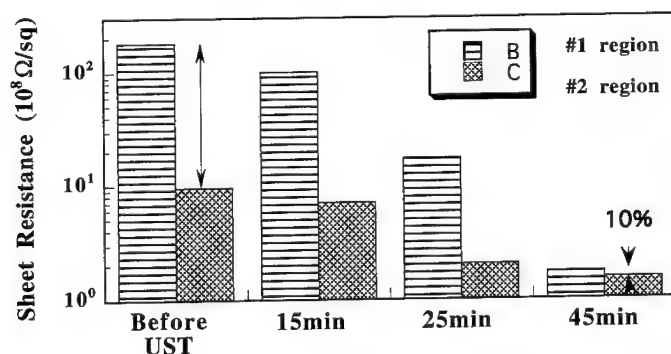


Fig.4 Improvement of resistance homogeneity in hydrogenated poly-Si film versus time of Ultrasound Treatment

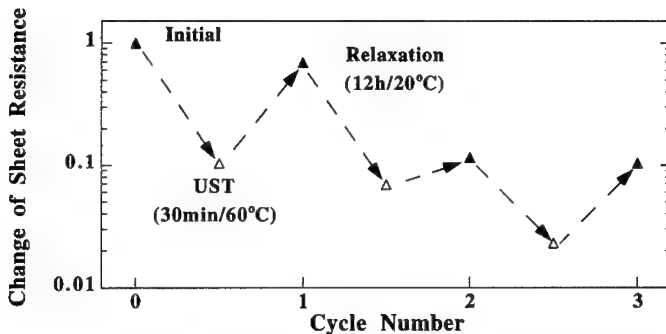


Fig.5 Stabilization of UST effect by using cyclic UST-relaxation-UST procedure

Finally, we applied the UST procedure to commercial poly-Si thin-film transistors subjected to plasma hydrogenation processing. The effect of UST on transistor characteristics is illustrated in Fig.6 by two I_D - V_G curves measured before and after poly-Si film with fabricated transistors was subjected to UST. A substantial decrease of the leakage current by a factor of as much as 10, was observed for a number of transistors with practically no change in the threshold voltage and drive current. At the present time, we do not have adequate data to specify a relevant mechanism responsible for UST reduction of the leakage current. However, the leakage current improvement is consistent with the hydrogenation of grain-boundary interface states after UST observed in this paper in the resistivity and SPV study.

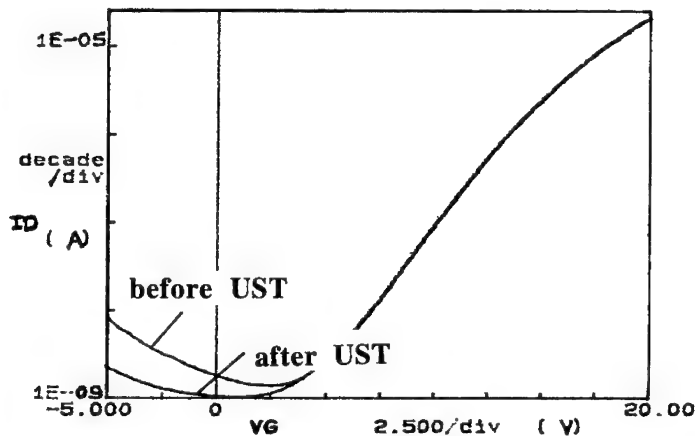


Fig.6 I-V characteristics of hydrogenated poly-Si thin film transistor demonstrating UST improvement of leakage current.

DISCUSSION

The phenomenon of the resistivity decrease due to poly-Si hydrogenation is the recognized as the passivation of inter-grain boundary trapping centers by hydrogen resulting in a decrease of grain boundary barriers [6]. Present experimental results imply that this process can be substantially enhanced by UST. We propose the following mechanism to tentatively account for the UST effect in poly-Si thin films. It is known that after hydrogenation of poly-Si thin films the total hydrogen concentration in the film exceeds the number of dangling bonds by as much

as two orders of magnitude [7]. Furthermore, it is also known that the fraction of passivated dangling bonds is often very low. Therefore, a significant reservoir of hydrogen is available in the hydrogenated film for the passivation of dangling bonds. It had been observed that this hydrogen in the reservoir is weakly bound (presumably, in the form of complexes or small H-induced platelets) and can be released by a low temperature annealing (460K) followed by rapid quenching [8]. The process of thermal liberation of hydrogen from the reservoir has an activation energy of about 1eV. This atomic hydrogen after fast diffusion to grain boundary regions can be captured by dangling bonds and form stable centers at room temperature or, alternatively, can form electrically active metastable H-related complexes. The Si-Si bonds strongly distorted by tensile stress at grain boundaries are a reasonable place to accommodate the atomic H released from H-reservoir. It is known that such centers are metastable defects and show a room-temperature relaxation of resistivity change [8]. We can postulate that UST enhances the hydrogen liberation from the reservoir (25min at 55°C), presumably, by decreasing the binding energy of atomic hydrogen in the reservoir. Moreover, UST can also increase the diffusivity of atomic hydrogen by reducing the activation energy of H-diffusion [9]. These suggestions follow examples of the established UST stimulated reduction of activation energy for dissociation of Fe-B pairs [3] and association of Cr-B pairs in silicon stimulated by the ultrasound [4]. The cyclic UST-relaxation-UST procedure finally brings together the released hydrogen and the dangling bonds at grain boundaries, by forming stable Si-H centers. This stable decrease of the sheet resistance may be in fact similar to the cyclic process of low temperature annealing - light activation of dangling bonds reported previously in thin film poly-Si [10].

CONCLUSIONS

We observed for the first time that ultrasound treatment applied to hydrogenated polycrystalline Si films provides the change of transport and recombination properties relevant to TFT applications. The process shows a relaxation behavior, but can be stabilized by cycling consecutive ultrasound treatment and relaxation. Ultrasound enhanced hydrogenation can be explained as UST stimulated release of atomic hydrogen from the H-reservoir followed by subsequent hydrogen trapping by the dangling bonds at grain boundaries and surface interface states. This UST mechanism can be responsible for the reduction of leakage current presently observed for commercial hydrogenated thin film transistors. By analogy with other semiconductors with grain boundaries, dislocations and point defects, UST may be an alternative (or complimentary) technique to improve the properties of polycrystalline silicon thin films and thin-film transistors for active matrix LCD application.

This work was supported by a grant from the Advanced Research Projects Agency.

REFERENCES

1. I.W. Wu, Tiao-Yuon Huang, W.B. Jackson, A.G. Lewis, and A. Chiang, *IEEE Electron Device Letters*, **12**, 181 (1991).
2. S. Ostapenko, W. Henley, S. Karimpanakkel, L. Jastrzebski, and J. Lagowski in Proceedings of International Display Research Conference (Monterey, California 1994), pp.299-302
3. S. Ostapenko and R. Bell, *Appl.Phys.Lett.*, **77** (10), (1995).
4. R. Bell, S. Ostapenko, and J. Lagowski. *This MRS Proceedings*.
5. S. Ostapenko, L. Jastrzebski, J. Lagowski, and B. Sopori, *Appl.Phys.Lett.*, **65**, 1555 (1994).
6. C.H. Seager and D.S. Ginley, *Appl. Phys. Lett.*, **34**, 337 (1979).
7. N.H. Nickel, N.M. Johnson, and W.B. Jackson, *Appl.Phys.Lett.*, **62**, 3285 (1993).
8. N.H. Nickel, W.B. Jackson, and C. van der Walle, *Phys.Rev.Lett*, **72**, 3393 (1994).
9. V.N. Pavlovich, *Phys.Stat.Sol (b)*, **180**, 97 (1993).
10. N.H. Nickel, W.B. Jackson, and N.M. Johnson, *Phys. Rev. Lett.*, **71**, 2733 (1993).

HYDROGEN PASSIVATION OF DEFECTS IN ELECTRON IRRADIATED POLYCRYSTALLINE SILICON SOLAR CELLS

R.R. BILYALOV AND B.M. ABDURAKHMANOV

Institute of Electronics, Department of Technical Electronics,
Uzbek Academy of Sciences, Akademgorodok, Tashkent 700143,
Uzbekistan

ABSTRACT

The effect of hydrogen passivation on photovoltaic performance of 1 MeV electron irradiated polycrystalline cast silicon solar cells is described. These cells were processed on cast p-type boron doped polycrystalline silicon substrates using standard technology. Passivation was made by low-energy hydrogen ion implantation on the front side. Cells performance was measured as a function of fluence, and it was found that the hydrogenated cell had the higher radiation resistance.

Defect behavior were studied using deep level transient spectroscopy and infra-red spectroscopy. It was shown that the concentration of vacancies ($E_c - 0,09$ eV), divacancies ($E_c - 0,23$ eV) and A-centers ($E_c - 0,18$ eV) is significantly lower in hydrogenated samples. This consistency strengthens the belief that hydrogen interacts with vacancy-type defects to prevent formation of the secondary radiation defects. It is confirmed by IR-measurements.

INTRODUCTION

The use of hydrogen in solar cells started when a grain boundaries and dislocations passivation in poly-Si was reported by C.H. Seager and D.S. Ginley [1]. Since this time the research and development efforts are concentrated in extending of H-passivation application. It is well known that the hydrogenation increases the efficiency of poly-Si solar cells due to passivation of electrical activity defects [2,3]. It was as well shown that the passivation by low-energy hydrogen ion implantation is preferable than by hydrogen plasma treatment due to the shorter processes time and the capability of controlling the ion energy [4]. The new very promising utilization of hydrogen passivation is the improvement of radiation characteristics of poly-Si solar cells for space application [5].

In this study the effect of hydrogen passivation on photovoltaic performance of 1 MeV electron irradiated polycrystalline silicon solar cells is presented. The defects occurring from radiation was studied using both deep level transient spectroscopy (DLTS) and infra-red spectroscopy (IR).

EXPERIMENTAL DETAILS

Samples (20mm x 20mm x 0,5mm) were cut from a directionally cast large grained (1-2 mm) polycrystalline silicon ingot, obtained as described in [6]. The substrates were p-type boron doped with a resistivity of 1-2 Ω cm. The n-p junction was formed by phosphorus diffusion at a depth of 0,7 μ m. The frontal contacts were obtained by vacuum deposition of Ti-Cu-Ni. On the backside of the samples Al was evaporated. Subsequently the samples were annealed at 300 °C for about 10 min in order to form an ohmic contact.

Hydrogenation was carried out by hydrogen ion implantation using a Kaufman ion source with an energy of 1,2 keV and a current density of 0,25 mA/cm². The detailed description of hydrogenation procedure was made in [7]. The finished solar cells were irradiated by electrons with an energy of 1 MeV and an integral fluence of $D=10^{13} - 10^{16}$ cm⁻². The radiation intensity was 10¹¹ cm⁻² sec⁻¹.

DLTS samples with area from 0,01 to 0,02 cm² were obtained by sawing a 2 x 2 cm² cells, etching and mounting them to TO-5 headers. DLTS measurements were taken using a 28-MHz capacitance bridge. All samples were stored in liquid nitrogen immediately after irradiations and after any measurements to prevent annealing at room temperature. The IR measurements were effectuated by means of a "SPEQORD - M80" and "PYE-UNICAM SP-3-300" equipped with a continuous-flow cryothermostat in the range of wavenumber 4000 - 400 cm⁻¹. The measuring temperature was in the range number 100 - 400 K and the resolution was 0,5 cm⁻¹.

RESULTS AND DISCUSSION

Fig.1 shows the I_{sc} and V_{oc} parameters of the hydrogenated (▲) and untreated (●) polycrystalline silicon solar cells versus 1 MeV electron fluence. With increasing irradiation dose the difference between the degradation rates of the passivated and untreated solar cells increases, reaching 6% of the maximum power at electron dose $D=10^{16}$ cm⁻². The critical integral electron fluence at which the I_{sc} decreases by 25% is 1,7 10¹³ cm⁻² for hydrogenated and 10¹³ cm⁻² for the untreated solar cell. The

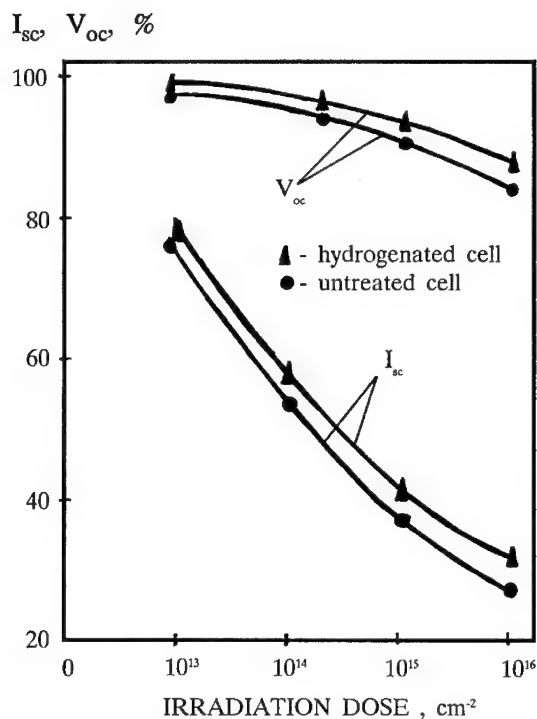


Fig.1

V_{oc} decreases by 12% and 16% respectively for hydrogenated and untreated cell after $D=10^{16} \text{ cm}^{-2}$. Therefore the radiation degradation of maximum solar cells power is determined mainly by the degradation of I_{sc} . In turn, I_{sc} decreases due to decreases in the minority carrier diffusion length.

The spectral response measurements of hydrogenated and untreated solar cell before and after 1 MeV electron irradiation shows the distinct shift in the decreasing in the minority carrier diffusion length. As was earlier shown the spectral response decreases by more than a factor of 3 when $D=10^{15} \text{ cm}^{-2}$ in the longwave region, while in the shortwave region the spectral response nearly constant up to an electron fluence of 10^{16} cm^{-2} [5]. In this case the slight shift of the peak toward shorter wavelength in hydrogenated solar cell is due to the increase in minority carrier diffusion length. The minority carrier diffusion length, which was determined from spectral response measurements is a factor of 1,5 higher in the hydrogenated than in the untreated solar cell.

The energy levels of the radiation-induced defect states found in electron - irradiated untreated polycrystalline silicon samples are given in Table 1. The identification of the radiation defects induced by electron irradiation was carried out in previous work [8].

Table 1

Type of defect	Charge state	Position of level
Divacancy	V_2^{-2}	$E_c -0,23$
	V_2^{-1}	$E_c -0,40$
A-center	$(V+O)^{\cdot}$	$E_c -0,18$
Boron vacancy	$(V+B)^+$	$E_v +0,45$
Vacancy	V^{\cdot}	$E_c -0,09$
	V^+	$E_v +0,11$
Interstitial Si	Si^+	$E_v +0,40$

The concentration of above mentioned defects especially divacancies ($E_c -0,23$ eV) and A-centers ($E_c -0,18$ eV) is an order of magnitude lower in the hydrogenated specimens, and the defects ($E_c -0,09$ eV) and ($E_v +0,4$ eV), which represent singly charged vacancies and interstitial Si atoms respectively, are not observed in hydrogenated samples. The A-center has been passivated by binding of Si dangling bonds with two hydrogen atoms. This thermal stable center is annealed only at 450 °C. In addition to direct passivation, hydrogen - vacancy interaction decreases the probability of secondary vacancy defects such as divacancies, A-centers etc.

The comparison of IR - spectrums before and after e-irradiation clearly shows the following. The absorption intensity at the some defects induced by electron irradiation in hydrogenated samples much lower than in untreated specimens. And absorption bands at 3571 cm^{-1} ($E_v +0,33$ eV), 3030 cm^{-1} ($E_v +0,38$ eV), 2632 cm^{-1} ($E_v +0,33$ eV) and 2439 cm^{-1} ($E_v +0,3$ eV) observed in untreated samples are not appeared in hydrogenated specimens. It is obvious that hydrogen neutralizes some of the radiation defects, and judging from effectiveness of passivation, the hydrogen is captured just immediately in defect formation process. On the other hand, one cannot exclude passivation due to the probable radiation-stimulated diffusion of free interstitial hydrogen atoms through the polycrystalline silicon.

CONCLUSION

Electron radiation testing of hydrogenated polycrystalline silicon solar cells indicates that the hydrogenation increases the radiation resistance. The absence of some electron induced radiation defects in hydrogenated samples and the decrease of the other defects concentration is due to the hydrogen incorporation with radiation defects. Therefore this hydrogenation technique may have significant implications in the area of photovoltaic space power. This study leads the way for more research on the hydrogenated polycrystalline silicon solar cells.

ACKNOWLEDGMENT

The authors would like to thank Dr. V.P. Chirva for his assistance with the electron irradiations experiments. We are also grateful to Prof. M.S. Saidov for discussion this work.

REFERENCES

1. C.H. Seager and D.S. Ginley, J. Appl. Phys. **52**, 1050 (1981).
2. J.C. Muller et al., Solar Cells, **17**, 201 (1986)
3. N. Lewalski, R. Shindler and B. Voss in Proc. 19th IEEE Photovoltaic Specialists Conference, (New York, 1987), p.1059.
4. J.C.Muller, A.Barhdadi, Y.Ababou and P.Siffert, Rev. Phys. Appl. **22**, 649, (1987).
5. B.M. Abdurakhmanov, R.R. Bilyalov, M.S.Saidov and V.P.Chirva, Appl. Sol. Energy **28** (3), 7-9 (1992).
6. B.M. Abdurakhmanov et al., Appl. Sol. Energy **28** (4), 8-14 (1992).
7. R.R. Bilyalov, M.S. Saidov and V.P. Chirva, Appl. Sol. Energy **26** (4), 40-42 (1990).
8. R.R. Bilyalov, PhD thesis, Tahkent Physical-Technical Institute, 1993.

INTERACTION OF ATOMIC HYDROGEN WITH CHALCOGENS IN GAAS

J. VETTERHÖFFER AND J. WEBER

Max-Planck-Institut für Festkörperforschung,
Postfach 800665, D-70506 Stuttgart, Germany

ABSTRACT

The passivation by hydrogen of the shallow donors sulfur, selenium, and tellurium in GaAs was studied by infrared absorption spectroscopy (FTIR), capacitance-voltage (C-V) depth profiling, and secondary ion mass spectroscopy (SIMS). Local vibrational mode (LVM) frequencies due to hydrogen-donor complexes agree with a microscopic model where the hydrogen atom is bound in the antibonding position to one of the donor's neighboring gallium atoms. Our results suggest a hydrogen penetration depth much greater than the passivated region, however the infrared active region coincides with the passivated part of the material.

INTRODUCTION

Hydrogen incorporation into semiconductors has been shown to be a very common process that occurs both during growth and during post-growth processing such as plasma etching, wet chemical etching or surface cleaning. These treatments can lead to a hydrogen diffusion up to several micrometers into the material. Hydrogen electrically passivates both shallow dopants as well as deep defects. Shallow dopant passivation leads to a decrease of free carrier concentration of up to one order of magnitude near the surface. This effect has been explained by a hydrogen bonding to the dopant atom rather than a compensation effect. Microscopic details of the hydrogen complexes can be obtained by infrared absorption spectroscopy. Vibrational excitation of the hydrogen atom (LVM) leads to very narrow absorption lines with frequencies very similar to those known for hydrogen containing molecules.

In the case of GaAs it is observed that all shallow dopants (C_{As} , Si_{As} , Ge_{As} , Be_{Ga} , Zn_{Ga} , Cd_{Ga} , Si_{Ga} , Sn_{Ga} , S_{As} , Se_{As} , and Te_{As}) are passivated by atomic hydrogen and for most of them vibrational lines have been reported[1]. Recently, we have reported vibrational modes after hydrogen treatment for the chalcogen donors sulfur, selenium, and tellurium[2] that have been confirmed at the same time by R. Rahbi *et al.*[3]. The analysis of the frequency dependence on the donor species led to a model where the hydrogen atom binds in the antibonding position to one of the gallium atoms next to the donor atom with the gallium-hydrogen bond along a $\langle 111 \rangle$ direction. This picture is in agreement with theoretical calculations performed by K. J. Chang[4] and by R. Rahbi *et al.*[3]. The complex has trigonal symmetry and the two absorption lines observed for each donor species are interpreted as a non-degenerate stretching mode and a lower lying two-fold degenerate bending mode.

In order to correlate the absorption measurements with the electrical passivation of the donor atoms, we have performed C-V depth profiling of the free carrier concentration after hydrogenation.

EXPERIMENTAL DETAILS

The samples used in this study for infrared absorption measurements consist of S- and Se-doped layers grown by metal-organic vapor phase epitaxy (MOVPE) and Se- and Te-doped layers grown by liquid phase epitaxy (LPE) on undoped semi-insulating GaAs substrates. The layer thicknesses varied between 2 and 10 μm with carrier concentrations from $2 \cdot 10^{18} \text{ cm}^{-3}$ to $1 \cdot 10^{19} \text{ cm}^{-3}$. In addition, Te-doped bulk material, grown by the liquid encapsulated Czochralski (LEC) technique, was used for the C-V depth profile measurements ($n = 2 \cdot 10^{17} \text{ cm}^{-3}$).

For passivation, the samples were exposed for 3 to 50 hours to a remote hydrogen or deuterium dc plasma in a parallel plate system with a plate voltage of 600 V. The samples were mounted on a heater block held at a temperature of 180–200°C and placed 10 cm downstream from the plasma with a bias voltage of about -300 V, that fixed the bias current to 50 μA . The gas pressure was held at 1 mbar.

Infrared transmission was measured at normal incidence with a BOMEM DA3.01 Fourier transform spectrometer, equipped with a liquid nitrogen cooled MCT detector as well as a liquid helium cooled Si:B detector. To avoid mounting stress, the samples were free-standing in the sample compartment of an exchange-gas cryostat, where the temperature was measured with a calibrated germanium resistor.

For C-V depth profile measurements, Schottky diodes were fabricated by evaporating Au Schottky contacts of 0.6 mm in diameter after dipping the sample into a dilute $\text{H}_2\text{SO}_4/\text{H}_2\text{O}_2/\text{H}_2\text{O}$ etch. Ohmic contacts were produced on the back side of the bulk samples by scratching an In/Ga alloy.

Secondary ion mass spectroscopy (SIMS) was performed on deuterated samples with a CAMECA IMS 4F apparatus, using a primary-ion source of cesium. A Talystep stylus profilometer was used for the depth calibration and a H-implanted GaAs specimen for the calibration of the absolute SIMS intensity.

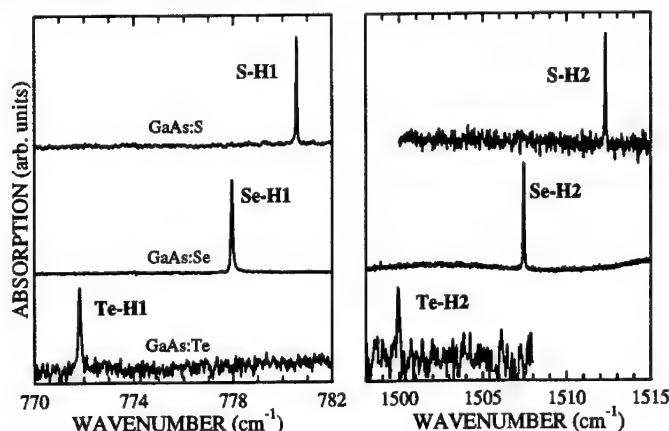


Figure 1: Typical spectra of the absorption lines found after hydrogen plasma treatment (0.025 cm^{-1} apodized resolution for X-H1 and 0.1 cm^{-1} for X-H2 lines).

Table I: Summary of LVM frequencies, their full width at half maximum (FWHM), relative integrated intensities, and r -values ($r = \frac{\omega_{X-H}}{\omega_{X-D}}$) at $T = 10$ K.

absorption line	line position (10 K)	FWHM (10 K)	relative intensity	r -value (10 K)
S-H1	780.58 cm^{-1}	0.045 cm^{-1}	7.8	1.4035
S-H2	1512.30 cm^{-1}	0.071 cm^{-1}	1	1.3895
S-D1	556.1 cm^{-1}	0.3 cm^{-1}	7.6	
S-D2	1088.4 cm^{-1}	0.4 cm^{-1}	1	
Se-H1	777.95 cm^{-1}	0.08 cm^{-1}	7.3	1.4035
Se-H2	1507.46 cm^{-1}	0.08 cm^{-1}	1	1.3896
Se-D1	554.3 cm^{-1}	0.6 cm^{-1}	≈ 20	
Se-D2	1084.8 cm^{-1}	0.7 cm^{-1}	1	
Te-H1	771.81 cm^{-1}	0.09 cm^{-1}	5.5	
Te-H2	1499.93 cm^{-1}	0.13 cm^{-1}	1	
Te-D1	550.0 cm^{-1}	0.6 cm^{-1}		
Te-D2	not detected			

RESULTS

Localized vibrational modes

After hydrogen plasma treatment, two new absorption lines were found for each donor species, a stronger one around 780 cm^{-1} labeled X-H1 ($X=\text{S,Se,Te}$) and a much weaker one, X-H2, around 1500 cm^{-1} (Figure 1). Substituting hydrogen by deuterium shifts the spectral positions of the lines to lower frequencies by a factor r close to $\sqrt{2}$ as expected for hydrogen LVMs that are very well described by a simple harmonic oscillator model. The precise ratios together with the line positions, line widths and relative intensities at $T = 10$ K are summarized in Table I. The intensity ratio of X-H1 to X-H2 is constant to within experimental error, manifesting that they originate from the same complex. We attribute

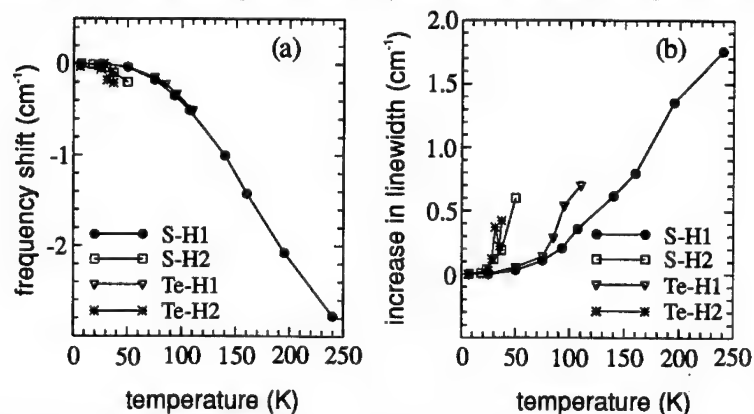


Figure 2: (a) Shift with temperature of the hydrogen absorption lines X-H1 and X-H2 ($X=\text{S,Se,Te}$). (b) The same for the line width (full width at half maximum).

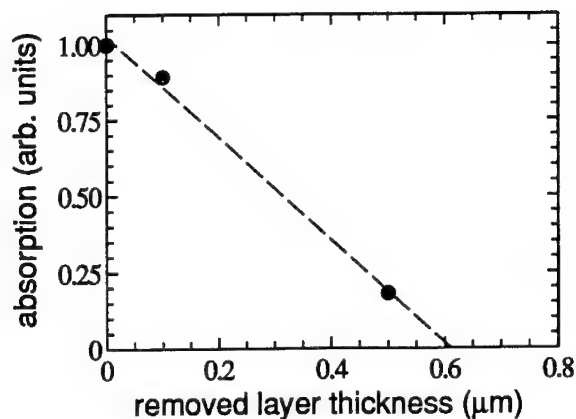


Figure 3: Decrease of absorption intensity of the Te-H1 line after successive removal of the surface layer. The doping level was $n=2.1 \cdot 10^{18} \text{ cm}^{-3}$ and the hydrogenation was performed at $T = 200^\circ \text{C}$ for 6 hours.

X-H1 to the bending mode of the bound hydrogen atom and X-H2 to the corresponding stretching mode.

All of the observed lines exhibit a strong temperature dependence. Increasing the measurement temperature above $T = 40 \text{ K}$ leads to a pronounced line broadening and a shift to lower frequencies (Figure 2). The weaker higher frequency lines X-H2 are observable only until $T = 50 \text{ K}$, the stronger lower frequency lines X-H1 up to 240 K .

In order to determine the layer thickness of the absorbing complexes, material was etched step-by-step from the surface by a $\text{H}_2\text{SO}_4/\text{H}_2\text{O}_2/\text{H}_2\text{O}$ etch. As a consequence, the absorption intensity decreases progressively. Extrapolating the absorption intensity to zero (cf. Figure 3) leads to an infrared active region with a thickness of $\approx 0.6 \mu\text{m}$.

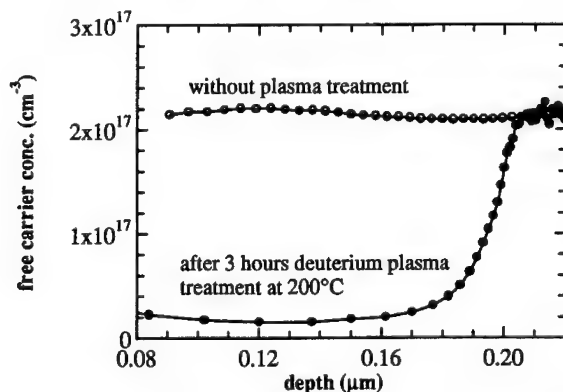


Figure 4: Electrical passivation of Te-doped GaAs after 3 hours hydrogen plasma exposure at $T = 200^\circ \text{C}$.

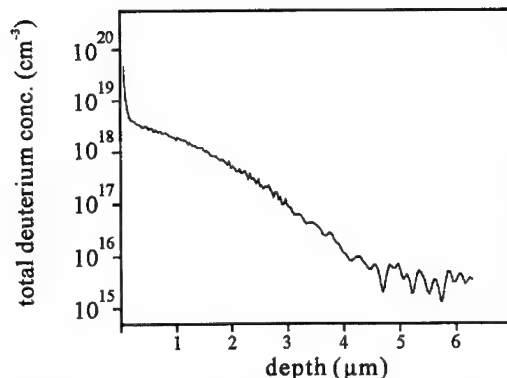


Figure 5: SIMS measurement of GaAs:Te ($n = 2 \cdot 10^{17} \text{ cm}^{-3}$) after 3 hours deuterium plasma treatment at $T = 200^\circ\text{C}$.

Electrical passivation and hydrogen penetration depth

We have monitored hydrogen trapping and detrapping from tellurium donors by capacitance-voltage profiling. By measuring the capacitance of a Schottky diode as a function of reverse bias voltage the depth dependent free carrier concentration can be calculated. These measurements were performed on the Te-doped bulk material ($n = 2 \cdot 10^{17} \text{ cm}^{-3}$). They show a passivation, after three hours of deuterium plasma exposure at 200°C , to a depth of about $0.2 \mu\text{m}$. In this region the carrier concentration has decreased by a factor of ten (Figure 4).

Simultaneously, a second sample of the same material was deuterated. Figure 5 shows the result of a SIMS measurement performed on this sample. Deuterium instead of hydrogen is used in order to increase the experimental sensitivity. The diagram shows that the deuterium penetrates much deeper into the sample than indicated by the electrical passivation. In contrast to the passivation depth of about $0.2 \mu\text{m}$, deuterium concentration decreases by a factor of 10 only after $2 \mu\text{m}$, and it is still detectable at a depth of $4 \mu\text{m}$. Up to a depth of $2 \mu\text{m}$ the total deuterium content is much higher than the donor concentration.

DISCUSSION

From Figure 1 it is evident, that there is a systematic dependance of the vibrational frequency on the mass of the donor atom. Increasing the donor mass leads to a decrease of the absorption frequency, indicating that the vibrational mode includes the donor atom. However, compared with the frequency-mass relationship found for hydrogen-group IV donor or for hydrogen-acceptor complexes[1], the chalcogen donor complexes exhibit only a very small mass dependance. This indicates that the hydrogen atom can not be directly bound to the donor but it must bind at least to a neighboring gallium atom.

A similar case is known for the hydrogen passivated group VI donors P, As, and Sb in silicon[5]. Substituting the phosphorus donor (mass: 31 a.u.) by antimony (mass: 122 a.u.) shifts the hydrogen stretching LVM only by 5 cm^{-1} from 1555 cm^{-1} to 1562 cm^{-1} . For these complexes a model has been proposed, where the hydrogen atoms binds in the

so-called antibonding position to a neighboring silicon atom of the donor. Applying this model to our case suggests a hydrogen-gallium bond at the antibonding site. The stretching frequency measured is in good agreement with Ga-H stretching mode frequencies of $\sim 1500 \text{ cm}^{-1}$ encountered in molecules[6], whereas the As-H stretching modes found in molecules are considerably higher ($\sim 2100 \text{ cm}^{-1}$).

This picture further is in agreement with the model proposed by Chang[4], which is based on *ab initio* pseudopotential calculations and that predicts a trigonal complex with a strong hydrogen-gallium bond along a $\langle 111 \rangle$ direction. The gallium-donor bond is weakened and the gallium atom relaxes by 0.78 \AA away from the donor to the hydrogen atom. However, no vibrational frequencies have been calculated. Similar calculations were performed by Rahbi *et al.*[3] confirming these results. The predicted frequencies are $\sim 845 \text{ cm}^{-1}$ ($\sim 600 \text{ cm}^{-1}$) for the X-H1 (X-D1) line and $\sim 1592 \text{ cm}^{-1}$ ($\sim 1131 \text{ cm}^{-1}$) for X-H2 (X-D2).

CONCLUSION

By application of high-resolution FTIR spectroscopy to hydrogen passivated chalcogen donors strong evidence for a microscopic model was found, where the hydrogen atom binds, in the antibonding position, to a gallium nearest neighbor of the donor species. This model explains the very weak frequency dependence on the donor mass and is in agreement with *ab initio* pseudopotential calculations[4, 3].

Furthermore, we have compared the depth of the infrared active region, the free carrier concentration profile, and the hydrogen penetration depth. The results suggest that the LVM absorption originates from the electrically passivated part of the sample and supports a microscopic picture for the donor passivation. In contrast, however, the total hydrogen content is much in excess of the donor concentration and its penetration depth is much deeper. Only a small part closer to the surface forms complexes with the donor species.

ACKNOWLEDGEMENTS

We wish to thank A.W.R. Leitch and J.R. Botha for the MOVPE samples and E. Bauser and S. Zehender for the growth of the LPE layers. We are grateful to H.J. Queisser for his continued interest and support, and acknowledge the technical assistance of H.-W. Krause and W. Heinz.

References

- [1] M. Stavola, Mater. Sci. Forum, 148-149, 251 (1994).
- [2] J. Vetterhöffer, J. H. Svensson, J. Weber, A. W. R. Leitch, and J. R. Botha, Phys. Rev. B 50, 2708 (1994).
- [3] R. Rahbi, B. Theys, R. Jones, B. Pajot, S. Öberg, K. Somogyi, M. L. Fille, and J. Chevallier, Solid State Commun. 91, 187 (1994).
- [4] K. J. Chang, Solid State Commun. 78, 273 (1991).
- [5] S. J. Pearton, J. W. Corbett, and M. Stavola, *Hydrogen in Crystalline Semiconductors* (Springer, Berlin, 1992).
- [6] K. P. Huber and G. Herzberg, *Molecular Spectra and Molecular Structure IV Constants of Diatomic Molecules* (Van Nostrand Reinhold Company, New York, 1979).

HYDROGEN PASSIVATION OF SHALLOW DOPANTS IN INDIUM DOPED BULK CdTe

Suma Gurumurthy, A.K. Sreedhar and H.L. Bhat

Department of Physics
Indian Institute of Science, Bangalore-560 012, India

and

B. Sundershesu, R.K. Bagai and Vikram Kumar

Solid State Physics Laboratory, Lucknow road, Delhi-110 054, India

ABSTRACT:

Hydrogen passivation effects in In doped n-CdTe upon exposure to rf hydrogen plasma have been studied by electrical and photoluminescence measurements. Shallow dopant passivation of approximately an order of magnitude at 150°C and 50% at 170°C is observed. No visual damage is seen. Reverse bias annealing effects are also studied. Results are discussed.

Introduction:

There has been increasing interest in hydrogen incorporation in semiconductors, as it causes profound modifications in the electrical and optical properties of these materials [1,2]. Most of the work reported so far has been mainly concerning the properties of hydrogen in silicon and gallium arsenide [3,4]. Relatively, few studies are reported in II-VI compounds. The first report of hydrogen incorporation was in polycrystalline CdTe films deposited by evaporation in H atmosphere and investigated by PL measurements [5] which showed that hydrogen contributed to reducing the incorrect bonds and improving the crystallinity. There have been reports of neutralization of acceptors in p-CdTe by implantation of hydrogen [6,7] and passivation of donors in n-CdTe by annealing under molecular H or D in sealed ampoules [8]. Svob et al [9] have demonstrated that hydrogen plasma could be used for etching cadmium telluride, thereby leaving a clean and nearly stoichiometric surface. On the other hand, substantial loss of cadmium has been reported when CdTe is exposed to atomic hydrogen [3]. Native oxide and thin tellurium layer removal from CdTe using H plasma has been reported by Nishibayashi et al [10]. Recently, incorporation of atomic hydrogen in CdZnTe has been studied by PL [11]. Here, we report new results on the passivation and reactivation of donors in indium doped n-CdTe upon exposure to rf hydrogen plasma, studied by I-V, C-V and PL measurements.

Experimental:

Single crystals of CdTe used in the present investigation were grown by the asymmetrical Bridgman technique [12]. Crystals were doped by Indium appropriately to obtain n type material of $3 \times 10^{17} \text{ cm}^{-3}$ donor concentration as well as high resistivity material. Samples were prepared from wafers cut parallel to (111) orientation and mechanically polished. They were degreased, chemically etched in 1% bromine in methanol for 5 mins followed by

rinsing in methanol for 1h to remove traces of bromine. After this, the samples were treated in 1N KOH in methanol for 5 mins to remove the tellurium film resulting in the bromine methanol etch [13]. Indium was deposited on the backside of the wafer and annealed at 160°C for 2 mins in a hydrogen atmosphere to form ohmic contacts. Gold Schottky dots of 0.6 mm diameter were deposited through a shadow metal mask at a pressure of 1×10^{-6} torr.

Hydrogenation was carried out by placing the samples in downstream plasma in a home-made plasma reactor operating at the frequency of 13.56 MHz. The plasma treatment was carried out at different temperatures for 1 h duration. The rf power density was fixed at $0.5\text{W}/\text{cm}^2$ and the pressure maintained at 0.5 torr.

Room temperature I-V and C-V measurements were carried out on all the samples. The active donor concentration profile was extracted out from the C-V measurements. Reverse bias annealing was carried out at different temperatures to study the thermal stability of dopant passivation. PL measurements on the control and hydrogenated samples were carried out at 4.2 K with a resolution of 0.5 meV using a MIDAC Fourier Transform PL system. Excitation source was the 5145 Å line of argon ion laser and the detector used was a liquid nitrogen cooled Ge-photodiode.

Results and Discussions:

The I-V curves for the control and hydrogenated diodes are shown in Fig. 1. Clearly, there is no significant difference between the two characteristics. This indicates that exposure to downstream hydrogen plasma in our system causes no surface damage. This is also verified by microscopic observations. This result is in contrast to earlier reports where significant surface degradation was observed after H plasma exposure [3]. Svob et al. [9] studied the temperature dependence of the etching rate and showed that exposure of CdTe to plasma at temperatures lower than 170°C would result in samples covered by a powdery layer. There is also no Schottky barrier modification due to hydrogen bombardment induced defects, unlike that reported for Si and GaAs [14]. These differences are perhaps due to the low energy and remote nature of hydrogen plasma employed in our experiments.

C-V depth profiles of the active donor concentration in the control and hydrogenated diodes are shown in Fig. 2 & 3. When sample is kept at 150°C, the passivation is over one order of magnitude but at 170°C the donor concentration is reduced only by factor of 2. The thermal stability of the dopant passivation was studied by carrying out reverse bias

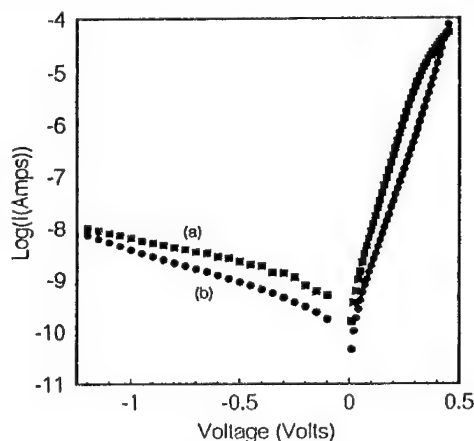


Fig.1. I-V Characteristics of (a) control and (b) hydrogenated Au/n-CdTe diodes.

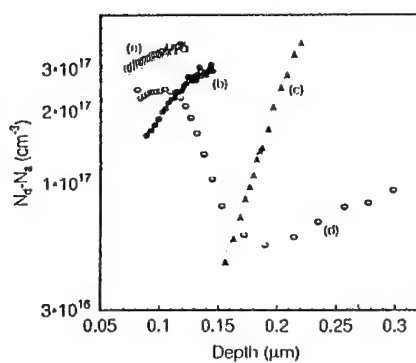


Fig.2. Net active donor concentration profiles for (a) control (b) hydrogenated at 170°C (c) hydrogenated at 150°C (d) RBA at 150°C for 10 mins, samples. (RBA carried out at 3V applied bias and on the sample hydrogenated at 150°C.)

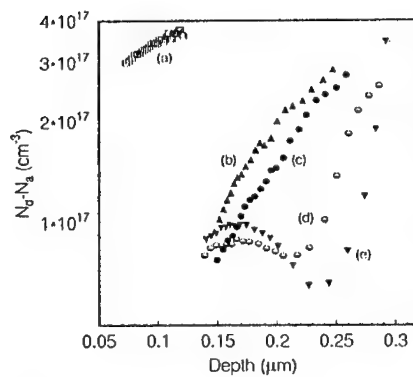


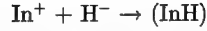
Fig.3. Net active donor concentration profiles for (a) control (b) hydrogenated at 150°C (c) RBA at 100°C for 30 mins (d) RBA at 125°C for 15 mins (e) RBA at 125°C for 45 mins, samples. (RBA carried out at 3V applied bias and on the sample hydrogenated at 150°C.)

annealing (RBA) [15] experiments at temperatures ranging from 100-150°C under a 3V applied bias. RBA at 100°C for 30 mins shows no reactivation, but further movement of hydrogen into the bulk as seen in Fig. 3 (curve c). At 125°C, 15 min treatment reveals interesting features. The active donor concentration is low near the surface but shows a plateau between 0.15 to 2μm and the edge of the passivation zone is further shifted into the bulk. When the treatment is for 45 mins at 125°C, the plateau is higher and shifted towards the surface. RBA treatment at 150°C, for 10 mins shows the plateau to shift to 0.1μm, with nearly complete reactivation of donors. This is shown in Fig. 2 curve (d). However, donors near the surface remain still passivated.

The donor profiles obtained here after RBA are different from those reported for silicon [16], GaAs [17,18] and InP [19]. The main difference is the low reactivation of donors in the surface region. During RBA following processes are likely to be taking place:

- (i) Release of atomic hydrogen, perhaps H^- from (InH) complexes.

$$(InH) \rightarrow In^+ + H^-$$
This may be accompanied by, $H^- \rightarrow H^0 + e^-$
- (ii) Drift of H^- towards the bulk under the influence of electric field.
- (iii) Retrapping of H^- by In donors to form passivated donors.



This is the dominant process during H plasma exposure and passivation.

- (iv) Diffusion of H^- into the bulk. This is likely to be dominant at the edge of the passivation zone.

RBA of the hydrogenated diodes results in the reactivation of the dopants near the surface and their passivation deeper inside the bulk. This is generally attributed to the thermal disassociation of the dopant hydrogen complexes (process (i)) and subsequent field directed drift of the charged hydrogen into the bulk (process (ii)). However, as the observed profiles are different from those reported for Si, GaAs and InP, it can be understood if we assume that there is considerable extra hydrogen available in the surface region. This is not unexpected since CdTe is likely to have more defects than group IV and III-V materials, which can share extra hydrogen. For the same reason hydrogen mobility will be smaller in CdTe. Hence, the supply of hydrogen from the surface region is slow and process (iii) seems to be dominant near the surface region. However, the hydrogen from the middle region seems to be escaping faster into the bulk thereby giving rise to the plateau. Passivation seen up to a greater depth can be explained by the diffusion and trapping of hydrogen by the donors in the bulk (process (iv)). Detailed modeling of the profile and reaction kinetics is being carried out.

The influence of hydrogen plasma passivation is seen in PL spectra of the control and hydrogenated high resistivity In:CdTe which is shown in Fig. 4. The PL intensity of the commonly found 1.42 eV band shown in Fig. 4a was found to increase after hydrogenation suggesting the passivation of non-radiative centers. Also, better resolution of the phonon replicas of the 1.42 eV band after hydrogenation indicates improvement in the crystallinity by passivation [5]. With regards to the 1.42eV defect peak there has been a lot of controversy, with different groups assigning different transitions to it [20]. Despite the prominence of 1.42eV bands and their long history of observation, the possible origin of this band still remains a matter of dispute and conjecture.

Evidence of the donor passivation can be seen from Fig. 4b wherein after hydrogenation the emission at 1.589 eV is found to have appeared. This peak is attributed to exciton bound to neutral V_{Cd}^0 [21]. The absence of this excitonic peak in the In-doped samples suggests that there are very few isolated V_{Cd}^0 's present in the In-doped material. In view of the accepted self-compensation models for II-VI compounds in which V_{Cd} plays a major role [22], it is more plausible that a considerable number of V_{Cd} 's are present but in the form of complexes with In atoms. The passivation of In donors by hydrogen, releases V_{Cd}^0 to trap excitons giving rise to 1.589 eV line. Additionally, we have seen that this peak disappears after cadmium annealing in uncompensated CdTe samples thereby confirming its relation to V_{Cd}^0 . The 1.586 eV also appears after hydrogenation. However, its origin is not well established. The PL spectra of low resistivity n-CdTe, used for electrical studies, also show similar behaviour for these two peaks after hydrogenation, though not pronounced. The peak at 1.544 eV in Fig. 4b (spectrum a) is attributed to a C-A like transition, with the acceptor being a singly ionized cadmium vacancy [23]. The hump seen at 1.523 eV is the LO phonon replica of 1.544 eV. However, a hump on the higher energy side of 1.544 eV which corresponds to a peak at 1.548 eV, remains after hydrogenation. This peak at

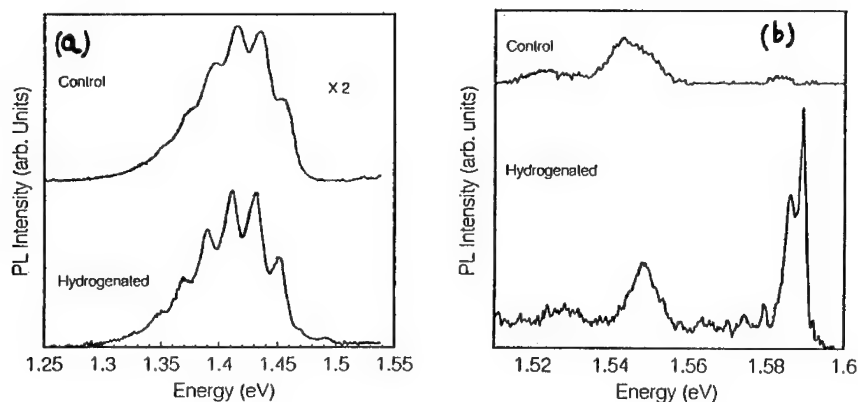


Fig.4. PL spectra at 4.2K of high resistivity CdTe:In (a) 1.42eV band and (b) edge emissions.

1.548 eV is also a C-A like transition from residual impurities [24]. The presence of this peak even after hydrogenation tells that it is the donors in the material that are passivated. The absence of any deep level peak at 1.1 eV which is generally attributed to doubly ionized cadmium vacancies [20] in control as well as hydrogenated samples points to the fact that there has been no loss of cadmium from the surface or the bulk of the sample during plasma treatment.

In conclusion, we have seen that atomic hydrogen incorporated by exposure to rf hydrogen plasma in n-CdTe at 150°C does not create any surface damage and has strongly reduced the indium donor activity. This effect must be considered if hydrogen plasma is to be used for etching of CdTe or for the removal of its native oxide. The reactivation kinetics of donors under RBA seems to be different from other well studied semiconductors. Manifestation of the donor passivation is seen in PL by the appearance of the acceptor bound excitonic peak.

Acknowledgement:

This work has been carried out under a joint project funded by Solid State Physics Laboratory, Delhi.

REFERENCES:

1. W.L. Hansen, E.E. Haller and P.W. Luke, IEEE Trans. Nucl. Sci. NS-29, 738 (1982).
2. J.W. Corbett, S.N. Sahu, T.S. Shi and L.C. Synder, Phys. Lett. A **93**, 303 (1983).

3. S.J. Pearton, J.W. Corbett and M. Stavola, Hydrogen in Crystalline semiconductors (Springer-Verlag, Berlin, 1992).
4. J.I. Pankove and N.M. Johnson, Hydrogen in Semiconductors, Semiconductors and semimetals, Vol 34 edited by, J.I. Pankove and N.M. Johnson (Academic Press, New York 1991).
5. T. Takamoto, H. Masamoto, S. Hongo and H. Bō, Jpn. J. Appl. Phys. 20 (9), 1757 (1981).
6. L. Svob and Y. Marfaing, Solid State Commun. 58(6), 343 (1986).
7. B. Biglari, M. Samimi, M. Hage-Ali and P. Siffert, Appl. Phys. A 43, 47 (1987).
8. L. Svob, A. Heurtel and Y. Marfaing, J. Cryst. Growth 101, 439 (1990).
9. L. Svob, J. Chevallier, P. Ossart and A. Mircea, J. Mater. Sci. lett. 5, 1319 (1986).
10. Y. Nishibayashi, Y. Tokumitsu, T. Imura and Y. Osaka, Jpn. J. Appl. Phys. 28 (10), 1919 (1989).
11. Y.F. Chen, C.S. Tsai, Y.H. Chang, Y.M. Chang, T.K. Chen and Y.M. Pang, Appl. Phys. Lett. 58 (5), 493 (1991).
12. R.K. Bagai and W.N. Borle, J. Cryst. Growth 94, 561 (1989).
13. P.M. Amirtharaj and F.H. Pollak, Appl. Phys. Lett. 45, 789 (1984).
14. Y.G. Wang and S. Ashok, Physics B 170, 513 (1991).
15. T. Zundel and J. Weber, Phys. Rev. B 39, 13549 (1989).
16. J. Zhu, N.M. Johnson and C. Herring, Phys. Rev. B 41(17), 12354 (1990).
17. G. Roos, N.M. Johnson, C. Herring and J.S. Harris, Appl. Phys. Lett. 59, 461 (1991).
18. S.J. Pearton, C.R. Abernathy and J. Lopata, Appl. Phys. Lett. 59, 3571 (1991).
19. S.J. Pearton, W.S. Hobson and C.R. Abernathy, Appl. Phys. lett. 61, 1588 (1992).
20. S. Gurumurthy, K.S.R.K. Rao, A.K. Sreedhar, H.L. Bhat, B. Sundershesu, R.K. Bagai and V. Kumar, Bull. Mater. Sci. 17 (6), 1057 (1994).
21. P.M. Amirtharaj and N.K. Dhar, J. Appl. Phys. 67 (6), 3107 (1990).
22. C. Canali, G. Ottaviani, R.O. Bell and F.V. wald, J. Phys. Chem. Solids 35, 1405 (1974).
23. C.E. Barnes and K. Zanio, J. Appl. Phys. 46(9), 3959 (1975).
24. N.S. Giles, K.A. Bowers, R.L. Harper, Jr., S. Hwang and J.F. Schetzina, J. Cryst. Growth 101, 67 (1990).

PLASMA-INDUCED ELECTRON TRAPS IN n-InP

YOSHIFUMI SAKAMOTO*, TAKASHI SUGINO*, KOICHIRO MATSUDA**
AND JUNJI SHIRAFUJI*

*Department of Electrical Engineering, Faculty of Engineering, Osaka University,
2-1 Yamadaoka, Suita, Osaka 565, Japan

**Horiba, Ltd., Miyanohigashi, Kisshoin, Minami-ku, Kyoto 601, Japan

ABSTRACT

Deep electron traps in n-InP introduced during plasma exposure have been studied by means of isothermal capacitance transient spectroscopy (ICTS). Three electron traps, ($E_c-0.21$ eV), ($E_c-0.34$ eV) and ($E_c-0.54$ eV), which are designated E2, E3 and E4, respectively, are detected in n-InP treated with H₂ plasma and by subsequent annealing. The E2 trap is induced by plasma exposure and the E3 trap is produced by thermal annealing. The E4 trap is generated by both plasma exposure and thermal annealing. These three traps are passivated with hydrogen atoms. The E2 trap density near the surface of hydrogen-plasma-treated samples is strongly enhanced by applying electric field because of dissociation of hydrogen from E2 trap. The E2 trap is annealed out with the activation energy of 1.5 eV and the attempt-to-escape frequency of $3.2 \times 10^{14} \text{ s}^{-1}$. Phosphine plasma treatment is effective in suppressing generation of these electron traps.

INTRODUCTION

In recent years, dry etching processes based on chemical reaction in a plasma have been introduced in the fabrication of compound semiconductor devices. A gas mixture of CH₄ and H₂ is often used for reactive ion etching of InP and related materials.[1] A significant drawback of plasma process is unavoidable defect generation at and/or near the surface of substrate by impinging energetic particles, leading to deteriorated performances of devices. Hydrogenation is effective in passivating the surface defects[2]. Defect passivation by hydrogen gives an influence on the Schottky barrier height of GaAs and InP contacts[3]. The thermal stability of hydrogen passivation of deep levels is of much interest from the point of surface control.

Our group has reported in a previous paper that five electron traps are detected in n-InP which suffers H₂ plasma treatment and subsequent annealing in a parallel-plate plasma reactor.[4] The five traps were designated E1, E2, E3, E4 and E5, the energy levels of which are 0.21, 0.51, 0.32, 0.54 and 0.63 eV, respectively, below the conduction band edge. The E1 trap is detected even in the untreated n-InP, while the E2 trap is generated by H₂-plasma treatment. Although the E3 and E4 traps are not detected in the H₂-plasma treated n-InP, these traps appear after annealing at 350 °C for 3 min and disappear again by H₂-plasma treatment after the annealing process. This experimental fact demonstrates that E3 and E4 traps are passivated by hydrogen atoms. The E5 trap was found during the annealing in the limited temperature range from 150 to 300 °C. There is a report on the characterizations of the E2 trap, the origin of which was supposed to be related to hydrogen[4]. However, it is not clear whether the plasma damage may give an influence on generation of the E2 trap. Therefore, it is meaningful to examine InP treated with He plasma, the mass of

helium being close to that of hydrogen atom. Moreover, generation of the E3 and E4 traps due to plasma damage can be confirmed eliminating hydrogen passivation by investigating He-plasma treated InP.

In this paper, it is described that E2 and E4 traps are introduced in n-InP by He-plasma treatment, while the E3 trap is produced by annealing. Also described are occurrence of hydrogen passivation of the E2 trap and reactivation under the applied electric field. Thermal annealing process of the E2 trap is also studied. It is demonstrated the reduction of E3 and E4 trap densities by PH₃-plasma treatment for the sample which E3 and E4 traps were generated intentionally.

EXPERIMENTAL

The samples used in the present experiment were n-type bulk InP grown by liquid encapsulated Czochralski (LEC) method. The (100) InP substrates had the electron concentration of $5\text{--}6 \times 10^{15} \text{ cm}^{-3}$. Ohmic contacts were prepared on the back side of the InP substrate by evaporating AuGeNi followed by alloying at 370 °C for 3 min. After the substrate was cleaned with acetone and deionized water, the surface was chemically etched with a solution consisting of H₂SO₄, H₂O₂ and H₂O (5:1:1) at 50 °C for 3 min.

After InP samples were placed on a grounded pedestal, which was located 18 cm away from the plasma region, the chamber was evacuated down to 3×10^{-6} Torr. Pure H₂ or He gas was introduced at the flow rate of 15 sccm. The gas pressure was regulated at 0.2 Torr. The substrate temperature was maintained constant at 95 °C. Plasma treatment was carried out in a remote plasma chamber in the present experiment[5]. Glow discharge was obtained by supplying RF power (13.56 MHz) of 35 W. Treatment time was fixed at 20 min. He-plasma treatment was carried out in order to examine whether E2 trap is inherent in H₂-plasma treatment or introduced simply by plasma damage. Immediately after the plasma treatment was finished, Schottky junctions were formed on the plasma-treated surface by in-situ evaporating Au.

ICTS measurement was carried out on the Schottky junctions to investigate deep electron traps induced at and/or near the surface of the plasma-treated InP by using an automated equipment (Horiba DA-1500). The diffusion potential of the Schottky junction necessary for setting the flat band condition was estimated from the true Schottky barrier height, which was obtained from the Richardson plot of the temperature dependence of the saturation current density, and the Fermi level position determined from the equilibrium electron concentration.

RESULTS AND DISCUSSION

Prior to investigation of the plasma treated InP, ICTS measurement was carried out for the sample annealed at 350 °C for 3 min in dry N₂ gas without plasma treatment. This is because it is necessary to understand the influence of annealing on trap generation in order to carry out the isochronal annealing experiment. Figure 1 shows the ICTS spectra for the annealing sample. E3 and E4 traps are detected at measurement temperatures of 200 and 300 K, respectively. The measurement region was from the surface to 0.1 μm in depth. The densities of the E3 and E4 traps were estimated to be $9.9 \times 10^{13} \text{ cm}^{-3}$ and $4.2 \times 10^{13} \text{ cm}^{-3}$, respectively. The E2 trap generated by H₂-plasma treatment was not detected for the

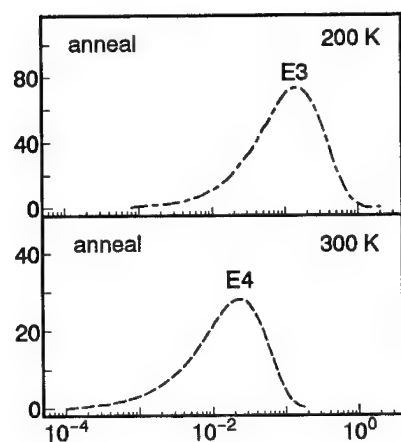


Fig. 1 ICTS spectra at 200 and 300 K for annealed InP, respectively.

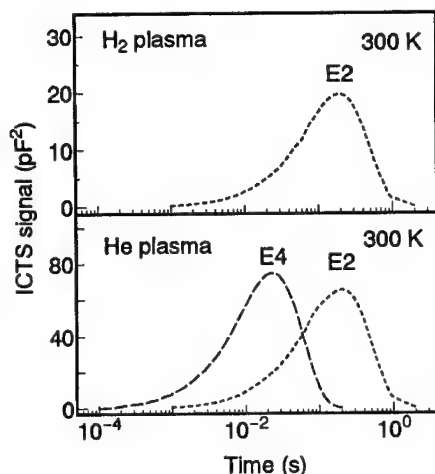


Fig. 2 ICTS spectra at 300 K for H₂- and He-plasma treated InP.

annealed sample.

Figure 2 shows the ICTS spectra of the samples treated with H₂ and He plasmas. The ICTS measurement was carried out at 300 K. In the sample treated with H₂ plasma, only E2 trap with a time constant τ of 2.0×10^{-1} s is detected. In the case of the He-plasma treatment, on the other hand, two peaks of ICTS signals are observed at the time constants of 2.0×10^{-1} s and 2.4×10^{-2} s, corresponding to E2 and E4 traps, respectively. However, E3 trap was not detected at the temperature of 200 K in both samples treated with H₂ plasma and He plasma. It is demonstrated in the present experiment that E2 trap is induced by both H₂ and He plasmas. Although E2 trap was tentatively related to hydrogen diffused into InP in a previous report[4], the present result suggests that E2 trap is attributed to plasma-induced defect. The E4 trap was generated by both annealing and He-plasma treatment, while the E3 trap was produced only by annealing. The activation energy and capture cross section of these electron traps detected here are summarized in Table I. It makes clear in the present experiment that the E2 and E4 traps are induced by the plasma treatment.

Table I: Summary of activation energy E_a , capture cross section σ_c , emission time constant τ and measuring temperature T for three traps of E2, E3 and E4.

State	E_a (eV)	σ_c (cm ²)	τ (s)	T (K)
E2	0.51	3.9×10^{-18}	2.0×10^{-1}	300
E3	0.32	1.2×10^{-18}	1.6×10^{-1}	200
E4	0.54	8.8×10^{-18}	2.4×10^{-2}	300

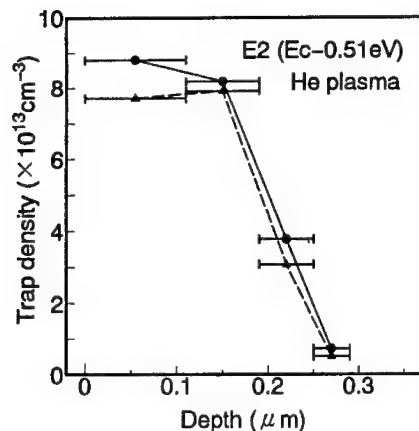


Fig. 3 In-depth profiles of the E2 trap density for He-plasma-treated sample before and after reverse bias stress. Solid circles and solid triangles indicate as-treated and reverse-bias-stressed samples, respectively.

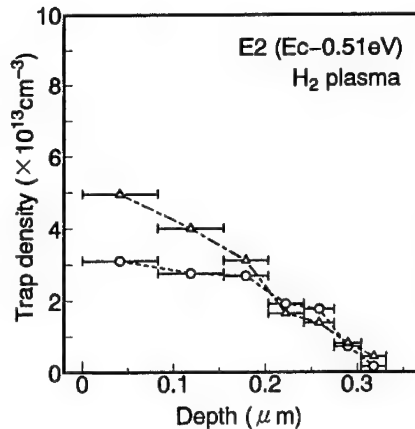


Fig. 4 In-depth profiles of the E2 trap density for H₂-plasma-treated sample before and after reverse bias stress. Open circles and open triangles indicate as-treated and reverse-bias-stressed samples, respectively.

The effect of reverse bias stress on the E2 trap density for a sample treated with He plasma is investigated where Schottky junctions suffered reverse bias stress (-1 V on Schottky metal electrode) for 60 min at room temperature. No marked variation in the in-depth profile is observed after the reverse bias stress as shown in Fig. 3. In clear contrast to this, the E2 trap density in H₂-plasma-treated sample was remarkably enhanced over the range $0.2 \mu\text{m}$ deep from the surface by applying reverse bias stress as shown in Fig. 4. The density averaged over the range from the surface to the depth of $0.08 \mu\text{m}$ increases up to $5.0 \times 10^{13} \text{ cm}^{-3}$. The E2 trap in the H₂-plasma-treated sample has the same activation energy and the capture cross section as those of the E2 trap generated by He plasma treatment. It was also confirmed that the E2 trap generated by He plasma treatment was partly passivated by H₂ plasma treatment. Therefore, there exist possibly the E2 trap and the hydrogen-passivated E2 trap in the H₂-plasma-treated sample. Increase of the E2 trap density in H₂-plasma-treated sample by reverse bias stress is suggested to be not due to generation of the E2 trap but due to reactivation of hydrogen-passivated E2 traps by dissociation of hydrogen.

The isochronal annealing experiment of E2 trap was carried out using He-plasma-treated samples. The samples were annealed in dry N₂ ambient for a constant time of 3 min. The annealing temperature was varied from 87 to 187°C . The bias condition was chosen to permit detection of relevant traps located in the region from the surface to $0.28 \mu\text{m}$ deep. The E2 trap density was not changed up to the annealing temperature of 127°C , being nearly equal to the initial value of $8.8 \times 10^{13} \text{ cm}^{-3}$ before annealing. The trap density began to decrease at annealing temperatures above 127°C . The trap density became undetectably low at annealing temperature above 187°C in the present isochronal annealing condition. In Fig. 5 the trap density N normalized to the initial value N_0 before annealing is plotted as

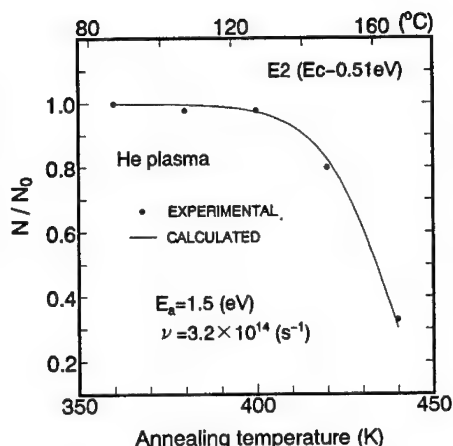


Fig. 5 Fraction of not-annealed E2 trap density as a function of annealing temperature.

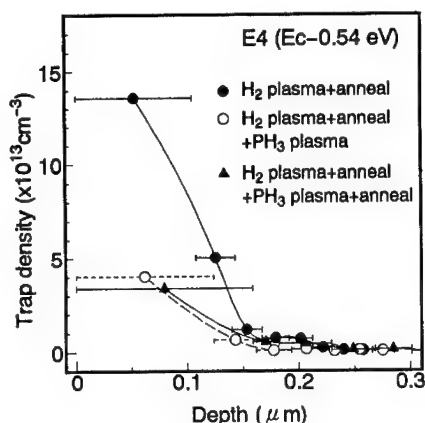


Fig. 6 In-depth profiles of E4 trap for InP treated by various processes.

a function of the absolute temperature T during annealing. The variation in the normalized trap density after each annealing is modelled by assuming first-order kinetics of the annealing process[6].

$$\frac{N}{N_0} = \exp \left\{ -t\nu \exp \left(-\frac{E_a}{kT} \right) \right\} \quad (1)$$

Therein t is annealing time. The values of attempt-to-escape frequency ν and activation energy E_a were adjusted to fit the calculated curve to the experimental points. The activation energy for annealing process of E2 trap and the attempt-to-escape frequency were finally determined to be 1.5 eV and $3.2 \times 10^{14} \text{ s}^{-1}$, respectively. These values are close to the values obtained in samples which were treated with H_2 plasma, followed by reverse bias stress[7].

The annealing out of E2 trap at a rather low temperature of 187 °C may imply that E2 trap is possibly due to simple point defects like Frenkel pairs and isolated vacancies. It has widely been reported that the irradiation with high-energy electrons and X-ray photons introduces simple lattice defects[8, 9] which can anneal rather easily with an activation energy, for example, of about 1 eV in n-InP[10].

It is well known that H_2 -plasma treatment causes preferential etching of phosphorus at the InP surface[11]. Therefore, PH_3 -plasma treatment was carried out in parallel-plate plasma reactor in order to make sure whether E4 trap may be related to phosphorus vacancies. Figure 6 shows the in-depth profiles of the E4 trap densities after various processes. E4 trap appears in the sample annealed at 350 °C for 3 min after H_2 -plasma treatment. However, the subsequent PH_3 -plasma treatment at 250 °C for 60 min leads to the marked reduction of E4 trap density in the depth region from the surface to 0.17 μm . This experimental result implies that E3 and E4 traps are associated with phosphorus vacancies or their complexes in InP. A behavior of the E3 trap was also observed similar to that of the E4 trap.

SUMMARY

The plasma-induced traps in n-InP have been investigated by ICTS measurement. It is demonstrated by He-plasma treatment that E2 trap ($E_c-0.51$ eV) and E4 trap ($E_c-0.54$ eV) are attributed to plasma-induced defects. H_2 -plasma treatment leads to the generation of E2 trap and simultaneous passivation of some fraction of the generated E2 trap. The reverse bias stress on Schottky junction can reactivate E2 trap passivated by hydrogen resulting in a remarkable increase in the E2 trap density in the surface region. The isochronal annealing experiment on the He-plasma-treated sample shows that the E2 trap is annealed out at a temperature as low as 187 °C. Assuming the first-order kinetics, the activation energy and the attempt-to-escape frequency of the annealing process are estimated to be 1.5 eV and $3.2 \times 10^{14} \text{ s}^{-1}$, respectively. E3 and E4 traps are perfectly passivated with hydrogen. It is observed that densities of these two traps are reduced in the case of PH_3 -plasma treatment indicating that these traps are related to phosphorus vacancies.

ACKNOWLEDGEMENT

The authors are much indebted to Dr. T. Shirakawa of Sumitomo Electric Industries Inc. for supplying InP wafers.

REFERENCES

1. U. Niggebrugge, M. Klug and G. Garus: *Inst. Phys. Conf. Ser.* **79** 367 (1985).
2. A. Frova and M. Capizzi: *Thin Solid Films* **193** 211 (1990).
3. R. L. Van Meirhaeghe, W. H. Laflere and F. Cardon: *J. Appl. Phys.* **76** 403 (1994).
4. T. Sugino, H. Ninomiya, T. Yamada, K. Matsuda and J. Shirafuji: *Appl. Phys. Lett.* **60** 1226 (1992).
5. Y. Sakamoto, T. Sugino, H. Ninomiya, K. Matsuda and J. Shirafuji: *Jpn. J. Appl. Phys.* **34** 1417 (1995).
6. W. L. Hansen, E. E. Haller and P. N. Luke: *IEEE Trans. Nucl. Sci.* **NS-29** 738 (1982).
7. T. Sugino, H. Ninomiya, K. Matsuda and J. Shirafuji: *Jpn. J. Appl. Phys.* **33** L267 (1994).
8. D. V. Lang: *Proc. Int. Conf. Radiation Effects in Semiconductors*, (Dubrovnik, 1967): *Inst. Phys. Conf. Ser.* **31** 70 (1977).
9. D. Pons and J. C. Bourgoin: *J. Phys. C: Solid State Phys.* **18** 3839 (1985).
10. J. Koyama, J. Shirafuji and Y. Inuishi: *Electron. Lett.* **19** 609 (1983).
11. C. W. Tu, R. P. H. Chang and A. R. Schlijer: *Appl. Phys. Lett.* **41** 80 (1982).

HYDROGEN DIFFUSION IN n-GaAs:Si UNDER HYDROSTATIC PRESSURE

B.MACHAYEKHI*, J.CHEVALLIER*, B.THEYS*, J.M.BESSON**, G.WEILL** AND G.SYFOSSE***

*Laboratoire de Physique des Solides de Bellevue, CNRS, 1 place Aristide Briand, 92195 Meudon Cedex (France)

** Physique des Milieux Condensés, URA 782, Université Pierre et Marie Curie, 4 place Jussieu, 75005 Paris (France)

*** Département des Hautes Pressions, Université Pierre et Marie Curie, 4 place Jussieu, 75005 PARIS (France)

ABSTRACT

It has recently been shown that deuterium diffusion experiments can provide information on the deepening of the hydrogen acceptor level in the band gap of $\text{Al}_x\text{Ga}_{1-x}\text{As}$ alloys with increasing x . In the present work, we report on the influence of hydrostatic pressure on deuterium diffusion in n-GaAs:Si. SIMS analysis reveals that the deuterium profiles in n-GaAs:Si are sensitive to hydrostatic pressure: the diffusion depth decreases and a plateau appears in the diffusion profile as the pressure is applied. The results are interpreted in terms of an increasing amount of the H^- species as pressure is applied. This increase is mainly attributed to a deepening of the H acceptor level with respect to the bottom of the Γ conduction band of GaAs. Qualitatively, this effect is similar to the deepening of the H acceptor level in $\text{Al}_x\text{Ga}_{1-x}\text{As}$ alloys as x increases.

INTRODUCTION

It is well established that hydrogen diffusion in n-GaAs and n-AlGaAs results in a neutralization of shallow donors and DX centers [1-3]. This neutralization effect arises from the formation of Si-H complexes which have been detected by vibrational spectroscopy [4,5]. It is also accepted now that hydrogen behaves as a deep acceptor in n-GaAs and n- $\text{Al}_x\text{Ga}_{1-x}\text{As}$ alloys and that the formation of the complex is due to a coulombic attraction between H^- and the Si^+ ionized donors [6].

Recently, hydrogen diffusion has been studied in n-GaAs:Si and n- $\text{Al}_x\text{Ga}_{1-x}\text{As}$:Si ($0 < x < 0.30$) as a function of temperature, silicon doping level and alloy composition. The hydrogen diffusion profile is strongly sensitive to these parameters which all vary the relative position of the Fermi level with respect of the hydrogen acceptor level and consequently the relative concentrations of H^- and H^0 [7]. From a modeling of these experimental data, we have been able to conclude that the hydrogen acceptor level deepens below the Γ conduction band as the alloy composition x increases. Extrapolation to GaAs indicates that the hydrogen acceptor level is located 0.10 ± 0.05 eV below the Γ conduction band of GaAs [8].

In this work, we report on the influence of hydrostatic pressure on the hydrogen diffusion in n-GaAs:Si since pressure is able to increase the band gap energy of GaAs in a manner somewhat similar to alloying.

EXPERIMENTS

It is clear that hydrogen diffusion experiments in n-GaAs:Si under hydrostatic pressure are very difficult to perform during hydrogen plasma exposure. For this reason, we applied a different procedure.

Buried silicon doped GaAs layers were grown by molecular beam epitaxy on semi-insulating GaAs substrates. The samples consisted of: 5000 Å of non intentionally doped (nid) GaAs buffer, 2 µm of silicon doped GaAs and 1 µm of nid GaAs. We used two different doping levels for the buried silicon doped GaAs layer: $5 \times 10^{18} \text{cm}^{-3}$ and $1.5 \times 10^{18} \text{cm}^{-3}$.

In a first step, deuterium was loaded in the nid GaAs top layer by exposing the samples to a r.f. deuterium plasma under the following conditions: r.f. power density = 0.12 W.cm^{-2} , $T = 150^\circ\text{C}$ and $t = 40 \text{ min.}$. SIMS experiments indicate that, under these conditions, deuterium diffusion is limited to the nid GaAs layer which will act as a hydrogen reservoir.

In a second step, samples were thermally annealed under argon pressure in the range of 1 to 700 MPa. Under these conditions, part of the hydrogen which is present in the reservoir diffuses into the buried silicon doped GaAs layer. These experiments were performed under three sets of annealing conditions:

- buried layers with $[\text{Si}] = 5 \times 10^{18} \text{cm}^{-3}$ were annealed at 200°C during 60 minutes under 1, 300, 500 and 700 MPa,
- buried layers with $[\text{Si}] = 1.5 \times 10^{18} \text{cm}^{-3}$ were annealed at 160°C during 3 hours under 1, 500 and 700 MPa,
- another series of buried layers with $[\text{Si}] = 1.5 \times 10^{18} \text{cm}^{-3}$ were annealed at 145°C during 8 hours under the same hydrostatic pressure conditions.

Secondary ion mass spectrometry (Cameca IMS 4f) was used to measure the deuterium profiles in the samples after each step. By comparison with deuterium implanted standards the absolute deuterium concentration was derived.

EVOLUTION OF THE HYDROGEN PROFILE WITH ANNEALING TIME.

Figure 1 shows the deuterium diffusion profile after exposure to the deuterium plasma (0.12 W.cm^{-2} , 150°C , 40 min.), to create the hydrogen reservoir in the nid GaAs layer. The profile is correctly fitted with a complementary error function indicative of the diffusion of a free hydrogen species which is taken to be H^0 [9]. The solubility of deuterium near the surface is close to 10^{20}cm^{-3} and progressively decreases to $3 \times 10^{17} \text{cm}^{-3}$ near the nid/silicon doped GaAs interface.

In this figure, we also report the evolution of the deuterium profile with time at 150°C in the samples with $[\text{Si}] = 1.5 \times 10^{18} \text{cm}^{-3}$ under thermal annealing in an argon atmosphere. During annealing, the deuterium partly diffuses towards the silicon doped buried layer and partly effuses out of the sample. After one hour annealing time, the deuterium concentration in the buried layer is still negligible. However, after about 1h30min., a deuterium diffusion regime is established in the buried layer with a constant hydrogen concentration C_S at the nid/silicon doped GaAs interface. This also holds true for 17h30 min. annealing time. The profiles are correctly fitted by a set of erfc functions with an effective diffusion coefficient $\approx 7 \times 10^{-14} \text{cm}^2/\text{s}$ at 150°C

provided we take into account a time delay t_0 of 1h30min, which is necessary to establish the diffusion regime with $C_S = \text{constant}$.

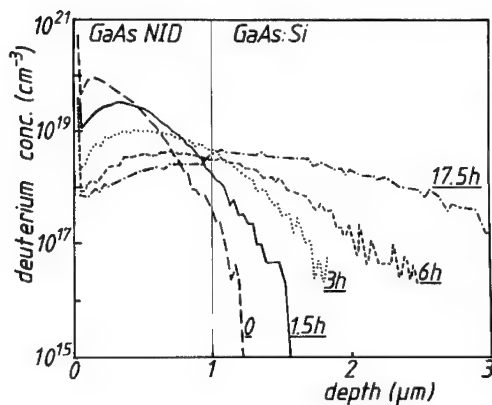


Figure 1: Deuterium diffusion profiles in a n-doped GaAs/silicon doped GaAs structure after plasma exposure at 150°C, 60 min., 0.12 W.cm⁻² and plasma exposure followed by annealing at 150°C for different durations.

The effective diffusion coefficient has also been deduced from the time dependence of the total amount $M(t)$ of deuterium diffusing into the silicon doped buried layer. Since the deuterium diffusion profile follows an erfc function dependence, the total amount $M(t)$ of deuterium can be expressed by the well known expression: $M^2(t) = 4C_S^2 D(t - t_0)/\pi$, where C_S represents the deuterium concentration at the n-doped/silicon doped interface, and D is the effective diffusion coefficient. The experimentally deduced value of D was again: 7×10^{-14} cm²/s.

Finally, we have found that this value is in very good agreement with the diffusion coefficient deduced from the deuterium diffusion profile in a n-GaAs:Si sample doped at the same level of 1.5×10^{18} cm⁻³ and directly exposed to the r.f. plasma at the same temperature.

We have checked the existence of the neutralization effect of silicon donors under hydrogen diffusion in the buried silicon doped layer after annealing. Electrical measurements have been performed on a thinner silicon doped buried layer ($e = 0.2 \mu\text{m}$, $n = 3 \times 10^{18}$ cm⁻³, $\mu_n = 1627$ cm²/V.s.), in order to establish a uniform hydrogenation in the buried layer after annealing. The thickness of the undoped cap layer was $0.5 \mu\text{m}$. The deuterium reservoir was formed by exposing the as-grown sample to the r.f. deuterium plasma (r.f. power = 0.12 W.cm⁻², $T = 150^\circ\text{C}$ and $t = 10$ min.). No change is observed in the electron concentration and the electron mobility of the buried silicon doped layer. The plasma exposure step was then followed by thermal annealing at 200°C for 60 min.. The deuterium concentration in the buried layer matches the silicon dopant concentration. The corresponding decrease of the free carrier concentration (2×10^{18} cm⁻³) and the increase of mobility (1975 cm²/V.s.) prove the existence of the neutralization effect of silicon donors.

HYDROGEN DIFFUSION IN n-GaAs:Si UNDER HYDROSTATIC PRESSURE.

Figures 2 and 3 show the deuterium profile of the reservoir after exposure to the plasma and the depth profiles of deuterium under annealing, while hydrostatic pressure is applied, for two structures with a buried GaAs:Si layer doped at a level of $5 \times 10^{18} \text{ cm}^{-3}$ and $1.5 \times 10^{18} \text{ cm}^{-3}$ respectively. As previously observed, we note an increase of the solubility of deuterium at the n/doped GaAs interface which is equal to the dopant concentration as a result of the H-dopant interactions [10]. In the more highly doped buried layer, one observes a modification of the deuterium diffusion profile, as the hydrostatic pressure is increased. We note that the erfc function is progressively replaced by a diffusion profile characterized by a plateau followed by a rapid decrease of the deuterium concentration. In both samples, the diffusion depth decreases as hydrostatic pressure is increased.

Figure 2: Deuterium diffusion profiles in a n/doped GaAs/silicon doped GaAs structure ($n = 5 \times 10^{18} \text{ cm}^{-3}$) after plasma exposure at 150°C , 40 min., 0.12 W.cm^{-2} and after plasma followed by annealing at 200°C , 1 hour under different hydrostatic pressures.

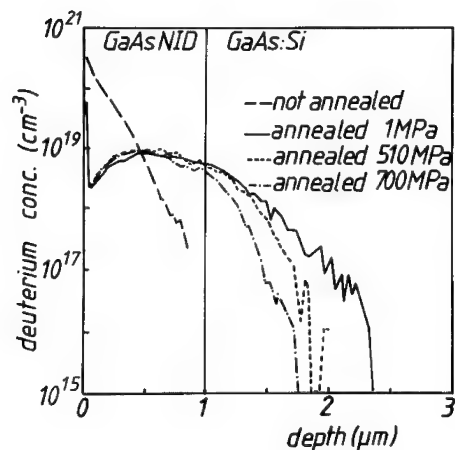
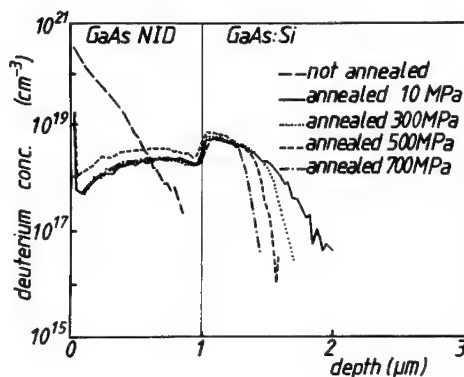


Figure 3: Same as figure 2 for a structure with a silicon doping level of $1.5 \times 10^{18} \text{ cm}^{-3}$. Annealing under hydrostatic pressure is performed at 160°C for 3 hours.

DISCUSSION

Since hydrogen introduces a deep acceptor level E_A in the band gap of n-GaAs:Si and n-AlGaAs:Si, we expect that the free hydrogen diffusing species are H^0 and H^- [8]. For this reason, a possible explanation of the modification of the deuterium profiles in the silicon doped buried layer, as the pressure is applied, would be that the diffusion coefficient of the various hydrogen diffusing species is pressure dependent. To check whether this assumption holds true for H^0 , we have studied the deuterium redistribution in semi-insulating GaAs bulk material as pressure is applied. We first exposed two semi-insulating GaAs samples to the deuterium plasma at 150°C during 40 min.. The plasma power was 0.12 W.cm⁻². Then, one of them was annealed under 1MPa argon atmosphere at 200°C for 60 min. and the other was annealed under 550 MPa argon pressure under the same time-temperature conditions. Figure 4 shows the deuterium diffusion profiles in semi-insulating bulk GaAs after exposure to plasma and also after plasma followed by annealing with and without the pressure applied. By estimating the diffusion coefficient of H^0 in samples where deuterium has been redistributed under thermal annealing with and without the hydrostatic pressure, we find a ratio $D_{H^0}(550\text{MPa})/D_{H^0}(1\text{MPa}) \approx 0.8$. Assuming that the diffusion coefficient of H^- is affected in a similar way by pressure, we conclude that the variations of the hydrogen diffusion coefficient with pressure are insufficient to explain the modification of the deuterium profiles in the silicon doped buried layer.

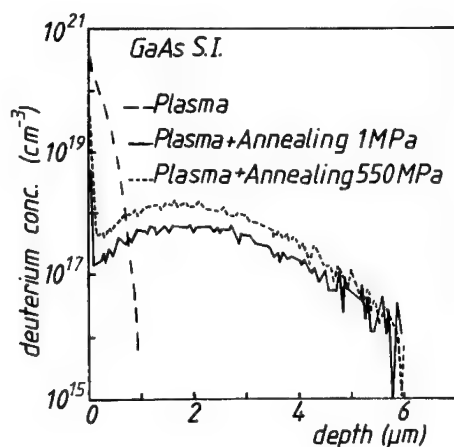


Figure 4: Deuterium diffusion profiles in bulk semi-insulating GaAs after plasma exposure at 150°C, 40 min., 0.12 W.cm⁻² and after plasma followed by annealing at 200°C, 1 hour under two different hydrostatic pressures of 1 and 550 MPa.

The hydrogen diffusion profile is also strongly sensitive to the position of the hydrogen acceptor level E_A with respect to the Fermi level E_F in GaAs because a modification of the energy difference $E_F - E_A$ implies a relative change in the concentrations of H^- and H^0 . The modifications of the hydrogen diffusion profile as hydrostatic pressure is increased strongly suggest an increase of H^-/H^0 with pressure and correspondingly an increase of $E_F - E_A$, assuming that E_F follows E_{Γ^-} . We also note a strong similarity between the above pressure dependence of the hydrogen diffusion profile in GaAs and the alloy composition dependence of these profiles in $Al_xGa_{1-x}As$ ($0 < x < 0.30$) published previously [7,8]. In both cases, we assign the modifications of the hydrogen diffusion profile to a deepening of the hydrogen acceptor level with respect to the bottom of the Γ^- conduction band of the material.

CONCLUSION

Hydrogen diffusion has been studied in n-type GaAs:Si under hydrostatic pressure. The modifications of the diffusion profiles with pressure have been interpreted as the result of a deepening of the hydrogen acceptor level with respect to the conduction band minimum. This result is qualitatively similar to the deepening of the hydrogen acceptor level in $Al_xGa_{1-x}As$ alloys as x increases.

ACKNOWLEDGEMENTS

The authors express their gratitude to E.CONSTANT from IEMN Villeneuve d'Ascq for providing samples and also to M.MILOCHE from LPM, Meudon for SIMS experiments.

REFERENCES

1. J.Chevallier, W.C.Dautremont-Smith, C.W.Tu and S.J.Pearson, Appl. Phys. Lett. **47**, 108 (1985)
2. J.C.Nabity, M.Stavola, J.Lopata, W.C.Dautremont-Smith, C.W.Tu and S.J.Pearson, Appl. Phys. Lett. **50**, 921 (1987)
3. R.Mostefaoui, J.Chevallier, A.Jalil, J.C.Pesant, C.W.Tu and R.F.Kopf, J. Appl. Phys. **64**, 207 (1988)
4. B.Pajot, R.C.Newman, R.Murray, A.Jalil, J.Chevallier and R.Azoulay, Phys. Rev. B **37**, 4188 (1988)
5. B.Pajot, Inst. Phys. Conf. Ser. **95**, 437 (1989)
6. G.Roos, N.M. Johnson, C.Herring and J.S.Harris Jr, Mater. Sci. Forum **83-87**, 605 (1992)
7. J.Chevallier, B.Machayekhi, C.M.Grattepain, R.Rahbi and B.Theys, Phys. Rev. B **45**, 8803 (1992)
8. B.Machayekhi, R.Rahbi, B.Theys, M.Miloché and J.Chevallier, Mater. Sci. Forum **143-147**, 951 (1994)
9. R.Rahbi, D.Mathiot, J.Chevallier, C.Grattepain and M.Razeghi, Physica B **170**, 135 (1991)
10. N.Caglio, E.Constant, J.C.Pesant and J.Chevallier, J. Appl. Phys. **69**, 1345 (1991)

NATIVE DEFECTS IN LOW TEMPERATURE GaAs AND THE EFFECT OF HYDROGENATION

R.E. PRITCHARD*, S.A. McQUAID*⁺, R.C. NEWMAN*, J. MÄKINEN[@], H.J. VON BARDELEBEN^o AND M. MISSOUS[#]

* Interdisciplinary Research Centre for Semiconductor Materials, The Blackett Laboratory, Imperial College, Prince Consort Road, London SW7 2BZ, UK

+ Present address: Departamento de Ingenieria Electronica, Universidad Politecnica de Madrid, Ciudad Universitaria s/n, 28040 Madrid, Spain

@ Laboratory of Physics, Helsinki University of Technology, 02150 Espoo, Finland

o Groupe de Physique des Solides, Centre National de la Recherche Scientifique, Université Paris VII, 2 place Jussieu, 75251 Paris CEDEX 05, France

Department of Electrical Engineering, UMIST, PO Box 88, Manchester M60 1QD, UK

ABSTRACT

GaAs grown at low temperatures by MBE has been doped with shallow impurities to $\sim 10^{19} \text{ cm}^{-3}$. A layer doped with Be acceptors was completely compensated and the simultaneous detection of As_{Ga}^0 and As_{Ga}^+ confirmed that the Fermi level was close to midgap and that compensation was partly related to As_{Ga} defects. There was no evidence for the incorporation of V_{Ga} in this layer. For Si-doped samples, more than 80 % of the donors were compensated and the detection of $\text{Si}_{\text{Ga}}\text{-V}_{\text{Ga}}$ pairs by infrared localized vibrational mode (LVM) spectroscopy indicated that V_{Ga} were at least partly responsible. Increasing the Si concentration suppressed the incorporation of As_{Ga} . Exposure of the Be-doped layer to a hydrogen plasma, generated a LVM near 2000 cm^{-1} which may be the stretch mode of a $\text{As}_{\text{Ga}}\text{-H-V}_{\text{As}}$ defect complex. For Si-doped layers, two stretch modes at 1764 cm^{-1} and 1773 cm^{-1} and a wag mode at 779 cm^{-1} relating to a H-defect complex were detected and we argue that the complex could be a passivated As antisite. The detection of characteristic hydrogen-native defect LVMs may provide a new method for the identification of intrinsic defects.

INTRODUCTION

Undoped GaAs grown at low temperatures of 200-250°C by molecular beam epitaxy (MBE) under high As_4/Ga beam equivalent pressure ratios (> 4) is As-rich^{1,2}. In as-grown material, this excess As is accommodated as interstitial defects (As_i)¹, As_{Ga} , and V_{Ga} ; according to theory, the latter defect can transform by a single atomic jump to a $\text{As}_{\text{Ga}}\text{-V}_{\text{As}}$ nearest neighbor pair complex³. Previous studies have led to estimated concentrations of $[\text{As}_i]$ (at least some as complexes with other native defects) in the range $\sim 10^{20}\text{-}10^{21} \text{ cm}^{-3}$, $[\text{As}_{\text{Ga}}] \sim 10^{19}\text{-}10^{20} \text{ cm}^{-3}$, $[\text{As}_{\text{Ga}}^+] \sim 1\text{-}5 \times 10^{18} \text{ cm}^{-3}$ and $[\text{V}_{\text{Ga}}] \sim 1\text{-}5 \times 10^{18} \text{ cm}^{-3}$. The presence of shallow impurities is expected to modify these concentrations so that the total energy is minimized³. For example, it should require less energy to form V_{Ga} defects (deep electron traps) in Si-doped LT-GaAs than in undoped and Be-doped LT-GaAs. Likewise, Be-doping should lower the formation energy for deep donor defects (As_{Ga} or $\text{As}_{\text{Ga}}\text{-V}_{\text{As}}$ defects).

In this paper we report a wide range of measurements on LT-GaAs to determine native

defect concentrations and their dependence on shallow impurity concentrations including positron annihilation (PA), near-bandedge infrared (NBE-IR) absorption, electron paramagnetic resonance (EPR), Hall and x-ray diffraction. A novel procedure has been to expose layers to a radio frequency (RF) hydrogen plasma and investigate the resulting hydrogen-native defect complexes spectroscopically using IR LVM absorption.

EXPERIMENTAL DETAILS

The GaAs epilayers were grown at a substrate temperature of 250°C by MBE on (001) SI LEC GaAs substrates. The growth rate was 1 $\mu\text{m}/\text{h}$ with an As_4/Ga beam equivalent pressure ratio (BEP) in the range 4-6. It has been reported previously² that varying the BEP ratio in this range has a negligible effect on the electrical and optical properties of LT-GaAs. Details of the layers examined are given in the table. The layer thicknesses were between 3 and 7.2 μm .

TABLE. Dopant concentrations measured by LVM spectroscopy and defect concentrations measured by NBE-IR absorption, LVM absorption, positron annihilation, x-ray and EPR.

Sample	Dopant	$n(p)$ $\times 10^{19}$ (cm^{-3})	LVM $\times 10^{19}$ (cm^{-3})	As_{Ga}^0 $\times 10^{19}$ (cm^{-3})	As_{Ga}^+ $\times 10^{18}$ (cm^{-3})	As_i $\times 10^{20}$ (cm^{-3})	V_{Ga} $\times 10^{18}$ (cm^{-3})
1	Undoped	-	-	4	<0.4	1.4	>1 ^(a)
2	Be	<0.001	1.8	1	6	0.4	<0.01 ^(a)
3	Si	0.08	1.5	1	<0.4	-	2 ^(b)
4	Si	0.02	1.2	0.7	NM	-	2 ^(b)
5	Si	0.4	1.9	<0.05	NM	-	4 ^(b)

NM - not measured, (a) obtained from positron annihilation measurements and (b) obtained from LVM IR absorption of $\text{Si}_{\text{Ga}}\text{-}V_{\text{Ga}}$ pairs.

LVM spectra were obtained using a Bruker IFS 120 interferometer operated at a resolution of 0.25 cm^{-1} and with the sample at a temperature of $\sim 10\text{ K}$. The concentrations of dopants occupying lattice sites were estimated from the integrated absorption coefficients (IA) of the LVMs using the calibrations for Si_{Ga} donors⁴ and Be_{Ga} acceptors⁵ in GaAs. NBE-IR absorption was detected at a sample temperature of 77 K using a double beam spectrometer and the concentrations of neutral As_{Ga}^0 defects were determined from the absorption coefficient at 1.18 eV using the 5 K calibration of Martin⁶. The excess As concentration was estimated from the lattice mismatch, $\Delta a/a_0$, between the epilayer and substrate (x-ray). The spin concentrations of As_{Ga}^+ defects were measured by EPR as described elsewhere⁷ and positron annihilation (PA) measurements⁸ to detect vacancy-type defects were performed at various sample temperatures (20-470 K) using slow, monoenergetic positrons implanted so as to reach different depths (up to $\sim 2\text{ }\mu\text{m}$). Hydrogen atoms were in-diffused by heating the layers at their growth temperature (250°C) for 6-72 h in an inductively-coupled RF hydrogen plasma (13.56 MHz, 50 W, 2 mbar).

RESULTS

Details of the defect concentrations measured in the various layers are given in the table. The salient points are that by comparison with the undoped layer, $[V_{Ga}]$ decreased by at least two orders of magnitude by doping LT-GaAs with Be to $2 \times 10^{19} \text{ cm}^{-3}$ while $[As_{Ga}]$ decreased by at least one order of magnitude by doping LT-GaAs with Si to $2 \times 10^{19} \text{ cm}^{-3}$.

After exposure of the Be-doped layer to a hydrogen plasma, the $H-Be_{Ga}$ stretch mode⁵ was not detected but a strong hydrogen stretch mode was observed at 1997 cm^{-1} with a half width at full maximum, $\Delta = 1.1 \text{ cm}^{-1}$ and $IA = 150 \text{ cm}^{-1}$ (Fig. 1a). Treatment in a deuterium plasma led to the observation of an isotopically shifted LVM at 1442.2 cm^{-1} with $\Delta = 0.7 \text{ cm}^{-1}$. Since there were no changes in the lineshape or IA of the isolated Be_{Ga} it was concluded that the passivated complex (designated $H-Z_1$) does not incorporate a Be atom. To our knowledge the $H-Z_1$ LVM line has not been reported previously for passivated epitaxial GaAs. After plasma treatment, antisite concentrations of $[As_{Ga}^0] = (9 \pm 1) \times 10^{18} \text{ cm}^{-3}$ and $[As_{Ga}^+] = (8 \pm 1) \times 10^{18} \text{ cm}^{-3}$ were measured for sample 2 implying, by comparison with the corresponding concentration for the as-grown material, that E_f had moved towards the valence band. This change in E_f is small even though the concentration of passivated centers was of the order of 10^{19} cm^{-3} (assuming the dipole moment of the $H-Z_1$ complex is the same as that for $H-Be_{Ga}$ ⁵). To investigate the thermal stability of the defect Z_1 , separate pieces of sample 2 were annealed (250-792°C) prior to hydrogen plasma treatment. Fig. 1 shows the associated LVM spectra. The IA of the $H-Z_1$ line decreased with increasing anneal temperature corresponding to the annealing behavior of As_{Ga}^0 and As_{Ga}^+ .

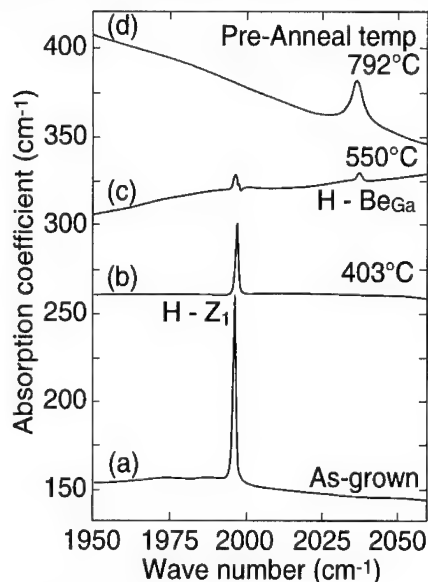


Fig. 1. IR absorption spectra from hydrogenated Be-doped LT-GaAs (a) unannealed and samples pre-annealed at (b) 403°C, (c) 550°C and (d) 792°C.

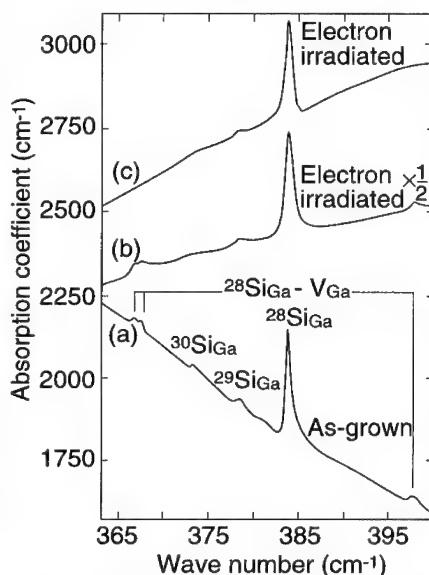


Fig. 2. IR absorption spectra from (a) sample 3, (b) electron irradiated sample 5 and (c) a stoichiometric Si-doped sample following electron irradiation. Irradiation with 2 MeV electrons removes the free carrier absorption.

defects in undoped LT-GaAs⁷. For the sample pre-annealed at 550°C, the stretch mode of the H-Be_{Ga} complex was just detectable indicating that E_f had moved towards the valence band after this anneal, as confirmed by Hall measurements. For the sample pre-annealed at 792°C, only the H-Be_{Ga} mode was detected.

The H-Z₁ line was detected as a weak feature with IA=8 cm⁻² and Δ=1.2 cm⁻¹ following plasma treatments of the undoped layer along with another weak hydrogen related stretch mode, H-Z₂, at a frequency of 1835 cm⁻¹ with IA~20 cm⁻² and Δ=2.5 cm⁻¹. [As_{Ga}⁰] did not change following plasma exposure and post treatment EPR measurements were not made.

LVM measurements of the Si-doped samples showed that all of the Si-atoms occupied Ga lattice sites (Fig.2) although the electron concentrations were much lower than the concentration of Si_{Ga} donors (table). The detection of Si_{Ga}-V_{Ga} second nearest neighbor pairs by LVM spectroscopy indicated compensation by deep V_{Ga} acceptors (Fig.2). V_{Ga} were also detected by PA measurements of sample 3 (> 10¹⁸ cm⁻³) and the positron trapping showed a temperature dependence below 300 K indicating the presence of negative ion-type centers⁸. After exposure of the Si-doped layers to a hydrogen plasma, the H-Si_{Ga} stretch mode was detected at 1717 cm⁻¹ for all layers (Fig. 3) and, for samples 3 and 4, two new absorption lines were detected at 1764 cm⁻¹ and 1773 cm⁻¹. The H-Si_{Ga} wag mode at 897 cm⁻¹ was also observed for all Si-doped samples (Fig. 4) and another new line was detected at 779 cm⁻¹ for samples 3 and 4. The *relative* strengths of the new absorption lines were independent of both passivation time and sample implying that they should be identified with a single complex. We attribute the two high frequency lines to stretch modes and the low frequency line to a wag mode of a hydrogen-native defect which we designate H-Z₃. For reasons which are not understood, we were unable to incorporate deuterium into samples 3 and 4 to establish the number of H atoms in the complex⁹. For sample 3, there was a decrease in [As_{Ga}⁰] by 30 ± 15 % (~3×10¹⁸ cm⁻³) from its as-grown value following plasma treatment.

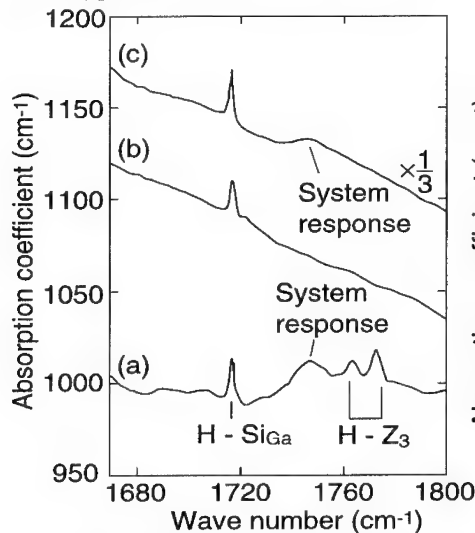


Fig. 3. IR absorption spectra from hydrogenated layers of (a) sample 3, (b) sample 5, and (c) a stoichiometric Si-doped sample.

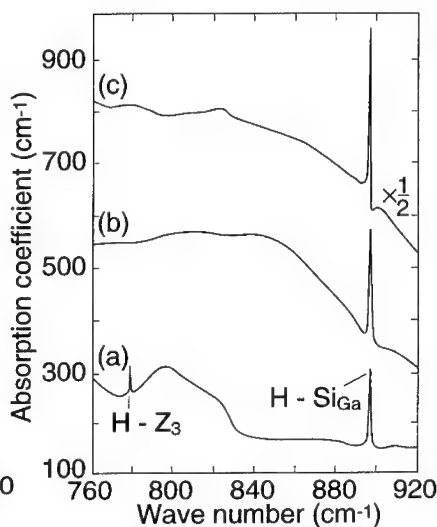


Fig.4. IR spectra from hydrogenated layers of (a) sample 3, (b) sample 5, and (c) a stoichiometric Si-doped sample.

DISCUSSION AND CONCLUSIONS

For the Be-doped layer, the concentration of V_{Ga} acceptor defects was below the detection limit (10^{16} cm^{-3}) indicating a suppression of at least two orders of magnitude compared with the undoped material. Conversely, doping layers with Si donors suppressed the formation of As_{Ga} donor defects by at least one order of magnitude to below the detection limit (10^{18} cm^{-3}). These results are in agreement with theoretical predictions³ relating to the formation energy of native defects and their concentrations as a function of the Fermi level. The electrical activity of As_i complexes is not known but according to theory¹⁰, isolated As_i atoms are negative-U centers that can be donors or acceptors and self-compensation could occur. It is therefore difficult to predict how $[As_i]$ will depend on the concentrations of grown-in shallow dopants. The lattice mismatch between the epilayer and substrate was greatest in the undoped LT-GaAs implying that the incorporation of Be_{Ga} or Si_{Ga} limits the incorporation of excess As atoms (As_i and As_{Ga}).

The layer doped with Be ($2 \times 10^{19} \text{ cm}^{-3}$) was completely compensated but no LVM lines from Be_{Ga} paired with deep donor defects were detected. Since $[As_{Ga}^0] \sim [As_{Ga}^+]$, it is inferred that E_F was pinned at the As_{Ga} ionization level, close to midgap. The detection of only $[As_{Ga}^+] = 6 \times 10^{18} \text{ cm}^{-3}$, however, implies that some other native donor defect with an energy level above that of As_{Ga} was also present. Possible hole traps are $As_{Ga}-V_{As}$ or As_i defects. For the undoped layer, no As_{Ga}^+ defects were detected while $[V_{Ga}^-] > 10^{18} \text{ cm}^{-3}$ was measured by PA. Since a high concentration of As_{Ga}^0 was determined, E_F must be more than a few kT above midgap. It is again inferred that some other deep donor center, shallower than As_{Ga} , must have been present in a concentration of at least 10^{18} cm^{-3} . The presence of $As_{Ga}-V_{As}$ and/or As_i hole traps could also explain the compensation mechanisms in undoped material.

Less than 20 % of donors in Si-doped samples contributed electrons to the conduction band and LVM measurements showed that 10-20 % of Si_{Ga} were complexed with V_{Ga} . Although each V_{Ga} may trap three electrons it is necessary to invoke the presence of another compensating defect at a concentration of $\sim 5 \times 10^{18} \text{ cm}^{-3}$ for each layer to account fully for the compensation. While this other defect may be the isolated V_{Ga} , we cannot confirm this proposal from PA measurements as it was only possible to determine a total vacancy concentration in excess of 10^{18} cm^{-3} . PA measurements did demonstrate the presence of a negative-ion center, however, which could account for the additional compensation. A possible candidate is a As_i^- defect.

It is found commonly that hydrogen passivation of shallow impurities moves E_F towards the midgap position. In our Si-doped LT-GaAs, this process is observed by the formation of H- Si_{Ga} pairs after which there is passivation of a deep donor defect (Z_3). During this second stage of passivation, $[As_{Ga}^0]$ decreased by ~ 30 % for sample 3 while the H- Z_3 LVMs were not detected following passivation of the Si-doped sample that showed no IR absorption from As_{Ga}^0 in its as-grown state (sample 5). Since As_{Ga}^0 is a double donor, its complete passivation would require two H atoms to form an H_2 - As_{Ga} complex. The detection of two stretch modes and one wag mode from a common complex would be similar to the observations⁹ for the H_2^+ defect in Si. In this defect, one hydrogen atom occupies a bond-centered site between two adjacent Si atoms while the other hydrogen atom is located in an anti-bonding (AB) site. Both hydrogen atoms give rise to a stretch mode and the atom in the AB site also gives rise to a wag mode. A similar arrangement of two hydrogen atoms around a neutral As_{Ga} defect has been shown to be a possible equilibrium configuration from pseudopotential local density functional calculations¹¹.

For the as-grown Be-doped layer, the Be_{Ga} acceptors were compensated and their passivation by hydrogen was not expected, in agreement with observations. Instead there was passivation of a deep level defect (Z_1) giving rise to an LVM at 1997 cm^{-1} . LVMs at 1998 cm^{-1} and 2001 cm^{-1} have been detected previously in proton implanted¹² and as-grown¹³ LEC GaAs respectively. The

application of uni-axial stress¹³ caused the line at 2001 cm⁻¹ to shift to lower energies, opposite to the usual response of LVMs due to hydrogen-shallow acceptor complexes, and was attributed to an H-As bond with a V_{Ga} nearest neighbor. We did not detect V_{Ga} in our Be-doped material and so alternatively the H-Z₁ defect could be a hydrogen atom paired with the As atom in a As_{Ga}-V_{As} complex, that is, the transformed V_{Ga}. A puzzling feature of these results is that although a high concentration (~10¹⁹ cm⁻³) of H-Z₁ defects was formed following passivation of the Be-doped layer, there was only a small change in E_F. Such behavior can be explained if Z₁ was a negative-U center with two levels straddling the 0/+ electronic level of the As_{Ga} defect.

H-Z₁ complexes (~5×10¹⁷ cm⁻³) were also detected in the undoped layer along with another defect-H complex (H-Z₂). This latter complex has been detected previously in proton implanted LEC GaAs¹² and was attributed to a H-Ga stretch mode. It is difficult to understand how such an interpretation could be valid for LT layers since hydrogen complexes involving V_{Ga}, As_i or As_{Ga} should give rise to stretching vibrations of H-As bonds.

In conclusion, we have identified point defects and established their role in compensation processes in LT-GaAs. Although it has not been possible to make definitive assignments of some compensating centers (e.g. As_i defects), we have found that electron traps other than V_{Ga} must be present in Si-doped LT-GaAs and deep donors other than As_{Ga} must be present in undoped and Be-doped LT-GaAs. Finally, we have demonstrated how the passivation of native defects by hydrogen in LT-GaAs can be investigated by IR absorption spectroscopy.

ACKNOWLEDGMENTS

The UK authors thank the Engineering and Physical Sciences Research Council (EPSRC), UK, for their financial help and Linda Hart for the x-ray measurements.

REFERENCES

1. K. Man Yu, M. Kaminska, and Z. Liliental-Weber, *J. Appl. Phys.* **72**, 2850 (1992)
2. M. Missous, and S. O'Hagan, *J. Appl. Phys.* **75**, 3396 (1994)
3. W. Walukiewicz, *Appl. Phys. Lett.* **54**, 2094 (1989)
4. R. Murray, R. C. Newman, M. J. L. Sangster, R. B. Beall, J. J. Harris, P. J. Wright, J. Wagner, and M. Ramsteiner, *J. Appl. Phys.* **66**, 2589 (1989)
5. P. S. Nandhra, R. C. Newman, R. Murray, B. Pajot, J. Chevallier, R. B. Beall, and J. J. Harris, *Semicond. Sci. Technol.* **3**, 356 (1988)
6. G. M. Martin, *Appl. Phys. Lett.* **39**, 747 (1981)
7. H. J. von Bardeleben, M. O. Manasreh, D. C. Look, K. R. Evans, and C. E. Stutz, *Phys. Rev. B* **45**, 3372 (1992)
8. C. Corbel, F. Pierre, K. Saarinen, P. Hautojärvi, and P. Moser, *Phys. Rev. B* **45**, 3386 (1992)
9. B. Bech Nielsen, J. D. Holbeck, R. Jones, P. Sitch, and S. Öberg, *Mater. Sci. Forum.* **143-147**, 845 (1994)
10. D. J. Chadi, *Phys. Rev. B* **46**, 9400 (1992)
11. A. Amore Bonapasta, *Mater. Sci. Forum.* **143-147**, 235 (1993)
12. J. Tatarkiewicz, A. Krol, A. Breitschwerdt, and M. Cardona, *Phys. Status Solidi B* **140**, 369 (1987)
13. B. Clerjaud, M. Krause, and C. Porte, in *Proc. 19th Int. Conf. Phys. Semicond.*, Warsaw, Poland, 1988, ed. W. Zawadzki (Institute of Physics, Polish Academy of Sciences) p.1175

HYDROGEN-RELATED ELECTRON TRAPS IN GaAs AND THEIR RELATION TO CRYSTAL STOICHIOMETRY

TATSUYUKI SHINAGAWA AND TSUGUNORI OKUMURA

Department of Electronics and Information Engineering, Tokyo Metropolitan University
1-1, Minami-ohsawa, Hachiohji, Tokyo 192-03, Japan

ABSTRACT

Deep-level formation upon plasma hydrogenation has been studied with n-GaAs grown by various methods. Four electron traps (EH0-EH3) were generated in As-rich n-GaAs crystals. No electron traps were observed in the LPE layer before and after hydrogenation. The hydrogen as well as excess arsenic defects are responsible for the formation of these deep levels. Two of the generated levels in our study, EH0/EH2, exhibit metastability and are identical to the M3/M4 levels reported by Buchwald *et al.* It can be speculated that both diffused hydrogen and already existing As antisite defects are responsible for the generation of the metastable defects.

INTRODUCTION

The properties of hydrogen impurities in semiconductors have been of much interest since hydrogen is a technologically important impurity present in virtually every step during the processing of semiconductor devices.¹⁾ The introduction of hydrogen into semiconductors is well known to passivate both shallow donor²⁾ and acceptor³⁾ impurities. While several deep levels in GaAs are deactivated by hydrogenation,⁴⁾ new deep level defects not present in the original material are created in the hydrogenated region.⁵⁻⁹⁾ Among these defects, a metastable pair of defects (M3 and M4), which were directly observed by deep level transient spectroscopy (DLTS), was found in n-GaAs grown by the metalorganic chemical vapor deposition (MOCVD) method by Buchwald *et al.*^{10,11)} The defect configuration can be completely converted from M3 to M4, and vice versa, by thermal annealing with and without applied bias. First indication that hydrogen is in some way responsible for the presence of the metastable states in MOCVD materials was done by Leitch *et al.*⁹⁾ However, the structure of the defect-hydrogen complex (M3/M4) is not clear.

In this paper, we present experimental evidence that hydrogen as well as arsenic antisite (As_{Ga}) defects are responsible for the generation of the metastable defects. Plasma hydrogenation was carried out on several kinds of GaAs crystals grown by different methods which provide different off-stoichiometric compositions. The DLTS data for the M3/M4 levels were examined in relation to the presence of the EL2 level in the as-grown state.

EXPERIMENTAL PROCEDURES

The GaAs crystals used in this study were grown by various methods: liquid phase epitaxy (LPE), vapor phase epitaxy with $AsCl_3$ (VPE), molecular beam epitaxy (MBE), boat grown method (BG), horizontal Bridgman method (HB) and liquid encapsulated Czochralski method (LEC). The donor (Si) concentration was $1-3 \times 10^{17} \text{ cm}^{-3}$ for almost all crystals except for LPE (undoped, $n = 4 \times 10^{15} \text{ cm}^{-3}$) and one LEC (#2: undoped, $n = 1 \times 10^{16} \text{ cm}^{-3}$) crystals. The substrates were cleaned in organic solvents (trichloroethylene, acetone and ethanol) and etched in a solution of $5H_2SO_4 + H_2O_2 + H_2O$ at 50 °C for 1min. After etching, In-Sn alloy and Ag were deposited by resistive-heating evaporation on the back of the substrate, followed by heat treatment at 400 °C for 5 min. Just before loading the substrates into a plasma processing chamber, the substrate surface was soaked in a $HCl:H_2O = 1:1$ solution at 50 °C for 2min in order to remove a native oxide layer formed during the above process.

The hydrogen plasma treatment was carried out in a remote RF (13.56 MHz, 50 W) plasma system with three electrodes in the chamber. The chamber was evacuated below 10^{-6} Torr prior to feeding a hydrogen gas (99.9999% pure). The distance between the glow-discharge plasma and the substrate holder was 15 cm and the substrate temperature was kept at room temperature. In this experiment, polarity of the substrate bias as well as insertion of the grid electrode between the plasma and the substrate did not affect the basic results except for the defect concentration due to different dosage of atomic hydrogen.

In order to characterize shallow donors as well as deep levels, Schottky diodes were fabricated by evaporating Al or Au on the top of the hydrogenated surfaces through a metal mask with openings of 0.3, 0.5, 0.7 and 1.0 mm in diameter. Standard current-voltage (I - V) and capacitance-voltage (C - V) measurements were carried out before deep level transient spectroscopy (DLTS) measurements. Deep levels were detected by using a homemade DLTS system with YHP 4280A 1MHz capacitance meter, which is computer automated with transient signals being digitally recorded for subsequent analysis. The capacitance difference signals were obtained by using the rectangle weighting function and the rate window was set to 400 ms for the purpose of spectrum comparison.

A series of isochronal anneals (10 min) were carried out at temperatures within $370\text{ K} < T < 420\text{ K}$ under specific bias conditions. For this experiments, the DLTS measurement was done only below 300 K in order to minimize the bias anneal effects during measurements.

RESULTS AND DISCUSSION

The crystals used in this work can be sorted into three groups in terms of crystal off-stoichiometry summarized in Table I: *Group A* includes LPE crystals grown from a Ga-rich solution, *Group B*, MBE, VPE and BG crystals considered to be slightly As-rich, and *Group C*, LEC#1, LEC#2 and HB crystals containing a large amount of excess As atoms.

TABLE I
THREE GROUPS IN TERMS OF CRYSTAL OFF-STOICHIOMETRY.

Group	Crystals	Off-stoichiometry	Dopant	Donor concentration ($\times 10^{17}\text{cm}^{-3}$)
<i>A</i>	LPE	Ga-rich	undoped	0.04
	MBE		Si	2
<i>B</i>	VPE	moderately As-rich	Si	3
	BG		Si	1
	HB		Si	1
<i>C</i>	LEC #1	highly As-rich	Si	1
	LEC #2		undoped	0.1

DLTS spectra for the as-grown samples are shown in Fig. 1. All signals are due to electron traps because of the use of Schottky diodes on n-type substrates. Neither LPE (*Group A*) nor VPE layers (*Group B*) showed any detectable peak in the as-grown state within the detection limit of $5 \times 10^{12}\text{ cm}^{-3}$. No EL2 signal was observed in MBE and BG crystals (*Group B*), although some broad signal was detected. On the other hand, the EL2 level was the dominant deep level in *Group C* (highly As-rich) crystals. In addition to the EL2 level, the EL5 and EL8 levels were detected in the undoped LEC crystal (LEC#2) and the HB crystal, respectively. These results are consistent with the literature¹²; LPE GaAs layers are free from electron traps and the EL2 level is not observed

in MBE layers grown at regular temperatures (550–650 °C). No detection of the EL2 level in the present VPE and BG samples can be partly attributed to suppression of As antisite formation due to donor doping over 10^{17} cm^{-3} .¹³⁾

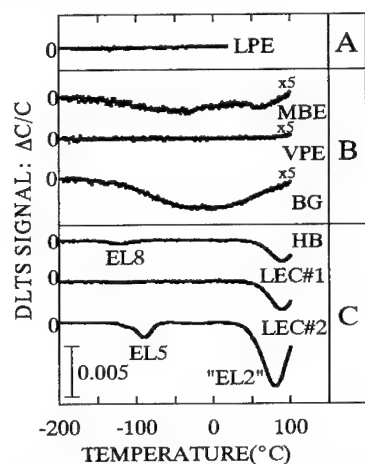


Fig. 1. DLTS spectra before hydrogenation for n-GaAs.

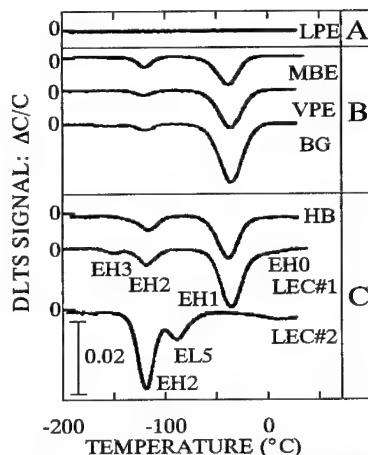


Fig. 2. DLTS spectra after hydrogenation for n-GaAs.

Figure 2 shows the DLTS spectra for the samples plasma-hydrogenated at room temperature. For the LPE crystal (Group A), no electron trap was generated even after exposure to hydrogen plasma. On the other hand, DLTS spectra were completely changed for Groups B and C after hydrogenation. The dominant peak, labeled EH1, was commonly observed around -40 °C except for the undoped LEC crystal (LEC#2), in which the depletion layer expands down to about 0.5 μm from the surface due to low electron density while in the other samples the depletion layer width ranged between 0.1 and 0.2 μm . Therefore, the EH1 level might be attributed to a hydrogen-related defect introduced in the near surface region, or Si atoms might be responsible for the formation of this level since all crystals in which the EH1 level was detected are intentionally doped with Si.

The second largest level commonly observed in the hydrogenated samples was labelled EH2, whose peak appeared in the very vicinity of the EL6 level.¹⁴⁾ At present, we cannot conclude whether the EH2 level is identical with the EL6 level. It is noted that the EH2 concentration was extremely high in the undoped LEC crystal (LEC#2) with high concentration of the EL2 level in the as-grown state. Closer look at the spectra indicates that a weak shoulder and a low peak appeared on the higher temperature side of the curves for two LEC crystals. These signals are attributed to one of the metastable states, labeled EH0 here, which grew by annealing above 400 K with forward bias. There was another minor level (EH3) which appeared after hydrogenation, although it was observed only in the LEC crystal (#1: $n=1 \times 10^{17} \text{ cm}^{-3}$).

The Arrhenius plots for four hydrogen-related levels (EH0-EH3) are shown in Fig. 3 and compared with the electron traps labelled by Martin *et al.*¹⁴⁾ and the hydrogen-related levels reported by several research groups.^{6, 10, 11, 15)} Among them, a pair of levels, M3 and M4 which exhibit metastability, were for the first time found in MOVPE GaAs reported by Buchwald *et al.*^{10, 11)} A complete conversion between the two configurations (M3/M4) can be achieved by thermal annealing under forward or reverse bias. The signature plot suggests that EH0, E3¹⁵⁾, A⁶⁾ and M3^{10, 11)} possess similar trap parameters, and that so do EH2, EL6¹⁴⁾, E1¹⁵⁾ and M4.^{10, 11)}

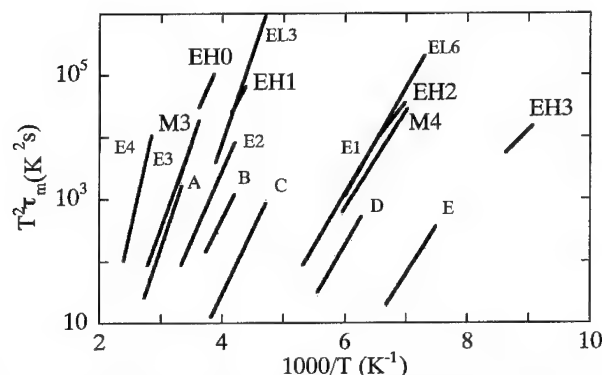


Fig. 3. Arrhenius plots of the four electron traps observed in hydrogenated n-GaAs compared to hydrogen-related metastable defects.

EL3,EL6: Martin et al., M3,M4: Buchwald et al., E1-E4: Tabata et al., A-E: Jalil et al.

In order to investigate the nature of the hydrogen-related levels (EH0-EH3) detected here, bias-annealing was carried out at temperatures of 390K– 420K with reverse bias of –3 V as well as forward bias of 0.4V. Figure 4 shows a typical variation of DLTS spectra upon bias-annealing for the LEC crystal (#1: $n=1 \times 10^{17} \text{ cm}^{-3}$), in which the EL2 peak was clearly observed in the as-grown crystal (*Group C*). The EH2 level disappeared upon forward-bias annealing at 410– 420 K for 10 min, and recovered after annealing with reverse bias. The EH0 peak was clearly observed after annealing at 410 K with forward bias. The behavior of the EH0 level was opposite to that of the EH2 level; it appeared and vanished after annealing at 420 K with forward and reverse bias, respectively. The conversion was completely reversible at this temperature. This metastability of the EH0/EH2 pair is identical with that of the M3/M4.^{10,11)} Furthermore, the EH0 level showed a strong Poole-Frenkel effect, which indicates a donor nature of defects, as shown in Fig. 5; the M3 level is also well known to show the Poole-Frenkel field emission of electrons.¹¹⁾ Therefore, it is concluded that the EH0/EH2 couple is exactly the same as the M3/M4 pair with metastability reported by Buchwald et al.^{10,11)} Two other crystals of *Group C* (HB and LEC#2) also showed the appearance of the EH0 level and the metastability between the EH0 and EH2 levels upon bias-annealing at 420 K.

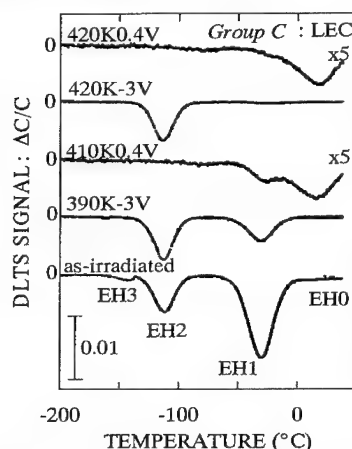


Fig. 4. Variation of DLTS spectra upon bias-annealing *Group C* : LEC #1.

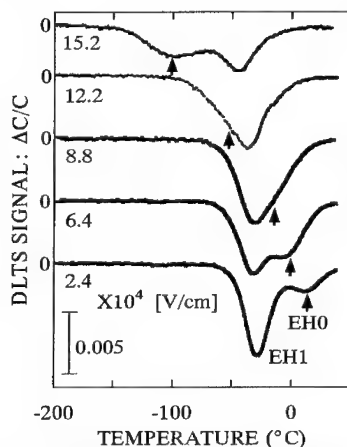


Fig. 5. Dependence of the DLTS spectra of the EH0 level on applied electric fields.

On the other hand, the crystals of *Group B* showed a different annealing behavior of deep levels, although they gave basically similar DLTS spectra in the as-hydrogenated state (see Fig. 2). Figure 6 shows a typical variation of DLTS spectra for the MBE layer upon bias annealing at 420 K. The EH2 level in the MBE layer completely vanished after the first annealing with reverse bias, while the reverse-bias annealing increased the concentration of the EH2 (M4) level in *Group C* (see Fig. 4). No DLTS signal for the EH0 (M3) level appeared in crystals of *Group B* even after annealing with forward bias. VPE and BG samples exposed to hydrogen plasma showed the same behavior as the MBE crystal. Therefore, the M3/M4 pair was not generated upon hydrogenation of *Group B* crystals without the EL2 defect in the as-grown state. It is not clear at present whether the state EH2 in *Group B* is identical with the EH2 in *Group C* or not.

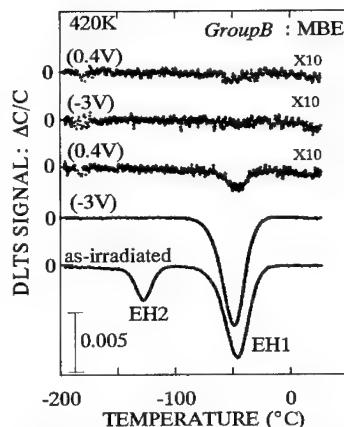


Fig. 6. Variation of DLTS spectra for the MBE layer (*Group B*) upon bias-annealing

Table II summarizes the appearance of the metastable pair of hydrogen-related defects in relation to the existence of the EL2 level. This result indicates a strong correlation between formation of the M3/M4 pair and the EL2 level (the As_{Ga} related defect). Although the crystals in *Group B* are also thought to be As-rich or grown in an As-rich atmosphere, the M3/M4 pair was not generated by exposure to hydrogen plasma. Tabata *et al.*¹⁵⁾ showed that the presence of an electron trap 0.33 eV below the conduction band (E1 in Fig. 3) is dependent on the As/Ga ratio in the MOCVD growth; they stated that arsenic interstitials could be responsible for the E1 level showing metastability, probably identical to M4. It is well known that the EL2 level is a major electron trap in MOCVD GaAs,¹⁶⁾ but they did not state the correlation between the EL2 level and the metastable defect. Very recently, Pfeiffer and Weber¹⁷⁾ concluded from the experiments with GaAs containing a high concentration of oxygen that both the oxygen impurity and diffused hydrogen are involved in the formation of the M3/M4 defects; the EL3 level, which is tentatively assigned to the off-center oxygen defect O_{As} ¹⁸⁾ was observed in their as-grown samples. However, we have not found any EL3 signal in the as-grown crystals even in *Group C*.

The dominant level (EH1) introduced in *Groups B* and *C* by hydrogenation monotonically decreased in concentration upon annealing irrespective of bias polarity. The signature plot apparently indicates that the EH1 corresponds to the EL3 level.¹⁸⁾ However, the annealing behavior as well as the slope in the Arrhenius plots are different between the EH1 and EL3 levels. The EH1 level might be identical with one of the ion sputter induced defects (E_{Ar} 10) reported by Aurret *et al.*^{19,20)}

TABLE II
SUMMARY OF THE RELATION BETWEEN THE METASTABLE DEFECTS AND THE EL2 LEVEL.

Group	Crystals	EL2 level	metastable defects
<i>A</i>	LPE	×	×
	MBE	×	×
<i>B</i>	VPE	×	×
	BG	×	×
<i>C</i>	HB	○	○
	LEC #1	○	○
	LEC #2	○	○

CONCLUSIONS

- (1) During plasma hydrogenation, four electron traps (EH0-EH3) were generated in As-rich n-GaAs crystals. No electron traps were observed in the LPE layer before and after hydrogenation. The hydrogen as well as excess arsenic defects are responsible for the formation of these deep levels.
- (2) Two of the generated levels in our study, EH0/EH2, exhibit metastability and are identical to the M3/M4 levels reported by Buchwald *et al.*
- (3) It can be speculated that both diffused hydrogen and already existing As antisite defects are responsible for the generation of the metastable defects.

ACKNOWLEDGEMENTS

We wish to thank S. Kuma and Y. Otoki of Hitachi Cable Co. for providing various kinds of GaAs crystals. We are also grateful to H. T. Kaibe and T. C. Lin of Tokyo Metropolitan University for their assistance with the sample preparation.

REFERENCES

- 1) S. J. Pearton, J. W. Corbett and M. Stavola, Hydrogen in Crystalline Semiconductors (Springer, New York, 1992).
- 2) Y. Chung, C. Y. Chen, D. W. Laner and Y. S. Park, *J. Vac. Sci. & Technol.* **B1**, 799 (1983).
- 3) N. M. Johnson, R. D. Burnham, R. A. Street and R. C. Thornton, *Phys. Rev.* **B33**, 1102 (1986).
- 4) J. Chevallier, B. Clerjaud and B. Pajot, Hydrogen in Semiconductor, Semiconductors and Semimetals Vol. 34, edited by J. I. Pankove and N. M. Johnson (Academic, San Diego, 1991) p. 447.
- 5) H. Y. Cho, E. K. Kim, S.-K. Min, J. B. Kim and J. Jang, *Appl. Phys. Lett.* **53**, 856 (1988).
- 6) A. Jalil, A. Heurtel, Y. Marfaing and J. Chevallier, *J. Appl. Phys.* **66**, 5854 (1989).
- 7) H. Y. Cho, E. K. Kim, S.-K. Min, K. J. Chang and C. Lee, *Appl. Phys. Lett.* **58**, 1866 (1991).
- 8) H. Y. Cho, E. K. Kim, S.-K. Min and C. Lee, *Phys. Rev.* **B43**, 14498 (1991).
- 9) A. W. R. Leitch, Th. Prescha and J. Weber, *Phys. Rev.* **B45**, 14400 (1992).
- 10) W. R. Buchwald, N. M. Johnson and L. P. Trombetta, *Appl. Phys. Lett.* **50**, 1007 (1987).
- 11) W. R. Buchwald, G. J. Gerardi, E. H. Pointdexter, N. M. Johnson, H. G. Grimmeiss and D. J. Keeble, *Phys. Rev.* **B40**, 2940 (1989).
- 12) K. W. Nauka, Imperfections in III/V Materials, Semiconductors and Semimetals Vol. 38, edited by E. R. Weber (Academic, San Diego, 1993) pp. 351-357.
- 13) J. Lagowski, H. C. Gatos, J. M. Parsey, K. Wada, M. Kaminska and W. Warkiewicz, *Appl. Phys. Lett.* **40**, 342 (1982).
- 14) G. M. Martin, A. Mitonneau and A. Mircea, *Electron. Lett.* **13**, 191 (1977).
- 15) A. S. Tabata, M. A. A. Pudensi and A. M. Machado, *J. Appl. Phys.* **65**, 4076 (1989).
- 16) P. K. Bhattacharya, J. W. Ku, S. J. T. Owen, V. Aebi, C. B. Cooper III, and R. L. Moon, *Appl. Phys. Lett.* **36**, 304 (1980).
- 17) G. Pfeiffer and J. Weber, *Materials Science Forum*, **143-147**, 873 (1994).
- 18) U. Kaufmann, E. Klausmann, J. Schneider and H. Ch. Alt, *Phys. Rev.* **B43**, 12106 (1991).
- 19) F. D. Auret, S. A. Goodman, G. Myburg and W. E. Meyer, *J. Vac. Sci. & Technol.* **B10**, 2366 (1992).
- 20) T. Shinagawa and T. Okumura, (unpublished).

HYDROGEN PASSIVATION OF SHALLOW DOPANTS IN InP STUDIED BY PHOTOLUMINESCENCE SPECTROSCOPY

SATHYA BALASUBRAMANIAN* AND VIKRAM KUMAR**

* Department of Physics, Indian Institute of Science, Bangalore -560 012,

** Solid State Physics Laboratory, Lucknow Road, Delhi - 110 054, India

ABSTRACT

The effect of hydrogenation on the photoluminescence (PL) of InP : Mg, InP : Zn and undoped n-InP is presented. An increase in the near band edge PL intensity due to passivation of non-radiative centers was observed in all the samples. A donor - acceptor pair transition was observed before hydrogenation in the InP : Mg sample and after hydrogenation in the InP : Zn sample due to the acceptor deactivation. In n-InP the enhancement of donor bound exciton after hydrogenation points to the absence of donor passivation.

INTRODUCTION

It is now well known that atomic hydrogen passivates shallow dopants as well as deep levels in virtually all semiconductors [1-5]. Hydrogen containing plasma has been used widely for III-V material processing [6]. Hydrogen passivation of non-radiative defect centers in the semiconductor bulk [7] and at interfaces of quantum wells [8,9] have also been reported. Photoluminescence (PL) spectroscopy has been used to study the passivation effects of hydrogenation. In GaP, Weber and Singh [3] have observed an increase in PL after hydrogenation along with the electrical deactivation of donors and acceptors. Hydrogen passivation of deep levels accompanied by an increase in PL was observed in n-GaAs [4]. Swaminathan, et al. [7] have observed a PL rise in p-InP after hydrogenation. In this paper, we report the effect of hydrogenation on the PL of InP : Mg, InP : Zn and undoped n-InP. We find a significant increase in the near band edge PL efficiency after hydrogenation along with acceptor passivation effects.

EXPERIMENTAL

The samples used in the present study are <100> oriented, liquid encapsulated Czochralski grown InP : Mg, InP : Zn and undoped n-InP crystals with room temperature carrier concentrations of $5.8 \times 10^{16} \text{ cm}^{-3}$, $3 \times 10^{18} \text{ cm}^{-3}$ and $6 \times 10^{15} \text{ cm}^{-3}$ respectively. The samples were degreased, etched in $\text{H}_2\text{SO}_4 : \text{H}_2\text{O}_2 : \text{H}_2\text{O}$ (1 : 1 : 8) solution, treated with dilute HF for native oxide removal and rinsed in running deionized water. Hydrogenation was carried out in a home-made plasma reactor operating at a radio frequency of 13.56 MHz following a method [10] to reduce preferential P loss during the treatment. The plasma treatment was carried out for a duration ranging from 1 to 2 hr at a temperature of $180 \pm 2^\circ\text{C}$. The RF power was fixed at 0.5 W/cm^2 and the pressure maintained at 0.5 torr.

PL measurements were carried out using a Midac Fourier Transform spectrometer. The PL spectra were recorded primarily at 4.2 K with the samples immersed in liquid He. The 5145 Å

line of the argon ion laser with a beam diameter of 1.1 mm was used as the excitation source. The PL signal was detected by a liquid nitrogen cooled Ge photodetector.

RESULTS AND DISCUSSION

Figure 1 shows the PL spectra of Mg doped InP before hydrogenation (control) recorded at 4.2 K with three different laser powers along with the spectrum after hydrogenation. In the control sample, for a laser excitation power of 1 mW, it can be seen that there are two peaks, one at 1.348 eV (referred to as low energy band (LEB)) and at 1.375 eV (referred to as high energy band (HEB)). In these samples, the conduction band to Mg acceptor (C-A) transition which occurs at an energy of 1.383 eV [11] is not observed. At an excitation power of 10 mW, the LEB shifts to 1.362 eV and hence, the 1.375 eV peak is not well resolved. The peak shift is calculated to be about 14 meV per decade change in excitation power. A peak shift of this magnitude suggests that the shallower center participating in this D-A pair transition has a higher ionization energy than the commonly observed shallow donors [12].

After hydrogenation, the D-A pair transition is below observable limits and only the HEB is observed as shown by curve (d) in Fig. 1 recorded for 1 mW laser power. The peak at 1.332 eV is the phonon replica of the HEB. The energy of the HEB does not change when the excitation intensity was varied over two orders of magnitude. The intensity of this transition is larger by a factor of 16 when compared to that of the control sample. This increased PL is due to the passivation of non-radiative recombination centers after hydrogenation and the suppression of the competing D-A pair transition. The absence of the D-A pair transition can be attributed to the passivation of acceptors by hydrogen wherein hydrogen bonds to the acceptors rendering them inactive as recombination centers. From the observation that the peak at 1.375 eV is present even after hydrogenation, we conjecture that it originates from a donor to valance band (D-V) transition as hydrogen is known to be an efficient passivant of acceptors in InP [5]. Since in the control sample, with increasing excitation, the D-A pair transition saturates at the energy position of this D-V transition, we observe that the same donor should be involved in both the transitions.

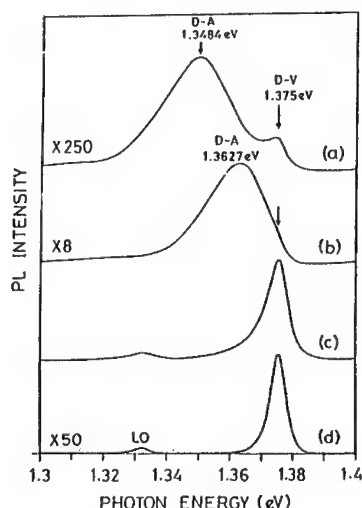


Fig. 1 4.2 K PL spectra of control (a-c) and hydrogenated (d) InP:Mg samples recorded at different laser powers; (a) 1 mW, (b) 10 mW (c) 100 mW and (d) 1 mW.

The PL spectra of InP:Zn recorded before and after hydrogenation are shown in Fig. 2 and Fig. 3 respectively. In the spectrum of the control sample recorded at an excitation intensity of 150 mW (Fig. 2) a deep band centered around 0.94 eV attributed to phosphorus vacancy related complexes [13] is observed. The near band edge emission occurs at 1.3862 eV which has been previously observed by Swaminathan et. al. [7]. In our sample, this band does not show any variation in peak position with excitation intensity and could not be involving any prominent D-A pair transition.

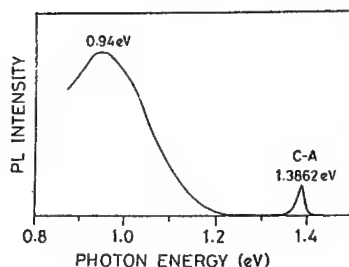


Fig. 2 4.2 K PL spectrum of InP:Zn samples recorded at 150 mW laser excitation power.

After hydrogenation (Fig. 3) the deep band is not observed pointing to the efficient passivation of the radiative deep centers by hydrogen. The C-A emission peak at 1.386 eV disappears and a new (D-A) emission is observed whose energy position depends on the excitation intensity. There is an increase by a factor of 50 in the near band edge emission after hydrogenation. The peak shift of the new D-A transition amounts to 7 meV per decade change in excitation power. A shift of this magnitude points to the involvement of a donor deeper than the commonly observed shallow donors. Recalling the results on InP:Mg samples where we observed an energy shift of about 14 meV per decade change in excitation power, a shift of 7 meV in InP:Zn samples leads to a conjecture that the donors present in the two samples are not the same. In Cd coped InP, a donor with $E > 56$ meV has been previously reported [12]. We thus note that donors of higher ionization energy than the normally observed shallow donors are present in p type InP crystals.

In InP:Zn samples, the D-A pair transition is observed after hydrogenation unlike in the case of InP:Mg. The reason for this can originate from the dopant and its concentration levels. In the InP:Zn samples, the acceptor concentration is high and the presence of the donors in smaller amounts may not

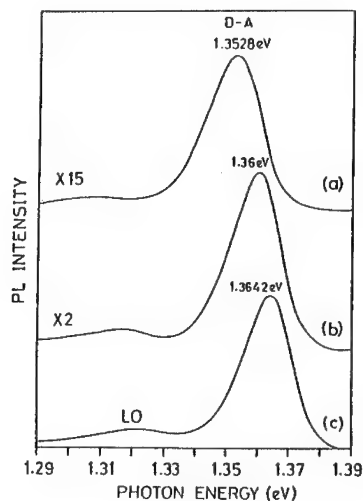


Fig. 3 4.2 K pl spectra of hydrogenated InP:Zn samples recorded at different laser excitation powers; (a) 5 mW, (b) 50 mW, and (c) 15 mW

give rise to any observable D-A pair transition. After hydrogenation, the active acceptor concentration is brought down which may facilitate the D-A pair emission to show up. In the case of InP : Mg, as the acceptor doping is moderate, the D-A pair transition is observed even in the control sample. After hydrogenation, D-V transition becomes dominant due to acceptor passivation. In an earlier work by Swaminathan and co workers [7], a new near band edge peak was observed which was attributed to hydrogenation induced damage. We observe such a peak in InP : Zn samples and explain it as the D-A pair transition which becomes observable following acceptor passivation by hydrogen. As it is observed after hydrogenation only in InP : Zn samples and not in InP : Mg samples we find that it is not created by hydrogenation.

Figure 4 shows the 4.2 K PL spectra of the control and hydrogenated n-InP. The transition observed at 1.4171 eV is due to neutral donor bound exciton (D-X) and the emission at 1.3738 eV is a D-A pair transition as it exhibits a shift of 0.4 meV towards higher energy per decade change in excitation intensity. The PL spectra of the hydrogenated InP sample shown in Fig. 4 exhibit a remarkable increase in the intensity of the bound excitonic transition in comparison with that of the control. An increase in the PL by a factor of about 265 is observed for a laser power of 50 mW. This enhancement clearly points to the passivation of non-radiative centers by hydrogen. The increase in intensity of the donor bound exciton after hydrogenation is in contrast to the earlier result obtained on n-GaAs [15]. In their case, a decrease in the intensity of the donor bound exciton was observed and was attributed to the passivation of donors by the formation of neutral donor-hydrogen complexes which was in accordance with the electrical measurements [16]. In the present work, the increase in the PL of donor bound exciton after hydrogenation suggests that there is negligible passivation of donors in n-InP though it does not rule out the donor passivation because the PL rise can be brought out by the passivation of non-radiative centers. But, C-V profiling of active donor concentration supports the fact that the donor passivation by H is negligible in n-InP.

CONCLUSION

In summary, we have studied the dopant passivation in InP due to hydrogenation by PL

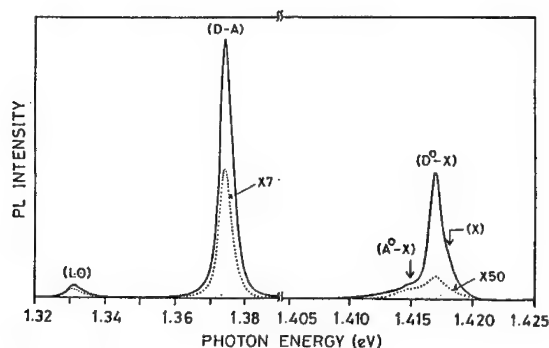


Fig.4 4.2 K PL spectra of unhydrogenated (dotted curve) and hydrogenated (solid curve) n-InP sample. The laser excitation power is 50 mW.

measurements. On hydrogenation, we observe a rise in near band edge PL intensity of all the samples studied which is attributed to the passivation of non-radiative centers by hydrogen. We observe a D-A pair transition before hydrogenation in the InP : Mg sample and after hydrogenation in the InP : Zn sample due to acceptor passivation by hydrogen. In n-InP, the increase in the PL of donor bound exciton after hydrogenation suggests negligible passivation of donors.

Acknowledgment

One of us (SB) acknowledges the Council for Scientific and Industrial Research, India for the award of Senior Research Fellowship. We thank Solid State Electronics Group, TIFR, Bombay and Dr. Shambhu K. Shastry for providing the samples used in this work, DST, India for partial financial support and DOE, India for the FTPL system.

References

- [1] S.J.Pearton, J.W.Corbett, and T.S.Shi, Appl. Phys. A 43, 153 (1987).
- [2] S.J.Pearton, J.W.Corbett and M.Stavola, Hydrogen in Crystalline Semiconductors (Springer, Berlin, 1992).
- [3] J.Weber and M.Singh, Mat. Res. Soc. Symp. Proc. 104, 25 (1988).
- [4] W.C.Dautremont-Smith, J.C.Nabity, V.Swaminathan, M.Stavola, J.Chevallier, C.W.Tu, and S.J.Pearton, Appl. Phys. Lett. 49, 1098 (1986).
- [5] W.C.Dautremont-Smith, J.Lopata, S.J.Pearton, L.A.Koszi, M.Stavola, and V.Swaminathan, J.Appl. Phys. 66, 1993 (1989).
- [6] V.Swaminathan, J.Lopata, S.E.G.Slusky, W.C.Dautremont-Smith and S.J. Pearton, Defect Control in Semiconductors, Ed. K.Sumino (Elsevier Science Publishers B.V., North-Holland, 1990).
- [7] J.M. Zavada, F. Voillot, N.Lauret, R.G.Wilson, and B.Theys, J.Appl. Phys.73, 8489 (1993).
- [8] S.M.Lord, G.Roos, J.H.Harris, Jr., and N.M.Johnson, J.Appl. Phys.73, 740 (1993).
- [9] T.R.Hayes, Indium Phosphide and related materials: Processing, Technology and Devices. Ed. Avishay Katz (Artech House, Boston, 1991).
- [10] Sathya Balasubramanian, Vikram Kumar, and N.Balasubramanian Appl. Phys. Lett. 64, 1696 (1994).
- [11] A.Yamada, Y.Makita, S.Kimura, H.Asakura, T.Matsumori, A.C.Beye, and K.M.Mayer, Mat. Sci. and Engg. B 9, 319 (1991).
- [12] V.Swaminathan, V.M.Donneley, and J.Long, J. Appl. Phys. 58, 4565 (1985).
- [13] H.Temkin, B.V.Dutt, and W.A.Bonner, Appl. Phys. Lett. 38, 431 (1981).
- [14] K.Hess, N.Stath and K.W.Benz J.Electrochem.Soc.121,1208 (1974).
- [15] J.Weber, S.J.Pearton and W.C.Dautremont-Smith Appl. Phys. Lett. 49, 1181 (1986)
- [16] J.Chevallier, W.C.Dautremont-Smith, C.W.Tu and S.J.Pearton Appl. Phys. Lett. 47, 108 (1985).

HYDROGEN-INDUCED PASSIVATION OF DEEP TRAPS IN n-GaAs:Si GROWN ON LT-GaAs

E.C. PALOURA^{a)}, A. GINOUDI^{b)}, B. THEYS^{c)}, J. CHEVALLIER^{c)}, C.B. LIOUTAS^{a)}, J. KALOMIROU^{a)}, M. LAGADAS^{d)} AND Z. HATZOPOULOS^{d)}.

^{a)} Aristotle Univ. of Thessaloniki, Department of Physics, GR-54006, Greece.

^{b)} University of Thrace, Dept. of Electrical and Computer Engineering, 67100, Greece.

^{c)} C.N.R.S., Lab. de Physique des Solides de Bellevue, F.92.195 Meudon Cedex, France.

^{d)} F.O.R.T.H.-I.E.S.L., GR-71110, Crete, Greece.

ABSTRACT

We study the hydrogen-induced passivation of interface traps in n-GaAs:Si, grown by MBE at 580°C, with a buffer layer grown at 200 to 250°C (LT-buffer). In the as-grown samples, the LT-buffer contains As-precipitates, with a density of $4 \times 10^{16} \text{ cm}^{-3}$ and a diameter that depends on the LT-buffer growth temperature and takes values in the range 4-8nm. The epilayer/LT-buffer interface in the as-grown samples is characterised by interface related traps which dominate the electrical behaviour of the epitaxial layer. Secondary ion mass spectroscopy profiling of deuterated samples reveals that ^2H has a nearly uniform concentration throughout the epilayer, while it accumulates at the interface. Hydrogenation induces a reduction of the interface trap concentration and a significant improvement of the carrier mobility values.

INTRODUCTION.

Recently, the interest in GaAs buffer layers grown at low temperatures (LT-buffer layers) became a subject of considerable interest. These layers are used as buffer layers for FET and HEMT applications¹ because, due to the high resistivity of the LT-buffer, the parasitic effects like side- and back-gating, which are due to the insufficient insulation between devices, are shown to be significantly reduced². In general, the quality of the active layer is acceptable for device fabrication, while the annealed LT-buffer suffers from point defects, such as As_i , As_{Ga} , V_{Ga} and As precipitates³. The dimensions and density of the As precipitates depend on the growth conditions (temperature and $P_{\text{As4}}/P_{\text{Ga}}$ ratio) and annealing temperature^{4,5,6}. The beneficial effect of atomic hydrogen into highly defective materials is of immediate interest, since it is known to passivate impurity and defect states in semiconductors⁷, while its thermal stability is often higher when it forms complexes with native defects⁸. However its effect on LT-buffer GaAs has not been studied in the past. In this paper we report on the effects of plasma hydrogenation on the electrical, transport and structural properties of GaAs/LT-GaAs structures, while the depth profile of the diffused hydrogen is determined by secondary ion mass spectroscopy (SIMS).

SAMPLE GROWTH AND EXPERIMENTAL DETAILS.

The samples were grown on (100) Si-GaAs substrates, by molecular beam epitaxy (MBE), using As_4 and Si as the n-type dopant. The growth rate was 1 $\mu\text{m/hr}$ and the beam equivalent pressure $P_{\text{As4}}/P_{\text{Ga}}$ was 15. After the initial decreasing, etching and outgasing of the substrates, an undoped buffer layer of 250nm was grown at 580°C.

Then the substrate temperature was ramped down to 200-250°C and 1µm LT-GaAs was grown. The 1.2µm thick n-GaAs epilayer was grown at 580°C, therefore, the LT buffer layer has been subjected to in-situ annealing at 580°C for 70 min⁵. The epilayer was capped by a 100nm n⁺-GaAs:Si doped layer (10^{18} cm^{-3}), which was used for the fabrication of improved ohmic contacts and as a protective layer against plasma induced surface damage during a number of hydrogenations.

The samples were subjected to hydrogenation using deuterium (^2H) and hydrogen (hereafter called ^2H -genation and H-genation, respectively). The H-genations were performed in a hydrogen glow discharge, at 13.56MHz, in a capacitively coupled quartz reactor. The samples were placed downstream from the RF electrode and they were H-genated at two different temperatures, 30°C and 150°C, for 4 hrs, at 150-300mTorr, with a power density of about 0.2 W/cm^2 . The hydrogenations using deuterium were performed in a parallel plate reactor operating at 13.56MHz, at 200°C, for 4hrs, with a power density of $0.05\text{--}0.08\text{ W/cm}^2$. The ^2H profile was measured using SIMS.

The AuGe ohmic contacts were fabricated with electron beam evaporation and subsequent annealing in N_2 at 380°C for 10min, while the Schottky barriers were fabricated with Au evaporation. The samples were characterised prior and after hydrogenation with Hall measurements, I-V and C-V characteristics, deep level transient spectroscopy (DLTS), SIMS and cross section transmission electron microscopy (XTEM).

RESULTS AND DISCUSSION.

The presence of arsenic precipitates in the LT-buffer, with a density of $4 \times 10^{16}\text{ cm}^{-3}$, is identified with XTEM measurements. The As precipitate diameter depends on the LT-buffer growth temperature and takes the values $4 \pm 0.5\text{ nm}$ and $8 \pm 2\text{ nm}$, for growth temperatures 200 and 250°C, respectively. A cross-section image from the sample grown at 250°C is shown in Fig.1. There is a characteristic difference in the distribution of the precipitates at the Si-GaAs/LT-buffer and the LT-buffer/n-GaAs interfaces. The distribution at the Si-GaAs/LT-buffer interface is a step-like function, i.e. the precipitates are confined in the LT-buffer (inset A in Fig. 1). Contrary to that, the LT-buffer/n-GaAs interface is diffuse and the As precipitates extend to a distance of about $0.2\mu\text{m}$ from the interface, into the epilayer. The interface morphology is the same in the samples grown at 200 and 250°C. Even though the existence of As precipitates in the epilayer has been observed in the past⁹, the thickness of the n-GaAs that contains As precipitates was not reported.

The free carrier concentration (n) and mobility (μ) as a function of temperature (4-300K), in the as-grown and hydrogenated film, after ^2H -genation at 210°C, for 75min, with a power density of 0.05 W/cm^2 , are shown in Fig.2(a) and (b), respectively. The LT-buffer layer was grown at 200°C. The free carrier concentration in the as-grown samples is 10^{16} cm^{-3} and decreases to $1.7 \times 10^{15}\text{ cm}^{-3}$, i.e. by a factor of 6, after hydrogenation at 210°C. In addition to that, the electron mobility at 100 K increases after hydrogenation from $11,750$ to $12,750\text{ cm}^2/\text{Vs}$. The corresponding changes, at room temperature, in the values n and μ for the sample with the LT-buffer grown at 250°C are: $n = 2.0 \times 10^{16}\text{ cm}^{-3}$, $\mu = 5000\text{ cm}^2/\text{Vs}$ in the as-grown state and $n = 4.6 \times 10^{15}\text{ cm}^{-3}$, $\mu = 5840\text{ cm}^2/\text{Vs}$ after hydrogenation. These results indicate that, as expected, the hydrogen atoms neutralise donor impurities by forming neutral H-donor complexes.

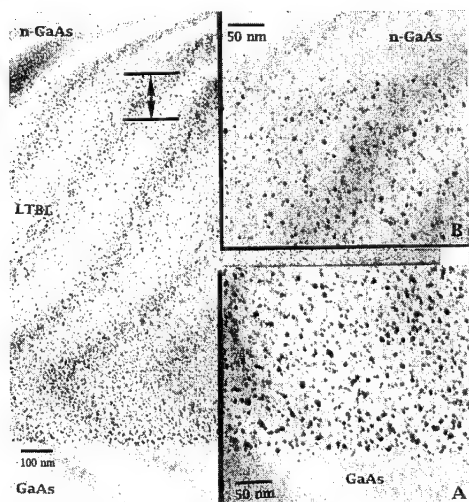


Fig. 1 : XTEM image of the sample with the LT-buffer grown at 250°C. The Si-GaAs/LT-buffer and LT-buffer/n-GaAs interfaces are shown, under magnification, in the insets A and B, respectively.

The barrier height and the ideality factor n of the Schottky barriers, as measured from I-V characteristics, on the as-grown samples are 0.8-0.9 eV and $n=1.1-1.3$, respectively. The barrier height does not change upon hydrogenation while the ideality factor increases to 1.2-1.5. The deterioration of the value on n could be related to residual surface damage induced by the H-generation.

The as-grown samples are characterised by a DLTS peak which has a strong bias dependence. The peak position, recorded for an emission rate of 200s^{-1} , shifts from 269 to 300 K, when the applied reverse bias varies from 0 to -4 V, as shown in Fig. 3. The spectra were recorded with a filling pulse height 0.5 V larger than the corresponding bias, and filling pulse width equal to 5 ms. This strong bias dependence is a characteristic property of interface traps^{10,11} which, at the present case, are localised at the n-GaAs/LT-GaAs interface. This interface is expected to be heavily defective⁶. Furthermore, it has been reported that the LT-buffer prior to annealing is characterized by a relative lattice expansion $\Delta a/a$ up to 0.15%, in the direction of growth. Although this lattice mismatch disappears after annealing at 580°C, due to the formation of As precipitates^{3,12}, the first layers of n-GaAs are grown on non-relaxed LT-GaAs material. As a consequence, the existence of residual outdiffused point defects at the interface is likely. These defects could favor the diffusion of excess As from the LT-GaAs into the n-GaAs epilayer, giving rise to As precipitates in the epilayer. Furthermore, it is expected that, beyond the geometrical interface, additional interfacial regions exist between the As precipitates and the surrounding GaAs¹³. It should be pointed out that interfaces related to the As precipitates introduce additional depleted areas in the interface region². Therefore, the distinction between the electrical phenomena related to the geometrical interface and the interfaces around the As precipitates is difficult.

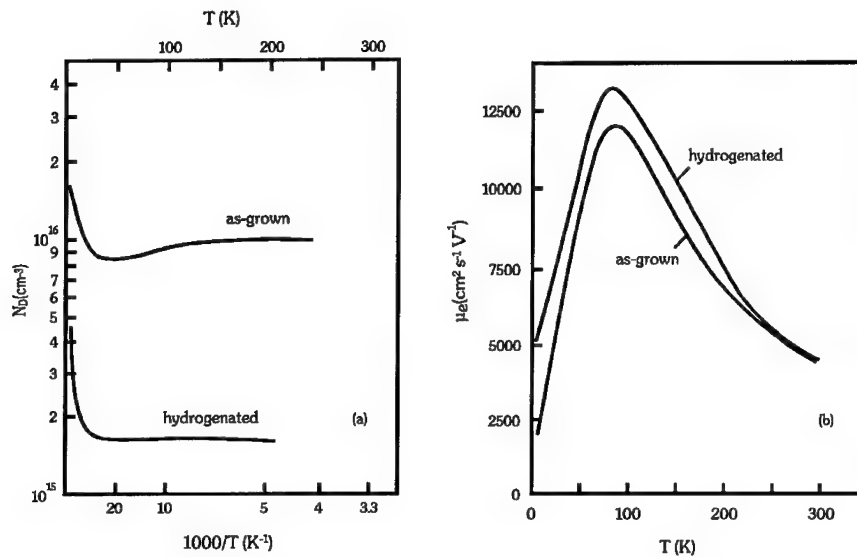


Fig 2 : Free carrier concentration (a) and mobility (b), as a function of temperature, prior and after hydrogenation.

DLTS measurements in the as-grown samples reveal that the interface trap concentration is reduced by a factor of 2-4 for an increase in the LT-buffer growth temperature from 200 to 250°C. After hydrogenation the DLTS peak decreases by a factor of 3 and 10 for hydrogenation temperatures of 30 and 150°C, respectively. Furthermore, ²H-genation at 210°C appears to be even more efficient for the passivation of the interface traps and reduces the DLTS peak to the detection limit. Even though a number of deep levels in highly resistive LT buffers have been identified in the past by thermally stimulated current measurements^{13,14,15}, we have not identified outdiffusion of deep bulk levels in the epilayer.

The heavy incorporation of hydrogen at the interface is also indicated by SIMS profiling. The strong ²H pile-up at the n-GaAs/LT-GaAs interface, obtained after a ²H plasma exposure of 2hrs, at 210°C with a power density of 0.08W/cm², is shown in Fig.4. This accumulation results from the bonding of hydrogen with defects and/or impurities at the interface, which could have resulted from the outdiffusion of the growth defects from the LT buffer during the in-situ annealing process.

Local charges in the region near the interface seem to be also related with the anomalous capacitance (C) versus temperature (T) behaviour of the Schottky diodes. C-T measurements performed under 0 V bias in the T-range 100-400K, show that the C increases as T decreases. This increase of the capacitance at low temperatures is not well understood, but after hydrogenation, although the trend remains the same, the relative changes between the capacitance C at 100 and 400K, i.e. the ratio $\Delta C/C = [C(100) - C(400)]/C(100)$, decreases by a factor of 3 to 10, as the degree of hydrogen incorporation, as determined by the hydrogenation conditions, increases.

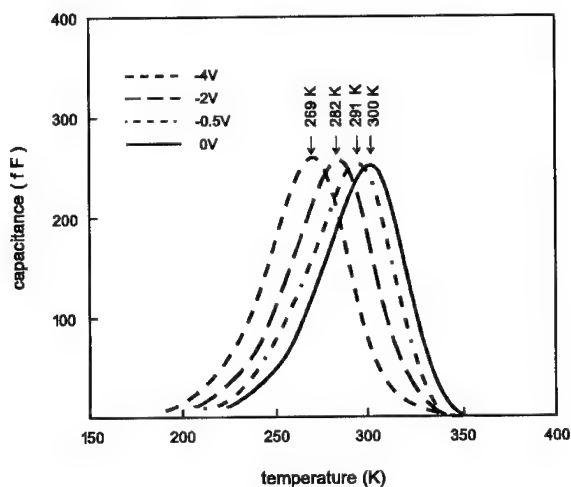


Fig.3 : Typical DLTS spectra from an as-grown sample (the buffer layer grown at 200°C).

We can assume that the defects responsible for the C-T behaviour are acceptor type, i.e. they are neutral when empty and negatively charged when filled. Thus the local charges increase when the traps are progressively filled, as the temperature decreases.

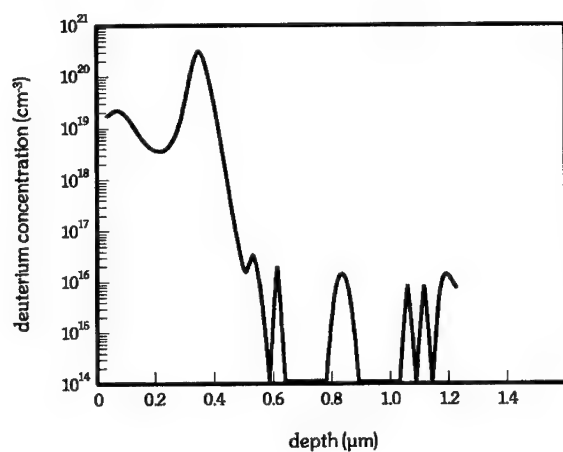


Fig. 4 : SIMS profile of the ^2H distribution in a sample ^2H -genated at 210°C, with a power density of $0.08\text{W}/\text{cm}^2$, for 2 hrs.

CONCLUSIONS

Our results, indicate that atomic hydrogen is effective in passivating interface-related defects in GaAs/LT-GaAs structures. Possible origin of these defects are the structural defects at the geometrical interface in combination with the interface regions surrounding the amorphous As precipitates, which are detected in the n-GaAs epilayer.

The existence of As precipitates in the annealed LT buffer and in the broad ($\approx 200\text{nm}$) n-GaAs/LT-GaAs interface, with a density of $4 \times 10^{16} \text{cm}^{-3}$ and a diameter in the range 4–8nm, was verified by XTEM measurements. The reported interface broadening is attributed to outdiffusion and precipitation of excess As from the LT-buffer. The LT-buffer/n-GaAs interface is characterised by electrically active interface traps, as detected by DLTS, with a concentration that depends on the growth temperature of the LT-buffer layer. Upon hydrogenation the trap concentration is reduced by a factor of 3–10, for hydrogenation temperatures 30 and 150°C , respectively. Furthermore, ^2H -generation at 210°C causes a reduction of the trap related DLTS signal to the detection limit of DLTS. An anomalous C-T behaviour, observed in these layers was not fully understood, but the value of $\Delta C/C$ decreases by a factor 3–10 after hydrogenation. The fact that hydrogen passivates efficiently the interface states was also supported by SIMS profiling, where the ^2H accumulation indicates the existence of a highly defective n-GaAs/LT-buffer interface. However, future work, including thermal stability studies would be useful for a more complete understanding of the interface related DLTS active defect. Finally, the decrease of the carrier concentration, as observed by C-V and Hall measurements, indicates the hydrogen induced passivation of shallow donors in the epilayer.

ACKNOWLEDGEMENTS : The authors wish to thank Mme Monique MILOCHE for the SIMS measurements. Partial financial support from the 91ED786 (G.S.R.T.) and PLATON programs is also acknowledged.

¹F. W. Smith, A. R. Calawa, C. L. Chen, M. J. Manfra and L. J. Mahony, IEEE Elect. Dev. Lett. **EDL-9**, 77 (1987).

²A. C. Warren, J. M. Woodall, J. L. Frecof, D. Grischkowsky, M. R. Melloch and N. Otsuka, Appl. Phys. Lett. **57**, 1331 (1990).

³M. Missous and S. O'Hagan, J. Appl. Phys. **75**, 3396 (1994).

⁴M. R. Melloch, N. Otsuka, K. Mahalingam, A. C. Warren, J. M. Woodall and P. D. Kirchner, MRS Mater. Res. Symp. Proc. **241**, 113 (1992).

⁵M. Lagadas, Z. Hatzopoulos, M. Calamiotou, M. Kayiambaki and A. Christou, MRS Mater. Res. Symp. Proc. **325** (1994) (in press).

⁶M. Lagadas (private communication).

⁷S. J. Pearton "Hydrogen in compound semiconductors" (Trans. Tech. Publications, Switzerland 1994).

⁸T. K. Woodward, J. E. Cunningham, W. Y. Jan and A. Kastalsky, Appl. Phys. Lett. **65**, 2174 (1994).

⁹J. M. Ballingall, P. Ho, R. P. Smith, S. Wang, G. Tessmer, T. Yu, E. L. Hall and G. Hutchins, MRS Mater. Res. Symp. Proc. **241**, 171 (1992).

¹⁰K. Yamasaki, M. Yoshida and T. Sugano, Jpn. J. Appl. Phys. **18**, 113 (1979).

¹¹E. C. Paloura, A. Ginoudi, G. Konstantinidis and G. Kiriakidis, Sensors and Actuators A, **33**, 63 (1992).

¹²D. C. Look, D. C. Walters, G. D. Robinson, J. R. Sizelove, M. G. Mier and C. E. Stutz, J. Appl. Phys. **74**, 306 (1993).

¹³W. S. Lau, T. C. Chong, L. S. Tan, C. H. Goo and K. S. Goh, Jap. J. Appl. Phys. **30**, L1843 (1991).

¹⁴Z.-Q. Fang and D. C. Look, Appl. Phys. Lett. **63**, 219 (1993).

¹⁵N. D. Jaeger, P. Dresser, N. Newman, A. K. Verma, Z. Liliental-Weber and E. R. Weber, Mater. Sci. Forum, **143-147**, 1599 (1994).

Part VI

Defect Issues in
Widegap Semiconductors

THEORY OF DEFECTS IN WIDE-BAND-GAP SEMICONDUCTORS

CHRIS G. VAN DE WALLE and JÖRG NEUGEBAUER

Xerox Palo Alto Research Center, 3333 Coyote Hill Road, Palo Alto, CA 94304

ABSTRACT

We discuss the application of state-of-the-art first-principles calculations to the problem of defects, impurities, and doping levels in semiconductors. Since doping problems are of particular relevance in wide-band-gap materials, we focus here on studies of ZnSe and GaN. For ZnSe, we discuss our latest insights in the influence of compensation and dopant solubility on the experimentally observed limitation of the free carrier concentration in *p*-type ZnSe. For GaN, we focus on the role of native defects in doping or compensation of the material, with particular emphasis on the *n*-type conductivity of as-grown GaN.

INTRODUCTION

First-principles calculations have had a major impact on the understanding of defects and impurities in semiconductors. The first applications of electronic structure methods focused on obtaining defect wave functions and levels in the band gap.^{1,2} With the advent of the capability to calculate total energies, it became possible to investigate the atomic structure of the defect; i.e., the stable position in the host lattice, the relaxation of the surrounding atoms, as well as the energy along a migration path.^{3,4,5} Calculations of hyperfine parameters also enabled more direct comparisons with experimental observations.^{6,7} More recently, formalisms have been developed to use the total energy of the defect to calculate its concentration, under the assumption of thermodynamic equilibrium.^{8,9} The same formalism can also be applied to the calculation of impurity solubilities.^{10,11}

The methods and computational approaches are, in principle, general in nature, and can be applied to any defect or impurity in any semiconductor. Some of the more interesting problems related to defect formation and doping occur in wide-band-gap semiconductors; these materials have therefore become a focus of intense theoretical research activity, in spite of the fact that they tend to be computationally more difficult to treat.

Wide-band-gap semiconductors have many exciting applications, ranging from high-temperature electronics to visible (or even UV) light emission. Groundbreaking research activities during the 1960's and 70's revealed problems related to doping of the materials – an obstacle that proved insurmountable at that time, and inhibited device applications. These problems were commonly attributed to *self-compensation*: the speculation was that formation energies for certain native defects (vacancies, self-interstitials, or antisites) can become very low in these materials, causing the defects to occur in such large quantities that they eliminate the electrical activity of the dopants.

It has recently become clear that self-compensation is not the show-stopping problem it was purported to be. State-of-the-art computations indicate that the formation energies of native defects are of the same magnitude as those in other semiconductors, such as Si or GaAs.^{9,12} Simultaneously, experimental successes in ZnSe and GaN have provided an existence proof for adequate doping levels – squelching the hypothesis that self-compensation

due to native defects would make doping impossible. Nonetheless, doping levels are still limited, and lower than desirable for certain device applications. The cause of conductivity in not-intentionally-doped material, specifically in GaN, is also still being debated. State-of-the-art first-principles calculations can fruitfully contribute to resolving such issues.

We will focus here on calculations for defects and impurities in ZnSe and in GaN, two semiconductors which have recently shown great promise as blue light emitters. We will first briefly review the underlying theoretical formalism and computational approach. In the remainder of the paper, we will discuss how the numerical results for native defects and dopant impurities can be used to understand the various factors that may limit doping, and to provide guidelines on how doping can be controlled or improved.

For ZnSe, we will focus on nitrogen doping, which has proven to be the most efficient way of obtaining *p*-type conductivity. Hole concentrations, however, are still lower than desired, a limitation which has been attributed to various causes, including solubility of the acceptor species¹¹; configurations, other than the substitutional site, assumed by the acceptor^{13,14}; and compensation by native defects, as well as formation of complexes between native defects and the nitrogen acceptor.^{11,15} We will describe our latest results and insights.

For GaN, we will mainly concentrate on the issue of *n*-type conductivity in the as-grown material. This *n*-type behavior has traditionally been attributed to nitrogen vacancies. We find, however, that nitrogen vacancies have a rather high formation energy in *n*-type material; therefore, in thermodynamic equilibrium, their concentration would be very low. We discuss various aspects of this problem, including kinetic limitations, formation of defect complexes or clusters, and doping by unintentional impurities.

FORMALISM

The equilibrium concentration, C , of a defect or impurity in the semiconductor is determined by its formation energy, E_{form} :

$$C = N_{\text{sites}} \exp \left[-\frac{E_{\text{form}}}{kT} \right] \quad (1)$$

where N_{sites} is the appropriate site concentration; e.g., for a substitutional impurity on the Se site in ZnSe, N_{sites} is the number of Se sites, $2.2 \times 10^{22} \text{cm}^{-3}$. Whether the assumption of thermodynamic equilibrium is satisfied or not depends on the mobility of various defects at the temperatures of interest.⁹ For ZnSe, the mobilities of native defects are high enough¹⁶ to justify invoking thermodynamic equilibrium. The mobility of the N vacancy in GaN, and its effect on our assumption, is discussed below. The energy appearing in Eq. (1) is in principle a Gibbs free energy. At the present stage of our work, we are not explicitly calculating vibrational entropies (a computationally very demanding task). Such entropy contributions cancel to some extent,¹⁷ and are small enough not to affect any qualitative conclusions; however, accurate calculations of vibrational entropies are gradually becoming feasible and will no doubt be carried out for various systems in the near future. The effect of entropy is included in an approximate way in the results we will present for ZnSe.

The formation energy of a N acceptor on a substitutional Se site (N_{Se}) in ZnSe is determined by the relative abundance of Zn, Se, and N atoms in the environment in which the crystal is grown. In a thermodynamic context, these abundances are described by the chemical potentials (energies of reservoirs) for the Se and N atoms, μ_{Se} and μ_{N} . The Zn chemical potential is not an independent variable, since the sum of μ_{Zn} and μ_{Se} has to be

constant and equal to the energy of a two-atom unit of ZnSe. Forming a substitutional N_{Se} acceptor requires the addition of one N atom to the crystal and the removal of one Se atom; the formation energy of the nitrogen acceptor in the negative charge state (which the acceptor assumes after donating a hole to the valence band) is therefore

$$E_{\text{form}}(\text{ZnSe}:N_{Se}^-) = \mathcal{E}(\text{ZnSe}:N_{Se}^-) - \mu_N + \mu_{Se} - E_F, \quad (2)$$

where $\mathcal{E}(\text{ZnSe}:N_{Se})$ is the total energy derived from a calculation for substitutional N, and E_F is the position of the Fermi level, which acts as the reservoir for electrons. Equation (2) illustrates the basic form of the expression for the formation energy; the expression is easily generalized to other defects and impurities.^{9,11}

The Se and N chemical potentials are variable parameters; they are, however, subject to the following boundary conditions. The upper limit of the Se chemical potential is given by ZnSe in equilibrium with bulk Se, while the lower limit is for ZnSe in equilibrium with bulk Zn; μ_{Se} can therefore vary over a range given by the heat of formation of ZnSe, ΔH . Following the notation of García and Northrup,¹⁵ a parameter λ is introduced which varies between zero (Zn rich) and one (Se rich):

$$\mu_{Se} = \mu_{Se(\text{bulk})} - (1 - \lambda)\Delta H. \quad (3)$$

To establish an upper bound on the chemical potential of the impurity (nitrogen), one needs to consider which other phases the element can form, either by itself, or in its interactions with the constituents of the host material. In the case of nitrogen, the bounds are due to formation of N_2 molecules, as well as formation of the compound Zn_3N_2 .

The energy $\mathcal{E}(\text{ZnSe}:N_{Se})$ is a quantity which can be obtained from first-principles calculations. Our well-tested approach is based on density-functional theory¹⁸ and *ab initio* pseudopotentials.^{19,20} Pseudopotential-density-functional calculations are commonly carried out with a plane-wave basis set (essentially expanding wave functions, etc., in Fourier series). The strong potential of the first-row element, nitrogen, and the strong localization of the 3d electrons in Zn and in Ga make such an approach challenging: high Fourier components have to be included in the expansions, significantly increasing the size of the matrices in the eigenvalue problem.

For the case of ZnSe, our choice was to use a *mixed basis* approach, in which a modest set of plane waves was supplemented by localized orbitals centered on the Zn atoms.²¹ For GaN, we have returned to the pure plane-wave method, but utilizing more tractable pseudopotentials²⁰ and a highly optimized code.^{22,23} The role of the Ga 3d electrons in GaN was discussed in Ref. [24]. All our calculations are carried out in a supercell geometry; two shells of host atoms around the defect or impurity are relaxed. More details about convergence and other aspects of the calculations can be found in Refs. [12] and [21].

DOPING LIMITS IN NITROGEN-DOPED ZnSe

Our first-principles calculations for $\text{ZnSe}^{9,11,21}$ addressed in detail the atomic and electronic structure of all native defects (isolated point defects), as well as various acceptor impurities (Li, Na, and N). The main conclusions emerging from that work were as follows: (a) The formation energy of all native point defects, for the allowed range of chemical potentials and Fermi-level positions, is high enough (and their concentration low enough) not to cause large amounts of compensation. (b) The acceptor impurities investigated in

our study all have a limited solubility at typical growth temperatures; the calculated trend in the solubilities also agrees with experimental observations of hole concentrations (Na exhibiting very low incorporation, Li rather higher, and N performing best, but still with limited hole concentrations). The calculated difference in solubility of these acceptor impurities in ZnSe versus ZnTe is also in agreement with experiment.^{25,26} (c) Incorporation of Li on interstitial sites (where it acts as a donor) is not a serious problem. We found that growth conditions (chemical potentials) which are optimized to maximize Li incorporation simultaneously minimize the occurrence of Li interstitials. We now elaborate on some of these findings, in light of more recent theoretical as well as experimental work.

The selenium vacancy

In (a) we pointed out that the formation energy of isolated native point defects was high enough for point defects not to pose a serious concern for compensation. In our study⁹ we carefully investigated many defect configurations and host relaxations. Nonetheless, one can never exclude the possibility of an unexpectedly large relaxation or a peculiar defect configuration, which may be overlooked in a standard search. In our original work,⁹ we argued that even if large additional relaxations would occur, they would be unlikely to affect our qualitative conclusions because the estimated relaxation energy²⁷ is small enough, and the formation energy of the unrelaxed defects large enough, not to lead to very small (relaxed) formation energies.

García and Northrup¹⁵ have recently shown that this argument does not hold in the case of the Se vacancy in the +2 charge state (V_{Se}^{2+}). Indeed, they found that the Zn atoms surrounding the Se vacancy move outward by 0.51 Å, lowering the energy by a whopping 1.6 eV. Taking this relaxation into account, García and Northrup found the Se vacancy to be the lowest-energy point defect in ZnSe.

In Ref. [9], such a large relaxation of V_{Se}^{2+} was not taken into account; the formation energy of the *unrelaxed* Se vacancy, under Zn-rich conditions ($\mu_{\text{Zn}} = \mu_{\text{Zn(bulk)}}$), and for a Fermi-level position at the top of the valence band, was found to be 1.87 eV; an estimated relaxation energy of 1.0 eV was then subtracted from this value. We have repeated the first-principles calculation for V_{Se}^{2+} , taking the large lattice relaxation predicted by García and Northrup into account, and find a relaxation energy of 1.58 eV – essentially the same as obtained in Ref. [15]. This relaxation energy lowers the formation energy to 0.29 eV, making the Se vacancy energetically slightly more favorable than the Zn interstitial, which we had previously found to be the dominant point defect.

This formation energy is still higher than the value obtained by García and Northrup.¹⁵ The reason for the discrepancy is not clear at this time. Some differences exist between the computational approaches: García and Northrup have used an approximation (the so-called nonlinear core correction) which allows them to treat the Zn *d* electrons as part of the atomic core, rather than explicitly including them as valence states. In addition, both types of calculations are carried out using density-functional theory in the local-density approximation and hence suffer from the well-known band-gap problem; it is conceivable that the resulting errors in the band positions (of defect levels as well as band edges) affect the formation energies in different ways, depending on whether the *d* electrons are explicitly included or not. More work will be needed to sort out these subtle points.

Irrespective of the discrepancy in the actual value of the formation energy, we agree with García and Northrup that the Se vacancy is the dominant point defect, and may occur in

large enough concentrations to allow experimental observation. [We note that Ando *et al.*²⁸ have reported a deep hole trap which exhibits a strong temperature dependence of the hole capture/emission rates, indicative of a center with large lattice relaxation.] However, we find that it would still not constitute a major form of compensation of the material. García and Northrup¹⁵ have also pointed out that compensation by an isolated point defect such as the Se vacancy may lead to a *reduction* of the hole concentration, but cannot cause a *saturation* of the free carrier concentration.

Complexes between native defects and substitutional acceptors

In our earlier work¹¹ we pointed out that Zn interstitials may form complexes with substitutional nitrogen acceptors. Such complexes are formed if a positive binding energy exists between the native defect and the acceptor; if this binding energy is large enough, the overall formation energy of the complex may be lower than that of the individual point defect. For this to happen, the binding energy of the complex needs to exceed the formation energy of the individual native defect. García and Northrup have addressed this issue for the case of As as the substitutional acceptor.¹⁵ They found that the binding energy of a (V_{Se} -As_{Se}) complex is 0.3 eV – a rather low value, ostensibly due to the fact that the constituents of this complex are only second-nearest neighbors in the lattice. They find, however, that a (Zn_i -As_{Se}) complex has a large binding energy, approximately 1.2 eV.

We have carried out calculations for a (Zn_i -N_{Se}) complex, yielding a binding energy of ~0.6 eV; i.e., not as large as the value obtained in Ref. [15] for (Zn_i -As_{Se}), but large enough to make the (Zn_i -N_{Se}) complex the prime candidate for a compensating center in ZnSe. We note that our own calculations for the (Zn_i -As_{Se}) complex produce a binding energy of 0.6 eV, i.e., the same as for (Zn_i -N_{Se}), and smaller than the value found in Ref. [15].

V_{Se} -N_{Se} complexes have been discussed in the literature; Hauksson *et al.* proposed this complex to explain the compensation observed in their samples.^{29,30} If (Zn_i -N_{Se}) complexes indeed occur in appreciable quantities, it should be possible to detect them experimentally. One possible technique of observation would involve dissociation of the complex, followed by drift of the Zn_i in an electric field – similar to an experiment designed and carried out for complexes between Li interstitial donors and Li_{Zn} acceptors.³¹ The resulting change in the doping profile can be detected in a C-V or small-signal AC-transmittance measurement. Other techniques, such as vibrational-mode spectroscopy, could also be very fruitful.

Compensation due to native-defect complexes

Figure 1 illustrates the dependence of the concentration of the acceptor species and the various compensating centers on the total nitrogen concentration, at 600 K. The nitrogen concentration is changed by varying the nitrogen chemical potential, μ_N , subject to the upper bounds discussed above. The curves are plotted up to the maximum achievable nitrogen concentration (i.e., the solubility limit). In Fig. 1 we also assume that the selenium chemical potential is fixed at the value which optimizes the incorporation of nitrogen on substitutional Se sites (i.e., maximizes the solubility) (see Ref. [11]); this value corresponds to $\lambda = 0.06$ [Eq. (3)], i.e., quite close to the Se-poor (Zn-rich) limit.

The formation energies for the native defects are those derived in Ref. [11]; similar to our previous work, we have included an estimated vibrational entropy of $5 k_B$ for each native defect and native-defect complex (note that, without this entropy contribution, the

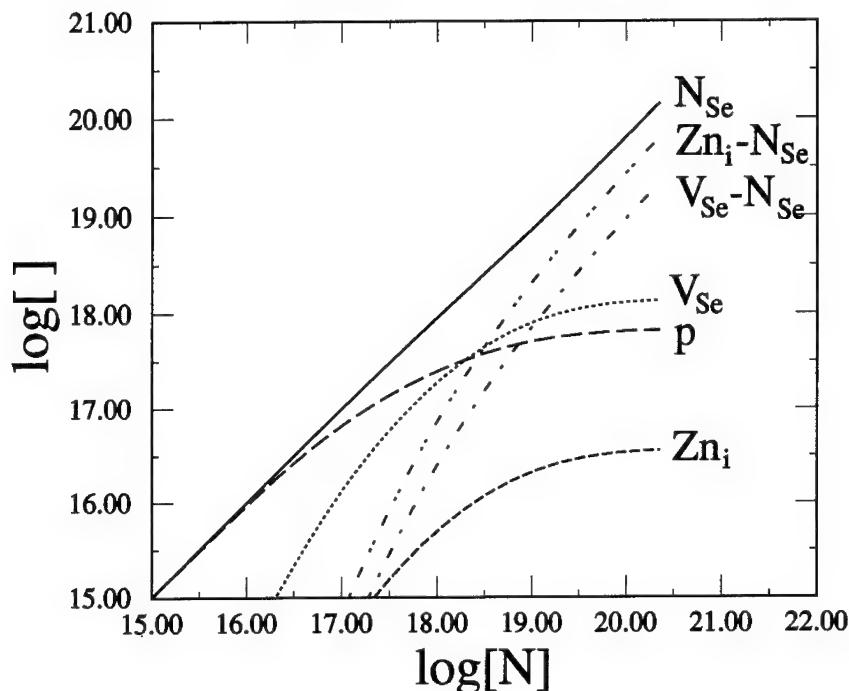


Figure 1:

Concentrations (per cm^3) of various species in N-doped ZnSe, as a function of total nitrogen concentration, at 600 K. The Se chemical potential is chosen to yield maximum solubility of N_{Se} [corresponding to $\lambda = 0.06$, Eq. (3)]. The curves are labeled according to the type of impurity or defect they correspond to; "p" indicates the hole concentration.

concentrations of the compensating defects would be almost two orders of magnitude lower than in Fig. 1). $(\text{Zn}_i\text{-}N_{\text{Se}})$ and $(V_{\text{Se}}\text{-}N_{\text{Se}})$ complexes are also included in Fig. 1, with binding energies of 0.6 eV and 0.3 eV, and appropriate degeneracy factors taking the equivalent geometries of the complexes into account. Note that the concentration of the isolated Zn interstitial is lower than in Fig. 5 of Ref. [11]; the reason is that most interstitials are now bound in $\text{Zn}_i\text{-}N_{\text{Se}}$ complexes. Under the conditions described here, the $\text{Zn}_i\text{-}N_{\text{Se}}$ complexes are the dominant compensating defects, causing a noticeable reduction in the hole concentration, which is also plotted in Fig. 1.

Figure 1 reflects the concentrations of various species at 600 K. If a sample is grown at this temperature, and subsequently cooled to room temperature, the concentrations of the defects may change, because various species (for instance, the Zn interstitial) are quite mobile. The room-temperature concentrations will depend on the mobility of the defects, the binding and dissociation energies of the complexes, and on the cooling rate.

Compensation by $(\text{Zn}_i\text{-}N_{\text{Se}})$ complexes causes the saturation of the hole concentration

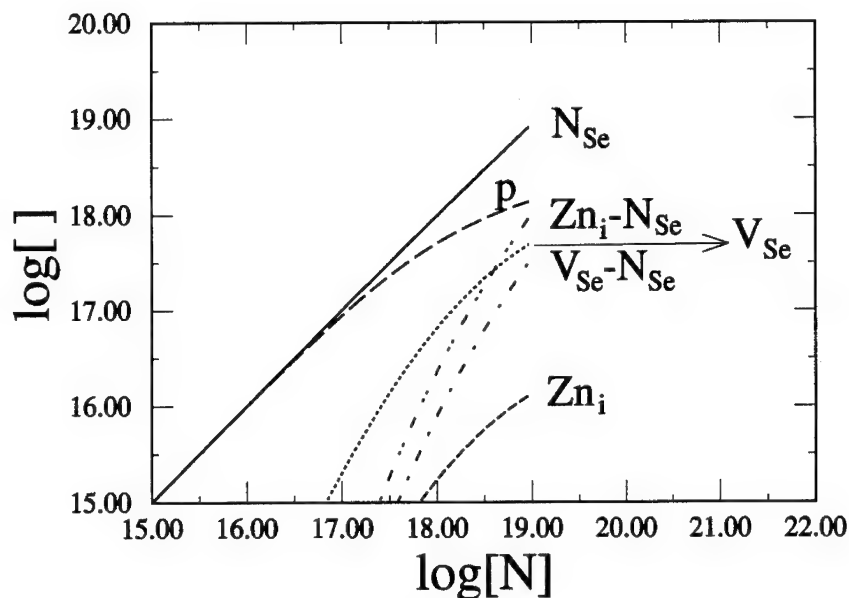


Figure 2:

Same as Fig. 1, except that the Se chemical potential is chosen corresponding to $\lambda = 0.15$.

observed in Fig. 1. Such a saturation of the carrier concentration as the nitrogen concentration is increased has been experimentally observed.^{32,33} However, it bears pointing out that the results displayed in Fig. 1 are quite sensitive to the Se chemical potential (i.e., to the details of the growth conditions). To illustrate this point, Fig. 2 shows the results obtained for a value of the Se chemical potential ($\lambda = 0.15$) which is only slightly different from the choice made in Fig. 1 ($\lambda = 0.06$). Note that the maximum concentration of nitrogen is now lower, since we have moved away from the point of maximum solubility. More importantly, however, note that the concentration of compensating defects has decreased – by as much as an order of magnitude, for similar N concentrations. The hole concentration is correspondingly increased, and no longer saturates at a plateau value.

The fact that the hole concentration is lower than the N_{Se} concentration is not solely due to compensation; because of the high ionization energy (110 meV, Ref. [34]), only a fraction of N_{Se} acceptors are actually ionized, pushing the hole-concentration curve below the N_{Se} curve. It has been suggested³⁵ that during device operation a larger fraction of the N_{Se} acceptors will actually be ionized than expected from purely thermal ionization.

If we continue to increase λ , we find that the degree of compensation is further reduced; at the expense, however, of N incorporation, due to the lower solubility. Our calculations show that if λ is raised above 0.3, the N_{Se} concentration falls below 10^{17} cm^{-3} . The fact that the effects of compensation are reduced as λ is increased (i.e., as the system becomes more Se rich) was also noted in Ref. [15]; however, the values of λ considered in Ref. [15] are *much* greater than in the work presented here. For values of λ as high as discussed

in Ref. [15] we find that the calculated N incorporation would become very low. Garcia and Northrup did not explicitly consider the formation energy of the N_{Se} species, and they allowed incorporation of the acceptor species above the solubility limit. Whether incorporation of the acceptor species occurs under equilibrium or non-equilibrium conditions has not been decisively established. Fan *et al.*³⁶ interpreted their SIMS and transport data on N-doped ZnSe and ZnTe as consistent with the notion of equilibrium incorporation, governed by solubility limits. More investigations are necessary, however.

Nitrogen on interstitial sites and nitrogen antisite defects

The possibility of incorporation of *nitrogen on interstitial* sites has also been raised. In Ref. [11], nitrogen interstitials located on tetrahedral interstitial sites in the lattice were examined and found to be prohibitively high in energy; nitrogen on substitutional Zn sites was similarly found to be unfavorable. These conclusions have been confirmed in recent calculations by Kwak.³⁷ Chadi and Troullier¹³ proposed split-interstitial configurations for nitrogen sharing a substitutional Se site with the Se atom; they did not, however, report energies of these configurations relative to the N_{Se} acceptor. Cheong *et al.*¹⁴ found that, among the configurations they investigated, neutral N_2 molecules would dominate in Se-rich material (in addition to N_{Se} , of course), while in Zn-rich material a split-interstitial complex consisting of two N atoms occupying a Se site would dominate.

Discussion of doping saturation effects

Various groups have published experimental results for carrier concentrations as a function of the total nitrogen concentration in the layer.^{32,33,38} [We presume that the quantity referred to as $N_A - N_D$ in these papers is actually the hole concentration, as measured in C-V measurements. In order to obtain the actual acceptor concentration, a further analysis would need to be carried out, taking into account that, due to the large ionization energy of the N acceptor, only a fraction of the dopants are ionized.] When the nitrogen concentration approaches 10^{18}cm^{-3} , the carrier concentration appears to saturate, and then decreases as $[N]$ is further increased. A saturation in the hole concentration would be consistent with a compensation mechanism, as described above and illustrated, for instance, in Fig. 1. However, a precipitous *decrease* in the carrier concentration for high $[N]$, as observed by Nishikawa *et al.*³² and by DePuydt *et al.*⁴⁰ cannot be attributed to compensation; some other mechanism needs to be invoked.

Kuo *et al.*³⁹ have reported an increase in the density of threading dislocations in ZnSe grown on GaAs substrates when the N concentration exceeds a certain critical value. We have previously suggested²⁵ that this increase is triggered by the fact that the dopant incorporation approaches the solubility limit; excess quantities of the dopant impurity may be incorporated as microprecipitates, which can act as nucleation sites for dislocation loops. This proposed explanation is consistent with the observation by the 3M group that the “critical acceptor concentration”, above which the hole concentration *decreases* (and the crystal quality degrades), depends on the type of acceptor. The measured values are 10^{16} , 10^{18} , 10^{19}cm^{-3} for Na, Li, and N doping, respectively; the trend in these values agrees very well with our calculated solubility limits for these acceptors.

Since the experimental observations reveal a *decrease* in the hole concentration at high acceptor concentrations, it is not clear whether the observed “plateau” in the carrier concen-

tration (around $[N] \approx 10^{18} \text{cm}^{-3}$ for nitrogen) should always be interpreted as a saturation effect that is due to compensation, or rather as the onset of an approaching downturn in the hole concentration. We have pointed out that the occurrence of compensation may also be a rather sensitive function of the growth conditions, as illustrated by Figs. 1 and 2, which differ only by a slightly different choice of Se chemical potential. Plots of carrier concentration vs. dopant incorporation therefore offer, in our opinion, no conclusive evidence regarding compensation. Other experiments, in which compensating defects are actually observed and identified, are required for that purpose. And we emphasize that our results suggest that compensation is not unavoidable – a careful choice of growth conditions can suppress the formation of compensating species.

DEFECTS AND DOPING IN GaN

Native defects

We have calculated the formation energy, as a function of Fermi level and of the atomic chemical potentials, for all native point defects in GaN. In previous work, we have found that the formation energies are largely insensitive to the structure (zincblende vs. wurtzite) of the material.²⁴ The results are displayed in Fig. 3, assuming Ga-rich conditions (which appear to be common in experimental growth situations). We immediately notice that the self-interstitials (Ga_i and N_i) and the antisite defects (N_{Ga} and Ga_{N}) have high formation energies, and are therefore very unlikely to occur in any significant concentration. The vacancies, on the other hand, have lower formation energies. Under conditions of thermodynamic equilibrium, a low formation energy is required for the defect to occur in large concentrations. We will focus here on the vacancy defects; more information about the atomic and electronic structure of all the native defects can be found in Ref. [12].

The nitrogen vacancy

Nitrogen vacancies have commonly been invoked to explain the n -type conductivity of as-grown GaN. Fig. 3 shows that the formation energy of the nitrogen vacancy (V_{N}) is actually quite high in n -type material (Fermi level high in the gap, near the conduction band). In thermodynamic equilibrium, the concentration of nitrogen vacancies should therefore be quite low, and they should not be responsible for the observed n -type conductivity. What about the possibility that incorporation of nitrogen vacancies occurs via a non-equilibrium process? Non-equilibrium implies that the concentration of nitrogen vacancies is prevented from reaching its equilibrium value, i.e., the nitrogen vacancies would be frozen in. This is only possible if the nitrogen species is sufficiently *immobile* to prevent any significant flux of nitrogen between the bulk of the material and a source or sink of nitrogen atoms. It is therefore important to study the diffusion properties.

Several channels can in principle contribute to the diffusion of nitrogen. Nitrogen could diffuse interstitially (and eventually annihilate vacancies); however, the high formation energy of the nitrogen interstitial (see Fig. 3) renders this diffusion mechanism unlikely. The other mechanism involves diffusion of the nitrogen vacancy. We have studied the migration path of the vacancy in detail⁴¹; the saddle point, which determines the height of the migration barrier, occurs for a position of the N atom midway between two vacancies (a so-called split-vacancy structure). The calculated migration barrier is ~ 4 eV, which should allow for

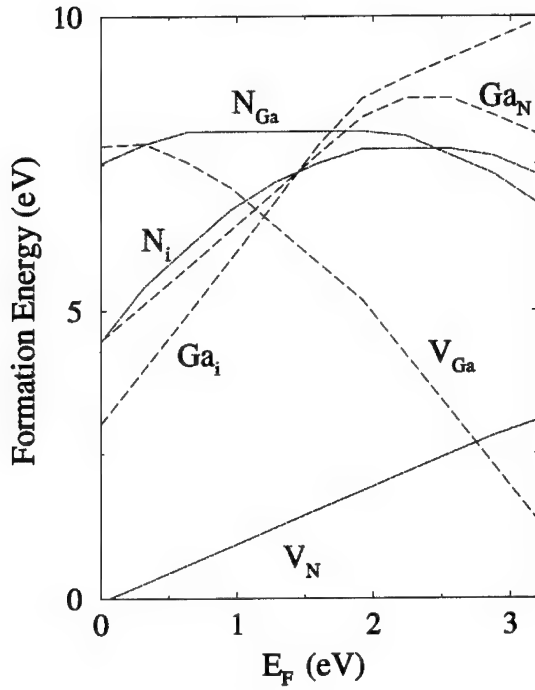


Figure 3:

Defect formation energies as a function of the Fermi level for all native point defects in GaN, under Ga-rich conditions ($\mu_{\text{Ga}} = \mu_{\text{Ga(bulk)}}$). $E_F = 0$ corresponds to the top of the valence band.

vacancy diffusion at the high temperatures at which growth of GaN is carried out. If one can assume efficient transport between the vacancy defects in the bulk and the reservoir of nitrogen atoms, the concentration of N vacancies will be allowed to reach its equilibrium value – which, as stated above, is *low* in *n*-type GaN.

Alternative explanations for the *n*-type conductivity in as-grown GaN

If nitrogen vacancies are not responsible, then what *is* the cause of the observed *n*-type conductivity? First, we stress that our conclusion about nitrogen vacancies applies to *isolated point defects*. It is still possible that a vacancy-related *complex* or *extended defect* is involved, if it acts as a donor. We also propose an alternative explanation for the *n*-type conductivity, namely that it is caused by unintentional incorporation of donor impurities. Silicon, oxygen, and carbon are common contaminants in the systems typically used for growth of GaN. We have performed first-principles calculations for these impurities,⁴² and found that silicon and oxygen indeed behave as donors, and can potentially be incorporated

in high concentrations. Carbon, if it is located on the Ga site (C_{Ga}) also behaves as a donor – however, this site is less favorable than the C_N site, on which C behaves as an acceptor.

Native defects as compensating centers

While we concluded that isolated nitrogen vacancies are unlikely to occur in *n*-type material, Fig. 3 shows that their formation energy is actually very low in *p*-type material. They could, therefore, play a role in compensating acceptors. Similarly, the Ga vacancy may have low enough energy to occur as a compensating center in *n*-type material. We note that our calculations for the Ga vacancy predict a level in the gap slightly more than 1 eV below the conduction band. While our error bars on the position of gap levels are rather large, it is tempting to suggest that the Ga vacancy may be responsible for at least some of the levels that have been experimentally observed in this energy region – and possibly also play a role in the infamous “yellow luminescence.”

In addition, in light of the preceding discussion of native-defect complexes in ZnSe, it is conceivable that complexes between the vacancies and impurities could occur, which could further lower the formation energy. For instance, in Si-doped *n*-type material, (V_{Ga} - Si_{Ga}) complexes might occur; however, given that the constituents of this complex are only second-nearest neighbors, the binding energy may be modest. In Mg-doped *p*-type material, on the other hand, (V_N - Mg_{Ga}) complexes may be formed, in which the constituents occur on neighboring lattice sites, and therefore may be more strongly bound. Our predicted low formation energy of the nitrogen vacancy in *p*-type material would also contribute to the likelihood of formation of such electrically neutral complexes.

ACKNOWLEDGMENTS

One of us (CVDW) gratefully acknowledges collaborations with D. B. Laks and S. T. Pantelides. We thank A. Garcia, N. M. Johnson and J. E. Northrup for useful discussions. This work is supported in part by ARPA and by the DAAD.

REFERENCES

- ¹ G. A. Baraff and M. Schlüter, Phys. Rev. Lett. **41**, 892 (1978).
- ² J. Bernholc, N. O. Lipari, and S. T. Pantelides, Phys. Rev. Lett. **41**, 895 (1978).
- ³ G. A. Baraff and M. Schlüter, Phys. Rev. B **28**, 2296 (1983).
- ⁴ Y. Bar-Yam and J. D. Joannopoulos, Phys. Rev. Lett. **52**, 1129 (1984).
- ⁵ R. Car. P. J. Kelly, A. Oshiyama, and S. T. Pantelides, Phys. Rev. Lett. **54**, 360 (1985).
- ⁶ H. Overhof, M. Scheffler, and C. M. Weinert, Mat. Sci. Forum **38-41**, 293 (1989).
- ⁷ C. G. Van de Walle and P. E. Blöchl, Phys. Rev. B **47**, 4244 (1993).
- ⁸ S. B. Zhang and J. E. Northrup, Phys. Rev. Lett. **67**, 2339 (1991).
- ⁹ D. B. Laks, C. G. Van de Walle, G. F. Neumark, and S. T. Pantelides, Phys. Rev. Lett. **66**, 648 (1991).
- ¹⁰ J. E. Northrup and S. B. Zhang, Phys. Rev. B **47**, 6791 (1993).
- ¹¹ C. G. Van de Walle, D. B. Laks, G. F. Neumark, and S. T. Pantelides, Phys. Rev. B **47**, 9425 (1993).
- ¹² J. Neugebauer and C. G. Van de Walle, Phys. Rev. B **50**, 8067 (1994).

- ¹³ D. J. Chadi and N. Troullier, *Physica B* **185**, 128 (1993).
- ¹⁴ B.-H. Cheong, C. H. Park, and K. J. Chang, to be published.
- ¹⁵ A. García and J. E. Northrup, *Phys. Rev. Lett.* **74**, 1131 (1995).
- ¹⁶ G. D. Watkins, in *Defect Control in Semiconductors*, edited by K. Sumino (Elsevier Science Publishers B. V., Amsterdam, 1990), p. 933.
- ¹⁷ G.-X. Qian, R. M. Martin, and D. J. Chadi, *Phys. Rev. B* **38**, 7649 (1988); N. Chetty and R. M. Martin, *ibid.* **45** 6089 (1992).
- ¹⁸ P. Hohenberg and W. Kohn, *Phys. Rev.* **136**, B864 (1964); W. Kohn and L. J. Sham, *ibid.* **140**, A1133 (1965).
- ¹⁹ D. R. Hamann, M. Schlüter, and C. Chiang, *Phys. Rev. Lett.* **43**, 1494 (1979).
- ²⁰ N. Troullier and J. L. Martins, *Phys. Rev. B* **43**, 1993 (1991).
- ²¹ D. B. Laks, C. G. Van de Walle, G. F. Neumark, P. E. Blöchl, and S. T. Pantelides, *Phys. Rev. B* **45**, 10965 (1992).
- ²² R. Stumpf and M. Scheffler, *Computer Phys. Commun.* **79**, 447 (1994).
- ²³ J. Neugebauer, to be published.
- ²⁴ J. Neugebauer and C. G. Van de Walle, in *Diamond, SiC and Nitride Wide Bandgap Semiconductors*, edited by C. H. Carter Jr., G. Gildenblat, S. Nakamura, and R. J. Nemanich, Materials Research Society Symposia Proceedings, Vol. 339 (Materials Research Society, Pittsburgh, Pennsylvania), p. 687.
- ²⁵ D. B. Laks, C. G. Van de Walle, G. F. Neumark, and S. T. Pantelides, *Appl. Phys. Lett.* **63**, 1375 (1993).
- ²⁶ C. G. Van de Walle and D. B. Laks, *Solid State Communications* **93**, 447 (1995).
- ²⁷ We estimated that relaxation energies would not exceed 1 eV.
- ²⁸ K. Ando, Y. Kawaguchi, T. Ohno, A. Ohki, and S. Zembutsu, *Appl. Phys. Lett.* **63**, 191 (1993).
- ²⁹ I. S. Hauksson, J. Simpson, S. Y. Wang, K. A. Prior, and B. C. Cavenett, *Appl. Phys. Lett.* **61**, 2208 (1992).
- ³⁰ B. N. Murdin, B. C. Cavenett, C. R. Pidgeon, J. Simpson, I. S. Hauksson, and K. A. Prior, *Appl. Phys. Lett.* **63**, 2411 (1993).
- ³¹ T. Marshall, *Physica B* **185**, 433 (1993).
- ³² Y. Nishikawa, M. Ishikawa, S. Saito, and G. Hatakoshi, *Jpn. J. Appl. Phys.* **33**, L361 (1994).
- ³³ S. Ito, M. Ikeda, and K. Akimoto, *Jpn. J. Appl. Phys.* **31**, L1316 (1992).
- ³⁴ K. Shahzad, B. A. Khan, D. J. Olego, and D. A. Cammack, *Phys. Rev. B* **42**, 11 240 (1990).
- ³⁵ P. M. Mensz, *J. Cryst. Growth*, **138**, 697 (1994).
- ³⁶ Y. Fan, J. Han, L. He, R. L. Gunshor, M. S. Brandt, J. Walker, N. M. Johnson, and A. V. Nurmikko, *Appl. Phys. Lett.* **65**, 1001 (1994).
- ³⁷ K. W. Kwak, D. Vanderbilt, and R. D. King-Smith, submitted to *Phys. Rev. B*.
- ³⁸ J. Qiu, J. M. DePuydt, H. Cheng, and M. A. Haase, *Appl. Phys. Lett.* **59**, 2992 (1991).
- ³⁹ L. H. Kuo, L. Salamanca-Riba, J. M. DePuydt, H. Cheng, and J. Qiu, *Appl. Phys. Lett.* **63**, 3197 (1993).
- ⁴⁰ J. M. DePuydt, private communication.
- ⁴¹ J. Neugebauer and C. G. Van de Walle, to be published.
- ⁴² J. Neugebauer and C. G. Van de Walle, in *Proceedings of the 22th International Conference on the Physics of Semiconductors*, Vancouver, 1994 (World Scientific Publishing Co Pte Ltd., Singapore), p. 2327.

THE ROLE OF IMPURITIES IN HYDRIDE VAPOR PHASE EPITAXIALLY GROWN GALLIUM NITRIDE

R. J. Molnar, K.B. Nichols, P. Maki, E.R. Brown and I. Melngailis
Massachusetts Institute of Technology, Lincoln Laboratory, Lexington, MA 02173-9108

ABSTRACT

Gallium nitride (GaN) films grown by hydride vapor phase epitaxy on a variety of substrates have been investigated to study what role silicon and oxygen impurities play in determining the residual donor levels found in these films. Secondary ion mass spectroscopy analysis has been performed on these films and impurity levels have been normalized to ion implanted calibration standards. While oxygen appears to be a predominate impurity in all of the films, in many of them the sum of silicon and oxygen levels is insufficient to account for the donor concentration determined by Hall measurements. This suggests that either another impurity or a native defect is at least partly responsible for the autodoping of GaN. Additionally, the variation of impurity and carrier concentration with surface orientation and/or nucleation density suggests either a crystallographic or defect-related incorporation mechanism.

INTRODUCTION

Recently, hydride vapor phase epitaxy (HVPE) of gallium nitride (GaN) has regained attention, primarily as a quasi-bulk technique to grow thick, free-standing films for use as substrates in the growth of device structures by other techniques, such as metalorganic vapor phase epitaxy (MOVPE) or molecular beam epitaxy (MBE)¹. While the literature is rich with studies of this growth technique, there has been wide speculation as to the origin of the residual donors in these films. Maruska and Tietjen speculated that these residual donors might be nitrogen vacancy native defects². While it has been subsequently shown both experimentally³ and theoretically⁴ that nitrogen vacancies are not likely, defect aggregates, possibly involving such a vacancy, cannot be ruled out.

Of course, a very important question is whether the residual donors in GaN (as well as InGaN) films can be completely accounted for by impurities. For example, it has been observed in the HVPE growth of Al-bearing films that strong exchange reactions between AlCl compounds and quartz reactor walls result in extremely high Si and O concentrations in films⁵. It is possible that, at the elevated temperatures (~1100°C) used in the growth of GaN, similar reactions could take place with GaCl compounds. Illegems and Montgomery⁶ have reported that impurity levels in their films were insufficient to completely account for the residual donors in their HVPE-grown films. However, their analytical methods, namely, spark source spectroscopy or uncalibrated secondary ion mass spectroscopy (SIMS), were not effective in accurately determining the impurities in these films, particularly for oxygen, which is known to act as a donor in GaN⁷. In this paper, therefore, we have investigated the residual donors in GaN films by Hall measurements as well as the concentration of suspected donors, i.e., silicon and oxygen, by calibrated SIMS analysis. Our results show that while oxygen is a predominate impurity, the sum of silicon and oxygen levels in many of the films is insufficient to account for the donor concentration observed in these films. In fact, the rather large ionization energy of oxygen donors (~78 meV)⁷ as well as compensation expected in such films strengthen the argument that the electron transport properties of GaN are at least partly determined by an as yet unidentified donor, either an impurity or native defect. Our results are consistent with the literature in suggesting that the incorporation of this defect as well as impurities such as oxygen and silicon is intimately related to the growth conditions, particularly during heteronucleation.

EXPERIMENTAL

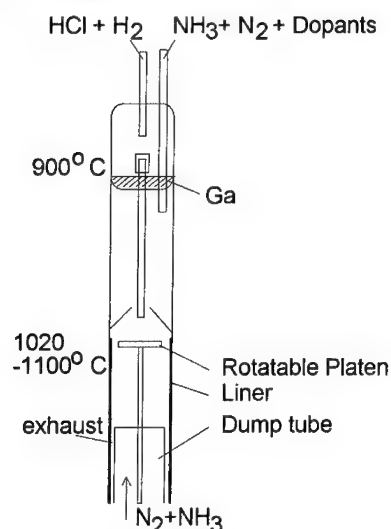


Figure 1-Schematic of HVPE reactor.

2000 sccm N_2 (main carrier). Under such conditions, growth rates of ~ 30 - $50 \mu\text{m/h}$ are typical depending on substrate position.

The surface morphology was investigated by both optical and electron microscopy. The films grown directly on (0001) Al_2O_3 exhibited a faceted hillock structure, as shown in Figure 2(a-d). The surfaces of these hillocks were defined predominately by $\{1\bar{1}01\}$ planes which gave way to (0001)-truncated surfaces with increasing growth temperature or decreasing growth rate, as has been observed in GaN films grown by MOVPE⁸. Additionally, by utilizing GaCl pretreatment methods described by Naniwae et al.⁹, we have been able to obtain smooth, featureless surfaces, as shown in Figure 3. These optically transparent films were determined to be single crystals by X-ray diffraction (XRD) with a high degree of internal cracking due to thermal stress at the GaN/ Al_2O_3 interface.

The films in this study were grown by a modified version of the chloride-transport HVPE process described by Maruska and Tietjen². In this process the Ga precursor is synthesized upstream in the reactor via a reaction of HCl gas (in an H_2 diluent) with Ga metal (at 900°C) to form GaCl. This precursor is then transported to the substrate area where it is mixed with NH_3 (in an N_2 carrier) to form GaN (at $\sim 1100^\circ\text{C}$). Our reactor differs from Maruska's in that the growth tube is arranged vertically to allow rotation of the substrate during growth to improve uniformity. Additionally, we have provisions to lower the substrate platen isothermally into a dump tube in which we counterflow NH_3 in a N_2 carrier (see Figure 1). This allows us to abruptly interrupt the growth and either change and equilibrate the flow of gas species in the main tube or slowly cool the substrate by further lowering the platen at the end of the growth. Typical flow rates in our system are 5 sccm HCl; 450 sccm NH_3 ; 100 sccm H_2 (HCl diluent); and

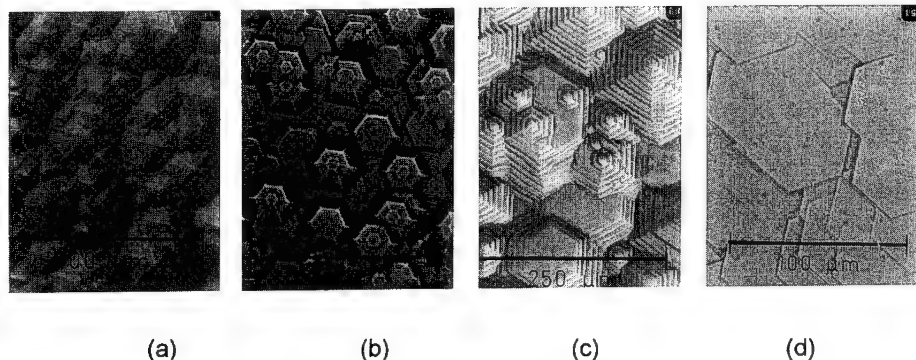


Figure 2 - Various surface morphologies obtained on (0001) Al_2O_3 .

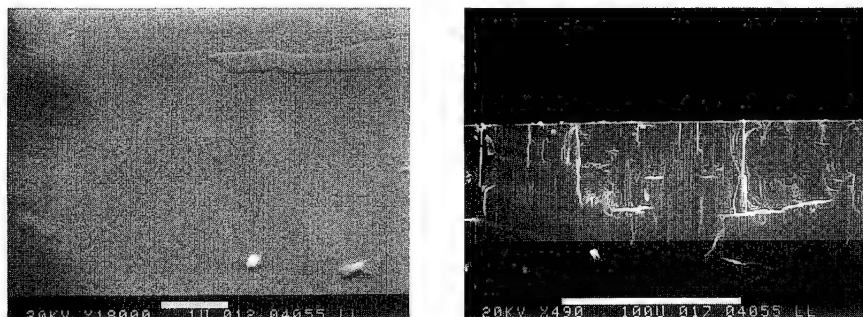


Figure 3 - Scanning electron micrographs of surface morphology and cross section of GaN film deposited using GaCl pretreatment.

In addition to the growth directly on (0001) Al_2O_3 , we have investigated the use of sputtered ZnO buffer layers as reported by Detchprohm et al.¹ The films were deposited in an RF sputtering system with a 5 in. diameter cathode, a 1:1 mixture of O_2 and Ar at 20 mT and RF power levels of 200 W. Reflection high energy electron diffraction patterns obtained from such buffers show a high degree of in-plane orientation with noticeable twinning, as shown in Figure 4. GaN films deposited on these buffers exhibit uniform film growth with large, low-angle hillocks indicative of a high lateral growth rate, as shown in Figure 5(a). Additionally, a small number of these hillocks (<5%) show spiral growth emanating from screw dislocations, as shown in Figure 5(b). To our knowledge, this is the first report of such defects observed in GaN. The dimensions of these features again indicate the high lateral growth rate.

We also investigated several other orientations of sapphire, namely the $(1\bar{1}00)$ and $(11\bar{2}0)$ planes, as well as (0001) off-axis Si-faced SiC substrates. For GaN films deposited on the $(1\bar{1}00)$ plane of Al_2O_3 , XRD indicate them to be monocrystalline and $(1\bar{1}03)$ oriented, similar to that reported by Hwang et al.¹⁰ The GaN films grown on $(11\bar{2}0)$ Al_2O_3 surfaces show (0001) orientation, as is commonly observed. The surface morphologies of these films are represented in Figure 6. It is interesting to note that while (0001) oriented GaN grown on (0001) Al_2O_3 , ZnO and SiC or $(11\bar{2}0)$ Al_2O_3 showed thermally induced cracking originating from the substrate/GaN interface, the GaN film grown on the $(1\bar{1}00)$ Al_2O_3 substrate did not. This may account for the somewhat higher mobility obtained for this orientation, as listed in Table I.

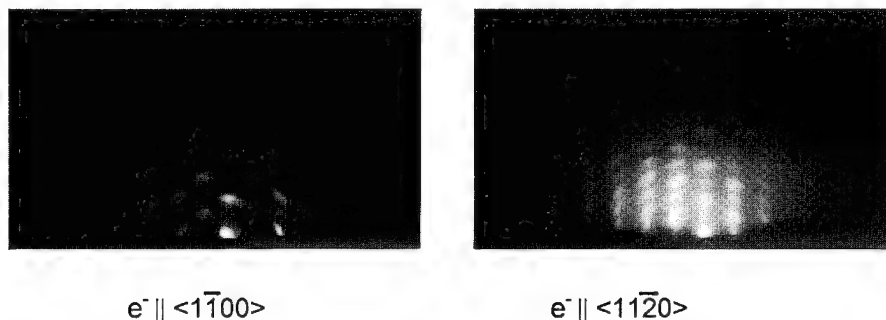


Figure 4 - Reflection high energy electron diffraction pattern obtained from ZnO buffer.

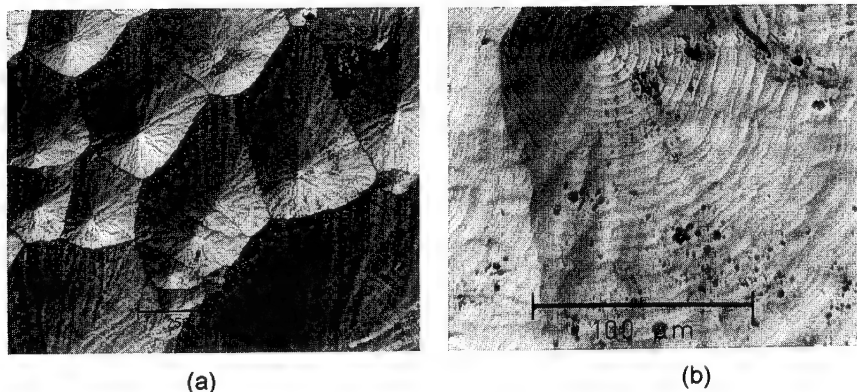


Figure 5 - Surface morphology of GaN films deposited on ZnO buffer.

The van der Pauw geometry was used to investigate the transport properties of the films. Rectangular pieces, ~5 mm on edge, were contacted with In solder and measured at room temperature in a magnetic field of 0.5 T and with a test current of 10 mA. For the sample shown in Figure 3, the severity of the thermal cracking led to excessive asymmetry in the measurements prohibiting accurate determination of the transport properties. However, the ability to readily form rectifying tungsten contacts with high breakdown voltage (~200 V) on this material suggests that the films are nondegenerate. Impurities levels in these films were determined by SIMS analysis using a Cs sputter beam and comparing signal levels with those obtained from ion-implanted GaN calibration standards¹¹. It is reasonable to expect that impurity concentrations determined by such normalization are accurate to within a factor of two. Table I shows the transport properties and impurity concentrations for Si, O and C as well as several other common impurities in the HVPE GaN films. A \leq sign indicates that impurity levels were at or below the detection limit indicated. For comparison, we have also indicated the results of SIMS analysis on an electron cyclotron resonance (ECR) plasma assisted MBE grown GaN film from our group. This sample was grown directly on (0001) Al_2O_3 in a similar fashion to Molnar et al.¹² except for the liner of the plasma source in this case being fabricated from pyrolytic boron nitride.

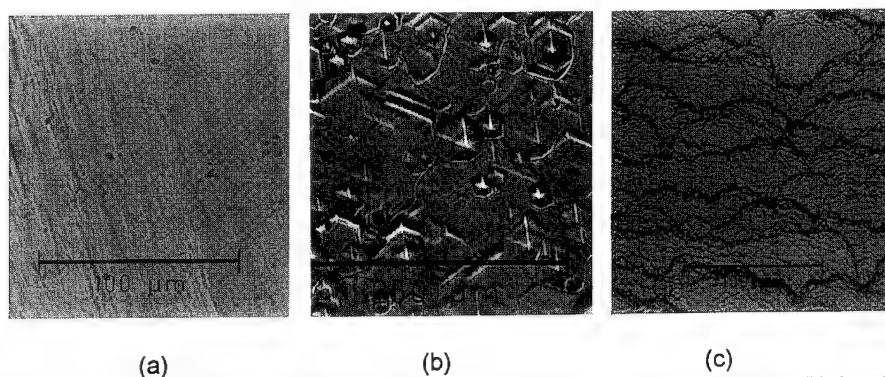


Figure 6 - Typical surface morphology for GaN films deposited on (a) (1100) Al_2O_3 , (b) (1120) Al_2O_3 and (c) (0001) SiC.

Table 1 - Material parameters of GaN films obtained from Hall and SIMS measurements.

Substrate	Growth Method	μ (cm ² /V.s)	n (cm ⁻³)	SIMS Impurity Concentration (cm ⁻³)					
				Si	O	C	H	Cl	F
(0001) Al ₂ O ₃	HVPE	124	1.0x10 ¹⁹	3x10 ¹⁷	3x10 ¹⁸	2x10 ¹⁶	7x10 ¹⁷	2x10 ¹⁶	≤1x10 ¹⁵
(0001) Al ₂ O ₃	HVPE	57	3.7x10 ¹⁸	4x10 ¹⁵	5x10 ¹⁷	≤5x10 ¹⁵	8x10 ¹⁶	2x10 ¹⁶	≤4x10 ¹⁴
(11 $\bar{2}$ 0) Al ₂ O ₃	HVPE	44	4.6x10 ¹⁷	≤3x10 ¹⁵	5x10 ¹⁷	≤5x10 ¹⁵	4x10 ¹⁸	2x10 ¹⁷	≤4x10 ¹⁴
(1 $\bar{1}$ 00) Al ₂ O ₃	HVPE	156	1.5x10 ¹⁸	8x10 ¹⁵	2x10 ¹⁸	≤2x10 ¹⁶	2x10 ¹⁷	≤7x10 ¹⁵	≤1x10 ¹⁵
(0001) ZnO	HVPE	93	1.7x10 ¹⁷	≤4x10 ¹⁵	2x10 ¹⁶	≤5x10 ¹⁵	3x10 ¹⁷	1x10 ¹⁷	≤4x10 ¹⁴
(0001) SiC	HVPE	125	1.6x10 ¹⁹	4x10 ¹⁶	1x10 ¹⁸	2x10 ¹⁶	2x10 ¹⁷	1x10 ¹⁶	≤6x10 ¹⁴
(0001) Al ₂ O ₃	ECR-MBE	270	2.5x10 ¹⁷	≤2x10 ¹⁵	2x10 ¹⁸	4x10 ¹⁶	4x10 ¹⁹	4x10 ¹⁵	7x10 ¹⁵

DISCUSSION

It is clear from the SIMS data that the HVPE films typically show low levels of carbon impurities, in many cases below the detection limit. This is likely the result of the high purity of the source materials, the extremely high growth rate and the inherent lack of hydrocarbon radicals in the Ga precursor, in contrast with MOVPE. This may also explain why HVPE GaN typically shows lower carrier compensation than material grown by other methods. The predominate impurity appears to be oxygen. While the source of this impurity is not yet known, reduction of the quartz cannot be ruled out. In films where dense, uniform nucleation is achieved, as is the case for the film grown on sputtered ZnO, the incorporation of impurities as well as residual donors is reduced. In fact, the film grown on the ZnO buffer shows oxygen and donor levels about a factor of ten lower than the other samples investigated. This is surprising in light of the inherent thermal instability of the ZnO buffer.

For convenience, the data of Table I is plotted in Figure 7 as the sum of suspected donor impurities (Si and O) vs room temperature carrier concentration. It is clear from the data that the residual donor levels, in at least some of these films, cannot be accounted for by the sum of the silicon and oxygen levels, even if one were to assume that these defects were completely ionized at room temperature. The data does, however, suggest that the incorporation of these impurities in the films is correlated with the growth conditions in similar ways as the undetermined donor. In particular, the nucleation and surface crystallography appear to play predominant roles in impurity incorporation, either through a crystallographic or defect-mediated process. Finally, it is important to note that, for the sample grown by ECR-MBE, the reduction in Si and O over those reported previously¹³ reinforces the notion that the quartz liner used in the previous study was a source of impurities in the GaN films.

CONCLUSIONS

GaN films have been grown by HVPE. The role that impurities play in determining the electronic properties of these films has been investigated. In particular, the levels of Si and O in some of the films was found to be insufficient to account for the observed donor concentrations.

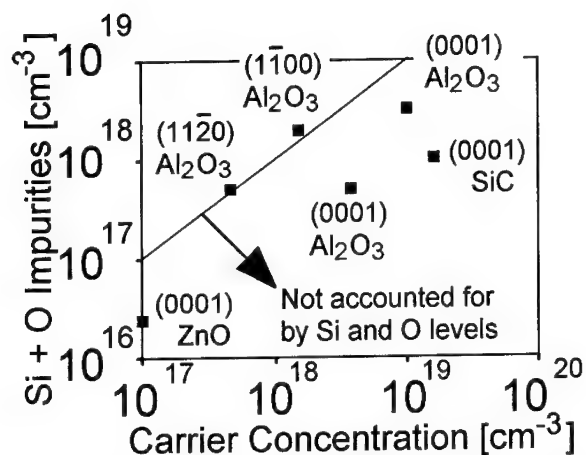


Figure 7 - SIMS O + Si levels vs carrier concentration for HVPE films investigated.

This suggests that either a native defect or undetermined impurity is at least partially responsible for the observed autodoping behavior in GaN.

ACKNOWLEDGEMENTS

The authors gratefully acknowledge the technical assistance of D. Hovey, R. Murphy, G. Iseler, C. Hoyt, R. Aggarwal and D. Calawa. This work is supported by the United States Air Force. Opinions, interpretations, conclusions and recommendations are those of the authors and are not necessarily endorsed by the United States Air Force.

REFERENCES

- ¹ T. Detchprohm, K. Hiramatsu, H. Amano and I. Akasaki, *Appl. Phys. Lett.* **61**, 2688 (1992).
- ² H.P. Maruska and J.J. Tietjen, *Appl. Phys. Lett.* **15**, 327 (1969).
- ³ W. Seifert, R. Franzheld, E. Butter, H. Sobotta and V. Riede, *Cryst. Res. Technol.* **18**, 383 (1983).
- ⁴ J. Neugebauer and C.G. Van de Walle, *Phys. Rev. B* **50**, 8067 (1994).
- ⁵ B. Baranov, L. Däweritz, V.B. Gutan, G. Jungk, H. Neumann and H. Raidt, *Phys. Status Solid. A* **49**, 629 (1978).
- ⁶ M. Ilegems and H.C. Montgomery, *J. Phys. Chem. Solids* **34**, 885 (1973).
- ⁷ B.C. Chung and M. Gershenson, *J. Appl. Phys.* **72**, 651 (1992).
- ⁸ T. Sasaki, *J. Cryst. Growth* **129**, 81 (1993).
- ⁹ K. Naniwae, S. Itoh, H. Amano, K. Itoh, K. Hiramatsu and I. Akasaki, *J. Cryst. Growth* **99**, 381 (1990).
- ¹⁰ J.S. Hwang, A.V. Kuznetsov, S.S. Lee, H.S. Kim, J.G. Choi and P.J. Chong, *J. Cryst. Growth* **142**, 5 (1994).
- ¹¹ Work was performed at Charles Evans and Associates, West, Job # 47916.
- ¹² R. J. Molnar, R. Singh and T.D. Moustakas, *J. Electron. Mater.* **24**, 275 (1995).
- ¹³ R.J. Molnar and T.D. Moustakas, *J. Appl. Phys.* **76**, 4587 (1994).

HIGH RESISTIVITY InAlN BY NITROGEN OR OXYGEN IMPLANTATION

J. C. ZOLPER,^a S. J. PEARTON,^b C. R. ABERNATHY,^b and C. B. VARTULI^b

^aSandia National Laboratories, Albuquerque, NM 87185-0603,

^bUniversity of Florida, Department of Materials Science and Engineering,
Gainesville, FL 32611

ABSTRACT

We report on the isolation properties of $\text{In}_{0.75}\text{Al}_{0.25}\text{N}$ implanted with either N or O for several doses and post-implant anneal temperatures. Sheet resistance versus anneal temperature data are reported for the various implants with a maximum sheet resistance of $\sim 1 \times 10^9 \Omega/\square$ achieved for a high dose N-implant annealed at 600 or 700 °C and $\sim 5 \times 10^8 \Omega/\square$ achieved for a high dose O-implant annealed at 600 °C. These sheet resistances correspond to a greater than three order of magnitude increase over the as-grown values. The compensating defect level for the highest resistance N-implanted sample has an estimate ionization level 580 meV below the conduction band edge. Implant isolation of InAlN is also compared to oxygen implant isolation of $\text{In}_x\text{Ga}_{1-x}\text{N}$ -- where only a 50 to 100 fold increase in sheet resistance is observed -- to study the effect of Al in the isolation scheme.

INTRODUCTION

The III-V nitride-containing semiconductors InN, GaN, and AlN and their ternary alloys are attracting renewed interest for application to visible light emitters^{1,2} and as the basis for high temperature electronics.³⁻⁵ Their attractive material properties include bandgaps ranging from 1.9 eV (InN) to 6.2 eV (AlN), an energy gap ($E_g(\text{GaN}) = 3.39 \text{ eV}$) matched to the short wavelength region of the visible spectrum, high breakdown fields, and relatively high carrier mobilities.⁶ For heterostructure field effect transistors (HFETs) and heterostructure LEDs and lasers, Al-containing ternaries should play a role as a barrier or modulation doping layer. In addition, for HFET structures, thermally stable implant isolation of the Al-containing layer will be desirable.

There have been limited reports of the implantation properties of the III-V nitrides or, in particular, the isolation properties of In-containing III-V nitrides. Early work by Pankove⁷ focused on the optical properties of GaN implanted with an array of elements while Khan investigated the implantation of Be or N in GaN⁸ and AlGa⁹ to improve Schottky barrier characteristics. For In-containing material the first report of their isolation properties was for F-implant $\text{In}_{0.37}\text{Ga}_{0.63}\text{N}$ and $\text{In}_{0.75}\text{Al}_{0.25}\text{N}$ for one dose.¹⁰ The F-implanted InAlN showed roughly a factor of 10 increase in sheet resistance to $\sim 5 \times 10^6 \Omega/\square$ after implantation and annealing at 500 °C while the InGa⁹ displayed a similar trend but with a slightly lower peak sheet resistance. More recently, the isolation properties of a range of In-fractions of InGa⁹ has been reported for both F, N, and O implantation at several doses.^{11,12} In addition, implant isolation of p- and n-type GaN by N-implantation has also recently been demonstrated.¹³

To further understand the ion/defect interaction in InAlN, we have studied the isolation properties of $\text{In}_{0.75}\text{Al}_{0.25}\text{N}$ implanted with either N or O for several doses and post-implant anneal temperatures. Both N and O implantation are candidates for forming thermally stable, chemically active, isolation in InAlN for two reasons. First, for N-implantation, a reduction in N-vacancies should reduce the as-grown conduction that is widely attributed to excess N-vacancies. Second, for O-implantation, an Al-O complex may be formed as is thought to occur in O-implanted AlGaAs.^{14,15,16}

EXPERIMENTAL

The $\text{In}_{0.75}\text{Al}_{0.25}\text{N}$ was grown by Electron Cyclotron Resonance Metal-Organic Molecular Beam Epitaxy (ECR-MOMBE) on (100) semi-insulating GaAs substrates. The group III sources were trimethylindium (TMI) and trimethylamine alane (TMAA) with atomic nitrogen generated by a 200 W, 2.45 GHz electron cyclotron resonance source (Wavemat MPDR).¹⁷ 75% InN was selected for the study since below 50% InN, as shown in Fig. 1, the layers are highly resistive. The samples are unintentionally doped with an electron concentration, as determined by room temperature Hall measurements, of $2 \times 10^{18} \text{ cm}^{-3}$ that is most likely attributable to N-vacancies or other chemical impurities (e. g. O or Si).¹⁸ Implants were performed using multiple energies to achieve an approximately uniform ion and damage profile throughout the epitaxial InAlN thickness of $\sim 440 \text{ nm}$. Both O and N ions were implanted at two dose schedules: 1) medium dose (dose at 40 keV = $5 \times 10^{13} \text{ cm}^{-2}$ with a corresponding ion peak concentration (N_p) equal to $8\text{--}10 \times 10^{18} \text{ cm}^{-3}$) and 2) high dose (dose at 40 keV = $5 \times 10^{14} \text{ cm}^{-2}$ with a corresponding $N_p \approx 8\text{--}10 \times 10^{19} \text{ cm}^{-3}$). Figure 2 shows the calculated ion profile using TRIM92¹⁹ for a medium dose N-implantation scheme. The samples were then annealed in a SiC coated graphite crucible in flowing Ar for 15 s. Pd/Au contacts were evaporated on the samples corners and room temperature Hall measurements were performed.

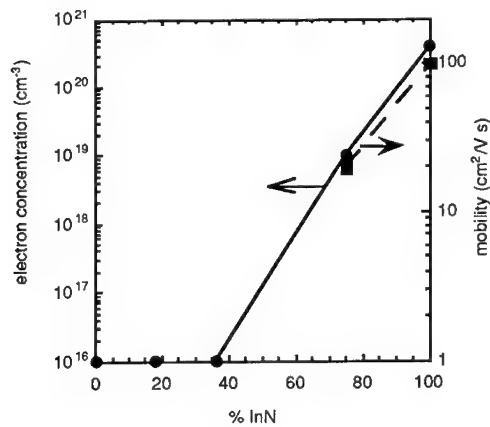


Figure 1: Electron concentration and mobility versus percent indium in $\text{In}_x\text{Al}_{1-x}\text{N}$ grown on SI-GaAs by ECR-MOMBE.

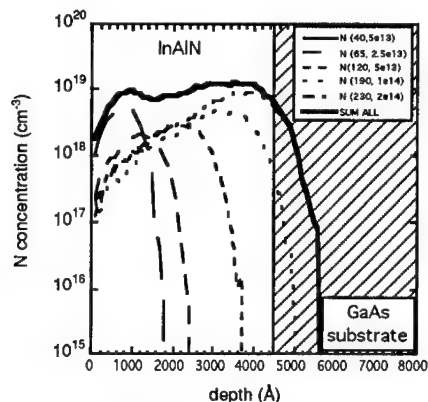


Figure 2: Example of the multiple energy implantation schemes used to achieve a nominally uniform ion and damage profile throughout the epitaxial InAlN layer. The profiles are for a medium dose N-implantation scheme (base dose = $5 \times 10^{13} \text{ cm}^{-3}$ at 40 keV, $N_p \approx 8 \cdot 10 \times 10^{18} \text{ cm}^{-3}$) as calculated with TRIM92.¹⁹

RESULTS AND DISCUSSION

Figure 3(a,b) shows the sheet resistance versus anneal temperature of the InAlN samples implanted with O (Fig. 3.a) or N (Fig. 3.b) at a medium or high dose. As noted on the figure, the as-grown resistivity was $\sim 1 \times 10^5 \Omega/\square$ with the high dose O-implanted sample achieving sheet resistances of $\sim 5 \times 10^8 \Omega/\square$ after a 600 °C anneal and the high dose N-implanted sample achieving a sheet resistance of $\sim 1 \times 10^9 \Omega/\square$ after a 700 °C anneal. This greater than 3 order of magnitude increase in sheet resistance for both O and N-implantation is in contrast to the roughly one order of magnitude increase reported for F-implanted $\text{In}_{0.75}\text{Al}_{0.25}\text{N}$ after a 500 °C anneal.¹⁰ The higher level of compensation achieved here may be a result of the lower initial carrier concentration in our material ($\sim 2 \times 10^{18} \text{ cm}^{-3}$) compared to that reported in the F-implanted material ($7.3 \times 10^{18} \text{ cm}^{-3}$) or indicate some degree of species dependent (chemical) compensation. The increase in p_s achieved here for InAlN is significantly higher than the 50-100 fold increase seen in F- and N-implanted InGaN as reported in ref. 11 or in O-implanted $\text{In}_{0.5}\text{Ga}_{0.5}\text{N}$ as seen in Fig. 4 and reported in more detail in ref. 12. The different compensation properties seen for InGaN and InAlN suggests a different ion/defect interaction in the Al-containing nitride than the Ga-containing nitride.

To examine the reduction of p_s beyond 700 °C extensive surface morphology and compositional analysis was performed using Auger electron spectroscopy (AES), Energy Dispersion Analysis by X-ray (EDAX), Scanning Electron Microscopy (SEM), Atomic Force Microscopy (AFM), and Hall measurements on unimplanted InAlN samples. The details of this study will be published elsewhere,²⁰ but several key points are summarized here. SEM micrographs of samples annealed at 800 °C and above showed evidence of In droplet formation on the surface. The composition of the droplets was confirmed as being primarily indium by performing EDAX on individual droplets. Samples annealed at 1000 °C also showed N loss as determined by AES. The combination of nitrogen loss and indium

segregation to the surface may contribute to the reduction in ρ_s seen in Fig. 3 for the higher temperature anneals and is the focus of additional studies.²⁰

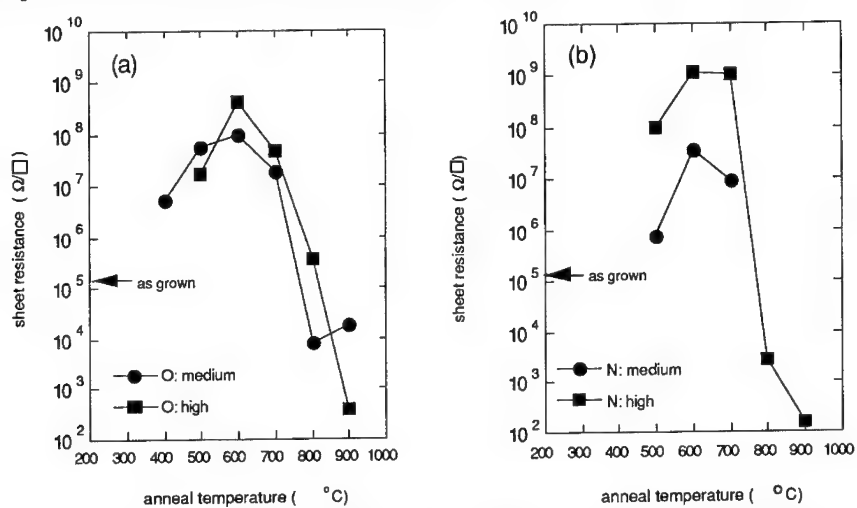


Figure 3: Sheet resistance versus anneal temperature for medium and high dose (a) oxygen and (b) nitrogen implants in $\text{In}_{0.75}\text{Al}_{0.25}\text{N}$.

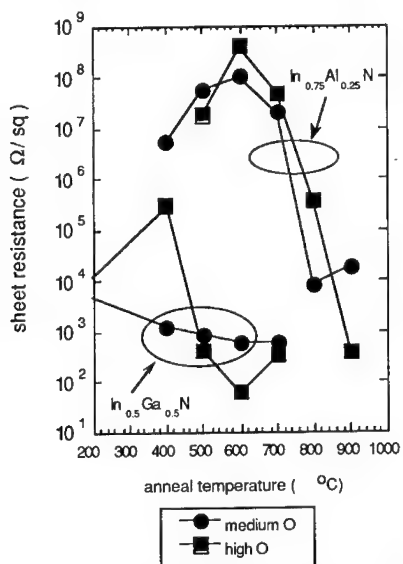


Figure 4: Sheet resistance versus anneal temperature for medium and high dose O-implanted $\text{In}_{0.5}\text{Ga}_{0.5}\text{N}$ and $\text{In}_{0.75}\text{Al}_{0.25}\text{N}$. The as-grown sheet resistances were $\sim 1 \times 10^5$ and $1 \times 10^4 \Omega/\square$ for InAlN and InGaN , respectively.

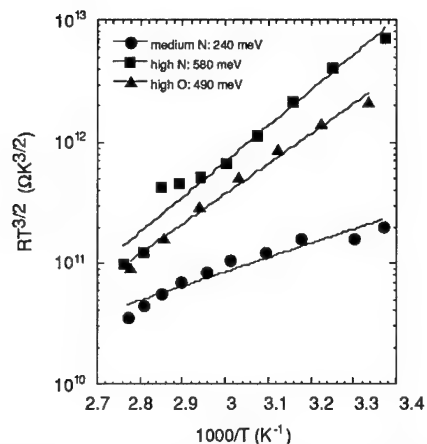


Figure 5: Arrhenius plot of the resistance/temperature product for estimating the ionization level of the compensating defect in medium and high dose N-implanted and high dose O-implanted InAlN after a 600 °C anneal. The levels are estimated as being 240, 580, and 490 meV below the conduction band edge, respectively, for the three samples.

To further probe the nature of the compensating defect, variable temperature Hall measurements were performed. Figure 5 is an Arrhenius plot of the sheet resistance/temperature product, from which the defect ionization level can be estimated, for the highest resistivity medium and high dose N-implanted samples and the high dose O-implanted sample annealed at 600 °C. The ionization energy for electrons from the defect level into the conduction band is estimated as 240 meV for the medium dose N-implanted sample, 580 meV for the high dose N-implanted sample, and 490 meV for the high dose O-implanted sample. These levels are high in the energy gap of $\text{In}_{0.75}\text{Al}_{0.25}\text{N}$ ($E_g \approx 2.51$ eV²¹) which is not optimum for realizing high resistivity material but is more typical of implant isolation in n-type InP and InGaAs.²² These levels are, however, sufficiently deep to achieve highly compensated, high resistivity InAlN as seen in Fig. 3. The fact that there is a dose dependence of the ionization levels may result from the existence of multiple defect states (e.g. damage related levels and chemical complex related levels).

CONCLUSION

The key results of this work can be summarized as follows:

1. Both O- and N-implantation are effective in realizing high resistivity ($\rho_s \geq 5 \times 10^8 \Omega/\square$) $\text{In}_{0.75}\text{Al}_{0.25}\text{N}$ after annealing in the 600 to 700 °C range.
2. The peak sheet resistance occurs at temperatures (600 to 700 °C) higher than the 500 °C reported for F-implant $\text{In}_{0.75}\text{Al}_{0.25}\text{N}$. This suggests there may be some degree of chemical activity for O- and N-implant isolation.
3. The ionization level for the compensating defect is high in the bandgap in $\text{In}_{0.75}\text{Al}_{0.25}\text{N}$ which is not optimum for implant isolation. This is similar to the defect position that is seen in n-type InP and InGaAs, but different from the situation

in other III-V semiconductors such as GaAs where the defect levels are near midgap.²³

4. Although the compensating defect is relatively high in the bandgap of InAlN, it is still sufficiently deep to realize highly compensated InAlN that is appropriate for device isolation.

Acknowledgments

The portion of this work performed at Sandia National Laboratories was supported by the U.S. Department of Energy under contract # DE-AC04-94AL85000. The work at the University of Florida is partially supported by a National Science Foundation grant (DMR 95-36533) and a University Research Initiative grant from AFOSR. The technical support of J. Escobedo at Sandia with implantation and annealing and the support of the MicroFabritech facility at UF is greatly appreciated.

References

- 1 S. Nakamura, T. Mukai, and M. Senoh, Appl. Phys. Lett., **64**, 1687 (1994).
- 2 I. Akasaki, H. Amano, M. Kito, and K. Hiramatsu, J. Lumin. **48/49**, 666 (1991).
- 3 S. C. Binari, L. B. Rowland, W. Kruppa, G. Kelner, K. Doverspike, and D. K. Gaskill, Electronics Lett., **30**, 1248 (1994).
- 4 M. A. Kahn, J. N. Kuznia, D. T. Olsen, W. J. Schaff, J. W. Burm, and M. S. Shur, Appl. Phys. Lett., **65**, 1121 (1994).
- 5 T. P. Chow and R. Tyagi, IEEE Trans. Electron. Dev., **41**, 1481 (1994).
- 6 S. Strite and H. Morkoç, J. Vac. Sci. Technol. B **10**, 1237 (1992).
- 7 J. I. Pankove and J. A. Hutchby, J. Appl. Phys., **47**, 5387 (1976).
- 8 M. A. Khan, R. A. Skogman, R. G. Schule, and M. Gershenson, Appl. Phys. Lett., **42**, 430 (1983).
- 9 M. A. Khan, R. A. Skogman, R. G. Schule, and M. Gershenson, Appl. Phys. Lett., **43**, 492 (1983).
- 10 S. J. Pearton, C. R. Abernathy, P. W. Wisk, W. S. Hobson, and F. Ren, Appl. Phys. Lett., **63**, 1143 (1993).
- 11 J. C. Zolper, S. J. Pearton, C. R. Abernathy, and C. B. Vartuli, Appl. Phys. Lett., in press
- 12 C. B. Vartuli, S. J. Pearton, C. R. Abernathy, J. D. MacKenzie, and J. C. Zolper, submitted to J. Vac. Science and Technology
- 13 S. J. Pearton, C. B. Vartuli, J. C. Zolper, C. Yuan, and R. A. Stail, submitted to Appl. Phys. Lett.
- 14 S. J. Pearton, M. P. Iannuzzi, C. L. Reynolds, Jr., L. Peticolas, Appl. Phys. Lett., **52**, 1540 (1989).
- 15 J. C. Zolper, A. G. Baca, and S. A. Chalmers, Appl. Phys. Lett., **62**, 2536 (1993).
- 16 J. C. Zolper, M. E. Sherwin, A. G. Baca, and R. P. Schneider, Jr., J. Elec. Mat., **24**, 21 (1995).
- 17 C. R. Abernathy, J. Vac. Sci. Technol. A, **11**, 869 (1993).
- 18 J. Neugebauer and C. G. Van de Walle, Phys. Rev. B, **50**, 8067 (1994).
- 19 J. F. Ziegler, J. P. Biersack, U. Littmark, *The Stopping and Range of Ions in Solids*, vol. 1, (Pergamon Press, New York, 1985) p. 202.
- 20 C. B. Vartuli, et al., to be published
- 21 A. F. Wright and J. S. Nelson, submitted to Appl. Phys. Lett.
- 22 S. J. Pearton, C. R. Abernathy, M. B. Panish, R. A. Hamm, and L. M. Lunardi, J. Appl. Phys., **66**, 656 (1989).
- 23 S. J. Pearton, Mat. Sci. Rep., **4**, 313 (1991).

DEEP LEVEL DEFECTS IN GaN CHARACTERIZED BY CAPACITANCE TRANSIENT SPECTROSCOPIES

W. GÖTZ*, N.M. JOHNSON*, R.A. STREET*, H. AMANO**, AND I. AKASAKI**

*Xerox Palo Alto Research Center, Palo Alto, California 94304, USA

**Department of Electrical and Electronic Engineering, Meijo University, Nagoya, Japan

ABSTRACT

Electronic defects in MOCVD-grown n-type GaN were characterized by conventional deep level transient spectroscopy (DLTS) and by photoemission capacitance transient spectroscopy (O-DLTS) performed on Schottky diodes. With DLTS two deep levels were detected with thermal activation energies for electron emission to the conduction band of 0.16 eV and 0.44 eV. With O-DLTS we demonstrate four new deep levels with optical threshold energies for electron photoemission of ~ 0.87 eV, 0.97 eV, 1.25 eV and 1.45 eV. The O-DLTS apparatus and the measurement are discussed in detail. We also report characterization of the Au-GaN barrier height of the Schottky diode by internal photoemission.

INTRODUCTION

The III-V nitrides are direct wide bandgap semiconductors that show great promise for both light emitting devices^{1,2} and high temperature / high power devices³. Consequently, there is intense interest in defect related properties of GaN and its alloys AlGa_{0.3}N and InGa_{0.3}N. For instance, the investigation of deep level properties of impurities and native point- or extended defects is essential to develop this materials system for device fabrication such as blue laser diodes.

Deep level transient spectroscopy (DLTS) is a sensitive spectroscopic tool for the characterization of electronic levels deep in the bandgap of semiconductors. However, conventional DLTS is of limited use in wide bandgap materials because it utilizes thermal energy for charge emission. Therefore, the accessible range of level energies in the gap is restricted to ~ 1 eV of either band edge, for typical trap parameters and practical measurement conditions. The application of photoemission capacitance transient spectroscopy (O-DLTS), also termed deep level optical spectroscopy⁴, overcomes this limitation by utilizing monochromatic light for carrier emission so that levels in the entire bandgap become accessible for characterization.

This study demonstrates the application of DLTS^{5,6} and O-DLTS⁷ for deep level characterization in n-type GaN grown on sapphire. With DLTS or O-DLTS, deep levels are commonly investigated in the space charge region of current rectifying devices such as Schottky diodes. To achieve reliable results with a high frequency capacitance measurement low series resistance of the device is essential. This can be particularly challenging when working with a semiconducting layer with low carrier mobility and on an insulating substrate. For this study Schottky diodes equipped with an Ohmic back contact and low series resistance were designed.

GaN MATERIAL AND SCHOTTKY DIODE FABRICATION

The GaN material used in this study was grown in an horizontal-type MOCVD reactor operating at atmospheric pressure. The substrate for heteroepitaxial growth was a polished (0001)-oriented sapphire crystal. To enable the fabrication of an Ohmic back contact two Si-doped epitaxial GaN layers with different doping concentrations were grown over the AlN buffer

layer⁵. The first layer of GaN, grown directly over the AlN, was $\sim 1.7 \mu\text{m}$ thick and heavily doped n^+ -type with a doping concentration of $\sim 2 \times 10^{18} \text{cm}^{-3}$. A semiconducting layer of n -type GaN was then grown on the n^+ layer to a thickness of $\sim 5 \mu\text{m}$ with a doping concentration of $1.9 \times 10^{17} \text{cm}^{-3}$.

Schottky diodes were fabricated by vacuum evaporating Au onto the n -type GaN layer through a shadow mask. The Ohmic back contacts were subsequently applied by evaporating Al over the laterally exposed n^+ layer. The metal films were approximately 150 nm thick.

The Schottky diodes were tested by current-voltage and capacitance voltage (C-V) techniques⁵. They exhibited excellent current rectification with low leakage currents (e.g., $\leq 0.5 \text{ mA} / \text{cm}^2$) and sufficiently low series resistance for the 1 MHz capacitance measurement. The dopant profile of the n -layer derived from the analysis of the C-V measurement was found to be uniform in the measured depth range from 60 to 140 nm below the surface. In anticipation of DLTS, C-V measurements were also conducted at various temperatures in the range from 100 K to 460 K. Above 130 K the electron concentration was unchanged within experimental uncertainty, with evidence for the onset of carrier freeze-out below 130 K.

DLTS ON MOCVD-GROWN n -TYPE GaN

The DLTS measurements were performed with a computer controlled system consisting of a Boonton (Model 7200) capacitance meter (ac signal: 1 MHz and 50 mV) to monitor the capacitance transients and a Nicolet (Model 4094) digital oscilloscope to record and average the transients. The trap-filling voltage pulses were supplied by a HP 8116A Pulse/Function generator. The reverse bias was set at 2 V and periodically pulsed to 0 V for trap filling. The width of the voltage pulse was 100 μs . Digitally averaged capacitance transients $C(t)$ from approximately 240 individual traces, were recorded for 200 ms after a pulse at 1 K increments over the temperature range from 100 K to 460 K, with the temperature held constant to within $\pm 0.1 \text{ K}$.

A representative DLTS spectrum for an n -type GaN Schottky diode is presented in Fig. 1. The DLTS signal, $|C(t_1) - C(t_2)|$, is displayed for delay times $t_1 = 2 \text{ ms}$ and $t_2 = 8 \text{ ms}$ ⁸. The spectrum reveals two DLTS peaks at 317 K (level 1) and 145 K (level 2), respectively, which arise from

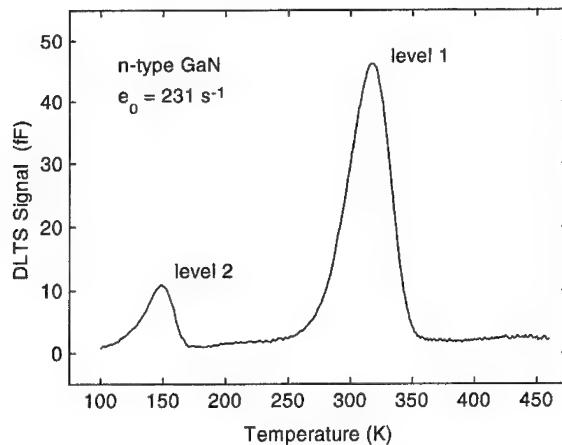


Fig. 1: DLTS spectrum for a Schottky diode on n -type GaN. The DLTS signal $|C(t_1) - C(t_2)|$ is shown for a spectrometer emission rate window $e_0 = 231 \text{ s}^{-1}$ (sampling delay times $t_1 = 2 \text{ ms}$ and $t_2 = 8 \text{ ms}$).

electron emission from two electronic deep levels. In the temperature range displayed in Fig. 1, no other deep level could be detected with the sensitivity of ~ 1 fF of our DLTS measurement.

The activation energies for electron emission of the deep levels were determined by an Arrhenius analysis of the electron emission time constants⁵. The analysis yields the activation energy with values of $E_1 = 0.46$ eV and $E_2 = 0.16$ eV. These energies have not been corrected for any temperature dependence of the electron capture cross section σ_n ($\sim T^0$). The uncertainty of these values is dominated by the unknown temperature dependence of σ_n . A temperature dependence of $\sigma_n \sim T^{-2}$ yields values of $E_1 = 0.49$ eV and $E_2 = 0.18$ eV. In addition, these values may be influenced by the Poole-Frenkel effect which significantly lowers the activation energies for electron emission from donor levels in the space charge region of a Schottky diode⁸.

The amplitude of each peak in the DLTS spectrum of Fig. 1 relates to the concentration N_T of the corresponding peak and was determined from the expression

$$N_T = \frac{2\epsilon_s^2 A^2 N_D \Delta C_{\text{peak}}}{C_r^3} (x_r^2 - x_p^2)^{-1} [\exp(-e_0 t_1) - \exp(-e_0 t_2)]^{-1}, \quad (1)$$

where ϵ_s is the permittivity, A is the diode area, N_D is the uniform ionized donor concentration, ΔC_{peak} is the amplitude of the emission peak in the DLTS spectrum, and e_0 is the emission rate window of the spectrometer given by $e_0 = \ln(t_2/t_1)/(t_2 - t_1)$. The parameters x_r and x_p are the distances from the surface at which the defect level intersects the Fermi level (or quasi-Fermi level) under reverse bias and pulse bias, respectively.⁵ The trap concentrations were determined to be $N_1 = (6.3 \pm 0.1) \times 10^{14} \text{ cm}^{-3}$ for level 1 and $N_2 = (7 \pm 1) \times 10^{13} \text{ cm}^{-3}$ for level 2.

O-DLTS ON MOCVD-GROWN n-TYPE GaN

A schematic of the O-DLTS apparatus is shown in Fig. 2. It utilized many of the components for recording the capacitance transients as described above for DLTS. During the measurement

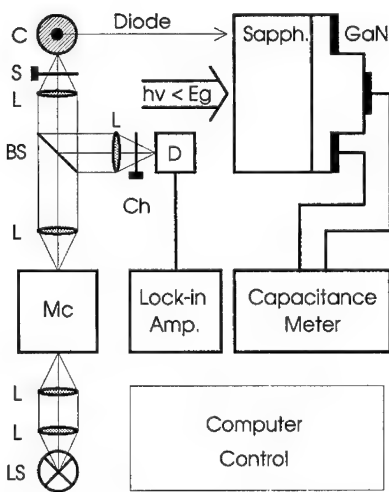


Fig. 2: Schematic of the photocapacitance transient apparatus

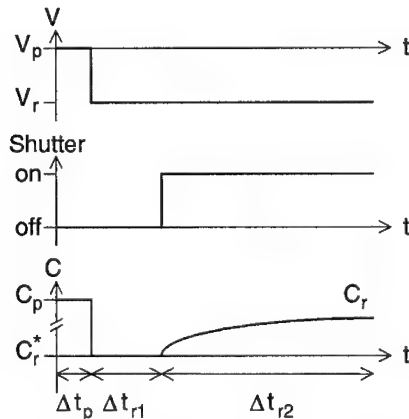


Fig. 3: Timing sequence of O-DLTS. Variations with time are depicted in the upper curve for the applied bias, the middle curve for the shutter position (illumination: on/off), and the lower curve for the capacitance of the Schottky diode.

the sample was placed in a continuous flow cryostat (C) and maintained at 150 ± 0.01 K. It was backside illuminated through the sapphire substrate with monochromatic light from a quartz tungsten halogen lamp (LS) and a double-grating monochromator (Mc) (10 nm resolution). The relative intensity of the incident light was continuously monitored by using a beam splitter (BS), light chopper (Ch) and a pyroelectric detector (D), with standard phase-sensitive detection.

A measurement cycle is depicted in Fig. 3 and will be described for the n-type GaN Schottky diode. Initially, the diode is unilluminated and under an applied reverse bias V_r ($= -3$ V) which induces a depletion width w_r ($= 116$ nm). The cycle is initiated by reducing the magnitude of the reverse bias to V_p ($= 0$) for a duration Δt_p ($= 10$ s); this collapses the depletion layer to a width w_p ($= 56$ nm) and induces trap filling by capture of free electrons. After reinstating V_r , the newly filled deep levels are metastably occupied. At this point in the cycle, with the GaN diode at 150 K there was no change in capacitance over a period of minutes. After a delay Δt_{r1} ($= 20$ s), the shutter is opened and the diode illuminated with monochromatic light. In the present study, the photon energy $h\nu$ was restricted to values less than one half of the bandgap in order to exclude minority-carrier transitions. Electrons photoemitted from metastably occupied levels to the conduction band drift out of the depletion layer, which increases the net positive space charge as revealed by an increasing depletion capacitance. At each wavelength, the light-induced capacitance transient was recorded for a period Δt_{r2} ($= 400$ s) and three individual recordings were digitally averaged to improve the signal-to-noise ratio. Data were recorded in the wavelength range from $1.9 \mu\text{m}$ (0.65 eV) to $0.8 \mu\text{m}$ (1.55 eV) with increments of $0.025 \mu\text{m}$.

An additional physical process must be considered in the interpretation of the photocapacitance data. Since the diode is under reverse bias during illumination, there is an internal photoemission of electrons from the metal contact into the semiconductor for photon energies greater than the Schottky barrier height for electrons. As these photoinjected electrons drift through the depletion layer, they can be captured by empty deep levels. The apparatus described above is readily modified to characterize the internal photoemission current by illuminating the diode with

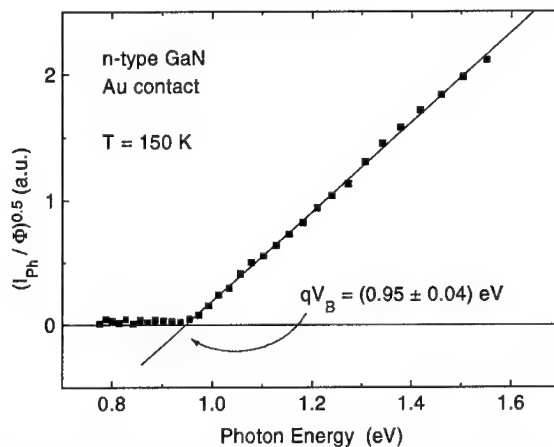


Fig. 4: Fowler plot for internal photoemission of electrons from a Au Schottky barrier into n-type GaN. The symbols refer to the experimental data and the solid line is a linear regression fit. The intercept of the fit with the horizontal axis determines the Au-GaN barrier height qV_B .

chopped monochromatic light and using standard phase-sensitive detection to monitor the diode photocurrent I_{ph} . The dependence of I_{ph} on $h\nu$ is accurately described by the Fowler relation⁹

$$I_{ph} = B\Phi_{ph} (h\nu - qV_B)^2, \quad (2)$$

where B is a proportionality constant, Φ_{ph} is the absorbed photon flux, and qV_B is the barrier height. In Fig. 4 is shown a Fowler plot, $(I_{ph}/\Phi_{ph})^{0.5}$ vs. $h\nu$, for the gold Schottky contact on n-type GaN. Extrapolation of the linear least squares fit to the horizontal axis yields a barrier height of (0.95 ± 0.04) eV. The electric field induced barrier lowering was calculated to be ~ 0.1 eV resulting in an estimated zero-field barrier height at 150 K of ~ 1.05 eV⁷.

In the photocapacitance transient measurement, the steady-state change in the diode capacitance due to illumination, ΔC_{ss} , is proportional to the steady-state change in the density of trapped charge (i.e., $\Delta C_{ss} \propto N_T - n_T$) for low trap densities (i.e., $N_T \ll N_D$)⁷

$$\Delta C_{ss} \propto N_T \left(1 + \frac{\sigma_T^n v_n n}{\sigma_T^O \Phi} \right)^{-1}, \quad (3)$$

where n_T is the density of occupied traps, σ_T^O is the optical cross section, Φ is the photon flux at the trap site, σ_T^n is the cross section for electron capture, v_n and n are the free electron velocity and concentration, respectively, and N_T is the trap density. For the purpose of evaluating the retrapping contribution of internally photoinjected electrons, the drift velocity was used to estimate the magnitude of the randomized hot-electron velocity in the depletion layer. Hence, ΔC_{ss} is directly proportional to the total trap density N_T provided that $\sigma_T^n v_n n / (\sigma_T^O \Phi) \ll 1$. Under photocapacitance measurement conditions with $h\nu = 1.55$ eV, the incident photon flux was

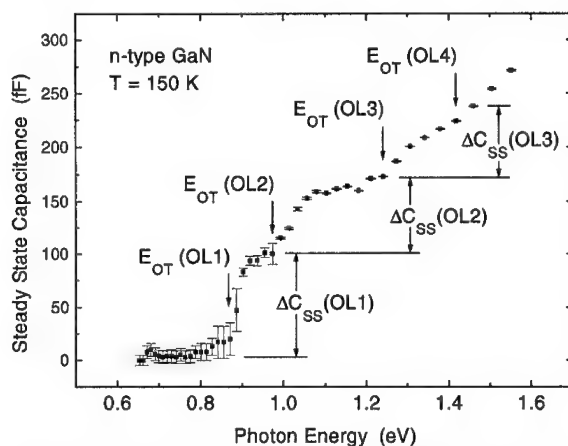


Fig. 5: Dependence of the steady-state photocapacitance ΔC_{ss} on photon energy $h\nu$ for a Schottky diode on n-type GaN. The spectrum displays distinct steps, marked by arrows, due to photo emission from four distinct deep levels, which are labeled OL1 - OL4. The magnitude of the steady-state photocapacitance for each of the deep levels is labeled $\Delta C_{ss}(OL\#)$ ($\# = 1$ to 4).

$\sim 2 \times 10^{16} \text{ cm}^{-2} \text{ s}^{-1}$ and the internal photocurrent was $\sim 2 \text{ pA}$, for which the inequality becomes $10^{-7} \sigma_T^h / \sigma_T^0 \ll 1$. For typical ranges of electron and photon cross sections, this inequality can reasonably be assumed to be satisfied. Then ΔC_{ss} relates to total trap densities, rather than to kinetically determined partial trap occupancies.

The dependence of the steady state photocapacitance on $h\nu$ is presented in Fig. 5 for n-type GaN. The spectrum increases monotonically with $h\nu$ because $\Delta C_{ss}(h\nu)$ is proportional to the sum of charge-change contributions from optically active deep levels that reside within an energy interval that extends up to $h\nu$. Each level introduces a step in the ΔC_{ss} spectrum, near its threshold energy E_{OT} . The spectrum in Fig. 5 displays four abrupt increases in slope each of which can be associated with a distinct deep level⁷. Each feature is identified by an arrow, with a label (i.e., OL1 - OL4) and the approximate threshold energy E_{OT} . The first two steps, at $\sim 0.87 \text{ eV}$ and $\sim 0.97 \text{ eV}$, are clearly resolved and followed by plateaus. The second two, at $\sim 1.25 \text{ eV}$ and $\sim 1.45 \text{ eV}$, are less well resolved but still suggest the onset of photoemission from additional deep levels.

With each step in Fig. 5 is associated a step height $\Delta C_{ss}(\text{OL}\#)$, which is proportional to the density of the corresponding deep level; saturation was not achieved for OL4 within our chosen range of $h\nu$ ($\leq 1.55 \text{ eV}$). The uniform density of deep levels $N_T(\text{OL}\#)$ was estimated from $\Delta C_{ss}(\text{OL}\#)$ and are $9 \times 10^{14} \text{ cm}^{-3}$ for OL1, $5 \times 10^{14} \text{ cm}^{-3}$ for OL2, and $6 \times 10^{14} \text{ cm}^{-3}$ for OL3.⁷

SUMMARY

Deep level defects in n-type GaN were detected and characterized using capacitance transient techniques (DLTS, O-DLTS). The newly detected deep levels in the upper half of the bandgap of GaN may play an important role in defect luminescence bands observed in GaN and may act as parasitic radiative or non-radiative recombination channels in light emitting devices. DLTS or O-DLTS studies could seek a correlation between growth conditions and the newly discovered traps and thus support the development of III-V nitrides as a materials system for laser diodes.

ACKNOWLEDGEMENT

The authors are pleased to thank C.G. Van de Walle, J. Neugebauer and D.P. Bour for helpful discussions and J. Walker for technical assistance. One of the authors (W.G.) acknowledges partial support by the Alexander von Humboldt Foundation, Germany. The work reported was supported by AFOSR and by the Ministry of Education, Science and Culture of Japan.

REFERENCES

1. I. Akasaki, H. Amano, N. Koide, M. Kotaki, K. Manabe, *Physica B* **185**, 428, (1993)
2. S. Nakamura, T. Mukai, and M. Senoh, *Appl. Phys. Lett.* **64**, 1687 (1994)
3. H. Morkoç, S. Strite, G. B. Gao, M. E. Lin, B. Sverdlov, and M. Burns, *J. Appl. Phys.* **76**, 1363 (1994)
4. A. Chantre, G. Vincent, and D. Bois, *Phys. Rev. B* **23**, 5335 (1981)
5. W. Götz, N.M. Johnson, H. Amano, and I. Akasaki, *Appl. Phys. Lett.* **65**, 463 (1994)
6. P. Hacke, T. Detchprohm, K. Hiramatsu, and N. Sawaki, *J. Appl. Phys.* **76**, 304 (1994)
7. W. Götz, N.M. Johnson, R.A. Street, H. Amano, and I. Akasaki, *Appl. Phys. Lett.* **66**, 1340, (1995)
8. N.M. Johnson, *Mater. Res. Soc. Symp. Proc.* **69**, 75 (1986)
9. R.H. Fowler, *Phys. Rev.* **38**, 45 (1931)

HYDROGEN DIFFUSION AND PASSIVATION IN InGaAlN ALLOYS

S.J. Pearton,* C.R. Abernathy,* J.D. MacKenzie,* C.B. Vartuli,* R.G. Wilson,** J.M. Zavada[†] and R.J. Shul^{††}

* Department of Materials Science and Engineering, University of Florida, Gainesville FL 32611

** Hughes Research Laboratories, Malibu CA 90265

[†] US Army Research Office, Research Triangle Park NC 27709

^{††} Sandia National Laboratories, Albuquerque NM 87185

ABSTRACT

Hydrogen is found to readily diffuse into InGaN, InAlN and InGaAlN epitaxial layers during plasma exposures at 170 - 250 °C for 40 sec - 30 min. The diffusivity of hydrogen is $> 10^{-11} \text{ cm}^2\text{s}^{-1}$ at 170 °C, and the native donor species are passivated by association with the hydrogen. Reactivation of these species occurs at 450-500°C, but the hydrogen remains in the material until ≥ 800 °C.

INTRODUCTION

The properties of hydrogen in group III nitrides and their alloys are attracting much recent attention because of the discovery that residual hydrogen remaining in Mg-doped GaN after MOCVD growth passivates the p-type doping and therefore that post-growth annealing is required to attain high conductivity.^(1,2) This problem will be especially evident in materials grown using NH_3 as the nitrogen precursor, but past studies in other III-V semiconductors have shown that metalorganics such as trimethylgallium, $\text{Ga}(\text{CH}_3)_3$, can also produce significant hydrogen incorporation.⁽³⁾ For photonic devices such as light-emitting diodes or heterostructure diode lasers, one will also need to understand the effect of hydrogen in ternary and quaternary nitrides, since these will comprise the active or cladding layers. In this paper we report on the thermal stability of electrical passivation in InGaN and InAlGaN grown on Al_2O_3 , Si or GaAs by metalorganic molecular beam epitaxy (MOMBE). We find that the electrical activity of passivated donors in these materials is restored by annealing at ≥ 450 - 500 °C, but that the physical removal of hydrogen requires temperatures ≥ 800 °C. This raises the question of what will happen during device fabrication steps such as CVD of dielectric films using SiH_4 or dry etching with CH_4/H_2 -based plasma chemistries. We find that hydrogen is also incorporated into the nitrides during plasma etching in a $\text{Cl}_2/\text{CH}_4/\text{H}_2/\text{Ar}$ discharge, during which the samples are held at a slightly elevated temperature (~ 170 °C).

EXPERIMENTAL

Samples of $\text{In}_x\text{Ga}_{1-x}\text{N}$ ($x = 1 - 0.25$), $\text{In}_{0.36}\text{Al}_{0.64}\text{N}$ and $\text{In}_{0.24}\text{Al}_{0.38}\text{Ga}_{0.38}\text{N}$ approximately 1 μm thick were grown on semi-insulating, (100) GaAs substrates at 500 °C in an Intevac Gas Source Gen II system.⁽⁴⁾ Other samples of AlN and InN were grown on Si or Al_2O_3 substrates at 500-700 °C under similar conditions. Triethylgallium (TEG), trimethylindium (TMI) and dimethylethylamine alane (DMEAA) were transported by He carrier gas and an electron cyclotron resonance (ECR) source operating at 2.45 GHz and 200 W forward power was used to provide the N_2 flux. The composition of the films was obtained from Rutherford Backscattering measurements. The epitaxial layers contained

both cubic and hexagonal phases, and were defective single crystal. The major structural imperfections present were microtwins and stacking faults. All of the material was nominally undoped, with n-type carrier concentrations of $\sim 3 \times 10^{17} \text{ cm}^{-3}$ for the InAlN, $\sim 5 \times 10^{19} \text{ cm}^{-3}$ for the InGaAlN and 10^{20} cm^{-3} for the InN due to the presence of native defects. These are generally assumed to be nitrogen vacancies.⁽⁵⁾ The AlN was semi-insulating. Some of the material was contacted with alloyed HgIn eutectic (400 °C, 60 sec) in a Van der Pauw pattern, while other sections were left blank. All of the samples were exposed to an ECR deuterium plasma for 30 min at 250 °C, with a process pressure of 10 mTorr and without any additional biasing of the samples position. Hall measurements were then performed on the contacted samples as a function of annealing temperature (300 - 500 °C), while Secondary Ion Mass Spectrometry (SIMS) was carried out using a Cs^+ ion beam on the blank samples annealed up to 900 °C for 5 min under a N_2 ambient. Other samples were exposed to ECR $\text{Cl}_2/\text{CH}_4/\text{D}_2/\text{Ar}$ discharges (flow rates of 10, 3, 15 and 10 sccm respectively) for 40 sec at 170 °C. The process pressure was 1 mTorr, the microwave power 850 W and the rf power applied to the sample position was 150 W, producing a dc bias of -165 V. The etch depth was $\leq 2000 \text{ \AA}$ on these films.

RESULTS AND DISCUSSION

Figure 1 shows the fraction of passivated donors remaining in both InAlN and InGaAlN as a function of post-hydrogenation annealing temperature. Both samples displayed a decrease in carrier concentration of approximately an order of magnitude after hydrogen plasma exposure, consistent with previous reports.⁽⁶⁾ Upon subsequent annealing the passivated donors begin to reactivate around 400 °C, and by 500 °C 78% of the lost carriers were restored in InAlN and 66% in the InGaAlN. The reactivation of the donors was fit to the relation:⁽⁷⁾

$$\frac{N_o}{N} = 1 - \exp \left[-\nu \exp \left(\frac{-E_d}{kT} \right) \right]$$

where N_o/N is the fraction of passivated centers reactivated by annealing at temperatures T for time t, ν is the attempt frequency (assumed to be 10^{14} s^{-1}) and E_d is the activation energy for reactivation. The recovery of the donor activity occurred over a slightly broader temperature range than generally observed for other passivated dopants in binary semiconductors, and is consistent with the presence of a Gaussian distribution of activation energies.⁽⁷⁾ This may be due to nitrogen vacancies with different numbers of specific group III neighbors surrounding them (i.e. 2 In and 2 Al versus 1 In and 3 Al). Assuming a Gaussian distribution of activation energies, we obtained values for E_d around 2.4 eV, with a full width at half maximum of $\sim 0.3 \text{ eV}$. The fact that reactivation of these donors occurs around 500 °C means that the apparent thermal stability is similar to that of passivated Mg acceptors in GaN.

SIMS profiles of deuterium in InAlN for as-hydrogenated plus subsequent 900 °C annealing treatments are shown in Figure 2. The initial plasma exposure at 250 °C for 30 min produces a very high deuterium concentration ($\sim 10^{21} \text{ cm}^{-3}$) throughout the epitaxial layer thickness, well in excess of the doping concentration. The sites to which this deuterium is bonded are at present unclear, but presumably involve the structural defects in the material. Annealing up to 800 °C did not measurably alter the deuterium profile, whereas annealing at 900 °C reduced the plateau concentration to $\sim 5 \times 10^{18} \text{ cm}^{-3}$. This is similar to the behavior in the component binaries reported previously.⁽⁸⁾ Similar data are

shown in Figure 3 for InGaAlN.

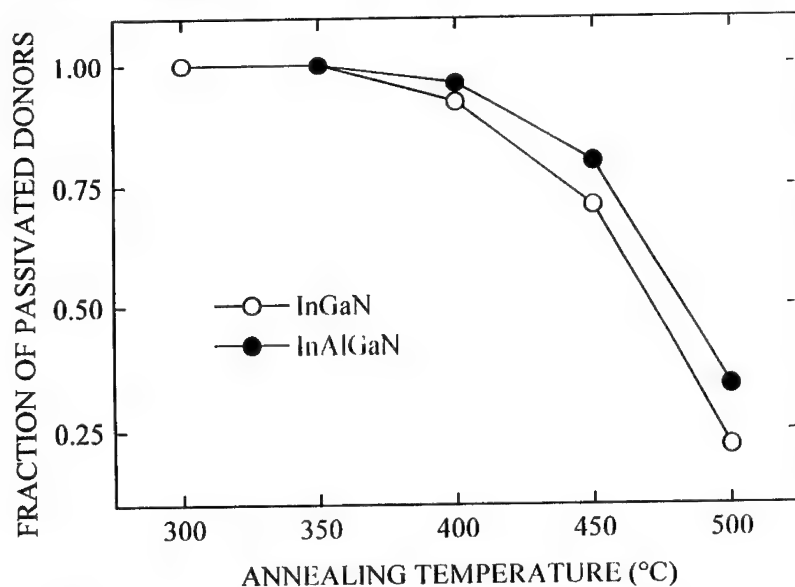


Figure 1. Fraction of passivated donors remaining in InAlN or InAlGaN after deuteration at 250 °C and subsequent annealing at different temperatures.

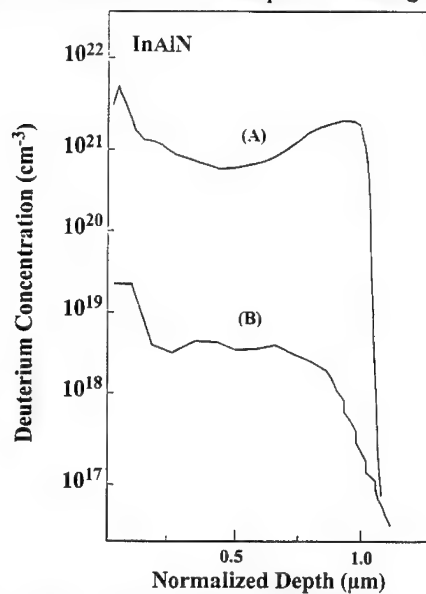


Figure 2. SIMS profile of deuterium in InAlN exposed to a) a D_2 plasma for 0.5 h at 250 °C, and b) after subsequently annealing at 900 °C.

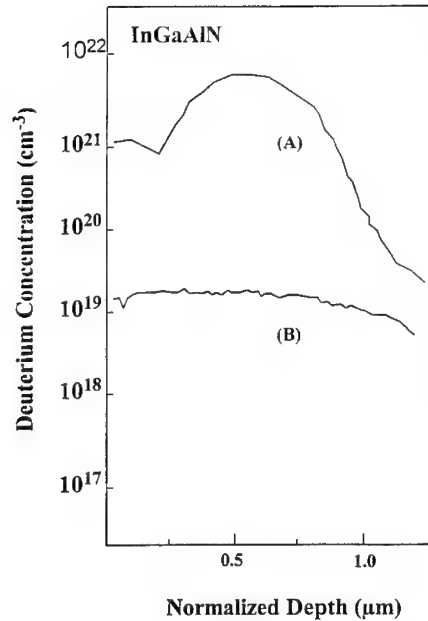


Figure 3. SIMS profile of deuterium in InGaAlN exposed to a) a D_2 plasma for 0.5 h at 250 °C, and b) after subsequently annealing at 900 °C.

Figure 4 shows the deuterium profile in GaN resulting from $Cl_2/CH_4/D_2/Ar$ plasma exposure. Approximately 10^{20} cm^{-3} peak deuterium concentration is incorporated, and the deuterium extends throughout the GaN layer and into the underlying Si substrate. Assuming a constant surface concentration of $2 \times 10^{20} \text{ cm}^{-3}$ we obtain an estimate for $D_D \geq 2.8 \times 10^{-11} \text{ cm}^2 \cdot \text{s}^{-1}$ at 170 °C in AlN. In the final case of InN (Figure 5) the profile shows a plateau shape typical of deuterium being trapped at defects, which in this material may be the native vacancies responsible for the strong as-grown n-type conductivity ($n \sim 10^{20} \text{ cm}^{-3}$). The deuterium has again permeated the entire epitaxial layer thickness, with a \sqrt{Dt} estimate yielding $D_D \geq 4 \times 10^{-11} \text{ cm}^2 \cdot \text{s}^{-1}$. Similar results are found for InAlN and InGaIn. One might have similar incorporation of hydrogen into III-V nitrides during PECVD of dielectrics for masking or passivation at typical temperatures of 200 - 400 °C.

CONCLUSION

Under our conditions, annealing in an inert ambient of N_2 or Ar at 450 - 500 °C is sufficient to fully reactivate all if the passivated carriers in the material, but substantially higher temperatures ($> 800 \text{ °C}$) are required to actually remove the hydrogen (or deuterium) from the crystal. This is because the neutral dopant or impurity-hydrogen pairs must first dissociate leaving the hydrogen to form more stable, but electrically inactive complexes such as H_2 molecules or larger clusters of hydrogen. It is only at higher temperatures that these are evolved from the material.

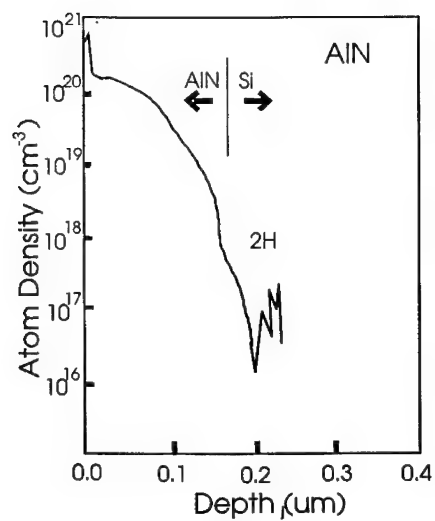


Figure 4. SIMS profile of deuterium in AlN/Si after a short etch in $\text{Cl}_2/\text{CH}_4/\text{D}_2/\text{Ar}$ ECR plasma.

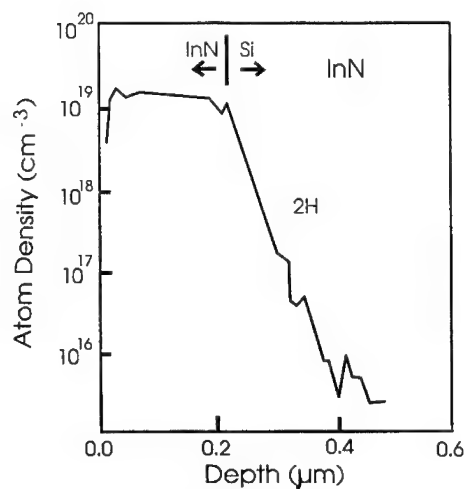


Figure 5. SIMS profile of deuterium in InN/Si after a short etch in $\text{Cl}_2/\text{CH}_4/\text{D}_2/\text{Ar}$ ECR plasma.

ACKNOWLEDGMENTS

The work at UF is partially supported by an NSF grant from the Division of Materials Research, an AFOSR University Research Initiative and an AASERT grant through USARO. The work at Hughes is partially supported by a US Army Research Office grant, while that at Sandia is supported by DOE contract # DE-AC04-94AL85000. The UF authors acknowledge the support of the staff of the MicroFabritech facility, while the technical assistance of P.L. Glarborg at Sandia is greatly appreciated.

REFERENCES

1. S. Nakamura, T. Mukai, M. Senoh and N. Iwasa, Jpn. J. Appl. Phys. 1992, **31** L139-L142.
2. H. Amano, M. Kito, K. Hiramatsu and I. Akasaki, Jpn. J. Appl. Phys. 1989, **29** L2112-L2114.
3. see, for example, M. Stavola, Mat. Sci. For. 1994, **148/149**, pp. 251-280.
4. C.R. Abernathy, J. Vac. Sci. Technol. A 1993, **11** pp. 869-875.
5. S. Strite and H. Morkoc, J. Vac. Sci. Technol. B 1992 **10** pp. 1237-1266.
6. S.J. Pearton, C.R. Abernathy, P. Wisk, W.S. Hobson and F. Ren, Appl. Phys. Lett. 1993, **63** pp. 1143-1145.
7. S.J. Pearton, J.W. Corbett and M. Stavola, *Hydrogen in Crystalline Semiconductors* (Springer-Verlag, Heidelberg, 1992).
8. J.M. Zavada, R.G. Wilson, C.R. Abernathy and S.J. Pearton, Appl. Phys. Lett. 1994, **64** pp. 2724-2726.

ATOMIC HYDROGEN IN GaN

JÖRG NEUGEBAUER AND CHRIS G. VAN DE WALLE

Xerox Palo Alto Research Center, 3333 Coyote Hill Road, Palo Alto, California 94304

ABSTRACT

Based on extensive first-principles total-energy calculations we study the electronic structure, atomic geometry and energetics of atomic hydrogen in cubic GaN. All charge states of hydrogen (H^+ , H^0 , H^-) are examined. For H^- the gallium tetrahedral interstitial site is energetically most stable. All other sites are much higher in energy, indicating a high diffusion barrier for H^- in GaN. H^+ favors positions on a sphere with a radius of $\approx 1 \text{ \AA}$ and a nitrogen atom in the center. Among these positions the nitrogen antibonding site is energetically most stable. An unexpectedly large negative- U effect ($U = -2.5 \text{ eV}$) indicates that H^0 is unstable.

INTRODUCTION

GaN is being pursued for the manufacturing of bright, highly-efficient blue and green light emitting diodes[1] and shows promise for producing blue/UV lasers and high-power, high-temperature devices. As-grown GaN is commonly n -type conductive. p -type conductivity has been more difficult to achieve. It was first shown by Amano *et al.* that p -type conductivity can be achieved by activating Mg-doped GaN using low-energy electron irradiation (LEEPI).[2] Subsequently, Nakamura showed that the activation of the Mg acceptors can also be achieved by thermal annealing.[3] Based on these observations it has been suggested that hydrogen plays a crucial role in passivating the Mg acceptors.[3, 4] This model of hydrogen passivation would be consistent with the fact that in MBE-grown GaN p -type conductivity can be achieved without any post-growth processing.[5, 6]

Whereas for the more traditional semiconductors like Si and GaAs the effects due to hydrogen passivation and diffusion are well understood, little is known about hydrogen in GaN. There are experimental indications that hydrogen passivates acceptor dopants by forming neutral acceptor-hydrogen complexes.[3, 7] However, there are no reports about hydrogen passivation of donors in n -type GaN.

In this paper we address the properties of isolated interstitial hydrogen in cubic GaN. In particular, we discuss the effect of the charge state on the position and the energetics of hydrogen in GaN. Results for hydrogen molecules and hydrogen-impurity complexes will be reported elsewhere.[8]

METHOD

Employing first-principles density-functional theory we have calculated total energy, electronic structure and atomic geometry for hydrogen in various interstitial positions and for all relevant charge states (H^+ , H^0 , H^-). The system is described by a 32-atom supercell. Atomic relaxation is fully taken into account. The wave functions are expanded in a plane-wave basis set with an energy cutoff of up to 60 Ry. The electron-ion interaction is described by soft Troullier-Martins pseudopotentials.[9] Details of the computational approach can be found elsewhere.[10, 11]

q	E_H^f (eV)	d_{N-H} (Å)	d_{Ga-H} (Å)	k	$3d$
1	-2.51	1.02	1.70	Γ	nlcc
0	-0.29	1.02	1.82	Γ	nlcc
-1	1.77	1.03	1.91	Γ	nlcc
1	-2.51	1.02	1.70	$(2 \times 2 \times 2)$	nlcc
0	0.79	1.03	1.82	$(2 \times 2 \times 2)$	nlcc
-1	4.31	1.03	1.91	$(2 \times 2 \times 2)$	nlcc
1	-2.31	1.00	1.75	Γ	3d
0	-0.82	1.00	1.76	Γ	3d
-1	0.71	1.01	1.76	Γ	3d

Table 1: Formation energy according to Eq. (1) and bond length to the nearest neighbors for hydrogen at the bond-center position in GaN. The results are given for all possible charge states. The calculations were performed using two different k -point samplings (Γ point and a $2 \times 2 \times 2$ Monkhorst-Pack mesh[13]). The Ga $3d$ electrons were treated in the non-linear core-correction (nlcc) or explicitly as valence electrons ($3d$).

The formation energy of hydrogen on an interstitial site in GaN is defined as:

$$E_H^f(q) = E_{\text{tot}}^{\text{defect}}(q) - E_{\text{tot}}^{\text{bulk}} - \mu_H - qE_F \quad . \quad (1)$$

Here q is the charge state of H, $E_{\text{tot}}^{\text{defect}}(q)$ is the total energy of H^q in GaN, $E_{\text{tot}}^{\text{bulk}}$ is the total energy of the corresponding bulk system and μ_H the chemical potential for hydrogen. For the following discussions we assume that μ_H is fixed at the energy of a free H atom, as a reference. E_F is the Fermi level which is set to zero at the top of the valence band.

Before presenting the results let us first discuss some convergence checks. In particular, we will discuss the role of the Ga $3d$ electrons and the k -point sampling. As shown earlier[12] an explicit treatment of the Ga $3d$ electrons as valence electrons ($3d$) is important to get accurate formation energies for the native defects. The non-linear core correction (nlcc), which is based on freezing in the atomic Ga $3d$ wave function, was found to be insufficient. However, as will be shown in the following discussion, the nlcc approximation is adequate to accurately describe interstitial hydrogen. This observation provides some insight into the bonding mechanism of hydrogen in GaN and allows us to significantly reduce the computational effort.

For the convergence checks we choose H at the bond center position. At this position the atomic relaxation of the GaN host atoms is largest and possible effects of k -point sampling and $3d$ electrons should be most significant. The results are listed in Table 1. Let us first discuss the k -point sampling. For all three charge states we find that the atomic positions are well described using only the Γ -point. The formation energy, however, agrees only for the +1 charge state. For the neutral and negative charge state we find deviations of more than 1 eV. An analysis of the electronic structure shows that neutral hydrogen at the bond-center position has a singly occupied defect level close to the conduction band. The fact that the formation energies agree only for the + charge state indicates a large dispersion of the defect level. Indeed, Figure 1 shows that the defect level extends over a range of 1.6 eV between the Γ and L -point. This dispersion is surprisingly strong considering the size of

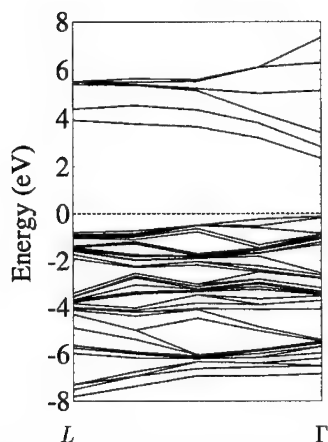


Figure 1: Band structure for H on a bond-center position in a 32 atom supercell. The dashed line marks the position of the top of the valence band. The first level above the zero line is the hydrogen defect level. The dispersion is due to the hydrogen-hydrogen interaction caused by the finite size of the supercell.

the supercell (32 atoms). For comparison, the corresponding dispersion of the level for H in Si is 0.5 eV.[14] The smaller lattice constant (about 20 % smaller than Si or GaAs) and the significantly smaller dielectric constant give rise to the large dispersion. There are two possible ways to avoid the dispersion: (i) the use of larger supercells (which quickly runs into the limits of even the most powerful supercomputers) or (ii) an appropriate k -point sampling. The idea behind (ii) is that the average of the defect level over the Brillouin zone is close to the defect level of an isolated defect.[14] The above discussion explains why the use of the Γ point for the Brillouin zone integration (although computationally very tempting) gives a insufficient description of defect levels. This problem continues to exist even in larger supercells.

If the Ga 3d electrons are allowed to relax the formation energy for the positive charge state changes only slightly. Further checks showed that the effect on energy differences between different sites is even smaller (< 0.1 eV). For the neutral and negative charge states, however, we find large deviations from the nlcc calculations. The reason is that the theoretical band gap is underestimated if the Ga 3d electrons are treated explicitly ($E_g = 1.7$ eV compared to 3.2 eV for nlcc), due to a 3 % increase of the lattice constant and the p - d repulsion.[8] The defect band, which near the Γ point lies at about 2.2 eV, therefore becomes a resonance in the conduction band when 3d relaxation is included. Since levels are occupied in order of increasing energy, the conduction band rather than the defect band is occupied, resulting in an underestimation of the transition levels and of the formation energy (Table 1). An analysis of the electronic states, however, shows that the position of the defect state in the band structure agrees within 0.1 eV with the nlcc calculation.

We can therefore conclude that for interstitial hydrogen the Ga 3d electrons can be treated in the frozen core approximation. Note however that the Ga 3d electrons are essential for a realistic description of native defects or substitutional impurities where Ga-N bonds are broken.[12]

q	site	E_H^f (eV)	d_{Ga-H} (Å)	d_{N-H} (Å)
1	AB _{Ga}	-0.22	1.78	-
1	AB _N	-2.61	1.96	1.03
1	BC	-2.51	1.70	1.02
1	C _N	-2.40	1.77	1.04
0	AB _{Ga}	0.76	1.76	-
0	AB _N	1.47	1.97	1.04
0	BC	0.79	1.82	1.02
0	C _N	1.39	1.75	1.07
-1	AB _{Ga}	1.66	1.74	-
-1	AB _N	5.43	1.98	1.04
-1	BC	4.31	1.91	1.03
-1	C _N	5.27	1.75	1.14

Table 2: Formation energy of hydrogen as defined by Eq. (1) for different interstitial positions and for all charge states of hydrogen. d_{Ga-H} gives the nearest-neighbor distance between Ga and H and d_{N-H} between N and H.

RESULTS

We have calculated the formation energy, atomic geometry and electronic structure for H in different interstitial positions. Particularly, in the following discussion we focus on the Ga antibonding site (AB_{Ga}), the N antibonding site (AB_N), the bond-center position (BC) and the C_N site. The C_N site lies at the center of a rhombus formed by two Ga atoms, a N atom, and the nearest tetrahedral interstitial site. For these sites the formation energy and the hydrogen distance to the nearest Ga atom and N atom are listed in Table 2.

Table 2 indicates that H⁺ prefers positions with a nitrogen atom as nearest neighbor. The calculated H-N bond length for all these positions is 1.02...1.04 Å and close to the experimental bond length of NH ($d_{N-H} = 1.04$ Å) and NH₃ ($d_{N-H} = 1.01$ Å).[15] Among these positions the N antibonding site is energetically most stable. All other sites, where a H-N bond cannot be formed (like the AB_{Ga}), are found to be energetically unfavorable.

The preference for the N antibonding site is in contrast with the behavior of H⁺ in Si or GaAs, where the BC position was found to be energetically most stable.[14, 16] This difference can be understood by noting the different character of the bulk chemical bond in GaN compared to GaAs and Si. In Si and GaAs there is a pronounced maximum of the charge density at the bond center due to the strong covalent character of these materials. For the more ionic GaN, however, there is no local maximum at the bond center but a monotonic increase in the charge density from Ga to N. Positively charged hydrogen, which is simply a proton, prefers a position where it obtains a maximum screening, i.e., it prefers sites with a high charge density. This explains the preference of H⁺ for the bond center position in Si and GaAs. In GaN the valence charge density exhibits nearly spherical symmetry around the nitrogen atom (as opposed to being concentrated in the covalent bond) which explains why all positions around the nitrogen atom are low in energy. At the bond-center position an extra energy cost needs to be paid due to the significant strain

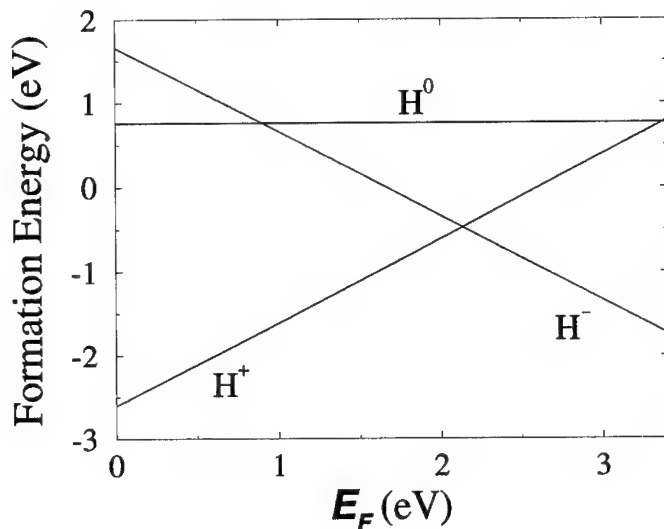


Figure 2: Formation energy as a function of the Fermi level for H^+ , H^0 , and H^- . $E_F = 0$ corresponds to the top of the valence band. The formation energy is referenced to the energy of a free H atom.

energy involved in relaxing the neighboring host atoms, rendering this site energetically favorable.

For neutral hydrogen we find much smaller energy differences (< 1 eV) between the different sites indicating a rather flat total-energy surface. The energetically most stable site is the Ga antibonding site. It is interesting to note that the Ga-H bond length for this site is only 0.1 Å smaller than the Ga-N bond length. Due to this coincidence the Ga antibonding site nearly coincides with the position of the tetrahedral interstitial site (T_d^{Ga}).

For negatively charged hydrogen we also find the Ga antibonding site (or T_d^{Ga}) to be energetically most stable. At this position the distance to the neighboring Ga atoms is maximized and the charge density has a global minimum. However, contrary to neutral hydrogen, the other sites are much higher in energy (> 3 eV), indicating much larger diffusion barriers than for H^- in Si or GaAs.

Based on the above analysis we obtain the energetically most stable position of H in GaN for each charge state. Using Eq. (1) the formation energy of atomic hydrogen in GaN can then be calculated as a function of the Fermi level. The result is shown in Fig. 2. The most striking feature in Fig. 2 is the large negative- U effect, with $U \approx -2.5$ eV. We conclude that neutral hydrogen is never a stable species. The negative- U behavior seems to be a property of hydrogen in semiconductors in general (see Ref. [14, 16]); however, the value found here for GaN is unusually large, and, to our knowledge, larger than any derived or predicted value for any defect or impurity in semiconductors. Finally, we note that while the current calculations were carried out for the cubic phase, we expect the behavior of H in hexagonal GaN to be very similar.[12]

ACKNOWLEDGMENTS

This work was supported in part by ARPA. One of the authors (J.N.) acknowledges financial support by the DAAD (German Academic Exchange Service).

References

- [1] S. Nakamura, T. Mukai, and M. Senoh, *Appl. Phys. Lett.* **64**, 1687 (1994).
- [2] H. Amano, M. Kito, K. Hiramatsu, and I. Akasaki, *Jpn. J. Appl. Phys* **28**, L2112 (1989).
- [3] S. Nakamura, N. Iwasa, M. Senoh, and T. Mukai, *Jpn. J. Appl. Phys* **31**, 1258 (1992).
- [4] J. A. Van Vechten, J. D. Zook, R. D. Hornig, and B. Goldenberg, *Jpn. J. Appl. Phys* **31**, 3662 (1992).
- [5] R. J. Molnar, T. Lei, and T. D. Moustakas, *Proc. Mater. Res. Soc. Symp.* **281**, 753 (1993).
- [6] M. E. Lin, C. Xue, G. L. Zhou, J. E. Greene, and H. Morkoc, *Appl. Phys. Lett.* **63**, 932 (1993).
- [7] M. S. Brandt, J. W. Ager III, W. Götz, N. M. Johnson, J. S. Harris, Jr., R. J. Molnar, and T. D. Moustakas, *Phys. Rev. B* **49**, 14758 (1994).
- [8] J. Neugebauer and C. G. Van de Walle, to be published.
- [9] N. Troullier and J. L. Martins, *Phys. Rev. B* **43**, 1993 (1991).
- [10] R. Stumpf and M. Scheffler, *Comp. Phys. Commun.* **79**, 447 (1994).
- [11] J. Neugebauer and C. G. Van de Walle, *Phys. Rev. B* **50**, 8067 (1994).
- [12] J. Neugebauer and C. G. Van de Walle, in *Materials Research Society Symposia Proceedings*, edited by C. H. Carter Jr., G. Gildenblat, S. Nakamura, and R. J. Nemanich (Materials Research Society, Pittsburgh, Pennsylvania, 1994), Vol. 339.
- [13] H. J. Monkhorst and J. D. Pack, *Phys. Rev. B* **13**, 5188 (1976).
- [14] C. G. Van de Walle, P. J. H. Denteneer, Y. Bar-Yam, and S. T. Pantelides, *Phys. Rev. B* **39**, 10791 (1989).
- [15] *CRC Handbook of Chemistry and Physics*, 73 ed., edited by D. R. Lide (CRC, Boca Raton, FL, 1993).
- [16] L. Pavesi and P. Gianozzi, *Phys. Rev. B* **46**, 4621 (1992).

PHOTOLUMINESCENCE STUDIES OF GaN AND AlGaN LAYERS UNDER HYDROSTATIC PRESSURE

C. Wetzel, W. Walukiewicz, E.E. Haller, H. Amano*, and I. Akasaki*

Lawrence Berkeley Laboratory, Berkeley, CA 94720, USA

*Dept. of Electrical and Electronic Engineering, Meijo University, Nagoya, Japan

Abstract

Wide bandgap GaN very often shows a high electron concentration. Although several impurities such as O and Si have been identified, the concentration is not high enough to account for the number of free carriers. As a consequence native defects namely the nitrogen vacancies are widely considered to be present at high densities. Several calculations predict different energy levels of this strongly localized defect. We present photoluminescence experiments of wurtzite GaN and AlGaN layers under large hydrostatic pressure to search for localized defects within the questionable energy range of 3.0 to 3.8 eV above the valence band edge.

Introduction

The growing interest in GaN and the wide bandgap III-V nitrides is driven by the recent demonstration of UV and blue light emitting devices [1]. This success has been achieved by a continuous basic research effort over the last few decades. Although promising device performances have been obtained, a great amount of details of the electronic and defect structure are still not understood. As observed in GaN material grown by many different techniques, it is very often highly n-type conducting in the range of 10^{18} - 10^{20} cm⁻³ [2]. However no impurities could be observed or identified by any technique at that high concentration. Secondary ion mass spectroscopy (SIMS) results indeed reveal incorporation of O or Si and both of those elements should act as a donor in GaN [3,4], yet concentration typically ranges about two orders of magnitude below the observed carrier concentration in highly conducting material [5-8]. Based on the presently available data, impurities can not be the major source of dopants in GaN. Consequently native defects are considered to be present in very high concentrations.

Calculations by several groups predict the charge states and the energy levels of native defects [9-11]. At present only isolated defects rather than complexes have been considered, and among group III vacancies, group V vacancies and antisites the nitrogen vacancy V_N is the best candidate to act as a donor. From several stoichiometry considerations this candidate has been favored in many publications [12,13]. However no experimental evidence of the existence of this

defect could be given so far. The model of Jenkins et al. [9] predict two levels A_1 and T_2 of the neutral V_N to lie close to the conduction band (CB). A_1 should be filled with two electrons and lie ~ 0.2 eV below CB whereas T_2 should carry one out of six electrons and lie ~ 0.6 eV above the CB. Being resonant with the CB the electron would auto-ionize, thermalize to the band edge and finally be bound in a hydrogenic state of the remaining fixed positive charge. Boguslawski et al. [10] predict both of those levels to lie within the CB, A_1 at $E_{CB} + 0.8$ eV, T_2 at $E_{CB} + 1.3$ eV. In a third calculation by Neugebauer and Van de Walle [11] existence of the resonant level T_2 has been confirmed, in contrast to the other predictions the A_1 level should lie within the valence band and should not contribute as a donor level. Interestingly a calculation of the formation energy in the same work denies the possibility of formation of high isolated V_N concentrations unless the material is highly p-type.

Here we present a photoluminescence study of autodoped highly conducting AlGa_{0.85}N and GaN layers applying large hydrostatic pressure in search for the possible level of V_N in the region of 3.0 to 3.8 eV. Being a strongly localized defect the energy levels of the V_N should be independent to a high degree from the energetic position of the band edges. Shifting the band edge by alloying, e.g. in AlGa_{0.85}N, or under hydrostatic pressure would then separate hydrogenic levels from levels of strongly localized defects. Such a behavior has been observed for several defects, e.g. in AlGaAs [14].

Experimental

Nominally undoped Al_{0.15}Ga_{0.85}N/GaN/sapphire heterostructure samples were grown by atmospheric pressure MOCVD using the technique of low temperature AlN buffer layers [15]. Layer thickness was 2 μ m (GaN) and 1 μ m (AlGa_{0.85}N). Low temperature (6K) PL was excited by a 10 mW, 325 nm line of a HeCd laser, dispersed by a 1 m double monochromator (SPEX) and detected by a UV sensitive photomultiplier tube using lock-in detection. Hydrostatic pressure was applied by means of a Merrill-Bassett type diamond anvil cell using the fluorescence of R₁ ruby lines at 6 K as secondary standard for the pressure determination [16].

Results

PL of the heterostructure at 0.7 GPa (a) and 3.4 GPa (b) in the vicinity of the bandgaps is presented in Fig. 1. Spectra are given for excitation from the AlGa_{0.85}N layer side (full lines) and the substrate side (dashed lines) (refer to the CB schematic in the inset). Luminescence of the AlGa_{0.85}N layer is blocked when excited from the substrate side and only a signal from the GaN layer is observed. Excitation from the top shows the shallow bound excitons of both of the layers

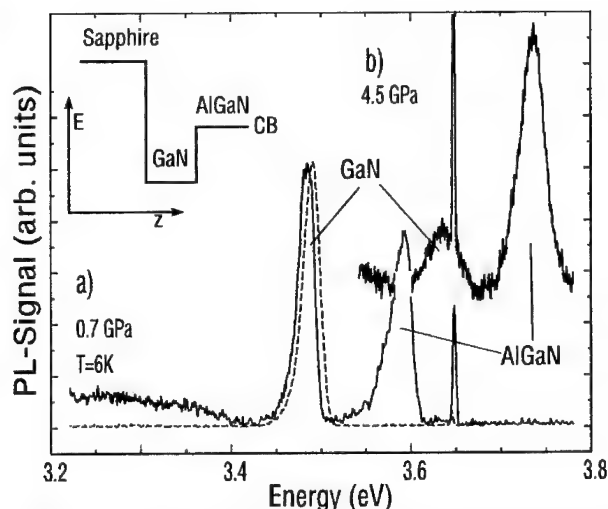


Figure 1: PL excitation from the AlGaN side (full line) and through the substrate (dashed line) at 0.7 GPa (a) and 4.5 GPa (b).

asymmetric lineshape with an exponential tail to the low energy side. This is especially obvious on a logarithmic scale (Fig. 3). Besides strain effects this tail width is very sensitive to the presence of a high density of defect states at this energy. In photoluminescence an additional very narrow line is observed in all spectra at 3.6466 eV and stems from a first order LO-Raman

and a defect related contribution on the lower edge of the spectrum. These defects are located in the AlGaN layer, as the luminescence can only be excited through the AlGaN band edge. There is a small separation of 6.7 meV (0.7 GPa) and 8.7 meV (3.4 GPa) in the excitonic luminescence of the GaN layer that corresponds to the band edge shift due to different bi-axial strain conditions on the lower and the upper GaN interfaces [17]. Both excitons show an

line of the HeCd laser in the diamonds of the pressure cell.

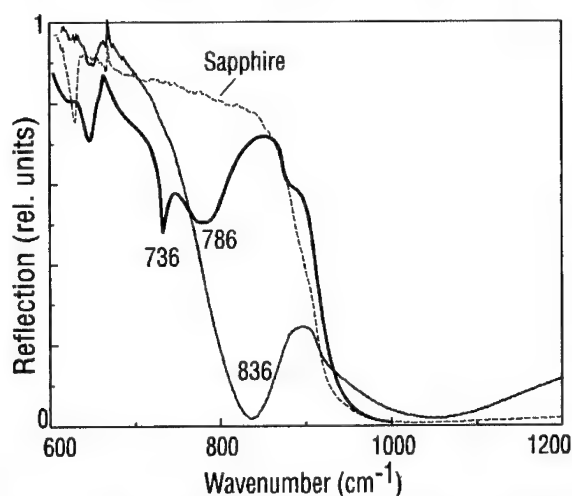


Figure 2: Infrared reflection of the heterostructures. The phonon-plasmon coupled modes reduce the reflection of the sapphire (dashed) reststrahlenband.

The high defect and carrier concentration in the individual layers of these films is confirmed by the infrared experiment in Fig. 2. Within the phonon region reflection is dominated by the reststrahlenband of the sapphire substrate with a high frequency edge at about 900 cm^{-1} . The layers on top of this mirror-like substrate give rise to pronounced dips at the energies of the LO

phonon-plasmon coupled modes in the individual layers. From the position and the line shape within an oscillator model of the dielectric function the carrier concentration is derived ($N = 1 \times 10^{18} - 2 \times 10^{18} \text{ cm}^{-3}$) using parameters of GaN [18].

According to the typical behavior of strongly localized defects a pressure dependence different from the band edges can be expected under hydrostatic pressure. Spectra are obtained from ambient pressure up to 7 GPa. The peak positions of the shallow bound excitons are collected in Fig. 4 (squares GaN, circles AlGaIn). Within our pressure range we find a linear shift of the exciton position with pressure.

$$\begin{aligned} dE/dp &= 43.7 \pm 1.0 \text{ meV/GPa in GaN} \\ &= 44.3 \pm 1.4 \text{ meV/GPa in Al}_{0.15}\text{Ga}_{0.85}\text{N}. \end{aligned}$$

For the ease of interpretation the spectra displayed in Fig. 2 on a logarithmic scale are corrected for the pressure shift of the GaN exciton. We thus realize that all features move parallel to the excitonic lines. The defect related features in the AlGaIn layer reveal a donor acceptor transition structure including several phonon replica. At higher pressure they are especially pronounced. The line width of the excitonic transitions shows only little change in the GaN layer (FWHM ~ 26 meV), in the AlGaIn layer it slightly increases up to ~ 35 meV at 4.6 GPa (marker B in Fig. 3). From the peak positions (Fig. 4) we derive a binding energy of the donor acceptor transition of 229 ± 7 meV with respect to the exciton or ~ 260 meV with respect to the band edge assuming an exciton binding energy of 30 meV. Phonon replica appear with energies of 85 to 96 meV in first and second order (see dotted lines in Fig. 4 parallel to excitonic shift).

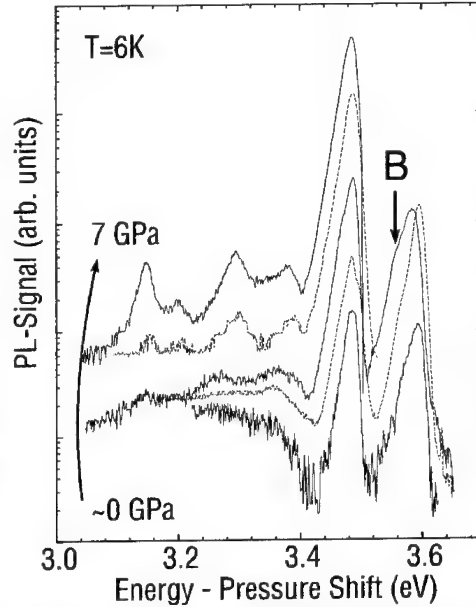


Figure 3: PL on a logarithmic scale versus the energy shifted by the pressure increase of the GaN excitonic gap.

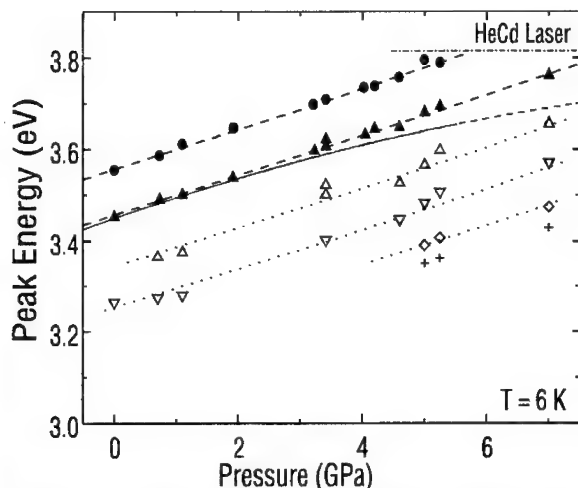


Figure 4: Peakposition of the excitonic transitions in AlGaIn (full circles) and GaN (full triangles). The dashed lines are the best linear fit. The defect related transitions are represented by open symbols. The dotted lines are guides for the eye parallel the excitonic shift. The full line is the result of Ref. [19].

Besides this feature we find no indication of strongly localized defects when shifting the excitons from 3.45 to 3.8 eV. We furthermore conclude that within the scope of our interpretation no strongly localized levels lie within the range of 3.45 to 3.7 eV above the respective valence band edge in our samples. In addition no strongly localized defect was observed in photoluminescence in the spectral range covered here down to 3.0 eV. It should be mentioned that other experiments indicate a crossing of the CB with a localized level at about 18 GPa [19] respective below 27 GPa [20].

Within the pressure range up to 7 GPa we find a linear dependence of the excitonic bandgap energies in GaN and $\text{Al}_{0.15}\text{Ga}_{0.85}\text{N}$. This is in contrast to available data from absorption in thick samples without substrate [21]. Up to pressures of 5.5 GPa a strong sublinear behavior was observed (drawn line in Fig. 4). Our findings might be related to the bi-axial strain present in our thin film structures as manifested in the GaN peak difference when looking from the top or the substrate side. Similar results are obtained on cubic GaN samples for $p \leq 5$ GPa [22].

CW acknowledges support by the Deutsche Forschungsgemeinschaft. Work partially supported by US DOE under Contract DE-AC03-76SF00098, and Ministry of Education, Science, and Culture of Japan Contracts 03243107, 06452114 and Hosono Bunka Foundation.

Discussion

From these experiments we conclude that all observed luminescence contributions in the AlGaIn/GaN heterostructure samples behave like hydrogenic defect levels. All spectral features in the heterostructure shift parallel to the band edges. There is a weak indication of a possible interaction with additional defect states in the AlGaIn excitonic luminescence at 4.6 GPa. However at 3.75 eV this line is close to the laser excitation and this could as well affect the line shape. Further investigations are necessary to clarify this point.

References

- [1] I. Akasaki, H. Amano, N. Koide, M. Kotaki, K. Manabe, *Physica B* **185**, 428 (1993).
- [2] A.S. Barker Jr. and M. Ilegems, *Phys. Rev. B* **7**, 743 (1973).
- [3] N. Koide, H. Kato, M. Sassa, S. Yamasaki, K. Manabe, M. Hashimoto, H. Amano, K. Hiramatsu, and I. Akasaki, *J. Crystal Growth* **115**, 639 (1991).
- [4] W. Seifert, R. Franzheld, E. Butter, H. Sobotta, V. Riede, *Cryst. Res. Technol.* **18**, 383 (1983).
- [5] B.C. Chung, M. Gershenzon, *J. Appl. Phys.* **72**, 651 (1992).
- [6] M. Ilegems, H.C. Montgomery, *J. Phys. Chem. Solids* **34**, 885 (1973).
- [7] R.J. Molnar, T.D. Moustakas, *J. Appl. Phys.* **76**, 4587, (1994).
- [8] R.D. Dupuis (private communication).
- [9] D.W. Jenkins, J.D. Dow, Min-Hsiung Tsai, *J. of Appl. Phys.* **72**, 4130 (1992).
- [10] P. Boguslawski, E. Briggs, T.A. White, M.G. Wensell, and J. Bernholc, Diamond, SiC and Nitride Wide-Bandgap Semiconductors, eds. C.H. Carter Jr, G. Gildenblat, S. Nakamura and R.J. Nemanich (*Mater. Res. Soc. Proc.* **339**, Pittsburgh, PA 1994) p. 693.
- [11] J. Neugebauer and C.G. Van de Walle, *Phys. Rev. B* **50**, 8067 (1994).
- [12] H.P. Maruska, J.J. Tietjen, *Appl. Phys. Lett.* **15**, 327 (1969).
- [13] J.I. Pankove, in Non-Stoichiometry in Semiconductors. *Proc. of Symp. A3 ICAM 91*. Edited by: K.J. Bachmann, H.-L. Hwang, C. Schwab, Amsterdam, Netherlands: North-Holland, 1992. p. 143-53.
- [14] M. Mizuta, M. Tachikawa, H. Kukimoto, and S. Minomura, *Jpn. J. Appl. Phys.* **24**, L143 (1985).
- [15] Y. Koide, H. Itoh, N. Sawaki, I. Akasaki, M. Hashimoto, *J. Electrochem. Soc.* **133**, 1956 (1986).
- [16] H.K. Mao, J. Xu, P.M. Bell, *J. Geophys. Research*, **91**, 673 (1986).
- [17] K. Naniwae, S. Itoh, H. Amano, K. Itoh, K. Hiramatsu, and I. Akasaki, *J. Crystal Growth*, **99**, 381 (1990).
- [18] C. Wetzel, D. Volm, B.K. Meyer, K. Pressel, S. Nilsson, E.N. Mokhov, P.G. Baranov, *Appl. Phys. Lett.* **65**, 1033 (1994).
- [19] P. Perlin, H. Teisseyre, T. Suski, M. Leszczynski, I. Grzegory, J. Jun, and S. Porowski, 22nd International Conference on the Physics of Semiconductors, Vancouver, Canada 1994. Ed. D.J. Lockwood (World Scientific Singapore 1995) p. 2383.
- [20] C. Wetzel, S. Fischer, W. Walukiewicz, E.E. Haller, P. Perlin, T. Suski, *Bulletin Am. Phys. Soc.* **40** (1), 416 (1995); C. Wetzel, W. Walukiewicz, E.E. Haller, I. Grzegory, S. Porowski, T. Suski, (unpublished).
- [21] P. Perlin, I. Gorczyca, N.E. Christensen, I. Grzegory, H. Teisseyre, and T. Suski, *Phys. Rev. B* **45**, 13307 (1992).
- [22] S.J. Hwang, W. Shan, R.J. Hauenstein, J.J. Song, M.-E. Lin, S. Strite, B.N. Sverdlov, H. Morkoç, *Appl. Phys. Lett.* **64**, 2928 (1994).

PHOTOCONDUCTIVITY AS A FUNCTION OF TEMPERATURE IN MOCVD GROWN GALLIUM NITRIDE FILMS

C. H. Qiu^(a), W. Melton^(b), and J. I. Pankove^(a,b)

(a) Astralux Inc., 2386 Vassar Drive, Boulder, CO 80303-5763

(b) University of Colorado, Dept. of Electrical Engineering, Boulder, CO 80309-0425

ABSTRACT

The optical absorption in gallium nitride (GaN) films was studied by photoconductivity (PC) spectroscopy at various temperatures. At all the measured temperatures, the photoconductivity per incident photon increases with photon energy $h\nu$ from 1.8 eV to 3.0 eV approximately as $\exp(h\nu/E_0)$. Surprisingly, the measured photoconductivity tail to the infrared becomes more pronounced in magnitude at lower temperatures. We suggest from the data that the photoconductivity is dominated by majority carriers, and that the quantum efficiency η for conducting electron and hole generation by across-gap excitation increases with increasing temperature.

INTRODUCTION

Gallium nitride (GaN) and its alloys with Al and In are potential candidate materials for blue-UV lasers, UV detectors, and high temperature electronics. This is evident from several impressive device achievements in the last few years, including the injection light-emitting diodes (LED),¹⁻⁴ solar-blind UV detector,⁵ and high temperature transistors^{6,7}. Surprisingly, the nitride materials seem to have high densities of structural and electronic defects. In fact, a broad distribution of states within the forbidden gap of GaN is revealed by both photoconductivity spectroscopy⁸ and photothermal deflection spectroscopy⁹. A high density of dislocations is also observed from the blue LEDs supplied by Nichia.¹⁰ Based on our measurements at room temperature, we suggested that there is a broad valence band tail in n-type GaN and a broad conduction band tail in p-type GaN.⁸ To ascertain this picture, we studied the photoconductivity spectra at lower temperatures where phonon assisted optical transitions are less probable. The new data not only support our model, but also reveal some interesting insights.

EXPERIMENTAL

The undoped n-type GaN thin films were grown on sapphire at Astralux in cold-wall low pressure metalorganic chemical vapor deposition (MOCVD) systems.⁸ The deposited films are epitaxial wurtzitic GaN as shown by X-ray diffraction. The p-type conducting films were grown at Meijo University in Japan. Sample 511 is undoped, exhibiting at room temperature a Hall mobility of 154 cm²/V-sec, an electron concentration of 1.3×10^{18} cm⁻³, and a strong near edge light emission. AA1 is p-type conducting, with a room temperature hole concentration of 6×10^{17} cm⁻³.

For the PC spectra measurement, a GE 1493 lamp was used as the light source. The radiation was filtered by a Perkin-Elmer model 12 monochromator equipped with a quartz prism. The photon flux vs. photon energy at the specimen was separately measured by replacing the specimen with an RCA 31025 photomultiplier, a PbS detector, and a calibrated Si detector. The photoconductivity was measured in a coplanar geometry with two indium contacts soldered to

the GaN surface, with samples placed on a cold finger cooled by a closed cycle helium refrigerator. The I-V curve is linear for n-type samples, whereas for p-type films the I-V curve is linear for voltages greater than 0.3 volts. A DC voltage was supplied to the sample through a series resistor. The DC voltage and the series resistor were chosen to minimize sample self-heating. The voltage output across either the sample or the load resistor, the one with the smaller resistance, was detected by the lock-in technique. The chopper frequency was 7 Hz. The PC signal decreases by a factor of two at a chopping frequency of about 20 Hz.

RESULTS AND DISCUSSIONS

The photoconductivity σ_{ph} corresponding to the incident flux F is given by:

$$\sigma_{ph} = eF(1-R)(1-e^{-\alpha d})[(\eta\mu\tau)_e + (\eta\mu\tau)_h]/d \quad (1),$$

where e is the electron charge, d is the film thickness, R and α are respectively the reflection coefficient and the absorption coefficient for the incident light. The sub-scripts e and h represent respectively the contribution of photo-excited electrons and holes to the photoconductivity. η , μ , and τ are respectively the quantum efficiency for photo-generation, the mobility, and the lifetime of the photo-excited carriers.

For each sample, the photoconductivity at all photon energies is much lower than the dark conductivity. Thus, the lifetime of the majority carriers is approximately independent of the photon energy because of the extremely small variation of the quasi-Fermi level. For clarity of later discussion, we shall define $r_e = (\mu\tau)_e / [(\mu\tau)_e + (\mu\tau)_h]$ for n-type samples and $r_p = (\mu\tau)_h / [(\mu\tau)_e + (\mu\tau)_h]$ for p-type samples to indicate the contribution of the majority carriers to PC. If we assume that electrons and holes excited to states within the forbidden gap are not mobile, photons with $h\nu$ several tenths of an eV less than E_g produce mostly mobile electrons in n-type GaN and mobile holes in p-type GaN. Thus, from equation (1)

$$\sigma_{ph}/F = e(1-R)\alpha(\eta\mu\tau)_e = e(1-R)\alpha(\mu\tau)_e \quad (\text{assuming } \eta=1) \quad (2),$$

for infrared light excitation of n-type sample ($\alpha d \ll 1$); and

$$\sigma_{ph}/F = e(1-R)\alpha(\eta\mu\tau)_h = e(1-R)\alpha(\mu\tau)_h \quad (3),$$

for infrared light excitation of p-type sample ($\alpha d \ll 1$); and assuming $\eta_e = \eta_h = \eta$,

$$\sigma_{ph}/F = e(1-R)\eta[(\mu\tau)_e + (\mu\tau)_h]/d \quad (4),$$

for across-gap light excitation ($\alpha d \gg 1$, e. g. at 3.6 eV). Thus, the PC spectra can be normalized at 3.6 eV to yield $1-e^{-\alpha d}$ for $h\nu$ close to E_g and $r_e\alpha d/\eta$ (or $r_p\alpha d/\eta$ if p-type) for $h\nu$ several tenths of an eV less than E_g , if the reflection coefficient R does not vary much with photon energy. We found that PC spectra measured with chopper frequencies of 5 -160 Hz yield identical normalized spectra, supporting our assumption that the lifetime of the majority carriers is independent of photon energy.

Fig. 1 is the normalized photoconductivity spectra of samples 511 and AA1. The spectra clearly show light absorption from near infrared to UV. Furthermore, the photoconductivity

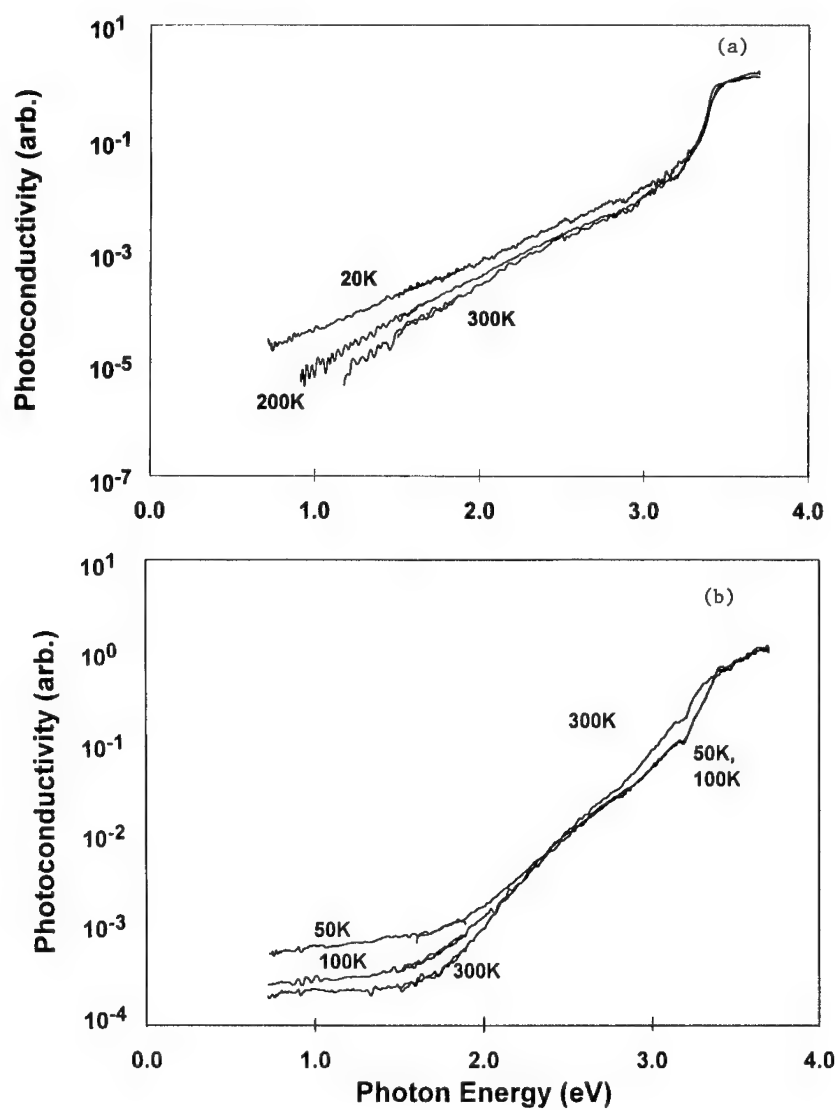


Fig. 1. Normalized photoconductivity spectra of n-type sample 511 (a), and p-type sample AA1 (b), measured at several temperatures.

response in the infrared is relatively more pronounced at lower temperatures. The normalized photoconductivity increases with photon energy $h\nu$ from 1.8 eV to 3.0 eV approximately as $\exp(h\nu/E_0)$. Contrary to the temperature dependence of the Urbach edge parameter,¹¹⁻¹³ the E_0 parameter in Fig. 1 increases when the sample temperature is lowered.

To understand the PC spectra, the photoconductivity measured at 3.6 eV and at 1.5 eV are plotted as a function of temperature in Fig. 2 for sample 511. When sample 511 is cooled, the photoconductivity excited by UV light decreases while the photoconductivity excited by infrared light increases.

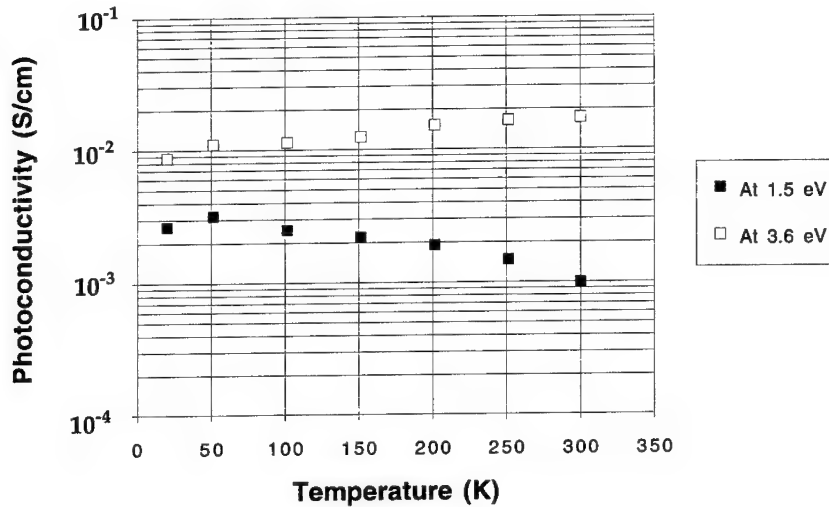


Fig. 2. Photoconductivity for n-type conducting sample GaN measured at 3.6 eV and at 1.5 eV as a function of temperature .

The decrease of photoconductivity with increasing temperature is termed as “thermal quenching” of photoconductivity, and is usually attributed to a decrease in majority carrier lifetime.¹⁴ In our case, we believe the electron lifetime at higher temperature is not shorter. In fact, the photocurrent decay of this sample is temperature-independent.¹⁵ Thus, from Eq. (2), the decrease of $\sigma_{ph}(1.5\text{eV})$ with increasing temperature suggests a decrease of $\alpha\mu_e$ with temperature. It is likely that the electron mobility μ_e peaks at ~50 K and decreases when T is increased further.

We suggest tentatively that $(\mu\tau)_e \gg (\mu\tau)_h$ for n-type material. The reported electron mobility μ_e in n-type GaN is at least a factor of 10 higher than hole mobility μ_h in p-type GaN. Further-more, our data suggested that there is a broad valence band tail in n-type GaN and a broad conduction band tail in p-type GaN.⁸ We thus expect that μ_h in n-type GaN is smaller than

μ_h in p-type GaN, because of the more pronounced valence band tail states in n-type GaN. Similarly, we expect $\tau_h < \tau_e$ in n-type GaN, since trapping in the valence band tail would reduce hole lifetime in the valence band.

With this background, we see that η , the quantum efficiency for mobile electron and hole generation, should increase with increasing temperature. Otherwise, $\sigma_{ph}(3.6 \text{ eV})$ in Fig. 2 would not increase with increasing temperature. The ratio of $\sigma_{ph}(3.6 \text{ eV})/\sigma_{ph}(1.5 \text{ eV})$ increases by a factor of six from 20 K to 300 K.

For p-type sample AA1, the photoconductivity measured at 3.6 eV and at 1.1 eV, are plotted as a function of temperature in Fig. 3. When the sample is cooled down, both $\sigma_{ph}(3.6 \text{ eV})$ and $\sigma_{ph}(1.1 \text{ eV})$ decrease. From Eq. (3), the decrease of $\sigma_{ph}(1.1 \text{ eV})$ may be attributable to a decrease of the hole lifetime τ_h . From 400 K to 100 K, the decrease of $\sigma_{ph}(3.6 \text{ eV})$ is very similar to the decrease of $\sigma_{ph}(1.1 \text{ eV})$. In other words, it reflects the decrease of the hole lifetime. From this result, we conclude that $(\mu\tau)_h \gg (\mu\tau)_e$ in p-type GaN. In other words, hole conduction dominates the photocurrent in p-type GaN, even though the electron mobility may be greater than the hole mobility. As a result, Eq. (4) simplifies to

$$\sigma_{ph}/F = e(1-R)\eta(\mu\tau)_h/d \quad (5),$$

for across-gap light excitation of p-type GaN.

From 100 K to 6 K, $\sigma_{ph}(1.1 \text{ eV})$ decreases only a little-indicating an almost constant τ_h , while $\sigma_{ph}(3.6 \text{ eV})$ decreases by a factor of seven. From Eq. (5), we are led to the conclusion that η , the quantum efficiency for mobile electron and hole generation, decreases with decreasing temperature. It appears to us that across-gap light creates excitons, which do not contribute to conductivity until they split up.

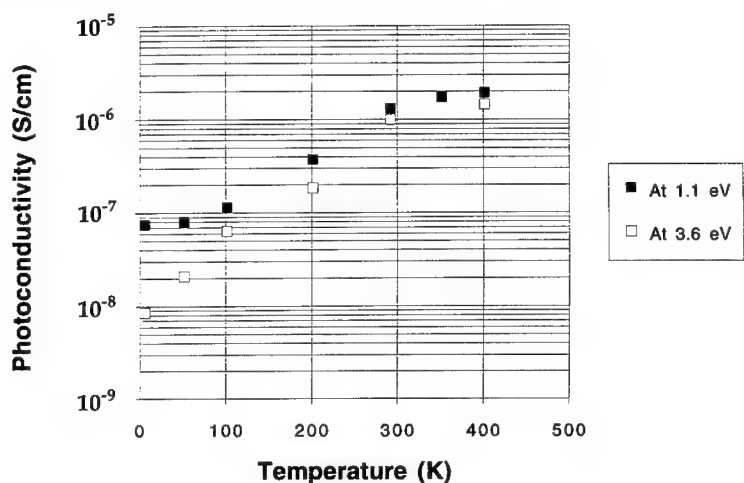


Fig. 3. Photoconductivity for p-type conducting GaN measured at 3.6 eV and at 1.1 eV as a function of temperature .

CONCLUSIONS

In summary, we measured the sub-band gap optical absorption in GaN films by photoconductivity spectroscopy to lower temperatures. Photoconductivity response is observed from near infrared to the near ultraviolet at all measurement temperatures for GaN films on sapphire. Such data support our earlier suggestion that there is a broad valence band tail in n-type GaN and a broad conduction band tail in p-type GaN. Furthermore, relatively more pronounced photoconductivity response in the infrared is observed at lower temperatures. We suggest that: (1) $(\mu\tau)_e \gg (\mu\tau)_h$ in n-type GaN, and $(\mu\tau)_h \gg (\mu\tau)_e$ in p-type GaN. In other words, the photo-conductivity is dominated by majority carriers; (2) η , the quantum efficiency for conducting electron and hole generation by across-gap excitation, increases with increasing temperature for both n-type and p-type samples. This result may be attributable to the dissociation of excitons.

ACKNOWLEDGMENTS

We are grateful to Profs. I. Akasaki and H. Amano for supplying the Mg-doped p-type conducting GaN samples used in this measurement. The work at Astralux was supported by BMDO/IST grant N00014-94-C-0171 and monitored by Mr. Max Yoder. Mr. Melton was supported by ARPA-URI grant N00014-92-1-1895.

References

1. H. Amano, M. Kito, K. Hiramatsu, and I. Akasaki, *Jpn. J. Appl. Phys.* **28**, L2112 (1989); I. Akasaki, H. Amano, M. Kito, and K. Hiramatsu, *J. Luminescence* **48/49**, 666 (1991).
2. S. Nakamura, T. Mukai, and M. Senoh, *Jpn. J. Appl. Phys.* **30**, L1998(1991); *Appl. Phys. Lett.* **62**, 2390 (1993); *ibid.* **64**, 1687 (1994).
3. B. Goldenberg, J. D. Zook, and R. Ulmer, *Appl. Phys. Lett.* **62**, 381 (1993).
4. R. J. Molnar, R. Singh, and T. D. Moustakas, *Appl. Phys. Lett.* **66**, 268 (1995).
5. M. Asif Khan, J. N. Kuznia, D. T. Olson, M. Blasinggame, and A. R. Bhattacharai, *Appl. Phys. Lett.* **63**, 2445 (1993).
6. M. Asif Khan, M. S. Shur, J. N. Kuznia, Q. Chen, J. Burm, and W. Schaff, *Appl. Phys. Lett.* **66**, 1083 (1995).
7. J. I. Pankove, S. S. Chang, H. C. Lee, R. J. Molnar, T. D. Moustakas, and B. Van Zeghbroeck, *IEDM 94*, p. 389.
8. C. H. Qiu, C. Hoggatt, W. Melton, M. W. Leksono, and J. I. Pankove, presented at the 2nd Int. Workshop on III-Nitrides, St. Louis, Oct. 1994, accepted for publication in *Appl. Phys. Lett.*
9. O. Ambacher, W. Rieger, and M. Stutzmann, presented at the 2nd Int. Workshop on III-Nitrides, St. Louis, Oct. 1994.
10. S. D. Lester, F. A. Ponce, M. G. Craford, and D. A. Steigerwald, *Appl. Phys. Lett.* **66**, 1249 (1995).
11. M. D. Sturge, *Phys. Rev.* **127**, 768(1962).
12. D. Redfield and M. A. Fromowitz, *Appl. Phys. Lett.* **11**, 138(1967).
13. D. Han, C. H. Qiu, and W. Wu, *Phil. Mag.* **B54**, L9(1986).
14. A. Rose, *Concepts in Photoconductivity and Allied Problems* (Wiley Interscience, New York, 1963).
15. C. H. Qiu, C. Hoggatt, Z. Zhang, M. W. Leksono, and J. I. Pankove, presented at the 41st national AVS meeting, Denver, CO, Oct. 1994 (unpublished).

TIME RESOLVED PHOTOLUMINESCENCE SPECTROSCOPY ON GaN EPITAXIAL LAYERS

B. K. Meyer, D. Volm, C. Wetzel[#], L. Eeckey^a, J.-Ch. Holst^a, P. Maxim^a, R. Heitz^a, A. Hoffmann^a, I. Broser^a, E. N. Mokhov^b, P. G. Baranov^b, C. Qiu^c and J.I. Pankove^c

Technische Universität München, Physik-Department E16, 85747 Garching, Germany

^aTechnische Universität Berlin, Institut für Festkörperphysik, 10623 Berlin, Germany

^bIoffe Physico Technical Institut, 194021 St. Petersburg, Russia

^cAstralux, Boulder, CO, USA

ABSTRACT

Free and bound exciton luminescences as well as donor-acceptor pair recombination of GaN epitaxial layers on 6H-SiC and sapphire substrates were investigated using time integrated and time resolved photoluminescence measurements at low temperatures. Lifetimes are determined for the donor bound exciton at 3.4722eV and for two acceptor bound excitons with energies of 3.4672eV and 3.459eV. Luminescences between 3.29eV and 3.37eV are identified as due to excitons deeply bound to centers located near the substrate-epilayer interface.

INTRODUCTION

Recent success in growth technology that allowed to produce p- type GaN¹, and the realisation of the first blue light emitting diodes² have revived widespread interest in this material. For further progress towards a GaN based blue or ultraviolet (UV) optoelectronic device a thorough understanding of the recombination mechanisms and the role of impurity related transitions is necessary. The formation of excitons, their capture by shallow impurities and defects, and the subsequent radiative decay is one of the most efficient recombination mechanisms in direct semiconductors. For GaN, investigations on the recombination dynamics have been restricted to donor-acceptor-pair (DAP) transitions³ and deeper luminescences⁴. The excitonic range of GaN is new ground regarding dynamical studies. In addition, the assignment of blue and UV luminescences of GaN to specific recombination processes has been tentative in some cases, as will be seen below. Here, luminescence transients can often give a fingerprint of the processes involved, thus allowing an identification of their nature.

EXPERIMENTAL

GaN epilayers were grown on 6H-SiC (0001) substrates using a modification of the sublimation sandwich method described earlier⁵. The samples prepared for this study have an epilayer thickness of 50 μm , exhibit n-conductivity and an electron mobility between 30 and 80 cm^2/Vs . They are nominally undoped⁶. The GaN layers on sapphire were grown by the metal organic chemical vapor deposition (MOCVD) technique at temperatures around 1030 $^\circ\text{C}$. The source gases were ammonia and Tri-Ethyl-Gallium. Further details can be found in ref.7. All layers were n-type with free carrier concentrations ranging from high 10^{17} cm^{-3} to 10^{19} cm^{-3} as determined by room temperature Hall effect measurements.

For time integrated and time resolved photoluminescence measurements the samples were excited by 5ps 100 kW/cm² laser pulses at 3.75eV from a frequency doubled dye laser which is pumped by a modelocked and frequency doubled Nd:YAG laser. The photoluminescence signal was analysed in a 0.35m subtractive double spectrometer and detected by a MCP photomultiplier. For time resolved measurements a single photon counting setup was used with a 50 ps FWHM response to the laser pulse. Employing convolution techniques the overall time resolution is enhanced to 15 ps. Some time integrated experiments were performed using the 325 nm line of a HeCd laser for excitation.

EXPERIMENTAL RESULTS AND DISCUSSION

In low temperature PL a number of near gap emissions is generally observed. They may be roughly classified into three groups as due to free and shallow bound exciton transitions between 3.45 eV and 3.48 eV (see Fig. 1.a), deeply bound exciton transitions between 3.31 eV and 3.37 eV (see Fig. 1.c and d) and donor-acceptor-pair (D-A) recombination at 3.27 eV (see Fig. 1.b). The donor acceptor pair band at 3.27eV which is followed by four clearly discernible phonon replica was first identified by Dingle and Illegems⁸ using time resolved luminescence spectroscopy. The acceptor could be Mg due to a memory effect in the reactor. However, this D-A pair band is also typical for undoped GaN in the absence of memory effects, and is thought to involve residual Carbon acting as a shallow acceptor.

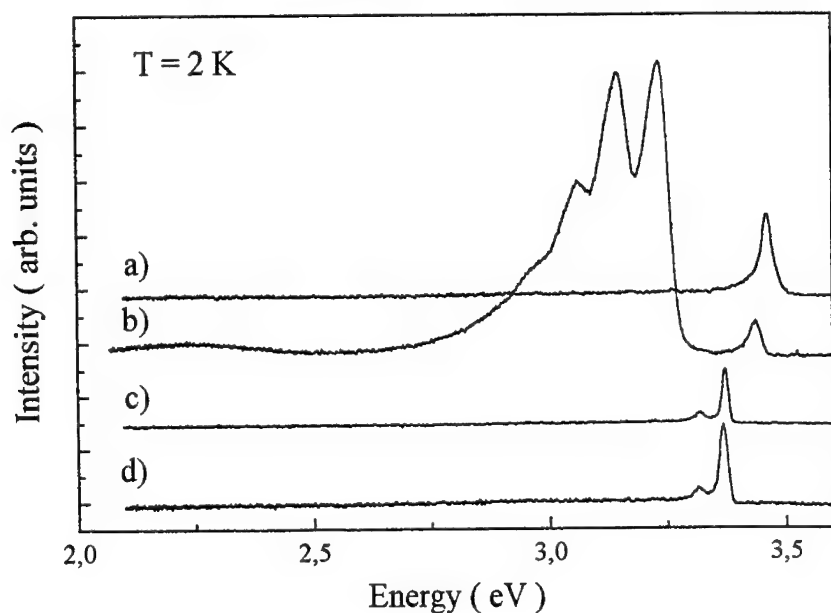


Fig. 1: Photoluminescence spectra for GaN epitaxial layers on sapphire substrates grown by MOCVD. The samples had free carrier densities of 5×10^{17} (a), 9×10^{17} (b), 2×10^{19} (c) and 7×10^{19} cm⁻³ (d) as determined by room temperature Hall effect.

We determined the carrier density by an analysis of the D-A pair transients (see Fig. 2) following the theory of Thomas et al.⁹ and obtained a concentration of $1 \times 10^{18} \text{ cm}^{-3}$. The parameters which enter are the Bohr radius of the donor $r_D = 13.5 \times 10^{-10} \text{ m}$, and the constant $W_{\text{max}} = 1.3 \times 10^8$.

When the carrier density is in the range of 10^{19} cm^{-3} the shallow bound exciton lines disappear and only the deeply bound exciton lines are seen (see Fig. 1.c,d).

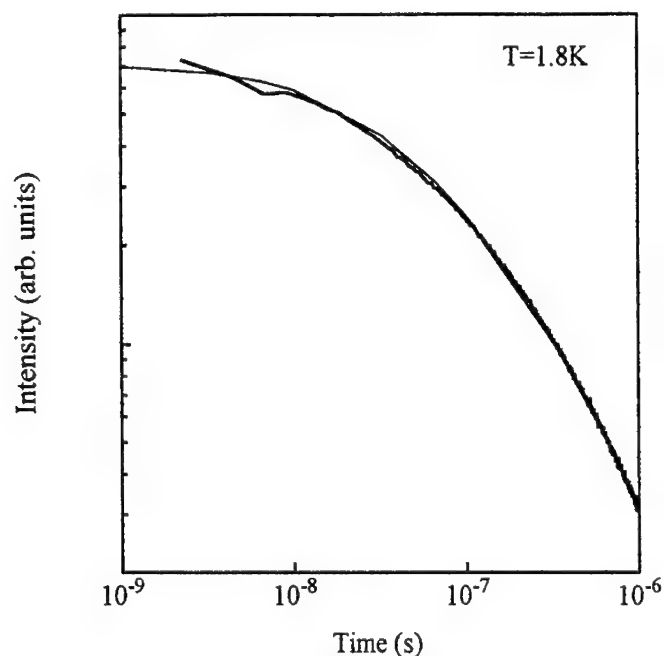


Fig. 2: Transient of the donor-acceptor pair luminescence in GaN. The drawn line is fit to the experimental data, for details see text.

For the GaN on SiC layers on the shallow and deeply bound excitons additional fine structure could be resolved. They are shown in Figs.3 and 4. In the first sample the dominant peak (2) is observed at 3.4722 eV with a FWHM of 5 meV (Fig. 3). Emission from GaN at 3.47eV is commonly ascribed to the recombination of an exciton bound to a shallow neutral donor and referred to as I_2 . Three minor structures are detected on the high and low energy shoulders of I_2 at 3.4805eV (FE), 3.4672eV (I_1'), and 3.459eV (I_1). The 3.4805 eV emission is due to the free exciton (FE) corresponding very well to FE recombination energies reported so far³. From data presented below and in agreement with Monemar and Lagerstedt¹⁰ we ascribe the emissions (3) and (4) to the recombination of excitons bound to two different neutral acceptors and therefore label them I_1' and I_1 . Luminescence transients taken in the range of the shallow bound exciton lines of sample A are shown in the inset of Fig. 3. The measurements are

represented by dotted curves. The labeling numbers correspond to the detection energies of the respective transients, referring to the luminescence spectrum of Fig. 3.

The partial overlap of the recombination lines and the spectral window of 3 meV during these time resolved measurements require a careful analysis of the transients. It was carried out using the convolution of the system response to the laser pulse with three independent exponential decays of different amplitudes. The obtained fits are represented by solid lines in the inset of Fig. 3. For the dominating I_2 (2) and the lower energy emissions I_1' (3) and I_1 (4) an unchanging set of time constants was obtained. Since the respective amplitudes of the three fitted exponential decays vary with the detection position the lifetimes of the bound excitons can unambiguously determined. They amount to 34 ± 5 ps for I_2 , 160 ± 15 ps for I_1 and 370 ± 40 ps for I_1' . For the free exciton a lifetime of 15 ps is obtained.

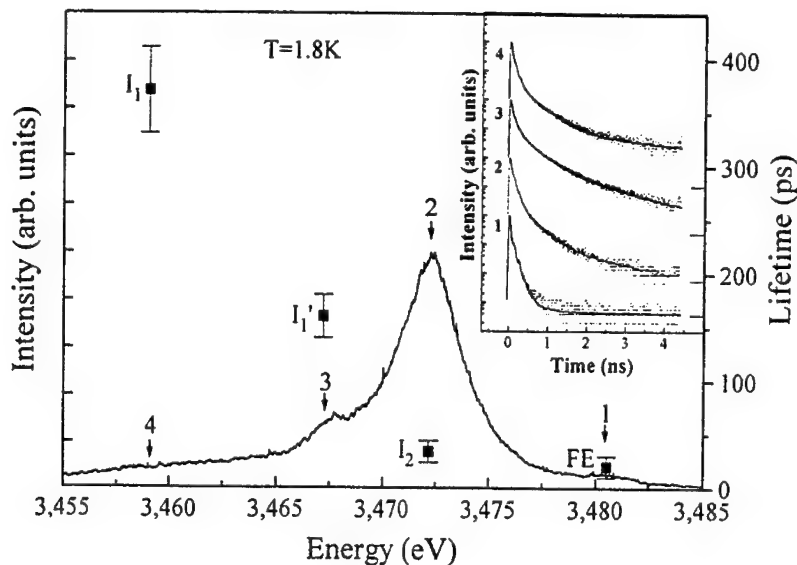


Fig. 3: Luminescence spectrum of GaN on SiC showing free and shallow donor bound exciton recombinations. At the transition energies marked with the numbers 1 to 4 luminescence transients were recorded (see inset); the dotted curves represent the measurements, full lines the pertaining fit.

These assignments of observed luminescence decay constants to the lifetimes of the shallow bound excitons are plausible also by a qualitative comparison of the four transients which are plotted on a logarithmic scale in Fig. 3. The short free exciton decay in transient (1) as well as the lifetime of 34 ps of the donor bound exciton observed in transients (2), (3) and (4) govern the decay for about the first 400 ps. As mentioned above, the time constant of the I_2 line is observed in all of these three transients because of the spectral overlap of the luminescence lines. Between 400 ps and about 2.5 ns on the time axis the line with the 160 ps time constant is dominating, most prominently at position (3), which is the I_1' transition energy. This justifies the

assignment of the 160 ps time constant to the I_1' recombination. The 370 ps time constant becomes most obvious after about 3 ns in transient (4). It is therefore identified as the lifetime of the I_1' complex.

Emission lines in the range between 3.31 eV and 3.37 eV are observed in many samples. In one sample - again with carrier densities around 10^{19} cm^{-3} - they appeared much stronger. The missing D-A recombination allowed to detect two weaker structures around 3.29 eV. We labeled all discernable lines L1 through L8 with increasing energy.

As can be seen in Fig. 4 the dominating 3.36 eV emission mainly consists of two peaks, L8 at 3.366 eV, and L7 at 3.360 eV, with line widths of about 4 meV. In addition, we resolve two weak structures L5 and L6 3.350 eV and 3.354 eV, respectively. At 3.311 eV we see the second prominent deeply bound exciton line L3. Its asymmetric lineshape on the high energy side is most likely caused by another weak line L4 around 3.32 eV. Two further weak lines L1 and L2 are resolved at 3.286 eV and 3.296 eV.

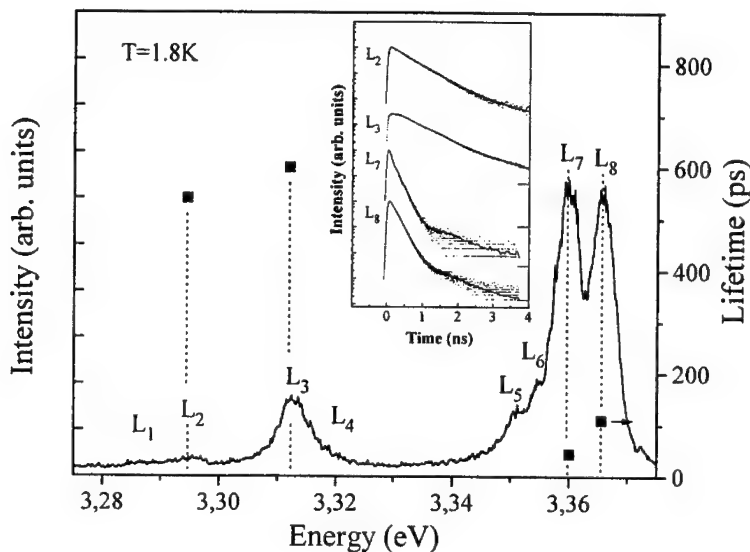


Fig. 4: Luminescence spectrum of GaN on SiC showing deeply bound exciton recombinations. At the transition energies marked with the numbers L1 to L8 luminescence transients were recorded, four of them are shown in the inset; the dotted curves represent the measurements, full lines the pertaining fit.

Several authors have reported luminescences from GaN in the range between 3.31 eV and 3.37 eV, lines L7 and L8 were observed by Pankove et al.¹¹. L3 at 3.311 eV was first reported by Dai et al.¹² along with L7 and L8 and tentatively ascribed to a DAP recombination. Recently, Hong et al.¹³ presented PL spectra on cubic epitaxial layers of GaN corresponding to the results of Dai et al.¹². The authors ascribed the higher energy lines around 3.36 eV to bound excitons and L3 to the DAP recombination of cubic GaN. However, the understanding of the

processes in this spectral range is still in a provisional state. We performed time resolved measurements to obtain additional information about the nature of these luminescences.

In the inset of Fig. 4 photoluminescence transients are shown taken at different spectral positions in this range (see Fig. 4). The exponential decay observed in all of these transients proves the excitonic character. In particular, the line L3 turned out to be of excitonic origin in contradiction to other interpretations^{12,13}. All transients exhibit a rise time constant of 20 ± 10 ps. This time constant corresponds to the formation of excitons and their capture by the centers causing the respective emissions. For L3 (transient (7) in Fig. 4) we observe an additional, weaker rise process which is governed by a time constant of 110 ± 10 ps. This corresponds exactly to the lifetime measured for L8. Obviously, there is an efficient energy transfer process from the center causing the emission L8 to that responsible for L3. A single center causing both emissions cannot be ruled out completely but seems very unlikely in view of the intensity ratio of these two lines. The lifetimes observed range between 45 ps for L7 and 650 ps for L3 which is very short regarding the excitonic localisation energy of about 110 to 180 meV for these lines. PL measurements by exciting the layer through the sapphire substrate showed that these luminescences are mainly localised near the interface. From the evidence collected to this point we conclude that these emissions are due to centers which are located predominantly present near the substrate-epilayer interface, e.g., at dislocations. The short lifetimes observed are primarily ascribed to efficient nonradiative processes in this structurally disturbed area.

CONCLUSION

In conclusion, we presented time resolved photoluminescence measurements of bound exciton recombinations in epitaxial GaN/SiC layers. Luminescences observed between 3.29 eV and 3.37 eV were identified as excitons deeply bound to centers located near the substrate-epilayer interface. An energy transfer process was found between the centers causing the lines at 3.366 eV and 3.311 eV.

present address: Lawrence Berkeley Lab., Berkeley, CA, USA

REFERENCES

1. H. Amano, M. Kito, K. Hiramatsu and I. Akasaki: Jpn. J. Appl. Phys. 28, L 2112 (1989)
2. S. Nakamura, M. Senoh, and T. Mukai, Appl. Phys. Lett. 62, 2390 (1993)
3. R. Dingle, D. D. Sell, S. E. Stokowski, and M. Ilegems: Phys. Rev. B 4, 1211 (1971)
4. P. Bergmann, Gao Ying, B. Monemar, and P.O. Holtz, J. Appl. Phys. 61, 4589 (1987)
5. Y.A. Vodakov, E. N. Mokhov, A. D. Roenkov and D. T. Saibekov, Kristall und Technik 14, 729 (1979)
6. C. Wetzel, D. Volm, B.K. Meyer, K. Pressel, S. Nilsson, E.N. Mokhov and P.G. Baranov, Appl. Phys. Lett. 65, 1033 (1994)
7. C.H. Qiu, C. Hoggatt, W. Melton, W.M. Leksono and J.I. Pankove (unpublished)
8. R. Dingle and M. Ilegems, Solid State Commun. 9, 175 (1971)
9. D.G. Thomas, J.J. Hopfield, and W. M. Augustyniak, Phys. Rev. 140, A202 (1965)
10. B. Monemar and O. Lagerstedt, J. Appl. Phys. 50, 6480 (1979)
11. J. I Pankove, J. E. Berkeysheiser, H. P. Maruska, J. Wittke: Solid State Commun. 8, 1051 (1970)
12. R. Dai, S. Fu, J. Xie, G. Fan, G. Hu, H. Schrey, C. Klingshirn: J. Phys. C 15, 393 (1982)
13. C. H. Hong, D. Pavlidis, S.W. Brown, and S.C Rand, J Appl. Phys 77, 1705 (1995)

DEFECT STUDIES IN n-TYPE GaN GROWN BY MOLECULAR BEAM EPITAXY

W. GÖTZ*, D.B. OBERMAN, AND J.S. HARRIS JR.

Solid State Electronics Laboratory, Stanford University, Stanford, California 94305, USA

ABSTRACT

GaN thin films grown by molecular beam epitaxy (MBE) were characterized by Hall effect measurements in the temperature range from 80 K to 500 K and by photoluminescence spectroscopy (PL) at 2 K and at 300 K. These films were grown by MBE utilizing either electron cyclotron resonance (ECR) plasma activated nitrogen gas or thermally cracked hydrogen azide (HN_3) as the source of chemically reactive nitrogen. The electrical properties of the GaN films grown by ECR plasma assisted MBE were found to vary with growth parameters, dominated either by shallow donors with activation energies (ΔE) in the range between 10 meV and 30 meV or deep donor levels ($\Delta E > 500$ meV). GaN grown by HN_3 gas-source MBE exhibited metallic conduction and electron mobilities $< 1 \text{ cm}^2/\text{Vs}$. However, these films displayed sharp photoluminescence lines at 3.360 eV and 3.298 eV and no deep level related luminescence, whereas only broad deep level related emission was observed in the PL spectra of the ECR plasma assisted MBE grown GaN films.

INTRODUCTION

The III-V nitrides are promising direct bandgap materials for photonic devices operating in the visible and near-uv wavelength range.¹ With the ability to grow lattice matched heterojunctions in the (AlGaIn)N mixed alloy system the fabrication of devices that make use of quantum well or superlattice structures such as diode lasers, resonators or waveguides should be possible.²

At present, the predominant growth technique utilized for III-V nitride devices is MOCVD. For example, the growth of high brightness blue/green light emitting diodes using an InGaN/AlGaIn heterostructure has been successfully demonstrated with this growth technique.^{3,4} However, all devices grown by MOCVD require postgrowth low energy electron beam irradiation (LEEBI) or thermal annealing to electrically activate acceptors.^{5,6} Total energy calculations suggest that hydrogen atoms present in the ambient during MOCVD growth readily diffuse in p-type GaN, bond to Mg and thus passivate the acceptors.⁷

GaN has been successfully grown by MBE, which furnishes growth conditions free of hydrogen and enables growth of III-V nitrides at significantly lower temperatures than MOCVD. ECR plasma activated nitrogen gas is commonly employed as an atomic nitrogen source in MBE growth of III-V nitrides (plasma assisted-MBE).^{8,9,10} With this technique, Mg-doping results in p-type GaN films without any postgrowth treatments.¹¹ Consequently, GaN p-n homojunction blue-violet light emitting diodes have been grown which require no postgrowth treatment for efficient operation.¹² However, films grown by this technique at high growth rates and, correspondingly, high plasma power levels suffer from ion irradiation damage creating electrically active defects.²

Alternative nitrogen sources for MBE growth of III-V nitrides that avoid ion irradiation damage are chemical gas sources, such as ammonia (NH_3), hydrazine (N_2H_4) or hydrogen azide (HN_3). HN_3 is the most reactive hydronitrogen source, has the lowest concentration of hydrogen byproducts and decomposes effectively at $\sim 300^\circ\text{C}$. HN_3 has been successfully utilized for MBE growth of GaN (HN_3 -GSMBE).¹³ With HN_3 , nitride films can be grown at temperatures as low as 500°C and at pressures far lower ($< 10^{-6}$ torr) than with the ECR-plasma source ($> 10^{-4}$ torr).¹³

This study evaluates GaN films grown by this novel growth technique of HN_3 -GSMBE as well as ECR-assisted MBE. Electrical and optoelectronic properties of unintentionally doped n-type GaN films were investigated by temperature dependent Hall effect and photoluminescence characterization at 2K and at 300 K.

EXPERIMENTAL

The GaN films used in this study were grown by MBE using a specially modified Varian Gen II system. Standard MBE furnaces were used to provide the Group III elements. A Wavemat ECR plasma source was used to grow some of the GaN films by plasma assisted-MBE. The HN_3 was synthesized in a reactor attached to the MBE system.¹³ HN_3 is chemically unstable and explosive unless stored at pressures < 100 torr. The GaN films were grown in the temperature range from 500°C to 860°C to a thickness of ~0.7 μm . The substrates were polished (0001)-oriented sapphire crystals. An AlN buffer layer 50 nm thick was first deposited on the sapphire at 500°C.

A Van der Pauw geometry was selected for the Hall effect measurements. Samples of $5 \times 5 \text{ mm}^2$ size were cut from the wafers. Ti (300 Å) and subsequently Al (1500 Å) layers were vacuum evaporated in the four corners of the samples to fabricate electrical contacts. The Ti/Al contacts exhibited ohmic current voltage characteristics in the entire temperature range of our measurement.

The Hall effect measurements were performed with a computer controlled system consisting of standard instrumentation for constant current supply and voltage detection. A Joule-Thompson high pressure nitrogen refrigerator was employed to control the sample temperature in the range from 80 K to 500 K. The magnetic field was 17.4 kGauss.

For the PL measurements the samples were mounted in a Janis DT cryostat and immersed in liquid He (2 K measurements). The PL spectra were excited with the 325 nm line of a 30 mW HeCd laser. A double grating monochromator with a resolution of 0.1 nm and a photo multiplier tube were used to measure the PL spectra.

HALL EFFECT CHARACTERIZATION OF MBE GROWN GaN FILMS

In Fig. 1, the electron concentrations of two unintentionally doped GaN samples grown by ECR-assisted MBE (# S33 (a) and # S34 (b)) are shown as functions of the reciprocal temperature. Sample # 33 and # 34 were grown at 600°C and 860°C with plasma powers of 150 W and 170 W, respectively. The electron concentrations $n(T)$ (squares in Fig.1) were derived from the experimental Hall constant $R_H(T)$ with the expression

$$n(T) = \frac{r_H}{qR_H(T)}, \quad (1)$$

where r_H is the Hall scattering factor and q is the electronic charge. The isotropic Hall scattering factor was assumed to be temperature independent and unity ($r_H \equiv 1$).

The solid lines in Fig. 1 result from a computation of the charge neutrality equation

$$n + N_{\text{comp}} = \sum_{i=1}^m \frac{N_i}{1 + (g_i/N_c) \exp(\Delta E_i/kT)}, \quad (2)$$

where N_{comp} represents the concentration of compensating acceptors and g_i is the degeneracy, which was assumed to be 2. N_c is the effective density of states in the conduction band and was

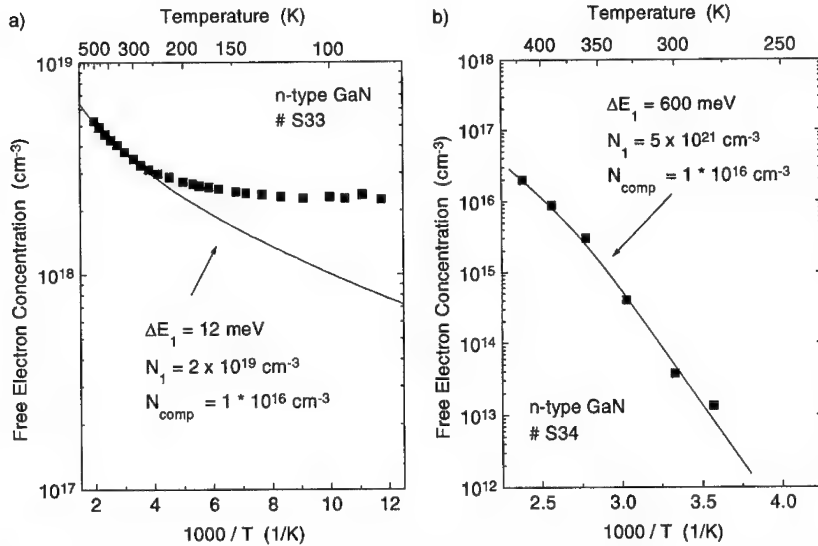


Fig. 1: Free electron concentration n vs. reciprocal temperature $1/T$ as obtained from Hall effect measurements of two n-type GaN samples # S33 (a) and # S 34 (b) (squares). The solid lines result from computations of the electron concentration with parameters as depicted in the figures.

calculated with an effective density of states mass of $0.2m_0$ ($N_C = 4.3 \times 10^{14} T^{3/2} \text{ cm}^{-3} \text{ K}^{-3/2}$). Eq. 2 is valid for a non-degenerate, n-type semiconductor with m independent donors. A single donor was assumed for the computations shown in Fig. 1. Activation energies ΔE_1 and concentrations N_1 for donors in samples # S33 and # S34 are depicted in Figs. 1a and 1b, respectively.

The temperature dependence of the electron concentration measured in sample # S33 can be described by a single donor with an activation energy of 12 meV. However, at temperatures below 200 K the electron concentration becomes independent of the sample temperature due to impurity band conduction. For sample # S34, which was grown at higher temperature and higher plasma power than sample # S33, a deep donor with an activation energy of ~ 600 meV dominates the temperature behavior of the electron concentration.

The Hall mobility μ_H was determined from the conductivity σ and R_H with the expression

$$\mu_H = \sigma |R_H|, \quad (3)$$

and was found to be $7 \text{ cm}^2/\text{Vs}$ and $3 \text{ cm}^2/\text{Vs}$ at room temperature (300 K) for samples # S33 and # S 34, respectively.

Fig. 2 displays typical Hall data taken on unintentionally doped n-type GaN (sample # S77) grown by HN_3 -GSMBE. Fig. 2a and 2b show the free electron concentration derived from the experimental Hall constant according to Eq. 1 and the resistivity, respectively, as functions of reciprocal temperature. In the entire temperature range from 100 K to 500 K of our measurement, the free electron concentration is temperature independent and as high as $\sim 10^{20} \text{ cm}^{-3}$. The resistivity ρ of sample # S77 decreases slightly with increasing temperature. This is due to an increase of the electron mobility at higher temperatures. The electron Hall mobility μ_H of sample # S77 increases from $\sim 0.2 \text{ cm}^2/\text{Vs}$ at 100 K to $\sim 0.5 \text{ cm}^2/\text{Vs}$ at 500 K.

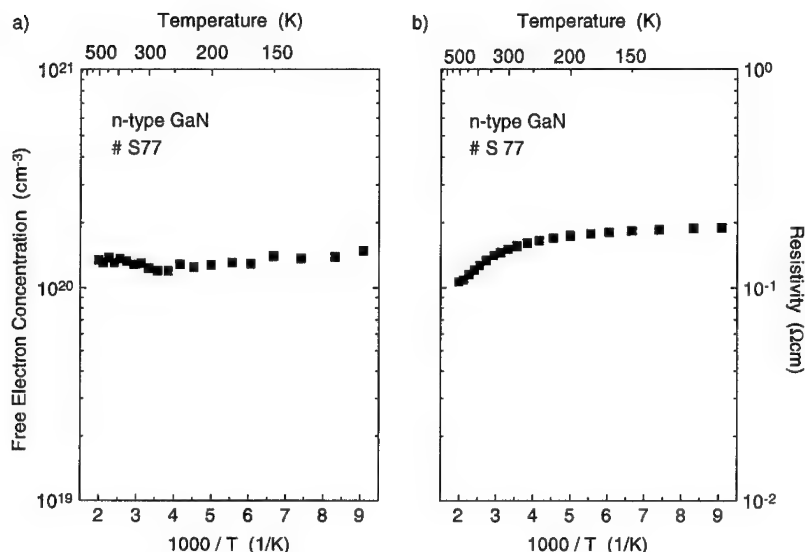


Fig. 2: Free electron concentration n (a) and resistivity ρ (b) vs. reciprocal temperature as obtained from Hall effect measurements on n-type GaN # S77 grown by HN_3 -GSMBE.

PL CHARACTERIZATION OF GaN GROWN BY MBE

Fig. 3 displays PL data obtained from GaN grown by plasma-assisted MBE (sample # S34, upper curves) and from HN_3 -GSMBE grown GaN (sample # S77, lower curves) in the spectral range from 350 nm (3.55 eV) to 700 nm (1.77 eV). These spectra were all taken with the sample at 300 K (dashed line) or 2 K (solid line).

The low temperature PL spectrum of sample # S34 reveals a deep level defect related PL signal but no band edge related luminescence. The spectrum is dominated by the “yellow” luminescence band centered at 2.3 eV. The defect band is approximately Gaussian shaped with a full width at half maximum of ~ 0.4 eV. No photoluminescence was detectable at room temperature.

PL spectra taken on GaN samples grown with HN_3 as a nitrogen source differ from the spectra described above for GaN grown by ECR plasma-assisted MBE. As an example, we show PL spectra taken on sample # S77 grown by HN_3 -GSMBE in the lower portion of Fig. 3. The low temperature PL spectra of sample # S77 is dominated by two sharp emission lines located at 3.36 eV and at 3.30 eV. The full width at half maximum of the 3.36 eV line is 5.9 meV. Room temperature spectra reveal a band edge related emission peak at 3.25 eV. No broad deep level related emission bands, such as the “yellow band” are observed in PL spectra of HN_3 -GSMBE grown GaN samples taken at 2 K or at 300 K.

DISCUSSION

Both nitrogen sources, ECR plasma excited N_2 and HN_3 , produced GaN material with electron mobilities below $10 \text{ cm}^2/\text{Vs}$ and high defect densities. The low mobilities indicate the presence of high compensation in the n-type GaN films. For GaN grown by ECR plasma-assisted MBE, the

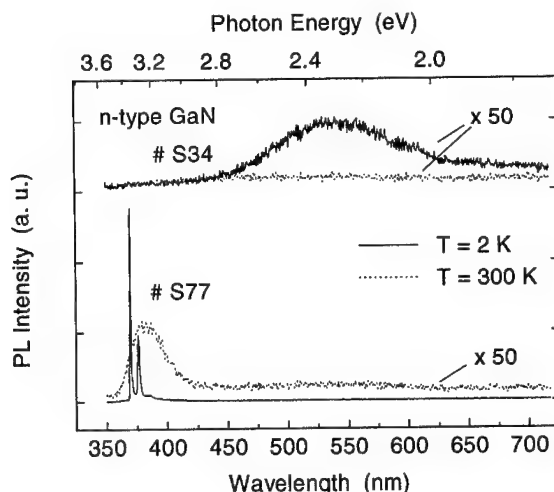


Fig. 3: PL intensity of GaN grown by ECR plasma assisted MBE (upper curves, sample # S34) and on GaN grown by HN_3 -GSMBE (lower curves, sample # S77) vs. wavelength. Spectra taken at 300 K are plotted as dotted and 2 K spectra are plotted as solid lines.

creation of unintentional background doping depends on growth parameters, in particular the substrate temperature and the plasma microwave power. Growth at lower temperatures and lower plasma powers results in films which are highly n-type. The electrical properties of these GaN films are dominated by shallow donors and defect band conduction as demonstrated in Fig. 1a for sample # S33. Sample # S33 was grown at 600°C with a plasma power of 150 W. For the shallow donors we determined activation energies in the range from 10 meV to 30 meV. The chemical nature of these shallow donors which are responsible for the autodoping phenomena in GaN and are found in both MBE and MOCVD grown material is not yet resolved. Nitrogen vacancies or oxygen impurities acting as donors are likely candidates.

The films grown with higher plasma powers and at higher temperatures are highly resistive. The Hall data of sample # S34 shown in Fig. 1b reveals a deep donor level with an activation energy of $\Delta E \sim 600$ meV and a concentration of $5 \times 10^{21} \text{ cm}^{-3}$. Sample # S34 was grown at 860°C with a plasma power of 170 W. Similar deep levels with an activation energy of ~ 500 meV have also been detected in MOCVD grown GaN by DLTS¹⁴. It is likely that an intrinsic defect prompted by ion bombardment² is responsible for the deep level observed in sample # S34. The n-type shallow background doping in these films is either not present or compensated.

The HN_3 -GSMBE GaN films investigated in this study exhibited metallic conduction with the free electron concentration being independent of the sample temperature. Such behavior may indicate defect band conduction or degeneracy due to high concentrations of shallow donors and acceptors. We believe that impurities such as Si, O, and Mg which act as shallow donors and acceptors, respectively, are incorporated during growth of GaN by HN_3 -GSMBE. Secondary ion mass spectroscopy analyses revealed the presence of Si and O in concentrations of $\sim 10^{20} \text{ cm}^{-3}$ in these films. The presence of these impurities which originate from chemicals used to synthesize HN_3 , poses a major problem for the growth of III-V nitrides with hydrogen azide since it is extremely difficult to purify¹³. However, PL spectra taken on HN_3 -GSMBE grown GaN films

demonstrate good luminescence properties. The spectra are free of deep level related emission bands and display a sharp emission line pair which consists of lines with transition energies of 3.360 eV and 3.298 eV. These lines are significantly deeper than the I_2 line at 3.478 eV which is commonly observed in n-type GaN and attributed to the recombination of a donor bound exciton.¹⁵ The radiative recombination that gives rise to the line pair in the PL spectra of the HN_3 -GSMBE grown GaN material involves at least one shallow defect level. Further studies are necessary to reveal the origin of these photoluminescence lines.

SUMMARY

GaN grown by ECR-plasma assisted MBE or by HN_3 -GSMBE were investigated by Hall effect and photoluminescence measurements. The formation of deep level defects which may result from bombardment by energetic ions generated in the nitrogen plasma was observed in GaN grown by ECR-plasma assisted MBE grown at high plasma powers. GaN grown by HN_3 -GSMBE was found to be free of deep level defects but the electrical properties of this material are affected by the insufficient purity of the HN_3 nitrogen source gas. SIMS analyses revealed impurity incorporation of Si and O in concentrations of $\sim 10^{20} \text{ cm}^{-3}$ in GaN films grown by HN_3 -GSMBE.

ACKNOWLEDGMENT

One of the authors (W.G.) is pleased to acknowledge support by the Alexander von Humboldt-Foundation in Germany. The authors are grateful to Noble M. Johnson and Robert. A. Street, Xerox PARC, for making available the Hall effect apparatus and the PL measurement system used in this study. The work was supported by ARPA on contract # MDA 972-94-1-0003.

REFERENCES

1. R.F. Davis, *Physica B* **185**, 1 (1993)
2. H. Morkoç, S. Strite, G. B. Gao, M. E. Lin, B. Sverdlov, and M. Burns, *J. Appl. Phys.* **76**, 1363 (1994)
3. I. Akasaki, H. Amano, N. Koide, M. Kotaki, K. Manabe, *Physica B* **185**, 428 (1993)
4. S. Nakamura, T. Mukai, and M. Senoh, *Appl. Phys. Lett.* **64**, 1687 (1994)
5. I. Akasaki, H. Amano, M. Kito, and K. Hiramatsu, *J. Lumin.* **48&49**, 666 (1991)
6. S. Nakamura, T. Mukai, and M. Senoh, *Jpn. J. Appl. Phys.* **30**, L1998 (1991)
7. J. Neugebauer and C.G. Van de Walle, presented at the 1995 MRS Spring Meeting, San Francisco CA, 1995 (unpublished)
8. M.J. Paisley, Z. Sitar, J.B. Posthill, and R.F. Davis, *J. Vac. Sci. Technol.* **A7**, 701 (1989)
9. S. Strite, J. Ruan, Z. Li, N. Manning, A. Salvador, H. Chen, D.J. Smith, W.J. Choyke, and H. Morkoç, *J. Vac. Sci. Technol.* **B9**, 1924 (1991)
10. T. Lei, M. Fanciulli, R.J. Molnar, T.D. Moustakas, R.J. Graham, and J. Scanlon, *Appl. Phys. Lett.* **59**, 944 (1991)
11. T.D. Moustakas and R.J. Molnar, *Mater. Res. Soc. Symp. Proc.* **281**, 753 (1993)
12. R.J. Molnar, R. Singh, and T.D. Moustakas, *Appl. Phys. Lett.* **66**, 268 (1995)
13. D.B. Oberman, H. Lee, W. Götz, and J.S. Harris Jr., to be published
14. W. Götz, N.M. Johnson, H. Amano, and I. Akasaki, *Appl. Phys. Lett.* **65**, 463 (1994)
15. R. Dingle, D.D. Sell, S.E. Stokowski, P.J. Dean, and M. Illegems, *Phys. Rev.* **B3**, 497 (1971)

* Permanent address: Xerox PARC, 3333 Coyote Hill Road, Palo Alto, CA 94304, USA

THE EFFECTS OF SINTERING ON THE MICROSTRUCTURE AND THE LUMINESCENT CHARACTERISTICS OF POLYCRYSTALLINE ZnS

R. MATTHEW ADAMS, PETER MASCHER, AND ADRIAN H. KITAI

Centre for Electrophotonic Materials and Devices, Department of Engineering Physics,
McMaster University, Hamilton, Ontario, Canada.

ABSTRACT

Positron annihilation spectroscopy and cathodoluminescence were employed to study changes in the microstructural and luminescent properties of pure and doped polycrystalline ZnS. All samples show evidence of defect clustering, when sintered at temperatures up to 400 °C, indicated by an increase in the average positron lifetime. The average lifetime of the undoped material is constant (at about 290 ps) from 300 to 700 °C, and then decreases beyond this temperature, due to the out diffusion of vacancy clusters. In comparison, the average lifetime for MnS doped material decreases beyond 600 °C. This decrease in the average lifetime is correlated with an increase in the luminescent intensity of the 585 nm Mn band, indicating that Mn compensation of zinc vacancies contributes to the decrease in the average lifetime. At sintering temperatures above 400 °C, the average lifetime of TbF₃ doped material decreases by ~3 ps / 100 °C, from a peak value of 285 ps, and then at 700 °C drops an additional 15 ps to 260 ps. At 650 °C a change from the distinct Tb spectrum to a broad band emission is observed. It is believed that these effects can be linked to the incorporation of Tb³⁺ ions on Zn²⁺ lattice sites.

1. INTRODUCTION

Polycrystalline ZnS is a wide band-gap semiconductor which is currently of great interest for the production of thin film electroluminescent devices. Dopants such as Mn and Tb produce emissions in the red, green and blue portion of the spectrum, as required for information display applications [1]. Our previous investigation of bulk polycrystalline ZnS, using positron annihilation spectroscopy (PAS), showed that significant microstructural improvements only occur at temperatures above 700 °C [2]. In this temperature range, sulphur self-diffusion and crystal re-growth are the important processes [3]. These findings are supported by the TEM work of Venghaus et al., who studied high temperature annealing of ZnS:Mn thin films [4]. For electroluminescent purposes, improvements in the microstructure of the active region should result in brighter and more efficient devices [5].

It is expected that the incorporation of dopants will modify the effects of thermal treatments. In this contribution, PAS and cathodoluminescence (CL) have been used to study the effects of sintering on pure ZnS powder, and ZnS with 5 mol% TbF₃ or 0.6 mol% MnS. The combination of both techniques can provide sensitive and unique information about changes in the microstructure of luminescent materials [6,7]. TbF₃ is chosen as the Tb source to facilitate the incorporation of the Tb³⁺ ion on a divalent lattice site, through the formation TbF₂²⁺ or TbF₂⁺ [13]. We have used MnS as a Mn source to preserve stoichiometry, and to reduce the amount of oxygen incorporated in the form of MnO.

2. EXPERIMENTAL DETAILS

High purity ZnS powder (99.99% by weight, $\sim 10\ \mu\text{m}$ diameter) was pressed isostatically at 30,000 psi for 3 min. Doped samples were prepared by adding 0.6 mol% MnS or 5 mol% TbF₃. After pressing, the samples were further cut into pellets, 10 mm in diameter and 2-3 mm thick. The samples were vacuum sintered for 4 hrs, at fixed temperatures, between 200 and 800 °C. During sintering, the pressure was maintained at 2×10^{-5} Torr and the temperature was controlled to within $\pm 3\ ^\circ\text{C}$. After each thermal treatment step, positron measurements were performed on the same pair of samples, and one sample from each doping set was removed for further study.

Positron lifetime measurements were performed using a spectrometer with a resolution (full width at half maximum) of 210 ps. The data was analyzed numerically using the programme PATFIT-88 [8] with a source correction to account for annihilations in the Al-foil containing the positron source (12 μCi of ²²NaCl). The spectra contained 7×10^6 counts, with at least two spectra collected for each data point. A more complete review of the experimental technique can be found in reference 9.

Cathodoluminescence was generated using electrons from a Perkin-Elmer grazing incidence electron gun, with an acceleration voltage of 4 kV. The resulting luminescence was analyzed using a 0.25 m monochromator with a photo multiplier tube and a lock-in amplifier. Intensities were measured using a Minolta LS-110 luminescence meter, which gives a measure of the total integrated intensity. A detailed description of the cathodoluminescence experiment is given in reference 10.

3. RESULTS AND DISCUSSION

3.1 Positron Lifetime Results

Despite high densification factors, large internal surface areas and inter-particle voids are characteristic features of pressed powder compacts. It is important to assess the effects of these structures on the positron annihilation characteristics. Prior to annihilation, positrons emitted from the nuclear decay of ²²Na will achieve thermal equilibrium within the sample through interactions with the lattice [9]. It is reasonable to assume that the positron will thermalize in the region of highest interaction probability, i.e., a powder grain. Considering that the diffusion length of a thermalized positron is on the order of 100 Å, the interaction volume of the positron is $\sim 1 \times 10^6$ times smaller than a grain of 1 μm diameter, and migration out of the grain is an unlikely process. Therefore, we expect that the positron lifetime spectrum will consist mainly of annihilations in the powder particles. The disappearance rate of the positrons from the sample is measured experimentally, and we will use the calculated average lifetime, $\langle\tau\rangle$, to describe this spectrum. For our samples, we interpret $\langle\tau\rangle$ to be a parameter which scales inversely with the average electron density of the material. An increase in the concentration or size of vacancy type defects causes an increase in this parameter.

Figure 1 shows $\langle\tau\rangle$ for all three sample types as a function of the sintering temperature. One can see that the value of $\langle\tau\rangle$ for the TbF₃ doped sample is consistently smaller, when compared to the other samples, over the entire range investigated. We attribute this difference to an increase in the average electron density introduced by the high concentration of large TbF₃ molecules. The general features of $\langle\tau\rangle$ as a function of sintering are similar for all three sets, and exhibit

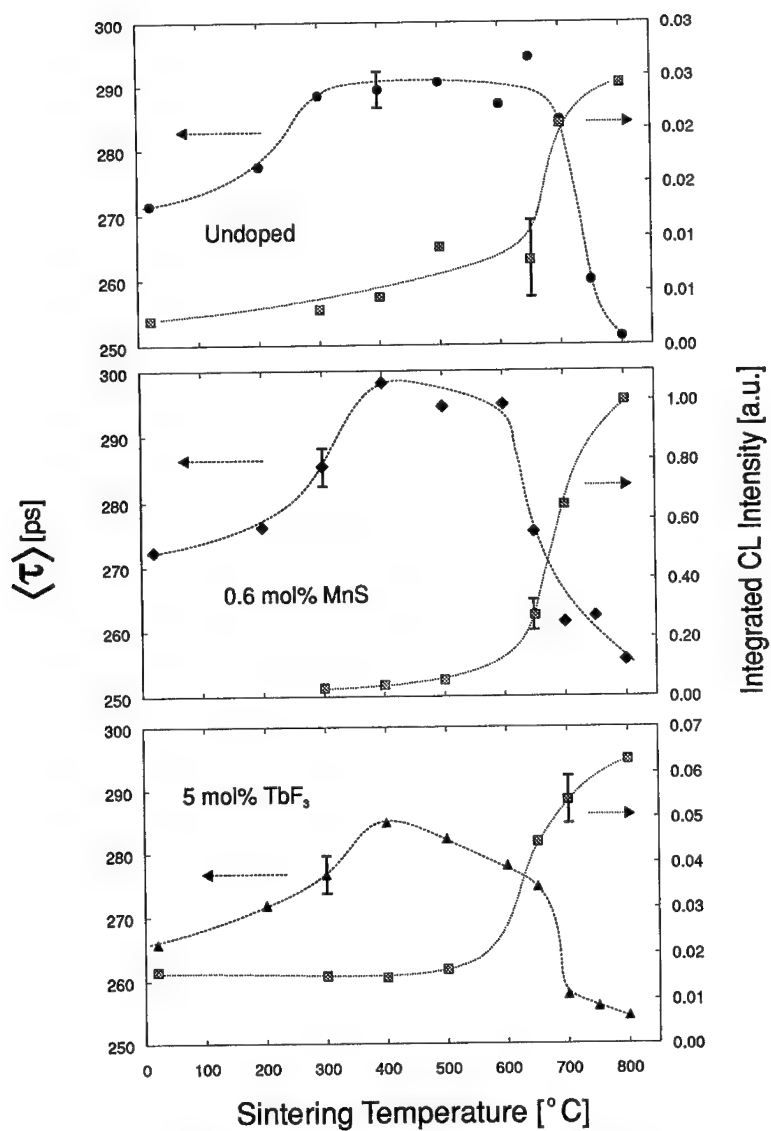


Figure 1. Average positron lifetime and integrated CL intensity as a function of sintering temperature

three distinct stages. The first stage is characterized by an increase in the average lifetime, followed by a plateau or a slight decrease, and then a final stage, a sharp decrease in $\langle\tau\rangle$ at the highest sintering temperatures.

The initial increase in the average lifetime likely is due to vacancy and void clustering, as has been observed in other semiconductors [11,12]. We attribute the final sharp decrease to the activation of self diffusion, causing out-diffusion of vacancies and voids. Beyond 700 °C, the rapid decrease in $\langle\tau\rangle$ is similar to observations made when sintering bulk CVD grown polycrystalline ZnS beyond this temperature [2]. We found earlier that for the CVD material, $\langle\tau\rangle$ stabilizes at 229 ± 3 ps. After processing at 800 °C, $\langle\tau\rangle = 252$ ps, for the powder pressed sample, which would seem to indicate that the out diffusion of the vacancy clusters is still incomplete. Due to significant mass loss at 800 °C, further microstructural improvements, with vacuum sintering, may only be feasible by increasing sintering times at 700 °C.

For the MnS doped material, $\langle\tau\rangle$ saturates between 400 and 600 °C, and the decrease in $\langle\tau\rangle$ begins at $T > 600$ °C. This is a slightly lower temperature than is found for the pure material, and the transition appears broader. The onset of significant dissociation of MnS, which has a lower melting point than ZnS (1600 °C compared to 1850 °C), is the likely reason for this shift to lower temperatures. Dissociated manganese and excess sulphur are available to diffuse into the ZnS lattice and potentially occupy vacancy sites in the stable ZnS, causing a decrease in $\langle\tau\rangle$.

Close examination of $\langle\tau\rangle$ as a function of sintering for the TbF₃ doped material reveals a few subtle differences. The saturation effect is not observed, rather, we find a slow, steady downward trend between 400 and 700 °C. Although diffusion of TbF₃ is not expected to be significant, Ogura et al. have reported that above 400 °C, TbF₃ begins to dissociate, and significant amounts of Tb³⁺ and TbF_x^{(3-x)+} are created [13]. A more mobile Tb³⁺ ion would be capable of diffusing into the ZnS, and residing in a V_{Zn} or a defect cluster. This would effectively remove a vacancy, or mask a larger cluster by inducing a local positive charge. Above 650 °C we find again a sharp decrease in $\langle\tau\rangle$. However, beyond 700 °C, the decrease in $\langle\tau\rangle$ is much less pronounced than in the previous two materials. As significant amounts of Tb³⁺ and TbF_x^{(3-x)+} are incorporated into the lattice, additional anion or cation vacancies are likely required to accommodate both the size and charge. Such an effect is observed in Al³⁺ doped material, where a nearest neighbour Zn²⁺ vacancy is induced [16].

3.2 Cathodoluminescence Results

Integrated cathodoluminescent intensities are also presented in Figure 1. All samples, regardless of doping show an increase in the CL intensity above 600 °C. However, to correctly interpret the data, the spectral dependence of these emissions must also be considered.

For the undoped material, all samples exhibit a broad self-activated emission band, which peaks at 495 nm (2.5 eV), as is shown in Figure 2. The shape and peak position of this band remains constant for all sintering temperatures. The cause of this luminescence is not completely clear, but it likely originates from an intrinsic zinc or sulphur vacancy

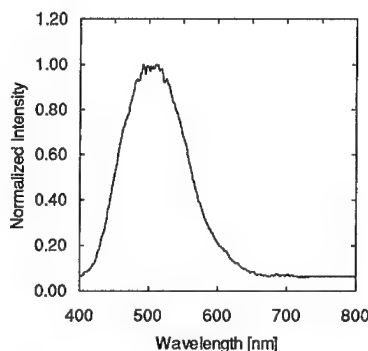


Figure 2. Characteristic CL spectrum from undoped polycrystalline ZnS

interacting with a nearest neighbour compensating impurity [14,15,16]. The increase in the luminescent intensity is potentially due to the introduction of new defects, or the activation/redistribution of co-activator impurity ions. In either case, the involvement of a vacancy type defect would appear contrary to our earlier statement that the decrease in $\langle\tau\rangle$ is indicative of a removal of vacancies. However, it is possible to reconcile these results in the following ways. On the one hand, point defects may be associated with the surface of a grain—as mentioned earlier, a region of the crystal not sampled by the positrons. The introduction of V_S through the evolution of S and the out-diffusion of excess Zn to the surface, is known to occur during vacuum sintering [3]. However, luminescence from V_S requires Cu co-activation [14], and Cu is not found to be present to within 1 ppb for the powder used. Another

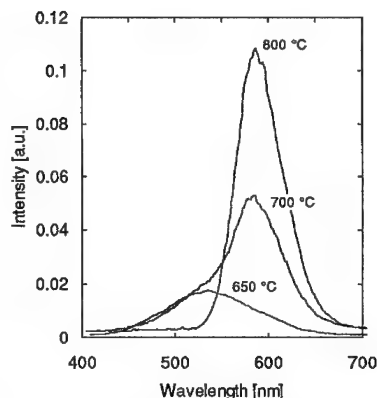


Figure 3. Spectral peak shift, due to the activation of the Mn luminescence

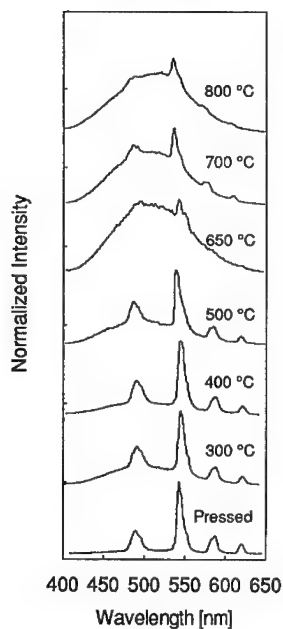


Figure 4. Development of the CL spectra in TbF_x doped samples

possibility is that the material is initially zinc deficient. For the ZnS powder used, impurity concentrations of Al, a known co-activator ion for V_{Zn} , are quoted to be ~ 0.004 at%, in which case the concentration of V_{Zn} , having been in excess, may not have yet dropped below this level. This would be consistent with the positron results which indicated that the out diffusion process was not yet completed, even at 800 °C. Sintering for longer times at 700 °C may quench or stabilize this self-activated emission. Further experiments will be required to substantiate this.

For the samples containing MnS, the increase in the integrated intensity appears to correlate with the decrease in $\langle\tau\rangle$. This increase is due to the activation of the familiar 585 nm Mn band, as is shown in Figure 3. In the as pressed state, the luminescence is similar to the undoped material. However, despite an increase in the intensity from the self activated band up to 650 °C, at 800 °C this luminescence appears to be quenched. Since it is well known that the 585 nm transition is allowed only when Mn^{2+} is properly coordinated in the ZnS lattice, the luminescence data would seem to confirm our interpretation of the changes in $\langle\tau\rangle$ as being due to an influx of Mn into the ZnS grains. If the self-activated emissions are due to the V_{Zn} -Al pair, substantial Mn compensation coupled with the out diffusion of defect structures, could result in the removal of this band.

The integrated luminescence intensity for the ZnS: TbF_x samples also increases as the sintering temperature increases.

In this case, however, it is not due to an activation of the intentional dopant luminescence, as is shown in Fig. 4. Up to 500 °C, the characteristic Tb lines are obtained and dominate the spectrum, although signs of an increasing broad background are apparent. The overall intensity of the luminescence remains essentially constant, as long as the spectrum retains the Tb signature. At 650°C the spectrum is swamped by the presence of a broad emission band, which appears to be similar to the self activated emission, both in shape and peak position. One possible explanation of these findings is that the combined heat treatment has resulted in a complete removal of fluorine from the sample. In this case, Tb^{3+} would be incorporated into the lattice in a manner similar to Al^{3+} , and would likely induce a nearest neighbour V_{Zn} , to accommodate its trivalent nature. In this case, the new $\text{Tb}^{3+}\text{-V}_{\text{Zn}}$ complex may well be acting in a manner similar to the $\text{Al}^{3+}\text{-V}_{\text{Zn}}$ complex resulting in a similar luminescent process.

ACKNOWLEDGMENTS:

This work is supported through grants from the Natural Sciences and Engineering Research Council of Canada (NSERC) and the Ontario Centre for Materials Research (OCMR).

REFERENCES:

- [1] E. Bringuier, J. Appl. Phys. **75**, 4291 (1994)
- [2] R.M. Adams, P. Mascher, and A.H. Kitai, accepted for publication in Appl. Phys. A, (1995).
- [3] M. Bredol, J. Merikhi, and C. Ronda, Ber. Bunsenges. Phys. Chem. **96**, 1770 (1992).
- [4] H. Venghaus, D. Theis, H. Oppolzer, and S. Schild, J. Appl. Phys. **53**, 4146 (1982).
- [5] Y. Nakanishi, Y. Fukuda, Y. Hatanaka, G. Shimaoka, Appl. Surf. Sci. **48/49**, 297, (1990).
- [6] J. Zhong, A.H. Kitai, and P. Mascher, J. Electrochem. Soc. **140**, 3644 (1993).
- [7] J. Brown, A.H. Kitai, and P. Mascher, J. Electrochem. Soc. **142**, 958 (1995).
- [8] P. Kirkegaard, N.J. Pedersen, and M. Eldrup, PATFIT-88: A Data-Processing System for Positron Annihilation Spectra on Mainframe and Personal Computers, (Risø National Laboratory, Dk-4000 Roskilde, Denmark, 1989).
- [9] S. Dannefaer, in Defect Control in Semiconductors, edited by K. Sumino (Elsevier Science Publishers, B.V., North Holland, 1990), p. 1561.
- [10] J. Zhong, M. Eng thesis, McMaster University, Hamilton On. Canada (1993)
- [11] S. Dannefaer, P. Mascher and D. Kerr, J. Appl Phys. **69**, 4080 (1991).
- [12] Y. Horii, K. Kawasuo, M. Hasegawa, Mater. Sci. Forum **105-110**, 1061 (1992)
- [13] T. Ogura, A. Mikami, K. Tanaka, K. Taniguchi, M. Yoshida, and S. Nakajima, Appl. Phys. Lett. **48**, 1570 (1986).
- [14] S. Shionoya, in Luminescence of Inorganic Solids, edited by P. Goldberg (Academic Press, New York, 1966), p. 205.
- [15] J. Nicholls, J. Davies, B. Cavenett, J. James, and D Dunstan, J. Phys. C. **12**, 361 (1979).
- [16] R. Watts, J. Mat.Sci. **8**, 1201 (1973).

STUDY OF DEEP LEVELS BY ADMITTANCE SPECTROSCOPY IN HIGH RESISTIVITY P-TYPE 6H-SiC SINGLE CRYSTALS.

A. O. Eywaraye, S. R. Smith and W. C. Mitchell
Wright Laboratory, Materials Directorate, MLPO
Wright-Patterson Air Force Base, Ohio 45433-7707

ABSTRACT

Deep levels in high resistivity p-type 6H-SiC has been studied using optical admittance spectroscopy (OAS). Besides the conductance peak due to the band to band transitions, there are three conductance peaks in the spectra of most of the samples. The conductance peak due to the vanadium donor ($0/+$) level at $E_V + 1.55$ eV is identified. The persistent photoconductance (PPC) at this defect was also studied. The decay kinetics of the PPC follow the stretched exponential form. The potential barrier against recapture of carriers was determined to be 220 meV for the vanadium donor level.

INTRODUCTION

Silicon carbide has excellent physical and electronic properties that make it the material of choice for the fabrication of electronic devices that can operate at high temperatures, high speeds, high frequencies and high power levels. Several silicon carbide based electronic devices have been fabricated with encouraging results¹⁻⁴. Because the bulk silicon carbide is grown at high temperatures, the resulting single crystals contain high concentration of chemical impurities. The most common chemical impurities incorporated during growth are nitrogen, boron, vanadium and titanium. Nitrogen and boron establish shallow levels and determine the conductivity of the crystals. Vanadium and titanium establish deep levels in the band gap of SiC^{5,6}; these levels influence the electrical and optical properties of the compound. Vanadium and titanium contaminants have been extensively studied with electron spin resonance (ESR)^{7,8}, photo-electron spin resonance (photo-ESR)⁹ and infrared absorption (IR)⁷. It is found from these studies that vanadium substitutionally occupies the silicon sites in the silicon carbide lattice in the following three charge states: $V^{3+}(3d^2)$ negative, $V^{4+}(3d^1)$ neutral and $V^{5+}(3d^0)$ positive. It therefore introduces both donor ($V^{4+}(3d^1)/V^{5+}(3d^0)$) and acceptor ($V^{3+}(3d^2)/V^{4+}(3d^1)$) levels in the band gap. The location of the donor level ($0/+$), which has been unambiguously determined, is at $E_V + 1.6$ eV for vanadium occupying the two quasi-cubic sites (k_1, k_2). For vanadium occupying the hexagonal site, the donor level is at $E_V + 1.3$ eV. The acceptor level ($-/0$) is located at $E_C - 0.6$ eV. Since the donor level of vanadium is close to the mid gap of SiC, vanadium can be used to control minority-carrier lifetime in SiC based rectifiers. Furthermore if sufficient quantities of vanadium are introduced to compensate the dominant residual impurity, semi-insulating substrates can be produced. Semi-insulating substrates are required for the fabrication of microwave devices. Therefore it is necessary to study further the deep levels in high resistivity p-type 6H-SiC.

Optical admittance spectroscopy^{10,11} is a more suitable technique for studying defect levels near mid gap without resorting to high temperature techniques. The optical admittance spectroscopy is a variation of thermal admittance spectroscopy. In the optical variation, the experiment is performed at a temperature where thermal emission of carriers from the defect is negligible. Carriers are then photoexcited from the defects to the conduction band or from the valence band to the defect levels. Optical admittance technique is spectroscopic that allows most of the defects within the band gap to be probed. Furthermore, the use of this technique makes it possible to study the optical behavior of a particular defect.

In this paper, we report the results of optical admittance spectroscopy studies of defects in high resistivity p-type 6H-SiC crystals. Kinetic studies of the slow build up of photoconductance and persistent photoconductance in high resistivity samples will also be reported.

EXPERIMENTAL DETAILS

Five bulk p-type 6H-SiC samples were obtained from three different sources. The three suppliers use the modified sublimation process to grow the crystals. The resistivity of the samples range from $125\Omega\text{-cm}$ to $10^8\Omega\text{-cm}$ at room temperature. All the samples were nominally undoped except for one sample that was intentionally doped with vanadium. After oxidation and cleaning¹², Ni was sputtered onto the silicon surface of the samples and annealed at 900°C for five minutes in an atmosphere of forming gas in order to form ohmic contact. Schottky diodes for admittance measurements were formed by magnetron sputtering Al dots of $600\text{ }\mu\text{m}$ in diameter through a shadow mask onto the carbon surface.

The optical admittance spectroscopy measurements were made with an HP4274A multifrequency LCR meter operated in high resolution mode at 20 kHz. Measurements were made at temperatures where thermal emission rates are negligible. This temperature varies from sample to sample and appears to depend on the resistivity of the sample. A 250W Xenon lamp and an Oriel monochromator model 77250 provided the monochromatic light used as the photexcitation source.

RESULTS AND DISCUSSIONS

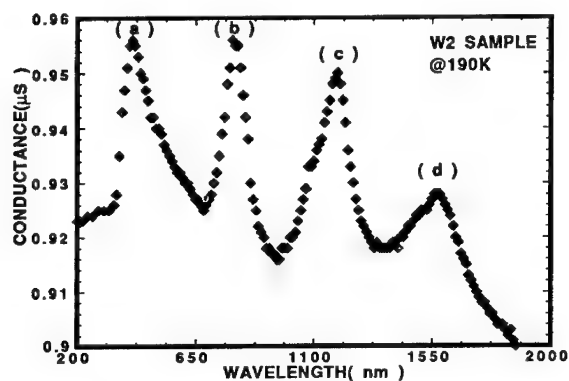


Figure 1. A typical optical admittance spectrum obtained at 190 K with diodes from one of the samples. The conductance peak (a) at 3.10 eV is due to the band to band transitions. The conductance peaks (b) at $E_V + 1.55$ eV, (c) at $E_V + 1.05$ eV and (d) at $E_V + 0.78$ eV are due to valence band to defect transitions.

1 and it corresponds to the excitation of carriers from the valence band to the conduction band. The value of 3.10 eV for the band gap of SiC at 190K is not unreasonable. As the wavelength is increased from $\lambda = 400$ nm, the additional conductance begins to decrease until it reaches its pre-illumination values at $\lambda = 700$ nm. This is due to the recombination of photoexcited electrons with holes in the valence band. Peak (b) is due to excitation of carriers from the valence band to a defect level at $E_V + 1.55$ eV. This is the donor level (0/+) of vanadium atom. In these high resistivity materials, the deep donor level of the vanadium impurity is ionized ($V^{5+}(3d^0)$) and electrons can be photoexcited into it. i.e. $V^{5+}(3d^0) + h\nu(1.55\text{ eV}) \rightarrow V^{4+}(3d^1) + h$. ESR experiments confirm that vanadium occurs in the positive charge state (D^+) in weakly p-type 6H-SiC. The extra hole created by the photo neutralization process changes the

Figure 1 shows a spectrum obtained at 190K when a diode from one of the samples was illuminated with light of various wavelengths. There are four conductance maxima (labeled a-e) in the spectrum. As the photon wavelength is increased, the additional conductance increases and reaches a maximum at $\lambda = 400$ nm (3.10 eV). This is the conductance peak labeled (a) in Fig.

conductance of the diode. As the wavelength of the light is scanned away from 800 nm, the number of holes generated is smaller and consequently the additional conductance is smaller. The energy position of $E_V + 1.55$ eV for the vanadium donor as obtained here agrees quite well with the value of $E_V + 1.6$ eV determined by photo-ESR. The vanadium related conductance peak (b) is observed in all the samples studied; the donor level for the hexagonal site at $E_V + 1.3$ eV is not observed in any of our samples. The conductance peak due to this level ought to occur in the spectrum at $\lambda = 954$ nm. The reason for this failure is not understood at present.

The conductance peak (c) is due to excitation of carriers from the valence band to a defect level at $E_V + 1.05$ eV. It is observed in all the samples studied; it may be a vanadium complex. The conductance peak (d) occurs in some samples but not in others. It may not be related to vanadium since it does not occur in the vanadium doped sample.

The photo conductance behavior of the defect at $E_V + 1.55$ eV was further studied by illuminating a diode from any of the samples at appropriate temperature with light of wavelength $\lambda = 800$ nm. This is the excitation wavelength of peak (b).

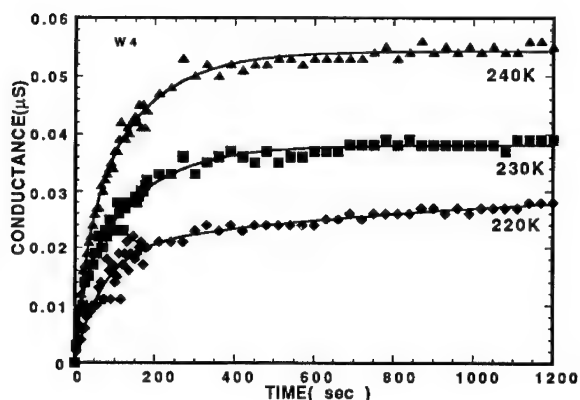


Figure 2. The variation of photoconductance G_p in a sample with illumination time at three representative temperatures ($T = 220, 230$ and 240 K). The dark conductance G_d has been subtracted from the data. The solid lines are fits to the experimental data using Eq. 1.

the following expression:

$$G_p = \sum_{i=1}^2 G_{\max}(i)(1 - e^{-\alpha_i t}) \quad (1)$$

where G_{\max} is the maximum photo induced change of the conductance and α is a rate associated with the persistent photoconductance build up process. The solid lines are the fits to the data using the above expression. Similar fits were made to the data from other samples. We see from this figure that G_p increases with temperature. For an exposure time of 400s, G_p increased from $0.022 \mu S$ at 220 K to $0.052 \mu S$ at 240 K; an increase of over 200%. If the carrier capture rate at the defect level is temperature dependent, then more carriers are captured as

Figure 2 shows the variation of the additional conductance G_p with illumination time under excitation with $\lambda = 800$ nm at representative temperatures ($T = 220, 230$ and 240 K). The dark conductance background has been subtracted. Similar photoconductance transients at different temperatures were obtained for each of the samples. These photoconductance transients can be described fully by

temperature is increased thereby increasing the photoconductance. This is exactly what is observed here.

When G_p reached its saturation value, the excitation source was turned off, and the decay of G_p was monitored as function of time. Figure 3 shows the decay of G_p at three representative temperatures, $T=195, 210$ and 220K . The curves have been normalized to unity at $t=0.0$, when the light was turned off. The dark conductance values have been subtracted out. At $T=195\text{K}$, the photoconductance is 50% of its initial level after 600s decay while at 220K it is only 15% of its initial level after 600s decay time. The decay is due to the capture of excess holes by the neutral vanadium donor level. The decay is clearly temperature driven and the data can be fitted with Williams-Watts exponential of this form:

$$G_p(t) = G_p(0) \exp \left[- \left(\frac{t}{\tau} \right)^\beta \right] \quad (2)$$

where G_p is the conductance at time t , $G_p(0)$ is the conductance at $t=0$, τ is the decay constant and β is the stretching factor.

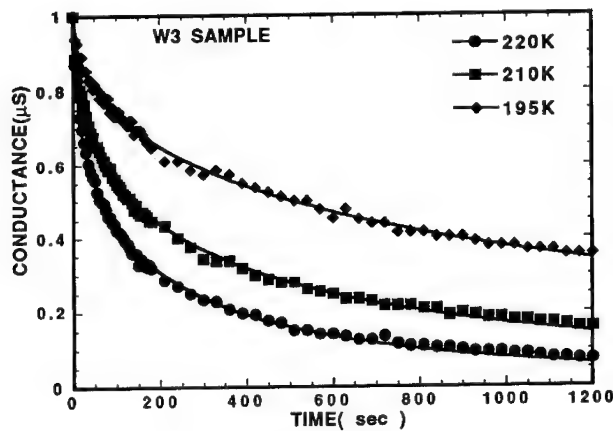


Figure 3. PPC decay curves were obtained at 195, 210 and 220 K. Each curve is normalized to unity at $t = 0$ when the light was turned off. The solid lines are fits to the data using the Williams-Watts exponential.

occurs a lattice rearrangement in the vicinity of the defect that leads to metastability. This lattice relaxation establishes a potential barrier that prevents the recapture of photo excited carriers. In our case, the ionized vanadium is neutralized and this causes lattice rearrangement in the vicinity of the defect. The established potential barrier prevents the excess holes from being captured by the neutral donor level thereby prolonging the photoconductance after the excitation source was turned off. The time constant τ is thermally activated and its temperature dependence is of this form:

$$\tau = \tau_0 \exp \left(\frac{E_{rec}}{KT} \right) \quad (3)$$

The solid lines through the data points in Fig. 3 are fits using the above expression. The decay of PPC in III-V, II-VI compounds and in n-type 6H-SiC follow the stretched exponential form similar to the results obtained here. But different mechanisms have been suggested as being responsible for the observed PPC in each material.

However, it is now generally accepted that upon ionization of a defect in certain materials, there

where τ_0 is the time constant without the potential barrier, T is the temperature, E_{rec} is the potential barrier and K is the Boltzmann constant.

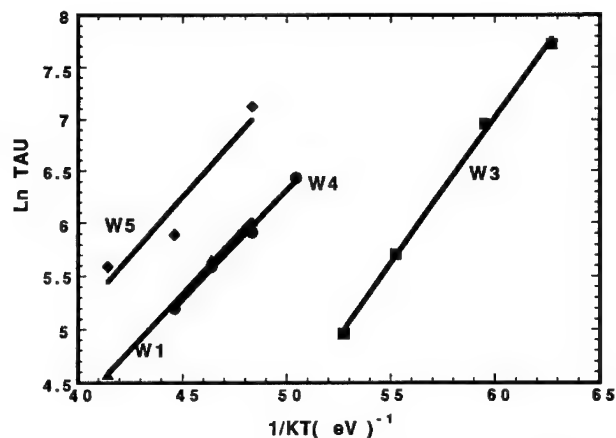


Figure 4. Plots of $\text{Ln } \tau$ vs $1/KT$ for four of the samples used in this experiment. The potential barrier height of 220 meV was obtained.

The potential barrier E_{rec} is obtained from the plot of $\text{Ln } \tau$ versus $1/KT$. Figure 4 shows the plots of $\text{Ln } \tau$ vs $1/KT$ for four of the samples used in this study. The straight lines through the data points are least squares fits to the data points. While the decay kinetics depend on the resistivity of the sample, the barrier height which is obtained from the slopes of the straight lines does not vary significantly from sample to sample. The average barrier height obtained for the vanadium donor level is 220 meV.

CONCLUSION

Optical admittance spectroscopy has been used to study deep defects in high resistivity p-type 6H-SiC. The vanadium donor level at $E_V + 1.55$ eV is clearly identified. The decay kinetics of G_D due to this defect were studied and found to follow the stretched exponential form. The potential barrier height of 220 meV was determined. The photoconductance due to the vanadium donor level persisted for several hours even at high temperatures.

ACKNOWLEDGEMENT

The authors would like to thank Dr. P. M. Hemenger for consistent support and encouragement. The work of one of us (SRS) was carried out under Air Force Contract No. F33615-91-C-5603. The authors would like to acknowledge the technical assistance of Paul Von Richter, Gerald Landis and Robert V. Bertke.

REFERENCES

1. P. G. Neudeck, D. J. Larkin, J. A. Powell, L. G. Matus and C. S. Salupo, Appl. Phys. Lett. **64**, 1386 (1994)
2. J. W. Palmour, J. A. Edmond, H. S. Kong and C. H. Carter Jr, Physica B **185**, 461 (1993)
3. H. Morkoc, S. Strite, G. B. Gao, M. E. Lin, B. Sverdlov, and M. Burns, J. Appl. Phys. **76**, 1363 (1994)
4. D. M. Brown, E. T. Downey, M. Ghezzi, J. W. Kretchmer, R. J. Saia, Y. S. Lui, J. A. Edmond, G. Gati, J. M. Pimbley and W. E. Schneider, IEEE Trans. Electron Devices **ED-40**, 325(1993)
5. K. Maier, H. D. Muller and J. Schneider, Materials Science Forum vols. **83-87**, 1183 (1992)
6. K. Maier, J. Schneider, W. Wilkening, S. Leibenzeder and R. Stein, Materials Science and Engineering, **B11**, 27(1992)
7. J. Schneider and K. Maier, Physica B **185**, 199 (1993)
8. M. Kunzer, U. Kaufman, K. Maier and J. Schneider, Materials Science and Engineering **B29**, 118 (1995)
9. J. Schneider, H. D. Muller, K. Maier, W. Wilkening, F. Fuchs, A. Dornen, S. Leibenzeder, and R. Stein, Appl. Phys. Lett. **56**, 1184 (1990)
10. G. Vincent, D. Bois and P. Pinard, J. Appl. Phys. **46**, 5173 (1975)
11. S. Duenas, M. Jaraiz, J. Vincente, E. Rubio, L. Bailon and J. Barbolla, J. Appl. Phys. **61**, 2541 (1987)
12. A. O. Evwaraye, S. R. Smith, M. Skowronski and W. C. Mitchel, J. Appl. Phys. **74**, 5269 (1993)
13. G. Williams and D. C. Watts, Trans. Faraday Soc. **66**, 80 (1970)
14. A. O. Evwaraye, S. R. Smith and W. C. Mitchel, J. Appl. Phys. ("To Be Published")

Part VII
Defect Characterization

LOCAL VIBRATIONAL MODE (LVM) SPECTROSCOPY OF SEMICONDUCTORS

EUGENE E. HALLER

Lawrence Berkeley Laboratory and University of California at Berkeley,
Berkeley, CA 94720 USA

ABSTRACT

Impurities and defects with masses smaller than the masses of the host semiconductor crystal atoms typically exhibit vibrational frequencies well above the phonon frequency spectrum. These vibrational modes produce sharp spectral absorption features in the infrared. Because of their strong spatial localization these modes are not affected by neighboring impurities and/or defects with concentrations up to 10^{19} cm^{-3} . This insensitivity is especially advantageous when the free carrier concentration must be reduced through the introduction of electron irradiation defects or when highly doped thin layers must be investigated. LVM spectroscopy with perturbations such as polarization of the probe light, uniaxial and hydrostatic stress, and isotope substitution has been highly successful in identifying the structure and composition of a large number of defect complexes. Hydrogen, in particular, forming a wide variety of complexes in elemental and compound semiconductors has been extensively studied with LVM spectroscopy. For example, it has been shown recently that nitrogen acceptors are hydrogen passivated in MOCVD grown ZnSe. Carbon and oxygen have been investigated in all major semiconductors with LVM spectroscopy. The extreme simplification of the spectrum of bond centered oxygen through isotope enrichment of several Ge crystals has been demonstrated. Additional recent investigations of importance to the currently much studied semiconductors will be reviewed.

INTRODUCTION

Local vibrational mode (LVM) spectroscopy assumes a very central role among the large number of semiconductor characterization techniques which have been developed over the years and which are continuously refined and improved. When applicable, this technique allows, in many cases, the precise identification of impurity species and their crystal lattice location with excellent sensitivity. LVM spectroscopy has become widely used by researchers exploring new approaches to doping, identifying dopant atom locations, and studying dopant complex formation. Processing engineers use LVM spectroscopy to determine the concentration of dispersed, bond centered oxygen or of carbon in a silicon wafer at various stages of fabricating complex integrated circuits.

LVM spectroscopy is a superb research technique in large part because of its spectroscopic

nature but it also serves as a quality control tool because it is sensitive, specific and quantitative.

The aim of this brief overview is to illustrate the above statements with recent examples and to point out areas for further fertile studies. Research and development of direct bandgap semiconductors for blue light emitting diodes and lasers, as well as the new possibilities offered by isotopically engineered semiconductors, are but two areas where LVM spectroscopy will make definitive contributions, foremost in doping (species and lattice location), in hydrogen passivation of dopants and in dopant interactions among themselves and with defects.

A further and very attractive aspect of LVM spectroscopy is its conceptual simplicity combined with direct and transparent data reduction as compared to many characterization methods which require elaborate data analysis schemes which cannot be easily tested or which escape physical intuition.

Space limitations do not allow a very detailed presentation of LVM practice and theory. The reader is referred to a number of excellent reviews of this topic. Barker and Sievers ¹ have given a detailed treatment of LVMs in semiconductors. Other classical texts have been written by Spitzer ² and Newman. ³

LVM SPECTROSCOPY

An impurity atom with a mass lower than the masses of the semiconductor host crystal atoms vibrates at a frequency which is higher than the fundamental lattice vibrations. Exceeding the maximum frequency which the crystal lattice can support, an impurity vibration cannot propagate through the crystal but remains highly localized very near the impurity site. The consequence is a well defined, high frequency vibrational mode which presents itself as a sharp absorption line in the infrared transmission spectrum of the crystal.

In its simplest form one describes the local vibration with a linear spring and ball model (Fig. 1). The frequency is given by:

$$\nu_{loc}^2 = C(A^{-1} + M_{lattice}^{-1}) \quad (1)$$

with C = effective spring constant, A = impurity atomic mass and $M_{lattice}$ = interaction mass of the lattice. $M_{lattice}$ is on the order of the sum of the nearest neighbor masses of the impurity.

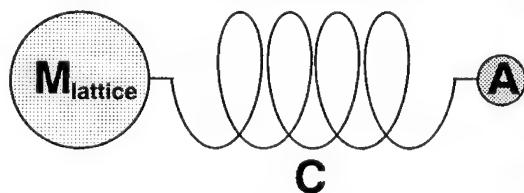


Fig. 1 A simple model for local vibrations of the impurity atom with mass A . The neighbors of the impurity atom are represented by $M_{lattice}$ and the bonds by the spring constant C .

Equation (1) readily illustrates a very important aspect of LVM spectroscopy: The impurity mass and the masses of the neighboring host lattice atoms directly affect the local mode frequency.

Deliberate substitution of one impurity isotope with another or isotopic engineering of the host lattice ⁴ leads to predictable frequency shifts. The most extreme case is the substitution of hydrogen ($A=1$) with deuterium ($A=2$) in crystals with large and therefore negligible M_{lattice} . The ratio of the hydrogen and the deuterium vibrational mode frequencies is close to $\sqrt{2}$ in this case. With high resolution Fourier transform instruments and the excellent quality of semiconductor crystals, much smaller isotope substitution caused frequency ratios can be measured accurately and easily today.

The simple relation given in equation (1) not only makes possible the identification of an impurity through isotope substitution but also the lattice location of the impurity. For example, we can readily decide if an amphoteric group IV impurity such as C or Si occupies an As or a Ga site in GaAs. Arsenic is monoisotopic with atomic mass $A=75$ while Ga has a natural composition of $A=69$ and $A=71$ in a 3:2 concentration ratio. An impurity on a Ga site is surrounded by four As atoms with one well-defined value of M_{lattice} , leading to a single sharp LVM line. On an As site the same impurity experiences several unique combinations of neighboring Ga atoms, leading to a total of nine distinct lines. Because of the close proximity of several of the resulting LVM lines, only five separate components have been resolved experimentally for Si_{As} and C_{As} .

We take a second example from the very large number of LVM studies with hydrogen passivated dopants in many different semiconductors. Whereas the vibrational mode frequencies of hydrogen bound to acceptors in silicon strongly depend on the acceptor impurity mass, the LVM frequencies of hydrogen passivating donors are insensitive to the donor impurity mass. The simple conclusion from this experimental observation is that hydrogen binds directly to acceptor dopants but does not bind to donor dopants. Both experiments and theory fully support this finding. ^{5,6}

To first order the value of C in equation (1) is a constant. For large amplitude vibrations, as they occur with hydrogen, nonlinearities become important and C must be described by a power series. The shift in LVM frequencies with lattice temperature is based on a change of C with the positions of the nearest neighbor atoms.

The successful study of a semiconductor sample with LVM spectroscopy requires the transmission of infrared light through the sample or Raman scattering of photons from a near surface layer. Transmission spectroscopy is most commonly used because of its high sensitivity and simpler instrumentation. Perhaps the most important limitation to transmission spectroscopy is free carrier absorption. Heavily doped samples have a very short extinction length for infrared photons. If thinning the sample is not feasible, an effective technique which was developed in the early phase of LVM spectroscopy makes use of radiation damage. Irradiation with 1 to 2 MeV

electrons or gamma rays introduces point defects. In most semiconductors these defects constitute deep level centers which remove the free carriers originating from the shallow dopants. Except for very high dopant concentrations ($>10^{18} \text{ cm}^{-3}$) the interaction between isolated point defects and the local vibrational modes remains small and can be neglected. For highly doped thin regions such as ion implanted layers, Raman spectroscopy is the tool of choice for the study of impurity LVMs.

Reducing the sample temperature typically improves the sensitivity and resolution of LVM spectroscopy. Coupling to multiphonon modes is reduced and the local oscillator Q-factor or lifetime increases. Reduction of the sample temperature to around 50 to 70 K leads to a very significant improvement over room temperature measurements but the highest resolution studies require sub-liquid helium temperatures. Superb Fourier transform spectrometers and a range of cryostats have been developed and are commercially available. With the exception of special and difficult cases, LVM spectroscopy has become a routine characterization tool.

HYDROGEN LVM SPECTROSCOPY IN SEMICONDUCTORS

In the past fifteen years the study of hydrogen in a wide variety of semiconductors has become a major area of research. The first electrical activity of hydrogen in a semiconductor was discovered in ultra-pure, hydrogen atmosphere grown Ge single crystals.⁷ Hydrogen activates the isoelectronic impurities Si and C in these crystals and turns them into shallow acceptor complexes.⁸ The neutral impurity oxygen forms a shallow donor complex when combined with hydrogen.⁹

The discovery of hydrogen passivation of shallow acceptors by in Si^{10, 11} and a few years later of shallow donors in Si¹² marks the beginning of a new sub-field of semiconductor research which has remained active worldwide to this date.

Hydrogen has been shown to passivate acceptors and donors by binding directly to the dopant atom or to a nearby host lattice atom. In the case of acceptors in Si, GaAs and other III-V compound semiconductors, hydrogen occupies one of the four bonds in the form of a proton Fig. (2).

In this bond centered (BC) position hydrogen is clearly bound to both neighbors, the acceptor impurity and a host lattice atom, though the relative bond strengths may differ. This model was established based on the sensitivity of the hydrogen stretch vibration frequency to the specific acceptor dopant species in a given semiconductor. For example, in silicon one finds the following hydrogen stretch vibration frequencies:

$$\nu_{\text{B-H}} = 1907 \text{ cm}^{-1}, \nu_{\text{Al-H}} = 2201 \text{ cm}^{-1}, \text{ and } \nu_{\text{Ga-H}} = 2171 \text{ cm}^{-1}.^{13}$$

Despite dedicated efforts, hydrogen-indium acceptor vibrational modes have not been observed.¹⁴

In sharp contrast, passivation of donors in silicon leads to LVM lines which are only very

weakly sensitive to the donor species. The hydrogen stretching vibrational frequencies of hydrogen-donor complexes are: $\nu_{P-H} = 1555.2 \text{ cm}^{-1}$, $\nu_{As-H} = 1561.0 \text{ cm}^{-1}$, and $\nu_{Sb-H} = 1561.7 \text{ cm}^{-1}$.¹⁵ These experimental findings in turn led to a model in which hydrogen binds to one of the Si neighbors of the donor in an antibonding position (Fig. 3).

A number of reviews^{6, 16} and books^{5, 17} have been written on hydrogen in semiconductors and the reader is referred to these for comprehensive information. Here we will focus on some of the early, key studies and on recent contributions. LVM spectroscopy has made to the understanding of hydrogen in semiconductors.

Uniaxial stress applied to Si samples containing acceptor-hydrogen complexes has been shown to align the symmetry axes of these complexes.¹⁸ The LVM lines show orientational splitting which in turn helps in determining the symmetry of the complexes. An especially elegant study of the boron-hydrogen center in Si showed that hydrogen can move relatively easily between the four bonds of the boron atom with its silicon neighbors.¹⁹ This motion can be frozen out at low enough temperatures. When stress is applied at high temperatures and during cooling down of the sample, the ratio of the intensities of LVM absorption lines for parallel and perpendicularly polarized light are a direct measure of the degree of alignment of the complexes. Removal of the stress and slow warming allows the center to reorient randomly with a certain time constant. An activation energy for the barrier between equivalent hydrogen positions in B-Si bonds of 0.19 eV has been determined in this way. Calculations of total energy surfaces for hydrogen moving through the Si lattice containing B acceptors find a barrier value of 0.2 eV between neighboring B-Si bonds in surprisingly good agreement with the experimental results.²⁰ An interesting question

regarding the type of hydrogen motion around the boron acceptor was raised by Stoneham.²¹ In view of the large zero-point energy of hydrogen in the boron-silicon bond corresponding to 0.12 eV, he suggested that tunneling may play a role. Because of the large relaxation of the boron and

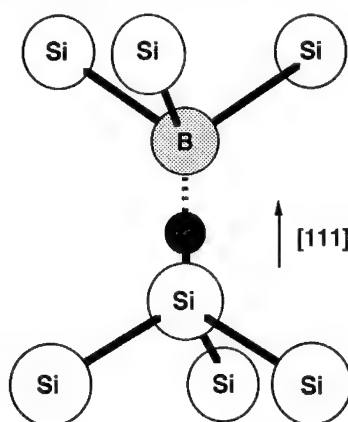


Fig. 2 Bond-centered configuration of the B-H complex in Si. The black sphere represents H.

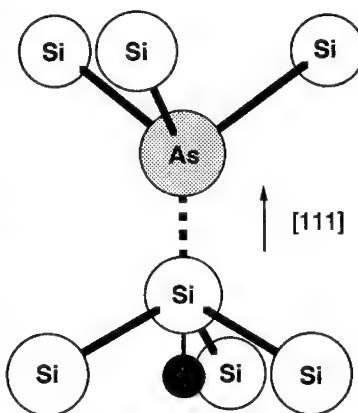


Fig. 3 Anti-bonding configuration of the As-H complex in Si. The black sphere represents H.

silicon atoms along the axis of the boron-hydrogen complex, tunneling is an unlikely process at low temperatures.²² At higher temperatures this question has been readdressed recently by Cheng and Stavola.²³ It is instructive to follow the evolution of such a basic question over time and to see how long it can take until it is finally settled.

LVM spectroscopy played as important a role in the detection and identification of hydrogen-dopant complexes in III-V semiconductors as it did in silicon. A very extensive body of experimental and theoretical results has accumulated over the years and has been documented in several reviews.^{6, 17, 24} We will summarize first some of the well-established results obtained with the best studied III-V semiconductor GaAs and then present some recent findings which have been obtained with GaP, GaN and ZnSe.

In close analogy with Si, a large number of acceptor-hydrogen and donor-hydrogen complexes have been discovered in group III-V semiconductors. Carbon-hydrogen is perhaps the most thoroughly studied complex in GaAs.²⁵ It is a technically important complex because carbon has become a preferred acceptor in GaAs due to its low diffusion coefficient and the very high concentration which can be achieved with MBE growth ($>10^{21} \text{ cm}^{-3}$). Taking all possible configurations of isotopic compositions (^{12}C , ^{13}C , ^1H , ^2H) and vibrational modes (stretch, wag, transverse, longitudinal) into account, one expects sixteen distinct infrared absorption lines. It is impressive that all sixteen modes have now been observed²⁶ and that good agreement is found between experiment and theory.²⁷ The model for carbon and other group IV acceptor-hydrogen complexes is shown in Fig 4a.²⁸ This model satisfies our intuition. The group IV acceptor has four bonds, three to the As neighbors and one to the bond centered hydrogen. The valence electrons of the As which are no longer bonded to the group IV acceptor, form three bonds to Ga neighbors and a lone electron pair. This is a common electron configuration (e.g. AsH_3).

The group IV dopants can, in principle, occupy the As or the Ga sites, i.e., they are amphoteric. While this behavior has been observed for Si, Ga, and Sn, C has never been found on Ga sites where it would act as a donor.²⁹

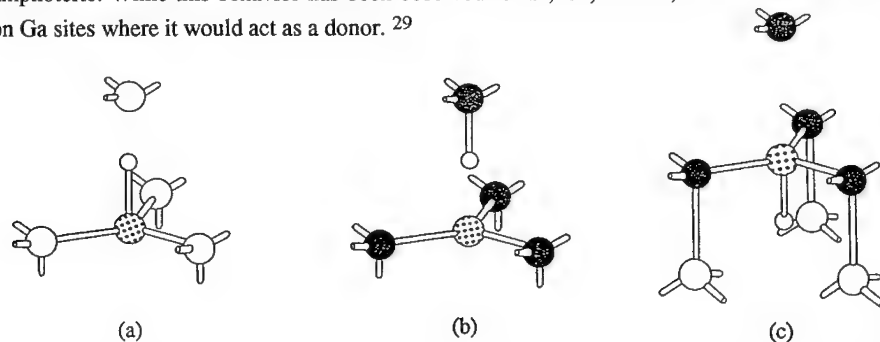


Fig. 4 Schematic representations of dopant-hydrogen complexes in III-V semiconductors; filled spheres: group V host lattice atom, empty spheres: group III host lattice atoms, dotted sphere impurity atom; a) group IV acceptor-hydrogen complex (e.g. $\text{GaAs:C}_{\text{As}}\text{H}$), b) group II acceptor-hydrogen complex (e.g. $\text{GaAs:Be}_{\text{Ga}}\text{H}$), c) group IV donor-hydrogen complex (e.g. $\text{GaAs:Si}_{\text{Ga}}\text{H}$). (Courtesy Refs. 28, 32)

There have been many hydrogen passivation studies of group IV acceptors in several III-V compounds other than GaAs. Recently an extensive study of $C_{As}-H$ complexes in AlAs epilayers has been reported.³⁰ Of the sixteen possible vibrational modes based on the model shown in Fig 4a, twelve have been measured. The frequencies of the various modes compare remarkably well with results from *ab initio* local density functional calculations and from a simple "spring and ball" harmonic oscillator. An intriguing aspect of the C-H vibrations in AlAs is the anti-crossing behavior of the carbon-like and the hydrogen-like modes shown in Fig. 5. It is important to notice that while hydrogen is mostly bound to the carbon acceptor it clearly senses the presence of the nearest Al host atom. This interaction is accounted for by the spring constant K_H^T .

The C-H complex in GaP has been investigated by Clerjaud.³¹ It can be aligned with uniaxial stress and frozen-in at low temperatures just like the B-H complex in Si. An activation energy for reorientation of 0.35 eV with a prefactor of $10^{12} s^{-1}$ has been determined. This relatively low energy gives strong support to the model shown in Fig. 4a. It again illustrates that the hydrogen is located in a potential energy minimum between carbon and one of its neighbors near the bond center rather than being bound exclusively to the carbon acceptor.

The group II acceptors have been studied in detail and, based on isotope effects and theory the model shown in Fig. 4b is the accepted configuration³². Recently the $Zn_{Ga}-H$ complex was discovered in GaP.³³ The stretch vibration frequency $\nu_H = 2379.0 \text{ cm}^{-1}$ is close to the value found for H passivated Zn in InP ($\nu_H = 2287.7 \text{ cm}^{-1}$) and the frequency ratios for the isotopes H and D are also similar $(\nu_H/\nu_D)_{GaP} = 1.3756$ and $(\nu_H/\nu_D)_{InP} = 1.3744$. The Zn-H bond-stretching frequency in a free molecule is only 1600 cm^{-1} . These findings strongly support the model shown in Fig. 4b. The hydrogen is more strongly bound to one of the phosphorus

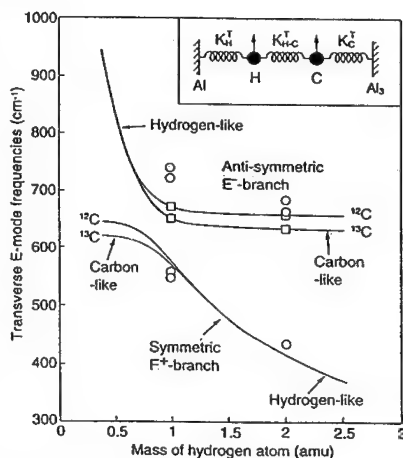


Fig. 5 Vibrational transverse E modes of the coupled masses shown in the inset, used as a simple model to represent the $H-C_{As}$ pair. The observed LVM frequencies were used to generate the spring constants using a least-squares fit. The curves show the variations in the frequencies when the mass of the hydrogen atom is regarded as an independent variable. The four 'carbon-like' modes (γ_2, E) detected for all possible isotopic combinations are shown by open squares. The frequencies predicted by *ab initio* theory are shown as open circles. The important feature is the anticrossing of the modes, which changes their effective identities (normal coordinates) for $H-C_{As}$ pairs compared with $D-C_{As}$ pairs (Courtesy Ref. 30).

neighbors of the Zn_{Ga} acceptor. The values of the frequency ratios are significantly smaller than the expected $\sqrt{2}$. Deviation from the simple harmonic oscillator potential (anharmonicity) is the most likely reason for this reduced value. Support for this assumption also comes from the observation that the deuterium related absorption line is more than a factor of 2 sharper than the hydrogen related line. The cause for this difference lies in the much smaller amplitude of the deuterium vibration.

Donors have been passivated in II-VI semiconductors and have been extensively studied with LVM spectroscopy. As in Si, donor-hydrogen complex formation is more difficult to achieve than acceptor hydrogen complex formation. A simple explanation for this difference comes from charge state arguments. In n-type materials where hydrogen assumes either a neutral or positive charge state, it readily forms immobile H_2 molecules.

An interesting question has been raised during studies of group VI donor passivation in GaAs.^{34, 35} All of their experimental findings support hydrogen bound to one of the Ga host atom neighbors of the group VI donor in an anti-bonding position. However they could not observe the small splitting of the hydrogen stretch vibration which is expected from the two Ga isotopes with masses $A = 69$ and $A = 71$ present in a 3:2 concentration ratio in natural Ga. This puzzle awaits an explanation.

A III-V family of semiconductors which are currently attracting much attention are the group III-nitride compounds. Whereas it is relatively easy to grow strongly n-type doped GaN, difficulties are encountered when large electrically active acceptor concentrations must be achieved. LVM spectroscopy of Mg doped GaN indicates hydrogen passivation of this acceptor through Mg-H complex formation.³⁶ It is expected that detailed LVM studies with these materials will help in understanding the doping limitations and may lead to ways of circumventing some of the problems.

For several reasons the number of LVM studies of hydrogen related centers in II-VI compound semiconductors is rather limited. The development of ZnSe and related compounds for blue light emitting diodes and lasers posed severe requirements for n- and p- doping. The acceptor N appears to be soluble at high concentrations. When grown under hydrogen-rich conditions, as they exist in organo-metallic vapor phase epitaxy (OMVPE), only a small fraction of the nitrogen atoms form electrically active acceptors. Wolk *et al.*³⁷ were first in finding the N-H stretch and wag vibration modes ($\nu_{\text{N-H}}(\text{stretch}) = 3194 \text{ cm}^{-1}$, $\nu_{\text{N-H}}(\text{wag}) = 783 \text{ cm}^{-1}$) in epitaxial layers of ZnSe:N,H grown on semi-insulating GaAs substrates, lending strong support to the argument that N is inactive because of hydrogen passivation. These LVM results were verified in part by Kamata *et al.*³⁸

Summarizing this section on H in semiconductors it can be stated that LVM spectroscopy has been the single most important technique regarding the determination of the structure of hydrogen containing complexes. Because of its low mass and the large mass ratio of the two stable hydrogen isotopes it is easily identified and detected with good sensitivity and excellent

resolution. The stretch vibration modes lie far above all other modes occurring in semiconductor crystals.

It is somewhat surprising that hydrogen escaped direct observation for such a long time. The major reason is related to the difficulty in introducing hydrogen in concentrations which far exceed solubility limits and in avoiding the formation of H_2 molecules which are rather immobile. It is expected that LVM spectroscopy will continue its important rôle in the study of hydrogen containing complexes in semiconductors.

LVM SPECTROSCOPY OF LOW MASS DOPANTS AND ISOELECTRONIC IMPURITIES IN SEMICONDUCTORS

Barker and Sievers¹ reviewed "optical studies of vibrational properties of disordered solids" in their nearly two hundred page article two decades ago. They listed vibrational mode frequencies of dozens of impurities in group IV, group III-V and group II-V semiconductors and some alloys. Their theoretical treatments are very accessible for the experimentalist and they give the depth necessary for a thorough understanding of the various features appearing in LVM spectra. In this article we will focus mainly on local modes which are produced by impurities with masses smaller than all the host atom masses. Other resonant vibrational modes such as gap modes and resonant modes will not be considered.

The major advances in LVM spectroscopy achieved over the past fifteen years originate in the significantly improved sample quality (crystallinity, purity), in new, easy to operate, very high resolution Fourier transform spectrometers and associated detectors and in the control of the isotopic composition recently achieved for some semiconductors. To illustrate these points we will review recent work reported on group IV and group III impurities in GaAs, on local modes of Mg in $Cd_{1-x}Zn_xTe$ and on oxygen in isotopically engineered Ge. All these examples illustrate clearly how the use of LVM frequency shifts, caused by impurity and host atom isotope composition leads, to an unambiguous determination of the impurity site and all its neighbors.

B, C and Si in GaAs

Simple intuition misleads us in assuming that B, as a group III element would always assume Ga positions in GaAs. Under Ga-rich growth conditions significant concentrations of B are found on As sites (B_{As}). The stable isotopes of B are ^{10}B and ^{11}B . With the small difference in mass between ^{10}B , ^{11}B and ^{12}C it is instructive to compare the LVM spectra of B_{As} and C_{As} . Leigh *et al*³⁹ have recently reported a high resolution study of B_{As} and C_{As} in GaAs. Figs. 6a) and 6b) show the very strong similarity between the LVM spectral signatures of $^{11}B_{As}$ and $^{12}C_{As}$. The similarity extends to the line intensity ratios and the line width. The five lines are due to a total of nine distinct modes. A perturbation theory for this C_{As} fine structure was

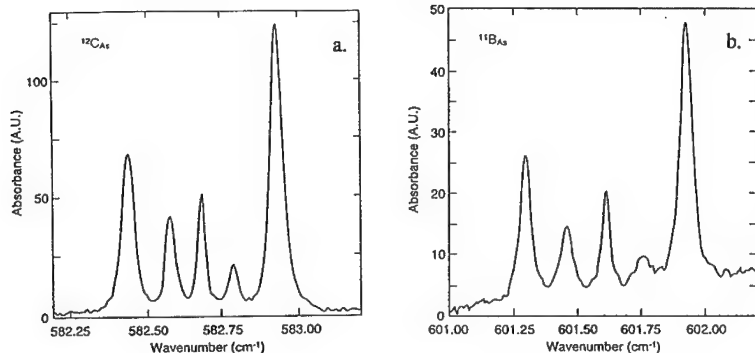


Fig. 6 a) The fine structure of the LVM line for $^{12}\text{C}_{\text{As}}$ in GaAs

b) The fine structure of the LVM line for $^{11}\text{B}_{\text{As}}$ in GaAs (Courtesy Ref. 39)

formulated some time ago.⁴⁰

The impurities can be surrounded by either four ^{69}Ga or ^{71}Ga host isotopes, creating the lowest and highest frequencies (a triplet each), by three ^{69}Ga and one ^{71}Ga isotope or *vice versa* three ^{71}Ga and one ^{69}Ga isotope each leading to two modes (a doublet and a triplet) and by two ^{69}Ga and two ^{71}Ga isotopes resulting in three singlet lines. Using the "direct embedded cluster method" described by Sangster *et al.*,⁴¹ the recent studies fit two force constants, the stretch constant between the impurity and the nearest neighbors and the bond bending constant.

After fitting the two constants, the calculated mode frequencies of the five observed lines agree with measurements to within 5 and in some case 6 digits for $^{10}\text{B}_{\text{As}}$, $^{11}\text{B}_{\text{As}}$, $^{12}\text{C}_{\text{As}}$ and $^{13}\text{C}_{\text{As}}$. Leigh *et al.*³⁹ also derived a relationship between the impurity isotope substitution shifts and the fine structure caused by the nearest neighbor host isotope effects. As long as a harmonic model is used one finds, based essentially on the expression given in equation (1) the following expression:

$$\left(\frac{\omega'}{\omega}\right)^2 = \frac{m}{m'} + 2\left(\frac{m}{m'} - 1\right) \frac{M}{\delta M} \frac{\delta\omega}{\omega} \quad (2)$$

ω , ω' and m , m' refer to the impurity LVM frequencies and masses respectively while M is the host isotope mass and δM the change (small!) is host isotope mass. The expression given in (2) has been tested with experimental values for ^{10}B , ^{11}B , and ^{12}C and ^{13}C and gives an accuracy of 1 in 10^5 ! It is this extremely good agreement between theory and experiment which gives us great confidence in the impurity site identifications proposed on the basis of LVM spectroscopy.

The possibilities for Si LVMs in GaAs are richer because this impurity, contrary to carbon, shows amphoteric behavior.⁴² The three stable isotopes of Si ($A = 28, 29, 30$) lead to sharp LVM lines when they occupy a Ga site and are surrounded by four monoisotopic ^{75}As host atoms. On the As site the most abundant ^{28}Si has been shown to produce a multi-line pattern

because of the different Ga isotope mass combinations. In addition to these modes corresponding to isolated Si impurities, new modes caused by $\text{Si}_{\text{Ga}}\text{-Si}_{\text{As}}$ donor-acceptor pairs and $\text{Si}_{\text{Ga}}\text{-V}_{\text{Ga}}$ have been identified. Further modes have been tentatively assigned to a complex involving Si_{As} and V_{Ga} .

A new Si related mode has been discovered in Si doped n-type GaAs under large hydrostatic pressure. Wolk *et al.*⁴³ assigned this mode to the metastable Si DX center which forms a deep localized electron state. The structure of the Si DX center has been proposed by Chadi and Chang⁴⁴ and consists essentially of a Si impurity bound only to three As neighbors. It moves along the broken bond direction away from the As neighbor by over one Ångström. From the ratio of the LVM lines of regular Si donors on Ga sites and Si in the DX configuration as a function of acceptor compensation, Wolk *et al.* were able to give experimental support for the predicted negative charge state of the DX center.

Mg in $\text{Cd}_{1-x}\text{Zn}_x\text{Te}$

The zincblende semiconductors CdTe and ZnTe and their alloy $\text{Cd}_{1-x}\text{Zn}_x\text{Te}$ are finding important applications as radiation detector materials,⁴⁵ as substrates for $\text{Hg}_{1-x}\text{Cd}_x\text{Te}$ epitaxy,⁴⁶ and in green and blue light emitting diodes and lasers.⁴⁷ The increased interest in these materials has led to significant efforts towards improving their crystalline quality and purity.

Low mass, electrically inactive impurities have recently been studied in detail in these II-VI compounds using LVM spectroscopy. We focus our discussion on Mg in Cd or Zn lattice positions. Natural Mg has three stable isotopes with atomic masses $A = 24$ (79%), 25 (10%), and 26 (11%). The expected three LVM lines are well resolved for Mg_{Cd} in CdTe (Fig. 7) and Mg_{Zn} in ZnTe (Fig. 8a).

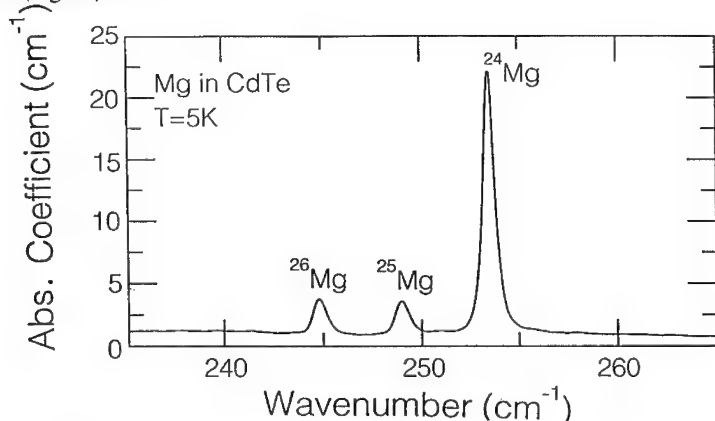


Fig. 7 Absorption spectrum of Mg_{Cd} local modes in CdTe (Courtesy Ref. 48)

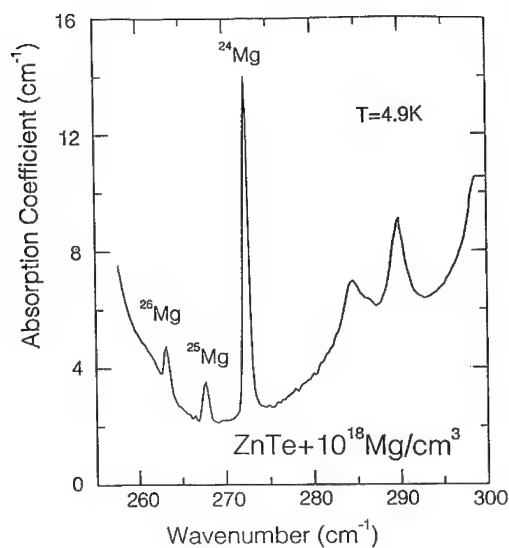


Fig. 8a Absorption spectrum of Mg_{Zn} local modes in ZnTe (Courtesy Ref. 48)

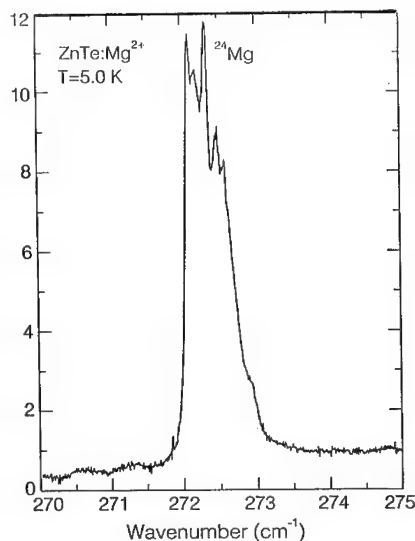


Fig. 8b Fine structure of the local mode of ^{24}Mg in ZnTe recorded with a 0.02 cm^{-1} resolution showing the effect of the four nearest neighbor Te atoms (Courtesy Ref. 48).

Surrounded by four Te atoms with isotopic masses ranging from $A = 120$ to $A = 130$ we expect significant fine structure due to nearest neighbor interactions between Mg_{Zn} and Te.

Sciaccia *et al.*⁴⁸ have succeeded in partially resolving this rich fine structure (Fig. 8b). As in the case of C_{As} in GaAs the various combinations of Te neighbors can be statistically evaluated and it should be possible to analyze the line shape in detail. This has not been accomplished so far, but it is evident that the intensity of the ^{24}Mg LVM line peaks on the low frequency side as one would expect from the abundance of the heavier stable Te isotopes (^{126}Te (19%), ^{128}Te (32%), and ^{130}Te (34%)).

Other group II isoelectric impurities such as Ca on group II host atom places and S_{Te} give rise to similar LVM spectra. A very interesting further complexity with additional physical information arises when a II–VI semiconductor with the wurtzite structure instead of zincblende structure is used for such LVM studies. The host lattice sites have a lower symmetry, reduced from tetrahedral (T_d) to trigonal (C_{3v}). This in turn leads to a splitting of the degenerate LVM lines of Mg, an effect which has been observed with CdSe by Sciaccia *et al.*⁴⁸.

A most interesting experimental result has been obtained with Mg LVM studies in a series of $\text{Cd}_{1-x}\text{Zn}_x\text{Te}$ with x ranging from 0 to 1.⁴⁸ The line position shifts linearly with x from

$\nu_{24Mg}(\text{CdTe}) = 253.3 \text{ cm}^{-1}$ to $\nu_{24Mg}(\text{ZnTe}) = 272.3 \text{ cm}^{-1}$ (Fig. 9a).

It appears that the local force constants given by the bonds of Mg to its four neighbors can be approximated by an effective value within the virtual crystal approximation (VCA) :

$$C_{\text{eff}} = C_{\text{Cd}}(1-x) + C_{\text{Zn}}x \quad (3)$$

The line width on the other hand follows a broadening pattern which is encountered for various physical properties in random alloys. The full width at half maximum (FWHM) is found to follow (Fig. 9b):

$$\text{FWHM} \propto x(1-x). \quad (4)$$

Electrical conduction in metal alloys follows the same kind of dependence.⁴⁹ When metal alloys order for special ratios of the individual constituents one observes sharp increases in electrical conductivity. It will be interesting to attempt to induce ordering in $\text{Cd}_{1-x}\text{Zn}_x\text{Te}$ and, if successful, to investigate the effect on linewidth.

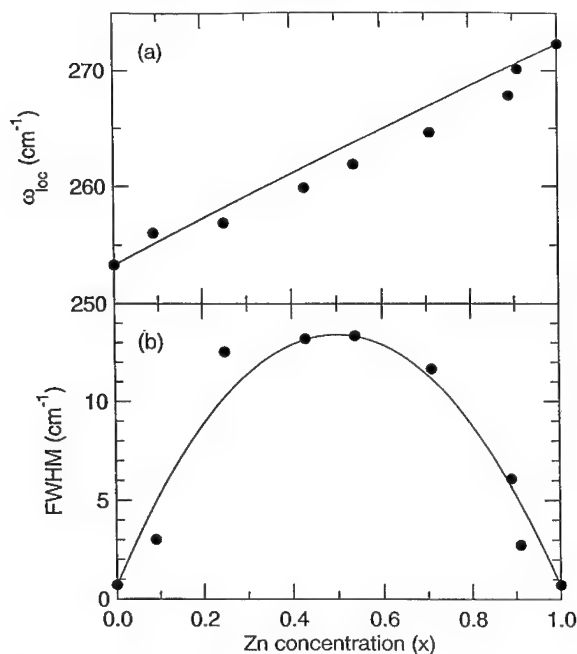


Fig. 9 a) Plot of the local mode frequency (ν_{loc}) of ^{24}Mg in $\text{Cd}_{1-x}\text{Zn}_x\text{Te}$ as a function of the Zn concentration x . The full circles are experimentally observed line positions and the line represents their dependence on x according to the virtual crystal model in which the Mg-Te force constant varies linearly with x . b) Full width at half maximum of the ^{24}Mg LVM in $\text{Cd}_{1-x}\text{Zn}_x\text{Te}$ as a function of x . The data fit a $x(1-x)$ dependence, typical for certain alloy properties (see text). (Courtesy Ref.48)

O in Isotopically Controlled Ge

Oxygen is one of the most important impurities in semiconductors. Crystals grown by the Czochralski technique from a melt contained in silica crucibles contain oxygen generated by the reduction of the crucible material by the melt. For the majority of Si based devices, oxygen is a desirable impurity because it can be used to form silica precipitates which are excellent gettering

centers for a wide range of undesirable impurities. Because of the importance of oxygen, a large number of studies have been performed over the past forty years. Kaiser, Keck and Lange⁵⁰ discovered the oxygen related infrared band near $9\mu\text{m}$ for Si and near $11.6\mu\text{m}$ for Ge. These bands have been assigned to stretching vibrations of the oxygen in its bond centered position. The "quasi-molecules" Si-O-Si and Ge-O-Ge with oxygen puckered away from the $\langle 111 \rangle$ axis have been successfully used to model the oxygen LVMs. All three normal modes ν_1 , ν_2 , and ν_3 of such a molecule have been found for Si at 30 cm^{-1} , 515 cm^{-1} and 1136 cm^{-1} , respectively. Coupling between the three modes due to anharmonicity was first suggested by Bosomworth *et al.*⁵¹.

Whereas natural Si consists of three stable isotopes with ^{29}Si present very dominantly at 92%, natural Ge consists of five isotopes: ^{70}Ge (21.23%), ^{72}Ge (27.66%), ^{73}Ge (7.73%), ^{74}Ge (35.94%), and ^{76}Ge (7.44%). In Si there exist five isotopic configurations for the Si-O-Si molecule while in Ge there are eleven combinations which lead to distinct oxygen LVM frequencies.

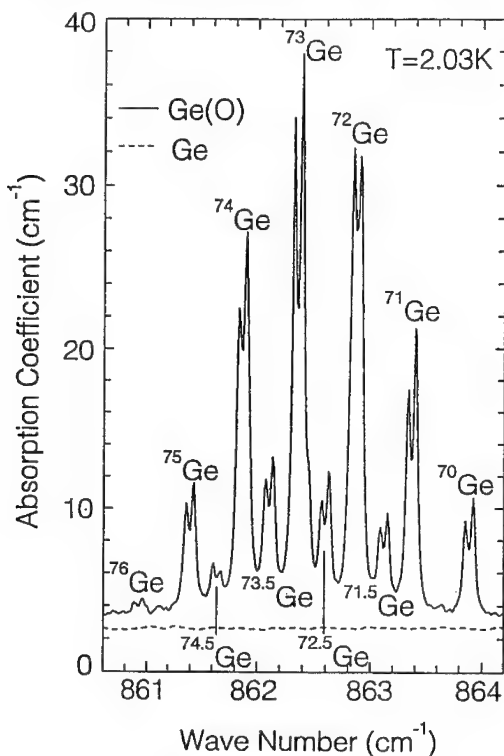
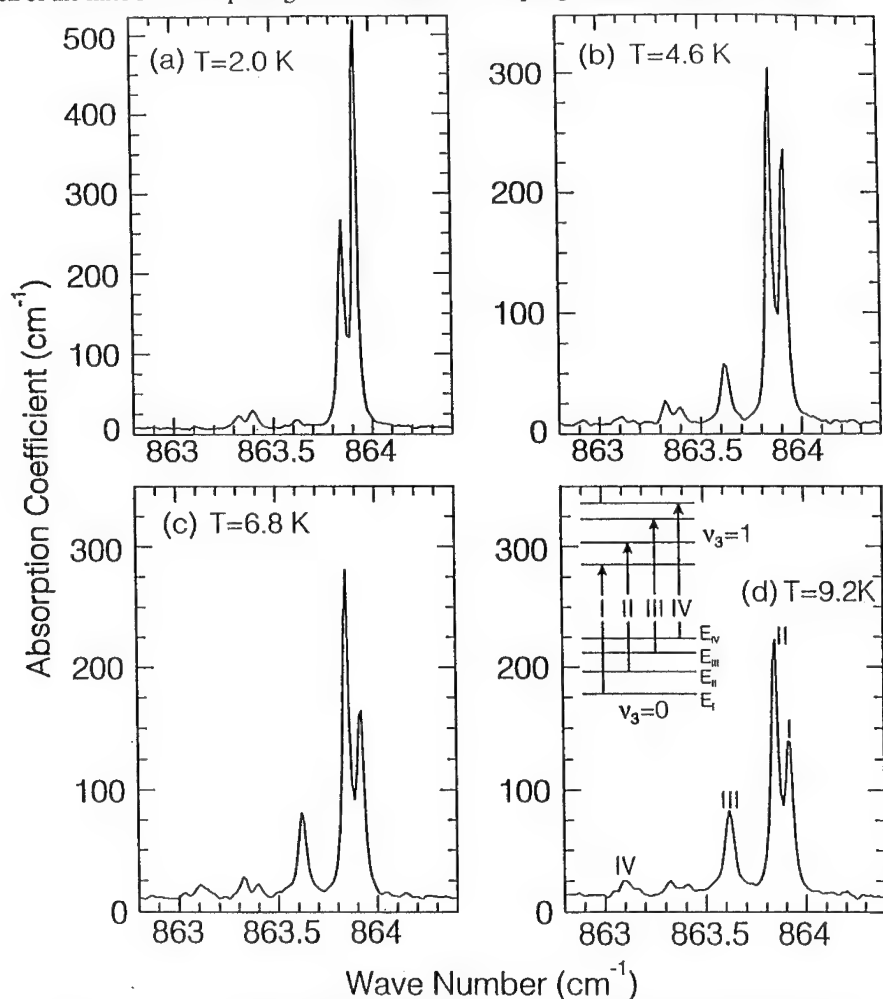


Fig. 10 High resolution spectrum of the ν_3 local mode vibrations in Ge of natural composition. There exist 11 distinct average masses of the two Ge isotopes neighboring O. The fine structure of each line is due to the coupling between the ν_2 and the ν_3 modes. (Courtesy Ref. 52)

The number of relevant mass combinations is smaller than the number of all possible combinations because only the average host atom mass or $\frac{1}{2}(A(^{73}\text{Ge}) + A(^{75}\text{Ge}))$ has an influence on the oxygen vibrational mode (e.g. $^{73}\text{Ge}-^{16}\text{O}-^{73}\text{Ge}$ and $^{70}\text{Ge}-^{16}\text{O}-^{76}\text{Ge}$ result in the same ^{16}O LVM frequency). Mayur *et al.*⁵² have recorded the oxygen LVM spectrum in natural and in isotopically controlled oxygen doped single crystals of Ge at very high resolution (Figs.10 & 11).

The individual lines in Fig. 10 are labeled with the average mass of the two immediate neighbors of the oxygen atom. There are no Ge isotopes with half masses or mass 71 and 75! Each of the lines shows a splitting which is due to the coupling of the ν_2 and the ν_3 modes.



Figs. 11 a) - d) Temperature dependence of the $\nu_2 + \nu_3$ coupling excitations in ^{70}Ge . The coupling excitations are identified in the inset in d). (Courtesy Ref. 52)

In Fig. 11 we see the $^{70}\text{Ge}-^{16}\text{O}-^{70}\text{Ge}$ LVM lines in an isotopically pure ^{70}Ge crystal as a function of temperature. The simplification of the LVM spectrum is as impressive as one would expect. The small double peak at 863.4 cm^{-1} is caused by the residual ^{72}Ge isotope present at $\sim 4\%$. The various components become thermally activated and from the dependences of their intensities on temperature, one can derive the energies of the ν_2 modes in the ground state of the ν_3 mode. The experimentally determined values are in good agreement for theoretical results obtained for a rigid rotor. Without the selective simplification of the oxygen. LVM spectrum made possible through isotope control, the $\nu_2 + \nu_3$ coupling could not have been investigated!

CONCLUSIONS

LVM spectroscopy has been used extensively to determine the lattice location of a large number of low mass impurities in many semiconductors. It is not necessary for an impurity to be electrically active or to have an unpaired electron spin as is required for electronspin resonance techniques. Identification of the impurity through impurity isotope shifts is unambiguous in very many cases. It is impossible to offer a comprehensive coverage of all the hydrogen related LVM studies performed in elemental group IV and compound groups III-V and II-VI semiconductors in the past fifteen years. The reason for the great popularity of the technique is based on the above statements regarding positive identification but also because of the good sensitivity of LVM spectroscopy, the large mass ratio between H and D and the possibility of using rather high impurity concentrations without loss of good resolution. This latter property is a direct consequence of the strong localization of LVMs.

LVM spectroscopy has been used productively with impurities other than H or D. Indeed, as long as the impurity mass is smaller than at least one of the host atom species we can observe gap modes. We have restricted our choice of examples to the simplest and clearest cases for which the impurity mass is smaller than all the host crystal constituents.

A new dimension for LVM spectroscopy has been opened by isotopically engineered semiconductors.⁴ The selective simplification achieved through isotope control has already lead to new results with O in Ge. It would be intriguing to test our knowledge about C_{As} in GaAs with isotopically "pure" $^{69}\text{Ga}^{75}\text{As}$ and $^{71}\text{Ga}^{75}\text{As}$ single crystals !

Some of the semiconductors which have recently attracted great interest because of applications in blue light emitting diodes have not been thoroughly investigated with LVM spectroscopy. To our knowledge there exists but one report on H passivation of acceptors in GaN which is based in part on hydrogen LVM spectroscopy³⁶. We expect many more studies to follow.

In closing it should be stated that LVM spectroscopy with high resolution Fourier transform spectrometers does not only produce exquisite spectra in many semiconductor studies, but it has found its place in semiconductor processing lines as a characterization tool. Dedicated

Fourier transform spectrometers are used to measure the concentrations of atomically dispersed oxygen in silicon at various processing stages. Based on these facts we foresee a very bright future for both broader and more refined uses of LVM spectroscopy in research, development, and fabrication.

ACKNOWLEDGEMENTS

I am indebted to my former and present students and many colleagues for fruitful collaborations and discussions involving the topic of LVM spectroscopy. I thank them for letting me use their results, some of them as yet unpublished, in this review. Special thanks go to R. Jeanloz, U.C. Berkeley for his support in acquiring a new, high resolution spectrometer. This work has been supported in part by AFOSR contract I49620-91-C-0082, USNSF grant DMR 94-17763 and by the Lawrence Berkeley Laboratory Directed Research and Development program through USDOE Contract DE-AC03-76SF00098.

REFERENCES

- 1.) A.S. Barker Jr., and A.J. Sievers, Rev. Modern Physics **47**, Suppl. 2 (1975)
- 2.) W.G. Spitzer, *Festkörperprobleme XI, Advances in Solid State Physics*, O. Madelung, ed. (Pergamon, Vieweg, Germany, 1971).
- 3.) R.C. Newman, *Infrared Studies of Crystal Defects*, (Taylor & Francis, London 1973); see also *Festkörperprobleme XXV, Advances in Solid State Physics*, P. Grosse, ed. (Vieweg, Braunschweig, 1985).
- 4.) E.E. Haller, J. Appl. Phys. **77**, (7) 2857 (1995).
- 5.) see articles in *Hydrogen in Semiconductors: Semic. & Semimetals* **34**, J.I. Pankove and N.M. Johnson, eds., (Academic Press, Orlando, FL, 1991).
- 6.) E.E. Haller, in *Handbook on Semiconductors Vol 3b*, S. Mahajan, ed., (Elsevier Science BV, Amsterdam 1994); pp. 1515-1555.
- 7.) E. E. Haller, "Hydrogen-Related Phenomena in Crystalline Germanium," Chapter 11 in : *Hydrogen in Semiconductors: Semiconductors and Semimetals Vol. 34*, J.I. Pankove and N.M. Johnson, eds., (Academic Press, Orlando, FL, 1991); pp 351-380.
- 8.) J. M. Kahn, R. E. McMurray, Jr., E. E. Haller and L. M. Falicov, Phys. Rev. B **36**, No. 15, 8001 (1987).
- 9.) B. Joos, E. E. Haller and L. M. Falicov, Phys. Rev. B **22**, 832 (1980).
- 10.) T. Sah, J.Y.G. Sun, J.J. Tzou, Appl. Phys. Lett. **43**, 204 (1983).
- 11.) J.I. Pankove, D.E. Carlson, J.E. Berkeyheiser and R.O. Wance, Phys. Rev. Lett. **51**, 2224 (1983).
- 12.) N.M. Johnson, C. Herring and D.J. Chadi, Phys. Rev. Lett. **56**, 769 (1986).
- 13.) M. Stavola, S.J. Pearton, J. Lopata, and W.C. Dautremont-Smith, Appl. Phys. Lett. **50**, 1086 (1987).

- 14.) M. Stavola, private communication.
- 15.) K. Bergman, M. Stavola, S.J. Pearton, and J. Lopata, Phys. Rev. B **37**, 2770 (1988).
- 16.) E.E. Haller, Semic. Sci. Technol. **6**, 73 (1991).
- 17.) see articles in *Hydrogen in Compound Semiconductors*, S.J. Pearton, ed., Materials Science Forum **148/9**, (Trans. Tech. Publ. 1994).
- 18.) K. Bergman, M. Stavola, S.J. Pearton, and T. Hayes, Phys. Rev. B **38**, 9643 (1988).
- 19.) M. Stavola, K. Bergman, S.J. Pearton, and J. Lopata, Phys. Rev. Lett. **61**, 2786 (1988).
- 20.) P.J.H. Denteneer, C.G. Van de Walle and S.T. Pantelides, Phys. Rev. B **39**, 10809 (1989) and Phys. Rev. Lett. **62**, 1884 (1989).
- 21.) A.M. Stoneham, Phys. Rev. Lett. **63**, 1027 (1989).
- 22.) G. Watkins, Proc. 15th Intl. Conf. Defects in Semiconductors, G. Frerenczi, ed. (Trans. Tech. Publ., Switzerland, 1989), p. 39.
- 23.) Y.M. Cheng and M. Stavola, Phys. Rev. Lett. **73**, 3419 (1994).
- 24.) R. Darwich, B. Pajot, B. Rose, D. Robein, B. Theys, R. Rahbi, C. Porte, and F. Gendron, Phys. Rev. B **48**, 17776 (1993).
- 25.) B. Clerjaud, F. Gendron, M. Krause and W. Ulrici, Phys. Rev. Lett. **65**, 1800 (1990).
- 26.) B.R. Davidson, R.C. Newman, T.J. Bullough, and T.B. Joyce, Semic. Sci. and Technol. **8**, 1783 (1993).
- 27.) R. Jones and S. Öberg, Phys. Rev. B **44**, 3673 (1991).
- 28.) J. Chevallier, B. Pajot, A. Jalil, R. Moustefaoui, R. Rahbi, and M.C. Boissy, Mat. Res. Soc. Proc. Vol. **104**, 337 (1988).
- 29.) M.J. Ashwin, B.R. Davidson, K. Woodhouse, R.C. Newman, T.J. Bullough, T.B. Joyce, R. Nicklin, and R.R. Bradley, Semic. Sci. Technol. **8**, 625 (1993).
- 30.) R.E. Pritchard, B.R. Davidson, R.C. Newman, T.J. Bullough, T.B. Joyce, and S. Öberg, Semic. Sci. Technol. **9**, 140 (1994).
- 31.) B. Clerjaud, D. Côte, W.-S. Hahn, and W. Ulrici, Appl. Phys. Lett. **58**, 1860 (1991).
- 32.) M. Stavola, S.J. Pearton, J. Lopeta, C.R. Abernathy, and K. Bergman, Phys. Rev. B **39**, 8051 (1989).
- 33.) M.D. McCluskey, E.E. Haller, J. Walker and N. M. Johnson, Appl. Phys. Lett. **65**, 2191 (1994).
- 34.) J. Vetterhöfer, J.H. Svensson, J. Weber, A.W.R. Leitch and J.R. Botha, Phys. Rev. B **50**, 2708 (1994).
- 35.) R. Rahbi, B. Theys, R. Jones, B. Pajot, S. Öberg, K. Somogyi, and M.L. Fille, Solid State Commun. **91**, 187 (1994).
- 36.) M.S. Brandt, J.W. Ager III, W. Götz, N.M. Johnson, J.S. Harris Jr., R.J. Molnar, and T.D. Moustakas, Phys. Rev. B **49**, 14758 (1994).
- 37.) J. Wolk, J.W. Ager III, K.J. Duxstad, E.E. Haller, N.R. Taskar, D.R. Dorman and D.J. Olego, Appl. Phys. Lett. **63**, 2756 (1993).

- 38.) A. Kamata, H. Mitsuhashi and H. Fujita, Appl. Phys. Lett. **63**, 3353 (1993).
- 39.) R.S. Leigh, R.C. Newman, M.J.L. Sangster, B.R. Davidson, M.J. Ashwin and D.A. Robbie, Semic. Sci. Technol **9**, 1054 (1994).
- 40.) R.S. Leigh and R.C. Newman, J. Phys. C: Solid State Phys **15**, L1045 (1982).
- 41.) M.J.L. Sangster, R.C. Newman, G. Gledhill, and S.B. Upadhyay, Semicond. Sci and Technol. **7**, 1295 (1992).
- 42.) R.C. Newman, Semicond. Sci. and Technol. **9**, 1749 (1994).
- 43.) J.A. Wolk, M.B. Kruger, J.N. Heyman, W. Walukiewicz, R. Jeanloz, and E.E. Haller, Phys. Rev. Lett. **66**, 774 (1991).
- 44.) D.J. Chadi and K.J. Chang, Phys. Rev. B **39**, 10063 (1989).
- 45.) P.N. Luke, Appl. Phys. Lett. **65**, 2884 (1994), see also papers in Nucl. Instr. & Meth. A **352**, No.1-3 (1994).
- 46.) see papers in Proc. *Producibility of II-VI Materials and Devices* , SPIE Proc. Vol. **2228** (1994).
- 47.) See papers in Proc. *6th Intl. Conf. on II-VI Compounds and Related Opto-electronic Materials* , J. Crystal Growth **138**, No.1-4 (1994).
- 48.) M. Dean Sciacca, A.J. Mayur, N. Shin, I. Miotkowski, A.K. Ramdas, and S. Rodriguez, Phys. Rev. B **51**, March 15 (1995), in press.
- 49.) C. Kittel, *Introduction to Solid State Physics*, 6th edition (John Wiley & Sons, Inc., New York, 1986), p. 582-3 (from C.H. Johansson and J.C. Linde, Ann. Phys. **25**, 1 (1936)).
- 50.) W. Kaiser, P.H. Keck and C.F. Lange, Phys. Rev. B **101**, 1264 (1956).
- 51.) D.R. Bosomworth, W. Hayes, A.R.L. Spray, and G.D. Watkins, Proc. Roy. Soc. London **A317**, 133 (1970).
- 52.) A.J. Mayur, M. Dean Sciacca, M.K. Udo, A.K. Ramdas, K. Itoh, J. Wolk, and E.E. Haller, Phys. Rev. B **49**, 16293 (1994).

SILICON DELTA DOPING IN GaAs : AN ONGOING ENIGMA

R.C. NEWMAN*, M.J. ASHWIN*, J. WAGNER‡, M.R. FAHY*, L. HART*, S.N. HOLMES*
AND C. ROBERTS*

* IRC Semiconductor Materials, The Blackett Laboratory, Imperial College of Science,
Technology and Medicine, Prince Consort Road, London SW7 2BZ, United Kingdom

‡ Fraunhofer Institut für Angewandte Festkörperphysik, Tullastrasse 72, D-79108 Freiburg,
Germany

ABSTRACT

Infrared (IR) absorption and Raman scattering are reported from the localized vibrational modes (LVM) of Al and Si δ -layer superlattices in MBE (100) GaAs grown at 400°C as a function of the total areal concentrations, $[Al]_A$ and $[Si]_A$ respectively. The Al superlattices show the expected behavior on passing from sub-monolayer (ML) to thicker layers (thin AlAs) since the impurities still occupy only Ga-sites. The behavior is very different from that found for Si δ -layers. In addition to Si_{Ga} reported previously, we now show that Si_{As} , $Si_{Ga}-Si_{As}$ pairs and the electron trap Si-X are also present in Si δ -layers and superlattices for $0.05 \leq [Si]_A \leq 0.5$ ML. The conductivity of these structures and the concentrations of substitutional Si in GaAs at all sites fall to zero for $[Si]_A > 0.5$ ML but a Raman feature at 470-490 cm^{-1} , attributed to the vibrations of covalent Si-Si bonds is then detected. This feature is not observed in structures containing very closely spaced dilute (0.01 ML) Si δ -planes. It is inferred that long-range Si diffusion does not occur in the bulk crystal, although there could be surface diffusion during Si deposition. The maximum measured carrier concentrations are always less than $2 \times 10^{19} cm^{-3}$, the DX limit. The redistribution of Si amongst the various lattice sites is discussed in terms of Si_{Ga} DX-like displacements occurring during growth, followed by local thermally activated diffusion jumps. It is speculated that As_{Ga} antisite defects and Ga-vacancies are produced by this process. The reason why the Si δ -layer is non-conducting remains unclear.

INTRODUCTION

Homogeneously silicon doped GaAs layers grown by molecular beam epitaxy (MBE) on (100) substrates are n-type with a carrier concentration (n) that initially increases monotonically with the silicon concentration, $[Si]$. At low doping levels essentially all the Si is present as isolated Si_{Ga} donors. At higher doping levels n passes through a maximum value, n_{MAX} , that depends on the growth temperature ($T(g)$) and then falls to much lower values at the highest doping levels [1]. For $T(g) = 580^\circ C$, n_{MAX} is $\sim 5 \times 10^{18} cm^{-3}$ [2,3], but higher values of $\sim 2 \times 10^{19} cm^{-3}$ have been reported for growth at $\sim 400-350^\circ C$ [4-7]. The limiting value of n_{MAX} may result from auto-compensation arising from the presence of Si_{As} acceptors, $Si_{Ga}-Si_{As}$ nearest neighbor pairs and a trap labeled Si-X ($T(g) > 400^\circ C$), DX-behavior ($T(g) \sim 400^\circ C$) or the introduction of Ga-vacancies that act as deep electron traps ($T(g) < 350^\circ C$) [8]. This limitation is unfortunate because for certain devices larger values of n are required [9-11].

An alternative doping method during MBE growth is to attempt to confine the Si_{Ga} donor atoms to a single plane, a process known as spike or delta (δ) doping [9-11]. Ionization

should then lead to a sheet of positively charged Si_{Ga} donors with electrons occupying states in minibands in the adjacent planar V-shaped potential [12]. The growth procedure is to interrupt the Ga-flux, deposit the required total areal concentration $[\text{Si}]_{\text{A}}$ of silicon and then to re-instate the Ga flux to produce an overgrowth of GaAs. In the work discussed here the As-flux is maintained throughout these steps. This sequence can be repeated many times at regular intervals to produce a δ -layer superlattice [13]. Because of surface segregation and diffusion of Si atoms during growth, $T(\text{g})$ should be no greater than 400°C to achieve "planar" confinement of the dopant [14]. At lower temperatures the layers contain unwanted intrinsic defects, while at higher $T(\text{g})$, electrical and optical measurements do not distinguish the properties of the δ -layer from those of the GaAs that becomes homogeneously doped immediately adjacent to the δ -layer as a result of the Si segregation and diffusion processes [13].

Previous infrared (IR) absorption measurements of the localized vibrational modes (LVM) of the Si atoms in δ -layer superlattices grown at 400°C revealed only the line from isolated Si_{Ga} donors, usually on a sharply rising background absorption due to free-carriers (Fig. 1) [13]. The concentration $[\text{Si}_{\text{Ga}}]$ initially increased as $[\text{Si}]_{\text{TOT}}$ increased (Fig. 2) but then passed through a plateau and fell to zero as $[\text{Si}]_{\text{A}}$ approached 0.5 monolayers (ML) per δ -layer ($3.4 \times 10^{14} \text{ atom cm}^{-2}$). The carrier concentration showed the same dependence on $[\text{Si}]_{\text{A}}$ and also fell to zero for $[\text{Si}]_{\text{A}} = 0.5 \text{ ML}$ (Fig. 2). This behavior was attributed originally to the formation of $\text{Si}_{\text{Ga}}\text{-Si}_{\text{Ga}}$ pairs in adjacent surface Ga-atom sites and to larger 2D islands modeled empirically by the solid line in Fig. 2. High resolution x-ray diffraction measurements confirmed that any spreading of the Si atoms was less than 2 ML for δ -layers with $[\text{Si}]_{\text{A}} = 0.5 \text{ ML}$ [15] but such measurements are not sufficiently sensitive to study dilute δ -layers [16].

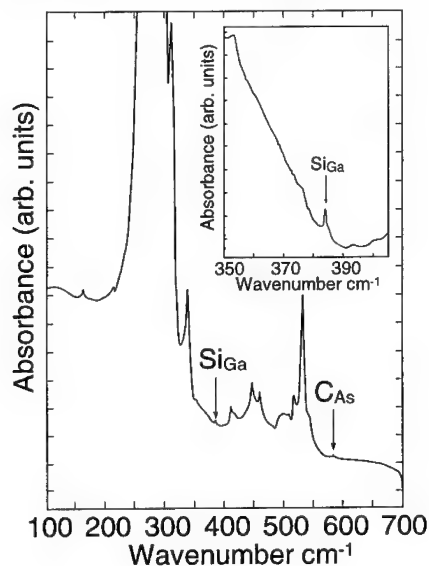


Figure 1.

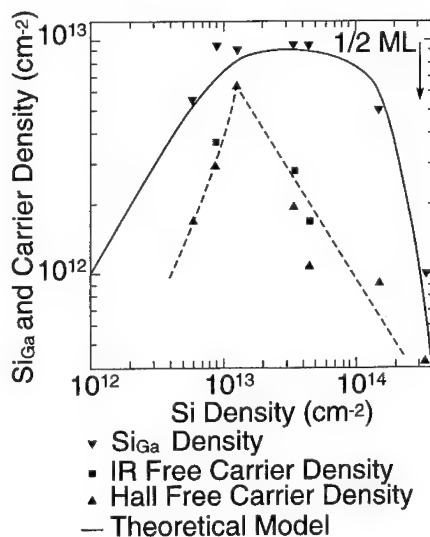


Figure 2.

Figure 1. IR spectrum from sample MV1347 (Table I) showing the Si_{Ga} LVM prior to subtraction of the two phonon and free carrier absorption.

Figure 2. Variation of the carrier concentration and $[\text{Si}_{\text{Ga}}]_{\text{A}}$ as a function of $[\text{Si}]_{\text{A}}$.

There are on-going attempts to explain the absence of IR absorption, and free carriers for $[\text{Si}]_{\text{A}} > 0.5$ ML and to determine the sites of the Si atoms after the surface layer is overgrown by GaAs. Recent Raman scattering measurements [17] have shown that for these large coverages a new spectral feature is present that is attributed to the vibrations of covalently bonded Si-Si aggregates. This feature had been observed in previous Raman studies [18] but measurements made on samples grown at $T(\text{g}) \geq 400^\circ\text{C}$ showed both this new feature and Si LVMs leading to some ambiguity of interpretation. This latter observation is in fact simply a result of Si surface segregation and / or diffusion out of the δ -layer, as discussed above. The new Raman measurements also showed that Si_{As} acceptors, $\text{Si}_{\text{Ga}}\text{-Si}_{\text{As}}$ donor-acceptor nearest neighbor pairs and a deep electron trap Si-X (speculated to be a planar $\text{As}_{\text{Ga}}\text{-Si}_{\text{As}}\text{-V}_{\text{Ga}}$ complex [19]) are present in addition to Si_{Ga} donors for $0.05 \text{ ML} \leq [\text{Si}]_{\text{A}} \leq 0.5 \text{ ML}$. Improved low noise IR LVM spectra, discussed below, are in agreement with these observations. There is an implication that either the as-deposited Si atoms do not occupy surface Ga-sites or that there is Si site switching during the overgrowth of the deposited layer, leading to the presence of Si-like inclusions. We shall also investigate a third possibility that (relatively) long-range Si diffusion occurs to produce 2-dimensional clusters by studying dilute (0.01 ML) Si δ -layer superlattices with interlayer spacings ranging from 200 to 1ML. In all the present investigations, the measured average volume carrier concentration never exceeded $\sim 2 \times 10^{19} \text{ cm}^{-3}$ as found for GaAs grown by other methods [19].

Before discussing the Si δ -layers we present the results of a parallel IR and Raman study of Al_{Ga} δ -layer superlattices that act as a reference system for the Si doped layers since all the Al atoms occupy Ga lattice sites [20]. These results demonstrate quite clearly the difference in the behavior of Al and Si impurities. There is a need (a) to explain why there is loss of IR absorption when $[\text{Si}]_{\text{A}} > 0.5 \text{ ML}$, (b) to find the lowest value of $[\text{Si}]_{\text{A}}$ when Si-Si pairs start to form, (c) to find the mechanism of formation of complexes such as Si-X and (d) to understand the structure of the 'Si-like δ -phase' observed for $[\text{Si}]_{\text{A}} \geq 0.5 \text{ ML}$.

EXPERIMENTAL DETAILS

Si δ -doped superlattices (Table I) were grown by MBE at 400°C , all with a nominal 500Å spacing but with different values of $[\text{Si}]_{\text{A}}$ per layer. After growth, the back surfaces of the semi-insulating GaAs substrates were polished to give wedge shaped samples. IR spectra were obtained over extended periods of ~ 20 h at a resolution of 0.25 cm^{-1} using a Bruker IFS120HR interferometer fitted with a liquid helium bolometer (Si detector) and with the superlattice samples held at $\sim 10 \text{ K}$. Spectra from semi-insulating (SI) GaAs reference samples were subtracted from the composite spectra to remove intrinsic two-phonon features. The free-carrier background was then also removed by subtracting a smooth curve (a polynomial of order three) to reveal the Si LVM spectrum more clearly. The concentrations of the various centers (Table I) were calculated using the calibration factor for which an integrated absorption coefficient (IA) $= 1 \text{ cm}^{-2}$ of the LVM corresponds to a concentration of $5 \times 10^{16} \text{ cm}^{-3}$ (see Ref. 3).

Raman spectra were obtained with samples at 77 K using a triple monochromator and a liquid nitrogen cooled Si charge-coupled detector (CCD) array. Spectra were obtained with the $x(y,z)\bar{x}$ geometry, where x, y and z refer to $[100]$, $[010]$ and $[001]$ directions. This technique also allowed us to study samples containing single δ -layers 50Å below the surface with values of $[\text{Si}]_{\text{A}}$ ranging from 0.01 ML to 2.0 ML. Spectra were obtained using 3.00 eV photons from a Kr^+ laser to produce resonantly enhanced scattering from Si donors (LVM at 384 cm^{-1}).

Table I. Details of δ superlattices with various values of $[\text{Si}]_A$

Sample	δ -plane spacing (\AA) (SIMS)	$[\text{Si}]_A$ (10^{12}cm^{-2}) (SIMS)	Si Concentration (10^{12}cm^{-2})					Hall (10^{12}cm^{-2})
			Si_{TOT}	Si_{Ga}	Si_{As}	$\text{Si}_{\text{Ga}}-\text{Si}_{\text{As}}$	$\text{Si}-\text{X}$	
SA10M54	460	5	13	13	--	--	--	3.9
SA2M12	485	6	5	5	--	--	--	1.7
SA10M55	490	14	25	21	--	--	4	5.0
SA2M09	420	14	9	9	--	--	--	6.5
MV1340	370	21	27	15	4	5	3	3.0
MV1342	385	35	26	12	4	3	7	2.0
SA10M57	475	67	29	14	5	3	7	3.0
MV1347	520	90	37	12	9	4	12	1.1
SA10M56	500	150	40	9	9	8	14	0.5
SA2M10	530	160	5	5	--	--	--	0.9
SA3M56	470	340	N.D.	--	--	--	--	0.4

Table II. Si δ superlattices with $[\text{Si}]_A = 0.01$ ML with various interplanar spacings.

Sample	δ -plane Spacing (ML)	No. of δ -planes	Intended $[\text{Si}]$ (10^{18}cm^{-3})	Mobility Hall (cm^2/Vs)	Carrier Concentration (10^{18}cm^{-3})		Si_{TOT} (10^{18}cm^{-3}) (Raman /IR)	Missing Si (10^{18}cm^{-3}) (Raman /IR)
					Raman	Hall		
SA7M26	1	500	212	--	*	--	66# 181☆	146# 31☆
SA7M27	2	400	106	250	*	6.3	46 93	60 13
SA7M28	5	400	39	489	20	13.5	20 20	19 19
SA7M29	10	200	21	767	15.4	14	15 16	6 5
SA7M35	20	200	12	894	10	9.3	11 8	1 4
SA7M33	50	200	4.2	1431	3.7	3.9	3.3 4.0	0.9 0.2
SA7M34	200	200	1.2	2707	--	0.86	-- 1.5	-- -0.3

* See text : # Raman data : ☆ IR data

IR, Raman and x-ray measurements were also made on Al δ -layer superlattices grown at 400°C on (100) Si GaAs substrates. The x-ray data were in excellent agreement with a previous IR calibration relating the integrated absorption coefficient (IA) of the Al_{Ga} LVM to the total concentration of [Al]_{Ga} present [20]. There was also agreement with measurements of [Al] from secondary ion mass spectrometry (SIMS).

In a second set of measurements on Si δ -layer superlattices the value of [Si]_A was set equal to 0.01 ML and the interplanar spacing was decreased from 200 ML to 1 ML (Table II). Hall effect and Shubnikov-de-Haas measurements showed that n increased initially but became very small for the layers with interplanar spacings of 2 and 1 ML. IR and Raman measurements now show that this loss of carriers is due to auto-compensation effects arising from the presence of Si_{As} and Si-X centers. Various other measurements including SIMS, x-rays and estimates of the carrier concentration n_{R2} , determined by Raman scattering from the frequency of the coupled phonon-plasmon ω_+ mode, were also made. In addition, a few samples were irradiated with 2 MeV electrons at 300 K to introduce deep electron traps at random sites in the crystal so that the free carrier absorption was lost. The Si_{Ga} IR LVM lost its Fano shape and appeared as a symmetrical absorption peak on a flat background.

INFRARED AND RAMAN STUDIES OF Al δ -LAYER SUPERLATTICES.

The Al δ -layer superlattices examined had intended areal concentrations [Al]_A = 0.1 ML (20 layers), 0.5 ML (20 layers) and 1.0 ML (100 layers) with interlayer spacings of 500 Å. High resolution x-ray diffraction showed that the actual values of [Al]_A were 0.25, 0.7 and 1.4 ML respectively [20]. There were more than 30 well-resolved satellites on each side of the 002 structure factor sensitive (chemical) x-ray reflection from the 1.4 ML sample and the spreading of the layer was confined to 6 Å according to modeling using dynamical theory. The layer with [Al]_A = 0.1 ML showed the IR LVM from isolated Al_{Ga} at 361 cm⁻¹ (10K) and there were small down-shifts to 358 cm⁻¹ for the other two layers as monolayer coverage was completed, corresponding to TO-like absorption from AlAs. It is important to note that the total integrated absorption coefficient (IA) continued to increase as [Al]_A increased (Fig. 3). Raman spectra also showed the Al_{Ga} LVM for the layer with the lowest value of [Al]_A but this feature lost intensity with the emergence of LO-like scattering from AlAs, as expected for the $x(y,z)\bar{x}$ geometry, for the layers with higher values of [Al]_A (Fig. 4).

These observations therefore provide a reference for the behavior of δ -layers as the impurity areal concentration increases from a sub-monolayer to complete monolayer coverage, provided the impurity atoms occupy only Ga-lattice sites. It was pointed out that the IR observations for the Al δ -planes were in sharp contrast to those for Si δ -layers reported in our earlier work where there was no detectable absorption, including that from Si_{Ga} donors (no other LVM lines were detected) when [Si]_A reached 0.5 ML [13]. As a consequence, it was inferred that Si_{Ga} atoms must have changed their lattice sites and / or their charge states as [Si]_A was increased [20]. An alternative possibility is that Si atoms were not located in surface Ga-sites immediately after deposition at this coverage.

RAMAN SCATTERING FROM Si: δ -LAYERS TO MONOLAYERS

Samples containing a single Si δ -layer 50 Å beneath the top surface were examined by

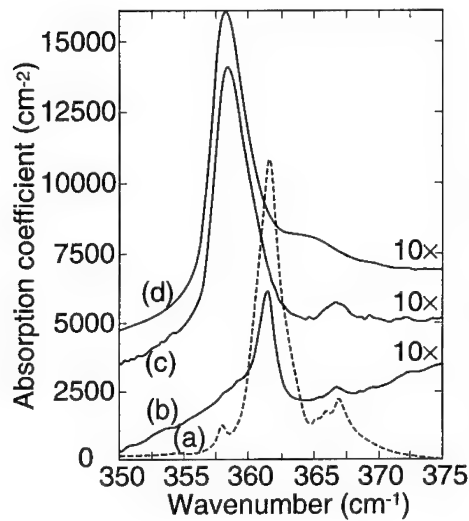


Figure 3.

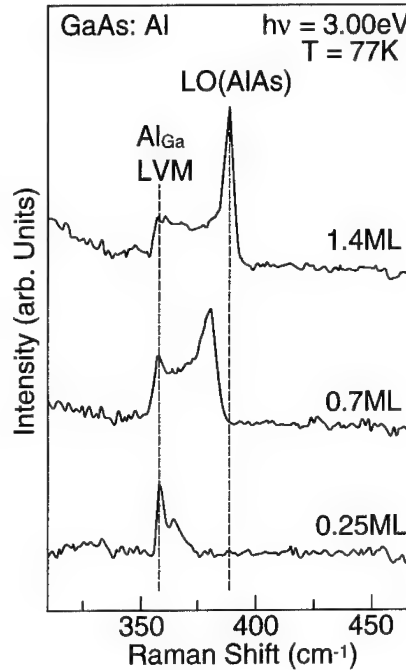


Figure 4.

Figure 3. IR Absorption spectra (b), (c) and (d) from samples with $[Al]_A = 0.25, 0.7$ and 1.4 ML. (a) is a reference spectrum from $Al_{0.02}Ga_{0.98}As$.

Figure 4. Raman scattering from Al δ -layers after subtraction of two phonon features.

Raman scattering as described previously for the Al δ -layers [17]. As $[Si]_A$ was increased, the LVM from Si_{Ga} donors increased, LVMs from $Si_{Ga}-Si_{As}$ appeared (Fig. 5) while Si_{As} and Si-X defects were also observed from some layers (not shown here). The strengths of all these lines reached plateau values and then decreased in strength as $[Si]_A$ was increased. No lines were detected for $[Si]_A = 0.5$ ML. The behavior of the Si_{Ga} donor line is the same as that reported in the earlier IR study (Fig. 2) but the observation of the other Si LVMs for layers with $[Si]_A$ as low as 0.1 ML, was unexpected since they were not detected previously. In addition, there was emergence of a new line close to 470 cm^{-1} for the layer with $[Si]_A = 0.5$ ML. This line increased in strength, sharpened and shifted to $\approx 490\text{ cm}^{-1}$ as $[Si]_A$ was increased to 2.0 ML (Fig. 5). A line close to this frequency has been observed previously [18,22] but a systematic study on passing from sub-monolayer δ -structures to layers with $[Si]_A > 1$ ML has not been reported.

These results can be understood provided the high frequency line [17] is assigned to a mode from covalently bonded Si-Si pairs since pairing of Si with As or Ga would not lead to a mode with such a high frequency. For comparison, IR LVMs from $Si_{Ga}-Si_{As}$ nearest neighbor pairs in GaAs give rise to an anti-symmetric mode involving a Si-Si stretch at 464 cm^{-1} but transverse modes, due primarily to stretching of Si-Ga and Si-As bonds occur at lower frequencies of 393 cm^{-1} and 367 cm^{-1} : a fourth symmetric stretching mode (so far undetected) is

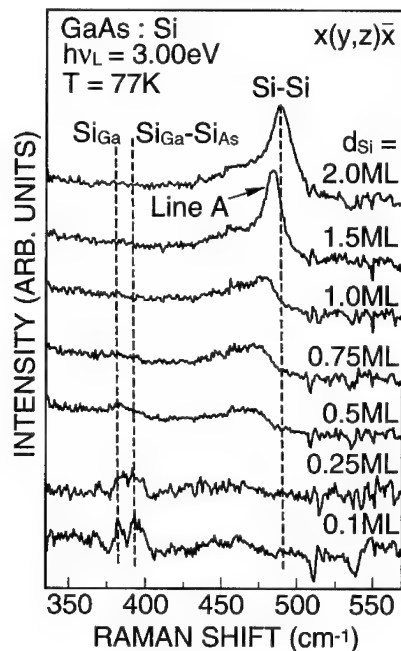


Figure 5.

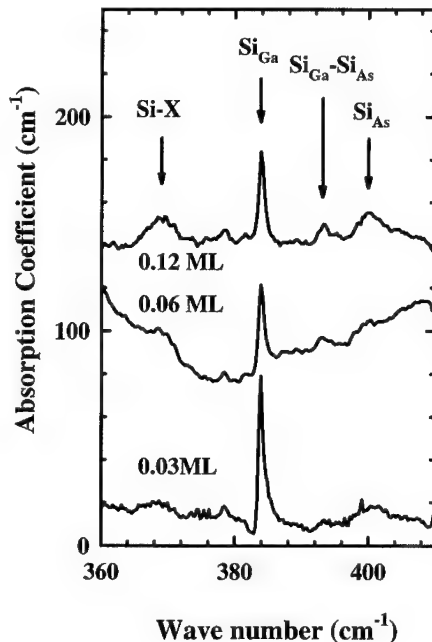


Figure 6.

Figure 5. Raman scattering from single δ -layers with various values of $[\text{Si}]_A$ after subtraction of two phonon features.

Figure 6. IR absorption from δ -superlattices (MV) with $[\text{Si}]_A = 0.03, 0.06$ and 0.12 ML after subtraction of two phonon and free carrier absorption.

expected at an even lower frequency near the Reststrahl absorption [19]. It is not understood why such lower frequency modes were not observed in the Raman spectra at high doping levels because a bilayer of Si with $[\text{Si}]_A = 0.5$ ML could not have covered more than 25% of the GaAs surface and so Si-Ga and Si-As bonds must be present. The scattering is the same as that expected from thin layers of (isolated) silicon, consistent with the absence of IR absorption since the dipole moment would then be small (zero). Small 2D-islands have been detected by high resolution transmission electron microscopy (direct lattice images) in similar samples [16] and the presence of these structures was inferred from tilts observed in x-ray reciprocal lattice maps. Unfortunately, neither of these techniques provides sufficient information to determine the chemical composition of the " δ -phase", but there is no reason to suppose that it is not simply bonded to the surrounding GaAs matrix.

An important point is that extrapolation of the strength of the Si-Si line shown in Fig. 5 from high values of $[\text{Si}]_A$ to below 0.5 ML, when the line broadens greatly, could imply the presence of covalently bonded Si-Si when $[\text{Si}]_{As}$ is as small as 0.05 ML, when lines from Si_{As} and Si-X appear. As the next step it was necessary to re-examine δ -superlattice structures by IR absorption to seek evidence for the presence of LVMs of these additional centers.

A RE-EXAMINATION OF IR SPECTRA OF Si δ -SUPERLATTICES

Low noise IR spectra, are shown in Fig. 6 after removal of the free carrier absorption. For $[\text{Si}]_A < 0.05 \text{ ML}$, only the LVM from Si_{Ga} donors is observed with a slight Fano profile due to interactions with the background electronic absorption. For thicker δ -layers, lines from Si_{As} , $\text{Si}_{\text{Ga}}\text{-Si}_{\text{As}}$ pairs and Si-X were clearly visible in agreement with the Raman spectra. However, once $[\text{Si}]_A$ reached 0.5 ML all the IR LVM and free carrier absorption was lost: no new lines were detected in spectra even for δ -layers up to 5 ML in thickness. This result is surprising because, as stated previously, Si-Ga and Si-As bonds would have been expected to be present and to give rise to IR active vibrational modes. Although the IR activity of Si-Si stretch modes could be small because of their symmetry, it should be remembered that isolated $\text{Si}_{\text{Ga}}\text{-Si}_{\text{As}}$ pairs with C_{3v} symmetry are fully active [19]. It has to be concluded that the Si-Si feature observed by Raman scattering is due to clusters of Si-Si paired atoms [23]. In that case, it is necessary to discover whether the clustering occurs during deposition of the Si atoms or is a result of long-range diffusion of the atoms to form a precipitated phase during the overgrowth of the layer by GaAs.

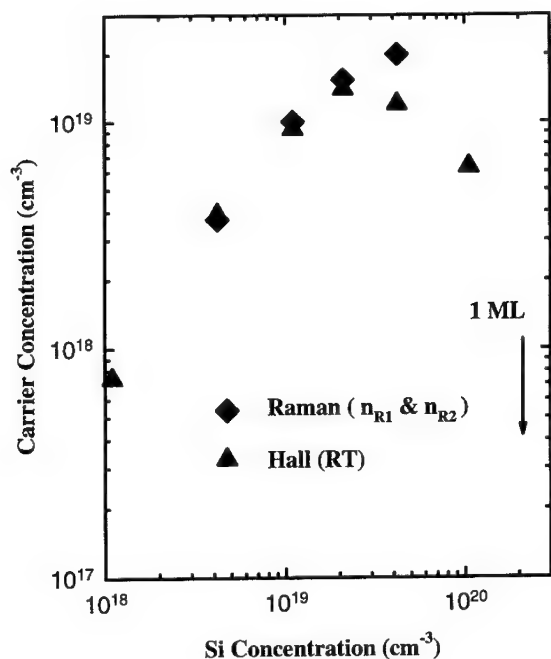


Figure 7.

Figure 7. Average volume carrier concentrations n_R and n_H for the samples listed in Table II.

IR ABSORPTION FROM DILUTE δ -LAYER STACKS.

Details of samples all containing δ -layers with $[\text{Si}]_A = 0.01 \text{ ML}$ but with various interplanar spacings are given in Table II. Previous Shubnikov-de-Haas measurements [21] showed that electrons were present in minibands for the 200 and 50 ML samples but since the behavior was essentially three dimensional for the other samples with more closely spaced layers we specify the carrier concentration per unit volume. Values of n_H (Hall) and n_{R1} and n_{R2} (Raman, see below) followed the intended doping level (Fig. 7) except for the samples with 1 ML and 2 ML δ -spacings, where carriers were lost. This unexplained result was reported previously but is now easily understood by reference to Figs. 8 and 9. After subtraction of the sloping backgrounds due to free carrier absorption from the IR spectra (Fig. 8), only the LVM

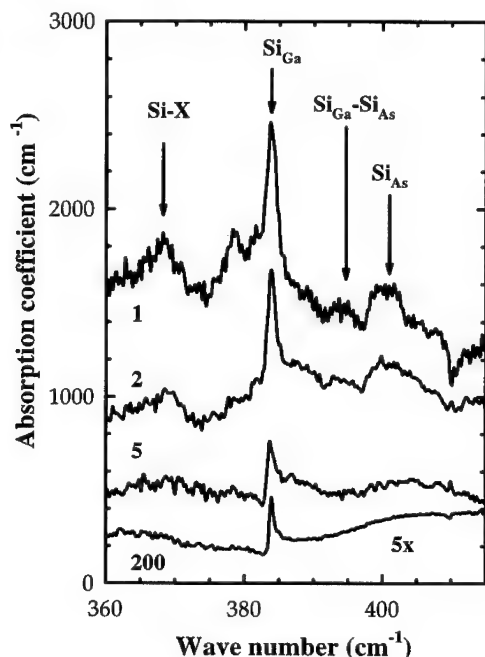


Figure 8.

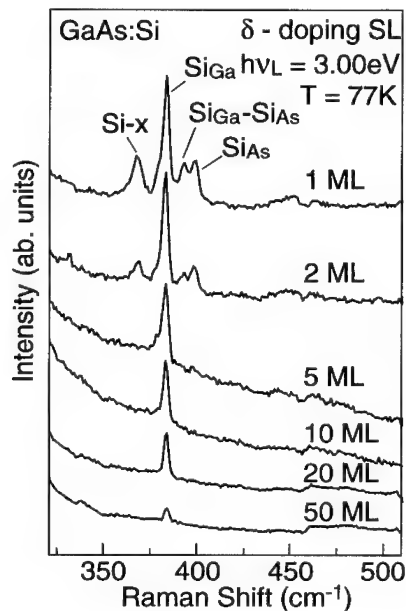


Figure 9.

Figure 8. IR spectra after removal of 2 phonon features and free carrier absorption for δ -layer stacks ($[\text{Si}]_A = 0.01 \text{ ML}$) with spacings of 200, 5, 2 and 1 ML.

Figure 9. Raman scattering for the same set of samples for interplanar spacings from 50 ML to 1 ML, after subtraction of 2 phonon features.

line from Si_{Ga} was present, except in the spectra for the 1 and 2 ML samples that also show LVMs from Si_{As} acceptors, $\text{Si}_{\text{Ga}}\text{-Si}_{\text{As}}$ pairs and Si-X . Estimates of the concentrations of these centers using reported calibrations indicate that complete compensation had occurred as a result of the Si incorporation in the additional sites for the 1 ML sample. The onset of this process occurred when the carrier concentration reached $\sim 1.3 \times 10^{19} \text{ cm}^{-3}$ (n_H). A value of n could not be measured by SdH measurements because of the small carrier mobility.

RAMAN SCATTERING FROM DILUTE δ -LAYER STACKS

The same set of samples was also examined by Raman scattering. After subtraction of two phonon features we obtained spectra (Fig. 9) that are clearly in close agreement with the IR measurements. The relative sizes of the LVM lines are slightly different for the two measurement techniques because of differences in the relative polarizabilities and IR absorption coefficients. Applying the Raman calibration for the LVM from Si_{Ga} [3,24] to all the LVM lines and assuming that the net donor concentration is equal to $([\text{Si}_{\text{Ga}}] - [\text{Si}_{\text{As}}] - [\text{Si-X}])$ led

to carrier concentrations, designated n_{R1} (Raman). Independent measurements of the coupled phonon-plasmon ω_c mode led to values of n_{R2} , using previously established calibrations [7]. These two quantities were in agreement for all samples (Fig. 7). In particular, it was found that $n_{R2 (MAX)} = 2 \times 10^{19} \text{ cm}^{-3}$ for the 5 ML sample but the carrier concentration was negligible for the 1 ML samples.

An important Raman result was that the LVM line due to covalently bonded Si-Si pairs was not detected in these samples, implying that the mechanism leading to the formation of pairs and larger 2D clusters is not long-range diffusion. It follows that pairing only occurs when $[\text{Si}]_A$ is high so that the atoms are in close proximity. These results do not however give information about whether local atomic jumps of Si_{Ga} and / or $\text{Si}_{\text{Ga}}\text{-Si}_{\text{Ga}}$ pairs take place when the δ -layer is overgrown with GaAs.

DISCUSSION

The present results have provided answers to some of the questions that have been posed. It is now clear from both IR and Raman measurements (Figs. 5 and 6) that silicon atoms are present as Si_{As} acceptors, $\text{Si}_{\text{Ga}}\text{-Si}_{\text{As}}$ donor acceptor pairs and Si-X defects once $[\text{Si}]_A$ exceeds about 0.1 ML ($3.4 \times 10^{13} \text{ atom cm}^{-2}$) and our earlier IR data [13] (Figs. 1 and 2) are superseded. When $[\text{Si}]_A$ exceeds ~ 0.5 ML there is the emergence of a Raman line attributed to the stretch modes of Si-Si covalent bonds. Extrapolation of the strength of this feature, that broadens as $[\text{Si}]_A$ is reduced, leads to the conclusion that such bonds could be present for $[\text{Si}]_A$ as low as 0.05 ML. It is implied that either the deposited Si atoms do not occupy only surface Ga-sites, or that Si diffusion jumps occur during overgrowth of the δ -layer. The latter process would explain the difference in the behavior of Si_{Ga} compared with Al_{Ga} impurities (Figs. 3 and 4). The possibility of long-range Si diffusion appears to be ruled out by the measurements made on the superlattice structures with $[\text{Si}]_A = 0.01$ ML as the layer spacing is reduced (Figs. 8 & 9), since line A (Si-Si) (Fig. 5) is not produced. It is possible, however, that some Si_{Ga} surface atoms undergo local diffusion jumps during the growth of the complete structure. Thus, a proposed interpretation made in a scanning tunneling microscopy study [25] that Si atoms occupy only Ga surface sites during deposition cannot be ruled out by the present observations.

When $[\text{Si}]_{\text{Ga}}$ is increased the Fermi level eventually rises to a position close to the DX level at $(E_c + 200 \text{ meV})$ [4]. According to theory [26], there are spontaneous displacements of the atoms towards interstitial sites at low temperatures when samples are subjected to a hydrostatic pressure $P > P_{\text{CRIT}}$ (Figs. 10a and 10b) and the Si atom becomes negatively charged. We therefore envisaged a structure for a "concentrated" δ -layer consisting of a raft of $\text{Si}_{\text{Ga}}^+ \text{-Si}_{\text{DX}}^-$ pairs arranged alternately [13,19]. Local density functional theory indicates that the displacement of a Si_{DX} atom is greater when it has a Si_{Ga}^+ neighbor (Fig. 10 c), than that for an isolated Si_{DX}^- defect. It is speculated that such displacements, occurring at the growth temperature (400°C), could lead to diffusion jumps of the Si atom. Diffusion jumps have been demonstrated for example for the conversion of $\text{Si}_{\text{Ga}}\text{-V}_{\text{Ga}}$ pairs to Si-X defects during annealing at only 350°C after MBE growth at 250°C [8]. Thus pairs of Si atoms in an original Si_{Ga} sheet could convert to $\text{Si}_{\text{Ga}}\text{-Si}_{\text{As}}\text{-As}_{\text{Ga}}$, $\text{Si}_{\text{Ga}}\text{-As}_{\text{As}}\text{-V}_{\text{Ga}}$ complexes or related defects, so that compensation is complete. Similar diffusion jumps of isolated Si_{Ga} atoms could lead to the formation of V_{Ga} . Migration and capture of the V_{Ga} by a second Si_{Ga} atom could then generate

Si-X and possibly other defects leading to electrical compensation, as in homogeneously doped GaAs.

It is still unclear however, why the Si-like δ -sheet does not show conductivity, even when continuous layers are present for $[\text{Si}]_A > 1$ ML. A possibility not so far considered is that there is a large density of interface states, as postulated for arsenic precipitates present in annealed low temperature MBE GaAs [27]. Evidence in support of a 'Si-like δ -phase' has also been provided by SIMS measurements of annealed (600°C) δ -layer superlattices (grown at 400°C) that have shown a local δ -layer concentration of $[\text{Si}] \approx 10^{21} \text{ cm}^{-3}$ (with $[\text{Si}]_A = 0.5$ ML) acting as a stable diffusion source of Si to the surrounding matrix with $[\text{Si}] \approx 2 \times 10^{19} \text{ cm}^{-3}$ [16]. In retrospect, it is clear that SIMS measurements showed the same behavior for δ -layers with $[\text{Si}]_A$ as low as 0.02 ML [28]. Capacitance voltage profiles described in this same study also indicated that the ' δ -phase' had a low conductivity.

It is of interest to note an IR feature at 376 cm^{-1} in Fig. 9 that is not usually observed, even in highly Si doped material: this feature was not observed in the corresponding Raman spectrum (Fig. 8) when the sample was illuminated with laser radiation. (The dip at 410 cm^{-1} is known to be due to a sharp 2-phonon feature that is not completely removed by the subtraction of the substrate spectrum). Previously, Wolk et al [29] measured LVM spectra of GaAs:Si at high hydrostatic pressures (5.0 K) and found a new line that they attributed to the Si DX-configuration. Their extrapolation of the frequency to zero pressure yielded a value of $376 \pm 1.5 \text{ cm}^{-1}$. It would be tempting to assign our 376 cm^{-1} feature to the DX state but further measurements on homogeneously doped samples have not reproduced the feature.

This work has clarified various issues but further studies are required to test our various speculations. Finally, it is important to recognize that the interpretation of SIMS data (Table I) is not straightforward for highly doped Si delta layers if a primary oxygen beam is used [30].

ACKNOWLEDGMENTS

The UK authors acknowledge discussions with Dr. R. Jones of Exeter University and the financial support of Engineering and Physical Sciences Research Council (EPSRC), UK.

REFERENCES

- [1] K. Köhler, P. Ganser and M. Maier, *J. Cryst. Growth* **127**, 720 (1993).
- [2] J. Maguire, R. Murray, R. C. Newman, R. B. Beall and J. J. Harris, *Appl. Phys. Lett.* **50**, 516 (1987).

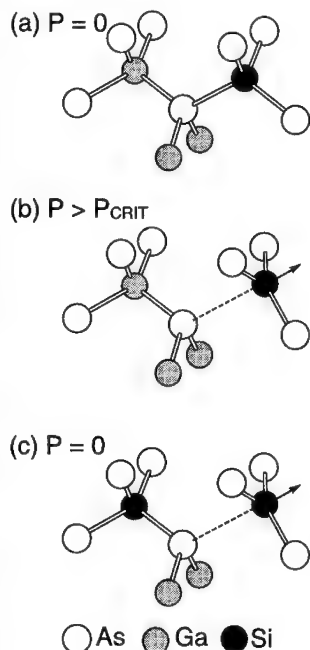


Figure 10
Figure 10. DX-displacements for Si_{Ga} and $\text{Si}_{\text{Ga}}\text{-Si}_{\text{Ga}}$ pairs.

- [3] R. Murray, R. C. Newman, M. J. L. Sangster, R. B. Beall, J. J. Harris, P. J. Wright, J. Wagner and M. Ramsteiner, *J. Appl. Phys.* **66**, 2589 (1989).
- [4] D. K. Maude, J.C.Portal, R.Murray, T.J.Foster, L.Dmowski, L.Eaves, R.C.Newman, P.Basmaji, P.Gibart, J.J.Harris and R.B.Beall, in *Physics of DX-centers in GaAs alloys (Solid State Phenomena 10)* ed. J. C. Bourgoin (Liechtenstein Sci.-Tech) p121.
- [5] M. Ogawa and T. Baba, *Jpn. J. Appl. Phys.* **24**, L572 (1985).
- [6] F. Briones, L. Gonzalez and A. Ruiz, *Appl. Phys.* **A49**, 729 (1989).
- [7] M. Ramsteiner, J. Wagner, P. Hiesinger, K. Köhler and U. Rössler, *J. Appl. Phys.* **73**, 5023 (1993).
- [8] S. M. McQuaid, R. C. Newman, M. Missous and S. O'Hagan, *Appl. Phys. Lett.*, **61**, 3008 (1992); *J. Cryst. Growth* **127**, 515 (1993).
- [9] K. Ploog, M. Hauser and A. Fischer, *Appl. Phys.* **A45**, 233 (1988).
- [10] E. F. Schubert, *J. Vac. Sci. Technol.*, **8**, 2980 (1990).
- [11] J. J. Harris, *J. Mat.Sci : Materials in Electronics*, **4**, 93 (1993).
- [12] A. Zrenner and F. Koch, in *Properties of Impurity States in Superlattice Semiconductors*, ed. C. Y. Fong, I. P. Batra and S. Ciraci, NATO ASI Series B (1988) Plenum NY) p1.
- [13] M. J. Ashwin, M. R. Fahy, J. J. Harris, R. C. Newman, D. A. Sansom, R. Addinall, D. S. McPhail and V. K. M. Sharma, *J. Appl. Phys.* **73**, 633 (1993).
- [14] J. B. Clegg and R. B. Beall, *Suf. Int. Anal.* **14**, 307 (1989).
- [15] L. Hart, M. R. Fahy, R. C. Newman and P. F. Fewster *Appl. Phys. Lett.* **18**, 2218 (1993).
- [16] L. Hart, M. J. Ashwin, P. F. Fewster, X. Zhang, M. R. Fahy and R. C. Newman, *Semicond. Sci. Technol* **10**, 32 (1994).
- [17] J. Wagner, R. C. Newman and C. Roberts, unpublished work (1995).
- [18] O. Brandt, G. E. Crook, K. Ploog, J. Wagner and M. Maier, *Appl. Phys. Lett.* **59**, 2730 (1991).
- [19] R. C. Newman, *Semicond. Sci. Technol.* **9**, 1749 (1994).
- [20] M. J. Ashwin, M. R. Fahy, L. Hart, R. C. Newman and J. Wagner, *J. Appl. Phys.* **76**, 7627 (1994).
- [21] A. J. Dewdney, S. Holmes, H. Yu, M. R. Fahy and R. Murray, *Superlattices and Microstructures* **14**, 205 (1993).
- [22] H.Tanino, H.Kawanami, H.Matsuhata, *Appl. Phys. Lett.* **60**, 1978 (1992).
- [23] R. Jones and S. Öberg, unpublished work (1995).
- [24] J. Wagner, *Mater. Sci. Forum* **65-66**, 1 (1990).
- [25] A.R.Avery, D.H. Holmes, J.L.Sudijono, T.S.Jones, M.R.Fahy and B.A.Joyce, *J.Cryst. Growth, Proc. MBE VIII*, in press (1995).
- [26] D.J.Chadi and K.J.Chang, *Phys. Rev. Lett.* **61**, 873 (1988).
- [27] A.C.Warren, J.M.Woodhall, P.Kirchner, X.Yiu, F.Pollak, M.R.Melloch, N.Otsuka and K.Mahalingam, *Phys. Rev.* **B46**, 4617 (1992).
- [28] R. B. Beall, J. B. Clegg, J. Castagné, J. J. Harris, R. Murray and R. C. Newman, *Semicond. Sci. Technol.* **4**, 1171 (1989).
- [29] J.A.Wolk, M.B.Kruger, J.N.Heyman, W.Walukiewicz, R.Jeanloz and E.E.Haller, *Phys. Rev. Lett.* **66**, 774 (1991).
- [30] V.K.M.Sharma, D.S.McPhail and M.R.Fahy, *Surface and Interface Analysis*, in press (1995).

APPLICATIONS OF SCANNING DEFECT MAPPING SYSTEM FOR SEMICONDUCTOR CHARACTERIZATION

KEVIN F. CARR*, N. CARLSON*, P. WEITZMAN*, B.L. SOPORI**, C. MARSHALL**,
AND L. ALLEN**

*Labsphere, Inc., Shaker Street, No. Sutton, NH 03260

**National Renewable Energy Laboratory, 1617 Cole Boulevard, Golden, CO 80401

ABSTRACT

A laser scanning system has been developed by the National Renewable Energy Laboratory for the rapid characterization of crystal defects in single- and poly-crystalline semiconductors. The scanning defect mapping system has been commercialized by Labsphere, Inc. as the PVScan 5000. In the unprocessed material, the system produces digital color maps of the spatial distributions of dislocations and grain boundaries simultaneously. After device fabrication, the PVScan 5000 is used to produce photoresponsivity maps of the light beam induced current (LBIC) on a photovoltaic device such as a solar cell or a photodetector. An additional feature is that it also measures the spatial distributions of optical reflectance, both specular and diffuse, which can be applied to the LBIC maps to determine the internal responsivity of the device. The internal responsivity is proportional to the minority carrier diffusion length of silicon devices. It may be possible, therefore, to determine the diffusion length for certain devices.

SIGNIFICANCE

The need for high speed techniques to characterize material and cell quality is driven by the increasing commercialization of PV energy. The fact that 70% of PV energy systems utilize low-cost single- and poly- crystalline silicon solar cells intensifies this need. Predicting the performance of low-cost materials requires analyzing the degree of spatial non-uniformities and identifying the sources of the non-uniformities. Localized regions of defects can be more detrimental to device performance than a uniform distribution.

Quality Assurance Purposes

In commercial PV silicon, the material non-uniformities are attributed to crystal defects, impurity segregation, and residual stress. These non-uniformities can be altered from the cell fabrication processes and new non-uniformities can be introduced as well. Fabrication induced non-uniformities can arise due to reflectance variations in surface texture and the application of anti-reflection coatings as well as spatial variation in the junction characteristics. It is imperative that an instrument capable of spatial analysis be used to determine device non-uniformities in order for the fabrication processes to be monitored and improved.

OPERATING PRINCIPLES

Defect Identification

Dislocations and grain boundaries in crystalline silicon can be simultaneously identified. The wafer sample must first undergo a treatment known as the "Sopori etch" to delineate the defects. The etch consists of $\text{HF}:\text{CH}_3\text{COOH}:\text{HNO}_3$ in the ratio 36:15:2. The etched defects will scatter incident laser light. Polishing prior to etching will reduce the scattering due to the surface roughness profile of non-defective areas.

The spatial distribution of the light scatter is different for dislocations than it is for grain boundaries.^{1,2} The amount and type of scatter will, therefore, identify the defects. Dislocations from circular etch pits will scatter light diffusely. As long as the etch pit diameter is known, the amount of diffuse scatter is proportional to the number of dislocations. In this way, a statistical count of the dislocation density can be performed. Etch pit diameter is controlled by careful monitoring of the etching process. Grain boundaries tend to form long grooves after etching. Light scatter from grain boundaries tends to be confined to a narrow 20° cone angle.

LBIC Measurement

The incident beam used to measure defect scatter from etched wafers can also be used to map the photocurrent responsivity of finished solar cells. Electrodes are attached to the cell contacts and the current measured with a picoammeter as the sample is scanned under the incident light beam. Directly measured LBIC is a function of the surface and bulk recombination and the surface reflectance loss.

Internal or bulk LBIC can be determined by isolating the reflectance effect. The reflectance, specular and diffuse, is easily measured by the same detectors used to differentiate dislocation and grain boundary scatter from etched wafers. The internal LBIC measured for incident radiation of a wavelength close to the bandgap of silicon is proportional to the minority carrier diffusion length. The diffusion length may be measured for multiple solar cell samples of similar collection efficiencies by calibrating with one cell whose diffusion length has been independently determined by a companion technique.

PVScan 5000

The PVScan 5000 is the first commercial instrument developed specifically for complete analysis of photovoltaic performance. It is capable of defect mapping of etched silicon wafers and LBIC mapping of finished solar cells.

Optical System

The optical system of the PVScan 5000 is illustrated in Figure 1.

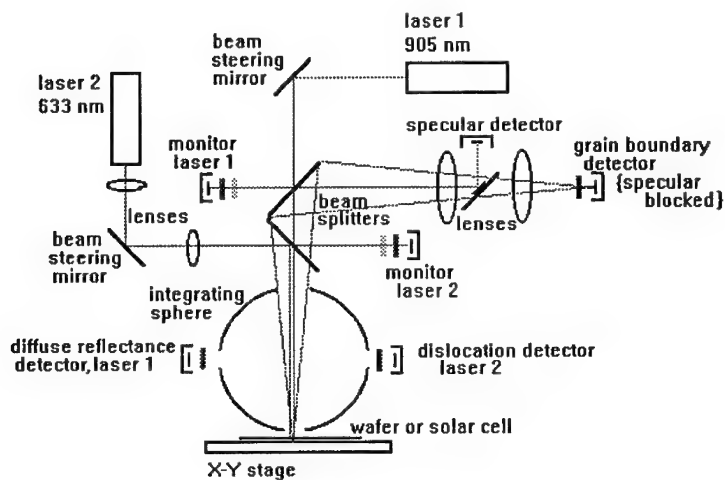


Figure 1 - Optical system of the PVScan 5000.

The light sources used are lasers to provide well collimated, intense incident beams. The lasers are unpolarized and are focused to 0.5 mm diameter spots incident on the sample surface. Two lasers are used. A helium-neon laser provides 633 nm radiation and is used primarily for defect mapping. The visible wavelength scatter resolves the etched defects. The second laser is a semiconductor diode type emitting radiation at a wavelength of 905 nm. This laser is used primarily for LBIC mapping since the longer wavelength will penetrate further into silicon devices. A Nd:YAG laser was considered since its wavelength of 1064 nm is closer to the bandgap of silicon, but the diode laser offered a more compact, robust and economical engineering solution. Either laser is selectable for any measurement procedure.

The collection optics of the PVScan 5000 are unique. An integrating sphere manufactured from Labsphere's proprietary Spectralon® material is used to collect the wide angle scatter from the dislocation etch pits as well as the diffuse reflectance used to determine the internal LBIC of solar cells. The integrating sphere includes two photodetectors, each filtered to respond to only one laser. A lens is used to collect the conical distribution of grain boundary scatter which exits the integrating sphere from the beam entrance aperture. The specular reflection is blocked from the grain boundary detector by a central aperture/mirror. The specular reflection is diverted to its own dedicated photodetector. Dichroic beamsplitters differentiate the laser wavelengths and optimize the reflectance or transmittance for each as required over the common optical path. Each laser beam is monitored for power fluctuations by individual detectors near the beamsplitters. Beam steering mirrors serve as alignment tools.

Instrument Features

The PVScan 5000 is a table-top instrument which requires only 2 feet by 2 feet of bench space. Samples are scanned under the laser beam with a precision, motorized X-Y stage. The photodetector signals are digitized and stored with the X-Y position signal for the stage. Samples are held to the stage by a vacuum pump within the instrument. The instrument is operated from an IBM compatible personal computer. MS-Windows[™] based software simplifies instrument operation and produces false color image maps of the collected data. The scans can be displayed on screen during data acquisition or stored and recalled for later analysis. The image color schemes can be altered by the system operator to optimize data resolution.

RESULTS

Figure 2 features the defect maps of a polycrystalline silicon wafer. The dislocation densities (at left) corresponding to the various gray scales are identified. A calibration sample is used to establish the scale. A qualitative analysis of the dislocation distribution is indicative of areas of high thermal stress during the crystal growing process. A strong variation in the dislocation distribution is expected to degrade cell performance due to the heavily dislocated regions acting as "sinks" or shunts for the rest of the device. The upper right image depicts a grain boundary map of the same sample. In comparing the images, it is evident that the two types of defects are clearly differentiated. A photograph of the etched sample is also included.

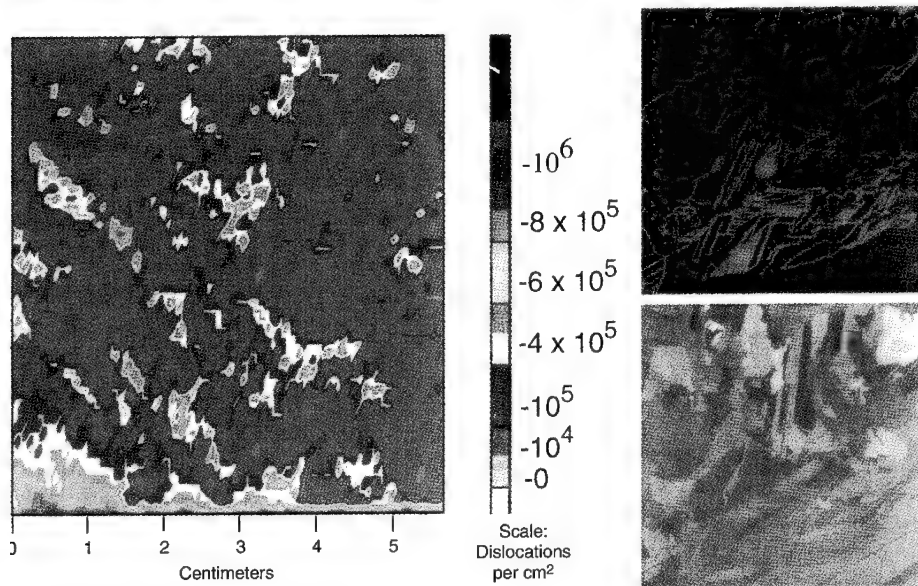


Figure 2 - A dislocation map and a grain boundary map of a polycrystalline silicon wafer

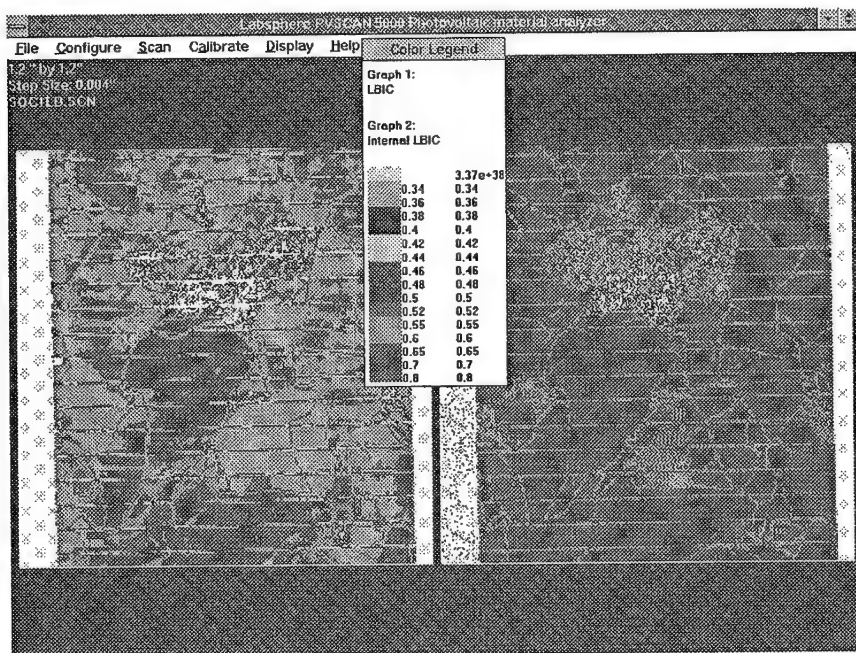


Figure 3 - LBIC maps of a PV silicon solar cell

Figure 3 depicts the results of an LBIC scan on a commercial silicon solar cell. The 905 nm diode laser was used to map a 1.2 inch by 1.2 inch area of the cell. The map on the left is the complete LBIC scan. The map reveals a clustered area of very low responsivity in the upper central portion of the scan area. This probably indicates a region of high dislocation density which could be confirmed by defect mapping an etched wafer prepared from the same ingot as this cell. The map on the right is the internal LBIC result after correcting by a subsequent reflectance scan on the same surface area. Note that the internal LBIC is more uniform following the reflectance loss correction. This may reveal non-uniformities incurred in the cell fabrication from application of the anti-reflection coating or other surface preparation process.

CONCLUSIONS

A laser scanning instrument, the PVScan 5000, is available for the complete characterization of photovoltaic semiconductor material. Digital maps of crystal defects, LBIC, and reflectance can be compared to fully optimize all phases of the manufacturing process. The instrument will prove invaluable to the manufacturing of low-cost solar cells.

REFERENCES

- ¹ B.L. Sopori, *Applied Optics* **27** (22), 4676-4683 (1988).
- ² B.L. Sopori, *J. Electrochem. Soc.* **135** (10), 2601-2606 (1988).

CHARACTERIZATION OF FAST DIFFUSING CHARGED DEFECTS IN SEMICONDUCTORS

T. HEISER*, A. ZAMOUCHE** AND A. MESLI*

*Laboratoire PHASE, UPR 292 du CNRS, BP20, 67037 Strasbourg Cedex 2, France

**Unité de Recherche Physique des Matériaux et Applications, Université de Constantine, route d'Aïn El Bey 25000, Constantine, Algérie

ABSTRACT

A novel technique is introduced to study fast diffusing charged defects in semiconductors. It is based on the capacitance change induced by ion drift in a reverse biased Schottky barrier. It is shown that such charge movement yields exponential capacitance transients, which contain information about the defect concentration and mobility. The method is checked on Li-diffused samples, where the extracted diffusion coefficient are in good agreement with literature data. It is next applied to interstitial copper (Cu_i) in silicon. In the proposed experiment Cu_i gives rise to a well defined signal which enables us to investigate near room temperature defect reactions involving Cu_i . The diffusion data extracted from copper diffused and quenched silicon samples establishes the origin of the signal. Near room temperature precipitation kinetics of Cu_i are studied and energy barriers are extracted.

INTRODUCTION

Fast diffusing charged defects play an important role in semiconductor physics for several reasons. Their high mobility together with their charged state are responsible for numerous diffusion limited defect reactions, like neutral acceptor-donor pair formation, occurring at relatively low temperatures. As a consequence, the host semiconductor electrical properties may be unstable and affect electronic device operations. Some of the 3d transition metals ($\text{Cu}, \text{Ni}, \text{Co}$) are the most famous examples. Unintentional contamination of silicon wafers by these impurities led to the request of efficient gettering techniques. Irradiation induced defects as well as hydrogen in silicon further illustrate the puzzling behaviour these fast diffusing species might display.^{1,2} Recently, chemomechanical polishing, using copper contaminated alkaline slurries, was found to introduce fast diffusing defects responsible for a resistivity increase across the whole wafer.^{3,4}

In this work we introduce a method to detect low concentrations of fast diffusing charged defects near room temperature and apply the technique to several defects which may not be observed by standard defect analyses, like for instance deep level transient spectroscopy (DLTS). In the first part we describe the principle of the technique and the model used to extract values of defect concentration and effective diffusion coefficient.

Next, lithium in silicon, whose properties are well known, is investigated and the results are compared to literature data.

Copper diffused samples are then investigated leading to values of its intrinsic diffusion coefficient. Copper-dopant interaction are studied as a function of dopant nature. Precipitation kinetics of copper are measured and the corresponding energy barrier is extracted.

Preliminary results in Ni diffused samples are also discussed.

EXPERIMENTAL METHOD

Electrical capacitance of pn junctions or Schottky diodes is often measured to study relaxation phenomena in low resistive semiconductors. Most frequently, capacitance transients are due to electrical carrier emission, following either electrical or optical excitation, and are used to detect extremely low concentrations of defects in semiconductors. A prerequisite for such analyses is the introduction by the defect of a deep level into the semiconductor energy band gap.

The capacitance change ΔC is proportional to $\int_0^W \rho(z, t) dz$, where $\rho(z, t)$ is the excess charge

distribution in the space charge region and W the space charge width.⁵

Deep level carrier emission generally leads to a time dependent charge distribution of the form $\rho(z, t) = g(z)f(t)$, where $f(t)$ corresponds to an exponential function. Analyses of the corresponding capacitance transients as a function of temperature is the core of the DLTS method.

Capacitance change may however also be induced by a spatial redistribution of the space charge. Indeed, if charged mobile defects are present in the host material, the electric field in the space charge region may induce defect drift, changing the charge distribution and hence leading to a capacitance transient. In that case, no deep level associated to the defect is needed. Such electric field enhanced migration is well known in silicon oxides and was shown to be responsible for MOS structure instabilities.⁶ Recently, capacitance transients due to hydrogen migration was investigated by Johnson et al^{2,7} and led to interesting information on hydrogen properties.

If the applied voltage is changed periodically, the ions will undergo, under certain conditions which are detailed below, a periodical drift. The corresponding capacitance signals can then easily be detected with a high signal to noise ratio. This method, labeled Transient Ion Drift (TID), was successfully used to measure the Cu diffusion coefficient in silicon at moderate temperatures.⁸

The necessary conditions to observe periodical ion drift are: uniform ion distribution, in the absence of electric field, over a distance large compared to W ; same charge as majority carriers; and sufficiently high mobility at temperatures where the device is still operational (depends on the semiconductor used). After each drift period, the initial flat distribution is reached again by thermal diffusion.

The resulting transient signals contain information about the defect concentration and effective mobility. These parameters may be estimated, if the analytical form of the signals is known. The experimental process, as well as the model we used to yield quantitative results, are detailed in reference [8]. The following simplifying assumptions were made:

- during the ion accumulation period, the thermal diffusion is negligible against drift,
- the defect density is much lower than the doping level (N_{dop}), leaving the electric field unaffected by the charge redistribution,
- the electric field decreases linearly with depth (uniform N_{dop}),
- no ions are lost due to outdiffusion or irreversible precipitation.

These assumptions are easily achieved in the experiments described below. It was shown in reference [8], that the resulting capacitance signal during the drift period has an exponential shape, with a time constant given by:

$$\tau = \frac{kT \epsilon}{q^2 D N_{dop}} \quad (1),$$

where ϵ is the semiconductor permittivity, k the Boltzmann constant, T the absolute temperature, q the ion charge and D the effective ion diffusivity. This rather astonishing result enables us to measure the temperature dependence of D and estimate the diffusion energy barrier in a similar manner than deep level energies are deduced from DLTS measurements. The signal amplitude is proportional to the initially uniform defect concentration over the depth which is scanned when the reverse bias is increased.

A characteristic feature of the TID signals is the ratio τ/t_d , where t_d is the time necessary to reestablish a uniform ion distribution. Experimentally, t_d corresponds to the minimum pulse width beyond which the TID signal amplitude saturates. It is equivalent to the trap filling time t_f in DLTS measurements. Due to the slow diffusion process compared to the drift, τ/t_d is much greater than unity, while the ratio t_e/t_f , where t_e is the carrier emission time, is generally lower than unity. Moreover, the bias dependence of τ/t_d is characteristic of the ion drift process.^{8,9} Hence, TID

signals, although similar to DLTS signals, may easily be distinguished from the latter, if the behaviour of the ratio τ/t_d is considered.

TID might be used either to study the diffusion properties of fast diffusing charged defects in semiconductors, or to detect their presence in the lattice. In the latter case, the comparison of estimated D values with established diffusion data can be used to determine the chemical nature of the defect. Both approaches will be illustrated below by the results obtained on Li and Cu diffused silicon samples. A further important point of the technique is the temperature range ($T < 480\text{K}$ for Si), within which the measurements can be performed. For these temperatures, charged mobile defects are often submitted to long range interactions leading to a reduced effective diffusivity. TID measurements with carefully chosen experimental conditions, might be used as a tool to investigate these interactions.

LITHIUM DOPED SILICON

Lithium has been intensively studied for nearly forty years, as it was used to compensate the acceptor dopants and to yield highly resistive materials for nuclear detectors. Its diffusion coefficient is well known, and its interaction with dopants and interstitial oxygen was investigated by Pell et al [10,11]. It is positively charged and highly mobile near room temperature. It is thus particularly well adapted to test the TID method.

We used boron doped epitaxial layers in order to avoid Li-O interactions. The dopant concentration ($N_{\text{dop}} = 6 \times 10^{14} \text{cm}^{-3}$) is too low to reduce significantly the Li diffusivity. High purity lithium was scratched on the wafer back side and annealed at 1030K for 5 hours. Schottky diode preparation are described elsewhere.⁸

The capacitance signals followed an exponential decrease down to less than 10 percent of the initial capacitance change. The residual linear capacitance decrease is probably due to the thermal diffusion of Li into the neutral region at the end of the accumulation period.

The results are shown on Fig.1, in comparison with literature data. The temperature dependence of the time constant followed an Arrhenius behaviour. The good agreement between both data indicates that values extracted from the TID signals, using expression (1), correspond to the intrinsic Li diffusion.

The same measurement on Li diffused Czochralski grown silicon are also reported on Fig.1. Significantly lower values are observed which reveal the presence of Li-O interactions.

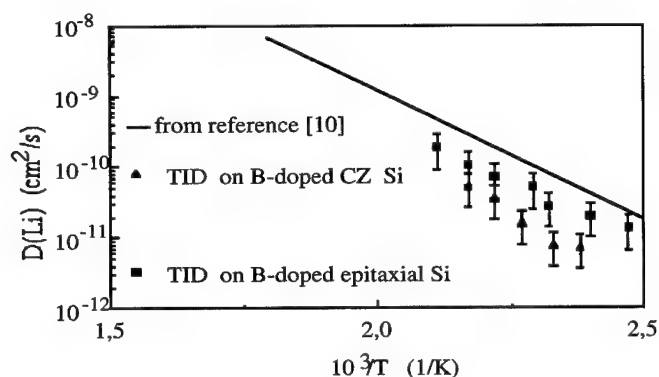


Fig.1:
Arrhenius plot
of the lithium
diffusion data in
Silicon

COPPER DOPED SILICON

Copper is known to be the fastest diffusing impurity in silicon and as a matter of course it is the most frequent metallic contaminant in silicon electronic devices. When dissolved on interstitial sites, its charge state was found to be positively charged.¹²

However, its low solubility limit at room temperature¹² as well as the absence of an associated deep level, makes the detection of interstitial copper (Cu_i) by 'standard techniques', like DLTS, impossible.

On the other hand, copper has been proposed by many authors as the most appropriate element for metallic interconnections in VLSI technology.¹³ In order to prevent copper in-diffusion, several groups studied the formation of diffusion barriers, detecting the presence of Cu in silicon via leakage current measurements.

Recently, copper was shown to be involved in the formation of a fast diffusing defect during chemomechanical polishing. The presence of low Cu concentrations (in the ppm range) in the polishing slurry was found to be sufficient to induce a huge acceptor passivation^{3,4}. The same defect was shown by Prescha et al,¹⁴ to be present after high temperature copper diffusion and thermal quenching.

In reference [8], TID measurements, done on copper diffused and quenched silicon, led to effective diffusion coefficients of the mobile defect, which can be related to its intrinsic value when coulombic copper-acceptor pairing is taking into account. The values coincide with literature data of Cu_i diffusion and lead to the identification of the diffusing defect as Cu_i atoms.

We performed similar measurements on Aluminium and Boron doped silicon in order to estimate the dependence of the pairing interaction on the chemical nature of the acceptor atom. High purity Copper was evaporated on both sides of the wafers. Samples were encapsulated in an argon filled quartz ampoule, thermally diffused at 1050°C for 30 minutes, and quenched into liquid nitrogen. In Boron doped samples, the diffusion coefficients extracted from TID signals, correspond to the intrinsic Cu_i diffusivity. The results are shown on Fig.2 and are compared to data obtained by Hall and Racette at high temperatures^{15,16} and to low temperature data extracted from C(V) measurements by Mesli et al.¹⁶ This good correlation indicates that Boron-Copper interaction is weaker than coulombic interaction.

In Al-doped samples, acceptor - Cu pairing was again sufficient to reduce Cu_i mobility. The pairing reaction constant can be described by: $\Omega = 4\pi R_c D_{\text{Cu}}/\nu$, where R_c is the capture radius and ν the acceptor-copper dissociation rate. R_c is given by $q^2/(8\pi\epsilon kT)$ if we assume the pair association rate to be described by long range coulombic interaction. The dissociation rates have been measured by Prescha et al¹⁴. The pairing reaction constants plotted on Fig.3, were obtained using expression $D_{\text{Cu}} = 4.5 \cdot 10^{-3} \exp(-0.39 \text{ eV}/kT)$, from reference [16].

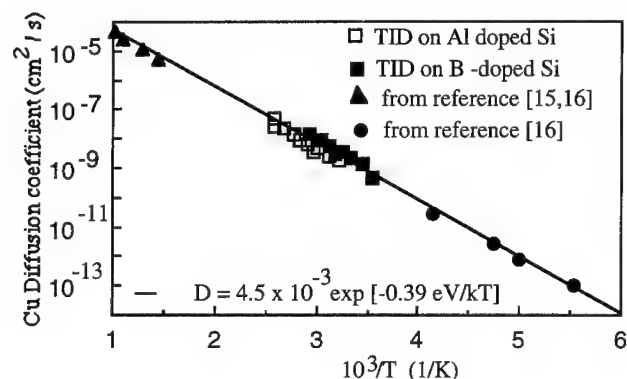


Fig2: Arrhenius plot of copper diffusion data in Silicon.

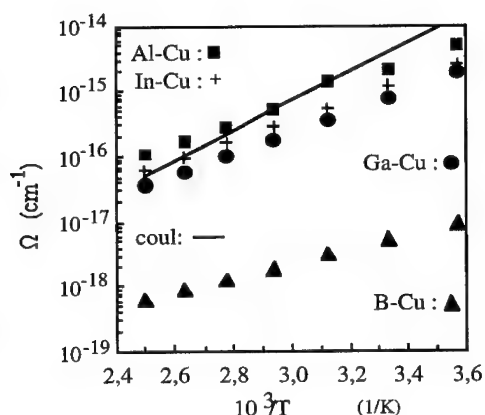


Fig3: Reaction constants of the acceptor-copper pairing

The sample is kept at a fixed temperature lower than 450K and TID signals are stored periodically. Cu outdiffusion should be negligible as the electric field constrains the positively charged Cu impurities to drift towards the bulk.

The signal amplitude decreases exponentially, and the Arrhenius plot of the time constants fits well to a straight line (see Fig.4). The free energy barriers obtained on In or Ga doped samples are given by: $E_{In}=0.60$ eV and $E_{Ga}=0.92$ eV. In spite of the higher energy barrier for Ga-doped samples, the diffusion rate observed in this material is higher than in the In-doped samples. If the precipitation process is assumed to be diffusion limited, these energy barriers correspond to the Cu_i diffusion energy, including acceptor-copper pairing. The pairing effect can be taken into account if the rate constants are corrected according to $\tau = \tau_{Tid}(1+\Omega N_{acc})^{-1}$. This leads to the following values: $E_{In}=0.4$ eV and $E_{Ga}=0.8$ eV.

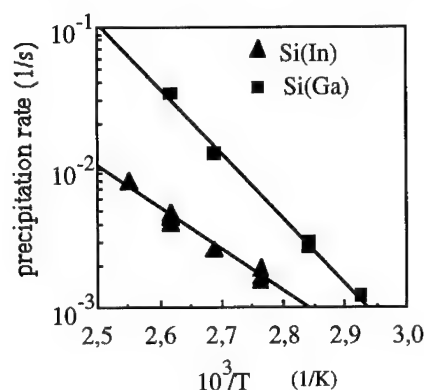


Fig.4: Copper precipitation rate observed by TID in In and Ga doped Si.

The results clearly show the reduced interaction of the B-Cu pair, compared to the other acceptor-Cu pairs, which behave almost like two point charges (solid line in Fig.3).

If the TID results obtained on Al-doped samples are corrected using results from Fig.3, a good agreement is again found with the literature diffusion data (see Fig.2). As a consequence of these results, TID signals may be used to detect the presence of low concentrations of Cu_i in silicon. The analyses of Cu_i low temperature precipitation kinetics is straight forward.

The values obtained in In-doped samples is close to the diffusion barrier extracted from the TID capacitance transients and agrees with a diffusion limited precipitation process. The results on Ga-doped samples, however, disagree with this simple model. More measurements are needed to understand this behaviour. We believe the purity of the samples (i.e. presence of microdefects, dislocations...) rather than the chemical nature of the dopant, to be responsible for these results.

NICKEL DOPED SILICON

Ni in silicon is known to behave similarly to Cu. It has a high diffusion constant and precipitate during thermal quenching. Its positive charge state¹² renders it susceptible to be detected by TID.

We used the same procedure to diffuse nickel into silicon and make electrical measurements.

No TID signal could be detected. This negative result might be due either to an unexpected nonpositively neutral charged state, or to faster precipitation rates, compared to copper precipitation.

In order to increase the possibility to detect Ni by TID, we will have to improve the cooling rate after Ni indiffusion and the time needed to realize Schottky contacts. These developments are currently under investigation.

SUMMARY

It was shown in this work that transient capacitance signals can be induced by ion drift in the depletion region of a Schottky barrier. For pulsed applied voltage, the resulting transients can be used to detect low concentrations of fast diffusing charged defects. The temperature dependence of the corresponding time constants yields information about effective diffusion coefficients of the defects. The temperature limitation of the technique is related to device operation. This constraint should be lower in large band gap material.

Application of the method to Li-diffused silicon led to diffusion data in good agreement with literature data. Reduced diffusivities were measured in Cz material, and were attributed to the well known Li-O interaction. The technique was shown to be able to detect low concentrations of interstitial copper in silicon and was used to estimate the dopant dependence of acceptor-copper pairing. The latter reaction fits well to a Coulombic long range interaction, for In, Ga and Al doped silicon. The interaction was found to be significantly weaker for boron-copper pairs. This particular behaviour of boron was already reported for H, Li and Fe-boron pairs. It might be due to additional lattice strain induced by the small size of Boron atoms in the silicon matrix.

Copper precipitation kinetics could be observed using TID analyses. In Indium doped samples the extracted energy barrier was consistent with a diffusion limited precipitation process.

Finally, no TID signal was found in Ni diffused silicon, as a consequence of a presumably faster precipitation process compared to Cu precipitation.

ACKNOWLEDGEMENTS

This work was supported by the joining program 91 MDU 163 between the university of Constantine (Algeria), the university of Strasbourg and CNRS.

The authors would like to thank Miss S.Clur for sample preparations and TID measurements.

REFERENCES

- ¹L.C.Kimerling, M.T.Asom, J.L.Benton, P.J.Drevinski, C.E.Caefer, *Mat.Sci.Forum* **38**,141(1988)
- ²N.M.Johnson and C.Herring, *Phys.Rev.B* **45**, 11379 (1992); *Phys.Rev.B* **46**,15554 (1992)
- ³H.Prigge, D.Gerlach, P.O.Hahn, A.Schnegg and H.Jacob,*J.Electrochem.Soc.***138**, 1385(1991)
- ⁴T.Zundel, J.Weber, B.Benson, P.O.Hahn, A.Schnegg and H.Prigge, *Appl.Phys.Lett.* **53**, 1426 (1988)
- ⁵H.Kukimoto, C.H.Henry and F.R.Merritt, *Phys.Rev.B***7**, 2486 (1973)
- ⁶M.Marciniak, *J.Electrochem.Soc.* **124**, 740 (1976)
- ⁷N.M.Johnson, C.Herring and C.G.Van de Walle, *Phys.Rev.Lett.* **73**, 130 (1994)
- ⁸T.Heiser and A.Mesli, *Appl.Phys.A* **57**, 325 (1993)
- ⁹A.Zamouche, T.Heiser and A.Mesli, *Appl.Phys.Lett.* **66**, 5 (1995)
- ¹⁰E.M.Pell, *Phys.Rev.* **119**, 1222 (1960)
- ¹¹E.M.Pell, *J.Appl.Phys.* **31**, 291 (1960)
- ¹²E.R.Weber, *Appl.Phys.A* **30**, 1 (1983)
- ¹³S.Q.Wang, *MRS Bulletin*, **19**, 30 (1994)
- ¹⁴T.Prescha, T.Zundel, J.Weber, H.Prigge, P.Gerlach, *Mat.Sci.Eng.B* **4**, 79 (1989)
- ¹⁵R.H.Hall and J.H.Racette, *J.Appl.Phys* **35**, 379 (1964)
- ¹⁶A.Mesli and T.Heiser, *Mat.Sci.Eng.B* **25**, 141 (1994)

NONCONTACT PHOTOCONDUCTIVITY AMPLITUDE TECHNIQUE TO CHARACTERIZE POLISHING-AND SLICING-INDUCED RESIDUAL DAMAGE IN SI WAFERS

Y. OGITA* M. NAKANO** and H. MASUMURA**

*Kanagawa Institute of Technology, Department of Electrical and Electronic Engineering,
Atsugi, Kanagawa, 243-02 Japan

** Shin-Etsu Handotai Co., Ltd., Shirakawa Lab., Nishi-shirakawa, Fukushima 961 Japan

ABSTRACT

The photoconductivity amplitude (PCA) technique with UV laser carrier excitation has been proposed to characterize surface property and subsurface damage. Combining this new technique with mechanochemical polishing has determined the depth profile of the slicing-induced residual damage. Combining SC1 cleaning with this technique allows to determine the depth profile of residual damage induced by mirror polishing. This result leads that the mirror polishing-induced damage can be removed by the SC1 cleaning.

INTRODUCTION

The reduction in device dimension in ULSI demands extremely high surface and subsurface quality of silicon wafers. The machining as slicing, lapping, and polishing causes unavoidable surface and subsurface damage[1]. The slicing causes deep residual damage in a subsurface. Therefore, the subsurface is finally removed by about 80-90 μm in one side to avoid defects in device production. The larger diameter of the ingot needs to minimize the residual damage and to evaluate precise damage depth for cost saving. On the other hand, mechanochemical polishing in a final wafer process causes residual damage in extremely thin layer of the subsurface. The damage has to be removed to avoid defects in the devices. Thus, we need a method to measure how it can be observed and removed and, how long the damage depth is.

The minority carrier recombination lifetime is known to be very sensitive to defects, heavy metal contamination and surface properties[2]. In order to characterize surface and subsurface properties, Ogita has proposed the UV mm-

wave technique which uses an ultra violet (UV) laser with extremely narrow photoexcitation time and with extremely thin penetration depth, and uses a mm-wave as the probe to detect information in a shallow layer due to the skin effect. Combining the UV photoexcitation and the mm-wave allows the direct measurement of carrier transportation in thin layer of the subsurface. The photoconductivity decay (PCD) which can be measured by the UV mm-wave technique, thus, has made it possible to characterize of contamination level in epitaxial layer of p/p⁺ and n/n⁺ Si wafer[3,4,5].

In this paper, a new technique using a photoconductivity amplitude (PCA) which can be measured by the UV mm-wave technique is proposed to characterize surface and subsurface properties based on detailed numerical analysis which correlates the PCA signal with a surface recombination velocity and a subsurface lifetime. Using the PCA technique, characterization of the residual damage induced by slicing is examined. Furthermore, characterization of the residual damage induced by mechanochemical polishing in the final mirror-polishing wafer

process is examined using the PCA technique.

PCA TECHNIQUE

The illumination light pulse causes the photoconductivity transient (PCT) as shown in Fig. 1. The PCA is defined as an amplitude

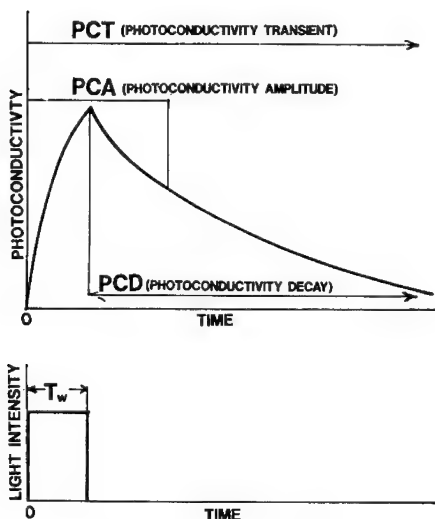


Figure 1 The definition of PCA

of PCT in initial time region with order of nanosecond as shown in the figure. Fig. 2

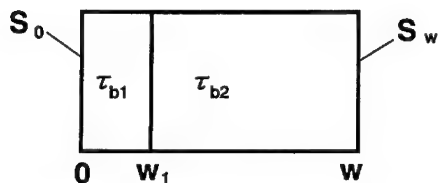


Figure 2 Calculation model for Si wafer

shows a calculation model of a Si wafer to calculate PCA signals depended on such parameters as S_0 and τ_{b1} . S_0 and S_w is a respective surface recombination velocity at a

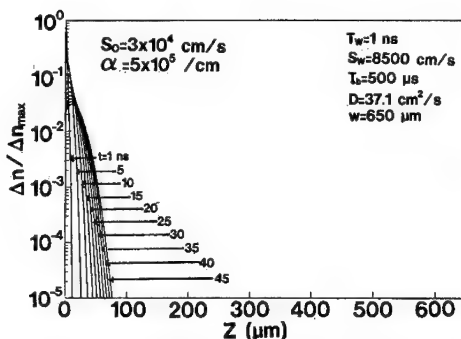


Figure 3 Flow profiles of carriers photoexcited

surface and a backface. τ_{b1} and τ_b is a subsurface carrier lifetime and a bulk lifetime, respectively. W_1 and w is a subsurface depth assumed and a wafer thickness, respectively. The wafer surface with S_0 is illuminated by a N_2 laser. The continuity equation of minority carriers was solved numerically under the boundary condition determined by S_0 and S_w shown in Fig. 2 and the initial condition of photoexcitation. In this calculation, an absorption coefficient $2 \times 10^5 \text{ cm}^{-1}$ (a penetration depth of 200 Å) and a pulse width of 1 ns as the photoexcitation condition were taken to fit the conditions of the experiment done here. The calculated results are shown in Fig. 3, 4 and 5. Fig. 3 shows profiles of flowing-carriers. We can roughly say that the carriers move with speed of order of 1 $\mu\text{m}/\text{ns}$ [6]. Therefore, if we can observe the signal in initial time region with order of nanosecond, we can obtain the information within several μm of the subsurface. Fig. 4 shows PCA signals depended on S_0 under $\tau_{b1} = \tau_{b2} = \tau_b = 500 \mu\text{s}$. The PCA signal decreases with increase of S_0 . We can see that the signal strongly depends on S_0 . Fig. 5 shows PCA signals depended on τ_{b1} . The PCA signal also decreases with decrease of τ_{b1} . We can see that the signal also depends on the subsurface lifetime.

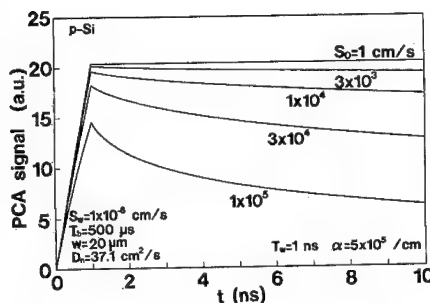


Figure 4 PCA signals depended on S_0

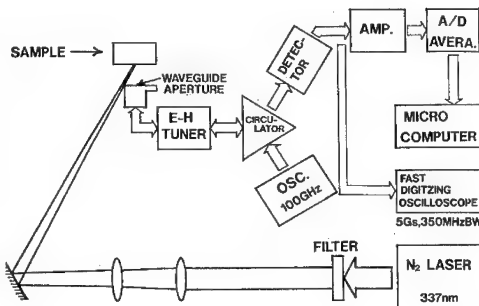


Figure 6 Schematic diagram of experimental setup for PCA measurement

From the above results, the PCA signal is dependent on both surface and subsurface quality. When a surface recombination velocity is decreased by means of a H-terminated treatment or when the velocity is

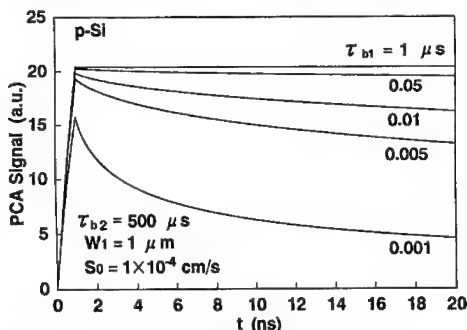


Figure 5 PCA signals depended on τ_{b1}

constant, i.e. the wafer owns the same surface property (e.g. surface roughness), the PCA signal reflects only subsurface quality.

MEASUREMENT SYSTEM

As shown in Fig. 6, the sample was illuminated by N_2 laser (Usho, AN-200) and irradiated by 100GHz millimeter wave generated by Gunn oscillator (Millitech, GDM-0). The photoconductivity change

caused by the illumination was detected by the millimeter wave probe as reflection change or conductance change. The signal was detected by the high speed detector and observed by the High speed digital oscilloscope (Lecroy, 9360) [3-5]. The signals were observed with 2GHz sampling in this experiment.

CHARACTERIZATION OF SLICING RESIDUAL DAMAGE USING PCA TECHNIQUE

6 inch CZ, p-type, 10 Ω cm silicon ingot was sliced using a inner diameter blade to be wafers with (100) plane and 783 μ m thick. The wafer samples was prepared especially for the experiments by Showa Denko Co., Ltd. Three samples named as A, B, C were scribed to be 1 cm square for the experiments. The PCA signals were measured through the lapping and polishing process as shown in Fig. 7. The polishing depth was determined from the sample thickenss measured by the dialgauge. Fig. 8 shows one example of PCA signals measured for the depth polished. The PCA value at the peak of PCA signals measured for respective sample is plotted for the depth in Fig. 9. In the lapping process, the PCA signal was not observed for the samples

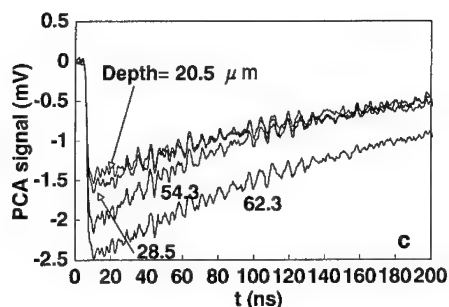
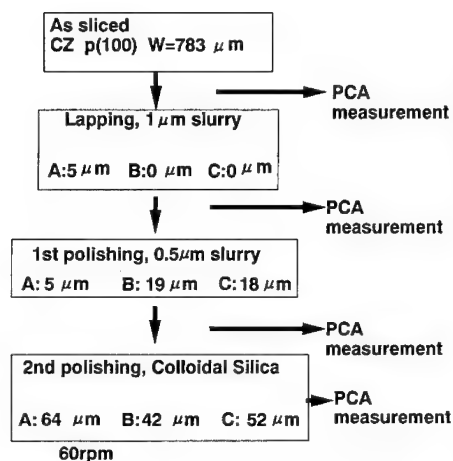


Figure 8 One example of measured PCA signals for depth

of A, C except for B as seen in Fig. 9. As seen from the figure, three PCAs rise abruptly by polishing with the colloidal silica with 600 Å and PH 9.8. This expresses that the damage induced by the slurry with 0.5 μm in the lapping process is removed by the polishing. After that, it increases till the saturation level. It seems to be saturation at the depth of 55–62

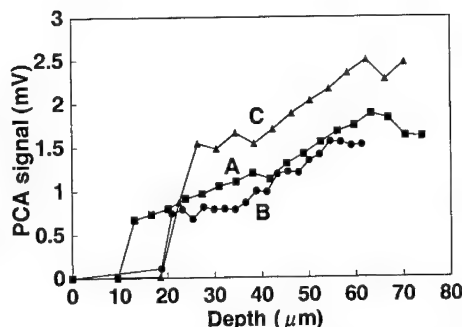


Figure 9 Measured PCA signals as a function of depth

μm. This indicates removal of the residual damage induced by the slicing. We think that this corresponds to the damage depth induced by the slicing. This value is larger than 20–50 μm which silicon makers have been saying it to be. The residual damage profile measured using the infrared depolarization was reported by Lundt[5]. The curve as a function of depth seems to be not still saturated at 40 μm depth. Thus, this deeper damage depth will be due to higher sensitivity of this PCA technique.

CHARACTERIZATION OF MIRROR POLISHING-INDUCED RESIDUAL DAMAGE

We examined whether the PCA signal can detect removing the residual subsurface damage induced in extremely thin layer by the mechanochemical polishing. The original sample was CZ, p-type Si wafers with (100) plane, 10 Ωcm and 620 μm thick. In order to remove the residual damage, SC1 cleaning was tried as the procedure shown in Fig. 10. Four samples with such different SC1 cleaning time as 30, 60, 90, 180 sec. were prepared. HF cleaning was done to decrease the surface recombination due to the H-terminated surface treatment. The samples had been kept in sealed wafer box to avoid the surface change due to the air exposure. The PCA

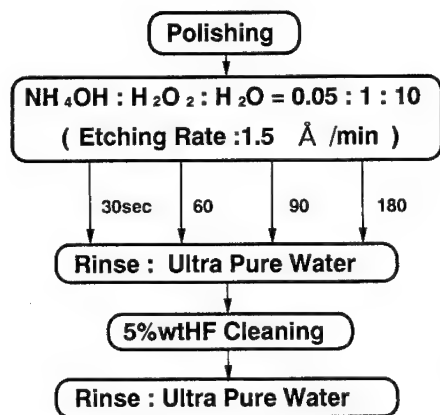


Figure 10 Sample preparation for characterization of mirror polishing-induced damage

signal were measured at 1 hour 45 min. late after taking them out from the box. PCA value at $t = 2$ ns of the PCA signals measured for four samples are plotted as a function of SC1 cleaning time in Fig. 11. In the same figure,

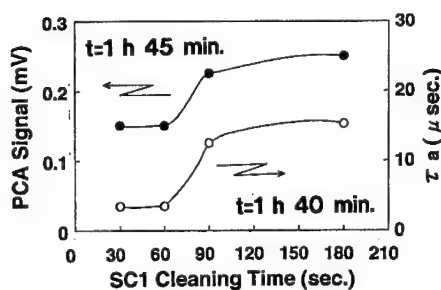


Figure 11 PCA signal as a function of SC1 cleaning time

the effective carrier lifetime τ_a is also plotted. The τ_a was obtained from the gradient of photoconductivity decay (PCD) in 2 ns - 1.3 μ s in initial time region. From the figure, we can see that the PCA and τ_a have similar curve shape and they approach the saturation level at SC1 cleaning for 180 sec. These

curves express the removing of mirror polishing-induced damage in the subsurface. To confirm validity of the above results, the another experiment was tried to characterize the damage by the photothermal displacement method using the damage monitor (Leo, PA-300) [7]. The result is shown in Fig. 12. The

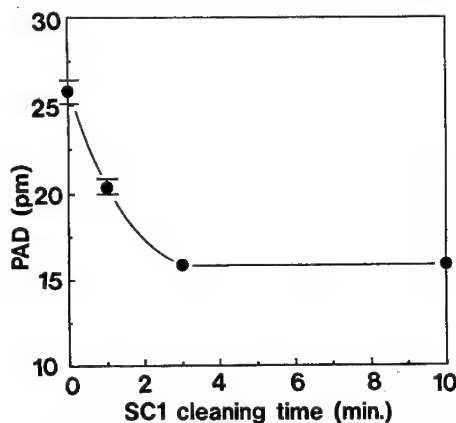


Figure 12 Photothermal displacement signal as a function of SC1 cleaning time

measurement was carried out within 10 min. after taking it out from the box. As seen from the figure, the signal approaches the saturation level by SC1-cleaning time for 3 min. This coincides with the result of PCA and the initial apparent lifetime τ_a . Furthermore, the contamination level in the subsurface measured was under the lowest limit or the same level in the equipment ICP-MS (Seikodenshi, SQP8000) used. Thus, the above results by two method do not reflect the contamination but reflects the subsurface damage. Furthermore, the same PCA measurement was again carried out for the same samples at 72 hours and 15 min. late after taking them out from the box. The result is shown in Fig. 13. The change of the PCA becomes smaller than that at 1 hour 45 min. late but the change is same as that. But, the change is still detected. The reason is that the influence on the subsurface damage to PCA signal is hindered by the increase of the

surface recombination by replacing Si-H bonds by H₂O, O₂ and others in the air. The damage depth is estimated to be 0.45 nm using etching speed of 0.15 nm/min. measured for the subsurface without a damage. The etching speed for the layer with damage must be larger than it. We can say that the damage depth is 0.45 nm at least. Even if we does not acquire the exact damage depth, we can conclude that the damage can be removed by the SC1 cleaning.

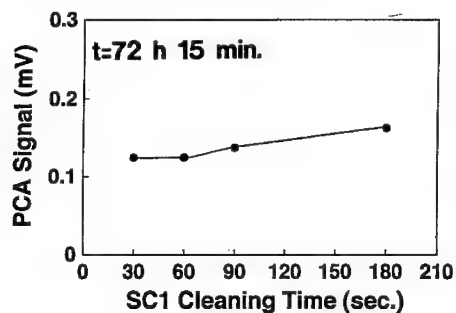


Figure 13 PCA signal as a function of SC1 cleaning time for the sample left in air for 72 hours 15 min.

CONCLUSIONS

The theoretical analysis shows that the PCA technique can be sensitive method for determining surface recombination velocity and subsurface carrier lifetime. The depth profile of slicing-induced residual damage can be measured by combining the PCA technique with the mechanochemical polishing. And the depth was obtained to be 55–62 μm in this experiment. The depth profile of the residual damage induced by the mirror polishing can be measured by combining the PCA technique with the SC1 cleaning. The mirror polishing-damage can be removed by the SC1 cleaning.

ACKNOWLEDGEMENTS

The authors would like to thank undergraduate students K. Komai and H. Shiraya of Kanagawa Inst. Tech. for the PCA measurements of polishing-induced damage and F. Takeoka and T. Yamamoto of the same Institute for the PCA measurements of slicing-induced damage.

REFERENCES

1. Lundt, N. Kerstan, A. Huber and P. O. Hahn, in *Semiconductor silicon/1994*, edited by H. R. Huff, W. Bergholz and K. Sumino (The electrochemical Society, Pennington, NJ, 1994) pp. 218–225
2. T. Abe, T. Itoh, Y. Hayamizu, S. Yokota and H. Yamagishi, in *Defect Control in Semiconductors*, edited by K. Sumino (North-Holland, Amsterdam, 1990) pp. 297–303
3. Y. Ogita, *Semicond. Sci. Tech.*, **7**, 1, A175–A179 (1992)
4. Y. Ogita, K. Yakushiji and N. Tate, in *Defect Recognition and Image Processing in Semiconductors and Devices*, edited by J. Jimenez (Institute of Physics, Bristol, UK, 1994) pp. 39–43
5. Y. Ogita, K. Yakushiji and N. Tate in *Semiconductor silicon/1994*, edited by H. R. Huff, W. Bergholz and K. Sumino (The Electrochemical Society, Pennington, NJ 1994) pp. 1083–1092
6. Y. Ogita, K. Shinbu, T. Katoh, M. Ishihara and T. Hirai, *The Japan Soc. of Appl. Phys. and Related Soc., Extended Abs.*, (1994 Spring), No. 2, P. 685 (29a-ZK-2)
7. S. Sumie, H. Takamatsu, H. Tsunaki, Y. Nishimoto and Y. Nakai, *Mat. Res. Soc. Symp. Proc.*, Vol. 236, (1992), pp. 241–246

NON-DESTRUCTIVE METHOD FOR SIMULTANEOUS MAPPING OF DIFFUSION LENGTH AND SURFACE RECOMBINATION VELOCITY

HANS-CHRISTOPH OSTENDORF AND ARTHUR L. ENDRÖS
Siemens Corporate Research and Development, D-81730 Munich, Germany

ABSTRACT

Bulk and surface recombination are the main material parameters that determine the performance of crystalline silicon solar cells. We present a new method for the nondestructive, simultaneous mapping of the diffusion length and the surface recombination velocity of a silicon wafer. The method uses the hardware of the electrolytical metal tracer (ELYMAT). The separation between bulk and surface recombination is achieved by illuminating the sample with laser beams of two different colors. By solving the diffusion equation for both laser penetration depths the diffusion length and the surface recombination velocity can be calculated from the measured diffusion currents. First experiments are presented which show the basic feasibility of the method.

INTRODUCTION

The development of crystalline silicon solar cells is heading steadily towards thinner devices, a trend which makes the quality of surface passivation more and more decisive for solar cell performance. In line with this it is necessary to have a nondestructive method of determining the minority carrier diffusion length (L) and the surface recombination velocity (S) *simultaneously* after every step of solar cell processing. Further requirements are the possibility of obtaining a map of L and S throughout the wafer, easy sample preparation, and a means of maintaining certain injection levels.

Methods for measuring the minority carrier lifetime of silicon samples are well known [1, 2]. However, the distinction between bulk and surface recombination is gaining more and more importance [3, 4]. However, no method complies with all the requirements given above. One of the established methods of measuring L is the electrolytical metal tracer (ELYMAT), which measures a *stationary* diffusion current generated by a laser [5]. This is very similar to a solar cell under short-circuit conditions. The simple theory enables a straightforward evaluation of the data. In addition, it is easy to obtain a given injection level.

Our newly developed method is an extension of the standard ELYMAT measuring modes. It does not depend on assumptions concerning the surface recombination velocity. In this paper we review the ELYMAT principle and describe our new "Two-Color Method". First experimental results are presented that show the applicability of the new method.

THE ELYMAT PRINCIPLE

The principle of the ELYMAT apparatus is shown in Figure 1a. The silicon sample is mounted in an electrolytical double cell. Both chambers can be filled with an aqueous solution of hydrofluoric acid (HF). The HF provides two large-area, transparent contacts to

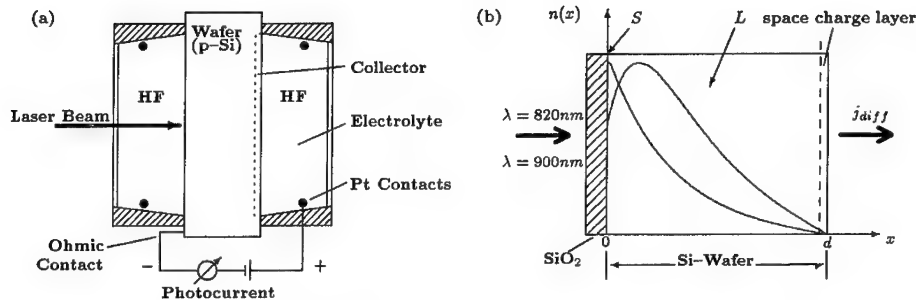


Figure 1: (a) Principle of the ELYMAT operation in back side photocurrent (BPC) mode. (b) Typical minority carrier profiles $n(x)$ generated by laser beams of different penetration depths (in BPC mode).

the sample. Depending on bias voltage the HF-silicon interface is either very well passivated [6] or acts as a collecting junction (for details see Ref. [5]). A third (ohmic) contact to the sample is realized by tungsten carbide needles.

A standard diffusion length mapping is achieved as follows: A laser beam generates carriers near the HF-passivated front surface of the wafer. The carriers diffuse through the depth of the wafer and are collected by a junction at the rear side (BPC mode). The photocurrent depends solely on L and the absorbed photon flux. The photon flux is determined by collecting the carriers at the front side of the wafer (FPC mode). L can then be calculated from the BPC and FPC photocurrents. Finally, scanning the laser beam over the sample yields a diffusion length mapping.

With a second measurement S can be determined, too [7]. However, this method is destructive and relies on the removability of the investigated surface layer.

THE TWO-COLOR METHOD

Our new "Two-Color Method" (TCM) attempts to overcome the limitations of the surface recombination measurement by not making assumptions concerning S during any measurement step. However, without HF passivation the photocurrent in BPC mode depends on both L and S . Therefore, at least two different measurements are necessary to determine L and S . In order to obtain those two measurements the sample is illuminated with laser beams of two penetration depths as outlined in Figure 1b. One of the laser beams generates minority carriers close to the front surface, i.e., the measurement is very sensitive to surface recombination. The second laser has a longer wavelength, so it generates carriers more homogeneously in the sample. This reduces the influence of the front surface on the photocurrent so that the measurement probes mainly the bulk of the material. By solving the diffusion problem a set of *two* equations is obtained which can be solved for L and S .

Theory

The theoretical evaluation of the measured photocurrents is based on a solution of the one-dimensional diffusion equation for the minority carriers. The front side of a sample

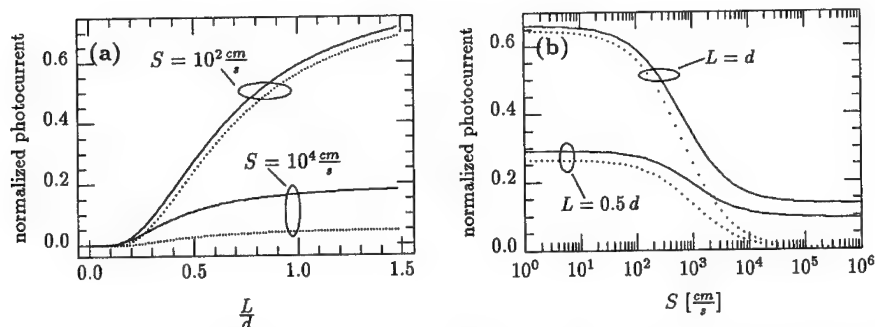


Figure 2: Dependence of the photocurrent in BPC mode on L (a) and S (b), respectively. (···) denotes a short, (—) a long penetration depth of the incident laser beam. The photocurrent is normalized to the absorbed photon flux. Diffusion lengths are given relative to the sample thickness d .

(thickness d) is illuminated by light of an absorption constant α . On the rear of the wafer the carriers are collected by the junction (see Figure 1b). This situation can be described by the differential equation for the minority carrier density $n(x)$:

$$D \frac{\partial^2 n}{\partial x^2} + (1 - R)\Phi \alpha e^{-\alpha x} - \frac{n(x) - n_0}{\tau} = 0, \quad (1)$$

with D being the diffusion constant of the minority carriers and n_0 being the minority carrier density in thermal equilibrium. R is the reflectivity of the front surface and Φ is the incident photon flux density. The boundary conditions are given by the surface recombination velocity S on the front side and by the collecting junction on the rear side.

This description is valid under the assumptions of low injection, a constant diffusion length across the thickness of the sample, and an ideal collecting junction. Solving the boundary value problem leads to the current density [8]

$$j = -\frac{e(1 - R)\Phi \alpha L}{1 - \alpha^2 L^2} \frac{(\alpha L + L \frac{S}{D}) [e^{-\alpha d} \cosh(\frac{d}{L}) - 1] + (1 + \alpha L \frac{L S}{D}) e^{-\alpha d} \sinh(\frac{d}{L})}{L \frac{S}{D} \sinh(\frac{d}{L}) + \cosh(\frac{d}{L})}, \quad (2)$$

i.e., j depends on L , S and α . Since equation (2) cannot be analytically solved for L , a numerical root finding process is applied to obtain the values of L and S .

Detection Range and Accuracy

In order to estimate the detection limits for L and S we investigated the dependence of the photocurrent in equation (2) on L and S . Typical results are plotted in Figure 2. Referring to Figure 2a it is obvious that the photocurrent depends strongly on L for $L \leq d$. For $L > d$ L has a weaker influence on the photocurrent, so the highest accuracy for L can be expected for $L \leq d$. From Figure 2b it is evident that the highest accuracy for S is in the intermediate range of S between $10^2 \frac{\text{cm}}{\text{s}}$ and $10^4 \frac{\text{cm}}{\text{s}}$. Additionally, L must exceed a minimum value of about $d/4$, otherwise the influence of the surface is too small for a reliable measurement of S . However, if L is too large for an accurate determination, S can nevertheless be calculated by assuming a value of, e.g., $L = 10d$, since the influence of L on the photocurrent can be neglected and S is the major recombination channel.

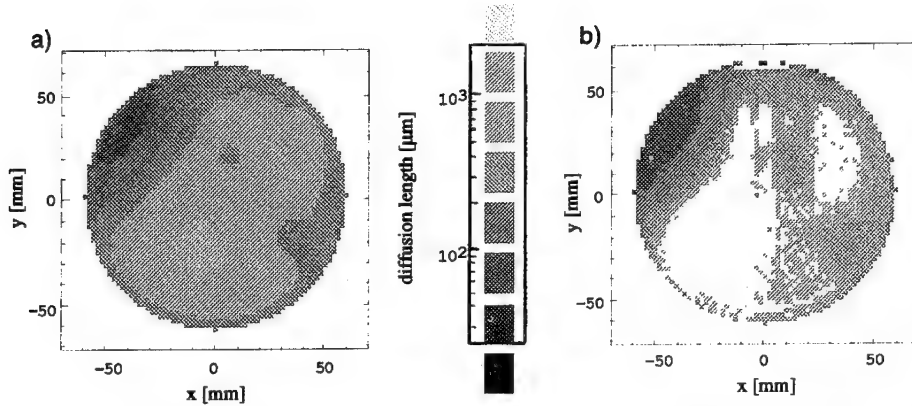


Figure 3: Diffusion length mappings determined by the standard ELYMAT method (a) and by the “Two-Color Method” (b).

EXPERIMENTS

In order to test the feasibility of the “Two-Color Method” measurements on samples with a wide range of L and S are necessary. As a first step we chose a wafer with a wide L variation from $100\mu\text{m}$ to $1000\mu\text{m}$ (see Figure 3a). The sample was p-type, (100)-oriented, with a thickness of $675\mu\text{m}$ and a resistivity of $5\Omega\text{cm}$. A thin chemical oxide was produced via a standard RCA cleaning procedure.

The measurements were made with laser wavelengths of 820nm and 900nm providing penetration depths of $14\mu\text{m}$ and $32\mu\text{m}$, respectively [9]. For each laser the photon flux was determined via an FPC measurement on the test wafer. To establish the same optical properties for all measurements the front cell was filled with deionized water during measurements 1 and 2 and filled with HF during measurement 3.

Three different BPC measurements were then performed on the test wafer:

1. $\lambda_{\text{laser}} = 820\text{nm}$, front surface covered with chemical oxide;
2. $\lambda_{\text{laser}} = 900\text{nm}$, front surface covered with chemical oxide;
3. $\lambda_{\text{laser}} = 820\text{nm}$, front surface passivated with HF;

RESULTS AND DISCUSSION

Following the standard ELYMAT procedure the L mapping was calculated from measurement 3 (subsequently called L_{ref}). Then the L_{ref} measurement was used together with measurement 1 to obtain the surface recombination velocity mapping S_{ref} . Using the “Two-Color Method” (TCM) measurements 1 and 2 were evaluated and lead to the mappings L_{TCM} and S_{TCM} .

Figure 3 shows the L mappings measured by the standard and the “Two-Color Method”. Comparing the two mappings it can be seen that there is an agreement in the (darker) areas of smaller L ($L < d$) but for larger L ($L \geq d$) the Two-Color Method shows more noise.

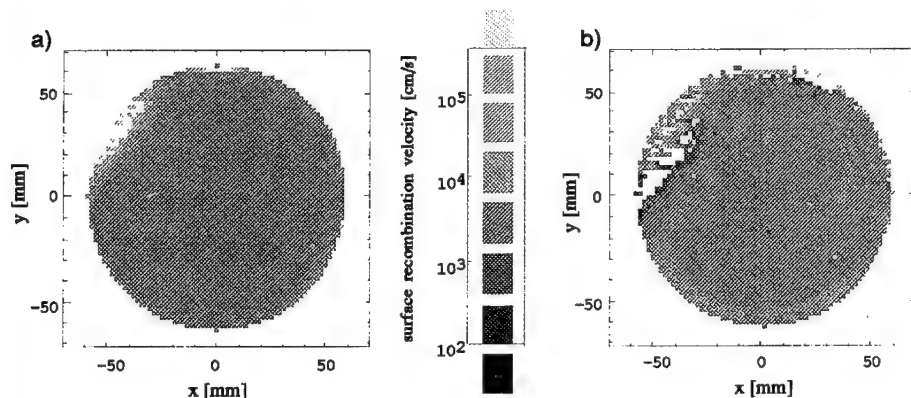


Figure 4: Surface recombination velocity mappings determined by the standard ELYMAT method (a) and by the "Two-Color Method" (b).

The "white spots" in Figure 3b are caused by the fact that the evaluation algorithm cannot find a sensible value for L , thus indicating that $L > d$. Calculating the relative deviation between the two mappings L_{ref} and L_{TCM} we find that 90% of the L values agree within an interval of $\pm 50\%$.

Figure 4 displays the S mappings measured by the standard and the Two-Color Method. It is obvious that an accurate measurement of S is not possible in regions of small L as visible in the upper left region of the wafer. But it is worth noticing that a determination of S with the Two-Color Method is possible even in those areas where a determination of L is impossible for the Two-Color Method. This is due to the fact that for large L the influence of L on the photocurrent is negligible. Both measurements lie well within the range of $10^3 \frac{cm}{s}$ to $10^4 \frac{cm}{s}$, but with the Two-Color Method the noise is somewhat larger. The relative deviation between the two measurements S_{ref} and S_{TCM} gives an interval of $[-40\%, +200\%]$, including 90% of the 2800 measured points.

The injected carrier densities were estimated to be about $1...2 \times 10^{14} cm^{-3} s^{-1}$ for both lasers. So the sample was in low injection condition during the measurements.

In Figure 5a the relative deviation of L versus L_{ref} is plotted for all 3001 points of the mapping. It is clearly visible that the deviations of L increase with increasing L_{ref} . This agrees closely with the theoretical considerations given above. The same analysis was performed in Figure 5b for the deviations in S . The decreasing accuracy of S in the "Two-Color Method" with decreasing L_{ref} is clearly visible. Again, this agrees with the theoretical findings.

SUMMARY

We developed a new method for a simultaneous, nondestructive measurement of diffusion length and surface recombination velocity without special assumptions on surface properties. The method includes the opportunity of obtaining a mapping of L and S over the whole sample and of maintaining certain injection levels. First experiments show the feasibility of measuring both recombination parameters with only two different laser colors. The applicability of the method was experimentally confirmed in the interval $0.2d < L < d$ for the

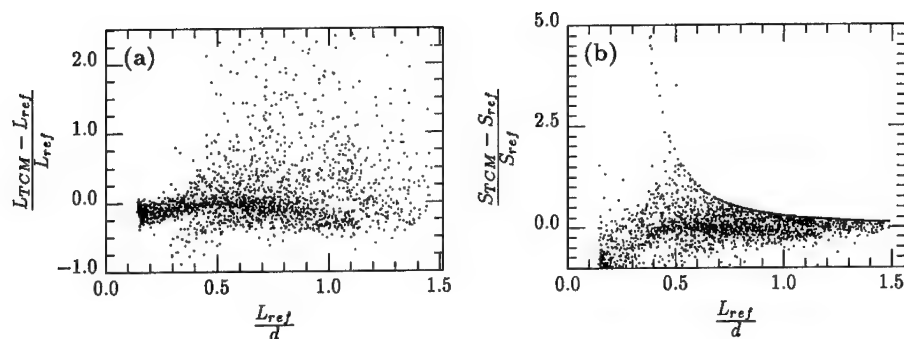


Figure 5: (a) Correlation between L and the relative deviation in L and S , respectively. L is normalized to the wafer thickness d .

measurement of L and $10^3 \frac{cm}{s} < S < 10^4 \frac{cm}{s}$ for the measurement of S . From the theoretical analysis a wider range of $10^2 \frac{cm}{s} < S < 10^5 \frac{cm}{s}$ for the measurement of S can be expected. Further improvements of applicability and accuracy seem to be possible by means of optimizing of the method and by using more than two laser colors, i.e., a wider range of penetration depths.

ACKNOWLEDGEMENT

We would like to thank D. Wecker, her group, P. Eichinger, and GeMeTec Company for allowing us access to the ELYMAT and for their continuous assistance. This work was supported by the Bundesminister für Forschung und Technologie.

REFERENCES

- [1] D. T. Stevenson and R. J. Keyes, J. Appl. Phys. **26**, 190 (1955).
- [2] A. M. Goodman, J. Appl. Phys. **32**, 2550 (1961).
- [3] S. W. Glunz, A. B. Sproul, W. Warta, and W. Wettling, J. Appl. Phys. **75**, 1611 (1994).
- [4] A. W. Stephens, A. G. Aberle, and M. A. Green, J. Appl. Phys. **76**, 363 (1994).
- [5] V. Lehmann and H. Föll, J. Electrochem. Soc **135**, 2831 (1988).
- [6] E. Yablonowitch, D. L. Allara, C. C. Chang, T. Gmitter, and T. B. Bright, Phys. Rev. Lett. **57**, 249 (1986).
- [7] V. Lehmann, private communication
- [8] S. M. Sze, *Physics of Semiconductor Devices*, 2nd ed. (John Wiley & Sons, New York, 1981), p. 800-803.
- [9] M. A. Green (Ed.), *High Efficiency Silicon Solar Cells*, (Trans Tech Publications, Brookfield, VT, USA, 1987), p. 228-230, and references therein.

INVESTIGATION OF RECOMBINATION PARAMETERS IN ION IMPLANTED LAYER-SUBSTRATE Si STRUCTURES

E. GAUBAS, K. JARAŠIŪNAS, A. KANIAVA, J. VAITKUS

Vilnius University, Institute of Material Science and Applied Research, Laboratory of Optical Diagnostics, Sauletekio 10, 2054 Vilnius, Lithuania

INTRODUCTION

Ion implantation is widely used technological process in the fabrication of semiconductor devices, and contactless techniques to monitor the implantation process and material quality are desired. The excitation-probe nondestructive optical techniques for separate determination of recombination parameters and control of low doses of implanted ions in Si are developed in this work.

A modified method of infrared as well as microwave absorption is based on variation of excitation depth of the sample. The mathematical model based on the solution of the continuity equation with layer-by-layer varying parameters, such as carrier bulk lifetime τ_b and coefficient of ambipolar diffusion D . The asymptotic decay time τ_{eff} is used as an experimental parameter to characterize recombination processes of material, and is described in effective depth approximation by analytical solution of this model. To determine recombination parameters of both layer and substrate, simultaneous investigation of τ_{eff} reconcilable changes at different excitation depth d_{eff} is required. The transient grating (TG) technique is based on sinusoidal refractive index modulation at the surface region by illumination with light interference pattern and subsequent light diffraction on this spatial structure.

Experimentally variations of d_{eff} are performed by changing the excitation light wavelength. Non-monotony of the asymptotic recombination time vs. implantation dose was revealed. In the range of doses 10^{12} - 10^{14} cm⁻² (for Ar⁺) carrier bulk lifetime decreases with implantation, while at higher dose values the superlinear increase of surface recombination and decrease of diffusion constant take place. Transient grating technique allows to determine low doses of B⁺ and P⁺ ions in the range of 10^{10} - 10^{15} cm⁻².

MATHEMATICAL MODEL

The asymptotic decay time τ_{eff} is measured as instantaneous recombination time τ_M for the slowest part of decay. The approximation of effective thickness [1] assumes that depth of penetration of generated excess carriers is limited by excitation light absorption (α_λ) and carrier diffusion: $d_{eff} = \alpha^{-1} + \sqrt{Dt_M}$ and $D_2 \partial n / \partial x|_{x=d_{eff}} = 0$. The accepted approximation is justified by the fact that the measured signal at each t_M is proportional to carrier concentration averaged over d_{eff} at wavelength of excitation in the range of strong absorption. The continuity equation is considered with stepwise changing coefficients as d_1, τ_1, s_1, D_1 and d_2, τ_2, s_2, D_2 for implanted layer and substrate, respectively. This task is solved for the typical boundary conditions accounted surface recombination as well as conjugation conditions at the structure interface included equality of diffusion flows and

excess carrier concentrations on it. This task may be solved by the method of variables separation. The concentration averaged over effective thickness is presented by the expression :

$$\langle n \rangle_d = n_0^* \sum_{j=1}^2 \sum_{m=1}^{\infty} \exp(-v_m t) [8L_{jm} \sin^2 y_{jm} / 2] / [y_{jm} + \sin y_{jm}] \quad (1)$$

where $n_0^* = n_0 / d_{eff}$ is initial stationary excess carrier concentration averaged over d_{eff} , $L_{jm} = (D_j / (v_m - \tau_j^{-1}))^{1/2}$, $y_{jm} = d_j / L_{jm}$ and v_m is the root of the transcendental equation:

$$p_1 [q_1 + tgy_1] / [1 - q_1 tgy_1] = p_2 \text{ctg}((d_{eff} - d_1) / L_2) \quad (2)$$

Here $p_j = L_j / D_j$, $q_j = D_j / L_j s_j$, $\tau_{eff} = v_1^{-1}$. This solution formally correlates with the solution for a homogeneous sample with $d_1 = 0$ and $d_{eff} = d$ as well as with the solution for homogeneous excitation of two layer structure when real carrier distribution profile is approximated by rectangular one with the average concentration n_0^* . The solution presented above is valid when the difference between bulk lifetimes in both layers is small and surface recombination prevails. If bulk lifetime in the implanted layer is the smallest among the other recombination times transcendental equation acquire the form:

$$p_1^* [1 + r_1] / [1 - r_1] = p_2 \text{ctg}((d_{eff} - d_1) / L_2) \quad (3)$$

where $L_{im}^* = (D_1 / (\tau_1^{-1} - v_m^*))^{1/2}$, $p_1^* = L_{im}^* / D_1$, $r_1 = \exp(-2y_1^*) [D_1 - s_1 L_1^*] / [D_1 + s_1 L_1^*]$. Although the expression for the averaged concentration acquires slightly different form ($\sin \rightarrow \sinh$), the dependence of concentration on time is characterized by v_m^* and remains the same. For the method based on the determination of asymptotic relaxation times at different excitation depths the main task is to solve transcendental equation. Computer simulation procedure (to get the best fit of measured and calculated asymptotic lifetime at different excitation depths for the same sample) includes consideration of both (2),(3) transcendental equations.

The transient grating technique is based on the additional spatial modulation of excess carriers generated within d_{eff} . Two-dimensional distribution of carrier concentration and its temporal evolution follows from the solution of continuity equation as well. Periodic modulation of carrier concentration (and, consequently, of refractive index given by Drude-Lorentz model) leads to light induced diffraction phenomena. The diffraction efficiency η_1 of the first diffraction order and its dependence on time, exposure and grating period Λ are the main characteristics to study recombination and diffusion parameters of material before and after ion implantation. Diffraction efficiency in the first diffraction order η_1 can be expressed via light-induced phase modulation by free carriers $\Phi = (2\pi g / \lambda)^* \int \Delta n(z) dz$, and the temporal behavior of η_1 is governed by effective recombination time τ_{eff} and diffusive time $\tau_D = \Lambda^2 / 4\pi^2 D$, according to simple relationship:

$$\eta_1 = J_1^2(\Phi) \approx (\pi g \langle n \rangle_d d_{eff} \exp(-4\pi^2 D t / \Lambda^2) / \lambda_p)^2 \quad (4)$$

where g is a coefficient of refractive index dispersion by free carriers and Δn is an instantaneous value of modulation of carrier concentration, induced by light interference pattern and governed by carrier recombination and diffusion. Due to superlinear

dependence of diffraction efficiency on carrier concentration, from one hand, and measurements of the diffracted signal in the dark field background, from the other hand, the sensitivity of transient grating technique is enhanced respectively to the other linear techniques. This technique allows one to determine low implantation doses via calibrated changes of diffraction efficiency.

EXPERIMENTAL TECHNIQUE

The investigations of asymptotic lifetime have been performed on p-type substrates implanted by Ar^+ ions. In order to eliminate the impact of substrate parameter variation, the Ar^+ ions of energy $E = 150$ keV were implanted on separate sectors of the face side of the same wafer. The initial values of recombination parameters (τ_2 , s_2 , D_2) have been measured on non-implanted sectors of the wafer and served as the substrate parameters in determining recombination parameters of implanted layer. Implantation dose Π at different sectors varied in the range of 10^{13} - 10^{16} ions/cm². The wafers with implantation dose varying from 10^{10} to 10^{15} cm⁻² of B^+ or P^+ ions were investigated by transient grating technique.

Experimental conditions approaching the requirements of the model were reached by optical excitation of the structure by pulsed YAG laser or by LED radiation with number of fixed wavelengths. An effective excitation depth changes due to the considerable difference of absorption coefficient α at the excitation wavelengths: $\alpha_1 \approx 10$ cm⁻¹ for $\lambda_1 = 1.064$ μm , $\alpha_2 \approx 300$ cm⁻¹ for $\lambda_2 = 0.94$ μm , $\alpha_3 \approx (0.6-1.0)10^3$ cm⁻¹ for $\lambda_3 = 0.78-0.84$ μm and $\alpha_4 \approx 8 \cdot 10^3$ cm⁻¹ for $\lambda_4 = 0.532$ μm . Generally, for determination of two layer structure parameters, the asymptotic time τ_{eff} for near surface excitation (λ_2 - λ_4) was measured at both face and rear wafer side. This means that $l \geq 4$ independent measurements have been performed.

The radiation λ_1 of the first (λ_1) and the second (λ_4) harmonics of solid state pulse laser ($\tau_L = 14$ ns, YAG: Nd^{3+}) was used for the bulk and surface excitation. The radiation of the second harmonic was also used for optical pump of the dye laser. The dye laser with tunable wavelength λ_3 radiation as well as light emitted by LED ($\tau_{\text{LED}} = 0.1$ μs) λ_2 serve for excess carrier generation near surface. Under the short pulse excitation ($\tau_L \leq \tau_{\text{eff}}$) the excess carriers are generated at d_{eff} determined by absorption coefficient. These carriers modulate the absorption of cw He-Ne laser ($\lambda_{p1} = 1.15$ μm) or microwave ($\lambda_{p2} = 3$ cm) radiation, which probes the excited region. The decay of absorption by excess carriers in time is recorded as relaxation curve by oscillograph, and data processing is performed by microcomputer. Relaxation reveals the transient non-exponential initial part and asymptotic part, which may be approximated by exponent.

Experiments by TG technique are carried out by using short pulses of YAG-laser both for excitation and probe. Excitation of excess carriers is performed by interference field of strongly absorbed laser radiation λ_4 while the weakly absorbed beam λ_1 probes the light induced grating. Grating spacing is changed by beam splitter. Diffraction intensity of the first diffraction order is measured in dark field background.

RESULTS AND DISCUSSION

The measurements of asymptotic lifetime τ_{eff} have been performed at the same point of the sample for four effective thickness: $d_{\text{eff}1} = d = 400 \mu\text{m}$, $d_{\text{eff}2} = 330 \mu\text{m}$, $d_{\text{eff}3} = 60-72 \mu\text{m}$, $d_{\text{eff}4} = 1-45 \mu\text{m}$, which are obtained by

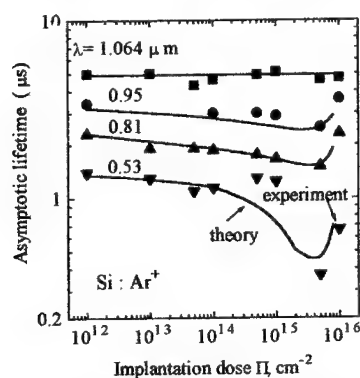


Fig. 1. Asymptotic lifetime vs implantation dose

changing the excitation wavelengths $\lambda_1 - \lambda_4$. The thickness of the implanted layer is considerably smaller than the effective diffusion length L of excess carriers and generation depth. This condition is accepted in the model of effective thickness. The dependencies of asymptotic lifetime on the dose of implantation at different excitation wavelengths are shown by points in Fig. 1. Solid curves represent the computed dependencies, obtained for fixed parameters $\tau_2 = 8 \mu\text{s}$, $D_2 = 15 \text{ cm}^2/\text{s}$, $s_2 = 3.5 \cdot 10^3 \text{ cm/s}$, $d_1 = 0.20 \mu\text{m}$, varying the set of parameters τ_1 , s_1 , D_1 . The set of parameters at any point should in the best way fit the experimental values τ_{eff} simultaneously for all depths of excitation. The τ_{eff} for nonimplanted sample

decreases with diminishing of d_{eff} . This means that the influence of the surface recombination on the integral parameter increases with decreasing effective thickness. For the bulk excitation (λ_1), when d_{eff} coincides with the wafer thickness d , and the thickness of implanted layer d_1 is negligibly small with respect to d_{eff} , τ_{eff} is independent on implantation dose within the error limits. A dependence of τ_{eff} on dose is only revealed, as should be expected, for inhomogeneous excitation ($d_{\text{eff}} < d$). τ_{eff} decreases with increasing the dose, and it increases with respect to previous τ_{eff} values, when the dose exceeds the value $\Pi = 5 \cdot 10^{15} \text{ cm}^{-2}$. The largest relative variation of τ_{eff} is revealed for the surface excitation (λ_4 , $d_{\text{eff}4}$). Non-monotonicity of the dose dependence $\tau_{\text{eff}}(\Pi)$ is caused by defects formation accompanied by competition between recombination and diffusion processes.

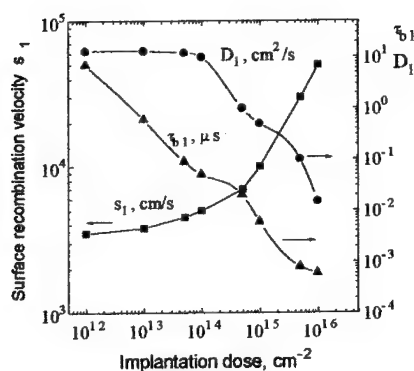


Fig. 2. Recombination parameters in implanted layer vs. implantation dose

The dependence of parameters τ_1 , s_1 , D_1 on the implantation dose has been determined from the best fit of the computed and experimental values of $\tau_{\text{eff}}(\lambda)$ (Fig. 2). The bulk lifetime in the implanted layer decreases by four orders of magnitude at $\Pi = 10^{16} \text{ cm}^{-2}$ with respect to the initial value. Approximately the linear variation of τ_1^{-1} vs. Π points to the relationship $\tau_1^{-1} \propto N_b$, where

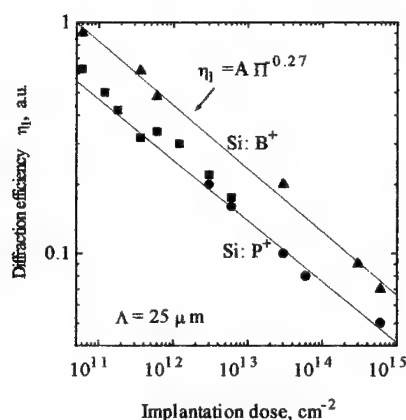


Fig.3. Diffraction efficiency, normalized to one before implantation, vs. implantation dose

N_i is a concentration of recombination centers. The diffusion constant D_1 and the surface recombination velocity s_1 vary non-linearly with dose. Significant variation is revealed for D_1 at $\Pi_{D1} \geq 10^{14} \text{ cm}^{-2}$ and for s_1 at $\Pi_{s1} \geq 10^{15} \text{ cm}^{-2}$. The obtained values $\Pi_{s,D}$ of accelerated variation of s, D correspond to the range of critical doses of amorphization in Si:Ar⁺. Complete amorphization of the implanted layer at $\Pi \geq 5 \cdot 10^{15} \text{ cm}^{-2}$ slows down the diffusion process to such a degree that τ_{eff} rises with further increasing of the implantation dose. Non-linear behavior of s_1, D_1 for $\Pi \geq 10^{14} \text{ cm}^{-2}$ points to the complexity of defect formation process, i.e. surface defects act as separate recombination centers slightly affecting s at $\Pi < 10^{14} \text{ cm}^{-2}$, but with increase of their concentration the complexes are formed causing nonlinear variation of s_1, D_1 in the range $\Pi = 10^{14} - 10^{16} \text{ cm}^{-2}$.

At higher doses of implantation the

recombination parameters should not change, because sputtering of the material takes place simultaneously with the generation of defects. Therefore, if the dose is increased due to the prolonged radiation, the recombination parameters saturate or weakly depend on the dose due to decrease of implanted layer thickness d_1 .

TG technique revealed the decrease of η_i in P⁺ or B⁺ implanted Si wafers starting from doses as low as 10^{10} cm^{-2} . The sensitivity for implanted dose can be approximated by power law dependence $\eta_i = A \cdot \Pi^{-0.27}$, (see Fig. 3), valid up to $\Pi = 6 \cdot 10^{14} \text{ cm}^{-2}$ in the range of ion energies from 20 to 120 keV. The coefficient A varied from 0.27 (B⁺) to 0.17 (P⁺) and reached its lower value for heavier ions, as As⁺, In⁺ or Tl⁺. Time resolved measurements of η_i revealed faster recombination times and lower diffusion coefficients, both for carriers and thermal one D_T , e.g. $\tau_{\text{eff}} = 100 \text{ ps}$, $D = 2 \text{ cm}^2/\text{s}$, $D_T = 0.65 \text{ cm}^2/\text{s}$ for case of P⁺ and $\Pi = 10^{13} \text{ cm}^{-2}$, $E = 100 \text{ keV}$ [2]. It was found that after the implantation dose approaches the threshold of amorphization, then $\eta_i \propto \Pi^{-1}$. The comparison of optical and photoelectrical properties have shown the existence of electrically active defects in the depth up to $1.3 \mu\text{m}$, essentially exceeding the projected mean range of implanted ions [3]. The TG technique also revealed a correlation between the photoelectric and elastic properties during the annealing of implanted Si wafers, which was attributed to interaction of dislocations and radiation-induced defects [4].

CONCLUSIONS

The performed theoretical and experimental studies of recombination processes in implanted Si structures show that a modified technique of light induced absorption of infrared and microwave radiation as well as transient grating technique allows one to determine parameters of implanted layers in non-destructive way. The change of excitation depth by varying the wavelength of light sources permits to measure recombination parameters. The variation of asymptotic lifetime of excess carriers in ion-implanted structures is due to simultaneous changes of bulk and surface recombination parameters, while a non-monotonic dependence of τ_{eff} vs. dose is determined by competition and redistribution of recombination flows at nonhomogeneous excitation. Power-law dependence of diffraction efficiency on implantation dose in Si:P⁺ and Si:B⁺ enables to determine low implantation doses by contactless transient grating technique and to study process of thermal annealing.

REFERENCES

1. J.Vaitkus, E.Gaubas, A.Kaniava, Lith.Phys.J. **32**, 434 (1992).
2. L.Jonikas, K.Jarašiūnas, J.Vaitkus, Phys. Stat. Sol. (a), **112**, 375 (1989).
3. J.Vaitkus, E.Gaubas, K.Jarašiūnas, M.Petrauskas, Semicond. Sci. Technol. **7**, A131 (1992).
4. N.Kvasov, L.Jonikas, K.Jarašiūnas, Sov. Phys. Semicond. **22**, 508 (1988).

PECULIARITIES OF DETERMINATION OF RECOMBINATION PARAMETERS AT MODERATE AND HIGH EXCITATION LEVELS IN SILICON WAFERS

E. GAUBAS, A. KANIAVA

Vilnius university, Department of Physics, Sauletekio 10, 2054 Vilnius, Lithuania

INTRODUCTION

Carrier lifetime is the most sensitive parameter to characterize defect structure of material. Simultaneous and reconcilable determination of integral parameters such as carrier lifetime, surface recombination rate, and concentration of local centers becomes very important for a technological monitoring of material quality. Consequently, development of nondestructive measurement techniques and computation algorithms is desired.

There are some well-known contactless techniques to determine carrier bulk lifetime, surface recombination rate based on the measurements of carrier decay [1-3]. These methods can be easily applied at low injection levels in the material with low defect concentration, when carrier lifetime is short or surfaces of wafer are passivated well. However, the parameters of wafer and sensitivity of the instrument determine the excitation level necessary to perform reliable measurements. On the other hand, investigations of the dependence of the recombination parameters on excitation level significantly enlarge the opportunities of detailed consideration of the problem. As a rule, the recombination parameters at moderate and high injection levels are dependent on carrier concentration and, consequently, the decay processes are nonlinear. In these cases no analytical solution can be found, and the numerical simulation of continuity equations is only possible. To minimize the number of uncertain parameters and to obtain the data with the lowest number of iterations, the reconcilable computer simulation procedures and experimental measurements are necessary. Thus, peculiarities of the determination of recombination parameters give rise, which are not encountered in well-known paradigm of separate measurements of surface and bulk recombination through asymptotic relaxation time of linear recombination.

In this work a few of experimental and computer simulation problems are discussed on the basis of the performed investigations on various batches of Si wafers. The instantaneous decay time is considered as the parameter of the first approximation for different type of nonlinearities. Algorithms and determined parameters are briefly discussed.

EXPERIMENTAL LIMITATIONS

The measurements of the excess carrier decay characteristics were performed by well-known pulse excitation/cw probe mode. The solid state and dye lasers as well as LED pulse radiation with discrete wavelengths λ in the range of 0.53-1.06 μm were used as excitation light sources. Pulse duration was in the range of $\tau_L = 10\text{-}100$ ns to satisfy the approximation of δ -pulse. The absolute values of excess carriers concentration must be measured for the consideration of nonlinear processes. The calibrated measurements of the light energy density per pulse are necessary. Due to experimental uncertainties the errors of these measurements may exceed 20%. On the other hand, to evaluate light induced carrier concentration (Δn) the data of the recombination parameters are necessary for more precise determination of Δn . Thus, the absolute values of Δn are obtained by the iteration procedure.

For the probe either the infrared (IR) radiation of cw He-Ne ($\lambda=1.15 \mu\text{m}$) laser or microwaves (MW) of 10 and 21 GHz were used. The response U of IR absorption by free carriers may be presented as follows:

$$U = k[(1-R) I_p \exp(-\sigma_\lambda n_0 d) (1 - \exp(-\sigma_\lambda \Delta n d)) - I_n] \quad (1)$$

Here I_p is the intensity of probe radiation, I_n is intensity of noises, d - wafer thickness, R - reflection coefficient, n_0 , p_0 are concentrations of equilibrium electrons and holes and Δn , Δp of excess ones, and σ_λ is effective cross-section of absorption by free carriers at probe wavelength λ . Coefficient k is the transfer function of optical/electrical signal of detector. Injection level is defined by parameter $\beta = (\Delta n + \Delta p) / (n_0 + p_0)$.

To enhance the sensitivity and dynamic range of instrument the intensity of the probe I_p is desired to be large. Although, the upper limit of I_p is restricted by the condition of the probe mode (i.e. $\Delta n_p / \Delta n_{ex} < 1$) and by the requirement to avoid heating of material. The preselection and statistical processing of data are necessary to minimize the noises I_n . The optimum of response for the sample with certain resistivity and thickness can be obtained at $\sigma_\lambda n_0 d = \ln(1+\beta)/\beta$, and for $\sigma_\lambda n_0 d > 1$ the only compromise is to enlarge I_p . In other cases U decreases to kI_n . In our experiments the measurements are reliable for wafers ($d \geq 300 \mu\text{m}$) with resistivity of $>0.05 \Omega\text{cm}$ for IR and $>2 \Omega\text{cm}$ for MW probe, respectively. Most of experimental restrictions for MW probe are similar to that of mentioned above for IR one.

MODELS AND ALGORITHMS

Most general model necessary for determination of recombination parameters including nonlinear recombination is based on solution of the system of one-dimensional continuity equations (separate for electrons $n = n_0 + \Delta n$ and holes $p = p_0 + \Delta p$):

$$\partial n / \partial t = D_n \partial^2 n / \partial x^2 - n / \tau_n - n / \tau_q + q / \tau_g - \gamma_j n^j \quad (a)$$

$$\partial q / \partial t = n / \tau_q - q / \tau_g \quad (b)$$

$$\partial n / \partial x \big|_{x=0, d} = \pm s_{0, d} n / D_n \quad (c) \quad (2)$$

$$n \big|_{t=0} = n_0 f(x), q \big|_{t=0} = q_0 \quad (d)$$

$$q + n = r + p \quad (e)$$

with boundary (c) and initial (d) conditions. Here the equations for electrons are presented, and the same equations must be added for holes by replacing $p \rightarrow n$, $r \rightarrow q$. These equations are conjugated by neutrality equation (e). The denotes are typical: τ_n , τ_q , τ_g are carrier lifetimes respectively to recombination, trapping and thermal generation, γ_j are coefficients of nonlinear Auger type recombination, $j = 2, 3, \dots$, q is concentration of trapped carriers. This system must be solved numerically, when trapping effect is significant. Experimental selection of the dominant processes as well as their parameters at fixed range of injection levels β is necessary. Recombination processes are described by the unified ($n=p$) equation (a) and unified instantaneous time τ_M if trapping can be neglected. The latter τ_M may characterize the bulk recombination τ_b in the case of homogeneous distribution of recombination defects.

Impact of surface recombination

Excess carrier concentration, averaged over the wafer thickness, is expressed by analytical solution of unified linear continuity equation as a series of space frequency v_m constituents: $\langle n \rangle_d = n_0 \sum_{m=1}^{\infty} A_m \exp(-(v_m^2 D + \tau_b^{-1}) t)$. The space frequency v_m is determined by transcendental equation:

$$\text{ctg } v_d = (Dv/(s_1 + s_2)) - s_1 s_2 / ((s_1 + s_2) Dv) \quad (3)$$

Transitional part of the decay kinetic, described by the sum of v_m constituents, is nonexponential due to different influence of higher space frequencies on various stages of relaxation process. The asymptotic relaxation time at exponential decay is traditionally measured to determine an impact of surface recombination. Space frequency v_1 determines the main surface constituent on relaxation time. The parameters of surface recombination can be determined when bulk lifetime τ_b is large and constant. Otherwise, τ_b can be separated, when impact of surface recombination is small. As an alternative to the surface passivation, the measurements of τ_{eff} at high injection level can be performed to characterize the same recombination centers by τ_{∞} of Shockley-Read-Hall (SRH) model, if $\tau_{\infty} < \tau_0$. In this case consideration of transcendental equation (3) is of paramount significance.

In the case of negligible surface recombination on one side of the wafer (e.g. $s_2 = 0$) the first constituent of eq.(3) right part remains only. In the latter case eq.(3) is transformed to reduced one: $\text{ctg } v_d = Dv/s_1 d$. The solution of reduced equation is governed either by surface recombination, when $D/s > d$, or by wafer thickness d when $d > D/s$. The one-direction diffusion to surface (s_1) appears if $s_2 = 0$. The solution of reduced equation $v_m d$ (which depends on the ratio $A = D/s_1 d$) can be approximated by functions: $F_1(Y) = [(15/2)(3Y+1)\{(1+4/5(3Y+1))^{1/2} - 1\}]^{1/2}$ for $m=1$ and $F_m(Y) = \pi(3Y/(3Y+1))\{[1+(4/[3Y^2(m-1)^2\pi^2])^{1/2} - 1]\}^{1/2}$ for $m \geq 2$. The cut-off angle $v_1 d$ (of the carrier concentration $n_0 \propto n_0 \cos v_1 d$ on the wafer surface in the stationarized case or at virtual boundary where opposite flows of carriers are quasistationarized for $v_m d$ within distances $v_m^{-1} = \sqrt{Dt}$) is expressed as follows: $v_1 d = F_1(A)$, when $A > 0.04$, and $F_1 \approx A^{-1/2}$ for $A \rightarrow \infty$, $s \rightarrow 0$; $v_1 d = (\pi - F_1(A^{-1})/2)$, when $A \leq 0.04$, and $F_1(A^{-1}) \approx A^{1/2}$ for $A \rightarrow 0$; $v_m d = (m-1)\pi + F_m(A)$, when $A > 0.1$, and $F_m(A) \rightarrow 0$ for $A, m \rightarrow \infty$; $v_m d = (m-0.5)\pi - F_m(A^{-1})$, when $A < 0.1$, and $F_m(A^{-1}) \rightarrow 0$ for $m \rightarrow \infty$. It can be noticed that $v_1 d$ decreases to zero when ratio A infinitely increases due to $s \rightarrow 0$, and it increases to $\pi/2$ when $A \rightarrow 0$ due to $s \rightarrow \infty$. The $v_1 d = \pi/2$ is the limit value for one-directional diffusion to surface. The higher the mode number m , the faster approach of $v_m d$ to its limit value of $m\pi$ is achieved. This latter is characteristic to exact solution of continuity equation with boundary conditions $s_1 = s_2 = \infty$.

For widely used approximation of equal surface recombination rates $s_1 = s_2$, the transcendental equation (3) can be easily transformed to reduced one when wafer thickness d is changed to $d/2$: i.e. two-directional task due to its symmetry is replaced by consideration of one-directional diffusion. The main features are also described by functions F_1 , F_m . Although, for two-dimensional case total range of $v_1 d$ values is $0 \leq v_1 d \leq \pi$ respectively to that of one-directional diffusion ($0 - \pi/2$). It is important to point out, that space frequency v_m , which characterize the carrier decay time, is determined by both the ratio A and the thickness d .

In the case of asymmetry of surface recombination rates, e.g. $s_1 > s_2$, solution of eq.(3) can be approximated by reduced one, when $D/(s_1 + s_2) \gg d$ and $d\sqrt{s_1 s_2}/D < \pi/2$. Then it can also be described by function F_1 . For asymmetric case the maximum of the stationarized excess carrier concentration must be shifted to slower surface recombination side when $d\sqrt{s_1 s_2}/D \leq \pi/2$. It can be

postulated that $d_1/d_2 = s_1/s_2$ and $d_1 + d_2 = d$, where the distances d_1 and d_2 define the position of maximum from surfaces of wafer. In this situation eq.(3) can be transformed as follows: $\text{ctg} \nu d = [D \nu d / s_1 d_1] (d_1/d)^2 - [s_1(d-d_1)/D \nu d]$. Its solution can be expressed by the function $F_3(Y_1, Y_2) = \{(15/2)(3Y_1+1)[<1+4(Y_2+1)/5(3Y_1+1)^2>^{1/2} - 1]\}^{1/2}$ and the reduced ratios $A_1 = (D/s_1 d_1)(d_1/d)^2$, $A_2^{-1} = (D/s_1(d-d_1))$. The cut-off angle can be expressed by function F_3 with different arguments: $\nu_1 d = F_3(A_1, A_2)$, when $Q = d \sqrt{s_1 s_2} / D < 1$; $\nu_1 d = \pi/2 - F_3(A_1^{-1}, A_2^{-1})$ for $Q \leq \pi/2$. Thus, the space frequency for stationarized carrier distribution can be obtained as follows $\nu_1 = (s_1/d_1 D)^{1/2}$ for $Q < 1$. The effective distance d_1 can be determined either by measuring of probing depth in the reflection mode for which the saturation of averaged concentration is achieved or by perpendicular scanning of the concentration profile by method proposed in [2]. When d_1 is determined and value of ν_1 is obtained from τ_{eff} , velocity of surface recombination s_1 can be calculated. Afterwards s_2 can be determined through s_1, d_1 .

Nonlinearities of SRH type and Auger bulk recombination

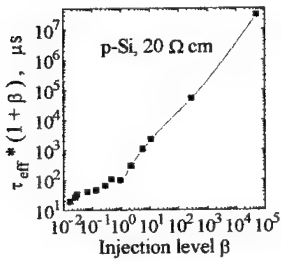


Fig.1. Asymptotic lifetime vs. injection level

dependence $\tau_{M \text{ SRH}}(1 + \beta) = f(\beta)$. The τ_0 and τ_∞ can be obtained from this linear dependence, and SRH model cannot be applied, when this characteristic is nonlinear. The illustration of such nonlinearity for p-Si 20 Ωcm wafer are shown in Fig.1. Thus, experimentally measured and approximated by exponent asymptotic time τ_{eff} represents the parameter τ_M , which changes with β and is in the range between τ_0 and τ_∞ . The activation energy of the recombination defects can be found by measurements of $\tau_{M \text{ SRH}}$ dependence on temperature, when $\tau_0 \geq \beta \tau_\infty$ and carrier generation from impurities is saturated. The $\tau_{\text{eff}}(T)$ will be distorted by $\beta(T)$ changes in other cases.

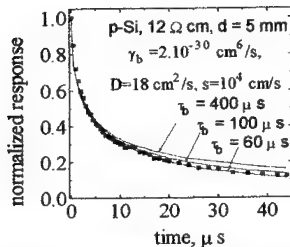


Fig.2. Nonlinear recombination decay

At moderate injection levels $\beta \geq 1$ even in the case of recombination via single level with small concentration of centers the instantaneous relaxation time τ_M depends on excess carrier concentration: $\tau_{M \text{ SRH}} = (\tau_0 + \beta \tau_\infty) / (1 + \beta)$. Consequently, the decay process is nonexponential. Here τ_0 is recombination time at low injection level, which contains dependence on temperature as well as activation energy of center. The high injection level time τ_∞ is independent on temperature. The validity of well-known SRH model can be estimated by linearity of

It seems attractive to perform measurements at $\beta \gg 1$ to avoid the instantaneous time $\tau_{M \text{ SRH}}$ dependence on the excess carrier concentration. Then τ_∞ is only determined by the defect concentration and their capture cross-section. Excess carrier concentrations, necessary to fulfill the condition $\beta \gg 1$ for Si of resistivity $\leq 20 \Omega \text{cm}$, are $\Delta n \geq 10^{16} \text{cm}^{-3}$. The impurity assisted ($\gamma_i = \gamma_2$) and band to band ($\gamma_b = \gamma_3$) recombination is essential [3] for this excitation level β . These nonlinear processes can be characterized by instantaneous lifetime: $\tau_{MA} = (\gamma_i \Delta n + \gamma_b \Delta n^2)^{-1}$. The

calculated and experimental decay curves at the presence of Auger recombination are presented in Fig.2.

Trapping effects

Another reason of discrepancy from the linear characteristic of $\tau_{M\text{ SRH}} = f(\beta)$ is a trapping effect. It may be caused either by the large concentration of defects M or by simultaneous action of numerous recombination levels. The main feature of this process is inequality of concentrations of excess electrons and holes ($\Delta n \neq \Delta p$) [4,5]. Asymptotic time will be determined by the longest of partial times (τ_n, τ_p). As a rule carriers of one type are trapped, and their lifetime is the smallest. At the presence of trapping the recombination process cannot be characterized by unified time for both type carriers. Inequality of lifetimes and concentrations of excess carriers leads to concentration dependent diffusion coefficient [4]: $D = (n+p)/((n/D_p) + (p/D_n))$.

Trapping is a pure transient phenomenon. It gives complementary information about the defects in material. Trapping disappears in the case of stationary excitation due to compensation of the flows of capture/thermal activation. Consequently, additional steady state illumination (AI) can efficiently compensate these flows, and it considerably changes the decay characteristics. A large variety of trapping point defects (slow as well as fast) is known [5]. Instantaneous time for the latter ones can be expressed as follows: $\tau_{Mtr} = \tau_n(1 + MN_{CM}/(n + N_{CM})^2)$. Here τ_n is lifetime of trapped carriers, M is concentration of traps, N_{CM} is effective density of states. Instantaneous time saturates, when $n \rightarrow 0$, and the trapping effect vanishes, when n is large. Thus, trapping coefficient $K = M/N_{CM}$ can be found from τ_{eff} changes with excitation (or calibration of AI) at $n \rightarrow 0$, and τ_{eff}/τ_n variation with temperature enables to obtain E_M . The most important feature of above analyzed trapping is decreasing of τ_{Mtr} with increasing of excess carrier concentration as well as with steady state additional illumination (Fig.3. NTD Si).

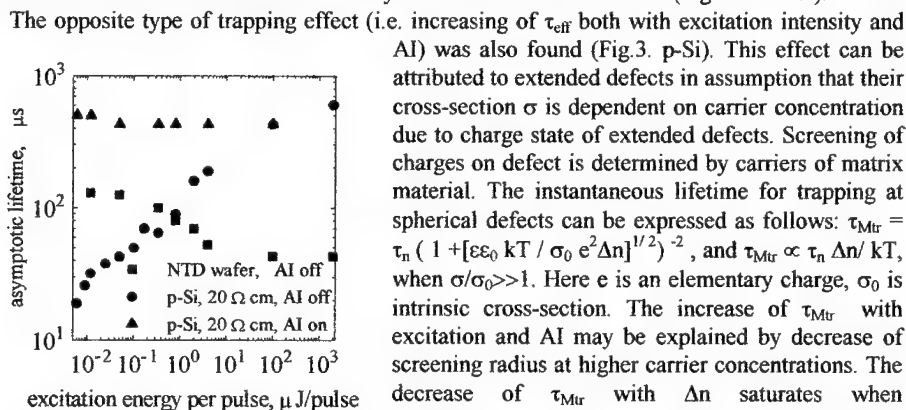


Fig.3. Asymptotic lifetime vs. excitation intensity

The opposite type of trapping effect (i.e. increasing of τ_{eff} both with excitation intensity and AI) was also found (Fig.3. p-Si). This effect can be attributed to extended defects in assumption that their cross-section σ is dependent on carrier concentration due to charge state of extended defects. Screening of charges on defect is determined by carriers of matrix material. The instantaneous lifetime for trapping at spherical defects can be expressed as follows: $\tau_{Mtr} = \tau_n(1 + [\epsilon\epsilon_0 kT / \sigma_0 e^2 \Delta n]^{1/2})^{-2}$, and $\tau_{Mtr} \propto \tau_n \Delta n / kT$, when $\sigma/\sigma_0 \gg 1$. Here e is an elementary charge, σ_0 is intrinsic cross-section. The increase of τ_{Mtr} with excitation and AI may be explained by decrease of screening radius at higher carrier concentrations. The decrease of τ_{Mtr} with Δn saturates when recombination efficiency of other centers is achieved, and it increases with Δn until cross-section decreases to geometrical one of extended defect. The geometrical cross-section σ_0 was evaluated to be of order $10^{-10} - 10^{-8} \text{ cm}^2$ by this model from $\tau_{Mtr}(\Delta n)$.

Algorithms and determined parameters

Table I. Recombination parameters of Si wafers

Wafers	s, cm/s	τ_b , μ s	D, cm ² /s	γ_b , cm ⁶ /s	M; E _M
p-Si, 12 Ω cm	10 ⁴	70	18	2 10 ⁻³⁰	
n-Si(NTD) oxidized etched	600 3600	227	8 13		10 ¹⁵ cm ⁻³ 0.28 eV

The simultaneous determination of the set of recombination parameters is based on the adjustment of experimental and calculated characteristics obtained by the least squares method. Either the asymptotic and instantaneous decay times

in transitional part or whole decay kinetic is adjusted to experimental data. Respectively, either functional $\sum_{i=1}^4 (\tau_M^{\text{calc}} - \tau_M^{\text{exp}})^2$ or functional $\sum_{i=1}^{250} (n^{\text{calc}} - n^{\text{exp}})^2$ is considered. The result of the procedure of adjustment significantly depends on the starting set of parameters. This set and the range of their possible changes is selected by experimental data of instantaneous time τ_M^{exp} and decay characteristic shape. The adjustment procedure is canceled, when absolute minimum of functional or boundary values of parameters is achieved. In the latter case the result (set of parameters) is used as start data for the next iteration, and/or algorithm is extended by including of additional models. Complementary experiments are performed in this situation.

The analytical solutions of bipolar continuity equation are used to determine surface and bulk recombination parameters. To account Auger type recombination excess carrier concentration decay is numerically simulated by method of finite elements. Results obtained by these procedures for p-Si, 12 Ω cm are presented in Table I. Coefficient of Auger process was found to be: $\gamma_b = 2 \cdot 10^{-30} \text{ cm}^6 \text{ s}^{-1}$, and set of recombination parameters s, τ_b and D were obtained for p-Si, $\beta \approx 100$. The set of recombination parameters at $\beta \geq 10$ and the parameters of traps determined from lifetime temperature dependence at different excitation levels for NTD Si are also presented in Table I.

CONCLUSIONS

The nonlinearities of recombination processes (SRH type recombination within the bulk and on surfaces, Auger type recombination or trapping) must be accounted in the analysis of recombination processes at moderate and high level of excitation. Reconcilable experimental measurements and numerical simulations are necessary to develop reliable algorithms for the simultaneous determination of recombination parameters. Recombination parameters obtained by these investigations are in agreement with analogous ones measured by other methods. Complex experimental investigation is necessary to minimize variables in the algorithms.

REFERENCES

1. K.L.Luke, L.J.Cheng, J.Appl.Phys. **61**, 2282 (1987).
2. J.Waldmeyer, J.Appl.Phys. **63**, 1977 (1988).
3. V.Grivickas, E.Gaubas, A.Kaniava et al., Lith.Journ.Phys. **32**, 307 (1992).
4. J.S.Blakemore. Semiconductor statistics. (Pergamon Press, 1962), Ch.8.
5. S.M.Ryvkin. Photoelectric effects in semiconductors (Consultants Bureau, New York, 1964), Ch.6.

APPLICATION OF ELASTIC MID-IR-LASER-LIGHT SCATTERING FOR NON-DESTRUCTIVE INSPECTION IN MICROELECTRONICS

VICTOR P. KALINUSHKIN*, VLADIMIR A. YURYEV*, OLEG V. ASTAFIEV*,
ALEXANDER N. BUZYNNIN*, AND NIKOLAY I. BLETSKAN**

*General Physics Institute of RAS, 38 Vavilov Street, Moscow, 117942, Russia

**Research and Production Association ELMA, Zelenograd, Moscow, 103482, Russia

ABSTRACT

Some possible applications of the low-angle mid-IR-light scattering technique and some recently developed on its basis methods for non-destructive inspection and investigation of semiconductor materials and structures are discussed in the paper. The conclusion is made that the techniques in question might be very useful for solving a large number of problems regarding defect investigations and quality monitoring both in research laboratories and the industry of microelectronics.

INTRODUCTION

Over 15 years, the method of low-angle mid-IR-light scattering (LALS) have been actively used by us for investigation of the large-scale electrically-active defect accumulations (LSDAs) in semiconductors (see e.g. Refs.[1–15] and references cited therein). We shall consider below some possible applications of LALS and techniques recently developed on its basis for solving some specific problems of material and structure testing in microelectronics.

BRIEF DESCRIPTION

For the beginning let us briefly remind the basic principles of LALS. This method is founded on elastic scattering of IR light by inhomogeneities of semiconductor crystals—like the method of laser tomography,—but in LALS, as distinct from the laser tomography, the scattering at relatively low angles is registered—from about 2° to less than 15° in crystal—and light with large wavelength is used as a probe emission—routinely the radiation of CO_2 - or CO-lasers with the wavelength of $10.6\ \mu\text{m}$ and $5.4\ \mu\text{m}$, respectively, is applied. Application of mid-IR-light makes the technique sensitive to the presence of domains with enhanced concentration of free carrier or changed conductance type (FCAs) and measuring in the above interval of angles allows one to observe defects with the sizes from several microns to several dozens of microns.^{1,2,9,11} (Writing FCAs we mean both manmade domains with changed carrier concentration or conductance type—e.g. doped domains of semiconductor structures—and natural LSDAs which always are FCAs.)

A number of procedures has been developed, which enable the distinguishing of the scattering by FCAs from that by different defects. These procedures consist in the investigation of the light scattering with different wavelengths or measuring the dependencies of the light scattering intensity on sample temperature.^{9,12,14,15} In addition, the latter procedure and the investigation of the influence of photoexcitation on light scattering intensity allows one to

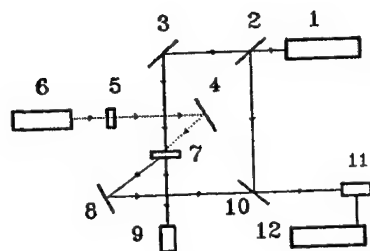


Figure 1: Optical diagram of angle-resolved LALS: (1) mid-IR-laser; (2,10) semitransparent mirrors; (3,4) mirrors; (5) filters; (6) exciting laser (used in LALS with photoexcitation); (7) sample; (8) movable mirror; (9,11) photoreceivers; (12) computer.

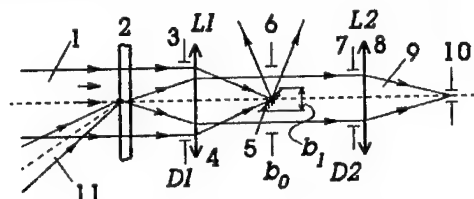


Figure 2: Optical diagram of the SLALS microscope: (1) mid-IR probe wave; (2) sample; (3,6,7) diaphragms; (4,8) lenses; (5) mirror or opaque screen; (9) scattered wave; (10) IR photodetector; (11) exciting light beam (used in OLALS).

determine thermal and optical activation energies of point centers in LSDAs.^{9,12} Moreover, LALS allows one to investigate large-scale recombination-active defects (LSRDs) and large-scale gluing centers (LSGCs) discriminating between those in near-surface layers—including epilayers—and those in substrate bulk: the former are studied by use of the surface optical excitation,¹⁶ while the latter are observed using the volume photoexcitation.^{1,8,10} (Typical examples of LSRDs are such defects as grain boundaries, dislocations, swirls, precipitates, their clusters and aggregations of recombination point centers.)

Presently, the two following schemes of LALS are developed. One of them—the conventional LALS or LALS with angular resolution—registers light scattered by all defects which are situated within the probe beam,^{2,10,12} see Fig.1. In the other—in scanning LALS microscopy or SLALS, which is a kind of the scanning laser microscopy,—every singular defects are visualized,^{17–20} see Fig.2. By combining these two schemes, one can determine concentration of defects, their spatial distribution, and hence, one can estimate the value of deviation of their dielectric constants from those of crystal bulk outside them $\Delta\epsilon$ (in the case of FCAs—and, as mentioned above, LSDAs always are FCAs,—the concentrations of free carriers in them, Δn , can be evaluated).^{9,10,14,15}

The LALS technique is of high sensitivity, it allows one to observe defects with the variation of dielectric constant $\Delta\epsilon$ down to 10^{-5} – 10^{-4} —i.e. with Δn down to 10^{13} cm⁻³. LALS is non-destructive and contactless, it has no limitations on the tested wafer diameter.

INDUSTRIAL AND LABORATORY APPLICATIONS

Let us dwell on some possible specific applications of LALS as the checking technique in the field of the industrial microelectronics.

Inspection of semiconductor wafer homogeneity

As mentioned above, LALS enables the observation of LSDAs with the sizes from several μm to several tens μm with point detect concentration in each of them down to 10^{13} cm^{-3} . This method permits the investigation of the LSDA composition and the influence of various thermal treatments and operations of an industrial technological cycle on them. Wafer mapping is possible by means of SLALS. Incoming control with posterior utilization of substrates in the production process and technological step checking by using free chips are also possible.

These techniques are well developed now and a prototype of the instrument is available.

Fig.3 demonstrates the images of LSDAs in different bulk semiconductors obtained with the SLALS microscope ($1 \times 1 \text{ mm}^2$ areas are presented). The microphotographs of LEC undoped InP (a), LEC InP:Fe (b), LEC SI GaAs annealed at 900°C in a sealed quartz ampule when produced (c), CZ Si:B with high (d) and low (e) epd, and CZ Si:B coated with 1200 \AA thick SiO_2 layer (f) are presented. White spots are the images of LSDAs. One can find more details on these pictures in Refs.[18-21].

The disadvantage of LALS (and SLALS) is its inability to discriminate between LSDAs situated in crystal bulk and ones located in near-surface layer. To remove this shortcoming, LALS tomography with longitudinal resolution down to $10\text{--}20 \mu\text{m}$ is now under development on the basis of SLALS. The solution of the problem does not seem to meet any difficulties. Its successful solving would enable the testing of homogeneity of "working" near-surface layers of wafers and epitaxial layers. Note that layer inspection is possible even if it is under coating or under other layer — up to the stage of metallization. For instance, the homogeneity of a silicon wafer under oxide layer may be checked — Fig.3(f) — as well as its near-surface layer.

Inspection of presence of LARDs in near-surface, near-interface and epitaxial layers

The methods of optical beam induced LALS (OLALS) and LALS with optical pumping,¹⁶ which may be used for such inspections, are the optical analogs of such well-known methods as EBIC and OBIC, yet they require neither Schottky barrier or $p\text{--}n$ junction nor complicated sample preparation. Like in the above case, a significant advantage of these techniques is their ability to test multilayer structures including layers covered with other layers. Also there are no limitations on sample size and resistivity in LALS. So wafer mapping, all-round incoming and step control with subsequent utilization of substrates in production cycle are possible.

Control of LSRDs in the substrate volume, including tomography, is also possible, but this is likely of interest for the production of γ -ray detectors, whose resolution is determined by LSDAs and LSRDs,¹⁰ various nuclear-ray counters, volume photodetectors, etc.

As of now, a cycle of experiments has been carried out, which have shown the possibilities of these methods.^{8,10,16,19,20}

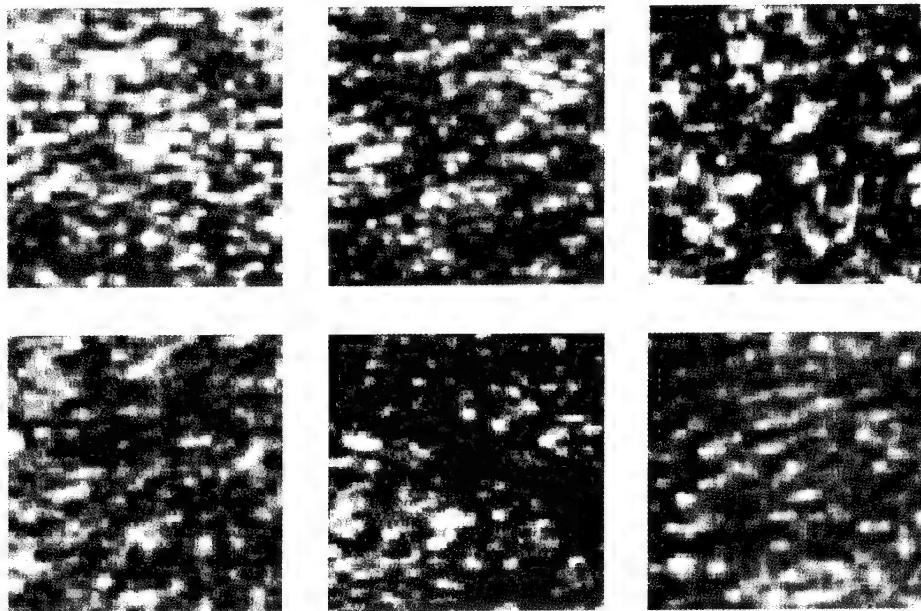


Figure 3: SLALS images of LSDAs in semiconducting wafers; the first row (left to right): undoped LEC InP (a); LEC InP:Fe (b); LEC SI GaAs annealed at 900°C (c); the second row (left to right): CZ Si:B, $\rho = 12 \Omega \text{ cm}$, high epd (d); CZ Si:B, $\rho = 12 \Omega \text{ cm}$, low epd (e); CZ Si:B (different establishment) under 1200 Å thick SiO₂ layer (f); $1 \times 1 \text{ mm}^2$, $\lambda_{sc} = 10.6 \mu\text{m}$. Amplification factors are equal in the following pairs of pictures: (a) and (b), (d) and (e). White spots in the photographs are the images of LSDAs.

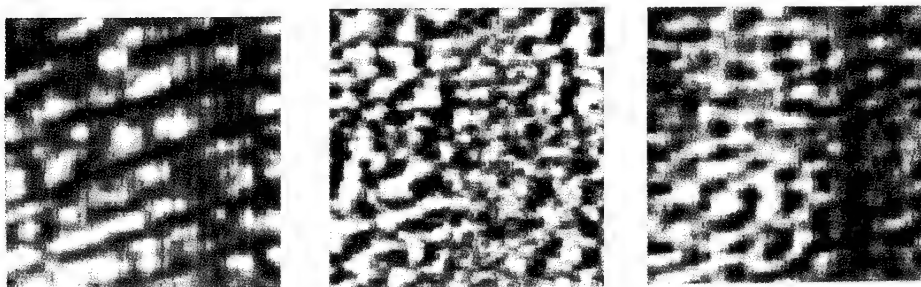


Figure 4: OLALS microphotographs of Si wafers, defects in near-surface layers (left to right): FZ Si:P, chemico-dynamic polishing (a); FZ Si:P, mechanical polishing (b); CZ Si:B under 1200 Å thick SiO₂ layer (c)—the same region as that given in Fig.3(f); $1 \times 1 \text{ mm}^2$, $\lambda_{sc} = 10.6 \mu\text{m}$, $\lambda_{ex} = 633 \text{ nm}$. Amplification factor in picture (b) is by 100 times greater than in picture (a), and that in picture (c) is by 10 times greater than in picture (a). The brighter image, the longer the non-equilibrium carrier effective lifetime is. The dark areas are the images of defective regions.

Fig.4 demonstrates the microphotographs of near-surface regions of Si wafers subjected to different polishing and oxidation procedures ($1 \times 1 \text{ mm}^2$ areas are presented). The images of FZ Si:P wafers after chemico-dynamic (a) and mechanical (b) polishing procedures, and the image of CZ Si:B wafer coated with 1200 Å thick SiO_2 layer (c) are given in this figure. The darker image, the shorter non-equilibrium carrier effective lifetime is. The focused 633-nm-wavelength radiation of 55-mW He-Ne laser was used in this experiment for electron-hole pairs photoexcitation in near-surface layers (see Fig.2).

Testing of specially doped areas

LALS may be also used for the inspection of such parameters of specially doped domains of semiconductor structures as their sizes, concentration of free carrier in them and surface resistance. The inspection of these parameters is also possible even after different layers are grown and coatings are given (until metallized). The domains with the sizes greater than $1 \text{ }\mu\text{m}$ and the variation of free carrier concentration greater than 10^{13} cm^{-3} can be tested. Nowadays, the development of a prototype of such instrument is being in the final stage.

Inspection of gettering process efficiency

We would like to specially emphasize that the above techniques might be very useful for the inspection of the gettering processes efficiency.²²

The presence of the gettering precipitates at the internal gettering process can be checked by OLALS or LALS with quasi-bulk photoexcitation. The presence and parameters of impurity atmospheres around the gettering precipitates can be checked by the conventional (angle-resolved) LALS and SLALS microscopy. The "working layer" may be tested by OLALS or LALS with surface photoexcitation.

The inspection of efficiency of the external gettering and gettering by implanted domains is also possible by the LALS-based techniques. The procedures proposed for these inspections are analogous to those described above for the internal gettering process.

CONCLUSION

So we can conclude that the LALS-based techniques might be a very effective non-destructive tool for solving a wide class of problems of materials and structures testing in modern microelectronics, which might be used both in laboratories and directly in the production cycle. We discussed only several most obvious possible applications of these techniques in this paper. We are sure, however, that they might find a great number of additional applications and be useful in many branches of microelectronics science and industry.

REFERENCES

1. V.V. Voronkov, T.M. Murina, G.I. Voronkova *et al.*, Fiz. Tverd. Tela **20**, 1365 (1978) [Sov. Phys. Solid State **20** (5), 1365 (1978)].
2. V.V. Voronkov, G.I. Voronkova, B.V. Zubov *et al.*, Fiz. Tverd. Tela **23** (1), 117 (1981)

- [Sov. Phys. Solid State, **23** (1), 65 (1981)].
3. V.V. Voronkov, G.I. Voronkova, V.N. Golovina *et al.*, J. Cryst. Growth **52**, 939 (1981).
 4. V.V. Voronkov, G.I. Voronkova, V.P. Kalinushkin *et al.*, Fiz. Tekh. Poluprovodn. **18** (12), 2222 (1984) [Sov. Phys. Semicond. **18** (12), 2222 (1984)].
 5. S.E. Zabolotskii, V.P. Kalinushkin, T.M. Murina *et al.*, Phys. Stat. Sol.(a) **88**, 539 (1985).
 6. N.V. Veselovskaya, V.V. Voronkov, G.I. Voronkova *et al.*, Fiz. Tverd. Tela **27** (5), 1331 (1985) [Sov. Phys. Solid State **27** (5), 1331 (1985)].
 7. A.V. Voronkova, V.P. Kalinushkin, T.M. Murina, and N.S. Sysoyeva Fiz. Tekh. Poluprovodn. **19** (10), 1902 (1985) [Sov. Phys. Semicond. **19** (10), 1902 (1985)].
 8. V.P. Kalinushkin, D.I. Murin, T.M. Murina *et al.*, Microelectronica **15** (6), 523 (1986) [Sov. Phys. Microelectronics **15** (6), 523 (1986)].
 9. S.E. Zabolotskii, V.P. Kalinushkin, D.I. Murin *et al.*, Fiz. Tekh. Poluprovodn. **21** (8), 1364 (1987) [Sov. Phys. Semicond. **21** (8), 1364 (1987)].
 10. Victor P. Kalinushkin, in *Proc. Inst. Gen. Phys. Acad. Sci. USSR, Vol.4, Laser Methods of Defect Investigations in Semiconductors and Dielectrics*, edited by A.A. Manenkov (Nova, New York, 1988) pp. 1-75.
 11. A.V. Batunina, V.V. Voronkov, G.I. Voronkova *et al.*, Fiz. Tekh. Poluprovodn. **22** (7), 1308 (1988) [Sov. Phys. Semicond. **22** (7), 1308 (1988)].
 12. V.V. Voronkov, V.P. Kalinushkin, D.I. Murin *et al.* J. Cryst. Growth **103**, 126-130 (1990).
 13. A.N. Buzynin, S.E. Zabolotskii, V.P. Kalinushkin *et al.*, Fiz. Tekh. Poluprovodn. **24** (2), 264 (1990) [Sov. Phys. Semicond. **24** (2), 264 (1990)].
 14. V.P. Kalinushkin, V.A. Yuryev, and D.I. Murin, Fiz. Tekh. Poluprovodn. **25**, 798 (1991) [Sov. Phys. Semicond. **25** (5), 798 (1991)].
 15. V.P. Kalinushkin, V.A. Yuryev, D.I. Murin, and M.G. Ploppa, Semicond. Sci. Technol. **7**, A255-A262 (1992).
 16. V.P. Kalinushkin, D.I. Murin, V.A. Yuryev *et al.*, in *Second International Symposium on Advanced Laser Technologies*, edited by V. Pustovoy and M. Jelínek, Proc. SPIE **2332**, 146-153 (1994).
 17. O.V. Astafiev, V.P. Kalinushkin, and V.A. Yuryev, in *Second International Symposium on Advanced Laser Technologies*, edited by V. Pustovoy and M. Jelínek, Proc. SPIE **2332**, 138-145 (1994).
 18. O.V. Astafiev, V.P. Kalinushkin, and V.A. Yuryev, Mater. Sci. Eng. B (submitted for publication).
 19. V.P. Kalinushkin, V.A. Yuryev, and O.V. Astafiev, presented at the First International Conference on Materials for Microelectronics, Barcelona, Spain, October 18-23, 1994 (Mater. Sci. Technol, 1995) (submitted for publication).
 20. O.V. Astafiev, V.P. Kalinushkin, and V.A. Yuryev, presented at the Ninth International Conference on Microscopy of Semiconducting Materials, Oxford, UK, March 20-23, 1995 (IOP Conf. Ser.) (submitted for publication).
 21. Vladimir A. Yuryev and Victor P. Kalinushkin, Mater. Sci. Eng. B (in the press).
 22. V.P. Kalinushkin, A.N. Buzynin, D.I. Murin, V.A. Yuryev, O.V. Astafiev, and A.I. Buvaltsev, presented at the First International Conference on Materials for Microelectronics, Barcelona, Spain, October 18-23, 1994 (unpublished).

Part VIII

**Ion Implantation and
Process-Induced Defects**

ACTIVATION OF IMPLANTED PHOSPHORUS IONS INTO SILICON BY FOLLOWED HYDROGEN ION IMPLANTATIONS

Y.HASEBE * ,H.OHSHIMA ** ,T.HATTORI * ,A.USAMI *** and Y.TOKUDA ***

* Research Laboratories,Nippondenso Co.,Ltd.,500-1 Komenoki,Nisshin,Aichi 470-01,Japan

** "Structure and function property",PRESTO,JRDC,5-9-4 Tokodai,Tsukuba 300-26,Japan

*** Department of Electronics,Aichi Institute of Technology,Yakusa,Toyota,Aichi470-03,
Japan

ABSTRACT

The activation of phosphorus implanted into n-type silicon (100) substrate by followed hydrogen ion(H^+) implantation was studied by means of spreading resistance technique(SR), secondary ion mass spectroscopy(SIMS) and transmission electron microscopy(TEM).

"The activation ratio" defined by carrier concentration divided by phosphorus concentration was used as a measure of activation of phosphorus. The H^+ energy, dose and dose rate dependence of activation ratio of phosphorus was investigated.

In the case of thermal annealing at 400 °C for 200 minutes the phosphorus atoms were not activated, on the other hand in the case of H^+ implantation at 400 °C the phosphorus atoms were activated and the activation ratio was increased almost proportionally with the dose. The SIMS data suggested that the depth profile of phosphorus atoms was not changed after activation by H^+ implantation. The activation ratio was increased with decreasing the dose rate. The TEM data suggested that the density of residual defects was reduced in the case of lower dose rate. The depth profile of activation ratio was similar to that of hydrogen atoms implanted at 20 °C. From these results the activation and recrystallization mechanism is discussed in the view of contribution of elastic collision process between H^+ ions and substrate atoms.

INTRODUCTION

In recent deep-submicron rule, electron devices need complex impurity profile in silicon substrate to avoid the short channel effect and so on. The temperatures in impurity doping processes become lower to reduce the broadening of the impurity profiles which induces short channel effect. For example Rapid Thermal Annealing(RTA)[1], solid state diffusion[2], laser-doping[3] or plasma-doping[4] have been investigated to form the ultra-shallow junction. For better device performance it is necessary to optimize impurity profile not only in near-surface region but also in bulk region. In bulk, it is difficult to optimize even if techniques mentioned above are used, because they are based on the impurity diffusion from surface. Especially it is difficult to form PMOS-type device. It is because of broadening of boron profile in activation. RTA is essentially a high temperature process, so the broadening cannot be avoided. The other techniques can be applied only to the near-surface region, so it is difficult to optimize the impurity profile in bulk region.

An energetic ion can deposit energy to nuclei or electrons directly at any depth. The nuclei are displaced from the initial lattice site and are diffused, electrons are excited to higher energy levels and the bond formation between substrate atoms can be enhanced. So ion implantation might have a possibility to activate an impurity atom in silicon substrate. Yoshinouchi et al.[5] investigated the activation of phosphorus in polycrystalline silicon film on SiO_2 which is induced by simultaneous

implantation of phosphorus ions and hydrogen ions. The sheet resistance of polycrystalline silicon film was reduced at a hydrogen ion dose over 10^{16} cm^{-2} . In their experiment as the simultaneous implantation was done, the role of hydrogen ions in activation of phosphorus was not clear. In order to clear the activation mechanism, we considered that two step implantation process should be done. At first step phosphorus ions were implanted, and at the second step the hydrogen ions (H^+) were implanted. In this way only the effects of H^+ ions irradiation can be extracted.

EXPERIMENTS

The substrate used was n-type silicon(100) wafer, which has a resistivity of between 8 and 12 $\text{ohm}\cdot\text{cm}$. We used a single crystalline silicon substrate to neglect the effects of grainboundaries, and investigated the activation at low temperature and the elimination of broadening in phosphorus profile with activation. 80keV phosphorus ions were implanted to a dose of $5 \times 10^{13} \text{ cm}^{-2}$ at 20 $^\circ\text{C}$, wafer was tilted by 7 degrees to the surface normal. H^+ ions are subsequently implanted at 400 $^\circ\text{C}$, the energy was ranging from 10 to 60keV, and the dose was ranging from 5×10^{14} to $3.65 \times 10^{15} \text{ cm}^{-2}$, dose rate was ranging from 8.6×10^{10} to $3.4 \times 10^{11} \text{ cm}^{-2} \text{ s}^{-1}$. The incident angle was normal to the surface to suppress the destruction of the recrystallized layer by H^+ implantation. 20% H_2 /Ar gas was introduced into ion source chamber of accelerator in H^+ implantation, where Ar was used for the enhancement of plasma-discharge.

In this paper we use the term "the activation ratio" of phosphorus, which is the measure of activation of phosphorus, is defined as the value of carrier concentration divided by phosphorus concentration. The carrier concentration was estimated by means of spreading resistance technique(SR), the phosphorus and hydrogen concentration was measured by means of secondary ion mass spectroscopy(SIMS). Total Activation ratio is obtained by the integration of activation ratio over the phosphorus implanted region. The residual damage was analyzed by means of transmission electron microscopy(TEM). The mechanism of activation is also discussed by comparing the depth profile of local activation ratio of phosphorus with the depth profile of implanted hydrogen atoms.

EXPERIMENTAL RESULTS AND DISCUSSION

Depth profiles of spreading resistance of phosphorus ion implanted sample after annealing at 400 $^\circ\text{C}$ for 200 minutes or after followed 30keV H^+ implantation to a dose of $1 \times 10^{16} \text{ cm}^{-2}$ (dose rate : $3.4 \times 10^{11} \text{ cm}^{-2} \text{ s}^{-1}$) at 400 $^\circ\text{C}$ are shown in Fig.1. There is no change in

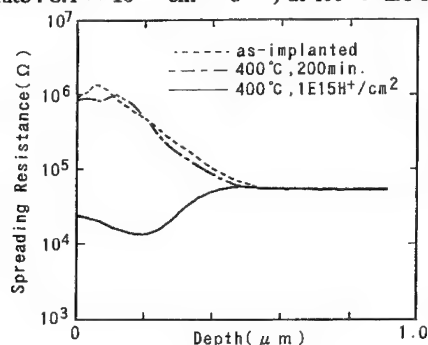


Fig.1 Depth profile of spreading resistance after thermal annealing at 400 $^\circ\text{C}$ or 30keV H^+ implantation at 400 $^\circ\text{C}$.

spreading resistance after annealing, on the other hand spreading resistance is decreased after H^+ implantation. This result indicates that the activation of phosphorus was induced by H^+ implantation at such low temperature of $400^\circ C$.

As the H^+ dose was increased, the more spreading resistance was decreased, which corresponds to the increase of activation ratio. The total activation ratio of phosphorus is plotted as a function of H^+ dose in Fig.2. The activation ratio is almost proportional to H^+ dose. The depth of the maximum activation ratio is about $0.3 \mu m$. The activation ratio becomes larger in the same depth profile at whole depth of phosphorus implanted region.

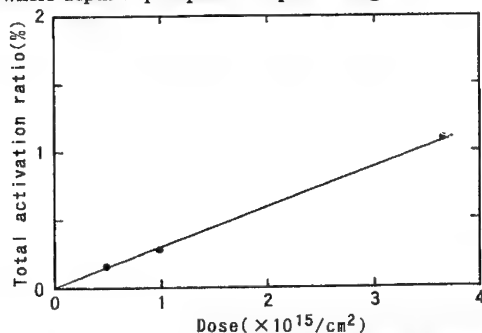


Fig.2 $30keV H^+$ dose dependence of total activation ratio implanted at $400^\circ C$.

The H^+ energy dependence of depth profile of spreading resistance at $400^\circ C$ is shown in Fig. 3. The H^+ dose was $1 \times 10^{15} cm^{-2}$. As the energy was increased from $10keV$, the spreading resistance was decreased and reached minimum at an energy of $30keV$. As the energy was more increased, the spreading resistance was increased and the depth of resistance minimum was shifted to deeper region. This shift indicates that the depth where the activation of phosphorus has occurred is changed with increasing energy. No clear change in depth profile of phosphorus was observed after H^+ implantation, which were measured by SIMS.

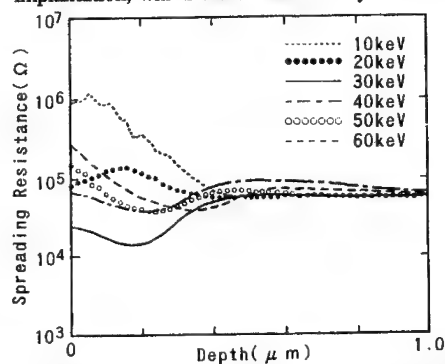


Fig.3 H^+ energy dependence of spreading resistance after implantation to a dose of $1 \times 10^{15} cm^{-2}$ at $400^\circ C$.

Hydrogen profiles implanted at $20^\circ C$ or $400^\circ C$ were measured by means of SIMS, which are shown in Fig.4. The H^+ energy was $30keV$ and its dose was $1 \times 10^{15} cm^{-2}$. They are normalized to the maximum concentration. They are different from each other, especially the depth profile of hydrogen is a terrace-like profile, which is attributed to the diffusion at $400^\circ C$. This is an evidence that the decrease in spreading resistance is attributed to the just activation not to the passivation effect of defect with hydrogen atoms.

For comparison, the depth profile of activation ratio after H^+ implantation at $400^\circ C$, whose dose rate was $8.6 \times 10^{10} cm^{-2} s^{-1}$, is also shown in Fig.4. It is also normalized to the maximum activation ratio. The hydrogen depth profile implanted at $20^\circ C$ is more similar to the

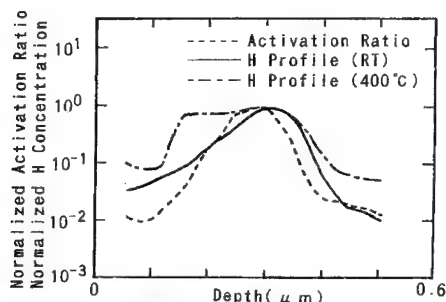


Fig.4 Normalized activation ratio and normalized depth profiles of hydrogen concentration implanted at 20 °C or 400 °C .

activation ratio profile than that implanted at 400 °C .

If activation of phosphorus is induced by inelastic collision between H^+ ion and substrate atoms, the activation ratio should be increased with increasing of H^+ energy, because the inelastic energy loss of incident ion becomes dominant at higher energy, and the activation ratio should be higher at near-surface region than in deep-bulk region. But the experimental results indicate that the most suitable energy for activation exists and the depth profile of activation ratio has maximum at depth of $\sim 0.3 \mu m$.

These results are understood in the view of contribution of elastic collision process between H^+ ions and substrate atoms. At first phosphorus ions are implanted into silicon substrate, when lattice defects such as interstitial silicon atoms and vacancies are formed, so the ratio of phosphorus atoms at substitutional lattice site is very small and cannot be acted as an activated donor. For the activation of phosphorus, rearrangement of silicon atoms and phosphorus atoms for recrystallization is necessary. The experimental result in Fig.1 indicates that the thermal annealing at 400 °C cannot cause the rearrangement mentioned above. On the contrary, the followed H^+ implantation can cause the rearrangement of substrate atoms. The incident H^+ ions give a kinetic energy to substrate atoms in elastic collision, and the collision cascades are formed with many displaced silicon atoms. The displaced silicon atom acts as an interstitial atom and diffuse to distant position from its initial lattice site, and its vacancy is also formed. At the end of collision cascade, if seed for recrystallization exists in contact with the region where collision cascade occurred, it is possible to recrystallize the damaged layer, and the phosphorus atoms near this region are diffused and has a possibility to go in the substitutional lattice site in crystallized region, which is to say a vacancy of silicon atom, and can be activated as a donor.

In this experiment the most suitable energy was 30keV, which is understood as follows. At this energy the highest efficiency of elastic energy deposition at the interface between the damaged region with phosphorus ion implantation and non-damaged single crystalline substrate to be a seed for recrystallization, which corresponds to the depth of $\sim 0.3 \mu m$, is considered to be realized. In Fig.4 the depth profile of hydrogen implanted at 20 °C is considered to be the very projected range distribution of incident H^+ ions. The profile of elastic energy deposition should be a little shallower than the projected range distribution, so the depth of deposited energy maximum corresponds to just the depth of the interface mentioned above and also corresponds to the depth of activation ratio maximum. It is considered that the highest recover of crystallinity in phosphorus implanted region and the highest activation ratio are realized at an incident energy of 30keV. In this case the peak concentration of retained hydrogen atoms is about $7 \times 10^{19} cm^{-3}$. The effect of hydrogen for passivation of phosphorus has not been cleared yet. The retained hydrogen atoms are released from surface after followed thermal annealing. Most of implanted hydrogen atoms are released after annealing at 700 °C for 20minutes.

The dose rate dependence of activation is also examined. 30keV H^+ dose rate dependence of depth profile of spreading resistance is shown in Fig.5. Its dose was $1 \times 10^{15} cm^{-2}$. The

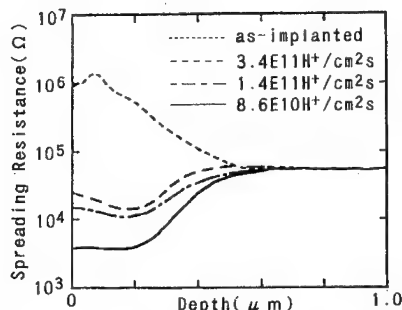


Fig.5 30keV H^+ dose rate dependence of spreading resistance after implantation to a dose of $1 \times 10^{16} \text{ cm}^{-2}$ at 400°C .

spreading resistance is decreased with decreasing the dose rate, which corresponds to the increase in activation ratio. This is the evidence that the activation is not induced by heating effect in H^+ implantation. At the dose rate of $8.6 \times 10^{10} \text{ cm}^{-2} \text{ s}^{-1}$ the activation ratio is reached to 55% at the depth of $\sim 0.3 \mu\text{m}$.

The total activation ratio is shown in Fig.6. The total activation ratio is reached to 4% at the dose rate of $8.6 \times 10^{10} \text{ cm}^{-2} \text{ s}^{-1}$. This activation ratio is considered to be increased with increasing the H^+ dose as mentioned above.

These results are understood in the view of the contribution of residual lattice defects. As mentioned above, the crystallinity of phosphorus implanted region is recovered by followed H^+ implantation, which corresponds to the decrease in the residual amount of lattice defects. The activation ratio is decreased by the residual lattice defects formed in H^+ implantation. It is considered that the amount of residual lattice defects is decided in a balance between the rate of formation and that of disappearance. The rate of formation is increased with increasing the dose rate, on the other hand, in the assumption that the rate of disappearance is decided with only the temperature, the residual amount of lattice defects is increased with increasing the dose rate. In the case of higher dose rate, even if the phosphorus atoms go in the substitutional lattice site, dangling bond is formed so the phosphorus cannot act as an activated donor. So the activation ratio is increased with decreasing the dose rate.

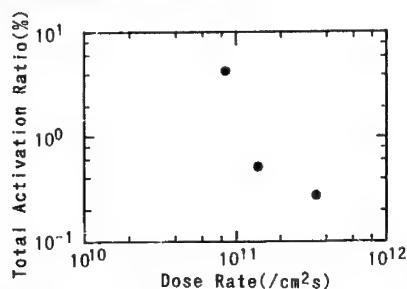


Fig.6 30keV H^+ dose rate dependence of total activation ratio.

The TEM photograph of activated region is shown in Fig.7. The H^+ dose was $1 \times 10^{15} \text{ cm}^{-2}$. Stratiform defect layer is observed near the interface between damaged region with phosphorus implantation and non-damaged single crystalline region at the dose rate of $3.4 \times 10^{11} \text{ cm}^{-2} \text{ s}^{-1}$. No clear image originated from large defects as mentioned above. This is the evidence that the recover of crystallinity is realized at lower dose rate.

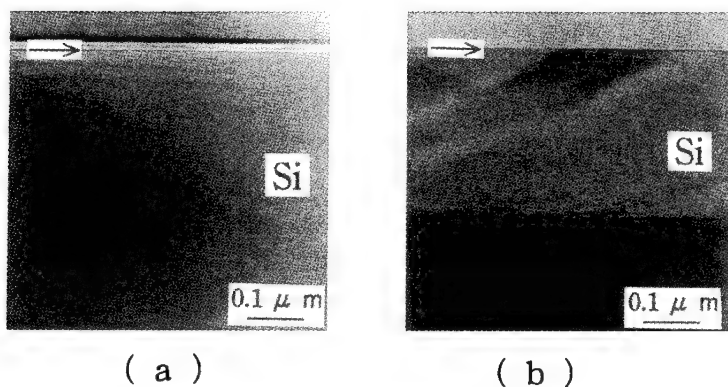


Fig.7 Cross sectional TEM photographs of samples activated by H^+ implantation at a dose rate of (a) $8.6 \times 10^{10} \text{ cm}^{-2} \text{ s}^{-1}$ and (b) $3.4 \times 10^{11} \text{ cm}^{-2} \text{ s}^{-1}$. The arrows correspond to the surface of silicon substrate.

SUMMARY

It was indicated that the activation of phosphorus implanted into silicon is induced by followed H^+ ion implantation at such low temperature of 400°C . For the activation, it is necessary to recrystallize the damaged layer.

The activation is induced by the rearrangement of substrate atoms in the collision cascade, which is formed by elastic collision between H^+ ions and substrate atoms. The position of collision cascade is important for the activation, especially energy deposition to the interface between damaged region formed with phosphorus implantation and nondamaged single crystalline region is very important.

REFERENCES

1. M.Miyake et al., Symp.VLSI Technology, 91(1987)
2. K.Tsukamoto et al., J.Appl.Phys. 48, 1815(1977)
3. D.G.Carey et al., IEEE Electron Dev.Lett. EDL-6, 291(1985)
4. K.Yamada et al., Jpn.J.Appl.Phys. Supplement 22-1, 157(1983)
5. A.Yoshinouchi, T.Morita, S.Tsuchimoto in Materials Modification by Energetic Atoms and Ions, (Mater.Res.Soc.Proc.268, Pittsburgh, PA, 1992) pp.383-388

PHOTOLUMINESCENCE OF EXTENDED DEFECTS IN SILICON-ON-INSULATOR FORMED BY IMPLANTATION OF OXYGEN

Y H QIAN*, J H EVANS*, L F GILES**, A NEJIM**, P L F HEMMENT**

* Centre for Electronic Materials and Department of Electrical Engineering and Electronics, UMIST, PO Box 88, Manchester, M60 1QD, UK

** Department of Electronic and Electrical Engineering, University of Surrey, Guildford, Surrey, GU2 5XH, UK

ABSTRACT

PL and TEM have been carried out on SIMOX structures before and after thinning the silicon overlayer by a process of sacrificial oxidation. The implantation and high temperature annealing schedules involved in fabricating SIMOX material result in threading dislocations and stacking fault tetrahedra and pyramids in the silicon overlayer. The optical activity of these extended defects is found to be low. However, after the sacrificial oxidation, strong dislocation related luminescence is observed, which is attributed to the presence of oxidation-induced stacking faults now present in the overlayer.

INTRODUCTION

The formation of silicon on insulator structures by Separation by Implanted Oxygen (SIMOX) is a well established technology which is compatible with VLSI processing. The silicon overlayer is a strong candidate for the active region of fully depleted CMOS devices, with reduced parasitic effects, good radiation tolerance and increased speed. A standard technique for the production of thin SIMOX is sacrificial oxidation, which does not involve any modification of the implant conditions, but may lead to the formation of oxidation induced stacking faults (OISF). If these defects occur in the active region of a device their associated electrical activity is known to degrade device performance[1].

Prior to the sacrificial oxidation, it is likely that the aggressive implantation and very high temperature annealing involved in the formation of SIMOX structures will result in residual defects in the silicon overlayer. Such defects include threading dislocations and intrinsic stacking fault tetrahedra and pyramids[2,3]. Therefore, coupled with the OISF present in thinned SIMOX structures, there is likely to be present in the active region a high concentration of extended defects which have the potential to act as generation-recombination centres.

It is difficult to assess the electrical quality of the active region of a SIMOX structure because of two factors: firstly, no current flows from front to back because there is a buried insulating layer and secondly, the silicon overlayer is thin (typically 2000Å to 3000Å) even before sacrificial oxidation, and surface and interface recombination cannot be deconvoluted from recombination occurring at defects within this layer. However, in the special case of extended defects in silicon, it is very likely that a defect that exhibits non-radiative deep level electrical activity, (such as is detected by Deep Level Transient Spectroscopy (DLTS)[4] and Electron Beam Induced Current), also exhibits radiative emission which can be characterised by photoluminescence (PL)[5]. PL is a non-destructive technique that characterizes material

within the electron-hole pair generation volume. If the 514nm line of an argon ion laser is employed as the excitation source with a penetration depth of approximately $1\mu\text{m}$ in silicon, this will generate carriers in the silicon overlayer and beyond the buried oxide and into the underlying silicon in our structures.

We have carried out PL on SIMOX structures which exhibit stacking fault tetrahedra and pyramidal (SFT/SFP) and threading dislocations in the overlayer to assess the level of exciton capture and subsequent radiative recombination at these defects. We have also carried out PL on SIMOX structures that have been thinned by sacrificial oxidation, and contain OISF. The extended defects in all layers were observed by plan view transmission electron microscopy (TEM) and cross sectional TEM (XTEM).

EXPERIMENTAL

The p-type SIMOX layer was formed by implantation of a dose of $1.79 \times 10^{18}/\text{cm}^2$ O^+ ions at 190 keV into silicon at a temperature of 600°C . The wafer was then annealed at 1320°C for 6 hours in an atmosphere of $\text{Ar} + 0.5\% \text{O}_2$. This resulted in a silicon overlayer thickness of 2040\AA determined by 1.5MeV He^+ Rutherford backscattering analysis. A sample cut from the wafer at this stage is identified as sample A in Table I.

In order to thin the sample, thermal oxidation was carried out at 900°C in a dry O_2 atmosphere, followed by an etch in HF to remove the oxide, which reduced the overlayer thickness to 500\AA (sample B). In order to establish the physical location of the centres giving rise to PL signals, we completely etched away the silicon overlayer and the buried oxide from one region of the oxidized wafer (sample C) and carried out PL on the remaining substrate. Extended defect types and densities were obtained using TEM analysis.

Table I: Summary of Sample History and Structure.

Sample Name	Details of Processing	Overlayer Thickness (\AA)
A	O^+ implantation. Annealing at 1320°C	2040
B	O^+ implantation. Annealing at 1320°C . Sacrificial oxidation	500
C	O^+ implantation annealing at 1320°C . Sacrificial oxidation. Removal of overlayer and oxide	n/a
D	O^+ implantation. Annealing at 1320°C . Cu diffusion	2040
E	O^+ implantation. Annealing at 1320°C . Sacrificial oxidation. Cu diffusion	500
F	Light surface damage. Dry oxidation at 1100°C	n/a

It is well known that a light amount of decoration by a transition metal such as Cu or Au increases the intensity of radiative emission from extended defects in silicon[6]. We have deliberately introduced a small amount of Cu by lightly touching samples A and B on the

back with cleaned copper wire and heating to 700°C for 15 minutes. This results in samples D and E, respectively, in Table I. Finally, we created OISF in bulk silicon by light surface damage and oxidizing at 1100°C. This provided a comparison of the dislocation-related emission when only OISF are present, sample F.

RESULTS

Fig. 1 shows a XTEM micrograph of sample A. This shows that stacking fault tetrahedra and pyramidal (SFT/SFP) are present at the top Si/SiO₂ interface with a density of $1 \times 10^7 \text{ cm}^{-2}$. These interface defects are very small with a length typically between 0.1 - 0.2 μm , and are not observed at the lower SiO₂/Si-substrate interface. In addition, sample A was etched with a specially developed defect etch for thin layers[7]. This showed that threading dislocations are also present in the silicon overlayer, and they extend from the SiO₂/Si interface to the surface. The density of these dislocations is $1 \times 10^5 \text{ cm}^{-2}$.

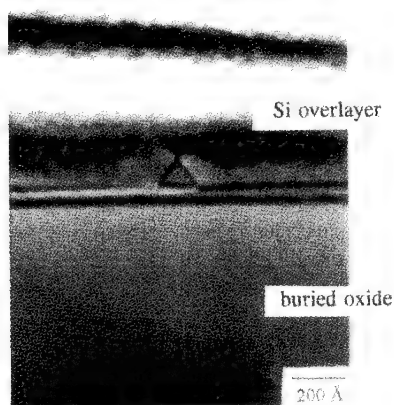


Fig.1 XTEM of sample A, showing a stacking fault tetrahedra at the upper Si/SiO₂ interface

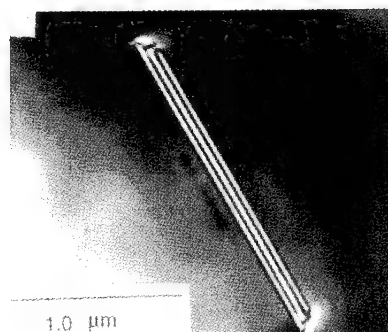


Fig.2 TEM of OISF in the silicon overlayer of the SIMOX structure after dry oxidation at 900°C for 24 hours

Fig.2 shows plan view TEM of the OISFs present in the thinned overlayer in sample B after sacrificial oxidation at 900°C for 24 hours. They are revealed to be well formed OISFs bounded by dislocation loops, with a mean length greater than 1 μm . However, the density of the OISFs is low, approximately $1 \times 10^4 \text{ cm}^{-2}$.

The PL spectra from samples A, B and C are shown in Fig.3. The PL from the SIMOX sample before sacrificial thinning (A) shows a small and broad dislocation-related emission feature centred at 0.814eV, while boron bound-exciton (BE) emission dominates at 1.098eV. The peak at 0.814eV is the dislocation-related D1 line[6]. PL from the sample that has experienced sacrificial oxidation (B) exhibits a larger feature at 0.814eV and the intensity of the bound-exciton peak is reduced relative to the dislocation related emission. PL from sample C is dominated by the boron bound-exciton recombination and no D1 line can be

detected.

The lightly copper decorated samples D and E were investigated by PL and the spectra are illustrated in Fig. 4. It can be seen from the PL spectra that the copper decoration reduces the dislocation-related luminescence originally detected from samples A and B. The bottom trace in Fig.4 shows a PL spectrum of the reference sample (F) containing OISFs near the surface of the silicon substrate, and consists of the lines D1 and D2, bot of which are commonly associated with OISFs[8].

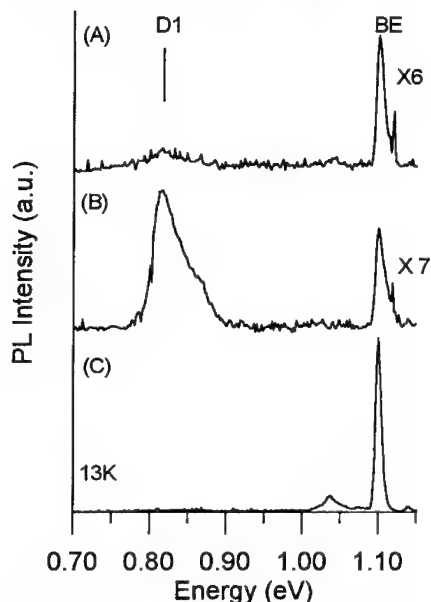


Fig.3 PL from SIMOX(A), thinned SIMOX(B) and substrate after removal of SIMOX top Si and buried oxide(C).

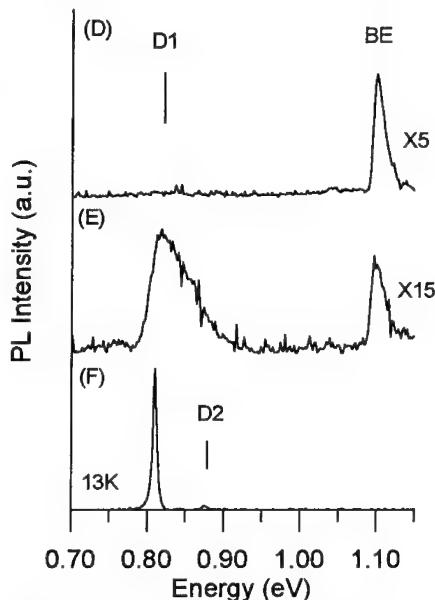


Fig.4 PL from sample Cu-dec. SIMOX(D), Cu-dec. thinned SIMOX(E), and OISF reference sample(F).

DISCUSSION

The particular processes involved in SIMOX technology, high-dose, high-energy O^+ ion implantation, combined with a very high-temperature anneal, has been shown in the past to be responsible for contamination and the formation of bulk and interface defects[9]. The high densities of threading dislocations and oxygen precipitates that resulted in the silicon overlayer were reported to produce D1 - D4 in PL spectra[10]. With the improvement of SIMOX processing technology, the threading dislocation problem has been greatly reduced, but other types of defects such as stacking fault tetrahedra and pyramids at the Si/SiO₂ interface are emerging as the most numerous defects[2,11,12]. The SFT/SFP in our samples have a high density of $1 \times 10^7 \text{ cm}^{-2}$. A crucial factor when considering any material system is whether an extended defect will have sufficient electrical activity to influence device parameters, and this issue can be partly resolved by examining the optical activity of the system.

PL spectra from silicon fall naturally into two regions: bound exciton emission above approximately 1.00eV and dislocation related emission which manifests itself as broader peaks

below 1.00eV. Our PL measurements from sample A, which has a relatively low density of threading dislocations but a high density of SFT/SFPs, shows little radiative emission in the dislocation emission portion of the spectrum (Fig. 3a). However, even a relatively low density ($1 \times 10^4 \text{ cm}^{-2}$) of OISFs in the very thin silicon overlayer of 500Å, sample B, gives rise to a much more intense D1 line in the PL spectrum. This implies that the OISF have much greater radiative recombination activity associated with them than the SFT/SFPs, and may therefore be more electrically active. If this is the case, then the sacrificial oxidation process has introduced generation-recombination centres into the region where devices will be fabricated in these substrates. This supposition is reasonable as it is known that OISFs in bulk silicon capture both majority and minority carriers[13].

Copper was introduced into sample A to establish whether the SFT/SFP were not detected because the defects were 'clean'. There is much in the literature (for example, references 4,6 and 8) which reports that deliberate decoration by copper of dislocations in silicon modifies the PL emission associated with the defects. A light decoration enhances the radiative emission, whereas heavy decoration reduces the emission. This latter result is due to the formation of copper precipitates which act as non-radiative centres that compete for excitons, thus reducing the radiative recombination paths in the excited region. In order to ensure that the experiment was carried out in the 'lightly' decorated regime, the copper was introduced from the back of the samples. Copper is a fast diffuser in silicon, but is approximately two orders of magnitude slower when diffusing through SiO_2 . Therefore it was assumed that only a small amount of copper passed through the insulating layer to decorate the extended defects in the overlayer.

The presence of extended defect-related PL often results in a decrease in the BE emission from the same sample, and it can be instructive to examine the ratio of the intensities of the two types of emission features. Table II shows the ratio, D1/BE, of the integrated intensities of D1 to the BE emission peak for samples A - E. The ratio is seen to dramatically increase after the overlayer has been thinned. This is attributed to the very efficient exciton capture by the OISFs associated with the local strain field, i.e. fewer excitons are able to diffuse deep into the substrate, which gives rise to the lower intensity of the 1.098eV peak.

Table II. Ratio of the intensities of the D1 line and the bound exciton emission line.

Sample No.	A	B	C	D	E
D1/BE	0.60	4.79	0.15	0.17	4.45

It can clearly be seen that the copper has diffused through the buried oxide and reached the extended defects in samples D and E because the ratios D1/BE in both samples have changed after copper decoration. As mentioned previously, if the copper decoration becomes considerable, the intensity of D1 will start to reduce, and this appears to be the case for both samples D and E. From this, we deduce that the extended defects were already decorated with an impurity before our decoration experiment, and that this enhanced the defect related luminescence from samples A and B. Inadvertent impurity incorporation can occur during a process such as ion implantation. This implies that even an unintentional decoration in sample A was not sufficient to cause the SFT/SFPs to exhibit a significant emission peak at 0.814eV, despite their high density. However, a density of OISFs that is lower does produce enough radiative centres to reduce the bound exciton recombination. This level of decoration means that the OISFs are likely to have associated deep non-radiative electronic states[5].

CONCLUSIONS

The process of forming SIMOX can result in the presence of threading dislocations and SFT/SFP in the silicon overlayer, but these extended defects have no detectable D-line emission measured by PL. It is inferred therefore that they have a low level of electrical activity and as such, will not contribute significantly to device degradation. By contrast, the OISF present in SIMOX structures that have been thinned by oxidation exhibit emission centred at 0.814eV (D1). This emission cannot be enhanced by light decoration of the OISF by copper. The PL spectra from the OISF is virtually identical to that measured for OISF in bulk silicon, and it is deduced that the OISF in the SIMOX overlayers have the potential to be generation-recombination centres. By etching off the buried oxide we have demonstrated that the D1 line originates from an extended defect in the silicon overlayer, and have thus shown that PL can be used as a sensitive analysis technique for layers as thin as 500Å.

ACKNOWLEDGEMENTS

One of us (YHQ) would like to acknowledge student support from the British Council. This work was partially supported by the UK EPSRC. LFG acknowledges support from CAPS, Brazil.

REFERENCES

1. B. O. Kolbesen, W. Bergholz, H. Cerva, F. Gelsdorf, H. Wendt and G. Soth, *Inst. Phys. Conf. Ser.* **104**, 421 (1990)
2. L. F. Giles, C. D. Marsh, A. Nejim, P. L. F. Hemment and G. R. Booker, *Nuclear Instrument And Method in Physics* **B84**, 242 (1994)
3. W. Coene, H. Bender and S. Amelinckx, *Philos. Mag.* **A52**, 369 (1985)
4. P. Omling, E. R. Weber, L. Montelius, H. Alexander and J. Michel, *Phys. Rev.* **B32**, 6571 (1985)
5. G. R. Lahiji, A. R. Peaker and B. Hamilton, *Inst. Phys. Conf. Ser.* **104**, 239 (1990)
6. E. C. Lightowers, V. Higgs, M. J. Gregson, G. Davies, S. T. Davey, C. J. Gibbings, C. G. Tupper, F. Schaffler A. Kasper, *Thin Solid Films* **183**, 235 (1989)
7. L. F. Giles, A. Nejim and P. L. F. Hemment, *Mat. Chem. and Phys.* **35**, 129 (1993)
8. J. H. Evans, J. Kaniewski, M. Kaniewka and J. S. Rimmer, *Semicond. Sci. Technol.* **7**, A41 (1992)
9. G. E. Davis, K. S. Jones, and S. Prussin, *MRS Sym. Proc.* **107**, 111 (1987)
10. W. M. Duncan, P.-H. Chang, B.-Y. Mao, and C.-E. Chen, *Appl. Phys. Lett.* **51**, 773 (1987)
11. J. Margail, J. M. Lamure and A. M. Papon, *Mat. Sci. and Eng.* **B12**, 27 (1993)
12. J. C. Park, J. D. Lee, D. Venables, S. Krause, and P. Roitman, *MRS Sym. Proc.* **279**, 153 (1993)
13. J. A. Davidson, J. H. Evans and A. R. Peaker, *Mat. Sci. and Eng.* **B24**, 167 (1994)

TYPE II DISLOCATION LOOPS AND THEIR EFFECT ON STRAIN IN ION IMPLANTED SILICON AS STUDIED BY HIGH RESOLUTION X-RAY DIFFRACTION

R. H. THOMPSON JR., V. KRISHNAMOORTHY, J. LIU, AND K.S. JONES

Department of Materials Science and Engineering, University of Florida, Gainesville, FL 32611

ABSTRACT

P-type (100) silicon wafers were implanted with $^{28}\text{Si}^+$ ions at an energy of 50 keV and to doses of 1×10^{15} , 5×10^{15} and $1 \times 10^{16} \text{ cm}^{-2}$, respectively, and annealed in a N_2 ambient at temperatures ranging from 700°C to 1000°C for times ranging from 15 minutes to 16 hours. The resulting microstructure consisted of varying distributions of Type II end of range dislocation loops. The size distribution of these loops was quantified using plan-view transmission electron microscopy and the strain arising from these loops was investigated using high resolution x-ray diffraction. The measured strain values were found to be constant in the loop coarsening regime wherein the number of atoms bound by the loops remained a constant. Therefore, an empirical constant of 7.7×10^{-12} interstitial/ppm of strain was evaluated to relate the number of interstitials bound by these dislocation loops and the strain. This value was used successfully in estimating the number of interstitials bound by loops at the various doses studied provided the annealing conditions were such that the loop microstructure was in the coarsening or dissolution regime.

INTRODUCTION

As the computer age advances so does the demand for smaller devices. VLSI circuit fabrication demands increasingly smaller dimensions to improve performance. Selective doping using ion implantation is an important aspect of the VLSI fabrication process. At high enough implant energies and doses the implant conditions are sufficient to amorphize silicon. Upon subsequent annealing at temperatures greater than 550°C solid phase epitaxial regrowth of the amorphous region occurs leaving behind Type II end of range dislocation loops at the original amorphous / crystalline interface^{1,2}. Previous studies have shown that this layer of dislocation loops causes a tetragonal distortion in the lattice resulting in a positive strain perpendicular to the wafer surface^{3,4}. Previous studies have also related this strain to the concentration and size of the dislocation loops^{4,5,6}. The aim of this study was to determine a relationship between the number of interstitials bound by the loops calculated using TEM and the strain evaluated using High Resolution X-Ray Diffraction (HRXRD). This relation would allow for the prediction of the number of interstitials trapped in loops using HRXRD which has the advantage of being a non-destructive analysis technique.

EXPERIMENTAL PROCEDURES

The experiments were conducted on p-type (Boron doped) (100) Czochralski grown silicon wafers with a resistivity of 5-10 ohm-cm. Wafers were implanted with $^{28}\text{Si}^+$ at an energy of 50 keV and doses of $1 \times 10^{15}\text{cm}^{-2}$, $5 \times 10^{15}\text{cm}^{-2}$, and $1 \times 10^{16}\text{cm}^{-2}$ using a Varian Ion Implanter. The ion beam was kept at a minimal current to reduce possible beam effects on the sample.

After implantation a 5500Å LPCVD SiO_2 cap layer was deposited on the samples to prevent oxidation during subsequent annealing. The samples were annealed in a N_2 ambient at temperatures of 700°C, 800°C, 900°C and 1000°C for times ranging from 15 minutes to 16 hours. After annealing the surface oxide was removed by dipping the samples in a buffered oxide etch solution (6:1 Hydrofluoric acid to Ammonium Hydroxide) until the surface became hydrophilic.

To measure the strain from the dislocation loops a Philips HR-1 system was modified by adding a Bonse-Hart collimator (see Figure 1) to increase resolution. This was necessary to detect the small magnitude of strain being measured. After appropriate system optimization of specimen rotation and tilt, omega/2 theta x-ray rocking curves were acquired using a small step size of 0.0005° and a time per step of 10 seconds. A comparison of rocking curves obtained with and without the Bonse-Hart collimator is shown in Figure 2 to illustrate the necessity of this addition.

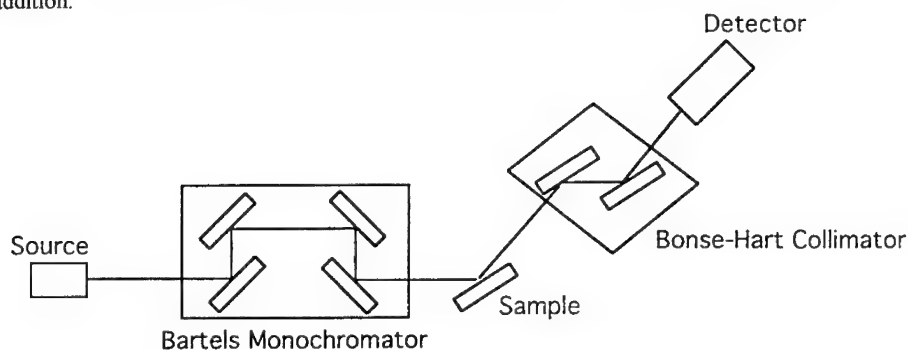


Figure 1. The Philips HR-1 HRXRD system with the addition of a Bonse-Hart Collimator

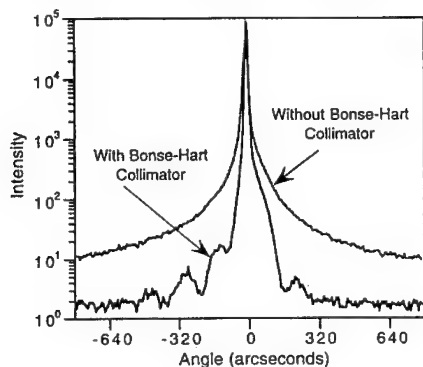


Figure 2. A comparison of x-ray rocking curves taken before and after the addition of the Bonse-Hart Collimator to the Philips HR-1 HRXRD system.

The x-ray rocking curves performed about the [004] reflection revealed satellite peaks to the left of the silicon substrate peak. The lower angle of these peaks indicates a lattice expansion. The outermost satellite peak has been previously shown to represent the maximum strain in ion implanted silicon (31). Rocking curve simulations were performed using strain profiles with the maximum positive strain centered at a depth corresponding to the loop layer. The results showed that the outermost satellite peak did indeed correspond to the maximum strain value.

Plan-view transmission electron microscopy (PTEM) samples were prepared by etching in a (1:3) HF/HNO₃ solution until the specimen was electron transparent. PTEM was performed using a JEOL 200CX electron microscope and the dislocation loops were imaged using a <220> reflection. The size distribution of the loops was evaluated using the micrographs and since the density of atoms on a <111> plane is known, the number of interstitials trapped by the dislocation loops was evaluated.

RESULTS AND DISCUSSION

The strain was calculated from the x-ray rocking curves using the following equation.

$$\epsilon_{\perp} = -\Delta\omega \times \cot(\Theta_B) \quad (1)$$

The evaluated strain is plotted versus annealing temperature in Figure 3. It can be seen that there appears to be three distinct regions of strain. The first region from 700°C to 800°C where the strain drops from 5046 ppm to 3210 ppm after a 15 minute anneal and from 4920 to 3420 ppm after a 2 hour anneal. In the second region from 800°C to 900°C the strain appears nearly constant at about 3400 ppm. In the third region from 900°C to 1000°C the strain drops from 3400 ppm to 1840 ppm after a 15 minute anneal and from 1846 ppm to below the detection threshold of the x-ray system after a 2 hour anneal.

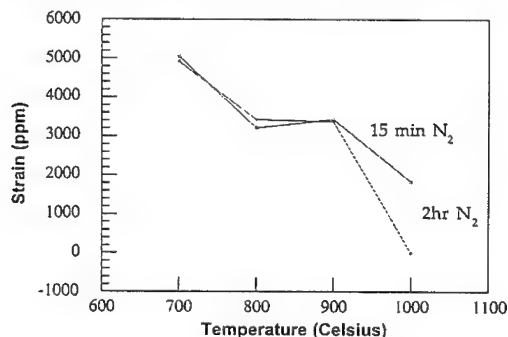


Figure 3. A plot of the maximum strain versus annealing temperature.

In order to understand the relevance of the 3 regions PTEM was performed on the various specimens. The micrographs from the 2 hour annealed samples are shown in Figure 4. The micrographs clearly show an increase in loop size with increasing temperature and at high

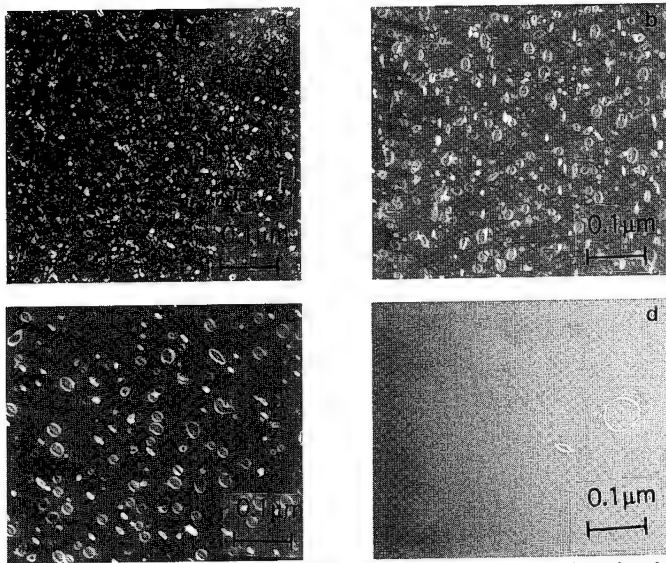


Figure 4. Plan View TEM micrographs of the type II end of range dislocation loops annealed in N_2 for 2 hours at a) 700°C, b) 800°C, c) 900°C and d) 1000°C.

temperatures a decrease in loop number density with increasing temperature. The total number of interstitials trapped in the dislocation loops was calculated and was compared with the strain values. The number of interstitials trapped in the loops and the strain for the 2 hour annealed samples are shown in Figure 5. It is important to note that the total strain in these samples would be the sum of the strain due to free interstitials in the lattice and the strain exerted by the dislocation loops on the surrounding Si lattice.

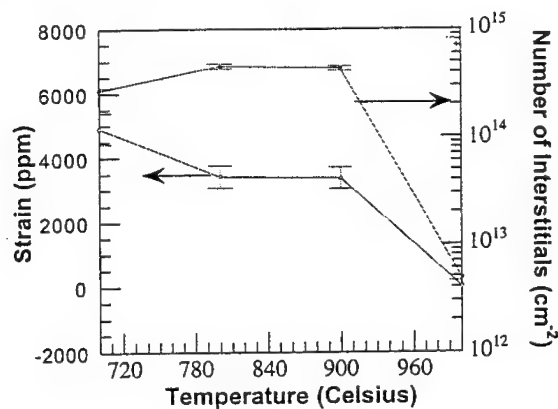


Figure 5. A plot of the number of trapped interstitials and the strain versus temperature for 2 hour anneals in N_2

In the 700°C to 800°C range, the number of interstitials trapped by the loops increases while the strain decreases with increasing temperature. This suggests that the dislocation loops are in the

growth stage. In this stage, therefore, the strain due to dislocation loops would increase with increasing temperature. However, the measured strain decreases with increasing temperature. As pointed out earlier, the total strain would be sum of the strain component due to dislocation loops and that from free interstitials. A free interstitial would typically exert greater strain on the lattice than would an interstitial trapped by a dislocation loop and hence the driving force for the formation of such loops. Annealing at increasing temperatures would allow free interstitials to diffuse to the loops (hence growing them). Therefore, the strain contribution from free interstitials would decrease with increasing temperature. Assuming that the total number of interstitials in the lattice decreases (due to recombination) or remains a constant the total strain would decrease with increasing annealing temperature.

In the 800°C to 900°C range, both the strain and the number of trapped interstitials remain nearly constant. This can be attributed to loop coarsening in this temperature regime wherein loops larger than a critical radius grow and those below this radius shrink². The net quantity of interstitials trapped in the dislocation loops would remain a constant in this regime and hence the strain should remain constant if the strain is solely dependent on the loop interstitial content. In the third stage from 900°C to 1000°C both the strain and the number of trapped interstitials decrease with increasing temperature. This can be explained by the occurrence of loop dissolution where the dislocation loops are no longer stable² and hence a lower number of trapped interstitials would lead to a lower strain value.

For temperatures greater than 800°C and for longer times there appeared to be a direct correlation between the number of trapped interstitials and strain. The interstitial numbers evaluated from PTEM and strain from x-ray were correlated in this regime and an empirical constant of 7.7×10^{-12} interstitials/ppm was determined.

Assuming that the strain is a direct function of the number of trapped interstitials (as in the coarsening and the dissolution regime), the empirical value should be able to provide the number of trapped interstitials if the strain is measured. To test the effectiveness of the constant in predicting the number of trapped interstitials samples of self-ion implanted silicon at doses of $1 \times 10^{15} \text{ cm}^{-2}$, $5 \times 10^{15} \text{ cm}^{-2}$, and $1 \times 10^{16} \text{ cm}^{-2}$ and at a constant energy of 50 keV were studied. The samples were annealed at a high temperature of 900°C for 30 minutes to allow for the diffusion of any excess free interstitials to sinks. X-ray rocking curves were obtained from these samples and the strain was calculated using Equation 1. The number of trapped interstitials was then calculated using PTEM micrographs from these samples. Figure 6 shows the number of trapped interstitials found using PTEM along with the calculated number of interstitials using the x-ray strain and the empirical constant.

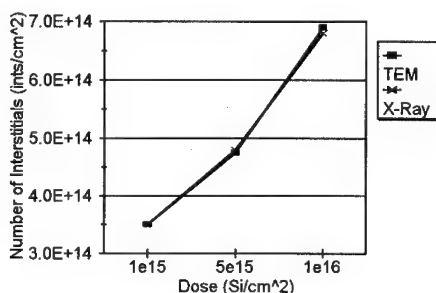


Figure 6. A plot of the number of interstitials found using PTEM along with the number of interstitials calculated using strain and the empirical constant.

The two values appear to correlate quite closely and therefore seems to indicate that the constant can be used to evaluate the number of trapped interstitials under conditions where loop growth is complete.

CONCLUSIONS

The data from this study has shown that there is a direct correlation between the x-ray strain and the number of interstitials trapped in Type II dislocation loops in the loop coarsening and dissolution regimes. The strain and interstitials trapped in the loops do not correlate in the loop growth regime. This was explained by noting that during loop growth there are free interstitials which not bound by the dislocation loops present in the Si lattice which also contribute to the measured strain. These free interstitials are indiscernible in PTEM and hence no discrete number can be obtained to relate these interstitials to strain. An empirical constant was determined (for the loop coarsening and dissolution regimes) that relates the number of interstitials trapped in Type II dislocation loops to strain evaluated by x-ray diffraction. This constant offers the possibility of evaluating the number of interstitials trapped in dislocation loops using x-ray diffraction, a non-destructive technique, instead of PTEM which is a laborious destructive technique.

REFERENCES

1. K.S. Jones, Ph.D. Thesis, University of California, Berkeley, 1987.
2. J. Liu, M.S. Thesis, University of Florida, Gainesville, 1994.
3. J.G.E. Klappe and P.F. Fewster, *J. Appl. Cryst.* **27**, 103 (1994).
4. P. Zaumseil, U. Winter, F. Cembali, M. Servidori, and Z. Sourek, *Phys. Stat. Sol.* **100a**, 95 (1987).
5. M. Servidori, *Nucl. Inst. Meth.* **B19/20**, 443 (1987).
6. M. Servidori and R. Fabbri, *J. Phys. D* **26**, A22 (1993).

CONTACTLESS EVALUATION OF THE SURFACE RECOMBINATION PROPERTY OF SILICON WITH AN ION-IMPLANTED LAYER

Akira Usami, Takanori Makino, Hideaki Yoshida, and *Etsuro Morita
Nagoya Institute of Technology, Gokiso, Showa, Nagoya 466, JAPAN
*Mitsubishi Materials Silicon Co.,Ltd., Nishisangao, Noda 278, JAPAN

ABSTRACT

The surface properties of silicon are investigated by the noncontact laser ($\lambda=774\text{nm}$)/microwave method. The effective surface recombination velocity (S_{eff}) at an n⁺n high-low junction interface is estimated by fitting the experimental decay curve for excess carriers with the theoretical decay curve. The results show that S_{eff} decreases as the dopant concentration increases and that S_{eff} at the n⁺n high-low junction formed with a dose of 1×10^{15} ions/cm² has values lower than 1cm/s. And it is shown that S_{eff} is inversely proportional to the potential barrier height of the n⁺n high-low junction. Similar results are obtained using an N₂ laser ($\lambda=337.1\text{nm}$) instead of a laser diode ($\lambda=774\text{nm}$, 904nm) as a carrier excitation pulse source.

INTRODUCTION

The improvement in the surface properties of silicon wafers has become more important for the silicon device performance and reliability as the device dimension decreases continuously. It is known that the surface properties are improved by forming a heavily doped layer on the surface with an ion implantation technique. This method is founded on a blocking property [1] of a high-low junction for minority carriers. Consequently, the recombination rate at the silicon surface is effectively reduced. This property has been used for the improvement in open circuit voltage and short circuit current of Back-Surface-Field (BSF) solar cells [2,3].

In this experiment, we have investigated the surface properties of silicon which has a heavily doped layer at the surface. The heavily doped layer was formed by an ion implantation technique to reduce the surface recombination velocity of silicon. The surface properties of silicon are evaluated by the noncontact laser/microwave method [4,5,6].

EXPERIMENTAL PROCEDURE AND SAMPLE PREPARATION

Figure 1 shows a schematic illustration of the apparatus based on the noncontact laser/microwave method used in this experiment. Excess carriers are injected by an irradiation of δ -pulsed light at a surface of a silicon wafer. After the irradiation, the injected excess carriers decrease by recombination. The decay

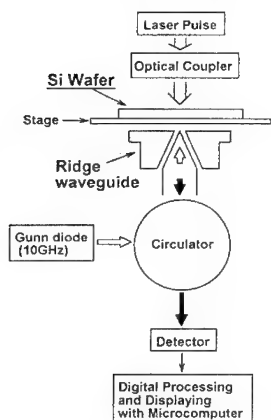


Fig.1 Schematic illustration of the system used in this experiment.

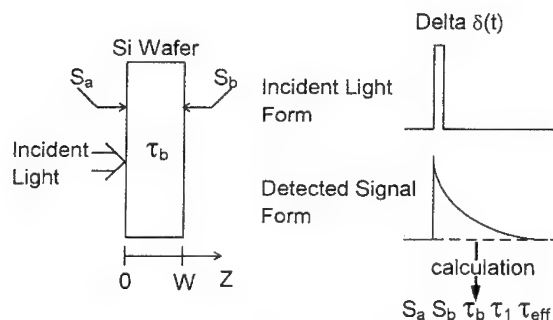


Fig.2 Schematic description of the noncontact laser/microwave method.

process for excess carriers is detected by 10GHz microwave from a Gunn diode. Consequently, minority carrier lifetimes, such as τ_1 , τ_{eff} , and τ_b mentioned later, are measured from the decay curve (the photoconductivity decay method). In this experiment, we used a laser diode (LD) ($\lambda=774\text{nm}$, pulse width=50ns) and an N_2 laser ($\lambda=337.1\text{nm}$, pulse width=1ns) as a carrier excitation pulse source. The irradiation light from these lasers is appropriate for the detailed investigations of the surface properties of silicon, because their optical penetration depths into silicon are shallow. We also used a LD ($\lambda=904\text{nm}$, pulse width=50ns) in this experiment.

Figure 2 shows the schematic description of the incident light, i.e. a carrier excitation pulse source, and the detected signal using the noncontact laser/microwave method. Decay of the detected signal intensity after the irradiation is initially nonexponential but then becomes almost exponential. Primary mode lifetime (τ_1), which is affected by both surface and bulk properties of a silicon wafer, means the time constant obtained from the latter part of the decay curve. Effective lifetime (τ_{eff}) means the time at which the value of the detected signal intensity decreases to $1/e$ of the maximum value. Bulk lifetime (τ_b) and the surface recombination velocity ($S : S_a, S_b$) of a wafer are also estimated from the detected signal intensity.

The theoretical decay curve is described by the solution of the continuity equation (1),

$$\frac{\partial}{\partial t} \Delta p(x,t) = -\frac{\Delta p(x,t)}{\tau_b} + D \frac{\partial^2}{\partial x^2} \Delta p(x,t) \quad (1)$$

subject to the initial condition (2), and the boundary conditions (3) and (4) as following.

$$\Delta p(x,0) = g_0 \exp(-\alpha x) \quad (2)$$

$$D \frac{\partial}{\partial x} \Delta p(x,t) \Big|_{x=0} = S_a \Delta p(0,t) \quad (3)$$

$$D \frac{\partial}{\partial x} \Delta p(x,t) \Big|_{x=W} = -S_b \Delta p(W,t), \quad (4)$$

where τ_b is the bulk lifetime, D the diffusion coefficient of the minority carrier, g_0 a constant, α the absorption coefficient for an irradiation light, W the thickness of the wafer, and S_a and S_b are the surface recombination velocities on the front and back surface of the wafer, respectively.

The wafers used in this experiment were one-side polished, 4-inch (100)-oriented n-type (resistivity of 8-12 $\Omega\cdot\text{cm}$, thickness of 500 μm) Czochralski (CZ) silicon. The P^+ ion implantations were performed at different implantation energies of 50, 70, and 100keV with doses ranging from 1×10^{12} to 1×10^{15} ions/ cm^2 for the polished face of the wafers. Hereafter, we call the implanted face the front surface. To form an n-n high-low junction, post-implantation annealings were carried out at 900 $^\circ\text{C}$ for 30min. A sample name, for example N-50-12, means that the type of conduction is n-type and that the ion implantation was performed at an implantation energy of 50keV with a dose of 1×10^{12} ions/ cm^2 .

We measured minority carrier lifetimes for these samples with irradiation of excitation light at a heavily doped layer side. The widths of the heavily doped layer for all the samples were much thinner than the optical penetration depth into silicon of the LD's used in this experiment. Thus, carriers can be fully excited below the heavily doped layer/substrate interface.

RESULTS AND DISCUSSION

A. Estimation of effective surface recombination velocity (S_{eff})

Figure 3 shows the decay curves for excess carriers of the samples implanted at an energy of 50keV with doses ranging from 1×10^{12} to 1×10^{15} ions/ cm^2 and subsequently annealed. The LD ($\lambda=774\text{nm}$) is used as a carrier excitation pulse source. The results show that τ_1 increases with dose. Figure 4 shows the dependence of τ_1 on dose with the energy as a parameter for all the samples. The results show that the values of τ_1 increase with dose for all the energies.

A high-low junction has a blocking property for minority carriers, and hence the surface recombination velocity is effectively reduced. (The effective recombination velocity is denoted as S_{eff} .) It has been reported that the reduction of S_{eff} by the high-low junction increases with width

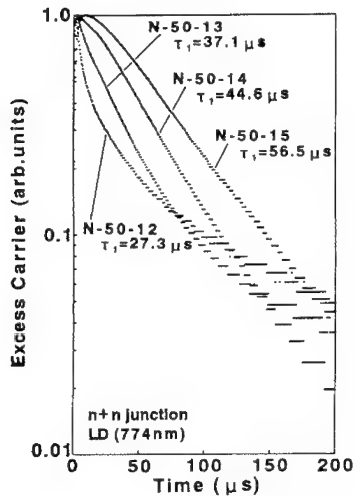


Fig.3 Decay curves for excess carriers of the samples implanted at an energy of 50keV with doses ranging from 1×10^{12} to 1×10^{15} ions/cm² and subsequently annealed.

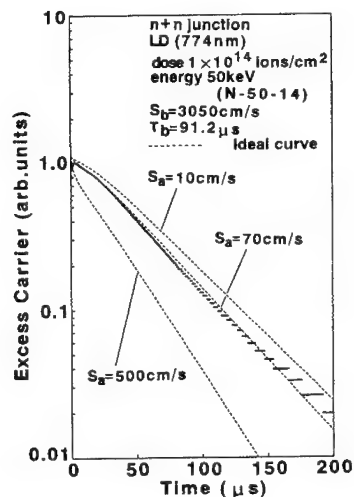


Fig.5 An example of the fitting for the sample N-50-14.

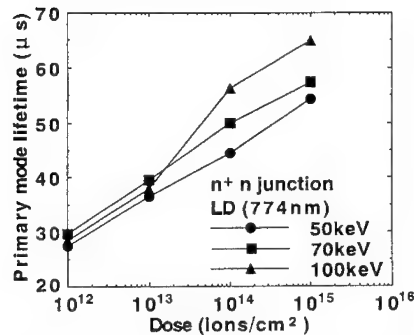


Fig.4 Dependence of τ_1 on dose with the energy as a parameter for all the samples.

and carrier concentration of the heavily doped layer [7, 8, 9].

Under the implantation conditions of a constant energy and different doses, the heavily doped layers formed after annealing have almost the same width, and the carrier concentration of the heavily doped layers increases with dose. Therefore, S_{eff} at the high-low junction interface is reduced more effectively at the higher dose owing to the blocking property for minority carriers. Thus, τ_1 increases with dose. As previously reported [10,11], τ_1 is affected by both surface and bulk properties of the sample. In figure 4, the value of τ_1 is mainly affected by S_{eff} , because the starting wafers have almost the same bulk properties. Thus, it is considered that the increase of τ_1 with dose represents the decrease of S_{eff} at the front surface with dose.

We estimated S_{eff} at the front surface by fitting the experimental decay curve with the theoretical decay curve. Figure 5 shows an example of the fitting for a sample implanted at 50keV with 1×10^{14} ions/cm² and subsequently annealed (N-50-14). The theoretical decay curve is obtained by equation (1), using $W=500\mu m$, $\alpha=1300cm^{-1}$ ($\lambda=774nm$), $D=10.4cm^2/s$, $\tau_b=91.2\mu s$, $S_b=3050cm/s$ with S_a as a parameter. The values of S_b and τ_b are determined by the separation of S and τ_b [12] for the experimental decay curves obtained from the back surface of the samples. The best fit is obtained when $S_a=70cm/s$. Thus, S_{eff} is 70cm/s in figure 5 (for the sample N-50-14). Similarly, S_{eff} is estimated for all the samples.

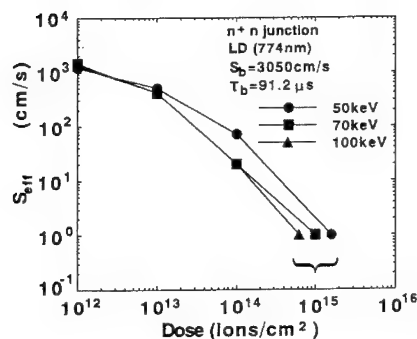


Fig.6 Dependence of S_{eff} on dose with the energy as a parameter for all the samples.

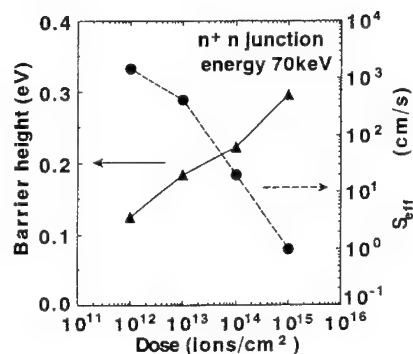
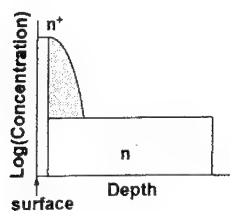
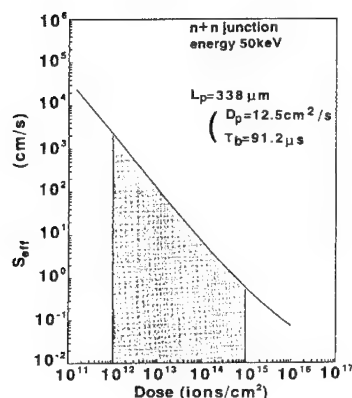


Fig.7 Dependences of S_{eff} and of the potential barrier height on dose for the samples implanted at 70keV with different doses.



(a)



(b)

Fig.8(a) A model of a carrier concentration profile. (b) Results for the numerical analysis of S_{eff} at an n^+n junction interface as a function of dose (an energy of 50keV) using the model in (a).

Figure 6 shows the dependence of S_{eff} on dose for all the samples. The results show that S_{eff} decreases with dose for all the energies. It should be emphasized that S_{eff} is reduced by forming the high-low junction and that the increase of τ_1 with dose represents the decrease of S_{eff} with dose. Figure 7 shows S_{eff} and a potential barrier height of an n^+n high-low junction as a function of dose for the samples implanted at 70keV. The potential barrier height were obtained from the dopant concentration profiles measured by secondary ion mass spectrometry (SIMS). These results indicate that S_{eff} were reduced because of the increase in the potential barrier height, which is due to the increase in the carrier concentration of a heavily doped layer with dose. Thus, the results were in good agreement with the results expected from the dependence of τ_1 on dose as mentioned above (figure 4).

S_{eff} at a high-low junction interface was investigated by the numerical analysis using a carrier concentration profile as shown in figure 8(a) [13]. (The effect of electric field and the dopant concentration on effective surface recombination velocity was reported in reference [13].) We investigated S_{eff} involving the recombination in the shaded region in figure 8(a) by the numerical analysis. Figure 8(b) shows the results for the numerical analysis of S_{eff} at an n^+n junction interface as a function of dose (an energy of 50keV) based on the model shown in figure 8(a). In figure 8(b),

L_p is the diffusion length of minority carriers and the shaded region represents the range of dose used in the present experiment. The results show that S_{eff} decreases with dose at a constant energy. This theoretical result coincides with the experimental result in figure 7.

B. Effect of doped layer on S_{eff} and τ_{eff} measured using an N_2 laser

We measured an effective minority carrier lifetime for the samples by the photoconductivity decay method using an N_2 laser ($\lambda=337.1nm$) as a carrier excitation pulse source. The wavelength of an N_2 laser is much shorter than those of the LD's ($\lambda=774nm, 904nm$).

Figure 9 shows the decay curves for excess carriers of the samples implanted at an energy of 70keV with doses ranging from 1×10^{12} to 1×10^{15} ions/cm² and subsequently annealed. The N_2 laser was used as a carrier excitation pulse source. In figure 9, the sample N-70-15 is also measured using the LD ($\lambda=904nm$). The result shows that τ_{eff} increases with dose. It is also shown that the value of τ_{eff} measured using the N_2 laser becomes equivalent to that measured using the LD ($\lambda=904nm$) for the sample implanted with a dose of 1×10^{15} ions/cm². The same results were obtained for the other energies. It is considered that the injected excess carriers diffuse quickly to the bulk while lifetimes are measured, though an irradiation light from the N_2 laser is absorbed in the heavily doped layer. The optical penetration depth into silicon of the N_2 laser is estimated to be about 0.01 μm . Figure 10 shows the diffusion length and the effective width of an n^+ -region as a function of dose for the samples implanted at 70keV [14]. In figure 10, it should be emphasized that the diffusion length is longer than the effective width of the n^+ -region.

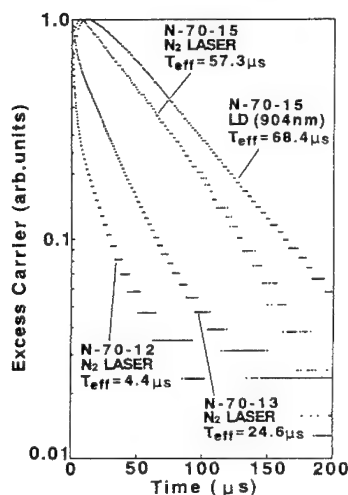


Fig.9 Decay curves for excess carriers of the samples implanted at an energy of 70keV with doses ranging from 1×10^{12} to 1×10^{15} ions/cm² and subsequently annealed. An N_2 laser and a LD ($\lambda=904nm$) were used as a carrier excitation pulse source.

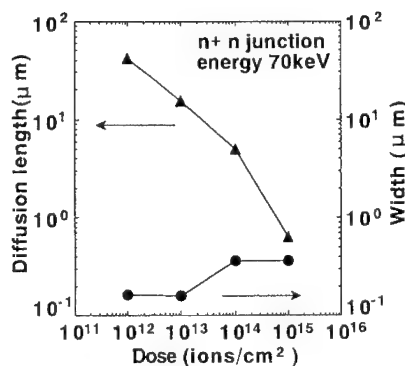


Fig.10 Dependences of the diffusion length and of the effective width n^+ -region on dose for the samples implanted at 70keV with different doses.

SUMMARY

We have investigated the surface properties of silicon which has a heavily doped layer at the surface. We measured minority carrier lifetimes for the samples using the noncontact laser/microwave method, where minority carriers were injected using a laser diode ($\lambda=774\text{nm}$). The results show that values of τ_1 increase with dose for all the energies. It is considered that the effective surface recombination velocity (S_{eff}) was reduced because of the increase in the carrier concentration of the heavily doped layer with dose. We estimated S_{eff} at an ion implanted surface. The results show that S_{eff} decreases with increasing dose for all the energies. This experimental result coincides with the theoretical result.

Furthermore, we measured an effective minority carrier lifetime for the samples by the photoconductivity decay method using an N_2 laser ($\lambda=337.1\text{nm}$) as a carrier excitation pulse source. Similar results were obtained using the N_2 laser instead of laser diode's ($\lambda=774\text{nm}$, 904nm) as a carrier excitation pulse source.

REFERENCES

- [1] R.W.Dutton and R.J.Whiter, IEEE Trans. Electron Devices, **ED-16**, 458 (1969)
- [2] J.G.Fossum, IEEE Trans. Electron Devices, **ED-24**, 322 (1977)
- [3] A.Usami and M.Yamaguchi, IEEE Trans. Nuclear Science, **NS-26**, 2874 (1979)
- [4] A.Usami, H.Fujiwara, N.Yamada, K.Matsuki, T.Takeuchi, and T.Wada, IEICE Trans. Electron., **E75-C**, 595 (1992)
- [5] A.Usami, T.Nakai, H.Fujiwara, S.Ishigami, and T.Wada, IEICE Trans. Electron., **E75-C**, 1043 (1992)
- [6] A.Usami, A.Ito, Y.Tokuda, H.Kano, and T.Wada, J.Cryst. Growth, **103**, 350 (1990)
- [7] J.R.Hauser and P.M.Dunbar, Solid-St.Electron., **18**, 715 (1975)
- [8] A.Sinha and S.K.Chattopadhyaya, IEEE Trans. Electron Devices, **ED-25**, 1412 (1978)
- [9] J.G.Fossum, R.D.Nasby, and S.C.Pao, IEEE Trans. Electron Devices, **ED-27**, 785 (1980)
- [10] A.Usami, Proc. IEEE Int. Conference on Microelectronic Test Structures, **4**, 1 (1991)
- [11] A.Usami, H.Fujiwara, T.Nakai, K.Matsuki, T.Takeuchi, and T.Wada, IEICE Trans. Electron., **E75-C**, 978 (1992)
- [12] A.Usami and T.Kushida, Oyo Buturi **50** 607 (1981) (in Japanese)
- [13] G.V.Ram and M.S.Tyagi, Solid-St. Electron., **24**, 753 (1981)
- [14] G.W.Taylor, H.M.Darley, R.C.Frye, and P.K.Chatterjee, IEEE Trans. Electron Devices, **ED-26**, 172 (1979)

ULTRASOUND DEFECT ENGINEERING OF TRANSITION METALS VIA METAL-ACCEPTOR PAIRS IN SILICON

RONALD E. BELL II, SERGUEI OSTAPENKO AND JACEK LAGOWSKI

Center for Microelectronics Research, University of South Florida
4202 East Fowler Avenue, MS ENB 118, Tampa, FL 33620-5350, USA

ABSTRACT

Experimental evidence is provided for ultrasound stimulated dissociation of metal-acceptor pairs in silicon, and also for enhanced diffusion of metal interstitials which may lead to enhanced pairing. The first effect is found dominant in Fe-doped p-type silicon where ultrasound causes low temperature dissociation of Fe-B pairs. This is in contrast to Cr-doped p-type silicon where ultrasound enhances the formation of Cr-B pairs due to enhanced diffusivity of Cr by as much as two orders of magnitude.

In this study, the metal-acceptor reaction was monitored in situ via corresponding changes of the minority carrier diffusion length measured by non-contact surface photovoltage. Ultrasound-stimulated pair reaction can be utilized for metal diagnostics for the silicon IC industry. Thus, with ultrasound, Cr-B pairing can be reduced from months to hours, making possible the identification of Cr via pairing kinetics in a reasonable period of time.

INTRODUCTION

Detection of transition metal impurities with high sensitivity is crucial for fabrication of integrated circuits (IC). As the dimensions of IC's decrease and the number of components per chip increase, metallic impurities become a real threat to IC yields, even at concentrations as low as 10^{10} atoms/cm³. The reduction of yield is associated with a degradation of gate oxide integrity in field effect devices, an increased leakage current in bipolar devices, and white spot defects in charge coupled devices.¹

Surface photovoltage (SPV) has been proven to have low detection limits for transition metals in silicon wafers approaching the part per quadrillion range.² This non-contact, real-time method is based on minority carrier diffusion length measurements combined with metal identification via donor-acceptor (D-A) pairing kinetics. In this paper, we discuss an application of ultrasound for alter D-A pairing reactions relevant to metal identification.

The application of ultrasound vibrations to semiconductors has been established as a means for altering defect related semiconductor properties.^{3,4} The corresponding ultrasound treatment (UST) of semiconductor crystals has been studied since the early 1980's,³ and has been shown to have significant effects on recombination properties. UST caused changes of the minority carrier diffusion length, L , has been recently observed in Czochralski (Cz) silicon wafers and in solar grade polycrystalline silicon.⁵

In silicon, key metal contaminants, such as chromium and iron, occupy interstitial sites. These fast diffusing, mobile species, Cr_i^+ and Fe_i^+ , behave as donors and tend to form nearest-neighbor coulombic pairs with substitutional boron acceptors, B_s^- .

Both interstitial metals and pairs act as recombination centers. In the case of Fe, the interstitial is about ten times more effective as a recombination center than the pair. For Cr, the situation is reversed and the pair is about twice as effective than Cr_i . These differences are the basis for determining

the metal concentration from changes in the minority carrier diffusion length caused by pairing or dissociation.

As discussed in References 6 and 7, the breaking of Fe-B (Cr-B) pairs is accompanied by a decrease (increase) of the minority carrier diffusion length value from L_0 to L_1 . L_0 is the initial minority carrier diffusion length when all metal species form pairs and L_1 is the final diffusion length value after "metal activation", when all pairs are broken. Activation is achieved by thermal treatment, optical pumping of minority carriers, or minority carrier injection by junction current. The concentration of metal is related to L_0 and L_1 by the following equation:

$$[N_{Fe(Cr)}] = C_{Fe(Cr)} \times (L_1^{-2} - L_0^{-2}) \quad (1)$$

where the constant $C_{Fe} \cong 7 \times 10^{16} \text{ [cm}^{-3}]$. For chromium, the exact value of C_{Cr} is, at present, not certain.

At any stage of pairing/dissociation reaction, the concentration of pairs and interstitials can be determined from the actual L value, which is between L_1 and L_0 . A pairing process is a first order reaction with a characteristic time constant τ_p given by:

$$\tau_p = 557T/D_i \text{ [B]} \quad (2)$$

where, $D_i = \text{const.} \exp(E_a/kT)$ is the diffusion length of the interstitial, E_a is the diffusion activation energy, k is the boltzmann's constant, T is the absolute temperature, and $[B]$ is the concentration of boron⁷.

EXPERIMENTAL PROCEDURE

Samples used in our study were boron doped Czochralski (Cz) silicon wafers with boron concentrations from 5×10^{14} to 10^{16} cm^{-3} . The iron concentration was $(0.8 \text{ to } 1.5) \times 10^{14} \text{ cm}^{-3}$. Chromium concentration was $(0.3 \text{ to } 5) \times 10^{13} \text{ cm}^{-3}$. $[B]$ was measured by the four point probe method, $[Fe]$ by the SPV optical techniques described in Reference 2, and $[Cr]$ concentration was determined by using deep level transient spectroscopy.

UST experiments utilized an ultrasound vibration apparatus (see Fig. 1) which consisted of a circular piezoelectric transducer mounted on a temperature controlled chuck (20 - 300°C), connected to a heating cooling system. The transducer (with frequencies ranging from 25 to 70kHz) was bound to the back surface of the sample. Ultrasound vibrations were generated by the power generator, controlled by a function generator. The sample was placed on the transducer and pressed against it with a Teflon pin. The acoustic strain, as measured by a miniature acoustic wave detector, had an amplitude of 10^{-5} to 10^{-4} . The temperature of the sample during UST and post-UST, was monitored in-situ by a thermocouple attached to the wafer surface.

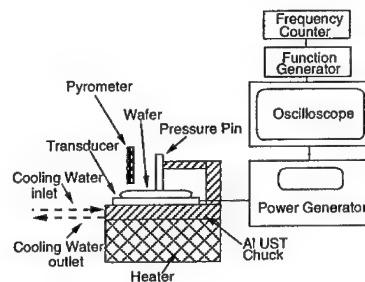


Fig. 1. UST Apparatus

A computer controlled commercial SPV system was used for non-contact measurements of the minority carrier diffusion length, L . The method used is analogous to that described in Reference 2.

RESULTS AND DISCUSSION

Chromium-Boron

The effect of ultrasound vibrations on the pairing of Cr-B at 65°C is shown in Figure 2. It is seen that the minority carrier diffusion length reaches the low L_0 value of 44 μm much faster when ultrasound is on. The initial state in this experiment corresponds to all pairs dissociated by previous thermal activation process (10 min. at 200°C and rapid quenching to room temperature). At room temperature, the Cr-B pairing is negligible due to low Cr diffusivity. Subsequent annealing at 65°C causes Cr-B pairing. For SPV measurements, 300°C annealing is stopped by placing the sample on water-cooled Al plate, which also served as the sample stage for SPV measurements. This is seen in Figure 2a. The minority carrier diffusion length reaches the low L_0 value of 44 μm much faster.

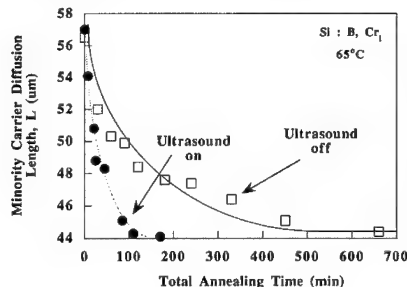


Fig. 2a. Diffusion length changes caused by Cr-B pairing.

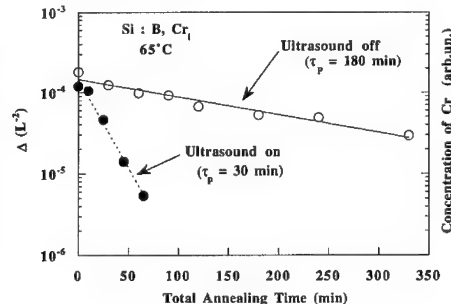


Fig. 2b. Cr-B Pairing kinetics.

The results from Figure 2a are replotted in Figure 2b as (\log of ΔL^{-2}) vs. time, in accord with Equation (1). Where $\Delta L^{-2} = L_1^{-2} - L_0^{-2}$. This plot reflects a decay of interstitial chromium due to pairing with boron. Both decays are exponential. However, a characteristic pairing time is six times shorter when ultrasound is on. Experiments were carried out for different annealing temperatures and the values of τ_p were then used to determine the Cr_i diffusion constant from Equation (2). Results for ultrasound on and off are presented in Figure 3. It is evident that ultrasound dramatically enhances Cr diffusivity.

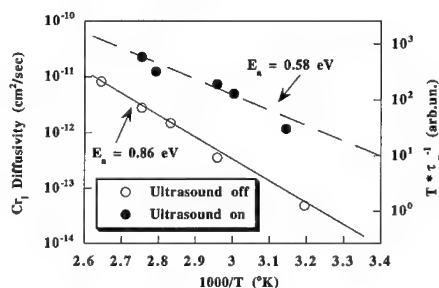


Fig. 3. Diffusivity of Cr determined from Cr-B pairing.

In accord with theory of UST effects, the enhanced diffusion is due to the transfer of energy from ultrasound wave to phonon gas and to the diffusing Cr. As a result, the diffusion activation barrier, E_a , is reduced to 0.58eV as compared to 0.86eV for thermal diffusion without UST.

After optimizing UST parameters, we were able to attain a reduction of Cr-B pairing time by as much as two orders of magnitude. In samples with $[B] = 1.2 \times 10^{16} \text{cm}^{-3}$, this allowed for the reduction of 800 minutes pairing time, without ultrasound, to only 8 minutes.⁶

Iron-Boron

A response of Fe-B pairing to UST is different than that of Cr-B. Fe diffusivity is about two orders of magnitude larger than that of Cr. Therefore, UST enhancement of pairing due to diffusivity increase is less significant. This provides a favorable condition for observing the opposite effect, i.e. the ultrasound induced braking of Fe-B pairs.

Corresponding results are shown in Figure 4. In this experiment, the initial pairing is achieved by long time (1 week) storing of sample at room temperature. The sample and transducer were then placed on a heated chuck and the UST started at 75°C at $t=0$. For SPV measurements, the sample was rapidly cooled to room temperature on an Al plate and the L value was measured in a matter of seconds. Annealing and UST were then resumed up to a net treatment time of about 80 minutes. Results in Figure 4 demonstrate a strong decrease of the diffusion length due to the UST. This decreasing of L corresponds to dissociation of Fe-B pairs caused by UST. Further annealing was performed with ultrasound off. The recovery of the diffusion length in that period is caused by the Fe-B pairing. The dashed line in Figure 4 is the behavior expected from thermal dissociation of Fe-B pairs at 75°C. Experimental points - filled squares - represent pair dissociation under UST. The recovery curve under "UST OFF" is calculated considering standard pairing theory controlled by Fe diffusion to immobile substitutional boron (Equation (2)).

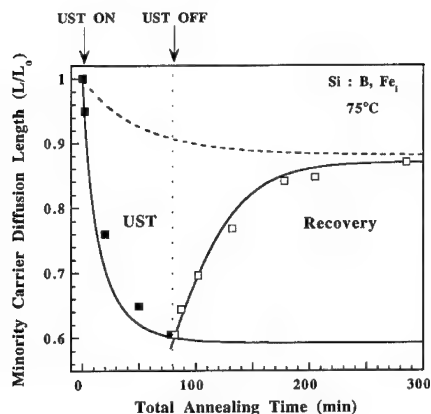


Fig. 4. Minority carrier diffusion length response to UST stimulated dissociation of Fe-B pair and subsequent pairing.

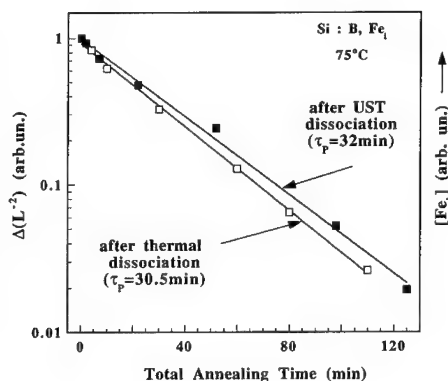


Fig. 5. Pairing kinetics after UST and after thermal pair dissociation.

It is important to emphasize that the pairing kinetics after ultrasound stimulated dissociation was the same as that after thermal pair dissociation. This is evident from Figure 5, which compares [Fe] decay at 75°C after UST and after thermal pair dissociation (200°C, 5 minutes annealing followed by quenching to 75°C on Al block). Both transients are exponential with practically the same pairing time constant very consistent with Fe-B pairing model and Equation (2).

The "jump" of an interstitial atom between two equivalent sites (nearest neighbors to the substitutional atom) occurs in two steps. In the first step, the interstitial atom moves to a distant site from the substitutional atom while, in the second step, it migrates to a new nearest-neighbor position, accomplishing a reorientation process.

Considering existing UST models, the ultrasound stimulated Fe-B pair dissociation can be explained similarly to the previously explored case of Li-B pairs. The ultrasound vibration can transfer elastic energy to anisotropic pair via the mechanism of acoustically forced pair reorientation.

The mechanism of pair reorientation is most effective at the following resonance condition.¹⁴

$$2\pi f = \omega_0 \exp(E_b/kT) \quad (3)$$

where f is the ultrasound frequency of the transducer, $\omega_0 = 10^{12}$ - 10^{13} s⁻¹ is the lattice phonon frequency and E_b is the pair binding energy. Substituting in Equation (3) the parameters of UST, $f = 70$ kHz and $T = 348$ K, we find $E_b \cong (0.44$ - $0.51)$ eV. This range is very close to electrostatic binding energy of the nearest neighbor coulombic pair in silicon (0.5-0.55)eV.¹¹ This confirms a feasibility of the pair reorientation mechanism.

PRACTICAL IMPLICATIONS

UST acceleration of Cr-B pairing can be of significance for determining Cr contaminants introduced during IC manufacturing, employing SPV measurement of the minority carrier diffusion length in conjunction with Cr-B pairing spectroscopy. The SPV approach is a leading method for measuring Fe contamination. Attempts to extend the approach to Cr have thus far failed because of approximately thirty times larger time periods are required for Cr-B pairing. Two orders of magnitude acceleration of Cr-B pairing by UST can, in principle, make the method faster than the standard technique used for Fe. However, for practical implementation, a further development of UST is needed for the capability of wafer scale ultrasound treatment of entire wafers up to 8 inches in diameter.

UST stimulated dissociation of Fe-B pairs can have a different application. By liberating Fe interstitials, it can provide a first step toward a new, low-temperature gettering of Fe. We have indeed demonstrated such a possibility for UST stimulated Fe gettering on grain boundaries in solar-grade silicon.¹²

SUMMARY AND CONCLUSION

Present results demonstrate a feasibility of effective, low-temperature engineering of chromium-boron and iron-boron pairs in silicon by ultrasound vibrations. The UST effects on Cr-B and Fe-B pairing is opposite. In the case of slowly diffusing chromium, the dominant UST effect is the enhancement of diffusivity, which leads to an acceleration of the pairing. In the case of iron, UST stimulated dissociation of pairs is realized. In the general case of any interstitial, donor-acceptor

pair, both effects should take place consistent with theoretical models of UST. Which effect is dominant will, however, depend on specific parameters and also on the critical conditions prior to UST.

We also conclude that UST engineering of pairs in silicon can have interesting, practical applications.

ACKNOWLEDGMENTS

The authors would like to thank MEMC Electronics Materials Company for the Fe and Cr doped wafers, Dr. Kamal Mishra for assistance with DLTS measurements and the staff of the Center for Microelectronics Research at the University of South Florida. This work was supported by grants from the National Renewable Energy Laboratory and Advanced Research Projects Agency.

REFERENCES

- ¹L. Jastrzebski, W. Henley, C. Neuse, *Solid State Technology*, Dec. (1992).
- ²J. Lagowski, A.M. Kontkiewicz, W. Henley, M. Dexter, L. Jastrzebski, P. Edelman, presented at the 5th International Conference on Defect Recognition and Image Processing in Semiconductors and Devices, 1993.
- ³I.V. Ostrovskii, V.N. Lisenko, *Sov. Phys. Solid State* **24**, 682 (1982).
- ⁴V.L. Gromashevskii, V.V. Dyakin, E.A. Sal'kov, S.M. Sklyarov, N.S. Khilimova, *Ukr. Fiz. Zh.*, **29**, 550 (1984).
- ⁵S.S. Ostapenko, N. Ikeda, F. Shimura, *Semiconductor Silicon*, 1994, edited by H.R. Huff, W. Bergholz and K. Sumino, PV/94-10, Electrochem. Soc. Proceed. Ser., Pennington, NJ, 1994, p. 856.
- ⁶K. Mishra, *Electrochemical Soc. Proc.*, 92-2, Extended Abstracts 426, October 1992, Toronto, Canada.
- ⁷G. Zoth, W. Bergholz, *J. Appl. Phys.* **67** 11, 1 June (1990).
- ⁸H.R. Huff, *Solid State Technology*, **26**, 211 (1983).
- ⁹L.C. Kimmerling, J.L. Benton, *Physica* **166B**, 297-300 (1983).
- ¹⁰E.R. Weber, *Applied Physics, A* **30**, 1-22 (1983).
- ¹¹H. Conzelmann, K. Graff, R. Weber, *Applied Physics A Solids and Surfaces*, **30**, 169-175 (1983).
- ¹²S.S. Ostapenko, R.E. Bell, *Appl. Physics Letters*, **77** (10), 15 May (1995).
- ¹³B.S. Berry, *J. Physics Chem. Solids*, **31**, 1827 (1970).
- ¹⁴R. de Batist, *Internal Friction of Structural Defects in Crystalline Solids* (American Elsevier, New York, 1972), p. 67.
- ¹⁵J. Lagowski, P. Edelman, A.M. Kontkiewicz, O. Milic, W. Henley, M. Dexter, L. Jastrzebski, A.M. Hoff, *Appl. Phys. Lett.* **63**, 3043 (1993).

INVERSION OF CONDUCTIVITY IN *p*-Si AFTER ION TREATMENT

ALEXANDER N. BUZYNIN*, ALBERT E. LUK'YANOV*, VYACHESLAV V. OSIKO*,
AND VLADIMIR V. VORONKOV**

*General Physics Institute of RAS, 38 Vavilov Street, Moscow, 117942, Russia

**Institute of Rare Metals, Bolshoi Tolmachevski, 5, Moscow, 109017, Russia

ABSTRACT

The results of electric parameters studies of silicon samples with unusual *p-n* junctions are presented. The junctions appeared after the treatment of homogeneous *p*-Si wafers by 1–5 keV energy argon ion irradiation at the temperature below 100°C and without doping by any *n*-type impurities. The model of this phenomena is discussed.

INTRODUCTION

An unusual *p-n* junction in Si crystal was revealed in Ref.[1] by using a scanning electron microscope (SEM) in electron beam induced current (EBIC) mode. The further studies² showed that a junction appears after an exposure of *p*-Si wafer to argon ion irradiation. This treatment was made before the deposition of metal coating to produce high quality Schottky barrier. The Schottky barriers or shallow *p-n* junctions are usually employed in SEM EBIC investigations of Si crystal microdefects and other inhomogeneities.

In our paper all available experimental results are discussed. The main attention is paid to the formation and diffusion of the self-interstitials (Si_i) due to irradiation by argon ions. The proposed model of the effect is based on the interaction of Si_i with the impurities, boron and oxygen.

EXPERIMENTAL

The *p*-Si wafers from B-doped CZ-crystals with various resistivity were processed by 1–5 keV Ar ions in gas discharge plasma. Then cleavages of the wafers were studied by SEM EBIC mode. The formation of a *p-n* junction was revealed. The formation of *n*-type region in *p*-type Si wafer after the Ar ion bombardement was confirmed by a simple thermo-probe technique: the thermo-EMF sign changed for the opposite one on the processed side of the wafer. It was also confirmed by the Hall effect data.

Typical examples of *p-n* junctions produced after exposure of the wafers to Ar ions are shown in Fig.1. Light or dark vertical strip is just the image of such *p-n* junction (the positive or negative contrast depends on the polarity of EBIC amplifier). The depth *h* of the junction (its distance from the processed surface of the wafer) was a nonlinear function of exposure duration *t*. No junction was found in control non-processed wafers. Some delay (1–15 min) in the junction movement was also observed. When *p-n* junction starts to move (as well as when it approaches the non-processed wafer side) its velocity is essentially reduced.

A typical *h(t)* plot is shown in Fig.2. The shape of the curve is similar to that of "error function" $\text{erf}(t/T)$ with a parameter *T* which is dependent on characteristics of the

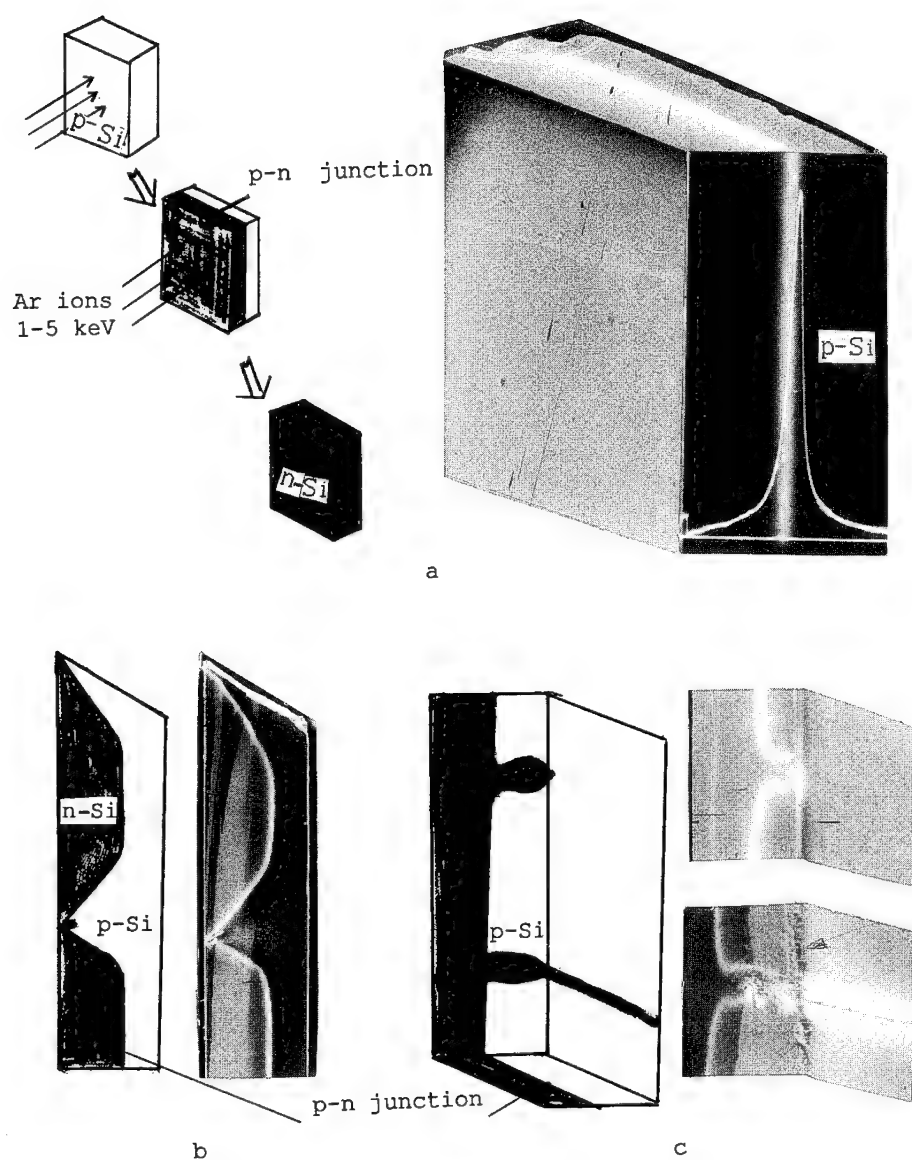


Figure 1: SEM microphotographs of cleavages of Si wafers with p - n junctions in secondary emission and EBIC modes: (a) practically straight p - n junction (light strip in image); (b) distortion of p - n junction form due to effect of a surface defect located on the treated side of the wafer and the wafer edge; (c) distortion of p - n junction form due to effect of a defect and a scratch on the untreated side of the wafer. The thickness of Si wafers is 0.45 mm.

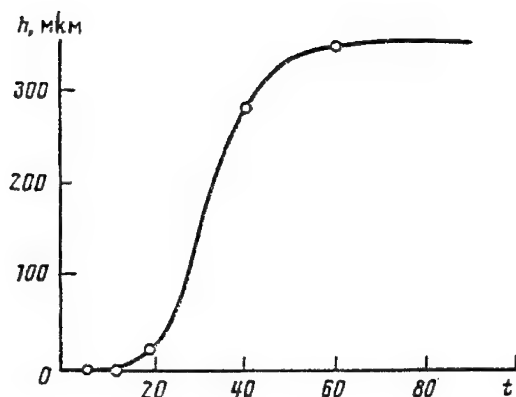


Figure 2: Typical plot of p - n junction depth h vs duration of Si wafer exposure to Ar ions. The bombardment by Ar ions (energy 1.5 keV, current density 1 mA/cm², sample temperature below 100°C) of one side of B-doped p -Si wafer ($\rho = 12\Omega\text{cm}$) caused the p - n junction formation.

sample as well as on the processing features. One may control the junction depth h within the range from several microns to several hundreds of microns by varying the processing duration. Particularly the junction may closely approach the unexposed by ions wafer side. The relation $h/\sqrt{t} = \text{const}$, which is the typical characteristic of diffusion processes, holds at $t > 20$ min. The slope of the curve $h(t)$ depends on the wafer thickness.

The influence of surface treatment and its defect structure on p - n junction movement was also revealed. When bright polished Si surface was treated by argon ions the junction movement is faster than that in samples of abrasion polishing. The extended defects of Si wafer surface as well as structural and impurity inhomogeneities also influenced the local p - n junction movement.

Fig.3 shows the effect of growth striations of an initial crystal on the form of em p - n junction image. One should note that EBIC oscillograms are practically symmetric for deep junctions. Thus the minority charge carrier diffusion length L remains almost constant in the course of p - n junction formation and movement (usually $L > 0.01$ mm). It means that the structural perfection of the crystal bulk is not much affected by Ar ion treatment.

The secondary-ion mass-spectrometry studies were performed to control the possible contamination of wafer during argon ion bombardment. The layer-by-layer etching of both the processed sample with a shallow p - n junction (if the depth $h < 1\mu\text{m}$) and the control (non-processed) sample showed that the content of various impurities was practically identical in both wafers. Therefore there was no additional doping of the wafer by n -type impurities in the course of Ar ion processing.

Hence the only cause of the p - n junction formation is a loss of boron acceptors and/or generation of donor defects by some reactions. The p - n junction was not found after the argon ion treatment of n -type Si single crystal: the acceptor-type conductivity did not appear. The p - n junction did persists after the annealing during several hours at 450°C.

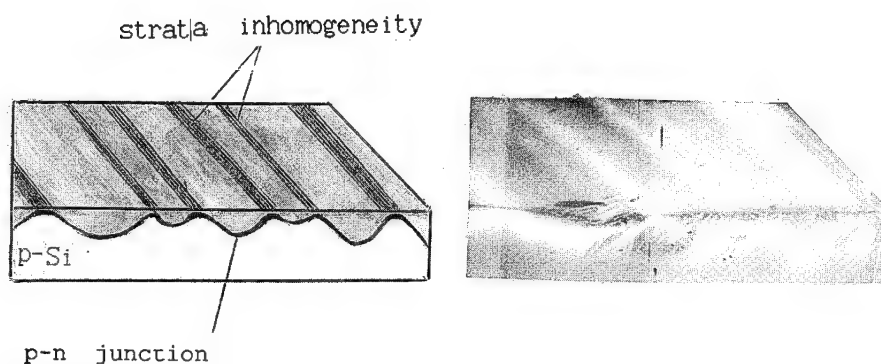


Figure 3: Distortion of the p - n junction form seen on cleavage due to strata inhomogeneity which is seen on the front surface of the wafer. The wafer thickness is $450\text{ }\mu\text{m}$.

However, one hour annealing at 750°C resulted in disappearance of the p - n junction, and the sample conductivity restored its initial value.

The four-probe resistivity measurement performed for some processed wafers (with p - n junction near the untreated wafer surface) showed that n -type resistivity was 3–5 times lower than the initial p -type resistivity which means that the produced electron concentration is about the same as the initial hole concentration.

The Hall effect measurements of two samples with a p - n junction in the wafer second half revealed that the electron concentration was one tenth of the initial hole concentration. Hall effect temperature dependence obtained for the n -type region of one of those samples demonstrated that:

- 1) the acceptor concentration is equal to only 1% of the initial boron concentration,
- 2) there are donor energy levels at $E_c = 60\text{ meV}$ and $E_c = 130\text{ meV}$ which are the well known levels of oxygen thermal donors of so called *BTD* family,³
- 3) the major donor level is $E_c = 80\text{ meV}$.

The I - V curves for our samples with p - n junctions are similar to those for usual Si diodes and depend on the quality of ohmic contacts to p - and n -regions. The C - V curves treated using many conventional models lead to contradictory results, which should be verified.

The samples (diodes with p - n junctions) were tested as prototypes of solar cells and detectors of radiation (electrons and ions). Encouraging results were obtained even with the simple ohmic contacts (Al baking, rubbing in In-Ga alloy, etc.). It allows to expect improvement of the performance of the mentioned devices after developing a simple low-temperature and ecologically pure technology of their production.

Variation of processing conditions allows to produce several p - n junctions rather than a single one inside the wafer (Fig.4), i.e., the structures of p - n - p , p - n - p - n , etc. types. These structures are feasible for manufacturing transistors and other more complex silicon devices.

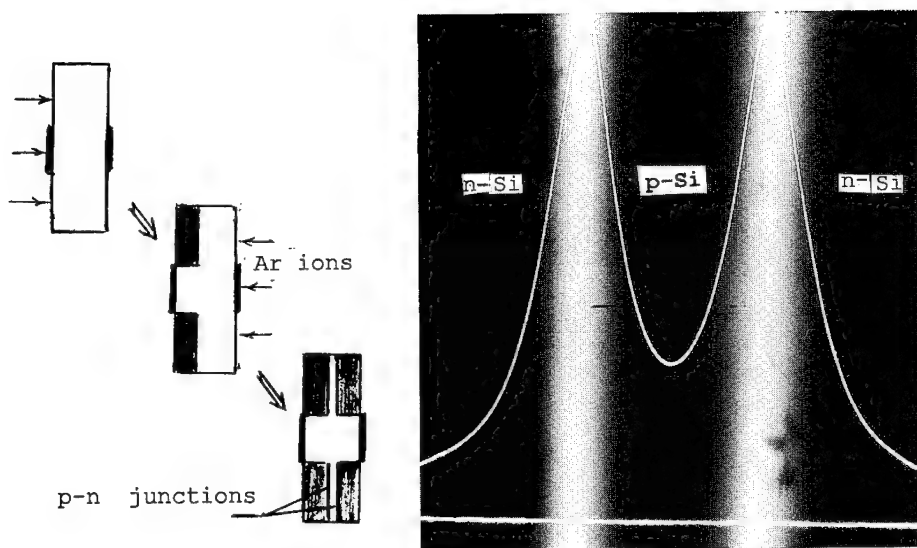


Figure 4: Oscillogram and zero level of EBIC signals for the sample with two p - n junctions, and a diagram of its fabrication.

DISCUSSION

What are the reasons of unusual p - n junctions formation in our experiments? It was already noted that the p - n junction formation is not related to any doping of the initial p -Si sample by n -type impurities from an external source in the course of Ar ion processing. In principle, such doping by some impurities from the ion processing chamber is not excluded, but our studies have shown that the doping is of low probability.

Therefore, one should look for such intrinsic point defects produced by Ar bombardement near the wafer surface, diffusing into the wafer bulk and reacting with the impurities (which are mostly oxygen and boron). As was mentioned above there are very low boron acceptor concentration in the converted n -region. The drastic decrease in the substantial boron concentration is most likely to be caused by in-diffusing Si_i , which kick out the boron atoms into interfaces.

Formation of oxygen thermal donors indicates to another plausible mechanism of boron loss which is also related to in-diffusing Si_i . Oxygen atoms are immobile at the temperature below 100°C during the Ar processing. Yet the Si_i may serve as vehicles for oxygen by forming fast-diffusing complexes silicon-silicon oxides.³ Thus the thermal donor formation (that is, oxygen aggregation) is strongly catalyzed by Si_i . Besides simple oxygen aggregates (double donors), oxygen aggregates including a boron atom may form; these are single

donors, and the major observed donor level ($E_c = 80$ meV) may be attributed to such donor complexes. It is likely that both mechanisms of B acceptor loss — kicking out and complexing with oxygen — occur simultaneously. While the types of Si_i reactions are just hypothetical the basic effect of Si_i in-diffusion is of a little doubt.

Indeed, the retardation of p - n junction in the vicinity of the wafer backside is naturally explained by sinking of Si_i to this surface, so that the Si_i concentration is reduced (and the conversion reaction rates are also reduced). Similar explanation is applied to a junction retardation near the wafer edge. Enhanced propagation of p - n junction near the backside extended defects (scratches) can be explained by gettering action of these extended defects (it is well known in device manufacture). This means that Si_i sinking is not to the surface itself, but to some near-surface microdefects which are locally gettered near an expended defect.

CONCLUSION

The deep p - n junction formation due to inversion of p - to n -type resistivity in B-doped p -Si wafers after low energy ion argon treatment below 100°C was discussed. The inversion may be due to interaction of self-interstitials with boron and oxygen atoms.

The authors express deep gratitude to N. A. Butylkina and A. I. Butylkin for some experimental results.

REFERENCES

1. A. N. Buzynin, A. E. Luk'yanov, N. A. Butylkina *et al.*, Bull. Acad. Sci. USSR Phys. Ser. **54**, 96 (1990)
2. A. E. Luk'yanov, A. N. Buzynin, A. I. Butylkin *et al.*, Scanning. **14**, 358 (1992)
3. V. V. Voronkov, Semicond. Sci. Technol. **8**, 2037 (1993)

SURFACE-ORIENTED OXYGEN MASS TRANSPORT DURING IMPLANTATION

A.B. DANILIN¹, L.A. CHARNYI², A.W. NEMIROVSKI^{1,2}, AND V.V. SARAIKIN¹

1. Centre for Analysis of Substances, 9, Elektrodnyaya st., 111524 Moscow, Russia.

2. Moscow Steel and Alloys Institute, 4, Leninsky Prospekt, 117936 Moscow, Russia.

ABSTRACT

The effect of implantation conditions on the localization of oxygen implanted with substoichiometric doses has been studied. Oxygen ions were implanted into Si wafers coated with a thin oxide film, which was etched off after the implantation. We used various implantation modes. After the implantation, the specimens were studied using SIMS and X-ray diffractometry. The concentration profiles suggest that at the lower implantation temperature, part of oxygen migrates toward the Si-SiO₂ interface. The effect does not refer to the usual enhancement of SIMS signal at the surface because the concentration peak is at a depth of about 25 nm. Calculated deformation profiles indicate a compression at the same depth, the effect being the strongest for the low current density. The result suggests that the superficial layer is rich in vacancial-type defects. The coincidence of the deformation and oxygen concentration maxima leads to the conclusion that oxygen migrates toward the surface in the form of A-centers. A similar phenomenon has been observed for sequential low-temperature implantation of oxygen and nitrogen.

INTRODUCTION

The design of layered structures in microelectronics materials using controlled defect-impurity reactions is an interesting and practically important trend of the advanced materials science. It has been shown [1] that the localization and, hence, the efficiency of substoichiometric ion beam synthesis of SiO₂ in Si can be considerably increased by choosing those implantation conditions which allow amorphous buried layers to be formed in the region of the highest oxygen supersaturation in as-implanted specimens. However, since the type and concentration profile of the radiation defects in Si largely depends on the implantation conditions [2], and the behavior of oxygen implanted with substoichiometric doses is related to those defects [3], we may assume that the oxygen concentration profile will also be determined by implantation mode. Thus, it is of interest to assess the effect of implantation conditions on the efficiency of ion beam synthesis. In particular, we would like to understand the role of dose rate and implantation temperature of oxygen, whose behavior is very sensitive to radiation defects, in Si enrichment with oxygen at the depth at which buried SiO₂ layer is to be formed during subsequent annealing.

The aim of this work was to investigate the influence of substoichiometric-dose oxygen implantation conditions on oxygen concentration profiles for oxygen implantation and sequential implantation of oxygen and nitrogen.

EXPERIMENTAL

O⁺ ions with an energy of 150 keV and a dose of $1.2 \cdot 10^{17} \text{ cm}^{-2}$ were implanted into n-type Si(100) with a resistivity of $4.5 \Omega \cdot \text{cm}$. Possible contamination of the superficial Si layer during implantation was avoided by coating it with a 30 nm thick SiO₂ layer. After the implantation, this film was etched off.

The specimens were heated using various methods, the temperature being controlled with a thermocouple. For ion beam heating, the wafer temperatures were 200 and 350 °C at current densities of 6 and $22 \mu\text{A} \cdot \text{cm}^{-2}$, respectively. Combined heating was performed using ion beam and a resistive heater and, at the above current density, the wafer temperature was 650 °C.

One of the specimens was treated in thermocycling mode: implantation with an ion current density of $22 \mu\text{A} \cdot \text{cm}^{-2}$ was interrupted three times with 5-min breaks in the implantation process.

As has been shown [1], specimens treated in thermocycling mode or with a low current density contain amorphous buried layers.

The sequential implantation of oxygen and nitrogen was performed under the following conditions: the doses, $0.5 \cdot 10^{17} \text{ O}^+ \cdot \text{cm}^{-2}$ and $1.0 \cdot 10^{17} \text{ N}^+ \cdot \text{cm}^{-2}$; the energy, 80 keV; the current density, $5 \mu\text{A} \cdot \text{cm}^{-2}$. During the implantation, the wafer temperature was about 200 °C. One of these specimens was studied as-implanted and the other was analyzed after annealing at 1200 °C for 4 h in an Ar atmosphere.

Concentration profiles were recorded on a Cameca IMS-3f spectrometer using Cz⁺ and Ar⁺ primary beams. The beam currents were 0.1 and 0.6 μA , respectively. The etch pit area was $250 \times 250 \mu\text{m}^2$.

Oxygen-implanted specimens were analyzed using X-ray diffractometry. We used the following principles. Rocking curves of deformed materials exhibit more than one peak [4]. The strongest sharp peak is referred to as the main peak and is produced by the perfect matrix. Other peaks are produced by the deformed regions according to the well-known Bragg law: $d \sin \theta = n \lambda$. The law suggests that, given constant wavelength λ and reflection order n , any change in the lattice parameter d should lead to an appropriate change in the Bragg angle θ and, hence, in the peak position on the rocking curve. One can also see that an increase in the lattice parameter of a layer (interstitial-type defects) will produce a negative displacement of the corresponding peak (i.e., the peak will shift toward lower angles). A decrease in the lattice parameter (vacancial-type defects) will shift the peak toward large angles.

Deformation profiles were restored by solving the well-known Takagi equations [5]. The idea used was as follows. Rocking curves of specimens with deformed layers exhibit oscillations of intensity due to the interference of X-ray beams reflected by two crystal regions which are located at two opposite sides of the deformation profile and have the same deformation. The periods, intensities and spreading of the oscillations depend on deformation profile parameters. The restoration was performed using specially written computer program [6]. It should be noted that two deformation profiles which are symmetrical about the middle of the layer would produce absolutely similar rocking curves because of the above described mechanism of reflection from a deformed layer. Thus, we had two alternative symmetrical profile patterns. We chose that pattern which is considered to be typical of ion implantation [7].

RESULTS AND DISCUSSION

Figure 1 presents concentration profiles of implanted oxygen. It is noteworthy that, in comparison with the specimen implanted at $22 \mu\text{A}\cdot\text{cm}^{-2}$ (350°C , profile 1), in other specimens (profiles 2-4) the concentration of oxygen in the outer profile wing is lower. The greatest depletion of oxygen is observed in the specimen implanted with low ion current density (profile 4). It can be seen (profiles 3 and 4) that oxygen depletion of the profile wings is accompanied by an increase in the oxygen concentration in the superficial silicon layer. Usually, this effect is believed to originate from enhanced secondary ion emission from the surface oxide layers. However, in our case the maximum of profile 4 is located at a certain depth. Figure 2 shows elastic deformation profiles in the buried layers, and oxygen concentration curves are also given there to compare with. The deformations in the superficial layers of the specimens implanted with radiation heating (350°C) and combined heating (650°C) were negligible. The concentration profile maximum of the specimen implanted at $6 \mu\text{A}\cdot\text{cm}^{-2}$ (Fig. 2) coincided with the deformation maximum.

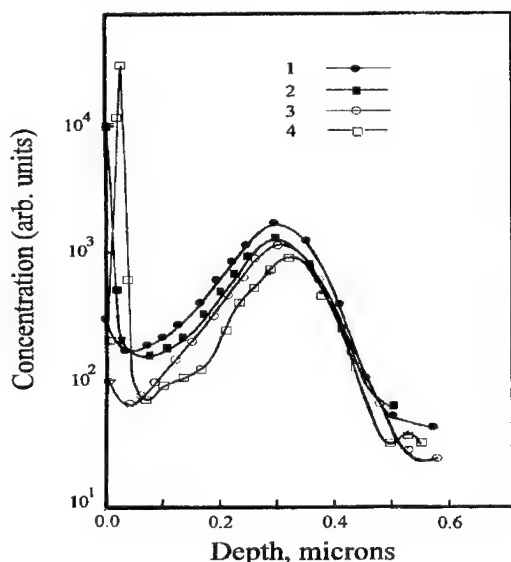


Figure 1. Oxygen concentration depth profiles. (1) Radiation heating; (2) Radiation heating (implantation with breaks); (3) Combined heating; and (4) Implantation at low current density.

As can be seen from Fig. 3, after low-temperature sequential implantation of oxygen and nitrogen at low ion current density, the oxygen profile has not a usual peak and the superficial silicon layer is rich in oxygen. Figure 4 shows that even after annealing at 1200°C for 4 h in an Ar atmosphere, the superficial silicon layer is still rich in oxygen.

The results can be interpreted as follows. Some of the radiation defects produced by implantation of light ions coagulate to stable complexes at the depth of the maximum elastic deformation. Other defects migrate to external sinks, such as the surface, where they may accumulate until the superficial layer becomes completely amorphous [8]. The remaining defects may annihilate. An increase in the ion current density or in the dose rate

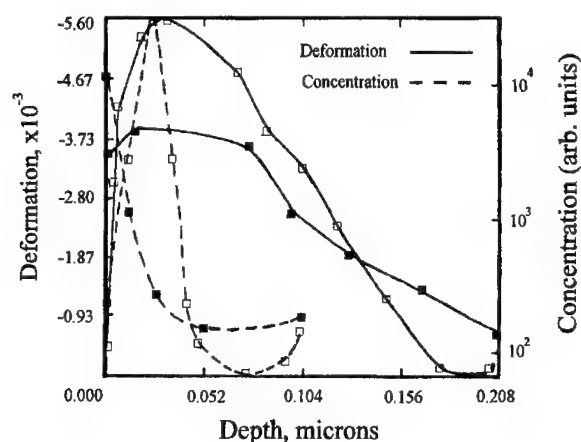


Figure 2. Elastic deformation profiles (inverted) and concentration profiles: (■) implantation with breaks and (□) implantation at low current density.

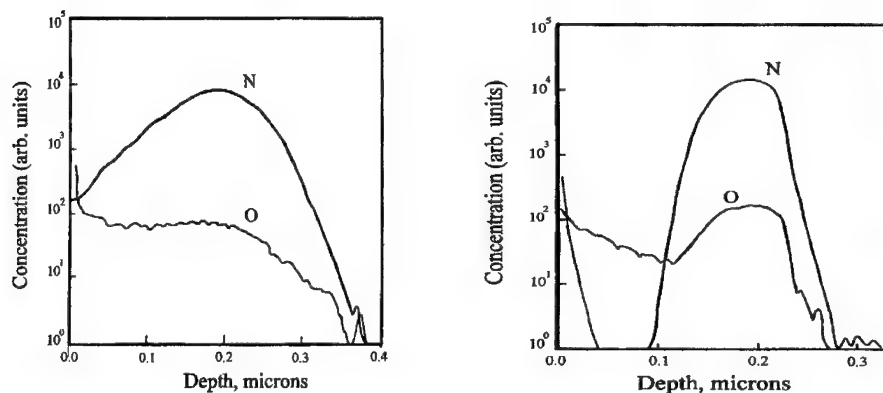


Figure 3. Oxygen and nitrogen depth profiles in as-implanted specimen.

Figure 4. Oxygen and nitrogen depth profiles in annealed specimen.

leads to an increase in the concentration of point defects generated in unit volume during unit time at the depth of the maximum deformation. Thus, the probability that complexes form should also increase. As a result, the amorphization dose decreases [9] and the mass transport of point defects toward the surface and their annihilation are hindered [10]. On the contrary, a decrease in the dose rate reduces the probability of direct defect accumulation and enhances their mass transport toward the surface [10]. As a result, the

amorphization dose increases [9] and the radiation defects accumulate in the thin superficial silicon layer [8, 10]. However, the real process is much more complex because of radiation heating which is proportional to ion current density [11]. The amorphization dose may then increase to an unachievable level, and only large complexes which are stable at a given implantation temperature may survive. Thus, oxygen implantation at a current density of $6 \mu\text{A}\cdot\text{cm}^{-2}$, which provided radiation heating to 200°C , produced an amorphous buried layer [1], and some point defects migrated to the surface, i.e., to the Si-SiO₂ interface. According to the sign of the elastic deformation, those defects were of vacancial nature. Accumulation of such defects in thin superficial Si layers has been observed earlier for implantation through SiO₂ film [12]. The superficial layer is simultaneously saturated with oxygen and vacancial-type defects due to the transport of V-O complexes toward the surface (Si-SiO₂ interface). This mechanism of oxygen mass transport has been shown to be possible at moderate temperatures [13]. For implantation with breaks, the temperature is relatively low for a noticeable period of time at early heating stages, and it seems that it is these stages that produce the buried layer. The transport of V-O defects toward the Si-SiO₂ interface becomes probable if temperature increases to its steady-state value. By and large, this implantation mode seems to be the most efficient because, obviously, it enables both accumulation and annealing of radiation defects.

The nature of the depletion at left profile wing after implantation at 650°C is completely different (profile 2, Fig. 1). It seems to originate from the formation of silicon oxides during high-temperature oxygen implantation [14]. The latter process includes several stages, the earliest of which are nucleation and growth of the nuclei. In the case under study, SiO₂ phase already exists on the wafer surface. Therefore, at an early stage of implantation when the inner sinks (silicon oxide precipitates) are not yet formed, oxygen atoms may move toward the Si-SiO₂ interface and, hence, the SiO₂ phase develops.

In case of sequential implantation of oxygen and nitrogen, a large amount of vacancial-type defects form during nitrogen implantation and produce V-O complexes. The migration of those complexes toward the surface is likely to produce the peculiar oxygen profile. However, the present implantation conditions do not influence the nitrogen profile, the pattern of which is quite usual. Obviously, the oxygen profile retains its general pattern in the superficial layer after annealing (Figs. 3 and 4).

Of course, the above models need to be verified by further experiments. Nevertheless, with account of well-known data on defect formation during implantation of light ions at various dose rates and wafer temperatures, as well as on the behavior of substoichiometric amounts of oxygen in silicon, the present assumptions appear to be reasonable.

CONCLUSIONS

Because of oxygen transport from the desired localization of buried SiO₂ layer, synthesis of such layers with substoichiometric oxygen doses may involve oxygen depletion even during implantation. We assume that, depending on implantation conditions, the depletion may be caused either by the transport of vacancy-oxygen complexes toward the surface, or diffusion of single oxygen atoms toward the protective SiO₂ film. This observation is of importance for substoichiometric ion beam synthesis of buried silicon dioxide and oxynitride layers.

ACKNOWLEDGMENTS

We wish to thank O.I. Vyletalina and A.F. Petrov for performing implantation and annealing. Special gratitude is expressed to A.A. Malinin for fruitful discussion of the results. We are also very grateful to MRS secretary Mrs. M. Geil, ISF staff and personally to Mr. G. Soros for making possible the presentation of the results.

REFERENCES

1. A.B. Danilin, A.A. Malinin, V.N. Mordkovich, V.V. Saraikin, and O.I. Vyletalina, Nucl. Instr. and Meth. in Phys. Res. **B82**, 431 (1993).
2. Physical Processes in Irradiated Semiconductors, edited by L.S. Smirnov (Nauka, Novosibirsk, 1977), p. 256 (in Russian).
3. K. Sumino, 2nd Inter. Autumn Meeting Proc. Gettering and Defect Engineering in Semiconductor Technology (GADEST 87), Garzau, Germany, 1987 (Akad. Weisenchaften DDR, Frankfurt (Oder), 1987), p. 218.
4. A.M. Afanas'ev, P.A. Aleksandrov, and R.M. Imamov, X-Ray Diagnostics of Superficial Layers (Nauka, Moscow, 1986), p. 96 (in Russian).
5. P. Zaumzeil and V. Winter, Phys. Status Solidi **A120**, 67 (1990).
6. K.D. Scherbachev, Private communication (1992).
7. Y. Akasaka, K. Yoneda, T. Sakurai, H. Nishi, S. Kawabe and A. Tohi, J. Appl. Phys., **44**, 1 (1973) 220.
8. A.I. Gerasimov, E.I. Zorin, P.V. Pavlov, and D.I. Tetelboum, Ibid. **A12**, 679 (1992).
9. B. Crowder, Ion Implantation in Semiconductors, Proc. US-Japan Seminar, edited by S. Namba (Kyoto, 1973), p. 63.
10. I.A. Abroyan and A.I. Titov, in Proceedings of 2nd USA-USSR Seminar on Ion Implantation, July 9-11, 1979, Puschino, edited by V.S. Vavilov and L.S. Smirnov (Inst. Semicond. Phys., Siberian Branch of Russian Acad. Sci., Novosibirsk, 1979), p. 335.
11. J.H. Freeman, D.J. Chivers, G.A. Gard, G.W. Hinder, B.J. Smith, and J. Stephen, in Ion Implantation in Semiconductors, edited by S. Namba (Plenum Press, New York, 1975), p. 55.
12. A. Vedono and S. Tanigawa, Defect Control in Semiconductors, edited by K. Sumino (Elsevier Science Publishers B.V., North-Holland, 1990), p. 495.
13. A.K. Tipping, R.C. Newman, D.C. Newton, and J.H. Tucker, Mater. Sci. Forum **10/12**, pt. III, 887-892 (1986).
14. K.J. Reeson, C.D. Marsh, R.J. Chater, J.A. Kilner, A.K. Robinson, K.N. Christensen, P.L.F. Hemment, G. Harbbeke, E.F. Stigmeier, G.R. Booker, and G.K. Celler, Microelectronics Engineering **8** (3/4), 163 (1988).

OBSERVATION OF VACANCY-OXYGEN COMPLEXES IN SILICON IMPLANTED WITH SUBSTOICHIOMETRIC DOSES OF OXYGEN IONS

A.I. BELOGOROKHOV^{1,2}, L.A. CHARNYI^{1,3}, A.B. DANILIN¹,
AND A.W. NEMIROVSKI^{1,3}

1. Centre for Analysis of Substances, 9, Elektrodnaya st., 111524 Moscow, Russia

2. Institute of Rare Metals, 156-517, Leninsky Prospekt, 117571 Moscow, Russia

3. Moscow Steel and Alloys Institute, 4, Leninsky Prospekt, 117936 Moscow, Russia

ABSTRACT

Cz-grown p-Si(111) specimens were implanted with O⁺ ions at an energy of 150 keV and doses of 0.25, 0.5, and 1.0 ($\cdot 10^{17}$) cm⁻². The implantation temperatures used were 350 and 650 °C. After the implantation, some of the specimens were annealed at 1000 °C for 1 h in a nitrogen atmosphere. IR data indicated the presence of vacancy-oxygen complexes both before and after annealing, irrespective of implantation temperature. Double-crystal X-ray rocking curves also showed that vacancy-type defects are present.

INTRODUCTION

Structural defects, including radiation-induced ones, are known to largely affect the behavior of reactive impurities, e.g., oxygen, in silicon [1]. Controlling of defect-impurity reactions in ion-implanted silicon is a promising method of engineering of layered structures with desired properties. Vacancy-type defects play a significant role in ion beam synthesis of oxygen-containing compounds in silicon. These defects may serve as centers of nucleation or heterogeneous phase formation [2-4]. SiO₂ precipitates offer an energetic advantage because of the difference in the densities of SiO₂ ($2.4 \cdot 10^{22}$ SiO₂/cm³) and Si ($5.0 \cdot 10^{22}$ Si/cm³) [4]. Furthermore, vacancy emission by vacancy complexes during annealing may enhance the transport of unbonded oxygen atoms toward the growing precipitates (the vacancy mechanism of oxygen diffusion has been described in [5]). On the other hand, the vacancies annihilate with interstitial Si atoms produced by SiO₂ growth and, hence, reduce the concentration of interstitial-type defects in the material [6]. Choice of those implantation conditions which provide for accumulation of vacancy-type radiation defects in the thin buried layer will considerably increase the efficiency of ion beam synthesis of buried SiO₂ layers in silicon [7].

Thus, study of solid state reactions which occur in silicon supersaturated with oxygen atoms and radiation defects is of a great practical interest.

EXPERIMENTAL

Double-side polished Cz-grown p-Si(111) specimens were implanted with 150 keV oxygen ions. The ion current density was 22 μ A/cm². Some of the specimens were heated by ion beam to max. 350 °C. Other specimens were implanted with combined heating by ion beam and a resistive heater. In that case, the highest temperature was 650 °C; it was monitored with a thermocouple. The implantation doses were 0.25, 0.5, and 1.0 ($\cdot 10^{17}$) cm⁻². Only the central parts of the specimens (2x2 cm²) were implanted. After the implantation, some of the specimens were annealed at 1000 °C for 1 h in a nitrogen

atmosphere. Bourret [6] reported that at this temperature, silicon oxides start to form in Cz-Si, the effect of thermal vacancy- and interstitial-type defects being negligible. We may assume that the result of low-temperature annealing should be largely determined by the reactions between oxygen atoms and radiation defects. In turn, both the type and the concentration of radiation defects depend substantially on implantation dose and temperature.

We recorded rocking curves of the defect layers using conventional technique [8]. Since interstitial-type defects produce greater relative distortions than do vacancy-type defects and, hence, X-ray diffractometry is less sensitive to the latter defects [8], we applied this method only to unannealed specimens implanted with the highest experimental oxygen dose ($1 \cdot 10^{17} \text{ cm}^{-2}$). Rocking curves were obtained in double-crystal setup according to [8] and are shown in Fig. 1. IR absorption spectra were recorded on a rapid-scanning IFS-113v (Bruker) Fourier-spectrometer in the range from 400 to 1200 cm^{-1} at room temperature. The wavelength resolution was not worse than 1 cm^{-1} . The spectra of unimplanted silicon were subtracted from the spectra of the implanted areas. The resultant spectra are presented in Figs. 2-4.

RESULTS AND DISCUSSION

As can be seen from Fig. 1, the rocking curves indicate a positive angular deviation of the peaks produced by the layers and, hence, a decrease in the lattice parameter due to compression deformations in the implanted layers. This situation is typical of layers which contain vacancy-type defects [8]. Note that an increase in the implantation temperature from 350 (curve 1) to 650 °C (curve 2) leads to only a quantitative change in the diffraction pattern: the deformation produced by the radiation defects becomes somewhat lower.

IR spectroscopy helped us to identify the type of the vacancy-type defects the presence of which was suggested by X-ray diffractometry. Figure 2, *a* shows that after implantation at 350 °C with a dose of $0.25 \cdot 10^{17} \text{ cm}^{-2}$ (spectrum A) the material exhibits several well-pronounced absorption bands and peaks. These are

(1) the peak at 515 cm^{-1} which can be attributed to interstitial oxygen atoms in the matrix [9];

(2) the peak at 607 cm^{-1} due to carbon atoms [9];

(3) the peak at 830 cm^{-1} produced by vacancy-oxygen (V-O) complexes [9];

(4) the wide band which spreads from 850 to 1050 cm^{-1} and can be related either to interstitial oxygen clusters around the V_2O complexes [10-12] or substantial damage of the layer [13]. The band may include absorption peaks in the range 1020 to 1050 cm^{-1} produced by SiO_x compounds ($x < 2$) [14];

(5) the band in the range 1070 to 1110 cm^{-1} which can be attributed either to SiO_2 microprecipitates (1083 cm^{-1} [14]) or to oxygen dissolved in silicon (1107 cm^{-1} [9]).

After implantation at 650 °C (spectrum B) the intensity of the peak produced by dissolved oxygen (515 cm^{-1}) is lower and the V-O peak disappears. Furthermore, the absorption in the range from 850 to 1000 cm^{-1} somewhat decreases, and in the range from 1020 to 1070 cm^{-1} it slightly increases. These observations indicate a decrease in the amount of interstitial oxygen atoms and oxygen involved in clusters around V_2O complexes and suggest a more efficient formation of substoichiometric silicon oxides. The latter assumption is quite reasonable since there are indications [15] that the higher is the oxygen implantation temperature the more intense is the phase formation during implantation.

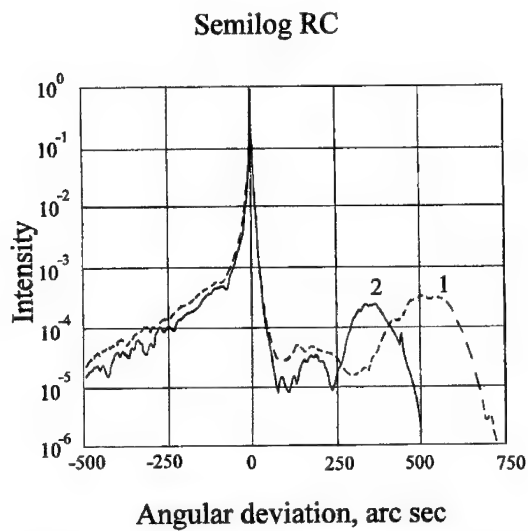


Figure 1. X-ray rocking curves of specimens implanted at (1) 350 and (2) 650 °C.

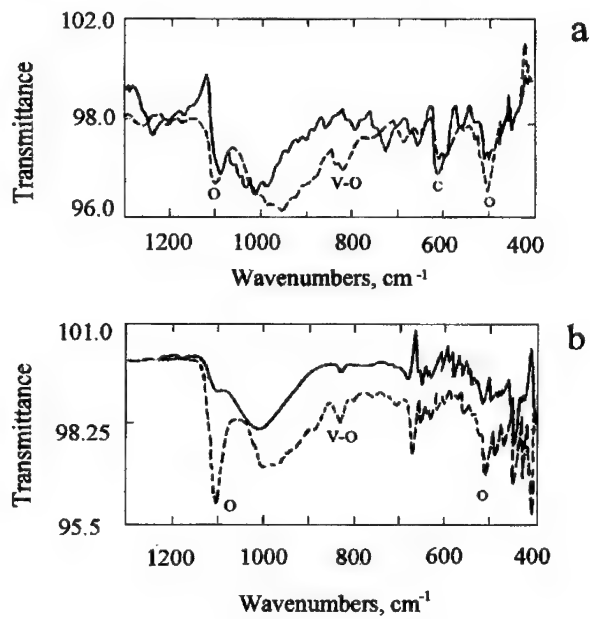


Figure 2. Transmittance spectra of specimens implanted with $0.25 \cdot 10^{17} \text{ O} \cdot \text{cm}^{-2}$ (a) before and (b) after annealing. Curve A (—) implanted at 350 and B (---) at 650 °C.

The drop at 1113 cm^{-1} can be attributed to a decrease in the concentration of $\text{C}_1\text{-O}_1$ complexes in comparison with the initial material (1115 cm^{-1} [5]).

The general pattern of the spectra remains the same for $0.5 \cdot 10^{17}\text{ cm}^{-2}$ (Fig. 3, *a*). However, even at 650°C (spectrum *B*) the V-O peak is still present and the band produced by oxygen clusters around V_2O complexes changes only slightly as compared to 350°C (spectrum *A*). Spectrum *B* shows that an increase in the efficiency of SiO_x formation is mainly caused by an increase in the fraction of oxygen dissolved in the matrix. Moreover, an increase in the implantation temperature avoids carbon contamination of the material.

After implantation at 650°C (spectrum *B*) the intensity of the peak produced by dissolved oxygen (515 cm^{-1}) is lower and the V-O peak disappears. Furthermore, the absorption in the range from 850 to 1000 cm^{-1} somewhat decreases and in the range from 1020 to 1070 cm^{-1} it slightly increases. These observations indicate a decrease in the amount of interstitial oxygen atoms and oxygen involved in clusters around V_2O complexes.

After implantation at 650°C (spectrum *B*) the intensity of the peak produced by dissolved oxygen (515 cm^{-1}) is lower and the V-O peak disappears. Furthermore, the absorption in the range from 850 to 1000 cm^{-1} somewhat decreases and in the range from 1020 to 1070 cm^{-1} it slightly increases. These observations indicate a decrease in the amount of interstitial oxygen atoms and oxygen involved in clusters around V_2O complexes and suggest a more efficient formation of substoichiometric silicon oxides. The latter assumption is quite reasonable since there are indications [15] that the higher is the oxygen implantation temperature the more intense is the phase formation during implantation. The drop at 1113 cm^{-1} can be attributed to a decrease in the concentration of $\text{C}_1\text{-O}_1$ complexes in comparison with the initial material (1115 cm^{-1} [5]).

The general pattern of the spectra remains the same for $0.5 \cdot 10^{17}\text{ cm}^{-2}$ (Fig. 3, *a*). However, even at 650°C (spectrum *B*) the V-O peak is still present and the band produced by oxygen clusters around V_2O complexes changes only slightly as compared to 350°C (spectrum *A*). Spectrum *B* shows that an increase in the efficiency of SiO_x formation is mainly caused by an increase in the fraction of oxygen dissolved in the matrix. Moreover, an increase in the implantation temperature avoids carbon contamination of the material.

Now we will dwell upon the role of annealing (Figs. 2, *b* - 4, *b*). It can be seen that the changes produced by annealing are minor and the general pattern of the spectra remains the same. At the lowest dose (Fig. 2, *b*) annealing fails to eliminate the vacancy-type defects and, furthermore, the V-O peak remains in the spectrum of silicon implanted at 650°C (spectrum *B*). The intensity of the absorption peaks of oxygen dissolved in silicon (1107 cm^{-1}) increased, especially for implantation at 350°C . This result may indicate a partial annealing and enlargement of the interstitial-type defects: oxygen atoms segregate to the defects and become optically neutral [1]. The shift of the V_2O absorption peak toward larger wavelength as a result of annealing has been observed earlier [11]. At a dose of $0.5 \cdot 10^{17}\text{ cm}^{-2}$ (Fig. 3, *b*), the major result of annealing is an increase in the concentration of oxygen dissolved in the silicon matrix. Annealing of specimens implanted with $1.0 \cdot 10^{17}\text{ cm}^{-2}\text{ O}^+$ also increases the concentration of dissolved oxygen, which conclusion can be made from the increase in the intensity of the absorption peaks at 515 cm^{-1} (Fig. 4, *b*). Spectrum *B* also has a small peak at 1107 cm^{-1} .

At 650°C , the transmittance of all the specimens, especially those which were implanted with $1.0 \cdot 10^{17}\text{ cm}^{-2}\text{ O}^+$ (Figs. 2, *b* - 4, *b*), increases in the range 600 to 900 cm^{-1} as compared to the specimens implanted at 350°C . This observation is usually attributed to an increase in the structural perfection of ion-implanted silicon [16]. An increase in oxygen implantation temperature is known to improve the quality of superficial silicon layers [17].

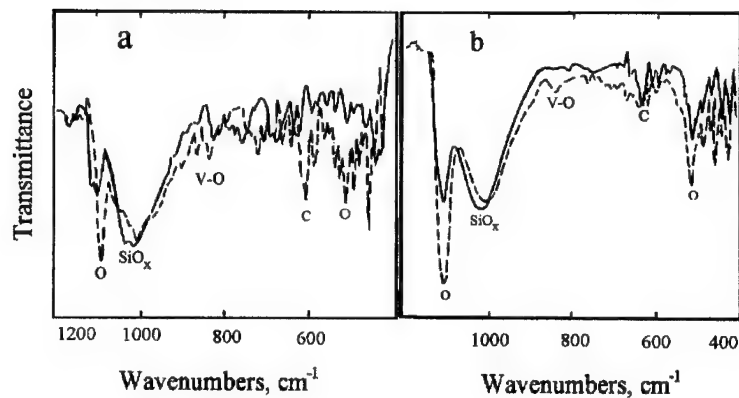


Figure 3. Transmittance spectra of specimens implanted with $0.5 \cdot 10^{17} \text{ O} \cdot \text{cm}^{-2}$ (a) before and (b) after annealing. Curve A (---) implanted at 350 and B (—) at 650 °C.

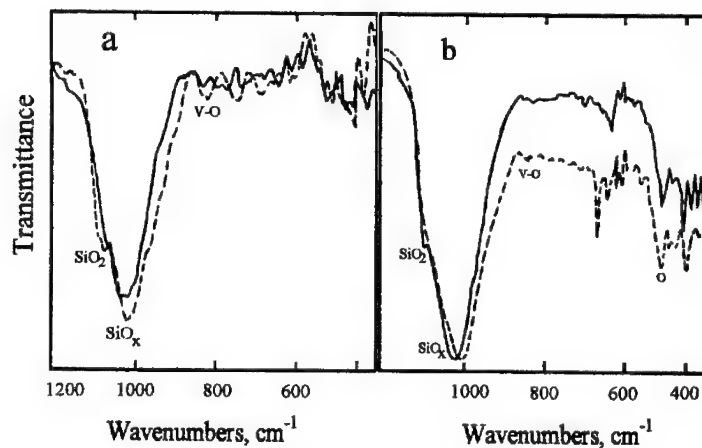


Figure 4. Transmittance spectra of specimens implanted with $1 \cdot 10^{17} \text{ O} \cdot \text{cm}^{-2}$ (a) before and (b) after annealing. Curve A (---) implanted at 350 and B (—) at 650 °C.

SUMMARY

The experiments showed that implantation of 0.25 , 0.5 , and $1.0 (\cdot 10^{17}) \text{ cm}^{-2}$ 150 keV O^+ ions into heated silicon produces quite a stable system of dissolved oxygen atoms, vacancy-oxygen complexes, precipitates of silicon oxides and, obviously, interstitial-type radiation defects which cannot be observed directly. The higher is the implantation dose and the implantation temperature the more efficient is the phase formation during

implantation and the less oxygen is bonded into vacancy-oxygen complexes. It is noteworthy that at high oxygen implantation doses which provide for a high silicon supersaturation with oxygen and radiation defects, the complexes are observed not only after implantation at 350 or 650 °C, but even after annealing at 1000 °C for 1 h.

REFERENCES

1. K. Sumino, 2nd Inter. Autumn Meeting Proc. Gettering and Defect Engineering in Semiconductor Technology (GADEST 87), Garzau, Germany, 1987. Akad. Weisenschaften DDR, Frankfurt (Oder), 218 (1987).
2. F. Shimura, H. Tsuya, and T. Kawamura, Appl. Phys. Lett. **37**, 483 (1980).
3. S.M. Hu, in Defects in Semiconductors, edited by J. Narayan and T.Y. Tan (North-Holland, Amsterdam, 1981), p. 333.
4. E.A. Maydell-Ondrusz and I.H. Wilson, Thin Solid Films **114**, 367 (1984).
5. A.S. Oates, R.C. Newman, J.M. Tucker, G. Davis, and E.C. Lightowers, Mater. Res. Soc. Symp. Proc. **59**, 59 (1986).
6. A. Bourret, Mater. Res. Soc. Symp. Proc. **59**, 223 (1986).
7. A.B. Danilin, A.A. Malinin, V.N. Mordkovich, V.V. Saraikin, and O.I. Vyletalina, Nucl. Instr. and Meth. in Phys. Res. **B82**, 431 (1993).
8. A.M. Afanas'ev, P.A. Aleksandrov, and R.M. Imamov, X-Ray Diagnostics of Superficial Layers (Nauka, Moscow, 1986) (in Russian).
9. R.C. Newman, Infra-Red Studies of Crystal Defects (Taylor and Francis, London, 1973), p. 187.
10. J.W. Corbett, G.D. Watkins, and R.C. McDonald, Phys. Rev. **135**, A1381 (1964).
11. J.L. Lindstrom and B.G. Svensson, Mater. Res. Soc. Symp. Proc. **59**, 45 (1986).
12. H.J. Stein, Defects in Semiconductors III, edited by H.J. von Bardeleben (Trans. Tech. Publ., Aedermannsdorf, 1986), p. 935.
13. H.J. Stein, Mater. Res. Soc. Symp. Proc. **104**, 173 (1988).
14. L. Diantong, Z. Lirong, W. Zhonglie, and P.L.F. Hemment, Nucl. Instr. and Meth. in Phys. Res. **B55**, 705 (1991).
15. K.J. Reeson, C.D. Marsh, R.J. Chater, J.A. Kilner, A. Robinson, K.N. Christiansen, P.L.F. Hemment, G. Harbeke, E.F. Steigmeier, G.R. Booker, and G.K. Celler, Microelectronics Engineering **8** (3/4), 163-174 (1988).
16. S.M. Hu, J. Appl. Phys. **51**, 59 (1980).
17. O.W. Holland, T.P. Screen, D. Faty, and J. Narayan, Appl. Phys. Lett. **45** (10), 1081-1083 (1984).

X-RAY TOPOGRAPHY OF STRAIN FIELDS INDUCED BY 100 MEV Ti^{7+} ION IRRADIATED Si(100)

B.B.SHARMA*, S.R.GUPTA*, R.K.SHARMA*, V.KUMAR*, U.TIWARI, P.SEN** AND G.K.MEHTA*****

*Solid State Physics Laboratory, Delhi - 110054, India.

**School of Physical Sciences, Jawaharlal Nehru University, New Delhi - 110067, India.

***Nuclear Science Centre, New Delhi -110067, India.

ABSTRACT

The lattice deformation caused by 100 MeV Ti^{7+} ion irradiation in Si (100) has been studied using X-ray topographic techniques. An important finding is the appearance of a strain field perpendicular to the ion beam direction in the irradiated region well separated from the projected range of implanted ions. This in-plane strain extends in the bulk of the sample and is not merely confined to the surface. The implanted region has been found to experience an out of plane strain which is expected to be tensile in nature.

1. INTRODUCTION

X-ray diffraction topography is a non-destructive technique to study defects on the surface and in the bulk of perfect crystals. It is particularly sensitive to very small lattice distortions, and low absorption of X-rays in most materials allows hundreds of μm thick crystals to be topographed in transmission. As it is possible to scan large crystals, this technique is unique in observing the spatial pattern of defect networks with a resolution of a few micrometers.

X-ray topography has been employed successfully to study the lattice changes introduced in semiconductors by low energy ions [1]. MeV ions employed recently for various applications such as buried layer formation, multiple implantation [2], etc., interact with the lattice mainly through electronic process in addition to the usual elastic collisions operative at KeV energies close to the end of the ions range. It is thus important to study the extent of lattice deformation in spatially separated electronic and elastic loss regions. In the present study X-ray topographic techniques have been employed to investigate lattice distortion close to the surface and in the bulk of the irradiated crystals. Controlled surface etching and subsequent topography is performed to extract information about the distribution of the strain in the depth of the crystal.

2. EXPERIMENT

2.1 High Energy Ion Irradiation

Si(100) single crystals, 500 μm thick, were irradiated with 100 MeV Ti^{7+} ions (dose $\sim 10^{12}$ ions/ cm^2) at NSC, Delhi with a 15 UD Pelletron. The irradiating ion beam passed through a metal grid placed $\sim 10\text{cm}$ above the sample as shown in Fig.1. The grid had $800 \times 800 \mu\text{m}^2$ square openings defined by metal strips of square cross section ($40 \times 40 \mu\text{m}^2$). Calculations using the Monte Carlo code 'TRIM' project a range of 20 μm for 100 MeV Ti in Si.

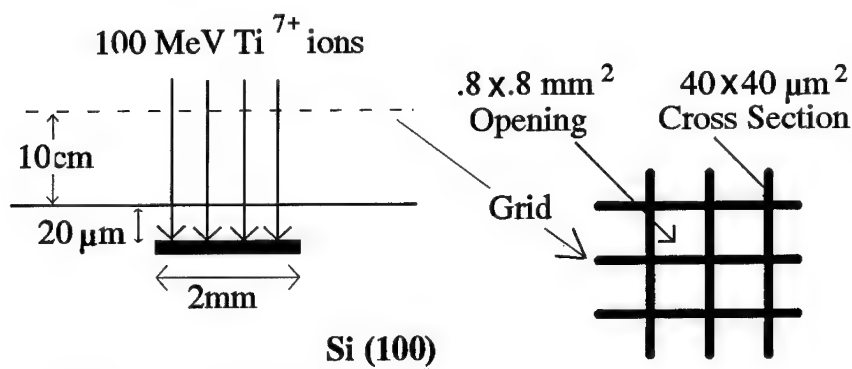


Fig.1 Irradiation Geometry

2.2 X-Ray Topography

Topographs were recorded in transmission and in reflection geometries with diffraction vectors (\mathbf{g}) suitably chosen to reveal the nature and the direction of the strain. Since the sample surface has (100) orientation, the diffraction vectors [022] and [400] suited for revealing the in-plane (parallel to the sample surface) and the out-of-plane (normal to the sample surface) strains respectively as the lattice deformation represented by the strain component (s) gives maximum contrast in a topograph when $\mathbf{g} \cdot \mathbf{s}$ is maximum.

The 022-topographs (transmission geometry, symmetric Laue) were recorded using $\text{MoK}\alpha$ and $\text{CuK}\alpha$ radiations. With $\text{MoK}\alpha$ ($\mu t = 0.8$, μ = absorption coefficient and t = sample thickness), mainly kinematic contrast is expected (thin crystal approximation) while with $\text{CuK}\alpha$ ($\mu t = 7$), the strain field is imaged in dynamic contrast (thick crystal approximation). The 400-topograph (reflection geometry - symmetric Bragg) was recorded with $\text{CuK}\alpha$ radiation. The depth explored in a reflection topograph is an important parameter. It is taken to be the depth

from where the diffracted beam emerges with 90% loss in intensity [3]. For **400** reflection it is $\sim 46 \mu\text{m}$, and thus covers the total range of the impinging ions ($\sim 22 \mu\text{m}$). A **311** reflection topograph was recorded with $\text{CuK}\alpha$ radiation to explore shallow surface region ($\sim 7.5 \mu\text{m}$), well separated from the elastic loss region near the location of the implanted ions. A **511** reflection topograph (asymmetric Bragg geometry) with a penetration of $\sim 54 \mu\text{m}$ was also recorded with $\text{CuK}\alpha$ radiation to investigate the elastic loss region in the interior of the sample.

3. RESULTS AND DISCUSSION

3.1 Surface Examination

In addition to the topographic examination of the strain fields, irradiated samples were also examined under an optical microscope, and with a scanning electron microscope in the secondary electron mode to see surface changes resulting from high energy ion irradiation. The microscopic examination revealed some scratches and a crack like feature (also visible in all the topographs), but the grid pattern was not visible. SEM at a comparatively high tube current (100 nA, 20 KV), however, clearly revealed the grid. Fig.2 shows the SEM image of the irradiated region. The masked regions are clearly defined by a sharp contrast at the boundaries. Since secondary electrons have a range of only a few nanometers, this image reveals the strain fields only at the surface.



Fig.2 SEM image (secondary electron mode) of irradiated Si (100).

3.2 X-Ray Topographic Study

As discussed in Section 2.2, the topographs were recorded with $g = [311]$, $[400]$, $[511]$ and $[022]$. The contrast features observed are now discussed.

The **311** topograph (Fig.3) explores a depth of only $7.5 \mu\text{m}$. There is no visible contrast in the irradiated region but the masked region directly below the metal grid appears in dark

contrast. As any strain whether \perp or \parallel to the sample surface would appear in this reflection in a kinematic contrast, it is inferred that only the masked regions are under strain.

The **400** and **511** topographs (Figs. 4a and 4b) with penetration depths of 46 and 54 μm respectively show the irradiated region in strong kinematic contrast. As the irradiated region has no contrast in the **311** reflection, the strain field in the elastic loss region (close to the ion range) is clearly responsible for this contrast. As the **[400]** diffraction vector lies along the surface normal, this strain definitely has an out-of-plane component.

The **022** transmission topographs (Figs. 5a and 5b) show no contrast in the irradiated region. Since **[022]** and **[400]** are mutually orthogonal diffraction vectors, it is inferred that the strain in the elastic

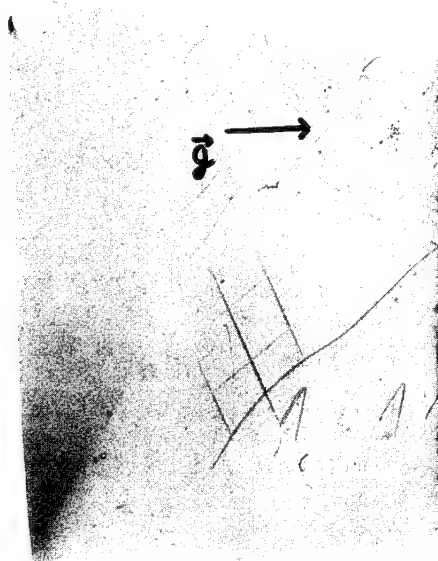


Fig.3 **311** reflection topograph, $\text{CuK}\alpha$ radiation.

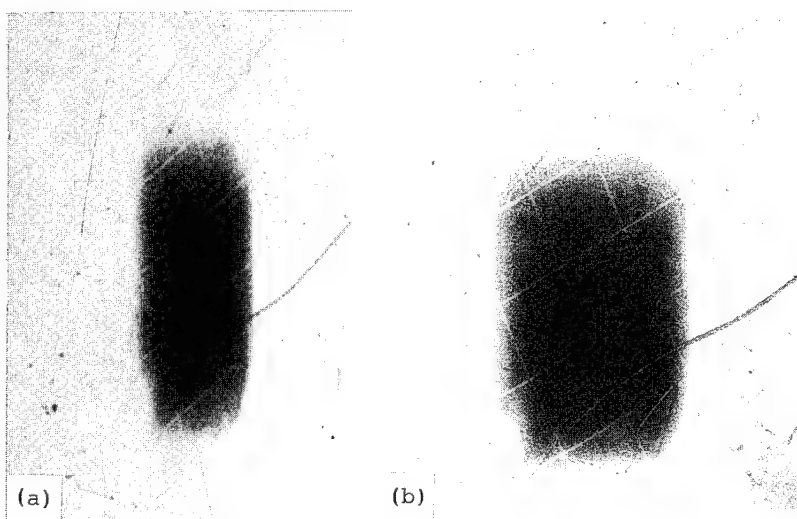


Fig.4 (a) **400** and (b) **511** reflection topographs, $\text{CuK}\alpha$ radiation.

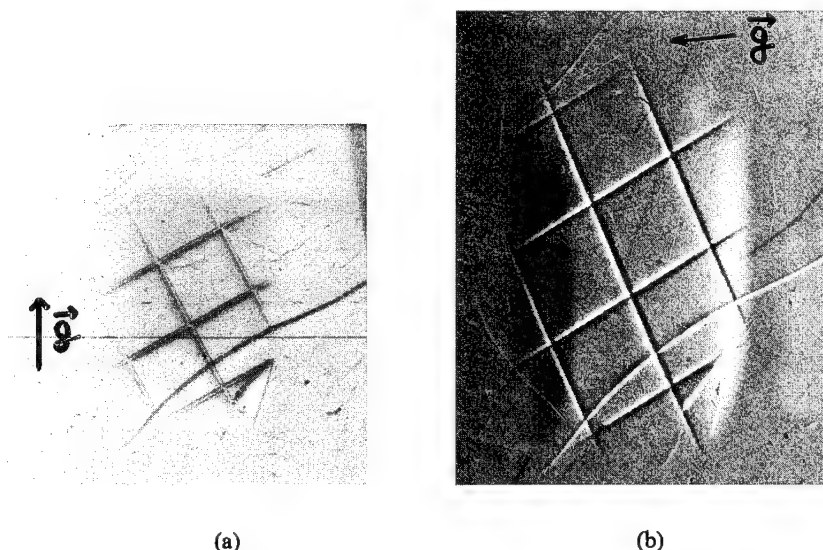


Fig.5 022 transmission topographs, (a) $\text{MoK}\alpha$ and (b) $\text{CuK}\alpha$ radiation.

loss region is almost entirely along the surface normal.

The 022 topographs, however, show the grid structure in strong contrast. The $\text{MoK}\alpha$ topograph (Fig. 5a) shows the masked region (grid) as a well resolved double line structure with a strong kinematic contrast at the edges and comparatively strain free region in between. This represents in-plane strain at the boundaries. The sense of this strain field can be inferred from the $\text{CuK}\alpha$ topograph (Fig. 5b) in which it is mapped in dynamic black-white contrast. This gets reversed by reversing g . An analysis based upon Penning-Polder theory [4] shows that the masked regions are under compressive stress.

Another significant feature seen in the $\text{CuK}\alpha$ topograph (Fig. 5b) are the two broad side bands (black on one side and white on the other) which define the limit of the impinging ion beam. The diffused appearance of side bands is a consequence of the gradual fall in the beam intensity at its limits. The strain field at the other two edges defining the incident ion beam are \perp to g , and therefore are not visible. A similar analysis shows that the strain is compressive in these regions.

The compressive nature of the strain along the grid and the side bands obtained from the $\text{CuK}\alpha$ topograph is consistent with the assumption that the irradiated surface region possesses tensile stress which accumulates at the surface discontinuities defined by the grid. This type of contrast is well known in topography of semiconductor crystals having discontinuous surface films [5].

To examine the depth distribution of strain fields in the irradiated samples, these were etched upto a depth of $\sim 8 \mu\text{m}$ in several steps and 022 and 311 topographs recorded at every step. No significant change in contrast features was observed. The in plane strain field is, thus, not a surface feature, but penetrates substantially deep below the surface.

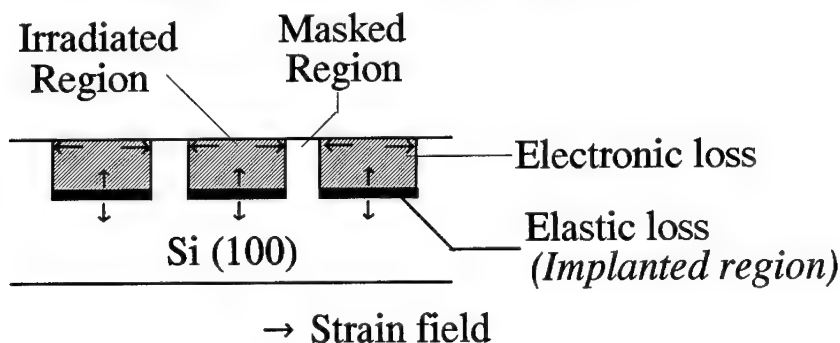
4. CONCLUSION

Strain induced by 100 MeV Ti^{7+} ion irradiation / implantation in Si (100) is mapped using X-ray topographic techniques.

The sense of dynamic contrast in 220-topographs confirms that the masked region is under compressive strain parallel to the sample surface. It indicates a tensile stress generated in the electronic loss region. This stress gets concentrated at the boundaries, as is commonly observed in case of discontinuous surface films under tensile stress on semiconductors. As revealed by etching experiments this in-plane strain extends in the bulk of the sample and is not confined to the near-surface region.

The implanted region experiences out-of-plane (along the surface normal) strain which is expected to be tensile in nature. Detailed analysis of 400-section-topographs has subsequently confirmed it. These results are being communicated separately.

A model of strain field as emerged from this study is shown below:



Acknowledgement

We acknowledge helpful discussion with Dr.W.N.Borle. One of the authors (UT) acknowledges financial grant from UGC, India.

References

- [1] Gerward L., Z Physik **259**, 313 (1973).
- [2] Borland J.O., Solid State Technology, Dec.1993, p. 28
- [3] Halliwell M.A.G., Childs J. B. and O'Hara S., *Proc. 1972 Symp. on GaAs (Instt.Phys., London, 1973)* p.98.
- [4] Penning P. and Polder D., Philips Res. Repts. **16**, 419 (1961).
- [5] Meieran E. S. and Blech I. A., J. Appl. Phys. **38**, 2913 (1967).

RELATION BETWEEN STRUCTURE AND CARRIER LIFETIME IN As - IMPLANTED GaAs

Z. Liliental-Weber, W. Swider, H. Kagiichi,* A. Claverie,** H.H. Wang,***
and J.F. Whitaker,***

Materials Science Division, Lawrence Berkeley Laboratory 62/203, Berkeley, CA 94720,

*University of California, Berkeley, CA 94720, ** CEMES-LOE/CNRS, BP 4347, F-31055,

Toulouse Cedex, France, Department of Materials Science, ***Center for Ultrafast Optical
Science, University of Michigan, Ann Arbor, MI 48109

ABSTRACT

The structure of As implanted GaAs layers before and after annealing are described and the relation between the structural quality and carrier lifetime was determined. Subpicosecond carrier lifetimes were found already for as-implanted layers, and this value changes only slightly after annealing in the temperature range up to 600°C. Annealing of As-implanted layers leads to the growth of As precipitates with a similar orientation relationship as those observed in low-temperature MBE-grown GaAs layers. However, it is still not clear whether point defects created by implantation or the As precipitates are responsible for the short carrier lifetime.

1. INTRODUCTION

Recent developments have shown that semi-insulating GaAs layers can be grown by molecular-beam epitaxy (MBE) with As-supersaturation at temperatures as low as 200°C (LT-GaAs)[1]. Such material contains about 1.5 % excess As, which leads to expansion of the lattice parameter of the layer [2,3]. The high density of As_{Ga} antisite defects ($\sim 10^{20} \text{ cm}^{-3}$) found in the as-grown layers leads to hopping conductivity. These layers become semi-insulating after annealing [1].

Arsenic-ion-implanted GaAs is potentially a substitute for LT-GaAs. Implantation conditions can be chosen so that the resulting As concentration for a typical 200 keV implantation with $1 \times 10^{16} \text{ ions/cm}^2$ gives a maximum 2% excess As at a depth of about 90 nm which is close to the concentration found in LT-GaAs. Annealed As-implanted GaAs layers show very similar properties to LT-GaAs layers. In this paper the relation between the structure and carrier lifetime for implanted layers will be described.

2. As-IMPLANTED GaAs LAYERS

Our earlier studies show that similar properties to those of LT-GaAs layers can be obtained using As ion implantation [4-8]. GaAs wafers (001) (n^+) were implanted with As ions. Two different implantation conditions were used: (1) an energy of 200 keV with As⁺ dose of $1 \times 10^{16} \text{ ions cm}^{-2}$ and (2) an energy of 180 keV with a dose of $3 \times 10^{15} \text{ ions cm}^{-2}$. The wafers were not cooled during implantation. Therefore, at the higher implantation dose, they could reach a temperature as high as $100^\circ\text{C} \pm 50^\circ\text{C}$.

The implantation conditions were chosen so that the resulting As excess concentration in the layer, defined as $(N_{As}-N_{Ga})/(N_{As}+N_{Ga})$, was a maximum of 2%, at a depth of about 90 nm. Based on simulation of As distribution in the layer for the particular implantation conditions, one would expect an excess As concentration comparable to those found in LT-GaAs layers from the surface to a depth of 200 nm [9]. The only structural difference between as-grown LT-GaAs layers and as-implanted layers was that the latter are amorphized from the sample surface to a depth of about 110 nm (Fig. 1). This amorphization of the as-implanted layers is in agreement with the “critical damage energy density” model, which has been used to describe the kinetics of GaAs amorphization by As bombardment [10]. The crystalline/amorphous (c/a) interface was only slightly undulated.

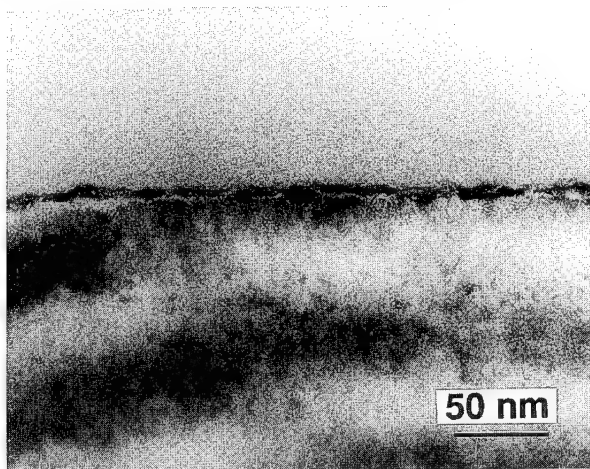


Fig. 1. An amorphous layer of GaAs sample formed after As^+ implantation at 200 keV with dose of 1×10^{16} ions cm^{-2} .

3. ANNEALED As-IMPLANTED GaAs

Arsenic implanted samples (with implantation at 200 keV and dose 1×10^{16} ions cm^{-2}) were annealed at different temperatures and at different times in order to observe solid phase regrowth (SPE) and formation of defects. It was noticed that annealing at as low a temperature as 200°C for 1 hr lead already to solid phase regrowth. These layers annealed at low temperature show different lattice parameter than the substrate (Fig. 2). Computer simulation of these rocking curves indicates a 0.36% expansion of the lattice parameter (Fig. 2a). By comparison with LT-GaAs layers [3] this suggests the presence of more than 2 % of excess As. Despite this high As concentration annealing at 200°C does not lead to the formation of visible As precipitates (Fig. 3a). This material is structurally very similar to as-grown LT-GaAs layers with except that annealed implanted layers have a much higher concentration of planar defects which are called end of range defects (EOR) found mostly just beneath the initial crystalline/amorphous (c/a) interface. The density of planar defects drastically decreases for 1 hr annealing at 350°C (Fig.

3b). No As precipitates were visible in the implanted part of the material annealed at this temperature. However, the expansion of the lattice parameter has decreased at this annealing temperature (Fig. 2b) and at 400°C only the substrate peak is visible with only a small shoulder due to the implanted layer. It has already been shown [11] that around 400°C the first visible clusters of As are formed in annealed LT-GaAs layers and the lattice parameter has decreased. Apparently the same behavior is revealed here for annealed As-implanted layers.

Annealing at 600°C for 15 s leads to the formation of clearly visible As precipitates (Fig. 4a) and also results in extra spots in the diffraction patterns. The orientation relationships of these precipitates are identical to those observed for LT-GaAs [12] e.g. $(0003)_{pp} \parallel (111)_m$ with $[1210]_{pp} \parallel [011]_m$ where the As structure is given in hexagonal units, with indices "pp" and "m" referring to precipitates and matrix, respectively. This is the most stable configuration for hexagonal precipitates and a cubic matrix and is associated with the lowest formation energy.

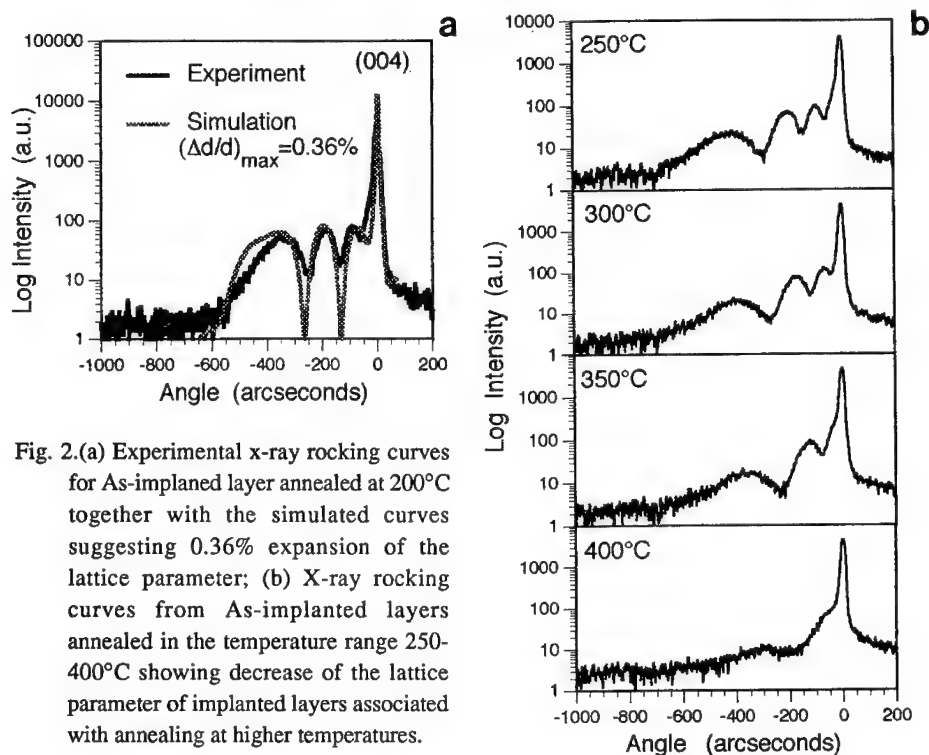


Fig. 2.(a) Experimental x-ray rocking curves for As-implanted layer annealed at 200°C together with the simulated curves suggesting 0.36% expansion of the lattice parameter; (b) X-ray rocking curves from As-implanted layers annealed in the temperature range 250-400°C showing decrease of the lattice parameter of implanted layers associated with annealing at higher temperatures.

There are four variants of these precipitates; details concerning those variants were described earlier [12].

Longer annealing times at 600°C led to the formation of faceted precipitates (Fig. 4). From a depth of 160 nm to about 500 nm many defects are seen with a characteristic "coffee-bean"

contrast. They are located beneath the former (c/a) interface, and they were identified as interstitial dislocation loops consisting of extra {111} planes. These interstitial loops result from the implanted atoms and also from displaced substrate atoms injected beneath the c/a interface.

Annealing of the samples implanted with a lower implantation dose (3×10^{15} ions cm^{-2} at 180 keV for 10 min at 600°C) led to practically the same conclusion, however the density of EOR defects and As precipitates was lower. The interstitial dislocation loops (typical “end-of-range” defects) were formed at distances of 120 nm to 260 nm from the sample surface [5]. Their density was estimated to be in the range of $1 \times 10^{10} \text{ cm}^{-2}$. Large dislocation loops were decorated by As precipitates.

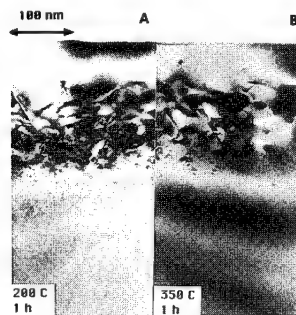


Fig. 3. Micrographs showing cross-section of the regrown GaAs layer after annealing for 1 hr at: a) 200°C, b) 350°C. Note decreasing density of planar defects after annealing at the higher temperature.

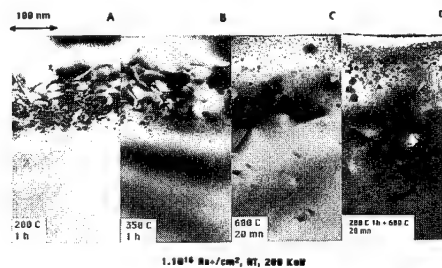


Fig. 4. Set of cross-sectional micrographs showing the microstructure of layers regrown at 600°C as a function of annealing time.

4. RESPONSIVITY AND CARRIER LIFETIME IN As-IMPLANTED GaAs

Transient reflectivity measurements were performed for implanted samples in a standard pump-probe configuration with 100-fs Ti:sapphire laser pulses at 850 nm in order to determine annealing conditions leading to materials with a fast carrier response. It was found that for annealing at 300°C or below carrier lifetime was much shorter than for layers annealed at 600°C. However, responsivity of layers annealed at 350°C or below was much lower (Fig. 5a).

These findings are in agreement with our earlier studies of LT-GaAs layers with pyramidal defects [13-14]. As was shown above a high density of planar defects can be detected in As-implanted layers annealed in the temperature range 200-350°C, and responsivity is affected by the presence of these defects. In addition, a long response tail was observed for these low annealing temperatures, similar to that observed for as grown LT-GaAs layers [13-14]. The nature of this tail is not clear, but it is speculated that it might be related to hopping conduction present in these layers. However, if implanted samples were annealed above 600°C, the optical response was typical of annealed LT-

GaAs layers (Fig. 5). This shows that annealing time is very critical, a well defined density of defects is needed in order to ensure short response time. A range of carrier lifetime were observed,

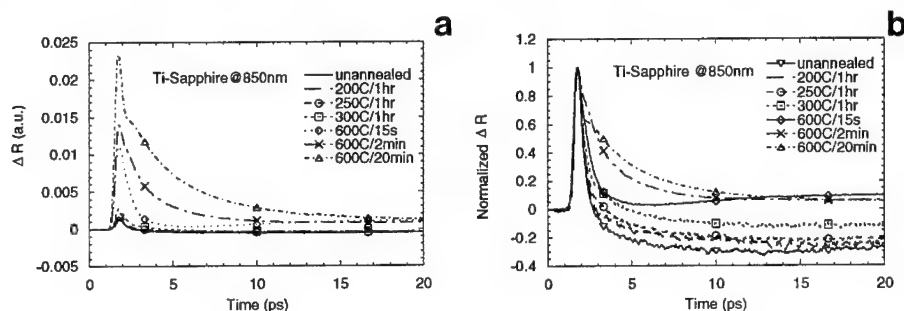


Fig. 5. a) Transient reflectivity for As-implanted GaAs annealed at different temperature and time; b) the same graph normalized from which 1/e decay time can be determined. Note a tail with a negative values for as-implanted sample.

although many of the samples exhibited subpicosecond response components.

Photoconductive switching characterization was performed on these samples as well using 100-fs laser pulses. The photoconductive gap had a 20 μm separation, and d_c bias on the detector was 5 V. The full-width-half-maximum (FWHM) of the detector response was 1.23 ps, and the 1/e fall time was 0.64 ps for the samples annealed at 600°C for 15 sec.

5. CONCLUSIONS

The results described in this paper show that As-implanted amorphous layers can be fully regrown by annealing at 200°C for 1 hr. However, a high density of planar defects is detected in the regrown part of the material. The density of these defects decreases for anneals at higher temperatures. The presence of these defects appears to be responsible for the lower response of the photoconductive switch built on this material, as was observed for as-grown LT-GaAs layers with pyramidal defects. These low annealing temperatures (200-350°C) do not lead to the formation of visible As precipitates. Both as-grown LT-GaAs layers and low temperature annealed implanted layers show the shortest carrier lifetime. The higher the growth temperature of LT-layers the longer the lifetime consistent with the decreasing concentration of As_{Ga} antisite defects.

Annealing at 600°C leads to the formation of As precipitates as was observed in LT-GaAs layers. In order to obtain a high density of As precipitates, implantation conditions need to be chosen carefully, followed by annealing. The density of extended defects in the implanted layers drastically decreases for annealing at higher temperature. Much larger As precipitates can be found in the vicinity of these defects compared to areas free of structural defects. The precipitate structure, its orientation relationship, and their distribution are very similar to those observed in low-temperature MBE-grown GaAs layers. Therefore, it appears to be possible to achieve good

quality semi-insulating GaAs layers at lower cost by using ion implantation.

The carrier lifetime in annealed As-implanted layers is only slightly longer compared to the as-implanted layers. The carrier lifetime increases for longer annealing time at 600°C. The work is in progress to elucidate the role of additional defects introduced by implantation compared to simple excess As and its distribution in the layer.

ACKNOWLEDGMENTS

This research was supported by AFOSR-ISSA-90-0009. The use of the Facility of the National Center for Electron Microscopy in Lawrence Berkeley Laboratory supported by the U.S. Department of Energy under Contract No. DE-AC03-76SF00098 is greatly appreciated.

REFERENCES:

- [1] F.W. Smith, A.R. Calawa, C.L. Chen, M. Manfra, and L.J. Mahoney, *IEEE Electron. Device Lett.* **9**, 77 (1988).
- [2] M. Kaminska, E.R. Weber, Z. Liliental-Weber, R. Leon, and Z. Rek, *J. Vac. Sci. Technol.* **B7**, 710 (1989).
- [3] Z. Liliental-Weber, W. Swider, K.M. Yu, J. Kortright, F. Smith, and A.R. Calawa, *Appl. Phys. A* **58**, 2153 (1991).
- [4] A. Claverie, F. Namavar, and Z. Liliental-Weber, *Appl. Phys. Lett.* **62**, 1271 (1993).
- [5] Z. Liliental-Weber, F. Namavar, and A. Claverie, *Ultramicroscopy*, **52**, 570 (1993).
- [6] A. Claverie, F. Namavar, and Z. Liliental-Weber, *Appl. Phys. Lett.* **62**, 1271 (1993).
- [7] F. Namavar, N.M. Kalkhoran, A. Claverie, Z. Liliental-Weber, E.R. Weber, P. Moise, S. Vernon, and V. Haven, *J. Elect. Materials*, **22**, 1409 (1993).
- [8] A. Claverie, L. Laanab, H. Kagiuchi, Z. Liliental-Weber, and E.R. Weber, *Proc. of 8-th Conference on Semi-insulating III-V Compounds*, Warsaw, Poland, June (1994) in press.
- [9] J.F. Ziegler, J.P. Biersack, and U. Littmark, *TRIM-Transmission of Ions in Matter*, 1991. See also *The Stopping and Range of Ions in Solids*, Pergamon, New York, 1985.
- [10] J. Beauvillain, A. Claverie, and K. Akmoum, *J. Phys. III (Fr.)* **2**, 407 (1992).
- [11] Z. Liliental-Weber, K.M. Yu, J. Washburn, and D.C. Look, *J. Elect. Materials*, **22**, 1395 (1993).
- [12] A. Claverie and Z. Liliental-Weber, *Phil. Mag.* **65**, 981 (1991).
- [13] Z. Liliental-Weber, S. Gupta, and F. W. Smith, in Semi-insulating III-V Materials, eds. C.J. Miner, W. Ford, and E.R. Weber (Institute of Physics Publishing, Bristol and Philadelphia, (1993) p. 135.
- [14] Z. Liliental-Weber, J. Ager, D. Look, X.W. Lin, J. Nishio, K. Nichols, W. Schaff, W. Swider, K. Wang, J. Washburn, E.R. Weber, and J. Whitaker, in Semi-insulating III-V Materials, ed. M. Godlewski (World Scientific Publishing Co. Pte. Ltd., Singapore, New Jersey, London, Hong Kong (1994) p. 305.

THE INFLUENCE OF NON-STOICHIOMETRY ON THE ELECTRICAL ACTIVATION OF n-TYPE DOPANTS IN InP

M.C. RIDGWAY*, C.M. JOHNSON* AND P. KRINGHØJ**

*Department of Electronic Materials Engineering, Australian National University, Canberra, Australia

**Institute of Physics and Astronomy, Aarhus University, DK-8000 Aarhus C, Denmark

ABSTRACT

The influence of implantation-induced non-stoichiometry on the electrical activation and depth distribution of Group IV (Ge and Sn) and VI (Se and Te) elements in InP has been investigated with a variety of analytical techniques. Electrical measurements indicate that P co-implantation can increase the electrical activation of the Group IV elements through reductions in amphoteric behaviour and dopant-defect complexes for Ge and Sn, respectively. The relative influence of P co-implantation increases as the dopant ion dose increases. Though others have demonstrated that co-implantation increases the electrical activation of Group II elements, similar observations were not apparent for Group VI elements, the latter attributed to the lack of Group VI element interstitial character.

INTRODUCTION

Group IV or VI elements implanted in InP preferentially occupy In or P lattice sites, respectively, and as a consequence, n-type conduction can be achieved with either species. The electrical activation of such dopants is governed by a variety of mutually exclusive factors including: dopant amphoteric behaviour (Group IV elements), solid solubility, dopant-defect complexes, implantation-induced non-stoichiometry and disorder, native-defect compensation and background-dopant gettering. In general, electrical activation decreases as ion dose increases with Group VI elements typically yielding greater electrical activation than Group IV elements. Figures 1(a) and (b) demonstrate these trends, showing electrical activation as a function of ion dose for both Group IV and VI elements.

The influence of the individual factors that govern electrical activation are necessarily dopant ion dose dependent. (For example, dopant solid solubility does not influence electrical activation at low ion doses). One such factor - non-stoichiometry - can be achieved through co-implantation with a lattice constituent and can significantly influence the electrical activation of Group II or IV elements. For example, an increase in electrical activation for Be, Ge and Sn has been achieved with P co-implantation as attributed to, respectively, decreases in dopant interstitial character [1], amphoteric behaviour [2-5] or dopant-defect complexes [3,4,6]. Figures 2(a) and (b) demonstrate this effect, showing carrier concentration as a function of depth for, respectively, Ge- and Sn-implanted InP with and without P co-

implantation. For the present report, the relative influence of non-stoichiometry has been investigated as a function of dopant ion dose for both Group IV and VI elements. Though the latter are confined to P lattice sites and hence, lack amphoteric behaviour, the observations cited above for Be [1] and Sn [3,4,6,7] demonstrate non-stoichiometry can also influence the electrical activation of non-amphoteric dopants.

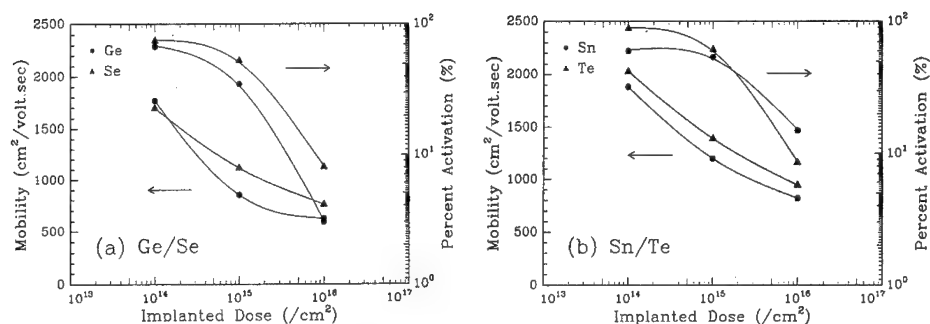


Figure 1. Average carrier mobility and electrical activation as function of ion dose for (a) Ge- and Se-implanted InP and (b) Sn- and Te-implanted InP. From reference [4].

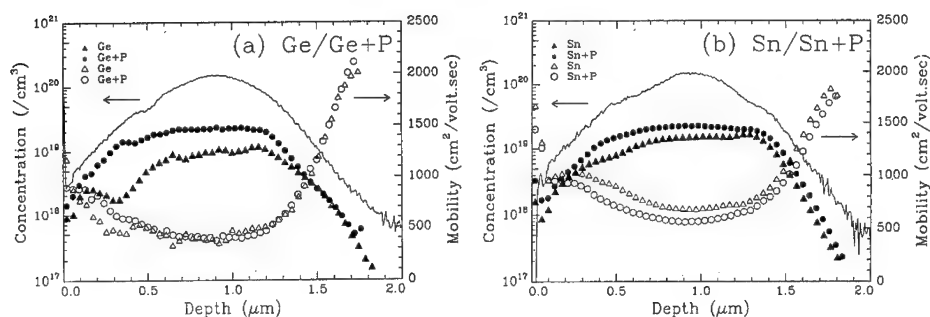


Figure 2. Carrier mobility and concentration as a function of depth (with and without P co-implantation) for (a) Ge- and (b) Sn-implanted InP for ion doses of 10^{16} /cm². From reference [3].

EXPERIMENTAL

Semi-insulating, (100) InP substrates were implanted at a temperature of 200°C with Group IV or VI elements over the ion dose range 10^{13} - 10^{16} /cm². Selected samples were further implanted with In and/or P ions with a dose equal to that of the dopant. For all ions, implantation energies were selected to yield a projected range of ~ 1 μ m. Samples were subsequently rapid thermally annealed in a N₂ ambient at 800°C for 10 sec with proximity capping. Sheet carrier concentrations were determined with Hall measurements using alloyed AuGe contacts in the van der Pauw geometry. Dopant depth distributions were measured with secondary ion mass spectrometry (SIMS) using O₂⁺ or Cs⁺ primary ion beams and detecting positive (Ge⁺ and Sn⁺) or negative (Se⁻ and Te⁻) secondary ions, respectively.

RESULTS AND DISCUSSION

Figures 3(a), (b) and (c) show the ratio of sheet carrier concentrations with and without co-implantation as a function of dopant ion dose for, respectively, Ge-, Sn- and Se-implanted InP. (Results for Te were comparable with those of Se and hence, are not shown.) Macroscopic stoichiometry was maintained in samples implanted with both In and P and thus, any slight decrease in electrical activation apparent for such samples is attributable to an increase in implantation-induced disorder.

At doses $> \sim 2 \times 10^{14}$ /cm², P co-implantation yields an increase in electrical activation for Ge and Sn through a decrease in either dopant amphoteric character or dopant/defect complexes as noted previously. At lesser doses, a decrease in electrical activation is consistent with an increase in implantation-induced disorder. At low doses, the electrical activation of both Group IV and VI elements approaches 100% and hence, the potential for increasing the electrical activation through co-implantation is necessarily slight. In fact, Fig. 3 demonstrates that P co-implantation can actually decrease electrical activation at low dopant ion doses. Conversely, at high doses, the relative influence of dopant amphoteric behaviour (Ge) and dopant/defect complexes (Sn) increases and hence, the effectiveness of P co-implantation, which inhibits such effects, also increases. For Se, note that P co-implantation does not have a significant effect on electrical activation. This result is in contrast to observations of Group II elements co-implanted with P ions as attributable to the different lattice site occupation for the Group II and VI elements.

In co-implantation yields a slight decrease in electrical activation for the Group IV elements, though the relative influence is minimal compared to that observed for P co-implantation. This is consistent with a preferential occupation of an In lattice site (Ge) or a complete lack of dopant amphoteric behaviour and/or the nature of the dopant/defect complex responsible in part for electrical inactivation (Sn). The electrical activation of Se is also insensitive to In co-implantation. Though P co-implantation yields an increase in electrical activation of Group II elements [1], a similar trend is evidently not observed for Group VI elements with In co-implantation. This is attributable to a lack of interstitial character for

Group VI elements as consistent with ion-beam measurements of the lattice site location of such dopants [8,9].

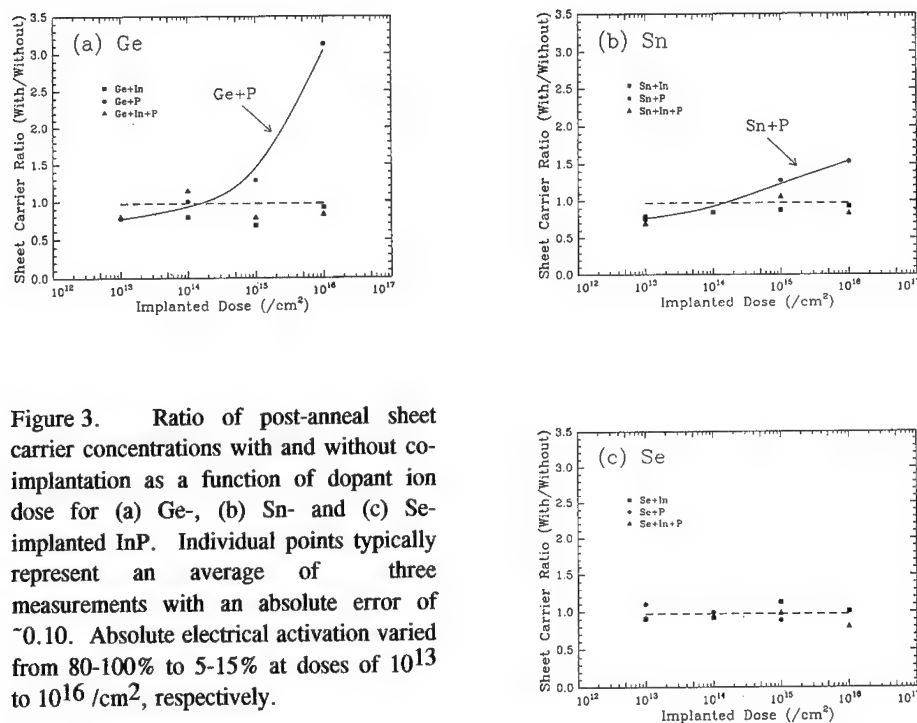


Figure 3. Ratio of post-anneal sheet carrier concentrations with and without co-implantation as a function of dopant ion dose for (a) Ge-, (b) Sn- and (c) Se-implanted InP. Individual points typically represent an average of three measurements with an absolute error of ~ 0.10 . Absolute electrical activation varied from 80-100% to 5-15% at doses of 10¹³ to 10¹⁶ /cm², respectively.

Figures 4(a), (b) and (c) show SIMS measurements of the post-anneal dopant depth distributions for, respectively, Ge-, Sn- and Se-implanted InP (for a dose of 10¹⁶ /cm²). (Results for Te were comparable with those of Se and hence, are not shown.) For all elements, no significant dopant diffusion, toward the surface or bulk, was apparent after annealing. In Fig. 4(a), note the precipitation-related redistribution (as verified with transmission electron microscopy) evident at concentrations $> 5 \times 10^{19}$ /cm³ in the sample co-implanted with P. The latter yields not only an increase in electrical activation but a decrease in Ge solid solubility. Both phenomena are the result of an increase and decrease in [Ge_{IN}]

and [GeP], respectively. Similar trends in dopant solid solubility have been observed in both Ge [10] and Si [11] where an enhanced solubility was evident in the presence of comparable donor and acceptor concentrations. For Sn-implanted InP, precipitation-related redistribution (as verified with transmission electron microscopy) is apparent in samples both with and without P co-implantation. These observations are consistent with a lack of amphoteric behaviour for Sn as noted above. In Fig. 4(c), no differences are evident in the Se depth distributions of samples both with and without In co-implantation and furthermore, no dissimilarities were observed relative to unannealed samples (the latter not shown).

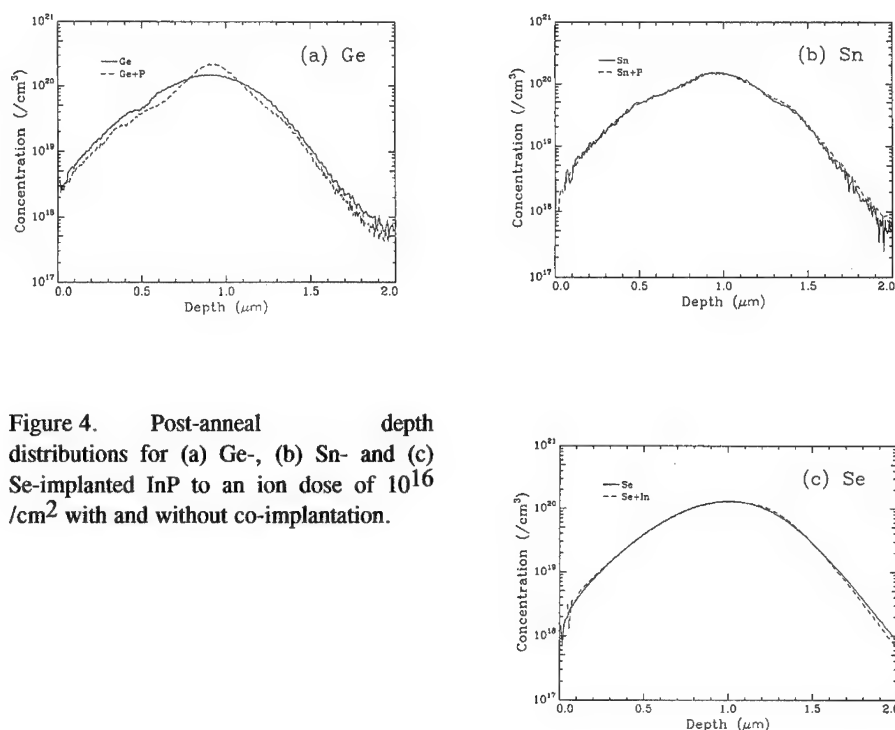


Figure 4. Post-anneal depth distributions for (a) Ge-, (b) Sn- and (c) Se-implanted InP to an ion dose of 10^{16} /cm² with and without co-implantation.

CONCLUSIONS

P and In co-implantation can increase and decrease, respectively, the electrical activation of both Ge and Sn. The relative influence of co-implantation is, however, dopant ion dose dependent as are the factors that contribute to electrical inactivation of such dopants. Precipitation-induced phenomena are apparent in post-anneal Ge and Sn depth distributions. Conversely, the electrical activation and depth distribution of Se and Te are insensitive to implantation-induced non-stoichiometry for the range of dopant ion dose and annealing conditions utilized in the present report.

ACKNOWLEDGEMENTS

We thank both the Australian Department of Industry, Technology and Regional Development and the Danish Natural Sciences Research Council for partial funding.

REFERENCES

- [1] A. Dodabalapur and B.G. Streetman, in Proceedings of the Symposium on Ion Implantation and Dielectrics for Elemental and Compound Semiconductors, eds. S.J. Pearton, K.S. Jones and V.J. Kapoor (The Electrochemical Society, New Jersey, 1990) p. 66.
- [2] M.C. Ridgway, C. Jagadish, T.D. Thompson and S.T. Johnson, in Proceedings of IPRM 1992 (IEEE, New York, 1992) p. 56.
- [3] M.C. Ridgway and P. Kringhøj, in III-V Electronic and Photonic Device Fabrication and Performance, eds. K.S. Jones, S.J. Pearton and H. Kanber (Mat. Res. Soc., Pittsburgh, 1993) p. 351.
- [4] M.C. Ridgway, P. Kringhøj and C.M. Johnson, *Nucl. Instrum. Meth.* **B96**, 311 (1995).
- [5] P. Kringhøj, *Appl. Phys. Lett.* **64**, 351 (1994).
- [6] M.C. Ridgway and P. Kringhøj, *J. Appl. Phys.* **77**, 2375 (1995).
- [7] P. Kringhøj and G. Weyer, *Appl. Phys. Lett.* **62**, 1973 (1993).
- [8] Q.F. Xiao, S. Hashimoto, W.M. Gibson and S.J. Pearton, *Nucl. Instrum. Meth.* **B45**, 464 (1990).
- [9] P. Kringhøj, *J. Appl. Phys.* **71**, 1748 (1992).
- [10] H. Reiss, C.S. Fuller and F.J. Morin, *Bell Syst. Tech. J.* **35**, 535 (1956).
- [11] N.B. Hannay, Solid State Chemistry (Prentice-Hall, New Jersey, 1967) p. 120.

ELLIPSOMETRIC MONITORING OF DEFECTS INDUCED BY ELECTRON CYCLOTRON RESONANCE ETCHING OF GaAs

P.G. SNYDER,* N.J. IANNO,* B. WIGERT,* S. PITTAL,** B. JOHS,** AND J.A. WOOLLAM**

*Center for Microelectronic and Optical Materials Research, and Dept. of Electrical Engineering, U. Nebraska-Lincoln, Lincoln, NE 68588-0511

**J.A. Woollam Co., Suite 39, 650 J St., Lincoln, NE 68508

ABSTRACT

Spectroscopic ellipsometry (SE) measurements were made during and after electron cyclotron resonance (ECR) etching of GaAs. The spectral range for *ex situ* measurements, 1.24-5 eV, included the E_1 , $E_1+\Delta_1$ critical points. The E_1 , $E_1+\Delta_1$ structure was red shifted by about 50 meV, and broadened, by etching with a mixture of methane, argon, and hydrogen. Exposure to a pure H_2 plasma caused greater red shifting and broadening, while a pure Ar ECR plasma produced only a slight red shift. The red shift is consistent with an increase in lattice constant of the order of 1%, in the top 10-30 nm. Broadening is consistent with crystalline lattice damage.

INTRODUCTION

The electron cyclotron resonance (ECR) based etching of GaAs and its compounds via $CH_4/Ar/H_2$ gas mixtures is well known.¹ This methane mixture yields reasonable etch rates, is insensitive to crystal orientation and is capable of etching a wide range of compounds. In order to study the surface damage caused by the etch process, we have used real time *in situ* spectroscopic ellipsometry (SE) to monitor the ECR etching of GaAs by $CH_4/Ar/H_2$ plasmas, as well as *ex situ* SE. We will show the effect of etching on the optical properties of the top 10-30 nm of the material, which is to red shift and broaden the critical point structure. Possible mechanisms for the red shifting are discussed.

EXPERIMENTAL

The vacuum chamber was turbo pumped by a Leybold 600 l/s pump, and the ECR system was a Microscience 900, which is a magnetic mirror type employing electromagnets and a 1000 W, 2.45 GHz power source. Gas flow into the chamber was controlled by an MKS flow control system. The substrate was water cooled, and could be biased. The substrates were polished (100) semi-insulating GaAs.

The *in situ* ellipsometer (model M-44 from J.A. Woollam Co.) was mounted on optical ports such that the light was incident on the sample at a nominal angle of 75° with respect to the surface normal. Simultaneous detection at 44 wavelengths covered the spectral range 416 to 755 nm. A scanning wavelength instrument, also from J.A. Woollam Co., was used for *ex situ* measurements from 1.24-5 eV. The supplied software incorporated the modeling and fitting features described below.

Ellipsometry

Ellipsometry measures the change in polarization state of a light beam reflected at non-normal incidence from the sample surface.² The change in polarization is given as a complex number ρ , related to the sample reflection properties by $\rho = R_p/R_s$, where R_p (R_s) is the complex reflection coefficient for light with electric field polarized parallel (perpendicular) to the plane of incidence. Spectroscopic ellipsometry is the measure of ρ as a function of photon energy $h\nu$, at one or more angles of incidence ϕ . The ρ data are sometimes converted to the pseudodielectric function for convenience:

$$\langle \epsilon \rangle = \langle \epsilon_1 \rangle + i\langle \epsilon_2 \rangle = \sin^2 \phi \left[1 + \tan^2 \phi \left(\frac{1 - \rho}{1 + \rho} \right)^2 \right]. \quad (1)$$

This is what the dielectric function would be if the sample were a simple substrate with isotropic uniform optical constants and no overlayers. To obtain information about individual layer thicknesses and optical constants, a multilayer model is used to calculate R_p and R_s for comparison with the measured ρ data. Selected model parameters are then varied (using the Levenburg-Marquardt algorithm) to minimize the error function:³

$$\chi^2 = \frac{1}{2N-M} \sum_{i=1}^N \left[\left(\frac{\psi_i^m - \psi_i^c}{\delta \psi_i} \right)^2 + \left(\frac{\Delta_i^m - \Delta_i^c}{\delta \Delta_i} \right)^2 \right]. \quad (2)$$

Here $\tan(\psi)$ and Δ are the magnitude and phase of ρ , m and c superscripts refer to measured and calculated values, the i subscript labels the different photon energies (and incidence angles, if more than one), $\delta \psi_i$ and $\delta \Delta_i$ are the standard deviations in the measured ψ and Δ values, N is the total number of measurements, M the number of model variables.

Model parameters include layer thicknesses and dielectric functions. The latter may themselves be modeled in various ways, or tabulated by photon energy. Dielectric function models include the Bruggeman effective medium approximation (EMA) for composite or porous materials.⁴ The general procedure is to develop the simplest model that gives a good fit to the data, is physically reasonable, and is consistent with whatever is independently known about the sample.

RESULTS

Figure 1 shows *in situ* $\langle \epsilon_2 \rangle$ spectra measured during etching with the $\text{CH}_4/\text{H}_2/\text{Ar}$ gas mixture, with flow rate ratios of 5/15/7 and total pressure of 1 mTorr, microwave power of 300 W, and rf induced dc bias of -150 V. The spectral range includes the E_1 critical point (2.9 eV). The initial spectrum (0 s) can be modeled as normal GaAs,⁵ with about 6 nm of overlayer. As etching begins the overlayer thickness is quickly reduced (4 s). This is evidenced in the $\langle \epsilon_2 \rangle$ spectrum as an amplitude increase at energies near E_1 , and an amplitude decrease at lower energies. Also at 4 s, a slight red shift and broadening of the E_1 peak are observable. The red shifting and broadening continue until both have nearly stabilized at 48 s.

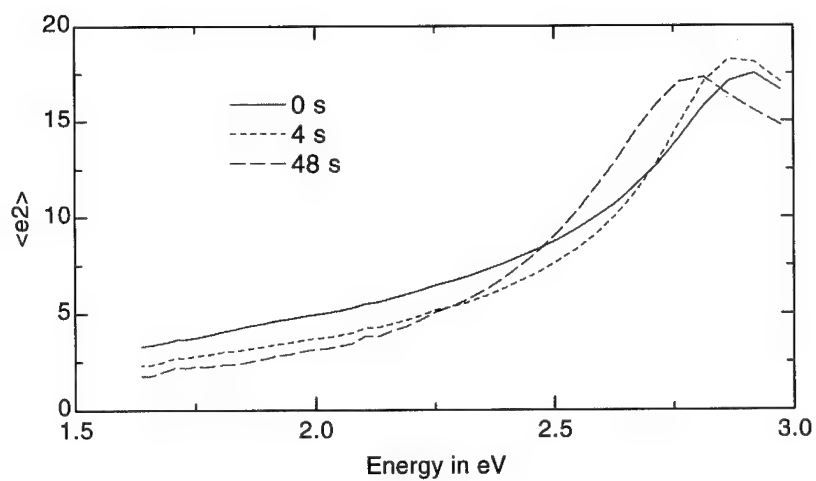


Figure 1. *In situ* pseudodielectric function (imaginary part) measured during GaAs etching with the methane mixture.

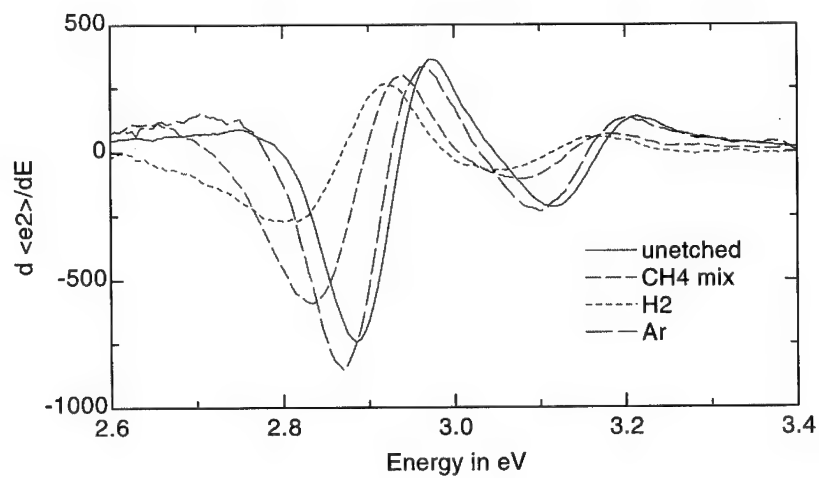


Figure 2. Second derivatives with respect to photon energy of *ex situ* $\langle \epsilon_2 \rangle$ measurements after etching.

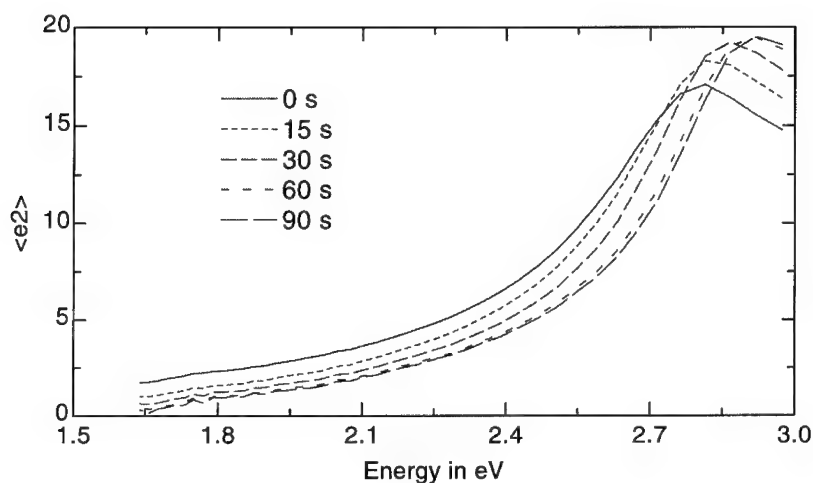


Figure 3. *In situ* $\langle \epsilon_2 \rangle$ measured during Ar etching of GaAs that was previously etched with the methane mixture.

Numerical second derivatives of *ex situ* measurements after etching with the methane mixture are shown in figure 2. A distinct red shift (about 50 meV) and broadening of the E_1 , $E_1 + \Delta_1$ structure are evident for the methane mixture etch. The red shift is not an artifact due to a difference in overlayer thickness. Also shown are data from samples etched in pure hydrogen (0.5 mTorr, 300 W microwave power, -100 V dc bias) and pure argon (1 mTorr, 200 W, -100 V). Hydrogen etching causes more pronounced red shifting and broadening than the methane mixture. Argon etching causes very little red shift, indicating little damage.

To determine bulk etch rates, a small surface region was covered by silver paint during the etch, then the paint was removed and the step height measured by profilometer. Etch rates were about 26 nm/minute for the methane mix, 37 nm/min for pure hydrogen, and 33 nm/min for the argon. These results are consistent with previously reported etch rates under similar conditions.¹

To determine the approximate thickness of the red shifted GaAs layer, a sample was etched first with the methane mix for several minutes (as in figure 1), then with argon to remove the damage layer. Figure 3 shows data taken during the argon etching. As the argon etch removes the red shifted layer, E_1 gradually blue shifts back towards its original value (the reverse of figure 1). Most of the red shifted layer is gone within a minute, implying that the red shifted layer due to methane etching is no more than about 30 nm thick. Similar runs were made starting with a hydrogen etch instead of the methane mix. These red shifted layers required over twice as long to etch away with the argon.

DISCUSSION

The above described measurements of etched bulk GaAs indicate a red shifting of the E_1 , $E_1+\Delta_1$ critical points in the top few tens of nm, associated with the presence of hydrogen in the plasma. We now consider the possible causes of the red shift. Ion implantation has been shown to convert the crystal near the surface into partly amorphous material.⁶ This causes a broadening of the E_1 , $E_1+\Delta_1$ critical point structure (in fully amorphous material the critical point structure is not resolved), but no shifting. Therefore simple amorphous damage, though likely present to some degree, is not the cause of the red shifting.

Effects which are known to cause critical point energy shifts include temperature, alloying, and strain. The temperature dependence of GaAs optical constants is known;^{7,8} in fact, SE can serve as a sensor for surface temperature.⁸ Increasing temperature broadens and red shifts the critical points, as in figure 2. However, the temperature that would be required to achieve the observed red shift is in excess of 200°C. After etching the red shift would decrease to zero as the sample cooled. This is not the case, since the red shift exists in steady state at room temperature (figure 2). Similarly, alloying with indium or antimony would cause red shifting and some broadening. There is no known source of these elements in the plasma, however, and Auger electron spectroscopy (AES) measurements did not show the presence of any new elements after etching.

The relation between strain and critical point shift has been calculated in a perturbation approximation.⁹ Hydrostatic strain (an isotropic change in lattice constant) causes an equal shift of E_1 and $E_1+\Delta_1$ in the same direction. The shift observed here, ~ -50 meV for the methane mixture etch, is consistent with approximately a 1% increase in lattice constant.

Others have also reported damage due to ECR plasma etching at room temperature, but no red shifting effects have been reported. Constantine *et al.* observed changes in photoluminescence intensity and I-V characteristics, when using a methane mixture with high rf bias.¹ Weegels *et al.* observed changes near the GaAs critical point structure in *in situ* reflectivity spectra during hydrogen ECR etching with bias, which they modeled as a partially amorphous damage layer.^{10,11} Their results for Ar etching, like ours, showed much less change in critical point structure than the hydrogen etching.¹⁰ In earlier work we described ECR etching of GaAs with a $\text{CCl}_2\text{F}_2/\text{O}_2$ gas mixture.^{12,13} In that case no red shift occurred, only a thin amorphous damage layer of a few nm.

Though the red shifting observed here may be explained by an increase in lattice constant, the mechanism by which this occurs is unknown. AES measurements showed a Ga rich surface for the hydrogen etch. This result implies a possible connection between stoichiometry and red shifting. We hypothesize that hydrogen reacts preferentially with arsenic within the lattice. As the product (reported as arsine¹⁴) volatilizes it may leave the near surface region nonstoichiometric and less dense than before, allowing the remaining material to expand slightly. The ready penetration of GaAs by hydrogen can explain the relatively large thickness of the red shifted layer. Some damage to the crystal structure must accompany the arsenic removal, accounting for the observed broadening. Note that even pure argon etching caused a small but measurable red shift, implying a small degree of strain-inducing damage for this case as well. However, most of the damage was amorphous. This material could be modeled reasonably well (but without reproducing the small red shift) with a damage layer about 5 nm thick modeled as an EMA mixture of amorphous GaAs¹⁵ and voids.

Whatever the mechanism for red shifting is, it is clear that *in situ* SE is a very sensitive tool for monitoring this and other types of damage in real time. In a single etch run several para-

meters may be varied (power, pressure, substrate temperature, *etc.*), and the effects of these changes on the damage can be seen immediately, without the need for moving the sample to a UHV surface analysis chamber or applying contacts for electrical measurements.

CONCLUSION

In situ spectroscopic ellipsometry has been used to investigate damage caused by electron cyclotron resonance plasma etching. A damage layer as much as several tens of nm thick was produced by $\text{CH}_4/\text{H}_2/\text{Ar}$ or pure H_2 etching with rf bias on the sample. The effect on the optical constants was to red shift and broaden the critical point structure of the GaAs in the damage layer. We hypothesize that the red shifting is due to crystal lattice expansion related to the reaction of hydrogen with arsenic, while broadening is due to amorphous damage. Ar etching caused relatively little damage. Ellipsometry is very sensitive to the surface region damage.

Acknowledgement

Research supported by U.S. Air Force Contract No. F33615-93-C-1297.

References

1. C. Constantine, D. Johnson, S.J. Pearton, U.K. Chakrabarti, A.B. Emerson, W.S. Hobson, and A.P. Kinsella, *J. Vac. Sci. Technol.* **B8**, 596 (1990).
2. R.M.A. Azzam and N.M. Bashara, *Ellipsometry and Polarized Light* (North-Holland, Amsterdam, 1977).
3. G.E. Jellison, Jr., *Appl. Opt.* **30**, 3354 (1991).
4. D.E. Aspnes, J.B. Theeten, F. Hottier, *Phys. Rev.* **B20**, 3292 (1979).
5. The tabulated GaAs optical constants used here were obtained by simultaneous fitting of data published by Aspnes and Jellison, and data measured at U. Nebraska-Lincoln.
6. M. Erman, J.B. Theeten, P. Chambon, S.M. Kelso, D.E. Aspnes, *J. Appl. Phys.* **56**, 2664 (1984).
7. P. Lautenschlager, M. Garriga, S. Logothetidis, M. Cardona, *Phys. Rev.* **B35**, 9174 (1987).
8. H. Yao, P.G. Snyder, J.A. Woollam, *J. Appl. Phys.* **70**, 3261 (1991).
9. F.H. Pollak, *Semiconductors and Semimetals* **32**, edited by T.P. Pearsall, p.40 (Academic Press, Boston, 1990).
10. L.M. Weegels, T. Saitoh, H. Ohashi, and H. Kanbe, *Appl. Phys. Lett.* **64**, 2661 (1994).
11. L.M. Weegels, T. Saitoh, H. Kanbe, *Appl. Phys. Lett.* **65**, 3117 (1994).
12. N.J. Ianno, S. Nafis, P.G. Snyder, B. Johs, and J.A. Woollam, *Appl. Surf. Sci.* **63**, 17 (1993).
13. S. Nafis, N.J. Ianno, P.G. Snyder, W.A. McGahan, B. Johs, and J.A. Woollam, *Thin Solid Films* **233**, 253 (1993).
14. T.R. Hayes, M.A. Dreisbach, P.M. Thomas, W.C. Dautremont-Smith, and L.A. Heimbrook, *J. Vac. Sci. Technol.* **B7**, 1130 (1989).
15. A. Gheorghiu and M.-L. Theye, *Phil. Mag.* **B44**, 285 (1981).

ELECTRON-BEAM-INDUCED TRANSFORMATION OF DEFECTS IN PROTON-IMPLANTED CdS SINGLE CRYSTALS.

V.B.MITYUKHLYAEV.

Research Center for Surface and Vacuum Investigations.
Andreyevskaya emb.2, Moscow, 117526, Russia.

INTRODUCTION

Since their discovery at the end of the last century, electrons have been used as the basis of the increasing number of analytical techniques: electron diffraction, electron microscopy, Auger electron spectroscopy, etc. Now it is known, that electron beams as part of an analytical technique can produce changes on the sample studied. In addition to the radiation damage when using high-energy (generally > 100 keV) beams, there are many effects caused by electrons with the energy below the threshold for direct "knock-on" displacement of atoms in the sample. Such effects have been observed for semiconductors, for example, CdS [1-3].

The interest in electron-beam effect on CdS is also due to the use of CdS in a number of electronic applications, particularly electron-beam-pumped semiconductor lasers [4]. Because the drawback of these lasers is their degradation in the course of operation, it is highly relevant to characterize the various electron-stimulated processes as fully as possible. In this study, electron-beam-induced transformation of defects, created by proton implantation in CdS, has been investigated using cathodoluminescence and electron-beam-induced current.

RESULTS AND DISCUSSION

Experiments were carried out in a scanning electron microscope "Camebax", equipped with the attachment for spectral cathodoluminescence investigations in the temperature range 80 to 300 K. The samples used were high purity wurtzite CdS single crystals with a resistivity of $50 \Omega \text{ cm}$. The (0001) surfaces were mechanically polished, etched in concentrated HCL and then implanted with H^+ (150 keV , 10^{15} cm^{-2}).

Cathodoluminescence spectrum of the CdS crystals before implantation at 300 K consists of the green ($\lambda_{\text{max}} = 510 \text{ nm}$) and broad red ($\lambda_{\text{max}} \sim 740 \text{ nm}$) bands (fig 1a).

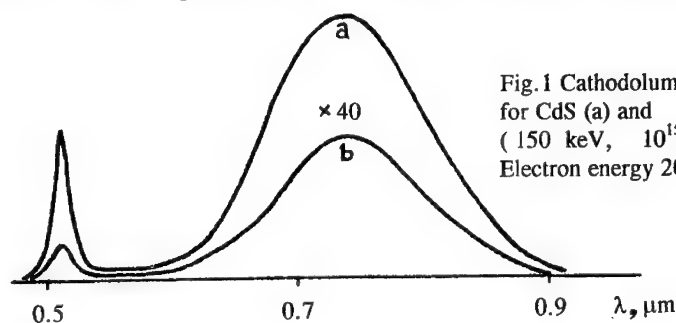


Fig. 1 Cathodoluminescence spectra for CdS (a) and proton-implanted (150 keV , 10^{15} cm^{-2}) CdS (b). Electron energy 20 keV. $T = 300 \text{ K}$

Now it is recognized [5,6] that green and red emissions are due to radiative transitions from the conduction band to the levels of interstitial sulphur (S_i) and $[V^{2+}_{Cd} + V^{2+}_S]^0$ complex respectively. After the proton implantation the intensity of integral cathodoluminescence at 20 keV decreases approximately by two orders of magnitude (fig 1b) as a result of the formation of implantation-induced non-radiative defect centers. It is worth mentioned that the penetration depth of 20 keV-electrons ($2\ \mu\text{m}$) is compared with the calculated projected range of implanted protons - $1\ \mu\text{m}$ [7].

During the 20 keV electron irradiation (with a beam current density of $10^{-1} - 10^{-5}\ \text{A cm}^{-2}$) the rise of the green and red bands of cathodoluminescence takes place and this process depends on the dose of irradiation (fig.2). These changes of recombination properties remain for at least several months after switching off the electron irradiation. It means that during this period the enhanced cathodoluminescence efficiency of the irradiated region (compared with the unirradiated one) does not change. Such a long-term modification of cathodoluminescence efficiency cannot be explained by the change in the charge state of semiconductor defects and hence electron-beam-induced transformation of defects occurs. It should be noted that in the course of measurements of cathodoluminescence intensity the dose of electron irradiation was much less than $10^{17}\ \text{cm}^{-2}$, so changes in semiconductor properties as a result of the measurements can be disregarded.

After annealing of the CdS crystals at 200°C for 1 hour cathodoluminescence intensities of irradiated and unirradiated regions become almost the same. The estimation shows that the annealing process have an activation energy of $\sim 0,7\ \text{eV}$ and this allows one to explain such a long-term modification of the semiconductor properties. Analysis of electron-beam-induced enhancement of cathodoluminescence intensity for green and red bands in the temperature range 80-300 K revealed that the enhancement rate is independent of the temperature and so the defect transformation is an athermal process.

Electron irradiation of the cleaved unimplanted CdS crystals does not change cathodoluminescence intensity at the irradiation dose up to $10^{18}\ \text{cm}^{-2}$ (only slight increase by 10-20% can occur). Besides, experiments were fulfilled on the CdS single crystals implanted with He^+ (300 keV, $10^{15}\ \text{cm}^{-2}$) instead of H^+ . He^+ ions create only radiation defects and do not form chemical bonds with substrate atoms, but have almost the same projected range ($\sim 1\ \mu\text{m}$) at 300 keV as protons at 150 keV [7]. These experiments revealed that the electron irradiation of CdS:He crystals does not cause any changes in cathodoluminescence intensity. So it can be concluded that electron-beam-induce

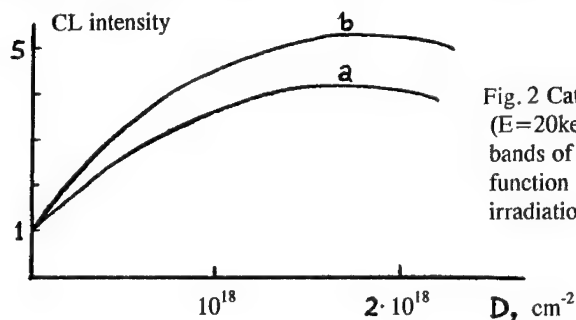


Fig. 2 Cathodoluminescence intensity ($E=20\text{keV}$) for green (a) and red (b) bands of proton-implanted CdS as a function of the dose of electron irradiation at 20 keV.

changes in the cathodoluminescence intensity of CdS are due to the transformation of radiation defects incorporating hydrogen.

In order to clarify the process of electron-beam-induced transformation of defects in proton-implanted CdS, the decay of conductivity induced by the electron beam was investigated. Two pads of 300 Å thick (separated by 0.5 mm) on the (0001) surface of CdS were prepared by vacuum evaporation of In. To provide ohmic contacts, 0.1 μF capacitor charged up to 150 V was discharged through these contacts. Conductivity measurements revealed that after the proton implantation a thin layer is formed near the surface, which conductivity is approximately two orders of magnitude higher than that of the substrate: removal by scraping of some micrometers of the surface layer results in approximately 50% rise of resistance between the contacts.

If electron beam strikes the region of CdS surface between the contacts, conductivity increases. In other words, conductivity induced by electron beam is formed due to the additional quantity of majority carriers - electrons. After switching off the electron beam the decay of conductivity lasts for tens of minutes (fig.3a). Besides, the analysis of such a long-term conductivity relaxation have shown that the decay curve can be approximated by logarithmic curve. If we suppose that the decay of conductivity is due to the recombination of electrons from the conduction band with holes trapped by centers of recombination, then the decay time is

$$\tau = (V S n)^{-1} \quad (1)$$

where V is the thermal velocity, S is the electron capture cross section, n is the concentration of electrons. Using for S a minimal magnitude $S_{\min} = 10^{-23} \text{ cm}^2$ [8] we get $\tau_{\max} \sim 0.1 \text{ s}$ and this magnitude can be treated as a maximum for our experimental conditions and the model used.

Hence, our experimental data contradict the conventional recombination model of uniform semiconductor. Nevertheless the long-term decay of electron-beam-induced conductivity can be explained using the model of non-uniform semiconductor where microscopic potential barriers occur [8]. It is known that these barriers formed by defect clusters, can be created in the course of implantation [9].

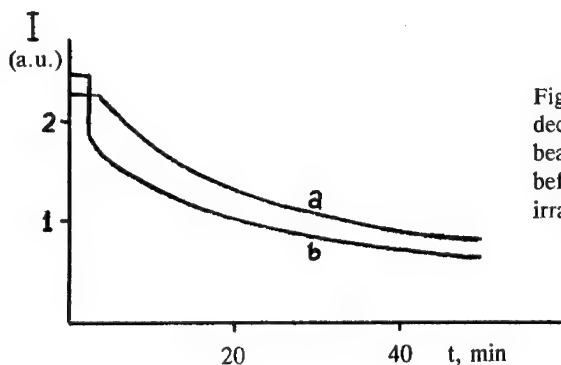


Fig.3 Electron-beam-induced current decay after switching off the electron beam for proton-implanted CdS before (a) and after (b) the electron irradiation (20 keV, 10^{18} cm^{-2})

According to [8], the lifetime (τ_n) of majority carriers (in our case - electrons) in the non-uniform semiconductor is

$$\tau_n = \tau_{n0} \exp(E/kT) \quad (2)$$

where τ_{n0} is the lifetime of electrons in the uniform semiconductor, E is the height of potential barriers.

Electron concentration n as a function of time after switching off the electron beam is determined by the expression [10]

$$n(t) = n(0) - (1/q^2) \epsilon k T R N \ln(1 + (G/N) t) \quad (3)$$

where q is the elementary charge, ϵ is the permittivity of CdS, kT is the thermal energy, R is the radius of clusters, N is the concentration of clusters, G is the carrier generation rate. This Equation is derived for the case of the overlapping of space charge regions of clusters, i.e. when $(4/3) \pi R^3 N > 1$.

After the electron irradiation (20 keV , 10^{18} cm^{-2}) the curve of conductivity decay changes markedly (fig.3b). Although the curve a of fig.3 can be approximated by the Eq (3) fairly well, it cannot be done for the curve b of fig.3 because of the fast decay at the initial moment after switching off the electron beam. This fast decay can be explained if we suppose that potential barriers of clusters drop after the electron irradiation and so their space charge regions do not overlap. Then apart from the recombination in the clusters, the recombination in neutral regions occurs, resulting in the fast decay at the initial moment after switching off the electron beam.

According to [8] the height of the potential barrier E of clusters in the non-uniform semiconductor determines the minority carrier lifetime

$$\tau_p = \tau_{p0} \exp(-E/kT) \quad (4)$$

So the decrease of E allows one to explain the rise of minority carrier lifetime τ_p and hence the increase of the cathodoluminescence intensity after the electron irradiation.

Thus, investigations using cathodoluminescence and electron-beam-induced current revealed that the electron irradiation (20 keV , 10^{18} cm^{-2}) of proton-implanted CdS results in the transformation of defect clusters, containing hydrogen and as a result of the transformation a potential barrier of the clusters drops.

To clarify the mechanism of defect transformation in proton-implanted CdS, an effect of free charge carrier generation due to the light excitation was studied, using 1W Ar laser ($0.488 \mu\text{m}$). Calculated rates of free charge carrier generation were approximately the same for the light and electron excitations. The experiments have shown the absence of any changes in the cathodoluminescence intensity of light-irradiated region of the crystal. So different theories of recombination-accelerated defect formation (for example, Bourgoin-Corbett [11] and Lang-Kimerling [12] mechanisms) cannot explain the observed phenomena in CdS. It is thought that the most probable mechanism in our case is analogous to that proposed to explain the electron stimulated desorption and known as the KF model [13]: the excitation and removal of a core electron from the substrate atom, followed by its Auger relaxation, leaves the atom in a repulsive potential, from which one or more atoms may be displaced from the equilibrium state.

CONCLUSIONS

1. Proton implantation (150 keV , 10^{15} cm^{-2}) of CdS crystals results in the formation of defect clusters in the near-surface region.
2. Irradiation of the proton-implanted CdS with 20 keV electrons causes transformation of the defect clusters and decrease of their potential barriers. As a result, the lifetime of minority carriers and cathodoluminescence intensity increase
3. Generation of free charge carriers by the light excitation does not cause the defect transformation in CdS:H. The probable mechanism of electron-beam-induced defect transformation is believed to be analogous to the KF model of electron stimulated desorption: the excitation and removal of a core electron from the substrate atom, followed by its Auger relaxation leaves the atom in a repulsive potential, from which one or more atoms may be displaced from the equilibrium state.

REFERENCES

1. B.A.Kulp and R.H.Kelley, J. Appl. Phys., **31**, 1057 (1960).
2. A.E.Cherednichenko, B.V.Novikov and G.V.Benemanskaya, J. Luminesc., **6**, 193 (1973).
3. V.B.Mityukhlyayev, Appl. Surf. Sci., **81**, 137 (1994).
4. J.L.Brewster, Appl. Phys. Lett. **13**, 385 (1968).
5. B.A.Kulp. Phys. Rev., **125**, 1865 (1962).
6. M.K.Sheinkman, N.E.Korsunskaya, I.V.Markevich and T.V.Torchinskaya, Izv. Akad.Nauk SSSR ser fiz., **40**, 2290 (1976). [Bull. Akad. Sci. USSR, Phys.Ser. **40**,1 (1976)]
7. J.F.Ziegler, J.P.Biersack, U.Littmark. The Stopping and Ranges of Ions in Solids (Pergamon press, New York, 1985), p.321.
8. M.K.Sheinkman and A.Y.Shik, Fiz. Tekh. Poluprovodn. **10**, 209 (1976) [Sov. Phys. Semicond.**10**, 164 (1977)]
9. R.F.Konopleva, A.A.Yufferev. Radiat. Eff., **29**, 193 (1976).
10. A.Y.Shik, Fiz. Tekh. Poluprovodn. **11**, 1758 (1977) [Sov. Phys. Semicond. **11**, 1235 (1978)].
11. J.C.Bourgoin and J.W.Corbett, Phys. Lett. **38**, 135 (1972).
12. P.V.Lang and L.C. Kimerling, Appl. Phys. Lett. **28**, 248 (1976)
13. M.L.Knotek and P.J.Feibelman, Surf. Sci. **90**, 78 (1979).

Part IX
Defects in Devices

DEFECTS AND FUTURE SILICON TECHNOLOGY

J. PALM AND L.C. KIMERLING

Massachusetts Institute of Technology, Department of Materials Science and Engineering, 77 Massachusetts Avenue, Cambridge, MA 02139

Abstract

The interaction between device technology and the control of defects has been strong since the first transistor. The rapid and unparalleled development of this technology can be monitored by changes in device size and process complexity, or reciprocally, in defect density. In the future the emphasis on computation functionality will shift to imaging and learning. In addition high volume manufacturing will cast an emphasis on capital cost, yield, effluent control and safety. These foci require the development of new sensitive defect assessment tools, the modelling of complex defect systems and the understanding of defect properties on the atomic scale. We shall illustrate this interplay between technology and materials science by topics in ULSI circuits, silicon photovoltaics and silicon microphotonics. For ULSI the control of both bulk and surface defects is decisive. The physical chemistry at the silicon surface plays a key role in metal contamination. We shall discuss the use of RF-PCD for in-line monitoring and investigation of reaction kinetics. Silicon for low cost, photovoltaic applications confronts problems involving complex defect systems, but comparatively simple processes. The goal is to optimize growth and cell processing. The objective of silicon microphotonics is to establish an IC compatible process technology for integration of optical interconnection with silicon electronics. By building the first silicon-based LED operating at $\lambda=1.54\text{ }\mu\text{m}$ at room temperature it has been shown that erbium doping is a viable approach. Codoping with F or O largely enhances the light output. We will show a process simulator for the Si:Er:F system as an example for ligand field engineering.

INTRODUCTION

Defects have always played a Janus-faced role in semiconductor device technology: the device performance fundamentally relies on intentionally introduced defects in the bulk, e.g., dopant impurities for p-n junctions, and at interfaces, e.g. Metal Oxide Semiconductor (MOS) structures. Likewise point defects are indispensable for standard processing steps, i.e., diffusion, oxidation and contact formation. Generated at elevated processing temperatures, however, they cannot be reduced to their thermal equilibrium concentrations due to slow reaction kinetics. In addition metal contaminants or implantation damage can be deleterious to subsequent processing and device performance, affecting leakage current, gate oxide integrity, and yield. The unparalleled development of

semiconductor technology has been fundamentally enabled by defect engineering, i.e., the strong interaction of material science and electrical engineering. We shall illustrate the challenges of defect related problems for the future Silicon technology by examples from three areas driving the industry: 1) operations constraints at the front end of device manufacturing: process monitor and control, safety and environment issues for Ultra Large Scale Integration (ULSI); 2) energy: limited fossil energy resources and environmental considerations motivate research on low cost devices for photovoltaic applications. 3) interconnects: whereas the preceding topics require incremental progress in understanding, a major breakthrough is demanded to overcome the principal limitations for electrical interconnects on ULSI devices given by propagation delay and power dissipation. Silicon microphotronics has this potential. Its concept is to merge the high functionality of silicon integrated circuits with the tremendous information carrying capacity of light transmission.

ULSI

The driving force for the progress of integrated circuit (IC) technology has been the demand for ever increasing speed and integration level. Imaging and learning will require even higher data rates and functionality than computing. The key approach to meet these demands has been scaling, i.e., the reduction of the feature sizes of the elementary IC components.

Figure 1 shows the exponential decrease of minimum feature length, i.e. gate width, junction depth and gateoxide thickness of MOSFET structures with time. The rate of about 13% reduction per year has led the present 0.35 μm generation with 0.15 μm junction depth and 90Å gateoxide thickness. This increase of integration level and logic gate speed is accompanied by the unfavorable increase of chip area, chip power dissipation and number of input/output pins. The tolerable defect density has to scale

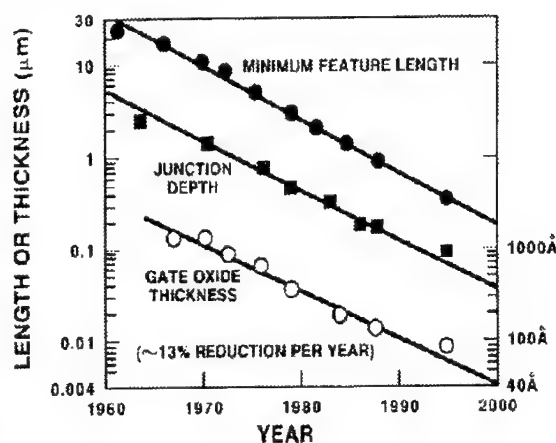


Figure 1 Scaling of MOSFET dimensions

reciprocally with the chip area. The outstanding question of the 1990s is: where and when will this progress saturate? The limiting materials and fundamental physics problems are interwoven with manufacturing constraints: yield, equipment investment and operating costs, safety and environmental issues.

The following section gives a short survey on defect related issues in ULSI technology.

Crystal Growth: The silicon boule size has been steadily increased in order to place more die on a single wafer. The technology focus has moved from dislocation control to point defect control. Doping homogeneity becomes a fundamental limit for the nanometer scale gate length. Statistical (Poisson) fluctuations in local dopant concentration will lead to variations of device performance parameters such as the MOSFET threshold voltage. Czochralski (CZ) grown material is the industry standard for mechanical strength and internal gettering capability. Increase of the boule diameter produces higher thermomechanical stress which threatens dislocation free growth.

Wafer Preparation: The mechanical specifications for a silicon wafer are the most demanding for any man-made object. Cutting, polishing and etching must now be accomplished with atomic precision. Wafer warpage, surface roughness and acceptor passivation by hydrogen are current issues. Contamination level requirements are projected to be below levels of spectroscopic detection for the next generation technology; as an example the specifications for bulk iron concentration will drop from $1 \times 10^{11} \text{cm}^{-3}$ (1995) to below $5 \times 10^9 \text{cm}^{-3}$ (2010). Gettering mechanisms are limited by low thermal budgets and complex circuit topography.

Junction Formation: Junction depths of $0.5 \mu\text{m}$ and gate oxide thicknesses of $0.04 \mu\text{m}$ are projected as technology limits. Ion implantation profiles with little dopant diffusion presently define the doping distribution making damage recovery a key issue. In addition, control of dopant profiles requires diffusion processes to be understood at the atomic scale.

Interconnection: The propagation delay due to resistivity and capacitance of the metal interconnects already exceeds the gate delay, i.e. transistor switching times. Increasing current densities and multilevel structures pose reliability limits through electromigration, i.e., the current induced transport of metal atoms, and stress. These limits may be overcome by silicon microphotonics as discussed below.

Process Monitor and Control: As wafer diameters and purity constraints increase, the costs of wafer and lost product become important. Single wafer processing offers an opportunity for enhanced in-line control.

Environmental and Safety Issues: The selection of materials and processes must fit within environmental and safety envelopes. Substitutes for chlorine based etches wet cleans and the standard HF treatments for oxide removal and surface passivation are needed.

Our recent work on Radio Frequency Photoconductance Decay addresses both technological and science issues: the need for sensitive detection tools and process monitors compatible with the IC manufacturing environment, as well as the need for a better understanding of reactions at the silicon surface during wafer preparation and processing [1,2]. In RFPCD the decay of excess carriers generated by a pulsed light source is measured as the change of inductance of a resonant RF circuit. Figure 2 shows the calculated dependence of the total, i.e. measured, lifetime τ_{meas} on bulk lifetime for different surface recombination velocities S [1]: the sensitivity of the system to surface recombination increases

with wafer quality. The technique is contactless and the wafer can be placed in Teflon beakers with cleaning solutions or HF. Therefore the change of surface properties by metal adsorption, passivation or oxidation can be measured in-situ.

The adsorption of copper has been measured in situ by adding copper into the dilute HF solution [2]. Figure 3 shows the degradation of the surface with time. The surface state concentration was obtained by calculating the surface recombination velocity from the measured lifetime. The total number of copper atoms was obtained by measuring the final copper coverage with TXRF for different Cu concentrations in solution.

With the equation

$$S = \sigma_{\text{Cu}} v_{\text{th}} N_{\text{T}} \quad (1)$$

the capture cross section σ_{Cu} can be determined: $\sigma_{\text{Cu}} = 2 \cdot 10^{-17} \text{ cm}^2$. This parameter gives the relationship between measured lifetime and surface state density N_{T} for all immersion times. The value of the capture cross section indicates atom by atom deposition for low copper concentrations. Considering the re-quired surface purity for ULSI processing steps the design of wafer cleans will be crucial. We recently proposed the use of E-pH or Pourbaix Diagrams for the understanding of the efficiency of cleaning solutions for the removal of different metal contaminants [2]. E-pH diagrams map stable phase fields, i.e. as metal, oxide or ion, as a function of redox potential E and the pH of the solution. Figure 4 shows the E-pH diagram for iron, displaying the stability regions for the various solid and ionic species. The phase boundaries (for different molarities) represent the change from positive to negative reaction potential for the E-pH diagrams map stable phase fields, i.e. as metal, oxide or ion, as a function of redox potential E and the pH of the solution. Figure 4 shows the E-pH diagram for iron, displaying the stability regions for the various solid and ionic species. The phase boundaries (for different molarities) represent the

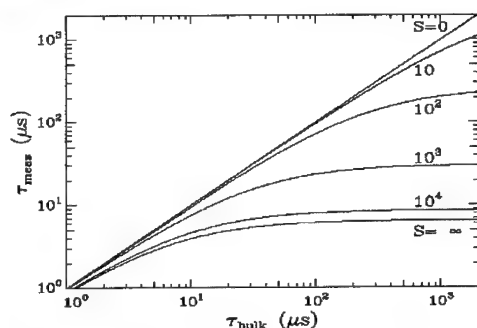


Figure 2 Calculated total lifetime vs. bulk lifetime for different surface recombination velocities S

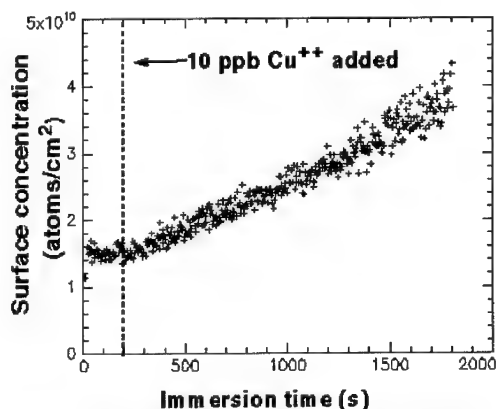


Figure 3 Surface state concentration calculated from the measured RFPCD lifetime as a function of immersion time.

change from positive to negative reaction potential for the dissociation reaction of the adjacent species, as shown in the case of Fe^{+++} and Fe_2O_3 .

Figure 5 shows the E-pH values for different cleaning solutions which are given by the reduction reactions of the oxidant (hydrogen peroxide). Since the cleaning solution SC1 falls in the stability region of a solid oxide phase in the Fe E-pH diagram, trace amounts of Fe present in the cleaning solution can lower the system free energy by forming Fe_2O_3 on the surface. Conversely, effective contaminant removal will occur when the cleaning solution lies in the stability region of a metal ion, as in the case of Fe in SC2.

This prediction can be confirmed by the effects of two different cleaning procedures on gate oxide integrity, monitored here by the measured lifetime. Wafers from two different vendors (A,B) were tested ($[B]=5 \times 10^{15} \text{ cm}^{-3}$, (100) grown, 20 cm diameter). Oxidation after an HF/SC1 clean lead to considerably lower lifetime values (A: $3 \mu\text{s}$, B: $33 \mu\text{s}$) than after the standard HF/SC1/SC2 clean (A: $592 \mu\text{s}$, B: $250 \mu\text{s}$). DLTS measurements confirmed the role of FeB pairs in lowering measured lifetimes.

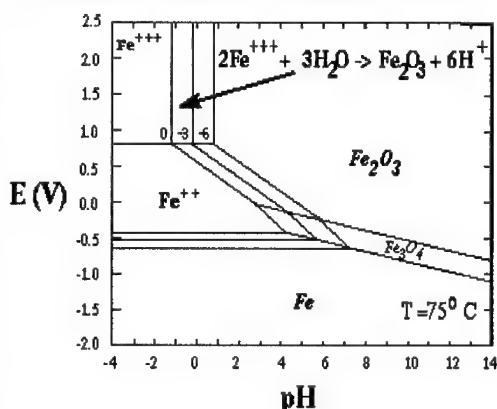


Figure 4 The E-pH diagram for Fe, showing phase boundaries for 10^{-6} , 10^{-3} and 1 molal concentrations in solution

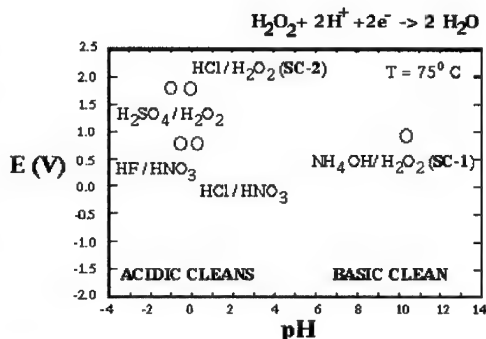


Figure 5 (E, pH) values for some standard cleaning solutions

Silicon Photovoltaics

Limited fossil energy resources and environmental issues are driving an increasing interest in renewable energy. Large scale terrestrial solar energy will have a huge market potential. Silicon is a favorable candidate as a solar cell material because of its abundance, its environmental safety and the immense available knowledge base. For solar cells to be the building block for photovoltaic power stations of Mega or Giga Watt output power it is self-evident that cost per area is the key parameter. Therefore the goal of materials research is to provide the knowledge base for low cost silicon growth and processing. Contrary to the ULSI technology the challenge is here to characterize, understand and simulate a system

containing a large density and variety of defects and to optimize a device with comparatively simple processing steps. The key device parameter is the conversion efficiency, i.e. the ratio of light intensity and electrical output power. Current research topics are: the development of cost effective growth processes such as ribbon or sheet growth, casting and planar solidification or simplified CZ growth; the interaction of impurities, predominantly oxygen, carbon and transition metals among each other and with grain boundaries and dislocations; and the advantages of process steps like passivation and gettering. Process monitors, cell characterization tools, especially mapping techniques, as well as modelling of process reactions and process design are important technological issues. Some aspects of defect reactions will now be discussed by the example of iron in silicon.

Iron is an ubiquitous contaminant coming from wafer preparation equipment, especially wafer cutting. As a fast interstitial diffuser iron can be a deleterious due to its electronic properties and the reaction with other defects. Well known is the pairing reaction with shallow acceptors. From the perspective of fundamental defect physics iron acceptor pairs allow the study of a variety of interesting phenomena like metastability, the pairing kinetics and the electronic structure. Interstitial iron introduces a deep donor state at $E_v + 0.38\text{eV}$ in the bandgap. After pairing with a shallow acceptor a level at $E_v + 0.1\text{eV}$ is introduced.

Iron boron pairs have also been studied in solar cell materials [3]. Figure 6 shows the room temperature EBIC micrograph of a grain boundary in boron doped multicrystalline cast silicon which has been intentionally contaminated by iron diffusion (state I). At 100K the bulk EBIC signal has dropped significantly indicating a decrease of the diffusion length. This behavior is expected for recombination at shallow states like the iron boron pairs. Adjacent to the grain boundary a bright zone demonstrates the gettering of iron by the grain boundary. In state II the iron boron pairs have been partially destroyed by forward biasing a Schottky junction. The room temperature EBIC signal has decreased due to the

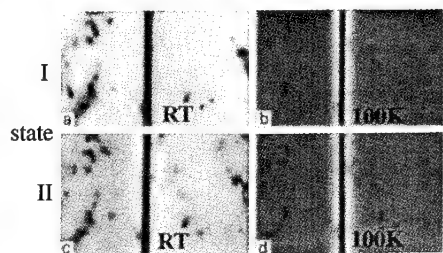


Figure 6 EBIC images of a grain boundary in multicrystalline silicon; state I: after iron diffusion; state II: after destruction of the FeB pairs.

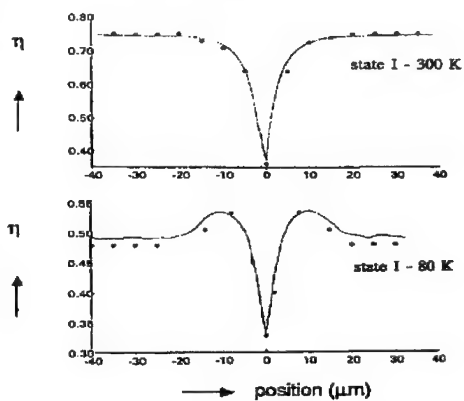


Figure 7 Measured and simulated EBIC profiles

introduction of deep interstitial iron levels. The EBIC signal can be simulated by Monte Carlo calculations (Fig. 7). The amount of iron gettered at the grain boundary has been determined to be $4 \times 10^{11} \text{ cm}^{-2}$. It should be noted that the EBIC efficiency is analogous to the solar cell efficiency, i.e. the presence of grain boundaries and their gettering activity can be advantageous in the sense of defect engineering.

Silicon Microphotronics

Microphotonic technology merges the high functionality of silicon integrated circuits with the tremendous information carrying capacity of light. The goal is to overcome the limits of metal based electronic interconnects, like propagation delay, crosstalk and reliability, by shifting the functions of clock signal distribution and input/output data transfer to an optical network integrated on the same chip.

One of the key components of this future technology is the silicon based light emitter. Our approach is the doping of

silicon with the rare earth erbium. We have fabricated the first room temperature operating silicon light emitting diode (LED) and demonstrated process compatibility with standard IC processing [4,5,6]. We will illustrate features of the Er/Si materials system. In order to achieve a sufficient light output Erbium has to be incorporated in concentrations above the solubility limit. We have studied the doping by deep implantation (range $\approx 1.5 \mu\text{m}$ for 4.5 MeV) and the optical activation by annealing. It has been found that co-doping with oxygen or fluorine [6] strongly enhances the luminescence. Figure 8 shows the dependence of PL intensity vs. annealing time for different F concentrations. The three different regimes are attributed to 1) damage recovery 2) F outdiffusion and 3) Er-F complex dissociation. In order to define the process window for optimum light output a process simulator has been developed: the Er and the F dopant profiles form the data input, process parameters are temperature and time. The key model parameters are the dissociation / formation enthalpies the Er-F complexes, the diffusion coefficient and the surface accumulation coefficient of fluorine.

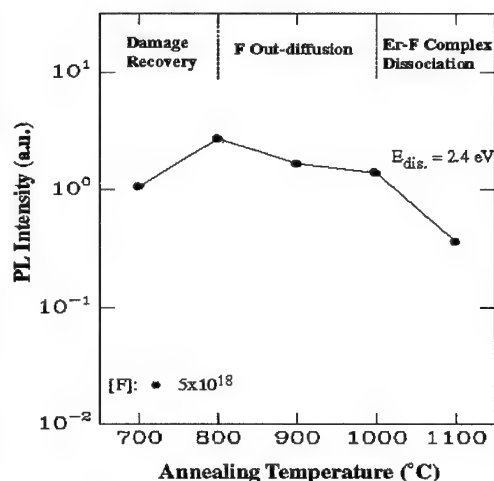


Figure 8 Effect of heat treatment on light output of the Si:Er-F system

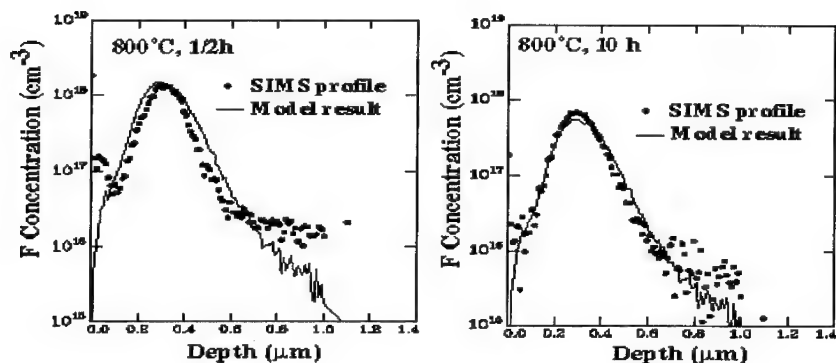


Figure 9 Measured and simulated F SIMS profiles

The formation enthalpies for three different complexes ErF , ErF_2 and ErF_3 in silicon are scaled according to the corresponding values in the gasphase. Simulated concentration profiles for the three complexes show that ErF_3 is the dominant one. Figure 9 shows the good agreement of simulated and measured SIMS profiles of the total F concentration for two annealing times. Figure 10 presents the comparison of the simulated and measured PL intensity. The deviations for short annealing times are due to the interaction with implantation defects which are not included in the model. Besides the materials properties of the Si:Er:Ligand system, Er in silicon is subject of fascinating and challenging defect related research. Current topics are the electronic structure of Er defect complexes and the excitation and quenching processes of the electroluminescence.

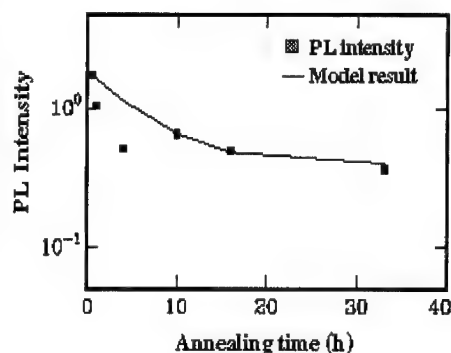


Figure 10 Measured and simulated PL intensity as a function of annealing time

Conclusion

We have shown that defects are both indispensable and deleterious for silicon technologies. Research on defects in silicon is driven by science (knowledge) and technology (applications). Three challenges for material science and defect physics have been outlined: the development of sensitive

defect assessment tools, the understanding of defect reactions on the atomic scale and simulation of complex defect systems.

Acknowledgments

The paper reviews work which was funded in parts by NREL, SRC, ARPA, Rome Laboratories and AFOSR. J. Palm is supported by the Deutsche Forschungs Gemeinschaft.

References

- [1] H. M'Saad, J. Michel, J.J. Lappe, and L.C. Kimerling, J.E.M., **23**, 487 (1994)
- [2] G. Norga, L.C. Kimerling, J.E.M. , **24**, 397 (1995)
- [3] M. Kittler, W. Seifert, M. Stemmer, J. Palm, J.A.P. , **77**, 3725 (1995)
- [4] F.Y.G. Ren, J. Michel, Q. Sun-Paduano, B. Zheng. H. Kitawa, D.C. Jacobson, J.M. Poate and L.C. Kimerling, Mat. Res. Soc. Symp. Proceedings, **298**, 415 (1993)
- [5] B. Zheng, J. Michel, F.Y.G. Ren, L.C. Kimerling, D.C. Jacobson and J.M. Poate, Appl. Phys. Lett. **64**, 2842 (1994)
- [6] F.Y.G. Ren, J. Michel, Q. Sun-Paduano, B. Zheng. H. Kitawa, D.C. Jacobson, J.M. Poate and L.C. Kimerling, Mat. Res. Soc. Symp. Proceedings, **301**, 87 (1993)

PROBING METAL DEFECTS IN CCD IMAGE SENSORS

WILLIAM C. MCCOLGIN, J.P. LAVINE, AND C.V. STANCAMPIANO
Eastman Kodak Company, Microelectronics Technology Division,
Rochester, NY 14650-2008

ABSTRACT

We have investigated the role of heavy metals in causing visible pixel defects in Charge Coupled Device (CCD) image sensors. Using a technique we call dark current spectroscopy, we can probe for deep-level traps in the active areas of completed image sensors with a sensitivity of 1×10^9 traps/cm² or better. Analysis of histograms of dark current images from these sensors shows that the presence of traps causes quantization in the dark current. Different metal traps have characteristic dark current generation rates that can identify the contaminant trap. By examining the temperature dependence of the dark current generation, we have calculated the energy levels and generation cross sections for gold, iron, nickel, and cobalt. Our results show the relationship of these traps to the "white spot" defects reported for image sensors.

INTRODUCTION

Charge Coupled Device (CCD) image sensors have made considerable progress in recent years. Higher resolution electronic cameras that incorporate sensors with from 1 to 25 megapixels are now commercially available.^{1,2} Such cameras are finding enthusiastic use in such diverse applications as electronic journalism, desktop publishing, and both professional and amateur astronomy, where the speed and convenience of the digital format are ideal. This progress in imager technology has built on the advances in memory chips; however, unlike memories, imagers have no redundancy for defective pixels. While individual defective pixels may be corrected with image processing, such correction is expensive and is limited to certain types of defects. Thus, it is essential to reduce the occurrence of defective pixels.

Defects from Contaminant Metals

One source of pixel defects in imagers is heavy metal contamination in the active area of the final device. This includes transition metals such as iron through copper and metals such as gold. Advances in materials processing have enabled silicon to be among the purest materials produced. And yet the requirements for future devices will be even more stringent. In order to maintain the steady progress of the last four decades, the Semiconductor Industry Association Roadmap calls for iron levels of less than 2×10^{10} cm⁻³ in silicon starting wafers by the year 2001 and for process steps to deposit less than 1×10^{10} cm⁻² of most transition metals.³ However, in imagers, as we shall see, the effects of even single, errant contaminant atoms may be observed.

These metals have several properties that make them hazardous for imagers.⁴ First, even though they have little to no solubility in silicon at room temperature, at processing temperatures of 1000°C their solubilities can increase by as much as seventeen orders of magnitude to 10^{17} cm⁻³, a potentially devastating level for a contaminant.^{4,5} Second, these metals are typically fast diffusers, capable of transiting a wafer thickness of 525 μ m in less than 30 s at the same 1000°C.⁶ This means that localized contamination can spread substantially across a wafer in the course of processing; sublimation may even spread it to adjacent wafers.⁷ When wafers cool, the solubility

drops much faster than the diffusion coefficient, so that the metals can migrate to interfaces where they can disrupt electrical structures. Finally, these metals form deep-level traps in silicon⁵ that facilitate the thermal generation of noise electrons, or dark current, that compete with signal electrons produced by light in an imager. Such contaminants have long been cited as a source of white spot image defects that are visible with no imager illumination. In the case of "bright point" defects, etching back to the silicon surface reveals extended defects present in the silicon, either caused by or decorated by metal precipitation.^{8,9} In the case of a fainter class of white spots called "dim points," etch backs do not reveal crystal defects; however, the occurrence of these dim points has been correlated with the presence of iron.¹⁰ The effects of specific metals in imagers have also been determined through deliberate contamination experiments.^{11,12} Figure 1a shows the high dark current resulting from iron. An iron wire was scribed across the back of this imager just before the last high temperature step in fabrication. The magnified view in Fig. 1b shows the spot-like nature of the dark current. We found that gold, nickel, and cobalt could also generate sufficient dark current to cause defective pixels. Clearly, eliminating these metals from image sensors is of high priority. One challenge, however, is to be able to detect them at levels well below those that affect the device.



Fig. 1a. Photograph from an image sensor with a bright streak caused by iron.

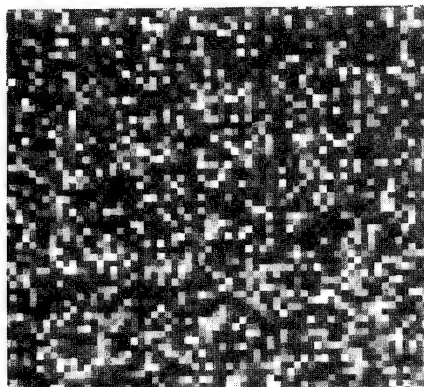


Fig. 1b. Enlarged view of Fig. 1a showing the spot-like nature of iron contamination.

DARK CURRENT SPECTROSCOPY

The demonstrated sensitivity of imagers to metal contamination can be turned to advantage to both study and monitor deep-level metal traps in image sensors. In imager systems where external temporal noise can be reduced or averaged out, the spatial distribution of dark current sources among the pixels of the imager chip can be examined. Some internal sources such as interface states can be eliminated through proper design and operating conditions.^{13,14} With enough sources of dark current removed, what remains is largely due to deep-level traps in the imager. These traps, distributed across an image sensor, can be studied at the spatial resolution of a single imager pixel by integrating the imager with no illumination and analyzing the resultant

image. Integrating for several seconds, instead of for the usual frame time of 1/30th s, amplifies pixel-to-pixel variations and allows details in the dark current image histograms to be resolved and analyzed. We call this technique dark current spectroscopy.

The image sensor used in this work was a KODAK KAI-0370 Image Sensor, a 2/3" video interline-transfer CCD imager. The imagers were studied at the wafer level on a probe station with a temperature-controlled chuck. The test temperatures were 55°C unless otherwise indicated. Hardware and software controls allowed us to investigate traps either in the photodiodes or in the CCD shift registers. Additional experimental details have been previously reported.¹²

Quantized Dark Current

When the dark current image data is plotted as a histogram^{10,15} of the number of pixels found at each value of dark current, we find that the dark current is quantized.^{12,16} This quantization is due to the discrete nature in which traps are distributed among the pixels of the image sensor. Figure 2 shows the quantization resulting from a single type of trap present in the photodiodes of the imager. In this histogram, many of the photodiodes of the sensor have no discernable traps. Their dark current, labeled J_0 , comes from other sources common to all the photodiodes. These pixels are found in the first peak to the right of the truncated zero reference in the figure. The second peak in the histogram represents pixels that have one trap present that is generating additional dark current at the rate of about 7 electrons/frame. The next peak, with twice the added dark current, is from pixels with two traps each. Succeeding peaks correspond to three, four, five, etc. traps per pixel. It is assumed that within a pixel, multiple traps act independently and their dark currents are additive. This assumption appears to be borne out by the equal spacings between peaks. This weak trap is occasionally seen in imagers without deliberate contamination and is believed to be due to interstitial iron. This identification will be discussed in some detail later.

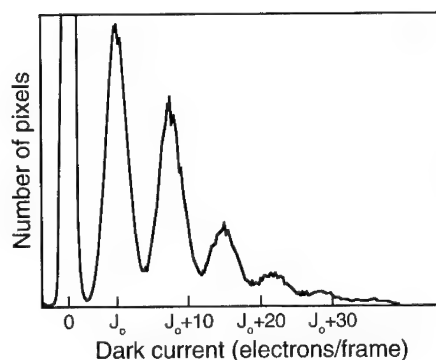


Fig. 2. Quantized dark current from the photodiodes of an interline-transfer imager. A single type of deep-level trap is present.

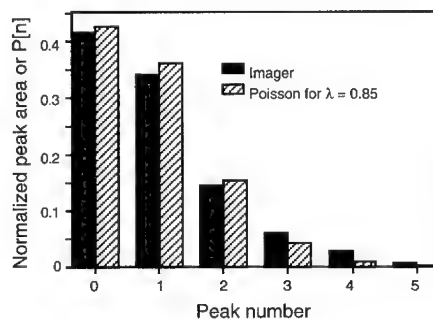


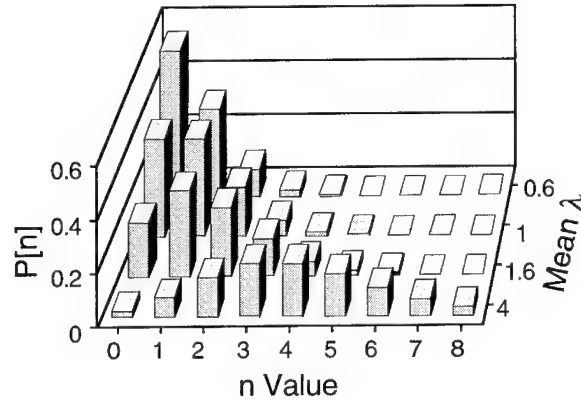
Fig. 3. Comparison of the fractional areas of the Fig. 2 peaks to the Poisson distribution. The peaks match 0.85 traps/pixel.

The spatial distribution of traps among the imager pixels is assumed to be Poisson with

$$P_n(\lambda) = \frac{\lambda^n}{n!} e^{-\lambda}, \quad \text{where } n = 0, 1, 2, 3, \dots, \quad (1)$$

and $P_n(\lambda)$ is the probability of finding exactly n traps in a pixel. The Poisson mean λ is the average number of traps per pixel. To compare Fig. 2 with the Poisson distribution, we can, by curve-fitting, calculate the area under each of the dark current peaks. Figure 3 shows that the fractional areas of the peaks fit closely to a Poisson distribution with a mean of 0.85, indicating an average of 0.85 traps per imager pixel. Since the electrically depleted volume of the photodiodes in this sensor is $50 \mu\text{m}^3$, the average trap concentration is $1.7 \times 10^{10}/\text{cm}^3$.

Fig. 4. Plots of the Poisson distribution $P[n]$ for different values of the Poisson mean λ .



The shape of the Poisson distribution changes sensitively with the Poisson mean, as is illustrated in Fig. 4. One can therefore estimate the average number of traps simply from the shape of the histogram. As Fig. 4 shows, when λ is less than one, the succession of peaks drops off quickly. For higher values of λ , the shape begins to approximate a skewed Gaussian curve.

The bandwidths of the quantized peaks in the histograms gauge the variability of the trap generation or the effects of the local environment in which the deep-level traps are located. We suggest that width σ_n of the n th peak in the histogram be given by the expression

$$\sigma_n = \sqrt{\sigma_0^2 + n\sigma_T^2}, \quad \text{where } n = 0, 1, 2, 3, \dots, \quad (2)$$

where σ_0 is the bandwidth of the dark current noise common to every pixel and σ_T is that of the trap. The bandwidths obtained from the histogram peaks in Fig. 2 compare well to the Eqn. (2) model for the values $\sigma_0 = 1.5$ and $\sigma_T = 0.8$ electrons/frame. In general, when σ_0 dominates, peaks in the histogram will appear equal in width; however, if σ_T is larger, the peak widths will begin to broaden as \sqrt{n} . This explains why higher n -value peaks become harder to resolve, and why evidence of the quantization may be lost when the average number of traps becomes too large.

Deep-Level Metal Traps

More can be learned about deep-level traps by examining imagers containing specific metals. Figure 5 contains dark current histograms from imagers on a wafer deliberately contaminated with Au. A trap due to the gold is present in the CCD shift registers with a spacing close to three times that of the weaker trap of Fig. 2. The Poisson mean in Fig. 5a is 0.16, from an imager located on the wafer some 5 cm from the scribed gold line. Figures 5b and 5c show successively higher levels of gold as the scribe line is approached, with averages of 1.7 and 3.6 gold atoms/pixel, respectively. Converting Poisson means to concentrations, we find that the gold on this wafer varies from $3 \times 10^9 \text{ cm}^{-3}$ at the wafer edges to about $1 \times 10^{12} \text{ cm}^{-3}$ near the actual scribe line. The shapes of the histograms follow the behavior expected from Fig. 4.

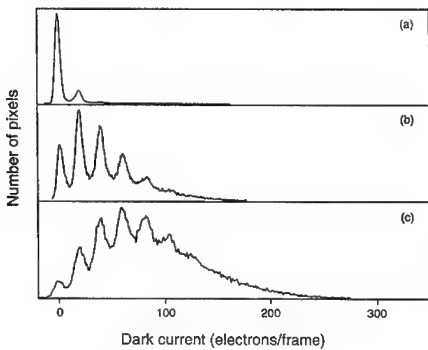


Fig. 5. Dark current histograms from imagers on a wafer deliberately contaminated with gold. The gold level increases from (a) to (c).

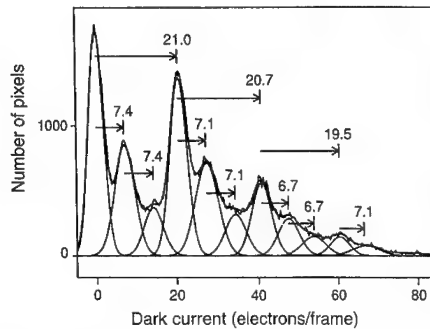
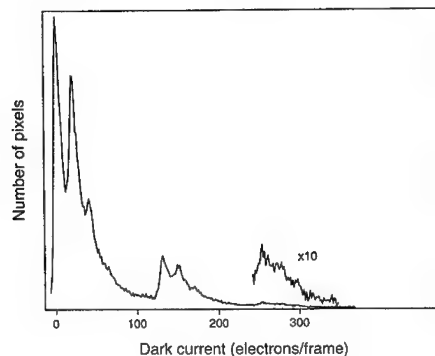


Fig. 6. Histogram of Au and Fe_i in the same imager. Peak spacings were determined by a curve fit of 12 Gaussians.

If more than one contaminant is present in an imager, multiple sets of peaks may appear in the histogram. Figure 6 shows a case where both gold and the interstitial iron trap are present. The histogram shows a series of gold peaks, each gold peak having associated with it the sequence of smaller-spaced peaks seen earlier. The peak spacings for each of the two different traps in Fig. 6 were obtained by fitting 12 Gaussian peaks to the dark current histogram. The two traps appear to act independently, each randomly distributed among the imager pixels and each with its own Poisson mean. Accordingly, pixels with any particular number of gold traps can also have zero, one, two, etc. of the weaker traps. The result is the "multiplet" sequence shown in the figure. The similarities of such dark current histograms to the spectra provided by several optical spectroscopic techniques have led us to refer to this as dark current spectroscopy.

Wafers with either Ni or Co contamination showed additional traps, each with the higher dark current generation rate of 132 electrons/frame at 55°C. Figure 7 shows the histogram obtained from an imager adjacent to a deliberate nickel scribe line. The nickel concentration here is about one nickel trap in every 5.5 photodiodes, or $3.6 \times 10^9 \text{ cm}^{-3}$. The smaller set of spacings is due to gold cross-contamination that occurred when wafers scribed with different metals were annealed together in the same furnace tube. Hence, the gold peaks in photodiodes without nickel are replicated in the sequences of peaks for both one and two nickel traps per pixel, just as in the case presented earlier for the two traps of Fig. 6.

Fig. 7. A deep-level nickel trap generating 132 electrons /frame at 55°C. Gold peaks from cross-contamination are also present.



We observed in Fig. 1 that iron causes very bright image defects in a relatively narrow region over the iron scribe line. The strong intensity of these defects would appear to preclude them from being point defects like the other metals. Instead, the iron has probably created extended lattice defects. Indeed, an etch back of some of the imagers revealed silicon defects present in a region over the iron scribe line. This was not observed for the other metals. Extended defects might be expected to have a broad range of potential generation rates and not to show effects of quantization. However, histograms from iron-contaminated die on several wafers showed new common peaks occurring at the large generation rates of about 2100, 3000, and 11,600 electrons/frame. For extended defects to appear as peaks, the defects must have similar enough dark current generation rates. For a sequence of peaks to occur, the individual peaks must be resolvable; that is, the variations in the generation rates must be somewhat smaller than the average generation rate itself. Such self-similarity is likely due to the uniformity of conditions across the wafer(s) as these defects formed. If this is true, different generation rates might be found for these large iron traps under different processing conditions.

We summarize the properties of the traps examined by listing their dark current generation rates in Table I. Their relationship to the white spot defects described earlier can now be set forth. For the imager used in this work, we have arbitrarily defined a dim point as any pixel whose photodiode dark current exceeds the imager mean by 350 electrons/frame or 10,500 electrons/s. Consequently, as few as three Co or Ni traps in a pixel form a dim point defect. Gold requires 18 traps and the weak interstitial iron trap would require 50 traps. At the other extreme, any one of the extended iron defects listed in Table I is sufficient to cause a noticeable image defect. Hence, an average low level of metals may not be enough if there are high local concentrations because defects in active device areas have getterred the metals.

TABLE I
DEEP-LEVEL TRAP GENERATION RATES

Trap	Point Defects				Extended Iron Defects		
	Interstitial Iron	Gold	Nickel	Cobalt	Trap 1	Trap 2	Trap 3
Generation Rate at 55°C (electrons/s)	213 (±5 %)	612	3960	3960	≈63,000	≈90,000	≈348,000

Constructive Use of Traps

The characteristic dark current generation rates observed for the different metal traps provides a sensitive analytical method for detecting and identifying these metal contaminants in imager device runs. In low-metal imagers, histogram peaks of 1/20th the main peak ($\lambda = 0.05$) are readily detectable. For the imager used in this work, the electrically depleted region in which traps can contribute dark current is about $50 \mu\text{m}^3$. That corresponds to a detection sensitivity of 1.0×10^9 traps/cm³. This permits completed imagers to be monitored at the wafer level for metal contaminants at levels lower than those currently considered to affect yield. And inherently, dark current spectroscopy is most sensitive to the metals of most concern for generating dark current.

One interesting use of traps is as a calibration source. When imagers are used in camera systems, there are system gains chained together, such as the on-chip amplifier gain and the gain of the external camera system. Using the gold generation rate of 612 electrons/s at 55°C from Table I, the overall system gain in units of volts/electron can be easily determined for any camera system if a trace amount of gold is present.

Trap Temperature Dependence and Cross Sections

We have found that for most of the deep-level traps described here, the dark current generation rate doubles about every 9°C. If the dark current spacings for gold from a histogram like those in Fig. 5 are plotted on an Arrhenius-type plot, straight lines are obtained, as shown in Fig. 8. Note that the peak spacings of the second and third gold traps superpose on those of the first gold trap, indicating similar trap behavior from pixels with different numbers of gold atoms present. On such a plot, the y-coordinate value at a given temperature helps determine the trap cross section for dark current generation.¹⁷ The position of the trap energy level E_t in the silicon bandgap is obtained from

$$\text{Peak spacing} \propto n_i(T) v \sigma e^{-|E_t - E_i|/kT} \quad (3)$$

Here n_i is the intrinsic carrier concentration at temperature T , v is the thermal velocity, k is Boltzmann's constant, σ is the trap cross section, and E_i is the intrinsic level.

Temperature dependences for a number of traps are plotted shown in Fig. 9 along with gold. Data for iron include the weak trap believed to be interstitial iron and some data for the large traps that are probably extended defects. Using Eqn. 3, one can calculate the trap energy levels and the generation cross sections. These are given in Table II.

TABLE II
TRAP ENERGY LEVELS AND CROSS SECTIONS

Trap	Interstitial Iron	Gold	Nickel	Cobalt
$ E_t - E_i $ (eV)	0.13-0.15	<0.03	<0.03	<0.03
σ (cm ²)	3×10^{-14}	1×10^{-15}	6.6×10^{-15}	6.6×10^{-15}

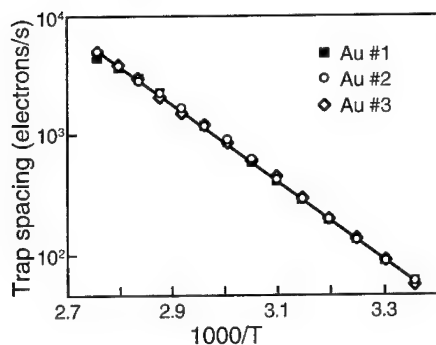


Fig. 8. Temperature dependence of gold peak spacings for 1, 2, and 3 gold traps/pixel. A line has been fitted to the combined data.

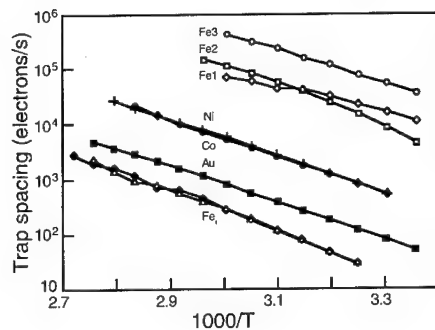


Fig. 9. Temperature dependence of several deep-level traps, including iron extended defects.

We compare our results from dark current spectroscopy in Tables I and II with values from the literature. We first note that the trap levels for Au, Ni, and Co are within kT of mid gap, whereas Fe_i is somewhat off gap. This yields a larger cross section for Fe_i than the value we previously reported for an unknown trap, assuming a mid-gap level.¹² Our Table II cross section for electron emission by Fe_i is within a factor of 2 of that found by Lemke¹⁸ and quoted by Heiser,¹⁹ $1.7 \times 10^{-14} \text{ cm}^2$ at 55°C. The present cross section for Au is in agreement with the value of $0.7 \times 10^{-15} \text{ cm}^2$ deduced from Fig. 11 of Tasch and Sah for a Au acceptor level at 0.54 eV below the conduction band.²⁰ The generation rate for Ni of Table I is reasonably close to the 3300 electron/s found by Jaraiz et al., for a mid-gap level;²¹ however, this is not the most common level reported for Ni.²² Cobalt has a mid-gap level, but its generation rate has been found by Yau and Sah²³ to be close to that of Au, whereas we cannot distinguish Co from Ni.

Provisional Identification of Iron

The weak trap of Fig. 2 shows some unusual properties that suggest it originates from some form of complex. The first property is temperature sensitivity. Figure 10 contains a series of histograms. The original one shows the unknown trap with a λ of about 0.45. A small amount of gold is also present. The second histogram was obtained after thermal treatment of the wafer in air at 200°C for 4 min. The effect of the anneal was to increase the λ of the unknown trap to >2 without affecting the gold, which means that the number of unknown traps increased about 5x. The additional histograms in the figure show that the imager recovered in time, first at 55°C and then at room temperature. It eventually returned to the initial condition. This type of behavior is reported for donor-acceptor complexes of the type FeX, where X includes such acceptors as B, Al, and Ga.²⁴ Of these, B is of particular interest because it is an intentional dopant, present in substantial quantity in these imagers. Other transition metal complexes with B have also been reported, such as MnB and CrB.²⁵ The interesting thing about the iron complexes is that they form shallow traps, too far off mid gap to be strong dark current generators. For example, the FeB pair level is located at $E_v + 0.1$, where E_v represents the valence band edge. Interstitial iron, however, has an energy level at $E_v + 0.4 \text{ eV}$, close enough to mid gap to generate dark

current. The energy level we calculate for this small trap from its temperature dependence is 0.43 eV.²⁶ The dissociation reaction reported for FeB at 200°C is indicated by the reaction:



At lower temperatures, the iron atoms still diffuse until they find a B atom and the complex reforms. Transformations of the type expressed in Eqn. 4 appear to explain the observed trap generation and recovery shown in Fig. 10.

The property that most strongly suggests that the weak trap is interstitial iron is the generation of this trap by strong light. For this experiment, the tip of a round fiber optic bundle from a light source was placed in direct contact with an imager on a wafer for 2 min. The light intensity was 150 mW with a spot size of 9 mm². Wafer temperature during the light exposure was 55°C, but the same effect occurs at room temperature. When the wafer was then placed on the probe station, a circular region of higher dark current was seen, as shown in Fig. 11. Dark current

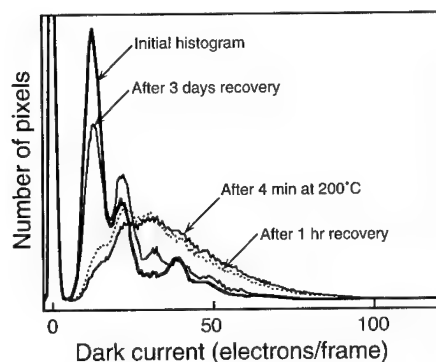


Fig. 10. Generation and subsequent recovery of the weak Fig. 2 trap from a 200°C anneal.

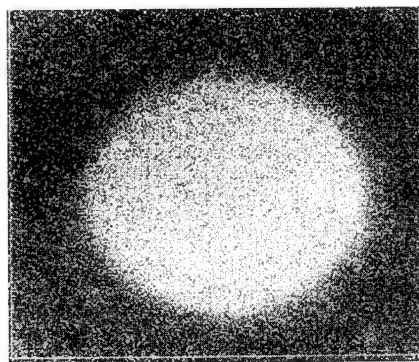


Fig. 11. Dark image of high dark current caused by prior exposure to a spot of intense light. The trap responsible appears to be Fe_i.

spectra of this region show an increase in the Poisson mean of the weak trap, as compared to the background regions, indicating that these traps are produced by light as well as thermally. The only reported complex we have found with this combination of properties appears to be FeB.²⁶ In fact, illumination of this type is used to identify and quantify iron contamination in wafers using the surface photovoltage technique.²⁷⁻²⁹ CrB will also dissociate with light, but only at about 90°C.³⁰⁻³² Moreover, the CrB complex is closer to mid gap than the Cr that would be released, so illumination of CrB contamination should produce a dark spot. Since iron is a common cleanroom contaminant and the FeB complex properties match the observed behavior for the weak trap, we provisionally identify this trap as interstitial iron. Chemically similar complexes such as MnB cannot be completely ruled out at present.

We also observed that this weak trap is generated at 55°C on the heated test chuck of the probe station, but only when imager clocking voltages are applied. Over a period of 5 hr of clocking, λ was observed in one case to increase from 0.45 to 1.0. Recovery to the initial level was observed with the clocking removed, just as for the temperature-induced case in Fig. 10. This is consistent with the reported behavior of FeB with electric fields.³³

Details of this weak-trap generation can be observed using a two-dimensional histogram plot, as shown in Fig. 12. To form this plot, two images were saved from the same imager at different times. Then for each image pixel, a point was plotted whose y- and x-coordinates are the initial and final dark current values, respectively, for that pixel. Since too many points are plotted in the figure to be individually seen, except at the edges of the clusters, the density of points in the plot is indicated by the pattern. Note that the points are plotted from image information, but the projections of the points onto the two axes would give the initial and final histograms. The histogram of the initial image showed a modest amount of the weak trap ($\lambda = 0.12$) and some gold present ($\lambda = 0.11$). The final histogram, after 2 hr of clocking at 55°C, indicated a drop in zero-trap pixels and an increase in peaks containing the weak trap to $\lambda = 0.24$. The Poisson mean for the gold did not change.

To interpret the two-dimensional histogram, note that pixels whose dark current is unchanged plot as points on the 45-degree line that passes through the origin. However, if new traps of a specific type have formed since the initial image, those pixel points will appear along a second 45 degree line displaced from the first line by this trap spacing. In Fig. 12, most of the new traps were produced in diodes that had no initial traps, simply because those pixels were the most plentiful. However, some of the pixels that originally had only one gold trap now have one gold and the new weak trap. Of the relative few that had only one weak trap, some now have a second weak trap, etc. If the new traps appear randomly in any pixel, the clusters of points along the second line will tend to replicate those of the first line. Note in Fig. 12 the beginnings of a cluster of points along a third line. These are from pixels that have gained two weak traps.

In the experiment of Fig. 12, standard histograms would indicate only a net generation of the weak trap. However, the two-dimensional histogram shows some back reaction is occurring. The cluster of points marked with an arrow in Fig. 12 are from pixels that originally had one weak trap, but later had none. So, even though the net driving force in an equation like Eqn. 4 is to the right, some back reaction still occurs and the two-dimensional histogram technique makes it apparent.

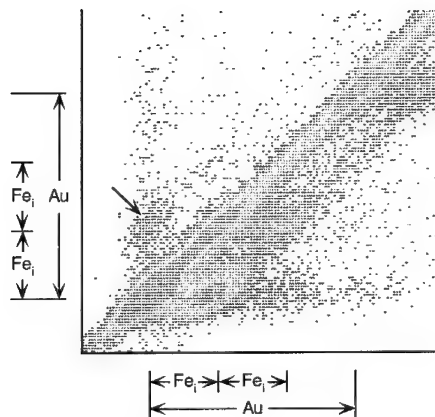


Fig. 12. Two-dimensional histogram showing Fe_i trap population changes for 100,000 pixels.

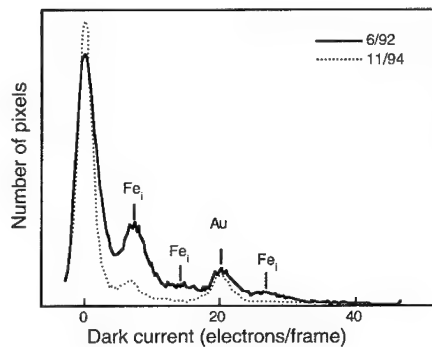


Fig. 13 Histograms from the same imager taken 29 months apart showing interstitial iron migration at room temperature.

One final note on interstitial iron is that it moves around in imagers at room temperature. Figure 13 shows an initial dark current histogram and a second one taken from the same imager two and one-half years later. Although curvefit analysis shows the gold level to be unchanged, the interstitial iron has largely disappeared; presumably the iron is now in the form of precipitates somewhere in the wafer. Exposure to light increases this trap level only slightly, so it is simply not present as FeB. Evidence that such potentially damaging contaminants as iron move around, albeit slowly, under normal storage conditions is disconcerting.

SUMMARY

We have shown some of the unfortunate effects of contaminant metals on solid-state image sensors and have mentioned the stringent purity conditions that must be met for present and future imagers. Fortunately, dark current spectroscopy provides a very high sensitivity for those metals that cause dark current defects. The distinctive generation rates of the different metals permit the identification and quantification of localized contamination spots and can even be used as calibration standards for test equipment. Since dark current spectroscopy is readily applied to imagers at the wafer level, it is very useful for monitoring metals in device runs at levels below those that would currently affect device yield.

REFERENCES

1. W.A. Miller, K.Y. Wong, and W.C. Chang in *The Physics and Chemistry of Imaging Systems, IS&T 47th Annual Conference*, (1994) pp. 649-651.
2. S.G. Chamberlain, S.R. Kamasz, C.R. Smith, W.D. Washkurak, M.G. Farrier, Tech. Dig. of the IEDM, 701 (1994).
3. The National Technology Roadmap for Semiconductors, Semiconductor Industry Association, 1994.
4. L. Jastrzebski, R. Soydan, G.W. Cullen, W.N. Henry, S. Vecrumba, J. Electrochem. Soc. **134**, 212 (1987); L. Jastrzebski, R. Soydan, H. Elabd, W. Henry, E. Savoye, *ibid.*, **137**, 242 (1990).
5. E.R. Weber, Appl. Phys. A **30**, 1 (1983).
6. D.R. Sparks and R.G. Chapman, J. Electrochem Soc. **133**, 1201 (1986).
7. M. Domenici, G.C. Ferrero, and P. Malinverni, in *Semiconductor Processing, ASTM STP 850*, edited by D.C. Gupta (American Society for Testing and Materials, 1984), p. 257.
8. R. Ogden and J.M. Wilkinson, J. Appl. Phys. **48**, 412 (1977).
9. J. van der Spiegel and G.J. Declerck, Solid-State Electron. **27**, 147 (1984).
10. Y. Okada, M. Okigawa, K. Kazui, Y. Kitamura, T. Furusawa, Opto-electronics **6**, 231 (1991).
11. W.C. McColgin, J.P. Lavine, J. Kyan, D.N. Nichols, J.B. Russell, and C.V. Stancampiano in *Defect Engineering in Semiconductor Growth, Processing and Device Technology*, edited by S. Ashok, J. Chevallier, K. Sumino, and E. Weber (Mater. Res. Soc. Proc. **262**, Pittsburgh, PA, 1992) pp. 769-774.
12. W.C. McColgin, J.P. Lavine, J. Kyan, D.N. Nichols, and C.V. Stancampiano, Tech. Dig. of the IEDM, 113 (1992).
13. N.S. Saks, IEEE Electron Device Lett., **EDL-1**, 131 (1980).
14. B.C. Burkey, W.C. Chang, J. Littlehale, T.H. Lee, T.J. Tredwell, J.P. Lavine, E.A. Trabka, Tech. Dig. of the IEDM, 28 (1984).

15. D.G. Ong and R.F. Pierret, IEEE Trans. Electron Devices, **ED-22**, 593 (1975).
16. R.D. McGrath, J. Doty, G. Lupino, G. Ricker, J. Vallerger, IEEE Trans. Electron Devices **ED-34**, 2555 (1987).
17. D.K. Schroder, IEEE Trans. Electron Devices, **ED-29**, 1336 (1982).
18. H. Lemke, Phys. Status. Solidi. (A) **76**, 223 (1983).
19. T. Heiser, A. Mesli, N. Amroun, Mater. Sci. Forum **83-87**, 173 (1992).
20. A.F. Tasch, Jr. and C.T. Sah, Phys. Rev. B, **1**, 800 (1970).
21. M. Jaraiz, S. Dueñas, J. Vicente, L. Bailón, J. Barbolla, Solid-State Electron. **29**, 883 (1986).
22. H. Kitagawa, S. Tanaka, H. Nakashima, M. Yoshida, J. Electron. Mater. **20**, 441 (1991).
23. L.D. Yau and C.T. Sah, Appl. Phys. Lett. **21**, 157 (1972).
24. K. Wünstel and P. Wagner, Appl. Phys. A **27**, 207 (1982).
25. H. Lemke, Phys. Status. Solidi. (A) **75**, 473 (1983).
26. L.C. Kimerling and J.L. Benton, Physica **116B**, 297 (1983).
27. G. Zoth and W. Bergholz, J. Appl Phys. **67**, 6764 (1990).
28. J. Lagowski, P. Edelman, M. Dexter, W. Henley, Semicond. Sci. Technol. **7**, A185 (1992).
29. J. Lagowski, P. Edelman, A.M. Kontkiewicz, O. Milic, W. Henley, M. Dexter, L. Jastrzebski, A.M. Hoff, Appl. Phys. Lett. **63**, 3043 (1993).
30. K. Mishra and R. Falster, ECS Extended Abstracts **92-2**, 632 (1992).
31. K. Mishra (private communication).
32. K. Mishra in *The Role of Point Defects and Defect Complexes in Silicon Device Processing*, edited by B.L. Soporì (Third NREL Workshop, Golden, CO, 1993), p. 57.
33. H. Kikuchi, A. Agarwal, S. Koveshnikov, and G.A. Rozgonyi, in *The Degradation of Electronic Devices due to Device Operation as well as Crystalline and Process-Induced Defects*, edited by H.J. Queisser, J.E. Chung, K.E. Bean, T.J. Shaffner, and H. Tsuya (Electrochem. Soc. Proc. **94-1**, Pennington, NJ, 1994) pp. 298-303.

CRYSTALLOGRAPHIC DEFECT RELATED DEGRADATION IN HIGH DENSITY MEMORY DEVICES

S. S. KIM* AND W. WIJARANAKULA**

*Texas Instruments, Inc., 13353 Floyd Road, MS 374, Dallas, Texas 75265

**Shin-Etsu, SEH America, Inc., 4111 NE 112th Avenue, Vancouver, Washington 98682.

ABSTRACT

Crystallographic defect related degradation in high density memory devices was investigated. The results indicate that the refresh time degradation and bit failure mechanism are directly related to the crystal originated defects generated during Czochralski crystal growth. Defects associated with vacancy aggregations are found to have a detrimental effect on the overall performance of memory devices. Other defects, such as oxide polyhedral precipitates, contribute to a high number of cumulative fail bits, particularly in the bottom section of the crystal.

INTRODUCTION

Degradation of memory device performance resulting from the leakage of stored charge has been one of the major problems in trench capacitor cell technology because the memory cell penetrates deep into the silicon substrate and hence is exposed directly to the crystallographic defects present in the silicon substrate. Several types of crystal originated defects which include the flow pattern defects (FPDs) [1], oxide polyhedral precipitates [2], crystal originated particles (COPs) [3], and laser scattering tomography defects (LSTDs) [4] have been identified in as-received Czochralski (Cz) silicon wafers. Because the generation of the crystal originated defects is driven by the point defect saturation during the crystal growth [5], the crystal growth conditions play a significant role in the defect generation [4,6-7]. The detrimental effect of the crystal originated defects on the gate oxide integrity in metal-oxide-semiconductor (MOS) capacitors [1] and the refresh-time of memory devices [2] has been established. Therefore, an understanding of the coupling effects between crystal growth conditions, crystal originated defect generation, and device performance are essential not just for the academic interest, but also for silicon material development for future commercial integrated circuit devices.

In this work, the performance of dynamic random access memory (DRAM) devices fabricated on wafers originating from Cz crystals grown under different cooling conditions will be examined.

EXPERIMENTAL

Memory devices were fabricated using a deep-trench structure [8] on 150 mm diameter p-type (100) CZ silicon wafers doped with boron at 1×10^{16} atoms/cm³. The wafers originated from two short crystals grown successively from a single batch of melt in the same growth furnace. The initial oxygen concentration in the wafers as determined by Fourier transform

infrared (FTIR) spectroscopy analysis and calibrated using the coefficient of $2.45 \times 10^{17} \text{ 1/cm}^2$ was between 6 and $7 \times 10^{17} \text{ atoms/cm}^3$. The radial variation in the oxygen concentration was below 10 %. The amount of substitutional carbon concentration was below the FTIR detection limit which is approximately $2.5 \times 10^{15} \text{ atoms/cm}^3$. The overall process steps for growing two short crystals were similar to those for a typical full-length crystal described elsewhere [9]. However, under the present experimental growth conditions, each short crystal experienced entirely different cooling conditions.

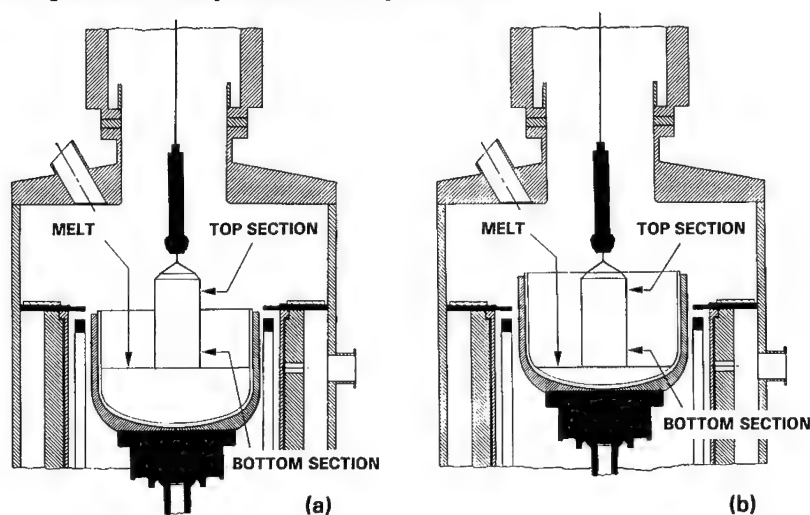


Figure 1: Schematic cross section of the CZ crystal growth furnace showing (a) the first and (b) second crystal prior to tailing off.

Figures 1a and 1b show the position of the first and second crystals prior to the tailing off process. From the figure it may be seen that during the growth of the second crystal, the melt level relative to the top of the crucible was lower than that during the growth of the first crystal. As a result, the heat radiation from the crucible sidewall to the surface of the second crystal was significantly more intense than that of the first crystal [9]. Therefore, the overall cooling rate of the second crystal was slower than that of the first crystal. In addition to the wafers originating from crystals with different cooling conditions, wafers originating from a magnetic CZ (MCZ) crystal containing interstitial oxygen atoms on the order of $3.5 \times 10^{17} \text{ atoms/cm}^3$ and epitaxial silicon wafers with an epitaxial layer thickness of $20 \text{ }\mu\text{m}$ were included as monitor wafers.

Prior to device processing, CZ wafers received a 4h denudation annealing at 1100°C in N_2 ambient. Ramping to 1100°C was done in dry O_2 ambient to avoid surface pitting. Wafers without the denudation annealing were also included for comparison. The refresh time testing was performed at 90°C . Other characterization techniques including the surface photovoltage (SPV) [10], transmission electron microscope (TEM), and non-agitated Secco etching [11] were also performed.

RESULTS AND DISCUSSION

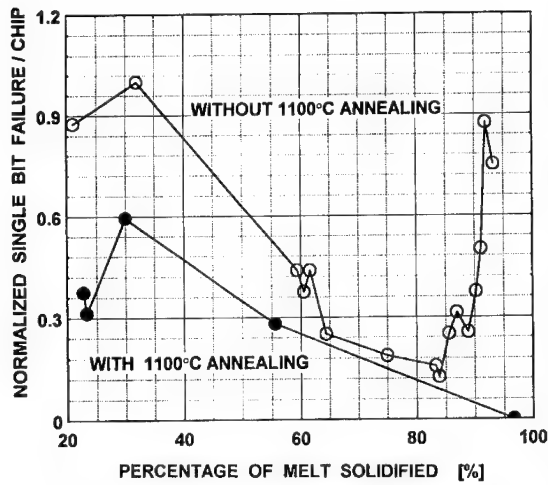


Figure 2: Effect of the denudation annealing on the single bit failure/chip.

Effect of the denudation annealing - Figure 2 shows a typical plot of the normalized single bit failure/chip, defined as the number of single bits failed at a given refresh time during the initial testing stage, as a function of percentage of melt solidified. From the figure, a 1100°C denudation annealing causes a drastic reduction in the number of single bit failures in the devices fabricated on the wafers originating, particularly from the bottom section of the crystal.

Effect of the crystal cooling rate - Figures 3a and 3b show the typical fail bit plots for the devices fabricated on the wafers originating from the first and second crystals, respectively. In the high refresh time region > 15 a.u. (arbitrary unit), devices fabricated on the wafers originating from the top section of the crystal perform much better than those from the bottom section. In the low refresh time region < 15 a.u., on the other hand, the number of cumulative fail bits in the bottom section of the crystal is lower than that in the top section, compared to Figure 1.

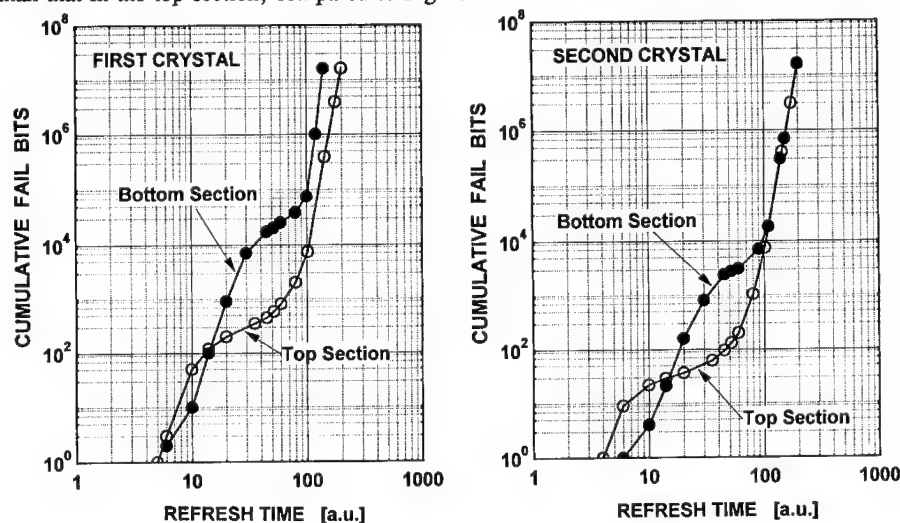


Figure 3: Fail bit plots in (a) first and (b) second crystal.

The cumulative fail bits were replotted as a function of crystal section in Figure 4. By comparing the fail bit plots within the crystal section, it is clearly seen that the devices fabricated on the wafers originating from the second crystal exhibit a lower number of cumulative fail bits than the first crystal.

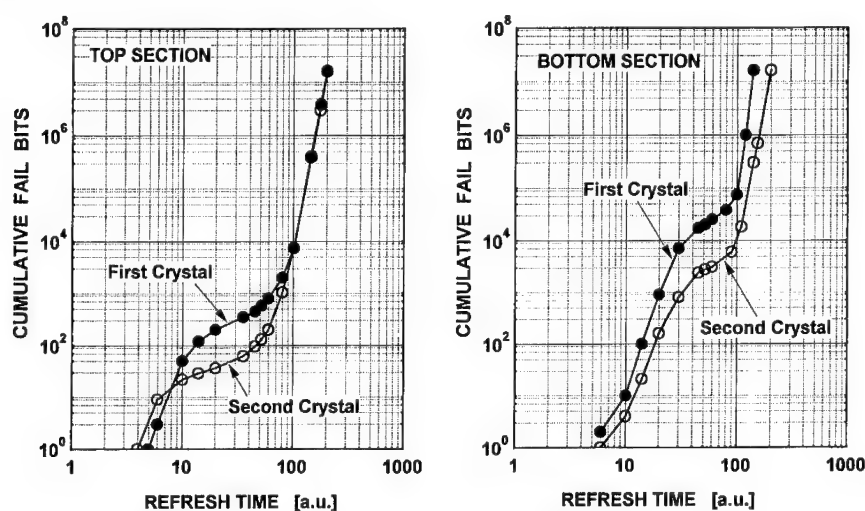


Figure 4: Fail bit plots in (a) top and (b) bottom section of the crystal.

From the above results, the denudation annealing appears to be effective in reducing the number of single bit failures in the low refresh time region. In the high refresh time region, a trend showing the devices fabricated on wafers originating from the bottom section of the crystal to have a higher number of cumulative fail bits than the top section is not influenced by the denudation annealing. Based upon the crystal growth theory and the results in Figures 3 and 4, it is intuitively clear that the devices fabricated on wafers originating from a crystal grown with a slow cooling rate exhibit a lower number of cumulative fail bits than those from a crystal grown with a higher cooling rate. Yamagishi, et al [6] reported that the COP and FPD densities in a crystal grown in a slow cooling furnace are reduced, compared to those in a crystal grown in a fast cooling furnace. A denudation annealing even at 1000 °C is capable of dissolving oxide microprecipitates in the silicon surface layer but not the flow pattern defects [11-13]. After reviewing the above information, it is concluded that defects associated with the vacancy aggregation such as the flow pattern defects have a detrimental effect on the overall performance of memory devices.

Defects in the bottom section of the crystal - Figure 5 shows the result from the SPV measurement on a wafer originating from the bottom section of the crystal after the well drive-in step. In the dark annular region, the minority carrier diffusion length is far below the average value which indicates that silicon in that region contains bulk traps. A short minority carrier diffusion length has been observed to be attributed to bulk stacking faults which are evolved from the grown-in oxide polyhedral precipitate shown in Figure 6.

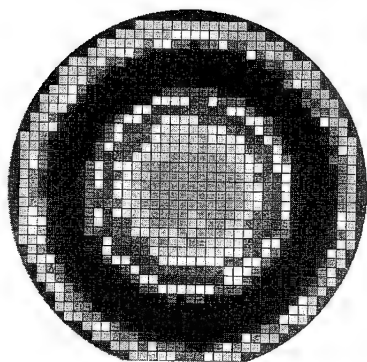


Figure 5:
Minority carrier diffusion length
distribution on the wafer originating
from the bottom section of the crystal.

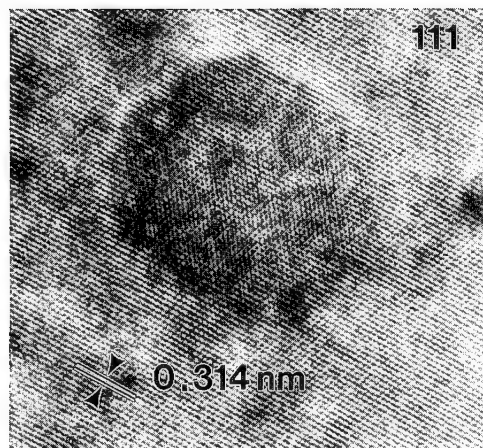


Figure 6: Oxide polyhedral precipitate in
an as-received wafer.

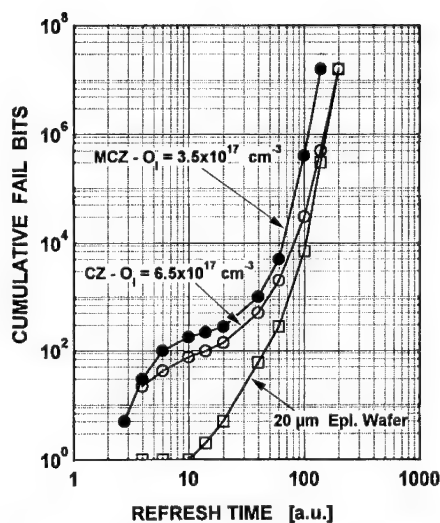


Figure 7: Effect of the bulk oxygen concentration on the fail bit plots.

condition, the characteristic of the fail bit plot, particularly in the tail region, may not be significantly affected by the concentration of interstitial oxygen atoms in the wafers.

Effect of the bulk oxygen concentration -
Figure 7 shows a comparison between the fail bit plots for devices fabricated on CZ, MCZ and epitaxial wafers, respectively. From the figure, it is observed that devices fabricated on epitaxial wafer exhibit the lowest number of cumulative fail bits, compared to those in devices fabricated on CZ or MCZ wafers. The reason is because the epitaxial layer is free from crystal originated defects including oxide microprecipitates [14-15]. In addition, it may be observed that the fail bit plots for the devices fabricated on the MCZ and CZ silicon wafers are comparable even though the interstitial oxygen concentration in the MCZ silicon wafers is approximately one half of that in CZ silicon wafers. This result implies that under a proper denudation annealing

SUMMARY

Crystallographic defect related degradation in high density memory devices was investigated. The results indicate that the refresh time degradation and bit failure mechanism are directly related to the crystal originated defects generated during Czochralski crystal growth. Defects associated with vacancy aggregations are found to have a detrimental effect on the overall performance of memory devices. Other defects, such as oxide polyhedral precipitates, contribute to a high number of cumulative fail bits, particularly in the bottom section of the crystal.

ACKNOWLEDGMENTS

The authors would like to thank the staff of the Silicon Products Departments at Texas Instruments, Incorporated for their technical support.

REFERENCES

1. H. Yamagishi, I. Fusegawa, N. Fujimaki, and M. Katayama, *Semicond.Sci.Technol.*, **7**, A135(1992).
2. S.S. Kim and W. Wijaranakula, *J.Electrochem.Soc.*, **142**, 553(1995).
3. J. Ryuta, E. Morita, T. Tanaka, and Y. Shimanuki, *Japan.J.Appl.Phys.*, **29**, L1947(1990).
4. K. Nakajima, J. Furukawa, H. Furuya, and T. Shingyouji, in *Semiconductor Silicon/1994*, edited by H.R. Huff, W. Bergholz, and K. Sumino (Electrochem.Soc.Proc., **94-10**, Pennington, NJ, 1994) pp.168-179.
5. W. Wijaranakula, Q.S. Zhang, K. Takano, and H. Yamagishi, in this proceeding.
6. H. Yamagishi, I. Fusegawa, K. Takano, E. Iino, N. Fujimaki, T. Ohta, and M. Sakurada, in *Semiconductor Silicon/1994*, edited by H.R. Huff, W. Bergholz, and K. Sumino (Electrochem.Soc.Proc., **94-10**, Pennington, NJ, 1994) pp.124-135.
7. M. Hourai, T. Nagashima, E. Kajita, S. Miki, S. Sumita, M. Sano, and T. Shigematsu, in *Semiconductor Silicon/1994*, edited by H.R. Huff, W. Bergholz, and K. Sumino (Electrochem.Soc.Proc., **94-10**, Pennington, NJ, 1994) pp.156-167.
8. B. Ahlbum, R. Novak, M. Galiano, and J. Olsen, in *ULSI Science and Technology 1991*, edited by J.M. Andrews and G.K. Celler (Electrochem.Soc.Proc., **91-11**, Pennington, NJ, 1991) pp.617-626.
9. W. Zulehner and D. Huber, in *Crystals: Growth, Properties, and Applications*, edited by J. Grabmaier (Springer-Verlag, New York, 1982) pp.3-143.
10. A.M. Goodman, L.A. Goodman, and H.F. Gossenberger, *RCA Rev.*, **44**, 327(1983).
11. W. Wijaranakula and J.H. Matlock, *J.Appl.Phys.*, **69**, 6982(1991).
12. W. Wijaranakula, *J.Appl.Phys.*, **75**, 3678(1994).
13. W. Wijaranakula, *J.Electrochem.Soc.*, **141**, 3273(1994).
14. W. Wijaranakula and M. Aminzadeh, *J.Appl.Phys.*, **67**, 1566(1990).
15. M. Miyashita, H. Hiratsuka, and Y. Matsushita, in *Defects in Silicon II*, edited by W.M. Bullis, U. Gösele, and F. Shimura (Electrochem.Soc.Proc., **91-9**, Pennington, NJ, 1991) pp.407.

IMPROVEMENT OF PIN PHOTODIODES ON THE SOI LAYER BY RAPID THERMAL ANNEALING

Yoshimaro FUJII*, Akira USAMI, Katsuhiro FUJIYOSHI,
Hideaki YOSHIDA and Masaya ICHIMURA

Nagoya Institute of Technology, Gokiso-cho, Showa-ku, Nagoya 466, Japan

*Hamamatsu Photonics K.K., 1126-1, Ichino-cho, Hamamatsu 435, Japan

ABSTRACT

Electrical properties of PIN photodiodes fabricated on the bonded silicon on insulator (SOI) wafers annealed at 900°C for 5 seconds were evaluated in order to investigate the effect of rapid thermal annealing (RTA) on SOI wafers. Traps in the SOI layers with different thicknesses (10, 30, 100 μm) were investigated using the deep level transient spectroscopy (DLTS) method. In the SOI layer with a thickness of 100 μm , a trap with deep energy level (about $E_c - E_t = 0.55$ eV) was observed and the concentration of the trap decreased from $5.0 \times 10^{11} \text{ cm}^{-3}$ to $1.5 \times 10^{11} \text{ cm}^{-3}$ by RTA. For PIN photodiodes on the 100 μm -thick SOI layer, the dark current decreased from 2×10^{-9} A to 6×10^{-10} A, and sensitivity uniformity for a 35 $\mu\text{m}\phi$ light spot and spectral responses were both improved by RTA. Lifetimes were obtained from open-circuit voltage (V_{oc}) decay curves for 940 nm and 655 nm light, and they increased from 37 μs to 57 μs and from 47 μs to 62 μs , respectively, by RTA. For thinner SOI layers (thickness=10, 30 μm), PIN photodiodes have good uniformity and low dark current, and their characteristics were not changed by RTA.

INTRODUCTION

The photo-IC that includes photo-sensors and operation circuits on the same chip has been used extensively. These devices have been fabricated on high resistivity epitaxial layers and required high integration density and operation speed. The silicon on insulator (SOI) is promising alternative structure that substitutes for bulk silicon wafers. The bonded SOI structure has been attractive in point of high speed, low power consumption and high radiation hardness, and many reports have been published [1,2].

However, electrical properties of the bonded SOI layer and device characteristics fabricated on them have not been investigated enough. We have already reported traps revealed by deep level transient spectroscopy (DLTS) method [3] in the bonded SOI wafer, and characteristics of photodiodes on the SOI layer were also evaluated [4,5].

Rapid thermal annealing (RTA) has been used to activate implanted impurities in Si wafers and has been reported to decrease defect density [6-8]. But RTA has not been used to annihilate residual stresses in the SOI layer. In this study, the effects of RTA on bonded SOI wafers and characteristics of PIN photodiodes on them are investigated.

EXPERIMENTAL PROCEDURE AND SAMPLES

We prepared three bonded SOI wafers with different SOI layer thicknesses (10, 30, 100 μm) and a normal FZ-Si wafer that is the same wafer as those used for bonded SOI layers. The resistivity of the SOI layer is about 1-2 $\text{k}\Omega\text{cm}$. An interfacial oxide layer about 0.5 μm thick was introduced by thermal oxidation on the substrate wafer. There is a high carrier

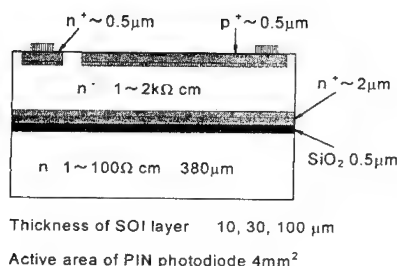


Fig. 1. Structure of PIN photodiode.

concentration region near the bonded interface. This region was formed by the thermal diffusion of Sb before the bonding. In order to bond completely, the wafers bonded at room temperature were annealed at 1100°C for 2 hours. In addition, the SOI wafers were annealed at 900°C for 5 seconds to investigate the effects of RTA on SOI wafers. PIN photodiodes were fabricated on the SOI layers and the FZ-Si wafer. Its active area is 4 mm². Figure 1 shows the sample structure used in this study.

Traps in the SOI layers were characterized using the DLTS method with a bipolar rectangular weighting function [9]. The double correlated DLTS (DDLTS) method [10] was used for the in-depth profiles of the trap concentration. To calculate these concentrations of the trap detected, carrier concentration profiles were measured by the capacitance-voltage (C-V) method.

For PIN photodiodes on the bonded SOI wafer, reverse current-voltage (I-V) properties, sensitivity profiles in the active area, and spectral responses were measured. In the sensitivity profile measurements, the incident light beam was irradiated vertically to the active surface of the photodiode. The measurements were made at three wavelengths 400, 800 and 1000 nm. The light spot size was approximately 35 μm in diameter and was linearly scanned so as to pass the center of the active area of PIN photodiodes. In addition, open-circuit voltage (V_{oc}) decay curves were measured after light pulse irradiation (pulse width 0.4 ms), and the minority carrier lifetime τ_p in the SOI layer was estimated by the following equation with approximations $V_0 \gg kT/q$, $\tau_p \gg t$ [11].

$$V = V_0 - \frac{kT}{q} \cdot \frac{t}{\tau_p} \quad (1)$$

In this measurement, the light sources were light-emitting diodes (LED) whose wavelengths were 655 nm and 940 nm.

RESULTS AND DISCUSSION

A. DLTS measurements

DLTS signals were measured over the temperature range of 50-280 K as shown in Figure 2. Dashed lines are DLTS signals before RTA and solid lines are those after RTA. In the 10 μm-thick SOI layer and the wafer before the bonding, no DLTS peak was observed. One DLTS peak was observed at about 270 K in the SOI layers before RTA with thicknesses of 30 μm and 100 μm. The energy levels of these traps were $E_c - E_t = 0.53$ and 0.56 eV, respectively. In the SOI layers after RTA with thicknesses of 30 μm and

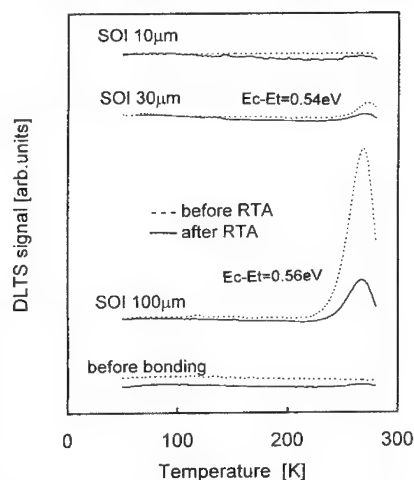


Fig. 2. DLTS signals observed in the SOI layer with different thicknesses (10 μm, 30 μm, 100 μm) and before bonding Si wafer.

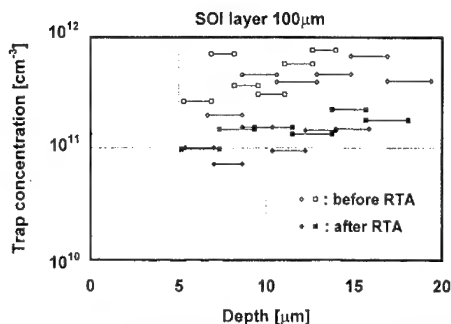


Fig. 3. In-depth profiles of the trap concentration in the SOI layer with a thickness of 100 μm .

DDLTS method. The traps exist homogeneously in the depth direction and the concentration decreased homogeneously after RTA. The mean value of the trap concentration before RTA was about $5.0 \times 10^{11} \text{ cm}^{-3}$ and that after RTA was about $1.5 \times 10^{11} \text{ cm}^{-3}$. This trap is believed to be generated after the bonding process because no trap was observed in the wafer before the bonding.

B. Characteristics of PIN photodiodes

Figure 4 shows dark current characteristics of PIN photodiodes at an applied reverse bias of 30 V and the total number of traps in the depletion region. These trap numbers were estimated from the in-depth profiles of the trap concentration. Both the dark current of the PIN photodiode and the total number of traps increased with increasing SOI layer thickness. The trap concentration of the SOI layer with a thickness of 10 μm was lower than the detection limit of our DLTS system. It is considered that the trap observed by the DLTS method acts as a generation center in the depletion region and increases the dark current. For the 100 μm -thick SOI layer, the dark current decreased with a decrease in this trap concentration by RTA. The increase rate of the dark current is different

100 μm , one DLTS peak was also observed. Their energy levels were $E_c - E_t = 0.55$ and 0.57 eV, respectively. The value of $E_c - E_t$ is a mean value of several samples in the same wafer. These traps detected for the SOI layers may be the same trap because they have a similar energy level. The magnitude of the DLTS peak detected in the SOI layer with a thickness of 100 μm decreased by RTA. For the SOI layer with a thickness of 30 μm , the magnitude of the DLTS peak was a little different from sample to sample, and it was slightly decreased by RTA.

Figure 3 shows in-depth profiles of the trap concentration in the SOI layer with a thickness of 100 μm measured by the

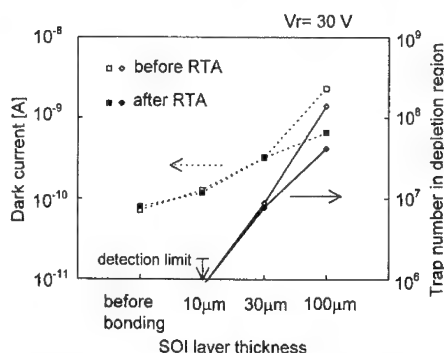


Fig. 4. Dark current characteristics and total trap concentration in depletion region.

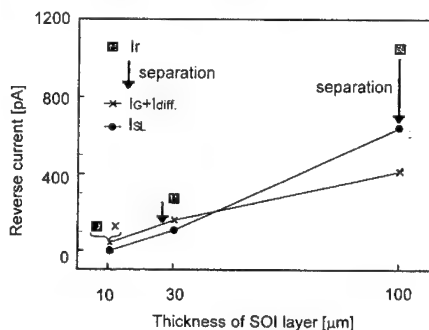


Fig. 5. Separation of diffusion-generation and surface leakage current component

from that of the total number of traps. Therefore the dark current will be partly due to some origin other than the bulk trap.

The diffusion current in the neutral region, the generation current in the depletion region and the surface leakage current constitute the reverse current of the PIN photodiode. Figure 5 shows the separated current components and the reverse current measured for the samples before RTA. The values of reverse currents were measured at reverse bias voltages at which the SOI layers were fully depleted. The diffusion current component is negligible compared with the generation current component. The generation current component was estimated from the following equation under the approximation $V \gg kT/q$ [12]

$$I_G = q \frac{n_i}{\tau_g} WA. \quad (2)$$

The surface leakage current component increases with increasing SOI layer thickness as shown in figure 5. It is considered that this component is due to generation at a surface defect in the surrounding side-wall of the PIN photodiode.

Figure 6 shows the sensitivity profiles of PIN photodiodes on the SOI layers. The wavelength of the light source was 1000 nm. The horizontal axis indicates the position in the active area and the vertical axis shows the sensitivity of PIN photodiodes. PIN photodiodes on the SOI layers with thicknesses of 10 μm and 30 μm have excellent uniformity and its uniformity was not changed by RTA (figure 6 (a), (b)). PIN photodiodes on the 100 μm -thick SOI layer before RTA showed inferior uniformity (figure 6 (c)). But after RTA, the PIN photodiodes showed good uniformity. The sensitivity at the middle of PIN photodiodes was inferior to that at the edge. We consider that the inferior sensitivity may be due to stress at the bonded interface. Figure 7 shows the sensitivity profiles of PIN photodiodes on the SOI layer with a thickness of 100 μm . When the reverse voltage of 30 V was applied, good sensitivity uniformity was obtained at $\lambda=1000$ nm (figure 7 (a)). By the applied reverse voltage, the depletion region was spread, and thus the carriers were generated in the depletion region and swept out by the electric field immediately. Therefore the sensitivity was not affected by the lifetime in the neutral region of the SOI layer. Figures 7 (b), (c) show sensitivity profiles at shorter wavelengths for PIN photodiodes without bias voltage. PIN photodiodes showed a little

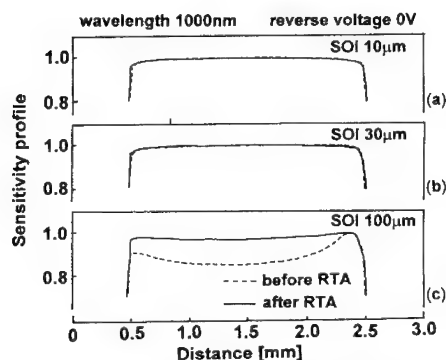


Fig. 6. Sensitivity profiles of PIN photodiodes on the SOI layer with a thickness of (a)10 μm , (b)30 μm , (c)100 μm at $\lambda=1000$ nm.

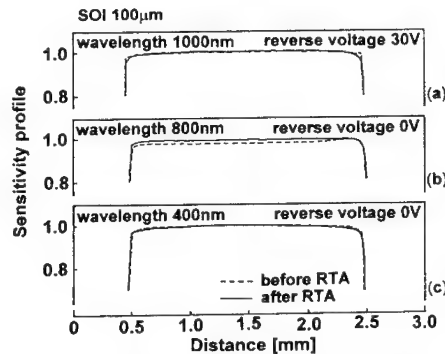


Fig. 7. Sensitivity profiles of PIN photodiodes on the SOI layer with a thickness of 100 μm at (a) $\lambda=1000$ nm ($V_r=30$ V), (b) $\lambda=800$ nm, (c) $\lambda=400$ nm ($V_r=0$ V).

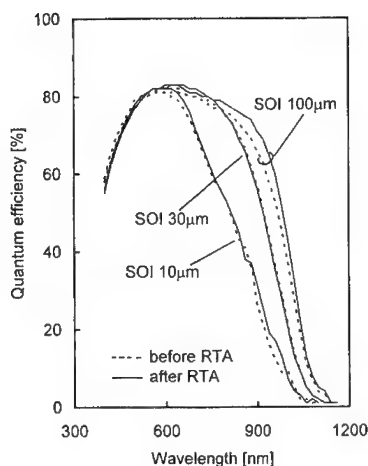


Fig. 8. Spectral responses of PIN photodiodes

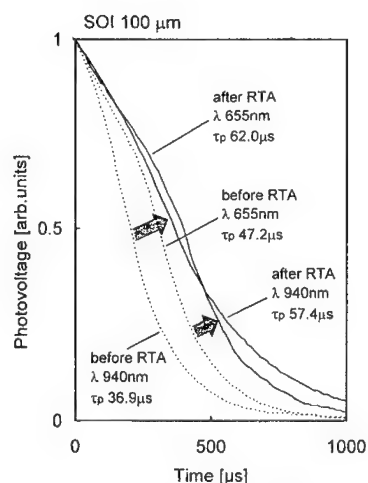


Fig. 9. Voc decay curves of PIN photodiodes on the SOI layer (100 μm) before RTA and after RTA ($\lambda=940, 655$ nm).

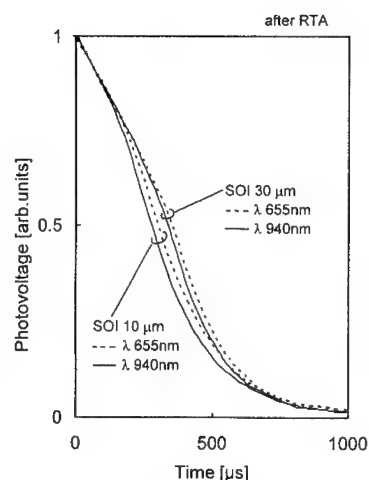


Fig. 10. Voc decay curve of PIN photodiodes on the SOI layer (10 μm, 30 μm) after RTA ($\lambda=940, 655$ nm).

wavelength	SOI 10 μm	SOI 30 μm	SOI 100 μm
655 nm	49.7 μs	48.9 μs	62.0 μs
940 nm	48.5 μs	49.9 μs	57.4 μs

poor uniformity at $\lambda=800$ nm and good uniformity at $\lambda=400$ nm. At the short wavelength (shorter 800 nm), the sensitivity depends on the quality of the PN junction rather than bulk properties, because the depletion width are larger than the penetration depth of the irradiated light.

Figure 8 shows the spectral responses of PIN photodiodes. The spectral responses were almost the same for all PIN photodiodes in the shorter wavelength range. The differences in the longer wavelength range is due to the different thicknesses of the SOI layer. By RTA, the spectral response of PIN photodiodes on the 100 μm-thick SOI layer was improved in the longer wavelength range. This will be because of improvement of the lifetime by RTA.

We measured Voc decay curves of PIN photodiodes. This decay curve depends on lifetime and surface recombination velocity. Figure 9 shows Voc decay curves of PIN photodiodes on the 100

μm -thick SOI layer and the minority carrier lifetime τ_p estimated from the decay curve. Dashed lines show the decay curves before RTA and solid lines show those after RTA. By RTA, the lifetime increased from 37 μs to 57 μs for $\lambda=940\text{ nm}$ and from 47 μs to 62 μs for $\lambda=655\text{ nm}$. This is consistent with the results of sensitivity profiles and spectral responses. Figure 10 shows the V_{oc} decay curves of PIN photodiodes on the SOI layers with thicknesses of 10 μm and 30 μm , and Table I shows the minority carrier lifetime τ_p of PIN photodiodes on each SOI layer. τ_p in the SOI layers with thicknesses of 10 μm and 30 μm was about 50 μs . The difference in τ_p between two wavelengths was observed for the SOI layer with a thickness of 100 μm . Most carriers are generated in the depletion region for $\lambda=655\text{ nm}$. On the other hand, most carriers are generated in the neutral region for $\lambda=940\text{ nm}$. Thus when the wavelength is longer, the value of τ_p is affected by the lifetime in the neutral region of the SOI layer.

From the sensitivity profile, spectral response, and V_{oc} decay curve measurements, we consider that the trap with $E_c-E_t \approx 0.55\text{ eV}$ acts as a recombination center. By RTA, these characteristics were improved with a decrease in the trap concentration.

SUMMARY

We have studied characteristics of the PIN photodiodes on bonded SOI wafers. From the DLTS measurements, a trap with an energy level $E_c-E_t \approx 0.55\text{ eV}$ was observed in the SOI layers (thickness=30, 100 μm). By RTA, this trap concentration decreased for the SOI layer with a thickness of 100 μm . I-V properties, spectral responses, and sensitivity profiles of the PIN photodiodes were measured. By RTA, the dark current was decreased and the lifetime estimated from V_{oc} decay curves increased for PIN photodiodes on the 100 μm -thick SOI layer. The sensitivity uniformity and spectral response were also improved by RTA. From the lifetime and dark current measurements it was found that the trap acts as a recombination and/or generation center. For thinner SOI layers, PIN photodiodes have low dark current and excellent sensitivity uniformity, and these characteristics were not changed by RTA.

REFERENCES

- [1] W. P. Maszara, J. Electrochem. Soc., **138**, 341 (1991)
- [2] T. Abe and Y. Nakazato, IEICE Trans. Electron., **E77-C**, 342 (1994)
- [3] D. V. Lang, J. Appl. Phys., **45**, 3023 (1974)
- [4] A. Usami, K. Kaneko, A. Ito, T. Wada and S. Ishigami, Semicond. Sci. Technol. **9**, 1366 (1994)
- [5] A. Usami, K. Kaneko, Y. Fujii and M. Ichimura, IEEE Trans. Electron Devices **42**, 239 (1995)
- [6] A. Usami, Y. Tokuda, M. Katayama, S. Kaneshima and Y. Wada, J. Phys. D : Appl. Phys., **19**, 1079 (1986)
- [7] J. B. Lasky, J. Appl. Phys., **54**, 6009 (1983)
- [8] K. L. Wang, S. Y. Liu, G. E. Possin, J. Karins, Jr and J. Corbett, J. Appl. Phys., **54**, 3839 (1983)
- [9] Y. Tokuda, N. Shimizu and A. Usami, Jpn. J. Appl. Phys., **18**, 309, (1979)
- [10] H. Lefèvre and M. Schulz, Appl. Phys., **12**, 45, (1977)
- [11] ERAD : Terrestrial Photovoltaic Measurement II, NASA CP-2010 (1976)
- [12] C. T. Sah, R. N. Noyce and W. Shockley, Proc. IRE, **45**, 1228 (1957)

CHARACTERIZATION OF MOS DEVICES FABRICATED ON CARBON IMPLANTED SILICON SUBSTRATES

IBRAHIM BAN*, MEHMET C. ÖZTÜRK*, KIM CHRISTENSEN**, AND
DENNIS M. MAHER**

* Department of Electrical and Computer Engineering, North Carolina State University,
P.O. Box 7911, Raleigh, NC 27695-7911, USA

** Department of Materials Science and Engineering, North Carolina State
University, P.O. Box 7907, Raleigh, NC 27695-7907, USA

ABSTRACT

In this study, we present characterization of Metal-Oxide-Semiconductor (MOS) capacitors fabricated on carbon (C^{14}) implanted silicon substrates. Carbon was implanted at an energy of 50 keV with doses ranging from $1 \times 10^{12} \text{ cm}^{-2}$ to $4.1 \times 10^{15} \text{ cm}^{-2}$. Metal-Oxide-Silicon (MOS) capacitors were fabricated and used to determine the MOS capacitance-voltage (C-V) and capacitance-time (C-t) behavior. These measurements revealed a strong correlation between carrier lifetime and the carbon dose. Degradation in lifetime was observed for carbon dose levels as low as $4 \times 10^{12} \text{ cm}^{-2}$. At carbon doses equal to and above $6.4 \times 10^{13} \text{ cm}^{-2}$, extremely low generation lifetimes were obtained ($\sim 10^{-7} \text{ sec}$). On the other hand, degradation in C-V characteristics was observed only for carbon doses above $2.7 \times 10^{14} \text{ cm}^{-2}$. Below this dose, both flatband voltage and interface trap density of the carbon implanted samples were comparable to those of the monitors. Analysis of the samples by cross sectional transmission electron microscopy revealed the absence of extended defects even in samples with high carbon dose levels.

INTRODUCTION

Carbon is one of the commonly found impurities in silicon. Carbon incorporation in silicon can occur during processes such as reactive ion etching(1), ion implantation and chemical vapor deposition. Carbon is generally considered as an electrically inactive impurity in silicon (2). However, there exists evidence in the literature linking structural defects in Si to the presence of carbon for levels above $1 \times 10^{16} \text{ cm}^{-3}$ (2, 3). It has been shown that carbon can cause degradation in reverse characteristics of power pn junctions fabricated on float-zone (FZ) wafers at concentration levels as low as $5 \times 10^{16} \text{ cm}^{-3}$ (3, 4). In these studies, emphasis was on power devices that were subjected to high temperature cycles ($>1200^\circ\text{C}$) for long times ($>10 \text{ hr}$). In dynamic memories fabricated on FZ substrates with moderate processing conditions, similar defects were not observed (3). Recently, Beck et al. has reported that oxide kinetics and oxide breakdown are both influenced by carbon in silicon (1). In silicon wafers implanted with carbon, they have observed changes in flatband voltage (V_{FB}) and interface trap density (D_{it}) and they have correlated these changes to the implant dose. Carbon is also known to cause precipitates in the presence of oxygen with high thermal budget heat treatments (5, 6, 7).

On the useful side, it has been shown that carbon can serve as a sink for silicon self-interstitials (8). Proximity gettering in silicon has been demonstrated by implanting carbon at relatively high dose levels ($\geq 1 \times 10^{14} \text{ cm}^{-2}$) and high energies (MeV) (9). However, excess leakage currents were observed in p-n junctions when depletion widths of these devices reached the carbon implanted region (10).

In this study, we have investigated the effects of carbon on MOS capacitance-voltage (C-V) and capacitance-time (C-t) behavior. One of our primary objectives was to study the

dependence of minority carrier generation lifetime on carbon level in silicon. We were particularly interested in moderate carbon levels typically found in silicon layers obtained by low pressure chemical vapor deposition (LPCVD). As such, carbon levels considered in this work are in general lower than those used in earlier studies. MOS capacitors were fabricated on silicon substrates implanted with carbon at different dose levels. The samples were characterized via C-V and C-t measurements. Carbon profiles were obtained by secondary ion mass spectroscopy (SIMS). Cross sectional transmission electron microscopy (XTEM) was used for defect analysis.

SAMPLE PREPARATION

MOS capacitors were fabricated on 1.9 - 2.3 Ω -cm Czochralski (CZ) grown, (100) oriented p-type substrates. Carbon ($m=14$) was implanted at 50 KeV at dose levels ranging from 1×10^{12} to $4.1 \times 10^{15} \text{ cm}^{-2}$ (Implant conditions are given in Table I). A 10 nm pad oxide was grown followed by LPCVD of a 300 nm SiO_2 layer at 400°C. Following a 1050°C/10 sec rapid thermal annealing (RTA) step for implantation damage annealing, the oxide was stripped, and a 225 Å gate oxide was grown at 800 °C by a dry/wet/dry cycle. This was followed by LPCVD of polysilicon. Polysilicon doping was achieved by phosphorus implantation and RTA at 1050 °C for 10 sec. Titanium (100 nm) and aluminum (800 nm) were evaporated for device contacts, and the back contact was formed by Al evaporation.

Table I. Carbon implant conditions.

Sample	Energy (keV)	Dose (cm^{-2})
C1	50	1.0×10^{12}
C2	50	4.0×10^{12}
C3	50	1.6×10^{13}
C4	50	6.4×10^{13}
C5	50	2.7×10^{14}
C6	50	1.0×10^{15}
C7	50	4.1×10^{15}
C8 (monitor)	-	-

RESULTS AND DISCUSSION

Fig. 1 shows carbon, oxygen, and phosphorus profiles in the monitor prepared with no carbon implantation. The polysilicon gate appears to be doped degenerately up to the oxide interface as indicated by the oxygen peak. The carbon level in polysilicon is $2 \times 10^{18} \text{ cm}^{-3}$ which is typical for conventional LPCVD systems. The SIMS oxygen and carbon background levels were obtained from a high-purity FZ silicon standard as $3 \times 10^{17} \text{ cm}^{-3}$ and $2 \times 10^{16} \text{ cm}^{-3}$ respectively. Thus, both carbon and oxygen levels in the substrate are below the SIMS detection limits.

Resulting carbon profiles in implanted samples after all high temperatures steps used in MOS capacitor fabrication are shown in Fig. 2. The carbon doses calculated from the depth profiles indicate an almost 50% carbon loss for wafers C1, C2, C3, and C4. A potential cause for

this loss is the two thermal oxides grown on carbon implanted wafers. However, in low dose samples, the comparable SIMS background levels may also be introducing error into our dose calculations. This difference was found to decrease for higher carbon doses (10% for C5, 6% for C6).

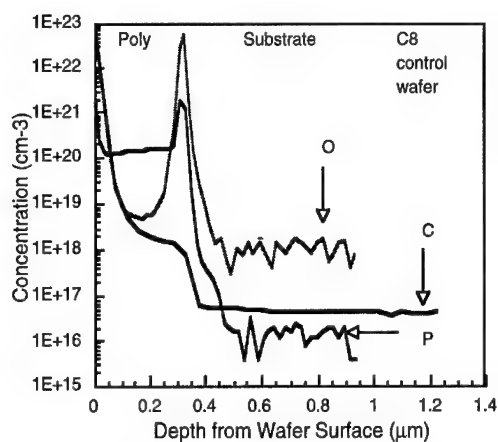


Fig. 1. The SIMS profile of oxygen, carbon, and phosphorus in a control wafer.

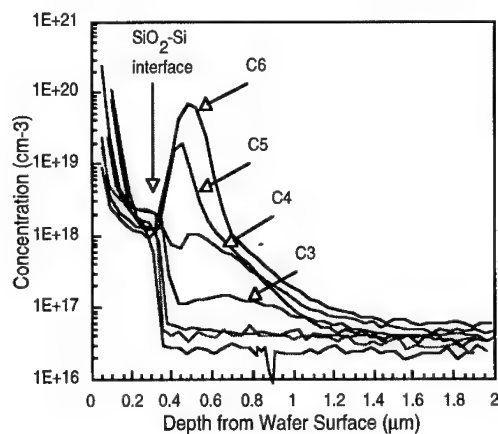


Fig. 2. Carbon Levels in implanted samples

Typical high and low frequency capacitance-voltage (CV) curves obtained from C1 are presented in Fig. 3(a). The profiles are practically identical to those obtained from the monitor (C8) prepared without carbon implantation. Fig. 3(b) shows the distribution of the interface traps across the bandgap for the same dose level. As shown, the midgap interface trap density (D_{it}) is $5 \times 10^{10} \text{ cm}^{-2} \text{ eV}^{-1}$ which is comparable to D_{it} levels obtained from the monitors. This behavior

was common to all samples with carbon doses ranging from 1×10^{12} to $6.4 \times 10^{13} \text{ cm}^{-2}$. For this dose range, flatband voltages obtained from the carbon implanted samples were also found to be comparable to those of the monitors. Therefore, under these conditions, it appears that carbon levels as high as 10^{18} cm^{-3} (after all thermal cycles) do not cause measurable degradation in MOS C-V characteristics. These results are in agreement with those of Beck et. al which showed degradation in D_{it} for carbon dose levels only higher than $1 \times 10^{14} \text{ cm}^{-2}$ (1). In our study, for dose levels above $2.7 \times 10^{14} \text{ cm}^{-2}$ (C5, C6, C7), an anomalous C-V behavior was observed. When these capacitors were biased to accumulation, the high frequency capacitance was found to be lower than the oxide capacitance indicative of another series capacitor. On the other hand, we were able to obtain normal low frequency C-V behavior from these samples. These findings imply that in these samples, hole concentration under the gate can not follow the 1 MHz signal used for the C-V measurement. This behavior may be attributed to hole traps previously observed in carbon implanted silicon samples (11).

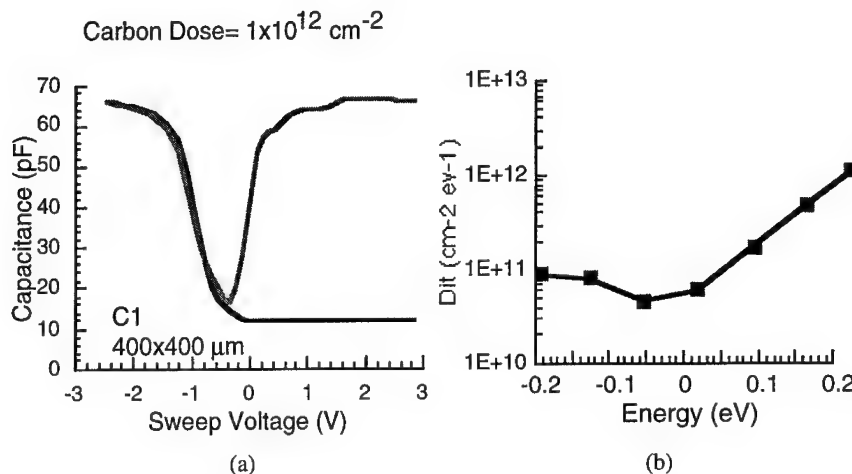


Fig. 3. (a) A typical C-V curve obtained from the wafer doped with $1 \times 10^{12} \text{ cm}^{-2}$
(b) the interface trap density of the device.

The same samples were also used to determine the minority carrier generation lifetime in silicon. In evaluating the effect of carbon on generation lifetime, one has to be concerned about defects that may be introduced by ion implantation. We believe that since carbon has an atomic mass only slightly above that of boron, the damage caused by C implantation can not be extensive. Therefore, the two 1050 °C/10 sec RTA steps (first after oxidation, second after poly implant) were expected to provide a sufficient thermal budget for damage annealing. To support this argument, several samples were characterized using cross-sectional Transmission Electron Microscopy (XTEM) to determine if the defects induced by ion implantation were annealed out during the high thermal budget cycles. The results of this analysis indicated that all samples including those implanted with carbon dose levels as high as $1 \times 10^{15} \text{ cm}^{-2}$ were free of extended defects. It should be noted that degradation in high frequency C-V behavior was observed for dose levels almost an order of magnitude below this level.

In lifetime measurements, we have used a technique first introduced by Zerbst (12). In this technique, a large voltage pulse is applied to an MOS capacitor. An inversion layer can not

form instantaneously since minority carriers have to be created via thermal generation in the substrate. This state is referred to as deep depletion. With time, minority carriers are generated and the MOS capacitor moves from deep depletion to inversion. During this relaxation period, the capacitance is measured as a function of time. This information can then be used to extract the generation lifetime. The time required for this transition to occur is commonly referred to as relaxation time. A long generation lifetime implies fewer carriers generated per unit time which corresponds to a longer relaxation lifetime. Since correct analysis is possible only if an acceptable C-V curve is obtained, lifetime measurements were performed only for C1, C2, C3, C4, and the monitors. A total of 15 samples were measured on each wafer. A Keithley™ Model 5958 C-V system was used for these measurements. Fig. 4(a) shows the measured relaxation time for a gate pulse of 4 V. The dashed line indicates the lowest relaxation time obtained from the monitors. As shown, the relaxation time with a carbon dose of 1×10^{12} (C1) is comparable to that of the monitors. For the higher carbon dose of $4 \times 10^{12} \text{ cm}^{-2}$, the relaxation time is still high, however, a wider distribution is obtained with some values below the dashed line. For higher carbon doses, a dramatic drop in the relaxation time can be observed. When the carbon dose is $6.4 \times 10^{13} \text{ cm}^{-2}$ (C4), the relaxation occurs almost instantaneously.

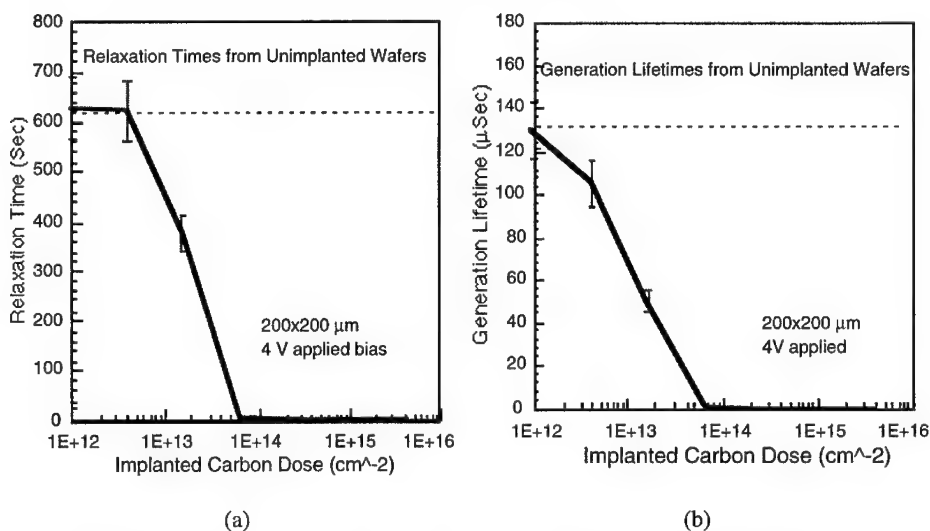


Fig. 4(a). The relaxation time with respect to the carbon implant doses (b) The generation lifetime with respect to implanted carbon dose.

The generation lifetimes extracted from the C-t measurements are plotted in Fig. 4(b). As expected, there exists a close agreement between the relaxation time and the generation lifetime (13). In agreement with the relaxation times measured, a carbon dose of $4 \times 10^{12} \text{ cm}^{-2}$ (C2) can cause measurable degradation in the substrate. For a carbon dose of $6.4 \times 10^{13} \text{ cm}^{-2}$, the generation lifetime in silicon is practically zero. Therefore, even though excellent high and low frequency C-V behavior was observed for all MOS structures considered in these measurements, there appears to be a substantial degradation material quality for dose levels above $4 \times 10^{12} \text{ cm}^{-2}$. This dose, which corresponds to a peak carbon concentration of $5 \times 10^{16} \text{ cm}^{-3}$ after all thermal steps, appears to be a threshold value in this experiment. What is significant about this result is

that such carbon levels can be readily incorporated in films grown by conventional LPCVD methods. This is especially a concern for epitaxial films.

CONCLUSIONS

In this work, MOS capacitors were fabricated on carbon implanted silicon. Carbon was implanted at 50 keV and at different dose levels. The capacitors with carbon doses ranging from 4×10^{12} to $6.4 \times 10^{13} \text{ cm}^{-3}$ exhibited normal high and low frequency C-V behavior. The capacitors with higher carbon doses were not even able to show the high frequency accumulation capacitance which we have attributed to the presence of hole traps. On the other hand, generation lifetime measurements revealed severe degradation for dose levels above $4 \times 10^{12} \text{ cm}^{-3}$ corresponding to a peak concentration of $5 \times 10^{16} \text{ cm}^{-3}$. This level is certainly in the range for films deposited by conventional LPCVD methods. Analysis of the samples by XTEM indicated removal of extended defects during high temperature cycles. Therefore, the observed degradation in lifetime can either be due to point defects which are not observable by XTEM or an electrical effect.

ACKNOWLEDGMENTS

The authors are grateful to Dr. R. Kuehn and the personnel of NCSU Microelectronics Laboratory for their technical assistance in sample preparation. This research was partially supported by NSF Engineering Research Centers Program through the center for Advanced Electronic Material Processing (grant CDR-8721545)

REFERENCES

1. R. B. Beck, T. Brozek, J. Ruzyllo, and S. D. Hossain, *J. Elect. Mat.* **22**, 689 (1993).
2. B. O. Kolbesen, in *Aggregation Phenomena of Point Defects in Silicon*, edited by E. Sirtl, and J. Goorissen (The Electrochemical Society, Princeton, NJ, 1983), pp. 155-175.
3. B. O. Kolbesen and A. Muhlbauer, *Sol. St. Elect.* **25**, 759 (1982).
4. N. Akiyama, Y. Yatsurugi, Y. Endo, and Z. Imayoshi, *Appl. Phys. Lett.* **22**, 630 (1973).
5. W. Zulehner, in *Aggregation Phenomena of Point Defects in Silicon*, edited by E. Sirtl, and J. Goorissen (The Electrochemical Society, Princeton, NJ, 1983).
6. S. Q. Feng, J. P. Kalejs, and D. G. Ast in *Oxygen, carbon, hydrogen, and nitrogen in crystalline silicon*, edited by J. C. Mikkelsen (Mat. Res. Soc. Symp. Proc. **59**, Pittsburg, PA, 1986) pp. 439-444.
7. F. Shimura, *J. Appl. Phys.* **59**, 3251 (1986).
8. S. Nishikawa and T. Yamaji, *Extended Abstracts of the 1992 International Conference on Solid State Devices and Materials*, 26-28 (1992).
9. H. Wong, N. W. Cheung, P. K. Chu, J. Liu, and J. W. Mayer, *Appl. Phys. Lett.* **52**, 1023 (1988).
10. H. Wong, N. W. Cheung, and S. S. Wong, *Nucl. Inst. Meth. Phys.* **B37/38**, 970 (1989).
11. O. O. Awadelkarim, B. A. Suliman, B. Monemar, J. L. Lindstrom, Y. Zhang, J. W. Corbett, *J. Appl. Phys.* **67**, 270 (1990).
12. J. S. Kang, D. K. Schroder, *Phys. Stat. Sol. (a)* **89**, 13 (1985).
13. D. K. Schroder, *Semiconductor Material and Device Characterization* (Wiley-Interscience, New York, 1990).

THE ROLE OF THE Si-SiO₂ (CVD) INTERFACE IN DEGRADATION EFFECTS FOR HIGH-SPEED BIPOLAR TRANSISTORS

J.-Q. LÜ*, S. SCHÖTTL*, E. STEFANOV*, F. KOCH*, R. MAHNKOPF** and H. KLOSE**

*Physik-Dept. E16, Technical University Munich, D-85747 Garching, Germany

**Siemens AG, Corporate R&D, D-81730 Munich, Germany

ABSTRACT

The intent of the present work is to analyze device degradation and reliability in terms of their microscopic origins. The base-emitter junction of the advanced, "double-poly", self-aligned bipolar transistor contacts the SiO₂ sidewall spacer. During normal circuit operation, the base-emitter junction experiences a reverse bias which as a stress in time degrades the current gain of the transistor. Both a decrease of the gain, as well as an increase in the noise are observed. The forward base current increase as a function of stress time follows $\Delta I_B \sim t^n$. We present evidence that the defects are occurring at the Si-SiO₂ interface from perimeter to area comparisons. The weak temperature dependence of the forward base current in degraded transistors shows that trap-assisted tunneling current through the Si-SiO₂ interface states is involved. The random-telegraph-signals observed for the first time in a silicon bipolar transistor are a direct identification of damage at the Si-SiO₂ interface. 2D simulation of the potential and field near the interface allows us to show that damage can be expected.

INTRODUCTION

The common, modern high-speed n-p-n bipolar transistor is based on a "double-poly", self-aligned planar structure in which the base-emitter junction contacts the SiO₂ sidewall spacer. During normal circuit operation, the base-emitter junction experiences a reverse bias which in time degrades the current gain of the transistor [1]. The knowledge of device degradation effects becomes more and more important with further miniaturization of bipolar transistors. A few studies have investigated the degradation effects in advanced self-aligned bipolar transistors using the hot-carrier concept [2-4]: electrons are accelerated by the applied field in reverse mode. They can gain so much energy, that they damage the Si-SiO₂ interface after injection across this interface. The accepted explanation is that the resulting interface traps are generation-recombination centers, causing an increase of the base current [4]. In the worst case it results in a short circuit.

This hot-carrier concept is further investigated in this work with high performance self-aligned Si n-p-n transistors, realized in a 0.5 μm -technology, with a cutoff frequency 25 GHz and a current gain β of 100. The experiments are performed over a range of device sizes. Evidence is found that the defects are occurring at the Si-SiO₂ interface from the perimeter to area comparisons. Further study of the temperature dependence of the forward current in degraded transistors shows that trap-assisted tunneling through the Si-SiO₂ interface states is involved. In order to identify the microscopic physical mechanisms we measured 1/f noise and found for the first time the random-telegraph-signals in a Si bipolar transistor. This is an identification of the damage at Si-SiO₂ interface. Modeling the potential and field shows where the damage could be expected.

MEASUREMENT OF DEGRADATION

Device Structure and Experiment Performance

The n-p-n bipolar transistors are fabricated using a 0.5 μm self-aligned technology similar to that proposed by [5]. The device cross section is shown in Fig. 1. The starting wafers are an n⁻-type epitaxial layer grown on an p⁻-substrate. The intrinsic p-base is formed with boron implantation and anneal. The extrinsic p⁺-base region is doped by B out-diffused from B implant

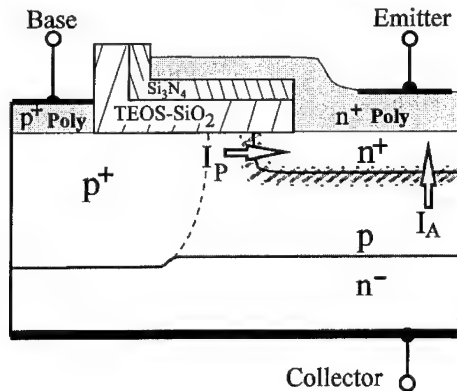


Fig. 1. The schematic cross-section of the bipolar transistor with the identification of perimeter current I_P and area current I_A .

p⁺-poly-Si during drive-in heat cycle. The As implant n⁺-polysilicon on the intrinsic p-base is self-aligned to the polysilicon base contact and separated by a sidewall spacer of Si₃N₄/TEOS-SiO₂. A subsequent drive-in is performed yielding the n⁺-emitter. The secondary ion mass spectroscopy (SIMS) profiling is used to measure the doping profiles of different regions. The concentrations of p⁺-extrinsic base, p-intrinsic base, n⁺-emitter and n⁻-collector are about 10²⁰ cm⁻³, 3×10¹⁸ cm⁻³, 10²⁰ cm⁻³ and 8×10¹⁶ cm⁻³, respectively. The sample sizes are listed in Table I, where A_{eff} is the effective emitter area, P the perimeter length around the emitter.

TABLE I. LIST OF THE DEVICE SIZES

Device	A_{eff} (μm^2)	P (μm)	P/A (μm^{-1})
A	0.4×2.9=1.16	6.6	5.69
B	0.8×2.9=2.32	7.4	3.19
C	0.8×20.5=16.4	42.6	2.60
D	1.6×2.9=4.64	9.0	1.94
E	7.7×7.3=56.21	30	0.53

The stress is carried out by applying a constant reverse bias (e.g. 3.5 V) on the base-emitter junction at room temperature. The stress time ranges from 0 up to 10⁶ s. The forward characteristics of each device are measured before the constant bias stress and then after each stress, at different temperatures (4.2 K to room temperature).

Degradation Effects

The typical forward I-V characteristics are shown in Fig. 2. An abnormal base leakage current at low forward bias is found with an ideality factor greater than two. Moreover, the forward base current changes up to greater than two orders of magnitude due to the stress, while the reverse current changes only about 10% at the reverse bias greater than 0.5 V. In spite of the nonideal base current, the collector current is ideal and the β is about 100 in the ideal region.

A method for characterizing the degradation of β is to plot ΔI_B , measured at a particular value of the forward bias V_{BE} , against the stress time t [4]. We found that $\Delta I_B \sim t^n$, where $n \sim 0.3$ for all devices with different sizes, and different biases V_{BE} when V_{BE} smaller than 0.6 V and greater than 0.1 V (see also Fig. 4).

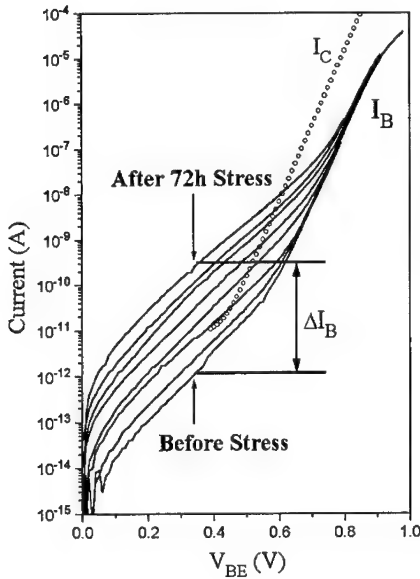


Fig. 2. Gummel plots showing the degradation of the base current I_B with increasing stress time for device A, stressed at reverse bias $V_R = 3.5$ V.

The nonideal I-V characteristics have been explained by assuming that a Shockley-Read-Hall recombination mechanism in the space charge region is responsible for the leakage current [2]. In fact, there are three current components [3], i.e. J_{diff} (diffusion current), J_{g-r} (generation and recombination current), and J_{tunnel} (tunneling current). This is valid for reverse and forward I-V characteristics, also for the perimeter current I_p and area current I_A as shown in Fig. 1.

In the reverse mode, the I-V characteristics show that the dominant current component is a band-to-band tunneling current J_{tunnel} that is relatively insensitive on defects. Thus, tunneling is responsible for the high reverse leakage current, therefore for the degradation effects. To identify the tunneling current as either a perimeter or an area component, the reverse base currents for the five device sizes (see Table I) are compared. The ratio of base currents is found to be approximately suited with the ratio of perimeters, which indicates the perimeter tunneling current is the dominant source of the degradation.

In the forward mode, the three current components J_{diff} , J_{g-r} , and J_{tunnel} have different voltage and temperature dependences. J_{diff} has an $\exp(qV/kT)$ dependence and J_{g-r} , an $\exp(qV/2kT)$ dependence, on the bias voltage and temperature. Since the Si is an indirect bandgap material, any observed tunneling current in forward bias is either phonon assisted or via intermediate energy states within the bandgap (excess tunneling current). Both have a strong dependence on bias voltage and are relatively insensitive to the temperature. The typical relation in phonon-assisted tunneling is $\exp(-(E_g(T) - E_p)^{3/2}/\mathcal{E})$, where E_g is the bandgap of the semiconductor material, E_p is the phonon energy, and is \mathcal{E} the junction electric field. On the other hand, the typical relation in excess tunneling [6] is $D_x \exp(q(V - V_{bi})/\alpha)$, where $V_{bi} = E_g(T) - q(V_p + V_n)$ is the built-in potential, α is a constant determined by the unity potential depletion layer width, D_x is the density of states in the forbidden gap at an energy $q(V_{bi} - V)$ above the top of valence band.

Based on the different voltage and temperature relations of the four current components, one can distinguish the dominant current component in the forward-biased base-emitter junction. A typical result of the base current as a function of temperature is shown in Fig. 3 measured at a fixed bias for a degraded device. Fig. 3 shows clearly that the base current does not follow the temperature dependence of $\exp(V/mkT)$, where m is the ideality factor. The fit curve is calculated using the excess current theory, and $E_g(T) = 1.17 - 4.73E-4 T^2 / (636 + T)$ (see [7]). This good agreement between the experiment data and fit data, associating the exponential voltage dependence as shown in Fig. 2, identifies the forward current as excess tunneling through the energy levels in the forbidden gap, for the low forward bias.

For the higher forward bias, the diode ideality factor still remains unity, which indicates that the diffusion current component of the base-emitter junction dominates at higher forward bias as expected. Therefore it is necessary to probe the origin of the excess tunneling current, i.e. whether tunneling occurs near the interface of Si/sidewall spacer, or in volume of the base-emitter junction and then what is the origin of the energy levels in forbidden gap.

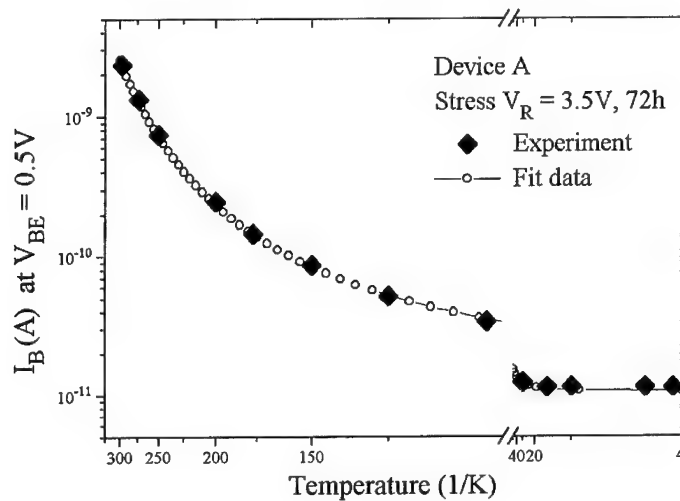


Fig. 3. Temperature dependence of the forward base current measured at $V_{BE} = 0.5V$. The fit data calculated using the excess current theory are well suited with the experiment data.

For the tunneling path, five devices (shown in Table I) have been used with a perimeter ratio $P^C : P^E : P^D : P^B : P^A = 6.45 : 4.45 : 1.40 : 1.12 : 1$ and an area ratio $A^C : A^E : A^D : A^B : A^A = 14 : 48 : 4 : 2 : 1$. The forward base currents I_B are measured for each device and normalized to the emitter perimeter P and area A , respectively in Fig. 4. The good agreement among the different curves in the top picture of Fig. 4 and the separate behavior in the low picture show clearly that the tunneling takes place along the perimeter of the emitter near the sidewall spacer. This is an evidence that the base current for low forward bias is a tunneling current assisted by the Si-SiO₂ interface states.

Because the reverse band-band tunneling current which leads to a degradation of the bipolar transistor, and the forward base tunneling current in lower bias are associated with the sidewall spacer, we are in favor of assumption that interface states (electronic states) are generated in the oxide (in particular sidewall oxide of the advance self-aligned transistor shown in Fig. 1) of devices subjected to reverse-bias stress. In order to further verify the generation of interface states, the $1/f$ noise measurement is performed.

The $1/f$ noise measurements are carried out using some components of the HP3048 phase-noise measurement setup. A constant forward current is applied to the base. The collector voltage fluctuations of the transistor are displayed as spectral power density of the voltage fluctuations $S_v(f)$. A typical $1/f$ noise is observed in our transistors. For devices without any stress the $S_v(f)$ is just like the ground noise spectra. For degraded devices the $S_v(f)$ rises typically by 20 dB after a stress ($V_R = 3.5$ V, 72 hours).

In research of the microscopic origin of the $1/f$ noise, particularly when the interface of Si-SiO₂ plays a role as postulated, it is suggested that random-telegraph-noise (RTN) switching should be observed by low temperature, analog to MOS structure [8]. We have found the RTN's signal for the first time (to our knowledge) in a bipolar transistor. It appears at the same forward bias as the excess current, which confirms the damage at the Si-SiO₂ interface.

DISCUSSION

The nonideal device characteristics discussed in the previous sections have been associated with the damage in the region of the Si-SiO₂ interface and the lateral base-emitter junction. To calculate the electric field distribution and the carrier temperature in this region is therefore very important in research of the microscopic origins of the degradation processes at reverse stress condition. Such calculations are carried out using the PISCES program for the 2D-distributions

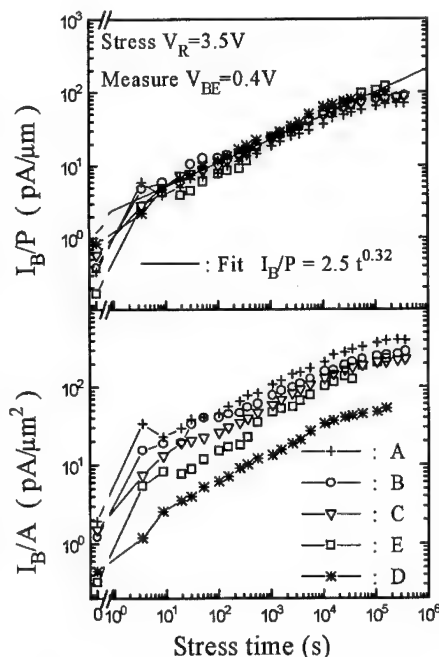


Fig. 4. Degradation of I_B are normalized to the emitter perimeter length (on top) and area (below), respectively, for different sizes.

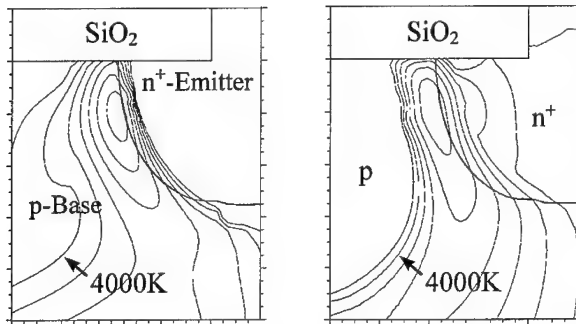


Fig. 5. 2D distribution of the electron (left) and hole (right) temperature for the reverse stress condition, $V_R = 3.5$ V. The step between the lines is $\Delta T = 1000$ K.

of potential, electric field and carrier temperature under the reverse stress condition. The result show that the maximum field (1.5 MV/cm) is situated near the Si-SiO₂ interface along the lateral base-emitter junction (the vertical component about 0.5 MV/cm). This high electric field can yield the reverse band-band tunneling current. A typical result for the distribution of carrier temperature (Fig. 5) shows that the electrons and holes have considerably higher temperature ($T_e \sim 10000$ K, $T_h \sim 8000$ K) under the sidewall spacer. As a result, one can expect that some of these hot carriers can inject into the sidewall spacer and generate the interface states and the border traps in SiO₂, which leads to a degradation of the bipolar transistor.

CONCLUSION

All the results of perimeter effects, temperature dependence and the noise measurement show that the Si-SiO₂ interface plays a very important role in the degradation mechanism of the advanced self-aligned bipolar transistors. In forward mode the dominant process is the interface state assisted tunneling process. In reverse mode the dominant process is the band-band tunneling process under the sidewall spacer. 2D simulations confirms that the damage is situated near the interface of SiO₂ and the base-emitter junction, due to the reverse bias stress. To make a high quality Si-SiO₂ interface and to decrease the electric field near the interface is therefore necessary in order to decrease the degradation effects for further scaled-down bipolar devices.

REFERENCE

- [1] S. P. Joshi, R. Lahri, and C. Lage, in *IEDM Tech. Dig.* 1987, 182.
- [2] S. A. Petersen and G. P. Li, in *IEDM Tech. Dig.* 1985, 22.
- [3] G. P. Li, T. C. C. Chen, C. T. Chuang, J. M. C. Stark, D. D. Tang, M. B. Ketchen, and L. K. Wang, *IEEE Electron Device Lett.* **EDL-8**, 338 (1987).
- [4] J. D. Burnett and C. Hu, *IEEE Trans. Electron Devices*, **35**, 2238 (1988).
- [5] K. Ehinger, E. Bertagnolli, J. Weng, R. Mahnkopf, R. Köpl and H. Klose, in *IEDM Tech. Dig.* 1991, 459.
- [6] A. G. Chynoweth, W. L. Feldmann, and R. A. Logan, *Phys. Rev.* **121**, 684 (1961).
- [7] C. D. Thurmond, *J. Electrochem. Soc.* **122**, 1133 (1975).
- [8] M. J. Kirton and M. J. Uren, *Adv. Phys.* **38**, 368 (1989).

INFLUENCE OF DISLOCATIONS ON THE I-V CHARACTERISTICS OF SILICON SOLAR CELLS

ROBERT MURPHY, BHUSHAN L. SOPORI AND DOUG ROSE
National Renewable Energy Laboratory, 1617 Cole Boulevard, Golden, CO 80401

ABSTRACT

This paper presents a phenomenological approach for analysis of dislocations in a large-area device like a solar cell. A microscopic model of a dislocation is used to calculate the local effects of a dislocation on the dark and the illuminated characteristics of a p-n junction device. A statistical approach is then used to empirically arrive at the I-V characteristics of a small-area device with a uniform distribution of dislocations. Finally, these results are applied to develop a network model to determine the terminal characteristics of a large-area solar cell of a known spatial distribution of dislocations. We show that the performance of a solar cell is influenced not only by the density of dislocations but also by their spatial distribution; heavily dislocated regions exert a disproportionately large degradation effect on the device characteristics.

INTRODUCTION

Dislocations are the dominant defects that control the performance of commercial solar cells fabricated on low-cost, large-grain, polycrystalline silicon substrates [1]. It is known that dislocations can increase the recombination of minority carriers in the bulk of the device, thus, reducing the photo-induced current of solar cells. Furthermore, the presence of dislocations propagating through the junction can influence its carrier collection properties, often leading to a decrease in the open circuit voltage and the fill factor. Although a wealth of knowledge exists about the bulk effects of dislocations, the information about the influence of dislocations on the device characteristics is rather scant. Many calculations that deal with dislocations in devices assume a uniform distribution of defects. However, in large-grain polycrystalline silicon used for solar cells, dislocations are present in certain preferred grain orientations. Thus, heavily dislocated regions can be adjacent to very low or zero dislocation regions. A theoretical modeling is needed to understand the effects of various distributions of dislocations on the solar cell performance.

In this paper we use a basic microscopic model of a dislocation to determine its recombination effects on a p-n junction device. These results are applied to determine the I-V characteristics of a small-area device having a uniform distribution of dislocations. This small-area device model is then extended into a network model that includes the effect of distribution of dislocations in a large-area device like a solar cell.

MODELING APPROACH

Our modeling approach includes three essential features:

1. The microscopic behavior of individual dislocations

The electronic effects of a dislocation in a localized region can be expressed in terms of a band model. Figure 1a illustrates the band diagram of a p-type silicon in the vicinity of a dislocation. The core of the dislocation has an energy distribution of interface states, N_s , and carries a net positive charge. This results in a built-in potential, V_d , that extends to a distance, w . For solar cell applications, the model must include the changes in the band structure due to illumination. Figure 1b illustrates band diagram under illumination. These models are well known and have recently been applied to analyze some effects of grain boundaries on solar cell performance [2-5]. The parameters of this model depend on the nature of the dislocations, the

properties of the substrate, and on the structure of the device. One can apply Poisson's equation to determine the surface recombination velocity at the edge of the space charge region ($r=w$). The effective surface recombination velocity, $S(w)$, can be expressed as:

$$S(w) \propto S(0) \exp(eV_d/kT) = N_s \cdot \sigma \cdot v (E_{fn} - E_{fp}) \exp(eV_d/kT) \quad (1)$$

where E_{fn} and E_{fp} are the quasi Fermi levels, σ is the capture cross section of electrons and holes, N_s is the effective interface state density, and v is the thermal velocity; V_d is the diffusion potential under illuminated condition.

Let us assume a sample of thickness t , and a dislocation density per unit area of N_d . If the number of traps per unit length of dislocation = N , then following the arguments similar to those of references [2-5], we can write an expression for effective volume concentration (N_r) of recombination centers as:

$$N_r \propto N_d^{1/2} \cdot N_s \cdot N (E_{fn} - E_{fp}) \exp(eV_d/kT) \quad (2)$$

From expression in equation (2), we can calculate the minority carrier lifetime due to dislocations, $\tau(N_d)$, as:

$$\tau(N_d) = (1/N_r) \propto \exp(-eV_d/kT-1) / \{ N_s \cdot \sigma \cdot v \cdot N_d^{1/2} \cdot N (E_{fn} - E_{fp}) \} \quad (3)$$

If the lifetime of dislocation-free material is τ_0 , the net lifetime is given by

$$1/\tau_{eff} = 1/\tau_0 + 1/\tau(N_d) \quad (4)$$

$$\tau_{eff} = \tau_0 \cdot \tau(N_d) / (\tau(N_d) + \tau_0). \quad (5)$$

Thus, dislocations can cause a reduction in the minority carrier lifetime in the bulk of the material, and that the lifetime due to recombination caused by dislocations is inversely proportional to $N_d^{1/2}$.

2. Statistical behavior of dislocations in a small-area P-N junction device

On a macroscopic scale, the dislocations in a small-area p-n junction device can be regarded as having two effects, as illustrated in Figure 2. (1) A statistical bulk effect that results in a decrease in the minority carrier lifetime, changes in the carrier mobility, and change in the resistivity. The dominant bulk effect appears to be a reduction in the minority carrier lifetime with an increase in the dislocation density, as shown above. Its effect on a p-n junction device is to increase the dark current component of the device which has a temperature dependence of (e/kT) . (2) An increased recombination in the depletion region due to a dislocation passing through the junction of the device. This component has a temperature dependence of $e/2kT$.

For a dislocation-free junction, the dark characteristics can be written as:

$$J_d = J_{01} \cdot \exp\{(-eV/kT) - 1\} + J_{02} \cdot \{ \exp(-eV/2kT) - 1 \} \quad (6)$$

where the saturation currents are given by standard expression (e.g. see reference 6) From the discussion above, the current in a dislocated device is also of the same form of equation (6). However, the saturation currents have higher values due to excess current components. It is clear that the effects of dislocations in a p-n junction device can be described simply in terms of J_{01} and J_{02} .

For a solar cell, the net current J is given by, $J = J_{ph} - J_d$, where J_{ph} is the photo-current due to solar illumination. J_{ph} can be written in a simple form as $J_{ph} = L_{eff} \times \phi$, where ϕ is the number of photons transmitted into the device, and L_{eff} is the effective minority carrier diffusion

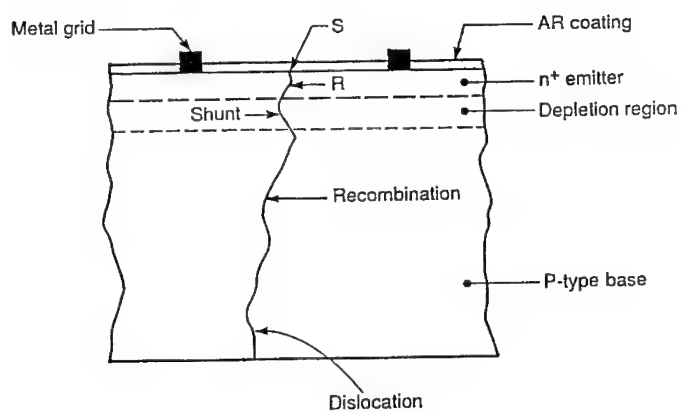
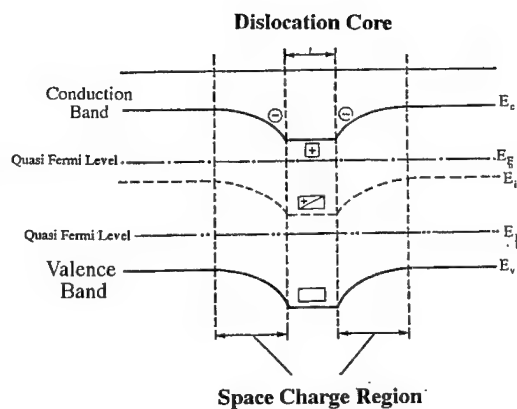
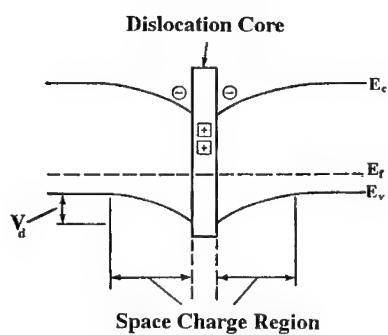


Figure 2
Illustration of the effect of dislocation in a p-n junction solar cell.

length in the base of the device $\{L_{\text{eff}} = (D \cdot \tau_{\text{eff}})^{1/2}\}$. Hence, it is seen that J_{ph} will decrease with an increase in the dislocation density. Consequently, we see that in a small-area p-n junction device the effect of dislocations is to reduce J_{ph} by lowering L_{eff} , and increasing the dark current J_{d} by increasing J_{01} and J_{02} .

Experience has shown that application of detailed theoretical calculations to study the effects of dislocations on the commercial cell performance is not very useful. This is primarily due to the fact that the parameters that describe dislocations are difficult to determine. Furthermore, these parameters vary from material to material. However, it is useful to directly obtain the values of $J_{01}(N_{\text{d}})$ and $J_{02}(N_{\text{d}})$ for practical ranges of dislocation density and apply this information to determine J_{d} . This information can be obtained by fabricating arrays of edge-passivated mesa diodes on the substrate [7]. These devices can be probed for dark and illuminated characteristics in a manner similar to solar cells.

Another component that appears in a device containing dislocations is due to impurity tunneling. This component has the form of

$$J \propto \exp(-eV/kT)$$

We believe that the tunneling component, that arises due to deep states, is significant only in the case of impurity precipitation at the dislocations [8]. Since in solar cell fabrication extensive gettering is used, this component can be quite small in "good" cells. In this paper we will neglect this component.

3. A network model describing the effects of the spatial distribution of dislocations in a large-area device

The microscopic and statistical models describe how each local region behaves as a solar cell. In order to describe how these local cells interact with each other to produce large-area cell characteristics, we have developed a computer network model which interconnects the local solar cells, as illustrated in Figure 3. It consists of a parallel combinations of current sources (photon generated current) and diodes (dark current). Each node in the matrix depicts a local cell, connected to other cells by a resistor representing the series resistance. The series resistance is approximated by the emitter sheet resistance between the adjacent elements and is constant. Each local region, having a known defect density, can be described by a dark current given by :

$$J_{\text{dark}} = J_{01} \left[e^{eV/kT} - 1 \right] + J_{02} \left[e^{eV/2kT} - 1 \right] \quad (7)$$

These dark current components of equation (7) correspond to the base and the depletion region recombination currents, respectively. Hence, a local cell element (n,m) in the network matrix of Fig. 3, is comprised of dark current sources of J_{01nm} , and J_{02nm} , and a corresponding light-induced current $J_{\text{ph},nm}$. One can represent

$$J_{01nm} = J_{01} \times F_{nm} \times \exp(eV/kT - 1)$$

and

$$J_{02nm} = J_{02} \times F'_{nm} \times \exp(eV/2kT - 1)$$

where J_{01} and J_{02} , that represent dark currents in the best device element. F_{nm} and F'_{nm} , are the factors representing the ratio of dark current normalized by the "best-device" current for each component. A finite element computer code, written in Microsoft Excel, is used to analyze the network.

As an example, we model a solar cell as an array of 5x20 devices connected through an emitter with a sheet ρ of 40 Ω/sq and connected to a bus bar as shown in Fig. 4. Let us assume that 20% area of this cell has a dislocation density of $10^6/\text{cm}^2$. We assume that there are only two

types of devices — the device elements (1,17) through (1,20) and (5,17) through (5,20), corresponding to 20% of the total cell area, have a high dislocation density of about $10^6/\text{cm}^2$; rest of the cell has zero dislocation density (zero-D). The effect of this dislocation density is accounted for by higher J_0 values and lower J_{ph} , as compared to the other elements. The values of J_{01} and J_{02} for dislocated regions are $7.2 \times 10^{-8} \text{ A/cm}^2$ and $9 \times 10^{-12} \text{ A/cm}^2$, respectively. The corresponding values for zero-D regions, are $3.6 \times 10^{-9} \text{ A/cm}^2$ and 4.5×10^{-13} , respectively. The J_{ph} value for the dislocation-free devices is assumed to be 35 mA/cm^2 . The values of J_{01} and J_{02} for the dislocation-devices are defined as fractions of the high-performance values. These values of dark current densities are taken from our earlier published results [7].

It is clear from Fig. 4 that the characteristics of each device operating in the connected cell configuration will be different from those in the isolated case. The characteristics of an isolated dislocation-device from node (1,17) is shown Figure 5. For comparison, a similar plot for a dislocation-free device, such as (1,1), is also shown in this figure. Figure 6 shows the I-V characteristics of the total cell, with 20% dislocation-devices, under AM 1.5 illumination. Also shown in the figure are total cell I-V characteristics for a cell consisting of 100% dislocation-free devices and a cell consisting of 100% dislocation-devices, for comparison. The values of V_{oc} , J_{sc} , and FF are as follows:

% area of high dislocation devices	$V_{oc}(\text{mV})$	$J_{sc}(\text{mA/cm}^2)$	FF
0	650	34.9	77.72
20	615	33	77.53
100	565	26	75.18

It is seen that while V_{oc} and J_{sc} drop as the fraction of the total cell covered by low-performance cell elements increases, the FF does not vary substantially.

It is instructive to determine how each cell element can act as a current generator or a sink as the cell is operated through different voltage conditions. Figure 7a shows the status of the current through each device when the entire cell is operating near the maximum power point ($V=0.5\text{V}$). The open white regions indicate that the device is generating current, while shaded regions indicate that the device element is acting as a "sink". It is seen that at the maximum power point of 0.5V, no cell, element is sinking the current. Figures 7b, 7c, and 7d show the status of the various devices at selected terminal voltages as the voltage increases toward 0.56V.

Conclusion

We have described a phenomenological approach to combine a microscopic dislocation model, statistical model for a small-area P-N junction containing dislocations, and a network model to couple non-uniformly distributed dislocation. The results of this model predicts:

- The primary effect of dislocations in silicon substrates have a primary effect is to degrade the cell V_{oc} . The severity of such a degradation depends on the distribution of the low performance regions and the nature of the defects and impurities present in these local regions.
- The mechanism of the degradation is manifested by local shunting of the cell, leading to internal current "sinks."
- The present model includes only two terms in the dark current. This model can be extended to include tunneling current to accommodate the effects of impurity segregation at the dislocations.

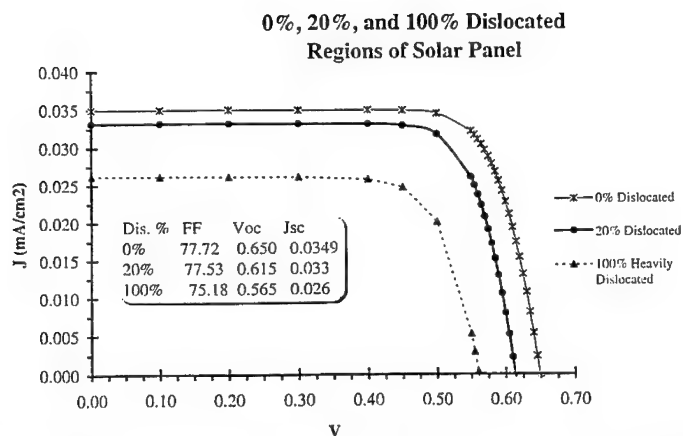


Figure 6. Calculated illuminated I-V characteristics of the total cell with 0%, 20%, and 100% dislocated regions

20% Highly Dislocated Block Region Panels

(Light gray region [generating current] and Dark gray region [sinking current])

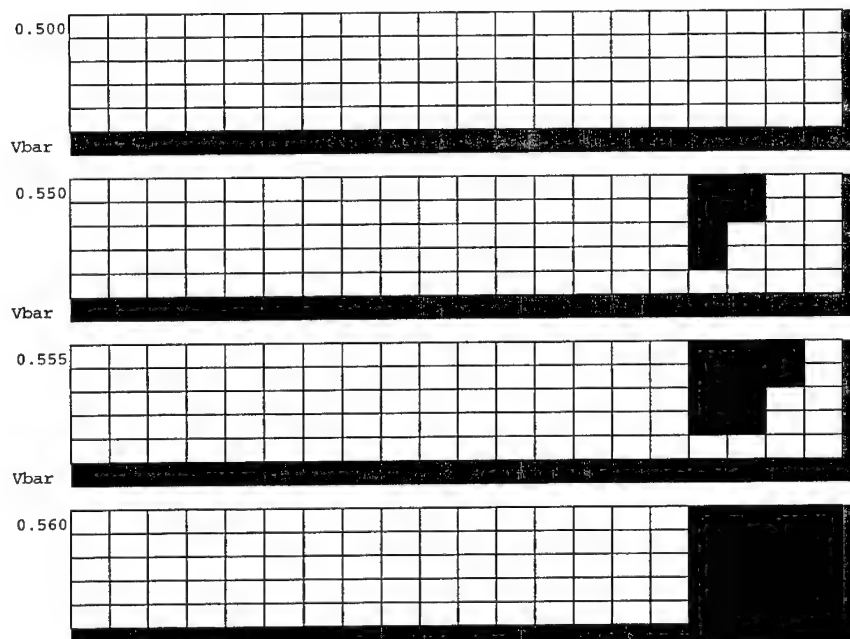


Figure 7. Illustration showing states of various cell elements.

Clear regions are current generators, while dark regions are "sinks." The cell operating voltages are indicated on the upper left corner of each figure

ACKNOWLEDGMENT

This work was supported by the U. S. Department of Energy under contract No. DE-AC02-83CH10093, and by NASA grant No. NGT-70338.

REFERENCES

1. B. L. Sopori, Solar Cells, 1, 237(1980).
2. H. C. Card and E. Yang, IEEE Trans. ED-24, 397(1977).
3. A. K. Ghosh, C. Fishman, and T. Feng, J. Appl. Phys. **51**, 446(1980).
4. J. C. Fossum and F. A. Lindholm, IEEE Trans. ED-27, 692(1980).
5. J. G. Fossum, A. Neugroshcel, F. A. Lindholm, and J. A. Mazer, Procd. IEEE PVSC, 184 (1980).
6. S. M. Sze, Physics of Semiconductor Devices, John Wiley, New York, 1981.
7. B. L. Sopori, Appl. Phys. Lett., 52, 1780(1988).
8. A. G. Chynoweth, W. L. Feldmann, and R. A. Logan, Phys. Rev. **121**, 684(1961).

EFFECTS OF LIGHT ON THE RESONANT TUNNELING IN SILICON QUANTUM DOT DIODE

CHEN DING AND RAPHAEL TSU

Department of Electrical Engineering, UNC Charlotte, Charlotte, NC 28223

ABSTRACT

The resonant tunneling via nanoscale silicon particles embedded in an a-SiO₂ matrix in a diode structure has revealed a range of intriguing observations such as extremely sharp peaks and steps and periodic oscillations in (conductance-voltage) G-V measurements. Recently we have discovered a drastic sharpening of the conductance peak with light. Phase measurements show that the effects of light may be understood by invoking the filling of charged traps.

Silicon resonant tunneling diodes are constructed of an amorphous silicon dioxide (a-SiO₂) double barrier, surrounding a nano-crystalline silicon (nc-Si) layer. The double barrier is sandwiched between a crystalline silicon (c-Si) substrate and aluminum (Al) contacts. The resulting metal /a-SiO₂/nc-Si/a-SiO₂/c-Si/ metal structure was first fabricated and investigated by Ye, Tsu, and Nicollian [1]. From the very first treatment of resonant tunnelling [2], the I-V should show peaks. However, due to the large Fermi sphere of the Al contact, peaks are present only in G-V as elaborated [3]. Figure 1 shows the diode structure fabricated by lithography with the active part isolated by field oxide. The thickness of the active part is typically 150 Å consisting of deposited silicon at room temperature followed by annealing and oxidation at 800 - 850°C resulting in nc-Si particles embedded in an a-SiO₂ matrix. The as-prepared diode structure shows almost no conduction before forming by passing current in the forward direction typically at +5 V at a current density of 100 A/cm². Forming is necessary to assure conduction path by removing the residue amorphous tissue regions between these nanoscale silicon particles [4].

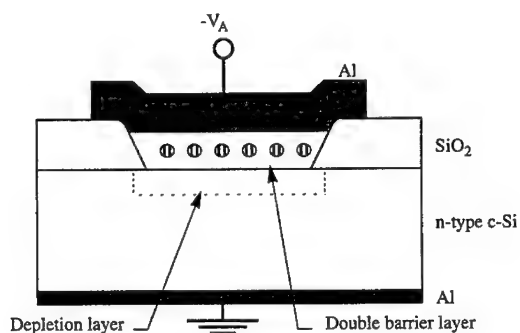


Fig. 1 Cross section of the silicon quantum dot diode.

Recently we have found that electrical forming is not necessary when highly phosphorus doped polysilicon gate is used instead of the Al-gate [5]. Before we discuss the effects of illumination by visible light, several typical I-V or G-V features will be summarized in order to have a better understanding of the highly surprising observations. Figure 2 shows a typical conductance G versus the reverse bias V . Note that this particular sample shows both the typical peak as well as the step in G-V. In 5% of the diode structures, slow conductance oscillations are observed [6]. And recently, the observations of the multiple steps, attributed to resonant tunneling initiated avalanche multiplication, have been quantitatively explained [7].

In the present work, we have focussed our transport measurements to include the phase shift versus bias voltage, Φ -V. We shall show that the observed light effect can be explained using the Φ -V measurements.

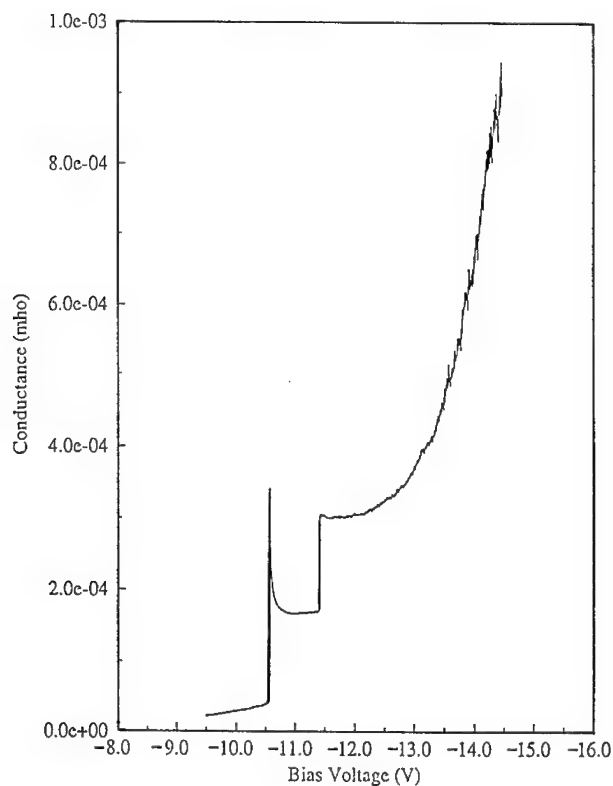


Fig. 2 Conductance versus bias voltage for a sample with both peak and step.

Under illumination with a focussed microscope light through a filter, typically steps in G-V are converted to peaks and peaks in G-V are significantly sharpened as shown in Fig. 3a and 3b. Using a Si filter, a Ge filter, a GaAs filter, and various Corning filters, it was established that light induced effects disappear when the photon energy falls below the fundamental bandgap of silicon. The presence of trapping centers in a resonant tunneling device introduces phase shifts analogous to a capacitance in a resistive circuit. Figure 4 shows the phase of the conductance G versus the applied bias voltage for a typical sample at 300 K, with light illumination (WL) and no illumination (NL). Note that the dip in phase $\sim 25^\circ$, near the peak in G-V is absent with illumination. The disappearance of a substantial phase shift may be interpreted by the filling of traps from light generated carriers, resulting in a stronger conductance peak. Since the generation of electron-hole pairs lowers the substrate resistance, the peaks are shifted toward lower bias voltage under illumination.

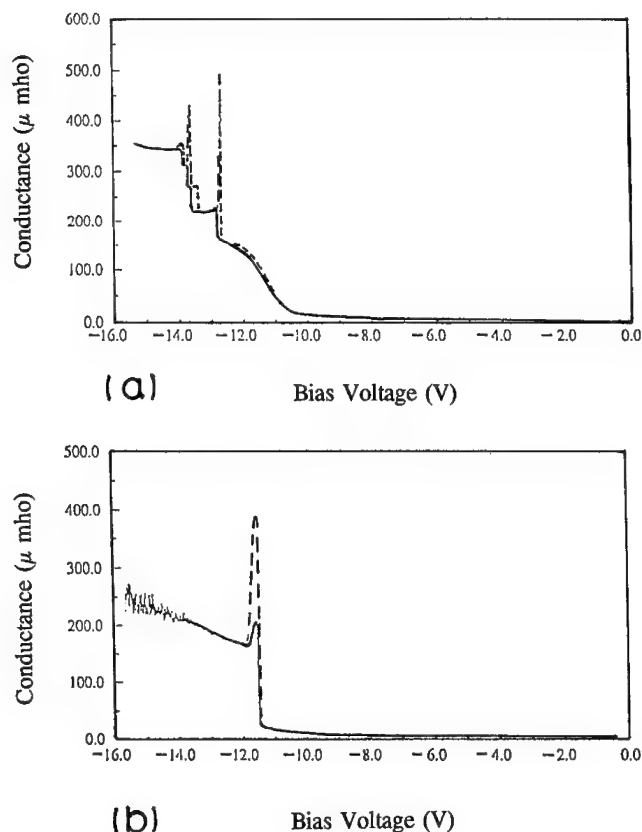


Fig. 3 Conductance versus bias voltage for two samples with illumination (dashed) and without illumination (solid).

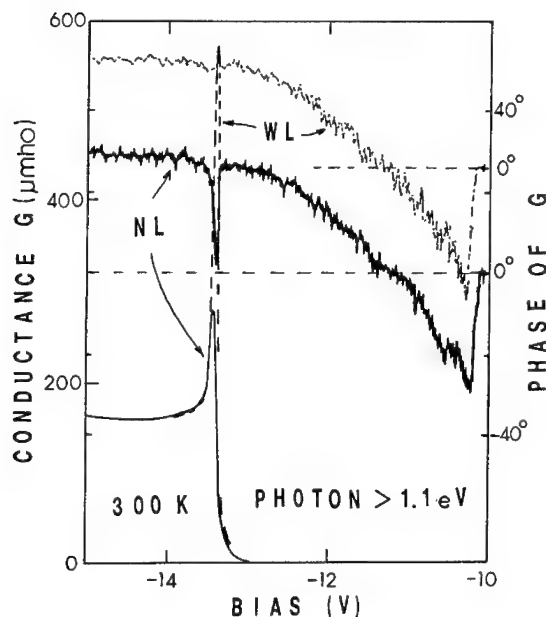


Fig. 4 Phase of the conductance G vs bias V for a typical sample, WL (with light) and NL (no light). G - V is also shown for comparison.

In summary, using Φ - V to corroborate G - V , we are able to establish that the features are enhanced with illumination due to filling of traps from photo-generated carriers. And Φ - V measurements represent a powerful technique for the study of traps in resonant tunneling. The frequency dependence of the Φ - V will be examined in future studies.

ACKNOWLEDGEMENTS

This research is supported by NSF, ARO, and ONR.

REFERENCES

1. Q. Y. Ye, R. Tsu, and E. H. Nicollian, *Phys. Rev. B* **44**, 1806 (1991).
2. R. Tsu and L. Esaki, *Appl. Phys. Lett.* **22**, 562 (1973).
3. R. Tsu, *Physica B* **189**, 235 (1993).
4. E. H. Nicollian and R. Tsu, *J. Appl. Phys.* **74**, 4020 (1993).
5. J. P. Ganasan, MS thesis, UNC Charlotte, 1995.
6. R. Tsu, X. Li, and E. H. Nicollian, *Appl. Phys. Lett.* **65**, 842 (1994).
7. D. W. Boeringer and R. Tsu, *Phys. Rev. B* **51**(15 May 1995).

A MODEL FOR THE FREQUENCY DEPENDENCE OF CHARGE PUMPING CURRENT IN POLYCRYSTALLINE SILICON THIN FILM TRANSISTOR

**GA-WON LEE, JUNG-YEAL LEE, DEUK-SUNG CHOI, SUNG-HOI HUR,
CHOONG-KI KIM and CHUL-HI HAN**

Department of Electrical Engineering, Korea Advanced Institute of Science and Technology,
Taejeon, Korea

ABSTRACT

Making a comparative study between MOSFET and polycrystalline silicon thin film transistor (poly-Si TFT) in applying the charge pumping method (CPM), the most distinctive difference was found in the relation of the charge pumping current (I_{cp}) versus the gate pulse frequency. According to the conventional theory, I_{cp} increases linearly with the gate pulse frequency. In poly-Si TFT, however, I_{cp} shows complicated dependence on frequency. We modeled the frequency dependence of I_{cp} in poly-Si TFT by considering the resistance of active poly-Si film. According to this model we can extract the parameters such as grain boundary trap density, substrate resistance, and capture cross section.

1. INTRODUCTION

Poly-Si TFT has been actively studied because of their capability of integrating on-panel driving circuit with active elements in AM-LCD's and three-dimensional LSI applications¹. But these advantages are constrained by the grain boundary traps. Therefore, to know the characteristics and density of grain boundary traps is very important in order to achieve proper control over these devices. There are several works about the grain boundary trap evaluation by measuring the channel current^{2,3}. Because the channel current is affected by the potential barrier formed by the grain boundary traps, the information about the grain boundary traps can be extracted from the measured channel current. However, the properties of the grain boundary traps found by this method is only effective ones not real ones.

For MOSFET, charge pumping method (CPM) has been used to find out the density of Si/SiO₂ interface traps. CPM was originally introduced by Brugger and Jesper⁶, which is based on a recombination process in the Si/SiO₂ interface states. This method can present the information like the spatial and energy distribution of interface states as well as the average density. Therefore, it has been known to be a very powerful and reliable method for the characterization of the interface trap properties.

Nowadays, CPM is also tried to poly-Si TFT by a few to evaluate the grain boundary trap density^{4,5}. But the direct application can cause some problems because the characteristic of poly-Si TFT is different from that of MOSFET. The most distinctive difference discovered by our experiment was in the relation of charge pumping current (I_{cp}) versus the gate pulse frequency (f). In MOSFET, I_{cp} increases linearly with frequency but in poly-Si TFT, even decreases in high frequency range. Therefore, we can see that significant error may be caused if the grain boundary trap density is evaluated in the improper frequency range where the conventional theory is violated.

In this paper, the physical processes involved with the unexpected phenomenon will be explained and the theoretical model will be also presented.

II. THEORETICAL MODEL

Conventional theory : Charge pumping current

While the n-channel MOSFET is forced by positive gate voltage, some of the electrons which form the inversion layer are captured by the surface states. And they recombine with the majority carriers from the substrate when the gate voltage is changed to drive the device into accumulation state. By repeating this sequence, a net current called charge pumping current flows. According to the conventional theory, I_{cp} is

$$I_{cp} = A_G f \{ q N_{it} + \alpha C_{ox} (V_G - V_t) \} \quad (1)$$

where A_G is gate area, f is gate pulse frequency, q is electronic charge, N_{it} is average density of interface states, C_{ox} is oxide capacitance, V_G is gate voltage, V_t is threshold voltage and α is the fraction of free carriers under the gate that recombine in the substrate forming geometric component.

Modified theory for poly-Si TFT

The resistance of poly-Si film has been known to be very large until the doping concentration is up to 10^{18}cm^{-3} ^{7,8}. This is because the disordered atoms at the grain boundary have the incomplete atomic bonding that creates a potential barrier by trapping carriers. This fact, however, has not been considered in applying the charge pumping method to poly-Si TFT although the resistance of undoped substrate can limit the ability of holes to transit into the gate area when the pulses are forced with high frequency. Of course, the substrate resistance also limits the electron transit but affects less because of the device geometry (Fig. 1(b)). Hence, we will expand the equations on the assumption that the electrons are supplied enough.

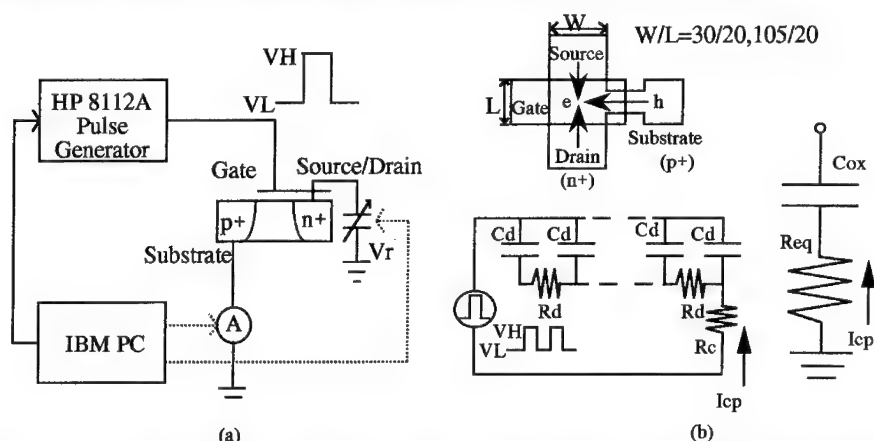


Fig. 1 (a) The experimental configuration. (b) The device structure and distributed model for charge pumping. C_d and R_d are the distributed capacitance and resistance which are experienced by holes(or electrons) during transition into the gate area. The last one is the lumped model.

If we calculate the amount of holes when the gate pulse is negative V_L (for the convenience, the distributed elements are substituted by lumped R_{eq} and C_{ox} such as Fig. 1(b)) assuming the duty cycle of gate pulse is 50%, then

$$Q_L(f) = \frac{|V_L - V_{FB}|}{R_{eq}} \int_0^{T/2} \exp\left(-\frac{t}{R_{eq}C_{ox}}\right) dt = |V_L - V_{FB}| C_{ox} \left\{ 1 - \exp\left(-\frac{1}{2R_{eq}C_{ox}f}\right) \right\} \quad (2)$$

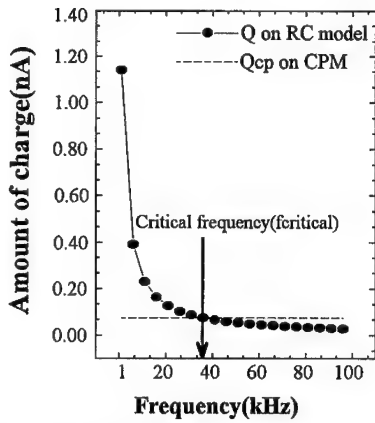


Fig.2 Comparison of the charges calculated on RC model and those necessary in charge pumping operation per one period. Parameters used in calculation are $R_{eq}=7.5G\Omega$ and $C_{ox}=0.23pF$ and $N_{gt}=5 \times 10^{10}cm^{-2}$.

where V_L is negative gate voltage, R_{eq} is equivalent resistance of TFT, T is the gate pulse period. In Fig. 2, we compared the amount of charge calculated on Eq. (2) and necessary in charge pumping based on Eq. (1). This figure shows that the magnitude of I_{cp} will be limited by the substrate resistance at higher frequency than $f_{critical}$. That is, the measured I_{cp} is mainly decided by the amount of holes supplied by substrate not by the trapped electrons in high frequency range above $f_{critical}$.

To analyze this substrate resistance effect on I_{cp} , we considered the time characteristic of traps. The trap time constant is used for average time for trapping and is expressed as follows (τ_d for donor and τ_a for acceptor states respectively)

$$\tau_d = \frac{1}{v_{th}\sigma_n n_s}, \quad \tau_a = \frac{1}{v_{th}\sigma_p p_s} \quad (3a),(3b)$$

where v_{th} is thermal velocity of carrier, σ_n and σ_p is capture cross section of electrons and holes and n_s , p_s is electron and hole concentration at surface respectively. Eq. (3), however, must be rewritten in poly-Si TFT if the band bending which causes p_s (or n_s) is limited by the large substrate resistance as mentioned above. Considering Eq. (2),

$$\tau_d(f) = \left[v_{th} \times \sigma_p \times \frac{|V_L - V_{FB}| \times C_{ox}}{qV_{sub}} \left\{ 1 - \exp\left(-\frac{1}{2R_{eq}C_{ox}f}\right) \right\} \right]^{-1} \quad (4)$$

where V_{sub} is the volume of channel. This trap time constant is dynamic with the gate pulse frequency. According to the above equation, the time constant gets longer as frequency increases. Therefore, the amount of carriers captured by traps for one period is reduced. This becomes evident when we calculate the density of the grain boundary trap states that participate in the charge pumping operation as shown below.

$$N_{gt}(f) = \int_{El}^{Eh} \int_0^{T/2} D_{gt}(E) \frac{c_p n_{-}(0) \exp(-t/\tau_d)}{N_t} dE dt = n_{-}(0) \left\{ 1 - \exp\left(-\frac{1}{2\tau_d f}\right) \right\} \quad (5)$$

where Eh and El is the high and low energy limit and the only traps located in this range can be evaluated by CPM. Eh and El is calculated by considering the capture and emission rate of traps⁹. The fact that the traps which contribute to the charge pumping current may be segregated by energy is the limit of CPM. But, if most trap states locate near mid gap, the error between real and evaluated trap density will be negligible. In Eq. (5), $D_{gt}(E)$ is grain boundary trap density per eV per unit area and assumed to be uniform, c_p is hole capture rate and $n_{-}(0)$ is the number of negatively charged traps at time $t = 0$ during the negative gate voltage. N_t is the total number of trap states located between El and Eh. To calculate $n_{-}(0)$, let's assume that there are two kinds of traps, that is, negatively charged and neutral. If the amount of capture and emission during the pulse transition is negligible, the number of negatively charged traps is⁹

$$n_{-}(0) = \frac{N_t \left\{ 1 - \exp\left(-\frac{T}{2\tau_a}\right) \right\}}{1 - \exp\left\{-\frac{T}{2}\left(\frac{1}{\tau_a} + \frac{1}{\tau_d}\right)\right\}} \quad (6)$$

But at high frequency, the pulse period is too short to reach steady state in capturing carriers. Then the amount of $n_{-}(0)$ may be different for each pulse train. Then Eq. (6) can be rewritten like below.

$$n_{-k}(0) = \left[n_{-1}(0) - \frac{N_t \left\{ 1 - \exp\left(-\frac{T}{2\tau_a}\right) \right\}}{1 - \exp\left\{-\frac{T}{2}\left(\frac{1}{\tau_a} + \frac{1}{\tau_d}\right)\right\}} \right] \exp\left\{-\frac{(k-1)T}{2}\left(\frac{1}{\tau_a} + \frac{1}{\tau_d}\right)\right\} + \frac{N_t \left\{ 1 - \exp\left(-\frac{T}{2\tau_a}\right) \right\}}{1 - \exp\left\{-\frac{T}{2}\left(\frac{1}{\tau_a} + \frac{1}{\tau_d}\right)\right\}} \quad (7)$$

where $n_{-k}(0)$ is the amount of negatively charged trap for kth pulse train and $n_{-1}(0)$ is the initial amount. By inserting Eq. (7) into (5), $N_{gt}(f)$ is expected to decrease at high frequency and if this reduced amount is large enough to cancel the increment of frequency, then I_{cp} will decrease in high frequency range.

In Fig. 3, the effect of substrate resistance on I_{cp} is simulated. As we can predict, R_{eq} is related directly with the distortion starting frequency.

III. EXPERIMENTAL RESULTS

The experimental configuration is the same with Fig. 1(a). Rectangular pulse was generated with the HP8112A pulse generator. Pulse amplitude was large enough to originate charge pumping current: $V_H > V_t$ and $V_L < V_{FB}$. Supply of V_r and measurement of DC substrate current were made with the modular DC source/monitor 4142B. And the complete experimental system was controlled by IBM PC.

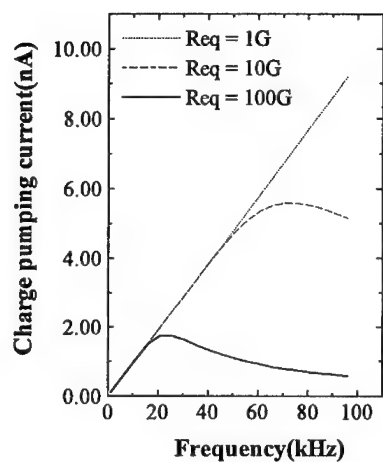


Fig. 3 The effect of equivalent resistance R_{eq} on charge pumping current.

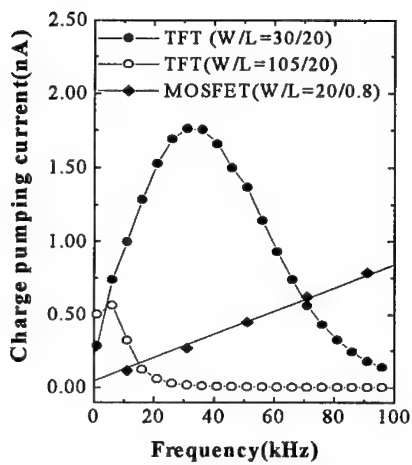
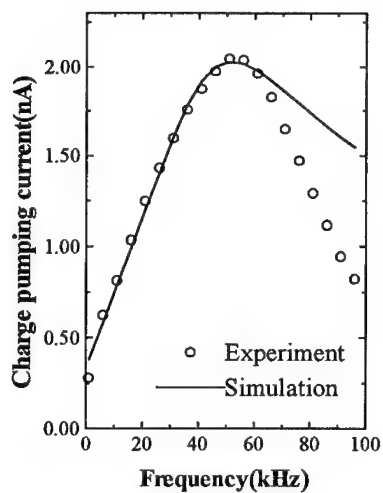
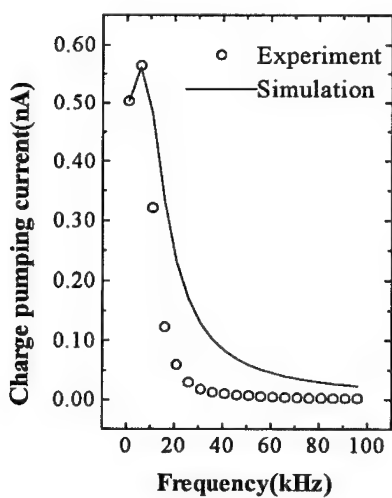


Fig. 4 Experimental values of I_{cp} in poly-Si TFT and MOSFET for gate pulse frequency.



(a)



(b)

Fig. 5 Simulation results and experimental values. (a) is for $W/L=30\mu\text{m}/20\mu\text{m}$ and (b) for $W/L=105\mu\text{m}/20\mu\text{m}$.

The devices are n-channel poly-Si TFT fabricated in the mid temperature(600°C). The thickness of gate oxide and poly-Si film is about 35nm, 100nm respectively. The ratio of width to length is 30 μ m/20 μ m and 105 μ m/20 μ m. For comparison, we prepared MOSFET whose W/L is 20 μ m/0.8 μ m.

In Fig. 4, the experimental results are illustrated. In low frequency, the device whose gate area is larger generates more charge pumping current. I_{cp} , however, starts to fall at lower frequency in W/L=105/20 than W/L=30/20. This is reasonable because longer width results in larger equivalent resistance for holes. But, in MOSFET I_{cp} is proportional to the gate pulse frequency linearly as predicted in Eq. (1).

The simulation results based on our new model coincides with the experiment as shown in Fig. 5. But difference becomes larger as the frequency increases. This may be originated in the fact that the distribution of grain boundary trap density for time constant isn't considered in our model. Therefore, further study is needed to obtain more advanced equation including the time constant distribution. And the extracted parameters are $R_{eq}=55G\Omega$, $N_{gt}=6.33\times10^{10}cm^{-2}$ for 30/20 and $200G\Omega$, $0.43\times10^{10}cm^{-2}$ for 105/20 with $V_H=5V$, $V_L=-5V$, $V_t=3V$, $V_{FB}=-1V$, $v_{th}=1.0\times10^7cm/s$ and $V_{sub}=3\times10^{-11}cm^{-3}$ and $9\times10^{-11}cm^{-3}$. N_{gt} is calculated from the slope of I_{cp} versus frequency in low frequency range. It can be conferred from the value of N_{gt} for 105/20 that there is already considerable degradation even in a few kHz range. In simulation, capture cross section is fixed to $4\times10^{-17}cm^2$ to focus the role of substrate resistance.

IV.CONCLUSION

We find out why the distortion in the relation of I_{cp} versus gate pulse frequency appears in poly-Si TFT. The large substrate resistance of undoped poly-Si film limits the transit ability of carriers and hence sufficient trapping cannot occur in higher frequency range than $f_{critical}$. Therefore, if we evaluate the density of grain boundary traps by conventional CPM theory, the gate pulse frequency must be chosen carefully. Our model, however, includes the distortion and so, can extract the substrate resistance and capture cross section as well as the density of grain boundary traps.

Calculated N_{gt} is somewhat low and this may be because tail states cannot be evaluated by CPM in our experimental condition. Therefore, we can guess that most of grain boundary traps are located in tail states not in mid-band as evaluated by a few^{8,10}. Therefore, to obtain more accurate value we correct our results by deviding with (E_h-E_l) .

REFERENCE

1. S. Morozumi, Japan Display Sym. Tech. Dig. 148 (1989).
2. K. Sasaki et.al., Dig.Tech.papers of 1989 IEEE Int. Solid-State Circuits, 34.
3. J. Levinson et.al., J. Appl. Phys. **53** (2), 1193 (1982).
4. M. Koyanagi et.al., IEDM Dig. 863 (1990).
5. M. Koyanagi et. al., IEEE Electron Device Letters, **13**, 152 (1992).
6. J. S. Brugler and P. G. A. Jesper, IEEE Trans. Electron Devices, ED-16, 297 (1969).
7. John Y.W. Seto, J. Appl. Phys. **46**, 5247 (1975).
8. H. C De Graff, M. Huybers and J. G. De Groot, Solide State Electron. **25**, 67 (1982).
9. R. A. Wachnik and J. R. Loweny, Solid State Electron. **29**, 447 (1986).
10. S.Hirae, M.Hirose and Y. Osaka, J. Appl. Phys. **51**, 1043 (1980).

ANALYSIS AND CONTROL OF THE PERFORMANCE-LIMITING DEFECTS IN HEM-GROWN SILICON FOR SOLAR CELLS

CHANDRA P. KHATTAK*, AND FREDERICK SCHMID*, MICHAEL CUDZINOVIC**,
MARTHA SYMKO**, AND BHUSHAN L. SOPORI**

*Crystal Systems, Inc., 27 Congress Street, Salem, MA 01970-5597

**National Renewable Energy Laboratory, 1617 Cole Boulevard, Golden, CO 80401-3393

ABSTRACT

Multicrystalline silicon ingots of 55 cm x 55 cm cross section, 100 kg have been grown by the Heat Exchanger Method (HEM). Controlled growth features have been used to produce large grain size, vertically oriented grain boundaries, large areas of twins with low defect density and rejection of impurities to the top of the ingot. Ambient control has reduced C, N, and O concentration and minimized precipitates with no detectable metallic impurities. High performance solar cells have been fabricated, and further improvements can be achieved by minimizing dislocation tangles and impurities in localized regions.

INTRODUCTION

It is recognized in the photovoltaic industry that crystalline silicon produced by ingot technologies can meet the near-term cost and efficiency demands for commercial production of high performance solar cells. For the long range, it is necessary to reduce the production cost of ingot technologies further to compete with the projected cost of alternative materials in thin film form. This can be done with larger ingots, and these cost reductions must not be achieved at the expense of degradation in quality of the material produced.

A number of multicrystalline ingot production processes [1-6] are being pursued for economic production of silicon ingots. One such process is the Heat Exchanger Method (HEM) which is a single crystal growth process adapted for multicrystalline silicon ingot growth. Ingots up to 55 cm x 55 cm cross section, weighing 100 kg have been produced with uniformity in properties to produce large area solar cells [7]. In an effort to further improve the performance of solar cells, emphasis has been placed on understanding the performance-limiting defects and impurities and developing procedures to control these defects and impurities.

Solidification by HEM with a nearly planar solid-liquid interface to produce large regions of nearly zero dislocation density have been developed. The control of the growth ambient yields material of low carbon and oxygen concentrations with minimal precipitate formation, residual metallic impurities, and only localized regions of dislocation networks.

HEAT EXCHANGER METHOD

The Heat Exchanger Method (HEM) is a single crystal growth process which is used in production for 20 cm and 25 cm diameter, high-quality sapphire crystals for optical applications [8-10]. Sapphire crystals up to 33 cm diameter have been grown in research and development.

This process was adapted for production of large, square cross-section silicon ingots for photovoltaic applications. Nearly single crystal ingots of 33 cm x 33 cm cross-section, 35 kg were produced [11]. It was demonstrated that the large grain multicrystalline areas of the ingot yielded solar cell performance similar to that of single crystal areas [12]. It was recognized that further cost reductions could be achieved by production of multicrystalline silicon ingots with uniformity in properties by decreasing the labor costs and increasing the growth rates. Modifications were made to the heat extraction system so that heat was extracted during the growth stage through the entire bottom of the crystal. An additional advantage was that as the cross-section of the ingot was increased, the heat extraction area increased correspondingly. The control system inherent in the HEM was retained even for multicrystalline silicon ingot growth. With this approach, a nearly planar solid liquid interface was produced. This resulted in material that had nearly vertical grain growth, low residual stress, low defects, and impurities. Silicon ingots of 44 cm x 44 cm, 80 kg were grown in production [13]. The cycle time of approximately 44 hours was similar to the 33 cm x 33 cm cross section, 40 kg ingots. The uniformity of large grain size and vertical orientation of the grain boundaries for a 44 cm square cross-section ingot is shown in Fig. 1.

Multicrystalline silicon ingot growth by HEM is carried out in a Si_3Ni_4 based coated silica crucible [7]. This coating prevents the attachment of the silicon ingot to the silica crucible at high temperatures and, therefore, cracking of the ingot is eliminated. At the melting point of silicon this coating is destabilized under vacuum and, therefore, argon gas is used as the growth ambient. The furnace pressure is controlled during the growth stage so that silicon contains low oxygen and carbon concentrations. The source of oxygen in silicon is primarily due to the silica crucible. When a non-oxide ceramic was used as a reusable crucible with HEM, the oxygen concentration in the silicon was reduced to less than 1 ppma [14]. Growth of multicrystalline silicon ingots by HEM is achieved by controlling the heat extraction through the bottom of the crucible. Therefore, a temperature gradient is imposed on the ingot during the growth stage. This temperature gradient can lead to stress in the ingot and, therefore, to a high defect density in the silicon. After complete solidification by HEM, the furnace temperature can be reduced below the melting point of silicon, and the temperature gradient on the ingot can be reduced to achieve annealing of the ingot prior to cool down. This in situ annealing of the ingot reduces the defect density in the silicon. In an effort to improve the quality of multicrystalline HEM silicon produced routinely, detailed characterization of defects and impurity contamination was carried out. This data was used to optimize the growth parameters of HEM. Most of this development was carried out for 33 cm x 33 cm size ingots, and after characterization, these procedures were implemented for the production of 44 cm square ingots. During this characterization emphasis was placed on mapping of properties so that the uniformity of improvements could also be evaluated.

DIRECTIONAL SOLIDIFICATION

Most impurities in silicon have an equilibrium segregation coefficient of less than one. Therefore, during directional solidification from the melt, highest purity silicon is solidified initially, and most of impurities are rejected in the last material to freeze. In addition, it is important that there are no impinging interfaces because, under these circumstances, the impurities will be dumped in these areas. It is also important that uniform growth rates are achieved with control of the solid-liquid interface. Therefore, for square cross section ingot

growth proceeding from the bottom of the crucible towards the top with a nearly planar solid-liquid interface, the last material to solidify should be near the top corners of the ingot.

Since silicon undergoes expansion upon solidification, the last material to freeze should be tips at the top corners of the ingot. Under these circumstances most impurities will be rejected near the top surface of an HEM ingot. Some contamination and stress is also expected near the outside surfaces of the ingot in contact with the crucible. Therefore, it is essential to remove the surface layer off an HEM ingot prior to use for photovoltaic applications. Detail characterization was carried out on the bulk of the ingot to quantify the degradation of material quality. It was observed that there was some degradation in material quality along the height of the ingot; however, there was no observable difference along the length and width of the ingot. The material close to the bottom and the top of the ingot showed some degradation, whereas the bulk of the remainder ingot showed uniformity in properties. Based upon this observation, characterization was carried out for silicon pertaining to top, middle, and bottom of the ingot.

CHARACTERIZATION

Different characterization techniques were used to characterize the top, middle, and bottom of HEM ingots. The top and bottom sections corresponded to areas within 2.5 cm from these surfaces. The characterization data reported pertains to typical values of several ingots; the trends were quite similar with some differences in absolute values.

Diffusion Length Measurements

A 10 cm x 10 cm wafer of HEM silicon was polished and mapped for diffusion length and lifetime. Data corresponding to a 10 cm diameter area of the wafer from the middle portion of the ingot is shown in Fig. 2. This data shows a high degree of uniformity with average value of diffusion length of $96 \pm 16 \mu\text{m}$ for as-grown silicon. The average lifetime value was $2.35 \pm 0.75 \mu\text{s}$. Data taken for a similar wafer corresponding to the top of the boule showed a diffusion length of 15 ± 12 with a maximum value of $121 \mu\text{m}$. This degradation is attributed to rejection of impurities near the top section of the ingot; however, localized areas still show long diffusion lengths. A sample corresponding to an area approximately 2.5 cm from the top surface exhibited a diffusion length of 67 ± 58 with localized area up to $269 \mu\text{m}$. This data shows that the degradation in diffusion length of as-grown silicon is limited to about 2.5 cm from the top surface of the boule for as-grown multicrystalline HEM silicon.

Carbon and Oxygen Concentrations

Samples of HEM silicon corresponding to top, middle, and bottom portions of a typical ingot were characterized for carbon and oxygen concentrations. This analysis was carried out using Fourier Transform Infrared (FTIR) spectroscopy, and diffusion length measurements were also carried out using SPV.

This data is shown in Table I for ingot #14. It can be seen from this data that the oxygen concentration decreases along the height of the ingot. This is attributed to the effect of

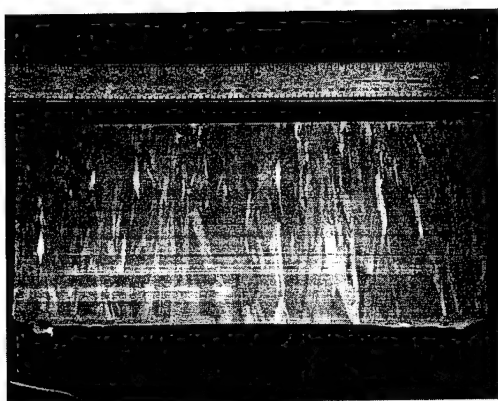


Figure 1: Photograph of a HEM silicon ingot. Note the large vertical grain growth.

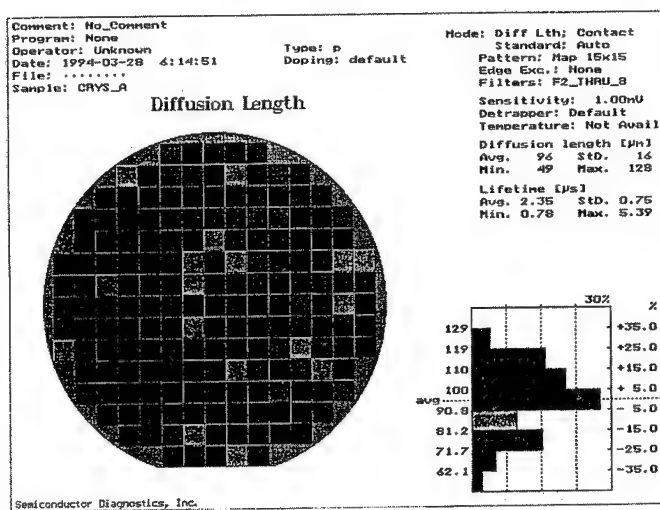


Figure 2: Diffusion length map of a 10 cm diameter area from the middle of an ingot. The diffusion length is very uniform over the region.

atmosphere during growth; the silicon at the bottom of the boule had minimal exposure to the ambient of the furnace as compared to the material at the top of the ingot, which showed significant reduction in oxygen concentration. The carbon concentration showed little change with a slight tendency to increase along the height for this boule; this slight increase was not always observed. The data on Table I also shows that the typical diffusion length values are quite uniform within the ingot except near the top of the ingot. Process changes were made to the HEM solidification to improve the uniformity of silicon for the bulk of the ingot, and the data for ingot 217K is also shown in Table I. For this ingot the sample designated top was taken approximately 2.5 cm from the top surface. It can be seen that for these samples, the diffusion length and carbon and oxygen concentrations show very good uniformity.

Slices from top, middle, and bottom sections of HEM multicrystalline silicon ingots were mapped for defect density using Rapid Scanning Defect Mapping System [15] at NREL. The samples showed low defect density, and a typical sample is shown in Fig. 3. The defect maps showed a low "background" defect density ($\sim 10^4 \text{ cm}^{-2}$), corresponding essentially to dislocation-free material. In some localized areas, the defect density increased, but only slightly. A wafer from a middle portion of the ingot was also characterized for defect distribution. This data for ingot 251K is shown in Fig. 4. This sample also shows low defect density with some localized areas of slightly higher defect density. Some of these localized areas were measured for diffusion length, and these values are also shown in Fig. 4. A comparison of the defect map for the diffusion length data shows very little correlation; even the higher defect density regions show long diffusion length.

Optical Microscopy

The characterization data on several HEM silicon ingots showed that generally, the material was of high quality with long diffusion lengths for as-grown material and low defect density in the bulk of the boule. However, there were localized areas which may be limiting the performance for photovoltaic applications. Emphasis was placed on characterizing these localized problem areas for defect density and impurities concentrations. Figure 5 shows three types of areas observed at 200X magnification for ingot 251K. The bulk of the material was typical of Figure 5a, showing a high density of parallel twins with regions of low defect density. Localized areas of dislocation tangles are shown in Fig. 5b. Figure 5c shows regions of low defect density, dislocation tangles, and dislocations in close proximity.

Impurity Analysis

The localized areas of high defect density were characterized by Auger Spectroscopy. It was expected that the regions of high defect density may be associated with high concentration of impurities as well. Auger Spectroscopy did not show detectable impurity concentrations in these areas. This may be because, even in these localized areas, the impurity concentration is below the detectability limit of Auger Spectroscopy. Samples of HEM silicon were, therefore, characterized at University of Southern Florida. Measurements of diffusion length along with Fe and Cr concentrations in dissolved form for as-grown multicrystalline silicon samples were carried out. Linear scans of diffusion lengths were used to measure the concentration of non-precipitated Fe and Cr in the present form of Fe-B and Cr-B pairs. The Fe and Cr concentrations

Sample	Carbon (ppma)	Oxygen (ppma)	Diffusion Length (μm)
Ingot 14: wafer 6	8.42	1.92	80
wafer 71	9.06	3.67	73
wafer 145	7.86	4.48	78
Ingot 217K, wafer 5	9.70	5.30	166
wafer 54	10.6	4.90	181
wafer 108	9.50	2.30	215

Table 1: This table shows the carbon and oxygen concentration and diffusion length versus position in HEM ingots.

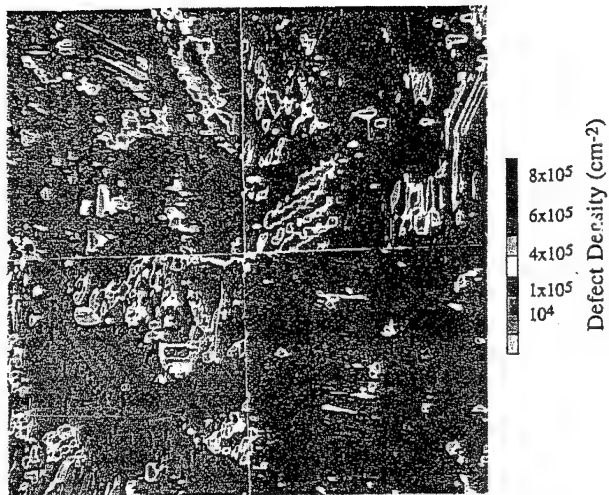


Figure 3: Typical defect density map of HEM silicon. There is a low background defect density with isolated regions of higher density.

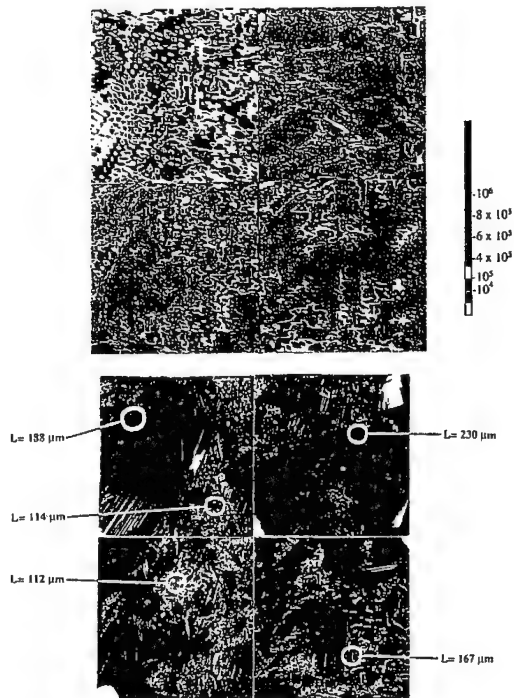


Figure 4: Defect density (a: top) and lifetime (b: bottom) map for an HEM wafer. Note the diffusion length is high even in high dislocation regions.

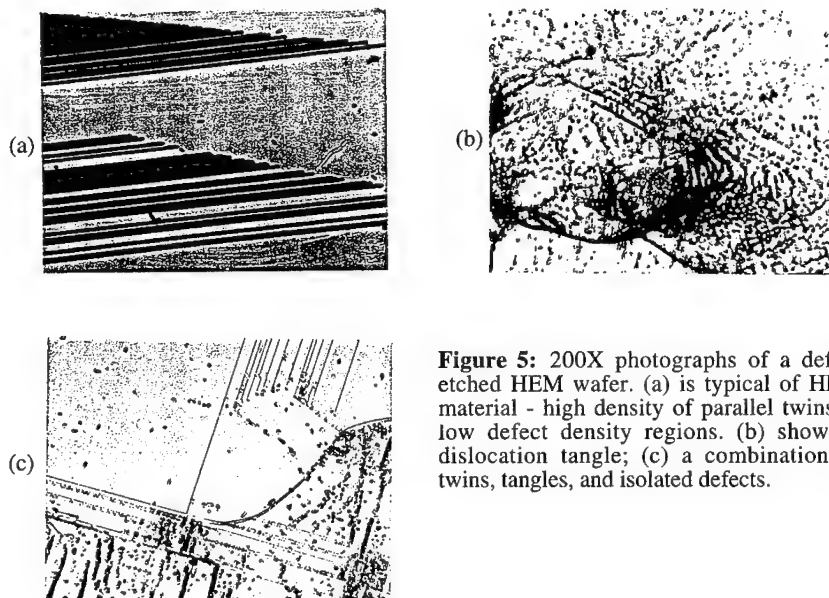


Figure 5: 200X photographs of a defect etched HEM wafer. (a) is typical of HEM material - high density of parallel twins in low defect density regions. (b) shows a dislocation tangle; (c) a combination of twins, tangles, and isolated defects.

were determined from changes in diffusion lengths upon optical and thermal activation, which led to the disassociation of Fe-B and Cr-B pairs, respectively and the formation of Fe and Cr interstitial. This data showed that the Fe-B pairs in HEM multicrystalline silicon is less than 10^{12} cm^{-3} . The primary metallic impurity detected in these samples was Cr, which was approximately at 10^{12} cm^{-3} level.

Solar Cell Performance

Multicrystalline HEM silicon has been used in solar cell fabrication at several laboratories. University Center of Excellence for Photovoltaics and Education, Georgia Institute of Technology, has produced 17.4% efficiency (1 cm^2 area) solar cells. Sandia National Laboratories produced several high performance devices of 42 cm^2 area and achieved up to 16.3% efficiency. HEM multicrystalline silicon has been used by Sandia to produce world's first multicrystalline silicon solar cell module with over 15% efficiency [16]. This has been achieved with production of large area cells that have a very narrow distribution [17]. A systematic evaluation of solar cell performance as a function of height of the ingot showed that the bulk of the material in the boule showed high performance with degradation for wafers corresponding to the very top and bottom of the ingots. Based upon the characterization data, the slight deterioration at the bottom of the ingot may be due to thermal stress because this material under goes maximum thermal gradient during ingot growth. The degradation near the top of the ingot may be due to segregation of the impurities during growth. Diffusion length mapping correlation of characterization data showed that the degradation of solar cell performance near the top of the boule was limited to a smaller distance, as compared to the characterization data. This discrepancy may be due to segregation of fast diffusing impurities (such as Cr) near the top of the ingot. During P diffusion, these impurities may be gettered, thereby leaving the substrate free of these impurities.

CONCLUSIONS

The HEM is a low-cost process capable of producing large $55 \text{ cm} \times 55 \text{ cm}$ cross-section multicrystalline silicon which is useful for making high efficiency solar cells. This single crystal growth process has been adapted to produce multicrystalline silicon ingots with large grain sizes, vertical orientation of the grain boundaries, low "average" dislocation density, large areas of twinning corresponding to low defect density. Controlled growth features of the process have been used for achieving effective segregation of impurities so that most of the impurities are rejected to the last material to freeze near the top of the ingot. Ambient control during the growth has allowed control of carbon and oxygen concentrations to lower values. Uniform growth conditions favor low precipitation of impurities and low density of particles. The precipitates in localized areas are a complex mixture of C, N, and O with no detectable metallic impurities. The Cr concentration observed (10^{12} cm^{-3}) can be gettered during the cell fabrication process, thereby leading to improved diffusion lengths in the multicrystalline silicon. The uniformity of properties of HEM silicon ingots is high, and the low diffusion length regions are limited to the surfaces of the ingot. High performance solar cells have been fabricated, and the limitation to further improved performance appears to be few localized regions of dislocation tangles and impurities at lower levels.

ACKNOWLEDGMENTS

A portion of the work reported in this paper was carried out under the Cooperative Research and Development Agreement (CRADA) between Crystal Systems, Inc. and the National Renewable Energy Laboratory (NREL). The authors thank W. K. Schubert for the solar cell fabrication and characterization data, and contributions from A. Rohatgi and L. Jastrzebski for solar cell fabrication and characterization of impurities are also appreciated.

REFERENCES

- [1] C. P. Khattak and F. Schmid, In: *Proc. 13th IEEE Photovoltaic Specialists Conf.*, Washington, D.C., 1978 (IEEE, New York) p. 137.
- [2] W. F. Regnault and K. C. Yoo, In: *Proc. 17th IEEE Photovoltaic Specialists Conf.*, Kissimmee, FL, 1984 (IEEE, New York) p. 286.
- [3] J. Fally and C. Guenel, In: *Proc. 3rd E. C. Photovoltaic Solar Energy Conf.*, Cannes, France, 1980 (Reidel, Dordrecht) p. 598.
- [4] D. Helmreich, In: *Silicon Processing for Photovoltaics II*, eds. C. P. Khattak and K. V. Ravi, 1987 (North-Holland, Amsterdam) p. 97.
- [5] I. A. Dorrity, B. J. Garrard and D. A. Hukin, In: *Proc. 10th E. C. Photovoltaic Solar Energy Conf.*, Lisbon, Portugal, 1991 (Kluwer, Dordrecht) p. 317.
- [6] W. Koch, W. Krumbe and I. A. Schwirlich, *Proc. 11th Photovoltaic Solar Energy Conf.*, Montreaux, Switzerland, 1992 (Harwood Academic Publ.) p. 518.
- [7] C. P. Khattak, F. Schmid and W. K. Schubert, *Proc. 1st World Conf. on Photovoltaic Energy Conv.*, Waikoloa, HI, 1994 (in press).
- [8] F. Schmid and D. Viechnicki, *J. Am. Ceram. Soc.* **53**, 528 (1970).
- [9] F. Schmid and C. P. Khattak, *Laser Focus* **19** (9) 147 (1983).
- [10] F. Schmid, C. P. Khattak and D. M. Felt, *Am. Ceram. Soc. Bull.* **73** (2) 39 (1994).
- [11] F. Schmid and C. P. Khattak, *Optical Spectra* **15** (5) 65 (1981).
- [12] K. A. Dumas, C. P. Khattak and F. Schmid, *Proc. 15th IEEE Photovoltaic Specialists Conf.*, Orlando, FL 1981 (IEEE, New York) p. 954.
- [13] C. P. Khattak, F. Schmid, D. W. Cunningham and J. G. Summers, *Proc. 22nd IEEE Photovoltaic Specialists Conf.*, Las Vegas, NV, 1991 (IEEE, New York) p. 976.
- [14] C. P. Khattak, F. Schmid, W. K. Schubert, M. Cudzinovic and B. L. Sopori, *Proc. 23rd IEEE Photovoltaic Specialists Conf.*, 1993 (IEEE, New York) p. 73.

-
- [15] B. L. Sopori, R. Murphy and C. Marshall, *Proc. 23rd IEEE Photovoltaic Specialists Conf.*, 1993 (IEEE, New York) p. 190.
 - [16] D. L. King, W. K. Schubert and T. D. Hund, *Proc. 1st World Conf. on Photovoltaic Energy Conversion*, Waikoloa, HI, 1994 (in press).
 - [17] W. K. Schubert, D. S. Ruby, P. A. Basore, J. M. Gee, M. E. buck and H. L. Tardy, *Proc. 1st World Conf. on Photovoltaic Energy Conversion*, Waikoloa, HI, 1994 (in press).

RESOLVING DEGRADATION MECHANISM IN CARBON AND BERYLLIUM DOPED HBT's USING PULSED MODE CURRENT STRESS

Y.C.CHOU AND G.P.LI

Department of Electrical and Computer Engineering, University of California, Irvine, CA. 92717

C.S.WU, PETER CHU, C.K.PAO AND T.C.CISCO*

Microelectronics Division, Hughes Aircraft Company, Torrance, CA 90505

* Radar System Group, El Segundo, CA 90245

ABSTRACT

The reliability of high performance carbon and beryllium-doped heterojunction bipolar transistors (HBT's) is investigated using a pulsed mode current stress. After the current stress, the collector current reduction (measured at a fixed V_{be}) and the inverted collector current ratio change (measured at two different reverse V_{be} biases) are used as measures of HBT degradation due to dopant acceptors migration. For carbon and beryllium doped HBT's, degradation was found to be only significant beyond a threshold current density (J_{th}), showing that the carbon doped devices have a higher J_{th} than that of the Be-doped HBT's. Beyond the J_{th} , the device degradation is insensitive to the stress current density but depends on the total stress charge. As a result, the device degradation mechanisms of electric field assisted dopant and carrier recombination enhanced dopant migration can be distinguished under pulsed mode current stress.

INTRODUCTION

While HBT technology has reached a certain degree of maturity, there is still little device reliability information available to warrant a widespread acceptance of this class of devices in military and commercial applications. This is partially due to the complicated device degradation characteristics associated with the device fabrication processes and to a lack of the understanding of device degradation mechanisms. Therefore, the investigation of degradation mechanisms on HBT devices is essential to help establish a credible reliability baseline for HBT technology.

M.E.Hafizi and O.Nakajima et al. were among the first to investigate the current induced degradation of I-V characteristics in Be-doped AlGaAs/GaAs HBT's under forward current stress^{1,2}. They attributed the mechanism to diffusion of the positively charged Be^+ interstitial atoms from the base into the emitter, resulting in a reduction of collector current and a B-E junction turn-on voltage shift. The diffusion of Be^+ interstitial is only activated under forward applied bias. On the other hand, based on the studies on degradation in tunnel diode, Masashi et al. identified the degradation mechanism in Be doped GaAs due to a recombination-enhanced impurity diffusion process³. Despite that the current induced degradation in Be-doped AlGaAs/GaAs HBT's can be suppressed either by Zn diffusion into extrinsic base layer² or a MBE growth condition of reducing substrate growth temperature and increasing As₄/Ga flux ratio^{4,5}, there is still no comprehensive understanding on the degradation mechanisms in Be-doped AlGaAs/GaAs HBT's.

In contrast to Be-doped HBT's, carbon-doped HBT's show better reliability results because of a smaller diffusion coefficient for carbon than for Be^{6,7}. Nevertheless, carbon-doped HBT's still degrade under forward current stress. The degradation characteristics depend on the process technology⁸, stress techniques⁹, recombination rates in the emitter-base space charge region¹⁰, surface passivation at the extrinsic base¹¹, and the generation of midgap traps in the base layer via electron-hole recombination process¹². Evidently, the major degradation mechanisms are very complicated. Thus, it is desirable to unveil the degradation mechanism in the HBT's. In this paper, we report the investigation of degradation mechanisms in Be- and C-doped AlGaAs/GaAs HBT's using a pulsed mode current stress.

EXPERIMENTS

A pulsed mode current stress was applied to Be- and C-doped AlGaAs/GaAs HBT's at room temperature. The emitter geometry of Be- and C-doped devices is $3 \times 10 \text{ } \mu\text{m}^2$ and $5 \times 5 \text{ } \mu\text{m}^2$, respectively. The HBT's layers were grown by molecular beam epitaxy (MBE) or metal organic chemical vapor deposition (MOCVD) for Be- and C-doped devices, respectively. The Be- and C-doped base layers have a doping concentration of $1 \times 10^{19} \text{ cm}^{-3}$ and $4 \times 10^{19} \text{ cm}^{-3}$, respectively. Both devices utilize a compositionally graded layer on both sides of the emitter layer.

Figure 1 shows a typical pulsed mode current stress setup for the reliability study. A HP 8610A programmable pulse generator was used to provide the stressing pulse signal. By adjusting the pulse width and height as well as the duty cycle, HBT's can be stressed at different current density but with the same amount of stress charge. A typical duty cycle is 1%. Consequently, device degradation induced by the conventional forward constant current stress such as ohmic contact migration and a self heating effect may be alleviated. A small resistor connecting to the emitter lead is used to measure the peak stress current density. The stress current density is in the range of $0.1 \text{ mA}/\mu\text{m}^2$ to $1 \text{ mA}/\mu\text{m}^2$.

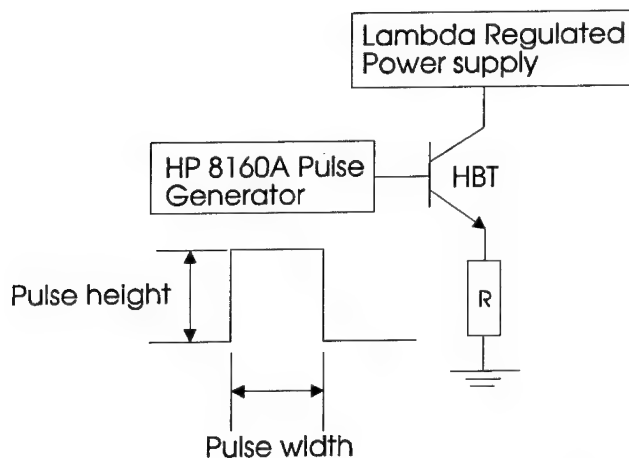


Fig. 1. Experimental setup for pulsed mode current stress.

INVERTED MODE MEASUREMENT

The collector current ratio (R ratio spectrum) measured at $V_{\text{hetero}}=2/0$ volt as a function of homojunction forward bias in the inverted mode configuration was used to resolve the degradation mechanism in Be-doped AlGaAs/GaAs HBT's under forward current stress¹³. The detailed derivation of the analytic equation and physical explanation of this novel technique can be found elsewhere¹³. Here, we adopt this technique for a measure of base dopant out diffusion in Be- and C-doped devices subjected to the pulsed mode current stress.

Figure 2 shows a typical experimental R ratio shape as a function of V_{homo} on Be-doped HBT's, illustrating the U-shape characteristic. At low V_{homo} , the ratio is governed by the reverse leakage current. The change of R is an indication of changes in the effective generation/recombination centers or the width variation in the space charge region. At high V_{homo} , the series resistance dictates the R ratio value. As a result, this part of R ratio curve can be used to monitor the contact integrity. In this paper, we use the bottom value of R ratio curve as an indicator of device degradation, i.e. the potential barrier formation due to acceptor dopant migration.

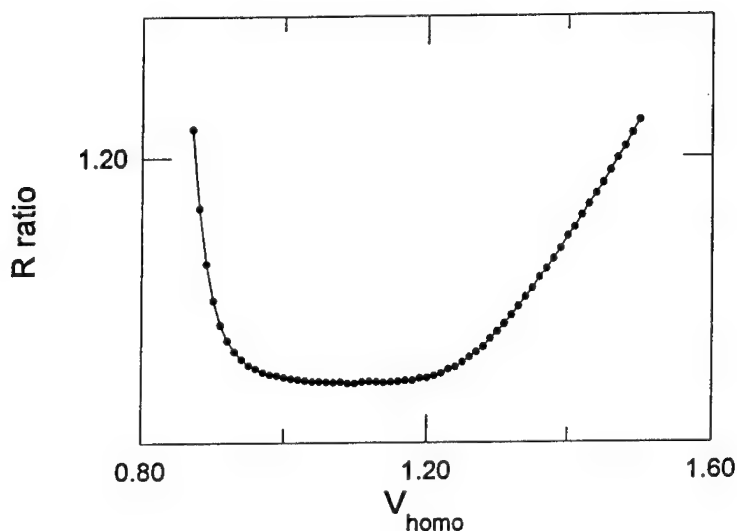


Fig. 2. The typical shape of a R ratio curve measured as a function of V_{homo} in the inverted mode configuration.

R ratio increase indicates that a conduction band barrier is formed in the heterojunction, resulting in a reduction of collector current¹³. In our experiment, an increase of R ratio was also observed under pulsed mode current stress, accompanying a decrease of collector current. As shown in Fig.3, the R ratio variation as a function of stressed current density also tracks well with collector current change. Therefore, collector current change is an alternative for measuring the device degradation.

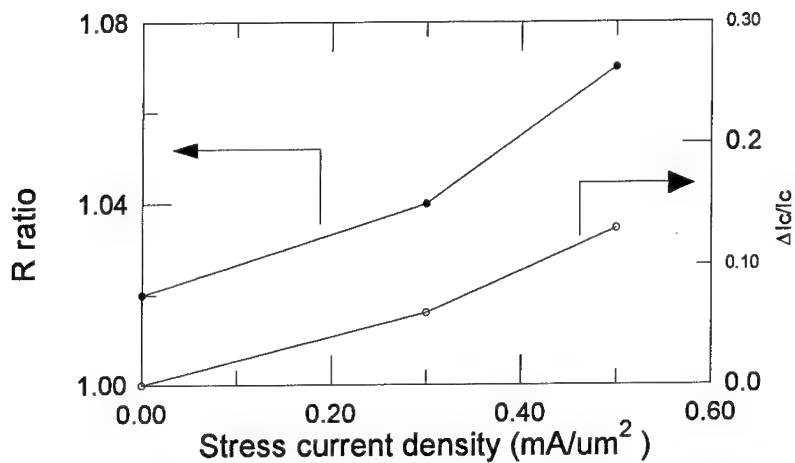


Fig.3 R ratio variation and collector change as a function of stress current density.

RESULTS AND DISCUSSIONS

The collector current changes as a function of stress current density and total stress charges in carbon-doped AlGaAs/GaAs HBT's are shown in Fig.4 (a) and (b) respectively. Clearly, a threshold of 0.5 mA/um^2 independent of total stress charge is observed. Beyond the threshold current density, the device degradation is found to be insensitive to the stress current density (for a fixed stress charge), but depends on the stress charge. The higher the stress charge is used, the more degradation in HBT's is observed.

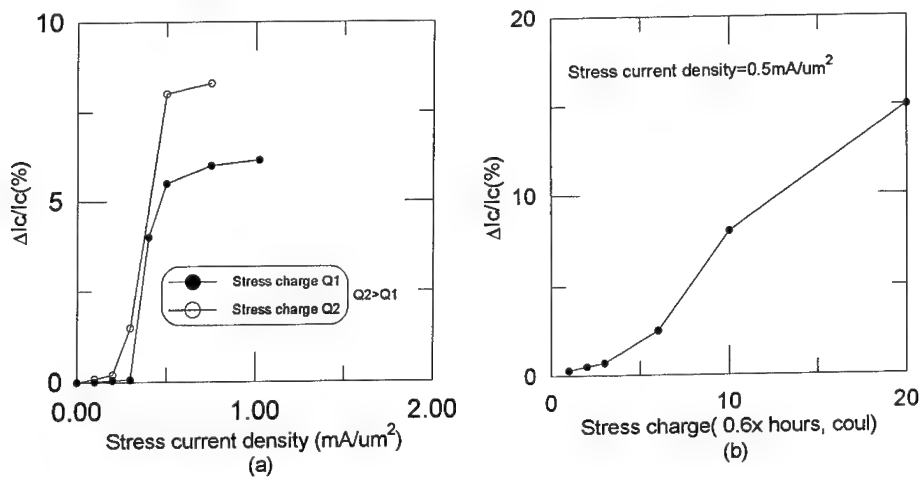


Fig. 4. (a) Collector current change versus stress current density in carbon-doped devices.
(b) Collector current change versus total stress charges in carbon-doped devices.

Figure 5 compares the stress results of Be- and C-doped AlGaAs/GaAs HBT's. While Be-doped devices shows a similar trend of threshold current density dependency, its value is smaller than carbon-doped devices. With the same stress charge as C-doped devices, J_{th} in Be-doped devices is approximately $0.25 \text{ mA}/\mu\text{m}^2$.

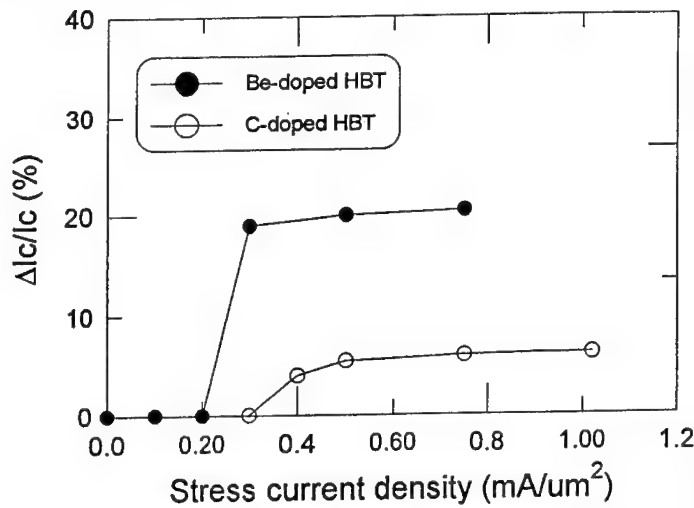


Fig.5 Collector current change versus stress current density in Be- and C-doped devices.

The device degradation is only observed in devices under forward current stress, suggesting that the degradation is related either to the minority carrier injection or to the applied electric field at the junction. If one believes the hypothesis of electric field assisted diffusion, the results of dopant migration in both carbon and Be doped HBTs during current stress imply that the interstitials of C or Be are positively charged in GaAs. The positively charged interstitials of C and Be are very unlikely to be observed in GaAs. In addition, the electric field assisted diffusion model could not explain the degradation results saturated at even higher stress current densities as shown in Fig. 5. On the other hand, the electron-hole recombination can take place upon the minority carrier injection and release its electronic energy to the lattice vibration, enhancing diffusion of vacancy/interstitial defects. When the interstitials of carbon or beryllium migrate to the Ga or As vacancy site, respectively, they become substitutional acceptors of Be_{Ga} or C_{As} , which are electrically activated at room temperature. If these events occur at the heterojunctions, the potential barrier for electron injection will increase, resulting in a reduction in collector current¹³. Based on this proposed model, a supply of vacancies and its subsequently limited enhanced diffusion to the heterojunction interface due to a finite number of recombination events may account for such an observation as the collector current reduction depends on the total injection charges (stress charges) and is insensitive to the stress current density as long as above the threshold. If a low stress current density (below threshold) is used, the process of enhanced diffusion of vacancies may be incoherent due to a random nature of diffusion process and thus a reduction of collector current is absent. On the other hand, the enhanced diffusion of vacancy is coherent and follows the current injection path for the stress condition above threshold. Following this argument, the observed threshold dependence on the C- and Be- doped samples can be attributed to the difference in the enhanced diffusion of associated Ga or As vacancies.

SUMMARY

We have performed the reliability investigation in Be- and C-doped AlGaAs/GaAs HBT's using a pulsed mode current stress. By using this stress technique, devices would not suffer from the contact migration and self-heating effects. An inverted Gummel measurement is used as a measure of device degradation. The devices start to show pronounced degradation after the stress current density reaches a threshold current density. The threshold current density of C-doped HBT's is higher than that of Be-doped devices. Beyond the threshold current density, the device degradation is not affected by the current density, but depends on the stress charge. It suggests that carrier recombination enhanced dopant diffusion should be a root cause of the device degradation.

REFERENCE

1. M. E. Hafizi, L.M. Pawlowicz, L.T. Tran, D.K. Umemoto, A.K. Oki, M.E. Kim and K.H.Yen, Technical Digest of GaAs IC Symposium, 1990, p329.
2. O. Nakajima, H. Ito, T. Nittono and K. Nagata, Technical Digest of International Electron Device Meeting, 1990, p.673.
3. Masashi Uematsu and Kazumi Wada, Appl. Phys. Lett.,58, 2015(1991).
4. D.C. Streit, A.K.Oki, J.R. Velebir, K.S. Stolt and D.K. Umemoto, J. Vac. Sci. Technol.B ,10, 853(1992).
5. D.C. Streit, A.K. Oki, D.K. Umemoto, J.R. Velebir, K.S. Stolt, F.M. Yamasa, M.E. Hafizi, S. Bui and L.T. Tran, IEEE Electron Dev. Lett.12, 472(1991).
6. T. Takahashi, Y. Yanaguchi, A. Sandhu, H. Ando, T. Fujii and N. Yokoyama, Jpn. J. Appl. Phys. 30, 3843(1991).
7. F. Ren, T.R. Fullowan, L. Lothian, P.W. Wisk, C.R. Abernathy, R.F. Kopf, A.B. Emerson, S.W. Downey and S.J. Pearton, Appl. Phys. Lett. 59, 3613(1991).
8. M.R.Frei, C.R. Abernathy, T.Y. Chiu, T.R. Fullowan, J.R. Lothian, R.K. Montgomery, S.J.Pearson, F. Ren, P.R. Smith, C.W. Snyder, B. Tseng, J. Weiner, and P.W. Wisk, presented at the Dev. Res. Conf., 1994.
9. Y.C. Chou, Y.H. Chang, G.P. Li, C.S.Wu, Peter Chu, C.K.Pao, D.C. Wang and T.C. Cisco, presented at the GaAs Reliability Workshop, 1994.
10. S.J. prasad and E. Hultine, presented at the GaAs Reliability Workshop, 1994
11. Y.H. Chang and G.P.Li, to be published in the Appl. Phys. Lett. 1995.
12. T. Henderson, D. Hill, W. Liu, D. Costa, H.F. Chau and A. Khatibzadeh, Technical digest of International Electron Device Meeting, 1994.
13. Y.H. Chang and G.P. Li, IEEE Trans. Electron Devices 40, 692(1993).

DEGRADATION OF InGaAs HIGH ELECTRON MOBILITY TRANSISTORS: THE ROLE OF CHANNEL COMPOSITION AND THICKNESS

MARJOHN MESHKINPOUR*, MARK S. GOORSKY*, DWIGHT C. STREIT**, THOMAS
R. BLOCK**, AND MIKE WOJTOWICZ**

*University of California, Los Angeles, CA 90024

**TRW Space and Electronics Group, Redondo Beach, CA 90278

ABSTRACT

In this study, we examined the performance of AlGaAs/InGaAs/GaAs pseudomorphic high electron mobility transistors with varying channel layer thicknesses for indium mole fractions of 0.21 and 0.24. For both compositions, we find that there is an optimum channel thickness above which the device performance is impaired. As expected the effective critical thickness of the $\text{In}_{0.21}\text{Ga}_{0.79}\text{As}$ layer is higher. Surprisingly, however, transmission electron microscopy of the device structures indicates that the device performance is not impaired by the presence of a linear array of misfit dislocations. In fact, the devices with highest performance have misfit dislocations indicating that defect engineering may lead to improved performance in these structures. Furthermore, we find that device structures with poor performance have misfit dislocations along both of the $\langle 110 \rangle$ directions. Triple axis x-ray diffraction provides a non-destructive estimate of the dislocation densities present.

INTRODUCTION

Two ways in which to improve the performance of high electron mobility transistors (HEMTs) are by increasing the InGaAs channel thickness and the indium content. Increasing the InGaAs channel thickness results in better electron confinement by lowering the energy levels in the channel quantum well and therefore increasing the conduction band offset. However, as the InGaAs channel thickness increases, the likelihood of forming misfit dislocations to relieve the strain in the layer also increases [1]. The Matthews-Blakeslee [1] critical thickness is an equilibrium criterion which has apparently been surpassed by growing under metastable conditions [2-5]; these studies have suggested the notion that pseudomorphic InGaAs layers can be grown in excess of their critical thicknesses without the onset of misfit dislocations. Increasing the indium content also improves the carrier confinement by increasing the conduction band offset. However, the critical thickness decreases with increasing indium content or misfit. Recently, there has been considerable interest in improving the performance of high electron mobility transistors (HEMTs) by varying the InGaAs thickness and/or composition [2,4,6-8]. To date, however, the correlation between device performance and the materials issues of actual HEMT structures have not been studied extensively.

EXPERIMENTAL PROCEDURES

Two sets of samples were grown by molecular beam epitaxy [9]. One set consisted of nine HEMT structures with $\text{In}_{0.21}\text{Ga}_{0.79}\text{As}$ channel widths varying from 75 Å to 300 Å. The other set had an $\text{In}_{0.24}\text{Ga}_{0.76}\text{As}$ channel layer varying in thickness between 70 Å and 220 Å. Beginning from the (001) semi-insulating GaAs substrate, these device structures consist of a GaAs buffer, an InGaAs channel, a 530 Å thick $\text{Al}_{0.25}\text{Ga}_{0.75}\text{As}$ barrier with a δ -doped Si layer, and a 50 Å GaAs cap. High resolution x-ray diffraction was performed on a Bede D³ diffractometer. Its setup has been described elsewhere [10]. In this study, transmission electron microscopy (TEM) was performed on a Phillips CM20 microscope. The TEM samples were prepared by jet polishing in a Southbay 550 jet polisher using a 0.1 vol% bromomethanol solution. Transport properties were determined using both Hall and rf measurements [9].

RESULTS AND DISCUSSION

Figure 1 shows the variation of the sheet carrier concentration and the cutoff frequency with increasing channel thickness. Initially, the sheet carrier concentration, N_s , increases with increasing channel thickness, and then begins to decrease for a channel width of 205 Å. For thicknesses below 205 Å, this trend can be attributed to the increase in carrier confinement with increasing channel width, and therefore the increase in the 2 DEG concentration. However, for thicknesses greater than 185 Å, the carrier concentration decreases. Between an InGaAs thickness of 185 Å and 205 Å, N_s drops by $0.2 \times 10^{12}/\text{cm}^2$. Rf measurements of fabricated device structures with 0.1 μm gates also show that f_T increases with channel thickness up to 185 Å, but then decreases substantially for devices with thicker channels. This is in agreement with the work of Moll et al. [5], which indicated that the sheet concentration is the relevant parameter in predicting device figures of merit like f_T .

In our previous work [10], triple axis reciprocal space maps showed the presence of diffuse scatter along at least one of the $\langle 110 \rangle$ directions for channel thicknesses greater than or equal to 150 Å. Transmission electron microscopy confirms that the cause of this diffuse scatter is the presence of misfit dislocations along one of the $\langle 110 \rangle$ directions. Thus, device performance is not impaired by the presence of a linear array of misfit dislocations. The degree of diffuse scatter has been quantified by calculating the area under a rocking curve about the substrate peak and dividing it by the peak intensity of that curve (integral breadth [11]). direction. Figure 2 shows the variation of this integral breadth for the preferred $\langle 110 \rangle$ misfit

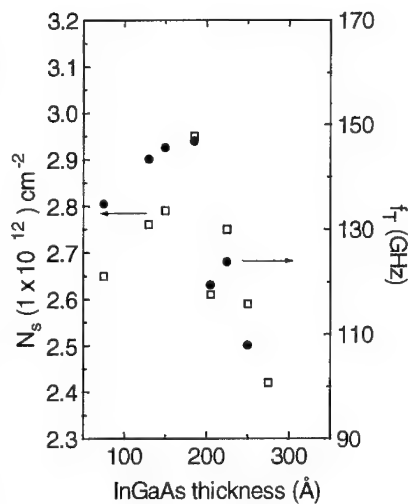


Figure 1. The variation of N_s (□) and f_T (●) with the $\text{In}_{0.21}\text{Ga}_{0.79}\text{As}$ layer thickness.

dislocation. Superimposed on that plot are the corresponding measured misfit dislocation densities. The correlation between the triple axis x-ray diffraction measurements and transmission electron microscopy is excellent. In fact, transmission electron microscopy indicates that for a channel layer thickness of 205 Å, misfit dislocations are present along both $\langle 110 \rangle$ directions suggesting that the onset of the second set of misfit dislocations is the cause for the drop in device performance.

Figure 3 shows the variation of the Hall sheet carrier concentration with increasing $\text{In}_{0.24}\text{Ga}_{0.76}\text{As}$ channel layer thickness. In this case, the drastic drop in carrier concentration occurs for a channel layer thickness of 190 Å. Thus, the effective critical thickness like the Matthews-Blakeslee critical thickness decreases with increasing strain in the layer. Furthermore, even though the maximum sheet carrier concentration is greater for the higher indium content HEMTs, its drop in N_s is more dramatic (e.g. a drop in N_s of $0.35 \times 10^{12}/\text{cm}^2$ occurs within a 15 Å increase in the InGaAs thickness). However, the maximum sheet carrier concentration is greater for the higher indium content HEMTs. TEM micro-

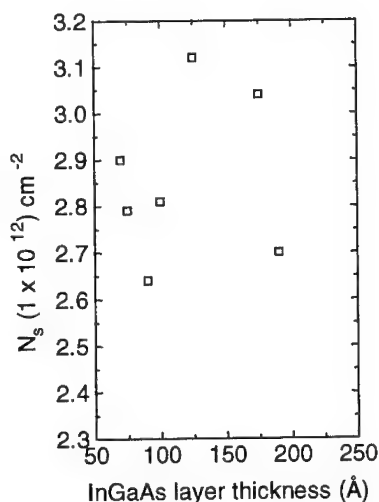


Figure 3. Variation of N_s with InGaAs layer thickness for $\text{In}_{0.24}\text{Ga}_{0.76}\text{As}$ HEMTs.

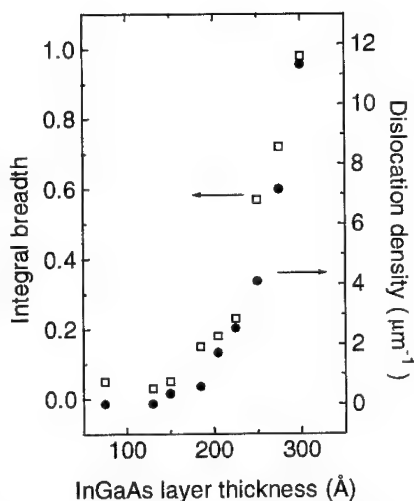


Figure 2. Comparison of integral breadth (□) and misfit dislocation density (●) for various $\text{In}_{0.21}\text{Ga}_{0.79}\text{As}$ channel thicknesses.

graphs of the $\text{In}_{0.24}\text{Ga}_{0.76}\text{As}$ HEMTs with channel thicknesses of 175, 190, and 220 Å are shown in figure 4. As in the case of the lower indium content HEMTs, the 60° misfit dislocations initially form only along one of the $\langle 110 \rangle$ directions. The second set of misfit dislocations forms for a channel thickness corresponding to the effective critical thickness (~ 190 Å). Another interesting result is the fact that at this higher indium content, segments of the $\langle 110 \rangle$ dislocations form edge misfit dislocations with line directions along one of the $\langle 100 \rangle$ directions. ((220), (2-20), (400) and (040) reflections were used to confirm that the dislocations along $\langle 100 \rangle$ are of edge character.) The origin of these misfit dislocations, however, is unclear. Some attribute [12] the edge dislocations to glide on $\{110\}$ planes suggesting that when the strain in the layer is large enough ($x > 0.35$), a second slip system is activated. Others claim that the $\langle 100 \rangle$ misfit dislocations are due to climb, and in fact have observed the presence of these $\langle 100 \rangle$ misfit dislocations for $x = 0.25$ [13] and $x = 0.2$ (upon annealing) [14]. In any case, all of these studies have cited nominal values for the InGaAs

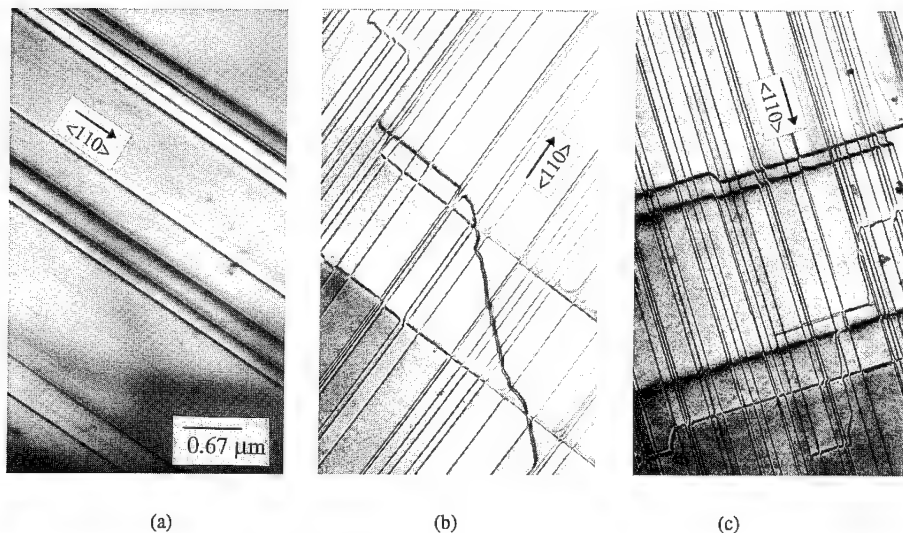


Figure 4. TEM micrographs of HEMTs with $\text{In}_{0.24}\text{Ga}_{0.76}\text{As}$ layers (a) 175 Å, (b) 190 Å, and (c) 220 Å thick.

composition. In this study, the indium mole fractions of the HEMT structures have been determined using high resolution x-ray diffraction [15] to within ± 0.005 . Thus, composition does indeed play a role in the onset of $\langle 100 \rangle$ misfit dislocations, yet the indium mole fraction at which these dislocations appear is much less than that claimed by Albrecht et al. [12].

Figure 5 shows the integral breadth and misfit dislocation density along the preferential $\langle 110 \rangle$ direction with increasing channel thickness for the higher indium content HEMTs. Like figure 2, the agreement between these two independent measurements is excellent. However, the rise in diffuse scatter with InGaAs layer thickness is steeper for the higher indium content HEMTs suggesting that the range of metastability is smaller.

Our results indicate that the device performance drops when the orthogonal array of misfit dislocations forms. It is still unclear whether the interactions between these orthogonal dislocations impairs the performance or whether the density of the first set of dislocations become significant enough to capture many of the electrons in the well.

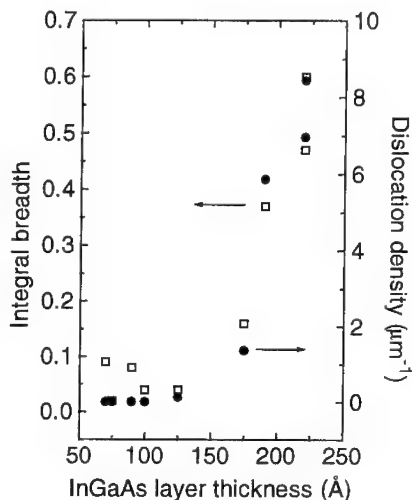


Figure 5. Comparison of integral breadth (□) and misfit dislocation density (●) for various $\text{In}_{0.24}\text{Ga}_{0.76}\text{As}$ thicknesses.

CONCLUSION

The effective critical thickness for HEMTs with $\text{In}_{0.21}\text{Ga}_{0.79}\text{As}$ and $\text{In}_{0.24}\text{Ga}_{0.76}\text{As}$ channels is approximately 205 Å and 175-190 Å, respectively. These values correspond to a drop in Hall sheet carrier concentration and the onset of the second set of misfit dislocations along $\langle 110 \rangle$. The correlation between high resolution x-ray diffraction measurements and transmission electron microscopy suggests that the former may be used to non-destructively estimate the density of misfit dislocations present in a device structure prior to further fabrication. We also observed edge misfit dislocations along $\langle 100 \rangle$ for the $\text{In}_{0.24}\text{Ga}_{0.76}\text{As}$ HEMTs.

ACKNOWLEDGEMENTS

This study has been funded by TRW, the UC MICRO program, the National Science Foundation (DMR 9208766) and the National Defense Science and Engineering Graduate Fellowship program.

REFERENCES

1. J.W. Matthews and A.E. Blakeslee, *J. Crys. Growth* **27**, 118 (1974).
2. L.D. Nguyen, D.C. Radulescu, M.C. Foisy, P.J. Tasker and L.F. Eastman, *IEEE Trans. Elec. Dev.* **36**, 833 (1989).
3. P.S. Peercy, B.W. Dodson, J.Y. Tsao, E.D. Jones, D.R. Meyers, T.E. Zipperian, L.R. Dawson, R.M. Biefield, J.F. Klem, and C.R. Hills, *IEEE Elec. Dev. Lett.* **9**, 621 (1988).
4. A. Fischer-Colbrie, J.N. Miller, S.S. Laderman, S.J. Rosner and R. Hull, *J. Vac. Sci. Technol.*, **B 6** 620 (1988).
5. N. Moll, M.R. Hueschen and A. Fischer-Colbrie, *IEEE Trans. Elec. Dev.* **35**, 878 (1988).
6. D.C. Streit, W.L. Jones, L.P. Sadwick, C.W. Kim, and R.J. Hwu, *Appl. Phys. Lett.* **58**, 2273 (1991).
7. T. Schweizer, K. Kohler, W. Rothmund and P. Ganser, *Appl. Phys. Lett.* **59**, 2736 (1991).
8. K. Maezawa and T. Mizutani, *IEEE Trans. Elec. Dev.* **37**, 1416 (1990).
9. D.C. Streit, K.L. Tan, R.M. Dia, J.K. Liu, A.C. Han and J.R. Velebir, *IEEE Elec. Dev. Lett.* **12**, 149 (1991).
10. M. Meshkinpour, M.S. Goorsky, G. Chu, D.C. Streit, T. Block and M. Wojtowicz, *Appl. Phys. Lett.* **66**, 748 (1995).
11. B.D. Cullity, *Elements of X-ray Diffraction*, Second Edition, Addison-Wesley Publishing Company, Inc., London, c. 1978.
12. M. Albrecht, H.P. Strunk, R. Hull, and J.M. Bonar, *Appl. Phys. Lett.* **62**, 2206 (1993).
13. J. Zou, C.T. Chou, D.J.H. Cockayne, A. Sikorski, and M.R. Vaughan, *Appl. Phys. Lett.* **65**, 1647 (1994).
14. Y. Chen, Z. Liliental-Weber, J. Washburn, J.F. Klem, and J.Y. Tsao, *Appl. Phys. Lett.* **63**, 2234 (1993).
15. M. Meshkinpour, M.S. Goorsky, K.M. Matney, D.C. Streit, and T.R. Block, *J. Appl. Phys.* **76**, 3362 (1994).
16. Y. Uchida, H. Kakibayashi, and S. Goto, *J. Appl. Phys.* **74**, 6720 (1993).

IMPROVED PERFORMANCE OF MESFET DEVICES WITH L.T.GaAs BUFFER LAYERS

M.LAGADAS¹, Z.HATZOPOULOS¹, F.KARADIMA¹, G.KONSTANTINIDIS¹,
N.KORNILIOS¹, C.PAPAVASILIOU¹ and A.CHRISTOU²

¹Institute of Electronic Structure and Lasers, Foundation for Research and Technology
Hellas, P.O.Box 1527, 71110 Heraklion, Crete, Greece

²University of Maryland, Dept. of Material Engineering, College Park, Maryland 20742,
USA

ABSTRACT

We have investigated the electrical properties of n-GaAs epilayers grown by MBE on the top of L.T.GaAs. The Hall mobility and the channel depth of the epilayer decreases as the growth temperature of the buffer decreases. The degradation of the electrical properties is attributed to the outdiffusion of precipitates and point defects from the L.T. buffer layer. The use of intermediate layers (GaAs grown at 400°C-600°C and GaAs/Al_xGa_{1-x}As (x=0.5, 1) superlattices) between L.T. buffer and n-GaAs active layers in MESFET devices improves the Hall mobility of the channel, the g_m and f_r performance of the devices. This improvement has been attributed to the AlGaAs layer which hinders the defects outdiffusion.

INTRODUCTION

Sidegating in molecular beam epitaxially grown FET devices has been eliminated by using high resistive GaAs buffer layers grown at low temperatures[1,2]. The high resistive layers provide good d.c. isolation (better than the other commonly used layers e.g. GaAs, AlGaAs/GaAs superlattices[3]), high d.c. output resistance and elimination of the kink effect during the device operation[4]. However the extrinsic transconductance g_m of MESFET's which employ the low-temperature buffer is 10% lower[3,5] and have 10% reduced unity gain cutoff frequency[5] than that of MESFET's with conventional buffer. These detrimental effects can be caused by point defects[2] and As-precipitates outdiffusion[6] which give rise to a lower charge concentration in the active layer on the top of the low temperature buffer.

In this work we investigate the effect of the growth temperature of the buffer layer on the electrical properties of the n-GaAs epilayers grown by MBE. Also the use of AlGaAs/GaAs superlattice and GaAs layers as barriers to defect outdiffusion between the active and the buffer layers in FET structures have been examined.

GROWTH AND CHARACTERIZATION

All layers were grown in a VGV80H MBE system, under As-stabilized conditions. (100)S.I.GaAs substrates were etched in (5:1:1) (H₂SO₄:H₂O₂:H₂O) at 70°C and

outgassed at 350°C for 1hr in UHV before been introduced in the deposition chamber. After the oxide desorption and the growth of 0.2µm GaAs layer at Tgr=580°C, the substrate temperature was ramped down to the low temperature without growth. L.T.GaAs was then grown at a growth rate of 1 µm/hr to the desired thickness. The n-GaAs active layers were grown at 580°C with a V/III beam equivalent pressure of 15.

In order to investigate the influence of the L.T.GaAs buffer layer on the electronic quality of the doped active layer, a 0.3 µm n-GaAs($2 \times 10^{17} \text{ cm}^{-3}$) layer were grown on the top of the 0.5µm L.T. buffer (fig.1). In these L.T. buffers the As-to-Ga BEP was 10. Electrolytic C-V profiling and Hall mobility at 300K in van de Pauw geometry with In contacts annealed at 400°C for 2mins were measured.

0.3µm n-GaAs,Tgr=580° C
0.5µm L.T.GaAs
0.2µm GaAs,Tgr=580° C
(100) S.I.GaAs

Fig 1.n-GaAs/LTGaAs structure for mobility and C-V profiling measurements

The FET structure consisted of 700Å⁰ n⁺-GaAs($2 \times 10^{18} \text{ cm}^{-3}$) and 1800Å⁰ n-GaAs ($4 \times 10^{17} \text{ cm}^{-3}$). Between the 0.7µm L.T. buffer (BEP=30 during L.T.growth) and the active layer of the device, AlGaAs/GaAs superlattice and GaAs intermediate layers were grown (the AlGaAs layers were grown at 600°C and the GaAs at 580°C). The structures of these layers are shown in Table1. The MESFET devices were fabricated with Au/Ge/Ni ohmic

contacts annealed at 410°C for 20secs , Ti/Pt/Au for the gate metalization. DC characterization of 1 µm gate length FET's was performed in order to measure the output resistance Ro and the variation of the transconductance as a function of the gate voltage.

RESULTS AND DISCUSSION

The electronic quality of the n-GaAs epilayers is strongly depended on the growth temperature of the buffer layer. The Hall mobility of the 0.3µm n-GaAs($2 \times 10^{17} \text{ cm}^{-3}$) as a function of the growth temperature of the buffer is shown in fig 2. For Tgr lower than 400°C there is a drastic decrease in the mobility of the n-GaAs epilayers. Electrolytic C-V

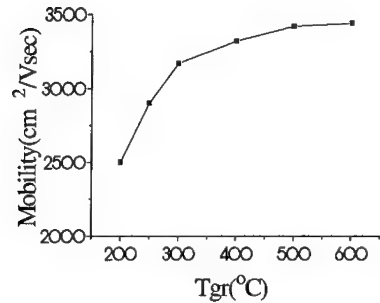
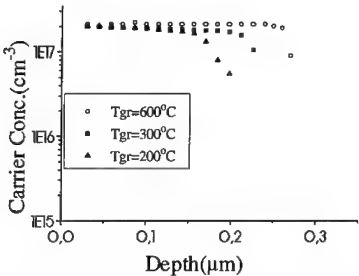


Fig 2. Mobility of n-GaAs epilayers as a function of the growth temperature of the buffer.

Fig 3. Electrochemical C-V profiling of n-GaAs epilayers as a function of the growth temperature of the buffer layer.



profiling of the doping of the n-type layer is shown in fig 3. The channel depth decreases gradually as the growth temperature of the buffer layer decreases. For the sample with the lower Tgr (200°C) the doped epilayer is almost 35% thinner (i.e. 1000Å⁰) than the sample with conventional buffer. The decreased channel depth cannot be attributed to the carrier diffusion due to the Fermi level difference between the n-type epilayer and the buffer layer. LT. GaAs is a highly resistive layer having Fermi level pinned almost at the middle of the band gap[7,8]. The built-in potential in the n-GaAs/L.TGaAs interface is expected to be lower than the V_{bi} in the n-GaAs/ GaAs interface (undoped GaAs grown by MBE at 580°C is p-type). The reduced V_{bi} leads to lower depletion width in the interface .

TEM observation on n-GaAs/L.T.GaAs structure has revealed As-precipitates outdiffusion to a depth of 2000Å⁰ into the epilayer [9] . The growth temperature was 250°C for the L.T. layers. The sample was annealed at 580°C for 1.5hrs. Based on this observation we believe that the decreased channel depth is attributed mainly to the precipitates outdiffusion. However trap outdiffusion from the buffer can not be excluded since the mobility degradation in samples with L.T. buffer reveals the presence of increased compensation ratio in n-GaAs layers. As the growth temperature of the buffer layer decreases the excess arsenic and point defects concentration increases giving rise to higher diffusion length of these defects during annealing. As a consequence the electrical properties of epilayers degrade , as we observed.

Table1 Growth and electrical characterization data for MESFET devises

Sample	Tgr of buffer	Intermediate layer	$\mu_{m,max}$ (mS/mm)	mobility (cm ² /Vsec)	f _T (GHz)	R _o (KΩ)
1335	600°C	-----	190	2730	13	1.3
1333	250°C	0.2μmGaAs,400°C 0.2μmGaAs,500°C 0.2μmGaAs,580°C	195	2720	---	0.5
1332	250°C	(300Å ⁰ Al _{0.5} Ga _{0.5} As /100Å ⁰ GaAs)x5 0.4μmGaAs,580°C	210	2750	14.5	1.5
1331	300°C	(100Å ⁰ AlAs /100Å ⁰ GaAs)x2 0.4μmGaAs,580°C	210	2710	14.5	1.5
1329	250°C	0.6μmGaAs,580°C	175	2600	8	1.6
1318	250°C	-----	155	2450	7.5	10

As the growth temperature of L.T. layers decreases their resistivity increases [10] giving better device isolation. On the other hand the electrical properties of doped epilayers degrade. In order to suppress the outdiffusion of defects, GaAs and AlGaAs/GaAs superlattices have been used, between the active and the buffer layers in FET structures. The growth temperature of L.T. buffer layers was 250°C and 300°C. Measurements of the channel mobility d.c. and r.f. characteristics of the devices are shown in Table 1. The Hall mobility was measured after the etching of the 700Å⁰ n⁺ cap layer.

The open channel current was 180-190mA/mm for all the devices except for the

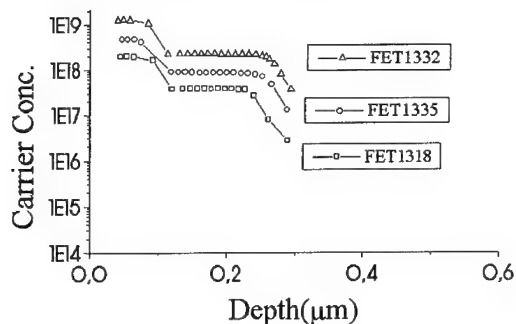


Fig 4. Electrochemical C-V of the doping profile in the FET structure. The curves are removed in their vertical position in order to compare the channel depth.

sample #1318 which has a current of 135mA/mm. The lower current for this sample is attributed to the shorter channel of this device. For that reason the pinch-off voltage for this structure was lower (-1.2Volts) than in the other devices (-1.4 Volts). The transconductance g_m was measured at $V_{DS}=2.5$ Volts and the d.c. output resistance R_o at $V_{GS}=0$ Volts.

The Hall mobility of the active epilayers is strongly dependent on the presence of intermediate layers between

the buffer and the doped channel. The lower mobility appeared in the sample with no intermediate layer, is an indication of increased compensation in the active layer. The growth of the 0.6μm GaAs intermediate layer had as a result to improve the mobility of the doped epilayer. However the mobility remains lower compared with the sample buffered by conventional GaAs. The use of GaAs grown at 400°C-600°C and AlGaAs/GaAs superlattices results in the recovery of the electrical activity of the epilayer.

The doping profile of FET's reveals that the channel depth is the same for all structures except for the sample which has no intermediate layers. In that sample the channel depth is 20% decreased (fig 4). The mobility and channel depth degradation resulted in lower transconductance of the device. Although the channel depth of the device with the 0.6μm GaAs intermediate layer grown at 580°C remains unaffected, the device appears to have lower g_m due to mobility degradation. The maximum g_m of the other structures, having L.T. buffer, being higher compared to that of the conventional sample is consistence with other reports in the literature [4 and ref. therein]. To our knowledge, our g_m values are the highest ever been reported for L.T. buffered devices (for L.T. GaAs layers grown at 250°C). The FET structures with superlattices are more effective for g_m enhancement. The increased transconductance cannot be caused by variation in the carrier concentration in the channel since the variations in our structures is less than 3% as extracted from C-V profiling. Also the samples with superlattice intermediate layers have improved f_T compared to the samples with only GaAs intermediate layers.

TEM observation of L.T. $\text{Al}_x\text{Ga}_{1-x}\text{As}/\text{L.T. GaAs}$ structures have revealed the presence of a precipitate depletion zone along the interface on the AlGaAs side[11]. Although the precipitate diffusion might be suppressed by the presence of the superlattices, it cannot affect the device performance, in our case, since the channel depth of the samples with GaAs intermediate layers remains unaffected by the presence of the L.T. buffer. Also the total thickness of the intermediate layers is much higher than the observed, as mentioned above, outdiffusion length of As-precipitates. PL and electrical measurements on n-GaAs/L.T. GaAs structures have revealed gallium vacancies diffusion from L.T. grown GaAs. ($x > 0.3$) layers inserted between L.T. GaAs and the Si-doped GaAs, suppresses the diffusion of V_{Ga} [12]. We suggest that superlattice layers act as a barrier in point defects diffusion giving rise to improved device performance. Further PL measurements are in progress to support this suggestion.

The transconductance g_m as a function of the gate voltage has the same profile for all devices with different buffer layers (fig 5). The maximum g_m occurs around

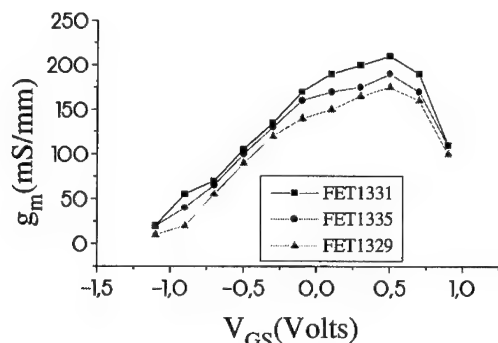


Fig 5. Transconductance as a function of the gate voltage.

$V_{GS} = +0.5$ Volts. The profile is characteristic of a FET structure with uniform doping in the channel in accordance with C-V measurements.

The output resistance R_o for devices buffered with L.T. GaAs is significantly higher compared to conventional devices [1,4]. This is attributed to the lower charge concentration in the channel. For this reason, R_o for FET structure with no intermediate layer in the buffer is higher compared to the other structures due to the decreased channel depth. On

the other hand the R_o for FET structures with intermediate layers is similar to that of the conventional ones.

CONCLUSION

Mobility and carrier concentration of n-GaAs epilayers are strongly affected by precipitates and traps outdiffusion from the L.T. GaAs. The degradation of the electrical properties is higher as the growth temperature of the buffer becomes lower. The use of intermediate layers between the buffer and the active layers in the FET structures improves the d.c. transconductance, the unity gain cutoff frequency and the Hall mobility of the channel. The improvement is more evident by using $\text{Al}_x\text{Ga}_{1-x}\text{As}/\text{GaAs}$ ($x = 0.5, 1$). We suggest that this improvement is mainly due to the suppression of point defect outdiffusion.

ACKNOWLEDGMENTS

Two of us (M.L and Z.H.) acknowledge partial support by the General Secreteriat for Research and Technology, Greece through project PENED91ED477. We want also to thank V.Foukaraki for her Hall measurements.

REFERENCES

- [1]F.W.Smith, A.R.Calawa, C.L.Chen, M.J.Manfra and L.J.Mahoney, IEEE Electron Devises Lett. **9**,77 (1988).
- [2]C.L.Chen, F.W.Smith, A.R.Calawa, L.J.Mahoney and M.J.Manfra, IEEE Transacions on Electron Dev. **36**(9),1546 (1989).
- [3]W.J.Schaff, L.F.Eastman , B.V.Rees and B.Liles , J. Vac. Sci. Technol **B2** (2),265 (1984).
- [4]J.Haruyama, N.Goto and H.Negishi, Appl. Phys. Lett. **61**(8),928(1992).
- [5]D.C.Streit, M.M.Hoppe, C.Chen, J.K.Lin and K.H.Yen ,J. Vac. Sci. Technol. **B10** (2), 819 (1992).
- [6]J.M.Ballingall, P.Ho, R.P.Smith, S.Wang, G.Tessmer, T.Yu, E.L.Hall and G.Hutchins in Low Temperature (LT) GaAs and Related Materials, edited by G.L.Witt, R.Calawa, U.Mishra and E.Weber (Mater.Res.Soc.Proc.241, Boston , Massachusetts,1991)pp.171-179.
- [7]D.C.Look, D.C.Walters, M.O.Manasreh, J.R.Sizelove,C.E.Stutz and K.R.Evans, Phys.Rev.B **42**(6),3578 (1990).
- [8]A.C.Warren, J.M.Woodall, J.L.Freeouf, D.Grischkowsky, D.T.McInturff, M.R.Melloch and N.Otsuka, Appl.Phys.Lett.**57**,1331 (1990).
- [9]A.Ginoudi, E.C.Paloura, B.Theys, J.Chevallier, J.Kalomiros, M.Lagadas and Z.Hatzopoulos ,MRS Proc.,this volume
- [10]T.Y.Chu,A.Dodabalapur, A.Srinivasan, D.P.Neikirk and B.G.Streetman, J. Cryst. Growth **111**,26 (1991)
- [11]K.Mahalingam, N.Otsuka, M.R.Melloch, and J.M.Woodall, Appl. Phys. Lett. **60**, 3253 (1992)
- [12] I.Ohbu, M.Takahama and Y.Umamara, Jpn. J. Appl. Phys. **31**,1647 (1992)

DEFECTS AND IMPURITIES IN MERCURIC IODIDE PROCESSING

J. M. VAN SCYOC*, R. B. JAMES*, T. E. SCHLESINGER**, AND T. S. GILBERT**

*Advanced Materials Research Department, Sandia National Laboratories, MS 9162, P.O. Box 969, Livermore, CA 94551

**Department of Electrical and Computer Engineering, Carnegie Mellon University, 5000 Forbes Avenue, Pittsburgh, PA 15213

ABSTRACT

In the fabrication of mercuric iodide (HgI_2) room temperature radiation detectors, as in any semiconductor process, the quality of the final device is very sensitive to the impurities and defects present. Each process step can change the effects of existing defects, reduce the number of defects, or introduce new defects. In HgI_2 detectors these defects act as trapping and recombination centers, thereby degrading immediate performance and leading to unstable devices. In this work we characterized some of the defects believed to strongly affect detector operation. Specifically, we studied impurities that are known to be present in typical HgI_2 materials. Leakage current measurements were used to study the introduction and characteristics of these impurities, as such experiments reveal the mobile nature of these defects. In particular, we found that copper, which acts as a hole trap, introduces a positively charged center that diffuses and drifts readily in typical device environments. These measurements suggest that Cu, and related impurities like silver, may be one of the leading causes of HgI_2 detector failures.

INTRODUCTION

Red mercuric iodide ($\alpha\text{-HgI}_2$) has been researched for almost three decades for use as a room-temperature radiation detector material. It has several properties which make it an extremely attractive material for this purpose. The high average atomic number of the constituent atoms ($Z_{\text{Hg}}=80$, $Z_{\text{I}}=53$, or $Z_{\text{avg}}=62$) results in a high efficiency for stopping photons into the low MeV range. The electron-hole pair creation energy of 4.2eV at room temperature leads to a sufficiently large signal response per photon. And finally, the room temperature bandgap of 2.13eV results in a resistivity on the order of $10^{14}\Omega\cdot\text{cm}$ and a dark current on the order of picoamps for typical device structures. These properties combine to give a material that has been used to produce some of the highest resolution room-temperature x-ray and gamma-ray detectors [1-4]. In addition, the capability for room temperature operation results in the possibility of compact spectrometer field instruments for applications such as environmental monitoring or special nuclear materials (SNM) monitoring.

However, these positive properties are balanced by several negative properties. Some of the basic properties of HgI_2 cause many of the problems. The fact that it is a compound semiconductor immediately leads to stoichiometry issues. The material has a relatively high vapor pressure at room temperature, and in addition, the iodine is generally preferentially sublimed at a faster rate, yielding mercury rich surfaces. The red tetragonal $\alpha\text{-HgI}_2$ phase undergoes a phase transition around 125°C to the yellow orthorhombic $\beta\text{-HgI}_2$ phase which destroys the crystallinity of the material upon return to room temperature. Finally, the material is mechanically very soft and also delaminates easily at the iodine layers.

The extrinsic factors that degrade mercuric iodides' usefulness are related to carrier trapping centers that are introduced into the material. These can arise from structural damage to the crystal or stoichiometric changes during the crystal growth and device fabrication processes. Of interest here, however, are the impurities that are introduced into the material, either from the original starting materials (generally mercuric chloride and potassium iodide), or further along in the fabrication. Several impurities are believed to play a role in mercuric iodide detectors, ranging from hydrocarbons to metallic elements. The impurities of interest here are copper and related metals.

These factors all lead to problems in the initial yield of high quality detectors, and the long term reliability of the detectors. These two problems combine to limit the applications of these sensors, particularly in the commercial arena. Given that the basic intrinsic material properties cannot be changed, one of the primary ways to improve the material is to identify the impurities that are deleterious to the detector performance, and work to reduce their presence. In this work we studied how copper and related impurities can be a prime source of problems in mercuric iodide detectors.

EXPERIMENTS AND RESULTS

Mercuric Iodide Detector Response

Mercuric iodide and other high resistivity room temperature semiconductor radiation detector materials allow for a very simple device structure. A bulk slab of material has simple ohmic contacts applied to opposite faces and a bias applied. The incoming x-ray or gamma-ray photon interacts with the semiconductor material yielding a number of electron hole pairs proportional to the photon energy. These carriers then drift in the applied field. This motion of carriers, or current pulse, is converted to a voltage pulse via a charge-sensitive preamplifier. This voltage pulse is then pulse-height-analyzed (PHA) and a count placed into the memory channel corresponding to the pulse magnitude. Therefore, the spectrum of event counts versus channel number, or pulse height, is directly proportional to the energy spectrum of the radiation seen by the detector, and the system can be thusly calibrated.

For this work a standard x-ray/gamma-ray detector characterization setup was used to measure the spectral response of a HgI_2 detector. A high voltage power supply was used to provide a negative bias to the entrance electrode. A custom-built box housed the detector under test and connected to a Tennelec TC170 charge sensitive preamplifier, modified for DC coupling, by way of a BNC connector. A Tennelec TC241 spectroscopy amplifier was used to shape the pulses from the preamplifier, and a The Nucleus MCA card and software were installed in a PC to collect the spectra. For the detector itself, a 1cm^2 by 2mm thick slab of mercuric iodide had 200Å thick 6.35mm diameter palladium contacts sputtered on each side and Pd wire leads aquadagged on. This is representative of the actual devices used in spectrometer systems. The detector was biased at -1000V and irradiated with a $1\mu\text{Ci}$ Americium-241 source placed about 2cm above the entrance electrode. Each spectrum was collected over a 1000s livetime. ^{241}Am has a gamma photon at 59.54keV and several x-ray escape peaks in the 14 to 21keV range. The gamma photopeak energy lies roughly in the center of the range of energies of interest for HgI_2 detector applications.

The previously given description of detector operation is an idealized model, in which the photopeak would be a one channel wide delta function at the appropriate pulse height for the number of carriers created by an incident photon (for example, the 14,176 electron-hole pairs for a 59.54keV gamma-ray). However, even in a "perfect" detector, i.e. one with complete charge collection, the peak would still be broadened to a gaussian shape because of carrier statistics. The more critical problem, however, is that many other processes degrade the spectral response more seriously. Anything that leads to a change in the voltage pulse height at the PHA greater than the digitization step size will lead to an error in the spectrum. The simplest possibility is that there is a constant amount of charge that is not collected, because it is trapped. This means that all of the pulses are reduced in magnitude, and the spectrum is thus shifted to lower channels. A constant change like this, although resulting in a reduction of the signal to noise in the system, can be "corrected" by simply recalibrating the energy scale. The more serious problem lies in the variable effects of real trapping processes. The trapping process is stochastic, such that the amount and timing of charge trapping is statistically broadened. Thus, events will have pulse heights reduced by different amounts. Therefore the photopeak is broadened on the low channel side. This is generally called "hole-tailing" as holes are usually the carriers trapped which lead to diminished pulses. Figure 1 shows the detector response of the mercuric iodide device above, which exhibits this hole-tailing problem. If the carriers that were trapped are released after the original pulse's collection time, the pulse heights of subsequent events can actually be larger than expected, though this rarely is visible in spectra, as the probability for the timing to be correct is low.

Finally, the problem of particular interest here, if the trapping process itself is changing, the effects on spectral response will be changing. Mercuric iodide detectors all exhibit this effect to some degree, particularly in the initial biasing characteristics. When a detector has been completely fabricated and is biased for the first time, the spectral response is very poor and changes significantly over time. It generally requires hours of bias for a device to stabilize to its high performance level. Figure 2 shows the evolution of the energy spectrum for the above detector, which actually required almost 200 hours to stabilize, as it was fabricated from material of lower than usual quality.

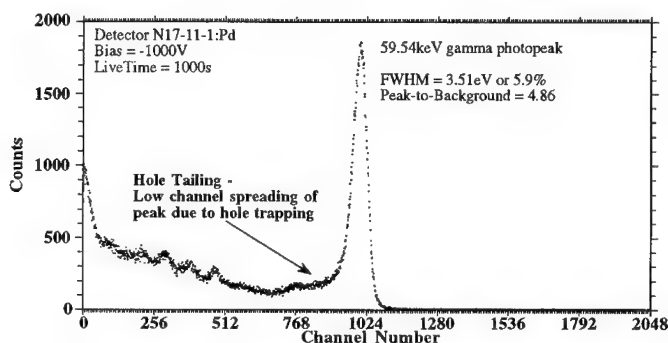


Figure 1. ^{241}Am spectrum from mercuric iodide detector exhibiting hole tailing.

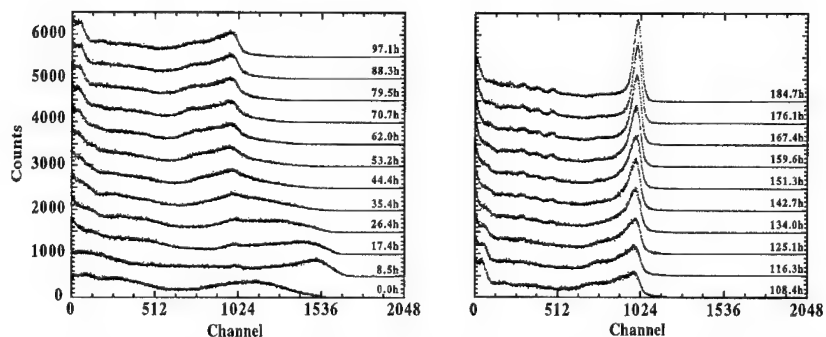


Figure 2. ^{241}Am spectrum versus time after initial biasing for mercuric iodide detector.

From Figure 2 one can study the detailed spectral evolution. After three days of biasing, the spectrum is just increasing in total counts and decreasing in peak widths. However, in the initial period, the first day in particular, the spectrum undergoes more substantial changes. There appear to be at least two separate peaks arising in the region of the expected gamma photopeak. One of these becomes the photopeak, while the peak at higher pulse height eventually disappears. As mentioned above, this higher than expected pulse height peak could be related to detrapping coincident with later events. However, the processes underlying this initial biasing behaviour require further study.

Impurities in Mercuric Iodide

Given that mercuric iodide is a somewhat primitive technology in semiconductor terms, impurities still tend to be present at significant levels. One set of methods for quantifying the elemental impurities are the Inductively Coupled Plasma Optical Emission and Mass Spectroscopy (ICP-OES and ICP-MS, respectively), which vaporize and ionize a sample solution with a plasma and measure the presence of a range of elements. The ICP-OES technique can generally measure down to the high ppb range, while the ICP-MS method can reach the high ppt region. Both of these techniques have been used on many HgI_2 samples, from initial material to purified material ready for crystal growth to completed crystals, as readily detectable levels of impurities are common. For example, copper is seen in the 100ppb to 1ppm level over a wide variety of samples, and therefore, it is fairly well accepted that copper is indeed present in most material [5]. Many of these impurities, such as copper, are electrically active, and thus are believed to be a prime cause of hole trapping. The presence of such an electrically active impurity would lead to a smaller signal and the distortion of the energy spectrum as seen in Figure 1 above.

Other experiments have shown that the impurities, as expected, can be equally well introduced during subsequent processing of the crystal for detector fabrication. Another good method for locating and identifying impurities present in a sample is low temperature photoluminescence (PL). PL has been used extensively on HgI_2 , and the material has a rich PL spectrum. In general, impurities can be detected down to the ppt level, but can rarely be quantified. One common step used throughout the fabrication process is the wet chemical etch in a dilute solution of potassium iodide (KI). The KI etch is used to remove mechanical damage from cutting, etc., and to remove the "aging" from the surface that results from the high vapor pressures of the Hg and I. Previous experiments have shown, however, that impurities in the KI solution are readily incorporated into the HgI_2 , and that these impurities readily diffuse throughout the sample in a matter of days. In addition sheet resistance measurements of thin film metal layers of copper have been conducted which showed that a large fraction of the Cu "disappears" into the HgI_2 . Therefore, copper can be introduced into the bulk material during the detector fabrication process as it readily diffuses throughout the sample, and it has been shown to degrade detector performance [6-10].

Leakage Currents Characterization

The existence of these mobile impurities complicates the carrier collection situation further. First, there is a current associated with the movement of any charged impurity itself, which leads to a heightened noise level. Secondly, the trapping effects of the impurity center varies unpredictably as the impurity moves in the bulk material. The previous work cited above demonstrated the high diffusivity of copper in HgI_2 . The experiment here demonstrates the mobility of the copper impurity in an electric field in mercuric iodide. In this experiment we intentionally doped a sample with a charge of copper. We then monitored the leakage current, or dark current, versus time to determine the movement of the copper-related centers.

The measurement system consisted of several instruments controlled and monitored by a personal computer via a GPIB (IEEE-488) interface. The sample was biased using a high voltage power supply capable of supplying up to 10mA at 500V. The sample bias voltage was monitored with a standard digital multimeter and stable within $\pm 1\text{V}$. The leakage current was measured with a Keithley Instruments 485 picoammeter, with resolution down to 0.1pA. Finally, a switching assembly was fabricated that allowed for computer controlled reversal of bias direction, and removal of bias for other measurements. With this setup the copper doped/contacted devices were biased and monitored over a period of days to capture the "transients" in the leakage currents.

The first set of samples used in this experiment were two similar 1cm^2 by 0.1mm thick HgI_2 crystals. A 6.35mm diameter, 2500Å thin film of high purity copper was sputter deposited onto one face of the sample, and a palladium lead was attached with aquadag. This translates to a doping level of about 2800ppm if the copper is distributed uniformly throughout the bulk of the HgI_2 . On the reverse side, an aquadag contact of similar area was made. The samples were then placed in a dark desiccator cabinet and connected to the measurement circuit. One sample had a positive 350V bias applied to the front, doping contact, while the other had the positive bias applied to the back contact, effectively giving a negative bias to the doping contact. In both cases

this translates to an electric field on the order of $3.5\text{V}/\mu\text{m}$, which is higher than the normal detector fields of $1\text{V}/\mu\text{m}$. This higher field accelerates the mobile processes. Figure 3 shows the results obtained for these two samples.

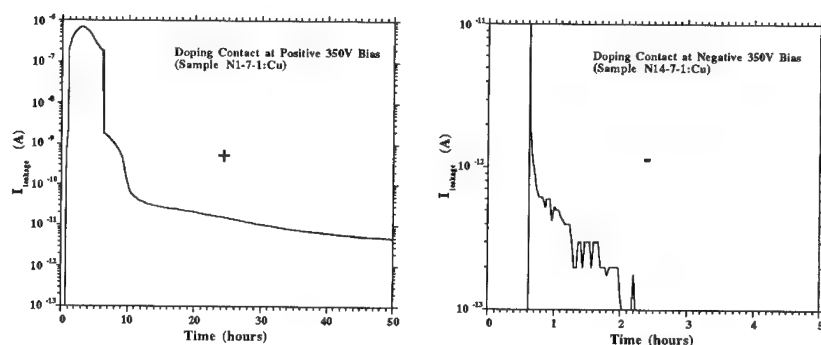


Figure 3. Leakage currents versus time for positively and negatively biased copper doping contacts on HgI_2 .

The leakage current for the positively biased sample exhibited a peak that sharply rose from the initial leakage current of 0.1pA to $0.7\mu\text{A}$. The peak decayed more slowly to a background leakage current of 5pA . This higher leakage level possibly indicates that the material had been damaged by the presence and movement of the high level of impurities, as the very initial leakage current was closer to the typical value for detectors.

Integrating the current gives the total charge moved, which should be representative of the impurities moved, as the intrinsic electron conductivity in the mercuric iodide is very low. The majority of the impurities, over 99%, appear to move in the first six hours. The total charge moved was $8.5 \times 10^{-3}\text{C}$, or 5.3×10^{16} single charges. This represents about 8% of the total number of atoms present in the deposited Cu film, assuming a singly charged impurity.

The negatively biased sample exhibited only a very small and brief current transient. Here $2.5 \times 10^{-9}\text{C}$ or 1.5×10^{10} single charges were moved. This is consistent with the view that the Cu forms a positively charged center, which is held at the negative contact. The transient that does occur is the movement of the few impurities that had diffused into the substrate back into the contact area.

These results show that the copper impurity, which may be a copper iodide (CuI) or something related, exhibits a single positive charge. The impurity drifts in the field as a positively charge carrier with an ionic mobility. For the second set of leakage current measurements one, different sample had the applied field periodically reversed. This experiment was done to confirm the above conclusions, and more importantly, to see if the copper impurities remain mobile after traversing the bulk of the mercuric iodide.

This sample was a 1cm^2 by 1mm thick HgI_2 crystal, with a 6.35mm diameter, 250\AA thin film sputtered onto one face. This translates to a doping level of about 28ppm, which is two orders of magnitude lower than the first two samples. This sample also had a 350V bias which now translates to an electric field on the order of $0.35\text{V}/\mu\text{m}$, which is one order of magnitude lower than before. Figure 4 shows the results obtained for this sample.

The leakage current for this sample exhibited a peak that sharply rose from the initial leakage current of 0.1pA to about 2nA . The peak decayed more slowly to a background leakage current of 0.2pA . The leakage current this time had returned more-or-less to its initial level, indicating that the material had not been damaged in this case because of the much lower level of impurities flowing through the sample. The majority of the impurities, over 97%, appear to move in the first four hours. The total charge moved was $4.3 \times 10^{-6}\text{C}$, or 2.7×10^{13} single charges. This represents about 0.04% of the total number of atoms present in the deposited Cu film. This amount is significantly lower than that of the first samples, most likely because of the lower field.

When the bias is reversed after one day a similar transient develops. Here $2.8 \times 10^{-6} \text{C}$ or 1.7×10^{13} single charges were moved, with 98% in the first two hours. This means that only 64% of the impurities moved back across. The remainder were either pinned somewhere in the bulk, or removed or stabilized at the back contact.

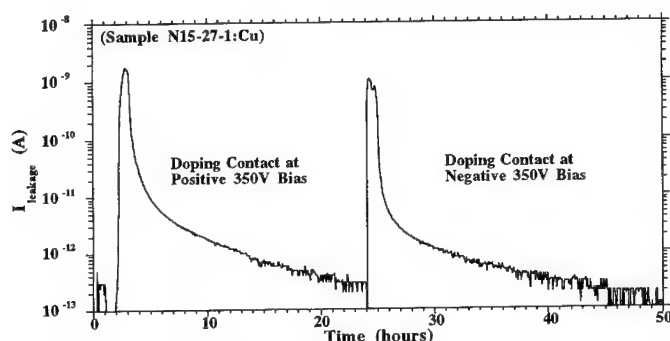


Figure 4. Leakage currents versus time for reversing field on copper doped HgI_2 .

CONCLUSIONS

Detector characterizations were used to highlight the degradation in performance frequently seen in mercuric iodide room temperature radiation detectors. This work sought to understand some of the causes of these failures by studying the copper impurities that are present in mercuric iodide and that are introduced during processing. Previous measurements revealed the high diffusivity of copper in mercuric iodide at room temperature. The leakage current measurements on doped samples shown here were used to demonstrate that the copper impurity is charged and mobile, and can easily be swept back and forth through the bulk crystal by an applied electric field. These measurements show how copper can affect the operation of detectors. In particular, the copper presents two means of detector failure. First, the presence of the copper introduces a defect center that traps carriers associated with the incoming photons, and leads to decreased and statistically broadened pulse heights. Secondly, the copper is seen to be mobile, which leads to changes in detector performance, particularly as the bias is changed. The movement of copper and similar impurities, such as silver, may actually be the cause of the needed conditioning time. When a detector is first biased, a fraction of the impurities are swept through the sample and remain at the back contact until the bias is removed when diffusion becomes the dominant mechanism. These results suggest that copper must be removed from and kept away from the mercuric iodide crystal and detector. Purifications are required to remove it from starting material, and the subsequent processing must be "clean".

ACKNOWLEDGMENTS

This work was supported by the U.S. Department of Energy

REFERENCES

1. L. van den Berg, Nucl. Inst. & Meth. in Phys. Res. A **A322**, 453 (1992).
2. A. J. Dabrowski, J. S. Iwanczyk, Y. J. Wang, M. Madden, and M. Szawlowski, Proc. of the SPIE **2007**, 19 (1993).
3. V. Gerrish and L. van den Berg, Nucl. Inst. & Meth. in Phys. Res. A **A299**, 41 (1990).

4. P. Olmos, G. Garcia-Belmonte, J. M. Perez, and J. C. Diaz, Nucl. Inst. & Meth. in Phys. Res. A **A299**, 45 (1990).
5. E. Soria, (private communication).
6. C. Y. Hung, X. J. Bao, T. E. Schlesinger, R. B. James, A. Y. Cheng, C. Ortale, and L. van den Berg, J. Appl. Phys. **73**, 4591 (1993).
7. X. J. Bao, T. E. Schlesinger, R. B. James, R. H. Stulen, C. Ortale, and A. Y. Cheng, J. Appl. Phys. **68**, 86 (1990).
8. X. J. Bao, Ph.D. Thesis, Carnegie Mellon University 1991.
9. R. B. James, X. J. Bao, T. E. Schlesinger, A. Y. Cheng, and V. M. Gerrish in *Semiconductors for Room-Temperature Radiation Detector Applications*, edited by R. B. James, T. E. Schlesinger, P. Siffert, and L. Franks (Mat. Res. Soc. Symp. Proc. **302**, Pittsburgh, PA, 1993) pp. 103-114.
10. J. M. Van Scyoc, T. E. Schlesinger, R. B. James, A. Y. Cheng, C. Ortale, and L. van den Berg in *Semiconductors for Room-Temperature Radiation Detector Applications*, edited by R. B. James, T. E. Schlesinger, P. Siffert, and L. Franks (Mat. Res. Soc. Symp. Proc. **302**, Pittsburgh, PA, 1993) pp. 115-120.

ROOM TEMPERATURE INFRARED ELECTROLUMINESCENCE FROM THIN-FILM POLYCRYSTALLINE CHALCOPYRITE $\text{Cu}(\text{In,Ga})\text{Se}_2$ -BASED DIODES

Miguel A. Contreras, John Webb, Andrew Tennant and Rommel Noufi
National Renewable Energy Laboratory, 1617 Cole Blvd., Golden, CO 80401

ABSTRACT

Evidence of room-temperature infrared electroluminescence from thin-film polycrystalline $\text{CuIn}_x\text{Ga}_{1-x}\text{Se}_2$ -based diodes ($0 < x < 0.4$) has been observed by Fourier transform spectroscopy using a FT-Raman spectrophotometer that operates in the near-infrared spectral region. Electroluminescence spectra from ternary CuInSe_2 and quaternary $\text{Cu}(\text{In,Ga})\text{Se}_2$ device structures are reported. In all electroluminescence cases we observe an approximate linear relationship of intensity to forward junction current. Film fabrication process determines to a great extent the optoelectronic properties of the emitters, and consequently, the characteristics of their luminescence spectra. Using a Gaussian multi-peak curve-fit routine to analyze electroluminescence spectra, we can deduce the position, width and relative intensity of the dominant optical transitions. Our purpose in this contribution is two-fold: (1) To report the room-temperature electroluminescence phenomena from chalcopyrite $\text{Cu}(\text{In,Ga})\text{Se}_2$ polycrystalline thin-films, and (2) to demonstrate electroluminescence as a viable technique to optically characterize $\text{Cu}(\text{In,Ga})\text{Se}_2$ materials using diode structures at RT.

INTRODUCTION

CuInSe_2 (CIS) belongs to the family of chalcopyrite I-III-VI₂ type of materials. With a direct bandgap of ~ 1.04 eV, it could be a potential low-cost material for infrared (IR) emitter/detector applications. In polycrystalline thin-film form, a near-stoichiometry Cu-deficient material is usually found to have p-type conductivity. Intrinsic point, line, and plane defects in the material influence to a great extent its optoelectronic properties. Cu antisites (Cu_{In}) and Cu vacancies (V_{Cu}) have been reported to provide acceptor levels within the energy gap [1,2].

By deconvoluting a given luminescence spectrum, for instance, into multiple Gaussian peaks, it is possible to extract information not only on the number of dominant optical transitions at RT, but also, on the width and amplitude of each such contribution to the overall spectrum [3]. It has been pointed out that even at cryogenic temperatures the highest energy transitions are still donor-to-acceptor-type transitions [2], therefore, we anticipate the resolved peaks with the highest energy to also correspond to subgap emissions. We look at Ga incorporation in a CIS matrix and its effect on some of the optical properties of CIGS. We note that the bandgap of ternary CIS can also be increased by adding Ga [4] or Al [5] (up to ~ 1.7 eV for CuGaSe_2 and up to ~ 2.6 eV for CuAlSe_2). Devices we report on in this paper were originally designed as solar cells and consist of emitters made from $\text{CuIn}_{1-x}\text{Ga}_x\text{Se}_2$ (CIGS) with $0 \leq x \leq 0.4$. Because of the limiting contact scheme in the solar cells, the excitation current to obtain electroluminescence (EL) data was kept to rather low values (< 10 A/cm²).

Figure 1 shows schematically the structure of the devices used in our experiments and a cross-section micrograph of a typical device. The preferred base substrate is a 3-mm-thick soda lime silica glass, but other substrates can also be used, including alumina (Al_2O_3), 7059 glass, and Mo metallic foils. The soda lime glass substrate is coated with a ~ 1 - μm Mo film by dc sputtering. The emitters—or absorbers, in the case of solar cells—were fabricated by different reaction pathways. For our interest, we examine and compare the luminescence characteristics of emitters made via (1) coevaporation (2) compound formation from Se-containing precursors, and (3) selenization. Detailed information on thin-film growth parameters and processing conditions are given elsewhere [6]. The emitter is then coated with a thin (~ 500 Å) intrinsic CdS layer by a chemical bath deposition (CBD) technique, followed by a transparent conductive oxide (TCO)—in our case, an RF sputtered bilayer of ZnO. The top contact is a metallic grid of e-beam evaporated Ni (500 Å) and Al

(3 μm). The finished devices incorporate a 1000-1300Å layer of MgF_2 that, in the case of solar cells, acts as an anti-reflective (AR) coating.

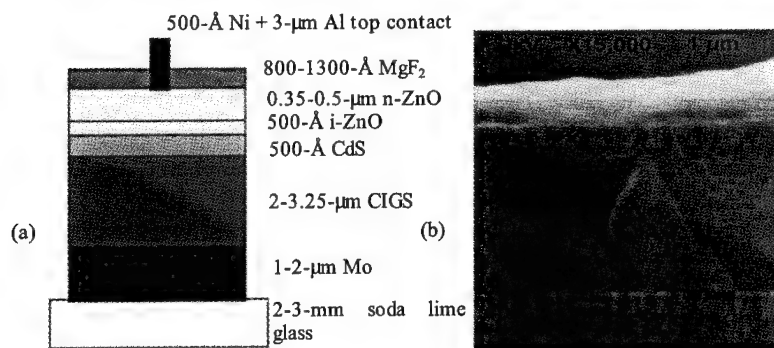


Fig. 1. (a) Schematics of device (not to scale), and (b) cross-section SEM of typical device.

RT IR ELECTROLUMINESCENCE

The luminescence measurements were made at 4 cm^{-1} (0.7 nm) resolution using an FT-Raman spectrophotometer as described in ref. [7]. One hundred interferometer scans were averaged and were Fourier-transformed into EL spectra for each device.

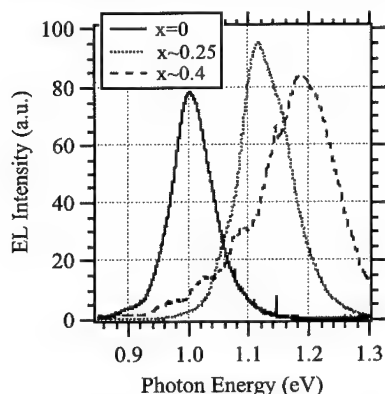


Fig. 2. EL spectra from CIGS devices

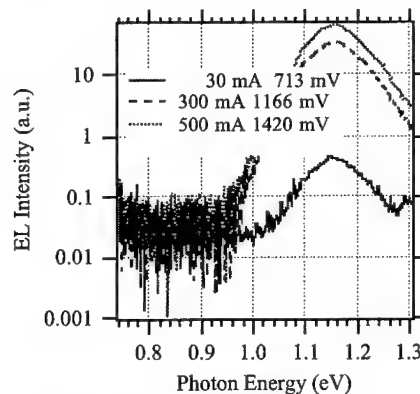


Fig. 3. EL intensity with forward current

First we demonstrate RT EL for emitters with different Ga contents $0 < x < 0.4$ (see Figure 2). We note the most intense EL emission from CIS (no Ga) is centered around 1.01 eV, with a full width at half maximum (FWHM) of $\sim 0.076\text{ eV}$ for an excitation of $\sim 1.16\text{ A/cm}^2$ and 1.032 V. This FWHM value corresponds to a width of about $3.04 \cdot kT$'s at RT (k is the Boltzmann constant), which is close to the FWHM values encountered in single-crystal GaAs samples ($\sim 1.5 \cdot kT$) [8]. We found the diodes to be very stable, and no signs of degradation in the intensity were observed after more than 60 min of continuous operation. Stability at longer times of operation has not been determined.

To investigate the quality of the junctions under emission, we forward-biased the diodes at three different junction current values and measured the EL intensity in each case. In all cases, i.e.,

ternary- and quaternary-based emitters, we observed that EL peak intensity follows an approximately linear relationship with current junction (see Figure 3). The junction area for the device used in obtaining Fig. 3 is 0.43 cm^2 ; therefore, the excitation current density values are 0.07, 0.7, and 1.16 A/cm^2 , respectively. Higher excitation currents were not possible because the contacts to the device were not designed to handle large current densities (one sun solar cells).

Of interest to our PV work are the effects of Ga incorporation in a base CIS matrix and comparisons between emitter/absorber films—and devices—that are fabricated by different procedures or reaction pathways. For this purpose, we prepared two sets of CIGS materials via (1) a coevaporation process and by (2) a 3-stage processing (compound formation from Se-containing precursors), both described elsewhere [5,7]. In both techniques we grew a ternary sample (no Ga) and another with a very small amount of Ga (0.4-1.1 at%). To make a fair comparison between them, the CIGS films have approximately the same composition, and the diodes (as solar cells) have an equivalent performance level (energy conversion efficiency 11%-13%). Table I shows a summary of composition data (electron probe microanalysis at 20 kV) for the CIGS films, along with the representative current-voltage (I-V) characteristics of the solar cells made from them.

Table I. Summary of CIGS film and PV device characterization

Sample (process)	M1201 (3-stage)	M1203 (3-stage)	C389 (coevap.)	C390 (coevap.)
Cu/In/Ga/Se at%	23.7/25.7/0/50.6	23.7/24.4/1.1/50.8	23.9/26.0/0/50.1	23.0/25.9/0.4/50.7
V_{oc} (mV)	480	478	461	458
J_{sc} (mA/cm ²)	37.5	33.7	36.9	38.2
Fill Factor (%)	74.9	68.2	72.1	71.8
Efficiency (%)	13.2	11.0	12.3	12.5

Table II. Summary of Gaussian multi-peak curve fitting for spectra in Figure 4. E_1 - E_5 are the resolved peak positions in eV. Peak widths are also given in units of eV.

Sample (process)	M1201 (3-stage)	M1203 (3-stage)	C389 (coevap.)	C390 (coevap.)
E_1 -peak width	0.953-0.059	0.937-0.047	0.764-0.023	0.819-0.041
E_2 -peak width	1.001-0.039	1.023-0.047	0.827-0.032	0.872-0.030
E_3 -peak width	1.031-0.064	1.092-0.031	0.879-0.024	0.913-0.913
E_4 -peak width	-	-	0.930-0.013	0.954-0.043
E_5 -peak width	-	-	0.950-0.073	0.999-0.060

The EL spectra from each sample listed in Table I, plus others with much higher Ga contents, are shown in Figure 4 (excitation current was $\sim 100 \text{ mA}$ for all samples). To analyze and compare the features of these EL spectra we have performed a Gaussian multi-peak curve fitting. We note that for the 3-stage process samples, the Gaussian multi-peak curve fitting for CIS and CIGS (with 1.1 at% Ga content) can be accomplished by 3 peaks, resulting in a residual error of less than 1%. On the other hand, the fitting for similar coevaporated films must be accomplished by a minimum of 5 peaks for a residual error of less than 5%. A summary of these results are presented in Table II.

The EL spectra in Figure 4 reveal that for both fabrication approaches there are substantial differences between the EL spectra of the resulting films, in spite of the similarities in film composition and PV device performance. Tanda et al [10] have already noted similar differences for films grown by coevaporation as compared to films grown by conventional selenization. We interpret the extra peaks needed to fit the EL spectra in coevaporated films as additional forbidden gap defect states/bands. On the other hand, the spectra from films fabricated by the 3-stage process can be resolved by 3 Gaussian peaks. This suggests that the reaction of Se-containing precursors (In_2Se_3 , Cu_2Se , others) to form the compound proceeds in such a manner as to produce films with superior uniformity and perhaps fewer defects overall.

The resolved peaks with the highest energy transitions (highlighted in Table II) compare very well with bandgap values reported in the literature. However, it is necessary to point out that these emissions (highest energy resolved peaks) more likely correspond to transitions that can be described as

$$h\nu = E_g - E_d - E_a \quad (1)$$

where $h\nu$ is the photon energy, E_g is the bandgap and E_d , E_a are the energies associated with the donor and acceptor levels. Rincón et al [11] reported an $E_g = 1.023 \pm 0.004$ eV at 7 °K obtained from luminescence data (this value obviously reduces even further at RT). Bougnot et al [12] gave $0.9 \leq E_g \leq 1.03$ eV calculated from transmission data (at RT).

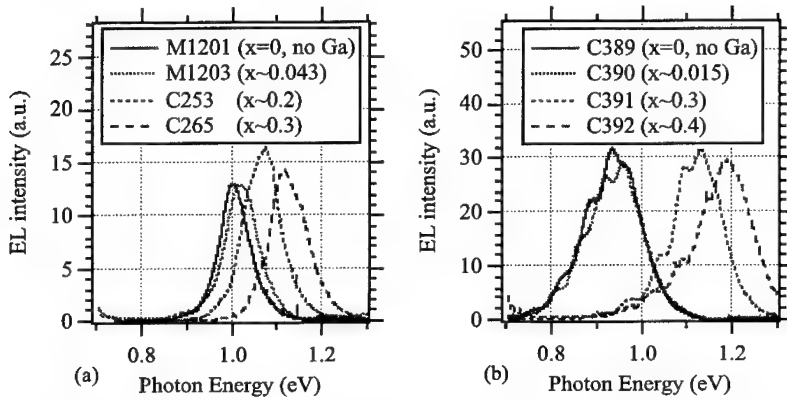


Fig. 4. EL spectra for films grown by (a) 3-stage process and (b) coevaporation process

It is important to note that in both semiconductor fabrication processes the addition of a small amount of Ga (~0.4-1.1 at%) has shifted the highest EL optical transition toward higher energy values—by 49-61 meV. A similar situation is observed for RT PL spectra taken from the bare CIGS films (C389 and C390). Here, the highest resolved peaks are at 0.960 eV for the sample with no Ga (C389) and at 0.983 eV for sample C390 with 0.4 at% Ga ($x=0.015$)—a shift of 23 meV. The same phenomenon is observed in the spectral response of PV devices (see Figure 5). We note that the spectral response data in PV devices are related to electron-hole pair generation/collection due to photon absorption from the solar spectrum. There are several ways that people attempt to determine bandgap values using spectral response data. Our approach is to extrapolate the linear region and to take the intercept at the horizontal axis as the bandgap value. From this argument, we determine $E_g \sim 0.96$ eV for sample M1201 (no Ga) and $E_g \sim 1.00$ eV for M1203 ($x=0.043$). Again, there is a shift toward higher energies (in the absorption edge in this case) of about 40 meV. The increase in the emission and absorption edges exceeds the expected shift based on bandgap enhancement arguments due to Ga alloying. From the relationship by Albin et al [4] for bandgap enhancement as a function of Ga content, we anticipate an increase in bandgap of 6 meV for $x=0.015$ and 18 meV for $x=0.043$ (near stoichiometry films). For Cu-poor films (Cu~19 at%) the bandgap increase is anticipated to be 11 meV and 32 meV for $x=0.015$ and $x=0.043$, respectively.

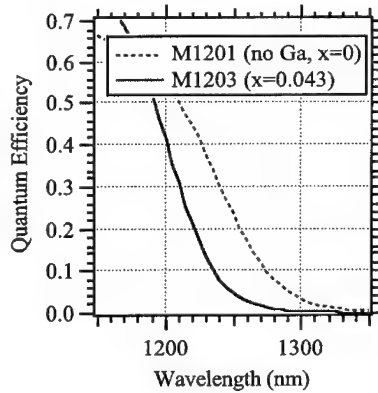


Fig. 5. Spectral response of PV devices

The shift we observe in the highest energy emissions is 49-61 meV. Therefore, from equation (1) it can be inferred that a new set of ionized luminescence centers (E_d', E_a') must be closer to the band edges than in the case of pure CIS. This can be explained in terms of a shift in the Fermi level position toward the valence band (VB). An indication that Ga could be either a passivating agent or an extrinsic dopant (for small amounts < 1at%). Conceivably, Ga incorporation in such small amounts (~0.4-1.1 at%) could aid in preventing point defects associated with donor states (such as In_{Cu} , V_{Se} , or In_i), hence balancing the material toward a more p-type conductivity. Walter et al [13] have shown that for high Ga content CIGS films the Fermi level clearly approaches the valence band.

Yet another possibility to explain the shift according to equation (1), is an additional enhancement of bandgap (assuming E_d, E_a to be at the same position as in the case of CIS) that could occur in conjunction with the Ga alloying mechanism. It is known that the bandgap of chalcopyrite semiconductor materials (and others) can be increased by subjecting the materials to a compressive stress state (hydrostatic pressures)[14]. Since the net effect of Ga incorporation is the shrinkage of the lattice, we anticipate intrinsic stresses to occur at low Ga concentrations. A rough estimate of an average strain can be computed assuming a uniform distribution of Ga in the bulk of the film. For $x=0.01$ there will be 100 atoms of In per atom of Ga, since the unit cell of CIS has 4 atoms of In, 4 atoms of Cu and 8 atoms of Se, it can be idealized that for every 25 CIS unit cells ($a_0=5.775 \text{ \AA}$ and $c_0=11.599 \text{ \AA}$) there will be one CIGS unit cell with 3 atoms of In and 1 Ga atom (a 25% Ga content unit cell with $a_1=5.739 \text{ \AA}$ and $c_1=11.473 \text{ \AA}$). The average volumetric strain can be computed as

$$\epsilon_v = [a_1^2 \cdot c_1 - a_0^2 \cdot c_0] / a_0^2 \cdot c_0 \quad (2)$$

yielding $\epsilon_v = -0.023$.

COMPARISON BETWEEN PL AND EL SPECTRA AT RT

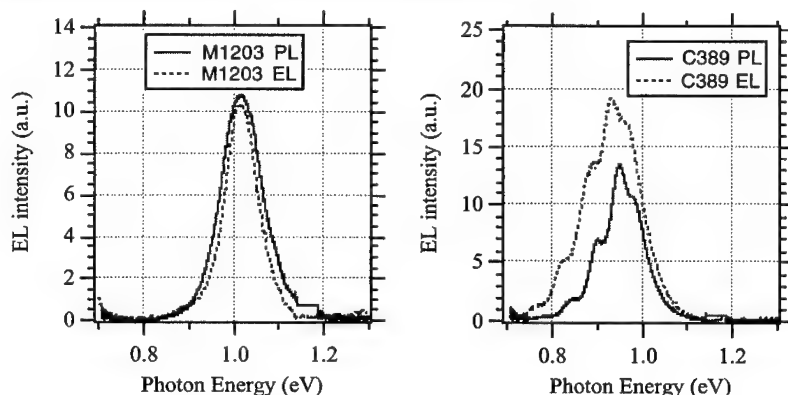


Fig. 6. Comparison of EL and PL spectra for samples with emitters grown by (a) 3-stage process and (b) coevaporation process.

PL spectra were obtained using an Nd-YAG laser operating in the 1.064- μm wavelength at <10 mW with a beam focused to ~50 μm . This excitation is much stronger (more intense) than EL excitation, and because of the small spot size we anticipate the excitation to yield information from just a few grains composing the material (grain size 1-3 μm). On the other hand, EL involves a much greater area, indeed, the whole junction area of 0.43 cm^2 in our devices.

Comparing the data from EL and PL in all samples analyzed, we notice that both signatures are qualitatively similar; but for samples with the highest density of defect states (coevaporated samples), the PL signature is shifted to slightly higher energy values—as compared to EL spectra. We believe this situation to be an effect of excitation intensity on luminescence output. Tanda et al [10] have reported the shift of the PL spectra toward higher energy values due to an increase in the excitation

intensity (laser power). In our samples, interestingly enough, this shift is less appreciable in CIGS films with lower defect densities (3-stage films) as compared to high-defect-density films (coevaporated)—see Figure 6.

CONCLUSIONS AND FINAL COMMENTS

Chalcopyrite polycrystalline CIS thin-films are demonstrated to be active infrared emitters. Onset of incoherent radiation emission is observed immediately after exceeding the built-in potential of the diodes (which depends on Ga content of the emitters). This demonstration of EL in such structures encourages us to pursue visible emission by alloying CIS with Al.

Data obtained via EL methods have proven to be a valuable aid in characterizing diode structures in the CIGS system. For our purposes, the technique has proven to be fast (no need to cool samples) and very reliable. Information obtained from it has the same character as PL data done at RT.

It is important to note that coevaporated films show distinct features very different from 3-stage processed films; nevertheless, this does not mean that all coevaporated CIGS films will behave the same way. Indeed, processing conditions such as substrate temperature, deposition rate, and cooling affect the properties of this material system in many ways. Under the right growth conditions it may be possible to obtain coevaporated films that behave (from a luminescence point of view) in a manner similar to 3-stage films.

ACKNOWLEDGMENTS

The authors wish to thank Alice Mason and Rick Matson, for compositional analysis and SEM micrographs; Brian Keyes, Tim Coutts, Dick Ahrenkiel, and Alex Zunger for technical discussions; James Keane and James Dolan for technical assistance in device fabrication and equipment readiness. This work was performed at NREL under Contract No. DE-AC36-83CH10093 to the US Department of Energy.

REFERENCES

- [1] S.M. Wasim, *Solar Cells*, **16** 289 (1986).
- [2] C. Rincón, C. Bellabarba, J. Gozález and G.S. Pérez, *Solar Cells*, **16** 335 (1986).
- [3] J.D. Webb, D.J. Dunlavy, T. Ciszek, R. Ahrenkiel, M. Wanlass, R. Noufi, and S. Vernon, *Mat. Res. Soc. Symp. Proc.*, **324** (1992).
- [4] D.S. Albin, J.J. Carapella, J.R. Tuttle, and R. Noufi, *Mat. Res. Soc. Symp. Proc.*, **228** (1992).
- [5] J.E. Jaffe and A. Zunger, *Physical Review B*, **28**, n. 10, 5822 (15 November 1983).
- [6] M. Contreras, J. Tuttle, A. Gabor, A. Tennant, K. Ramanathan, S. Asher, A. Franz, J. Keane, L. Wang, and R. Noufi. *Proceedings of the 1st World Conference in Photovoltaic Energy Conversion*, Hawaii, Dec 5-9 1994. (IEEE PVSC 1994) (to be published)
- [7] J.D. Webb, M. Contreras, and R. Noufi, *Proceedings of the 1st World Conference in Photovoltaic Energy Conversion*, Hawaii, Dec 5-9 1994. (IEEE PVSC 1994) (to be published)
- [8] *Physics of Semiconductor Devices*, 2nd Edition. S.M. Sze, Wiley & Sons, 1981 p. 686
- [9] A. Gabor, J. Tuttle, D. Albin, M. Contreras, R. Noufi and A. Hermann, *Appl. Phys. Lett.* **65** (2), 198 (11 July 1994).
- [10] M. Tanda, S. Manaka, A. Yamada, M. Konagai, and K. Takahashi, *Jpn. J. Appl. Phys.*, **32** Pt. 1, No. 5A, 1913, (1993).
- [11] C. Rincón, C. Bellabarba, J. Gonzáles, and G. Sánchez-Pérez, *Solar Cells*, **16** 335 (1986).
- [12] J. Bougnot, S. Duchemin and M. Savelli, *Solar Cells*, **16** 221 (1986).
- [13] T. Walter, R. Menner, M. Ruckh, L. Kasër, and H.W. Schock, *Proceedings of the 22nd IEEE PVSC*, Las Vegas, Nevada, October 7-11, 1991, (IEEE, New York) p. 924.
- [14] Ternary Chalcopyrite Semiconductors: Growth, Electronic Properties, and Applications. Shay and Wernick, (International series of monographs in the science of the solid state, v. 7) Pergamon Press, 1975, p. 97

Part X

**Interfaces, Quantum Wells
and Superlattices**

ELECTRONIC PROPERTIES OF IDEAL AND INTERFACE-MODIFIED METAL-SEMICONDUCTOR CONTACTS

WINFRIED MÖNCH

Laboratorium für Festkörperphysik, Gerhard-Mercator-Universität Duisburg, D-47048 Duisburg, Germany

ABSTRACT

Barrier heights in metal-semiconductor contacts may be modified by interlayers. The effects of atomic interlayers are due to interface dipoles. With the restriction to nearest-neighbor interactions and monovalent interlayer atoms, they may be described as interface molecules which consist of an interlayer and a substrate atom. If the interlayers are thicker than a few atomic layers their two interfaces with the metal and with the semiconductor will be non-interacting. Both types of interfaces are described by the model that interface-induced gap states determine the alignment of the bands and the electronegativity difference describes the charge transfer across the interface. The present paper discusses and analyzes experimental data for H-modified diamond and silicon, Al/Si/GaInP, and metal/ Si_3N_4 /Si Schottky contacts.

INTRODUCTION

Metal-semiconductor contacts play an essential role in semiconductor devices. Such contacts are either ohmic or rectifying. The latter ones, which are also called Schottky contacts, are depleted of mobile carriers on their semiconductor side [1] and the current transport is determined by an energy barrier which equals the energy distance between the Fermi level and the edge of the respective majority-carrier band right at the interface.

Large barrier heights are required for effective Schottky diodes and for gate contacts in metal-semiconductor field-effect transistors (MES-FETs), to name two examples. For the design of such devices, it is required to know about the barrier heights of ideal, i.e., intimate, abrupt, laterally homogeneous, and defect-free metal-semiconductor contacts. For specific applications, a tailoring of barrier heights is desirable. The present paper is organized such that the chemical trends of barrier heights in ideal metal-semiconductor contacts are briefly reviewed in the next section. The third section then describes the influence of interface doping on barrier heights and the fourth and the fifth section are devoted to the discussion of sub-nm and nm-scale interfacial layers, respectively, on the barrier heights.

IDEAL METAL-SEMICONDUCTOR INTERFACES

The alignment of the band structures across ideal metal-semiconductor interfaces is determined by the continuum of metal-induced gap states (MIGS) [2-6]. They represent the wavefunction tails of the metal electrons into the semiconductor in the energy range where the conduction band of the metal overlaps the band gap of the semiconductor, i.e., between the valence-band maximum of the semiconductor up to the Fermi level right at the interface. The MIG

states derive from the virtual gap states (ViGS) of the complex band structure of the semiconductor and their character varies across the band gap from predominantly donor- to predominantly acceptor-like close to the valence-band and the conduction-band edge, respectively. The respective branch point lies at the middle of the dielectric band gap, which is the relevant band gap rather than the minimum one. Intuitively, this branch point is also called the charge neutrality level (CNL) of the MIGS since the net charge in the MIGS has negative sign, is zero and changes to positive sign when their CNL is above, coincides with, and drops to below the Fermi level, respectively.

The covalent bonds in heteropolar diatomic molecules are partially ionic. Pauling [7] correlated the ionicities of such single bonds with the difference of the atomic electronegativities of the atoms involved. Chemical bonds also exist at interfaces and, therefore, charge transfer will also occur across interfaces between solids. In thermal equilibrium, interfaces are electrically neutral. Thus, the charge densities Q_m on the metal and Q_s on the semiconductor side of metal-semiconductor contacts are equal but of opposite sign and the condition of charge neutrality may be written as

$$Q_m + Q_s = 0. \quad (1)$$

In generalizing Pauling's concept, the charge transfer across solid interfaces is modeled by the electronegativities of the two materials in contact [6]. For metal-semiconductor contacts, one then obtains

$$-Q_m = Q_s \propto X_m - X_s, \quad (2)$$

where X_m and X_s are the electronegativities of the metal and the semiconductor, respectively. The charge density on the semiconductor side of an ideal metal-semiconductor contact,

$$Q_s = Q_{mg}^s + Q_{sc}^s, \quad (3)$$

consists of the space-charge density Q_{sc}^s and the net charge density Q_{mg}^s in the continuum of metal-induced gap states.

If the MIGS have a constant density of states, the MIGS-and-electronegativity model just outlined gives a linear dependence of the barrier heights in metal-semiconductor contacts on the difference of the metal and semiconductor electronegativities [8,9], i.e.,

$$\Phi_{Bn}^s = W_{ci}^s - W_F = \Phi_{cni}^s + S_x^s (X_m - X_s) \quad (4)$$

and

$$\Phi_{Bp}^s = W_F - W_{vi}^s = \Phi_{cni}^{s*} - S_x^s (X_m - X_s) \quad (5)$$

for *n*- and *p*-type semiconductors, respectively. The subscripts ci and vi denote the energies of the conduction- and the valence-band edges right at the interface, respectively. This is explained schematically in Fig 1.

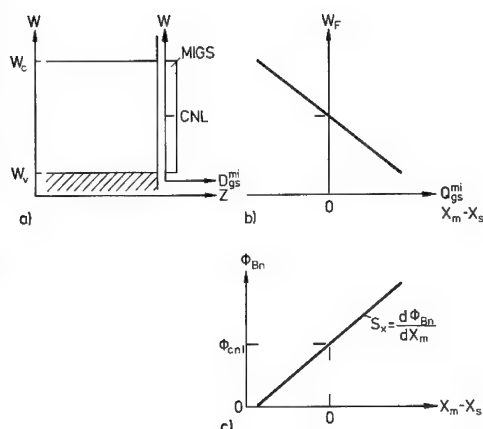


Fig. 1 Band diagram (a), charge transfer (b), and barrier height (c) at metal-semiconductor contacts containing a continuum of metal-induced gap states with constant density of states across the band gap (schematically). From Ref. 8.

The energy positions $W_{cnl}^s - W_{vi}^s$ and, what is the same, the zero-charge-transfer barrier heights

$$\Phi_{cnl}^s = W_{ci}^s - W_{cnl}^s \quad (6)$$

and

$$\Phi_{cnl}^{s*} = W_{cnl}^s - W_{vi}^s, \quad (7)$$

respectively, of almost all semiconductors were calculated by applying various theoretical methods and were also named differently. However, the branch points of the virtual gap states of the complex semiconductor band structure evaluated by Flores and coworkers [3,10] and by Tersoff [5], the dielectric mid gap energies calculated by Cardona and Christensen [11], the average hybrid energies given by Harrison and Tersoff [12] as well as the average bonding-antibonding energies calculated by Wang et al. [13] are conceptually identical.

The analysis of experimental as well as of numerical data from theoretical calculations revealed the relation [6,9]

$$A_x / S_x - 1 = 0.1(\epsilon_\infty - 1)^2 \quad (8)$$

between the slope parameter S_x in (4) and (5) and the electronic contribution ϵ_∞ of the static dielectric constant of the semiconductor. For contacts between solids, Miedema's electronegativities [14] are preferred over Pauling's scale since Miedema evaluated his values from properties of solid metals. One then finds $A_x \approx 0.86$.

For one and the same metal on a specific semiconductor, the barrier heights Φ_{Bn}^s and Φ_{Bp}^s measured with n - and p -type substrates, respectively, were always found to add up to the width W_g^s of the minimum band gap of the semiconductor, i.e.,

$$\Phi_{Bn}^s + \Phi_{Bp}^s = W_g^s \quad (9)$$

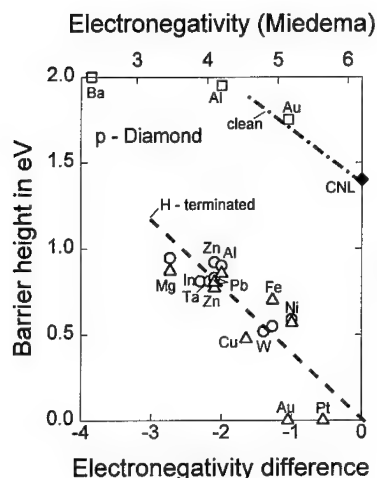


Fig. 2 Barrier heights of *p*-diamond Schottky contacts as a function of the difference of metal and carbon electronegativities. From Ref. 21

within the limits of experimental error, see, for example Refs. 15-19. Obviously, the density of states of the MIGS around their charge neutrality level is always sufficiently large so that the changes of the space-charge density, when the doping of the semiconductor is altered from *n*- to *p*-type, cause no measurable variations of the energy difference $W_{cni}^s - W_F$. Consequently, the space-charge density Q_{sc}^s may be neglected in (3) and, by this, also in (1).

The majority of experimental barrier heights does not fit the predictions of the MIGS-and-electronegativity model. This is not surprising since this approach assumes ideal metal-semiconductor interfaces. Deviations from what results from the MIGS-and-electronegativity model were attributed to fabrication-induced defects [20] and chemical [21] as well as structural interface dipoles [22,23] which will be discussed in the next section.

Contrary to the MIGS model just outlined, the unified defect model [24] postulates that at metal-semiconductor interfaces the Fermi level is pinned by the energy levels of defects. For GaAs Schottky contacts specifically, As_{Ga} antisite defects were proposed [25]. They are double-donors with their 0/+ and +/+ charging levels at approximately 0.7 and 0.5 eV above the valence-band maximum, respectively. According to the unified defect model, the Fermi level at metal contact on *n*- and *p*-type GaAs will be pinned at these As_{Ga} levels. This is possible only if additional spectator defects of acceptor character are present [26]. The barrier heights determined with 14 different metals on *n*- and *p*-type GaAs [27] were found to add up to $\langle \Phi_{Bn} + \Phi_{Bp} \rangle = 1.37 \pm 0.07$ eV on the average. This experimental finding does not support the unified defect model but confirms the MIGS mode. The deviation of the average value from the width of the GaAs band gap, 1.43 eV at room temperature, is accounted for by the difficulties and the large margins of error in determining the small barrier heights on *p*-GaAs.

ATOMIC INTERLAYERS: EXTRINSIC INTERFACE DIPOLES

Modification of barrier heights by means of interface doping was frequently tried. A most extensive set of experimental results was reported by Aoki and Kawarada [28] for metal contacts

on hydrogen-terminated {100}-oriented *p*-diamond surfaces. These data are plotted in Fig. 2 as a function of the difference $X_m - X_C$ between the electronegativities of the metals used and carbon. A least-squares fit to the experimental data yields

$$\Phi_{Bp}(H) = 0.017 - 0.37(X_m - X_C) \text{ [eV]} .$$

The dashed line illustrates the quality of the fit. The dash-dotted line, on the other hand, represents the chemical trend of the barrier heights

$$\Phi_{Bp} = 1.4 - 0.3(X_m - X_C) \text{ [eV]}$$

as predicted by the MIGS model for ideal metal-diamond contacts. The energy position of the CNL was taken from the calculations by Cardona and Christensen [11] and the slope parameter was evaluated by applying (8). The experimental data for Al and Au contacts with "clean" interfaces are well reproduced by the MIGS line while the data point for Ba deviates by approximately 0.5 eV. Irrespective of the metal used, all barrier heights reported by Aoki and Kawarada [28] for contacts on H-terminated *p*-diamond are lower by approximately 1 eV with respect to what is predicted by the MIGS model for ideal contacts. This parallel shift of the data points obtained with H-terminated surfaces suggests that the same mechanism is effective at all these metal-diamond interfaces. Mönch [21] explained these experimental findings by H-induced interface dipoles. This interpretation is also supported by metal contacts prepared on H- and on S-terminated Si(111) surfaces which will be discussed next.

Figure 3 displays current/voltage (*I/V*) characteristics of one diode each prepared by evaporation of lead onto a clean *n*-Si(111)-7x7 and a H-terminated *p*-Si(111):H-1x1 surface [29]. The barrier heights were evaluated as 0.64 and 0.7 eV, respectively. Relation (9) then predicts barrier heights of 0.4 to 0.5 eV for Pb contacts on *p*-Si(111)-7x7 and *n*-Si(111):H-1x1 surfaces. Experimentally, ohmic *I/V* curves were observed. Simulations demonstrated that such behavior is to be expected for barrier heights lower than approximately 0.5 eV and large series resistance.

The experimental findings with both diamond and silicon Schottky contacts indicate hydrogen-induced changes $\delta\Phi_B(H)$ of the barrier heights. They will be of the same size but of different sign on *n*- and *p*-type substrates. The barrier heights of interface-modified Schottky contacts may be written as

$$\Phi_{Bn}^{im} = \Phi_{Bn}^s - \delta\Phi_B \quad (10)$$

and

$$\Phi_{Bp}^{im} = \Phi_{Bp}^s + \delta\Phi_B , \quad (11)$$

where Φ_{Bn}^s and Φ_{Bp}^s denote the barrier heights with no interface doping. The experimental data just discussed then give

$$\delta\Phi_B(H-C) = -1 \text{ eV} \text{ and } \delta\Phi_B(H-Si) = +0.25 \text{ eV} .$$

The hydrogen-induced variations of the barrier heights thus have opposite sign in diamond and silicon Schottky contacts. This observation is easily explained by Pauling's concept on the correlation of the partial ionic character of covalent bonds and the difference of the atomic elec-

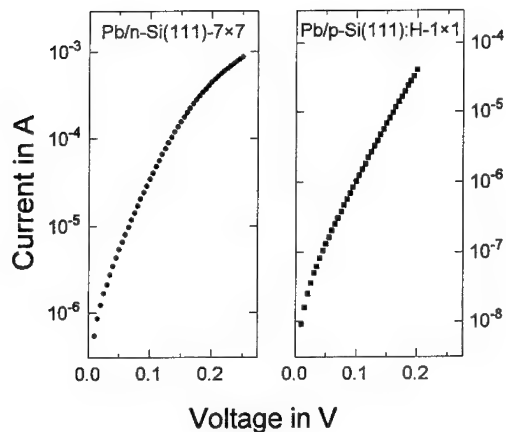


Fig. 3 Current/voltage characteristics of Pb/*n*-Si(111) and Pb/*p*-Si(111) contacts at room temperature. The diode areas measure $9.3 \times 10^{-3} \text{ cm}^2$. From Ref. 29

tronegativities. Considering nearest-neighbor interactions only, the chemical bond between a monovalent interlayer atom (ia) such as hydrogen and a substrate atom (s) may be described as a diatomic molecule. These "interface molecules" are heteropolar and thus have a dipole moment. The ionic character of single bonds is given by

$$\Delta q_i = 0.16|X_{ia} - X_s| + 0.035(X_{ia} - X_s)^2. \quad (12)$$

This is a revised version [30] of a relation originally proposed by Pauling. Pauling's electronegativity scale will be used here since it was designed for diatomic molecules. The electronegativities relevant in the present discussion are $X_{\text{Si}} = 1.9$, $X_{\text{C}} = 2.55$, and $X_{\text{H}} = 2.2$. One thus obtains C-0.06-H+0.06 but Si+0.05-H-0.05 interface dipoles. The opposite orientation of the hydrogen-induced dipoles immediately explains the reduction of the barrier heights on H-modified *n*-silicon but *p*-diamond Schottky contacts.

Another example are Pb/S/Si(111) contacts with a monolayer of sulfur at the interface [31]. Again, Pb/S/*p*-Si(111) contacts are rectifying with barrier heights of $0.69 \pm 0.02 \text{ eV}$ while with *n*-Si substrates ohmic *I/V* characteristics were observed. The sulfur interlayer changes the barrier heights by $\delta\Phi_B(\text{S-Si}) \cong +0.25 \text{ eV}$ with regard to "clean" interfaces. Sulfur has an electronegativity $X_{\text{S}} = 2.58$ and this value gives Si+0.12-S-0.12 dipoles. Their component normal to the interface is oriented the same as Si-H interface dipoles and this explains that both the H- and the S-induced changes of the barrier height have identical sign.

Extrinsic interface dipoles may be described by electric double layers [22]. The drop in potential energy across such a dipole layer changes the barrier height by

$$\delta\Phi_B = \pm(e_0 / \epsilon_{ms}\epsilon_0)p_i N_d, \quad (13)$$

where ϵ_{ms} and N_d are the interface dielectric constant and the area density of the dipoles, respectively, and ϵ_0 and e_0 are the permittivity of vacuum and the electronic charge, respectively. The orientation of the dipoles determines the sign of $\delta\Phi_B$. It is positive when the positive charge

of the dipoles is on the semiconductor side and vice versa. In a point charge model, the dipole moment may be approximated by

$$p_i = e_0 \Delta q_i d_d, \quad (14)$$

where $e_0 \Delta q_i$ and d_d are the charge and the length of the dipoles, respectively. For hydrogen atoms this simple approach is justified since their polarizability is extremely small. If interfaces are doped with atoms with larger covalent radii and then larger polarizabilities, the mutual interaction of the interface dipoles will lower their dipole moment as a function of their area density [32]. The dipole charge is approximated by relation (12) and the dipole length is taken as the sum of the covalent radii r_{ia} and r_s of the atoms involved, i.e.,

$$d_d = r_{ia} + r_s. \quad (15)$$

By inserting respective values, relation (13) gives

$$\delta\Phi_B(\text{H-C}) = -1.86/\epsilon_{ms} [\text{eV}] \text{ and } \delta\Phi_B(\text{H-Si}) = +1.00/\epsilon_{ms} \epsilon_i [\text{eV}].$$

Interface dielectric constants were estimated as $\epsilon_{ms} \cong 2$ for diamond [33] and $\epsilon_{ms} \cong 4$ for GaAs Schottky contacts [34]. With these values, the hydrogen-induced changes of the barrier heights result as $\delta\Phi_B(\text{H-C}) \cong -1$ eV for diamond and $\delta\Phi_B(\text{H-Si}) \cong +0.25$ eV for silicon Schottky contacts with H-interlayers in excellent agreement with the experimental findings presented above.

Quite recently, Saiz-Pardo et al. [35] calculated the change of barrier heights induced by an interlayer of hydrogen atoms in K/Si(111) contacts. They used a self-consistent LCAO method supplemented with a local-density prescription to calculate many-body effects. The hydrogen-interlayer in K/H/n-Si(111) contacts was found to form a dipole layer and to decrease the barrier height by 0.23 eV in comparison to undoped interfaces. This theoretical result reproduces the experimental findings at Pb/H/Si(111) contacts and confirms the simple dipole model described above.

SUB-nm INTERLAYERS

Schottky contacts were also modified by interlayers measuring more than just one monolayer. As an example, Al/Si/Ga_{0.52}In_{0.48}P contacts shall be considered [36]. The inclusion of a 0.6 nm thick Si layer or, in other words, four layers of silicon atoms between Al and GaInP was found to increase the barrier height by 0.17 eV from 0.86 to 1.03 eV for *n*-type but to reduce it by 0.08 eV from 0.93 to 0.85 eV on *p*-type GaInP substrates. These experimental results will be explained by applying the concept outlined above not only to metal-semiconductor contacts but also to interfaces between two semiconductors.

The band gaps of semiconductors generally differ in width. Therefore, discontinuities of the band edges are expected to exist at abrupt semiconductor heterostructures. The valence-band offsets represent an overlap of the valence band of the one semiconductor with the band gap of the other one. In this energy range, the wavefunctions of the valence electrons of the first semiconductor will tail into the second one. As at metal-semiconductor interfaces, these wavefunction tails are derived from the virtual gap states of the complex band structure of the respective semiconduc-

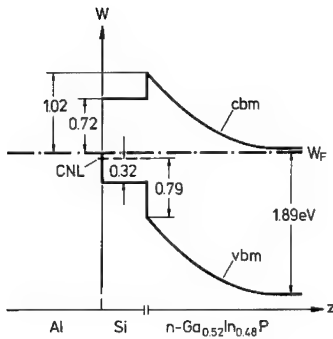


Fig. 4

Fig. 4 Schematic band diagram for Al/Si/n-Ga_{0.52}In_{0.48}P contacts; CNL: charge neutrality level of ViGS, vbm: valence-band maximum, cbm: conduction-band minimum; energies in eV. The thickness of the Si layer, 0.6 nm, is exaggerated with regard to the width of the GaInP depletion layer, approximately 85 nm. Schematic band diagram for Al/Si/n-Ga_{0.52}In_{0.48}P contacts; CNL: charge neutrality level of ViGS, vbm: valence-band maximum, cbm: conduction-band minimum; energies in eV. The thickness of the Si layer, 0.6 nm, is exaggerated with regard to the width of the GaInP depletion layer, approximately 85 nm.

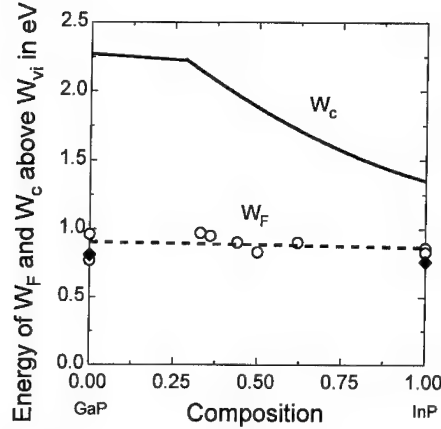


Fig. 5

Fig. 5 Position of the Fermi level at Al/n-Ga_{1-x}In_xP contacts [38] and position of the conduction-band minimum of Ga_{1-x}In_xP both relative to the valence-band maximum. From Ref. 22.

tor. This concept then predicts that the branch points of the ViGS or, what is the same, the dielectric mid-gap energies of the semiconductors in contact align across their interface. In case that the electronegativities of the two semiconductors differ an additional interface dipole will be present. The valence-band discontinuity may then be written as [10]

$$\begin{aligned} \Delta W_v &= W_{vi}^{sr} - W_{vi}^{sl} = (W_{cni}^{sl} - W_{vi}^{sl}) - (W_{cni}^{sr} - W_{vi}^{sr}) + D(X_r - X_l) \\ &= \Phi_{cni}^{sl*} - \Phi_{cni}^{sr*} + D(X_r - X_l). \end{aligned} \quad (16)$$

The subscripts r and l denotes the two semiconductors in contact. Generally, the dipole contribution $D(X_r - X_l)$ is small and may be neglected in most semiconductor heterostructures since the electronegativities of most semiconductors are almost equal. It is worth mentioning that in addition to the interface-induced gap states in the energy range of the band-edge discontinuities no gap states exist in ideal, i.e., abrupt, epitaxial, and defect-free semiconductor heterostructures.

Figure 4 displays a schematic band scheme of an Al/Si/n-GaInP contact. The Al/Si and the Si/GaInP interfaces are treated as non-interacting. This seems to be justified since the charge decay-lengths of the interface-induced gap states amount to approximately 0.3 nm only, see, for example, Ref. 22. Any voltage drop across the silicon interlayer may be neglected since its thickness measures 0.6 nm only. In thermal equilibrium, the Fermi levels in the metal and in the n-GaInP substrate line up. The barrier height of Al/Si contacts amounts to 0.72 eV [37] and the silicon CNL is slightly below the Fermi level since Al is somewhat less electronegative than silicon. At the Si/GaInP interface, the charge neutrality levels of the two semiconductors line up.

Tersoff's calculations [5] place the branch point of the ViGS in silicon by 0.32 eV above the valence-band maximum. The charge neutrality level in $\text{Ga}_{0.52}\text{In}_{0.48}\text{P}$ may be obtained by interpolation.

Figure 5 displays the positions of the Fermi level above the valence-band top evaluated from experimental barrier heights of $\text{Au}/n\text{-Ga}_{1-x}\text{In}_x\text{P}$ contacts [38] and the respective band gaps. The dashed line is a least-squares fit to the data points and the diamonds represent calculated energy positions of the charge neutrality levels of GaP and InP [5]. These data indicate that the energy position of charge neutrality level with relative to the valence-band maximum varies linearly as a function of composition. The same conclusion is reached from $\text{Au}/\text{Al}_{1-x}\text{Ga}_x\text{As}$, $\text{Al}/\text{Al}_{1-x}\text{Ga}_x\text{As}$, and $\text{Au}/\text{GaAs}_{1-y}\text{Py}$ Schottky contacts as well as $\text{GaAs}/\text{Al}_{1-x}\text{Ga}_x\text{As}$ heterostructures, see, for example, Ref. 22.

The data presented in Fig. 5 place the charge neutrality level of $\text{Ga}_{0.52}\text{In}_{0.48}\text{P}$ at 0.79 eV above the valence-band maximum. This gives an offset of the valence-band maxima at $\text{Si}/\text{Ga}_{0.52}\text{In}_{0.48}\text{P}$ interfaces of 0.47 eV. Since the band gap of $\text{Ga}_{0.52}\text{In}_{0.48}\text{P}$ measures 1.89 eV at room temperature, the interface-induced gap states model predicts a barrier height of 1.02 eV for $\text{Al}/\text{Si}/\text{Ga}_{0.52}\text{In}_{0.48}\text{P}$ contacts. This result perfectly agrees with the experimental value. The barrier heights of $\text{Al}/\text{Si}/n\text{-Ga}_{0.52}\text{In}_{0.48}\text{P}$ and $\text{Al}/\text{Si}/p\text{-Ga}_{0.52}\text{In}_{0.48}\text{P}$ contacts, 1.03 eV and 0.85 eV, respectively, add up to 1.88 eV. This experimental result again confirms relation (9) since $\text{Ga}_{0.52}\text{In}_{0.48}\text{P}$ has a band gap of 1.89 eV at room temperature.

The MIGS model predicts a barrier height of approximately 1.05 eV for intimate $\text{Al}/n\text{-Ga}_{0.52}\text{In}_{0.48}\text{P}$ contacts [22]. However, $\text{Al}/n\text{-Ga}_{0.52}\text{In}_{0.48}\text{P}$ contacts with no Si interfacial layer have barrier heights of only 0.86 eV [36] to 0.95 eV [39]. This reduction may be attributed to interface defects which might result from alloying. The formation enthalpy of AlP, -164 kJ/mol, is considerably larger than the respective values for GaP and InP, -122 and -75.3 kJ/mol, respectively. The silicon interlayer then simply acts as a spacer which separates the reactive Al from the GaInP and prevents strong chemical reactions and, by this, the formation of defects.

NANO-SCALE INTERLAYERS: MIS STRUCTURES

Metal-insulator-semiconductor (MIS) structures with thin insulating interlayers behave electrically like Schottky contacts. The barrier heights of such devices depend on the nature of the insulator, its thickness, and the specific metal used. Sobolewski and Helms [40] investigated silicon MIS structures with ultrathin silicon nitride layers as insulator and six different metal contacts. The barrier heights were evaluated from the capacitance/voltage characteristics of these $\text{M}/\text{Si}_3\text{N}_4/\text{Si}$ structures. Figure 6a displays their results. Irrespective of the contact metal, the barrier heights vary linearly as a function of the nitride thickness. The sign of slope parameter is negative for n - and positive for p -silicon but the least-squares fits to the data give the same absolute values of the slope parameter irrespective of the type of doping and of the contact metal. A similar behavior is known from MOS contacts with silicon dioxide as interlayer.

MIS structures possess a metal-insulator and an insulator-semiconductor interface. Both may be treated by applying the concept described above for metal-semiconductor contacts and semiconductor heterostructures, respectively, since insulators may be considered as semiconductors with extremely wide band gaps. For MIS structures, the condition of charge neutrality may be

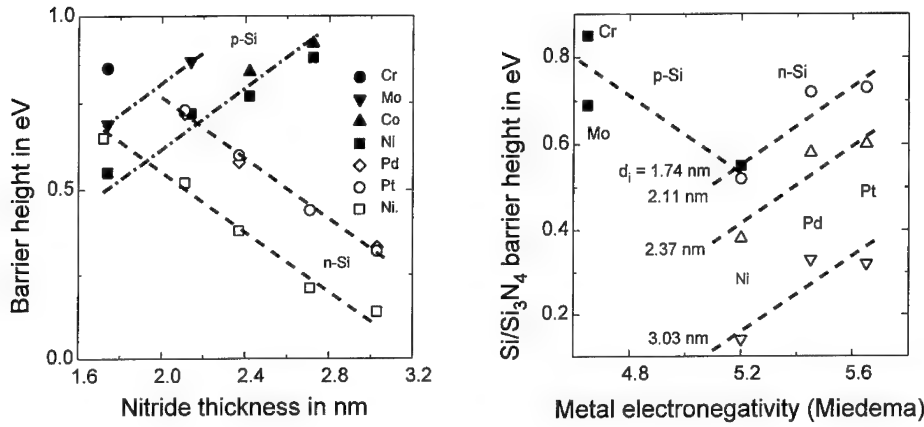


Fig. 6 Barrier heights of metal/Si₃N₄/Si contacts as a function of nitride thickness for a variety of metals (a) and as a function of metal electronegativity for the same nitride films (b). Data from Ref. 40

written as

$$Q_m + Q_i + Q_s = 0 \quad , \quad (17)$$

where the insulator charge density Q_i consists of two components, the charge density Q_f^i at the insulator-semiconductor interface and a space-charge density Q_{sc}^i . The barrier height $\Phi_{Bn}^i = W_{ci}^i - W_F$ and the zero-charge-transfer barrier height $\Phi_{cni}^i = W_{ci}^i - W_{cni}^i$ of the metal-insulator interface are analogously defined as the respective quantities of metal-semiconductor contacts, see (4) and (6). Figure 7 shows schematically a band diagram of MIS structures. In thermal equilibrium the different energy contributions at MIS structures add up as

$$\Phi_{Bn}^i = \Delta_i + \Delta W_c^{is} + \Phi_{Bn}^s \quad , \quad (18)$$

where the conduction-band offset at the insulator-semiconductor interface is given by

$$\Delta W_c^{is} = \Phi_{cni}^i - \Phi_{cni}^s - D(X_i - X_s) \quad . \quad (19)$$

X_i is the electronegativity of the insulator. The space charge in the semiconductor and in the Inserting of (18) and (19) into (20) gives

$$\begin{aligned} \Phi_{Bn}^s &= (\Phi_{Bn}^i - \Phi_{cni}^i) + \Phi_{cni}^s - (e_0 / \epsilon_i \epsilon_0) Q_f^i d_i + D(X_i - X_s) \\ &= S_x^i (X_m - X_i) - (e_0 / \epsilon_i \epsilon_0) Q_f^i d_i + \Phi_{cni}^s + D(X_i - X_s). \end{aligned} \quad (21)$$

The barrier height Φ_{Bn}^s at the insulator-semiconductor interface will thus decrease proportional

References

1. W. Schottky, *Naturwissenschaften* **26**, 843 (1938).
2. V. Heine, *Phys. Rev.* **138**, A 1689 (1965).
3. E. Louis, F. Yndurain, and F. Flores, *Phys. Rev. B* **13**, 4408 (1976).
4. S.G. Louie and M.L. Cohen, *Phys. Rev. B* **13**, 2461 (1976).
5. J. Tersoff, *Phys. Rev. Lett.* **52**, 465 (1984); *Surf. Sci.* **168**, 275, (1986).
6. W. Mönch, in *Festkörperprobleme* (Adv. in Solid-State Physics) vol. 26, ed. by P.Grosse (Vieweg, Braunschweig, 1986), p. 67.
7. L. Pauling, *The Nature of the Chemical Bond*, 2nd ed. (Cornell Univ. , Ithaca, NY, 1960).
8. W. Mönch, in *Gallium Arsenide Technology* Vol. II, ed. by D.K. Ferry (Sams & Co., Carmel, Ind., 1989).
9. W. Mönch, *Appl. Surf. Sci.* in print.
10. C. Tejedor and F. Flores, *J. Phys. C* **11**, L19 (1978).
11. M. Cardona and N.E. Christensen, *Phys. Rev. B* **35**, 6182 (1987).
12. W.A. Harrison and J. Tersoff, *J. Vac. Sci. Technol. B* **4**, 1068 (1986).
13. R.-Z. Wang, S.-H. Ke, and M.C. Huang, *J. Phys.: Condens. Matter* **4**, 8083 (1992).
14. A.R. Miedema, F.R. de Boer, and P.F. de Chatel, *F. Phys. F* **3**, 1588 (1973).
15. M.J. Turner and E.H. Rhoderick, *Solid-State Electron.* **11**, 291 (1968).
16. B.L. Smith and E.H. Rhoderick, *Solid-State Electron.* **14**, 71 (1971).
17. J.R. Waldrop, *J. Vac. Sci. Technol. B* **2**, 445 (1984).
18. M.O.Aboelfotoh and N.K. Tu, *Phys. Rev. B* **34**, 2311 (1986).
19. N. Newman, M. van Schilfgarde, and W.E. Spicer, *Phys. Rev. B* **35**, 6298 (1987).
20. W. Mönch, *Phys. Rev. Lett.* **58**, 1260 (1987); *Phys. Rev. B* **37**, 7129 (1988).
21. W. Mönch, *Europhys. Lett.* **27**, 479 (1994).
22. W. Mönch, *Semiconductor Surfaces and Interfaces* 2nd ed. (Springer, Berlin 1995).
23. R.F. Schmitsdorf, T.U. Kampen, and W. Mönch, *Surf. Sci.* in print.
24. W.E. Spicer, I. Lindau, P. Skeath, and C.Y. Su, *J. Vac. Sci. Technol.* **17**, 1019 (1980).
25. E.R. Weber, H. Ennen, U. Kaufmann, J. Windscheif, and J. Schneider, *J. Appl. Phys.* **53**, 6140 (1982).
26. W. Mönch, *Surf. Sci.* **132**, 92 (1983).
27. J. Waldrop, *J. Vac. Sci. Technol. B* **2**, 445 (1984).
28. M. Aoki and H. Kwarada, *Japan. J. Appl. Phys.* **33**, L708 (1994).
29. T.U. Kampen and W. Mönch, *Surf. Sci.* in print.
30. N.B. Hanney and C.P. Smith, *J. Am Chem. Soc.* **68**, 171 (1946).
31. A. Stockhausen and W. Mönch, unpublished.
32. J. Topping, *Proc. Roy. Soc. A* **114**, 67 (1927).
33. J. Ihm, S.G. Louie, and M.L. Cohen, *Phys. Rev. Lett.* **40**, 1208 (1978).
34. R. Ludeke, in *Metallization and Metal-Semiconductor Interfaces*, ed. by I.P. Batra (Plenum, New York, 1989), p. 39.
35. R. Saiz-Pardo, R. Rincon, and F. Flores, *Appl. Surf. Sci.* in print.
36. T.J. Miller, G.B. Backes, and M.I. Nathan, *J. Appl. Phys.* **76**, 7931 (1994).
37. R.J. Archer and M.M. Atalla, *Ann. New York Acad. Sci.* **101**, 697 (1963).
38. T.F. Kuech and J.O. McCaldin, *J. Vac. Sci. Technol.* **17**, 891 (1980).
39. E.Y. Chang, Y.-L. Lai, K.-C. Lin, and C.-Y. Chang, *J. Appl. Phys.* **74**, 5622 (1993).
40. M.A. Soblewski and C.R. Helms, *Appl. Phys. Lett.* **54**, 638 (1989).

EFFECT OF RF POWER ON THE CHARACTERISTIC PARAMETERS OF W/n-GaAs SCHOTTKY CONTACTS FABRICATED BY RF SPUTTERING

A. Singh, G. Aroca and L. Velásquez

Laboratorio de Semiconductores, Departamento de Física, Universidad de Oriente,
Apartado 188, Cumaná 6101 Sucre, Venezuela

ABSTRACT

W/n-GaAs/In Schottky contacts of area 1.75 mm^2 were fabricated by deposition of W on (100) n-GaAs by rf Sputtering using rf power values in the range 200-400 Watt. The I-V and high frequency C-V measurements at 300 K, in the 200 Watt W/n-GaAs Schottky contact indicated that W formed a good rectifying contact to n-GaAs, with a rectification ratio (r) of 270, ideality factor (n) of 1.39, reverse saturation current (I_0) of $1.2 \times 10^{-6} \text{ A}$ and the C-V barrier height (ϕ_{bo}) of 1.6 V. However, n and I_0 increased, whereas r and ϕ_{bo} decreased for the W/n-GaAs Schottky contacts prepared using higher rf power. For the 300 Watt W/n-GaAs contact, the values of 70, 1.70, $6.3 \times 10^{-6} \text{ A}$, and 1.2V for r , n , I_0 and ϕ_{bo} , respectively, were estimated. The low frequency forward bias capacitance (or surface defect density) was an order of magnitude higher in the 300 Watt contact than in the 200 Watt contact. This fact suggested that the degradation in the quality of W/n-GaAs Schottky contacts fabricated by using high rf power was caused by high density surface defects created during sputter deposition of W on n-GaAs.

INTRODUCTION

GaAs is one of the of the most important III-V compound semiconductor in the view of its technological applications in photonic and fast electronic devices. Among these devices are solar cells, light emitting diodes (LEDs), laser diodes, microwave mixer diodes, metal-semiconductor field effect transistors (MESFETs) and their integrated circuits. GaAs has also important applications in high temperature electronic devices which are vital components in the oil, lumber, avionics, automotive and nuclear power industries, and sensors for high temperature operation. The technology of gallium arsenide integrated circuits where MESFET is one of the main components requires a gate metal with high thermal stability on GaAs, because the fabrication process involves annealing at high temperatures upto 800° C^1 . Among the various refractory metals, W is an attractive choice as gate electrode because of its high temperature resistance, high work function and low electrical resistivity²⁻⁵.

RF Sputtering is one of the most commonly used techniques for the fabrication of W films and Schottky barriers. However, RF Sputtering introduces defects at or near the metal-semiconductor interface which degrade the quality of the Schottky junctions. This effect can be minimized by using appropriate fabrication conditions. The aim of this paper is to investigate the effect of rf power on the characteristic parameters of the W/n-GaAs Schottky junctions prepared by RF sputter deposition of W, on the chemically etched polished surface of n-GaAs, using the current-voltage (I-V), 1 MHz capacitance-voltage (C-V) and intermediate frequency capacitance-frequency/voltage (C-f/V) techniques.

EXPERIMENTAL TECHNIQUE

The n-GaAs (100) single crystals doped with Si, used in this work were purchased from Crystal Specialties⁶. Prior to metal deposition, the samples were degreased with acetone and methanol at 40° C for 10 min., rinsed with deionized (DI) water and dried with N₂ gas. To remove the native oxide, the samples were then chemically etched with HCl : H₂O (1:1) solution at room temperature for 10 min., rinsed with DI water and dried with N₂. To obtain ohmic contact, In metal was sputter deposited on the unpolished surface of n-GaAs, using a RF power of 50 watts with argon pressure of 6.5 x10⁻³ Torr, followed by a 3.5 hr. anneal in Ar atmosphere at 390° C. The W/n-GaAs Schottky junctions A, B and C were fabricated by deposition of W on the chemically etched polished surface of n-GaAs by RF Sputtering using rf powers of 200 Watt for 45 min., 300 Watt for 30 min. and 400 Watt for 22.5 min., respectively. All the W Schottky contacts were 1.75 mm² in area. Full details of fabrication of ohmic and rectifying contacts to n-GaAs are described elsewhere⁷.

The I-V characteristics of the W/n-GaAs/In Schottky diodes were measured using a Keithley 617 electrometer, a Keithley 480 picoammeter and a Hewlett-Packard 6160A power supply. The 1 MHz C-V measurements were made using a Boonton 72B capacitance meter. The small signal *ac* capacitance (C_M) and conductance (G_M) of the W/n-GaAs/In Schottky diodes as a function of applied *dc* bias (V_a), in the frequency range 0.2-100 KHz, were simultaneously measured with a two phase PAR-5204 lock-in amplifier.

EXPERIMENTAL DATA AND ANALYSIS

The I-V characteristics of the In ohmic contact to n-GaAs (100):Si are described elsewhere⁷. For the W/n-GaAs/In Schottky diodes A, B and C, the room temperature forward and reverse currents measured as a function of applied voltage (V_a) are shown in Fig. 1, and the values of the rectification ratio obtained from this data are listed in Table I. The voltage drop across the rectifying barrier (V) was obtained from the relation

$$V = V_a - IR_s \quad (1)$$

where R_s is the series resistance and had a value of 4 ohms in our case⁷. For the W/n-GaAs junctions A, B and C, the experimental values of $\ln[I/(1-\exp(-qV/kT))]$ vs V, under forward bias, shown in Fig. 2, were described by the relation⁸

$$I = I_0 \exp \left(\frac{qV}{nkT} \right) \left[1 - \exp \left(-\frac{qV}{kT} \right) \right], \quad (2)$$

where I₀ is the reverse saturation current. The ideality factor n is defined by⁸

$$\frac{1}{n} = \frac{kT}{q} \frac{d}{dV} \ln [I / (1 - \exp(-qV/kT))], \quad (3)$$

The fit of the experimental values of $\ln[I/(1-\exp(-qV/kT))]$ vs V (Fig. 2, discrete points in the linear region) to Eq. (2) (Fig. 2, solid lines) provided the values, n and I₀, given in Table I.

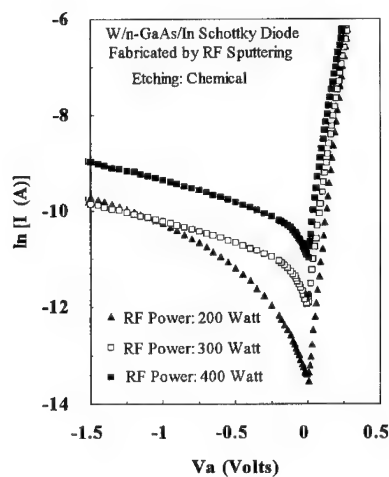


FIG. 1 Comparison of the I-V characteristics of the W/n-GaAs/In Schottky diodes A, B and C.

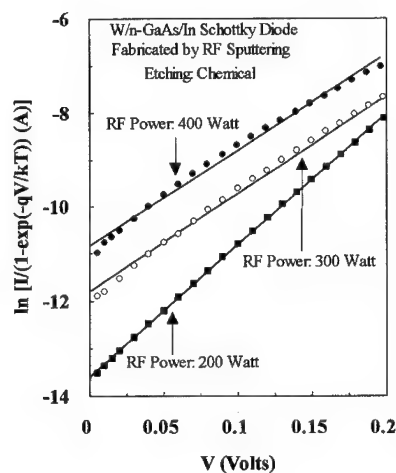


FIG. 2 $\ln [I/(1-\exp(-qV/kT))]$ vs V plots for the W/n-GaAs/In Schottky diode A, B and C

TABLE I

Summary of the electrical parameters obtained from the I-V data for the W/n-GaAs/In Schottky Diodes, fabricated by RF Sputter deposition of W at different rf powers, on the chemically etched polished surface of n-GaAs.

Device	RF Power (Watt)	n	I_0 (A)	r
Diode A	200	1.39	1.2×10^{-6}	270
Diode B	300	1.70	6.3×10^{-6}	70
Diode C	400	1.89	2.0×10^{-5}	50

The 1 MHz C^{-2} vs V data under reverse bias shown in Fig. 3, fitted well to Mott-Schottky relation⁹ with the values of 1.6 V and 1.2 V for the barrier heights (ϕ_{bo}) and $6.4 \times 10^{16} \text{ cm}^{-3}$ and $4.9 \times 10^{16} \text{ cm}^{-3}$ for the carrier concentrations (N_A-N_B) for the diodes A and B, respectively.

The C_M - V data in the frequency range 0.2-100 KHz, was corrected for series resistance¹⁰⁻¹¹ to obtain the junction capacitance C . Some typical C - V/f plots for the diode B are shown in Fig. 4, and the C - V/f plots for the diodes A and B are compared in Fig. 5. The frequency variation of C with the applied bias as a parameter, for the diode B is shown in Fig. 6.

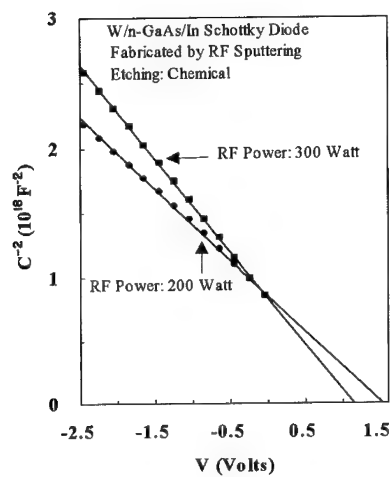


FIG. 3 C^{-2} vs V at 1 MHz for the W/n-GaAs Schottky diodes A and B

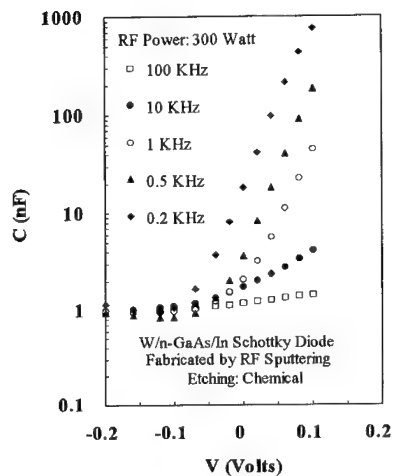


FIG. 4 C vs V at different frequencies for the W/n-GaAs Schottky diode B

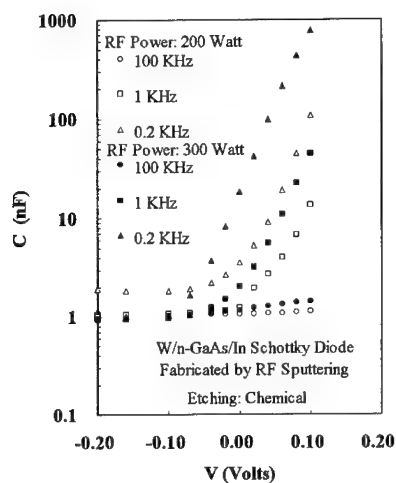


FIG. 5 Comparison of C vs V plots at different frequencies for the W/n-GaAs/In Schottky diodes A and B.

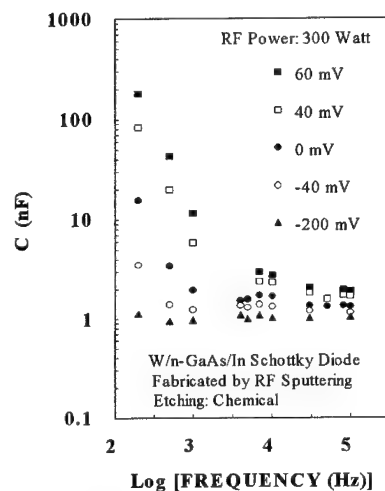


FIG. 6 Frequency dispersion of the junction capacitance in the W/n-GaAs/In Schottky diode B.

The frequency variation of C in the diodes A and B is compared in Fig. 7. The surface defects capacitance, C_p in the diodes A and B was obtained from $C(V, \omega)$ data by using the

procedure explained elsewhere^{10,12} and is shown in Fig. 8. The experimental values of C_p (Fig. 8, discrete points) were fitted to the theoretical relation¹³

$$C_p = \frac{qAN_{ss}\tan^{-1}(\omega\tau)}{\omega\tau} \quad (4)$$

where A is the area of the rectifying contact, ω the angular frequency of the ac signal, N_{ss} the energy density of the surface defects (surface states) and τ their relaxation time. The solid lines in Fig. 8 represent the best fit of the measured values of C_p (Fig. 8, discrete points) to Eq. (4).

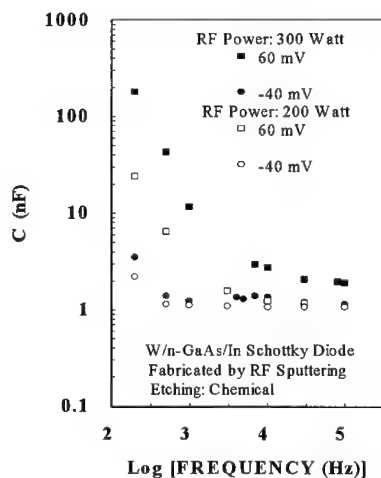


FIG. 7 Comparison of frequency dispersion of the junction capacitance in the Schottky diodes A and B.

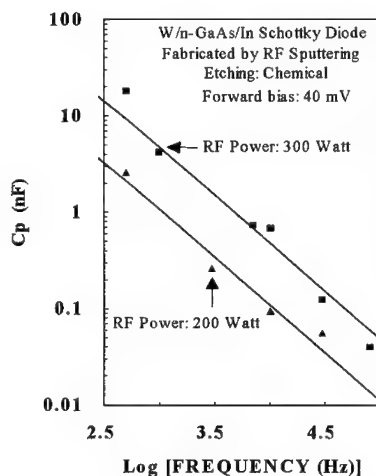


FIG. 8 Frequency variation of the surface defects capacitance at 40 mV in the Schottky diodes A and B.

DISCUSSION

From the I-V data shown in Fig. 1, the values of 270, 70 and 50 for r , for the diodes A, B and C, respectively, were obtained (Table I). The values of 1.39, 1.70 and 1.89 for n , and 1.2×10^{-6} A, 6.3×10^{-6} A and 2.0×10^{-5} A for I_0 , for the W/n-GaAs/In diodes A, B and C, respectively, were estimated from the forward I-V data (Fig. 2, Table I). These facts suggested that in the W/n-GaAs/In diodes, fabricated by RF Sputter deposition of W onto the chemically etched surface of n-GaAs, r decreased, n and I_0 increased, with the increase in rf power.

The 1 MHz C^2 -V characteristics for the diodes A and B fitted very well to the Mott-Schottky theory, over a wide range of reverse bias voltages (Fig. 3), indicating the abrupt nature of the W/n-GaAs junctions. However, the values of 1.6 V and 1.2 V for ϕ_{bo} , for the diodes A and B, respectively, obtained from the C-V data, were much higher than the values of 0.68 V and 0.78 V, obtained from the forward I-V data⁷. Such disagreement between the values of ϕ_{bo}

obtained from the two methods has been reported by other workers^{14,15}, and may be attributed to complicating effects of interfacial layer with fixed charges and surface defects.

For the diode B, the frequency dispersion of C was large under forward bias, but small under reverse bias (Fig. 4 and 6), which suggested that the defects at or near the metal/n-GaAs interface were responsible for this effect. The low frequency forward capacitance in the diode B was an order of magnitude higher than in the diode A (Figs. 5 and 7). The fit of the experimental values of C_p at 40 mV (Fig. 8 discrete points) to Eq. (4) (Fig. 8, solid line), provided the values of $1.8 \times 10^{13} \text{ eV}^{-1} \text{ cm}^{-3}$ and $3.5 \times 10^{12} \text{ eV}^{-1} \text{ cm}^{-3}$, for N_{ss} in the diodes B and A, respectively, with $\tau = 4.1 \text{ ms}$; which indicated that, the surface defects density in the diode B was five times higher than in the diode A.

In conclusion, the deposition of W by RF Sputtering at a rf power of 200 watt, onto the chemically etched polished surface of n-GaAs, formed a good quality Schottky contact. However, the rectifying quality of the W/n-GaAs junctions degraded with the increase in rf power. The density of the surface defects in the 300 watt diode (diode B), obtained from the C-f/V data was five times higher than in the 200 Watt diode (diode A) which suggested that the degradation in the quality of W/n-GaAs Schottky contacts fabricated by using high rf power was caused by high density surface defects created during sputter deposition of W on n-GaAs.

ACKNOWLEDGMENTS

This work was supported by the Consejo de Investigación de la Universidad de Oriente under contract No. CI-05-022-00456/94.

REFERENCES

1. N. Yokoyama, T. Mimura, M. Fukuta and H. Ishikkawa, *International Solid-State Circuits Conference, Digest of Technical papers*, Edited by L. Winner (IEEE, New York, 1981), p. 219.
2. B. L. Smith and M. Abbot, *Solid-State Electron.* **15**, 361 (1972).
3. L. J. Brillson, R. E. Viturro, M. L. Slade, P. Chiaradia, D. Kilday, M. K. Kelly and G. Margaritondo, *Appl. Phys. Lett.* **50**, 1379 (1987).
4. S. S. Lau, W. X. Chen, E. D. Marshall, C. S. Pai, W. F. Tse and T. F. Kuech, *Appl. Phys. Lett.* **47**, 1298 (1985).
5. K. M. Yu, J. M. Jaklevic and E. E. Haller, *Appl. Phys. A* **44**, 177 ((1987).
6. Crystal Specialties, 2853 Janitell Road, Colorado Springs, Co 80906 USA
7. A. Singh and L. Velásquez, (submitted for publication to *J. Appl. Phys.*)
8. E. H. Rhoderick and R. H. Williams, *Metal-Semiconductor Contacts*, Clarendon Press, Oxford (1988), p. 99.
9. A. Singh, K. C. Reinhardt and W. A. Anderson, *J. Appl. Phys.* **68**, 3475 (1990)
10. A. Singh, *Solid St. Electron.* **28**, 223, (1985)
11. A. Singh, P. Cova and R. Masut, *J. Appl. Phys.* **74**, 6714 (1993)
12. A. Singh, P. Cova and R. Masut, *Mater. Res. Soc. Symp. Proc.* **318**, 515 (1994).
13. K. Lehovec, *Appl. Phys. Lett.* **8**, 48 (1966).
14. C. Fontaine, T. Okumura and K. N. Tu, *J. Appl. Phys.* **54**, 1404 (1983).
15. Y. Kuriyama, S. Ohfuji and J. Nagano, *J. Appl. Phys.* **62**, 1318 (1987).

HIGH TEMPERATURE I-V AND C-V CHARACTERISTICS OF A Al/n-GaAs/In SCHOTTKY BARRIER TYPE DEVICE

A. Singh and N. Marcano

Laboratorio de Semiconductores, Departamento de Física, Universidad de Oriente, Apartado 188, Cumaná 6101, Sucre, Venezuela

ABSTRACT

Al/n-GaAs Schottky barrier type diode was fabricated by thermal deposition of Al on chemically etched polished surface of (100) n-GaAs at a pressure of 4×10^{-6} Torr. Back ohmic contact to n-GaAs was prepared by thermal deposition of In, followed by a 90 min. anneal in Ar atmosphere at 390°C . The C^{-2} vs V characteristics were quite linear for reverse bias voltages in the range 0-4 V. Over the temperature range 300-360 K, the values of the barrier height and the net carrier density ($N_D - N_A$), obtained from the C^{-2} -V data, were in the range 1.33-1.26 V and 4.3×10^{16} - $5.0 \times 10^{16} \text{ cm}^{-3}$, respectively. The forward I-V data over the temperature range 300-400 K, indicated that the electrical current across the Al/n-GaAs Schottky junction was transported by the mechanisms of generation-combination (GR) in the space charge, thermionic emission (TE) and ohmic leak current. A value of (1.20 ± 0.04) V for the zero bias barrier height was deduced from the temperature dependence of the TE reverse saturation current. The barrier height deduced from the I-V data was practically independent of temperature. The 20% change in $N_D - N_A$ with temperature, obtained from the C-V data, and important contributions of the GR and leak currents to the total forward current, suggested the presence of defect levels in the surface space charge layer in n-GaAs, which may be responsible for the discrepancy in the values of the barrier height obtained from the I-V and C-V data.

INTRODUCTION

Aluminum on GaAs has good stable thermal properties¹, and inspite of the surface oxidation problems, it is suitable for use as a Schottky metal for temperatures up to 400°C , and is widely used as a Schottky gate in practical GaAs MESFETs, and as a Schottky metal for characterization of deep levels in GaAs¹. Due to the technological importance of GaAs, full understanding of the nature of the electrical properties of the Al/n-GaAs junction is important.

There are some reports in literature on the analysis of the I-V characteristics of the Al/n-GaAs/In Schottky diodes^{2,3} in terms of the simple thermionic emission (TE) theory. However, to best of our knowledge, simultaneous analysis of the forward current-voltage/temperature (I-V/T) and high frequency capacitance-voltage/temperature (C-V/T) data has not been reported. In this work, we present high temperature I-V/T and 1 MHz C-V/T data for a Al/n-GaAs/In Schottky barrier type diode. The I-V/T data was analyzed in terms of a theoretical model which took various current-transport mechanisms and their temperature dependence into consideration. A non-linear least-squares fit method was used to separate the contributions of the different mechanisms, and the temperature dependence of the TE reverse saturation current thus obtained, was used to estimate the correct values of ϕ_{bo} , which were compared with the ones obtained from the C-V/T data.

EXPERIMENTAL METHOD

The Si-doped (100) n-GaAs substrate⁴ was chemically etched for 10 min. with HCl:H₂O (1:1) solution. Ohmic contact to the unpolished n-GaAs surface was obtained by thermal evaporation of In at a pressure of 3×10^{-6} Torr, followed by a 90 min. anneal at 390° C. High barrier Al/n-GaAs Schottky contact was prepared by thermal evaporation of Al dot of area 1.76×10^{-2} cm² at a pressure of 4×10^{-6} Torr, onto the chemically etched polished surface of n-GaAs. The In and Al contacts to n-GaAs were prepared, using a vacuum system with an oil diffusion pump.

The Al/n-GaAs/In Schottky diode was mounted in a liquid-nitrogen cryostat and its temperature was controlled and measured by a Stanton Red Croft 706 temperature programmer. The forward current-voltage (I-V) measurements were performed using Keithley 617 and 616 electrometers and a Hewlett-Packard 6106A power supply. The 1 MHz C-V measurements were made using a Boonton 72B capacitance meter.

EXPERIMENTAL DATA AND ANALYSIS

The I-V/T characteristics of the In contact to n-GaAs:Si were ohmic over a wide range of temperatures, with a value of $\approx 1 \Omega$ for the electrical resistance⁵. The 1 MHz C⁻² vs V data shown in Fig. 1, fitted well to the Mott-Schottky relation⁶, with the values of the diffusion potential (V_{do}), zero bias barrier height (ϕ_{bo}) and net carrier density ($N_D - N_A$) given in Table I.

A set of high temperature $\ln[I/(1 - \exp(-qV/kT))]$ vs V plots are shown in Fig. 2. For temperatures in the range 300-380 K, the experimental curves showed a central linear region with bends at both ends (Fig. 2). The length of the linear segment increased with the increase in temperature, and at 400 K, the curved part completely disappeared. The I-V data in the linear region was described by the Eq. (3.13) in Ref. 7, with an ideality factor (n) of 2.2 ± 0.1 .

Using a non-linear regression program "CURFIT", we tried to fit the experimental values of the forward current (Fig. 2) to the equation

$$I = I_1 + I_2 + I_3 + I_4, \quad (1)$$

where I_1 , I_2 , and I_3 are the currents due to thermionic emission (TE), thermionic field emission (TFE) and generation-recombination (GR) mechanisms in space charge region, respectively, and I_4 is the ohmic leak current due to inhomogeneities and surface defects in the metal-semiconductor (M-S) interface. However, the experimental I-V data did not fit to the complete Eq. (1). Then, the I-V data was fitted to different combination of two or three of the terms which exist on the right side of Eq. (1), and finally, it was found that the voltage dependence of the forward current shown in Fig. 2, was well described by the equation

$$I = I_1 + I_3 + I_4, \quad (2)$$

where I_1 , the current due to TE mechanism is given by⁷

$$I_1 = I_{t0} \left[\exp \left(\frac{qV}{kT} \right) - 1 \right], \quad (3)$$

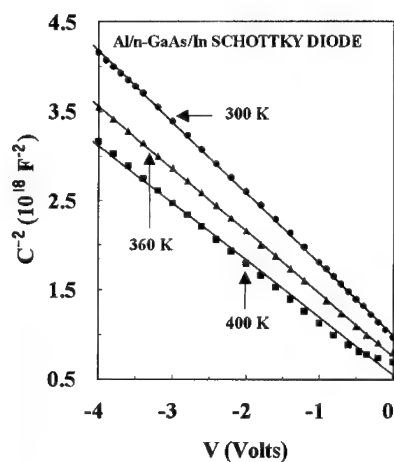


FIG. 1 1 MHz C^2 vs V characteristics at high temperatures, for the Al/n-GaAs/In Schottky diode.

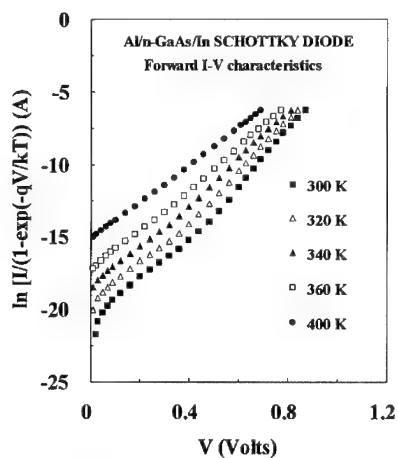


FIG. 2 $\ln [I/(1-\exp(qV/kT))]$ vs V plots for the Al/n-GaAs/In Schottky diode, at high temperatures.

TABLE I

Summary of the electrical parameters for the Al/n-GaAs/In Schottky diode, determined from the C - V/T and I - V/T data.

T (K)	$N_D - N_A$ (10^{16} cm^{-3})	V_{d0} (V)	(C - V) ϕ_{b0} (V)	(I - V) ϕ_{b0} (V)
400	5.4	1.04	1.12	1.16
380	5.1	1.09	1.14	1.18
360	5.0	1.18	1.26	1.21
340	4.8	1.22	1.29	1.21
320	4.6	1.28	1.33	1.20
300	4.3	1.26	1.32	1.19

and the TE reverse saturation current, I_{to} is defined by⁷

$$I_{to} = AA_{eff}T^2 \exp \left[\frac{-q(\phi_{bo} - \Delta\phi_{bo})}{kT} \right], \quad (4)$$

where A_{eff} is the modified effective Richardson constant, q the magnitude of the electron charge, and the barrier height lowering at zero bias due to image force ($\Delta\phi_{bo}$) defined by the Eq. (1.26a) in Ref. 7, has a value of 0.036 V for the Al/n-GaAs/In Schottky diode presented in this work. The GR current, I_3 is given by⁷

$$I_3 = B(V_{do} - V)^{1/2} \exp \left(\frac{qV}{2kT} \right) \left[1 - \exp \left(\frac{-qV}{kT} \right) \right], \quad (5)$$

with

$$B = \left[\frac{2q \epsilon_s A^2}{\tau^2 (N_D - N_A)} \right]^{1/2} \left[\frac{2\pi k (m_e^* m_h^*)^{1/2}}{h^2} \right]^{3/2} T^{3/2} \exp \left[-\frac{E_g}{2kT} \right], \quad (6)$$

where m_e^* and m_h^* are the effective masses of electrons and holes, respectively, E_g the semiconductor energy gap, and τ the life time of the charge carriers in the space charge region. The ohmic type leak current, I_4 is given by

$$I_4 = \frac{V}{R_1} \quad (7)$$

where R_1 is the resistance which limits the ohmic part of the leak current. The values of I_{to} , B and R_1 , obtained from the above fitting procedure are given elsewhere⁵. The experimental I-V data at 340 K (Fig. 3, discrete points) gave an excellent fit to the Eq. (2) (Fig. 3, solid curve I). To show the relative importance of the TE, GR and leak current mechanisms, I_1 , I_3 and I_4 are also plotted in Fig. 3. For temperatures in the range 300-400 K, the experimental values of $\ln [I_{to}/T^2]$ vs $1000/T$ (Fig. 4, discrete points) fitted well to the theoretical Eq. (4) (Fig. 4, solid line) with

$$\begin{aligned} \phi_{bo} - \Delta\phi_{bo} &= (1.16 \pm 0.04) \text{ V} \\ A_{eff} &= (4.2 \pm 0.5) \times 10^{-2} \text{ A cm}^{-2} \text{ K}^{-2} \end{aligned} \quad (8)$$

Substituting the experimental values of I_{to} in the Eq. (4), using A_{eff} from the Eq. (8), and $\Delta\phi_{bo} = 0.036$ V, the values of ϕ_{bo} were calculated and are listed in Table I.

From the experimental values of B^5 , the values of $\ln [B/T^{1.5}]$ vs $1000/T$ were calculated, which fitted well to the Eq. (6) with $E_g = (1.37 \pm 0.03) \text{ eV}$.

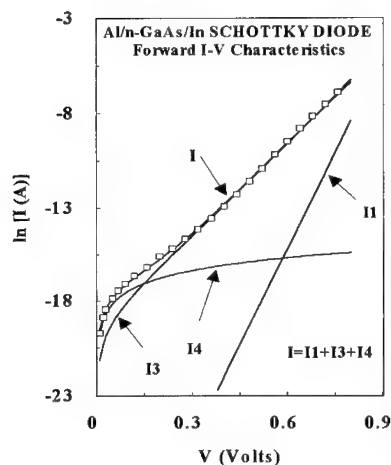


FIG. 3 Fit of the forward I-V data at 340 K (points) to Eq. (2) (solid curve I).

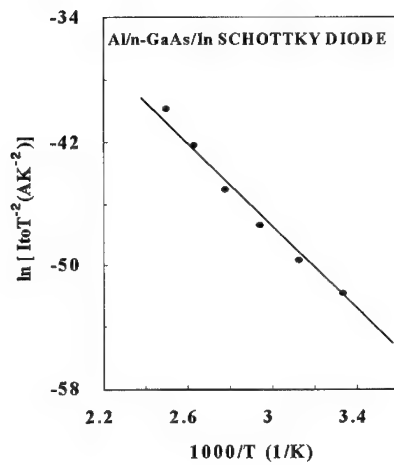


FIG. 4 Activation plot based on TE saturation reverse current (I_{10}).

DISCUSSION

For temperatures in the range 300-360 K, the C^{-2} vs V characteristics at 1 MHz, for the Al/n-GaAs/In Schottky diodes fabricated by thermal evaporation method, were quite linear over a wide range of reverse bias voltages (Fig. 1), indicating the abrupt nature of the M-S junction. However, the C^{-2} vs V data at 400 K showed an upward curvature at small reverse bias voltages which may be due to the presence of the acceptor type traps near the M-S junction. Over the temperature range 300-400 K, the values of $N_D - N_A$, obtained from the slope of the C^{-2} - V curves (Fig. 1), varied by 25% (Table I). This fact provided an evidence for the existence of the donor type defect levels in the space charge layer.

The I - V / T characteristics for the Al/n-GaAs/In Schottky diode shown in Fig. 2, manifested a strong non-ideal behavior which suggested that the pure TE mechanism was not responsible for the forward current transport in this device. The experimental forward data for the Al/n-GaAs/In Schottky diode was analyzed in terms of a theoretical model in which the TE, GR and ohmic leak current mechanisms were simultaneously present. The excellent fit of the experimental forward I-V data shown in Fig. 3 (discrete points) to the theoretical Eq. (2) (Fig. 3, solid curve I), permitted the separation of the contributions of the GR, TE and ohmic leak currents to the total forward current flowing through the Al/n-GaAs Schottky junction (Fig. 3, solid curves I_1 , I_3 and I_4). Three distinct regions were identified: (i) $V < 180$ mV, where the highest contribution to the forward current came from the ohmic leak current (I_4), the second place corresponded to the GR current (I_3) and the thermionic emission current (I_1) was negligible; (ii) $180 \text{ mV} < V < 580 \text{ mV}$, where the GR current dominated over the TE and ohmic leak currents; and (iii) $V > 580 \text{ mV}$, where the currents I_3 and I_1 occupied the first and second place, respectively, and I_4 was negligible.

Our value of $\phi_{bo}=1.19$ V at 300 K (Table I), obtained from the I-V/T is much greater than the value of $\phi_{bo}=0.71$ V, reported by Hasegawa et al³ for their Al/n-GaAs/In Schottky diode fabricated using a vacuum system with an oil diffusion pump. The reason for this discrepancy seems that these authors have obtained ϕ_{bo} from the room temperature I-V data with $n=1.5$, using the simple TE model which holds only for n close to 1. On the contrary, we have used a more realistic method of analysis which permits the determination of a correct value for the barrier height even from a highly non-ideal I-V/T data.

For temperatures in the range 300-360 K, the values of ϕ_{bo} , obtained from the I-V/T data, even after making image force lowering, were systematically slightly lower than those obtained from the C-V/T data (Table I). This difference may be due to the effect of the defect levels in the surface space charge layer, which was not taken into account in the C-V method.

The value of the semiconductor energy band gap, $E_g=1.37\pm0.03$ eV, obtained from the slope of the $\ln[B/T^{1.5}]$ vs $1000/T$ plot⁵, agreed within experimental error, with the value of 1.42 V, reported for the E_g of GaAs⁸. This fact along with the other results obtained from the TE reverse saturation current, indicated the validity of the theoretical model used for the analysis of the high temperature forward I-V/T data for the Al/n-GaAs/In Schottky diode.

In summary, the increase of N_D-N_A with the increase in temperature was attributed to the presence of the donor type defects in the space charge layer. The bias dependence of the measured forward current in the Al/n-GaAs/In Schottky diode over the temperature range 300-400 K, was very well described in terms of a theoretical model in which the current transport mechanisms of generation-recombination in space charge region, ohmic leak current, and thermionic emission, simultaneously contributed to the total forward current. The large values of the ohmic leak, GR currents at low, and high forward bias voltages, respectively, also provided an evidence of the presence of a considerable amount of interface defects.

ACKNOWLEDGMENTS

This work was supported by the Consejo de Investigación de la Universidad de Oriente with Contract No. CI-05-022-00456/94.

REFERENCES

1. C. J. Palmstrøm and D. V. Morgan, in *Gallium Arsenide*, edited by M. J. Howes and D. V. Morgan (Wiley and Sons Ltd, 1985, New York) p. 195
2. R. van de Walle, R. L. Van Meirhaeghe, W. H. Laflère and F. Cardon, *J. Appl. Phys.* **74**, 1885 (1993).
3. F. Hasegawa, M. Onomura, C. Mogi and Y. Nannichi, *Solid-St. Electron.* **31**, 223 (1988).
4. Crystal Specialties, 2853 Janitell Road, Colorado Springs, Co 80906 USA.
5. A. Singh and N. Marcano (submitted for publication to *J. Appl. Phys.*).
6. A. Singh, K. C. Reinhardt and W. A. Anderson, *J. Appl. Phys.* **68**, 3475 (1990).
7. E. H. Rhoderick and R. H. Williams, *Metal-Semiconductor Contacts* (Clarendon, Oxford, 1988) Chap. 3, pp 97, 99-100.
8. A. Fahrenbruch and R. H. Bube, *Photovoltaic Solar Energy Conversion* (Academic Press, New York, 1983) p 42.

**TEMPERATURE DEPENDENCE OF METAL-SEMICONDUCTOR
CONTACTS ON 6H-SiC. S.R. Smith*, A.O. Ewaraye, and W.C.
Mitchel, Wright Laboratory, WL/MLPO, 3005 P St., Wright-Patterson AFB,
OH 45433-7707**

ABSTRACT

We have examined the temperature dependence of the barrier height of Au, Ag, Ni, and Al, metal-semiconductor contacts on n-type 6H-SiC, and Al metal-semiconductor contacts on p-type 6H-SiC. The barrier height was determined from the $(1/C^2)$ vs V_R characteristics of the contacts at temperatures ranging from 300K to 670K. The measurements were made at 1 MHz. These measurements were compared to I-V measurements at various temperatures, and to the behavior predicted by standard models.

INTRODUCTION

The precise nature of the metal-semiconductor (m-s) contact is still not fully understood,¹ however, two major theories have been put forth to explain why a metal on a semiconductor has the characteristics that it does.^{2,3} One of these theories is that the metal induces interface states in the band gap of the semiconductor and that these metal-induced-gap-states (MIGS) pin the Fermi level and hence control the height of the barrier at the interface.^{4,5} The other theory invokes defects, created at the interface by chemical reactions between the metal and the semiconductor, which control the position of the Fermi level, and hence, the barrier height.^{3,6} It should be possible to discern which of these mechanisms is at work by examining the temperature dependence of the barrier height. This is so because the temperature dependence of the barrier should follow the individual motion of the respective band edge if MIGS are controlling the position of the Fermi Level. On the other hand, if defects control the position of the Fermi level, it is the ionization entropy of the defects which would control the temperature dependence of the barrier height.³

A vast number of electronic devices involve the use of m-s contacts, and the pre-eminent property of ms Schottky contacts is the barrier height at the m-s interface.⁷ The value of the barrier height may be determined by current-voltage (I-V), capacitance-voltage (C-V), or

photoemission measurements.^{8,9} The more popular of these are the I-V and CV measurements. Van Otterloo and Gerritsen¹⁰ have determined that CV measurements more accurately yield the flat-band barrier height. In addition, it is relatively easy to obtain CV data as a function of temperature.

EXPERIMENTAL DETAILS

We have investigated, as a function of temperature, the electrical behavior of m-s Schottky diodes fabricated on both n- and p-type 6H-SiC using the metals Au, Ag, Ni, and Al. The range of temperatures was from 300K to 670K (27C to 397C). We determined the m-s contact barrier height from CV measurements performed at 1 MHz, using an HP 4280A CV Meter-Plotter. A MicroManipulator HSM hot stage and temperature controller were used to provide the high-temperature environment. Four-point current-voltage (IV) measurements were also made at various temperatures. Metals were deposited by either RF sputtering, e-beam evaporation, or DC magnetron sputtering, onto carefully prepared surfaces. The surface preparation consisted of cleaning in organic solvents (trichloroethylene, acetone, methanol), H₂SO₄ at 50 C; three cycles through a 5:3:3 solution of HCl:H₂O₂:H₂O followed by a 10% solution of HF:H₂O, then a DI H₂O (18 M-ohm) rinse; the specimens were then stored briefly in methanol and blown dry with N₂ just before insertion into the deposition chamber. Some specimens were oxydized in wet oxygen at 1150 C for four hours, and subsequently etched in HF and stored in methanol prior to insertion into the deposition chamber. No difference in the results were noted.

The quality of the diodes was determined from the linearity of the C⁻² vs V curve at room temperature (300 K). The intercept (V_i) of a linear least squares fit to this portion of the curve was then used to calculate the flat-band barrier height according to the relationship¹¹

$$\phi_b = -V_i + V_0 + 2kT$$

where k is Boltzmann's constant, T is the temperature in Kelvins; V₀ = (kT/q)ln(N_C/N_D), where N_C is the effective density of states in the conduction band (for n-type material) and N_D is the net doping density as determined from the slope of the C⁻² vs V curve. Because the calculation of N_C involves the use of the effective mass, m*, and no reliable value for a temperature dependent effective mass exists, we have plotted the intercept value, ie. the diffusion potential, versus temperature. In those

cases where we felt that a value for the barrier height would serve better, we have used the room temperature value for m^* .

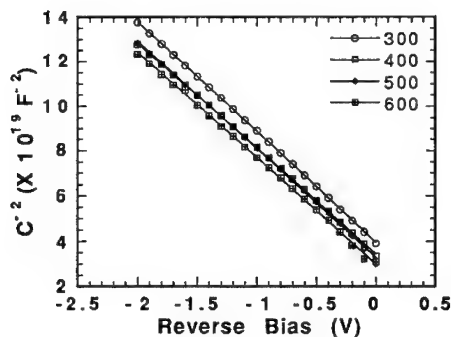


Figure 1. C^2 vs V curves at four temperatures for an Al m-s contact on n-type 6H-SiC.

increased to determine the degree of ionization of the dominant impurity, since the value of N_D is used in the calculation of the barrier height.

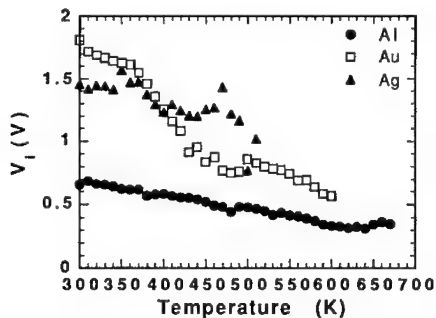


Figure 2a. Diffusion potential plotted as a function of temperature for three m-s contacts on n-type 6H-SiC.

narrowing.^{11,12} The p-type barrier height increases with temperature and at a similar rate as the n-type barrier height decreases. (fig 2b) It is not clear from these measurements which band edge is moving the most, nor is the direction of movement clear. It is conceivable that the band edges are moving downward relative to the Fermi level, and that the valence band edge is moving somewhat faster than the conduction band edge.

Figure 1 shows the C^2 vs V data plotted for various temperatures. The diode was Al on n-type 6H-SiC. The linearity of the data is apparent. The progression of the intercept to smaller values is also apparent. Similar results were obtained for each metal studied. The

concentration profile was also monitored as the temperature was

Figures 2a and 2b show the results of CV measurements on m-s contacts to n- and p-type 6H-SiC, respectively. It is clear that for n-type material that the barrier lowers with increasing temperature. The band gap is narrowing in this temperature range; however, fits to the data

yield a slope that is ten to twenty times the rate of band gap

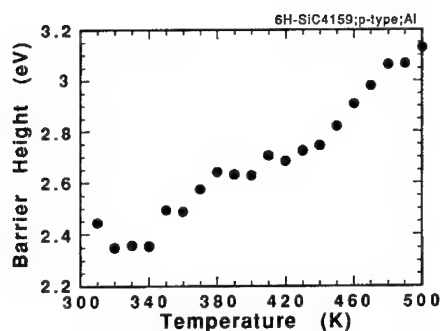


Figure 2b. Calculated barrier height for an Al m-s contact on p-type 6H-SiC, plotted as a function of temperature.

rapid rise in the value of the p-type barrier height. Because of the apparent motion of both band edges it is difficult to distinguish between the two models of barrier formation. Further work using midgap defect states as references will help determine the absolute motion of the band edges.

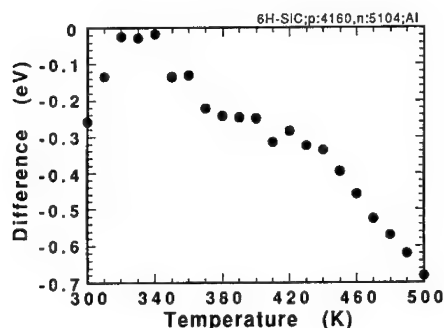


Figure 3. Deviation of the sum of the calculated barrier heights of Al m-s contacts on p- and n-type 6H-SiC from the calculated temperature dependent band gap.

while those on p-type material increase. Applications involving the use of m-s contacts on these materials must take this temperature dependence into account. A distinction between two competing theories of barrier formation could not be made since the change in barrier height of both n- and p-type contacts was large.

Figure 3 shows the deviation of the sum of the barrier heights of Al on n- and p-type 6H-SiC from the band gap value as a function of temperature. The barrier heights were calculated using a fixed value for the effective masses. The sum of the barrier heights increasingly exceeds the

band gap values as the temperature is increased.

This is attributable to the

CONCLUSIONS

We have observed that the barrier height of m-s Schottky contacts changes dramatically with temperature above 300 K. The rate of change is ten

to twenty times the rate of band gap narrowing. Barrier heights for n-type material decrease,

REFERENCES

1. R.H. Williams, *Contemp. Phys.* **23**, 329-351, (1982)
2. Heinz K. Henisch, Semiconductor Contacts An Approach to Ideas and Models, (Clarendon, Oxford, 1989) p. 25.
3. P. Revva, J.M. Langer, M. Missous, and E.R. Peaker, *J. Appl. Phys.* **74**, 416 (1993).
4. E.H. Rhoderick and R.H. Williams, Metal-Semiconductor Contacts, Second Edition, (Clarendon, Oxford, 1988).
5. Raymond T. Tung, Contacts to Semiconductors, Fundamentals and Technology, edited by L.J. Brillson, (Noyes, Park Ridge, NJ, 1993,) p. 176.
6. W.E. Spicer, P.W. Chye, P.R. Skeath, C.Y. Cu, and I. Lindau, *J. Vac. Sci. Technol.* **16**, 1422 (1979)
7. B.L. Sharma and S.C. Gupta, *Sol. St. Technol.* **May**, 1980, p. 97; *Sol. St. Technol.* **June**, 1980, p. 90.
8. Henry A. Wynands, M.L. Hartsell, and Bradley A. Fox in Diamond, SiC and Nitride Wide Bandgap Semiconductors, edited by Calvin H. Carter, Jr., Gennady Gildenblat, Shuji Nakamura, and Robert J. Nemanich (Mater. Res. Soc. Symp. Proc. **339**, Pittsburgh, PA, 1994) p. 235.
9. C.R. Crowell, S.M. Sze, and W.G. Spitzer, *Appl. Phys. Lett.* **4**, 91 (1964).
10. J.D. van Otterloo and L.J. Gerritsen, *J. Appl. Phys.*, **49**, 723 (1978)
11. Dieter K. Schroder, Semiconductor Material and Device Characterization, (John Wiley & Sons, New York, 1990), p134.
12. A. Michael Cowley and Robert A. Zettler, *IEEE Trans. Electron Dev.* **ED-15**, 761 (1968).

SURFACE MORPHOLOGY INVESTIGATION OF Au AND Pt ELECTROLESS CONTACT ON ZnCdTe CRYSTAL BY ATOMIC FORCE MICROSCOPY

ZHIYU HU, ZHIHUA HU, K.T. CHEN, M.A. GEORGE, A. BURGER AND W.E. COLLINS
Center for Photonic Materials and Devices, Department of Physics, Fisk University, Nashville, Tennessee 37208, U.S.A.

ABSTRACT

Gold and platinum metal contacts have been deposited on the cleaved and etched surfaces of ZnCdTe single crystals by "electroless" method from AuCl_3 , PtCl_2 and PtCl_4 aqueous solutions with different concentrations and deposition times. Atomic Force Microscopy (AFM) has been employed to reveal the surface morphology of metal contacts and it was found that for AuCl_3 and PtCl_2 solutions, the surface morphology and grain size are similar, and uniformly distributed. The surface morphology on contact made from PtCl_4 shows a larger grain size, higher roughness and non-uniformity. The effect of different heat treatments to the surface morphology will be discussed.

INTRODUCTION

Improvements in the quality of $\text{Zn}_x\text{Cd}_{1-x}\text{Te}$ (ZCT) single crystals have made them useful as suitable substrates for the growth of epitaxial $\text{Hg}_x\text{Cd}_{1-x}\text{Te}$ and $\text{Hg}_x\text{Zn}_{1-x}\text{Te}$ films, used as infrared detectors ¹ and as room temperature gamma ray detectors with better energy resolution.^{2,3} In order to obtain higher perfection crystals for effective nuclear radiation detectors, high resistivity material is required. Consequently, it is an important task to characterize the surface structure and composition of $\text{Zn}_x\text{Cd}_{1-x}\text{Te}$ crystal. Atomic Force Microscopy (AFM) is suitable for examining the surface characterization of nonconducting materials with near atomic resolution.⁴ A series of experiments have been carried out using AFM to survey various treated, Au or Pt coated and uncoated n-type $\text{Zn}_x\text{Cd}_{1-x}\text{Te}$ ($x=0.05$) single crystal surfaces.

These treatments which were applied on the crystal surfaces were, in most cases, similar to the ones used in device preparation procedures. The native surfaces were first studied under ambient conditions then the surfaces were freshly etched in Br-MeOH, gold contacts on cleaved/etched ZnCdTe surfaces were applied by electroless deposition. The simple and reliable electroless gold deposition, which was introduced by Kroeger and DeNobel,⁸ has been used to apply electric contacts from gold chloride solutions. The Au/p-type CdTe contact (producing ohmic contact) has been employed in the fabrication of polarization free detectors.^{9,10} The same deposition method has been studied for making Au/n-type CdTe contact which created a Schottky contact with 0.8 eV barrier height.¹¹ In order to gain the knowledge how different metal contacts affect the crystal surface, studies of electroless platinum contacts were performed with various treatments.

In our experiments, heat treatments have been applied to the surfaces before and after the contacting procedure. Etched, gold contacted wafers were annealed in both air and vacuum environments at different temperatures. Obvious changes in morphology and chemical composition have been observed after treatment. Studies correlating sample treatment to the Schottky diode characteristics and the surface modifications have been completed.

EXPERIMENTAL

1. Crystal growth and sample preparation

$\text{Zn}_x\text{Cd}_{1-x}\text{Te}$ ($x=0.05$) single crystals were grown from the melt by using the travelling heater method (THM), shown in Figure 1.¹² The starting materials were purchased from Alfa as 99.999% (metal basis) pure tellurium, 99.9999% pure cadmium and 99.9999% pure zinc.⁶ A laboratory-made apparatus with two source heaters has been employed to zone-refine the tellurium. A charge of 75 g tellurium was loaded into a clean and outgassed quartz ampule, evacuated and sealed. Zone refining was performed for a total of 45 passes at 1.5 cm/hour. The central part of the zone-refined ingots were mixed with the other starting elements and loaded into 15 cm long quartz ampules, evacuated and sealed. The synthesis reaction was performed in a laboratory-built rocking furnace kept at 800 °C for one week. A three-zone vertical furnace was employed to grow the crystals for the melt near the melting temperature of the alloy (1100 °C) using a heater translation rate of 0.5 cm/ 24 hours. Large grain single-crystal ingots having 1 cm diameter and about 8 cm long were obtained from a 20 cm charge. Samples were cut and polished to a size of 5 x 5 x 1 mm for surface characterization.

As during the fabrication of real ZnCdTe devices, the crystals were exposed in air for different periods of time. Similar conditions were applied when electric contacts were prepared. The crystal, Sample *C*, was freshly cleaved along the (110) plane and examined by the AFM, then gold contacts (Sample *CG*) were deposited using AuCl_3 aqueous (100 ppm concentration) solution for one minute. For Sample *E*, the crystal has been imaged by the AFM right after being etched by 5% Br-MeOH solution (2 min.). A gold contact was placed on the same region by using AuCl_3 aqueous solution (100 ppm concentration) for one minute, Sample *EG*. Heat treatments have been applied by annealing the samples in vacuum tube or in air for one hour at 300 °C, 400 °C and 500 °C, Sample *EGV3*, *EGV4*, *EGV5* and *EGA* respectively. By using the same method, two platinum contacts were applied on the etched crystal surface by using PtCl_2 (Sample *EP2*) and PtCl_4 (Sample *EP4*) aqueous solution (100 ppm concentration) for one minute. Normally, the contact size is about 3 mm in diameter dropped for reaction. For Sample *EP2A* and Sample *EP2V*, PtCl_2 contacted ZnCdTe crystals have been annealed in air or dynamic vacuum tube at 300 °C for 60 minutes. AFM measurement and observation have been utilized following each treatment.

2. Atomic force microscope

Our morphological analysis was performed on the Digital Instruments NanoScope II and NanoScope E.⁴ Considering the softness of the material surface, V-shaped, gold-coated silicon nitride cantilevers having a force constant of 0.06 N/m was employed in order to prevent the unnecessary surface deformation.

RESULTS AND DISCUSSION

Initially, the morphology of cleaved ZnCdTe surface as well as cleaved, gold coated samples were studied. Figure 1 (a) shows AFM images obtained on a ZnCdTe (110) surface (Sample *C*). Cleavage steps can be clearly observed, with a step height of about 1.5 nm. Higher

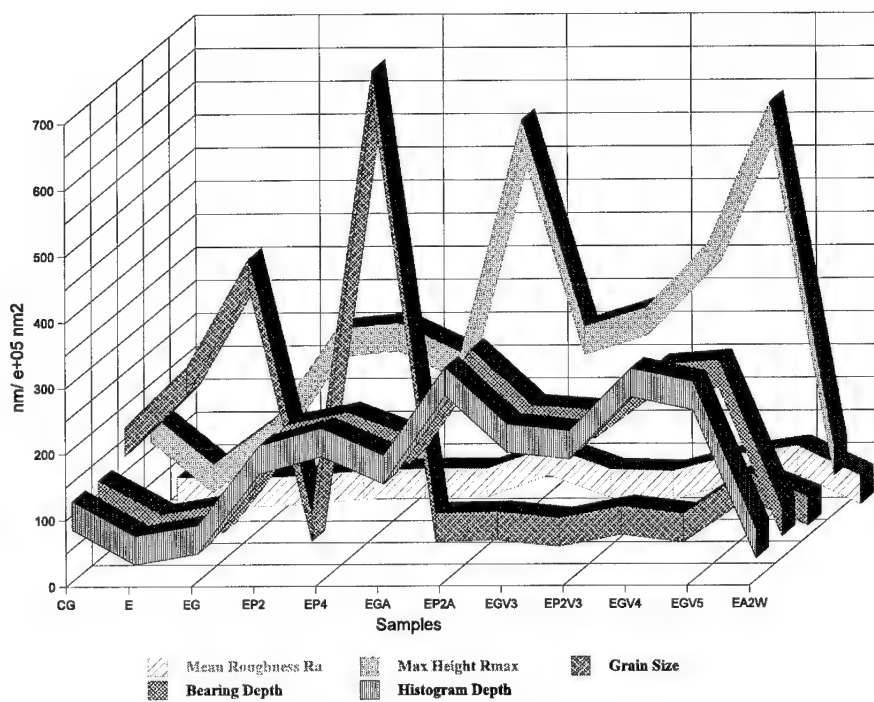


Chart I: AFM analysis results

magnification AFM image, Figure 1 (b), shows an average grain diameter of 40 nm on the gold covered region (Sample **CG**). Figure 1 (c) , Sample **CG**, presents the interface between gold contact and ZnCdTe crystal surface. On the left side of Figure 1(c) there is the gold contacted area, the right side is the cleaved crystal surface. The vertical change at the interface is less than 5 nm. Figure 1 (d) shows a magnified view of the second interface which was laid in the contact region. Discontinuous and uncovered (windows) areas can be seen along the interface. The depth of the "windows" are about 20 nm.

Figure 2 (a), Sample **E**, shows top view of three freshly Br-MeOH etched ZnCdTe surface. The surface contains a relatively homogenous (the average surface roughness was about 25 nm) grain structure resulting from the etching process. Previous studies which involved experimental techniques such as X-ray photoelectron spectra and low temperature photoluminescence, indicated that freshly etched samples of CdTe and ZnCdTe contained an excess of Te⁰ when examined immediately after etching, while surfaces left in ambient were covered with a thin layer consisting mainly of tellurium oxides^{6,13-16}. In present study, we have found that both the surface roughness and chemistry are strongly affected by the annealing treatments. Figure 2 (b) shows the surface features have changed upon gold deposition reflecting the morphology of the as deposited gold film, (Sample **EG**). The morphology and grain size are identical compared with the gold-coated, cleaved surface. Platinum contacted crystal are shown in Figure 2 (c) and 2 (d), Sample **EP2** and **EP4** representatively. From these images, one could early indicate that both PtCl₂ and PtCl₄ depositions form ellipsoid sharp features on the surface comparing with ball sharp on the gold coated surface. Their sizes are generally larger than gold deposition meanwhile surface roughness* is also increased remarkably, shown in Table I. In the large scanning size images which are not shown here, we notice that platinum contacts create some large-sized (>1~2 μm) crystal-like features forming in the deposit processing. PtCl₄ thin film has larger grain size and higher roughness than PtCl₂ thin film. Better uniformed distribution was found on the PtCl₂ contacted surface.

When the gold films were annealed in air at 300 °C for an hour, Figure 3 (a), Sample **EGA**, there is a dramatic change in the surface morphology of the as-deposited gold film. The grain size grew by a factor of 2-3, as well as the surface roughness. When a similar gold film was annealed in vacuum at 300 °C for 60 minutes, (Sample **EGV3**) there was an increase in the mean grain diameter as well as a roughening of the surface and the images are shown in Figure 3 (b). New surface morphology has been formed, however, both grain size and roughness did not enlarge as much as those annealed in air. Heat treatments have also been applied on PtCl₂ coated ZnCdTe crystal, Sample **EP2A** (annealed in air at 300 °C for 60 minutes) and Sample **EP2V3** (annealed in vacuum at 300 °C for 60 minutes). Shown in Figure 3 (c) & (d), we found there were morphologically changing on both samples. Similarly as gold coated samples, the one annealed in air had rougher surface than the one annealed in vacuum which can be seen in Table I.

* The surface roughness is the mean value of the surface relative to the center plane and is calculated using:

$$Ra = \frac{1}{LxLy} \int_0^{Lx} \int_0^{Ly} |f(x,y)| dx dy$$

Where $f(x,y)$ is the surface relative to the Center Plane and Lx and Ly are the dimensions of the surface.

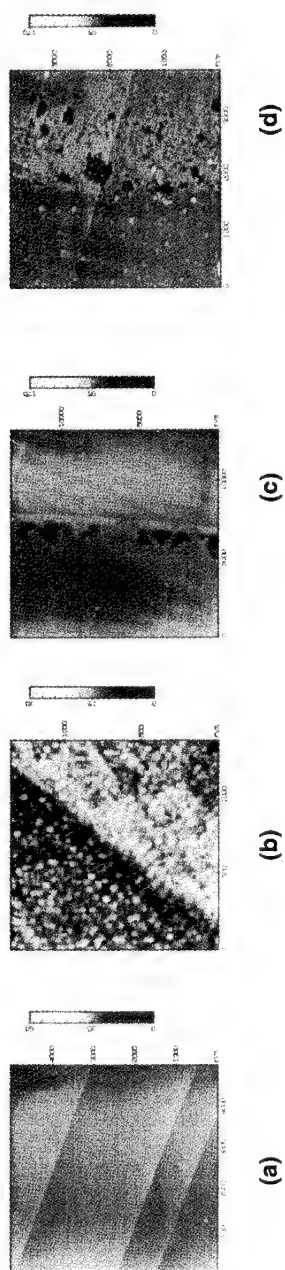


FIGURE 1: (a) Freshly cleaved ZnCdTe (110) surface; (b) AuCl_3 contacted on cleaved ZnCdTe surface; (c) First interface between gold thin film and cleaved surface; (d) Second interface between gold thin film and cleaved surface

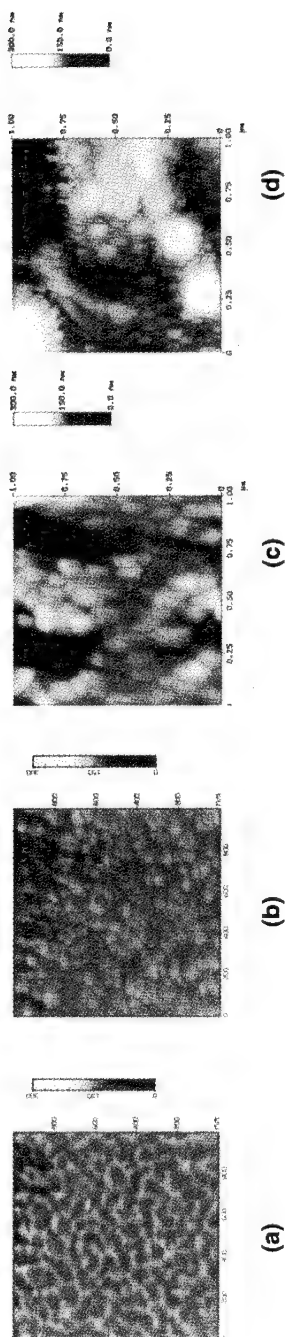


FIGURE 2: (a) Br-MeOH etched ZnCdTe surface; (b) Etched and AuCl_3 contacted; (c) Etched and PtCl_2 contacted; (d) Etched and PtCl_4 contacted

Table I

Sample	CG	E	EG	EP2	EP4	EGA	EP2A	EGV3	EP2V3	EGV4	EGV5	EA2W
Mean Roughness Ra nm	4.14	1.79	5.34	13.22	15.88	15.68	48.6	14.11	11.32	35.6	49.2	3.59
Max Height Rmax nm	134.2	56.8	125	261.3	270.4	225.4	576.4	264.2	293.2	390.3	602.9	80
Grain Size $e+005 \text{ nm}^2$	145	237	401	15.9	684.1	14.8	16.5	6.8	24.6	12.9	75.9	37.8
Bearing Depth nm	97.9	46.5	62	181.5	200	164.8	296	210	203	271.1	278.4	54.2
Histogram Depth nm	99.5	46.6	63	183.1	209	167.4	300.9	214.5	204.2	298.6	278.4	54.3

CG -- Cleaved and AuCl_3 coated
 E -- Etched by using 5 % Br-MeOH
 EG -- Etched and AuCl_3 coated
 BP2 -- Etched and PtCl2 coated
 BP4 -- Etched and PtCl4 coated
 EGA -- Etched, AuCl_3 coated and annealed at 300 OC in air 60 min.
 EP2A -- Etched, PtCl2 coated and annealed at 300 OC in air 60 min.
 EGV3 -- Etched, AuCl_3 coated and annealed at 300 OC in vacuum 60 min.
 EP2V3 -- Etched, PtCl2 coated and annealed at 300 OC in vacuum 60 min.
 EGV4 -- Etched, AuCl_3 coated and annealed at 400 OC in vacuum 60 min.
 EGV5 -- Etched, AuCl_3 coated and annealed at 500 OC in vacuum 60 min.
 EA2W -- Etched and aged in the ambient for two weeks

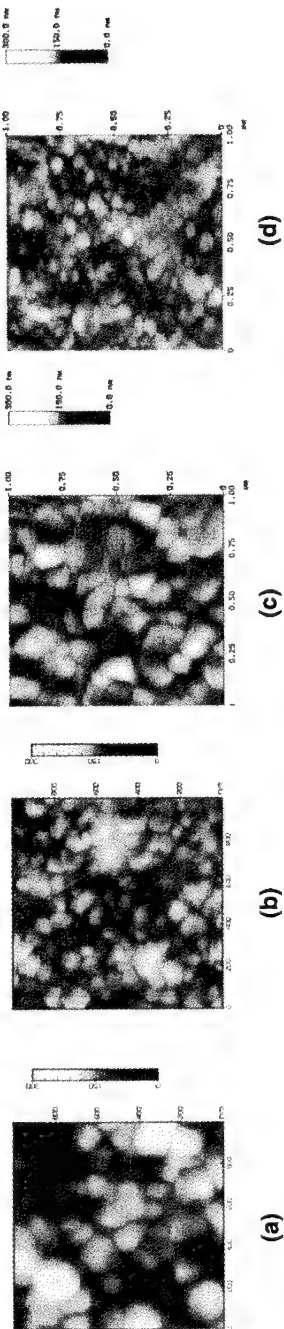


FIGURE 3: (a) Etched and AuCl_3 contacted ZnCdTe then annealed in air at 300°C for 60 minutes; (b) Etched and AuCl_3 contacted ZnCdTe then annealed in vacuum at 300°C for 60 minutes; (c) Etched and PtCl_2 contacted ZnCdTe then annealed in air at 300°C for 60 minutes; (d) Etched and PtCl_2 contacted ZnCdTe then annealed in vacuum at 300°C for 60 minutes;

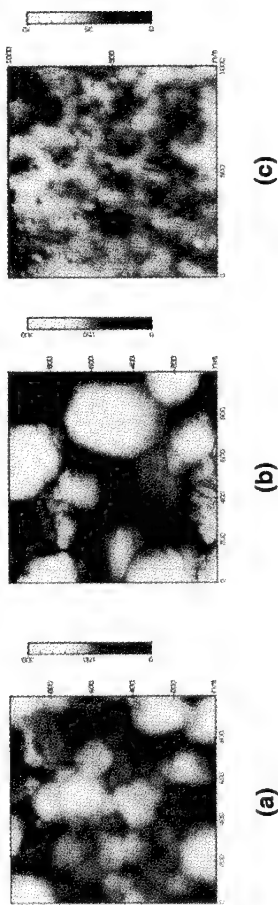


FIGURE 4: (a) Etched and AuCl_3 contacted ZnCdTe then annealed in vacuum at 400°C for 60 minutes; (b) Etched and AuCl_3 contacted ZnCdTe then annealed in vacuum at 500°C for 60 minutes; (c) Etched and AuCl_3 contacted ZnCdTe then aged in the ambient for two weeks

Further more, studies of the gold film annealed in vacuum at 400 °C (Sample *EGV4*) and 500 °C (Sample *EGV5*) for 60 minutes were presented in Figure 4 (a) and Figure 4 (b). As one can see the higher the annealing temperature was, the rougher surface emerged, as well as the grain size. The aging effects have also been investigated in our experiment. In the Figure 4 (c), Sample *EA2W*, we present the etched ZnCdTe surface aged in the ambient for two weeks. Comparing this with the freshly etched surface, after exposure to air the new structures have been formed on the surface during two weeks period. It appears that aging in air and the heat treatment produce similar effects to the etched, uncoated ZnCdTe surface.

Besides the AFM studies, additional measurements by Scanning Auger Electron Spectroscopy (SAES), X-ray Photoelectron Spectroscopy (XPS) , low temperature photoluminescence (PL), and dark current-voltage (I-V) curves have been applied on the gold coated ZnCdTe surface. I - V measurement enabled us to show a correlation between the Schottky diode characteristics and the chemical species/defects that are formed on the surface or in the region just beneath the Au/ZCT interface.^{5,6,7} As the time concerning, we did not get any chance to employ those techniques on the platinum contacted ZnCdTe surface before we send out this paper. However, the results will be presented in the near future.

CONCLUSIONS

In conclusion, the environment treatments led to strong modifications of the n-type ZnCdTe crystal surface for both as-cleaved and as-etched. The investigation of the process of thin gold and platinum film depositions on n-type ZnCdTe crystal surface indicates that the surface morphology and chemical modifications occurring during annealing and oxidation treatments. Both films show similar behaviors under same condition. Those changes directly related with the I-V characteristics of devices. The low level of current in the reverse bias achieved with vacuum annealed samples could approach the level of those required for X-ray detector performance in the Schottky diode mode of operation. In the future deeper studying will be introduced for platinum and other metal contacts, and passivation/encapsulation procedures geared towards improved radiation detection devices.

ACKNOWLEDGEMENT

This work was performed through funding provided by the NASA through the Fisk Center for Photonic Materials and Devices, Grant# NAGW-2925 by the Office of Naval Research, Contract # BMDO/ONR N 00014-93-1-1344, and the NASA Lewis Research Center Grant No. NAG3-1430.

REFERENCES

- 1). A. A. Khan, W. P. Allred, B. Dean, S. Hooper, J. E. Hawkey and C. J. Johnson, J. Electron. Mater. 15 (1986) 181.
- 2). E. Reiskin and J. F. Butler, IEEE Trans. Nucl. Sci. 35, (1988).
- 3). J. F. Butler, C. L. Lingren and F. P. Doty, IEEE Trans. Nucl. Sci., 39 (1992) 605.
- 4). Y. E. Stausser and M. G. Heaton, American Lab., May (1994).
- 5). M. A. George, W. E. Collins, K. T. Chen, Zhiyu Hu, S. U. Egarievwe and A. Burger, J.

Appl. Phys., Vol. 77, No. 6, 15 March (1995).

- 6). M. A. George, M. Azoulay, Jayatirtha H. N., A. Burger, W. E. Collins and E. Silberman, Surface Science, 296 (1993) 231.
- 7). M. Azoulay, M. A. George, A. Burger, W. E. Collins and E. Silberman, J. Vac. Sci. and Technol. B 11 (5) (1993) 1782.
- 8). F. A. Kroeger and D. DeNobel, J. Electron. 1, (1955) 190.
- 9). F. V. Wald and R. O. Bell, Contract AT (11-1) 3545, USAEC 1974.
- 10). A. Musa, J. P. Pompon, J. J. Grob, M. Hage-Ali, R. Stuck, and P. Siffert, J. Appl. Phys. 54 (6) (1983) 3260.
- 11). J. Tuskova and R. Kuzel, Phys. Status Solidi A10 (1972) 91.
- 12). R. Triboulet, Proc. 3rd Int. Conf. on CdTe, P. Siffert, A. Cornet (eds.), Strasbourg, 171, (1971).
- 13). M. Suita and T. Taguchi, Nucl. Instr. Meth. in Phys. Res., A283 (1989) 268.
- 14). M. H. Patterson and R. H. Williams, J. Phys. D: Appl. Phys. 11(1978) 183.
- 15). D. E. Aspnes and H. Arwin, J. Vac. Sci. Technol. A 2 (3) (1984) 1309.
- 16). A. J. Ricco, H. S. White and M.S. Wrighton, J. Vac. Sci. Technol., A2(2) (1984) 910.

METASTABLE DEFECT AT Si-SiO₂ INTERFACES

Z. Jing, G. Lucovsky, and J. L. Whitten

Departments of Physics, Chemistry, Materials Science and Engineering, and Electrical and Computer Engineering, North Carolina State University, Raleigh, NC, 27695.

ABSTRACT

An important issue in semiconductor device operation is the rate at which current or voltage stress creates defects that degrade eventually device operation. Based on recent results on nitrated gate dielectrics, we have concluded that bonded-H at the Si-SiO₂ interface plays a role in the formation of metastable defects that can be activated, and subsequently neutralized, by sequential trapping of injected holes and electrons. In this paper, differences in defect behavior for Si-SiO₂ interfaces that have exposed to nitrogen (N-) atoms or N-H groups are discussed. Based on these results, a microscopic model for interfacial defects is proposed.

INTRODUCTION

A paramount issue in semiconductor device processing is reliability; e.g., under operating conditions, do specific local bonding arrangements at the Si-SiO₂ interface contribute to the rate at which electronically-active defect states are created by current or voltage stress? The resolution of this question is particularly important for VLSI and ULSI devices in which the gate dielectric thicknesses are about 10 nm or less. For example, for devices in which the gate oxides are 5 nm or less, defects, and defect generation at, or in the immediate vicinity of the Si-SiO₂ interface can be significantly more important than in the bulk of the oxide layer itself [1].

As dielectrics are decreased to have oxide equivalent dielectric thickness as small as about 3 nm for 0.1 μ m feature size devices, there is increasing interest in incorporating nitrogen into these oxide layers in order to: i) increase device reliability, ii) prevent boron diffusion from p⁺ polysilicon gate electrodes in PMOS structures, and iii) reduce tunneling currents through the use of physically thicker oxides [2-5]. At the present time it is not clear whether there is an optimum distribution of N-atoms that will satisfy simultaneously all of these three requirements, or whether trade-offs will be required to optimize initial performance, with long term reliability.

In the course of studies on nitrated dielectrics prepared by low thermal budget plasma-assisted processing approaches [6-7], we have observed that selective introduction of N-atoms at the Si-SiO₂ interface, or in the bulk of the dielectric layer as in oxide-nitride-oxide (ONO) multi-layer dielectrics is strongly dependent on the N-atom source gas, and on post-oxidation and/or post-deposition thermal exposures. In particular the experimental results reported in Refs. 5-7 suggest that H-atoms, in particular N-H groups can serve as precursor sites for defect formation and/or generation either during the post-deposition device processing, and/or during device operation via current or voltage stress.

This observation derives in part from studies that have been performed on the thermal stability of H-atoms in hydrogenated silicon nitride alloys (Si₃N₄:H) where the experimental results have demonstrated that H-evolution, which occurs at temperatures as low as 400-500°C, may involve near neighbor SiN-H groups in which the H-atoms participate in weak electrostatic H-bonds, as well as in stronger bonds with the N-atoms of the SiN-H group [6-7]. Since H-atoms are generally present at Si-SiO₂ interfaces (e.g., as a result of post metallization anneals (PMA) in ambient that contain H₂), this has lead us to focus on initially-passive local bonding arrangements at Si-SiO₂ interfaces which involve H-atoms, and which can act as precursor sites for stress-induced defect generation.

It is believed that H-atoms compensate what otherwise would be Si-atom dangling bond defects, and thereby contribute to decreased levels of interface trapping states denoted as D_{it}. What has not been recognized to date is that H-atoms bonded directly to Si-atoms at the Si-SiO₂ interface can form *hydrogen bonds* with N-H groups or oxygen atoms of the SiO₂ network and

possibly reduce reliability. This paper explores the properties of these H-bonds, and focuses on their metastability with respect to charge capture occurring during device operation. Section 2 reviews results on defects at nitrated Si-SiO₂ interfaces. Section 3 proposes a mechanism for defect generation that is based on qualitative differences in bonding between N-atoms and N-H groups at Si-SiO₂ interfaces. Section 4 presents the results of model calculations that support the defect generation mechanisms suggested in Section 3. Section 5 gives a brief summary.

II. DEFECTS AT NITRIDED SI-SiO₂ INTERFACES

Metal-oxide-semiconductor (MOS) capacitors were formed by 300°C plasma processing [1]: (i) a remote plasma-assisted oxidation using either O₂ or N₂O [7] followed by (ii) a remote PECVD deposition of SiO₂. Some devices were exposed to direct or remote plasma excitation of NH₃[2,3]. Table I includes mid-gap D_{it} (also known as the P_b center in the EPR literature) for three types of devices prepared with pre-deposition oxidations using (i) either a) O₂ or b) N₂O, but with no post-deposition exposures to excited NH₃, and (ii) O₂, with post-deposition exposures to excited species from NH₃ plasmas. Also included in the table are interfacial densities of N atoms obtained from the analysis of SIMS data. The loss of H-atoms from N-H groups at the interface is assumed to occur at annealing temperature of ~900°C, paralleling behavior in bulk hydrogenated silicon nitride films as monitored by IR before and after annealing.

Table I - Mid-Gap D_{it} and N-Concentration at Si-SiO₂ Interfaces

Processing	D _{it} (cm ⁻² ·eV ⁻¹)	Nitrogen (cm ⁻²)
Plasma-Oxidation - O ₂ , 400°C	1 × 10 ¹⁰	N - 1.6×10 ¹⁴
Plasma-Oxidation - N ₂ O, 400°C	1 × 10 ¹⁰	N - 8.5×10 ¹⁴
Exposure to NH ₃ - 400°C	2-5 × 10 ¹¹	NH - >5×10 ¹⁴
Exposure to NH ₃ - 800°C	1 × 10 ¹⁰	NH - >5×10 ¹⁴

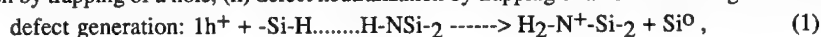
These results show (i) about the same D_{it} values for pre-deposition oxidations using O₂ and N₂O, with no exposures to plasma excited NH₃, but (ii) significantly higher values of D_{it} where pre-deposition oxidation using O₂ and oxide deposition were followed by an exposure to species from an NH₃ plasma. For processing conditions which included a 400°C PMA (i) the intentional incorporation of N atoms (as contrasted with NH groups) in the immediate vicinity of the Si-SiO₂ interface from the N₂O oxidation did not lead to any significant changes in D_{it} with respect to interfaces at which N atom concentrations were lower by a factor of ~5, whereas (ii) the incorporation of NH groups at the Si-SiO₂ interface (from an NH₃ plasma) resulted in significant increases in D_{it}. Three different procedures using plasma-excited NH₃ gave comparable increases in D_{it}: (i) exposure of oxide dielectrics to species from an NH₃/He discharge with no film deposition, and deposition of (ii) nitride layers, and (iii) oxynitride alloy layers for composite dielectrics. For processing which included the plasma excitation of NH₃, a 30s RTA at 900°C reduced D_{it} levels to about the same values as in devices without the NH₃ exposures.

MODEL FOR DEFECT METASTABILITY

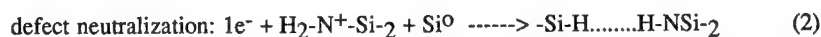
Figure 1a shows the ideal Si/Si-Oxide interface without defects, H- or N-atoms. Figure 1b shows the real Si/Si-Oxide interface with defects and H-atoms, but no N-atoms. The positively charged O atom is bonded to three atoms and is over-coordinated. The *ab initio* calculations presented below show that trapping a hole at an O-atom site that is H-bonded to an Si-H group can lead to the formation of a three-fold coordinated positively-charged oxonium center in the dielectric and a neutral dangling bond at the Si-SiO₂ interface. Similarly, trapping of a hole at an N-H site that is H-bonded to an Si-H group, can lead to the formation of a four-fold coordinated ammonium center and a Si-atom dangling bond. The stabilities of these over-coordinated and positively charged sites have been shown to be stable with O-H and N-H bond energies in excess of 4.5 eV. The same type of calculations indicates that trapping of an electron at the over-coordinated positively-charged sites is destabilizing in the sense that the H-atom is displaced back to the Si-atom, returning the local arrangement to its original configuration with a Si-H bond which is

once more coupled to the O-atom or N-H group through a H-bonding interaction.

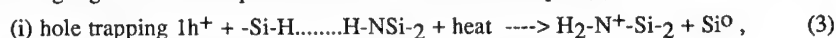
The proposed model for defect metastability at Si-SiO₂ with NH group is illustrated in Fig. 2, where a complete cycle of metastable bonding, including defect creation and annihilation is shown. The H-bonds that couple interfacial Si-H groups to highly electronegative atoms or groups in the dielectric in the immediate vicinity of that interface are integral components of a precursor site for charge trapping reactions that can lead to defect generation. The model is based on a premise, substantiated by the *ab initio* calculations presented below, that trapping of charged carriers at local bonding sites that include H-bonding arrangements is a mechanism that can promote defect metastability without the loss or diffusion of H-atoms. In this model, the equations for (i) defect creation by trapping of a hole; (ii) defect neutralization by trapping of an electron are given below:



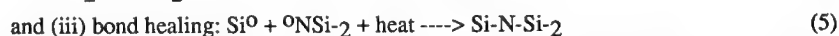
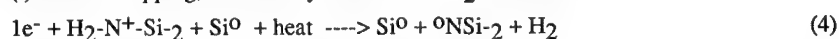
and



The trapping of a hole at a neutral site starts the process leading to the creation of charged ammonium center, H₂-N⁺-Si₂, and a neutral Si-atom dangling bond, Si⁰. The trapping of an electron on the ammonium center destabilizes that center leading a loss of a H-atom, which becomes reattached to the Si-H and an H-N-Si₂ group, that are connected via the H-bonding interaction and therefore are in the initial bonding arrangement. The coinage in this defect metastability process is the H-atom. It is initially bonded to the Si-atom, and weakly associated with the NH group with Si-H and N.....H distances of ~0.15 and 0.25 nm, respectively. After hole trapping, the Si-H distance is increased to greater than 0.2 nm, and the N-H bonding distance is decreased to ~0.17 nm. It has been implicitly assumed that the defect metastability cycle described by equations (1) and (2) occurs at room temperature. If the electron hole and trapping both occur at elevated temperatures, then H₂ release, and the subsequently linking up of the resulting Si and N-atom dangling bonds is then possible. This is illustrated in Eqns. (3) - (5):

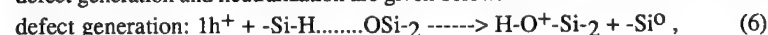


(i) electron trapping, followed by release of an H₂ molecule;

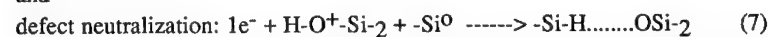


The experimental results suggest that defect neutralization is promoted by low temperature annealing (<300°C), whilst H₂ formation, followed by defect healing is driven at higher temperatures: 400-800°C for H₂ formation, and >800°C for defect healing.

Before discussing support for this model from *ab initio* calculations which serve to establish the stability of the four-fold coordinated, positively-charged H₂-N⁺-Si₂ group, and the instability of the four-fold coordinated neutral H₂-N-Si₂ group, we indicate the way the same type of defect metastability mechanism can be applied to materials with bonded O, as in hydrogenated silicon oxides. The link between the NH- and O-bonding arrangements derives from the fact that NH-groups and O-atoms are chemically equivalent, (i.e., isoelectronic), with each being capable of forming two partially covalent bonds in their neutral states, as in the respective ammonia and water molecules, H₂-NH and H₂-O, and three partially-covalent bonds when positively charged as in the respective ammonium and oxonium configurations, NH₄⁺ and OH₃⁺. The reaction equations for defect generation and neutralization are given below:



and



Elimination of bonded-H from Si-H and Si-OH groups, with the formation of H₂ can occur via a series of reactions that parallel Eqns. (3)-(5). There is also evidence for a process in which H₂O molecules can be eliminated from near-neighbor Si-OH groups that are interconnected through H-bonding interactions. At this point, we shall proceed to discuss the results of *ab initio* calculations for defect generation/defect metastability processes.

MODEL CALCULATIONS

In this work, calculations are carried out for the full electrostatic Hamiltonian of the system using GAMESS program[8]. For the ammonium complex, the positively charged N atom is bonded to two H atoms and two Si atoms which are terminated by six H atoms. For the oxonium complex, the positively charged O atom is bonded to one H atom and two Si atoms which are terminated by six H atoms. All of the boundary H atoms are positioned along ideal tetrahedral bond directions and the Si-H bond length is taken to be 1.48 Å. The active regions of the ammonium and oxonium complexes are shown in Fig. 3 (the boundary H atoms are not shown).

The N-H bond length in the positively charged ammonium is computed to be 1.01 Å and the N-H bond energy is found to be 4.97 eV. The neutral ammonium is found to be unstable. At the equilibrium geometry of the positively charged ammonium, the neutral ammonium is 1.51 eV unstable against H loss. The O-H bond length in the positively charged oxonium is computed to be 0.96 Å and the O-H bond energy is found to be 5.65 eV. Similar to ammonium, the neutral oxonium is found to be unstable. At the equilibrium geometry of the positively charged oxonium, the neutral oxonium is 3.35 eV unstable against H loss.

The next question we need to address is whether there exists an energy barrier to the transfer of H atom between -SiH and (NHSi-2)⁺ or (OSi-2)⁺. The -SiH bond in Si-SiO₂ interfaces is simulated by H₉Si₃SiH, i.e., the -SiH bond is backbonded by three Si atoms which are terminated by nine H atoms. The Si-H bond length is taken to be 1.48 Å and all the nearest neighbor Si-Si distances are maintained as in the bulk, 2.35 Å. Fig. 4(a) shows the relative energy of (H₉Si₃SiH)-(NHSi-2)⁺ as a function of the N-H distance at three Si-N distances of 2.5, 3.0 and 3.5 Å (the reference energy is the energy of (H₉Si₃SiH) + (NHSi-2)⁺). At large Si-N distance where there is no interaction between (H₉Si₃SiH) and (NHSi-2)⁺, there clearly exists an energy barrier to the transfer of H atom, since the SiH bond has to be broken which is about 3.5 eV before the formation of a stronger N-H bond. At the Si-N distance of 3.5 Å, Fig. 4(a) shows that as H moves from -Si, the energy of the system increases slightly and then decreases dramatically due to the formation of the stronger NH bond. At the Si-N distance of 3.0 Å, the energy of the system decreases monotonically as H moves from -Si to the positively charged ammonium complex. At the Si-N distance of 2.5 Å, the energy of the system is greater than zero and the system is unstable. This calculation shows that H atom can transfer from -SiH to a positively charged ammonium complex without any barrier at Si-N distances in the range of 2.5 to 3.5 Å.

Similar calculations are carried out for the transfer of H atom between -SiH and the positively charged oxonium complex. Fig. 4(b) shows the relative energy of (H₉Si₃SiH)-(OSi-2)⁺ as a function of the OH distance at three Si-O distances of 2.5, 3.0 and 3.5 Å (the reference energy is the energy of (H₉Si₃SiH) + (OSi-2)⁺). At large Si-O distance where there is no interaction between (H₉Si₃SiH) and (OSi-2)⁺, there clearly exists an energy barrier to the transfer of H atom, since the SiH bond has to be broken which is about 3.5 eV before the formation of a stronger O-H bond. At the Si-O distance of 3.5 Å, Fig. 4(b) shows that as H moves from -Si, the energy of the system increases slightly and then decreases dramatically due to the formation of the stronger OH bond. At the Si-O distance of 3.0 Å, the energy of the system decreases monotonically as H moves from -Si to the positively charged oxonium complex. At the Si-O distance of 2.5 Å, the energy of the system is much higher than the energy at the Si-O distance of 3.0 Å, suggesting that this geometrical configuration is unlikely to occur. This calculation shows that H atom can transfer from -SiH to the positively charged oxonium complex without any barrier at some Si-O distance in the range of 2.5 to 3.5 Å.

DISCUSSION AND SUMMARY

Our calculations show that trapping a hole at an O-atom site that is H-bonded to an Si-H group can lead to the formation of a three-fold coordinated positively-charged oxonium center in the dielectric and a neutral dangling bond at the Si-SiO₂ interface. Similarly, trapping of a hole at an N-H site that is H-bonded to an Si-H group, can lead to the formation of a four-fold coordinated ammonium center and a Si-atom dangling bond. These over-coordinated and positively charged

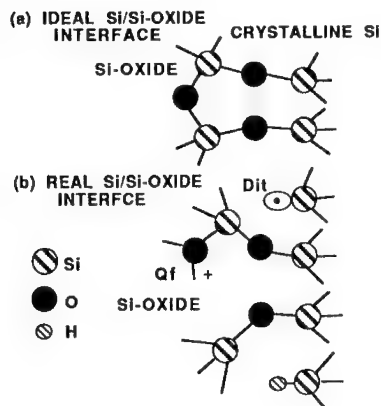


Fig. 1 (a) The ideal Si/Si-Oxide interface without defects, H- or N-atoms. (b) The real Si/Si-Oxide interface with defects and H-atoms, but no N-atoms. The positively charged O atom is bonded to three atoms and is over-coordinated.

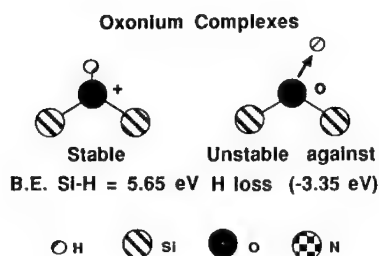
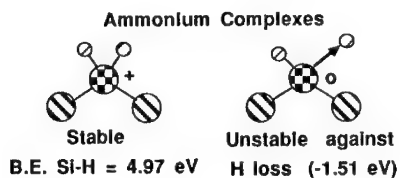


Fig. 3 The active regions of the ammonium and oxonium complexes (the boundary H atoms are not shown). (directly above)

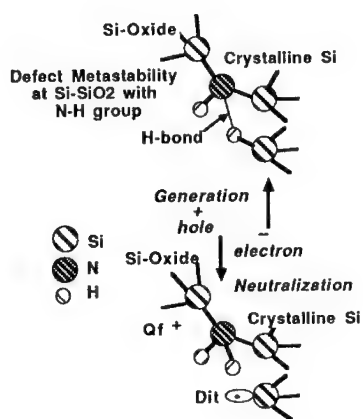


Fig. 2 The proposed model for defect metastability at Si-SiO₂ with NH group, where a complete cycle of metastable bonding, including defect creation and annihilation is shown.

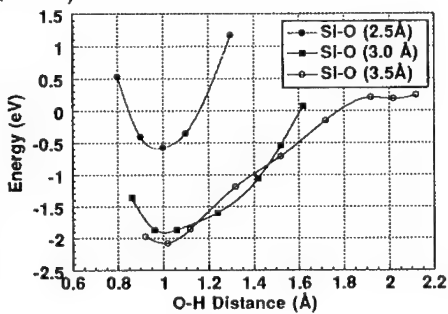
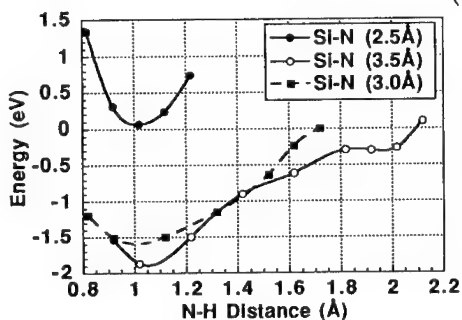


Fig. 4 The relative energy of: (a) (H₉Si₃SiH)-(NHSi-2)⁺ as a function of the N-H distance for Si-N distances of 2.5, 3.0 and 3.5 Å (the reference energy is that of (H₉Si₃SiH) + (NHSi-2)⁺). The relative energy of (b) (H₉Si₃SiH)-(OSi-2)⁺ as a function of the OH distance at Si-O distances of 2.5, 3.0 and 3.5 Å (the reference energy is that of (H₉Si₃SiH) + (OSi-2)⁺).

sites are stable with O-H and N-H bond energies in excess of 4.5 eV. On the other hand, the same type of calculations indicates that trapping of an electron at the over-coordinated positively-charged sites is destabilizing in the sense that the H-atom is displaced back to the Si-atom, returning the local arrangement to its original configuration with a Si-H bond which is once more coupled to the O-atom or N-H group through a H-bonding interaction. The effects of sequential hole and electron trapping establishes these bonding environments as metastable, with generation/neutralization reactions, respectively, at an H-bonded, O-atom site. The H-atom motion associated with these reactions is displacive, so that the defect generation/neutralization cycle does not require H-atom diffusion, or any other H-atom transport process.

The difference in defect behavior that include N, and NH groups is due to aspects of local bonding arrangements that involve H-bond formation. This type of bonding is possible when Si-H groups are in close proximity to both Si-O-Si and Si-NH-Si linkages as in Si-SiO₂ interfaces with NH groups, but not when N atoms bonded only to Si are in close proximity to Si-H bonds at Si-SiO₂ interfaces. This is a manifestation of the different symmetries of the non-bonding pair on the N-atoms in (i) a planar configuration of a N-atom with three-Si neighbors and (ii) a near tetrahedral arrangements as in an NH group that is attached to two Si atoms.

Since N-atoms bonded only to Si-atoms at Si-SiO₂ interfaces cannot produce additional H-bonding configurations, but only reduce the number of such interactions involving near-neighbor Si-H groups and Si-O-Si linkages, we would expect no increases in D_{it} at Si-SiO₂ interfaces processed with the O₂ and N₂O pre-oxidation step, even though the number of N-atoms in the immediate vicinity of the Si-SiO₂ interface is increased by a factor of about 5. In contrast, the values of D_{it} are significantly higher if NH species are allowed to accumulate at the Si-O-Si interface during processing.

Acknowledgments

Research, the NSF Engineering Center for Advanced Electronic Materials Processing at North Carolina State University, the North Carolina Sematech Center of Excellence.

References

1. G. Lucovsky et al., J. Vac. Sci. Technol. B12, 2839 (1994).
2. Yi Ma, T. Yasuda, S. Habermehl and G. Lucovsky, J. Vac. Sci. Technol. B11,(1993) 1533.
3. Yi Ma and G. Lucovsky, J. Vac. Sci. Technol. B12, 2504 (1994).
4. G. Lucovsky, Y. Ma, S.S. He, T. Yasuda, D.J. Stephens and S. Habermehl, Mater. Res. Soc. Symp. Proc. 284, 34 (1993).
5. S.S. He, M.J. Williams, D.J. Stephens and G. Lucovsky, J. Non-Cryst. Solids 164-166, 731 (1994).
6. Z. Lu, M.J. Williams, P.F. Santos and G. Lucovsky, J. Vac. Sci. Technol. A13 (1995), submitted.
7. D.R. Lee and G. Lucovsky, J. Vac. Sci. Technol. A13 (1995), submitted.
8. GAMESS, General Atomic and Molecular Electronic Structure System, M. Dupuis, D. Spangler, and J. J. Wendoloski, National Resource for Computations in Chemistry Software Catalog, University of California, Berkeley, CA (1980), Program QG01.

COMPARATIVE STUDY OF EXPERIMENTAL TECHNIQUES FOR BORON PROFILING AT POLY-Si/SiO₂ INTERFACE

M. FURTSCH*, J. BEVK*, J. BUDE*, S. W. DOWNEY*, K. S. KRISCH*, N. MORIYA*, P. J. SILVERMAN* AND H. S. LUFTMAN**

* AT&T Bell Laboratories, 600 Mountain Avenue, Murray Hill, NJ 07974

** AT&T Bell Laboratories, Breinigsville, PA 18031

ABSTRACT

Electrical characterization of MOS structures and device modeling require accurate information about dopant concentration, particularly at the poly-Si/SiO₂ interface. We compare four experimental techniques (secondary ion mass spectrometry SIMS, resonant ion mass spectrometry RIMS, differential Hall effect profiling, and spreading resistance analysis) to measure boron and free carrier concentrations in poly-Si, SiO₂ and crystalline Si. We find that no single technique completely characterizes the entire MOS structure, and that spreading resistance analysis in particular substantially underestimates the free carrier concentration at the poly-Si/SiO₂ interface. We conclude that in most cases of technological interest the magnitude of the poly depletion effect scales with the average carrier concentration at some distance away from the interface and that the interfacial effects, such as dopant segregation, are of only secondary importance. These findings are supported by theoretical modeling of capacitance-voltage behavior of boron-doped MOS capacitors.

INTRODUCTION

In dual gate CMOS technology, sufficient dopant activation throughout the polysilicon layer is essential to ensure optimal device and circuit performance. Polysilicon depletion near the gate oxide interface, in particular, degrades the transistor performance by reducing the channel carrier concentration and in turn the device transconductance and drain saturation current.

Obtaining accurate dopant/carrier profiles for the entire MOS structure is experimentally challenging and often requires extensive processing¹. In this study, we compare four experimental profiling techniques on boron doped polysilicon gate structures. We conclude that differential Hall effect profiling yields the most direct and accurate information about the carrier distribution at the poly-Si/SiO₂ interface. We gain additional insight about the dopant activation from the C-V measurements and from theoretical modeling of the C-V behavior of the boron-doped MOS capacitors.

EXPERIMENTAL DETAILS

For this investigation we used 5", phosphorus-doped Si(100) wafers, with a resistivity of 3-5Ωcm. Following the gate oxide formation (70Å dry oxide grown at 800°C), 2000Å of undoped, amorphous silicon was deposited at 550°C in a LPCVD reactor. Elemental boron was then implanted into the amorphous Si layer with an energy of 10 keV and a dose of 5·10¹⁵ cm⁻². All wafers were processed by rapid thermal annealing (RTA) at 1030°C for 10s, followed by furnace anneals ranging from 750°C to 900°C for 1h. The dopant and free carrier profiles were

subsequently analyzed utilizing four different experimental techniques:

1. Secondary ion mass spectrometry (SIMS) was performed using a 2 keV Cs⁺ primary beam; boron concentration profile was deduced from the BSi⁻ signal.

2. Resonant ionization mass spectrometry (RIMS) utilized a 6 keV Xe⁺ primary ion beam in combination with a 249.7nm laser light, produced by frequency doubling of an excimer-pumped dye laser². In the RIMS measurement, the neutral sputtered atoms get post-ionized, therefore reducing the matrix effects. This method is particularly sensitive for B-doped silicon.

3. Spreading resistance analysis (SRA) was done at a commercial laboratory³, using standard techniques. A bevel angle of 0.0034° and 2.5μm step increments were used in the measurements.

4. Differential Hall effect (DHE) profiling of lithographically patterned samples was carried out on a commercially available automated system⁴. Each cycle consisted of anodic oxidation of 30-100Å of poly-Si, oxide stripping and I-V measurement. Depending on the carrier concentration, 20 to 60 points were taken for each profile.

In order to correlate the measured doping profiles with device electrical parameters, we measured the C-V characteristics of a series of MOS capacitors that were subjected to different thermal treatments. These measurements were performed on 200μm x 200μm capacitors using a Keithley Model 5957 C-V tool. High-frequency and quasistatic measurements were performed simultaneously. The value of the poly-depletion effect was determined by dividing the quasistatic capacitance measured in the inversion region by the capacitance obtained in accumulation.

RESULTS AND DISCUSSION

Figure 1 shows various concentration profiles obtained by the four different experimental techniques for a wafer where an RTA step at 1030°C for 10s was followed by a furnace anneal at 800°C for 60 min. The SIMS and RIMS boron profiles look very much alike. A peak concentration of $\sim 7 \cdot 10^{21} \text{cm}^{-3}$ about 250Å from the surface clearly corresponds to the implantation peak. During the RTA process, boron readily diffused through the poly-Si layer to the SiO₂ interface, resulting in an average conc. away from the implantation peak of $\sim 2 \cdot 10^{20} \text{cm}^{-3}$.

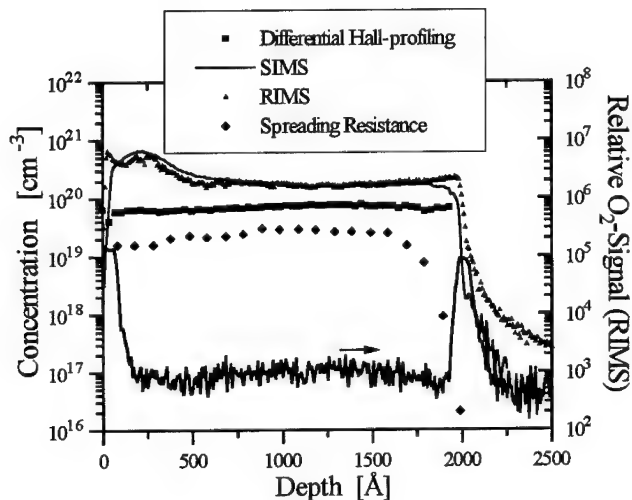


Figure 1:
Comparison of the four pro-
filing techniques for a boron-
doped polysilicon gate.

The only noticeable difference between the RIMS and SIMS data occurs at the poly-Si/SiO₂ interface, presumably because of the matrix effects.

The profiles obtained by DHE and SRA measurements differ qualitatively from the RIMS and SIMS data. The boron implant peak is not observed, and the average concentrations measured within the poly-Si are considerably lower. This is to be expected, since SIMS and RIMS detect the total dopant concentration, including atoms which are not incorporated into the silicon crystal lattice and are therefore not electrically active. The boron peak seen in the SIMS and RIMS profiles is due to the fact that the implant dose was higher than the dose corresponding to the boron solid solubility at the RTA temperature of 1030 °C ($\sim 3.0 \cdot 10^{15} \text{ cm}^{-2}$). Any excess boron will therefore not diffuse away but rather be left behind in the form of electrically inactive defects and clusters.

Additional furnace annealing at temperatures up to 900 °C will have very little effect on the overall boron SIMS and RIMS profiles within the polysilicon layer, since very little long range diffusion will take place. The carrier concentration, on the other hand, measured by DHE and SRA, may decrease dramatically because of the boron precipitation out of the supersaturated solid solution that requires only short range diffusion. The extent of this decrease depends both on the temperature and the length of the furnace anneal (reflecting both thermodynamic and kinetic considerations) and is a subject of a separate study³. Additional differences between SIMS and RIMS profiles can be seen in the SiO₂ layer and in the channel region and these have been discussed extensively elsewhere².

In Figure 2, we further analyze the profiles obtained with DHE and SRA, respectively. There are two major differences in the profiles. First of all, the average boron concentration throughout the poly-Si layer is by about a factor of 3 higher when measured with DHE profiling and secondly, the carrier concentration derived from the spreading resistance measurements drops below 10^{19} cm^{-3} at least 250 Å from the SiO₂ interface. This would indicate a substantial poly-depletion that is not consistent with the C-V measurements, as discussed later.

While spreading resistance analysis is rather straightforward and very accurate for measuring the resistivity profile $\rho(x)$ throughout the poly-Si layer, it has one major shortcoming: for the subsequent calculation of the carrier concentration $N(x)$ one has to know the value for the mobility $\mu(x)$ for boron-doped poly-Si:

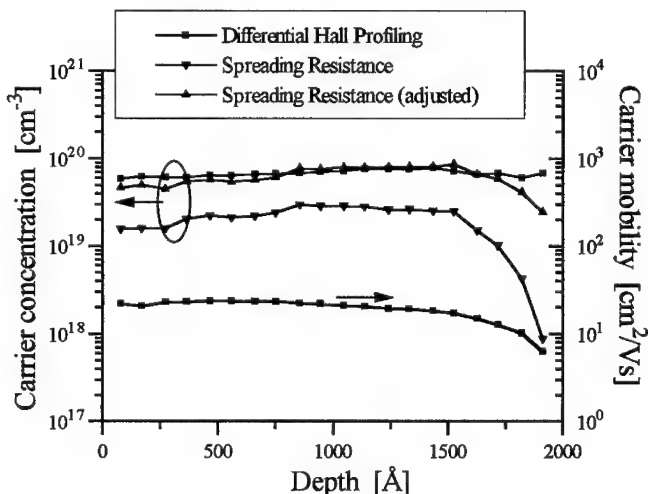


Figure 2:
Adjustment of the spreading
resistance data.

$$N(x) = \frac{1}{q \cdot \mu(x) \cdot \rho(x)} \quad (1)$$

In practice, the mobility values for carriers in single-crystalline Si are usually used in the calculation and this was done also in our case. The large discrepancy between the DHE and SRA carrier concentration profiles suggests that this approximation is rather questionable. With grain boundaries acting as scattering centers, the hole mobility in polycrystalline Si is reduced with respect to the single crystalline value. Near the interfaces with air and SiO₂, the mobility is expected to drop further due to additional interface scattering.

The unique feature of the differential Hall effect profiling is that it not only gives information on the carrier concentration profile, but also yields a profile of the carrier mobility throughout the analyzed layer. An example of this is shown in the bottom part of figure 2. The mobility of bulk poly-Si is a factor of 2.5 to 3 lower than for crystalline Si with the same doping level and by almost an order of magnitude near the poly-Si/SiO₂ interface. As shown in figure 2, recalculation of the carrier concentration profile, originally derived from the SRA, by using the experimental Hall mobility leads to an almost perfect match of both profiling techniques. Thus, depending on the mobility values used, the carrier concentration profiles obtained using spreading resistance measurements do not necessarily reflect the actual carrier distribution and must be treated with caution.

As stated earlier, another difference between the dopant and carrier concentration profiles is their dependence on the thermal processing. RIMS and SIMS plots remain virtually unchanged after the furnace anneals; the major change in the dopant profile had already occurred during the initial RTA step at 1030°C. On the other hand, the carrier concentration profiles are very sensitive to the subsequent furnace anneals. Figure 3 shows differential Hall effect profiles for two samples: the first was subjected only to the RTA process, the second was subsequently annealed at 850°C for 1 hour. Both carrier profiles are flat throughout the poly-Si layer, but differ in the absolute value of the carrier concentration. The corresponding SIMS profiles are not affected by the additional furnace anneal. The difference in the differential Hall effect profiles is due to the temperature dependent solid solubility of B in Si. The values of the solid solubility for poly-Si and crystalline Si are almost identical; however, since the solid solubility is considerably lower at 850°C than at

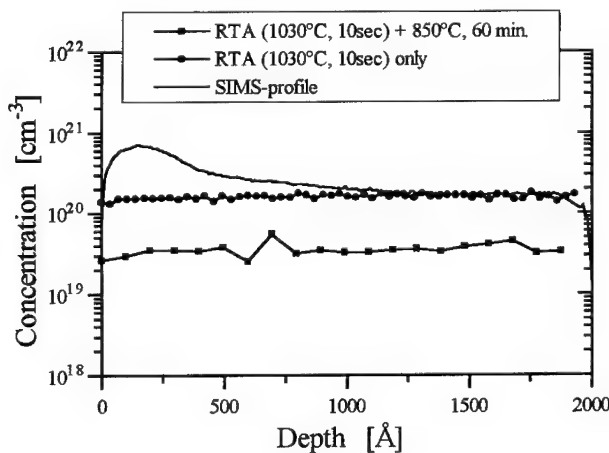


Figure 3:
Differential Halleffect
profiles as a function
of thermal treatment

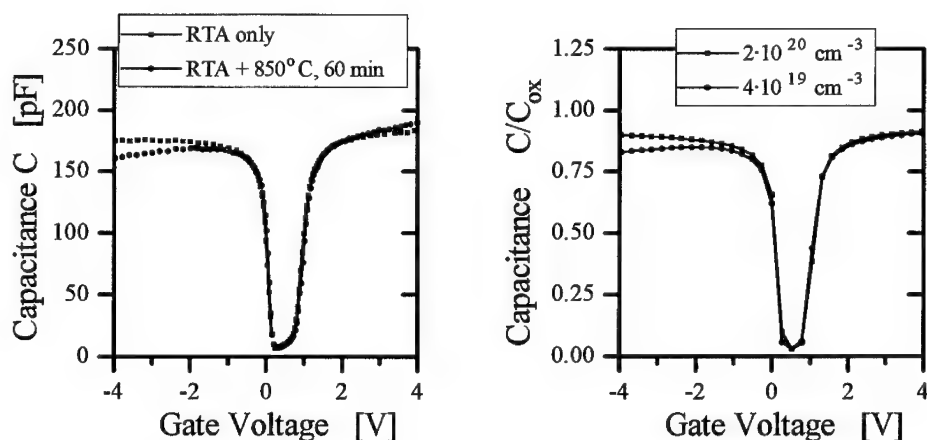


Figure 4: Experimental (left) and theoretical C-V curves for MOS capacitors with boron doped polysilicon gates

the RTA temperature of 1030°C, some of the previously activated boron atoms precipitate out of the solid solution during the furnace anneal and the total carrier concentration drops. Figure 3 also shows that in the region with constant dopant concentration (i. e., away from the implant peak) the SIMS and DHE curves overlap after the initial RTA step, implying complete activation.

Since device performance is ultimately of more interest than carrier concentration, the electrical characteristics of capacitors measured with the C-V method have a greater practical significance. The average carrier concentration throughout the poly-Si layer and, in particular, close to the poly-Si/SiO₂ interface is crucial in determining the C-V behavior. Figure 4a shows the measured quasistatic C-V curves for the samples of figure 3. The two curves especially differ in the inversion regime; the capacitance for the RTA-only sample stays constant, whereas the capacitance of the post-furnace annealed sample decreases with increasingly negative gate voltage. This is due to the fact that the carrier concentration close to the poly-Si/SiO₂ interface is low enough that a depletion layer is formed. This layer increases in width with increasing gate voltage, reducing the total capacitance. On the other hand, the carrier concentration in the RTA-only sample is sufficiently high that no depletion layer is formed, and the capacitance therefore remains unchanged. This behavior is consistent with simulation results obtained with recently developed modeling techniques⁶. Figure 4b shows the simulated quasistatic C-V curves for samples with poly-Si uniformly doped with $2 \cdot 10^{20} \text{ cm}^{-3}$ (approximately corresponding to the RTA-only sample) and $4 \cdot 10^{19} \text{ cm}^{-3}$ carriers (corresponding to the RTA and furnace annealed sample). The match with the measured C-V curves is excellent.

The value of the depletion effect and the carrier concentration throughout the poly-Si layer are inversely related. Figure 5 shows this relationship for a variety of samples annealed at different temperatures and therefore having different carrier concentrations⁵. There is a linear dependence between the logarithm of the average carrier concentration and the value of the depletion effect. The implications of this relationship on the optimized device performance and processing limitations are discussed elsewhere⁵.

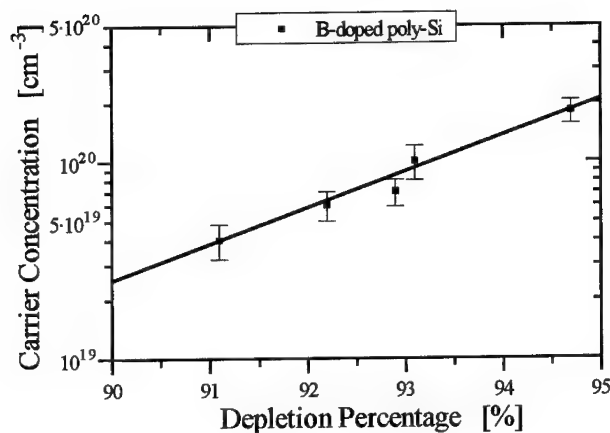


Figure 5:
Depletion percentage vs.
carrier concentration

CONCLUSIONS

We compare four different experimental techniques to measure boron and free carrier concentration in poly-Si. After an initial RTA step that diffuses the implanted boron up to the poly-Si/SiO₂ interface, SIMS and RIMS profiles remain insensitive to any additional furnace anneals. The carrier profiles deduced from the spreading resistance measurements depend sensitively on the correct values for the carrier mobility. The hole mobility in poly-Si is typically a factor of 2-3 lower than in single-crystalline Si; near the interfaces, additional scattering further reduces the carrier mobility. Using the mobility values obtained from differential Hall effect profiling, the carrier profiles based on the spreading resistance measurements look very much like the differential Hall effect profiles. This method, although experimentally more complicated, is the best technique to measure carrier concentration near the critical poly-Si/SiO₂ interface. We find a simple empirical relationship between depletion effect and carrier concentration.

ACKNOWLEDGEMENTS

The authors would like to thank L. Manchanda, G. E. Georgiou and L. C. Feldman for stimulating discussions.

REFERENCES

1. W. W. Lin, IEEE Electron Device Lett. **15**, 51 (1994).
2. S. W. Downey, A. B. Emerson, G. E. Georgiou, J. Bevk, R. C. Kistler, N. Moriya, D. C. Jacobson and M. L. Wise, J. Vac. Sci. Technol. **B13**, 167 (1995).
3. Solecon Labs, Inc., San Jose, CA, USA.
4. Bio-Rad, Mountain View, CA, USA.
5. J. Bevk *et al.*, to be published in the *Journal of Electronic Materials*.
6. K. S. Krisch, J. Bude and L. Manchanda, Proceedings of the *Symposium on Diagnostic Techniques for Semiconductor Materials and Devices* (Electrochemical Society), 12 (1994).

ATOMIC STRUCTURE OF THE INTERFACES BETWEEN SILICON DIRECTLY BONDED WAFERS

M Benamara¹, A Rocher¹, A Laporte^{2,3}, G Sarraayrouse², L Lescouzères³, A PeyreLavigne³, M Fnaiech⁴ and A Clavier¹

¹ CEMES-LOE/CNRS, 29 rue Jeanne Marvig, BP 4347, 31055 Toulouse Cedex (France).

² LAAS/CNRS, 7 av. du Colonel Roche, 31077 Toulouse Cedex (France).

³ Motorola Semiconducteurs S. A., Av. Général Eisenhower, 31023 Toulouse Cedex (France).

⁴ Faculté des Sciences de Monastir, 5000 Monastir (Tunisie).

ABSTRACT

The so-called Direct Wafer Bonding (DWB) technique opens new possibilities for the electronic industry but still suffers from the poor knowledge we have of the microstructure of these interfaces and hence of their electrical activity. In this work, we have extensively used Transmission Electron Microscopy techniques in plan-view and cross-section to identify the structure of the interfaces found between two bonded silicon wafers. The general structure of these interfaces is that of a perfect grain boundary and evidently depends on the misorientation between the two bonded wafers. A twist component in the range $0 < \theta < 13^\circ$ creates a square network of pure screw dislocation whereas an unavoidable tilt component ($< 0.5^\circ$) is compensated by a periodic array of 60° dislocation lines perpendicular to the tilt direction. Therefore, the regularity of these networks can be disrupted by the presence of steps (of up to several nanometers) in the interface plane. Silicon oxide precipitates are seen heterogeneously distributed on the interface with preferential nucleation sites on the dislocations.

INTRODUCTION

The direct wafer bonding (DWB) technology where two materials of different compositions or doping levels are bonded together at the atomic level opens new possibilities for the realization of electronic devices¹. With regard to bipolar devices and high voltage integrated circuit applications, it is investigated as an attractive technique since it has the potential for inexpensively producing thick and doped epilayers including n-n, p-p and p-n type junctions. For such applications, the electrical properties of the bonding interface are of crucial importance and were shown, contrary to what it is required, to be not free of anomalies most probably related to residual impurities or crystallographic defects. It has been shown that the electronic transport across such interfaces is restricted by a potential barrier resulting from charged interfacial states^{2,3}. However, the origin of these interfacial states remains still unknown because of the poor knowledge we have of the microstructure of these interfaces. It is the purpose of this work to carry out a complete transmission electron microscopy (TEM) study of these interfacial structures in an effort to improve our understanding of their electrical properties. From a fundamental point of view, this study consists in a considerable outgrowth of previous investigations of (001) twist boundaries in silicon⁴⁻⁷.

EXPERIMENTAL

Polished 4-inch, (001) oriented, 525 μm -thick, CZ-grown type, and lightly boron doped (10^{15} cm^{-3}) silicon wafers were cleaned in an automatic equipment aimed at rendering their surfaces hydrophobic. Then, pairs of wafers were put in contact by manual assembling in a class 10 clean room with the wafer flats intentionally misoriented from aligned to about 15° . Afterwards, the bonded wafers pairs were annealed at 1200°C for 50 mn in an N_2 ambient. The TEM studies were performed with a JEOL 200 CX and a Philips CM20 microscopes operating at 200 kV, using conventional images and diffraction patterns, on both cross-section and plan-view samples.

RESULTS

1) GENERAL OBSERVATIONS

The figure 1.a is a bright field image showing the general view of a bonding interface when the electron beam is closed to the [001] direction. Large domains are periodically separated by dark lines. Amorphous precipitates of silicon oxide are often seen located at the interface. The largest of them are connected to the black lines. The overlapping of the two misoriented crystals gives rise to double-diffraction effects (fig 1.c). Moiré fringes are resulting from this double-diffraction effect and arise owing to the interference essentially between the (220) reflections of the two crystals. They appear in the imaging mode as it is shown in the fig 1.b. These fringes give no direct information about the boundary structure but they show that the two crystals are misoriented around their common $\langle 001 \rangle$ axis. In this case, the moiré spacing is measured to be equal to $d = 23 \pm 1 \text{ \AA}$. From this value, one can deduce the corresponding twist angle⁵ $\theta = 4.8 \pm 0.2^\circ$.

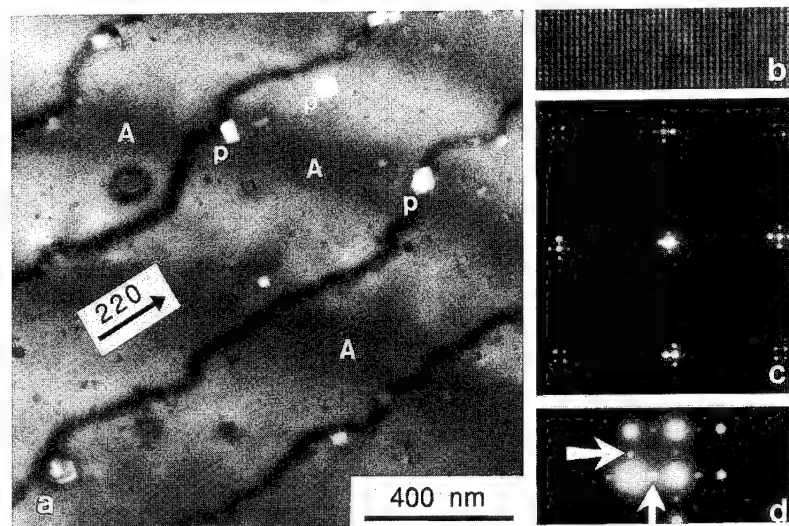


figure 1: a) BF plan-view micrograph taken under [001] zone axis. Note the formation of terraces (A) resulting from a small tilt misorientation and oxide precipitates (P) mostly connected to the 60° dislocation lines. b) the moiré fringes, seen within terraces and parallel to $\langle 110 \rangle$ directions. c) diffraction pattern along the [001] zone axis. The sharp extra-satellite spots that are pointed by the arrows in fig 1.d attest of the periodicity of the dislocation network on a large scale.

2) GBD accomodating low-angle twist component

As expected from cristallography of low-angle twist boundaries⁸, the structure of the interface consists of two orthogonal sets of screw dislocations. The Burgers vectors parallel to the dislocation lines are $\mathbf{b}_1 = a/2[110]$ and $\mathbf{b}_2 = a/2[\bar{1}10]$. The dislocation spacing is given by the relation, $Dd = b/2 \cdot \sin(\theta/2)$ (1), where θ is the twist misorientation angle.

a) $\theta < 1^\circ$

Figure 2 is a typical multibeam plan-view image from one of these low-angle boundaries. For such angles, the dislocation spacing is still large enough ($Dd > 220 \text{ \AA}$ for $\theta < 1^\circ$) so that the entire network can be easily imaged in strong beam conditions, as expected from the diffraction contrast theory⁹. The corresponding twist angle was found from the moiré spacing

(see §3.1) to be $0.58^\circ \pm 0.03^\circ$. The separation distance between dislocations is directly measured on this image to be $Dd=380\text{\AA}$. No distance correction needs to be carried out since dislocations of the same set possess the same Burgers vector.

b) $1^\circ < \theta < 7^\circ$.

As the misorientation is increased, the grain boundary dislocation spacing becomes smaller and the network becomes more regular because of the attractive forces tending to hold them

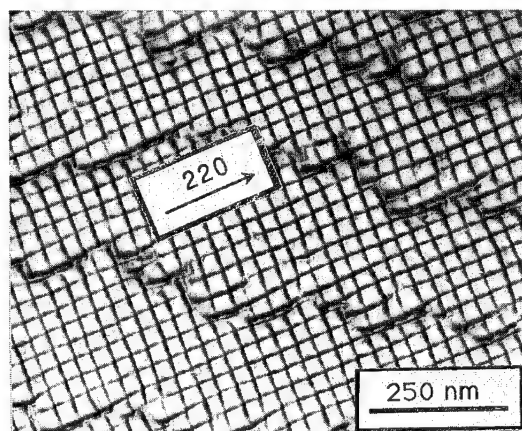


figure 2: Typical BF multibeam plan-view image from the interface of two lightly misoriented wafers. The multiple diffraction condition is satisfied by using simultaneously the 220, $\bar{2}20$ and 040 reflections. The square array of screw dislocations is disrupted by the 60° dislocation lines. Note the perfect grating of such spaced dislocations.

together in a uniform array. In this case, the structure cannot be observed in multibeam nor in two beams conditions because of the strong contrast arising from the moiré patterns. This moiré contrast may also induce confusions as its periodicity is half the separation distance between dislocations. Thus, the best way to determine the structure is to image it using the weak-beam technique because moiré contrasts rapidly fade when the deviation from the exact Bragg condition increases. Figures 3.a et b are "weak-beam" images of the sample presented in fig. 1: each of them shows one set of the screw dislocation, the other one being out-of-contrast. The dislocations appear in the images as continuous and straight white lines. Their spacing is measured to be equal to 46\AA . This is in good agreement with the value deduced from the relation (1) with the twist misorientation angle 4.8° . The interfacial stress is therefore minimized by this two sets of screw dislocations.

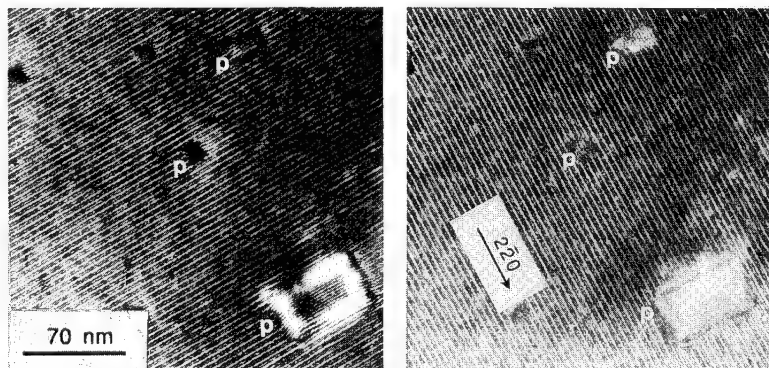


figure 3: Weak-Beam plan-view TEM images showing each of them one set of screw dislocations.

It is known that planar periodic grain boundary dislocation network examined by electron diffraction gives rise to specific reflections. These GBD reflections are arranged in a network which characteristics are directly connected to the GBD network. They must be carefully analysed to avoid confusion with spots resulting from double-diffraction effect⁷.

For a twist boundary consisting of a square grid of screw dislocation with spacing D_d examined under normal incidence, the diffraction pattern consists of a square array of spots spaced $1/D_d$ centered around the two crystal reflections and in the same orientation as the square GBD's grid¹⁰. This square grid of extra spots is shown in fig 1.d

c) $\theta > 7^\circ$.

The analysis of the diffraction pattern becomes a precious tool when the GBD structure cannot be determined from the image. It usually happens for dislocations rendered invisible because too closely spaced: when the corresponding misorientation angle is above 7° . In this case, it is easier to detect the periodic network through the presence of the array of the screw dislocation reflections though their intensity is known to decrease when decreasing D_d . Thus, a misorientation angle of 13.5° leads to the formation of a screw dislocation array detectable in the diffraction pattern [11]. Note that this sample corresponds to the maximum misorientation angle used in this work and we still do not know whether larger angles can also produce the same type of GBD network.

3) GBD accommodating low-angle tilt component

The interfacial structure always exhibited an uncontrolled small tilt component. This tilt component ($<0.5^\circ$) corresponds to a small rotation around random axes of the boundary plane. As a result, the interface consists of flat (001) terraces separated by steps lying along the direction perpendicular to the tilt direction. These steps are formed by the addition of families of 60° dislocation lines periodically located at the interface and that all have the same component perpendicular to the interface, $a/2=2.7 \text{ \AA}$. They are clearly observed in all samples even when the screw dislocation network cannot be detected when too closely spaced. Their spacing does not depend on the screw dislocation network. In the sample seen in fig 1, they appear as the dark lines 400 nm wide spaced. This allows us to precisely determine the tilt angle from which they originate to be 0.04° . The characteristics of this tilt angle (direction and magnitude) are in good agreement with those deduced from the shift of the Kikuchi lines in the diffraction pattern.

When one of these lines is examined under different diffraction conditions as in fig 4.a, it can be seen that the separation distance between the screw dislocation on either side of this dislocation is increased by half of the usual spacing. This change in spacing is because the screw component of this dislocation is half of the other dislocation. Another remarkable feature is that the other set of screw dislocation is systematically offset by half of its periodicity when it crosses this line (fig. 4.b). The reason of this offset is that the four nodes at which this 60° dislocation meets screw dislocations split into three fold nodes.

If the twist angle is below 1° , all dislocations segments are distinguishable in the image. In such cases, it is possible to carry out an analysis of the resulting configuration following the Frank's procedure^{12,13}. Fig. 5 shows, for instance, how a 60° dislocation lying along $[110]$ with Burgers vector $\mathbf{b} = a/2[\bar{1}01]$ intersecting the screw dislocation with Burgers vector \mathbf{b}_1 will appear in the network. At the meeting point, these two dislocations react to form a third dislocation with $\mathbf{b}_3 = \mathbf{b}_1 + \mathbf{b} = a/2[011]$ provided $b^2 + b_1^2 > b_3^2$ and \mathbf{b} , \mathbf{b}_1 make an angle larger than 90° . Before the reaction takes place, the 60° dislocation \mathbf{b} had an edge component in the plane of the interface. After the reactions, the two 60° dislocations segments with \mathbf{b} and \mathbf{b}_3 have an equal but opposite edge component. The total edge component vanished and is essentially

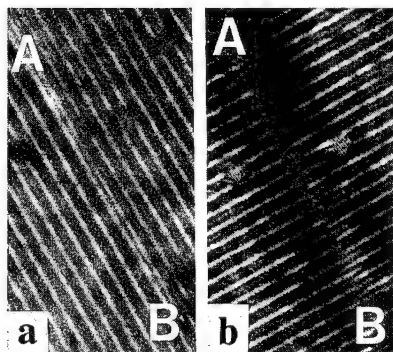


figure 4: Weak-Beam images of a 60° dislocation lying along AB

a) $g=\bar{2}20$, the dislocation appears as a straight and white line which direction is the same of the screw dislocation one.

b) $g=\bar{2}20$, note the shift of the other set of screw dislocations when it crosses AB.

accommodated by the offset of the screw dislocation. As seen in fig. 6, the appearance of these two 60° dislocations at the interface increases the screw dislocation spacing by $0.5 Dd$ since their efficient component in compensating the twist misorientation is $a/4[110]$. The low-energy configuration is achieved when angles between dislocations change to 120°.

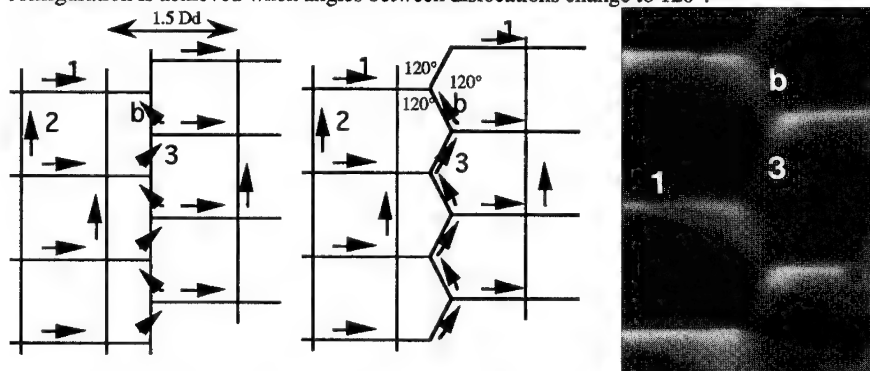


figure 5: Interaction between a 60° dislocation lying along $[110]$ with Burgers vector b and screw dislocations with Burgers vector b_1 .

4) Large steps

The regularity of the network is usually not total but disrupted by the addition of $\{111\}$ steps of up to several nanometers in height which do not act in accommodating the crystal misorientation. These steps are seen in only some of the investigated samples and their origin is believed to be an neighboring unbonded area. They are not arranged with a regular periodicity as the separation distance vary from up to a few tens of micrometers. Fig. 6 shows some of these steps when the electron beam is closed to the $\langle 001 \rangle$ direction. These steps look like broad ribbons lying along the two $\langle 110 \rangle$ directions. The corresponding schematic diagram of a perspective view of the actual structure deduced from tilting experiments is shown below.

SUMMARY AND CONCLUSION

Although wafers were Cz grown type, no oxide layer was encapsulated at the bonding interface whatever the twist misorientation angle. This is not surprising since it is well-known that the HF cleaning procedure prior to bonding is the best way to reduce the amount of oxide at the interface. A grain boundary is formed with all dislocations presents as part of the equilibrium boundary structure. All these dislocations are located at the interface and allow the structure to be fully relaxed with no extended volume defects.

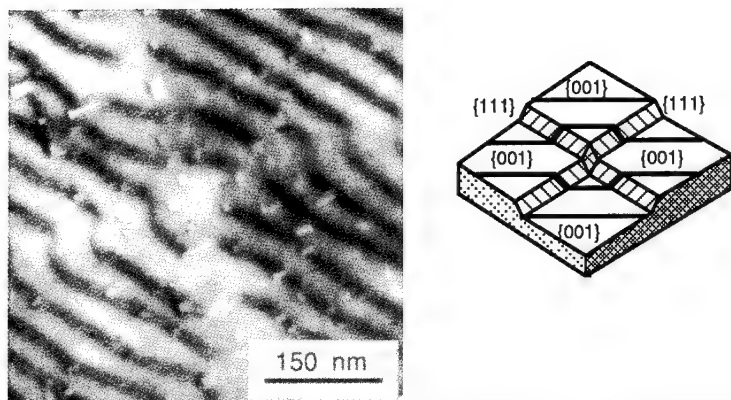


figure 6: a) BF image along [001] zone axis showing two large {111} steps which appear as two ribbons lying along the $\langle 110 \rangle$ directions. b) Schematic diagram of the actual structure.

The general structure of these interfaces is that of a perfect grain boundary and evidently depends on the misorientation between the two bonded wafers. A twist component creates a square network of pure screw dislocation whereas an uncontrolled tilt component ($<0.5^\circ$) is compensated by a periodic array of 60° dislocation lines perpendicular to the tilt direction. Therefore, these low-angle equilibrium boundaries possessing perfect structure are sometimes disrupted by the presence of steps (of up to several nanometers) in the interface plane.

We must emphasize that since the reproducibility of the electrical characteristics of these interfaces is of prime importance, significant efforts have to be spent to master the relative misorientation between wafers. Moreover, the 60° dislocations are seen to be preferential nucleation sites for oxide precipitates and thus the tilt component has also to be mastered.

Finally, TEM experiments are well suited for the study and optimization of the process conditions needed for the routine production of directly bonded semiconductor structures.

1. Bengtsson S., (1992) J. of Electronic Materials, 21 (8), 841-862.
2. Laporte A., Sarabayrouse G., Lescouzères L., PeyreLavigne A., Benamara M., Rocher A. and Claverie A., 1994, Proc. 6th Int. Symp. on Power Semi. Dev. & ICs, 293-296.
3. Engstrom O., Bengtsson S., Andersson G. I., Andersson M. O. and Jauhiainen A., (1992) J. Electrochem. Soc., Vol. 139, No 12, 3638-3644.
4. Föll H. and Ast D., 1979, Phil. Mag. A 40 (5), 589-610.
5. Benamara M., Rocher A., Laânb L., Claverie A., Laporte A., Sarabayrouse G., Lescouzères L. and PeyreLavigne A., 1994, CRAS Paris 318 (2) 1459-1464.
6. Gafiteanu R., Chevacharoenkul S., Gösele U. M., Tan T. Y., 1993, Microscopy of Semiconducting Materials 134, 87.
7. Carter C. B., Föll H., Ast D. G. and Sass S. L., 1981, Phil. Mag. A 43 (5), 441.
8. Bollmann W., 1970, Crystal Defects and Crystalline Interfaces (Editors: Springer-Verlag).
9. Kang J.M., 1993, Ph. D. Thesis, University of Toulouse III.
10. Guan D. Y. and Sass S. L., 1973, Phil. Mag. A 27, 1211.
11. Benamara M., Rocher A., Laporte A., Sarabayrouse G., Lescouzères L. PeyreLavigne A. and Claverie A., 1995, Microscopy of Semiconducting Materials, in press.
12. Frank F. C., 1954, Defects in Crystalline Solid, London, Physical Society.
13. Zhu and C.B. Carter, 1990, Phil. Mag. A 62 (3), 319.

DIRECT WAFER BONDING OF PREAMORPHIZED SILICON WAFERS.

A. LAPORTE^{1,3}, G. SARRABAYROUSE¹, M. BENAMARA², A. CLAVERIE², A. ROCHER², L. LESCOUZERES³ and A. PEYRELAVIGNE³.

¹ LAAS-CNRS, 7 Avenue du Colonel Roche, 31077 Toulouse Cedex.(France)

² CEMES/LOE-CNRS, 29 rue Jeanne Marvig 31055 Toulouse Cedex.

³ MOTOROLA S.A, Av. Général Eisenhower, BP1029 31023 Toulouse Cedex

ABSTRACT

This paper presents the comparison of the structural and electrical characteristics of Si/Si bonded interfaces depending on whether the surface layers were rendered amorphous by high dose ion implantation prior to annealing or not. While the general structure of the interfaces is the same when the wafers are preamorphized more precipitates are seen in the interface along with a few extended defects propagating into the volume. The most striking difference between both procedures is that the Spreading Resistance profile is more complicated in shape and difficult to master in the case of preamorphized wafers. Careful TEM analysis shows that only in this case the interfacial region is stressed in contrast with the fully relaxed structure obtained by direct bonding of crystalline wafers.

For these reasons, there is little chance that the preamorphization technique will benefit to the bonding procedure of direct Si wafers.

INTRODUCTION

The Direct Wafer Bonding technique opens new possibilities for the realization of structures such as : sensors ¹, micro-machined structures ² and Silicon On Insulator substrates ³. In this last case, the presence of unbonded areas (voids) constitutes the most important problem to be solved. Voids can be practically eliminated by a proper control of the silicon cleaning and contacting procedures.

A different application is that of electronic devices and circuits : rectifier, IGBT, bipolar transistor and smart power devices ^{4, 5, 6, 7, 8}. In this case, direct Si-Si interfaces are to be formed and thus, not only the mechanical but also the electrical characteristics of the bonded interfaces are critical parameters.

In a previous study, we have investigated the effect of a Si-Si bonded interface on the electrical characteristics of a high voltage vertical bipolar transistor ⁸. The degradations of the transistor performances were associated with electrically active defects at the bonded interface giving rise to an interfacial potential barrier and/or to carriers lifetime degradation.

Several subsequent structural studies by Transmission Electron Microscopy in plan-view of bonded interfaces have shown interfacial defects such as screw dislocations, 60° dislocations and SiO₂ precipitates ^{9, 10, 11, 12} with densities controlled by the initial characteristics of both wafers and the bonding procedure. The potential barrier that is evidenced on these structures can be accounted for by positively charged interfacial states most probably related to the extended defects. Since these defects are formed when the two Si monocrystals reconstruct a low-energy configuration interface (a grain boundary) that depends on the relative crystallographic orientation of the two surfaces put in contact, it is of interest to study the structure and electrical characteristics of bonded Si-Si interfaces formed by annealing of amorphous surfaces.

These interfaces are expected to be different as the Solid Phase Epitaxial (SPE) regrowth of the a-layer is known to lead to the formation of dislocation loops (EOR) beneath the former crystalline/amorphous interfaces¹³ that will emit Si-interstitial atoms toward the interface upon annealing¹⁴. Moreover, the behavior of the SPE regrowth of amorphous materials kept in contact can not be easily predicted.

This paper presents the comparison of the structural and the electrical characteristics of Si/Si bonded interfaces depending on whether the surface layers were rendered amorphous by high dose ion implantation prior to annealing or not.

EXPERIMENTAL CONDITIONS

Polished 4-inch, (001) oriented, P-type (10-15 $\Omega\cdot\text{cm}$), Czochralski (CZ), silicon wafers were amorphized with Ge⁺ implantation at 70 KeV with a dose of $7 \times 10^{14} \text{ cm}^{-2}$. XTEM has shown that the resulting amorphous layers were of about 700Å.

The wafers were then cleaned with the following sequence : organic removal, native oxide etching in diluted HF, water rinse and drying in warm nitrogen. Pairs of hydrophobic surfaces were manually contacted in a class 10 clean room with no intentional misorientation. The bonded heat treatment was performed in N₂ ambient at 1200°C during 50 minutes. Afterwards one face of the wafer was ground down to 50 micrometers from the bonded interface. Three types of bonded interface have been prepared (Table 1).

Name of the samples (Bonded interface)	Wafer 1 (Before the bonding)	Wafer 2 (Before the bonding)
Si/Si	monocrystalline Si(100)	monocrystalline Si(100)
"Mono-implant" Si	amorphous Si (700Å)	monocrystalline Si(100)
"Double-implant" Si	amorphous Si (700Å)	amorphous Si(700Å)

Table 1: Types of bonded interface.

Afterwards, the presence or the absence of voids was checked by infrared thermography. Macrovoids were sometimes observed due to particles at the surfaces before contacting or due to initial surface stress.

For each wafer, two small sections were cut at the center and two others near the edge. Bevels were prepared for electrical characterization by the Spreading Resistance (SR) technique.

Samples from each bonded wafers were prepared for microstructural analysis by Electron Transmission Microscopy (TEM) in plan-view. With these observations the relative tilt and twist angles of the wafers as well as the densities of the amorphous SiO₂ precipitates and of the interfacial defects at the bonded interfaces can be measured^{9, 11}.

STRUCTURAL ANALYSIS BY TEM

The microstructure of Si/Si interface has been extensively described elsewhere in this proceeding¹¹. It consists of perfectly and periodical arrays of screw and 60° dislocations that compensate the relative misorientation between the two crystals. These dislocations are organized so that the whole structure is fully relaxed with no extended defects propagating into the bulk of one of the wafers. Numerous SiO₂ precipitates are seen decorating these interfaces with densities depending on the dislocation content¹².

The "mono-implant" and "double-implant" Si interfaces are different from the Si/Si one. In addition to the usual interfacial defects, volume defects with a spacing of a few tens of micrometers are also visible (fig.1). As it can be seen in the image, they are bounded to the {111} plane of the matrix and are shown to be micro-twins.

Moreover, analysis of the moiré fringes seen in the bright field plan-view images shows that these interfaces are strained. Indeed, the most striking feature of these moiré patterns is their

irregularity (fig.II). Indeed from place to place, the moiré spacings and directions are different. These variations were never seen on typical Si/Si bonded interfaces¹¹ and are the result of strain induced variations of the interatomic distances. Another remarkable feature is that the moiré spacing is clearly seen to be not equal to half the separation distance between dislocations. This is firstly because the tilt axis is not a $\langle 100 \rangle$ -type direction of the interface plane and hence the densities of 60° dislocations lying along these two $\langle 110 \rangle$ directions are drastically different (fig.III). Moreover, the tilt angle is of the same magnitude as the twist angle and since the 60° dislocations also have an efficient component that can compensate the twist misorientation, the screw dislocation network is not squared but appears rectangular.

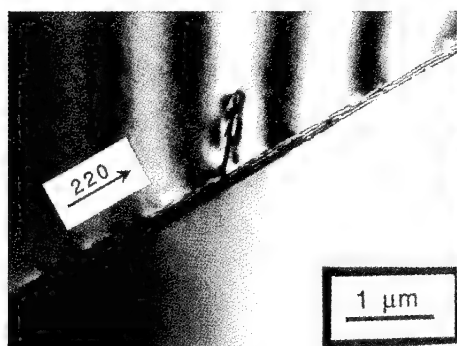


Fig.I Cross-section image of volume defects at the preamorphized bonded interfaces. These planar defects lie on $\{111\}$ planes.

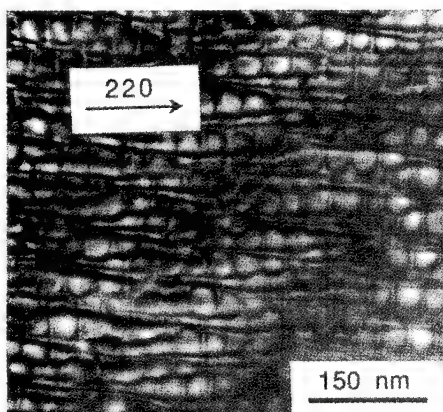


Fig.II TEM plan-view imaging the stress at the "mono implant" Si interface. Note the irregularity of the moiré fringes.

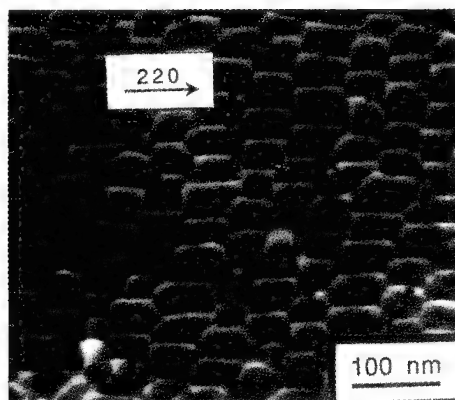


Fig.III TEM image of the "mono-implant" Si showing one set of screw dislocation. 60° dislocations are also visible in the image.

Typical results quantifying the structure and composition of the different interfaces are shown in Table 2.

Samples	Si/Si	"Mono- implant" Si	"Double- implant" Si
Screw dislocations density (km/cm ²)	5	4.2	12.5
60° dislocations density (km/cm ²)	0.4	1.8	4
SiC precipitates density (cm ⁻²)	-	10 ⁷	2.10 ⁷
SiO ₂ precipitates density (cm ⁻²)	10 ⁹	4.10 ⁹	9.10 ⁹
Volume defects density (μm ⁻¹)	-	1/50	1/200

Table 2 : Summary of the different defect densities for the three kinds of interfaces

SPREADING RESISTANCE RESULTS

For the Si/Si bonded interface, the SR peak increases near the interface (Fig.IV) and the bonded interface is revealed by Schimmel etching near the maximum resistance. When one or two surfaces are preamorphized prior to annealing, the shape of the SR peak changes ("mono-implant" and "double-implant" Si samples). In these two cases, the resistance increases before the interface, then decreases near the interface (fig.V) and the bonded interfaces are revealed by etching close to the position where the resistance reaches its lowest value.

Note that the asymmetry of the SR profile does not necessarily reflect an asymmetry of the carrier distribution since it can be well explained by measurements artifacts ¹⁵.

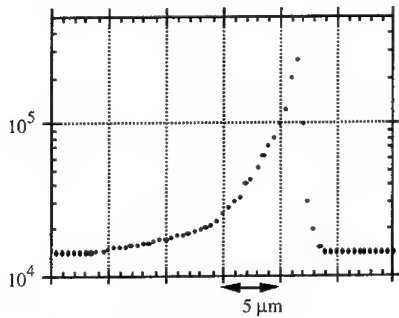


Fig.IV SR profiles of Si/Si bonded interface.

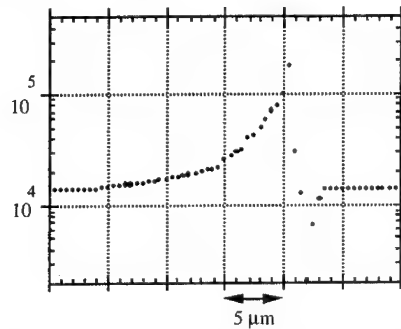


Fig.V SR profiles of "mono-implant" and "double-implant" Si bonded interface.

DISCUSSION AND CONCLUDING REMARKS

The observed increase of the Spreading Resistance near the Si/Si bonded interface (fig.IV) is due to positively charged interfacial states that leads to a potential barrier and to a carrier depletion. The origin of these states is very probably linked to the interfacial defects seen in the interface plane ^{10, 11, 12}.

In the case of the interfaces obtained after annealing of amorphized wafers, the change in the Spreading Resistance shape indicates that the electrical characteristics of these interfaces are

definitely different and obviously more complicated than those obtained after bonding of two crystalline wafers.

The defects densities (screw and 60° dislocations) are of the same order of magnitude and thus cannot explain the observed differences. In previous studies, we have shown that higher densities of screw and 60° dislocations could affect the magnitude of the SR profile but not its shape¹². The difference in terms of precipitate densities (SiC and SiO₂) is not high enough to be suspected of significantly altering the interfacial electrical characteristics. There is also little chance that the defects extending into the volume of the wafers can explain this change since there are seen in small numbers.

Thus, we have to consider that, contrary to the interfaces obtained after bonding of crystalline wafers that succeed in relaxing the whole structure, the material obtained by bonding amorphized wafers is heavily stressed and this can be measured on images showing the moiré fringes. Stress induced strain is known to affect the characteristics of semiconducting materials through various mechanisms^{16, 17}. While the most obvious of them is the resulting changes in terms of mobility and gap width, indirect effects also exist such as "anomalous" dopant diffusion in the vicinity of the strained regions. Indeed, Ishigami et al. have already observed this type of SR profiles when two Si wafers are assembled with a ring pattern¹⁷. In this case, they have measured by SIMS an increase of the boron concentration near the interface and a large stress in its vicinity by X-rays.

In our case, we have shown that the stress is localized near the interface and thus, some regions are under compressive stress and others under tensile stress. This residual stress can give rise to a driving force for enhancing the boron diffusion in its gradient region. Hence, it is expected that the boron concentration will increase near the interfacial region leading to a local decrease of the resistance.

Another explanation that cannot be ruled out is the change of the electrical characteristics of strained semiconductors. For example, the carrier mobility changes under stressed conditions and it is known that, in a P-doped and stressed substrate, the mobility substantially increases^{16, 17}.

In summary, this paper presents the comparison of the structural and electrical characteristics of Si/Si bonded interfaces depending on whether the surface layers were rendered amorphous by high dose ion implantation prior to annealing or not. While the general structure of the obtained interfaces is the same that for direct bonding of crystalline materials, more precipitates are seen in the interface along with a few extended defects propagating into the volume. The most striking difference between both procedures is that the Spreading Resistance profile is more complicated in shape and difficult to master in the case of preamorphized wafers. Careful TEM analysis shows that only in this case the interfacial region is stressed in contrast with the fully relaxed structure obtained by direct bonding of crystalline wafers. While more experimental characterizations including SIMS experiments are to be carried out to make this point clearer, there is little chance that the preamorphization technique will benefit the bonding procedure of direct Si wafers since the overall electrical characteristics get more complicated and even more difficult to reproduce than in the case of direct bonding of crystalline wafers.

REFERENCES

1. F. Secco d'Aragona and L.J. Ristic, *Sensor technology and devices*, Artech House Editor, (1994), 157-201.
2. Dino R. Ciarlo, Proc. of the 2nd Int. Symp. on Semiconductor wafer Bonding, (1993), 313-326.
3. W.P. Maszara, G. Goetz, A. Caviglia and J.B. McKitterick, J. Appl. Phys., 64 (1988) 4943.
4. Donald L. Hughes, Proc. of the 2nd Int. Symp. on Semiconductor wafer Bonding, (1993), 17-31.
5. A. Nakagawa, K. Imamura and K. Furukawa, Toshiba Review No161, 34, 1987

6. Parkes, E. Murray, H.S. Gamble, B.M. Armstrong, S.J.N. Mitchell and G.A. Armstrong, in Extended Abstracts 1991 Electrochemical. Soc. Fall Meeting, Vol.91-2, Phoenix, p.724 (1991)
7. H. Ohashi, K. Furukawa, M. Atsuta, A. Nakagawa and K. Imamura, IEDM Techn. Dig., IEEE, New York, (1987) 678.
8. A. Laporte, M. Bagnères, D. Stutzemberger, J.M. Reynes, G. Sarrabayrouse ", 7th Int. Symp. on Power Semiconductor Devices & ICs", Yokohama (Japon), May 1995.
9. M. Benamara, A. Rocher, L. Lanaab, A. Claverie, A. Laporte, G. Sarrabayrouse, L.Lescouzères et A. PeyreLavigne, CRAS Paris, 318 II (1994), 1459-1464.
10. A. Laporte, G. Sarrabayrouse, A. PeyreLavigne, L. Lescouzères, M. Benamara, A. Rocher and A. Claverie, Proc. of the 6th Int. Symp. on Power Semiconductor Devices & ICs, Davos (1994), 293-296.
11. M. Benamara, A. Rocher, A. Laporte, G. Sarrabayrouse, A. PeyreLavigne, L. Lescouzères, M. Fnaiech and A. Claverie, this proceeding.
12. A. Laporte, G. Sarrabayrouse, A. PeyreLavigne, L. Lescouzères, M. Benamara, A. Rocher, L. Lanaab, A. Claverie , 3rd Int. Symp. on Semiconductor wafer Bonding, May 1995, Reno.
13. B. de Mauduit, L. Laânab, M.M. Faye, A. Claverie, C. Bergaud and A. Martinez, Nucl. Instr. and Meth., B84 (1994), 190-194.
14. A. Claverie, L. Laânab, C. Bergaud, A. Martinez and D. Mathiot, Nucl. Instr. and Methods in Phys. Res. B, B96 (1995), 202-209.
15. W. Wijaranakula, Jpn. J. Appl. Phys., 32 (1993), 3872-3878.
16. H. Schlötterer, Solid. State Electronics, 11 (1968), 947-956.
17. S.I. Ishigami, Y. Kawai, H. Furuya, T. Shingyouji, Jpn. J. Appl. Phys. Vol. 32 (1993), 4408-4412.

EFFECT OF FERMI LEVEL PINNING AT THE SURFACE DURING OMVPE GROWTH

R.M. COHEN,* C.Y. CHEN,* W.M. LI,* D.S. SIMONS, ** and P.H. CHI**

*Dept. of Materials Science and Engineering, Univ. of Utah, Salt Lake City, UT 84112

**NIST Chemical Science and Technology Laboratory, Gaithersburg, MD 20899

ABSTRACT

During organometallic vapor phase epitaxy of GaAs, the Fermi energy is found to be pinned ≈ 200 meV below the intrinsic Fermi energy on a (100)-oriented surface. This was determined by making the first comparison of Zn concentration, N_{Zn} , obtained from growth with that obtained at equilibrium, all under the same nominal ambient conditions. Donor solubility has been found to be virtually unchanged during growth of n- or p-type GaAs, and this is strong evidence that the Fermi level remains pinned at essentially the same energy during growth of n- or p-type GaAs. Consistent with Fermi level pinning, we find (1) the N_{Zn} is supersaturated in the epilayer for the ambient growth conditions used, (2) a large excess concentration of positively charged Ga interstitials can be grown into n-type GaAs and which diffuses into nearby p-type layers, causing (3) the Zn diffusivity, $D_{Zn} \sim 10^{-13}$ cm²/s, out of buried npn layers to be essentially independent of the ambient conditions. Annealing of a heavily Zn-doped layer at the surface can lead to $10^{-16} < D_{Zn} < 10^{-13}$ cm²/s at $T=800$ °C simply by varying the Zn partial pressure over its commonly used range. Use of In-doped spikes in n- and p-type GaAs suggest that interstitial point defects have a strong effect on the group III diffusion.

INTRODUCTION

Conclusions are often made about diffusion mechanisms after analyzing diffusion or interdiffusion data with thermodynamic mass action expressions. For a system consisting of two phases, say, a GaAs wafer in contact with gas, and three components, Ga, As, and a dopant, the Gibbs phase rule demands that exactly three degrees of freedom be controlled. The degrees of freedom which are typically controlled are the temperature, T , and the As and dopant partial pressures, P_{As4} and P_{dop} . When these are controlled, then all other thermodynamic parameters (dopant solubility, concentration of point defects, etc.) are well defined at equilibrium and an experiment will be reproducible if the point defects can approach equilibrium quickly. Diffusivity may then be written as a function of the three controlled variables, $D=D(T, P_{As4}, P_{dop})$. However, only when the dopant concentration in the wafer, N_{dop} , is close to equilibrium with P_{dop} , may one express D in terms of the Fermi level, E_f , i.e., $D=D(T, P_{As4}, E_f)$. We have demonstrated¹ that N_{dop} almost never approaches equilibrium with P_{dop} during organometallic vapor phase epitaxy (OMVPE), and that the use of $D=D(T, P_{As4}, E_f)$ can be very misleading. In this paper, we provide additional evidence for Fermi level pinning at the surface during growth and show that it is the major reason why N_{dop} and P_{dop} do not equilibrate during OMVPE.

EXPERIMENTAL

GaAs epilayers were grown by atmospheric pressure OMVPE on Si-doped GaAs substrates, (100)-oriented and cut 2° off toward (110). Growth was performed in a rectangular OMVPE quartz reactor with a cross section of 2x5 cm. Sources used include tertiarybutylarsine (TBAs), trimethylgallium (TMGa), dimethylzinc (DMZn), dimethylditelluride (DMDTe), and CCl₄. H₂, of 5N purity, was passed through a commercially available metal hydride filter to obtain a purity of better than 7N (with respect to O₂ and H₂O). Electronic mass flow controllers were used to accurately control gas flows, and an electronic temperature controller was used to keep the sample temperature constant. An IR lamp was used to heat a graphite susceptor during growth. During annealing or diffusion studies, the susceptor was replaced with a graphite block which fit snugly inside the quartz. As described elsewhere,¹ the samples and their GaAs proximity caps were

placed in a slit cut in the block during annealing. Growth parameters for the p-type layers have been described elsewhere.¹ Dopant concentration was maximized in pnpn structures by using a growth temperature of $T_g=650^\circ\text{C}$ for the n-type layers and $T_g=575^\circ\text{C}$ for the p-type layers. For growth of the npn layers, $T_g=600^\circ\text{C}$. Characterization included electrochemical capacitance-voltage (ECV) profiling, and secondary ion mass spectroscopy (SIMS). SIMS profiles were made with a Cs^+ primary ion beam at an impact energy of 14.5 keV for C, In, and Te, and 5.5 keV for Zn. Concentration values were determined by comparison with ion implanted standards. The instrumental background concentration is approximately $1 \times 10^{18} \text{ cm}^{-3}$ for C, but it is much lower for the other elements measured. The depth scale was obtained by stylus profilometry of individual craters with an estimated uncertainty of $\pm 3\%$.

RESULTS AND DISCUSSION

Fig. 1 shows the solid solubility of Zn, N_{Zn} , as a function of P_{Zn} at $T=700^\circ\text{C}$ and constant P_{As_4} . The triangles represent the approximately constant N_{Zn} near the GaAs surface, as measured by SIMS, after Zn was diffused into undoped epilayers from the gas phase, and a line is drawn through the data with an $N_{\text{Zn}} \sim P_{\text{Zn}}^{1/2}$ dependence. The other data points show the results of OMVPE growth. The squares represent data taken by ECV profiling, and two of those points were verified with SIMS (diamonds). The growth results are similar to those reported by others,^{2,3} i.e., $N_{\text{Zn}} \sim P_{\text{Zn}}$, up to the solid solubility limit.¹

Interestingly, both curves can be understood by assuming solid-vapor equilibrium between species in the vapor (v) and the ionized Zn and holes, h^+ , in the solid (s), via $\text{Zn(v)} + 1/4\text{As}_4\text{(v)} \leftrightarrow \text{Zn-As(s)} + h^+$. The resulting mass action expression, $pN_{\text{Zn}} = K_p P_{\text{Zn}} P_{\text{As}_4}^{1/4}$, can be used to describe N_{Zn} after either growth or diffusion, assuming that equilibrium can be approximated. Thus, after Zn in-diffusion from the vapor, the region where $N_{\text{Zn}}=p=\text{constant}$ just below the surface should exhibit an $N_{\text{Zn}} \sim P_{\text{Zn}}^{1/2}$ dependence. This same dependence also would be observed during growth if $p=N_{\text{Zn}}$ at the growing surface. However, if the Fermi energy is pinned at the surface during growth, i.e., $p_{\text{surf}}=\text{const.}$, then $N_{\text{Zn,surf}} \sim P_{\text{Zn}}$ is predicted. During growth, $N_{\text{Zn,surf}}$ becomes the Zn concentration in the epilayer, and this results in a nonequilibrium, but metastable, $N_{\text{Zn,epilayer}}$ (assuming that the Zn cannot diffuse rapidly enough to change N_{Zn} during growth). We have shown¹ that the crossover of the two lines in Fig. 1, at $N_{\text{Zn}} \approx 3 \times 10^{17} \text{ cm}^{-3}$, provides an estimate of the pinned Fermi energy, E_f , relative to the intrinsic Fermi energy, E_i , and intrinsic carrier concentration, n_i , of $(E_i - E_f)_{\text{surf}} = kT \ln(p_{\text{surf}}/n_i) \approx 200 \text{ meV}$, during OMVPE growth of Zn-doped GaAs at $T=700^\circ\text{C}$.

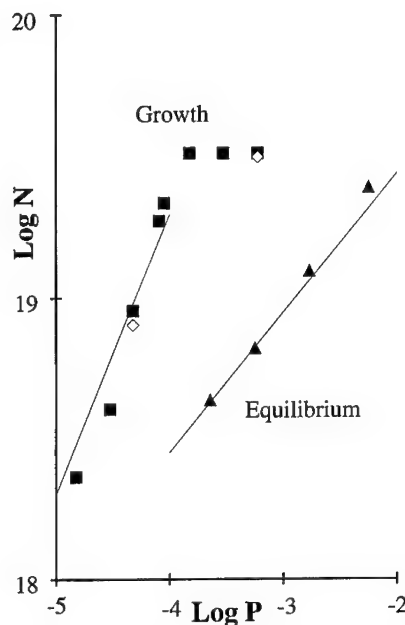


Fig. 1. $\text{Log } N_{\text{Zn}} (\text{cm}^{-3})$ vs $\text{Log } P_{\text{Zn}} (\text{atm})$, from growth (squares from CV, diamonds from SIMS) and from equilibrium experiments (triangles). A line with slope of 1/2 is shown with the equilibrium results, and a line with slope unity is shown with the growth results.

It is also of interest to determine whether pinning occurs during the growth of n-type GaAs, and, if so, where the Fermi level is pinned. We (and others) have observed a nominal $N_{Te} \sim P_{Te}$ for group VI elements rather than the $N_{Te} \sim P_{Te}^{1/2}$ expected⁴ from the mass action expression, $nN_{Te} = K_n P_{Te} P_{As_4}^{-1/4}$, if $n = N_{Te}$ at the growing surface. This suggests that pinning does occur during OMVPE growth of n-type GaAs, but experiments analogous to those performed with Zn, i.e., in-diffusion from the vapor, are impractical because of the low diffusivity of our donors.

An alternate approach is to measure the shift of the surface Fermi energy during growth of an npn structure. Keeping a constant P_{Te} and P_{As_4} during the entire growth, the mass action expression predicts that the equilibrium N_{Te} will increase more than an order of magnitude during growth of the p-type layer. Fig. 2 shows the results of growing an n-type layer with Te, and adding a large concentration spike of C during the growth. There is an insignificant change in N_{Te} as the carrier density closely follows the dopant concentration (confirmed by ECV). Attributing the small change of N_{Te} in the p-region entirely to a shift in $E_{f,surf}$, the shift is estimated to be

$$\Delta E_{f,surf} = kT \ln(n_{p\text{-region}}/n_{n\text{-region}}) < 20 \text{ meV.}$$

This is very strong evidence that the Fermi energy is pinned weakly p-type independent of the polarity of the dopant, i.e., $(E_i - E_f)_{surf} \approx 200 \text{ meV}$ during n-type as well as p-type OMVPE on the (100)-oriented surface of GaAs.

A pinned Fermi energy has implications which go far beyond the solubility of dopants. Analogous to dopants, the equilibrium concentration of charged point defects will be determined by reactions, such as $V^0 + e^- \leftrightarrow V^-$ which relates neutral and singly charged vacancies. Since the equilibrium concentration of neutrals, $[V^0]$, is independent of E_f ,⁴ the resulting mass action expression, $[V^-] = K_v [V^0] n$, illustrates that the concentration of any charged point defect will be strongly affected by the Fermi level pinning during growth. Unless the characteristic diffusion length of the defect is large, its concentration after growth (and perhaps even after annealing) will be determined primarily by $E_{f,surf}$ during growth rather than the equilibrium N_{dopant} . For the pinning described above, one expects to obtain a supersaturation of positive point defects and an undersaturation of negative point defects during OMVPE growth of n-type GaAs, and the opposite during growth of heavily p-type GaAs.

Deppe⁵ suggested that the emitter push effect observed in npn structures could be related to a Fermi energy which was pinned at the surface near midgap. He pointed out that the triply charged Ga vacancy, V_{Ga}^{3-} , which was then thought to control diffusion, would be undersaturated in the grown epilayer. Deppe proposed that a particular Frenkel reaction in an n-type epilayer,

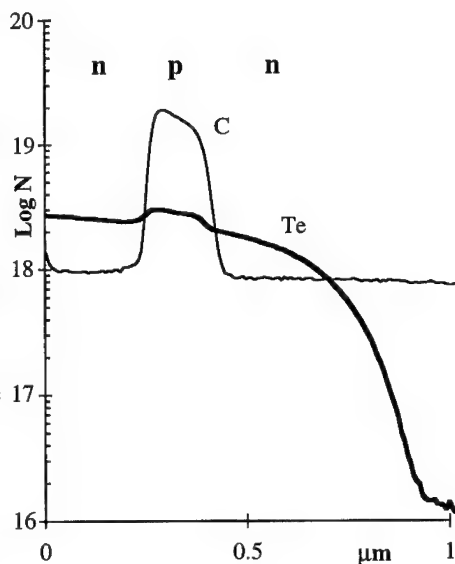


Fig. 2. Log N_{Te} and N_C (cm^{-3}) vs depth (μm). The lack of change in the Te concentration as the GaAs becomes p-type is striking. This is strong evidence that the Fermi level remains pinned at the same energy during growth of n-type and p-type GaAs. The instrumental background for $N_C \approx 1 \times 10^{18} \text{ cm}^{-3}$.

$\text{Ga}_{\text{Ga}} \leftrightarrow \text{V}_{\text{Ga}}^{3-} + 3\text{h}^+ + \text{I}_{\text{Ga}}^0$, would produce sufficient neutral interstitials, I_{Ga}^0 , to cause widening of an adjacent group II-doped base via the kick-out mechanism. This reaction is logically consistent with observations of that period, but it is likely to be a slow reaction when going to the right because of the large energy required to remove substitutional Ga.

Using the new Te source, DMDTe, which has allowed growth of unusually high electron concentrations of $n \geq 1 \times 10^{19} \text{ cm}^{-3}$,⁶ we have grown pnpn structures demonstrating a large emitter push effect. Fig. 3 shows the concentration profiles for Zn, Te, and In in an as-grown epilayer of sample CY132B. In this sample, it is worth emphasizing that Zn was turned on after Te was turned off, and Te was turned on after Zn was turned off. Separate experiments have confirmed that growth of the top Te-doped layer is responsible for the Zn

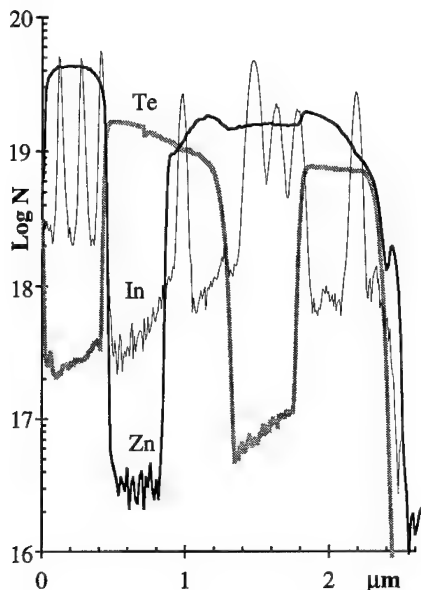


Fig. 4. Log N (cm^{-3}) vs depth (μm) measured after annealing a piece of CY132 at $T=800^\circ\text{C}$, $P_{\text{TBA}}=3 \times 10^{-3} \text{ atm}$, and a nominal $P_{\text{Zn}}=0$. A small diffusion of Zn out of the top layer can be seen, and contrasted to the large diffusion of Zn out of the buried layer.

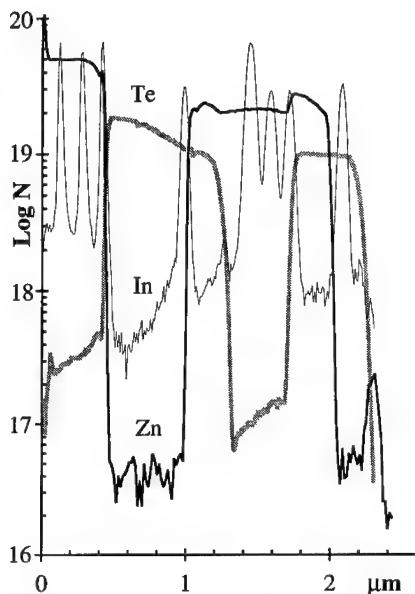


Fig. 3. Log N of In, Te, and Zn (cm^{-3}) vs depth (μm) for the as-grown sample, CY132B. The width of the buried Zn-doped layer has doubled during growth of the following layers because of trapped I_{Ga}^+ which entered during growth of the second Te-doped layer.

diffusion out of the buried layer. This buried Zn layer widens tremendously during the $t=25 \text{ min.}$ growth of the top two layers, even though there is virtually no diffusion out of the top Zn-doped layer.

The minimal Zn diffusion out of the top layer demonstrates that there is no significant flux of interstitials from the Te-doped layer into the top layer. This suggests that I_{Ga} generation by the Frenkel reaction is very slow. Assuming a singly charged positive

I_{Ga}^+ , it is easy to show⁴ that at equilibrium,

$$\left[\text{I}_{\text{Ga, surf}}^+ \right] / \left[\text{I}_{\text{Ga, bulk}}^+ \right] = n_{\text{bulk}} / n_{\text{surf}} \sim 10^4$$

for the conditions used here. We propose that the pinned p-type surface leads to (1) I_{Ga}^+ being trapped in the n-type epilayer at a supersaturated concentration during growth of n-type GaAs, and (2) this I_{Ga}^+

diffuses both back to the surface and into the buried Zn-doped region. Positive interstitials diffusing into the buried p-type layer will remain trapped there by the electric field of the two pn junctions. The trapped I_{Ga}^+ are expected to enhance the diffusion of any element, i.e., Zn and any other elements sensitive to the kick-out mechanism.

After annealing a piece of this sample at $T=800^\circ\text{C}$, $P_{TBAs}=3\times 10^{-3}$ atm, and a nominal $P_{Zn}=0$ atm for $t=1$ hr, substantially more Zn diffusion was observed out of the buried Zn-doped layer, but essentially none out of the top Zn-doped layer, as can be seen in Fig. 4. At a temperature of $\approx 150^\circ\text{C}$ above that used during growth, it is reasonable to expect an increase in the equilibrium V_{Ga} and I_{Ga} concentrations. However, diffusion out of the top Zn-doped layer is minuscule, and this provides strong evidence that the Frenkel reaction does not produce any significant quantity of I_{Ga} in the top n-type layer during annealing. It is interesting to make an order of magnitude estimate of the effective D_{Zn} associated with these two layers after annealing under the "same" ambient conditions. Out of the top layer, $D_{Zn}\sim 10^{-16}$ cm²/s while out of the bottom Zn-doped layer, $D_{Zn}\sim 10^{-13}$ cm²/s. Both Zn-doped layers are, in fact, far from equilibrium. The top Zn-doped layer is far from equilibrium because $N_{Zn}=0$ is the equilibrium concentration corresponding to $P_{Zn}=0$. In the buried layer, the Zn diffusion during annealing can be

understood in terms of (1) the excess I_{Ga}^+ , remaining trapped in the Zn-doped layer after growth, kick out and replace Zn atoms, (2) the resulting I_{Zn}^+ , although also trapped by the electric field of the pn junctions, diffuse a short distance into the pn junction, kick out and substitute onto Ga sites, and (3) the resulting I_{Ga}^+ move back into the neutral p-region to repeat the process. Experimental evidence for the positively charged I_{Zn}^+ and a more complete discussion of this process is presented elsewhere.⁷

After annealing another piece of CY132 at $T=800^\circ\text{C}$, $P_{TBAs}=3\times 10^{-3}$ atm, and $P_{Zn}=5.7\times 10^{-3}$ atm for $t=1$ hr, the profiles changed to those shown in Fig. 5. The diffusion of Zn out of the buried layer is similar to that seen in Fig. 4. The top Zn-doped layer has diffused into the Te-doped layer, and its diffusivity is clearly less than that observed at $T=650^\circ\text{C}$ using essentially the same P_{Zn} .⁸ This is simply a result of thermodynamics:⁹ relative to $P=1$ atm standard conditions, the activity of Zn at a fixed P_{Zn} , $a_{Zn}=P_{Zn}/P_{Zn}^0$, depends upon temperature through the vapor pressure of pure Zn, P_{Zn}^0 . One immediate result of this is that N_{Zn} in the top layer approaches its equilibrium value near the surface, which we have estimated from separate experiments to be $1\text{--}2\times 10^{19}$ cm⁻³ for the conditions associated with Fig. 5. For comparison, $N_{Zn,eqm}=5\times 10^{19}$ cm⁻³, at $T=650^\circ\text{C}$ and the same partial pressures, as can be seen in Ref. [8]. Another effect of lower

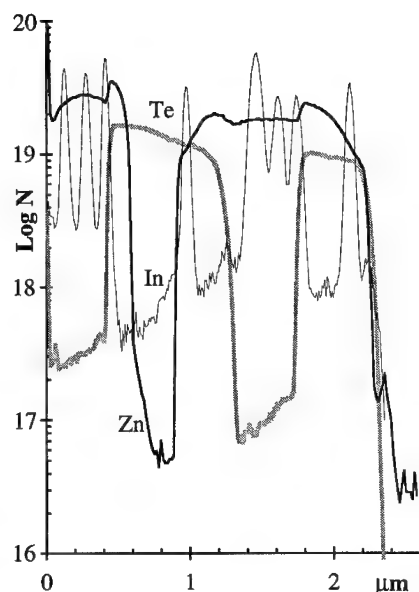


Fig. 5. Log N (cm⁻³) vs depth (μm) measured after annealing a piece of CY132 at $T=800^\circ\text{C}$, $P_{TBAs}=3\times 10^{-3}$ atm, and $P_{Zn}=5.7\times 10^{-3}$ atm. Significant diffusion of Zn out of both Zn-doped layers is now visible. Note that N_{Zn} near the surface has dropped to essentially its equilibrium value.

a_{Zn} at $T=800^\circ\text{C}$, compared to the nominally identical conditions at $T=650^\circ\text{C}$, appears to be a lower concentration of I_{Zn}^+ and thus lower Zn diffusivity.

A pinned Fermi energy which affects the concentration of charged point defects during growth is expected to have an impact on any measure of self-diffusion using neutral markers. Markers, consisting of concentration spikes of In, were grown into each layer of the pnpn structure and can be seen in Figs. 3-5. In the top Zn-doped layer of Figs. 3 and 4, interdiffusion on the group III sublattice is no larger than our resolution limit, i.e., $D_{\text{III}} \leq 10^{-17} \text{ cm}^2/\text{s}$. In Fig. 5, $D_{\text{III}} \sim 10^{-16} \text{ cm}^2/\text{s}$ is found in the top Zn-doped layer. In addition, $D_{\text{III}} \sim 10^{-16} \text{ cm}^2/\text{s}$ is measured in the buried Zn-doped layer where I_{Ga}^+ have been trapped since growth. These results indicate that a kick-out mechanism enhances $D_{\text{In-Ga}}$ when I_{Ga}^+ is present. Moreover, in the n-type layers $D_{\text{In-Ga}}$ is unmeasurably small. This is somewhat surprising because we expected that (1) the weak In-As bond would make In an excellent marker for a vacancy mechanism, and that (2) In would not move significantly by an interstitial mechanism because its large radius would preclude such diffusion. The $D_{\text{In-Ga}}$ in the Te-doped layers are lower than expected based upon the model of Tan and Gosele¹⁰ which predicts a measured $D_{\text{III}}(800^\circ\text{C}) = D_i \{n/n_i\}^3 \approx 10^{-20} \{1.5 \times 10^{19} / 8 \times 10^{16}\}^3 \approx 10^{-13} \text{ cm}^2/\text{s}$, or $\sim 10^4 \times$ larger than observed. The gradual conversion of the Te-doped layers to Zn-doped layers does not appear to account for this difference. The excess I_{Ga}^+ generated during growth in the Te-doped layer is expected to cause a sharp drop in the vacancy concentration via the Frenkel reaction, and the recovery of the $[V_{\text{Ga}}]$ back to its equilibrium value is expected to be slow.⁸ However, at present it is unclear how quickly the n-type crystal returns to equilibrium.

In summary, the work presented here shows that Fermi energy pinning at the surface of (100)-oriented GaAs is weakly p-type, $E_f - E_v \approx 200 \text{ meV}$, for growth of both p- and n-type GaAs with typical OMVPE conditions. This pinning accounts for not only the unity slope of the dopant solubility, i.e., $N_{\text{dopant}} \sim P_{\text{dopant}}$, but also a grown-in nonequilibrium concentration of charged point defects. It has been shown that nonequilibrium defect concentrations can become trapped by the electric field associated with pn junctions and is responsible for the so-called emitter push effect. Because we found that two Zn diffusion fronts separated by $< 1 \mu\text{m}$ can be characterized by diffusivities that differ by several orders of magnitude after annealing under nominally identical ambient conditions, we have not compared our diffusivities with those reported by others (taken under still different nonequilibrium conditions). These results and others should be useful for device application because an understanding of defect incorporation during growth and annealing should lead to new strategies to control diffusion in device regions.

Support from NSF through contract number DMR-9024848 is gratefully acknowledged.

- 1 W.R. Reichert, C.Y. Chen, W.M. Li, J.E. Shield, R.M. Cohen, D.S. Simons, P.H. Chi, J. Appl. Phys. **77**, 1902 (1995).
- 2 R.W. Glew, J. Cryst. Growth **75**, 91 (1984).
- 3 K. Okamoto, H. Mawatari, K. Yamaguchi, A. Noguchi, J. Cryst. Growth **98**, 630 (1989).
- 4 R.M. Cohen, J. Appl. Phys. **73**, 4903 (1993).
- 5 D.G. Deppe, Appl. Phys. Lett. **56**, 370 (1990).
- 6 W.M. Li and R.M. Cohen, submitted to J. Cryst. Growth.
- 7 C.Y. Chen, R.M. Cohen, D.S. Simons, P.H. Chi, submitted to Appl. Phys. Lett.
- 8 R.M. Cohen, C.Y. Chen, W.M. Li, D.S. Simons, P.H. Chi, presented elsewhere in this symposium.
- 9 C.Y. Chen and R.M. Cohen, submitted to J. Cryst. Growth.
- 10 T.Y. Tan and U. Gosele, Mater. Sci. Engineering **B1**, 47 (1988).

RADIATIVE RECOMBINATION PROCESSES IN BORON MODULATION-DOPED SiGe QUANTUM WELLS

I. A. BUYANOVA^a), W. M. CHEN, A. HENRY, W. X. NI, G. V. HANSSON, and
B. MONEMAR
Department of Physics and Measurement Technology, Linköping University, S-581 83
Linköping, Sweden

ABSTRACT

The radiative recombination processes of the two-dimensional hole gas formed in SiGe quantum wells (QWs) due to modulation doping are studied in details by photoluminescence (PL) spectroscopy. Boron-modulation-doped Si/Si_{1-x}Ge_x/Si heterostructures grown by molecular beam epitaxy (MBE) are studied. It is shown that charge transfer of holes from the doped Si layers causes the filling of the SiGe QWs leading to an appearance of a broad asymmetric PL band with a characteristic sharp high energy cut-off and enhanced recombination near the Fermi edge. A reduction of this PL enhancement is observed with an increase of measuring temperature. The PL bandwidth and the high energy cut-off are found to vary with either the doping level or the spatial separation between the delta-doped layers and the QWs. This PL band is argued to arise from the recombination of the holes in the QWs and electrons confined near the QWs as a result of the band bending induced by the delta-doping. The shape of the PL band with enhanced intensity near the Fermi edge are discussed in terms of the phase space filling and many-body effects.

INTRODUCTION

Modulation doping of semiconductors has attracted great interest from both fundamental and technological point of views. The effect of delta doping in GaAs and Si-based structures was demonstrated nearly 10 years ago. The recent advance in molecular beam epitaxy (MBE) makes possible the fabrication of high quality Si-based modulation-doped structures and encourages the detailed investigations of their physical properties. Recent studies of modulation doped Si and SiGe quantum wells (QWs) include intersubband absorption measurements [1, 2] and magnetotransport studies [3 - 6] of the two-dimensional (2D) electron or hole gas formed due to the modulation-doping. Very little has been done by photoluminescence (PL) spectroscopy, which has previously been successfully used to retrieve detailed information on the optical and electronic properties of 2D systems in III-V heterostructures [7 - 12]. This is mainly due to the fact that high quality Si and SiGe samples suitable for optical studies have only been available recently.

In this paper we report on the detailed photoluminescence studies of radiative recombination processes in boron-modulation-doped Si/SiGe/Si heterostructures. We shall show that the main photoluminescence (PL) process in such structures is the recombination between free electrons and the two-dimensional hole gas (2DHG), formed in the SiGe quantum well (QW) due to the carrier transfer from the doped regions. The observed strong dependence of the PL spectra on the structure parameters, such as the doping concentration and the spacer thickness, as well as on the experimental conditions, e.g. measurement temperature and photo-excitation intensity, is discussed in terms of many-body phenomena, such as the Fermi edge singularity.

EXPERIMENTAL

Samples investigated were grown in a Balzers UMS 630 Si MBE system on n-type (100) Si substrates (300 Ω cm), having a 1000 Å undoped Si buffer layer. The structures consist of a

strained $\text{Si}_{0.8}\text{Ge}_{0.2}$ QW placed between two boron-doped Si layers separated by undoped silicon spacers with the thickness ranging from 250 Å to 500 Å - Fig.1. The B-doping was done at

Si-cap layer	1200 Å
Si:B	35 Å
Si	250 - 500 Å
SiGe	500 Å and 30 Å
Si	250 - 500 Å
Si:B	35 Å
Si-buffer	750 Å
Si substrate	

Fig. 1. The basic Si/SiGe/Si quantum well structure with symmetrical modulation doping.

500°C to reach a sheet doping concentration of $1 \times 10^{13} \text{ cm}^{-2}$. SIMS measurements revealed that the B-doping profiles were significantly broadened due to the B segregation, leading to unintentional B doping in the Si spacers and also in the SiGe QW. The structures were finally capped by a nominally undoped, 1200 Å thick Si layer. Reference samples of similar structures were also grown without the modulation-doping in the Si barriers with or without the same doping in the SiGe QW. The sheet carrier densities in the SiGe QWs, estimated from the Poisson's equation by taking into account the actual B doping profiles, are $2.5 \times 10^{12} \text{ cm}^{-2}$ and $4.0 \times 10^{12} \text{ cm}^{-2}$ for structures with a 500 Å and 250 Å spacer, respectively. These values are in agreement with results from Hall effect measurements.

The PL measurements were performed in a temperature range 2-70 K. PL was excited by an Ar-ion laser and was dispersed with a SPEX 1-m double-grating monochromator and detected by a liquid-nitrogen-cooled North Coast Ge detector.

Hydrogen passivation was accomplished at about 200 °C for 60 min, inside a quartz reactor with a remote dc H plasma at a pressure of 2.0 mTorr.

RESULTS AND DISCUSSION

Fig. 2a and b (solid curves) represent PL spectra measured for the modulation-doped structures with 500 Å (a) and 250 Å (b) spacers. The spectra exhibit the no-phonon and phonon-assisted broad asymmetric PL bands with the maximum position of the no-phonon (NP) line ranging from 1.05 eV to 1.07 eV. (The substrate-related PL from Si, observed at higher photon energies, is not shown in the figure for clarity). This PL appears only after modulation doping and is never observed for the undoped structures. The observation of a pronounced NP line as compared to the transverse optical (TO) phonon replica, detected 58 meV below the NP band, is considered as characteristic for SiGe due to a strong alloy scattering. The shape of the band with an abrupt high energy cut-off is, however, significantly different from both the near-band gap excitonic PL detected in our undoped reference structures and the localized excitonic emission [13], known to be observed under low excitation conditions. We thus propose that this asymmetric PL is related to the recombination of the 2DHG in the SiGe QW and electrons confined near the QW due to band bending, induced by the modulation doping. The asymmetric line shape of the band, with increased PL intensity towards the higher energies followed by an abrupt high energy cut-off, reflects the energy distribution of optical matrix elements in indirect band gap materials, such as SiGe. The width of the band is then determined by the filling of the QW, while the high energy cut-off of the spectra represents the Fermi level position (E_F) with respect to the ground heavy-hole (HH) subband. The values of E_F estimated from the width of

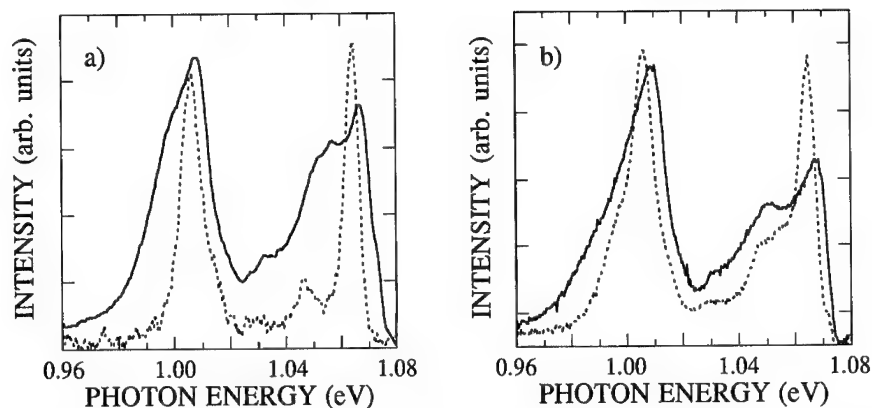


Fig. 2. Normalized photoluminescence spectra at 2K from the SiGe QWs with 500 Å spacer (a) and 250 Å spacer (b). Spectra of the as-grown and the hydrogen-passivated samples are shown as the solid and dashed curves, respectively.

the TO replica of the PL bands, measured with low excitation density (Fig.3), are ~ 30 meV and 50 meV for the structures with 500 Å and 250 Å spacers, respectively. These experimentally determined Fermi level positions agree reasonably well with the values of 26 and 48 meV estimated by solving the Poisson's equation.

To prove further the participation of the 2DHG in the PL transitions, hydrogen passivation of the structures investigated has been performed. Such a hydrogen treatment has previously been

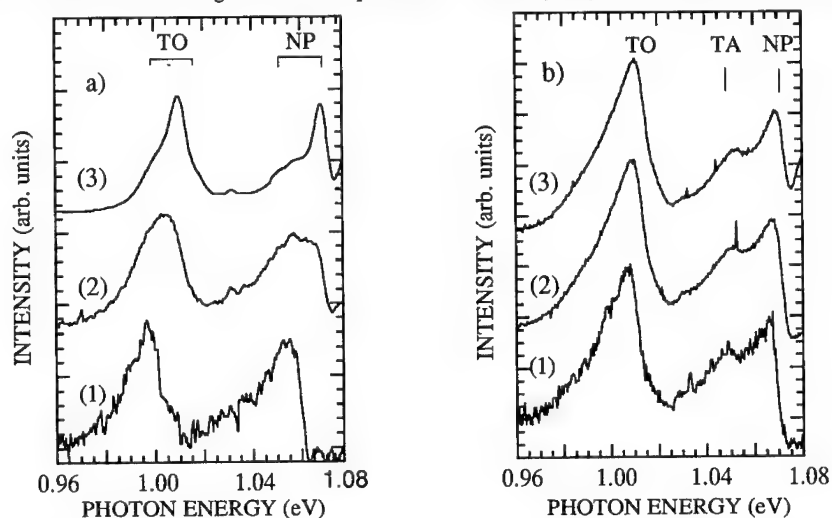


Fig. 3. Excitation dependent PL spectra measured at 2 K from the SiGe QWs with 500 Å spacer (a) and 250 Å spacer (b). The excitation densities are equal to 0.05 W/cm² (1), 0.8 W/cm² (2) and 3.5 W/cm² (3).

shown [14] to deactivate the effective boron-dopant density in modulation-doped Si layers, thus providing the possibility to vary easily the 2DHG density in the structures. The PL spectra recorded after the hydrogen passivation of the QWs with 500 Å and 250 Å spacers are shown as the dashed curves in Fig. 2a and b, respectively. For the structure with 500 Å spacer the PL spectrum of the passivated sample resembles the emission usually observed for undoped SiGe QWs with typical sharp phonon-assisted excitonic transitions [13]. For the QW with 250 Å spacer and, thus, higher free hole concentration, the partial decrease of the 2DHG density is observed after hydrogen treatments. We consider this PL behaviour as a direct evidence for the involvement of the 2DHG in the PL transitions.

The distinct feature of the asymmetric PL bands, appearing due to the modulation doping, is their strong dependence on the structure parameters, such as the doping concentration and the spacer width, as well as on the experimental conditions, e.g. measurement temperature and photo-excitation intensity. The excitation dependent PL spectra are shown in Fig. 3. A clear shift towards higher energies with increasing excitation power is observed, followed by an abrupt enhancement of the PL intensity at the Fermi edge (Fig. 3a) for the sample with 500 Å spacer. We suggest that this abrupt increase is attributed to the many-body interaction between the confined hole-plasma and photogenerated electrons, i.e. the Fermi edge singularity (FES) [7 - 12], based on a number of experimental facts. Firstly, the temperature-dependent PL spectra shown in Fig. 4 exhibit the expected [7 - 12, 15 - 17] behaviour of the Fermi edge singularity. The enhancement effects are strongly reduced with increasing temperature and are no longer observable at temperatures higher than 42 K. Such temperature dependence allows us to discard an alternative model for the abrupt PL enhancement, i.e. reappearance of the excitonic recombination of the QW

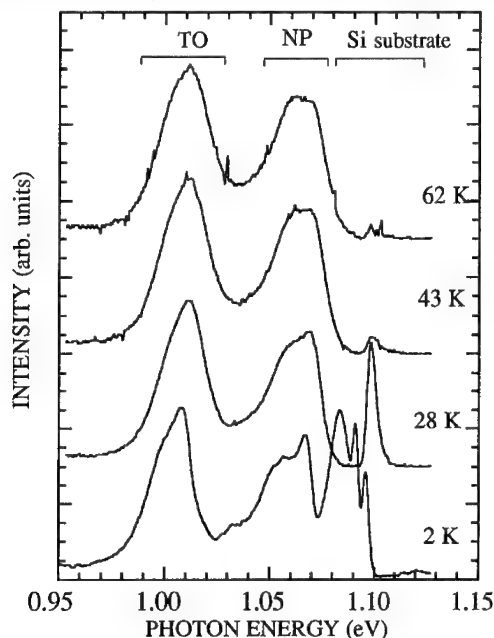


Fig. 4. Normalized temperature-dependent PL spectra of the SiGe QW separated by a 250 Å spacer, with a photo-excitation density of 2 W/cm².

under a flat-band condition reached due to an intense photo-excitation. This is based on the experimental observation that the thermal quenching of the excitonic PL is minimal up to 77 K for the reference sample under the same growth conditions but without the modulation-doping. Additional evidence will be provided in combination with the discussion below.

Two dominant mechanisms have been considered in the literature to be responsible for the FES in modulation doped III-V QWs [7 - 12]. One is the effect of the minority-carrier localization

due to alloy fluctuation and interface roughness, and the other is the scattering between the electronic states near the Fermi energy and the next unoccupied subband. If the first mechanism was dominating, the FES would have been present in all the SiGe QW samples studied since the electron localization in these samples with the same alloy composition and the same QW width is expected to be very similar. This is not the case. The experimentally observed FES varies between the samples, depending critically on the sample structure and the experimental conditions, particularly on the Fermi level position with respect to the next unoccupied hole subband. As an example, we show in Fig.3b PL spectra from the SiGe QW separated by 250Å spacer, where no FES can be observed for photo-excitation intensity up to 3.5 W/cm², although similar asymmetric PL bands are present. The localization of the minority carriers as the mechanism for the FES can therefore be excluded for the SiGe QWs studied in this work.

Theoretical calculations of Hawrylak [15] show that the FES effect should be rather weak when the Fermi level lies far from the next unoccupied subband. To test whether this mechanism is responsible, we have experimentally tuned the separation between the Fermi energy and the next unoccupied subband. This was done either by varying the structure parameters such as the spacer and the doping concentration, or by varying experimental conditions such as the photo-excitation intensity and the bias across the structures.

The charge transfer to the QW critically depends on the separation between the doped layer and the QW. Reducing the distance between the QW and the doping layer results in a stronger charge transfer and thus a higher filling of the QW with 2DHG. This will move up the Fermi level position, so that the next hole subband becomes readily populated. This explains the absence of the FES for the QW separated by 250Å spacer (Fig.3b), where the estimated Fermi level position is about 50 meV above the bottom of the first HH subband and thus higher than the second hole subband [2, 18]. By reducing the doping concentration of the same structure due to hydrogen passivation of the B dopants, and thus reducing the filling of the QW, the FES could be recovered as shown by the dashed curve in Fig.2b.

An increase of the photo-excitation intensity will move up the E_F position in the QWs towards the next higher hole subband, due to the effects of the band filling and the band flattening caused by neutralization of the B dopants. Since the estimated separation between the first heavy hole (HH) subband and the next hole subband (believed to be the first light hole (LH) subband [2, 18, 19]) in such structures is comparable with the Fermi energy of the 2DHG, with increasing excitation intensity the Fermi level can closely approach the LH subband, providing a resonant condition for efficient scattering of the 2DHG. The existence of this Fermi edge resonance will lead to an abrupt enhancement of the PL intensity near the Fermi edge (Fig.3). Alternatively, the phase space filling of the 2DHG up to the LH subband could as well give rise to a normal excitonic transition related to the LH subband. This higher-energy LH emission should be favoured with increasing temperature as compared to the HH-related PL band, which is inconsistent with our temperature dependent studies. In contrary, a thermal quenching was observed as shown in Fig. 3, which rules out the possibility of observing the LH exciton. The absence of the LH exciton can be explained by an insufficient occupation due to an efficient hole relaxation to the lower HH subband when the Fermi energy is still below the bottom of the LH subband. The LH excitonic transitions should also be suppressed after a certain filling of the LH subband, which is the case for the SiGe QW structure with the 250 Å spacer discussed above.

An alternative way to vary the Fermi level position with respect to the LH subband is to apply an external electric field across to the structures [11] and thus to change slightly the band bending. The appearance of the 1.066 eV NP line attributed above to the FES, was clearly observed for some gate voltages, which can be considered as an additional evidence in favour of the model proposed.

The experimental facts discussed above give strong support for an efficient scattering between the states at E_F and the adjacent unoccupied subband as the dominant mechanism responsible for the FES. This observation is quite remarkable, considering the indirect bandgap nature of the SiGe QWs. Since the mix-in of the $k=0$ contribution is not expected to significantly alter the matrix elements for optical transitions, we believe that it is rather the transfer of the excitonic effect from the unoccupied subband due to the many-body correlation that is mainly responsible for the FES in the SiGe QWs.

SUMMARY

In conclusion, the radiative recombination processes in modulation doped Si/SiGe/Si heterostructures have been studied by photoluminescence spectroscopy. It is shown that the main photoluminescence process in such structures is the recombination between the free electrons and the two-dimensional hole gas, formed in the SiGe quantum well (QW) due to the carrier transfer from the doped regions. The observed strong dependence of the PL properties on the structure parameters, such as the doping concentration and the spacer width, as well as on the experimental conditions, e.g. measurement temperature and photo-excitation intensity, is discussed in terms of many-body phenomena, such as the Fermi edge singularity. The dominant mechanism responsible for the FES has been shown to be the nearly resonant scattering of holes from states near the Fermi edge and the next unoccupied 2DHG subband. This work provides the first direct evidence that the FES concept remains highly relevant even for an indirect bandgap semiconductor such as SiGe.

References

a) On leave from the Institute of Semiconductor Physics, Ukrainian Academy of Sciences, Kiev, Ukraine

1. J. S. Park, R. P. G. Karunasiri, Y. J. Mii, and K. L. Wang, Appl. Phys. Lett. **58**, 1083 (1991).
2. F. Fromherz, E. Koppensteiner, M. Helm, G. Bauer, J. F. Nutzel, and G. Abstreiter, Phys. Rev. **B 50**, 15073 (1994).
3. H. J. Gossmann, and F. C. Unterwald, Phys. Rev. **B47**, 12618 (1993).
4. H. H. Radamson, M. R. Sardela, O. Nur, M. Willander, B. E. Sernelius, W. X. Ni, and G. V. Hansson, Appl. Phys. Lett. **64**, 1842 (1994).
5. T. K. Carns, X. Zheng, K. L. Wang, S. L. Wu, and S. J. Wang, Journal of Vacuum Science and Technology B **12**, 1203 (1994).
6. R. Loo, L. Vescan, A. Hartmann, R. Apetz, U. Zastrow, T. Schäpers, A. Leuther, C. Dieker, and H. Lüth, Phys. Rev. **B50**, 18113 (1994).
7. M. S. Skolnick, J. M. Rorison, K. J. Nash, D. J. Mowbray, P. R. Tapster, S. J. Bass, and A. D. Pitt, Phys. Rev. Lett. **58**, 2130 (1987).
8. Y. F. Chen, L. Y. Lin, J. L. Shen, and D. W. Liu, Phys. Rev. **B46**, 12433 (1992).
9. Y.-H. Zhang, D.-S. Jiang, and K. Ploog, Appl. Phys. Lett. **60**, 2264 (1992).
10. W. Chen, M. Fritze, A. Nurmikko, C. Colvard, D. Ackley and H. Lee, Phys. Rev. Lett. **64**, 2434 (1990).
11. Q. X. Zhao, P. O. Holtz, B. Monemar, E. Sörman, W.M. Chen, C. Hallin, M. Sundaram, J. L. Merz, and A. C. Gossard, Phys. Rev. **B43**, 7354 (1991).
12. M. S. Skolnick, D. W. Whittaker, P. E. Simmonds, T. A. Fisher, M. K. Saker, J. M. Rorison, R. S. Smith, P. B. Kirby, and C. R. H. White, Phys. Rev. **B43**, 7354 (1991).
13. L.C. Lenchyshyn, M.L.W. Thewalt, J.C. Sturm, P.V. Schwartz, E.J. Prinz, N.L. Rowell, J.-P. Noël and D.C. Houghton, Appl. Phys. Lett. **60**, 3174 (1992).
14. V. Arbet-Engels, K.L. Wang, R. P. G. Karunasiri, and J. S. Park, Appl. Phys. Lett. **59**, 2248 (1991).
15. P. Hawrylak, Phys. Rev. **B44**, 3821 (1991); P. Hawrylak, *ibid.* **B44**, 6262 (1991).
16. G. D. Mahan, Phys. Rev. **153**, 882 (1967).
17. S. Schmitt-Rink, C. Ell and H. Haug, Phys. Rev. **B33**, 1183 (1986).
18. S. K. Chun, D. S. Pan, and K. L. Wang, Phys. Rev. **B47**, 15638 (1993).
19. E. Corbin, K.B. Wong and M. Jaros, Phys. Rev. **B50**, 2339 (1994).

INTRODUCTION OF RADIATIVE ISOELECTRONIC COMPLEXES DURING MOLECULAR BEAM EPITAXIAL GROWTH OF Si AND Si_{1-x}Ge_x/Si SUPERLATTICES

KAREN L. MOORE*, OLIVER KING**, DENNIS G. HALL*, JOZE BEVK*** AND
MATTHIAS FURTSCH***

*University of Rochester, The Institute of Optics, Rochester, NY 14627

**University of Maryland, Laboratory for Physical Sciences, College Park, MD 20740

***AT&T Bell Laboratories, Murray Hill, NJ 07974

ABSTRACT

Radiative isoelectronic impurity complexes consisting of pairs of Be atoms that bind excitons can be formed in both Si and SiGe/Si superlattices during growth by molecular beam epitaxy. We describe the conditions under which these radiative complexes can be formed and show that they can be localized in the alloy layers of a superlattice. Experimental results from samples with grown-in Be are compared to previous results from ion implanted samples. Superlattices of varying well widths are examined and a narrowing of the no-phonon linewidth is observed.

INTRODUCTION

The introduction of radiative impurity complexes into indirect-band-gap semiconductors is of fundamental and practical importance. Due to the k -conservation rule, efficient, band-to-band, radiative transitions are forbidden in indirect-band-gap semiconductors. For indirect materials to play a role in semiconductor light source technology, alternative radiative mechanisms must be explored. To date, visible-wavelength gallium phosphide (GaP) light-emitting diodes use the mechanism of impurity-related optical emission to advantage. In that case, nitrogen,¹ zinc-oxygen,² and cadmium-oxygen³ impurities form isoelectronic (isovalent) complexes that bind excitons. Those isoelectronic bound excitons (IBEs) radiatively decay to emit light.

IBE emission from various impurity complexes in crystalline silicon (Si) has been reported for sample temperatures $T \leq 200\text{K}$.⁴⁻⁹ The Be isoelectronic impurity can, in many ways, be considered the prototype IBE system. Originally discovered in the early 1970s,¹⁰ the neutral complex is known to consist of a pair of Be atoms that act together to trap first an electron, and then a hole via the electron's Coulomb potential, to form a localized bound exciton system.¹¹ An intense no-phonon line near the wavelength $\lambda = 1.149\text{ }\mu\text{m}$ ($E = 1.08\text{ eV}$) for temperatures $T < 80\text{K}$ is observed as the exciton radiates. Thewalt *et al.* estimate the oscillator strength to be approximately 1.5×10^{-3} .¹² The exciton can be optically or electrically excited; external efficiencies as high as 1% have been reported for the former.¹³ By investigating the properties of the Be isoelectronic complex in indirect-band-gap semiconductors, our understanding of the

general behavior to be expected of such complexes is furthered.

We recently demonstrated that the same impurity complex can be formed in Si-rich, silicon-germanium ($\text{Si}_{1-x}\text{Ge}_x$) alloys¹⁴ and SiGe/Si superlattices.¹⁵ In the alloys, the no-phonon emission wavelength follows a linear trend with the germanium fraction x , over the composition range $0 \leq x \leq 0.2$. In those experiments, the samples were grown by molecular beam epitaxy (MBE) and Be was introduced via post growth ion implantation. With the introduction of impurities during MBE growth, it is possible that implant damage may be avoided and greater flexibility is afforded in placing the impurities at a desired location. We demonstrate here that under proper conditions, radiative beryllium IBE complexes can be formed via codeposition during MBE growth both in Si and in the alloy layers in a SiGe/Si superlattice. The optical characteristics of the resulting samples are compared with those obtained from implanted samples.

EXPERIMENTAL RESULTS AND DISCUSSION

The Si and $\text{Si}_{1-x}\text{Ge}_x$ layers studied in this investigation were grown by MBE. Details on the growth technique and the sample quality and characteristics can be found elsewhere.^{14,16} The crystal quality of the samples is shown to be excellent through Rutherford backscattering measurements. Be was introduced into one sample through standard ion implantation. For the remaining samples, Be was introduced during growth by using a shuttered boron nitride effusion cell containing approximately 1g of solid 99.999%-pure Be. Several Be outgassing procedures and Be cell temperatures T_{Be} were used before finding a set of Be deposition parameters that produced acceptably repeatable results. Details about the dependence of the Be concentration on the Be-cell temperature are published elsewhere.¹⁷

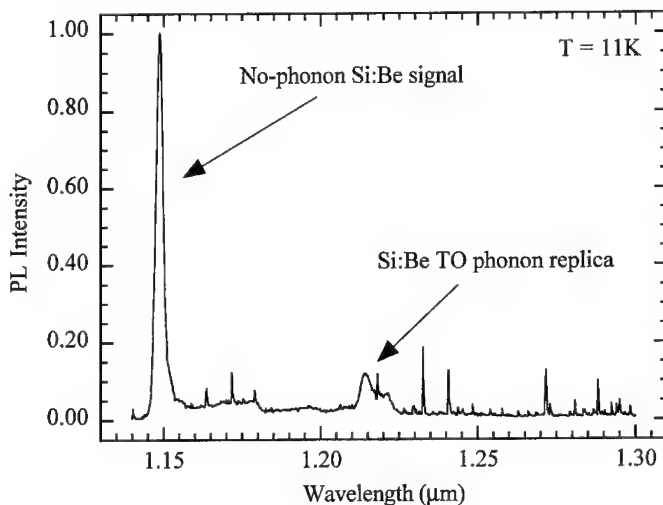


FIG. 1. PL spectrum of a Be-doped Si layer grown by MBE.

Photoluminescence (PL) measurements were performed on samples mounted in a closed-cycle helium cryostat (Air Products) in which the sample temperatures could be controlled from $T=10$ to 300K . The spectra presented in this paper were all measured for a sample temperature $T\sim 11\text{K}$. The samples were optically excited using the 676 nm line from a Coherent Kr^+ ion laser. Luminescence collected from each sample was chopped at approximately 100 Hz , dispersed using a McPherson grating monochromator, and detected using a liquid-nitrogen-cooled Northcoast Ge photodetector and a Stanford Research lock-in amplifier.

A typical PL spectrum for a 50-nm -thick layer of Be-doped Si, grown onto an undoped Si substrate, is pictured in Fig. 1. During growth, the Be-cell temperature was approximately $T_{\text{Be}}=775^\circ\text{C}$, as measured by an *in situ* thermocouple in contact with the outside wall of the effusion cell; the growth temperature was $T\sim 500^\circ\text{C}$. This measured spectrum, showing a strong no-phonon line near wavelength $\lambda=1.149\text{ }\mu\text{m}$ accompanied by a phonon replica, is essentially identical to that obtained when a similar Si substrate is ion implanted with Be. Typically, to activate strong luminescence from Si ion implanted with Be, a post-annealing process (10 min. at 590°C) is necessary. However, no post-growth annealing was required to observe the luminescence from the samples with grown-in Be, indicating that Be pairs are formed during Si growth. This formative process is of critical importance for obtaining luminescence. SIMS (secondary ion mass spectrometry) analysis performed on the sample of Fig. 1 revealed a Be concentration of $\sim 7\times 10^{17}\text{ cm}^{-3}$ in the MBE-grown layer.

Radiative Be complexes have also been incorporated into SiGe/Si superlattices. To allow for comparisons with the results of our previous work,^{15,17} several superlattices (SLs) were grown and examined. The first structure, SL50I, is the same structure as reported in Ref. 15: ten periods of $\text{Si}_{0.92}\text{Ge}_{0.08}/\text{Si}$ ($50/100\text{ }\text{\AA}$ layer thicknesses), ion implanted with $2\times 10^{13}\text{ Be ions/cm}^2$ at an energy of 40 keV . The next superlattice, denoted SL50, is composed of ten periods, with each period made up of a $50\text{-}\text{\AA}$ -thick layer of $\text{Si}_{0.92}\text{Ge}_{0.08}$ and a $100\text{-}\text{\AA}$ -thick layer of Si. The alloy layers were grown at a temperature $T\sim 450^\circ\text{C}$, and the shutter in front of the Be effusion cell was opened only during growth of the central 17\AA of each alloy layer, during which the Be-cell temperature was held at $T_{\text{Be}}\sim 800^\circ\text{C}$. The first 20\AA of each Si layer was

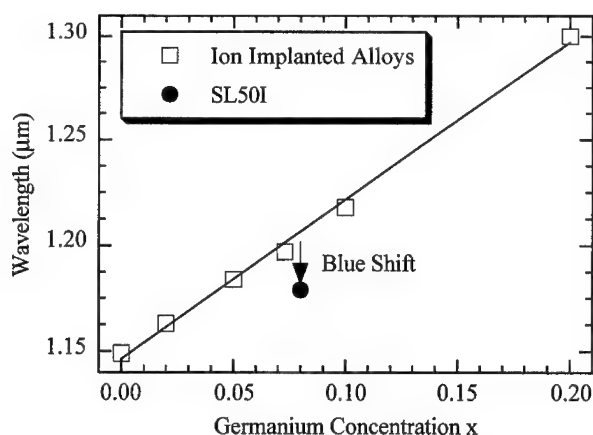


FIG. 2. Dependence of Be-related no-phonon emission wavelength on germanium concentration in ion implanted alloy (open squares) and SL (filled-in circle) samples.

grown at a temperature $T \sim 300^\circ\text{C}$, after which the growth temperature was raised to $T \sim 550^\circ\text{C}$ to complete the Si layer growth. Finally, the superlattice denoted SL20 is comprised of twenty periods, with each period consisting of a 20-Å-thick $\text{Si}_{0.92}\text{Ge}_{0.08}$ layer and a 100-Å-thick Si layer. The growth temperatures were similar to those of SL50, however, the shutter in front of the Be effusion cell was opened only during growth of the central 11 Å of each alloy layer. Similar to the Si samples previously described, the superlattices with grown-in Be exhibited the Be-related emission without post-growth annealing.

Figure 2 is a comparison of the peak emission wavelength of the Be complex for bulk alloys and SL50I. One can note that the position of the Be IBE no-phonon peak for the ion implanted SL is blue shifted from that of the bulk alloy. As discussed in Ref. 15, the peak wavelength blue shift for SL50I can be understood by noting that implantation produces Be distributed throughout the alloy and Si layers. Theoretical modeling reveals that the binding energy of the exciton varies with the position in the SL of the Be pair to which the exciton is bound. Since the Be distribution is spread out in the SL, the no-phonon line is shifted and broadened from that of the alloy. (Actual spectra are pictured in Fig. 1 of Ref. 15.)

The introduction of Be impurities during MBE growth provides increased control over the location of the Be compared to ion implantation. Our attempts to control the position of Be atoms by opening the shutter in front of the Be cell only during growth of the central portions of the alloy layers were successful. The upper curves in Fig. 3 show that the Be-related no-phonon emission line for SL50 and an ion implanted 8% bulk alloy are located at the same wavelength. The absence of a blue shift, as observed in SL50, strongly argues that the Be is reasonably well confined in the alloy layers of the SL. Additionally, the prediction made in Ref. 15 is confirmed by the fact that the no-phonon line from the grown-in SL (SL50) occurs at the same wavelength as that from the thick alloy. However, the linewidth has not decreased to that of the implanted

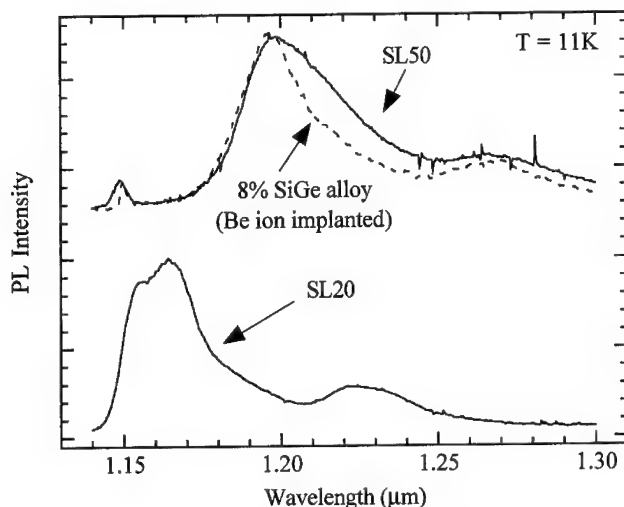


FIG. 3. Top: PL spectra from a $\text{Si}_{0.92}\text{Ge}_{0.08}/\text{Si}$ SL (500/100 Å layer thicknesses) Be-doped during MBE growth (solid line), and from a thick Be ion implanted (~ 5000 Å) $\text{Si}_{0.92}\text{Ge}_{0.08}$ alloy film (dashed line). Bottom: PL spectrum from a $\text{Si}_{0.92}\text{Ge}_{0.08}/\text{Si}$ SL (20/100 Å layer thicknesses) Be-doped during MBE growth.

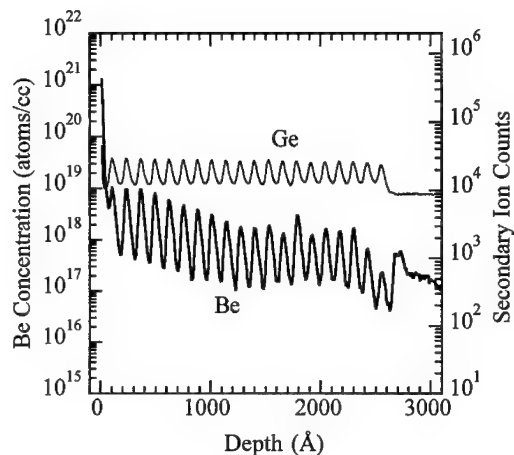


FIG. 4. SIMS measurement of the Be concentration for the $\text{Si}_{0.92}\text{Ge}_{0.08}/\text{Si}$ (20/100 Å layer thicknesses) SL doped during MBE growth (lower solid curve in Fig. 3). $T_{\text{Be}} \sim 800^\circ\text{C}$. Ge line indicates the location of the alloy layers.

alloy which implies that other factors are at work in the grown-in samples.

The lower curve in Fig. 3 is a PL spectrum from SL20, $\text{Si}_{0.92}\text{Ge}_{0.08}$ (20Å/100Å layer thicknesses). Again, the photoluminescence was observed without post-growth annealing, although the peak signal strength was decreased by a factor of ~ 2 from that of SL50. Several details of this spectrum are of interest. First, there exists an apparent blue shift of the entire spectrum, relative to that of SL50. A narrowing of the no-phonon line is also seen. Both of these effects suggest possible quantum confinement of the excitons in the alloy layers. The degree to which quantum confinement contributes to these experimental observations is currently under investigation.

SIMS analysis of the superlattices provides additional evidence that the Be is localized in the alloy layers. Figure 4 shows the results of a SIMS measurement performed on SL20 (Fig. 3 lower curve). The rapid increase of the Be concentration near the sample surface is caused by the expected surface layer of Be (or beryllium oxide). This effect can be reduced by etching the samples in either hydrofluoric (HF) acid or a combination of hydrochloric and HF acids prior to SIMS analysis. The concentrations labeled on the left vertical axis of the SIMS plot apply only to the Be curve. The curve for the Ge data is present only to indicate the locations of the alloy layers in the SL. A couple points should be highlighted to aid in the interpretation of Fig. 4. First, the Be concentration varies periodically as a function of depth and tracks the Ge concentration, indicating that the Be atoms are more highly concentrated in the alloy layers than in the Si barrier layers. Second, given that we attempted to introduce Be only into the central region of each alloy layer, and that the alloy layers are only 20Å thick, due to the limited depth resolution of the SIMS technique some degree of averaging is produced in Fig. 4. We estimate the peak Be concentrations to exceed $1 \times 10^{18} \text{ cm}^{-3}$, in agreement with the measured integrated Be dose per SiGe layer of $\sim 8.5 \times 10^{11} \text{ cm}^{-2}$.

CONCLUDING REMARKS

Radiative Be isoelectronic complexes are incorporated during MBE growth of Si and SiGe/Si superlattices. The fact that the no-phonon Be IBE emission is present, with no further processing, is clear evidence that the required Be pairs are being formed during the growth process. Be-cell temperatures in the range of 700-800 °C produce Be concentrations on the order of 10^{17} - 10^{18} cm⁻³. The absence of a blue shift in the PL spectrum for the grown-in superlattice (SL50), compared to an identical ion implanted sample, confirms a previous prediction. Both the no-phonon line narrowing and the blue shifted spectrum for SL20 suggest possible quantum confinement of the exciton.

The authors are grateful to Henry Luftman for the SIMS measurements. The authors acknowledge the support of the U.S. Air Force Office of Scientific Research.

REFERENCES

1. D. G. Thomas, J. J. Hopfield, and C. J. Frosch, Phys. Rev. Lett. **15**, 857 (1965).
2. T. N. Morgan, B. Welber, and R. N. Bhargava, Phys. Rev. **166**, 751 (1968).
3. C. H. Henry, P. J. Dean, and J. D. Cuthbert, Phys. Rev. **166**, 754 (1968).
4. J. Weber, W. Schmidt, and R. Sauer, Phys. Rev. **B21**, 2401 (1980).
5. G. Mitchard, S. A. Lyon, K. R. Elliot, and T. C. McGill, Solid State Commun. **29**, 425 (1979).
6. P. L. Bradfield, T. G. Brown, and D. G. Hall, Phys. Rev. **B38**, 3533 (1988).
7. M. O. Henry, D. J. Becket, A. G. Steele, and M. L. W. Thewalt, Solid State Commun. **66**, 689 (1988).
8. T. G. Brown and D. G. Hall, Appl. Phys. Lett. **49**, 245 (1986); P. L. Bradfield, T. G. Brown, and D. G. Hall, Appl. Phys. Lett. **55**, 100 (1989).
9. R. A. Modavis and D. G. Hall, J. Appl. Phys. **67**, 545 (1990).
10. R. K. Crouch, J. B. Robertson, and T. E. Gilmer, Jr., Phys. Rev. **B5**, 3111 (1972).
11. M. O. Henry, E. C. Lightowers, N. Kiloran, D. J. Dunstan, and B. C. Cavenett, J. Phys. **C14**, L255 (1981).
12. M. L. W. Thewalt, S. P. Watkins, U. O. Ziemelis, E. C. Lightowers, and M. O. Henry, Solid State Commun. **44**, 573 (1982).
13. T. G. Brown, P. L. Bradfield, D. G. Hall, and R. A. Soref, Opt. Lett. **12**, 753 (1987).
14. R. A. Modavis, D. G. Hall, J. Bevk, B. S. Freer, L. C. Feldman, and B. E. Weir, Appl. Phys. Lett. **57**, 954 (1990).
15. R. A. Modavis, D. G. Hall, J. Bevk, and B. S. Freer, Appl. Phys. Lett. **59**, 1230 (1991).
16. J. Bevk, J. P. Mannaerts, A. Ourmazd, L. C. Feldman, and B. A. Davidson, Appl. Phys. Lett. **49**, 286 (1986).
17. K. L. Moore, O. King, D. G. Hall, J. Bevk, and M. Furtch, Appl. Phys. Lett. **65**, 2705 (1994).

A SYSTEMATIC STUDY OF THE STRUCTURAL AND LUMINESCENCE PROPERTIES OF P-TYPE POROUS SILICON

H. YOON AND M. S. GOORSKY

University of California, Los Angeles, Department of Materials Science and Engineering,
Los Angeles, CA 90095-1595

ABSTRACT

The structural and luminescence properties of (001) p-type porous silicon samples ($\rho \sim 0.1\text{--}0.2 \Omega\cdot\text{cm}$) fabricated electrochemically under various conditions were investigated using high resolution double and triple axis diffraction and photoluminescence spectroscopy. We show the sensitivity of the structure of the porous silicon to the current density in the range of 10-50 mA/cm², HF acid concentration in the range of 15% - 30%, and the evolution of the structure with time. We have found a systematic dependence of the amount of strain in the porous silicon layer (PSL) on the current density. The effect of the HF concentration is such that at 25% and 30% HF, PSLs are formed which are crystalline and strained, but at a lower HF concentration (15%), strained layers are not formed. The perpendicular strain in the layer increases linearly with storage time but the in-plane lattice constant of the porous silicon remains matched to the substrate. Further, we utilized x-ray reciprocal space maps to observe that, with storage time, there is an increase in the diffuse scattering from the PSL due to an increase in the range of tilts in the layer. Room temperature photoluminescence emission was observed for all 15% and 25% HF samples, but not for all 30% HF samples. Higher peak luminescence energy was obtained with lower HF concentration. Finally, we note the relationship between the strain in the PSL and the luminescence properties.

INTRODUCTION

Since the first report of visible light emission from porous silicon (PS) was made in 1990 by Canham¹, much of the research has focused on the optical and electrical properties of this material. The possibility of utilizing silicon in optoelectronic applications has a great technological importance, and this has driven researchers to gain a fundamental understanding of the light emitting properties of PS. Among the several proposed interpretations of the light emission from PS, they are mainly based on the quantum size effect,^{1,2} or by the surface effect.³ However, in the past few years, little attention has been given to the relationship between the structural and luminescence properties of PS. In particular, to our knowledge, no study has shown how the strain in the porous silicon layer (PSL) influences the luminescence behavior.

The PS structure is greatly dependent on the fabrication parameters such as hydrofluoric (HF) acid concentration and current density, as well as the resistivity of the starting substrate.^{4,5} Young et al.⁶ investigated the lattice expansion of p-type PS of various resistivities to the HF concentration and current density and found no systematic dependence of strain on these parameters. They claimed that the resistivity of the substrate mainly determine the amount of strain in the PSLs. In other studies, Takemoto et al.⁷ found that higher current density resulted in larger strain in p+ PSLs; Sugiyama et al.⁸ showed that the PS lattice parameter expands slightly with storage time while the crystalline quality degrades (degradation was deduced from their

double crystal x-ray study). In this study, we investigate porous silicon produced on moderately doped p-type substrates.

In contrast to Young et al.,⁶ we found a systematic dependence of the amount of strain in p-type PS on the current density and a noticeable dependence on the HF concentration. We also investigated the structural change of PS over storage times of several months and find that the amount of strain increases linearly with time and that the intensity of the x-ray scattering from the PSLs decreases with time. Further, by using asymmetric x-ray reflections, the layers are observed to be fully coherent with the substrate. Triple axis x-ray technique has been used to determine the origin of the diffuse scattering originating from the PSL. Photoluminescence (PL) measurements on these samples show that the HF concentration is the fabrication parameter which has the greatest influence on the material's luminescence properties. A slight blue-shift of the peak intensity is observed with lower HF concentration. Typical peak luminescence energy at room temperature occurs ~ 1.7 eV with a FWHM of about 0.35 eV.

EXPERIMENTAL PROCEDURE

Four inch diameter (001) oriented p-type (boron doped) silicon substrates with a resistivity of 0.1-0.2 $\Omega\cdot\text{cm}$ were used. Standard RCA cleaning was done prior to etching.⁹ Aluminum was evaporated on the back side of the wafers to allow uniform current distribution. Samples were prepared in a Teflon cell which exposed an area of about 50 cm^2 . A gold-plated cylindrical grid which has the same diameter as the exposed substrate surface was used as the cathode, which allowed uniform samples to be fabricated. Current densities of 10 to 50 mA/cm^2 , HF (49%)-Ethanol electrolyte concentrations of 15% (HF:Ethanol::1:3.3 by volume), 25% (1:1.4), and 30% (1:0.92), and etching times of 5-15 minutes were used. Samples were rinsed in deionized water for ~ 30 seconds after the etching process. All samples were stored in closed containers, removed from light, and were exposed to ambient conditions (air, room lighting) only during the experimental measurements. Ten samples using the following parameters were fabricated and investigated in this study.

Table I. Fabrication parameters for PS samples used in this study.

15% HF	25% HF	30% HF
#1: 10 mA/cm^2 , 10 min.	#4: 10 mA/cm^2 , 10 min.	#7: 10 mA/cm^2 , 15 min.
#2: 30 mA/cm^2 , 5 min.	#5: 30 mA/cm^2 , 10 min.	#8: 20 mA/cm^2 , 15 min.
#3: 50 mA/cm^2 , 10 min.	#6: 50 mA/cm^2 , 10 min.	#9: 30 mA/cm^2 , 15 min.
		#10: 50 mA/cm^2 , 15 min.

A Bede D³ high resolution x-ray diffractometer was used for the structural analysis of these samples. This system uses a (111) silicon channel cut collimator and a (111) silicon monochromator in a (+,-,-) setting to condition the Cu $K\alpha_1$ beam. This beam conditioning axis (axis 1) and the sample (axis 2) constitute the double axis x-ray setup. Using this technique, the perpendicular strain $(\Delta a/a)_\perp$ was measured using the (004) reflection while the relaxation, or the parallel strain $(\Delta a/a)_\parallel$, was measured using asymmetric reflections. Triple axis x-ray diffraction technique employs a third axis which uses a (111) silicon channel cut analyzer crystal in a (+,-,+,) configuration. Using this technique, x-ray reciprocal space maps were made which show the amount of scattering due to lattice parameter variation and that due to mosaic spread.

A Spectra-Physics Model 2020 Argon ion laser was used for room temperature photoluminescence measurements. All measurements were taken using the 514.5 nm line at 0.3 W. The detection system included a frequency chopper, a Stanford Research Systems SR530 lock-in amplifier, a Jobin Yvon HR640 monochromator (0.64 m, 1200 gr/mm), and an S-1 type photomultiplier tube.

RESULTS AND DISCUSSION

Figures 1 and 2 show the strain evolution with storage time (samples stored in closed containers) for samples fabricated using 25% HF and 30% HF, respectively. The strain is

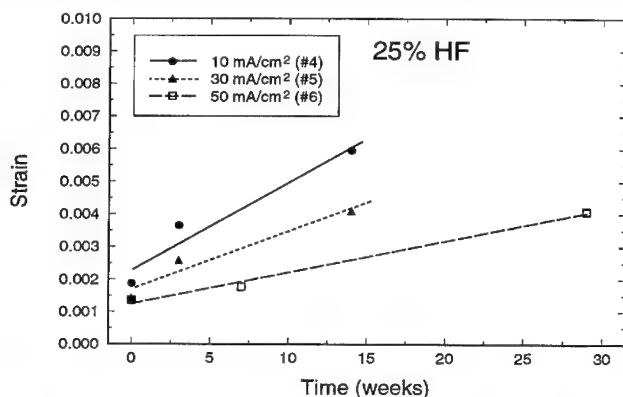


Figure 1. Strain evolution with storage time of porous silicon for 25% HF samples.

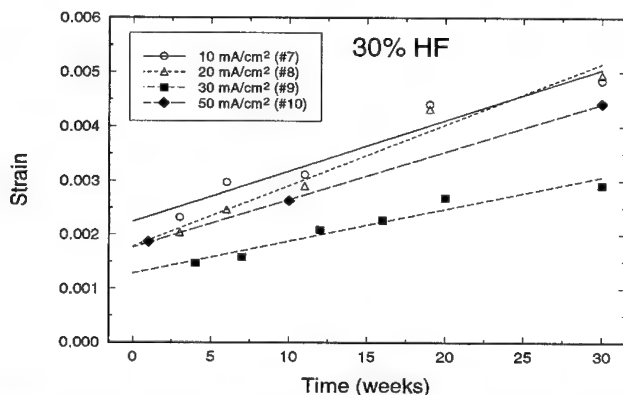


Figure 2. Strain evolution with storage time of porous silicon for 30% HF samples.

calculated from the angular separation of the substrate and the layer peaks in the (004) x-ray rocking curves using the formula $(\Delta a/a)_\perp = -\Delta\theta \cot\theta_B$ where $\Delta\theta$ is the angular separation and θ_B is the Bragg angle. Samples fabricated using 25% HF and 30% HF are initially strained (perpendicular lattice expansion) by approximately $1-2 \times 10^{-3}$, which is comparable to values

obtained by other groups.^{6,8,10} Samples fabricated using 15% HF, which have the highest porosity, did not form strained layers. Young et al.⁶ also did not observe diffracted peaks from PSLs of high porosity. In our study, the strained layers are coherent with the substrates, as determined by using asymmetric reflections.

The amount of strain has been found to increase linearly with time as shown in Figure 1 (25% HF) and Figure 2 (30% HF). In addition, the rate at which the strain increases varies for different samples. For the 25% HF samples, the amount of strain approximately doubles every 4, 6, and 10 weeks, for the 10, 30, and 50 mA/cm² samples, respectively. For the 30% HF samples, the amount of strain doubles every 10-11 weeks for the 10, 20, and 30 mA/cm² samples, and every ~17 weeks for the 50 mA/cm² sample. So clearly, the strain rate is dependent on both the current density and the HF concentration. The dependence we observe is such that lower current density and lower HF concentration produce higher strain rates. For example, the 30% HF samples are more "stable" in that their structure changes more slowly with time compared to the 25% HF samples.

An interesting behavior is observed in the relationship between the amount of strain and the current density. In other studies, the amount of strain has been found to increase with the current density⁷ and with porosity¹¹; however, the substrates used in these studies were p+ silicon. Our results do not show this behavior. As seen in Figure 1, for the 25% HF samples, higher current density results in less strain in the layers. For the 30% HF samples (Figure 2), the same trend is observed up to a current density of 30 mA/cm², but reverses at 50 mA/cm². These results are consistent with the work done by Herino et al.⁴ in which porous silicon produced on lightly doped p-type substrates exhibited a "U-shaped" behavior in the porosity vs. current density relationship. They observed the following values of porosity at various current densities: ~64% at 10 mA/cm², down to ~59% at 20 mA/cm², and back up to ~61% at 50 mA/cm². From our results (Figure 2), it is seen that at a current density of 10 mA/cm², the amount of strain is relatively high, then decreases for 20 mA/cm², and further decreases to our "minimum" at 30 mA/cm²; then at 50 mA/cm², we observe an increase in the amount of strain. By correlating these results, we are able to explain this "anomalous" behavior and suggest that the amount of strain in the PSLs of our samples is indeed dependent on the porosity of the PS.

Using the triple axis x-ray technique, reciprocal space maps (RSMs) were made to observe the diffuse scattering from the porous layers. Figures 3a and 3b are RSMs of sample #9

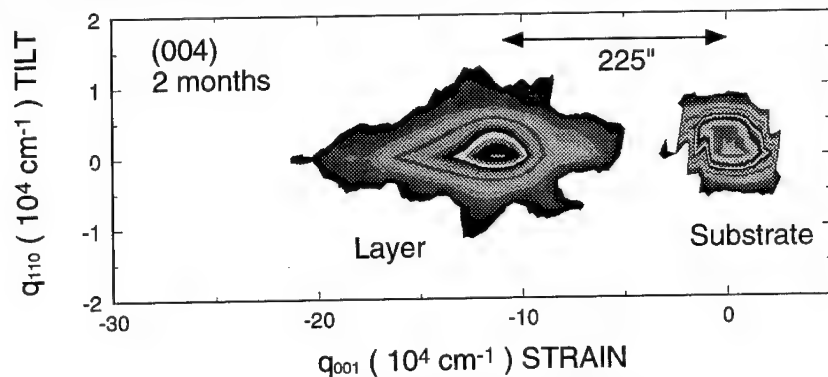


Figure 3a. (004) x-ray reciprocal space map of sample #9 two months after fabrication. Isointensity contours are plotted, represented by the different levels of grey shading.

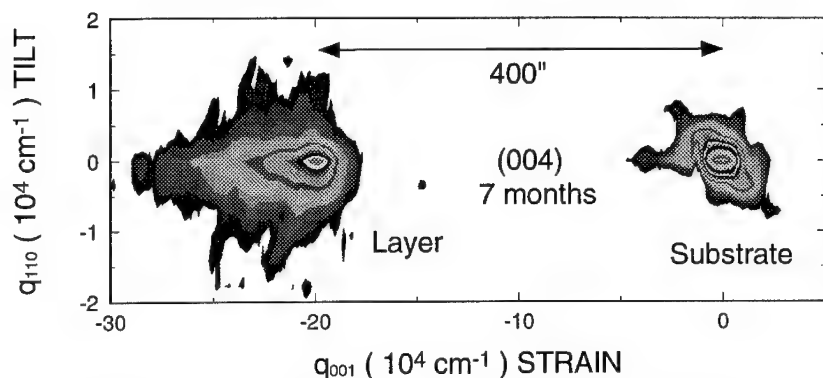


Figure 3b. (004) x-ray reciprocal space map of sample #9 five months after fabrication. Isointensity contours are plotted, represented by the different levels of grey shading.

for 2 and 7 months after fabrication, respectively. The crystalline quality of the PSL has slightly degraded within this time period, as seen by the wider spread in the q_{110} direction (tilt) for the scan taken at 7 months. With regards to the strain (lattice constant) variation, we observe the following. First, the strain distribution in the layer is more asymmetric at 7 months than at 2 months, indicating that the PS lattice parameter expands non-uniformly with time. Second, the overall strain distribution has decreased at 7 months, shown in Figure 3b by the shorter extension in the strain direction.

Figure 4 shows the room temperature photoluminescence spectra for samples #3, #6, and #9. Generally, there was an increasing trend of PL intensity (visibly observable) and peak energy

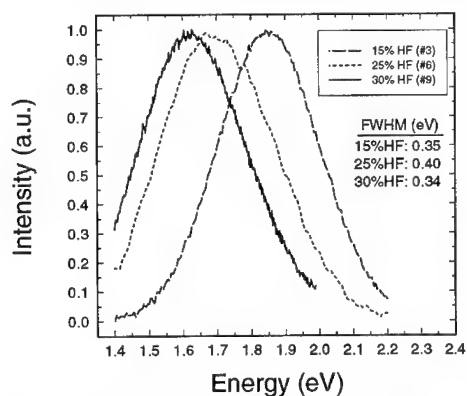


Figure 4. Room temperature photoluminescence spectra of samples #3, #6, and #9.

position with decreasing HF concentration, consistent with other experiments.¹² The peak intensity occurs at 1.85, ~1.7, and ~1.62 eV for the 15%, 25%, and 30% HF samples, respectively. All 15% and 25% HF samples display similar PL emission, but for the 30% HF samples, only the one shown in the figure (30 mA/cm²) and also sample #10 (50 mA/cm²) exhibited measurable PL emission. The 15% HF samples exhibited strong PL emission and it remained stable while no significant peak shift occurred even after 5 months. So far, no significant changes (shape and peak position) in the PL emission spectra have been observed with storage time for any of the samples. There was a slight dependence of the peak position on the

current density only for the 15% HF samples, as higher current density resulted in slightly higher PL energy.

In correlating the PL emission to strain, we have not yet found a distinct and/or systematic relationship between the two, as similarly strained PSLs prepared under different

conditions have different luminescence properties. For example, the initial strain in the 25% and 30% HF samples are similar but stronger PL intensity and higher PL peak energy are obtained from the 25% HF samples. Consequently, there are other factors that influence the luminescence of PS. However, the 15% HF samples, which show no strain, exhibit even stronger PL intensity and higher energy than the 25% HF samples, indicating that strain (either the presence or the absence of it) does indeed influence the PL emission.

CONCLUSION

The structural and luminescence properties of various p-type porous silicon samples were investigated. HRXRD has been used to determine that there is a systematic dependence of strain in the PSL with current density, and that the strain increases with storage time, with the rate depending on the initial structure. X-ray reciprocal space maps were used to show that there is an increase in diffuse scattering from the PSL due to mosaic tilt in the structure. The HF concentration played a key role in both the formation of strained layers and the PL emission. PS structures that exhibit no strained layers were formed using a low HF concentration, but the PL emission was strongest and most stable for these “unstrained” samples. We also obtained different PL properties (intensity and peak energy) for similarly strained PS fabricated using different conditions. A slight blue-shift trend was observed with decreasing HF concentration and also a small blue-shift trend with increasing current density for the 15% HF samples.

ACKNOWLEDGMENTS

This research has been funded by the UC Energy Research Group, Grant #930513.

REFERENCES

1. L.T. Canham, Appl. Phys. Lett. **57**, 1046 (1990).
2. V. Lehmann and U. Gösele, Appl. Phys. Lett. **58**, 856 (1991).
3. Y.H. Xie, W.L. Wilson, F.M. Ross, J.A. Mucha, E.A. Fitzgerald, J.M. Macaulay, and T.D. Harris, J. Appl. Phys. **71**, 2403 (1992).
4. R. Herino, G. Bomchil, K. Barla, C. Bertrand, and J.L. Ginoux, J. Electrochem. Soc. **134**, 1994 (1987).
5. M.I.J. Beale, J.D. Benjamin, M.J. Uren, N.G. Chew, and A.G. Cullis, J. Crystal Growth **73**, 622 (1985).
6. I.M. Young, M.I.J. Beale, and J.D. Benjamin, Appl. Phys. Lett. **46**, 1133-35 (1985).
7. K. Takemoto, H. Sugiyama, and O. Nittono, Extended Abstracts of the 1991 International Conference on Solid State Devices and Materials, Yokohama, 1991, pp.252-54.
8. H. Sugiyama and O. Nittono, ISIJ Int. **29**, 223-28 (1989).
9. W. Kern and D.A. Poutinen, RCA Rev. **31**, 187 (1970).
10. D. Bellet, G. Dolino, M. Ligeon, P. Blanc, and M. Krisch, J. Appl. Phys. **71**, 145-49 (1992).
11. K. Barla, R. Herino, G. Bomchil, J.C. Pfister, and A. Freund, J. Crystal Growth **68**, 727 (1984).
12. D.L. Naylor, S.B. Lee, J.C. Pincinti, and B.E. Bouma in Light Emission from Silicon, edited by S.S. Iyer, R.T. Collins, and L.T. Canham (Mater. Res. Soc. Proc. **60**, Pittsburgh, PA, 1992) pp. 111-116.

SPACE CHARGE LAYERS AT THE POROUS SILICON SURFACE

S.Z. WEISZ,* J. AVALOS,* M. GOMEZ,* A. MANY,** Y. GOLDSTEIN,** AND E. SAVIR**

*Department of Physics, University of Puerto Rico, Rio Piedras, PR 00931

**Racah Institute of Physics, The Hebrew University, Jerusalem 91904, Israel

ABSTRACT

Pulse measurements on the porous-Si/electrolyte system are employed to determine the surface effective area and the surface-state density at various stages of the anodization process used to produce the porous material. Such measurements were combined with studies of the luminescence spectra and scanning tunneling microscopy (STM). Both the effective area and the luminescence intensity are found to increase with anodization time, reaching maximum values for the *same* anodization time (1–2 minutes). In most cases, they decrease monotonically with further anodization. The surface state density, on the other hand, *decreases* with anodization time from the initial value of $\sim 10^{12}$ cm⁻² for the virgin surface, down to $\sim 10^{11}$ cm⁻² at the common anodization time for which both the effective area and the luminescence intensity are peaked. The surface-state density increases upon further anodization, reaching a value of at least 10^{13} cm⁻² after ~ 10 minutes of anodization. Apart from its intensity, the luminescence spectrum is essentially independent of anodization time. The common peak of the spectra is at about 700 nm. The STM measurements reveal a pronounced surface roughness. Preliminary results indicate that for 1 – 2 minute anodization (maximum effective area), the roughness scale is of the order of 1 – 2 nm. After 10-minutes anodization, on the other hand, the roughness microstructure becomes finer (roughness scale of only 0.5 – 0.7 nm). These findings indicate that the various characteristics studied are closely interrelated. Such information may help in understanding the luminescence mechanism, but further work is required in order to interpret more fully the results presented.

INTRODUCTION

Porous silicon,¹⁻⁴ obtained by certain electrochemical etching procedures applied on crystalline Si surfaces, exhibits high luminescence efficiencies in the visible range. Secondary electron microscopy (SEM) and transmission electron microscopy (TEM) show^{3,5} that highly luminescent porous silicon has a coral-like structure consisting of a continuous hierarchy of columns and pores. Typical lengths of the columns are a few tens of nanometers, while their average radius is a few nanometers. It is quite clear now that the *visible* luminescence originates from the band-gap enlargement due to quantum confinement in these structures.⁴ At the same time, the reasons for the high-efficiency luminescence are still under active debate.^{4,6} Quite a few suggestions have been made regarding this issue. Notably, that it is the amorphous⁷ or microcrystalline⁸ nature of the porous Si that is responsible for the phenomenon, or that the formation of silicon compounds such as siloxene (Si₆O₃H₆) or other species of Si-H, Si-O and Si-F bonds are involved in the luminescence.⁹

Perhaps the most fundamental question in the study of porous silicon concerns the mechanism of the luminescence process. One way of gaining further insight into this process is to carry out a variety of measurements on samples of different porosity. To that end we have employed combined studies of the effective surface area of the porous surface, the surface-state density, the luminescence spectrum and the surface morphology. Such studies were carried out at different stages of the anodization process and thus for different morphologies of the porous surface. The effective surface area and the surface state characteristics are determined by pulse measurements¹⁰ on the porous-Si/electrolyte system. This system is particularly suitable since a capacitive contact to the terrain of the porous surface is best achieved by an electrolyte. The luminescence spectra are measured by conventional methods while some features of the morphology are derived from STM scans. We find that there is a fairly close correlation between

the characteristics derived from these measurements. For example, maximum luminescence intensity is associated with maximum effective area and minimum surface-state density. The morphology of the surface at this stage of the anodization is characterized by a surface roughness scale of 1 – 2 nm. Further anodization reduces the luminescence intensity and increases the surface-state density, while the structure of the surface becomes finer (roughness scale of 0.5 – 0.7 nm). It thus appears that the effective area and the surface-state density play an important role in the luminescence process. We believe that the approach used here is promising and that further work along these lines should yield more detailed information on the luminescence process.

EXPERIMENTAL

The starting material was high-grade n-type silicon wafers of resistivity in the range 1 – 5 Ω -cm. An n+ layer was diffused into one of the faces to form an ohmic contact. The wafer was cut into square samples of 0.7x0.7 cm² in area. Each sample was attached to a cylindrical teflon cell via a Kalrez O-ring, the sample constituting the bottom of the cell, with the free surface facing upwards. In order to prepare the porous surface,^{1,4,11} a solution of HF, water and ethanol (1:1:2) was poured into the cell. A platinum electrode was immersed in the solution and a spring contact was attached to the n+ contact. The sample was illuminated (through the transparent solution) by a halogen lamp providing a flux of ~100 mW/cm². The anodization of the Si surface was performed by a current of 13 mA (100 mA/cm²).

The characteristics of the porous-Si/electrolyte interface were studied at different stages of the anodization process, starting from the "virgin" surface and up to an anodization time of 20 minutes. To that end, the anodizing solution was replaced after each anodization stage by an indifferent (non-reactive) electrolyte (an aqueous solution of KCl). The measurement technique applied to the semiconductor/electrolyte (S/E) interface has been described elsewhere,¹⁰ and will be reviewed only briefly here. A short voltage pulse of duration $T = 5 \mu\text{sec}$, applied between the Pt electrode and the sample's n+ contact, is used to charge up the interface region. The voltage drop across these electrodes, measured just after the termination of the pulse ($T + dT$), represents to a very good approximation the change δV_s in barrier height across the semiconductor space-charge layer induced by the applied pulse. If an insulating layer, such as an oxide, is present at the semiconductor surface, the measured voltage drop is $\delta V_s + \delta V_g$, where δV_g is the drop across the insulating layer. Obviously, $\delta V_g = Q_{\text{tot}}/C_g$, where Q_{tot} is the total charge density induced at the surface and C_g is the "geometric" capacitance of the insulating layer (per cm²). Q_{tot} is obtained from the voltage V_c developed across a large series capacitor C , again at the termination of the pulse. Pulses of varying amplitude are applied singly, one per data point taken. In this manner possible damage to the porous surface is minimized.

In general, Q_{tot} is made up of three components:

$$Q_{\text{tot}} = \delta Q_{\text{sc}} + \delta Q_{\text{ss}} + Q_L, \quad (1)$$

where δQ_{sc} is the change in the free space-charge density, δQ_{ss} is the change in surface-state charge density, and Q_L is the charge density that has leaked across the interface due to imperfect blocking of the S/E interface. In order to determine each component of Q_{tot} , the platinum electrode is shorted to ground by an electronic switch at $T + dT$, where dT is very short (0.1 – 0.2 μsec), just sufficient to permit accurate readings of δV_s and V_c right after the termination of the pulse. At this point, charge redistribution between C and the S/E interface begins to take place. In the first stage, the free charge δQ_{sc} and its equal counterpart in C discharge relatively fast through the low resistance of the sample and the electrolyte. The decay constant associated with this process is typically several microseconds. As a result, V_c decays to the value $\delta Q_{\text{ss}}/C$, δQ_{ss} being the charge remaining in C after the fast decay process. Thereafter, V_c decays to zero usually much more slowly, as electrons trapped in the surface states by the charging pulse are thermally re-emitted into the conduction band. The decay time is larger the deeper the surface states are located energetically and the lower the temperature.¹² If charge leakage exists, V_c does not decay to zero but to the level Q_L/C . Subsequently it remains practically constant since the leaked charge has been lost from the interface and the remaining charge Q_L on C cannot be

dissipated. This behavior enables the separate determination of the three components in Eq. (1), all as functions of δV_s . In porous silicon Q_L is insignificant and will not be considered here. In what follows, we shall express these components in terms of electron densities: $\delta N_s = -\delta Q_{sc}/q$ and $\delta N_{ss} = -\delta Q_{ss}/q$, where q is the absolute magnitude of the electronic charge.

In most cases a space-charge layer already exists at the semiconductor surface, before applying any bias. It is characterized by an equilibrium barrier height V_{s0} and an equilibrium surface electron density N_{s0} . If surface states are present, there may also be an equilibrium density N_{ss0} of occupied surface states. V_{s0} and N_{s0} can be determined quite accurately from measurements in the depletion range.¹³ The entire plots of N_s and N_{ss} vs. V_s can then be constructed by using the relations $V_s = V_{s0} + \delta V_s$, $N_s = N_{s0} + \delta N_s$, and $N_{ss} = N_{ss0} + \delta N_{ss}$. So much so in the absence of an insulating layer (such as an oxide) at the semiconductor surface. If such a layer is present, the as-measured barrier height, i. e., the measured voltage drop between the Pt electrode and the n+ contact just after the pulse termination, yields $V_s + V_g$, where V_g is the voltage drop across the insulating layer.

The luminescence of the porous Si was excited by a 10 mW He-Cd laser beam ($\lambda = 442$ nm). The luminescence spectra at different stages of the anodization process were measured by a Controlled Development spectrometer. The surface morphology of the porous sample was checked by both SEM and STM.

RESULTS

Typical results¹⁴ of the free surface-electron density N_s (squares) and the density of occupied surface states N_{ss} (triangles) against the as-measured barrier height $V_s + V_g$ as obtained for an etched virgin silicon surface, are displayed in the semilog plot of Fig. 1. In the depletion range, N_s is negative but, because of the logarithmic scale used, the plot is that of $-N_s$. The dashed curve represents the theoretical dependence of N_s on V_s for an oxide-free surface ($C_g = \infty$, $V_g = 0$), as derived from a solution of Poisson's equation for the value of the electron bulk concentration n_b marked in the figure. It is seen that this curve does not account well for the data in the accumulation range. The best fit, represented by the solid curve, was obtained by assuming the presence of an oxide layer of $C_g = 2 \mu\text{F}/\text{cm}^2$, corresponding to an oxide thickness of ~ 1 nm. (In

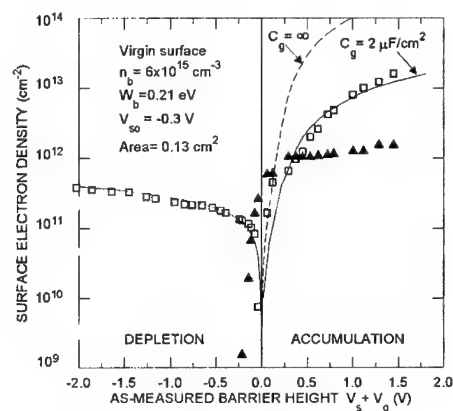


Fig. 1. Free surface electron density N_s (squares) and density of occupied surface states N_{ss} (triangles) vs. the as-measured barrier height $V_s + V_g$ for a virgin Si surface. The dashed and solid curves are theoretical plots of N_s .

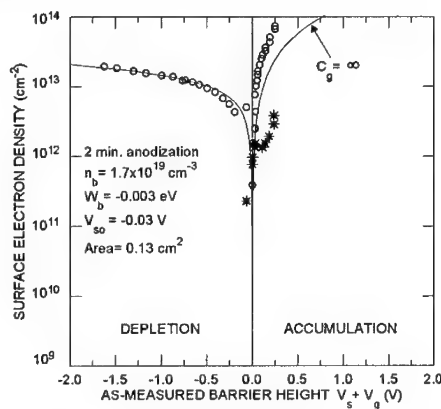


Fig. 2. N_s (circles) and N_{ss} (crosses) vs. $V_s + V_g$ for a porous surface obtained after the virgin sample of Fig. 1 had been anodized for 2 minutes. The surface area is assumed to be unchanged.

the depletion range, the dashed and solid curves very nearly coincide.) The surface-state electron occupancy N_{ss} is seen to rise from a low value up to a saturation level which remains constant over a considerable range. The plateau, which corresponds to completely occupied surface states, yields a total surface-state density of $\sim 10^{12} \text{ cm}^{-2}$. Analysis of these data shows also that the surface states are essentially discrete in energy, located $\sim 0.2 \text{ eV}$ below the conduction-band edge. The energy separation W_b in the bulk between the conduction-band edge and the Fermi level, and the sample area are also marked in the figure.

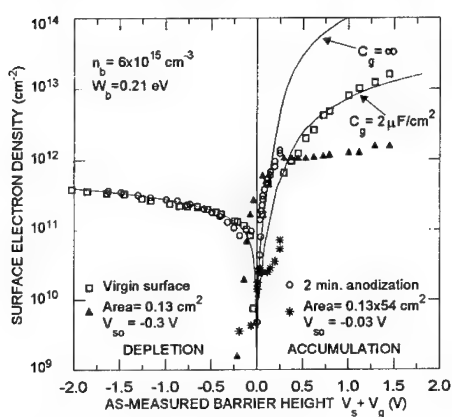


Fig. 3. Comparison of the data of N_s and N_{ss} for the virgin surface of Fig. 1 (squares and triangles) with those for the porous surface of Fig. 2 (circles and crosses). The latter data were scaled down by assuming the surface area to be multiplied by an area factor of 54.

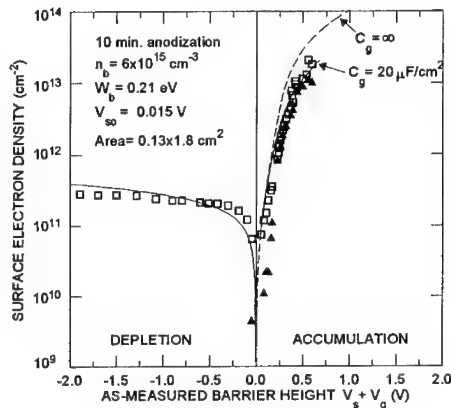


Fig. 4. N_s (squares) and N_{ss} (triangles) vs. $V_s + V_g$ for a porous surface obtained after further anodization (10 minutes altogether).

Similar results of N_s (circles) and N_{ss} (crosses) obtained for a porous surface after the sample of Fig. 1 has been anodized for 2 minutes are shown in Fig. 2. For this anodization time the luminescence intensity was maximal. The solid curve is theoretical, for the n_b value (marked) that yields the best fit to the data in the depletion range. It is seen that this value is more than three orders of magnitude higher than that obtained for the virgin silicon sample. This, in itself, is not impossible since the high n_b value may possibly reflect a higher free-electron density and/or localized bulk-state density in the porous silicon. However, the observation that in the accumulation range the experimental points (circles) lie considerably above the theoretical curve is much more difficult to reconcile. It can be shown that in order to account for this behavior, one must assume the presence of a few times 10^{20} cm^{-3} localized states in the porous region, which is unlikely. It is more reasonable to suppose that it is the effective area of the porous surface that has increased, as is also expected from the high porosity of the surface (see Fig. 7).

Figure 3 compares the data of N_s and N_{ss} vs. $V_s + V_g$ for the virgin surface of Fig. 1 (squares and triangles) and for the porous surface of Fig. 2 (circles and crosses). The latter data were adjusted by assuming the effective surface area to be much larger than the original area. The area factor, 54 in this case, was chosen in order to scale down the as-measured points (Fig. 2) so as to fit best the theoretical curve in the depletion range corresponding to the virgin surface. It is immediately seen that by applying this procedure, the N_s data in the accumulation layer are accounted for very well by the theoretical curve for $C_g = \infty$. This also indicates that the porous surface is essentially oxide free, at least up to the time of the measurement. As to the surface states, their density has decreased by about an order of magnitude compared to their density on the virgin surface.

In Fig. 4, N_s (squares) and N_{ss} (triangles) are plotted against $V_s + V_g$ for a porous surface obtained after 10-minute anodization of the same sample (minimal luminescence intensity). The area factor is now only 1.8. The dashed and solid curves of N_s are theoretical, the former for $C_g = \infty$ and the latter for $C_g = 20 \mu\text{F}/\text{cm}^2$ (oxide thickness of $\sim 1\text{\AA}$). The surface-state occupancy (triangles) reaches $\sim 10^{13} \text{ cm}^{-2}$ but no plateau was attained. This leads to the conclusion that the total surface-state density is at least 10^{13} cm^{-2} .

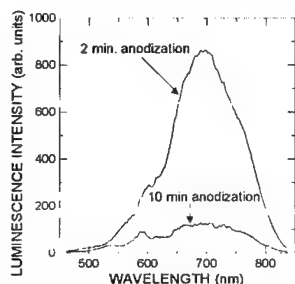
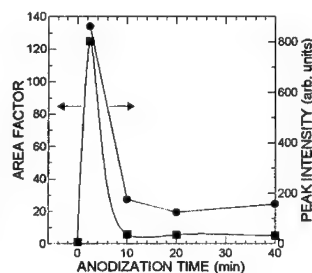


Fig. 5. Luminescence spectra obtained after 2-min. (upper curve) and 10-min. anodization (lower curve).

Fig. 6. Surface area factor (squares) and peak luminescence intensity (circles) as functions of anodization time.



The luminescence spectra of porous silicon obtained after 2-minute anodization (upper curve) and 10-minute anodization (lower curve) are displayed in Fig. 5. These spectra demonstrate the decrease in the luminescence intensity from its maximum value as the anodization time is increased. The shapes of the two spectra are similar, both attaining a peak at $\sim 700 \text{ nm}$.

In Fig. 6 the surface area factor (squares) and peak luminescence intensity (circles) are plotted against the anodization time. The area factors were derived from measurements of the type shown in Figs. 1 – 4, while the luminescence data were taken directly from spectra such as those displayed in Fig. 5. Note that the two curves passing through the respective points vary very similarly. In particular they are peaked at essentially the same anodization time (~ 2 minutes).

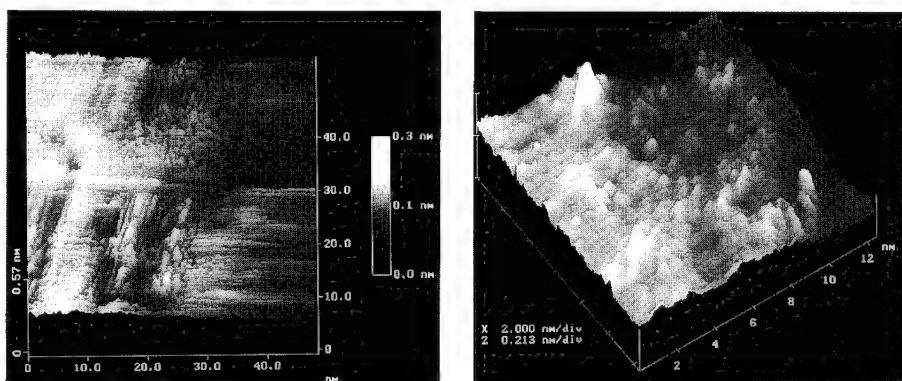


Fig. 7. STM scans of porous Si taken after 1-minute (left) and 9-minute (right) anodization times.

Figure 7 displays STM scans of porous Si, taken after 1-minute anodization (left scan), when the luminescence intensity is high, and after 9-minute anodization time (right scan), when the luminescent intensity is low. The surface roughness scale is in the range of 1 – 2 nm in the former case and 0.5 – 0.7 nm in the latter.

CONCLUSION

There is a close correlation between the effective surface area, the luminescence intensity, the surface-state density, and the microstructure of porous silicon. It should be stressed, however, that the derived effective areas provide only lower limits for the actual areas. For one thing, it is possible that the electrolyte does not penetrate all the pores and hence may not contact the entire area. In addition, the n_H value in the porous region may be lower than that in crystalline Si, which is another reason for the effective areas derived from the space charge measurements to be lower than the actual areas. Nevertheless, the observation that the effective area and the luminescence intensity vary in a very similar manner indicates that the effective area is a meaningful concept and constitutes a good measure for the luminescence efficiency. Moreover, it appears that surface states also play an important role in the luminescence process. Our finding that the luminescence intensity is largest when the surface-state density is lowest and is low when the surface-state density is high suggests that non-radiative transitions via the surface states can partially quench the luminescence.

The observed surface roughness (roughness scale of 1 - 2 nm) at maximum luminescence intensity is compatible with the supposition that the *visible* luminescence is due to quantum size effects. The decreased effective area after prolonged anodization, when the surface microstructure is finer, is not understood at present. One would expect the effective area to increase the finer the microstructure, unless the contact area between the porous surface and the electrolyte is drastically reduced.

We believe that the approach used in this study, in which several characteristics are simultaneously monitored on surfaces of varying porosity, is very promising. We expect that further work along these lines might shed more light on the mechanism and nature of the luminescence process in porous silicon.

ACKNOWLEDGMENT

The authors are indebted to Dr. A. Manivannan for taking the STM pictures. This work was supported by a National Science Foundation EPSCoR grant EHR-9108775 and by the Volkswagen Foundation, Hannover, Germany.

REFERENCES

1. L.T. Canham, Appl. Phys. Lett. **57**, 1046 (1990).
2. I. Amato, Science **252**, 922 (1991).
3. A.G. Cullis and L.T. Canham, Nature **353**, 335 (1991).
4. For the recent developments in this field see: Z.C. Feng and R. Tsu, *Porous Silicon* (World Scientific, Singapore, 1994).
5. F. Koch *et al.*, Proc. 20th Int. Conf. Semiconductor Physics (World Scientific, Singapore, 1992), p. 148.
6. F. Koch, Mat. Res. Soc. Symp. Proc. **298**, 319 (1993).
7. R.P. Vasquez, R.W. Fathauer, T. George, A. Ksendzov and T.L. Lin, Appl. Phys. Lett. **60**, 1004 (1992).
8. J.S. Foresi and T.D. Moustakas, Mat. Res. Soc. Symp. Proc. **256**, 77 (1992).
9. M.S. Brandt, H.D. Fuchs, M. Stutzmann, J. Weber and M. Cardona, Solid State Commun. **81**, 307 (1992).
10. M. Wolovelsky, J. Levy, Y. Goldstein, A. Many, S.Z. Weisz and O. Resto, Surf. Sci. **171**, 442 (1986).
11. S.F. Chung, S.D. Collins and R.L. Smith, Appl. Phys. Lett. **55**, 675 (1989).
12. A. Many, Y. Goldstein, and N.B. Grover, *Semiconductor Surfaces* (North-Holland, Amsterdam, 1971).
13. S.Z. Weisz *et al.*, J. Phys. Chem. Solids **51**, 1067 (1990).
14. A. Many *et al.*, J. Phys.: Condens. Matter **5**, A133 (1993).

REVERSIBLE AND IRREVERSIBLE LIGHT-INDUCED CHANGE OF PHOTOLUMINESCENCE IN POROUS SILICON

SUK-HO CHOI AND BYOUNG-HUN MUN

Department of Physics, College of Natural Sciences, Kyung Hee University, Suwon
449-701, Korea

ABSTRACT

We have investigated the light-induced change of photoluminescence(PL) and its recovery in porous silicon. The exposure of the porous silicon to continuous laser light in vacuum results in the quenching of the PL intensity, which is almost fully recovered by simply keeping the samples in vacuum or in air at room temperature for a few days. When the light exposure is done in air, the PL spectra of the samples with initial PL peak at 800 nm are blue-shifted to the peak position at 740 nm and the samples with the initial PL spectrum peaked at 740 nm shows only a rise of PL intensity without any change of its peak position. Fourier transform infrared(FTIR) studies suggest that the light-induced change of PL in air is a irreversible process and occurs as a result of optically induced replacement of some of the Si-H bonds with O-Si-H bonds or adsorption of oxygen with hydrogen loss.

INTRODUCTION

Visible room-temperature photoluminescence(PL) observed on electro-chemically etched porous silicon(PS)¹ has recently received considerable attention because of its potential as a promising material for Si-based optoelectronic devices. However, the physical mechanism of the strong photoluminescence is not understood yet, although several models have been suggested, namely, quantized effects, siloxene derivatives, chemisorbed molecules on the surface of porous Si, and the formation of amorphous Si. Moreover, many authors have reported on the instability of the PL in PS, especially the change of the PL after long time illumination, whose results are sometimes inconsistent with one another. For example, it has been reported that the PL degradation by exposure to laser light in air is caused by oxygen adsorption² or hydrogen desorption³, but Shih et al.⁴ report on the PL enhancement associated with oxygen molecules attached to the Si surface during laser exposure in air. Whether the light soaking induces the PL degradation or enhancement is also known to depend on the laser power density and the HF acid concentrations for anodization⁵. A correlation between PL spectrum and surface species in PS has been demonstrated by annealing experiments⁶. In contrast to the intensive work for the light-induced change of the PL in PS by many researchers, there have been few reports on its recovery. In this study, we report light-induced changes of PL in air as well as in vacuum and their recovery for PS.

EXPERIMENTAL

The porous Si samples were prepared by anodizing (100) p-type Si wafers with a resistivity of 20 Ω cm in a solution of HF(49 %) : ethanol(99 %) : H₂O = 5 : 13 : 15 at a constant current density. The samples used in this study are classified into 2 groups. The current density and the anodization time are 50 mA/cm² and 5 min for group 1, 30 mA/cm² and 60 min for group 2, respectively. The structure of the electrochemical cell used in this work is similar to that described in the literature⁷. Electrical contact was made on the back side of the wafers by evaporating an aluminum thin film at a substrate temperature of 150 °C in high vacuum. The anodized surface layer in the

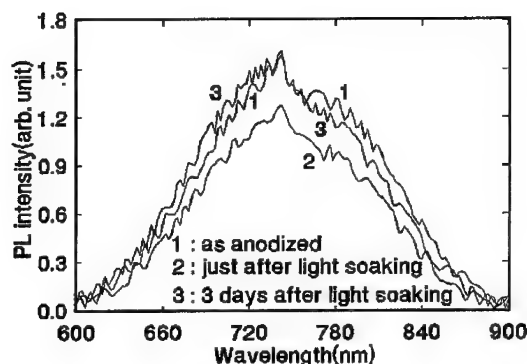


Fig. 1. The change of PL spectra after light soaking in vacuum and its recovery for porous silicon samples of group 1.

sample was observed to be 15 - 25 μm thick through cross sectional view of scanning electron micrograph. The PL system includes an Ar ion laser with an emission wavelength of 488 nm, a 1 m monochromator, a GaAs cathode photomultiplier, and a lock-in amplifier. The spot size of the incident laser was about 2 mm. For the measurements in vacuum the specimen was mounted on the cold finger in the vacuum chamber (base pressure $< 10^{-4}$ torr) of a closed-cycle refrigerator. All measurements in this work were done at 300 K.

RESULTS AND DISCUSSIONS

Fig. 1 shows the effect on PL of light soaking in vacuum and its recovery. The PL spectrum of as-prepared porous silicon peaks at 740 nm, typical of the samples of group 1 prepared as described above. After preparation, the samples were subjected to constant 13 W/cm^2 illumination in vacuum for 1 hour, which resulted in a 10 - 20 % drop in their PL intensity without any change of the peak position. The PL intensity of the photo-degraded samples is almost fully recovered simply by keeping them in air or in vacuum at room temperature for a few days, as seen in Fig. 1. The incident light intensity during the spectral measurements was reduced to as low as 0.5 W/cm^2 for minimizing the light induced change of PL.

Fig. 2 represents the intensity of the peak of the PL spectrum (740 nm) as a function of time for the samples used in Fig. 1. The PL signal was monitored under exposure to constant light intensity of 13 W/cm^2 in vacuum. The PL intensity degrades with illumination time, similar to the results of previous authors^{2,8}. After this 1st illumination, the sample was kept in vacuum for 3 hours without illumination and then, the PL intensity was remeasured as a function of time under same conditions as before. The PL intensity is almost fully recovered to the maximum value, but it decays with illumination time faster than the 1st PL degradation. The slower decay form of the PL degradation was repeated after the photo-degraded samples were kept at room temperature in air or in vacuum for a few days. These results indicate that the PL degradation in vacuum consists of slow and fast processes, both of which are easily recovered at room temperature.

When the light exposure is done in air, the PL spectra of the samples of group 2

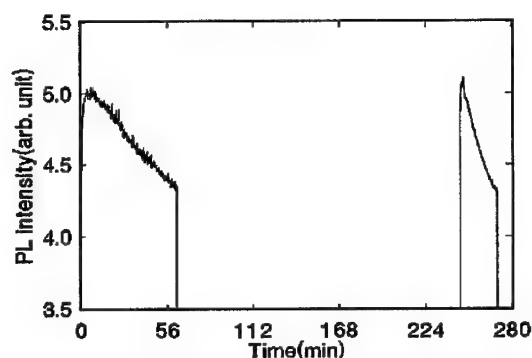


Fig. 2. Intensity of the peak of the PL spectrum (740 nm) as a function of time in vacuum under continuous laser light of 13 W/cm^2 for the samples of group 1.

with initial PL peak at 800 nm are blue-shifted to the peak position at 740 nm, as seen in Fig. 3. The samples of group 1 with the initial PL spectrum peaked at 740 nm shows only a rise of PL intensity without any change of its peak position after illumination in air. The light-induced change of PL in air was not recovered even if the samples were annealed in vacuum at 160°C for 1 hour. Fig. 3 shows an enhancement of the PL intensity over the entire range of wavelength by that annealing.

Fig. 4 shows plots of the PL intensity as a function of time at 700 and 800 nm under same conditions of light soaking in air as used above (13 W/cm^2 , 1 hour). The PL intensity decreased abruptly during first a few minutes and then, gradually increased with time. The 1 hour light-exposure caused a strong increase in the PL intensity at 700 nm, but a small decrease in the PL intensity at 800 nm, which is

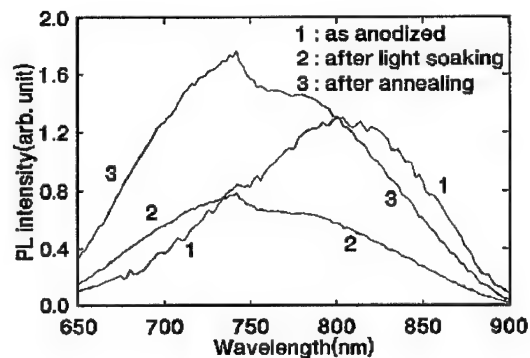


Fig. 3. The change of PL spectra after light soaking in air and annealing in vacuum for porous silicon samples of group 2.

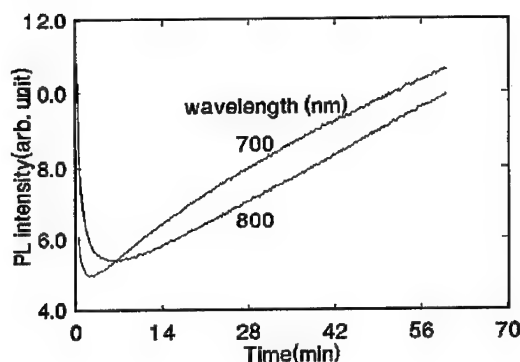


Fig. 4. The PL intensity at 700 and 800 nm as a function of time in air under continuous laser light of 13 W/cm^2 for the samples of group 2.

consistent with the blueshift of the PL spectrum in Fig. 3.

The photoirradiation effect was examined through FTIR measurements. Just after anodization, clear absorption peaks of the Si-H mode without background oxygen at 631 cm^{-1} , the $\text{O}_3\text{-Si-H}$ mode at 879 cm^{-1} , Si-H₂ scissors mode at 914 cm^{-1} , and the Si-O-Si asymmetric stretching mode at 1065 cm^{-1} were observed in the samples of group 2, as seen in Fig. 5. In the range of wave number above 2000 cm^{-1} , Si-H₂ mode at 2110 cm^{-1} and O-Si-H mode at 2258 cm^{-1} were also observed. For investigating the light-induced effect with the FTIR measurements, a wide area of the sample surface should be irradiated uniformly. Therefore, the laser light was set to go through a beam expander before reaching the sample surface.

After light soaking in air, the intensity of the hydride modes at 631 cm^{-1} and 914 cm^{-1} decreased, but the 879 cm^{-1} peak corresponding to $\text{O}_3\text{-Si-H}$ mode increased remarkably, which shows the well-known binding phenomena of Si-H and Si-H₂ with the O ion in the PS layer. The Si-O-Si mode at 1065 cm^{-1} also showed a small increase after illumination. The FTIR measurements for the samples of group 1 also shows similar behaviors except that Si-H₂ peak at 914 cm^{-1} was too small initially for detection. These results suggest that the irreversible change of PL occurs as a result of optically induced replacement of some of the Si-H and Si-H₂ bonds with $\text{O}_3\text{-Si-H}$ or adsorption of oxygen with hydrogen loss. Annealing the irradiated samples at 160°C in vacuum gave a reduction only in the H-related peaks at 631 cm^{-1} and 914 cm^{-1} with almost no change in the O-related peaks at 879 cm^{-1} and 1065 cm^{-1} . This indicates that even the annealing cannot recover the light-induced change of PL in air, instead it gives a rise in the PL intensity which seems to be caused by the reduction of some of the Si-H and Si-H₂ bonds. The FTIR peaks above 2000 cm^{-1} remains almost constant by light soaking or annealing.

There are many reports about the light-induced change of PL intensity and its peak wavelength, which has been commonly explained based on H desorption or O adsorption. However, a lot of data contradict one another. Oxidation of the silicon in the photo-degraded sample has been confirmed by the growth of the SiO_2 , which instead results in the PL enhancement during laser exposure in air according to the data of Shih et al.⁴ Nakajima et al.⁹ has reported that the increase in PL intensity after oxidation is accompanied by a reduction in the Si-H₂ band as well as in the Si-H band. In contrast, it has been observed that an increase of Si-H by annealing up to 250

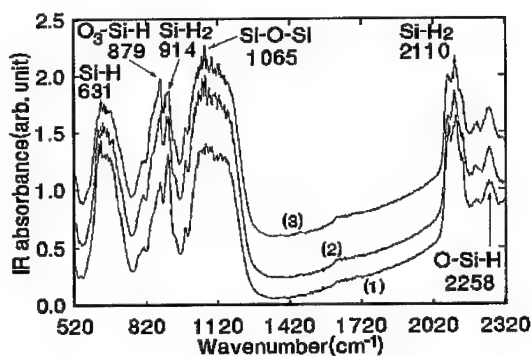


Fig. 5. The change of FTIR absorbance spectra for porous silicon samples of group 2 after light soaking in air and annealing in vacuum: (1) as anodized, (2) after light soaking in air, (3) after annealing in vacuum.

°C results in an increase in the PL intensity⁶. Moreover, the growth of the O-related bands on the surface of PS can cause a blueshift^{6,9} or a redshift¹⁰ in the PL spectra.

Based on the above discussions and our experimental results, we assume that silicon oxides and silicon hydrides are related to the emission process of the PL spectra at 740 nm and 800 nm, respectively. Then, as H-related FTIR peaks (Si-H and Si-H₂) decrease and O-related peaks (Si-O-Si and O₃-Si-H) increase, the PL peak at 800 nm decreases and the PL peak at 740 nm increases. Whether the light soaking in air induces an enhancement or a degradation of PL depends on the degree of oxidation or hydride formation on the surface of as-prepared PS, which equally applies to the change of PL after annealing or oxidation of PS. From these considerations, it is possible to explain the previous reports of PL enhancement or degradation.

In contrast, all peaks observed in the FTIR spectrum are almost similar before and after illumination in vacuum for the samples of group 1 as well as group 2, which suggests that the reversible degradation of PL is not related to chemical adsorption or desorption. Chemical adsorption is a chemical reaction accompanied by an activating process with an activation energy, while physical adsorption usually needs no activation energy and so, the physical adsorption and desorption arise more easily. The origin of PL degradation in vacuum and its recovery is not clear at present, but it seems to be related to the physical adsorption and desorption of rarefied gas molecules in vacuum. We are not able to make FTIR measurements of the sample after irradiation in vacuum to see if some molecular complex changes arise because the FTIR and the PL systems are so apart from each other.

CONCLUSIONS

It has been shown that the light-induced change of PL is reversible in vacuum, but irreversible in air. The degradation of PL during light soaking in vacuum consists of slow and fast processes, both of which are almost fully recovered at room temperature with the latter much faster than the former. Light soaking in air reduces the intensity of the PL spectrum peaked at 800 nm, but enhances that peaked at 740 nm, which is not recovered even by annealing at 160°C for 1 hour. The FTIR spectra suggest that

the irreversible change of PL in air occurs as a result of optically induced chemical adsorption of oxygen or hydrogen loss. The reversible change of PL in vacuum seems due to physical adsorption or desorption, judging from almost lack of any changes in FTIR spectra after light soaking in vacuum.

ACKNOWLEDGMENTS

The present studies were supported by the 1993 Research Fund of Kyung Hee University.

REFERENCES

1. L.T. Canham, *Appl. Phys. Lett.* **57**, 1046 (1990).
2. Z.Y. Xu, M. Gal, and M. Gross, *Appl. Phys. Lett.* **60**, 1375 (1992).
3. R.T. Collins, M.A. Tishler, and J.H. Stathis, *Appl. Phys. Lett.* **61**, 1649 (1992).
4. S. Shih, K.H. Jung, J. Yan, D.L. Kwong, M. Kovar, J.M. White, T. George, and S. Kim, *Appl. Phys. Lett.* **63**, 3306 (1993).
5. P.D. Stevens and R. Glosser, *Appl. Phys. Lett.* **63**, 803 (1993).
6. L. Tsybeskov and P.M. Fauchet, *Appl. Phys. Lett.* **64**, 1983 (1994).
7. D.R. Turner, *J. Electrochem. Soc.* **105**, 402 (1958).
8. M. Ben-Chorin, A. Kux, and I. Schechter, *Appl. Phys. Lett.* **64**, 481 (1994).
9. A. Nakajima, T. Itakura, S. Watanabe, and N. Nakajima, *Appl. Phys. Lett.* **61**, 46 (1992).
10. Y.M. Weng, Zh.N. Fan, and X.F. Zong, *Appl. Phys. Lett.* **63**, 168 (1993).

Part XI

**Defect Properties, Reaction,
Activation and Passivation**

CHEMISTRY OF POINT DEFECT IN SILICON AND ITS APPLICATIONS IN SEMICONDUCTOR TECHNOLOGY

S. PIZZINI, S. BINETTI, M. ACCIARRI
INFM- Department of Physical Chemistry and Electrochemistry,
Via Golgi, 10 20133 Milano (Italy)

Abstract

The chemistry of the interactions between point defects and impurities is discussed by considering first the general thermodynamic and kinetic aspects of these reactions, deserving major attention to the identity of the stable chemical species eventually formed and to the boundary conditions for diffusion controlled and reaction controlled interaction processes.

The second part of the paper is instead dedicated to the analysis of the chemistry of carbon, oxygen, hydrogen and point defects in silicon, which is a system of major technological interest.

We postulate that at low enough temperatures, when homogeneous nucleation processes are slow, spinodal decomposition assists oxygen aggregation phenomena. We postulate, also, on the basis of the existing knowledge, that carbon and hydrogen favour alternative reaction paths for oxygen in the due of clustering processes and discuss the hydrogen-enhanced oxygen diffusivity in the frame of a conventional trapping model.

Introduction

While in Semiconductor Physics studies about the interaction between defects are a relatively recent issue, they have been for years one of the most relevant topics in Solid State Chemistry.

Among others, studies which dealt with the thermodynamics and kinetics of point defect interactions in non-stoichiometric transition metal (TM) oxides indicated that point defect clusters of increasing complexity and of well defined configuration are formed in the course of oxidation or reduction processes [1]. These clusters are considered to be the precursors of the stable, stoichiometric phases which are the final result of the chemical reaction.

These kinds of processes are reminiscent of those occurring during the decomposition of metastable oxygen-silicon solid solutions or during the association of iron with acceptors in iron doped p-type silicon, where some of the polyatomic species formed during the early stages of defect-defect interaction are considered in hundreds of papers [2], [3], [4] the direct or indirect forerunners of the final equilibrium segregating phases.

As emphasized by Sumino [5], however, most of the work in Semiconductor Physics has been concentrated so far on the characterization of isolated defects and impurities or of grown-in clusters. Much less attention, with some notable exceptions [6], has, instead, been paid to the study of the chemical identity of the complex formed, to the reactivity

of isolated defects or/and impurities as well as to the kinetics of the defect-defect interactions even in systems of technological interest.

Thus, the interaction of defects in covalent semiconductor lattices is still an intriguing question, not only for the reasons given above and for intrinsic experimental difficulties, but also for the large number of independent variables which must be considered and for the need of individuating exactly the chemical identity of the complexes formed.

A typical example of this last problem deals with the configurations of the interstitial defect couples [7][8] in semiconductors with the diamond structure, where the interstitials might be covalently bound (split, bond centered, delocalized) or non-bonding and possibly ionized when sitting in tetrahedral or hexagonal sites. In this last case there is, moreover, increasing evidence of spin density redistribution from TM impurities located in an interstitial position to the silicon lattice [9].

Here, the specific bond character influences also the thermodynamic stability of the complex with the metal in different oxidation states, and therefore its stability dependence upon changes of the Fermi level.

In fact, while electrostatically bound, charged-defect pairs [7][10] can easily change their charge state, with relatively little influence on their stability, a covalently bound defect complex, with all electrons shared, would require bond reconstruction in order to perform equivalent charge-state changes.

Considering that the main aims of a chemical study about defect-defect interactions are to determine the type of bonding, the equilibrium configuration, the thermodynamic stability of the complex species found and the kinetics of reactions, we will concentrate first our attention on the thermodynamics and kinetics of defect-defect interactions in semiconductors.

The second part of this paper will be devoted, instead, to the discussion of one single case of defect-defect interaction in silicon, where sufficient accumulated experience exists and where silicon which can be depicted as a diluted, multinary phase where impurities and point defects behave as chemical species distributed in a covalently bonded silicon atoms matrix.

Thermodynamics and kinetics of point defects interactions

Thermodynamics

A first key feature of the thermodynamic behavior of condensed phases, even in the case of complete equilibrium conditions, is that point defects and impurities add an unknown number of chemical components to the system. Thus, not only the degrees of freedom of the system are not "a priori" necessarily determined, but the chemical potential of a specific solute, and then its equilibrium concentration as an isolated chemical species in the homogeneous phase, depends on the occurring of chemical interactions between that solute and the other impurities and/or the point defects.

As the chemical potential of an impurity is also depending on the local stress associated to size misfit and the charge state is affected by the Fermi potential and then by the dopant concentration, the solubility and then the segregation coefficient of an impurity between two homogeneous phases, or between a bulk phase and a subsurface phase of different composition, as it happens in the case of a p-n junction, is an a priori undefined

function of steric and chemical factors.

The so called "enhanced solubility model" often used, in spite of many chemical naiveties, to explain impurity gettering [11] or the "solute drag model", used to deal with the segregation of impurities at extended defects [12] relies at least in part on these factors.

Last, but not least, the presence of equilibrium or non-equilibrium concentrations of point defects (vacancies and interstitials) might strongly affect the thermodynamics of the system, as a consequence of defect-impurity interactions. In fact, not only the bound impurity-point defect pair might induce a local relieve of the mechanical stress associated to size misfit, but the incorporation of point defects might favor the coherent growth of an impurity-defect cluster in the solvent matrix.

Eventually, local stresses associated to inhomogeneous cooling induce a non-homogeneous distribution of the mechanical potential

$$P = \left(\frac{\delta E}{\delta V} \right)_{s, n_1, \dots, n_j} \quad (1)$$

within the solid phase and local fluctuation of temperature during growth might induce local density fluctuations in the silicon phase.

It is therefore well understandable that even in the case of thermodynamically stable and homogeneous solutions, containing one or more solutes in very diluted conditions, they might not necessarily behave as ideal solutions. In fact the impurities can interact with themselves or with point defects as well as with the lattice atoms forming pairs or more complicated clusters, when their mobility is sufficiently high and the interaction enthalpy ΔH_{int} is large enough to get a Boltzmann factor $\frac{-\Delta H_{int}}{kT} \gg 1$.

The interaction enthalpy, or the binding energy E_b , determines therefore the thermal stability of the defect clusters, with the obvious consequence that electrostatically bound complexes, like the H-B or the Fe-B pairs, with binding energies of the order of 0.5 eV [7] are thermally labile, while covalently bounded complexes, like the C-O or the $V_{Si} - O$ ones, with binding energies of the order of few eV should be stable in a largest temperature range.

More complicated features can be exhibited by supersaturated, metastable or unstable solid solutions [13], [14], see fig.1.

Here, depending on the composition, the homogeneous phase transformation can be initiated, respectively, by a nucleation process, which involves local density or concentration fluctuations of large amplitude or by a spinodal decomposition, which involves long-range composition or density fluctuations of small or infinitesimal amplitude in the case of unstable solutions.

As an example, as metastable solid solutions of oxygen in silicon lie well inside the miscibility gap, defined by the coexistence curve of fig.1, spinodal decomposition might play a crucial role in the segregation features of oxygen and carbon, as we will show in the next Section.

Additional complication arise in this case, as it is known that vacancies and interstitials might assist not only the precipitation of the silica and silicon carbide in a conventional nucleation, growth and coarsening process, by supplying the needed excess or defect volume [15], but could also assist the homogeneous growth of coherent clusters of the second phase during a spinodal decomposition, if we assume that long range density fluctuations are associated to point defect density fluctuations.

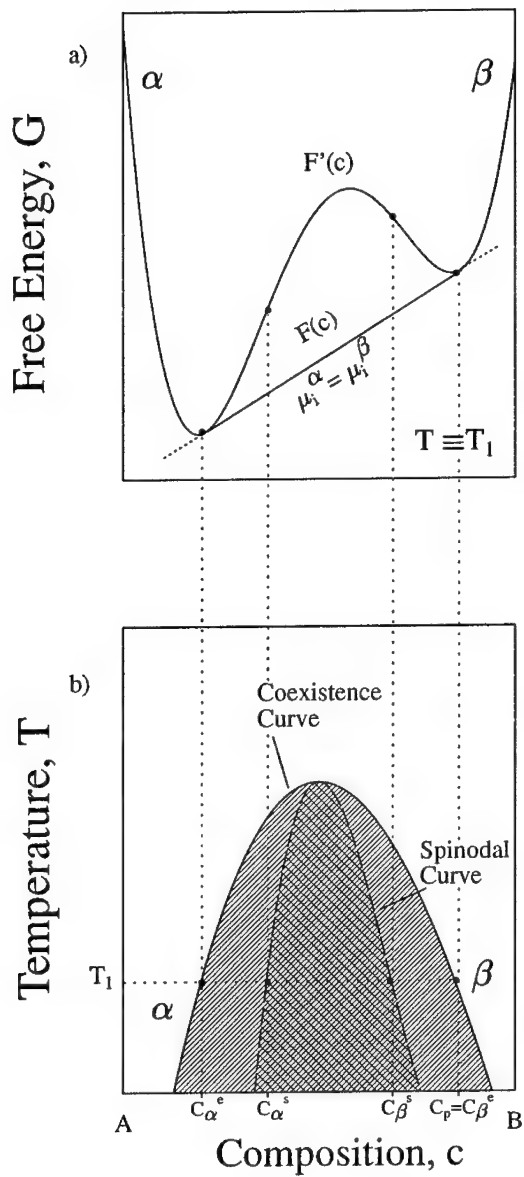


Figure 1: a) Schematic free energy versus composition curves at temperature T_1 ; b) Phase diagram of a binary model alloy with constituent A and B. $F'(c)$ represents a "constraints free energy" which should be overcome in any decomposition processes.

Kinetics: reaction rates and capture processes

As emphasized already by Hu [16] in 1969, and later by Estreicher [17] the attractive interaction of impurities and point defects plays a crucial role in many physical properties of semiconductors, including the impurity diffusivity.

On the other hand, the formation rate of a stable defect pair, which might be considered the simplest kind of a complex species, and which occurs according the reaction $A+B \rightarrow AB$, might be either reaction or diffusion limited.

In the first case, the absolute rate constant k_r for the defect complex formation is given by the equation:

$$k_r = \nu \exp\left(-\frac{\Delta H}{kT}\right) \quad (s^{-1}) \quad (2)$$

where the activation enthalpy ΔH is the saddle point enthalpy in a configurational coordinate (CC) diagram [8] and, then, the reaction rate R_r is much smaller than the supply rate R_d of reactants diffusing from the bulk towards the reaction site.

The saddle point enthalpy in the configurational space contains all energy terms associated to bond breaking or reconstruction, local stress set-up, charge state changes, etc., when we displace, as an example, one atom (or defect) and its reaction partner from the initial, non bonded configuration to the bonded, pair configuration.

Considering that the pair dissociation rate R_d can be calculated using eq.1, with an activation enthalpy $\Delta H + \Delta H_b$ (where ΔH_b is the binding enthalpy), the fraction f of the paired species is simply given by the relation

$$f = \frac{R_r}{R_d} = \exp\left(-\frac{\Delta H_b}{kT}\right) \quad (3)$$

Depending on the kind of interaction (electrostatic, covalent) the binding enthalpy ΔH_b can be estimated to range within 0.5 eV to few eV.

When the bimolecular reaction is, instead, diffusion limited, the formation of a stable pair can be discussed using the model formulated by Waite [18]. This model postulates, under the radiation boundary conditions, that when the pair separation is smaller by an amount Δr_o of the critical collision distance r_o the reaction is not longer diffusion controlled but proceeds according to a first-order chemical kinetics with a rate constant k^* . When the pair is instead at a distance $r = r_o - \Delta r$ with $\Delta r \rightarrow 0$, an increasing possibility exists that a reflection process might occur in parallel to the capture.

Under these conditions, when $mt \rightarrow \infty$, the reaction rate is

$$R_s = -\frac{dC_A}{dt} = -\frac{dC_B}{dt} = 4\pi r_o^2 D \left(\frac{\beta}{r_o\beta + 1}\right) C_A C_B \quad (4)$$

where t is the time, $\beta = k^* \frac{\Delta r_o}{D}$, $m = D \frac{(r_o\beta + 1)}{(r_o)^2}$ and $D = D_A + D_B$

while for values of $mt \rightarrow 0$ and for $r_o\beta \ll 1$, the rate is simply given by

$$-\frac{dC_A}{dt} = -\frac{dC_B}{dt} = 4\pi r_o^2 \Delta r_o k^* C_A C_B \quad (5)$$

Both rates are simply second order rates, but in the first case only the reaction is diffusion limited. Apparently, the absolute value of the diffusion coefficient D and that of the chemical reaction constant k^* , and then the values of m and β play the major role

in determining the reaction kinetics. Furthermore, when one species is a fast diffuser, D coincides with the diffusion coefficient of the fast diffuser and the value of $r_o\beta$ satisfies easier the condition $\beta r_o \ll 1$, for which the reaction is no more diffusion controlled. We will use these considerations when discussing the oxygen aggregation reactions in silicon in the following Section.

In the presence of charged defects, and therefore of long range electrostatic fields, the capture radius r_o is a large multiple of one interatomic distance, and in this case the capture rate is never diffusion controlled.

Aggregation of oxygen to oxygen clusters and interaction of interstitial oxygen with defects

Kinetic features of the oxygen segregation at low temperatures in a silicon matrix

Oxygen is one of the most studied impurities in silicon. As an interstitial impurity, forming a bent-bridged bond between two lattice silicon atoms, it is optically active in the IR and its concentration, which ranges within 10^{17} and 10^{18} cm^{-3} in Czochralski (CZ) silicon, is conventionally measured from its room temperature absorbance at 1106 cm^{-1} , using a calibration factor deduced from chemical and nuclear absolute measurements [19],[20].

Oxygen in CZ silicon is always in supersaturated conditions and, therefore the system tends to drift spontaneously to equilibrium conditions in the absence of mechanical or configurational constraints. Being a very reactive impurity, oxygen it is also potentially capable to saturate dangling bonds and to form oxygen-impurity complexes.

However, when we take as a qualitative measure of the reactivity the values $E_r = -\Delta G_f / \epsilon$, where ΔG_f is the free energy of formation of a compound in Kcal/atom at 273 K and ϵ is the static dielectric constant of silicon, we could see, as an example that carbon, with a value of 0.56 eV competes with oxygen having a value of 0.37 eV in bonding with silicon and that C-O complexes, with $E_r = 0.95 \text{ eV}$ seem to compete with Si-O and Si-C clusters having the silica or the SiC structure, respectively.

We expect, therefore, a strong effect of carbon in the chemistry of oxygen in silicon, as in fact is experimentally well shown.

Moreover once suitably precipitated as oxide from the solution, oxygen is eventually capable to getter metallic impurities and to segregate preferentially at grain boundaries and dislocations, alone or together with other impurities. In this last case, heterogeneous nucleation might compete with the homogeneous one, thus affecting the subsequent oxide growth processes [21].

For all these reasons, the chemistry of oxygen in silicon is one of the most challenging, but complicated, cases we might deal with for illustrating some chemical aspects of defect-defect reactions of technological interest.

As it is well known that above 650°C heterogeneous oxygen nucleation processes begin to play a major role [22], while there is instead no upper temperature limit for carbon, which is known to be very difficult to be segregated from a Si-C solution [23], we will restrict our interest to temperatures up to $450\text{--}500^\circ\text{C}$, where the Si-O-C system could be treated as a pseudo-homogeneous solution.

The first problem we encounter above approximately 350°C ¹ in carbon free Si-O solutions is relative to the kinetics of the process of oxygen segregation, which, in spite of more than 20 years of intensive research, still represents a puzzling question [24].

In fact, if we assume that:

a) the initial distribution of oxygen is almost completely uniform while neglecting the small oxygen concentration fluctuations associated to turbulence convection during the growth process [25]

b) the loss $\Delta[O]$ of the IR-active oxygen is associated to an oxygen clusterization process in the homogeneous phase,

c) the formation rate of higher polymers is fast and presumably not diffusion controlled, considering that the calculated diffusivity of the dimer is some 10^8 times larger than that of O_i [17], [26]

the formation of the smallest polymers (dimers) and than of the overall process in its initial state should be rate determined by the oxygen diffusivity via a capture process (see Section 2, eq.4).

However, instead of measuring an activation energy of 2.56 eV, which is the activation energy for the oxygen diffusion, the experimental value of the activation energy for the oxygen polymerization amounts only to 1.76 eV.

Similar conclusions can be deduced following the simultaneous formation of a small, but constant fraction of EPR-, IR- and electrically- active complex species [27], which present the character of shallow donors and which are conventionally called thermal donors (TD). The process of TD formation occurs in fact with an activation energy of 1.76 eV [17].

However, as the ratio $-\frac{\Delta[O]}{\Delta N_{TD}}$ is constant and independent of the time and of the initial concentration of oxygen², and, therefore, the major amount of oxygen segregates under a form which is not IR-active, it appears that TD are by-products of the main process of segregation of oxygen and that their formation rate of formation is faster with respect to the main process of oxygen segregation.

Considering that the initial reaction rate depends approximately on an n power of the O_i concentration (where n varies between 4 for low oxygen samples to about 2.4 for high concentration samples) [30],[31] but that n tends asymptotically to a value of 2 at low ($T \leq 400^{\circ}\text{C}$) temperatures [27], this discrepancy in the activation energy is associated to a discrepancy in the segregation rate of oxygen and in the initial formation rate of TD. In fact, using a value of $5 \cdot 10^{-8} \text{ cm}$ for r_o , a value of $10^{-20} \text{ cm}^2 \text{ s}^{-1}$ for the oxygen diffusivity and 10^{18} cm^{-3} for the oxygen concentration, one gets from equation 4, written as

$$\frac{d(O_i)_2}{dt} = 8\pi r_o D_{O_i} [O_i]^2 \quad (6)$$

with $D = 2 D_{O_i}$, $r_o \beta \gg 1$, $\Delta r_o = 10^{-9} \text{ cm}$, and $k^* > 1 \text{ s}^{-1}$

values of oxygen losses of the order of $10^{10} \text{ cm}^{-3} \text{ s}^{-1}$. Instead, from the initial values of the TD formation in as grown silicon containing an initial oxygen concentration of $1.06 \cdot 10^{18} \text{ cm}^{-3}$ [31] we have oxygen losses of the order of $5\text{-}6 \cdot 10^{12} \text{ cm}^{-3} \text{ s}^{-1}$, a factor of 500 larger (see fig.2)

¹this is not the lowest temperature limit, but the temperature at which kinetic hindrances make the system very difficult to be studied

²it takes in fact a value within 8 and 10 [28] [29]

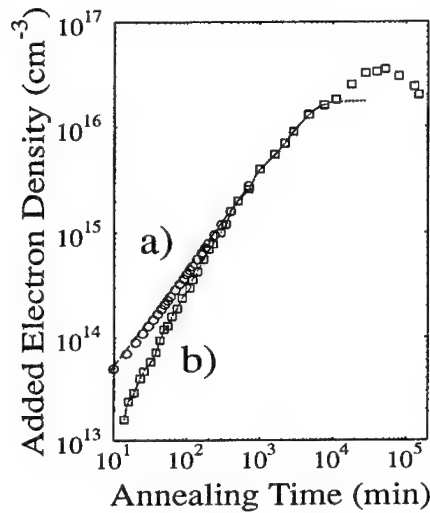


Figure 2: Effect of a dispersion treatment on the behavior of thermal donor generation a) before dispersion, b) after dispersion

Therefore, we have to evocate either an enhanced oxygen diffusivity or we must assume that some spatial correlation exists among isolated interstitial oxygen atoms, such to decrease locally the interatomic distance or/and that a sufficient amount of preexisting dimers exists in solution.

These last might be responsible of the high-initial rate of oxygen clustering, being the fast-moving species.

A remarkable indication that some spatial correlations do exist within isolated oxygen atoms is given by the results of measurements of the recovery of stress induced dichroism in as-grown CZ silicon carried out by Stavola et al. [32], considering that stress induced dichroism measures a local effect.

They found in fact an enhanced diffusivity of oxygen in a range of temperatures between 270 and 400 °C, which well corresponds with our range of interest. From these measurements an activation energy for the diffusivity of 1.96 eV was determined.

Some enhancement of the oxygen diffusivity can be deduced, also by recent oxygen loss measurements carried out by Newmann [27].

Instead, after an high temperature ($T = 1350$ °C) treatment for 20 h in vacuum, stress dichroism recovery measurements turn out to diffusivity values which are in extremely good agreement with the earlier Mikkelsen [33] values.

Considering that at 450 °C homogeneous nucleation occurs at a negligible rate [22] the only way to get spatial correlations in an homogeneous, impurity supersaturated matrix is the occurring of a spinodal decomposition. We come to then to the conclusion that the enhanced oxygen diffusion of oxygen in silicon in the temperature range of TD formation is an artifact due to oxygen concentration fluctuations, which disappear only after a long annealing at high temperatures. Apparently, the activation energy found is

that of the chemical reaction which should be in fact, rate determining.

This conclusion well agrees with the measurements of Kamiura [31], which showed in fact that the initial TD formation rate decreases of a factor 6 after an oxygen dispersion treatment at 1350 °C in Ar (see fig.2 b).

Effect of hydrogen on the diffusivity of oxygen

A possible explanation of the enhanced oxygen diffusivity comes from the recent discovery that not only hydrogen enhances dramatically the TD formation in CZ silicon [17] but also that the oxygen diffusivity is enhanced by about three orders of magnitude in undoped silicon by the presence of hydrogen [34].

One of the consequences of this enhancement is that the activation energy for oxygen diffusion drops from 2.56 eV to 2 eV, close enough to the activation energy values found for the rate of formation of TD.

Incidentally, these results are in very good agreement with previous theoretical anticipations [17], which led to the conclusion that hydrogen present in silicon at a concentration of 10^{15} cm^{-3} enhances by a factor of $3.5 \cdot 10^9$ the oxygen diffusivity and with our present knowledge about the possibility that hydrogen might be a systematic contaminant of CZ silicon.

The model proposed by Estreicher [17] to explain these results starts from the consideration that OH bonds are weaker than Si-O bonds (see as an example the bond strengths in SiO and OH, which amount 8.29 and 4.43 eV, respectively). Thus, the formation of OH bonds is not involved in the fast oxygen diffusion and the fast diffusion step consists in the capture of an hydrogen sitting in a T_d position by a interstitial oxygen, with a configuration at the transition point consisting in one hydrogen close to the BC position initially occupied by oxygen, while the interstitial oxygen sits as a nearest neighbor to a BC position.

We suppose, therefore, that hydrogen, being an highly mobile species, provides a faster reaction channel for oxygen aggregation processes, which are therefore not limited by normal oxygen diffusivity.

We can suppose that in presence of hydrogen the diffusion coefficient of oxygen is actually an effective diffusion coefficient which can be calculated using the following expression [35]

$$D_{eff} = \frac{D_{O-H}}{1 - 2x + 2x\nu^* \exp \frac{E_b}{kT}} \quad (7)$$

where D_{O-H} is the hydrogen-enhanced diffusion coefficient of oxygen, x is the atomic fraction of oxygen atoms sitting in normal interstitial positions, ν^* is the ratio of the frequency factors of oxygen sitting in hydrogen "bounded" positions and in normal interstitial positions and E_b is the binding energy of oxygen trapped in a normal interstitial position, taken equal to 2.56 eV.

In turn, D_{O-H} according to Estreicher[17] is given by

$$D_{O-H} = 4\pi r_c N_H D_H \frac{d^2}{6} \quad (8)$$

where d is the net displacement of oxygen associated to the capture of an hydrogen atom (calculated as $2.07 \cdot 10^{-8} \text{ cm}$), N_H is the concentration of hydrogen in solution, r_c is

the capture radius (taken equal to 5.10^{-8} cm) and D_H is the normal diffusivity of hydrogen in silicon.

In the case of a solid solution of hydrogen in silicon with $N_H = 10^{15} \text{ cm}^{-3}$, $N_O = 10^{18} \text{ cm}^{-3}$ and $D_H = 9.410^{-3} \exp\left(\frac{-0.48}{kT}\right) \text{ cm}^2 \text{ s}^{-1}$ we can estimate for D_{O-H} a value of $1.710^{-17} \text{ cm}^2 \text{ s}^{-1}$ and an activation energy of 2.08 eV if we take for the product $\nu^* x$ a value of 10^{-8} , which indicates that almost all oxygen diffuses via hydrogen assistance.

These results are in quite good agreement with those measured by McQuaid [34] in CZ silicon annealed for two h in an atmosphere of hydrogen at 900 °C.

Effect of carbon and point defects

The oxygen segregation and the TD formation is not only influenced by the presence of hydrogen, but also by the presence of carbon [36], which strongly depresses the formation of TD at 450 °C.

From IR measurements, moreover, we know that in the presence of substitutionally dissolved carbon, a fraction of carbon sits in next nearest position to an oxygen atom, giving rise to a satellite of the main oxygen band at 1106 cm^{-1} [37], [38] at 4 K.

Using a deconvolution procedure, we have carried out a systematic search of this band in the FTIR-spectra measured at 100 K on 18 different as-grown samples presenting different carbon to oxygen ratios. On some of these samples, presenting a carbon to oxygen ratio ranging from 1.70 to 0.18 we have done the same measurements at 100 K after a 100 h annealing at 723 K.

The results are reported in fig.3, which shows that the absorbance at 1104 cm^{-1} is proportional to the product of the C and O concentration in the samples treated at 450 °C. This dependence, which obeys the conventional chemical equilibrium conditions, can be taken as an indication of the formation of a stable C-O complex, or better of a O-Si-C complex of unknown concentration.

Incidentally, this kind of dependence of the absorbance at 1104 cm^{-1} rules out the hypothesis advanced by Lindstrom et al. [39] that the band at 1104 cm^{-1} might be associated to thermal donors, as it appears independent of their presence.

It is however interesting to observe not only that the critical amount of carbon needed to suppress the TD formation is almost equivalent to the stationary concentration of TDs after a sufficiently long annealing period at 450 °C (see fig.4),

but also that in solutions containing relatively large amounts of both oxygen and carbon carbon does increase significantly at $T > 400$ °C the oxygen clusterization [39],[40], as it is also shown in fig.5 [41].

There is, therefore, a conclusive evidence that carbon provides a route for alternative oxygen aggregation processes [39], which might imply the partial co-segregation of carbon as IR-active C-O complexes and/or IR-inactive SiC [40],[41].

Thus, the question which arises is whether in the temperature range 350-550 °C a complete thermodynamic equilibrium exists within TD and $C_{Si} - O_i$ complexes in solution or the TD formation in oxygen-rich solutions is depressed by carbon for kinetic or configurational reasons and, further one, whether the process is assisted by point defects.

In order to discuss this last question, we have first to recall that the C-O complexes giving rise to the absorbance at 1104 cm^{-1} are very labile species, which can be

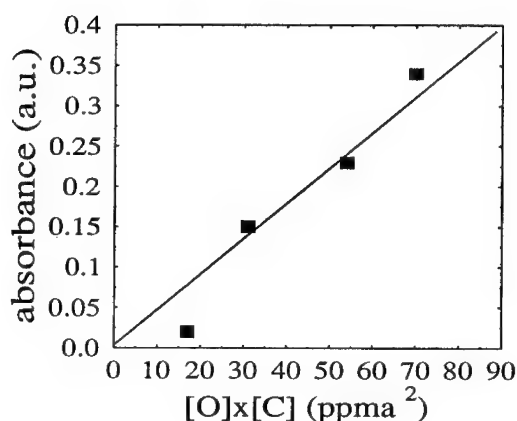


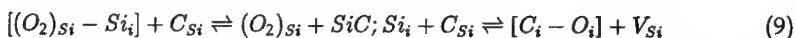
Figure 3: Dependence of the absorbance at 1104 cm^{-1} on the product of the carbon and oxygen concentration

decomposed at temperatures above $500\text{ }^{\circ}\text{C}$, but that $C_i - O_i$ complexes begin to be stable in this temperature range.

Additionally, we have to remind that TD are not the direct precursors of the stable phase which segregates at high temperatures. In fact, they might be destroyed by a very short treatment at $650\text{ }^{\circ}\text{C}$, when nucleation processes begin to run at a sufficiently large rate [22].

Eventually, it seems reasonable to rise the hypothesis that TD originate from the collapse of an oxygen dimer to a pseudo-molecular oxygen in a substitutional position, associated to an interstitial in a neighbor T_d position. This configuration is almost equivalent to that theoretically studied by Deak et al. [43] and used by Lindstrom et Hallberg [42] to explain the effect of carbon on the clustering of oxygen atoms at $450\text{ }^{\circ}\text{C}$.

Then, if the electrical activity of TDs depends on the presence of a bound $(O_2)_{Si} - Si_i$ couple, carbon represents an ideal mean for their deactivation. It provides in fact the conditions for the formation of stable $C_i - O_i$ complexes and of SiC nuclei, according to the following reactions:



which also account for our previous observation about the stoichiometric amount of carbon needed to suppress the electrical activity of TD.

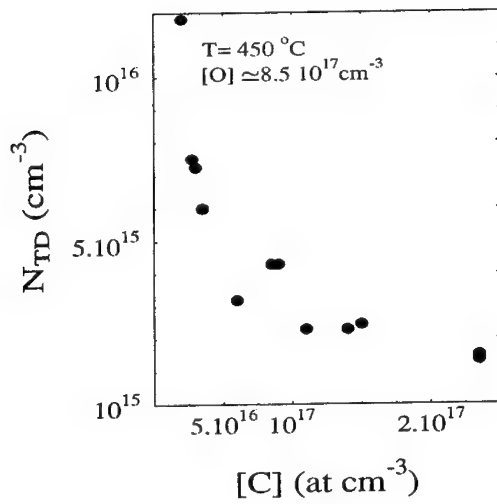


Figure 4: Concentration of TDs after a long annealing at $450\text{ }^{\circ}\text{C}$ versus the concentration of carbon [after [36]]

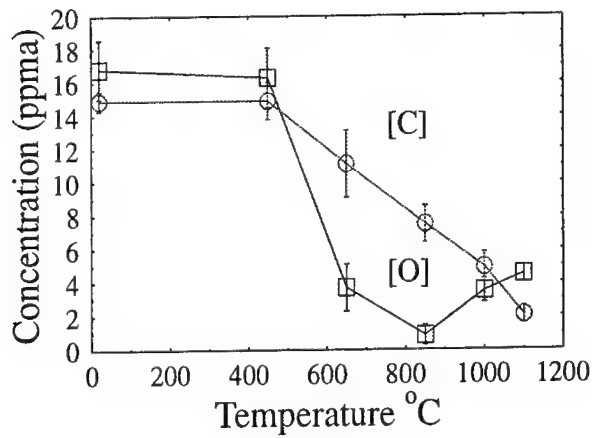


Figure 5: Co-segregation of oxygen and carbon in a sequence of 24h annealing steps in argon at increasing temperatures

Conclusions

In our attempt to discuss the features of the interactions among some ad hoc selected defect species in an homogeneous phase consisting of impurity-doped semiconductor silicon, we have shown, as expected, that the reactivity, the local configuration, the bond strengths and the diffusion coefficient of impurities play the major role in the reaction kinetics.

We have found that the classical Waite model helps in discussing the kinetics of reactions occurring in these solid, homogeneous phases, showing that they can be parameterized in terms of a chemical rate constant, k^* , of the diffusion coefficients D , of a collision radius r_o and of an effective capture radius $r_o - \Delta r$.

Eventually, we have tried to give a comprehensive view of the chemical synergies among oxygen, carbon and hydrogen, which look, at least qualitatively in good agreement with most of the literature data available, if we assume that the enhanced oxygen diffusivity needed to account for the homogeneous oxygen clustering processes originates either from hydrogen-assisted oxygen diffusion or from the presence of spatial correlations. These last are supposed to come from the spinodal decomposition of the unstable solid solutions of oxygen in silicon during the post-growth cooling process.

Acknowledgments

The authors are greatly indebted to the European Community to have supported this work within the Joule II Project.

References

- [1] C.N.R. Rao, J. Gopalakrishnan, New directions in solid state Chemistry, Cambridge University Press (Cambridge, 1986)
- [2] A.B. Van Oosten, PhD Thesis, University of Amsterdam (1989)
- [3] Semiconductor Silicon 1977, 1981, 1986, 1990, The Electrochem Soc. Inc., (1977, 1981, 1986, 1990) and references cited herein.
- [4] T.V. Mashovets, *Sov. Phys. Semicond.* **18**, 5 (1982)
- [5] Sumino in: *Solid state Phenomena*, Vol. 6 & 7, TransTech Publ. (Zuerich, 1989) pp. 197-210
- [6] M.Orlowski in: Semiconductor Silicon 1994, Vol. 94-10, The Electrochem. Soc. (1994). pp.579-592
- [7] L.C. Kimerling, M.T. Asom, J.L. Benton, P.J. Drevinsky, C.E. Caefer, *Materials Science Forum*, Vols. 38-41, TransTech Publ., Zuerich,(1989) pp. 141-150
- [8] G.D. Watkins, *Materials Sci. Forum*, Vols. 38-41, TransTech Publ., Zuerich(1989) pp.39-50

-
- [9] W. Gehlhoff, U. Rehse, Solid State Phenomena, Vols. 6 & 7, TransTech Publ., Zuerich (1989) pp.257-264
- [10] J.H. Crawford,Jr. L.M. Slifkin, Point defects in solids, Plenum Press (1972) Vol.I
- [11] J.S. Kang, D.K. Schroder, J. Appl. Phys. **65**, 2974 (1989)
- [12] S. Pizzini in: Defects in Electronic Ceramics, edited by S. Pizzini TransTech Publications; Zuerich (1993) , pp.81-120
- [13] K.F. Kelton, Crystal Nucleation in liquids and glasses, Solid State Physics, Vol.45; H. Ehrenreich, O. Turnbull Eds. Academic Press (New York) 1991 pp. 75-177
- [14] R. Wagner, R. Kampmann, Homogeneous second Phase Precipitation, in Materials Science and Technology, Vol.5 R.W.Cahn, P. Haasen, E.J. Kramer Edt. VHC, Weinheim, (1991) pp.213-303
- [15] S.M. Hu, J. Electrochem. Soc. **138**, (1992) 2066
- [16] S.M.Hu, Phys. Rev. **180**, 773 (1969)
- [17] S.K. Estreicher, Phys.Rev. B **41**, 9886 (1990)
- [18] T.R. Waite, Phys. Rev. **107**, 463 (1957)
- [19] R. Murray, K. Graff, B. Pajot, K. Strijkmans, S. Vandendriessche, B. Gripink, H. Marchandise, J. Electrochem.Soc. **139**, 3582 (1992)
- [20] A. Baghdadi, W.M. Bullis, M.C. Croarkin, Yue-zhen Li, R.I. Scace, R.W. Series, P. Stallhofer, M. Watanabe, J. Electrochem. Soc. **136** (1989) 2015
- [21] S.Acerboni, S.Pizzini, S.Binetti, M.Acciarri, J.Appl.Phys. **76**, 2703 (1994)
- [22] K.Wada, N.Inue in :Semiconductor Silicon 1986, Vol. 86-4, The Electrochem. Soc. 1986) pp.778-789
- [23] W.J. Taylor, T.Y. Tan, U. Goesele, Appl. Phys. Lett. **62**, 3336 (1993)
- [24] in: Diffusion in solids, Unsolved problems edited by G.E. Murch, TransTech Publ., Zuerich, (1992) pp.189-206
- [25] P.Rava, H.C. Gatos, J. Lagowski, Appl. Phys. Lett. **38**, 274 (1981)
- [26] L.C.Snyder, J.W. Corbett, P. Deak, R. Wu in: Defects in Electronic Materials, MRS Volume 104 (1987) pp.179-184
- [27] C.A. Londos, S.A. McQuaid, M.J. Binns, R.C. Newman, J.H. Tucker, Solid State Phenomena, Vol.32-32, TransTech Publ. (Zuerich,1993) pp. 161-166
- [28] R.C. Newman, J.H. Tucker, S.A. McQuaid, Materials Sci. Forum, Vol. 83-87, TransTech Publ. Zuerich, 1992, pp. 87-92
- [29] K.D. Glinchuk, N.M.Litovchenko, Z.A. Salnik, phys. stat. sol. (a) **71**, 83 (1982)

- [30] in: Defects in Electronic Materials, MRS Volume 104 (1987) pp.189-192
- [31] Y. Kamiura, K. Endo, J. Appl. Phys. **61**, 2478 (1987)
- [32] M. Stavola, J.R. Patel, L.C. Kimerling, P.E. Freeland, Appl. Phys. Lett. **42**, 73 (1983)
- [33] J.C. Mikkelsen, Appl. Phys. Lett. **40**, 336 (1982)
- [34] S.A. McQuaid, R.C. Newman, J.H. Tucker, E.C. Lightowers, R.A.A. Kubiak, M. Goulding, Appl. Phys. Lett. **58**, 2933 (1991)
- [35] C.A. Wert, R.C. Frank, Ann. Rev. Mater. Sci. **13**, 139 (1983)
- [36] J. Lerouelle, These Universite Pierre et Marie Curie, Paris 6 (1980)
- [37] R.C. Newman, Infra-red Studies of crystal defects, Taylor & Francis (London) 1973
- [38] G.S. Oehrlein, J.L. Lindstroem, J.W. Corbett, Appl. Phys. Lett. **40**, 241 (1982)
- [39] J.L. Lindstrom, H. Weman, G.S. Oehrlein, phy.stat. sol.(a) **99**, 581 (1987)
- [40] F. Shimura, J. Appl. Phys. **59**, 3251 (1986)
- [41] S. Pizzini, S. Binetti, M. Acciarri, S. Acerboni, phys. stat. sol.(a) **138**, 451 (1993)
- [42] J.L. Lindstrom, T. Hallberg, Phys. Rev. Lett. **72**, 2792 (1994)
- [43] P. Deak, L.C. Snyder, J.W. Corbett, Phys. Rev. Lett. **66**, 747 (1991)

BISTABILITY OF DEFECTS IN SEMICONDUCTORS

Masashi Mizuta

Fundamental Research Laboratories, NEC Corporation
34 Miyukigaoka, Tsukuba, Ibaraki 305, Japan

Abstract

The DX center in AlGaAs alloy is reviewed as an example of bistability of defects in semiconductors. Also presented is some technological importance of the defect bistability.

Introduction

Imperfection or defect, by word itself, is undesirable but sometimes it plays a key role in controlling the property of material. The DX center in AlGaAs alloy was undesirable in that this defect induces strange phenomenon such as persistent photoconductivity, PPC, at low temperatures, and it also induces technological problem of device instability and doping problem in this alloy system. Defect or impurity bistability has been known for a long time for many cases but people believed, and in many cases this was, due to atomic rearrangement of a complex defect. For a complex it is easy to think the transformation of relative location of constituent atoms which is induced by charge state change. But a single substitutional impurity has long been thought to be quite stable.

Less than ten years ago, it has been shown from the hydrostatic pressure experiment that the DX is composed of single substitutional donor impurity and has bistable character. Since then accumulating experimental evidence, and theoretical prediction give the picture now that the bistable behavior of single substitutional impurity is quite common even in the tetrahedrally coordinated semiconductors, which have the strong directional bonding or hybridization character. This phenomenon leads in some cases to drawback in technologically important properties of the material. But, in certain case, this defect bistability itself can be useful.

DX problems in AlGaAs alloy

N-type impurities such as Si, Ge, S, Se in GaAs are known to form effective-mass donor states with very little central cell effect. In $\text{Al}_x\text{Ga}_{1-x}\text{As}$, however, the donor state becomes deep, for alloy composition x exceeding ~ 0.25 . Chand et al. reported a comprehensive study of the alloy dependence of binding energy for a Si donor in AlGaAs alloy system¹⁾. The donor state becomes exceedingly deep in AlGaAs which cannot be extrapolated from simple increase in conduction band parameter (electron mass). This leads to problem of doping, for which maximum attainable carrier concentration severely decreases for higher x due to an increase in activation energy. Furthermore, the DX behavior can be thought as one of the carrier saturation mechanism in this alloy system²⁾.

At the same time from this alloy composition range, a strange effect, the so-called persistent photoconductivity (PPC) starts to appear³⁾. This phenomenon has been known in the direct gap

AlGaAs, but later the same PPC effect was observed in the indirect region⁴⁾. The mechanism or condition for the PPC is also related technological problem of device instability; I-V collapse, which occurs at low temperature in the HEMT structure, can recover under the condition which induces the PPC⁵⁾.

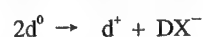
These led to the model of the large-lattice relaxation for the DX by Lang⁶⁾, however, the corresponding defect was assumed to be a complex, such as donor and unknown defect X, which originally thought to be Arsenic vacancy. The DX is thus named. At this point the story was self-explanatory and no question arouse. We had been studied this alloy system and had a question whether it is possible to have almost 100% donor becomes complex on alloying ? This can be tested by pressurize GaAs since conduction band structure and its indirect-direct order can be simulated by an application of pressure.

Pressure experiment reveals that shallow effective mass donor in atmospheric pressure GaAs can be converted to the DX deep level in alloy-analogue system⁷⁾. Since donor doped in GaAs can not convert to be a complex with any other defect at room temperature, the important conclusion is that the DX is composed of a substitutional impurity, in one case acting as a shallow effective mass state, in the other, the deep DX center. The experiment can be viewed that the deep level is originally embedded or resonant with conduction band and this can be pulled down (relative to the Fermi level or edge of conduction band) by alloying or pressure so that the deep level can accommodate appreciable number of electron upon injection. In normal pressure GaAs, shallow effective mass like level is ground state and the resonant deep level is excited state. This shallow-deep instability can occur in AlGaAs, but in this case the energy location of two levels is interchanged: the ground state of the donor is the DX and effective mass state is the excited one. After optical excitation at low temperatures, existence of the effective mass state is experimentally confirmed and steady change of electron population to shallow state is the PPC so that the PPC itself can be regarded as deep-shallow transition.

Shallow - deep instability of a substitutional donor

Shallow-deep instability can be thought quite general phenomenon: all the impurity has its characteristic core derived deep level and if this level is separated, for some reason, by a thermal barrier from shallow effective-mass like level, the center should show shallow-deep instability. The question is how these two states are possible for a single substitutional donor and what is the cause of thermal barrier. The main course of understanding was still along with the large lattice relaxation model given by Lang.

Recent first principles theory predicted the doubly electron captured DX state (negative-U state) and the corresponding the broken bond configuration⁸⁾.



This can be viewed as pseudo-Jahn-Teller effect as that antibonding T_2 state of the impurity atom lifted to A_1 which becomes the ground state upon two electron capture and consequent $\langle 111 \rangle$ direction (C_{3v}) lattice distortion, for which energy loss due to electron-electron repulsion is compensated by energy gain by Jahn-Teller distortion or lattice relaxation. This

naturally explains the lack of any signal from paramagnetic resonance measurements which have been tried rigorously without success. Several important experimental results have been reported in support for the negative U model. Simultaneous doping of Si to GaAs:Ge facilitates source for second or additional electron capture to the Ge DX so that quantitatively one Ge DX captures two electrons⁹⁾. Local Vibrational Mode (LVM) spectroscopy results show that the new LVM, corresponding to the DX, appears beyond a certain pressure and also verify that shallow donor (d) still exists even beyond the threshold pressure in equal concentration to the DX¹⁰⁾. Here, two electron nature was positively identified although a rigid experimental verification of bond breaking configuration is lacking.

More general view of bistability is represented as sp^3 - sp^2 transformation. Since for the shallow state, an impurity is regarded as tetrahedrally coordinated (sp^3). Upon broken bond configuration, an impurity Si is 3-fold coordinated (sp^2). An interesting analogue of transformation between sp^3 - sp^2 transfer is diamond-graphite system, although the activation energy is too high to induce real material transformation at room temperature. Also recently found carbon nanotube¹¹⁾ and fullerene (or C60) are also within the same system. Nanotube is more sp^2 like and C₆₀ is more sp^3 like from their shapes. But in more detailed view, the stability of dangling bond $p\pi$ -orbital is always fulfilled by delocalization; for graphite and carbon nanotube or even C60, the conduction band of these materials is composed of π orbital¹²⁾. At single defect like the DX, however, energy gain due to the delocalization cannot be expected, so that p -orbital is stabilized only through sp^3 hybridization which is achieved either by breathing mode relaxation (this is basically unchanged sp^3) or by bond breaking type relaxation ($\langle 111 \rangle$) at a position far beyond the $\langle 111 \rangle$ Arsenic plane until lattice elastic energy loss stops the motion. Therefore the sp^3 - sp^2 transformation is somewhat oversimplified view. Saito et al. considered the situation and found even in broken bond configuration $p\pi$ bond still tends to hybridize to gain energy¹³⁾. Actually an important chemical trend of the DX properties are understood in this hybridization concept: the DLTS activation energy can be estimated by the total energy difference between sp^2 -position and final displaced position ($sp^{2+\epsilon}$). This clearly explains the large activation energy for Si ($sp^{2+0.4}$), small for Sn ($sp^{2+0.2}$), and the same activation energies for group VI donors for which host As displaces instead of donor itself, since group VI donors is difficult to make sp -hybridization. This agreement has the importance for the origin of microscopic mechanism of thermal barrier for the bistability, i.e., the barrier is for Si to pass through sp^2 configuration where $p\pi$ -nonbonding state is quite unstable; the sp^2 configuration is close to Si being at (111) Arsenic plane.

Remaining problem in the DX mechanism

For capturing electrons to the DX, simultaneous two electron capture is highly unlikely. The existence of intermediate one-electron state is crucial although this intermediate state (which would be picked up by spin resonance technique) was not detected. This is also important issue for device problems like HEMT I-V collapse. So far the ground state DX is undetected by paramagnetic resonance and this is reasonable considering negative-U nature of the DX. For the case of Sn donor, however, a paramagnetic center is detected and thought as one electron state, D^0 or original A_1 state¹⁴⁾. However, in experiments, it always requires light irradiation for detecting the paramagnetic center and this is somewhat different from what naturally expected from A_1 (DX⁰) state.

For Sn impurity it is peculiar that DLTS always detects two peaks even for GaAs, both of them show the DX character. One can think coexistence of the DX and $D^0(A_i)$, but from pressure dependence of DLTS behavior (Fig. 1), high temperature peak B (due to D^0 ?) actually lies lower than the normal DX (Fig. 2). Then, the lack of paramagnetic signal under dark can not be understood. From the above discussion, the high temperature peak B could also represent two electron state, for which it may be the host-atom displaced configuration from small sp hybridization nature of Sn, or other possibilities may be breathing mode relaxation or bond-breaking relaxation other than $\langle 111 \rangle$ direction. In any case Sn is quite interesting case for looking into the details of the DX mechanism.

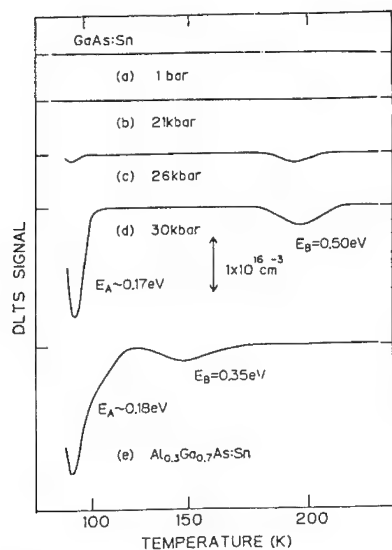
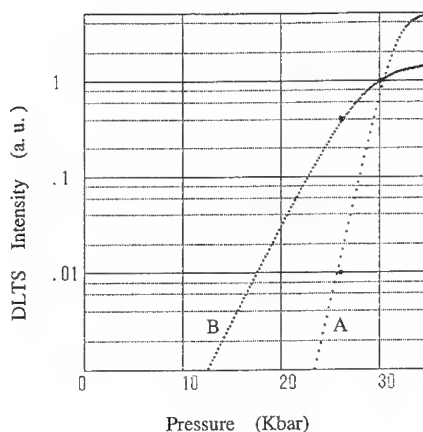


Figure 1
DLTS spectra for LPE GaAs:Sn under various hydrostatic pressures ((a) - (d)). Also shown in (e) is for AlGaAs:Sn ($x=0.3$).



Trap A : $E_{DLTS}=0.17\text{eV}$, $E_{DXA}-E_C=0.259\text{eV}$
Trap B : $E_{DLTS}=0.5\text{eV}$, $E_{DXB}-E_C=0.220\text{eV}$

Figure 2
DLTS signal intensity as a function of pressure. Energy levels are determined assuming the pressure coefficient of the levels as 3.8meV/Kbar .

The DX center in other materials

In the above, the DX in AlGaAs is described as most extensively studied case but single atom bistability can now be found in many semiconductors although the mechanism and involvement of single impurity are not necessary definitive¹⁵. An interesting case is acceptor type impurities, AX center ? In MgZnSse the PPC like phenomenon has been observed¹⁶. This is important issue in considering heavy p-type doping in these II-VI compound semiconductors required for light emitting devices.

Bistability for an application

A known example of technological use of defect bistability is F-center formation in alkali halide, used in an imaging plate, an X-ray or electron beam written storage device. The mechanism of F-center formation is similar to the DX mechanism but in this case the defect is intrinsic in nature in ionic crystal. Recent experiment utilizing the DX PPC effect to introduce localized carrier plasma is found to be potentially promising for optical storage or interconnection switching device application¹⁷⁾. The DX in PPC state produces shallow effective mass state or degenerated free carrier depending on donor concentration. This change is stable at least at low temperatures and also the spatial resolution of carrier plasma region is quite small due to Coulombic attraction from the ionized donor. The resultant refractive index change (Δn) has been shown to be very large, as high as Δn reaching $\sim 1\%$. Room temperature operation should have strong impact in technology.

Acknowledgments

The author acknowledges H. Kukimoto, J. Yoshino, M. Tachikawa, A. Oshiyama, Y. Mochizuki, M. Saito, T. Baba, K. Mori, J. D. Chadi, R. A. Linke, and T. Thio for collaboration and discussion.

References

- 1) N. Chand, T. Henderson, J. Klem, W. T. Masselink, R. Fisher, Y-C. Chang and H. Morkoc, Phys. Rev. B30(1984) 4481.
- 2) T. N. Theis, P. M. Mooney and S. L. Wright, Phys. Rev. Lett. 60(1988)361.
- 3) R. J. Nelson, Appl. Phys. Lett. 31(1977) 351.
- 4) M. Mizuta, K. Mori, Phys. Rev. B37(1988)1043.
- 5) A. Kastalsky and R. A. Kiehl, Inst. Phys. Conf. Ser. 79(1985)535; Y.Hori, M. Kuzuhara, N. Samoto, and T. Ito, IEEE Trans ED 39(1992)2720.
- 6) D. V. Lang and R. A. Logan, Phys. Rev. Lett. 39(1977)365; D. V. Lang, R. A. Logan and M. Jaros, Phys. Rev. B19(1979)1015.
- 7) M. Mizuta, M. Tachikawa, H. Kukimoto and S. Minomura, Jpn. J. Appl. Phys. 24 (1985) L143; M. Tachikawa, M. Mizuta, H. Kukimoto and S. Minomura, Jpn. J. Appl. Phys. 24 (1985)L821.
- 8) D.J.Chadi and K.J.Chang: Phys. Rev. Lett. 60 (1988) 2187; Phys. Rev. B39(1989) 10063; S.B. Zhang and D.J.Chadi: Phys. Rev. B42 (1990) 7174; J.Dabrowski and M. Scheffler, Mat. Sci. Forum vol.83-87 (1992) p.735.
- 9) T.Fujisawa, J.Yoshino and H.Kukimoto: Jpn. J. Appl. Phys. 29 (1989) L388.
- 10) J.A.Wolk, M.B.Kruger, J.N.Heyman, W.Walkiewicz, R.Jeanloz and E.E.Haller: Phys. Rev. Lett. 66 (1991) 774.
- 11) S. Iijima, Nature 354(1991)56.
- 12) S. Saito and A. Oshiyama, Phys. Rev. Lett. 66(1991)2637; N. Hamada, S. Sawada and A. Oshiyama, Phys. Rev. Lett. 68(1992)1579.
- 13) M.Saito, A.Oshiyama and O.Sugino: Phys. Rev. B45 (1992) 13745; M.Saito, A.Oshiyama

-
- and O.Sugino: Phys. Rev. B47 (1993) 13205; M.Saito, and A.Oshiyama, Phys. Rev. B48(1993) 11804; M.Saito, and A.Oshiyama: Modern Phys. Lett. 7(1993)1567.
- 14) M.Fockele, J.-M.Spaeth, H.Overhof and P.Gibart: Mat. Sci. Forum, vol.83-87(1992) p.835.
- 15) P. M. Mooney, J. Appl. Phys. 67(1990)R1.; K. J. Malloy and K. Khachaturyan, *Semiconductors and Semimetals*, ed. by Willardson, Beer and Weber(Academic, New York, 1993).
- 16) J. Han, M. D. Ringle, Y. Fan, R. L. Gunshor and A. V. Nurmikko, Appl. Phys. Lett. 65 (1994)3230.
- 17) R. A. Linke, T. Thio, J. D. Chadi and G. E. Devlin, Appl. Phys. Lett. 65(1994)16; T. Thio, R. A. Linke, G. E. Devlin, J. W. Bennett, J. D. Chadi and M. Mizuta, Appl. Phys. Lett. 65(1994)16; R. L. MacDonald, R. A. Linke, J. D. Chadi, T. Thio, and G. E. Devlin, Optics Lett. 19(1994)2131.

INTERACTION BETWEEN EL5 AND EL6 IN BULK GaAs

HIROYUKI SHIRAKI, YUTAKA TOKUDA* AND KOICHI SASSA

Central Research Institute, Mitsubishi Materials Corporation, 1-297 Kitabukuro-cho, Omiya, Saitama, Japan

*Department of Electronics, Aichi Institute of Technology, 1247 Yachigusa Yakusa, Toyota, Aichi, Japan

ABSTRACT

The interaction between EL5 and EL6 in the n-type bulk GaAs have been observed by using isothermal constant-capacitance voltage transient spectroscopy (CCVTS). Each CCVTS spectrum of EL5 and EL6 was broader than a theoretical one expected for a single level, and was found to be consistently interpreted by two main trap components. With the increase of the filling pulse duration in a wide range, one component of EL6 decreased to about 50 % of its initial value, while one component of EL5 increased and saturated. This variation in peak heights could be reversed by controlling electron occupation fractions of EL5 and EL6 by application of two adjacent filling pulses. Such interaction between both levels was commonly observed in n-type bulk GaAs independent of carrier density.

INTRODUCTION

The knowledge of deep levels in compound semiconductor materials is important for both device application and physics. Especially, the control of both spatial distributions and concentrations of deep levels is a serious problem in device fabrication and crystal growth. In the case of GaAs, a great deal of efforts have been devoted to understanding properties of the midgap donor EL2 which plays an important role in semi-insulating characteristics. In contrast to this, other deep levels in GaAs have drawn much less attention. Properties of medium-deep levels (EL5 and EL6) in GaAs materials have been studied by some authors [1,2,3,4,5]. However, the detailed behaviors such as the electron emission and capture kinetics of these levels have not been clarified.

In this work, we describe the observation of interaction between EL5 and EL6 in the n-type bulk GaAs grown by three different methods. The electron emission and capture kinetics of EL5 and EL6 were studied by using the isothermal constant-capacitance voltage transient spectroscopy (CCVTS) instead of the conventional constant-voltage capacitance transient method. The reversible defect reaction between both levels was commonly observed in n-type bulk GaAs independent of carrier density.

EXPERIMENTAL

N-type GaAs samples were prepared from crystals grown by three different growth methods : horizontal Bridgman (HB) method, liquid encapsulated Czochralski (LEC) method, and arsenic-pressure-controlled Czochralski (PCZ) method [6,7] in which a GaAs crystal was grown under

an arsenic pressure in a hot wall chamber without any encapsulant on the melt surface. Net shallow donor concentrations (N_{SDA}) in the samples, which were determined by capacitance-voltage (C-V) measurement at 80 K, ranged from $1.6 \times 10^{14} \text{ cm}^{-3}$ to $4.5 \times 10^{16} \text{ cm}^{-3}$.

The CCVTS measurements were performed isothermally on Au-Schottky diodes fabricated on the chemically etched (100) surfaces by using the combination of a 1MHz capacitance meter and a feed-back circuit. Au-Ge/Ni ohmic contacts were made on the back surface of the samples. Changes in the applied voltage of the diode while the capacitance is kept constant were measured at selected temperatures for long time duration following a filling pulse. Then the data were processed with a computer into CCVTS spectrum by using rate window scan method with a bipolar rectangular weighting function [8,9]. If the carrier emission from a trap level takes place in an exponential, the voltage transient is exactly exponential without any approximation in the constant capacitance method. This technique is also free from the distortions due to the change in the depletion layer thickness during the transient.

RESULTS AND DISCUSSION

Figure 1 shows typical DLTS spectra for a HB sample recorded with six different rate windows. As shown in Fig. 1 (b), the peak height of EL6 decreased remarkably by using a longer filling pulse duration. This kind of change in DLTS spectra was observed in all n-type GaAs samples used in this study. However, there is an inevitable ambiguity with the conventional DLTS measurement whether the decrease of the EL6 peak height is only due to the long filling pulse duration, because temperature was swept during the measurement. Therefore, we investigated the electron emission and capture kinetics of EL5 and EL6 in detail by using the isothermal CCVTS method.

Typical isothermal CCVTS spectra for three samples with various net shallow donor concentrations are shown in Fig. 2. If each of the trap EL5 and EL6 consists of a single level, the CCVTS spectra have to be described well by two individual levels. But, both spectra corresponding to these traps were broader than the theoretical spectrum expected for a single trap level. This fact means that both EL5 and EL6 consist of multi-components. Then, we tried to determine necessary components of the measured spectra using the method of least-squares fitting. As a result, the CCVTS spectra were found to be described well by six trap levels labeled A_1 , A_2 , A_3 , A_4 , A_5 , and A_6 . These components were represented by solid lines in Fig. 2. Each CCVTS spectrum of EL5 and EL6 in all samples was found to consist mainly of two trap components.

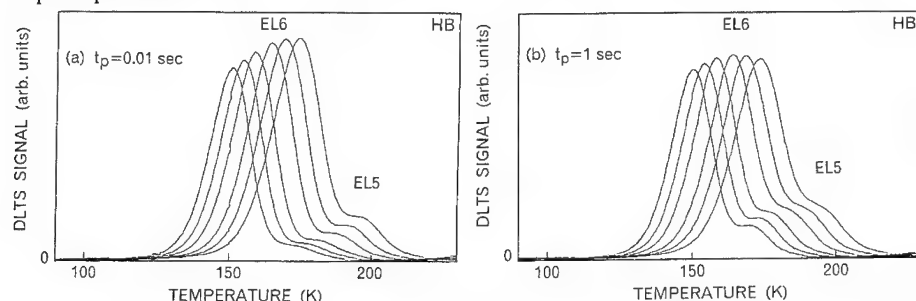


Fig. 1. Conventional DLTS spectra of a HB sample measured with filling pulse duration of (a) 0.01 and (b) 1.0 sec by using six different rate windows.

To obtain the activation energies for thermal emission of the six traps, the CCVTS measurements were carried out at seven temperatures. From Arrhenius plots, the activation energies were determined to be 0.24, 0.32, 0.36, 0.37, 0.40, and 0.38 eV for traps from A₁ to A₆, respectively.

Figure 3 shows three typical CCVTS spectra of EL5 and EL6 measured at 160 K with the filling pulse duration varied. As the filling pulse duration increases, the component A₅ of EL5 increases, while the component A₄ of EL6 decreases. Other components remained almost constant. Similar results were obtained for other samples. The peak height of a trap is independent of filling pulse duration, if the capture rate is large enough. If a trap level is caused by defects associated with lattice relaxation, the peak height increases and saturates, as the filling pulse duration increases. Therefore, the change in the A₄ peak height as seen here cannot be understood straightforwardly. Figure 4 shows the filling time dependence of the CCVTS peak heights of the four individual components (A₃, A₄, A₅, and A₆ as seen in Fig. 3) at 160 K. The peak heights of A₄ and A₅ remained almost constant in the filling pulse duration less than 0.1 sec. In a long range of filling pulse duration, however, the peak height of A₄ which gradually decreases to about 50 % of its initial value, while the peak height of A₅ increases and saturates.

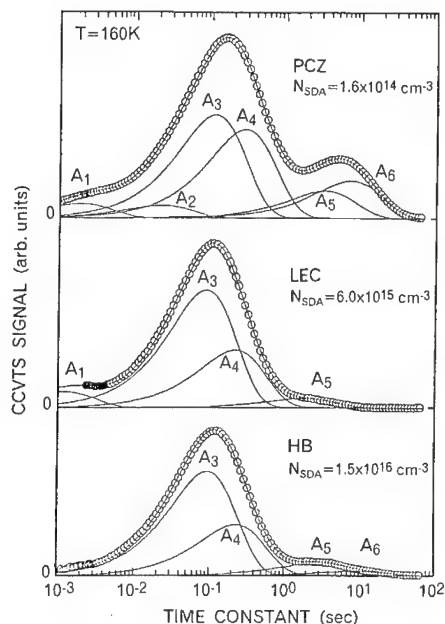


Fig. 2. Isothermal CCVTS spectra of three samples with various net shallow donor concentrations measured at 160 K with filling pulse duration of 0.1 sec. Open circles represent experimental spectra, and solid lines are calculated components.

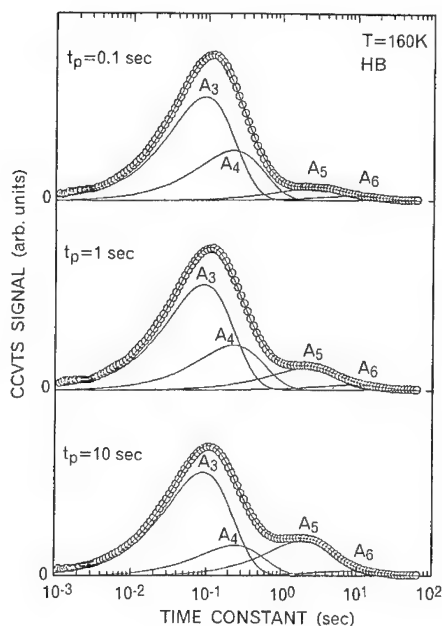


Fig. 3. Isothermal CCVTS spectra of a HB sample measured at 160 K with filling pulse duration of 0.1, 1, and 10 sec.

If the concentration of a trap is higher than the carrier concentration, the carriers emitted from the level play an important role in capture kinetics. Under such a condition, the capture rate of the trap decreases as the filling time increases. If the emission rate becomes larger than the capture rate, trapped electrons can be reemitted from the level to the conduction band, which should lead to the decrease in the concentration of observable defects. However, the characteristic behaviors of A_4 and A_5 were commonly observed in all samples independent of net shallow donor concentration. Therefore, the decrease in the A_4 peak height cannot be understood within the framework of charge redistribution model [10,11,12].

On the other hand, assuming that the trap A_5 has an activation energy for electron capture, the electron capture cross section of trap A_5 is estimated to be smaller than a few times 10^{-24} cm^2 from the experimental data at 160 K in Fig. 4. As a result, the activation energy for electron capture of trap A_5 is nearly equal to that for electron emission. This means that the net thermal depth of A_5 disappears in the configuration-coordinate description. Therefore, the dependence of the peak heights of A_4 and A_5 on the filling pulse duration is anomalous and cannot be explained within the framework of normal emission and capture kinetics.

In order to explain the characteristic behaviors of A_4 and A_5 , it is necessary to take account of some interaction among them. Because the reemission process mentioned above can be ignored, one possibility is that part of trapped electrons are transferred directly from the trap A_4 to A_5 . Another possibility is that a part of the trap A_4 is transformed into the trap A_5 . In other words, the component A_4 of the trap EL6 and the component A_5 of the trap EL5 are two states of a bistable center.

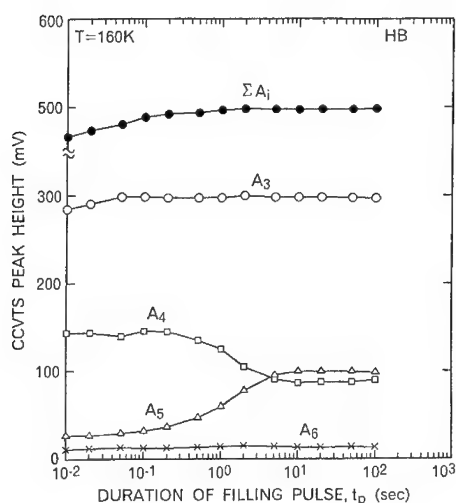


Fig. 4. Filling time dependence of CCVTS peak heights of the four individual traps.

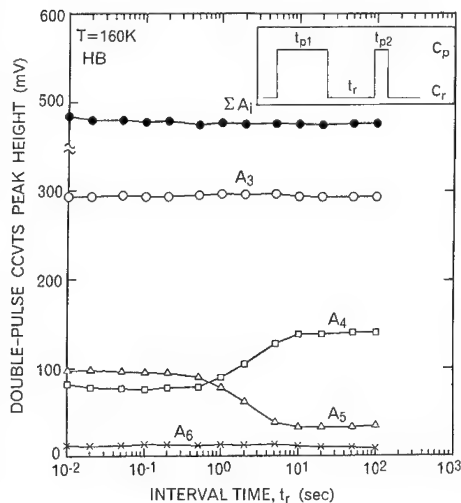


Fig. 5. Plot of double-pulse CCVTS peak heights of the four individual traps as a function of interval time between two correlated pulses. The inset illustrates the pulse sequence used in this study.

To clarify whether these traps are of bistable nature or not, we performed CCVTS measurements with two adjacent filling pulses. We selected the pulse width t_{p1} of 10 sec for the first pulse with which the trap A₄ and A₅ could reach their "steady-states". The pulse width t_{p2} of 0.1 sec was selected for the second pulse with which only A₄ could capture electrons from the conduction band. We performed CCVTS measurements as a function of interval time t_i between two correlated pulses. The electron occupation fractions of A₄ and A₅ could be controlled by selection of the interval time t_i . As a result, we can obtain the concentration of the filled A₄ trap just after the second pulse application and the concentration of the filled A₅ trap at the end of the selected interval time. We named this method "double-pulse CCVTS".

Figure 5 shows the interval time dependence of the double-pulse CCVTS peak heights of the four individual components measured at 160 K. The trap A₄ and A₅ remained in their "steady-states" for the interval time less than 0.2 sec. As the interval time increases, the peak height of A₄ gradually increases to about twice its initial value, while the peak height of A₅ decreases and saturates.

It is noticeable that the variations in peak heights of A₄ and A₅ as seen in Fig. 4 could be reversed by controlling electron occupation fractions of these traps just before the second pulse application. According to the carrier transfer model mentioned above, the peak height of A₄ should remain at its saturated value by electron capture during the second pulse application independent of the interval time t_i . Therefore, this reversible behavior is the direct evidence that the interaction between A₄ and A₅ is not due to the carrier transfer from one trap level to another one, but due to an electronically controlled bistable reaction. Further investigation of the interaction between EL5 and EL6 is in progress.

CONCLUSION

We investigated the electron emission and capture kinetics of EL5 and EL6 in the n-type bulk GaAs by using isothermal CCVTS and C-V measurements. Each CCVTS spectrum of EL5 and EL6 was found to consist of two trap components. Anomalous filling time dependence of CCVTS peak heights for these components was observed in a long range of filling pulse duration, i.e., one component of EL6 decreased to about 50 % of its maximum, while one component of EL5 increased and saturated. This variation in peak heights could be reversed by controlling electron occupation fractions of EL5 and EL6 by controlling the interval time between two adjacent filling pulses in the application of isothermal double-pulse CCVTS method. The interaction between these two levels was commonly observed in n-type bulk GaAs independent of carrier density and growth method. It was proposed that these components of EL5 and EL6 are bistable levels each other.

REFERENCES

1. Y. Kitagawara, N. Noto, T. Takahashi, and T. Takenaka, Appl. Phys. Lett., **48**, 1664 (1986).
2. Z. Q. Fang, T. E. Schlesinger, and A. G. Milnes, J. Appl. Phys., **61**, 5047 (1987).
3. J. H. Zhao, T. E. Schlesinger, and A. G. Milnes, J. Appl. Phys., **62**, 2865 (1987).
4. W. Siegel, G. Kuhnle, H. A. Schnider, H. Witte, and T. Flade, J. Appl. Phys., **69**, 2245 (1987).

-
5. H. Shiraki, Y. Tokuda, and K. Sassa, in *Defect Engineering in Semiconductor Growth, Processing and Device Technology*, edited by S. Ashok, J. Chevallier, K. Sumino, and E. Weber (Mater. Res. Soc. Proc. 262, Pittsburgh, PA, 1992) p.105.
 6. K. Tomizawa, K. Sassa, Y. Shimanuki, and J. Nishizawa, Inst. Phys. Conf. Ser., **91**, p.435 (1987) (Int. Symp. GaAs and Related Compound, Heraklion, Greece).
 7. T. Atami, K. Shirata, H. Takahashi, K. Sassa, and K. Tomizawa, Inst. Phys. Conf. Ser., **129**, p.25 (1992) (Int. Symp. GaAs and Related Compound, Karuizawa, Japan).
 8. Y. Tokuda, N. Shimizu, and A. Usami, Jpn. J. Appl. Phys., **18**, 309 (1979).
 9. Y. Tokuda, M. Hayashi, and A. Usami, J. Phys.D, **14**, 895 (1981).
 10. Z. Su, and J. W. Farmer, Appl. Phys. Lett., **59**, 1362 (1991).
 11. Z. Su, and J. W. Farmer, Appl. Phys. Lett., **59**, 1746 (1991).
 12. Z. Su, and J. W. Farmer, Mater. Sci. Forum, **83-87**, 817 (1992).

THE KINETICS OF CAPTURE AND EMISSION OF DISCRETE DX RELATED CENTERS IN
SILICON DOPED AlGaAs USING TIME ANALYZED TRANSIENT SPECTROSCOPY

SANDEEP AGARWAL* AND Y.N. MOHAPATRA**

*Dept. of Electrical Engineering

**Dept. of Physics, Indian Institute of Technology Kanpur - 208 016, INDIA

ABSTRACT

The kinetics of multiple DX related emission centers are studied using the isothermal Time Analyzed Transient Spectroscopy (TATS) of constant capacitance voltage transients. Four distinct emitting centers have been obtained using higher order TATS in the same silicon doped $\text{Al}_{0.33}\text{As}_{0.67}$ sample without use of hydrostatic pressure. Accurate identification of the multiple DX states has allowed a better understanding of the charge redistribution process during capture. Improved resolution due to increase in order of spectroscopy has enabled quantitative fitting of spectral lineshape and thus accounting for degree of nonexponentiality associated with each of the four discrete centers. The capture kinetics of these centers are studied over six orders in magnitude of filling time. The resulting quality of kinetic data makes possible detailed quantitative comparison with kinetics predicted by positive U and negative U models of DX centers. We show that our data is in agreement with positive U model of DX center.

INTRODUCTION :

Gallium arsenide and related III-V compound alloys, when doped with commonly used donor impurities from group IV and VI, give rise to the well known^{1,2} deep level defect called DX centers. Though there has been extensive studies on these centers using capacitance transient techniques such as deep level transient spectroscopy (DLTS), limitations inherent to this technique has inhibited a thorough quantitative understanding of trapping phenomena, specially in relation to the occurrence of multiple emission states associated with the same donor impurity. Though earlier studies on silicon related DX centers in AlGaAs has led to an identification of four silicon related donor states ascribed to alloy induced disorder², it has so far not been possible to test the model using

relative concentrations of these multiple levels. Moreover it is also known that these multiple levels are not independent centres and insufficient understanding of their coupling mechanism has led to severe problems both in interpretation and experimental observation of DX phenomena.

In addition, there is controversy regarding the charge state of these deep levels. Absence of EPR signal and recent *ab initio* calculations^{3,4} has led to a widespread belief that the Hubbard correlation energy of these centers is negative and therefore bind two electrons spontaneously instead of one. A study of time evolution of the multiple states has the promise of resolving this controversy as well.

In this work, the multiple DX related emission centers are studied using the isothermal Time Analyzed Transient Spectroscopy (TATS), which is demonstrated to be better suited for resolving multiple states and for detailed line-shape analysis. Four distinct features have been obtained using higher order TATS in the same silicon doped $\text{Al}_{0.33}\text{As}_{0.67}$ sample. A systematic observation of these levels has helped us in studying the kinetics of capture and emission of these multiple levels. This in turn enables us to test the statistics predicted by nearest neighbour alloy disorder models of multiplicity and more importantly the charge state of the DX centre. Our results are surprisingly in good agreement with positive U models of Si related DX centre in AlGaAs.

1. TIME ANALYZED TRANSIENT SPECTROSCOPY (TATS)

Since DLTS is a temperature scanning technique, the temperature dependence of the strength of transients and coupling between multiple states lead to a severe lineshape distortion of the spectrum⁵ even in the case of constant capacitance DLTS in which there is no non-exponentiality on account of high donor concentration. In general the lineshape of the DLTS spectrum depends on the activation energy and capture cross-section of the trap⁵. The difficulties inherent in DLTS processing of the DX emission transient have led us to explore spectroscopic methods which (a) do not involve temperature scanning, (b) do not have dependence of lineshape on trap parameters and (c) have sufficient resolving power to distinguish between closely spaced peaks. In this study we have used an isothermal method, termed time analyzed transient spectroscopy (TATS)¹⁴, which is based on the following general definition of n^{th} order spectroscopy (S_n) of an exponential transient:

$$S_n = \left(\frac{t}{\tau}\right)^n \exp\left(-\frac{t}{\tau}\right) \quad (1)$$

where (τ) is the time constant of the transient. TATS is implemented by finite difference realizations of differential operators, which in the limit $\Delta t \rightarrow 0$ give eqn.(1). Out of many possible realizations of TATS we have constructed our spectra as:

$$S_n(\ln(t)) = \sum_{i=0}^n A_i V(\ln(t) + n\alpha) \quad (2)$$

where V is the transient signal in $\ln(t)$ and α is a fixed difference in the $\ln(t)$ scale. For $n = 1$, and with a choice of $A_0 = 1$, $A_1 = -1$, $S_1(\ln(t))$ becomes the finite difference version of first order differentiation of the transient with respect to $\ln(t)$. In this case the TATS spectrum reduces to what is popularly referred to as rate window scan method. In general, $n > 1$ corresponds to higher order spectroscopy. Increasing the order of spectroscopy leads to smaller linewidths of the peaks thereby resulting in higher resolving power at the cost of signal to noise ratio and longer data storage. We have used several TATS realizations, each with a different trade-off between noise, resolution and data storage. For convenience we present our results in this letter using a TATS signal constructed as in eqn.(1) with a set of coefficients $\{A_i\}$ used for n^{th} order filtering of transient signals by Crowell and Alipanahi⁶.

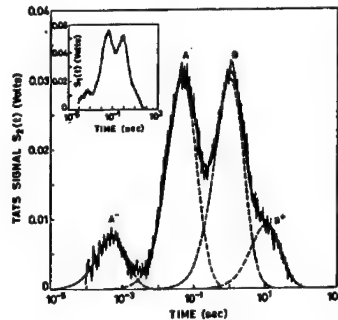
EXPERIMENTAL DETAILS

We have made constant capacitance transient measurements in silicon doped, MBE grown, $\text{Al}_{0.33}\text{Ga}_{0.67}\text{As}$ Schottky diodes. The doping concentration estimated by C-V measurement was $4 \times 10^{17} \text{ (cm)}^{-3}$. The experimental setup consisted of PC controlled acquisition of transients with capabilities for DLTS and TATS analysis. The capacitance was monitored using a Boonton model 72B Capacitance Meter. A Keithley 194A High Speed Voltmeter was used for digitization of voltage transients. Approximately 3×10^4 data points were acquired for each transient. Pulse filling was performed by zero-biasing the Schottky diode for the desired duration.

RESULTS AND DISCUSSION

Fig.1 shows a second order TATS spectrum of a transient acquired in a $x=0.33$ alloy sample, with a first order spectrum in the inset for comparison. The transient was obtained at a temperature $T=180$ K after a filling time of $50 \mu\text{s}$. The broken lines in the figure are simulated curves for individual centres each with a Gaussian distribution of activation energy of only 20 meV and the solid line is fitted to the sum of all the four such centres. Our results suggest that (a) there are four discrete DX related states, observable in the same sample even in high composition alloys, and (b) there is a small Gaussian distribution of activation energies of each of these states. The activation energies of the states were determined to be 0.305 , 0.395 , 0.447 and 0.479 eV and details of critical comparison with data collated from the literature will be given elsewhere⁷. The small broadening observed increases to a maximum of 30 meV for $x=0.5$ composition indicating that its origin related to long range disorder.

FIGURE 1: Second order TATS spectrum of DX center measured at 180 K with a fill pulse duration of $50 \mu\text{s}$. Inset depicts the corresponding first order TATS spectrum. Solid and Dashed lines are the fitted curves (see text).



The relative concentrations of the four peaks are dependent on the time for which capture is allowed to occur. From fitting of TATS curves of the for each filling time, we obtain the time development of relative concentrations of the four states. Figure 2 shows a typical set of curves for two different temperatures and compositions. Note that the time axis is in log scale and changes occur over six orders of magnitude in time. The time evolution of the concentrations are non-monotonic⁹⁻¹⁰. This effect has been attributed to charge distribution¹⁰ among the multiple levels. The occupancy of the shallower states increase initially, losing out their carriers to the deeper ones through emission to the conduction band.

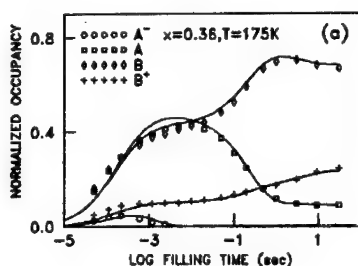


FIGURE 2: Time Evolution of occupancies of the four DX states as a function of logarithm of filling time.

The origin of four distinct centers has mostly been attributed to the existence of four distinct second nearest neighbour (nn) alloy configurations of the deep donor^{2,8}. It is claimed that the peaks A⁻, A, B and B⁺ correspond to four different nn configurations of Gallium and Aluminum, i.e. (3 Ga, 0 Al), (2 Ga, 1 Al), (1 Ga, 2 Al) and (0 Ga, 3 Al) respectively. One of the crucial issues in the study of DX center has been the validation of this hypothesis. The time evolution of occupancies of the four levels would according to this hypothesis be controlled by the statistics predicted by the nearest neighbor alloy and the the number of electrons involved in the transitions.

Since each silicon atom can relax to any of the four possible interstitial sites there can be 35 different distributions associated with each stae. Hence this demands solution of 35X4 coupled kinetic equations. However not all interstitial configurations are present in each distribution and the set of equations reduces to 80. The set of ordinary first order coupled differential eqauations have been solved numerically with the assumption that all electrons in the sample are coming from silicon donors. Only those density of states are included in the computation which are more than 0.05% of the total defect concentration. Hence the number of equations used varies from 7 at $x=0.04$ to a maximum of 80 at $x=0.5$. The experimentally obtained values of emissiion rates are used. Hence only the capture coefficients and realistic values of compensation are used as fitting parameters. The solid lines in Fig.2 correspond to the solution obtained from such a calculation assuming that DX is a positive U state. We find that the nature of coupling is such that time evolution of occupancy cannot be reconciled to negative U model of the defect. Specially if realistic values of compensation in these sample is taken into account the statistics of negative U fails to explain the

experimental data miserably. Note that model distinction is stark around the composition range $x=0.3$ since all the four states have significantly noticeable change in occupancy with filling.

It is important to point out that though large number of equations are involved in model calculations, the coupling between the states over such wide range of time, temperature and composition put severe restrictions on fitting. It is in fact remarkable that such good fits to four variables over 5-6 orders of magnitude can be obtained in spite of such severe constraints of statistics. We also find that our fitting is extremely sensitive to composition and hence our results provide the first quantitative test of nearest neighbor alloy disorder origin of multiple states.

In summary, we have presented evidence for the existence of four DX related centers, all observed in the same high composition aluminum gallium arsenide sample using an isothermal method termed TATS. The time evolution of the occupancies of the four states can be reconciled to a positive U model of the defect in conjunction with statistics predicted by nearest neighbor alloy disorder of multiple levels.

ACKNOWLEDGEMENTS:

We are grateful to Dr. B.M. Arora and Dr. S. Anand for providing the samples and to R. Sharan and Vijay A. Singh for thoughtful suggestions and comments.

REFERENCE LIST

1. D.V. Lang in *Deep Centers in Semiconductors*, edited by S.T. Pantelides (Gordon and Breach, New York, 1986), chapter 7; P.M. Mooney, J. Appl. Phys. 67, R1 (1990).
2. P.M. Mooney, J. Appl. Phys. 67, R1 (1990)
3. D.J. Chadi and K.J. Chang, Phys. Rev. Lett. 61, 873 (1988)
4. D.J. Chadi, Phys. Rev. B 46, 6777 (1992).
5. S. Agarwal, Y.N. Mohapatra and V. A. Singh, J. Appl. Phys. (in press)
6. C.R. Crowell and S. Alipanahi, Solid St. Electron. 24, 25 (1980).
7. S. Agarwal, Y.N. Mohapatra, V.A. Singh and R. Sharan, J. Appl. Phys. (1995) in press
8. T.N. Morgan, J. Electron. Matls. 20, 63 (1991)
9. Y.N. Mohapatra and V. Kumar, J. Appl. Phys. 68, 3431 (1990).
10. Z. Su and J.W. Farmer, Appl. Phys. Lett. 59, 1746 (1991).

DX-LIKE CENTERS IN IV-VI

DMITRIY R. KHOKHLOV

Physics Department, Moscow State University, Moscow 119899, Russia

ABSTRACT

Up to the recent times it was believed that observation of the DX-centers is restricted to the rather wide-bandgap III-V and II-VI semiconductors. However it becomes obvious now that some of the narrow-gap IV-VI semiconductors doped with the group III elements reveal the features of DX-centers. A range of features, such as negative-U behavior, large lattice relaxation, metastability of the local excited states, narrow bandgap - make the effects resulting from the DX-like behavior much more complicated than in the "classical" materials with the DX-centers. We review the most unusual recent results obtained in the field that originate from the specifics of the DX-like centers in IV-VI.

INTRODUCTION

The problem of DX-centers in semiconductors attracts a lot of experimental and theoretical efforts for more than 15 years. The main feature of these centers is a strong electron-lattice coupling leading to formation of a barrier in the configuration-coordinate space between the states of a system with the different number of localized electrons. Besides, strong polarization of a lattice in the impurity environment results in some cases in the negative-U character of impurity centers. This combination leads to the appearance of a range of unusual effects due to the impurity subsystem, such as Fermi level pinning, persistent photoconductivity and photomemory¹.

Specific features of the DX-centers are extensively used in the modern physics of semiconductors. Until recently investigation of the DX-centers was restricted to the rather wide-bandgap III-V and II-VI semiconductors. The microscopic structure of the DX-centers in III-V is quite well established now both experimentally and theoretically^{1,2}.

Impurity states in the mostly narrow-gap IV-VI semiconductors reveal a lot of specifics. Huge values of a dielectric constant and small effective masses make the binding energy of the hydrogen-like states extremely small, and all of the observed levels of impurities or defects are deep³.

Up to the recent times it was believed that the DX-centers are absent in the narrow-gap semiconductors, in particular, in the IV-VI materials. However it turned out that the properties of impurity centers arising in the group III-doped IV-VI semiconductors are quite similar to the features of the DX-centers. For instance, the Fermi level pinning and the persistent photoconductivity have been observed³. On the other hand there is a considerable difference from the effects due to the "classical" DX-centers in the relatively wide-gap III-V and II-VI semiconductors.

First of all, the characteristic energies of the photoconductivity spectra are much smaller than in the III-V and II-VI materials with the DX-centers, and are comparable with the value of the LO-phonon energy. It results, first, in a considerable experimental difficulties since it requires an extremely thorough screening of a sample from the background infrared radiation. Any part of the

experimental setup with the temperature above 10 K may be the source of such a radiation. Secondly, this circumstance does not allow to separate in energy the effects defined by the electron and the lattice subsystems.

Besides that, the long-term relaxation processes and the metastable electronic states may be observed in IV-VI irrespectively on the position of the impurity level³, in contrary to the DX-centers in III-V and II-VI, for which this kind of effects arise in most of the cases when the DX-state energy level lies within the gap¹.

Finally, the excited one-electron impurity states are shallow for the "classical" DX-centers, whereas they are deep and metastable for the IV-VI³, i.e. they are separated by a barrier in the configuration-coordinate space from both ground impurity states and the extended electron states. It is the most crucial circumstance that results in the appearance of a range of strong and unusual non-equilibrium effects. The most interesting of them are reviewed in the this paper.

PHENOMENA RELATED WITH THE DX-LIKE CENTERS IN IV-VI

Giant negative magnetoresistance

If $\text{Pb}_{1-x}\text{Sn}_x\text{Te}$ alloys are doped with indium in an amount exceeding the concentration of other electrically active impurities or defects, then the Fermi level E_F becomes pinned by the deep "DX-like" level. The position of this pinned E_F with respect to the conduction and the valence band edges is defined by the alloy composition. For $x < 0.22$ E_F lies within the conduction band, in the tin content range $0.22 < x < 0.28$ it crosses the gap, and enters the valence band at $x > 0.28$ giving rise to the free hole concentration⁴. When the Fermi level is pinned within the gap, the dielectric state of a system is realized. In this state the free carrier concentration in thermal equilibrium is defined only by the thermal excitation from the DX-like level. It results in an extremely high alloy resistivity $\rho > 10^6 \Omega\cdot\text{cm}$ at the liquid helium temperatures since the ground impurity states are very well localized, and the conductivity via the impurity level is practically absent. In these conditions the sample conductivity becomes non-Ohmic, it is defined by the monopolar electron injection⁵.

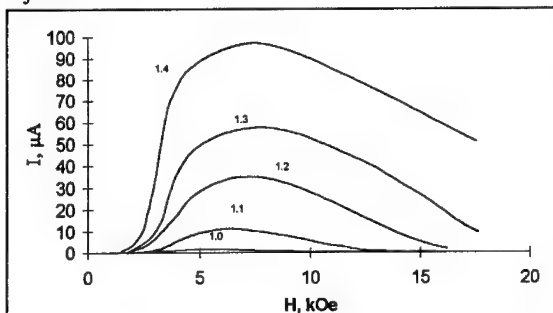


Fig.1. Dependence of the sample current on the magnetic field applied for $\text{Pb}_{0.75}\text{Sn}_{0.25}\text{Te}(\text{In})$ at $T = 4.2 \text{ K}$ ⁵. The figure near the curve is the voltage applied to the sample (in V).

The effect of giant negative magnetoresistance has been observed for this kind of alloy $\text{Pb}_{0.75}\text{Sn}_{0.25}\text{Te}(\text{In})$ where the Fermi level is pinned in the gap, at $\sim 25 \text{ meV}$ below the bottom of the conduction band⁵. The sample was cooled down to $T = 4.2 \text{ K}$. Then the DC voltage was applied to the sample contacts, and the sample current I was measured as a function of the magnetic field applied H . The experiment results are shown in Fig.1. It turns out that there is a pronounced maximum of conductivity at $H_{\text{max}} \sim 0.5 \text{ T}$, i.e. the negative magnetoresistance effect.

The effect amplitude is really giant: the ratio $I(H_{\max})/I(H=0)$ may exceed 10^6 depending on the voltage applied.

The above-mentioned effect was the first observed manifestation of the metastable impurity states in the galvanomagnetic effects in the group III-doped IV-VI. The explanation proposed in the paper ⁵ to account for the effect is the following. Application of a voltage to the cooled sample results in the injection of electrons from the contacts. The injected electrons become trapped to the metastable excited local states that lie in energy lower than the conduction band bottom. These states are separated by a barrier in the configuration-coordinate space from both ground impurity states and extended electron states. Application of a magnetic field pushes the metastable local level above the conduction band bottom, and the trapped injected electrons transfer to the conduction band giving rise to the sample conductivity.

Selective photoconductivity

The gallium-doped PbTe reveals the Fermi level pinning and the persistent photoconductivity effects, as well as the indium-doped lead telluride-based alloys ⁶. However there are some differences from the case of indium doping. First of all, the Fermi level is pinned in PbTe(Ga) only in some definite gallium content range $N_{\text{Ga}}^{\min} < N_{\text{Ga}} < N_{\text{Ga}}^{\max}$. Outside of this range gallium acts as a donor impurity, and the Fermi level lies in one of the allowed bands. When $N_{\text{Ga}}^{\min} < N_{\text{Ga}} < N_{\text{Ga}}^{\max}$ the Fermi level is pinned close to the middle of the bandgap providing the seminsulating state of the semiconductor. The Fermi level pinning effect was reported to exist in some other gallium-doped lead telluride-based alloys $\text{Pb}_{1-x}\text{Mn}_x\text{Te}(\text{Ga})$ and $\text{Pb}_{1-x}\text{Ge}_x\text{Te}(\text{Ga})$ ^{7,8}. The persistent photoconductivity effect in all of the Ga-doped lead telluride-based alloys is observed at $T < T_c = 80 \text{ K}$. The features of this effect look quite analogous to the case of the indium-doped materials, so it is reasonable to consider the origin of the DX-like behavior to be the same.

A peculiar feature of the photoconductivity in PbTe(Ga) is the appearance of the selective far-infrared photoresponse at $\omega_0 \sim 155 \text{ cm}^{-1}$ (Fig.2) ⁹. This effect is very unusual and quite surprising. Indeed, the energy corresponding to the photoresponse wavelength is much smaller than any characteristic energy of the electronic spectrum, i.e. the energy gap and the thermal

excitation energy of the ground impurity state. On the other hand, ω_0 is quite close to the energy of the LO-phonon in PbTe $\omega_{\text{LO}} = 110 \text{ cm}^{-1}$. Therefore it looks reasonable to consider this photoconductivity line as originating from the optical excitation of a local vibrational mode. The mechanism of the photoresponse could be the following. The background radiation excites one electron from the ground two-electron impurity state, and the impurity center is transferred to the metastable one-electron local state lying nearby the bottom of the conduction band. If then the local vibrational mode is excited by the incident

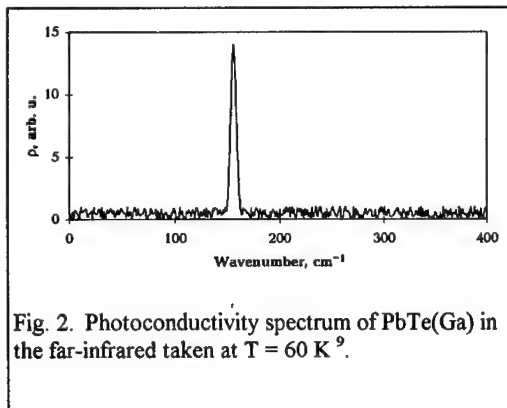


Fig. 2. Photoconductivity spectrum of PbTe(Ga) in the far-infrared taken at $T = 60 \text{ K}$ ⁹.

far-infrared radiation, the electron localized on a metastable impurity state may overcome small

barriers separating it from the conduction band and thus may take part in the photoconductivity. As the excitation of a local mode is resonant in frequency, the photoresponse should be resonant, too⁹.

Microwave effects

Strong photoresponse observed in the In- and Ga-doped lead tin tellurides has made very attractive the idea to construct the infrared detector based on these materials. Using of the persistent photoconductivity effect for the purpose of radiation detection has a considerable advantage: the incident radiation flux is internally integrated in the photodetector. On the other hand, one needs to know how to return the sample quickly to the initial "darkness" state in order to be able to operate in the regime of periodical accumulation and successive fast quenching of the photosignal.

The problem of the persistent photoconductivity quenching in $\text{Pb}_{1-x}\text{Sn}_x\text{Te(In)}$ was most effectively solved by application of the strong and short microwave pulses to the sample¹⁰. The complete and stable quenching of the accumulated photosignal for 10 μs was possible with the help of this technique. The microwave frequency in the pulse was ~ 300 Mhz with the power of 0.9 W. All the applied aspects of the problem and the parameters of a respective photodetector are summarized in¹¹. Here we will concentrate mostly on the new effects appearing under the action of the microwave radiation.

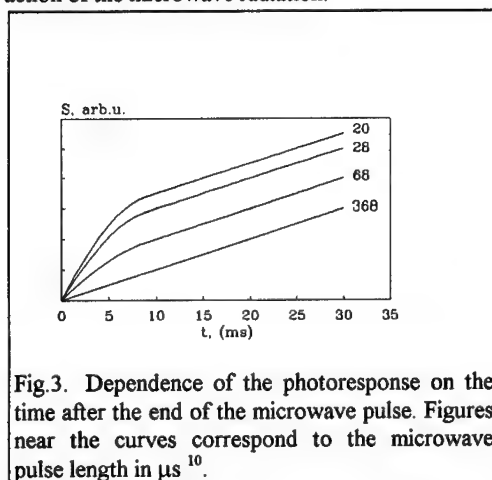


Fig.3. Dependence of the photoresponse on the time after the end of the microwave pulse. Figures near the curves correspond to the microwave pulse length in μs ¹⁰.

Application of a short microwave pulses not only quenches the persistent photoconductivity, but affects also the photoresponse after the end of the pulse. It was shown in¹⁰, that if the persistent photoconductivity is quenched by the pulses of minimal necessary length and amplitude, the quantum efficiency η of a photoresistor increases up to $\sim 10^2$, whereas out of this regime of quenching $\eta \sim 1$ (Fig.3).

The qualitative scheme of the processes involved proposed in¹⁰ is the following. Application of the short microwave pulse leads to the transition of electrons from the conduction band to the metastable state. The barriers separating

these states from the extended and the ground ones are rather small ($W \sim 1 \text{ meV}$ ¹²), that is why the longer microwave pulse returns all previously excited electrons to the ground local state. So the short microwave pulse results in the excess population of the metastable states. Some of the metastable centers may form a cluster with strong internal interaction. Under these conditions excitation of one electron from this cluster to the extended state leads to reconstruction of the center crystalline surrounding and to the avalanche transition of electrons localized on the metastable centers in the cluster to the conduction band. The result is the increase of the quantum efficiency.

The microwave quenching of the persistent photoconductivity is due to the direct interaction of the microwave radiation with free electrons. Indeed, no lattice heating after the microwave pulse has been observed¹³. One of the possible explanations of the microwave quenching effect is heating of electron gas not accompanied by the lattice heating. In this case one would expect independence of the quenching efficiency on the microwave frequency. However there exists some evidence that this effect is resonant in frequency. The following experiment has been performed in¹⁴. A $\text{Pb}_{1-x}\text{Sn}_x\text{Te(In)}$ sample cooled down to 4.2 K was included in two electric circuits. The first one was used for the DC measurements of the sample conductivity, the second - for the microwave "pumping" of the sample. The microwave generator could sweep the frequency in the range (0-500) MHz. The pumping power was ~ 50 mW, which is much lower then the minimal power necessary for quenching ~ 900 mW. The dependence of the sample DC conductivity σ as a function of a pumping frequency ω has been measured. In the initial "darkness" state there was no conductivity in all frequency range (fig.4). As the infrared radiation

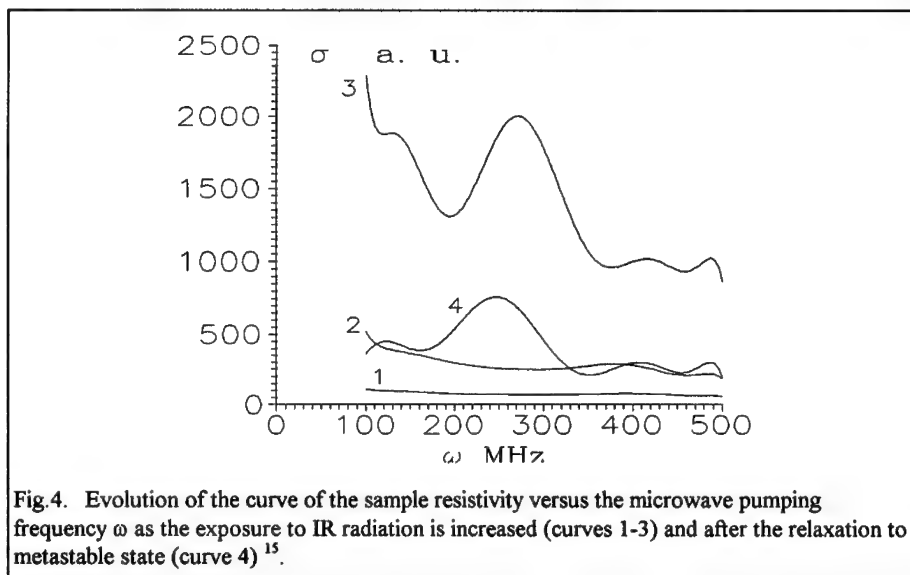


Fig.4. Evolution of the curve of the sample resistivity versus the microwave pumping frequency ω as the exposure to IR radiation is increased (curves 1-3) and after the relaxation to metastable state (curve 4)¹⁵.

exposure increased, a sharp peak on the $\sigma(\omega)$ dependence appeared on the background of a total conductivity rise. After the infrared radiation source was switched off, the conductivity slowly relaxed to the initial state, but the rate of this relaxation was much higher out of the peak, then in the peak region. So one could reach the state when the sample conductivity was absent for all the frequencies except for the region of a peak. It is interesting to note that there was no zero-frequency DC conductivity. Position of this peak did not depend on the electric field applied, but depended strongly on magnetic field. Sensitivity of the sample conductivity in the region of the peak to the action of the infrared radiation was much higher then for the initial "darkness" state of a sample. It is clear that though all of the electrons are localized, as it is evidenced from the absence of the DC conductivity at $\omega = 0$, the state of the system is different from the initial "darkness" one. The authors of¹⁴ do not give any clear interpretation of the effect, but there is some evidence to believe that it is related with the quantum efficiency stimulation effect. Indeed, both of them are observed in the same microwave frequency range. One can expect that the relaxation to metastable impurity states plays an important role in both these effects.

SUMMARY

The unusual non-equilibrium effects observed in the group III-doped IV-VI semiconductors are not restricted to those reviewed in the present paper, their range is much more wide. The idea of this paper is to demonstrate that the features of the impurity centers appearing in the above-mentioned materials are in many respects similar to the DX-centers in III-V and II-VI. However the physics of the DX-like centers in IV-VI is much more complicated, mainly due to the fact that the metastable impurity states play an important role in the non-equilibrium processes.

ACKNOWLEDGMENTS

The research described in this paper was supported in part by Grant No. MBB300 from the International Science Foundation and the Russian Government, by Grant of the Russian Foundation for the Fundamental Research and by Grant of the Dutch Organization of the Scientific Research (NWO).

REFERENCES

1. P.M.Mooney, J. Appl. Phys., **67**, R1 (1990).
2. D.J.Chadi and K.J.Chang, Phys. Rev. Letters **61**, 7 (1988).
3. B.A.Akimov, A.V.Dmitriev, D.R.Khokhlov and L.I.Ryabova, Phys. Stat. Sol. (a) **137**, 9 (1993).
4. B.A.Akimov, L.I.Ryabova, O.B.Yatsenko and S.M.Chudinov, Fiz. Tekh. Poluprovodn. **13**, 752 (1979) [Sov. Phys. Semicond. **13**, 441 (1979)].
5. B.A.Akimov, A.V.Nikorich, D.R.Khokhlov and S.N.Chesnokov, Fiz. Tekh. Poluprovodn. **23**, 668 (1989) [Sov. Phys. Semicond. **23**, 418 (1989)].
6. B.A.Akimov, N.B.Brandt, A.M.Gas'kov, V.P.Zlomanov, L.I.Ryabova and D.R.Khokhlov, Fiz. Tekh. Poluprovodn. **17**, 87 (1983) [Sov. Phys. Semicond. **17**, 53 (1983)].
7. B.A.Akimov, S.A.Belokon', Z.M.Dashevskiy, K.N.Egorov, V.M.Lakeenkov, A.V.Nikorich, and L.I.Ryabova, Fiz. Tekh. Poluprovodn. **25**, 250 (1991).
8. B.A.Akimov, A.V.Albul, I.I.Ivanchik, L.I.Ryabova, E.I.Slyn'ko and D.R.Khokhlov, Fiz. Tekh. Poluprovodn. **27**, 351 (1993).
9. A.I.Belogorokhov, I.I.Ivanchik and D.R.Khokhlov, Proceedings SPIE **1575**, 3476 (1991).
10. B.A.Akimov and D.R.Khokhlov, Semicond. Sci. Technol. **8**, S349 (1993).
11. S.N.Chesnokov, D.E.Dolzhenko, I.I.Ivanchik and D.R.Khokhlov, Infrared Phys. **35**, 23 (1994).
12. I.I.Zasavitskiy, A.V.Matveenko, B.N.Matsonashvili and V.T.Trofimov, Fiz. Tekh. Poluprovodn. **20**, 214 (1986) [Sov. Phys. Semicond. **20**, 135 (1986)].
13. B.A.Akimov, N.B.Brandt, D.R.Khokhlov and S.N.Chesnokov, Pis'ma v Zh. Tekh. Fiz. **14**, 731 (1988) [Sov. Tech. Phys. Lett. **14**, 325 (1988)].
14. D.E.Dolzhenko, I.I.Ivanchik, A.V.Nikorich, D.R.Khokhlov and S.N.Chesnokov, Pis'ma v Zh. Eksp. Teor. Fiz. **55**, 125 (1992) [Sov. Phys. - JETP Lett. **55**, 119 (1992)].

LOW TEMPERATURE ANNEAL OF THE DIVACANCY IN p-TYPE SILICON

M.-A. TRAUWAERT, J. VANHELLEMONT, H. E. MAES, A.-M. VAN BAVEL*,
G. LANGOUCHE*, A. STESMANS* and P. CLAUWS**
IMEC, Kapeldreef 75, B-3001 Leuven, BELGIUM
*K. U. Leuven, Celestijnenlaan 200D, B-3001 Leuven, BELGIUM
**U. Gent, Krijgslaan 281-S1, B-9000 Gent, BELGIUM

ABSTRACT

Results are reported of a Deep Level Transient Spectroscopy (DLTS) study of the conversion of the divacancy, with energy level at $E_v+0.19\text{eV}$, to a level at $E_v+0.24\text{eV}$ after anneal at temperatures below its dissociation temperature (300°C). In literature both levels have been associated with the donor level of the divacancy.

Diodes processed on p-type Float Zone (FZ) and Czochralski (Cz) silicon wafers with boron concentration between 0.2 and $3 \times 10^{15} \text{ cm}^{-3}$ are irradiated with 2 MeV electrons. Before and after anneal (200°C and 250°C) DLTS spectra are recorded to get a full electrical characterisation of the induced defects.

The observed conversion is proposed to be a gradual transformation of the divacancy to a divacancy-oxygen complex.

INTRODUCTION

The silicon divacancy has been extensively studied by using a wide range of experimental techniques. Three deep levels in the silicon bandgap are identified to belong to the divacancy: a donor level in the lower half of the bandgap and two acceptor levels in the upper half (V_2^{\pm} at $E_c-0.23\text{eV}$ and V_2^0 at $E_c-0.42\text{eV}$). However, a dispersion of experimental values for the energy position of the donor level ($V_2^{0/+}$) is found in literature with values reported around either $E_v+0.20\text{eV}^{1-3}$ or $E_v+0.24\text{eV}^{4-6}$. Londos measured an activation energy of 0.19eV for the 80K irradiation induced divacancy and assumed that this lower value is due to a Si self-interstitial which is loosely bond to the divacancy.⁷ During heating to room temperature, he observed an increase of the activation energy as the complex dissociates, liberating the Si self-interstitials. In n-type silicon an anomalous annealing behaviour of the divacancy was reported by Wang and co-workers.⁸ A two step annealing process was proposed, whereby the divacancy partially converts to another complex at low temperature ($240-300^\circ\text{C}$), while at higher temperatures the dissociation process dominates.

In the present paper the thermal behaviour of the divacancy in p-type silicon at temperatures below its annealing temperature is investigated by means of the DLTS technique. DLTS is well-known to be a very sensitive electrical characterisation

technique, presenting however the drawback that only the signature (activation energy and capture cross-section) and the concentration of the deep levels are deduced, without giving any structural or chemical information. For defect identifications one has therefore to rely on literature or on correlation with other techniques.

EXPERIMENTAL RESULTS

Two types of n^+p diodes were investigated, processed on Cz and FZ p-type silicon wafers, with measured interstitial oxygen content after diode processing of about 10^{18}cm^{-3} and less than 10^{16}cm^{-3} , respectively. The background boron concentration is $2.6 \times 10^{15}\text{cm}^{-3}$ for the Cz specimen and $1.8 \times 10^{14}\text{cm}^{-3}$ for the FZ ones. The irradiations are performed with a 2-MeV electron beam at fluences ranging between 5×10^{14} and $2 \times 10^{16}\text{cm}^{-2}$. During the irradiation the samples are kept below 50°C by means of water- and forced air-cooling. Anneal treatments are performed at 200°C and 250°C , with the samples encapsulated in vacuum quartz tubes or within an argon environment to minimise contamination during anneal.

Figure 1 shows a typical DLTS spectrum obtained on an irradiated p-type Cz diode before (full line) and after (dotted line) the low temperature anneal.

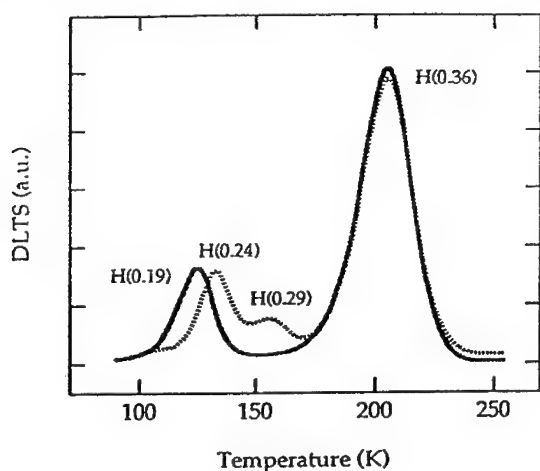


Figure 1
A typical DLTS spectrum (rate window = 223s^{-1}) of a 2-MeV electron irradiated p-type Cz diode before (full line) and after (dotted line) anneal at 200°C for 10 days. The typical reverse voltage and the filling pulse height were 5V and 4.5V, respectively. H refers to hole traps with the emission energy given in eV between brackets.

Each DLTS band corresponds to an energy level in the silicon bandgap. The activation energy of the defect level can be deduced by following the capacitance transient resulting from the thermal emission of trapped carriers from the deep energy levels within a depletion region towards the energy bands, as a function of temperature. In principle the capture cross-section is obtained from a semilog plot of the fraction of traps remaining empty at the end of the filling pulse versus the

filling pulse duration. The slope of the theoretical appearing straight line is proportional to the capture rate. However, due to capture in the carrier tails, deviations from the straight lines are observed. A first order correction can be performed following Meijer et al.⁹, by subtracting the edge region contribution from the measurement data, as shown in Figure 2. However, the fact that the fitted straight line through the data does not contain the point (0,0), indicates that the influence of the edge region has not completely vanished.

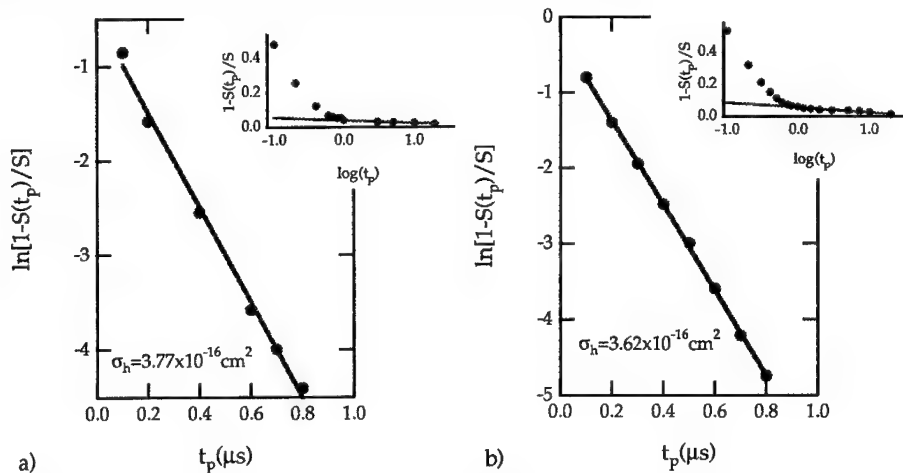


Figure 2

Capture cross-section of the hole levels a) H(0.19) and b) H(0.36): measured DLTS band height $S(t_p)$ at 120 and 205K, respectively. The inset shows the edge region contribution. The experimental data after subtraction this contributing are plotted in the main graph.

The H(0.36) band is a majority carrier trap with an activation energy $(0.360 \pm 0.005)\text{eV}$ and a hole capture cross-section $\sigma_h = 3.6 \times 10^{-16} \text{ cm}^2$. This deep level is associated with a C_iO_i -complex in the Cz substrates and with a C_iC_s -complex in the FZ ones, based on correlation with photoluminescence measurements.^{10, 11} The defect band with an energy level at $E_v + (0.192 \pm 0.005)\text{eV}$ and capture cross-section $\sigma_h = 3.8 \times 10^{-16} \text{ cm}^2$ is reported in literature to be the donor level of the divacancy. After anneal the H(0.36) level remains almost unchanged as the C_iO_i complex is one of the most stable complexes (stability: 400-425°C) of all the observed interstitials-related deep levels in silicon.¹ A new level H(0.29) is observed, correlated by Kimerling and co-workers with the B_iC_s -complex.¹² This complex is formed at 150°C, following the dissociation of the B_iO_i complex, which acted as a minority trap in p-type silicon before anneal. The most surprising observation however, is the apparent gradual transformation with increasing anneal time of the H(0.19) band to a new DLTS band with activation energy 0.24eV and $\sigma_h \sim 10^{-14} \text{ cm}^2$. This defect level has also been associated in literature with the donor level of the divacancy.

DISCUSSION

The conversion from H(0.19) to H(0.24) during the low temperature anneal does not happen at once. The p-type FZ diodes show the appearance of intermediate DLTS bands after anneal times between 5 and 10 days at 200°C. The H(0.19) band is still present in the FZ diodes after a 5 day anneal at this temperature. In 8 days annealed samples the DLTS band replacing the H(0.19) level corresponds to an energy level at $E_v+0.22\text{eV}$. Only after 10 days at 200°C we observe a final band H(0.24). Annealing of 20 days at 200°C reveals no further effect. For anneals performed at 250°C the transformation time is of the order of hours. On the other hand the H(0.19) band was still present in the DLTS spectrum after storing the samples at room temperature for more than 1 year.

In Cz substrates a similar conversion behaviour is observed, but after much shorter anneal times. After an anneal of only 5 days at 200°C the H(0.19) level is already completely converted into the H(0.24) level. The isothermal anneal behaviour at 250°C of the divacancy in Cz diodes has been followed in detail and the result is shown in Figure 3. Again the gradual evolution is observed from 0.19eV to 0.24 eV but only after passing through a minimum after an anneal of 20 minutes. A similar minimum is also observed during isothermal anneal treatments at 240 and 270°C.

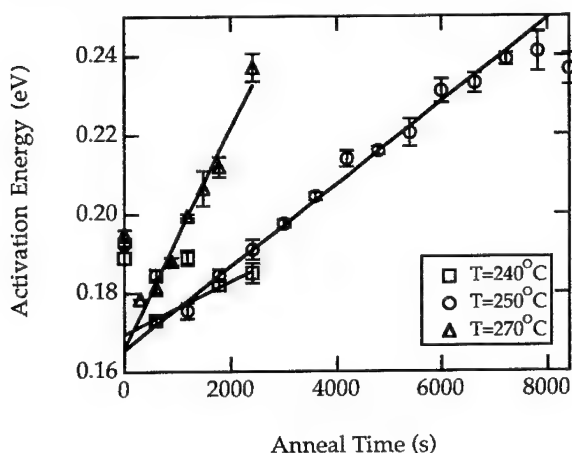


Figure 3

Changes in activation energy of H(0.19) due to isothermal annealing at 240, 250, and 270°C.

It is unlikely that the observed gradual evolution from H(0.19) to H(0.24) is due to a continuous transformation of the defect structure. An alternative explanation is that two different defect complexes are involved. The proposed mechanism is that during thermal treatments the initial (I) band will gradually anneal out, accompanied by the gradual appearance of the final (F) band. The observed intermediate DLTS spectra result from the superposition (S) of the DLTS bands related with the initial and the final defect structures: $S = I_{1-x} + F_x$ with x the fraction of the initial state which has already annealed out. However, due to the insufficient resolution of the DLTS system on the one side and to the specific defect parameters of the initial and final state on the other side, it is not possible to observe two

different well-resolved DLTS bands. The linear relationship between the activation energy, extracted from the isothermal anneal experiment, and the anneal time (Figure 3), suggests that the initial defect structure might have a lower activation energy than 0.19eV. Extrapolation of the straight lines through the data gives $(0.167 \pm 0.002)\text{eV}$. The average of the experimentally determined activation energies after long enough anneal times equals $(0.236 \pm 0.005)\text{eV}$. Corresponding capture cross-sections can be determined in a similar way yielding $(0.8 \pm 0.1) \times 10^{-16}\text{cm}^2$ and $(1.1 \pm 0.5) \times 10^{-14}\text{cm}^2$. Using the above determined signatures for the initial (I) and final (F) defect, the simulation shows that one always obtains one DLTS band with an apparent activation energy and apparent capture cross-section between 0.16eV and 0.24eV and between 10^{-16}cm^2 and 10^{-14}cm^2 respectively. By comparing the performed simulations with the experimental observations, the remaining fraction of the initial state as a function of the anneal time is determined (Figure 4).

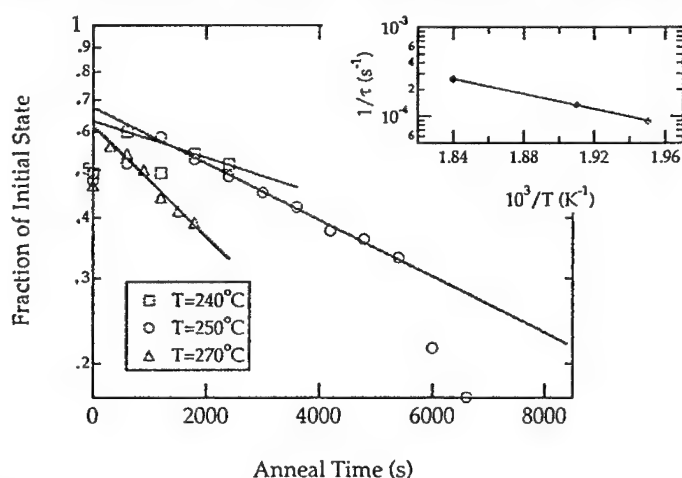


Figure 4

Fraction of initial state as a function of annealing time at various temperatures. In the inset: the annealing rate of the initial state as obtained from the main figure, versus inverse temperature.

The annealing reaction in the considered time interval is likely to be first order and may be fitted by a simple exponential expression of the form: $N(t) = N_0 \exp(-t/\tau)$, giving the thermally activated annealing rate $1/\tau = 2 \times 10^3 \exp(-0.85\text{eV}/kT) \text{s}^{-1}$. Wang et al. reported an annealing rate of $3 \times 10^3 \exp(-0.86\text{eV}/kT) \text{s}^{-1}$ dominating in the temperature range from 240 to 300°C for the divacancy in n-type silicon.⁸ The most important still remaining question is the nature of both (initial and final) defect structures. Recently, Londo assumed an interaction with a Si self-interstitial to explain the lower energy value.⁷ In his opinion the $E_V + 0.24\text{eV}$ level corresponds thus with the divacancy. Observations reported in previous work indicate that oxygen plays a role in the transformation.¹³ In oxygen rich wafers (Cz) much shorter anneal times are required to reach the $E_V + 0.24\text{eV}$ level, compared with the oxygen poor ones (FZ).

Based on these observations it is proposed that the observed defect conversion is a transformation of the divacancy into a V_2O complex (H(0.24)). Oxygen is present in

much higher concentration in the Czochralski wafers leading to the observed faster conversion.

Furthermore the high temperature isochronal (from 250 to 400°C, during 15-min.) annealing behaviour of the final H(0.24) level is consistent with results reported in literature for V₂O complexes as reported by Lee and Corbett.¹⁴

There are also some indications from the performed isochronal anneals that the complex formation has still not come to an end. Activation energies are determined of E_V+0.24eV, E_V+0.26eV and E_V+0.29eV after a 15-min. anneal at respectively 200°C, 300°C and at 360°C. These DLTS bands might originate from the formation of multivacancy-oxygen complexes.

ACKNOWLEDGEMENT

Part of this work was performed under IIKW contract 4.0007.93. M.-A. Trauwaert is indebted to the Flemish Fund for Technological Research (IWT) for her fellowship. A.-M. Van Bavel is indebted to the Belgian Fund for Scientific Research (NFWO) for her fellowship. W. Mondelaers is acknowledged for the 2 MeV electron irradiations which were performed in the linear accelerator (LINAC) of the University of Gent.

REFERENCES

- 1 P. J. Drevinsky, C. E. Caefer, L. C. Kimerling and J. L. Benton, *Defect control in Semiconductors* (Amsterdam, Elsevier, 1990), p. 341.
- 2 C. A. Londos, *Phys. Rev. B* **35**, 7511 (1987).
- 3 M. Asghar, M. Zafar Iqbal and N. Zafar, *J. Appl. Phys.* **73**, 4240 (1993).
- 4 P. M. Mooney, L. J. Cheng, M. Süli, J. D. Gerson and J. W. Corbett, *Phys. Rev. B* **15**, 3836 (1977).
- 5 G. D. Watkins and J. W. Corbett, *Phys. Rev.* **138**, 543 (1965).
- 6 L. C. Kimerling, *Proceedings of the International Conference on Radiation Effects in Semiconductors* (Dubrovnic, 1976), p. 221.
- 7 C. A. Londos, *Phys. Stat. Solidi (a)* **132**, 43 (1992).
- 8 F. P. Wang, H. H. Sun and F. Lu, *J. Appl. Phys.* **68**, 1535 (1990).
- 9 E. Meijer and H. G. Grimmeiss, *J. Appl. Phys.* **55**, 4266 (1984).
- 10 G. Ferenczi, C. A. Londos, T. Pavelka, M. Somogyi and A. Mertens, *J. Appl. Phys.* **63**, 183 (1988).
- 11 J. Vanhellemont, A. Kaniava, E. Simoen, M.-A. Trauwaert, C. Claeys, B. Johlander, R. Harboe-Sørensen, L. Adams and P. Clauws, *IEEE Trans. Nucl. Sci.* **41**, 479 (1994).
- 12 L. C. Kimerling, M. T. Asom, J. L. Benton, P. J. Drevinsky and C. E. Caefer, *Materials Science Forum* **38-41**, 141 (1989).
- 13 M.-A. Trauwaert, J. Vanhellemont, H. E. Maes, A.-M. Van Bavel, G. Langouche and P. Clauws, *Appl. Phys. Lett.*, in press, May (1995).
- 14 Y.-H. Lee and J. W. Corbett, *Phys. Rev. B* **13**, 2653 (1976).

ARE THE MODELS OF THE TRIPLY CHARGED GALLIUM VACANCY AND DOUBLY CHARGED GALLIUM INTERSTITIAL ALIVE OR DEAD?

R.M. COHEN,* C.Y. CHEN,* W.M. LI,* D.S. SIMONS, ** and P.H. CHI**

*Dept. of Materials Science and Engineering, Univ. of Utah, Salt Lake City, UT 84112

**NIST Chemical Science and Technology Laboratory, Gaithersburg, MD 20899

ABSTRACT

We have found that the measured diffusivity can be quite different than predicted by recent models of multiply-charged defects. Key problems dealing with the measurement and the interpretation of diffusion mechanisms are discussed. Using a few common variations in GaAs epilayer growth, we have obtained diffusivities which range over several orders of magnitude at the same temperature. Making use of the relatively weak In-As bond, we have used In as a marker to measure group III interdiffusion, D_{III} . D_{III} is consistent with the results of others using Al as a marker in n-type GaAs, but orders of magnitude smaller than predicted by the triply charged Ga vacancy, V_{Ga}^{3-} , model of Tan and Gosele. Although diffusion can be attributed to a negatively charged vacancy in n-type GaAs, In is found to often move by a kick-out mechanism in p-type GaAs. It appears likely that many early experiments with n- and p-type GaAs-AlAs interdiffusion were affected by large concentrations of Ga interstitials, I_{Ga} , caused by Fermi energy pinning at the growing surface. We present the first direct experimental evidence for the existence of a positively charged Ga interstitial. Our results, combined with those of others, suggest that V_{Ga} has a single negative charge associated with it. Because epilayer growth conditions appear to cause the point defect concentrations to deviate substantially from equilibrium, we conclude that the exact charge states of V_{Ga} and I_{Ga} still remain to be determined.

INTRODUCTION

Conclusions are often made about diffusion mechanisms after analyzing diffusion data with thermodynamic mass action expressions. For a system consisting of two phases, say, a GaAs wafer in contact with gas, and three components, Ga, As, and a dopant, the Gibbs phase rule demands that exactly three degrees of freedom be controlled. The degrees of freedom which are typically controlled are the temperature, T , and the As and dopant partial pressures, P_{As4} and P_{dop} . When these are controlled, then all other thermodynamic parameters (dopant solubility, concentration of point defects, etc.) are well defined at equilibrium and an experiment will be reproducible if the point defects can approach equilibrium quickly. Diffusivity may then be written as a function of the three controlled variables, $D=D(T, P_{As4}, P_{dop})$. However, only when the dopant concentration in the wafer, N_{dop} , is close to equilibrium with P_{dop} , may one express D in terms of the Fermi level, E_f , i.e., $D=D(T, P_{As4}, E_f)$. We have demonstrated¹ that N_{dop} almost never approaches equilibrium with P_{dop} during organometallic vapor phase epitaxy (OMVPE), and that the use of $D=D(T, P_{As4}, E_f)$ can be very misleading. We have shown elsewhere^{1,2} that Fermi level pinning at the surface is the major reason why N_{dop} and P_{dop} do not equilibrate during OMVPE growth.

These details are critically important for the interpretation of diffusion mechanisms because point defect models almost always assume that the point defect concentrations are at their equilibrium values prior to the start of diffusion. Assuming, for simplicity, that diffusion occurs on the Ga sublattice via Ga vacancies, V_{Ga} , one expects that the ratio of the diffusivity measured in the extrinsic crystal (e) to that measured in the intrinsic crystal (i) is related to the vacancy concentrations, $[V_{Ga}]$, via $D_e/D_i = [V_{Ga,e}]/[V_{Ga,i}]$. If the vacancies all have a negative charge of magnitude, β , then it is easy to relate $[V_{Ga,e}]/[V_{Ga,i}]$ to electron concentration, n , and the intrinsic electron concentration, n_i , $[V_{Ga,e}]/[V_{Ga,i}] = (n/n_i)^\beta$ and thus $D_e/D_i = (n/n_i)^\beta$. This is the essence of the model proposed by Tan and Gosele,³ i.e., $D=D(T, E_f)$ in GaAs. Based upon a

report of Mei et al.,⁴ which indicated $D_{\text{Al-Ga}} \sim n^3$ in a Si-doped GaAs-AlAs superlattice, Tan and Gosele concluded that $\beta=3$.

To date, no one appears to have addressed the question of whether the point defects in Mei's structure could ever have approached equilibrium. The AlAs-GaAs superlattice was grown by molecular beam epitaxy and consisted of six adjacent layers (each 0.3 μm thick) differing in their Si concentration. It was assumed that the vacancy concentration in each layer quickly approached its equilibrium value during high temperature annealing with a GaAs proximity cap. It can be shown that only a small amount of sublimation is required to provide a well defined P_{As} , P_{Ga} , and even P_{Si} above the sample surface. However, it is physically impossible for the charged point defects in the adjacent layers to be in equilibrium with each other and with the ambient partial pressures. For example, when the characteristic diffusion length of the V_{Ga} is comparable to, or larger than, the epilayer thickness, the dopant concentration will be essentially constant throughout the epilayer. Conversely, if the characteristic diffusion length of the V_{Ga} was short compared to the 0.3 μm thickness of each layer, then the diffusivity will not depend upon the partial pressures during annealing, i.e., the $[V_{\text{Ga}}]$ in each layer is a strong function of the growth conditions and independent of the annealing ambient pressures. In this paper, we show that nonequilibrium point defect concentrations may persist in GaAs well after growth, i.e., into later annealing cycles, and that the diffusion resulting from those anneals may be strongly influenced by the growth conditions.

EXPERIMENTAL

GaAs epilayers were grown by atmospheric pressure OMVPE on Si-doped GaAs substrates ($N_{\text{Si}}=5\text{--}10 \times 10^{17} \text{ cm}^{-3}$), (100)-oriented and cut 2° off toward (110). Growth was performed in a rectangular OMVPE quartz reactor with a cross section of $2 \times 5 \text{ cm}$. Sources used include tertiarybutylarsine (TBAs), trimethylgallium (TMGa), dimethylzinc (DMZn), dimethylditelluride (DMDTe). H_2 , of 5N purity, was passed through a commercially available metal hydride filter to obtain a purity of better than 7N (with respect to O_2 and H_2O). Electronic mass flow controllers were used to accurately control gas flows, and an electronic temperature controller was used to keep the sample temperature constant. An IR lamp was used to heat a graphite susceptor during growth. During annealing or diffusion studies, the susceptor was replaced with a graphite block which fit snugly inside the quartz. As described elsewhere,¹ the samples and their GaAs proximity caps were placed in a slit cut in this block for annealing. Epitaxial layers of thickness 1.2 μm were grown for the interdiffusion studies. A nominally rectangular In profile was grown in the top 0.3 μm to minimize the effects of any point defect outdiffusing from the substrate. For the pn-pn structures, dopant concentration was maximized by using a growth temperature of $T_{\text{g}}=650^\circ\text{C}$ for the n-type layers and $T_{\text{g}}=575^\circ\text{C}$ for the p-type layers. Characterization included electrochemical capacitance-voltage (ECV) profiling, and secondary ion mass spectroscopy (SIMS). SIMS profiles were made with a Cs^+ primary ion beam at an impact energy of 14.5 keV for In and Te, and 5.5 keV for Zn. Concentration values were determined by comparison with ion implanted standards. The depth scale was obtained by stylus profilometry of individual craters with an estimated uncertainty of $\pm 3\%$.

RESULTS AND DISCUSSION

Four In-doped, n-type, samples were simultaneously annealed using $T=900^\circ\text{C}$ and $P_{\text{TBAs}}=1.6 \times 10^{-2} \text{ atm}$ for $t=1 \text{ hr}$. The surface morphology was mirror-like after annealing under these conditions. The In concentration profiles are shown before (shaded line) and after (solid line) annealing in Fig. 1a-1d. Sublimation of the sample appears to be small. In has been used as an interdiffusion marker because the In-As bond is much weaker than the Ga-As bond, and it is expected to be an excellent marker to indicate a vacancy mechanism. Samples WL160 and WL177 were grown at $T_{\text{g}}=600^\circ\text{C}$ with a constant $N_{\text{Te}}=6 \times 10^{18}$ and $2 \times 10^{18} \text{ cm}^{-3}$, respectively. Samples

WL159 and WL176 were grown at $T_g=700^\circ\text{C}$ with a constant $N_{Te}=1.7\times 10^{18}$ and $1.5\times 10^{19}\text{ cm}^{-3}$, respectively.

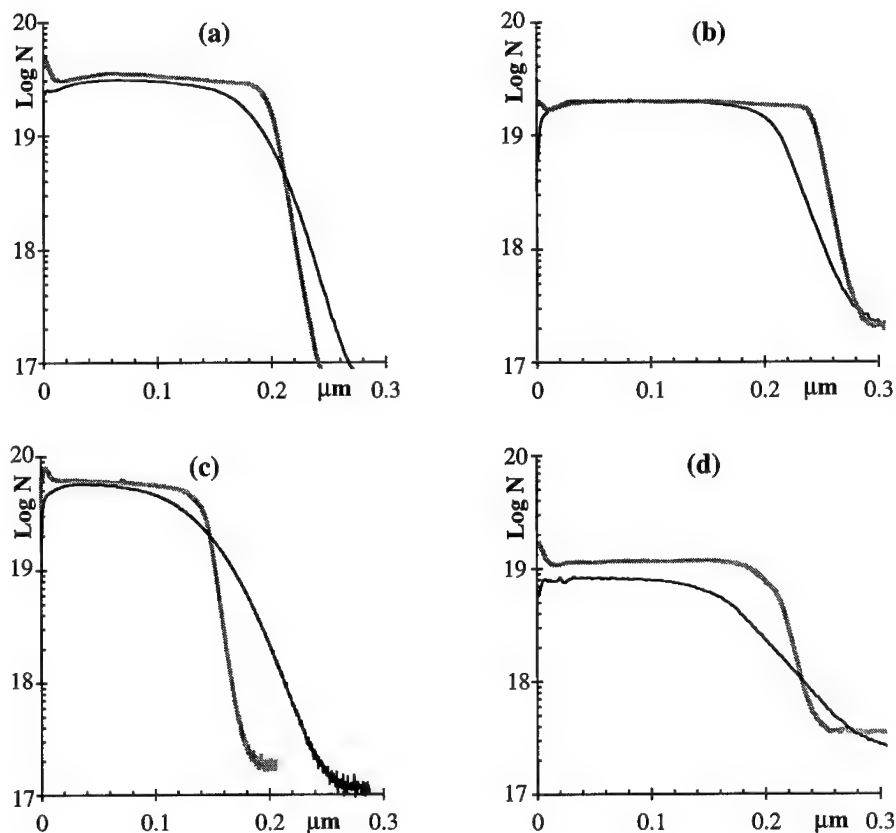


Fig. 1. $\text{Log } N_{\text{In}} (\text{cm}^{-3})$ vs depth (μm) before (shaded lines) and after (solid lines) annealing at $T=900^\circ\text{C}$ for (a) WL159, (b) WL177, (c) WL160, and (d) WL176, which were grown with $n=1.7\times 10^{18}$, 2×10^{18} , 6×10^{18} , and $1.5\times 10^{19}\text{ cm}^{-3}$, respectively.

D_{In} was calculated assuming that the starting N_{In} profile was perfectly rectangular.⁵ The solid symbols in Fig. 2 summarize D_{In} vs N_{Te} for these samples, and there is no significant difference attributable to the growth temperature. The shaded line shows the predictions of Tan and Gosele for a triply charged V_{Ga} .³ Triangles show the results of Mei et al.⁴ for Si-doped GaAs-AlAs interdiffusion at $T=900^\circ\text{C}$. Later results from Mei et al.⁶ for interdiffusion in Te-doped GaAs-AlAs at $T=900^\circ\text{C}$ are shown by open circles. The result of ^{69}Ga - ^{71}Ga interdiffusion reported by Tan et al.⁷ at $T=900^\circ\text{C}$ in nominally undoped GaAs is shown by the shaded square at $n_i(900^\circ\text{C})=2\times 10^{17}\text{ cm}^{-3}$. These data have also been divided by $P_{\text{As}_4}^{1/4}$ to account⁸ for the different P_{As_4} used in the different experiments: ≈ 1 atm in the isotopic interdiffusion, $\approx 4\times 10^{-3}$ atm in our

experiments, and $\approx 3 \times 10^{-7}$ atm⁹ in the Mei experiments. The adjusted data is shown by open squares (except for the one isotopic result) and together they represent the expected D_{III} for a Ga vacancy mechanism at $P_{As_4}=1$ atm and $T=900$ °C, assuming that the vacancies have equilibrated. A dashed line with unity slope is shown for comparison. The slope of the line passing through the data points is expected to provide³ the charge state of the V_{Ga} (if the point defect concentrations have equilibrated with the ambient vapor). We believe that such equilibration could not have occurred in multilayer samples such as those used by Mei, and, as discussed below, equilibration in our uniformly doped layers may not have been reached. Thus, we regard any assignment of a single negative charge to the V_{Ga} as preliminary.

We have also grown pnpn structures and annealed them under various conditions. The as-grown concentration profiles for Zn, Te,

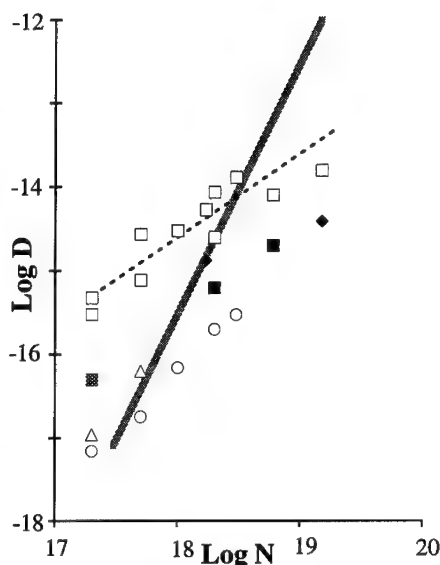


Fig. 2. $\log D_{In-Ga}(900\text{ °C})$ (cm^2/s) vs \log donor concentration (cm^{-3}). Our results for epilayers grown at $T_g=600$ and 700 °C are shown by the filled squares and diamonds, respectively. The dashed line illustrates a slope of unity, and the shaded line a slope of three. D_{Al-Ga} measured by Mei et al. using the dopants Si^4 or Te^6 is shown by open triangles or circles, respectively. D_{Al-Ga} measured by Tan et al.⁷ in a nominally undoped sample is shown by the shaded square.

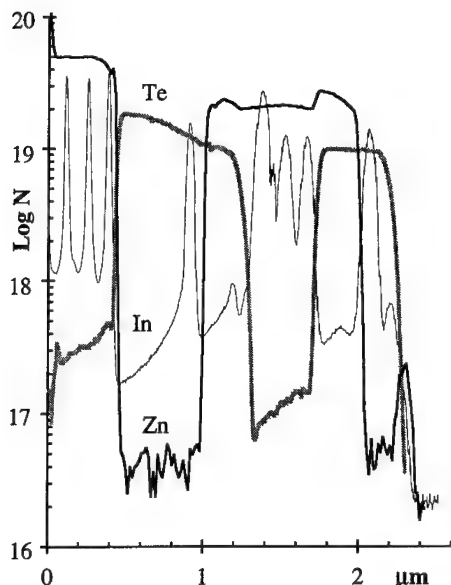


Fig. 3. $\log N$ (cm^{-3}) of In, Zn, and Te vs depth (μm) taken for the as-grown sample, CY132B. The width of the buried Zn-doped layer has doubled during growth of the two following layers because of trapped I_{Ga}^+ .

and In markers are shown for sample CY132B in Fig. 3. The profiles are slightly different than shown previously¹⁰ because the SIMS measurements shown in Fig. 3 have been run a second time to improve the resolution of the In profile. The most striking feature in Fig. 3 is the extended diffusion of Zn out of the buried Zn-doped layer during the growth process. It is worth emphasizing that Zn was turned on when Te was turned off, and Te was turned on when Zn was turned off. As discussed elsewhere,^{2,10} the large D_{Zn} is the result of positive Ga interstitials, I_{Ga}^+ , trapped in the Zn-doped layer after having been generated at the surface during growth of the second

n-type layer. Changes in the In markers in the buried Zn-doped layer suggest that a little self-diffusion has occurred via any mechanism. The magnitude of the positive charge on the interstitial remains unknown at present.

It is worth pointing out that one may obtain unusually large diffusivities at low temperatures. Fig. 4 shows the profiles of another piece of the original sample after annealing at $T=650^\circ\text{C}$, $P_{\text{TBA}_3}=2.1 \times 10^{-3}$ atm, and $P_{\text{Zn}}=5.1 \times 10^{-3}$ atm for $t=2$ hr. The SIMS conditions used to take the data for Fig. 4 were the same as those used to take the data of Fig. 3. The $D_{\text{In}} \sim 10^{-15}$ cm²/s in the top layer is approximately an order of magnitude larger than it was at $T=800^\circ\text{C}$ using essentially the same partial pressures.² $D_{\text{In}} \leq 10^{-17}$ cm²/s in the Te-doped layers, and this is approximately 100x lower than predicted.³ This discrepancy

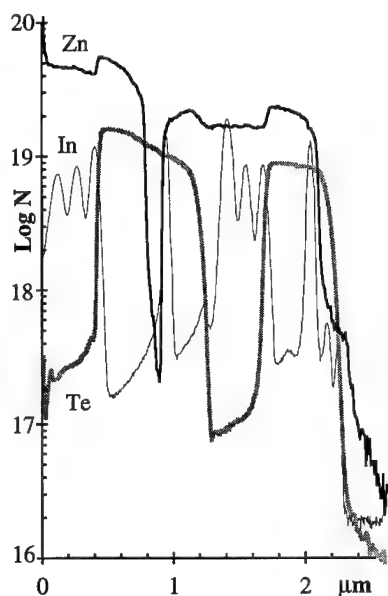


Fig. 4. Log N (cm⁻³) vs depth (μm) after annealing a piece of CY132 for $t=2$ hr with a nominally equilibrium P_{Zn} and P_{As_4} at $T=650^\circ\text{C}$. Even though the substitutional N_{Zn} in the top p-type layer is close to equilibrium with the ambient used, I_{Zn}^+ enter from the vapor, move to the pn junction, kick out I_{Ga}^+ , and the I_{Ga}^+ diffusing back to the surface kick out In and enhance the marker diffusion.

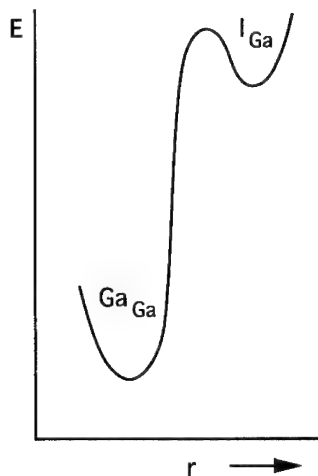


Fig. 5. An energy vs reaction coordinate diagram illustrating the generic Frenkel reaction, $\text{GaGa} \rightarrow \text{I}_{\text{Ga}} + \text{V}_{\text{Ga}}$. An important implication of this is that any excess I_{Ga} entering GaAs is likely to reduce the $[\text{V}_{\text{Ga}}]$ quickly, but because of the larger energy required to increase the $[\text{V}_{\text{Ga}}]$, a relatively long time is required to return the crystal to equilibrium.

does not appear to be accounted for simply by the fact that the Te-doped regions eventually become p-type. However, any thermodynamic interpretation of this data would be inappropriate because all of the experiments are fundamentally far from equilibrium even though three degrees of freedom were controlled. We have proposed that the rapid Zn diffusion out of the buried Zn-doped layer is caused^{2,10} by (1) a grown-in excess $[\text{I}_{\text{Ga}}^+]$, which (2) kicks out Zn into interstitial sites in the buried layer, (3) the resulting I_{Zn}^+ diffuses into the pn junction, kicking out I_{Ga}^+ which (4) drifts back into the buried layer because of the electric field and repeats the kick-out process. This kick-out mechanism continually widens the In

spikes and is relatively insensitive to temperature (compare Fig. 4 to result of $T=800\text{ }^{\circ}\text{C}$ anneals reported in Ref. [2]). Further details are discussed elsewhere.¹⁰

Of key importance in n-type layers is the generation of I_{Ga}^{+} during OMVPE (and presumably other forms of VPE) and its effect on the V_{Ga} concentration. Assuming a simple model, we write $\text{Ga}_{\text{Ga}} \rightarrow \text{I}_{\text{Ga}}^{+} + \text{V}_{\text{Ga}}^{-}$ and see that the interstitial and vacancy concentrations scale inversely through a mass action relation, i.e., $K = [\text{I}_{\text{Ga}}^{+}][\text{V}_{\text{Ga}}^{-}]$. As shown elsewhere,² the Fermi level pinning during growth of n-type GaAs may enhance $[\text{I}_{\text{Ga}}^{+}]$ by as much as $\sim 10^4$. This implies that $[\text{V}_{\text{Ga}}]$ (in any charge state) will be sharply lower than its equilibrium value after growth. This concept is illustrated by the configuration coordinate diagram shown in Fig. 5. This figure is intended to show that a relatively large energy is required to convert a substitutional Ga into an I_{Ga} , but a relatively small amount of energy is required to go in the other direction, i.e., to plug up vacancies whenever I_{Ga} is in excess. The figure also emphasizes that the reaction rates are inherently different, i.e., $[\text{V}_{\text{Ga}}]$ will drop relatively quickly when an influx of I_{Ga} occurs, but a relatively long time is required for $[\text{V}_{\text{Ga}}]$ to recover to its equilibrium value after an excess $[\text{I}_{\text{Ga}}]$ disappears. It is largely for this reason that further work is needed to determine the extent to which the results summarized in Fig. 2 were affected by the growth conditions.

In summary, $\text{D}_{\text{In-Ga}}$ ($900\text{ }^{\circ}\text{C}$) has been found to be similar to D_{III} previously estimated using Ga-Al and ^{69}Ga - ^{71}Ga . The dependence of $\text{D} \sim n$ rather than $\text{D} \sim n^3$ suggests that a single electron (rather than 3) is associated with V_{Ga} . However, it is unclear whether the V_{Ga} concentration has equilibrated, and thus whether any interpretation of the charge state is appropriate. We are presently investigating this. Present experiments provide the first experimental evidence that I_{Ga} is positively charged and can be trapped by the electric field of adjacent pn junctions. This has been shown to lead to enhanced diffusion via the kick out mechanism, and cause the so-called emitter push effect. At present, the magnitude of the positive charge on the I_{Ga} must be regarded as unknown.

Support from NSF through contract number DMR-9024848 is gratefully acknowledged.

References.

- 1 W.R. Reichert, C.Y. Chen, W.M. Li, J.E. Shield, R.M. Cohen, D.S. Simons, P.H. Chi, J. Appl. Phys. **77**, 1902 (1995).
- 2 R.M. Cohen, C.Y. Chen, W.M. Li, D.S. Simons, P.H. Chi, presented elsewhere in this symposium.
- 3 T.Y. Tan and U. Gosele, Mater. Sci. Engineering **B1**, 47 (1988).
- 4 P. Mei, H.W. Yoon, T. Venkatesan, S.A. Schwarz, J.P. Harbison, Appl. Phys. Lett. **50**, 1823 (1987).
- 5 J. Crank, The Mathematics of Diffusion, 2nd ed. (Oxford University Press, London, 1975), p. 39.
- 6 P. Mei, S.A. Schwarz, T. Venkatesan, C.L. Schwartz, E. Colas, J. Appl. Phys. **65**, 2165 (1989).
- 7 T.Y. Tan, H.M. You, S. Yu, U.M. Gosele, W. Jager, D.W. Boeringer, F. Zypman, R. Tsu, S.T. Lee, J. Appl. Phys. **72**, 5206 (1992).
- 8 R.M. Cohen, J. Appl. Phys. **67**, 7268 (1990).
- 9 Landolt-Bornstein Handbook, New Series, ed. by O. Madelung (Springer-Verlag, New York, 1982), Group III, vol. 17d, p.374.
- 10 C.Y. Chen, R.M. Cohen, D.S. Simons, P.H. Chi, submitted to Appl. Phys. Lett.

SOME PECULIARITIES DURING CREATION AND DESTRUCTION OF THE NATIVE DEFECTS WITH THE NEGATIVE CORRELATION ENERGY IN SEMICONDUCTORS

SEMYON D. SAVRANSKY

Physics Department, The City College, The City University of New York,
New York, NY 10031, USA E-mail: sds@scisun.sci.ccny.cuny.edu

ABSTRACT

The creation of negative-U defects (NUD) is a spin-dependent process, that could be used for getting information about NUD themselves; and the NUD destruction is accompanied by the Coulomb's repulsion between charge carriers.

THE SPIN-DEPENDENT NUD CREATION

The concept [1] of the native defects having the effective negative Hubbard correlation energy (NUD) well describes properties of various semiconductors [2-4]. The entirely-filled singlet NUD creation takes place at some atomic potentials during the successive self-trapping of two similar charge carriers (e.g., electrons) that must have opposite spins according to Pauli's exclusion principle.

One can consider the *two electrons and one atomic potential finite size's* system of a disordered semiconductor for simplification. As the mean free path of excess electrons is very small (or the radius of charge carrier's wave-function is short), they can interact effectively only with few neighboring localized states at each moment. Let the "first" electron, with the spin s_1 , occupy the bare localized state of a half-filled NUD and form an exchange-bound pair with the "second" electron, with the uncorrelated spin s_2 , in another neighboring localized or extended state. The probability of this is W . The evolution of this pair may be developed either by its destruction or by the self-trapping of the "second" electron at the same potential which the "first" electron has occupied, i.e., by the creation of the entirely-filled NUD at some atomic potential during time t_L . After life-time $t_U \sim t_0 \exp(|U|/kT)$, the NUD destroyed and again created after a period of about t_U/W , where k is Boltzmann's constant and $1/t_0$ is the vibration frequency in correspondent atomic potential, $1/t_0 \sim 10^{11} - 10^{13}$ Hz, $W \sim 5 \cdot 10^{-2}$ and $|U| \sim 0.5$ eV [1-3]. At the period of t_0/W the NUD are created and destroyed in other potentials. Let us stress that native NUD are metastable at all temperatures T , and the NUD concentration N fluctuates at the value $N^{1/2}$.

Spin-dependent processes are caused by the spin selection rule and the singlet-triplet transitions in the electron pairs [4-8]. An interaction of unpaired electrons with small magnetic fields leads to the singlet-triplet transitions during NUD creation. The mechanism of the magnetic field effect on the spin dynamics cannot be associated with the changes in the energetic of the NUD creation. The energy of any magnetic interaction in the spin system under consideration is several orders of magnitude lower than the thermal energy 1.5kT. The influence

of low magnetic fields H is reduced to the change of the singlet-triplet transition time t_{ST} in processes with pairs of particles with non-zero spins s_i ($i=1,2$). The following relations occur if the spin subsystems are isolated from other subsystems for a time comparable to the spin relaxation time t_r , and t_{ST} is shorter than the process's characteristic time:

$$t_{ST} < t_L, t_{ST} \leq t_r. \quad (1)$$

Therefore, the creation of NUD is a spin-dependent process [4] similar to the spin-dependent chemical reactions [5,6] and/or to the spin-dependent electron - hole recombination in semiconductors [7,8].

The time of NUD creation from the similar charge carriers' pairs $t_L \sim t_0 \exp(E/kT_D)$ is determined by the multiphonon process of self-trapping at the localized level, where E is the bare energy ~ 0.1 eV, T_D is the Debye temperature $\sim 100 - 400$ K. Usually t_L is about 10^{-7} second and $t_r \sim 10^{-4} - 10^{-8}$ second in the semiconductors with NUD [4,9]. The time t_D is determined by the thermal velocity of the "second" charge carriers in the extended states and by the localization radius for the "first" charge carrier, or this time is determined by the energy E for the charge carrier in the localized states. In the former case t_D is about 10^{-8} second, while in the latter case $t_D \sim 10^{-7}$ second. Usually the values of t_{ST} are about $(3 - 5) \cdot 10^{-9}$ second [6-8]. Therefore, relations (1) are valid in the typical semiconductors with NUD the charge carrier's spin-relaxation time is longer than the singlet-triplet transition time and the latter is shorter than characteristic time of the NUD creation from two similar charge carriers in the localized states.

For an investigation of the magnetic fields influence on dynamics of charge carriers one need to solve the following set of equations for spin-density matrices p :

$$dp(t)/dt = -iLp(t) - Fp(t) + Gp(t) - Rp(t), \quad (2)$$

where L is the Liouville superoperator; F is a superoperator of the NUD formation in the Liouville space, G and R are dynamic and relaxation operators. The action of the time-independent superoperator L is given by:

$$Lp(t) = H_t p(t) - p(t) H_t, \quad (3)$$

and the action of the time-independent superoperator F may be written in two forms:

$$Fp(t) = L[Psp(t) + p(t)Ps]/2 \quad \text{or} \quad Fp(t) = Psp(t)Ps. \quad (4)$$

The action of the relaxation operator leads to t_r variations in a magnetic field H , and the dynamic operator describes stochastic effects of the pairs' creation and destruction. Here H_t is the total spin-Hamiltonian and $P_s = |S\rangle\langle S|$ is the singlet projecting operator. Generally the total spin-Hamiltonian may be written as:

$$H_t = H_{hf} + H_{ex} + H_Z = h \sum_i s_i \sum_j B_{ij} I_{ij} - hJ(2s_1 s_2 + 0.5) + \alpha H \sum_i g_i s_i, \quad (5)$$

so it describes the hyperfine interaction, the exchange interaction of charge carriers' spins, and the Zeeman interaction of these spins with the external magnetic fields. Here h is Planck's quantum of action, α is Bohr's magneton, $J = J_0 \exp(-r/a)$ and J_0 is an exchange interaction constant, g is Lande's splitting factor, r is the intercharge carrier distance, a is the shortest radius of a localized charge carrier wave-function, and B is constant of hyperfine interaction with nuclear spin I .

For investigation of this influence one needs to solve the following set of evolution equations for spin-density matrices of electrons p_e , their pairs p_{ee} and the donor-like NUD p_U :

$$dp_e/dt = -i[H_t, p_e] - (p_e^0 - p_e)/t_r - W p_e \otimes p_e + p_{ee}/t_D + W p_U/t_U, \quad (6)$$

$$dp_{ee}/dt = -i[H_t, p_{ee}] + W p_e \otimes p_e - p_{ee}/t_D - (P s p_{ee} P s)/t_L, \quad (7)$$

$$dp_U/dt = (P s p_{ee} P s)/t_L - W p_U/t_U, \quad (8)$$

where p_e^0 is the electron spin-density matrix in the zero magnetic field. One can write similar equations for holes, their pairs and the acceptor-like NUD.

The general quasi-stationary solution of the equations (2)-(8) depends on the features of the charge carriers' kinetic during the NUD creation. Since the latter is not known at present, one can treat the problem by considering the different mechanisms of the low magnetic fields influence on the self-trapping at the NUD, i.e., using a simplification of the Hamiltonian H_t .

The mechanisms of the magnetic field influence on the NUD creation

The hyperfine interaction mechanism is based on the interaction between the spins of the electron's pair and magnetic nuclei due to the term H_{hf} of the total spin-Hamiltonian. When $H = 0$ the singlet (S) state is mixed with all triplet (T_0 , T_- and T_+) states and the probabilities of the NUD creation from each of them are equal:

$$1/t_L^0 = 1/t_L(S) + 1/t_L(T_0) + 1/t_L(T_-) + 1/t_L(T_+) = 4/t_L(S). \quad (9)$$

The S-T₀ and T₊-T₋ levels are splitting if $H > 0$. The transition between S and T₀ is realized, but S-T₋ and S-T₊ transitions are suppressed if the level splitting energy $E_s(H)$ is greater than the energy of a level's width γ . In this case

$$1/t_L^H = 1/t_L(S) + 1/t_L(T_0) + b[1/t_L(T_-) + 1/t_L(T_+)] = 2(1+b)/t_L(S), \quad 0 < b < 1. \quad (10)$$

As the inequality $1.5\langle g \rangle \langle r \rangle^3 < H_s$ is satisfied, one can neglect the dipole-dipole interaction during self-trapping at the NUD with the mean radius $\langle r \rangle$ that is not larger than 25 Å [4,10]. The parameter b is equal to zero if $E_s \gg \gamma$, which is realized in the saturating magnetic fields H_s about 100 Oe. In accordance with the equations (9) and (10), the applied DC magnetic fields suppress the NUD creation. The concentration beside the impurity atoms of the NUD becomes in the K times lower in H_s :

$$K = (1+b)(1/t_D + 1/t_L^H)/2(1/t_D + 1/t_L^0) \quad (11)$$

The Zeeman mechanism is based on the difference between the Lande splitting factors for the electrons in pairs. The wide spectra of the localized and extended states exist in any disordered semiconductor with NUD [4]. This feature leads to the g -factors dispersion by relatively high values δg about 10^{-2} [9], and to the importance of the Zeeman mechanism. In the framework of this mechanism the NUD creation is possible if s_1 and s_2 are in a singlet state when $H = 0$ for a really slight spin-orbit interaction in semiconductors, which yields to

$$1/t_L^0 = 1/t_L(S). \quad (12)$$

When $H > 0$, the singlet state is mixed with the triplet T₀ state because Larmor spin's precession frequencies are different due to the term H_Z of the total spin-Hamiltonian. Hence the probability of NUD creation reads as

$$1/t_L^H = 1/t_L(S) + 1/t_L(T_0) = (1+c)/t_L(S), \quad 0 < c < 1. \quad (13)$$

In accordance with the equations (12) and (13) the external magnetic fields H stimulate the NUD creation, and their concentration becomes in the Q times higher in the saturating magnetic fields $H_s \sim 3\text{kOe}$:

$$Q = (1+c)(1/t_D + 1/t_L^0)/(1/t_D + 1/t_L^H). \quad (14)$$

The exchange interaction intensively affects the electrons' dynamics during their self-trapping due to the strong localization of the electrons' wave-functions and intimate-range attractive potentials of the half-filled NUD. The exchange interaction takes off the degeneracy of singlet and triplet energy levels, which makes $S-T_0$ transitions more difficult. Then the characteristic DC magnetic fields that stimulate the spin-dependent self-trapping on the NUD increase up to

$$H^* \sim \{4J_t + [2 + t_r(2/t_D + 1/t_L - W/t_U)]\}^{1/2} / \alpha |g_i - g_j| \cdot [3 + t_r(3/t_D + 1/t_L - W/t_U)]^{1/2}. \quad (15)$$

At $H = H_s$ the exchange interaction not destroys the spin-dependent process. The characteristic DC magnetic fields that stimulate the spin-dependent self-trapping on the NUD increase due to the exchange interaction J .

The relaxation mechanism is capable of working only when the relation $t_{ST} \sim t_r$ is valid, i.e., it occurs solely in a short temperature interval. The relaxation mechanism can be realized if the Lande splitting factor has some anisotropy and, then, the longitudinal and/or transverse relaxation times vary in H . Usually this mechanism is not important for semiconductors [4,7,8].

THE EQUILIBRIUM NUD DESTRUCTION

The non-equilibrium destruction of NUD is connected with the Auger recombination [11,12].

Interpretation of the quasi-stationary capacitance - voltage characteristics of the Schottky barrier at the metal-semiconductor interface [13], AC conductivity in As_2Te_3 and GeSe_2 amorphous films [14] time-of-flight experiments with As_2Se_3 glass [15] and in some other experiments leads to the very high pre-exponential attempt-to-escape frequencies $f \sim 10^{17}$ Hz connected with charge carrier's thermalization out of NUD. Sometimes these f explained by very high (0.1 eV) electronic overlap integral [15], but this integral is about $4 \cdot 10^{-3}$ eV [9], and, in fact, this interpretation is incorrect. In the conventional solid state theory the correlation between f and the typical phonon frequencies F is based on the negligible electron-lattice interaction [16], but this interpretation is invalid because of the strong electron-lattice and electron-electron interactions at NUD in correspondent semiconductors.

These anomalous high f observed in the experiments [13-15] are connected with the Coulomb repulsion between charge carriers in the pairs during the equilibrium NUD

destruction. When the polaronic shift W decreases at some i-site occupied by a native NUD due to thermal atomic vibration, the Coulomb repulsion C between two electrons or two holes added to the phonon energy. Since the typical size of the native NUD is about 3\AA [3,4], this mechanism can provide f up to 10^{18} Hz, because $C/F \sim 10^3 - 10^5$. Note, that the repulsion between the similar charge carriers at the thermal destruction of a NUD (or a bipolaron) could lead to high f in other similar materials.

These results have demonstrated that the application of the NUD's concept provides a powerful tool for understanding some new processes in correspondent semiconductors.

The financial support from the Committee of Concerned Scientists, Inc. and the Organizing Committee of MRS'95 Spring Meeting is gratefully acknowledged and I wish to thank Professors H. Cummins and S. Ashok for their help.

References

1. P.W. Anderson, Phys. Rev. Lett. **34**, 953 (1975).
2. N.F Mott and E.A. Davis, Electronic Processes in Non-Crystalline Materials, (Clarendon Press, Oxford, 1979).
3. M.I. Klinger, Phys. Repts. **165**, 275 (1988).
4. S.D. Savransky, Sov. J. Phys. Chem. Glasses **13**, 659 (1987); *ibid.* **13**, 896 (1987).
5. R.M. Salikhov, Yu.N. Molin, R.Z. Sagdeev and A.L. Buchachenko, Spin Polarization and Magnetic Effects in Radical Reactions, (Budapest, Akademia Kiado, 1984).
6. U.E. Steiner, T. Ulrich, Chem. Rev. **89**, 51 (1989).
7. Ya.B. Zel'dovich, A.L. Buchachenko and E.L. Frankevich, Sov. Usp. Fiz. Nauk **155**, 3 (1988).
8. B. Spivak and F. Zhou, Phys. Rev. E, **49**, 2623 (1994).
9. P.C. Taylor, Noncrystalline Semiconductors, edited by M. Pollak **1**, 69 (1987).
10. S.D. Savransky, Solid State Communications **79**, 843 (1991).
11. S.D. Savransky, Phil. Mag. Lett. **66**, 91 (1992).
12. S.D. Savransky in Proc. Int. Conf. "Hopping and Related Phenomena 5", Edited by C.J. Adkins e.a., (Singapore, 1994) p. 117.
13. G.A. Bordovsky and M.R. Kanichev, Fizika i Techn. Poluprovodn. [Soviet Phys. Semiconductors] **24**, 527 (1990).
14. J.J. Hauser, Phys. Rev. B, **31**, 2133 (1985).
15. G. Pfister and H. Scher, Phys. Rev. B, **15**, 2062 (1977).
16. J.H. Ziman Principles of the Theory of Solids, (Cambridge University Press, Cambridge, 1972).

CLASSICAL AND RAPID THERMAL PROCESS EFFECTS ON OXYGEN AND CARBON PRECIPITATION IN SILICON

K. Mahfoud, M. Loghmarti, J.C. Muller and P. Siffert.
Lab. PHASE (UPR du CNRS n°292), BP20, F-67037 Strasbourg Cedex2, FRANCE

ABSTRACT

We report observations on the effects of rapid thermal annealing on oxygen and carbon content of different single and multicrystalline silicon materials.

From the comparison between the resulting effects of conventional and short thermal annealing, we can deduce that the increase of the concentration of interstitial oxygen after a rapid thermal annealing (RTA) is due to the dissociation of some microprecipitates in silicon, which is significantly affected by the initial oxygen content, thermal history, defects and impurity content such as carbon.

1. INTRODUCTION

The study of oxygen precipitation in silicon continues to be a topic of considerable current interest. It has been investigated extensively because of its role in hardening of the silicon lattice and in impurity gettering during device processing [1- 6].

In general, oxygen precipitation behaviour in silicon is governed by interstitial oxygen concentration and processing temperatures, especially by the supersaturated oxygen content at these temperatures. The secondary factors involved are related to the impurity content, defects and crystal thermal history [7- 9].

Many fundamental aspects of nucleation and growth of oxide precipitates have been studied, the amount and morphology of oxygen precipitates is a very complex problem. Up to now, the interactions between oxygen, carbon and metal impurities, point defects, aggregates responsible of the changes in silicon electrical properties during a thermal processing are not completely understood [10- 16].

In this work we have compared the effect of conventional and rapid thermal annealing on the oxygen precipitation in different silicon materials.

Our motivation in this experiment is the understanding of the oxygen concentration evolution and of the mechanism of its precipitation in bulk silicon.

2. EXPERIMENTAL PROCEDURE

Single crystal and polycrystalline silicon samples were used in our experiments. The polycrystalline material "Polix" was provided by Photowatt, and issue from different ingots, "P" type boron doped, identified by the letters A, B, C and D in the table and figures.

The sample thickness ranged between 400 μ m and 1mm, and both surfaces were polished (Double Side Polished DSP). The infrared absorption measurements at 1107 and 605 cm^{-1} , corresponding to the interstitial oxygen and substitutional carbon bands respectively, were carried out with a Perkin-Elmer 983G double beam grating infrared spectrophotometer. All spectra were recorded at room temperature using air in the reference beam. The calibration factors were $(3.03 \pm 0.19) \times 10^{17} \text{cm}^{-2}$ for interstitial oxygen and $(1.00 \pm 0.03) \times 10^{17} \text{cm}^{-2}$ for substitutional carbon [17- 18]. Special attention was taken in order to perform infrared absorption measurements exactly at the same position within the samples to avoid effects of a possible inhomogeneous distribution of impurities.

The Rapid Thermal Process (RTP) unit used here was a FAV4 model of JIPELEC (Grenoble, FRANCE), with temperature monitored by an infrared pyrometer .

The resistivity was measured by the four-point probe method. It is to be noted that before each treatment the samples were carefully cleaned in 25% HF for 2 min.

A first group of samples was subjected to successive isochronal 25sec heating steps from 450 to 1050°C whereas a second set of samples was used to study the dissociation and precipitation of oxygen. For this purpose the following two steps annealing were performed:

- CTA (1050 °C / 6 hours) + RTA (1050 °C / 25 sec)
- RTA (1050 °C / 25 sec) + CTA (1050 °C / 6 hours).

where CTA and RTA are Classical and Rapid Thermal Annealing respectively.

3. RESULTS and DISCUSSION

The concentrations of interstitial oxygen and substitutional carbon found in the different materials used are summarized in table I which give also the resistivity values.

Table I: Oxygen, Carbon and resistivity of the different materials used in the experiment.

Sample	[Oi] (ppma)	[Cs] (ppma)	ρ ($\Omega \cdot \text{cm}$)
CZ	13.0	< 0.5	10
Polix A	20.0	12.0	2.5
Polix B	13.0	10.0	1.5
Polix C	15.0	11.0	2.0
Polix D	5.4	18.0	1.2

It should be noted that Polix material presents a significant grain boundary (GB) recombination activity [19].

Figure 1 gives the evolution of the interstitial oxygen content in the different materials versus the annealing temperature for a 25 sec RTA. We can observe that, in the Polix sample "A", oxygen concentration is constant in the lower temperature range and increases for the highest temperatures. In both the other Polix samples, the evolution seems to be more complicate as a precipitation step seems to appear.

The evolution of the minority carrier diffusion length was witnessed by Surface PhotoVoltage (SPV). Figure 2 shows the evolution of the minority carrier diffusion length as function of the rapid thermal annealing temperature during 25 sec. We have observed a systematic degradation of the L_D values for all the materials. This strong degradation is due to the activation of defects, which can be related to the dissociation of complexes or to a subsequent contamination with quick diffusing metals [20]. The degradation in Polix "A" which contains more oxygen is more pronounced compared to Polix "D" which contains a large excess of carbon compared to oxygen.

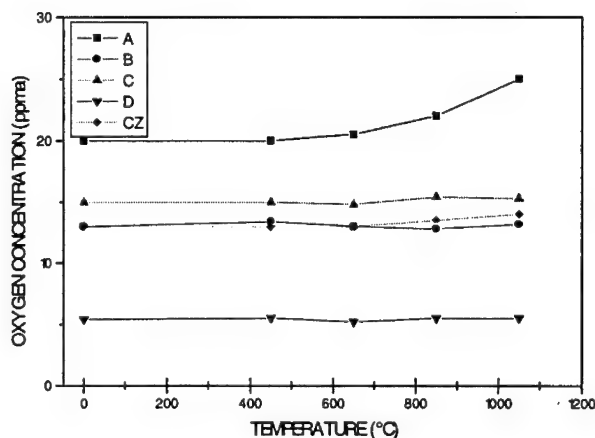


Figure 1 Evolution of interstitial oxygen concentration as function of the rapid thermal annealing temperature

We think, that a clear correlation between the oxygen content and the L_D evolution versus the annealing temperature can be found.

For the second point of our study we have tried to evidence the precipitation or dissociation process by using two kinds of annealing. First the classical one (CTA) with a slow cooling rate (2C/mn) which facilitates the precipitation and secondly the rapid one (RTA) characterized by a very fast cooling rate (>300C/sec) which inherently induces a quenching effect. During this step dissociation of precipitates and activation of impurities can occurs [21].

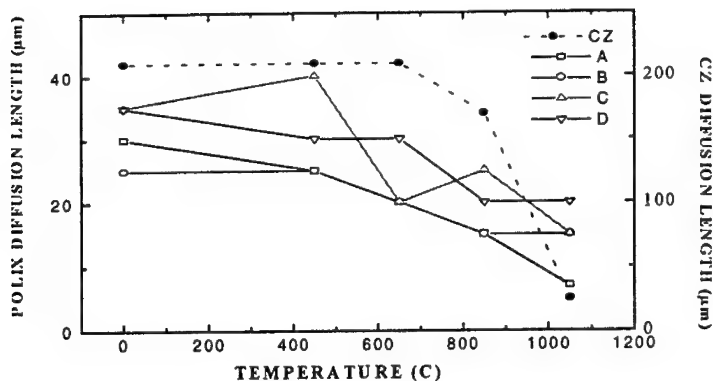


Figure 2 Degradation of bulk minority carrier diffusion length after a rapid thermal annealing during 25 sec

We have processed the wafers in this way, and also in the reverse way (RTA followed by CTA). We have taken, in particular, the samples from the previous study, the Polix "A" which have the highest oxygen content, the Polix "B", "C" and Polix "D" which has a largely lower oxygen content (see table I) and as reference the same CZ material.

Figure 3 and Figure 4 summarize the results of this two steps annealing. It appears that the amount of precipitated oxygen after CTA varied considerably with the material applied. We can observe for sample "A" that the oxygen concentration decreases significantly after the conventional annealing confirming that the precipitation occurs for this sample with high-oxygen content (≈ 20 ppma). After a subsequent RTA some dissolution of these precipitates seems to occur, which induces an increase of the oxygen concentration.

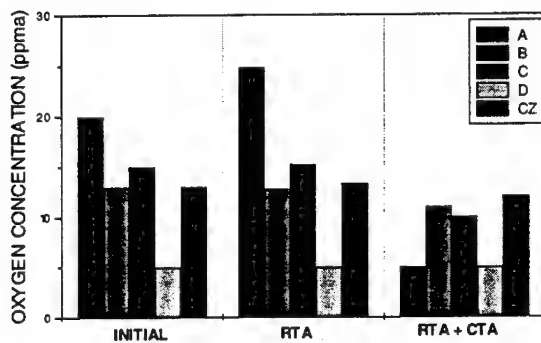


Figure 3 Interstitial oxygen content variations after a two step anneal RTA-CTA

When performing, first, a 25sec RTA at 1050C we found an increase of the [Oi] content in the Polix "A", indicating that some precipitates, can already exist at the initial state and were dissociated by RTA. Secondly, as before we have a strong reduction of the [Oi] concentration after a subsequent CTA processing confirming the efficiency of the slow cooling rate to promote the precipitation of oxygen and probably of other residual impurities as well.

For sample "D", which presents a low oxygen content (≤ 5 ppma) and high carbon nothing occurs after the different annealing cycles. For an intermediate oxygen content (13 to 15 ppma) corresponding to the Polix "B" and "C" samples and to the CZ one, we did not find systematically the same evolution as seen before for the Polix "A" sample. The effect is less pronounced than in the high-oxygen sample "A". The precipitation shown for Polix "B" and "C" (fig 3) and the dissociation for the CZ and Polix "C" are much more lower than in polix "A".

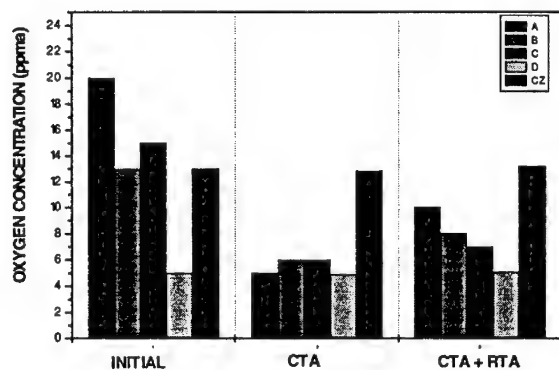


Figure 4 Changes of interstitial oxygen concentration after the two-step annealing CTA-RTA.

4. CONCLUSION

The results up to now obtained can be so summarized as follow:

- 1- Rapid Thermal Annealing can dissociate some oxygen precipitates existing in silicon material. This dissociation is accompanied by a degradation of the bulk diffusion length.
- 2- The effect of RTA on oxygen precipitation is strongly depending on the thermal history of the material, the initial oxygen content and the existing precipitates in the material.
- 3- In summary, the CTA-RTA and reverse annealing cycles were very useful in order to evidence the precipitation and dissociation effects in silicon.

ACKNOWLEDGEMENT

The authors would like to acknowledge the financial support of the FRENCH ADEME, the CNRS in the ECOTECH program and the Multichess II project (JOULE-CT92-0179) of the commission of the European Community D6 XII.

They also acknowledge Dr. Sarti for his grateful assistance and Polix samples supply.

REFERENCES

1. S. M. Hu, J. Electrochem. Soc. **139**, 2066 (1992).
2. F. Shimura, H. Tsuya and T. Kawamura. Appl. Phys. Lett. **38**, 867 (1981).
3. S. K. Pang and A. Rohatgi. J. Electrochem. Soc. **138**, 523 (1991).
4. W. Wijaranakula. J. Appl. Phys. **72**, 2713 (1992).
5. W. K. Tice and T. Y. Tan, Appl. Phys. Lett. **28**, 564 (1976).
6. M. L. Polignano, G. F. Cerofolini, H. Bender, C. Claeys and J. Reffle. Phys. Stat. Sol. (a). **103**, 307 (1987).
7. Y. Shimanuki, H. Furuya, I. Suzuki and K. Murai, Jpn. J. Appl. Phys. **24**, 1594 (1985).
8. H. Zimmerman and R. Falster. Appl. Phys. Lett. **60**, 3250 (1992).
9. K. Wada, H. Nakamishi, H. Takaoka and N. Inoue, J. Cryst. Growth. **57**, 535 (1982).
10. G. S. Oehrlein, J. L. Lindström and J. W. Corbett, Appl. Phys. Lett. **40**, 241 (1982).
11. W. Wijaranakula and J. H. Matlock, J. Electrochem. Soc. **138**, 2153 (1991).
12. A. Poggi and E. Susi, J. Electrochem. Soc. **138**, 1841 (1991).
13. W. Eichhammer, Vu-Thuong-Quat and P. Siffert, J. Appl. Phys. **66**, 3857 (1989).
14. D. Mathiot, Appl. Phys. Lett. **58**, 131 (1991).
15. W. Lin and A. S. Oates, Appl. Phys. Lett. **56**, 128 (1990).
16. C. J. Varker, J. D. Whitfield and P. L. Fejes in Defects in Semiconductor II, edited by S. Mahajan and J. W. Corbett (Mater. Res. Soc. Proc. 14, New York, 1983) pp.187-193.
17. R. Murray, K. Graff, B. Pajot, S. Vandendriessche, B. Griepink and H. Marchandise, J. Electrochem. Soc. **139**, 3582 (1992).
18. R. C. Newman and J. B. Willis, J. Phys. Chem. Solids. **26**, 373 (1964).
19. S. Pizzini, D. Narducci and M. Rodot, Revue Phys. Appl. **23**, 101 (1988).
20. J. R. Jr. Davis, A. Rohatgi, R. H. Hopkins, P. D. Blais, P. Rai-Choudhury, J. R. McCormick and H. C. Mollenkopf, IEEE Trans. Electron. Devices. 1980, 677.
21. B. Hartiti, J. C. Muller and P. Siffert. Appl. Phys. Lett. **59**, 425 (1991).

STUDIES OF DEFECTS IN ZnO BY POSITRON ANNIHILATION

WERNER PUFF ^{*}, SEBASTIAN BRUNNER ^{*}, PETER MASCHER ^{**}, and ADAM G. BALOGH ^{***}

^{*} Institut für Kernphysik, Technische Universität Graz, Petersgasse 16, A-8010 Graz, Austria

^{**} Centre for Electrophotonic Materials and Devices, Department of Engineering Physics, McMaster University, Hamilton, Ont. L8S 4L7, Canada

^{***} FB Materialwissenschaft, FG Dünne Schichten, Technische Hochschule Darmstadt, Hilpertstraße 31, 64295 Darmstadt, Germany

ABSTRACT

In order to investigate the basic properties of radiation-induced defects in ZnO crystals, positron annihilation lifetime and Doppler-broadening measurements were performed on crystals sintered for 18 hours at 1200 °C and irradiated with 3 MeV protons at 223 K. The irradiation induced a colour change of the specimens from the original yellowish-white to dark orange or even brown. Isochronal annealing experiments showed three annealing stages, centred at about 150 °C, 500 - 550 °C, and 750 °C, respectively. These stages are related to the annealing of variously sized vacancy complexes.

INTRODUCTION

ZnO has been the subject of a variety of investigations due to its unique physical properties and applications in commercial devices such as, as a phosphor for display panels and as varistors for electrical surge suppression. There also exist a few studies on defects in this material and especially the effects of particle irradiation on the properties of ZnO [1-8]. These investigations were done mainly by EPR and optical measurements. Nevertheless, basic properties of radiation-induced defects in ZnO are not yet fully understood, but it is believed that the radiation-induced colour changes originate from radiation-induced oxygen vacancies [2, 4, 9], which are in the singly-positive charge state.

Positron annihilation spectroscopy (PAS) is an effective tool to investigate defect systems in semiconductors [10]. In recent years, PAS has been applied in several cases to investigate the defect system in polycrystalline semiconductors. Quite a few of these investigations addressed ZnO and ZnO-based ceramics [11-19] and single crystals as well [20, 21].

In this contribution, we report the results of a PAS study on proton irradiated polycrystalline ZnO. The study focusses on the annealing behaviour of radiation-induced defects and defect clusters formed during the annealing.

EXPERIMENTAL DETAILS

High purity ZnO (at least 99.999% by weight), obtained from Johnson Matthey (AESAR) Ltd., was pressed into pellets, 10 mm in diameter and 1-1.5 mm in thickness. Each pellet was pressed under the same pressure of 10,000 psi. The details of the sintering procedure are described elsewhere [19]. The specimens sintered at 1200 °C for 18 hours were irradiated with 3 MeV protons to a dose of 1.2×10^{18} p/cm². The temperature of the specimens was kept below

- 50 °C during irradiation. The 30 min isochronal annealing from room temperature up to 1250 °C was carried out in air.

The positron annihilation lifetime and Doppler-broadening measurements were performed at room temperature. For the lifetime measurements, a conventional spectrometer was used with a time resolution of 190 ps full width at half maximum (FWHM). The positron source itself was used in the well-known sandwich configuration and was prepared by deposition of about 10 μCi of $^{22}\text{NaCl}$ on a 0.81 mg/cm^2 Al foil. Each lifetime spectrum was accumulated over a 24 hr period which resulted in at least 7×10^6 counts. This is necessary in order to be able to properly resolve defect related defect components, and up to three spectra were collected per data point. Numerical analysis of the data was performed by the PFPOSFIT program [22] with a source correction to take into account the annihilations in the Al-foil containing the positron source. This program fits a number of lifetime components and their respective intensities together with the resolution function of the measuring system to the measured spectrum. The value of an individual lifetime component is determined by the positron state at the site of the annihilation (i.e., bulk or defect states), while the corresponding intensities are related to the number of positrons annihilating from this state. In this investigation, all the lifetime spectra could be decomposed into three or four components. The longest of these was, however, an essentially constant term of about 1.5 ns with not more than 0.3 % intensity. This term could easily be separated from the actual spectra and will not be discussed further.

The Doppler-broadening of the annihilation line was measured using an intrinsic Ge detector with a resolution (FWHM) of 1.18 keV at 497 keV (close to the 511 keV annihilation γ energy). Digital stabilization on the annihilation peak and on a reference peak (^{207}Bi) was employed. Each measurement lasted 3000 seconds and was repeated at least 10 times. A total of about 4×10^7 counts were recorded for each spectrum. The numerical analysis of the Doppler spectra was performed by determining the shape parameter, S, defined as the ratio of the amount of counts in a fixed central portion of the spectrum and the total amount of counts.

RESULTS AND DISCUSSION

Table 1 shows the positron lifetimes and intensities together with the values of the S parameter before and after proton irradiation, and after annealing at 1250 °C. The values before irradiation are in very good agreement with earlier measurements [19]. The lifetimes τ_m and τ_b are the mean lifetime and the bulk lifetime, respectively, as calculated by the positron two-state-

Table 1: Observed positron lifetimes and intensities, the calculated values of the bulk and the mean lifetime, together with the S parameter for ZnO samples before irradiation, after irradiation with 3 MeV protons to a dose of $1.2 \times 10^{18} \text{ cm}^{-2}$, and after annealing at 1250 °C.

	τ_1 [ps]	I_1 [%]	τ_2 [ps]	I_2 [%]	τ_b [ps]	τ_m [ps]	S
before irr.	164	60.4	230	39.6	185	190	0.4208
after irr.	173	47.8	273	52.2	214	225	0.4304
after ann.	167	64.1	224	35.9	184	187	0.4214

trapping model [23]. The bulk lifetime is of particular importance since it refers to annihilations from the "perfect" crystalline regions of the crystal and hence is a material constant. Earlier measurements [18] gave a value of $\tau_b = 183 \pm 4$ ps, which is in excellent agreement with the value given in Tab. 1.

Recently it was shown [18], that the two lifetimes in well sintered samples ("before irr." in Tab. 1) result from annihilations in the nearly perfect lattice and defects therein. It was also shown that for such samples the influence of the grain boundary and the surface regions is very small or even negligible. A direct assignment of the observed defect lifetime to a specific type of defect is complicated by the fact that at the present time, no theoretical estimates exist for positron lifetimes in ZnO and that the defect configurations in sintered samples might be strongly influenced by the quality of the basic material [18, 19]. If one takes the ratio τ_D/τ_B to characterize a defect, our value of 230 ps yields, with a bulk lifetime of 185 ps a ratio of $\tau_D/\tau_B = 1.24$, in excellent agreement with the proposed value of 1.1-1.3 for monovacancies in compound semiconductors [24]. Lifetime and Doppler-broadening measurements down to 10 K show nearly no temperature dependence, an indication that the observed defect is in a neutral charge state [10, 25]. This also suggests that this defect is rather a vacancy complex than a monovacancy, since monovacancies are negatively (V_{Zn}) or positively charged (V_O) at room temperature [8].

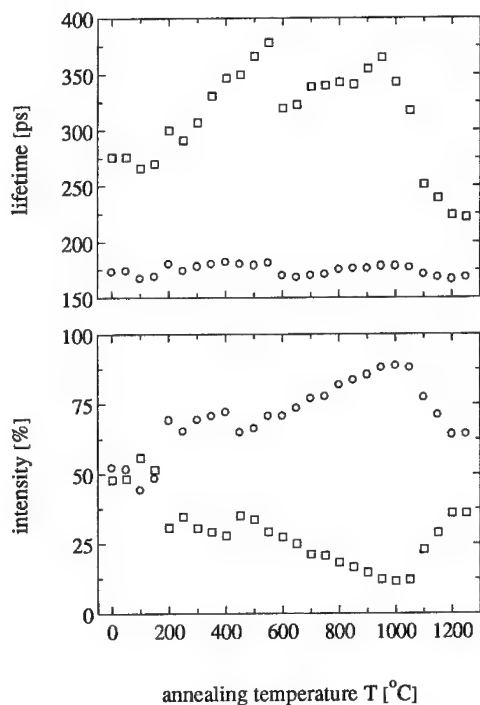


Fig. 1: Lifetimes τ_1 (O) and τ_2 (\square) and corresponding intensities as a function of isochronal annealing temperature obtained by a two-term analysis. Typical errors are ± 2 ps for τ_1 , ± 7 ps for τ_2 . The errors for the intensities are about $\pm 1.5 - 2.0$ %.

After irradiation, the lifetime of the defect component increases to 273 ps (Tab. 1). The ratio τ_D/τ_B now amounts to 1.49, which is in good agreement with the proposed value of 1.46 for divacancies [24]. The observed lifetime therefore, is a strong indication for the existence of the

$(V_{Zn})_2$ -centre, a defect which also has been seen after irradiation with rather high electron doses [6]. It is worth noticing that the bulk lifetime, τ_B , increases to a value of 214 ps after irradiation, which is much longer than the value of 185 ps in the well annealed sample. Changes in this parameter are often an indication for the introduction upon irradiation of non-vacancy defects - sometimes in large concentrations. Such defects can constitute so-called shallow positron traps with lifetimes close to the bulk value. More detailed data analysis of temperature dependent measurements down to 10 K are in progress and will be reported elsewhere. The deviation of τ_B from the true bulk value makes the simple trapping model inapplicable and we therefore, cannot make any assessment of the concentration of the defects.

The annealing data first were analysed with two significant lifetime components. Figure 1 shows these lifetimes and the corresponding intensities as a function of isochronal annealing. As one can see, the longer lifetime component τ_2 , which is attributed to positrons annihilating from the defect state is, for annealing temperatures between 200 and 1050 °C significantly longer than 273 ps. Actually, the lifetime values increase from 270 ps after annealing at 150 °C to 378 ps at 550 °C. This shows that this lifetime component consists of at least two contributions, one stemming from the divacancy-type defects, with a lifetime of 273 ps, and the other from even larger complexes.

In a next step, we tried to split the longer lifetime component into two components: one with a lifetime of $\tau_2 = 273$ ps and the other one with $\tau_3 = 370$ ps. This value was chosen from the data after 500 and 550 °C annealing and from the proposed ratio for larger defect clusters $\tau_D/\tau_B = 1.9 - 2.0$ [24]. Fig. 2 shows the intensities of the three lifetime components as a function of isochronal annealing. In Fig. 3, the changes of the S parameter and the mean lifetime are shown. It is evident from this figure that there exist three distinct annealing stages: at 150 °C, 500 - 550 °C, and 750 °C, respectively.

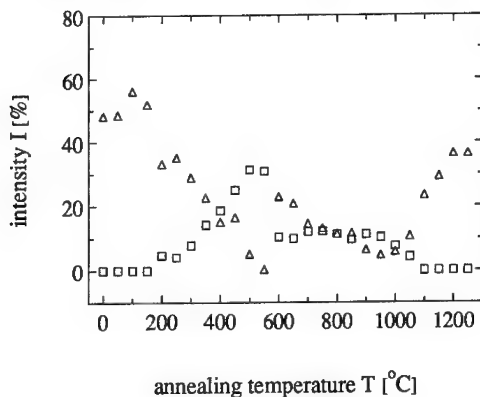


Fig. 2: Intensities I_2 (Δ) and I_3 (\square) of the defect related components of a three-term analysis with fixed lifetimes $\tau_2 = 273$ ps and $\tau_3 = 370$ ps as a function of isochronal annealing.

The intensity of the second component (I_2), which has been attributed to divacancy-type defects, shows a steady decrease from 150 °C up to 550 °C, at which temperature the component disappears entirely. At the same time the intensity of the third component (I_3) increases and reaches a maximum value of about 30 % after annealing at 500 °C. At 600 °C, the intensity of this component drops to about 10 % up to 950 °C and vanishes thereafter. After annealing at 1100 °C the longest lifetime component has disappeared.

After annealing at 600 °C, the second component appears again, and the intensities I_2 show a steady decrease up to 950 °C. At the moment it is not clear if the same defects are appearing again or if there are other defects with a lifetime close to 273 ps. For annealing temperatures between 600 and 750 °C, an additional longer component, with an intensity of about 2 % appears indicating that even larger complexes are formed at these annealing temperatures. For annealing temperatures above 1100 °C there are only two lifetime components left, eventually attaining the values for the well sintered samples at 1200 °C. Interestingly, the annealing behaviour of the radiation-induced discolouration of the samples is considerably less complex. The samples lose their colour quite continuously over a broad temperature range until, after annealing at 800 °C they have entirely reverted to their original yellowish-white appearance. Comparing this with the annealing curves of the positron data (Figs. 1 and 2), one can conclude that the colour centres are not directly related to the defect structures seen by the positrons. Similar conclusions were drawn earlier [18] regarding the correlation of vacancy-type defects and luminescence centres in ZnO.

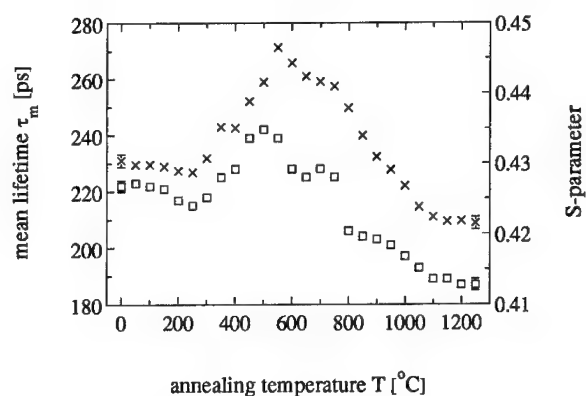


Fig. 3: Mean lifetime, τ_m , (\square) and Doppler-parameter S (\times) as a function of annealing temperature. Typical error bars are shown.

ACKNOWLEDGEMENTS

The proton irradiation was done at the Institut für Kernphysik, J.W. Goethe University, Frankfurt/Main, Germany. The authors wish to thank Dr. H. Baumann for carrying out the irradiation. This work was supported by the Fonds zur Förderung der Wissenschaftlichen Forschung of Austria and the Natural Sciences and Engineering Research Council of Canada.

References

- 1 W.E. Vehse, W.A. Sibley, F.J. Keller and Y. Chen, Phys. Rev. **167**, 828 (1968)
- 2 J.M. Smith and W.E. Vehse, Phys. Lett. A **31**, 147 (1970)
- 3 A.L. Taylor, G. Filipovich and G.K. Lindeberg, Solid State Commun. **8**, 1359 (1970)
- 4 D. R. Locker and J.M. Meese, I.E.E.E. Trans. Nucl. Sci., **19**, 237 (1972)
- 5 D. Galland and A. Herve, Solid State Commun. **14**, 953 (1974)

-
- 6 B. Schallenger and A. Hausmann, *Z. Physik B* **23**, 177 (1976)
 - 7 B. Schallenger and A. Hausmann, *Z. Physik B* **44**, 143 (1981)
 - 8 A. Pöpl and G. Völkel, *phys. stat. sol. (a)* **125**, 571 (1991)
 - 9 G.D. Watkins, in *Proc. Int. Conf. Rad. Effects in Semiconductors*, (Inst. Phys., London, 1977) pp. 95
 - 10 S. Dannefaer, in *Defect Control in Semiconductors*, edited by K. Sumino (Elsevier Science Publishers, North Holland, 1990) pp. 1561
 - 11 M. Noguchi, T. Mitsuhashi, T. Chiba, T. Tanaka, and N. Tsuda, *J. Phys. Soc. Japan* **32**, 1242 (1972)
 - 12 R. Pareja, M. A. Pedrosa, and Gonzales, in *Positron Annihilation*, edited by P.C. Jain, R.M. Singru, and K.P. Gopinathan (World Scientific Publ. Co., Songapore, 1985) pp. 708
 - 13 P. Fernández, N. de Diego, J. del Río, and J. Llopis, *J. Phys.: Condens. Matter* **1**, 4853 (1989)
 - 14 T.K. Gupta, W.D. Straub, M.S. Ramanachalam, J.P. Schaffer, and A. Rohatgi, *J. Appl. Phys.* **66**, 6132 (1989)
 - 15 M.S. Ramanachalam, A. Rohatgi, J.P. Schaffer, and T.K. Gupta, *J. Appl. Phys.* **30**, 8380 (1991)
 - 16 G.H. Dai, Q.J. Yan, Y. Wang, and Q.S. Liu, *Chem. Phys.* **155**, 275 (1991)
 - 17 T. Miyajima, H. Okuyama, K. Akimoto, Y. Mori, L. Wei, and S. Tanigawa, *Appl. Phys. Lett.* **59**, 1482 (1991)
 - 18 J. Zhong, A.H. Kitai, P. Mascher, and W. Puff, *J. Electrochem. Soc.* **140**, 3644 (1993)
 - 19 W. Puff, S. Brunner, and P. Mascher, *The Physics of Semiconductors*, edited by D.J. Lockwood (World Scientific Publ., Singapore, 1995) pp. 2439
 - 20 R.M. de la Cruz, R. Pareja, R. Gonzáles, L.A. Boatner, and Y. Chen, *Phys. Rev. B* **45**, 6581 (1992)
 - 21 N. Tomiyama, M. Takenaka, and E. Kuramoto, *Materials Sci. Forum* **105-110**, 1281 (1992)
 - 22 W. Puff, *Comput. Phys. Commun.* **30**, 359 (1983)
 - 23 P. Hautojärvi, *Positrons in Solids* (Springer, Berlin, 1979)
 - 24 G. Dlubek and R. Krause, *phys. stat. sol. (a)* **102**, 443 (1987)
 - 25 M.J. Puska, C. Corbel and R.M. Nieminen, *Phys. Rev. B* **41**, 9980 (1990)

DEFECT REACTION AND ELECTRICAL PROPERTIES OF IRON IN N-TYPE SILICON

HAJIME KITAGAWA AND SHUJI TANAKA

Department of Electronic Materials Engineering, Fukuoka Institute of Technology, Wajiro-Higashi, Higashi-ku, Fukuoka 811-02, Japan

ABSTRACT

Since the first report by our group in 1992, iron-related defects in n-type silicon has been found to exhibit unusual in-diffusion and annealing properties. We review in this paper the recent progress in understanding the electrical and diffusion properties of iron-related defects in n-type silicon. We have shown from DLTS and Hall effect that iron in n-type silicon is electrically ionized and introduce one donor level at $E_c-0.41$ eV (level C) and, at least, one acceptor level at $E_c-0.21$ eV (level B). The donor character of former level has been confirmed by a Poole-Frenkel effect. The concentrations of two centers introduced are in the order of 10^{13} cm⁻³ at maxima. In-diffusion behavior of levels B and C show that these levels are intermediate states in a consecutive reaction of iron-related complex formation. Low-temperature isothermal annealing experiments from the room temperature to 200°C suggest that iron-related donor is formed, in part, by the electrostatic attractive force between two point charges.

INTRODUCTION

Diffusion and electrical properties of iron in n-type silicon has less been paid attention compared with in p-type silicon mainly because it has been generally believed that iron does not ionize in n-type silicon [1, 2] except several reports [3-7]. However, the consistency between researchers remains poor. We have shown from DLTS and Hall effect [6] that iron in n-type silicon is electrically ionized and introduce a donor level at $E_c-0.41$ eV (hereafter referred to as the level C) and, at least, one acceptor level at $E_c-0.21$ eV (hereafter referred to as the level B).

The multilevel introduction by iron implies that positively charged and negatively charged iron states coexist in n-type silicon. Introduced concentrations of the levels B and C decrease with increasing the diffusion time. In addition, these iron-related defects turn into other different defects during storage at room temperature or upon low temperature annealing. Such in-diffusion and annealing behaviors suggest that these defects are due to iron-related complexes, especially that the electrically active complexes are intermediate states in the iron-related consecutive reactions.

The purpose of the present paper is to review our results obtained up to date for the diffusion and electrical properties of iron in n-type silicon. At first, the level confirmation of iron will be made by means of Hall effect and deep level transient spectroscopy (DLTS). In-diffusion and low-temperature isothermal annealing characteristics will then be presented to characterize the iron-related defects.

EXPERIMENTAL

Phosphorus-doped n-type, float-zoned and dislocation-free silicon crystals were used throughout the present study. Both faces of the silicon crystal slices were coated with evaporated iron to attain the well-defined diffusion. The sample was heated for the diffusion in a flowing nitrogen gas atmosphere. The diffusion heat treatment was terminated by pulling out the slice to the cool region of the quartz furnace tube. DLTS and steady-state capacitance were measured on a Schottky barrier diode made by the gold evaporation. The concentration of the iron-related defects was evaluated by the DLTS peak height and the steady-state capacitance. Isothermal annealing was performed in the temperatures between the room temperature and 200 °C. One control sample was always prepared for each iron-diffused sample under the same conditions as those of the iron diffusion.

RESULTS

Level Confirmation

Four levels related to iron have been confirmed through a series of the present studies. Donor or acceptor characters of these levels and concentrations have been determined using combined analyses of Hall effect and DLTS [6]. Fig.1 shows the typical DLTS spectra of iron-doped n-type silicon and its control sample. Electron traps A and B are acceptors and C donor [6]. The another acceptor labeled X emerges in the low-temperature annealing or the room-temperature storage for period longer than one month [6] (see Fig.4).

The level C exhibits a Poole-Frenkel field emission effect as expected for donors in n-type silicon which was measured by DLTS [8]. We used three kinds of silicon samples containing phosphorus of 4.0×10^{13} , 2.0×10^{14} and $4.0 \times 10^{15} \text{ cm}^{-3}$. Electron emission rate of the level C is proportional to $F^{1/2}$, where F is the electric field. Any other iron-related traps did not exhibit the Poole-Frenkel effect.

In-diffusion Process of Levels B and C

The introduction of levels B and C was comprehensively examined. The concentrations introduced at diffusion temperatures of 1160 and 1190 °C as functions of diffusion time t_D are

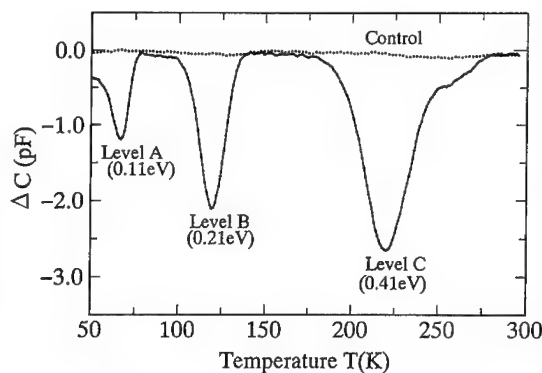


Fig.1. DLTS spectra of n-type silicon as doped with iron and the control sample. Iron was diffused at 1160 °C for 15 min. The measuring condition: reverse bias -5 V, rate window 0.5/5.0 ms, and injection pulse width 500 μ s.

shown in Fig.2 . Until about $t_D=50$ min, the concentrations increase with the increase of t_D , and about 10^{13} cm $^{-3}$ of level B and 1.7×10^{13} cm $^{-3}$ of level C are introduced at maxima. On the other hand, the concentrations introduced decrease with the increase of t_D in the heat treatment longer than 50 min. It should be noted that (1) the concentration higher than the order of 10^{13} cm $^{-3}$ cannot be introduced even at the elevated diffusion temperature, (2) the introduction seems to be irreversible, i. e., the concentration decreased with longer heat treatment does not recover even if following evaporation and diffusion processes for iron are applied and (3) the in-diffusion behavior of levels B and C is qualitatively identical. Therefore, the thermal equilibrium concentration of iron-related defects cannot be defined.

Isothermal Annealing

The donor state (level C) decays even during the room temperature storage [6,7]. Fig.3 shows concentrations of iron-related defects as a function of storage time at room temperature. In addition to levels B and C, the level X emerges and found to increase the concentration with a room-temperature storage time while concentrations of levels B and C decay. It should be noted that, as shown in Fig.3, the decay rate of the level C is about four orders of magnitude lower than that observed for interstitial iron Fei in p-type silicon [9].

For a longer storage, defects were found to turn into other different states and become in-

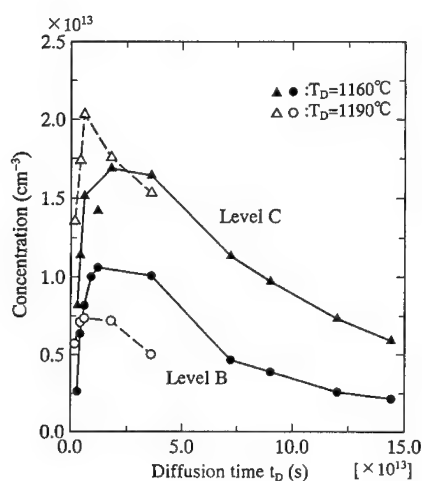


Fig.2. Concentrations of levels B and C introduced 1160°C as functions of diffusion time.

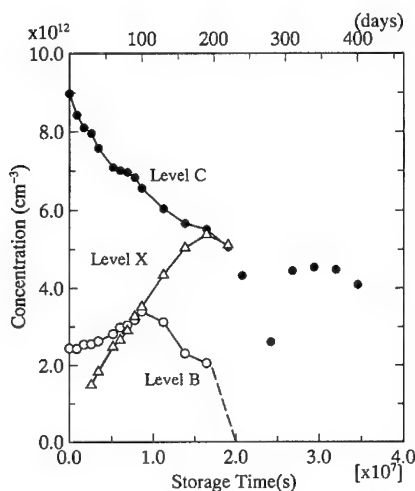


Fig.3. Concentrations of each iron-related level as functions of storage time at room temperature.

active eventually. Fig.4 shows DLTS spectra for the as-diffused sample (a) and for samples which have been stored at room temperature for 10 days (b), 100 days (c) and 220 days. Solid curves are the experimental DLTS spectra and broken curves are the results calculated for resolving the overlapped DLTS signals. While the electron traps B and C decay, the trap C splits into 2 electron traps as shown in Fig. 4(d) in the 220-days stored sample. For more longer annealing (for example 1 year), more traps appear and eventually they tend to turn into electrically inactive species.

The concentrations of level C decay exponentially in the low-temperature annealing, indicating that the level C dissociates. The decay constant τ of the level C is plotted against the reciprocal of the annealing temperature $1/TA$ in Fig.5 with the open circle. The least squares fit gives $\tau = 1.2 \times 10^{-4} \exp(0.65 \text{ eV}/kT)$ (s), where k is the Boltzmann's constant.

DISCUSSION

The acceptor and donor characters of iron-related levels indicate the presence of negatively charged iron states and positively charged iron states. In addition, the anomalous in-diffusion behavior of levels B and C shown in Fig.2 cannot be ascribed to a simple one-atom species. The probable explanation is based on the consecutive reaction model of the iron-related complex formation. Consider some complex α of a combination of an interstitial iron atom (Fe_i) and other defect U . Assuming that α turns into another state β which is electrically inactive, one can see that the concentration of α has a maximum value at $t = [\ln(k_1/k_2)] / (k_1 - k_2)$, where k_1 and k_2 are the rate constants of the reactions $\text{Fe}_i + U \rightarrow \alpha$ and $\alpha \rightarrow \beta$, respectively. Although this is only hypothetical, the in-diffusion results sug-

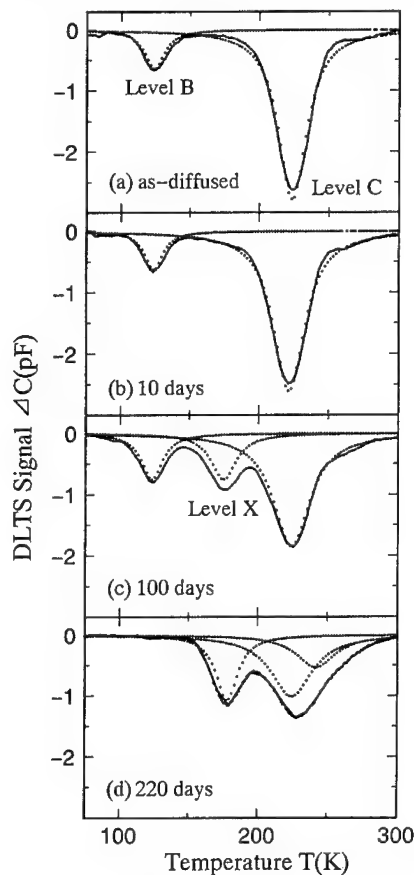


Fig.4. DLTS spectra for as-diffused sample (a) and for samples stored at room temperature for 10 days (b), 100 days (c) and 220 days (d). Dotted curves show the calculated results for resolving the overlapped DLTS peaks.

gest that the observed B and C defects are intermediate states of iron-related complexes produced by a consecutive reaction.

Such an interpretation is in accordance with the low-temperature annealing behavior of the level C shown in Fig.5. The decay of level C means the transfer of the level C to electrically inactive defects. Furthermore, as shown in Fig.4, the transfer accompanies the production of several new defects and they tend to become inactive during long-time annealing. The activation energy, 0.65 eV, of decay constant τ of level C is comparable to an electrostatic pair binding energy which should be about 0.5 eV for two point charges in silicon located at the tetrahedral interstitial sites and nearest substitutional sites.

For the positive charge, ionized phosphorus atoms are probable candidate for pairing. However, we have found that the in-diffusion characteristics as well as the decay constant do not depend on the phosphorus concentration in the silicon crystal.

Therefore we take the view that the donor state associates and dissociates by the defect reactions of iron atoms with impurity atoms other than phosphorus.

On the other hand, the negative charge is difficult to be modeled in iron-doped n-type silicon. If substitutional iron atoms are present, the existence of the negatively charged iron atoms may be possible as a results of tetrahedral bonds at the substitutional sites. However the presence of substitutional iron atoms has not yet been confirmed experimentally in spite of the prediction by Weber *et al.* [10].

Although it is premature to determine the composition of the iron-related complexes from the present work, the EPR results will provide some suggestion for probable pictures. Van Kooten *et al.* [11] have concluded from EPR measurements that Fei-Fei pair and the Fe_i complex are the intermediate states in the thermal clustering process of Fei. They [11] observed the disappearance of Fei-Fei center around the room temperature, indicating that there is a strong preference for further iron aggregation at this center. This mentioning for the iron aggregation process is qualitatively in good agreement with the consecutive reaction model of iron-related defect formation. If Fei-Fei pairing is possible and the bonding consists partly of an electrostatic attractive force, this means that Fei⁻ and Fei⁺ states can coexist in silicon. Even if the Fei⁻ state is present and the iron-related defect state is related to the Fei⁻ state, this charge state will be only a small fraction of total iron because the iron-related defects can be introduced in the order of 10¹³ cm⁻³ within the present experimental conditions while the solid solubility of iron should be in the order of 10¹⁶ cm⁻³ at 1150°C.

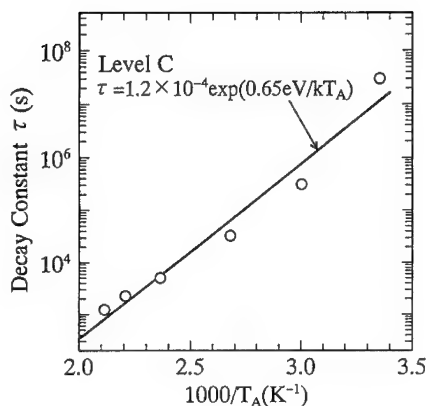


Fig.5. Decay constant τ in the isothermal annealing of level C as a function of the reciprocal of annealing temperature.

CONCLUSION

Some understanding of the introduction of iron-related defects in n-type silicon has obtained from the in-diffusion and annealing studies. The small fraction of iron atoms dissolved into n-type silicon is ionizable and forms some electrically active complexes. These complexes will be the intermediate states of the progressing defect reactions during the iron aggregation formation process. However, further work is needed to complete the picture.

REFERENCES

- [1] C. Schmidt, Appl. Phys. **17** 137 (1978).
- [2] G. A. Adegboyega, A. Poggi and E. Susi, Phys. Status Solidi (a) **118** 491 (1990).
- [3] L. C. Kimerling, J. L. Benton and J. J. Rubin, Defects and Radiation Effect in Semiconductors 1980 (Inst. Phys. Conf. Ser. 59, London, 1981) p.217.
- [4] K. Nakashima and M. Chijiwa, Jpn. J. Appl. Phys. **25** 234 (1986).
- [5] K. Kakishita, K. Kawakami, S. Suzuki, E. Ohta and M. Sakata, Jpn. J. Appl. Phys., **65** 3923 (1989).
- [6] H. Kitagawa, L. C. Kimerling and S. Tanaka, J. Electronic Materials **21** 863 (1992).
- [7] H. Kitagawa, S. Tanaka and B. Ni, Jpn. J. Appl. Phys. **32** L1645 (1993)
- [8] H. Kitagawa and S. Tanaka, submitted to Jpn. J. Appl. Phys.
- [9] H. Nakashima, T. Isobe, Y. Yamamoto and K. Hashimoto, Jpn. J. Appl. Phys. **27** 1542 (1988).
- [10] E. R. Weber and H. G. Rietz, J. Appl. Phys. **51** 1484 (1980).
- [11] J. J. van Kooten, E. G. Sieverts and C. A. J. Ammerlaan, Solid-State Commun. **64** 1489 (1987).

MODIFICATION OF RECOMBINATION ACTIVITY OF DISLOCATIONS IN Si AND SiGe BY CONTAMINATION AND HYDROGENATION

M. KITTLER*, W. SEIFERT* AND V. HIGGS**

* Institut für Halbleiterphysik, PSF 409, 15204 Frankfurt(Oder), Germany

**King's College, Strand, London WC2R 2LS, UK

ABSTRACT

Temperature-dependent (80 ... 300 K) measurements of dislocation recombination activity by the electron-beam-induced-current (EBIC) technique are reported. Controlled Cu contamination (ppb to ppm range), chemomechanical polishing and hydrogenation treatments were applied to alter dislocation properties. Increasing Cu level is found not only to increase the electrical activity of misfit dislocations in SiGe/Si structures at 300 K, but also to change its dependence on temperature. At low contamination, shallow centres control dislocation activity while deep centres are characteristic at higher Cu levels. Heavy Cu contamination results in very strong recombination activity which is attributed to precipitates. Chemomechanical polishing has an effect which is analogous to medium Cu contamination. Hydrogenation was found to passivate recombination activity at 300 K, but did not show pronounced effects on activity at low temperature.

INTRODUCTION

The electrical properties of dislocations have been the subject of investigations for a long time already. Understanding of dislocation properties is not only of practical interest from the point of view of devices, but is a fundamental issue as well. Although substantial amount of experimental data has been collected, there is still a lot of open questions (e.g. /1/).

Electron-beam-induced-current (EBIC) investigations have largely contributed to the current state of knowledge about dislocations. In particular, EBIC imaging and measurements of contrast c in dependence on temperature T and beam current I_b (initiated by an early work of Kimerling et al. /2/) turned out to be a very valuable experimental tool. Applied by the Oxford group to dislocations in plastically deformed Si, this technique revealed a positive $c(T)$ and a negative $c(I_b)$ slope. The experimental results were interpreted as due to a potential barrier around the dislocations, see /3/. However, in recent studies the opposite $c(T)$ behaviour (negative slope) was observed for dislocations in plastically deformed Si /4/, for dislocations in cast multicrystalline Si and for misfit dislocations in SiGe/Si structures /5,6/.

At the first glance it may look confusing that the same type of dislocations prepared in different laboratories by plastic deformation exhibits opposite $c(T)$ behaviour. The most likely explanation is a different degree of contamination by impurities. Fig. 1 illustrates this possibility for dislocations generated during a deformation experiment. The scratch in the middle of the micrographs served as dislocation source. The micrograph on the right was taken at 300 K and shows a zone of reduced dislocation activity around the scratch. At larger distance from the scratch, dislocations exhibit pronounced recombination activity. At 80 K (left image) all dislocation are active, which demonstrates that dislocations near the scratch show

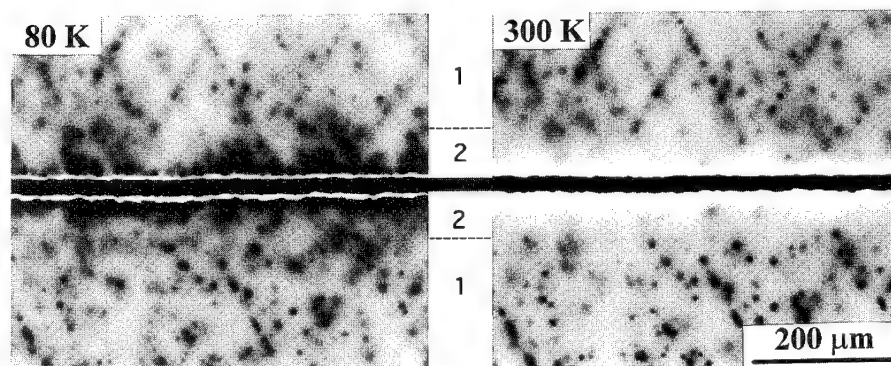


Fig. 1: Recombination activity of dislocations in a p-type CZ-Si sample at 300 and 80 K (dislocations introduced by plastic deformation at 700°C). Note the difference in the temperature dependence of contrast of dislocations close (region 2) and far (region 1) from the scratch.

another $c(T)$ behaviour than those far away. Scratches are known to getter impurities, so the difference in dislocation behaviour is probably due to different contamination. Contamination is also supposed to be responsible for the experimental fact that, even in the same SiGe/Si sample, misfit dislocations of both positive and negative $c(T)$ slope can be observed [7].

In the following we report results of EBIC studies of dislocation activity after different treatments. The results are based on EBIC imaging and contrast measurements in the temperature range 80 ... 300 K. As pointed out in [8,9] the type of temperature behaviour allows at least to draw qualitative conclusions about the centres responsible for the recombination activity observed. Type-1 behaviour, characterized by a positive $c(T)$ slope is attributed to deep centres or charged defects. Type 2 with a negative $c(T)$ slope is believed to be caused by shallow centres. The measurements were carried out at 30 keV beam energy and beam currents around 50 pA, using evaporated Schottky contacts as collecting junctions. For more experimental details see e.g. [10].

INFLUENCE OF CONTAMINATION ON MISFIT DISLOCATION ACTIVITY

SiGe/Si epilayers grown by chemical vapour deposition (CVD) and supplied by North Carolina State University were used for the experiments. The common structure of these samples was as follows: (100) Si substrate, Si buffer layer, SiGe alloy layer (2% Ge, 2 μm), and Si cap (3 μm) on top. In such structures a network of perpendicular sets of 60° misfit dislocations arises at the SiGe interfaces. The density of misfit dislocations can be controlled by Ge content and layer thickness. So, these dislocations are considered a well-defined 'model defect'.

A controlled Cu contamination of the samples was obtained by backplating from a Cu salt solution and a 800°C anneal for Cu drive-in. The Cu content in solution was measured by Atomic Absorption Spectroscopy and the surface concentration was checked by Total X-ray Reflection Fluorescence. Using this procedure, the Cu volume concentration could be varied from sub-ppb to ppm range [11].

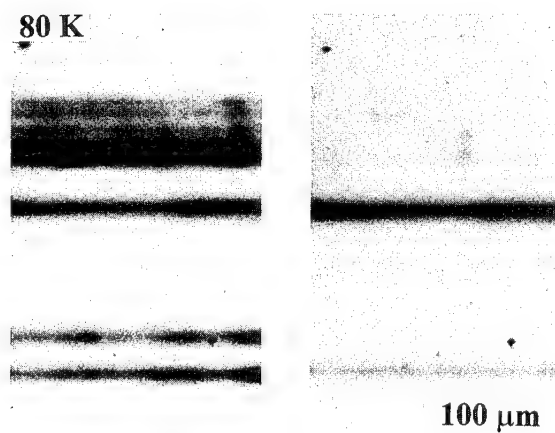


Fig. 2: Recombination activity of misfit dislocations in a slightly Cu contaminated sample at 80 and 300 K (EBIC, 30 keV). The numbers indicate the contrast in per cent.

In the as-grown samples no contrast could be observed at 300 K (detection limit of our set-up better than 0.2%). Only upon cooling the dislocations became visible, with a very small contrast of about 0.4% at 80 K [10]. This behaviour is denoted type II, because $c(T)$ has negative slope as type 2, but the contrast level is much lower.

At low Cu contamination (ppb range), different types of $c(T)$ behaviour can be observed. Some dislocations have substantial recombination activity at 300 K already, others are nearly invisible at room temperature but exhibit a steep contrast increase on cooling. Fig. 2

illustrates this experimental fact. Neighbouring dislocations/dislocation bundles are seen to behave in a completely different way. There is one dislocation bundle with a positive $c(T)$ slope corresponding to type-1 behaviour. Detailed measurements for this bundle revealed a contrast approximately proportional to $T^{0.5}$. Other dislocations show clearly type-2 behaviour. Certain dislocations in the samples exhibit a mixture of both types. At the lowest Cu level (~1ppb) the majority of dislocations shows type-2 behaviour. For higher Cu levels (~15ppb) dislocations with positive $c(T)$ slope (type 1) are dominating.

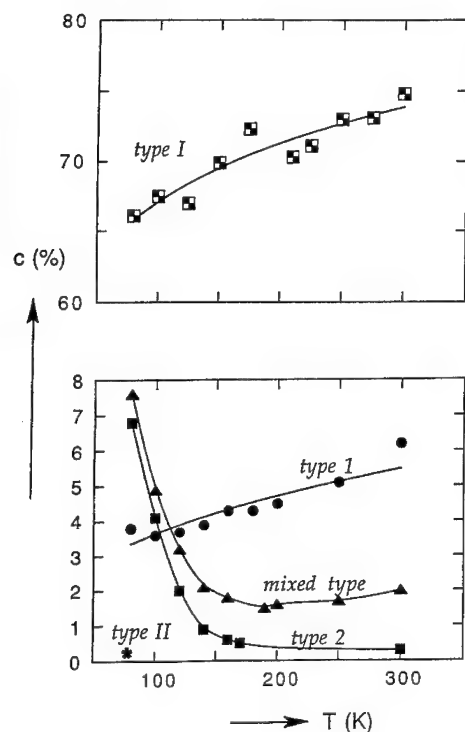


Fig.3:EBIC contrast c of misfit dislocations vs. temperature T for different Cu contamination levels: as-grown - type II, low Cu - type 2 \rightarrow mixed \rightarrow type 1, high Cu - type I.

In the high Cu contaminated samples (ppm range) a positive slope is found for the majority of dislocations, too. However, contrast is extremely large and has a weaker dependence on temperature than type-1 contrast in low Cu samples. This behaviour is denoted type I here. TEM investigations revealed Cu silicide precipitates at the dislocations.

Results of temperature-dependent contrast measurements for the different Cu contamination levels are summarized in Fig. 3. Starting from 'clean' as-grown material with type-II dislocations, all other types of contrast behaviour are obtained by increasing contamination level. At low contamination we have type-2, then type 1 and eventually type I at the highest levels.

POLISHING-INDUCED DISLOCATION ACTIVATION

Recently, chemomechanical polishing has been reported to lead to a substantial decoration of defects [12]. A similar observation concerning the electrical activity of dislocations in cast multicrystalline silicon has been described in [13]. More detailed studies showed that dislocations in the virgin as-grown material are nearly inactive at 300 K, but gain pronounced recombination activity at low temperatures (type - 2 behaviour). After polishing, there is pronounced contrast already at 300 K which slightly decreases on cooling (type-1 behaviour) - see Fig. 4. Thus, the dislocation activity is controlled by shallow centres in the as-grown state

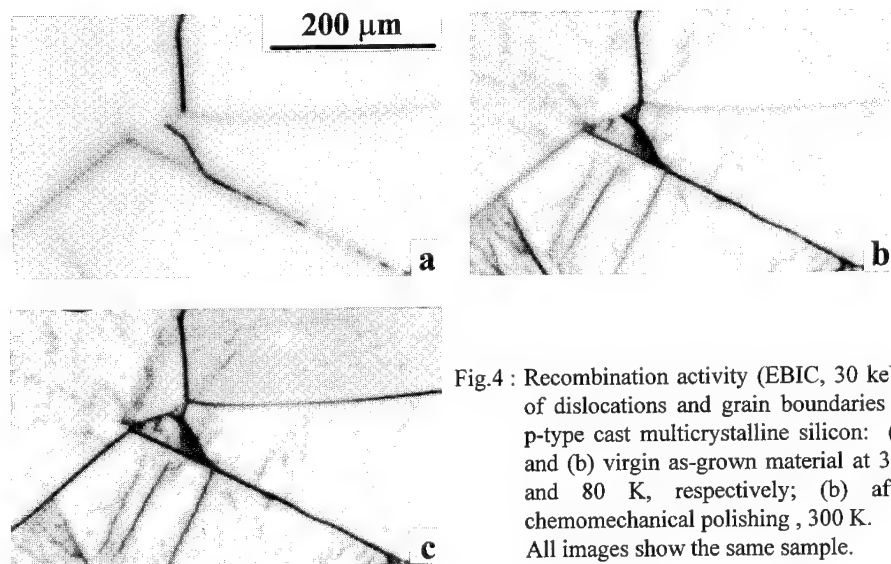


Fig.4 : Recombination activity (EBIC, 30 keV) of dislocations and grain boundaries in p-type cast multicrystalline silicon: (a) and (b) virgin as-grown material at 300 and 80 K, respectively; (c) after chemomechanical polishing, 300 K. All images show the same sample.

while dislocation recombination properties are governed by deep centres after chemomechanical polishing. Hence, polishing leads to the introduction of deep centres. Interestingly, dislocation activation is not restricted to a thin layer near the surface, but was revealed to extend at least 50 μm in depth. Annealing at temperatures in the range 500 ... 1000°C was found to remove deep

centres again. All the changes in recombination activity of dislocations could be monitored as well by EBIC diffusion length measurements /13/.

EFFECT OF HYDROGENATION

Hydrogenation experiments were carried out at 300°C in a hydrogen plasma (5-10 Torr, 13.5 Mhz). All samples were RCA cleaned prior to treatment and placed downstream of the plasma /11/.

Hydrogenation is found to have a positive effect on those dislocations which are already active at room temperature. This is true both for polishing-activated dislocations in multicrystalline silicon and misfit dislocations. The dislocation activity at 300 K decreases considerably due to hydrogenation, however the dislocation remain active at low temperature, i.e. hydrogenation does not remove dislocation activity, but transforms type-1 into type-2 behaviour (Fig. 5).

Type-2 dislocations are usually not influenced by hydrogenation. Only in few cases we observed a slight reduction of activity of those dislocations. Never hydrogenation succeeded in restoring the low-activity state II of misfit dislocations existing before contamination. For misfit dislocations of type-I we could not reveal any significant influence of hydrogen treatment.

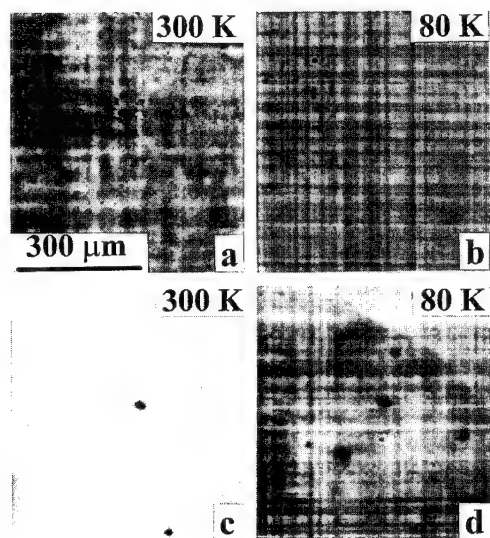


Fig. 5: Influence of hydrogenation on recombination activity (30 keV) of Cu contaminated misfit dislocations: (a) and (b) activity before hydrogenation, (c) and (d) after hydrogenation.

CONCLUSION

The results obtained clearly demonstrate that dislocation recombination behaviour is determined by the contamination level.

Dislocations in clean as-grown material are nearly inactive (type II). The negative slope of $c(T)$ points to shallow centres. Two explanation can be proposed: (i) true intrinsic dislocation property caused by the dislocation strain field and (ii) strongly reduced activity of normally type-2 dislocation by hydrogen (hydrogen is used as carrier gas during CVD layer growth). As hydrogenation experiments never restored type II behaviour it seems that type II activity is the intrinsic dislocation property.

Low contamination levels of misfit dislocations lead to type-2 activity which is attributed to shallow centres. At higher concentration deep centres are revealed (type 1). Behaviour indicating deep centres is observed also after chemomechanical polishing. Hydrogenation is found to passivate room temperature recombination activity of both misfit dislocations and dislocations in multicrystalline Si, leaving activity at low temperatures essentially unaffected. This means that hydrogenation passivates deep centres or transforms them into shallow ones. For polishing-activated dislocations in multicrystalline Si, simple annealing in a wide range of temperatures had the same effect.

At very high Cu contamination levels extremely strong recombination activity is observed. According to recent calculation /14/, this requires a minimum radius of the recombination-active region of about 1 μm , compared to radii in the nm range for dislocations of normal activity. This result can be understood, if we assume that Cu silicide precipitates decorating the dislocations form internal Schottky barriers with depletion regions widths of nearly 1 μm . This suggestion is supported by apparent similarities to the recombination behaviour of individual NiSi_2 platelets /15/.

To summarize, increasing contamination is not only established to result in an increase of activity, but also to induce qualitative changes of recombination properties. Dislocation of different origin behave in a similar way.

ACKNOWLEDGEMENTS

The authors thank North Carolina State University for supplying samples with misfit dislocations, S. Pizzini (Milano, Italy) for deformed samples and C. Ulhaq-Bouillet (Strasbourg, France) for TEM investigations. Parts of the work were supported by the German Federal Ministry of Education and Research, Bonn under contract number 0329536H.

- /1/ V.V.Kveder, in Gettering and Defect Engineering in Semiconductor Technology, edited by H.G. Grimmeiss, M.Kittler and H. Richter, Solid State Phenom. Vols. **32-33** (1993), p. 279; V. Higgs, *ibid.*, p. 291; Z.J. Radzimski, A. Buczkowski, G.A. Rozgonyi, *ibid.*, p.309
- /2/ L.C. Kimerling, H.J. Leamy, J. R. Patel, Appl. Phys. Lett. **30**, 217 (1977)
- /3/ P.R. Wilshaw, T.S. Fell, G.R. Booker, in Point and Extended Defects in Semiconductors, edited by G. Benedek, A. Cavallini, W. Schröter (Plenum, New York, 1989), p. 243
- /4/ S. Kusanagi, T. Sekiguchi, K. Sumino, Appl. Phys. Lett. **61**, 792 (1992)
- /5/ Z.J. Radzimski, T.Q. Zhou, A.B. Buczkowski, G.A. Rozgonyi, D. Finn, L.G. Hellwig, J.A. Ross, Appl. Phys. Lett. **60**, 1096 (1992)
- /6/ M. Kittler, W. Seifert, Z.J. Radzimski, Appl. Phys. Lett. **62**, 2513 (1993)
- /7/ M. Kittler, W. Seifert, Scanning 15, 316 (1993)
- /8/ M. Kittler, W. Seifert, phys. stat. sol. (a) **138**, 687 (1993)
- /9/ M. Kittler, W. Seifert, Mater. Sci. Eng. B **24**, 78 (1994)
- /10/ M. Kittler, W. Seifert, V. Higgs, phys. stat. sol. (a) **137**, 327 (1993)
- /11/ V. Higgs, M. Kittler, Appl. Phys. Lett. **65**, 2804 (1994)
- /12/ S.A. McHugo, W.D. Sawyer, Appl. Phys. Lett. **62**, 2519 (1993)
- /13/ M. Kittler, W. Seifert, G. Morgenstern, J. Electrochem. Soc. **140**, 556 (1993)
- /14/ C. Donolato, phys. stat. sol.(a) **135**, K13 (1993)
- /15/ M. Kittler, J. Lärz, W. Seifert, M. Seibt, W. Schröter, Appl. Phys. Lett. **58**, 911 (1991)

RECOMBINATION AT OXIDATION INDUCED STACKING FAULTS IN SILICON

J A DAVIDSON*, J H EVANS*, M VANDINI** and A R PEAKER*

* Centre for Electronic Materials and Department of Electrical Engineering & Electronics,
University of Manchester Institute of Science and Technology, Sackville Street, Manchester,
M60 1QD, UK

** Department of Physics, Bologna University, Via Imerio 46, 40126 Bologna, Italy

ABSTRACT

We have characterised the recombination at Oxidation Induced Stacking Faults (OISF) by employing a combination of DLTS and Minority Carrier Transient Spectroscopy (MCTS). The recombination rate at traps associated with the OISF has been compared with recombination at a conventional point defect also present in the silicon. We find that the effect of small amounts of decoration by copper is to increase hole capture rates at electron filled traps. Infra Red Beam Induced Current measurements are consistent with this in that they also indicate that decoration causes enhanced recombination at the extended defects.

INTRODUCTION

Oxidation induced stacking faults (OISF) in silicon can result from oxidation processes even when the oxidation times are short. Their presence is known to adversely affect device performance when in the active region. However, conventional point defect analysis cannot be applied to such defects, because they include interacting charge sites arranged along a one-dimensional line. This results in a localised electric field around the extended defect.

Kolbesen et al[1] showed that the effect of OISF in silicon is to produce an increase in the junction leakage current in power devices and studies by Ourmazd et al[2] have shown that the recombination activity of OISF in silicon is located around the Frank partial dislocations which bound the OISF. Previous studies of the electrical properties of OISF have employed Deep Level Transient Spectroscopy (DLTS) to characterize electron traps associated with OISF in n-type silicon[3]. A trap was observed whose spatial concentration profile correlated with that of the Frank partial dislocations. Moreover, electron capture by this state exhibits a logarithmic dependence on time [4]. Such non-exponential capture is a characteristic property of deep levels associated with extended defects [5]. The same behaviour has been reported for minority carrier traps associated with OISF in n-type silicon [6]. In this work, a trap was observed with a measured hole capture rate that is approximately exponential (point defect-like) at low occupancy, but a reduced capture rate is observed as the occupancy is increased.

We report here a study of non-radiative recombination at the traps associated with OISF characterized using a combination of DLTS and Minority Carrier Transient Spectroscopy (MCTS)[7] in a single measurement. We have also considered the effects of transition metal contamination on the electrical properties of the OISF. This was achieved by decorating the

defects with a small amount of copper. The DLTS results are compared to recombination measurements carried out by IRBIC.

EXPERIMENTAL

The silicon used in this work consisted of n-type epitaxial layers, doped with $2 \times 10^{15} \text{ cm}^{-3}$ phosphorus grown on CZ n^+ substrates. The silicon surface was oxidised for 10 minutes in dry oxygen at 1100°C , followed by 90 minutes in a steam ambient, followed by a final oxidation in dry oxygen for 10 minutes. This process creates Oxidation Induced Stacking Faults (OISF) with a mean length of $13 \mu\text{m}$, and a density of $2 \times 10^5 \text{ cm}^{-2}$. The oxide was then removed, and samples containing OISF to be decorated were lightly stroked on the rear surface with clean copper wire; these samples were subsequently annealed under dry nitrogen at 750°C for 30 minutes. Semi-transparent gold Schottky diodes were then deposited on the wafer surface.

Electrical characterization was performed using DLTS and Minority Carrier Transient Spectroscopy (MCTS). In the latter, the electrical fill pulse of DLTS is replaced by a pulse of above-bandgap light, originating from a GaAs/AlGaAs laser diode emitting at 860 nm . Minority carriers generated that lie within a diffusion length of the depletion region edge may diffuse into the space charge region, creating a minority carrier flux that is available for capture by deep levels. The electric field excludes majority carriers from this region.

Recombination cannot be characterized by DLTS or MCTS used in isolation because the process requires the capture of both majority and minority carriers. Considering the case of a recombination centre in the lower part of the bandgap in n-type material, MCTS may be used to analyze only the hole capture by this centre; DLTS will not detect the centre as it cannot emit to the conduction band. In order to characterize electron capture by this level, the combination of the two techniques into a single measurement (MCTS+DLTS) is used. In this, the level is initially filled with holes by using a long light pulse. Immediately after this pulse terminates, electrons are injected into the diode via a forward bias pulse, during which electrons will be captured to the level and lower the hole occupancy. Since the height of the peak in the MCTS spectrum is proportional to the hole occupancy, a reduction in peak height will ensue. As the duration of the electron injection pulse is increased, there will be further reduction in the hole occupancy and the corresponding peak height. Ultimately, the injection pulse will be sufficiently long that the level will become entirely electron occupied. At this point, the hole emission peak in the spectrum will no longer be detected. Alternatively, the recombination centre may lie in the upper part of the bandgap. In this case, the converse technique (DLTS+MCTS) is used. Here, the pulse sequence described above is interchanged and the reverse description applies.

If a deep level exhibits ideal point defect-like behaviour, the capture rate during the secondary pulse in these techniques will decrease exponentially as the pulse duration is increased. A Shockley Hall Read model may then be used to derive the relevant carrier capture cross-section. In this manner, both the electron and hole capture cross-sections of a point defect anywhere in the bandgap may be determined. This is extremely useful in assessing the ability of an individual deep level to act as a recombination centre.

Infra-Red Beam Induced Current (IRBIC) experiments were carried out at room

temperature with zero bias applied to the semi-transparent Schottky diode. Above band gap light (600nm) was used, in order to ensure that the Frank partial dislocation bounding the OISF was entirely within the e-h pair generation volume. The level of contrast in the IRBIC image was monitored to assess relative recombination strengths of OISF related traps.

RESULTS AND DISCUSSION

Figure 1 shows typical DLTS spectra, curves (a) and (b), and an MCTS spectrum, curve (c). Curves (a) and (c) are measured from silicon containing nominally clean (not deliberately decorated) OISFs, and curve (b) shows the effect on the DLTS spectrum of a small amount of decoration by copper. The peaks are labelled Au[-/0] for the gold acceptor, Au[+/0] for the Au donor, Au for other gold related defects[6], S_e for the electron trap related to the presence of the OISF and S_h for the OISF hole trap. The gold peaks are always present in such samples, which is due to pipe diffusion along the dislocation, because gold is used to fabricate the Schottky diodes. Gold related traps cannot be detected in identical silicon with (gold Schottky diodes) that has not been oxidised. The activation energies of the Au traps are in good agreement with those reported in the literature for the gold donor and acceptor. The activation energy of the S trap depends upon the experimental conditions during DLTS which affect the occupancy, and the degree of decoration[4]. However, it can be seen from Fig 1 that the S_e trap moves to a higher temperature after decoration with copper, in agreement with previous reports of the effect of decoration [3].

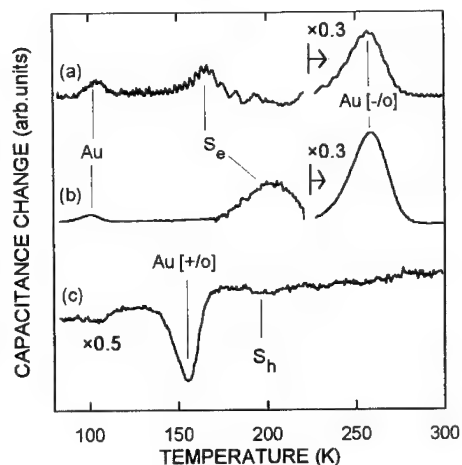


Figure 1. DLTS (a), (b) and MCTS (c) of silicon containing OISF, nominally clean (a), (c), and decorated with copper, (b). The rate window was 20 s^{-1} .

Figure 2 illustrates DLTS+MCTS of silicon containing decorated OISF. The spectra do not include the high temperature gold acceptor, for clarity, as the recombination properties and capture cross sections of this defect are well known [8]. A 10 ms electron pulse was sufficient to effectively fill the traps in the DLTS measurement. It can be seen that the S_e peak reduces rapidly with increasing laser (hole filling) pulse length and is no longer detected after a fill pulse $\geq 50 \mu\text{s}$. Since, in this experiment, the trap is initially filled with electrons (majority carriers) the reduction in the peak height is due to subsequent hole capture.

Figure 3 shows the hole capture behaviour of S_e traps with and without copper decoration. The Au-related trap has also been examined in order to provide an internal calibration against which the S_e level may be compared. For the undecorated OISF, both levels exhibited similar (point defect-like) characteristics when refilled with holes [6]. However, when Cu decoration is present, the S_e peak intensity reduces at a faster rate than that of the gold related trap,

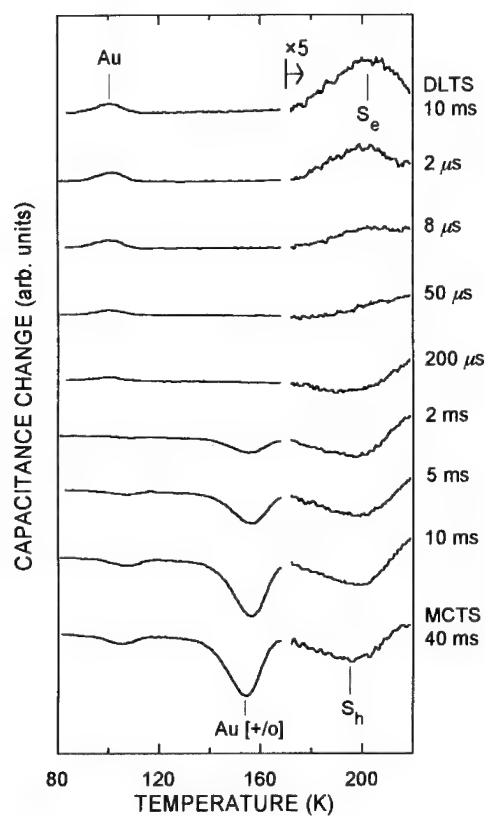


Figure 2.
DLTS + MCTS of n-type silicon containing decorated OISF. The laser (hole) pulse lengths are indicated on the right for all but the top curve which corresponds to DLTS only (no hole pulse). The bottom curve is MCTS only (no electron pulse). The rate window was 20 s^{-1} .

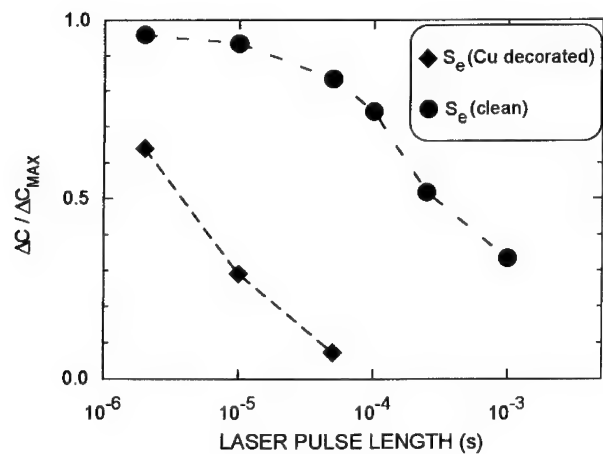


Figure 3.
The change in peak height as the DLTS is combined with MCTS (DLTS + MCTS), for nominally clean (●) samples and decorated samples (◆). Peak heights are normalized to DLTS peak heights (ΔC_{MAX}).

indicating that the efficiency of the S_e level as a recombination centre is dramatically increased. The difference in this behaviour is similar to that observed in IRBIC measurements on OISFs. The addition of Cu as a lightly decorating impurity to the OISF causes an enhancement in the beam-induced current contrast from 9% to 18%; this indicates a large increase in the recombination rate after copper decoration.

Figure 4 shows MCTS+DLTS of silicon containing decorated OISF. The spectra are shown up to a measurement temperature of 220 K as in Fig 2. The peak labelled S_h , due to emission from hole-filled traps, reduces in intensity very rapidly as electrons are injected by forward biasing the diode. At a DLTS fill pulse length above $1\text{ }\mu\text{s}$ this peak can no longer be detected. This is similar behaviour to that of the S_e trap in the upper half of the band gap, shown in Fig 2.

Ideal point-defect-like behaviour of the gold donor (peak $\text{Au}[+/0]$) should produce a further reduction in the intensity of this peak when DLTS fill pulses above $1\text{ }\mu\text{s}$ are applied. Interestingly, in this experiment, this is not observed; a negative peak is seen in every spectrum

in Fig 4. This indicates that hole emission is still taking place after DLTS pulse lengths of $170\text{ }\mu\text{s}$. Previous capture cross section measurements of this gold related defect in silicon containing OISF [6] have demonstrated that exponential capture, a phenomenon associated with point defects, occurs for electron capture at the gold acceptor and hole capture at the gold donor. However, in samples used in this work the gold is only present at all because there are stacking faults present, and it is reasonable to suppose that the gold atoms are located near the fault planes. The extended defects cause strain fields and therefore the gold is likely to be in a region of perturbed crystallinity. This is a key factor in the behaviour detected in an experiment such as MCTS+DLTS where there are competing capture and emission processes. If the gold atom is in a region of slight band bending due to an extended defect, the local electron concentration, and hence the electron capture rate, will be reduced. Similarly, the local hole concentration may increase. This would explain why hole emission is always observed in

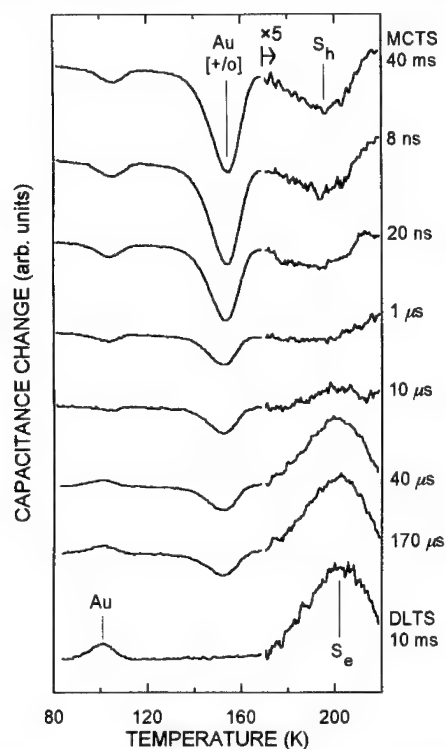


Figure 4. MCTS + DLTS of silicon containing decorated OISF. The top curve is MCTS only and the bottom curve is DLTS only. The rate window was 20 s^{-1} .

this experiment for the gold donor, even when a substantial time is allowed for electron capture via the bias pulse. Apart from the hole emission from the gold donor trap, $\text{Au}[+/0]$, the curve in Fig 4 with a $170\ \mu\text{s}$ DLTS fill pulse is identical to the curve at the bottom which is pure DLTS i.e. no hole pulse.

CONCLUSIONS

We have combined the techniques of DLTS and MCTS to characterize recombination properties of OISF related traps in silicon in both halves of the band gap, and examined the effect of decoration. Both majority carrier traps and minority carriers traps associated with the OISF exhibit recombination when exposed to carriers of the opposite polarity. The recombination strength of the electron trap (in the upper half of the band gap) is enhanced when small amounts of copper decorate the OISF. This correlates with IRBIC measurements, in which increased contrast (increased recombination) at the stacking faults is observed after decoration.

ACKNOWLEDGEMENT

Part of this work was sponsored by a NATO Collaborative Research Grant.

REFERENCES

- [1] B.O. Kolbesen, W. Bergholz, H. Cerva, F. Gelsdorf, H. Wendt and G. Zoth, *Inst. Phys. Conf. Ser.* **104** 421 (1989).
- [2] A. Ourmazd, P. R. Wilshaw and G. R. Booker, *Physica B* **116**, 600 (1983).
- [3] J. Kaniewski, M. Kaniewska and A.R. Peaker, *Appl. Phys. Lett.* **60**, 359 (1992).
- [4] Y. Qian, J.H. Evans and A.R. Peaker, *Inst. Phys. Conf. Ser.* **134**, 121 (1993).
- [5] W. Schröter, I. Queisser and J. Kronewitz, *Inst. Phys. Conf. Ser.* **104**, 75 (1989).
- [6] J.H. Evans, J.A. Davidson, M. Saritas, M. Vandini, Y. Qian and A.R. Peaker, to be published in *Mat. Sci. Tech.*
- [7] R. Brunwin, B. Hamilton, P. Jordan and A.R. Peaker, *Electron. Lett.* **15**, 348 (1979).
- [8] R.H. Wu and A.R. Peaker, *Solid-State Electron.* **25**, 643 (1982).

SURFACE PASSIVATION AND THE ULTRAFAST OPTICAL RESPONSE OF LOW-TEMPERATURE-GROWN GaAs

H. H. WANG*, J. F. WHITAKER*, K. AL-HEMYARI**, AND S. L. WILLIAMSON**

*Center for Ultrafast Optical Science, University of Michigan, Ann Arbor, MI 48109-2099

**Picometrix, Inc., P.O. Box 130243, Ann Arbor, MI 48113-0243

ABSTRACT

Metal-semiconductor-metal photodetectors fabricated using low-temperature-grown GaAs have been passivated using AlGaAs cap layers in order to understand the influence of surface states and fields on the properties of these detectors. It has been found that passivation has little effect on the time response or persistent photoconductive tails associated with the detectors, but that responsivity and dark current can be enhanced in certain circumstances. The dependence of the temporal response on optical fluence and dc-voltage bias were observed for both passivated and unpassivated detectors.

INTRODUCTION

The presence of surface states in GaAs has hindered the development of electronic devices, as demonstrated by, for example, the inability to produce a MISFET technology analogous to the Si MOSFET, and the degradation of gain in heterojunction bipolar transistors using AlGaAs/GaAs materials.¹ In the field of optoelectronics, the surface states in semi-insulating GaAs (SI-GaAs) strongly affect the photoexcited carrier lifetime due to the large surface field and surface recombination velocity they induce.² Moreover, in transit-time-limited, metal-semiconductor-metal (MSM) photodetectors, the so called "low-frequency gain" phenomenon, which decreases frequency response and increases the possibility of breakdown from non-uniform fields, is also present due to the surface states near the contacts.³

Since the discovery of low-temperature-grown GaAs (LT-GaAs), an increasing number of electronic and optoelectronic applications have been developed for epitaxial materials with ultrafast relaxation-times, high resistivities, and high breakdown voltages.⁴ Due to its unique properties, LT-GaAs has been employed, for instance, as a buffer layer sandwiched between an n-active layer and a semi-insulating GaAs substrate⁵ to eliminate the side-gating effects of MESFET devices. In optoelectronic applications, LT-GaAs has been used to realize an ultrafast photodetector (in one instance⁶ having a 3-dB bandwidth ≥ 375 GHz, and a responsivity ~ 0.2 A/W) due to its subpicosecond photoexcited carrier lifetime and reasonably high mobility. However, despite the fact that LT-GaAs is extensively used to make both commercial and laboratory ultrafast photodetectors, there has been little study of the impact of surface states on its optoelectronic properties. The goal of this paper is to present the effect of surface states on high-speed, LT-GaAs, MSM photodetectors in terms of dark current and low- and high-frequency performance.

For the fast-response photoconductive devices, four parameters have been investigated to see if they are affected by surface passivation. These are listed as follow: the dark current, which determines the noise level and thus impacts on the detector signal-to-noise ratio (SNR); the time response, frequently estimated as the $1/e$ relaxation time of an exponential decay, which provides information about carrier trapping and detector temporal resolution; tail response or persistent photoconductive decay, which represents a second, bandwidth-limiting time constant in the response and has been attributed to hopping conductivity in LT-GaAs; and amplitude response, which is used to determine the responsivity and the signal-to-noise ratio (SNR).

THEORETICAL CONSIDERATIONS

We will first estimate the effect of passivation on the time and amplitude response of an MSM detector, while the dark current will be considered later. Although there are many reported studies of surface states for conventional GaAs, there is little information on the LT-GaAs surface. It was suggested by Look, *et al.*⁷ that a high density of surface states exists on LT-GaAs, possibly due to the oxidation of arsenic atoms (*i.e.*, As₂O₃). These surface states are typically electron traps as in conventional GaAs. These trapped electrons near the surface produce a large gradient of potential within a 100-Å-thickness, and thus the corresponding built-in electric field is very large (rough estimates find it to be larger than 100 KV/cm). Therefore, when carriers are photoexcited in an LT-GaAs detector, the total response of the detector is governed by both bulk recombination and the surface.

Due to the very high density of defect states in LT-GaAs arising from the presence of excess arsenic, the bulk recombination time for the material is approximately 1 ps (for a growth temperature around 230°C), which gives a recombination rate of 10¹² s⁻¹. The recombination rate from the surface is approximately equal to the surface recombination velocity (SRV) divided by the epilayer thickness.² For GaAs, the SRV is about 10⁴ cm/s for an air-exposed wafer. If the epilayer of a photodetector is 1-μm thick, then the surface recombination rate is on the order of 10⁸ s⁻¹, which is much less than for bulk recombination. Therefore, from the perspective of the total number of recombined carriers, the surface recombination has a negligible contribution to the detector temporal response.

The response of LT-GaAs MSM detectors in the time domain typically has another component, however. This is a persistent, photoconductive tail which is due to the photoresponse of LT-GaAs (for T_g > 220°C) and is believed to arise due to hopping conductivity of carriers in the high density of bulk defect states. There is no evidence that the presence of surface defect states affects this hopping conductivity since it takes place through the much greater number of bulk defect states, and thus we expect no difference in the photoconductive tails after detector surface passivation.

In terms of photoconductivity amplitude, the photocurrent collected by the electrodes is not only determined by the carrier lifetime, but it also depends on the geometrical structure of the detector. If the photocurrent that the detector can collect is primarily contributed by carriers that are generated near the surface, then the surface field will have an impact on the photocurrent, and therefore the performance of the detector. The current density flowing into the contacts can be expressed as follows (for simplicity only the electron current is considered):

$$J_n = q(n(t) \mu_n (E_b + E_s) + D_n \nabla n(t)) \quad (1)$$

where E_b is the bias field, and E_s is the surface field. For a material with very short carrier lifetime like LT-GaAs, which has a mobility, μ_n , of about 100 cm²/V-s, the saturation velocity of the electrons is around 10⁷ cm/s. The anode can then only collect photoelectrons from an area within ~ 1000 Å of the contact for a sample of 1-ps carrier lifetime. Therefore, the 10% of photoelectrons that make up the conduction current experience a surface field that tries to drive them down towards the substrate, decreasing their chances of reaching the metal. However, with a passivated cap layer on top of the LT-GaAs, this effect can be eliminated and the responsivity of a photodetector should be improved.

DEVICE FABRICATION

To better prepare the surface of GaAs, sulfur-related chemical^{1,2} and solid-state⁸ passivation techniques have been introduced to diminish the effects of the dangling bonds. In general, a

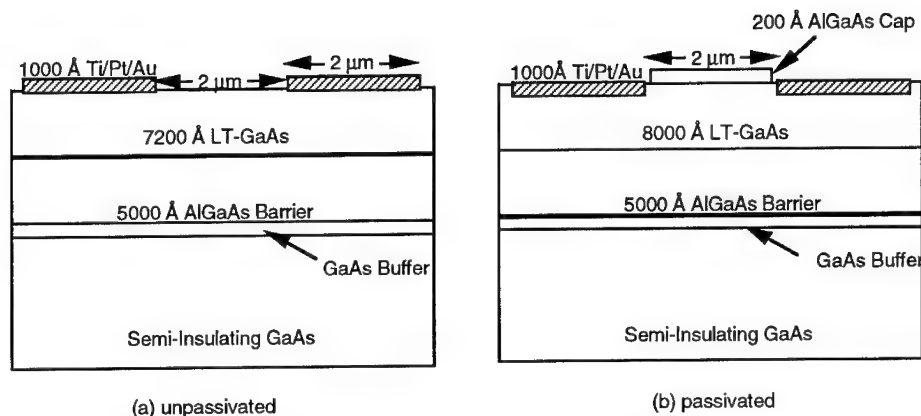


Figure 1. Cross section of LT-GaAs MSM photodetectors and material layers.

density of surface-states of 10^{11} cm^{-2} could be passivated by the above techniques, but not without fabrication concerns. To be specific, we have determined that while passivation of GaAs with ammonium sulfide is quick and universally applicable, its lack of stability after only hours of exposure in an ambient laboratory environment is at best an inconvenience. It is also not clear how completely this technique passivates a surface. The solid-state, PECVD technique may also be used with arbitrary samples, but it is somewhat more difficult to implement, and we have not yet perfected its fabrication. Perhaps the most simple solution, and the one followed for samples described throughout this work, was to prepare the LT-GaAs epitaxial layers studied with a 200-Å-thick layer of AlGaAs covering them. This passivation provides an optimized LT-GaAs surface, without a significant density of trap states, and it does not absorb photons of red and infrared light.

Two LT-GaAs wafers were grown at 270°C and 300°C in order to investigate the effect of this passivation. The material structure is shown in Fig. 1. The bottom AlGaAs layer was grown primarily to prevent any substrate current injection. The unpassivated samples were prepared by using a wet etch ($\text{H}_3\text{PO}_4/\text{H}_2\text{O}_2/\text{H}_2\text{O}$) to remove the AlGaAs cap layer. For the passivated samples, only the area where the metal was to be deposited was etched, so that the region between the fingers of the MSM was passivated by the remaining AlGaAs. A Ti/Pt/Au electrode with 1000-Å thickness was evaporated through standard photolithographic techniques to form the 2-μm-wide fingers of the detector pattern. In order to measure the high speed electrical signal output from the photoexcited detector, a 1-cm-long coplanar strip transmission line with 50-μm separation was defined with the MSM detector in between the lines and 5 mm from each end.

EXPERIMENTAL RESULTS

DC Measurements

The I-V curve for the detectors fabricated on the samples grown at $T_g = 270^\circ\text{C}$ is shown in Fig. 2. The four sets of data in the semi-log plot each have one curve for a passivated detector and one curve for an unpassivated detector. The bottom two curves are measured in the dark, and the other three sets were measured under three different cw laser power levels. As shown in the plot, the photocurrent for the passivated detector was always larger than that of the unpassivated one by 30 to 80% for different optical power levels at biases less than 10 V. This suggests that the passivated

sample collects more carriers than the unpassivated one. Another advantage of passivation for these two samples is that the dark current for the passivated sample is much smaller than for the unpassivated one at biases higher than 10 V. Since the SNR is inversely proportional to the square root of the dark current, the passivated sample can be biased up to 20 V without significantly degrading the SNR. This phenomenon might be explained by the presence of surface-state traps near the contacts which would capture carriers and create a space-charge region. This would create a non-uniform field distribution, thus increasing the injection of charge from the contacts and as a result, increasing the dark current. The clamping of current for the passivated sample at high bias can not be explained by the photodetector already reaching its transit-time-limited regime, as for SI-GaAs MSM detectors. Therefore, further investigation must be done to explain this phenomenon.

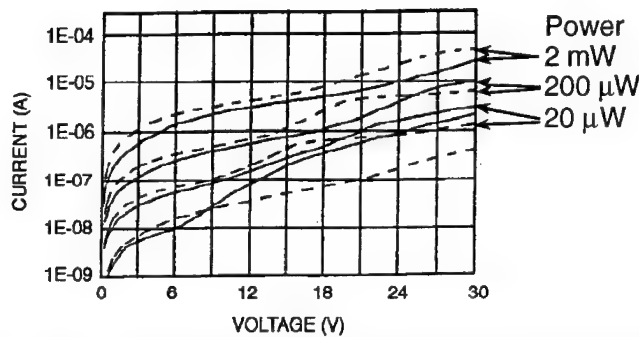


Figure 2. I-V curves for 270°C LT-GaAs MSM detectors. Dotted lines are for the passivated sample and solid lines for the unpassivated one. Dark current is the bottom set of two curves, with the other curves corresponding to three, cw optical power levels at $\lambda = 810$ nm.

The I-V curves for the detectors on the LT-GaAs grown at 300°C are shown in Fig. 3. Note that the optical power levels are different than for the data on the $T_g = 270^\circ\text{C}$ detectors. The photocurrents for the passivated and unpassivated detectors are nearly the same across almost the entire bias range. This indicates that the passivation has little advantage in terms of responsivity for

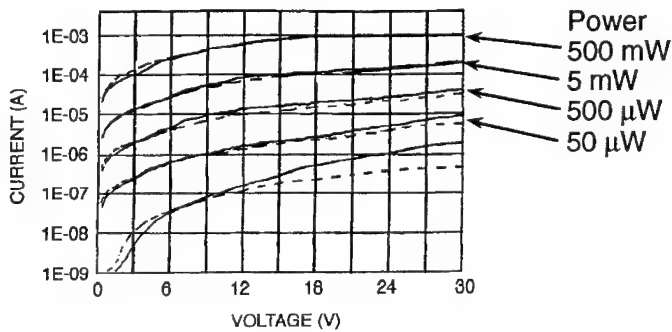


Figure 3. I-V curves for 300°C LT-GaAs MSM detectors. The dotted lines are for the passivated sample and solid lines for the unpassivated one. Dark current is the bottom set of two curves, with the successively higher sets of curves corresponding to four, cw optical power levels (50 μW , 500 μW , 5 mW, and 500 mW) at $\lambda = 810$ nm.

these detectors on the LT-GaAs with $T_g = 300^\circ\text{C}$. This is as expected for this material, since the carrier lifetime is longer and the mobility is higher than for the wafer with $T_g = 270^\circ\text{C}$. Thus the fraction of photocurrent contributed by the carriers near the surface is smaller than for the detectors grown on the LT-GaAs grown at higher temperatures. However, in terms of dark current, the passivated detector using material with $T_g = 300^\circ\text{C}$ is still superior to the unpassivated one, and the passivated detector will thus have a higher SNR. Also, from Fig. 3, it was determined that the MSM detector was not reaching its transit-time-limited current since no current clamping was observed up to a bias of 30 V (the curve tracer allowed a current maximum of 1.0 mA).

Pulse Measurements

In order to test the time response of the detectors, a standard, external-electro-optic sampling technique was employed using a freely-positionable probe tip. The laser source was a Spectra-Physics Tsunami, 100-fs pulse laser, which had 2 watts of output power with a repetition rate of 76 MHz and a wavelength of 810 nm. The laser was split into two beams, and with variable attenuation for the pump beam, an input excitation average power between 100 μW and several tens of mW was utilized. A LiTaO_3 crystal tip with a second-order-nonlinear-optical response (in this case, the Pockels effect) was placed between the coplanar strip lines within 100 μm of the MSM detector. The second laser beam was focused into the electro-optic probe and was modulated by the time-varying electric field – which was proportional to the detector photocurrent – on the coplanar transmission line.

The transient photoresponse for the detectors on the LT-GaAs with $T_g = 270^\circ\text{C}$ is shown in Fig. 4. The inset plot is the response for samples on the material with $T_g = 300^\circ\text{C}$. Since the laser power for the measurements of the detectors on the different materials was different, and also since the electro-optic sampling calibration may have been different for the different detectors, the peak amplitude was normalized to 1.0 for each plot. The transient photoresponses were virtually unchanged from the passivated to unpassivated samples for the detectors using materials of both growth temperatures. This indicates that the pulse width does not broaden when the surface states are passivated, and is experimental confirmation that a passivated surface will not degrade the speed of the photodetectors. Another significant result in Fig. 4 was that the photocurrent tails rising for the $T_g = 300^\circ\text{C}$ detectors (both passivated and unpassivated) were much higher than the $T_g = 270^\circ\text{C}$ detectors. This may be due to another current injection mechanism, which is not yet understood, and further investigation is needed. In each case, however, the tails did not change with passivation, as expected if they were due to hopping conduction.

SUMMARY

The dc and high-frequency optical response of LT-GaAs were measured with respect to the passivation of detectors employing the novel materials. The AlGaAs passivation layers were found to be more important for MSM photodetectors using LT-GaAs grown at 230 and 270°C rather than 300°C , since more photocarriers that produce photocurrent are affected by the surface field when the MSM is biased in the lifetime-limited regime. For LT-GaAs grown at higher temperatures, low-frequency gain typically occurs after the bias reaches its transit-time-limited regime. However, for LT-GaAs with a carrier lifetime of only several picoseconds, the transit time limit is not reached, although there is evidence that other injection mechanisms also become active. It is possible that surface passivation may be able to prevent some of this undesired injection. In terms of long-term reliability, the passivated cap layer can also help prevent material near the contact from earlier breakdown due to non-uniform field distribution.

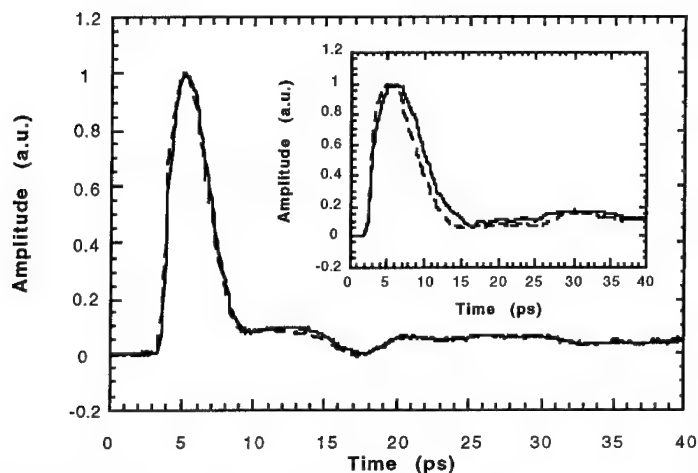


Figure 4. Transient photoconductive response of 270°C (inset for 300°C) LT-GaAs MSM detectors. Passivated (unpassivated) detectors are plotted with solid lines (dotted lines).

This research was sponsored by the Air Force Office of Scientific Research, Air Force Materiel Command, USAF, under grant number DOD-G-F49620-95-1-0227. The US Government is authorized to reproduce and distribute reprints for Governmental purposes notwithstanding any copyright notation thereon. Additional support provided by the National Science Foundation through the Center for Ultrafast Optical Science under STC PHY 8920108. We thank D.C. Look at Wright-Patterson AFB for providing the LT-GaAs substrates.

References

1. C.J. Sandroff, R.N. Nottenburg, J.-C. Bischoff, R. Bhat, *Appl. Phys. Lett.* **51**, 33 (1987).
2. E. Yablonovitch, C.J. Sandroff, R. Bhat, T. Gmitter, *Appl. Phys. Lett.* **51**, 439 (1987).
3. M. Klingenstein, J. Kuhl, J. Rosenzweig, C. Mogilestue, A. Hülsmann, Jo. Schneider, K. Köhler, *Solid-State Electronics* **37**, 333 (1994).
4. D.C. Look, *Thin Solid Films* **231**, 61 (1993).
5. C. L. Chen, F.W. Smith, A.R. Calawa, L.J. Mahoney, M.J. Manfra, *IEEE Trans. Electron Devices* **36**, 1546 (1989).
6. Y. Chen, S.L. Williamson, *Appl. Phys. Lett.* **59**, 1984 (1991).
7. D.C. Look, J.T. Grant, J.R. Sizelove, *Appl. Phys. Lett.* **61**, 1329 (1992).
8. J. S. Herman, F.L. Terry, Jr., *J. Vac. Sci. Technol. A* **11**, 1094 (1993).

PASSIVATION STUDIES ON AlGaAs SURFACES SUITABLE FOR HIGH POWER LASER DEVELOPMENT

C.EDIRISINGHE^{1,2}, H.E.RUDA^{1,2}, I.KOUTZAROV¹, Q.LIU¹, L.JEDRAL¹, M.G.BOUDREAU³, M.BOUMERZOU³, J.BROWN³, P.MASCHER³, A.MOORE⁴, AND R.HENDERSON⁴.

1) Electronic Materials Group, Department of Metallurgy and Materials Science, 2) Department of Electrical and Computing Engineering, University of Toronto, Toronto, Canada, M5S 1A4

3) Centre for Electrophotonic Materials and Devices, Department of Engineering Physics, McMaster University, Hamilton, Canada, L8S 4L7

4) EG&G Canada, Optoelectronics Division, 22001 Dumberry, Vaudreuil, Canada, J7V 8P7

ABSTRACT

We report on the optical characterization of sulphur (S) passivated $\text{Al}_x\text{Ga}_{1-x}\text{As}/\text{GaAs}$ surfaces using photoluminescence (PL) and surface photovoltage (SPV) measurements. Both techniques show an enhancement in the near bandgap signal intensity, implying a reduction of the non-radiative recombination rate at the surface. To counter the instability of S-passivation, due to re-oxidation, dielectric layers of silicon nitride were deposited using electron cyclotron resonance plasma enhanced chemical vapour deposition (ECR-PECVD); the deposition of dielectric layers up to 100nm thick does not appear to cause significant deterioration or stress at the insulator/AlGaAs interface. The dielectric layers are shown to be resistant to oxidation, and effective in maintaining the passivation effect over a period of weeks.

INTRODUCTION

High power AlGaAs lasers are used in optical fibre communication systems as the pump source for erbium-doped fibre amplifiers. However, these laser diodes suffer from intense non-radiative recombination in the vicinity of the laser facets, which leads to catastrophic optical damage. While certain techniques to control this degradation mechanism include specially designed waveguides to maintain optical intensities below critical levels, S passivation aims to reduce the surface recombination velocity near the facets, and, thus, extend the lifetime of these lasers [1]. Previous studies have shown that the effect of S treatment is to remove metallic native oxides, such as Ga_2O_3 , Al_2O_3 [2], followed by the formation of S bonded to Ga, Al and As at the surface. While the layers protect against re-oxidation, [3] the passivation is unstable and lasts, typically, only tens of hours.

To maintain the effect of the passivation over time an effective capping layer must be used [4]. A combination of a low damage deposition technique and a chemically inert film is required to maintain and stabilize the passivation. Electron cyclotron resonance plasma enhanced chemical vapour deposition (ECR-PECVD) satisfies the first criteria [5], while silicon nitride is used effectively to encapsulate AlGaAs/GaAs devices. The capping layer must have good adhesion, low stress, and high density to act as an effective diffusion barrier, particularly for water vapour. Impurities in the silicon nitride, particularly hydrogen, must be chemically stable if present at all.

EXPERIMENTAL DETAILS

Our investigation was carried out on epitaxial layers of AlGaAs grown on Si-doped n-GaAs (100) substrates by MOCVD. The wafers were degreased using acetone, methanol and DI water. Next, the wafers were 'pre-etched' in a standard solution of $\text{H}_2\text{SO}_4:\text{H}_2\text{O}_2:\text{H}_2\text{O}$, (1:8:500), at room temperature. The sulphur passivation procedure involved soaking the samples in ammonium sulphide solution, $(\text{NH}_4)_2\text{S}$, (20%) at 65°C . The samples were checked optically for any signs of poor surface morphology using the Nomarski technique. After S-passivation, samples were loaded into the ECR-PECVD system for the deposition of the capping layer. Silicon nitride thin films were deposited using a nitrogen/argon mix as the plasma environment, while trisdimethylaminosilane (TDAS) was used as the silicon source. The deposition pressure was typically 2 mTorr, with a TDAS partial pressure of 0.1 mTorr . Depositions were carried out at an input microwave power density of 2.5 Watts/cm^2 while the substrate temperature was approximately 100°C . A deposition rate of 50 \AA/min is obtained for these conditions. Prior to the deposition, samples were outgassed at the deposition temperature to obtain a chamber pressure of less than $2 \times 10^{-7}\text{ Torr}$. In order to avoid damage to the passivation layer the sample was partially shuttered during the first minutes of deposition in order to obtain a "low damage" film approximately 50 to 70 \AA thick, as measured by in situ ellipsometry. During deposition, a significant contribution to the substrate temperature comes from the plasma itself. Although it is difficult to measure accurately, the substrate temperature can be as much as 150°C higher than indicated by the thermocouple measurement, depending on the process gases.

The PL measurements used a 488nm Ar^+ ion and a 633nm He-Ne laser as the excitation sources. Samples were mounted inside a cryostat that allowed measurements to be made over a temperature range from 15K to 300K . The PL was dispersed through a 0.5m Chromex grating monochromator, and detected using a calibrated Si photodiode. The setup for PL measurements was also easily modified for SPV; a $100\text{W tungsten halogen}$ lamp was filtered through the same monochromator and focussed onto the samples. Standard procedures were adopted for measuring the SPV spectra, using identical conditions for both treated and untreated samples [6].

To determine the composition of the SiN layers, Fourier transform infrared spectroscopy (FTIRS), Auger electron spectroscopy (AES), and Rutherford backscattering spectrometry (RBS) were used. Appropriate substrates for each technique were also coated during the fabrication of the capping layer. For FTIRS, double sided polished, semi-insulating silicon was used. For AES a higher doping level was used to avoid electron beam charging effects. For the RBS measurements a polished carbon substrate was used to provide a more accurate measure of the concentration of the various components in the film.

RESULTS AND DISCUSSION

Effect of Chemical Treatment

The near bandgap (NBG) PL intensity enhancements after S-treatment varied with x ; typically, the enhancement factor for n-type $x=0.11$ was ~ 20 times, and ~ 5 times for p-type $x=0.29$ and 0.38 . The variations may be attributed to the differences in conduction type and possibly carrier concentration [7]; furthermore, previous experimental studies [2] have revealed the high stability of the Al oxide for higher x , which is not completely removed by the S-passivation. In order to facilitate the removal of native oxides, we observed that 'pre-etching' the

surfaces in acid-peroxide-DI water prior to S-treatment contributed to the overall success of the passivation treatment.

After chemical treatment, the bulk recombination rate remains unperturbed and, so, any change in PL implies a change in the non-radiative recombination at the surface. Fig. (1) shows the PL spectra for the p-type $x=0.29$ $\text{Al}_x\text{Ga}_{1-x}\text{As}$ after pre-etching and S-treatments. By measuring the PL intensity as a function of excitation power and temperature, the higher energy NBG peak at 1.884eV was identified as due to bound exciton emission, and the peak at 1.874eV as due to impurity related transitions involving shallow carbon acceptors (e°A) [8]. As seen in Fig. 1(c), the impurity related peak reduces by a factor of 5, while the bound exciton peak is enhanced by a comparable amount. This confirms that one of the consequences of S- treatment is the removal of impurities at the surface. It was also observed that the impurity related peaks became more prominent for higher x , as reported for typical MOCVD grown AlGaAs [9]. Below bandgap peaks, D and C, were also observed at 1.350eV and 1.485eV respectively. From previous studies [10], the origin of C may be probably due to the donor acceptor pair recombination involving the [Si-V] complex. In all samples studied, the location of the two peaks was virtually the same. As the temperature was raised, the intensity of peak D quenched faster than C.

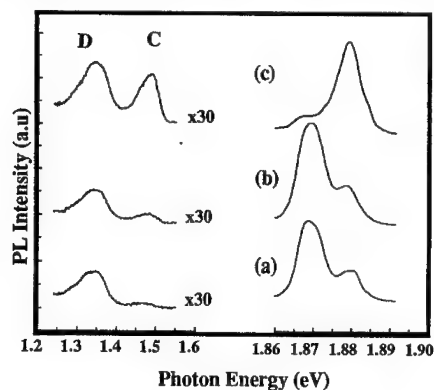


Figure 1: $x=0.29$, $\text{Al}_x\text{Ga}_{1-x}\text{As}$ at 18K:
a) as-grown b) pre-etched only
c) S-treated.

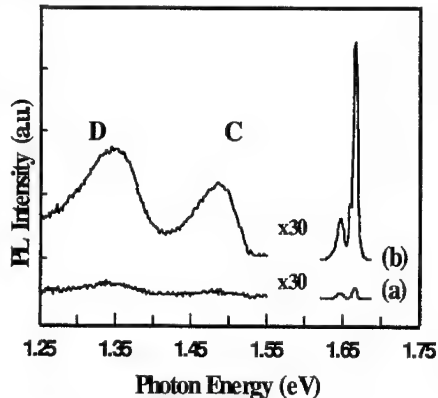


Figure 2: $x=0.11$, $\text{Al}_x\text{Ga}_{1-x}\text{As}$ at 18K:
a) as-grown b) S-treated.

Fig. (2) shows the PL spectra for the n-type, $x=0.11$ $\text{Al}_x\text{Ga}_{1-x}\text{As}$ after S-treatment. Again the NBG peaks were composed of a free to bound emission involving the shallow carbon acceptors (e°A), and bound exciton emissions that are just resolved into two components after treatment. It is possible to further resolve the separate excitonic peaks and tentatively assign them (analogous to results for GaAs [11,12]) to donor bound, and acceptor bound excitons; however, in a 'relative' PL study, the PL from one surface is compared to another, and, so, the primary concern is the enhancement factor of the generic bound exciton peak after etching and dielectric layer deposition.

Influence of Dielectric Deposition on S- treated Surfaces

Fig. (3) shows the NBG PL spectra for the n-type $x=0.11$, capped layers with two different thicknesses (100nm and 300nm), with and without S-treatment. The dielectric layer index of refraction is lower than the substrate index, resulting in changes in both the excitation intensity and the PL intensity due to the change in the substrate reflection coefficient. In a 'relative' PL study, therefore, only the intensities of capped surfaces were compared. We did not, however, observe a significant decrease in intensity after capping (fig. (3a,b&d)), confirming that the surfaces are not deteriorated by the ECR-PECVD process and are, most likely, free of PL degrading defects [13,14]. The S-treatment also appears to have withstood the deposition process as is evident from a 30% higher PL signal compared to the as-grown, capped surface. The enhancement of the D^0X exciton peak, at 1.6634eV, is 50% greater than the A^0X peak, at

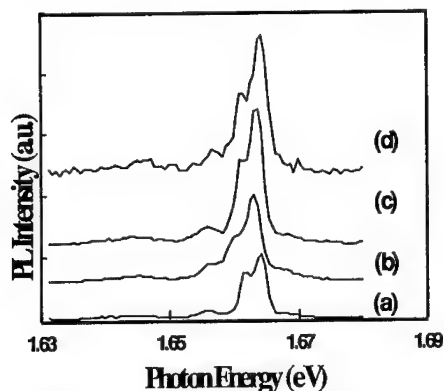


Figure 3: NBG PL spectra for $x=0.11$ at 18K: **a)** as-grown, uncapped, **b)** 300nm SiN capped, S-treated, **c)** 100nm SiN capped, S-treated, **d)** as-grown, 100nm SiN capped.

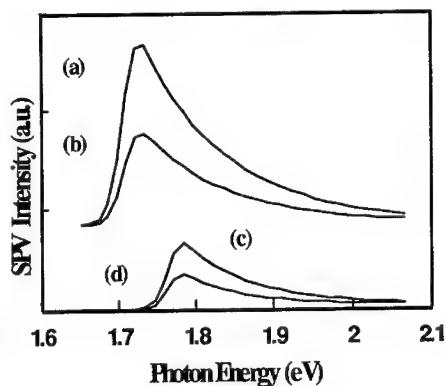


Figure 4: SPV spectra for NBG at room temperature: **a)** $x=0.21$, S-treated, capped, **b)** $x=0.21$, as-grown, capped **c)** $x=0.29$, S-treated, capped, **d)** $x=0.29$, as-grown, capped.

1.6612eV, (fig. (3c)) a feature that was observed at S-treated, uncapped surfaces as well. The dielectric layer deposition on an untreated surface also gave a similar effect (fig. (3(b,d))), and may be related to the incorporation of silicon centres at the surface [15]. It is difficult to interpret any PL peaks shifts as due to stress in capped samples because of a gradient of x in the epitaxial layers which varies with thickness [16]; however, the peaks for the 300nm capping layer were broader (fig. 3(b)) and the enhancement ratio negligible compared to the 100nm layer capped surfaces.

SPV spectra (fig. (4)) of the S-treated, capped sample also showed a clear and uniform enhancement over the whole NBG spectral range; this corresponds to a clear reduction in the surface recombination velocity. A monolayer of sulphur will not change bulk properties of the material such as light absorption and carrier diffusion. However, S-termination can reduce the effective surface recombination due to a reduction in the amount of surface bound oxygen, changes in the surface geometric/electronic structure and possible changes in the near surface concentration of defects. Thus the SPV enhancements reflect the improvement of the surface

properties after treatment rather than any perceptible changes in the bulk of the $\text{Al}_x\text{Ga}_{1-x}\text{As}$ layers. These SPV findings, thus, confirm the overall findings of the PL measurements.

Since we have used a non-conventional silicon source, TDAS, for the deposition of the SiN capping layers, the film properties should be discussed. We have found significant variations in both the material properties, and in their dependence on deposition parameters when compared to films deposited using silane [17]. Fig (5) shows the FTIRS spectrum of a 300nm film deposited using a 4:1 ratio of nitrogen to argon as the plasma environment. Note the high level of bonded

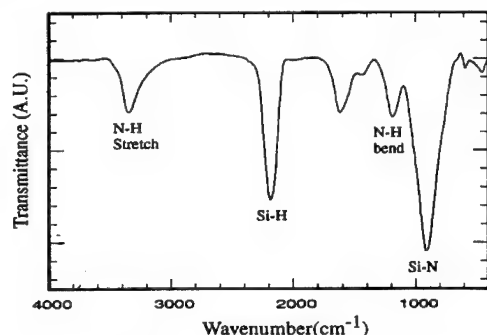


Figure 5: FTIRS spectrum of a 300nm SiN layer.

hydrogen. The hydrogen concentration is estimated to be $3 \times 10^{22} \text{ cm}^{-3}$ [18]. We have found that the level of oxygen contamination in the film is very sensitive to the partial pressure of oxygen in the chamber. An air leak with a partial pressure of $5 \times 10^{-7} \text{ mTorr}$ produced films with a significant oxygen content, as determined from RBS measurements. The absorption peak in the FTIRS spectrum near 1600 cm^{-1} is tentatively assigned to H-N-H bonds, and was correlated with the level of argon in the plasma. Fig. (6) shows the composition of the SiN film as a function of the depth obtained from AES measurements. There is a high level of carbon; however, there has not been significant oxidation of the film, even after 1 week exposure to air. This is confirmed by PL and SPV measurements that showed a stable enhancement ratio over this period of time.

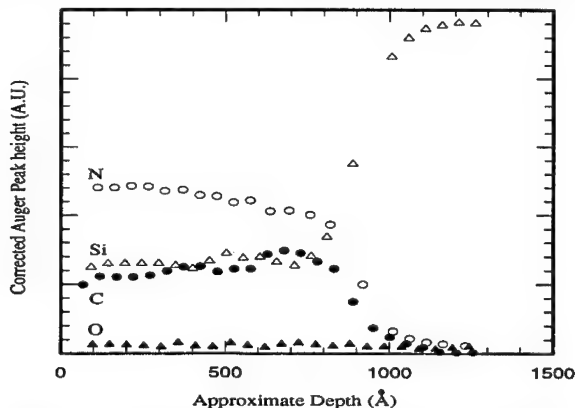


Figure 6: Auger depth profile of a 100nm SiN capping layer.

CONCLUSIONS

We have demonstrated that using a certain combination of pre-etchants and sulphur treatment, AlGaAs surfaces can be successfully passivated, whilst maintaining a good surface morphology suitable for laser facets. ECR-PECVD was shown to be a suitable technique for capping S-treated surfaces, and maintaining the passivation effectiveness for a period of weeks.

ACKNOWLEDGEMENTS

This work was supported by grants from the Natural Sciences and Engineering Research Council of Canada, and the Ontario Centre for Materials Research.

REFERENCES

1. H.Kawanishi, H.Ohno, T.Morimoto, S.Kaneiwa, N.Miyauchi, H.Hayashi, Y.Akagi, Y.Nakajima and T.Hijkata, in Ext. Abstr. 21st Conf. Solid. State Devices and Mat., Tokyo, 337 (1989).
2. H.Ohno, H.Kawanishi, Y.Akagi, M.Koba, T.Hijkata, in Chemical Perspectives of Microelectronic Materials II, edited by L.Interrante, K.Jensen, L.Dubois, and M.Gross (Mat. Res. Soc. Symp. Proc., **204**, Pittsburgh, PA, 1991), pp.65-70.
3. G.Guel, E.Armour, S.Sun, S.Srinivasan, K.Malloy and S.Hersee, *J. Electronic Mater.*, **21**, 1051 (1992).
4. W.Hobson, U.Mohideen, S.Pearson, R.Slusher, and F.Ren, *Electron Lett.*, **30**, 233 (1994).
5. S.Dzioba, R.Rousina, *J. Vac. Sci. Tech. B*, **12** (1), 433 (1994).
6. Annual Book of ASTM Standards, American Society for Testing and Materials, F, 1990, pp.390-391.
7. K.Uchida, S.Nakatsuka, *Jpn. J. Appl. Phys.*, **32**, L883 (1993).
8. G.Wicks, W.Wang, C. Wood, L. Eastman, L. Rathbun, *J. Appl. Phys.* **52** (9) Sept. (1981).
9. T.Kuech, E.Veuhoff, D.L. Woolford, J.A. Bradley, *Inst. Phys. Conf. Ser.*, UK, **74**, 181 (1985).
10. P.L.Souza and E.V.Rao, *J. Appl. Phys.* **67**, 7013 (1990).
11. L.Pavesi, M.Guzzi, *J. Appl. Phys.* **75** (10), 4779 (1994).
12. S.Olsthorn, F.Driessen, D.Frigo, L.Giling, Int. Symp.GaAs and Related Compounds, *Inst. Phys. Conf. Ser.*, **136**, (1993), pp.779-784.
13. A.Lamas, A.Gobbi, *Mat. Science and Eng.* **B23**, 142 (1994).
14. A.Piccirillo, R.Marzano, A.Gobbi, P.Bagnoli, *Applied Surface Science*, **52**, 295 (1991).
15. G.Gerardi, F.Rong, E.Poindexter, M.Harmatz, H.Shen, W.Warren, in Amorphous Insulating Thin Films, edited by J.Kanicki, W.Warren, R.Devine, M.Matsuma, (Mat. Res. Symp. Proc.) **284**, Pittsburgh, PA, 1993, pp.601-607.
16. D.Aspnes, W.Quinn, M.Tamargo, M.Pudensi, S.Schwarz, M.Brasil, R.Nahory and S.Gregory, *Appl. Phys. Lett.* **60** (10), 1244 (1992).
17. M.Boudreau, M.Boumerzoug, P.Mascher, P.E.Jessop, *Appl. Phys. Lett.* **63** (22), 3014 (1993).
18. W.A.Lanford and M.J.Rand, *J. Appl. Phys.* **49**, 2473 (1978).

PASSIVATION OF InGaAs/GaAs VERTICAL-CAVITY SURFACE-EMITTING LASERS BY AMORPHOUS GaAs DEPOSITION

HYO-HOON PARK, BYUENG-SU YOO, MIN SOO PARK*, JAEJIN LEE,
HAE GWON LEE, AND EL-HANG LEE

Electronics and Telecommunications Research Institute, Taejeon 305-600, Korea

*Visiting from the Department of Materials Science and Engineering, Korea Advanced
Institute of Science and Technology

JAE-HEON SHIN AND YONG HEE LEE

Department of Physics, Korea Advanced Institute of Science and Technology, Taejeon
305-701, Korea

ABSTRACT

We report for the first time a successful application of semi-insulating amorphous GaAs layer for surface passivation of index-guided vertical-cavity surface-emitting lasers. The amorphous GaAs layers on ion-beam-etched active region and mirror layers provide a significant improvement, more than 20%, in the threshold current density and differential quantum efficiency. The improvement of these performances is attributed to low defect density at the surface of active layers induced by amorphous GaAs.

I. INTRODUCTION

Vertical-cavity surface-emitting lasers (VCSELs) are considered promising light sources for applications in optical parallel processing, optical communications and optical interconnections. Some of the important performance characteristics to be improved for a wide range of applications are threshold current, light output power, single mode emission, and controllability of polarization. Of these, the improvement of the threshold current is the most critical issue for large scale integration of VCSEL devices. Post type index-guided SELs have advantages in achieving low threshold current performances due to a strong confinement of optical field and current, as compared to gain-guided SELs. However, etching through the active region exposes the edge of the quantum wells, thus inducing surface recombination currents through the etched sidewall. Many efforts have been made to reduce the surface recombination. Young *et al.* [1] reported sulfide passivation by dipping the etched wall in an ammonium sulfide solution and achieved a 25% reduction in surface recombination velocity and a submilliamp threshold current for 8 μm devices. Wu *et al.* [2] introduced regrowth of epitaxial layers of undoped GaAs and *n-i-p-i* doped $\text{Al}_{0.2}\text{Ga}_{0.8}\text{As}$ on the surrounding of etched VCSEL posts. They obtained low threshold currents and single mode emissions with 8 and 16 μm devices. In our work here, however, we first demonstrate the effectiveness of semi-insulating amorphous GaAs (a-GaAs) in burying the active region of VCSEL devices, thus achieving performance improvement by more than 20% both in the threshold current and differential quantum efficiency.

II. EXPERIMENTAL

For this work, we used a periodic gain InGaAs/GaAs VCSEL structure with a two-wavelength-thick (2λ) cavity. The epitaxial structure was grown by metal-organic chemical vapor deposition. The top (p-doped) and bottom (n-doped) DBR mirrors consist of, respectively, 16 and 23.5 periods of AlAs/GaAs quarter wave stacks. The detailed laser structure was described in previous reports [3,4]. We fabricated bottom-emitting lasers using chemically-assisted ion beam etching (CAIBE) with chlorine. The device procedures are sketched in Figs. 1(a)-(e). Ti(20Å)/Au(3000Å)/Ni(1600Å) metal dots were used as p-contact and mask layers for CAIBE. The laser posts were etched through the active region to the top layer of the bottom mirror by in-situ monitoring of etch depth using laser reflectometry. [5] After CAIBE, the sample was immediately rinsed with deionized water, and then it was slightly etched using a solution of $\text{H}_2\text{SO}_4:\text{H}_2\text{O}_2:\text{H}_2\text{O}$ (1:8:1000) for 10-20 sec to remove residual chlorine and ion-damaged layer on the etched sidewall. The etched sample with about $5 \times 5 \text{ mm}^2$ size was divided into two pieces. One piece was entered for measurement without additional surface treatment. Another piece was deposited by GaAs using molecular beam epitaxy technique at 160°C for 2.5 h under the As/Ga ratio of 20. The thickness of *a*-GaAs layer was about $2.5 \mu\text{m}$. The amorphous state of the deposited GaAs was identified from X-ray-diffraction measurements. In other works, too, it has been reported that *a*-GaAs phase is formed under deposition conditions similar to ours. [6] The resistance of *a*-GaAs layer was larger than $900 \Omega\text{cm}$ from I-V measurement for a sample deposited on a semi-insulating GaAs substrate. The *a*-GaAs layer on the p-type metal contact of VCSEL devices was removed by reactive ion etching using chlorine and argon. Figures 2(a) and 2(b) show scanning electron micrographs of as-etched devices and *a*-GaAs deposited devices, respectively.

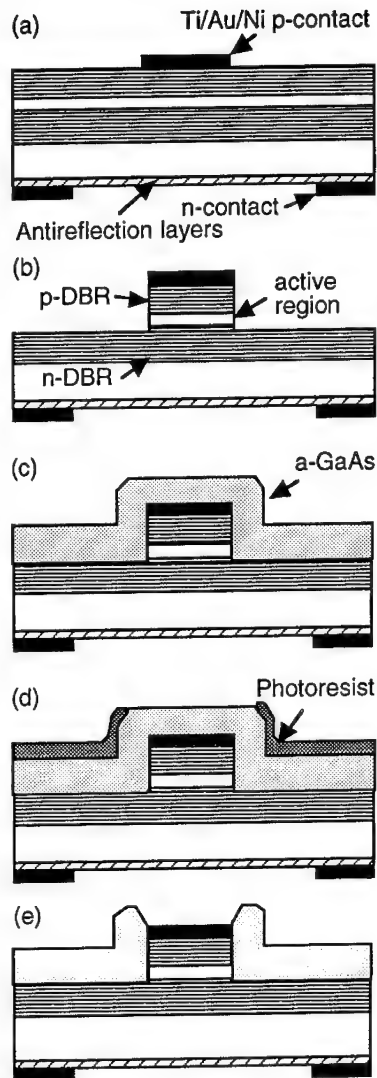


Figure 1. Schematic of the fabrication process for amorphous-GaAs-deposited surface-emitting lasers.

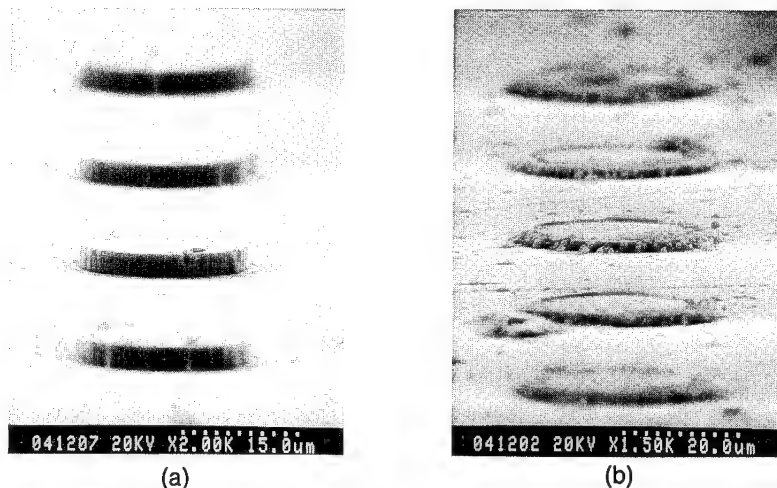


Figure 2. Scanning electron micrographs of (a) as-etched and (b) amorphous-GaAs-deposited surface-emitting lasers.

III. DEVICE CHARACTERISTICS

The device characteristics were measured at room temperature without a heat sink. Figures 3(a) and 3(b) show the light output power versus current (L-I) characteristics measured from CW operation for (a) as-etched devices and (b) *a*-GaAs deposited devices. The lasing wavelength was around 990 nm at threshold currents and was found to shift to longer wavelength up to 995 nm with increasing current. In Fig. 3, we present the best L-I curves among the data obtained for each size of devices. The threshold currents measured from as-etched circular devices [Fig. 3(a)] with 15, 20, 25, 35 and 40 μm diameters are 2.5, 4.3, 4.6, 8.2 and 6.0 mA, respectively. Threshold currents of *a*-GaAs deposited devices [Fig. 3(b)] with 20, 25, 30, 35 and 40 μm diameters are 2.1, 2.9, 3.4, 4.1 and 5.1 mA, which are significantly lower than the data seen in Fig. 3(a).

Figure 4 shows the data of threshold current densities, J_{th} , for the as-etched and *a*-GaAs deposited devices. The data points are somewhat scattered even on the same device size. In Fig. 4, the lowest values of J_{th} for each sizes of the as-etched devices are in the range of 480 - 1350 mA/cm^2 and those of the *a*-GaAs deposited devices are 380 - 500 mA/cm^2 . This result indicates that the *a*-GaAs deposition reduced J_{th} by more than 20%. The average values of J_{th} for each size seen in Fig. 4 are also significantly decreased after deposition of *a*-GaAs. Figure 5 shows the data of external differential quantum efficiencies, η_{ex} , for the same devices. The average values of η_{ex} for each sizes are also significantly increased by the passivation treatment.

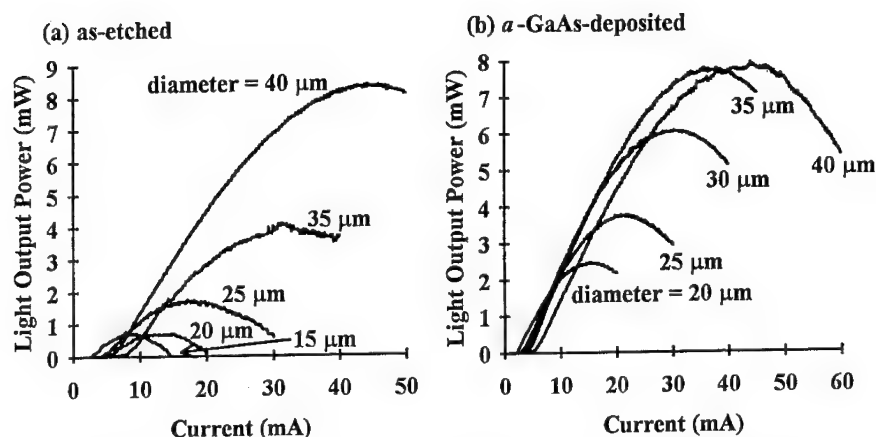


Figure 3. CW light output characteristics for (a) as-etched and (b) amorphous-GaAs-deposited surface-emitting lasers.

The threshold current density seen in Fig. 3(b) approaches the best values for VCSELs. Recently, Deppe *et al.* [7] recorded 350 A/cm^2 threshold current density from an InGaAs VCSEL in which the current injection region is defined by lateral oxidation of a surface AlAs layer on active cavity and CaF/ZnSe layers are used as top mirror layers. Yoffe *et al.* [8] reported a threshold current density of 380 A/cm^2 from air-post lasers with an *in-situ* grown Al top contact. Compared to the output power characteristics of their devices, our passivated devices show much higher values in maximum power and differential quantum efficiency. We note, however, that the whole performances of the passivated devices, seen in Figs. 3-5, are not so good as the as-etched air-post devices reported in our previous work [3]. We used the same epitaxial wafers for these works, but the device performances showed considerable differences depending on run-to-run (or chip-to-chip), due to non-uniform epitaxial quality and/or process control. Thus, the effect of a-GaAs deposition was investigated using the specimens within a small area and following the same process except the a-GaAs deposition.

The improvement of the threshold current density and differential quantum efficiency by a-GaAs deposition, seen in Figs. 4 and 5, is believed to be originated from a low defect density at the surface of active layers induced by passivating effect of a-GaAs. If the defect density drops with the passivation, nonradiative surface recombination of carriers is reduced, resulting in both a decrease of threshold current density and an increase of differential quantum efficiency [9]. For the defect density at the interface between a-GaAs and crystalline GaAs, few studies have been reported. However, it is known that the network of a-GaAs bonding has a tetrahedral character which is close to the structure of crystalline GaAs [10]. Thus, we expect that the surface defects on the InGaAs/GaAs layers buried by a-GaAs must be much low, as compared to the layers buried by other dissimilar passivation materials, such as silicon nitride or polyimide.

In addition to the passivation effect, the deposition of a-GaAs provides several

advantages in the fabrication process of VCSEL devices. We can achieve planarization of the deep-etched laser posts by appropriate control of the deposition thickness. Also, the low temperature process simplifies the experimental schemes, especially, for the formation of non-alloyed ohmic contacts on the top-mirror, which is required for bottom-emitting lasers.

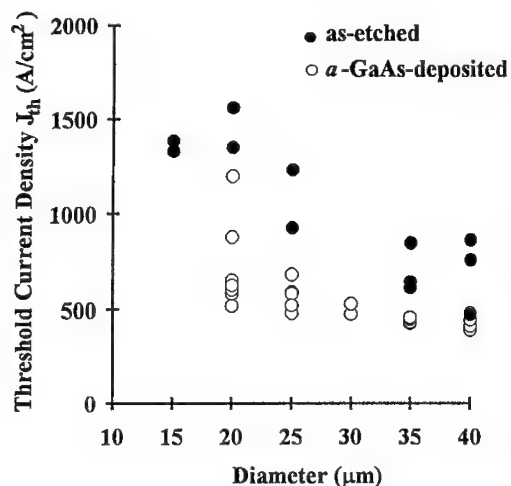


Figure 4. Threshold current densities for as-etched and amorphous-GaAs-deposited surface-emitting lasers.

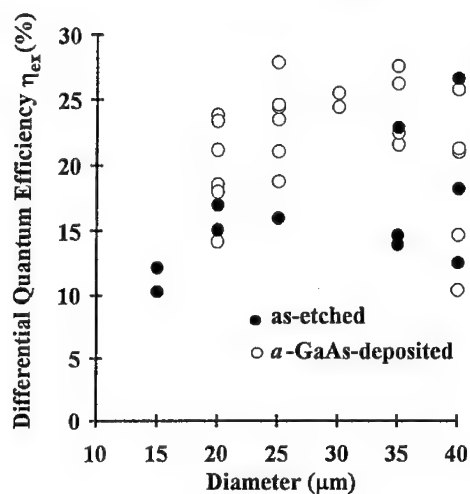


Figure 5. Differential quantum efficiencies for as-etched and amorphous-GaAs-deposited surface-emitting lasers.

IV. SUMMARY

We have demonstrated the surface passivation of index-guided surface-emitting lasers by low temperature deposition of a-GaAs. The threshold current density and differential quantum efficiency were improved more than 20% after the a-GaAs deposition.

ACKNOWLEDGMENTS

This work has been supported by the Ministry of Information and Communications, Korea.

REFERENCES

1. D.B. Young, A. Kapila, J.W. Scott, V. Malhotra, and L.A. Coldren, *Electron. Lett.* **30**, 233 (1994).
2. Y.A. Wu, C.J. Chang-Hasnain, and R. Nabiev, *Electron. Lett.* **29**, 1861 (1993).
3. B.-S. Yoo, H.-H. Park, and E.-H. Lee, *Electron. Lett.* **30**, 106 (1994).
4. H.-H. Park and B.-S. Yoo, *ETRI Journal*, in press.
5. J.Y. Yoo, J.H. Shin, Y.H. Lee, H.-H. Park, and B.-S. Yoo, *Optical and Quantum Electron.* to be published.
6. D.J. Eaglesham, L.N. Pfeiffer, K.W. West, and D.R. Dykaar, *Appl. Phys. Lett.* **58**, 65 (1991).
7. D.G. Deppe, D.L. Huffaker, C.C. Lin, and T.J. Rogers, *Conference on Lasers and Electro-Optics 1994 Technical Digest Series*, vol. **8**, pp. CPD2-1/3 - 6/8 (1994).
8. G.W. Yoffe, W.C. van der Vleuten, M.R. Leys, F. Karouta, and J. H. Wolter, *Electron. Lett.* **30**, 794 (1994).
9. G.P. Agrawal and N.K. Dutta, *Semiconductor Lasers*, 2nd ed. (Van Nostrand Reinhold, New York, 1993) pp.55-64.
10. C. Molteni, L. Colombo, and L. Miglio, *Phys. Rev. B*, **50**, 4371 (1994).

SULFIDIZATION IN ALCOHOLIC SOLUTIONS:
A NEW SURFACE PASSIVATION METHOD FOR GaAs.

VASILY N. BESSOLOV, ANDREW F. IVANKOV, ELENA V. KONENKOVA, AND
MIKHAIL V. LEBEDEV

A.F.Ioffe Physico-Technical Institute, Russian Academy of Sciences, Politekhnikeskaya 26,
St.Petersburg, 194021, Russia.

ABSTRACT

A new approach to GaAs surface passivation is suggested which consists in the treatment of GaAs in sulfide solutions in which different alcohols are used as solvents. It has been found that the photoluminescence efficiency of sulfide-treated GaAs associates with the dielectric constant of the solvent being used. With the decrease of dielectric constant value the PL intensity of sulfidized GaAs increases. Sulfidizing in isopropanol-, butanol- or t-butanol-based solutions leads to the formation of sulfide coat which PL properties remain constant even after strong laser irradiation. The effect of the solvent on the GaAs PL efficiency is explained within the framework of hard and soft acids and bases. Thus the use of alcohol-based sulfide solution with low dielectric constant value greatly reduces surface recombination losses in sulfide-treated GaAs.

1. INTRODUCTION

III-V semiconductors have a large density of surface states which pin surface Fermi level near the middle of semiconductors bandgap. The passivation of these states is a vital problem for semiconductor technology in view of the progress in miniaturization of electronic devices in recent years. It is known that the treatment of III-V semiconductor surface by different sulfides leads to dramatic decrease of the surface state density which considerably reduces the rate of the surface recombination [1].

In order to greatly reduce the surface recombination rate it is necessary to passivate the surface states which are the closest to the middle of the bandgap. From chemical point of view such states are the soft acid Lewis centers which are highly polarizable [2]. According to the principle of hard and soft acids and bases [3] such soft acid centers could be passivated by soft bases. The sulfide-ions are exactly such soft bases [2] and therefore they are quite suitable for III-V surface passivation. Since for an effective passivation the presence of protons is necessary [4] the surface passivation occurs usually in solutions. As a solvent on such solutions a protic liquid as water is used as a rule. However the other protic liquids, namely isopropanol, used as the solvent for sulfide solution lead to more effective passivation of the surface states in GaAs [5].

In this paper we compare the photoluminescence properties of GaAs treated by different sodium sulfide solutions in which various protic liquids have been used as solvents.

2. EXPERIMENTAL

We have treated n-GaAs(100) epi-layers ($n=4 \cdot 10^{15} \text{ cm}^{-3}$) grown on semi-insulating substrates by MOCVD. The thickness of the layers was 5-10 μm . They were treated by immersing in solutions in which sodium sulfide ($\text{Na}_2\text{S} \cdot 9\text{H}_2\text{O}$) was dissolved in different solvents up to saturation. The solvents used were water, ethanol, isopropanol, butanol and t-butanol. The immersion time was about 1 min. In aqueous solutions the samples were treated at different temperatures and in alcohol-based solutions the treatment was carried out at room temperature. After the sulfide treatment the samples were rinsed in the pure solvents in use and then dried in air.

Photoluminescence (PL) was excited by a Xe-laser ($I=3.0 \text{ kW/cm}^2$) at room temperature. The band edge PL peak intensity of untreated GaAs was 0.15-0.20 units. The degradation of the PL properties of sulfide-treated GaAs was studied by the measurement of the intensity of band edge PL peak at continuous irradiation of the semiconductor surface by laser light.

The results obtained are the following. After the sulfide treatment the band edge PL peak intensity of GaAs considerably increases. The PL intensity of GaAs treated in aqueous sulfide solutions is increased with the treatment temperature (Fig. 1).

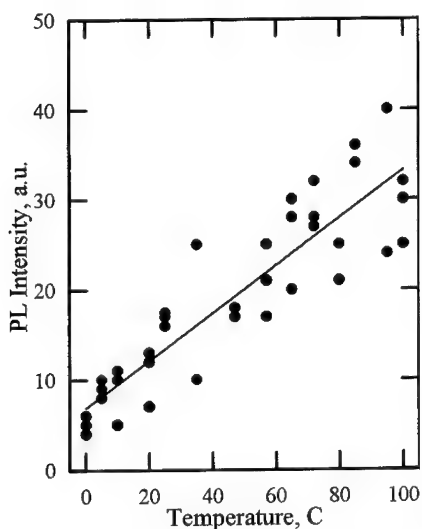


Fig. 1 Dependence of the PL intensity of the GaAs treated in aqueous sulfide solution on the treatment temperature.

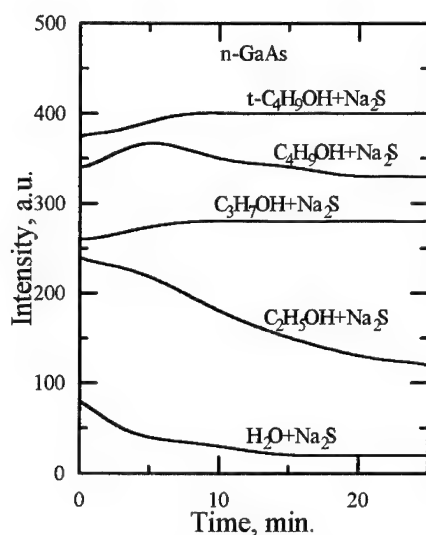


Fig.2 Variation of the PL intensity of GaAs treated in different solutions.

The PL intensity of sulfide treated GaAs depends on the solvent being used in the process of passivation (Fig.2). The greatest increase (by a factor 570) of the PL intensity of sulfide-treated GaAs relative to that of the untreated one has been achieved in t-butanol-based sodium sulfide solution. The sulfide treatment of semiconductor surface in alcohol-based solution in general leads to the increase of the PL intensity to a greater extent than in the aqueous solutions. For instance, the PL intensities of GaAs treated in isopropanol-based solution and t-butanol-based solution are higher by factors of 2.5 and 3.5 respectively than those of GaAs treated in aqueous solution at room temperature. It should be noted that the pretreatment of the semiconductor before sulfidizing in $\text{H}_2\text{SO}_4\text{:H}_2\text{O}_2\text{:H}_2\text{O}$ (1:8:500) etch solution did not lead to any increase of the PL intensity of GaAs treated in any solution.

The degradation of the properties of the sulfide-treated GaAs surface also depends on the solvent being used (Fig.2). The PL intensity of GaAs treated in aqueous solutions at any temperature under Xe-laser irradiation rapidly drops down to typical intensity values of untreated GaAs. The PL intensity of GaAs surface treated in ethanol-based solutions also decreases with time of the laser irradiation but to a lesser extent. On the contrary, the Xe-laser irradiation does not affect the PL properties of GaAs treated in isopropanol, butanol, or t-butanol-based solutions.

3. DISCUSSION

The values of the increase of the PL intensity of GaAs treated in different solutions are associated with the dielectric constant of the solvent being used (Fig.3).

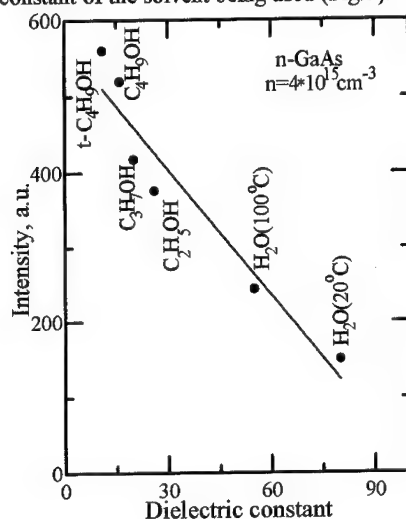


Fig.3 Dependence of the increase of the PL intensity of sulfide treated GaAs on the dielectric constant of the solvent. The increase refers to the intensity of untreated sample.

With the decrease of the dielectric constant the PL intensity of sulfide-treated GaAs increases. This dependence could be explained as follows.

Let us consider the variation of global hardness of the electronic system of the sulfide ion S^{2-} in the solution with the decrease of the solvent dielectric constant.

It is known that the dielectric constant of a polar liquid depends on the polarizability and the dipole moment of its molecule; with the increase of polarizability the dielectric constant decreases. Note that the molecules of the alcohols used as the solvents in the study have practically the same dipole moment.

The calculation of the parameters of the sulfide-ion has been done in the framework of the Thomas-Fermi-Dirac model. The radius of the electronic shell of the sulfide ion has been calculated as 3.9 Å. The global hardness of the sulfide-ion is dependent on the potential of the electrons in its shell [6].

An equilibrium distance on which the molecules of the dipole solvent settle down will be increased with the increase of the polarizability of the molecule i.e. with the decrease of the dielectric constant of the solvent [7]. For example in water the equilibrium distance will be equal to 2.2 Å, and in t-butanol its equal to 3.2 Å. So, the molecules of the solvent would penetrate to the outer region of the electronic shell of the sulfide ion.

The dipole potential of the solvent molecules surrounding sulfide-ion will lower the potential of the electrons occurring inside the region surrounded by the solvent molecules. Therefore the global hardness of the sulfide-ion will decrease. With an increase of the

equilibrium distance the region in which the potential of the electrons decreases will be enlarged which result in the greater decrease of the global hardness. That is, the global hardness of the sulfide -ion should decrease with the dielectric constant of the solvent.

With the decrease of the global hardness of the sulfide-ion and if there are enough protons in the solution for passing a photoelectrochemical reaction of sulfidizing [4] the possibility appears to passivate more soft surface states which are the nearest to the middle of the gap according to the hard and soft acids and bases principle. Therefore the sulfide passivation of GaAs in the alcohol-based solutions which have a low dielectric constant should be more effective than that in aqueous solutions.

4. CONCLUSION

It has been shown that the sulfide treatment of GaAs in alcohol-based solutions leads to an essential decrease of surface recombination losses compare with the commonly used passivation in aqueous sulfide solutions. With the point of view of the degradation of the properties of sulfidized GaAs such treatment also more promising. It has been found that the PL efficiency of sulfide-treated GaAs increases with the decrease of the dielectric constant of the protic solvent being used.

ACKNOWLEDGMENTS

The research described in this paper was made possible in part by Grant N R1V300 from the International Science Foundation and by Grant N 95-03-09330 from Russian Foundation for Basic Research.

REFERENCES

1. E.Yablonovitch, C.J.Sandroff, R.Bhat, and T.Gmitter, Appl. Phys. Lett., **51**, 439, (1987).
2. S.R.Lunt, P.G.Santangelo, and N.S.Lewis, J. Vac. Sci. Technol. A., **9**, 2333 (1991).
3. R.G.Pearson, J. Am. Chem. Soc., **85**, 3533 (1963).
4. V.N.Bessolov, M.V.Lebedev, E.B.Novikov, and B.V.Tsarenkov, J. Vac. Sci. Technol. B., **11**, 10 (1993).
5. V.N.Bessolov, A.F.Ivankov, E.V.Konenkova, and M.V.Lebedev, Pis'ma Zh. Tekh. Fiz., **21**(1), 46-50 (1995) [Tech. Phys. Lett. **21**, 20 (1995)].
6. M.Berkowitz, S.K.Ghosh, and R.G.Parr, J. Am. Chem. Soc., **107**, 6811 (1985).
7. E.A.Moelwyn-Hughes, The chemical statics and kinetics of solutions, (Academic Press, London and New York, 1971).

EFFECTS OF ADDITIVE ELEMENTS ON ELECTRICAL PROPERTIES OF TANTALUM OXIDE FILMS.

HISAYOSHI FUJIKAWA AND YASUNORI TAGA

TOYOTA Central R&D Laboratories, Inc., Nagakute-cho, Aichi-gun, Aichi-ken, 480-11, Japan

ABSTRACT

Ta₂O₅-based composite films prepared by magnetron sputtering have been investigated with respect to their dielectric properties. As additive third oxides, Y₂O₃ and WO₃ were found to be effective in improving insulating properties without decreasing their dielectric constant. Furthermore, electrical properties of Ta₂O₅-Y₂O₃ films were investigated by measuring the current-voltage characteristics in the temperature range from 100 to 330 K. Measurement of temperature dependence of the leakage current revealed that the conduction mechanism at RT changed from the Poole-Frenkel type to the Fowler-Nordheim tunneling type by adding Y₂O₃ into Ta₂O₅. Based on the detailed analysis of the results, it is concluded that the addition of Y₂O₃ into the Ta₂O₅ film is effective in the reduction of defect density without high-temperature annealing and the alteration of electrical conduction mechanisms of the films.

INTRODUCTION

High dielectric constant insulators have been widely required for thin film capacitors in scaled-down large scale integrated circuits (LSI) applications. In the last decade, Ta₂O₅ films have been the most promising material for dynamic random access memory (DRAM) fabrication,[1] because of their high breakdown field strength and dielectric constant. Of the many proposed techniques for device processing, chemical vapor deposition (CVD) has been accepted because of its excellent step coverage for trench and stack cell structures. Annealing in O₃ or O₂ gas has reduced the leakage current of the CVD films to an adequate level for the storage capacitor application.[2,3] On the other hand, it has been also demanded that highly insulating Ta₂O₅ films should be prepared at the low temperature because of the limitation of LSI processes. Nomura and Ogawa have indicated that the Ta₂O₅-Al₂O₃ thin films prepared by radio frequency (rf) reactive sputtering at a substrate temperature of 200 °C exhibited highly dielectric properties. [4] The mixing of another third oxide with Ta₂O₅ is a unique method of forming the high performance films, and this method is suitable for low-temperature device processing.

In the present work, we showed that the addition of another oxide such as Y₂O₃ or WO₃ to the Ta₂O₅ film was effective in improving the insulating properties.[5] In addition, the conduction mechanism of the Ta₂O₅-Y₂O₃ composite films were investigated in comparison with the Ta₂O₅ films by measuring the current-voltage characteristics at various temperatures.

EXPERIMENTS

Ta₂O₅ films and composite films were deposited on n-type silicon (100) substrates (0.01 Ω•cm) by rf magnetron co-sputtering with multiple-targets of Ta₂O₅ and additive oxide ceramics of 99.9 % purity which were bonded to the copper cooling plates. Reactive sputtering was performed using sputtering gas of Ar and 30% O₂. The substrate temperature was kept constant

at 300 °C during the film deposition. The composition of these films was controlled by an input rf power into each targets. The film thickness was measured by ellipsometry and the composition of the composite films was determined by the Rutherford back scattering spectroscopy (RBS).

Al electrodes were formed on the oxide films by vacuum evaporation using a stainless mask. The electrode area was 0.002 cm². The electrical properties were evaluated with the metal / insulator / semiconductor (MIS) structure. The leakage current-voltage characteristics were measured with a semiconductor parameter analyzer (HP4145B). The breakdown field strength (Ebd) was defined as the field at a leakage current density of 1 μA/cm². The relative dielectric constant (εr) was evaluated from the high frequency capacitance-voltage curves measured with a 1MHz capacitor meter (HP4280A). Furthermore, the Ta₂O₅ films and the Ta₂O₅-20 at.% Y₂O₃ composite films with a thickness of about 20 nm were made and their conduction mechanisms were investigated in detail. Post-annealing was not performed for the low temperature device processes. Electrical transport properties were examined by temperature dependent leakage current measurements between 100 and 330 K with a semiconductor parameter analyzer. Furthermore, in order to clarify the conduction transport mechanisms, the leakage current-voltage characteristics at various temperatures were re-plotted in the various forms based on several conduction models. Activation energy measurements were made from Arrhenius plots of the temperature-dependent leakage current, and these were used along with the current-voltage relationships to clarify the dominant transport process.

RESULTS AND DISCUSSION

Composite films were prepared by adding one of the nine kinds of oxides such as Al₂O₃, Bi₂O₃, GeO₂, Nb₂O₅, SiO₂, TiO₂, WO₃, Y₂O₃, and ZrO₂ into the Ta₂O₅ matrix. The concentration of the additive oxides was about 30 at.% except for the case of WO₃. In adding WO₃, the W concentration was about 3 at.%. The electrical properties were measured with the MIS structure as mentioned above. Here, the figure of merit was defined as a product of the relative dielectric constant and the breakdown field strength. The value is equivalent to the maximum storage charge of the films, which indicates performance of the capacitor films.

Figure 1 shows the breakdown field strength and the relative dielectric constant of the composite films. The broken line in the figure indicates the value of the figure of merit. The properties of the Ta₂O₅ film without adding another oxide are denoted by an open circle. In the case of the composite films, the symbols of the additive elements are described in the open circles. As shown in Fig. 1, Al₂O₃ and SiO₂ are effective in improving the breakdown field strength of Ta₂O₅. In increasing the relative dielectric constant of Ta₂O₅, Nb₂O₅ is an effective oxide. However, Bi₂O₃, GeO₂, ZrO₂, and TiO₂ have no effect on improving the dielectric properties of Ta₂O₅. The figure of merit of these composite films mixed with one of the above oxides and Ta₂O₅ matrix is less than that of Ta₂O₅ films. On the other hand, Y₂O₃ and WO₃ are effective in raising the figure of merit of Ta₂O₅, because the breakdown field strength of the composite films increases without reducing the relative dielectric constant.

Ta₂O₅-Y₂O₃ composite film had the largest value of the figure of merit among these composite films. Therefore, Ta₂O₅-Y₂O₃ composite films were investigated with regard to the dependence of the dielectric properties on the Y concentration. Figure 2 shows the breakdown field strength and the relative dielectric constants as a function of the Y concentration. The concentration is defined as the atomic percentage of the metal element in the oxide films. The broken lines in these figures indicate the breakdown field strength or the relative dielectric

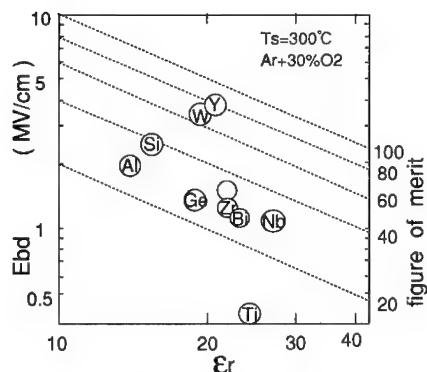


Fig. 1. The relationships between the breakdown field strength and the relative dielectric constant of the composite films. The symbols of the additive elements are described in the open circles. The properties of Ta_2O_5 films are denoted by the open circle. The broken lines indicate the value of the figure of merit.

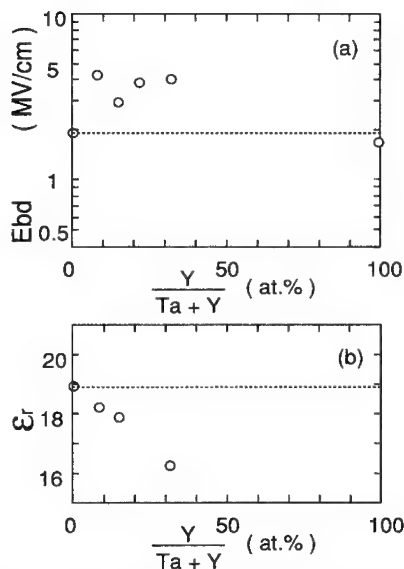


Fig. 2. (a) The breakdown field strength and (b) the relative dielectric constant as a function of the Y concentration.

constant of the Ta_2O_5 film. As can be seen from in Fig. 2(a), the optimum concentrations of Y in the films are 10 - 30 at.% with respect to the maximum breakdown field strength of the composite film. As shown in Fig. 2(b), the relative dielectric constant of the composite film reaches the value of Y_2O_3 with increasing concentration of Y. In addition, typical current density-applied electric field (J-E) characteristics at room temperature (RT) in MIS capacitors for the Ta_2O_5 film and the $\text{Ta}_2\text{O}_5\text{-Y}_2\text{O}_3$ composite film are shown in Fig. 3. The leakage current for the $\text{Ta}_2\text{O}_5\text{-Y}_2\text{O}_3$ composite film is smaller than that for the Ta_2O_5 film in a high electric field range. This indicates that the addition of Y_2O_3 into the Ta_2O_5 film is effective in improving the insulating properties. It is also suggested that the conduction mechanism of the $\text{Ta}_2\text{O}_5\text{-Y}_2\text{O}_3$ film is different from that of the Ta_2O_5 film particularly in the high electric field range at RT.

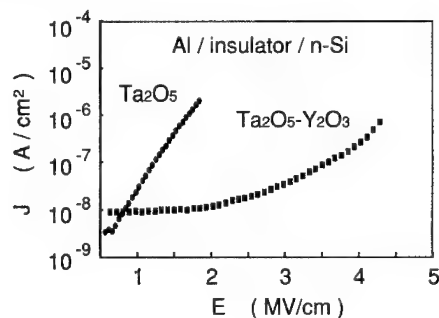


Fig. 3. Typical current density - electric field characteristics at room temperature in MIS capacitors for the Ta_2O_5 film and the $\text{Ta}_2\text{O}_5\text{-Y}_2\text{O}_3$ composite film.

It is worth examining the conduction mechanisms of these films more closely. In order to investigate the conduction mechanisms of the Ta_2O_5 film, the activation energy of the leakage current was determined from Arrhenius plots of $\log J$ vs $1000/T$ for the Ta_2O_5 film at various electric fields. Results are shown in Fig. 4. There are two distinct activation energies corresponding to two different dominant conduction mechanisms. The values of activation energy at an electric field of 1.8 MV/cm are 0.012 eV for low temperature (100 - 170 K) range and 0.12 eV for high temperature (170 - 320 K) range. In the high temperature range (at RT), since the activation energy is large, it cannot be a tunneling mechanism. It is seen that the dominant mechanism at the high temperature and the high electric field is consistent with field-assisted thermal excitation conduction such as a bulk-limited Poole-Frenkel or an electrode-limited Schottky emission.

Figure 5 shows the Poole-Frenkel plots [6] in $\log(J/E)$ and $E^{1/2}$ for the leakage characteristics of the Ta_2O_5 film. Linear relations are obtained at the high temperature (> 170 K). In the case of the Poole-Frenkel conduction, n value (slope) is generally selected between 1 and 2 as indicated in Fig. 5. Therefore, the experimental slope at RT ($n=1.5$) supports the Poole-Frenkel conduction mechanism in the Ta_2O_5 films. It must be pointed out, however, that another possibility is the electrode-limited Schottky emission.[6] This relationship is similar to the Poole-Frenkel characteristic, that is, $\log J$ instead of $\log(J/E)$ is linear with $E^{1/2}$. However, the slopes of the experimental plots were steeper than that of the theoretical plots of Schottky emission. In addition, the observed dependence of the leakage current on the measurement temperature as shown in Fig. 4 is not as steep as predicted by the Schottky process. From these results, it is clear that the conduction in the Ta_2O_5 film at RT agrees with the bulk-limited Poole-Frenkel emission. It is also found that the trap level is 0.48 eV which is calculated from the activation energy (0.12 eV).

Furthermore, the conduction mechanisms in the Ta_2O_5 - Y_2O_3 composite film were also investigated. Figure 6 shows the Arrhenius plots of $\log J$ vs $1000/T$ for the Ta_2O_5 - Y_2O_3 composite film. There are two values of activation energy for low temperature range (< 300 K) and high temperature range (> 300 K), the critical temperature is higher than that for the Ta_2O_5 film as shown in Fig. 4. At a moderate electric field of 2 MV/cm, the leakage current is independent

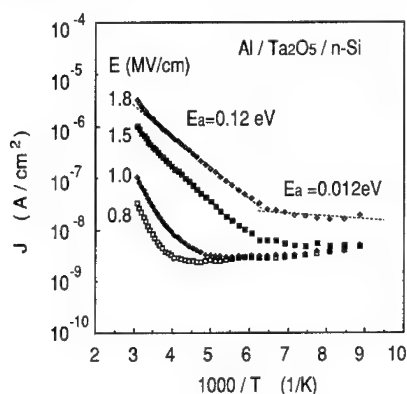


Fig. 4. Arrhenius plots of temperature-dependent leakage current for the Ta_2O_5 film.

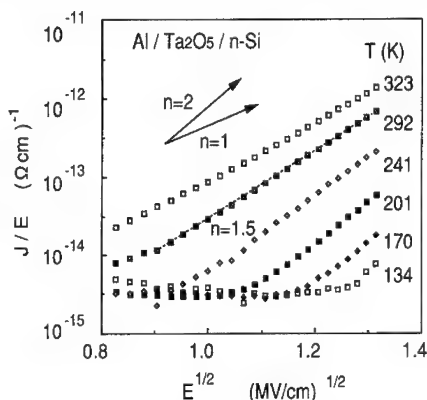


Fig. 5. Poole-Frenkel plots of leakage characteristics for the Ta_2O_5 film.

on the measurement temperature. It is considered that the leakage current at RT is due to the tunneling emission because of the low value of activation energy around RT. These results indicate that the thermal excitation emission surmounted the barrier of Si/Ta₂O₅-Y₂O₃ is not the dominant conduction below RT.

Furthermore, Fig. 7 shows the Fowler-Nordheim plots [7] in $\log(J/E^2)$ vs $1/E$ for the Ta₂O₅-Y₂O₃ composite film. At temperatures below 300 K, linear relations are obtained in the high field range (>4 MV/cm). This result strongly indicates that the leakage current at temperatures below 300 K in the composite film is due to the Fowler-Nordheim tunneling emission. The energy difference (Φ_b) between the Fermi level of n⁺-Si and the conduction band of Ta₂O₅-Y₂O₃ composite film is estimated to be 1.2 eV from the data in Fig. 7. Thermally excited leakage current surmounted the barrier between the Si substrate and the composite film, that is Schottky emission, is negligible because the Φ_b is very large.

From the above results, the Poole-Frenkel conduction due to the 0.48 eV traps is dominant for the Ta₂O₅ film at RT. For the Ta₂O₅-Y₂O₃ film, the Fowler-Nordheim tunneling is the dominant conduction at RT because of a decrease of the trap density and a rise of the barrier height between the Ta₂O₅-Y₂O₃ film and n⁺-Si. The addition of Y₂O₃ into Ta₂O₅ film results in a change of the conduction mechanism at RT from the Poole-Frenkel bulk-limited emission to the Fowler-Nordheim tunneling.

Many researchers reported some possibilities on the origins of the leakage current in the Ta₂O₅ films. As a result, it was considered that the leakage current was caused by impurities, oxygen vacancies, void formation, and grain boundary grooving.[2,4,8,9] In particular, it was indicated that the presence of water in Ta₂O₅ films is important in determining the conduction process.[10-12] For our Ta₂O₅ films, the leakage current of the Ta₂O₅ films was much smaller for annealed films at a low temperature of 450 °C in N₂ than for as-deposited film. As a result, this change of the leakage current suggests the presence of water in the Ta₂O₅ films. Furthermore, H⁺ ions in the films were observed by SIMS.[5] It seemed that H⁺ ion is a component of water or OH⁻ ions in the films. Consequently, it is considered that the unstable water component incorporated into the Ta₂O₅ films is the origin of the leakage current. [11,12] In view of the combination of Y atoms, it is reasonable that unstable water related to traps is combined by

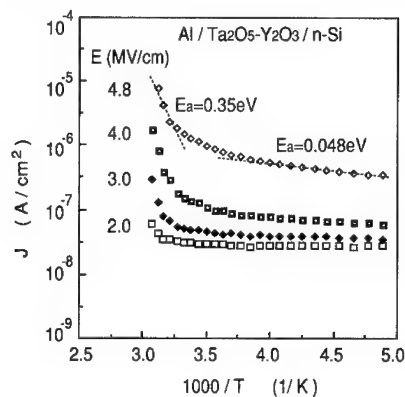


Fig. 6. Arrhenius plots of temperature-dependent leakage current for the Ta₂O₅-Y₂O₃ film.

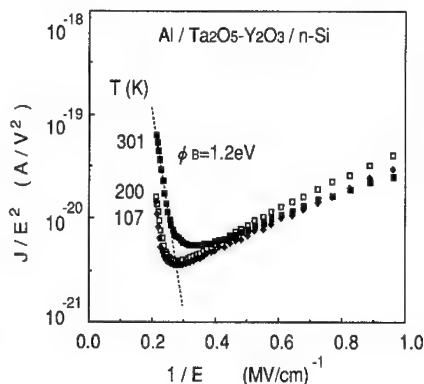


Fig. 7. Fowler-Nordheim plots of leakage characteristics for the Ta₂O₅-Y₂O₃ film.

Y^{3+} ions for the Ta_2O_5 - Y_2O_3 film. This is because the oxygen affinity value of Y is much larger than that of Ta. The water related to the traps in the films is believed to be stabilized, and the density of traps is reduced by adding Y^{3+} into the Ta_2O_5 films. Consequently, the leakage current of the Ta_2O_5 film was reduced by the addition of Y_2O_3 as shown in Fig. 3.

CONCLUSION

Ta_2O_5 and composite films such as Ta_2O_5 - Y_2O_3 and Ta_2O_5 - WO_3 prepared by the magnetron sputtering were investigated with respect to their insulating properties. In order to improve the dielectric properties of the Ta_2O_5 films, an addition of Y_2O_3 or WO_3 to the Ta_2O_5 films was effective in low temperature processing without annealing. Furthermore, conduction mechanisms in sputtered Ta_2O_5 films and Ta_2O_5 - Y_2O_3 composite films were investigated by measuring the current-voltage characteristics at various temperatures. For the Ta_2O_5 films, the Poole-Frenkel conduction due to 0.48 eV traps under the conduction band was the dominant current transport mechanism at RT. On the other hand, the Fowler-Nordheim tunneling was the dominant mechanism for Ta_2O_5 - Y_2O_3 films at RT. The barrier height between the composite film and the n^+ -Si substrate was estimated to be 1.2 eV. The addition of Y_2O_3 into the Ta_2O_5 film resulted in a decrease in the trap density and a change of the conduction mechanisms at RT from the bulk-limited Poole-Frenkel to the Fowler-Nordheim tunneling.

References

1. H.Shinriki and M.Nakata, IEEE Trans. Electron Devices **ED-38**, 455 (1991)
2. S.Tanimoto, M.Matsui, K.Kamisako, K.Kuroiwa, and Y.Tarui, J. Electrochem. Soc. **139**, 320 (1992)
3. S.Kamiyama, P.Y.Lesaichere, H.Suzuki, A.Sakai, I.Nishiyama, and A.Ishitani, J.Electrochem.Soc. **140**, 1617 (1993)
4. K.Nomura and H.Ogawa, J.Electrochem.Soc. **138**, 3701 (1991)
5. H.Fujikawa and Y.Tagu, J.Appl.Phys. **75**, 2538 (1994)
6. S.Banerjee, B.Shen, I.Chen, J.Bohman, G.Brown, and R.Doering, J.Appl.Phys. **65**, 1140 (1989)
7. S.Zaima, T.Furuta, Y.Koide, and Y.Yasuda, J. Electrochem. Soc. **137**, 2876 (1990)
8. S.Kimura, Y.Nishioka, A.Shintani, and K.Mukai, J.Electrochem. Soc. **130**, 2414 (1983)
9. M.Matsui, H.Nagayoshi, G.Muto, S.Tanimoto, K.Kuroiwa, and Y Tarui, Jpn.J.Appl.Phys. **29**, 62 (1990)
10. H.Matsunaga, A. Suzuki and T. Yabumoto, Jpn. J. Appl. Phys. **19**, 71 (1980)
11. Peter L. Young, J.Appl.Phys. **47**, 235 (1976)
12. S.Oshio, M.Yamamoto, J. Kuwata, and T.Matsuoka, J.Appl.Phys. **71**, 3471 (1992)

Phase separation of $\text{Si}_{1-x}\text{Ge}_x$ alloys

Eunja Kim and Young Hee Lee
Department of Physics and Semiconductor Physics Research Center,
Jeonbuk National University, Jeonju 560-756, R. O. Korea

ABSTRACT

We generate liquid and amorphous $\text{Si}_{1-x}\text{Ge}_x$ alloys for various Ge compositions using *ab initio* molecular dynamics approach. The electronic bonding characters and structural properties are discussed in terms of radial distribution function, bond angle distribution, and order parameters. Although the order parameters suggest approximately random alloy for all compositions, the snapshots reveal clearly phase separation. We will discuss how the phase can be separated in SiGe alloy system.

INTRODUCTION

SiGe alloy system is one of the strong candidate for optoelectronic devices on Si-based technology. Although liquid (*l*-) and amorphous (*a*-) Si have been extensively studied, *l*- and *a*-SiGe alloy systems have not been fully understood both theoretically and experimentally. Current technology uses the gas-source or solid-source Molecular Beam Epitaxy (MBE) system to grow SiGe superlattices and alloys. The SiGe alloy can also be utilized for high electron mobility devices with control of Ge concentration. [1] The *l*- and *a*-SiGe phases are intermediate states when the crystalline (*c*-) SiGe is formed from the SiGe gas phase. It is thus important to understand the physical properties of *l*- and *a*-SiGe phases. In addition the growth of Ge on Si surface introduces an extra problem of lattice mismatch which causes eventually the island formation depending on the free energy of the surface. In order to study *l*-SiGe alloy, one has to generate the structures. The *l*-Si and *l*-Ge systems have been studied theoretically by melting the crystalline phase. [2,3] The classical [1,4] and semiempirical approaches [2] have been implemented for *l*-Si system. Although these approaches are often very practical, in particular for the calculation of the dynamical properties, the validity of such approaches with effective potentials may be limited in many cases, and hence is difficult to predict detailed quantitative properties for a particular material. For this reason an *ab initio* molecular dynamics (MD) method has been introduced for *l*-Si system which gave an excellent agreement with experiment. [5]

Both X-ray diffraction experiment [6] and first principle calculations [7] have shown that the rhombohedral (RH) phase of *c*-SiGe alloy ($x=0.5$) is stabler than the zinc-blende (ZB) phase. It is generally well known that the Ge atoms are easily segregated onto the surface during the epitaxial growth on Si(100) surface. [8] The previous study by the Stillinger-Weber potential has also shown the segregation of Ge atoms in the SiGe alloy surface. [9] However, none of the work has been done on *l*-SiGe alloys. To our knowledge, *a*-SiGe alloys have not been studied theoretically mainly due to the difficulty in generating a reliable structure.

In this paper, the *ab initio* MD approach is introduced to an extensive and detailed studies of structural properties of *l*- and *a*-SiGe alloys. *a*- $\text{Si}_{1-x}\text{Ge}_x$ alloys show a tendency to phase separation (or clustering effect) at all the compositions, although the calculated order parameters suggest approximately random alloys.

THEORETICAL APPROACHES AND SIMULATIONAL DETAILS

We adopt *ab initio* MD simulation scheme developed by Car and Parrinello (CP). [10] The ionic and electronic forces are derived separately from an effective Lagrangian based on the local density approximation. This method has been successfully applied for many

semiconducting systems, i.e., the system with a finite single particle energy gap E_g , which determines the electron time scale μ / E_g . One can select conveniently small values of μ such that the electronic degree of freedom acquires only a very small classical kinetic energy to follow ions adiabatically. Under these conditions ionic trajectories, initially lying on the Born-Oppenheimer(BO) surface, deviate from it very slowly on the time scale of MD simulation. In the case of liquid SiGe alloys, which are metallic, we observe the thermal equilibration between the electronic and ionic systems, i.e., a substantial energy transfer from the ionic to the electronic system, resulting in the spontaneous reduction of the ionic temperatures due to the energy transfer to the electrons. This process cannot be fully eliminated but may be controlled by the choice of μ since in a finite size system, even in a metal E_g is not exactly zero. [11] In $\text{Si}_{1-x}\text{Ge}_x$ alloy system, a cubic supercell containing 64 atoms with periodic boundary conditions and Γ -point sampling in Brillouin-zone (BZ) are used. To consider the interaction between valence and core electrons we use the pseudopotentials by Bachlet, Hamann, and Schlüter(BHS) [12] with the *sp* nonlocality for both Si and Ge. The energy cutoff for the plane-wave expansion is 12 Ry, which corresponds to about 6000 plane waves. This number varies slightly with Ge composition. We have done a convergence test by studying Si_2 and Ge_2 dimers with different kinetic energy cutoffs. [13]

The *l*-Si and *l*-Ge shrinks by about 10 and 15%, respectively, when melted. [14]. Since there are no data for the volume shrinkage of liquid $\text{Si}_{1-x}\text{Ge}_x$ alloys, these can be extracted from the Vegard's law;

$$v_{l-\text{Si}_{1-x}\text{Ge}_x} = \frac{1}{2} \left(\frac{m_{l-\text{Si}}}{\rho_{l-\text{Si}}} + \frac{m_{l-\text{Ge}}}{\rho_{l-\text{Ge}}} \right) \quad (1)$$

where $m_{l-\text{Si}} = (N_{\text{Si}}M_{\text{Si}})$, $m_{l-\text{Ge}} = (N_{\text{Ge}}M_{\text{Ge}})$, $\rho_{l-\text{Si}} = 2.53 \text{ g/cm}^3$, and $\rho_{l-\text{Ge}} = 5.51 \text{ g/cm}^3$, which represent the densities of pure liquid Si and Ge, respectively. [14] For example, in the case of $x = 0.5$, $N_{\text{Si}} = 32$, $N_{\text{Ge}} = 32$, $v = 1297.2781 \text{ \AA}^3$. This gives the size of the simulation box $L = v^{1/3} = 10.906 \text{ \AA} = 20.6103 \text{ a.u.}$

The melting temperatures of Si and Ge are 1410 and 936 °C, respectively. [15] In order to generate liquid $\text{Si}_{x-1}\text{Ge}_x$ alloys, we should increase temperature above the melting point of the alloy ($T_m \sim 1450 \text{ K}$). The initial positions of the Si and Ge atoms are randomized at their ideal crystal lattice sites. The electrons are minimized to be at the ground state with this initial configuration. The electron fictitious mass is chosen to be 300 a.u. During the MD simulation the time step is fixed at 5τ where τ is taken to be $0.24 \times 10^{-16} \text{ s}$. The system is equilibrated with ions microcanonically for 500 steps. Then the system is heated to 2000 K for 1000 steps. The system is further run for 1000 steps with microcanonical ensemble. Then the temperature is increased to 4000 K and we run 1000 steps by dynamical annealing and 1000 steps further in microcanonical ensemble. We confirm at this stage that the system is completely melted. The temperature is decreased by 500 K and we run 500 steps in canonical and microcanonical ensembles, consecutively. This procedure is repeated till the temperature reaches 2000 K. As previously mentioned, there is a chance that the electronic and ionic motions could be coupled because of the smaller energy gap E_g . In fact we observed a systematic temperature decrease of ions due to the energy transfer. We suppress the electron temperature to be less than 40 K by minimizing the electronic energy whenever it exceeds this value. Once the system is fully equilibrated, the electron kinetic energy is stabilized. We decrease the temperature of the system to 1500 K such a way that the temperature is decreased by 100 K for every 500 steps of dynamical annealing and 800 steps in microcanonical runs. We try to keep the quenching rate $\sim 10^{15} \text{ K/sec}$ in this procedure. This system is further run for 1000 steps in microcanonical run. The equilibrium properties for liquid structures are then obtained by averaging over next 7000 steps (0.84 ps).

In order to obtain the *a*- $\text{Si}_{1-x}\text{Ge}_x$ alloys we further quench the system as follows. Starting from the final liquid structure, we decrease the temperature by 100 K at every 700 steps and then equilibrate the system for 300 steps. The average quenching rate is about $0.8 \times$

10^{15} K/sec. This value is similar to the quenching rate used to generate *a*-Si in the previous studies. [2,10] The system is further equilibrated for 1000 steps in microcanonical ensemble. The equilibrium properties are then obtained after for next 10,000 steps (~ 1 ps). We keep the same quenching procedure for all Ge compositions since the structures strongly depend on the thermal history.

RESULTS AND DISCUSSION

It is known experimentally that two ordered phases exist in crystalline $\text{Si}_{0.5}\text{Ge}_{0.5}$ alloys. [6] The typical ZB phase has four heteropolar bonds whereas the RH phase has three heteropolar (75 %) and one homopolar (25 %) bonds. The energy of the RH phase is lower by 7 meV/atom than that of the ZB phase. [13] $l\text{-Si}_{1-x}\text{Ge}_x$ alloys introduce thermal effect where the free energy of the system must be the minimum. With $x=0.5$ where the entropy of mixing takes its maximum values, the random alloy with equal number of homopolar and heteropolar bonds would be preferred.

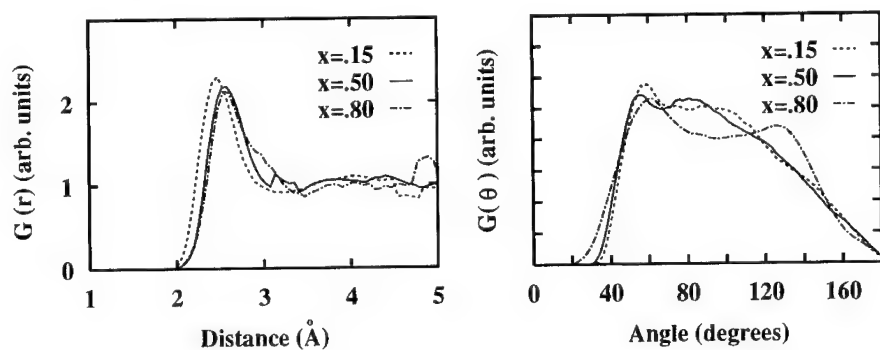


FIG. 1. Radial distribution functions and bond angle distribution functions of liquid $\text{Si}_{1-x}\text{Ge}_x$ alloy in terms of various Ge compositions. Open and black ones represent Si and Ge atoms, respectively.

Figure 1 shows the radial distribution function (RDF) and the bond angle distribution function (BADF) for various Ge compositions at liquid (high) temperature. As the Ge concentration increases, the peak position moves toward larger values, as expected, although the difference between $x=0.5$ and 0.8 is almost negligible. We note that extra bumps near the first minimum position are observed at high Ge compositions. This extra bump was analyzed by calculating the RDFs for each species. [13] This bump has also been observed experimentally for pure *l*-Ge system. Therefore, we believe that it originates from the *l*-Ge system. The BADF shows two main peaks. The first peak near 60 degrees originates from the Si-Si floating bonds which are analyzed by the BADFs for each species. The second peak is a characteristic of a covalent bonding. With $x=0.15$ the BADF still follows the similar behavior of *l*-Si system. [13] With $x=0.5$ the second peak position is shifted to near 90 degrees, indicating stronger *p*-bonding character. At $x=0.8$, the second peak is shifted to around 140 degrees, which is a characteristic $\beta\text{-Sn}$ like *l*-Ge structure. [13]

Figure 2 shows the RDF and the BADF for various Ge compositions at low temperature. As the Ge composition increases, the first peak position gets larger and the peak intensity decreases. The first minimum position also shifts to larger values. The BADFs of *a*- $\text{Si}_{1-x}\text{Ge}_x$ alloys are, however, different from those of *l*- $\text{Si}_{1-x}\text{Ge}_x$ alloys. The floating bonds near 50 degrees disappear at $x=0.15$ and 0.8 whereas they still exist at $x=0.5$. The fact that the second peak positions are shifted to 100 degrees at $x=0.15$ and 0.5 shows that the alloy

structures recover the tetrahedral bonding character. At higher Ge composition ($x=0.8$) the peak appears near 90 degrees, suggesting that the alloy still has strong p bonding character.

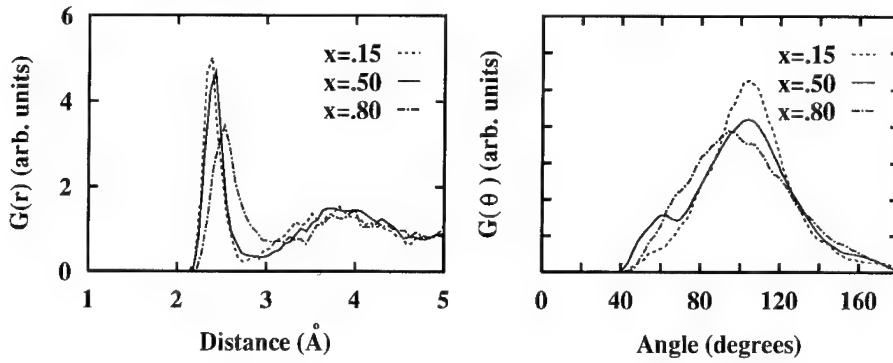


FIG. 2. Radial distribution functions and bond angle distribution functions of amorphous $\text{Si}_{1-x}\text{Ge}_x$ alloy in terms of various Ge compositions. Open and black ones represent Si and Ge atoms, respectively.

In order to investigate the ordering of the alloys, we calculate order parameters. We define the order parameter $P_{IJ} \equiv \bar{n}_{IJ} / \sum_K \bar{n}_{IK} \times 100\%$, where $\bar{n}_{IJ} \equiv \sum_i N_i / N_I$. Here N_I is the number of I -type atom, n_{IJ} the number of neighbors between I and J species from an I site. Thus the P_{IJ} is the probability that an atom next to an I -type atom would be J -type atom. For perfectly random alloys, P_{AA} is the probability that an atom next to an A -type atom is A is x and P_{BB} is $1 - x$ for A_xB_{1-x} alloy.

Table I shows the calculated order parameters for various Ge compositions. One sees that the system presents a tendency to behave like a random alloy. The system reaches a thermal equilibrium when the free energy $F = U - TS$ is a minimum. At high temperature, the entropy term plays a dominant role, i.e., the atoms prefer to be in random positions. One can see from the table that both P_{AA} and P_{BB} decrease with increasing temperature at all compositions, simply indicating that the free energy is minimized by maximizing the entropy term.

TABLE I. Order parameters of amorphous and liquid $\text{Si}_{1-x}\text{Ge}_x$ alloys for various x . n_{ij} and P_{ij} are defined in the text. A and B stands for Si and Ge atoms, respectively.

x (%)	T (K)	\bar{n}_{AA} (P_{AA})	\bar{n}_{AB} (P_{AB})	\bar{n}_{BA} (P_{BA})	\bar{n}_{BB} (P_{BB})
15	300	3.58 (85)	0.61 (15)	3.37 (85)	0.60 (15)
	1500	5.04 (79)	1.33 (21)	7.19 (87)	1.04 (13)
20	300	3.77 (82)	0.83 (18)	3.25 (84)	0.64 (16)
	1500	5.25 (82)	1.20 (18)	4.70 (85)	0.83 (15)
50	300	2.56 (57)	1.94 (43)	1.94 (47)	2.15 (53)
	1500	3.20 (47)	3.59 (53)	3.59 (50)	3.58 (50)
80	300	1.76 (35)	3.28 (65)	0.84 (16)	4.34 (84)
	1500	1.12 (16)	5.72 (84)	1.46 (18)	6.68 (82)
Crystalline order parameters					
50 (ZB)	0	4(100)		4(100)	0
50 (RH)	1(25)	3(75)		3(75)	1(25)
0 (pure Si)	4(100)	0		0	0
100 (pure Ge)	0	0		0	4 (100)

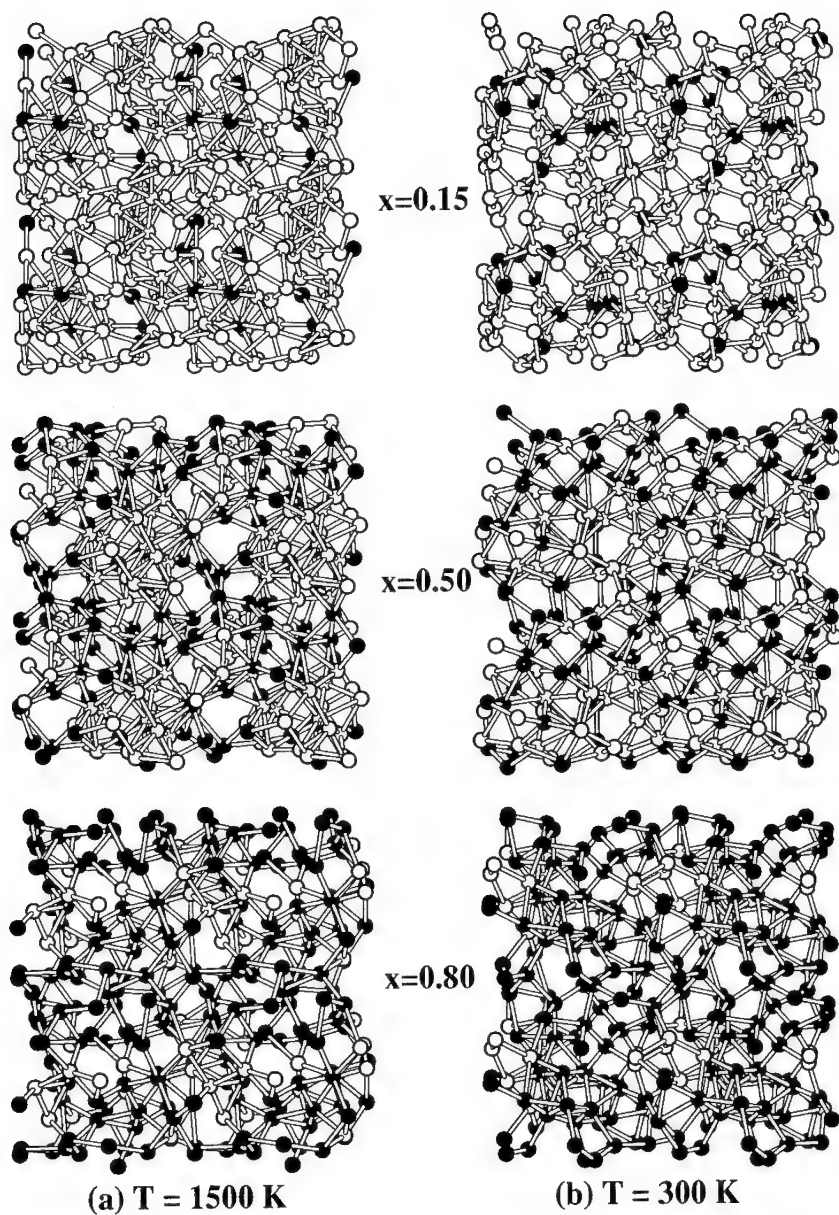


FIG. 3. The snapshots of liquid and amorphous $\text{Si}_{1-x}\text{Ge}_x$ alloys for various compositions. Open and black ones represent Si and Ge atoms, respectively.

We illustrate the snapshots of the l - and α - $\text{Si}_{1-x}\text{Ge}_x$ alloys for various compositions in Fig. 3. Although the order parameters suggest approximately random alloys, the snapshots at low temperature reveal a clustering effect at all compositions. The clustering effect becomes blurred at high temperature. In fact it has been suggested [7] that the SiGe alloy belongs to "type-II ordering" (i.e., low temperature bulk ZB or RH SiGe) where the system is unstable towards decomposition at sufficiently low temperatures unless the activation barriers is overcome. We generated α - $\text{Si}_{1-x}\text{Ge}_x$ alloys by quenching from liquid phase. At such high temperature the thermal energy is enough to overcome the activation barriers such that the system is fully relaxed. The strain is released by clustering to the like-atoms. This phenomenon is similar the relaxation of the strained layers. The clustered alloy produces some defects such as dangling bonds and floating bonds in α - $\text{Si}_{1-x}\text{Ge}_x$ alloys where the dangling bonds are formed mostly on Ge sites when $x \geq 0.15$. This will be discussed elsewhere.

SUMMARY

We have generated l - and α - $\text{Si}_{1-x}\text{Ge}_x$ alloys for various compositions using *ab initio* MD method. The radial distribution function reveals extra bumps near the first minimum position at high temperature for $x \geq 0.5$, similar to the β -Sn like bonding character of pure l -Ge system. At low temperature the contribution from the floating bonds is not observed at $x=0.15$ and 0.8 . Although the order parameters suggest approximately random alloys for all compositions, the snapshots reveal clearly the clustering effect at low temperature.

This work was supported by the Korea Science and Engineering Foundation (KOSEF) through the Semiconductor Physics Research Center (SPRC) at Jeonbuk National University.

-
- [1] D. Monroe, Y. H. Xie, E. A. Fitzgerald, and P. J. Silverman, Phys. Rev. B **46**, 7935(1992).
 - [2] E. Kim and Y. H. Lee, Phys. Rev. B **49**, 1743(1994).
 - [3] A. Arnold, N. Mauser, and J. Hafner, J. Phys:Condens. Matt. **1**,965(1989). Phys. Rev. B **46**, 7935(1992).
 - [4] F. H. Stillinger and T. A. Weber, Phys. Rev. B **31**, 5262 (1985).
 - [5] I. Stich, R. Car and M. Parrinello, Phys. Rev. B **44**, 4262(1991).
 - [6] A. Ourmazd and J. C. Bean, Phys. Rev. Lett. **55**, 765(1985).
 - [7] J. L. Martins and A. Zunger, Phys. Rev. Lett. **56**, 1400(1986).
 - [8] A. Schaefer, J. Q. Broughton, J. C. Bean, and H. H. Farrel, Phys. Rev. B **33**, 2999(1986); J. Q. Broughton, J. A. Schaefer, J. C. Bean, and J. Tersoff, Phys. Rev. Lett. **63**, 1164(1989).
 - [9] P. C. Kerlres and J. Tersoff, Phys. Rev. Lett. **63**, 1164(1989).
 - [10] R. Car and M. Parrinello, Phys. Rev. Lett. **55**, 2471(1985); in *simple Molecular systems at Very High Density*, vol. **186** of *NATO Advanced Study Institute, series B*; Physics, edited by A. Polian, P. Loubeyre and N. Boccara(Plenum, New York, 1989).
 - [11] L. Kleinman and D. M. Bylander, Phys. Rev. Lett. **48**, 1425(1982).
 - [12] G. B. Bachelet, D. R. Hamann, and M. Schlüter, Phys. Rev. B **26**, 4199 (1982)
 - [13] E. Kim, and Y. H. Lee, and M. Parrinello, J. Kor. Phys. Soc. **28**, s172, (1995)
 - [14] V. M. Glasov, S. N. Chizhevskaya, N. N. Glagoleva, "Liquid Semiconductors", (Plenum, New York, 1969).
 - [15] F. Hoffmann, A. Schulze, Phys. Z. **38**, 901(1937); E. S. Greiner, J. Metals **4**, 1044(1952).

INCORPORATION OF HYDROGEN IN SiO_2 AND Si_3N_4 THIN FILMS DEPOSITED BY ECR-CVD

J. BROWN*, M. BOUDREAU*, M. BOUMERZOU*, P. MASCHER*, T.E.
JACKMAN*,***, S.Y. TONG***, and H. HAUGEN***

*Centre for Electrophotonic Materials and Devices, Department of Engineering Physics,
McMaster University, Hamilton, Ontario, Canada, L8S 4L7.

**Institute for Microstructural Sciences, NRCC, Ottawa, Ontario, Canada, K1A 0R6.

***Accelerator Laboratory and the Institute for Materials Research, McMaster University,
Hamilton, Ontario, Canada, L8S 4L7.

ABSTRACT

Hydrogen incorporation in ECR-CVD silicon oxynitride films deposited using tris dimethylaminosilane (TDAS) as the silicon precursor was investigated. The as-deposited silicon dioxide films were shown to contain little hydrogen (<2%) as determined by both FTIR and nuclear reaction analysis (^{15}N profiling). Films were obtained with high breakdown fields (>10 MV/cm) and low interface state densities ($2 \times 10^{11} \text{cm}^{-2}$) on silicon without special surface preparation. Silicon nitride films were found to contain large hydrogen concentrations, both bonded and unbonded, which evolved from the film due to beam irradiation during ^{15}N profiling. We were able to demonstrate that dilution of the nitrogen plasma with both hydrogen and argon was effective in avoiding problems of trace oxygen contamination and poor film adhesion, and reducing the hydrogen concentration in the nitride films.

INTRODUCTION

The use of electron cyclotron resonance-chemical vapour deposition (ECR-CVD) for depositing high quality films of silicon dioxide or silicon nitride has received a great deal of interest due to the improved film characteristics compared to conventional CVD [1]. Among the advantages of ECR-CVD is the increased activation of species present in the plasma, allowing for lower substrate temperatures during deposition, and less damage to the substrate due to the reduction of high energy ion bombardment. This makes the technique more compatible with the increased temperature sensitivity of modern semiconductor processing.

Several different silicon sources are now commonly employed, the most frequent being silane (SiH_4) whose pyrophoric nature leads to concerns about gas handling safety. In this work, we have employed a safer organosilicon source, tris dimethylaminosilane (TDAS, $\text{C}_6\text{H}_{19}\text{N}_3\text{Si}$). This source is a non volatile liquid at room temperature, and is delivered to the system through a low pressure mass flow controller. The main feature of the molecule is the existence of direct Si-N bonds which results in an increased deposition rate for silicon nitride films when compared with traditional silane sources. Also, the reaction pathways are different from those found for silane based processes which results in films with markedly different growth characteristics and film properties. Because of these

differences, it is necessary to examine the growth and properties of silicon oxide and nitride films deposited using this precursor and determine the viability of the source for use in semiconductor processing.

EXPERIMENTAL DETAILS

Details regarding the ECR-CVD system at McMaster and the TDAS silicon source can be found in a previous publication [2]. During growth, the film refractive index and thickness were monitored using an in situ ellipsometer. The films were re-analyzed with an ex situ ellipsometer, to detect any changes occurring as a result of possible oxidation of the film upon removal from the vacuum system. The film composition was determined using Rutherford backscattering spectrometry (RBS). To facilitate the separation of the different RBS peaks, polished carbon [3] was used as the substrate material for the calibration measurements. The carbon was cleaned in trichloroethylene, acetone, methanol and deionized water to remove any organic contaminants present on the surface.

The total hydrogen content of the film was determined, as a function of depth, by nuclear reaction analysis (^{15}N profiling) [4]. The total bonded hydrogen present in the films was determined from the Fourier transform infrared (FTIR) spectroscopy measurements using the techniques of Lanford and Rand [5]. To reduce the effects associated with scattering, double polished highly resistive Si wafers were employed for the FTIR measurements.

The dielectric properties of the films were studied by capacitance-voltage (C-V) and current-voltage (I-V) measurements. To provide the necessary depletion region for a reliable extraction of the film properties from the C-V measurements, films were deposited on p-type $\langle 100 \rangle$ Si with a resistivity of $10\ \Omega\text{-cm}$. The substrates were dipped in a 10:1 solution of deionized $\text{H}_2\text{O}:\text{HF}$ prior to growth to remove any native oxide. The interface state density was determined from the high frequency (1MHz) C-V curve using the method of Terman [6]. A Hewlett Packard semiconductor parameter analyzer was used for I-V measurements. Electrical contacts were provided by evaporated aluminum.

RESULTS AND DISCUSSION

Silicon Dioxide Films

One of the most demanding applications for these dielectric films is as gate insulators in metal oxide semiconductor (MOS) device structures. It is therefore of great practical importance to be able to obtain films with desirable electronic characteristics: large breakdown voltages, small leakage currents, and low interface state densities. Silicon dioxide films were studied as a function of the TDAS flow during deposition. The flow of oxygen was fixed at 20 sccm and the substrate temperature at 200°C for this set of experiments. For low TDAS flow rates (<1.3 sccm) films with dielectric strengths in excess of 10 MV/cm could be obtained. The interface state densities were found to be approximately $2 \times 10^{11}\ \text{cm}^{-2}$ at mid-gap. While this value is reasonable, lower values should be obtainable through more aggressive cleaning and subsequent passivation of the substrate

to film deposition. Such work is in progress. Films grown at TDAS flows greater than 1.3 sccm were found to be conductive, and therefore were unacceptable for electronic device applications.

FTIR measurements were found to be a sensitive probe of the film quality. Figure 1 shows the film refractive index, and the Si-O stretching frequency vs. TDAS flow. The film index was found to be constant at 1.46 well beyond the maximum flow rate found acceptable for films with good electrical properties. Obviously, the refractive index is not a good indicator of the actual film quality. The Si-O stretching frequency, however, shows a linear variation with TDAS flow, clearly demonstrating an evolving difference between the films. The increased conduction at high flow rates is most likely associated with defect states present in the forbidden gap of the films. These states, perhaps the result of dangling bonds, would alter the local bonding arrangements of the SiO₂ molecules. This would, in turn, alter the vibrational frequency of the IR active bonds.

The level of hydrogen present in silicon oxide films is often a concern when silane is used as the silicon source, due to the associated degradation of the film's physical properties [7]. No Si-H or O-H peaks were observable in the FTIR spectrum, as is shown in Figure 2, and ¹⁵N profiling indicated a total hydrogen content below 2 at%.

Silicon Nitride Films

Silicon nitride films have a wide range of applications such as gate insulators and as the high refractive index material in thin film interference filters. It is therefore of technological interest to be able to grow combinations of oxides, nitrides, and oxynitrides in the same processing chamber. Unlike oxygen, nitrogen plasmas are not easy to maintain and can pose stability problems [1]. Using plasmas of pure nitrogen as the processing gas often leads to films with large amounts of stress, poor adhesion, and large hydrogen concentrations [8]. In an attempt to overcome these problems, various combinations of nitrogen, argon and hydrogen were used as the processing gases. Argon has been found to stabilize the plasma, and increase the ion density, while the inclusion of hydrogen as a processing gas has previously been found to lower the hydrogen content present in ECR-CVD films [9]. During ¹⁵N measurements, it was observed that irradiation by the probing beam caused hydrogen to evolve from the film. It was therefore difficult to reliably extract the hydrogen concentration from these measurements. However, the concentration of bonded hydrogen in all these films was sufficiently large to allow quantitative estimations from the FTIR spectrum, using the methods outlined by Lanford and Rand [5]. A typical transmission spectrum is shown

Table I: Hydrogen Content as a Function of Plasma Dilution.

Process Gases	Hydrogen Content (cm ⁻³)
N ₂	7.2x10 ²²
N ₂ /Ar	3.8x10 ²²
N ₂ /H ₂	1.1x10 ²²
N ₂ /H ₂ /Ar	1.2x10 ²²

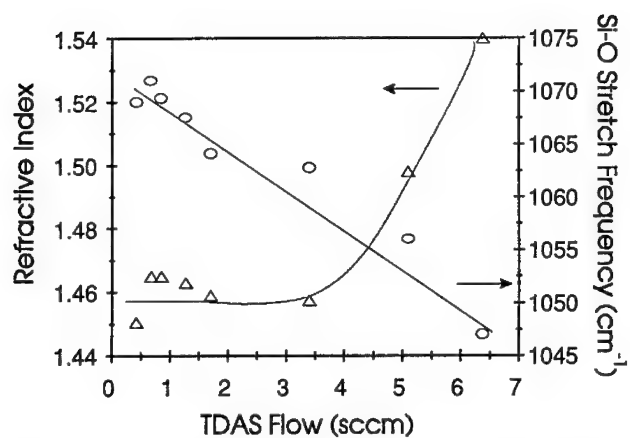


Figure 1: Refractive index (Δ) and frequency of the Si-O stretching vibration (o) versus TDAS flow.

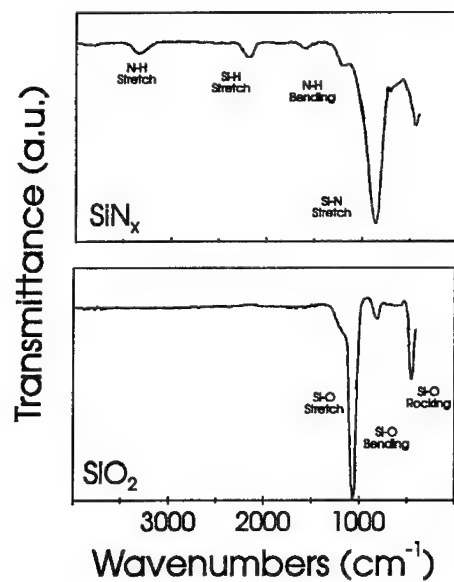


Figure 2: FTIR spectrum for silicon dioxide and silicon nitride films.

in Figure 2. Average hydrogen concentrations for the various growth conditions are shown in Table I. The addition of hydrogen to the plasma was consistently found to reduce the concentration of bonded hydrogen present in the film, when compared to a pure nitrogen or an argon-diluted plasma. However, the use of hydrogen was also found to result in unstable films which would bubble or crack, indicative of increased stress and poor adhesion. The addition of argon eliminated this problem, most likely due to the fact that argon acts to increase the cracking of both the N_2 and TDAS molecules thus creating more reactive species at the substrate surface. The result are films with improved bonding to the substrate. The best quality films were achieved through the addition of both argon and hydrogen, giving lower bonded hydrogen concentrations in the films and improved film stability.

ECR-CVD reactors must be operated at significantly lower operating pressures when compared with other CVD and PECVD systems. This causes an increased sensitivity to oxygen contamination through poor vacuum practice or small leaks in the system. For example, it was found that a background partial pressure of oxygen of 5×10^{-7} Torr resulted in oxygen contamination of the films, greatly reducing the refractive index. Also, the films, in some cases, continued to oxidize once removed from the system further reducing the refractive index. Figure 3, which shows the refractive index versus the oxygen fraction present in the film, demonstrates the consequences. The addition of hydrogen to the plasma was found to greatly reduce the sensitivity of the films to the incorporation of oxygen, most likely through the formation of water which subsequently would be pumped from the system before it could be incorporated in the films. The electrical characterization of these films is on going and will be reported in a future publication.

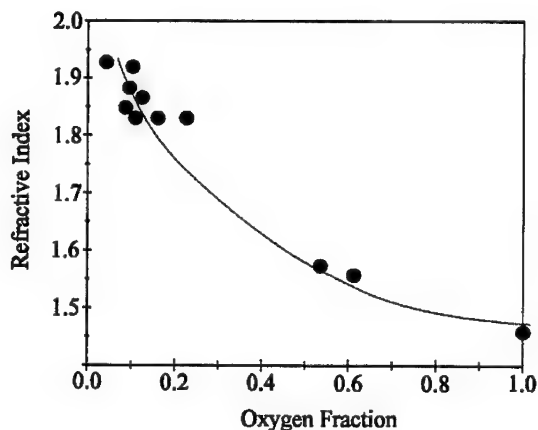


Figure 3: The refractive index versus the oxygen fraction in the deposited films (percent oxygen/(percent oxygen+percent nitrogen)).

CONCLUSIONS

This dimethylaminosilane has been shown to be a promising, and safer alternative to silane for ECR-CVD of silicon oxide and silicon nitride films. Good quality silicon dioxide was deposited with good electrical characteristics and minimal hydrogen incorporation. Silicon nitride films with reduced hydrogen incorporation and improved adhesion were obtained through the dilution of the processing gases with argon and hydrogen. The use of hydrogen was also found to reduce the sensitivity of the process to contamination by oxygen present in the background.

ACKNOWLEDGMENTS

This work was supported by the Natural Sciences and Engineering Research Council of Canada, and the Ontario Center for Materials Research. We would also like to thank Mr. Eugene Tan for valuable discussions and assistance.

REFERENCES

1. Y. Manabe, T. Mitsuyu, J. Appl. Phys., **66**, 2475, (1989).
2. M. Boudreau, M. Boumerzoug, P. Mascher, P.E. Jessop, Appl. Phys. Lett., **63**, 3014, (1993).
3. Alpha Research Chemicals and Accessories, Johnson Matthey, P.O. Box 8247, Ward Hill, Ma, 01835 0747.
4. S.Y. Tong, H.K. Haugen, M.G. Boudreau, M. Boumerzoug, and P. Mascher, in: The Physics of Semiconductors, edited by D.J. Lockwood (World Scientific, Singapore 1995), p. 2359.
5. W.A. Lanford and M.J. Rand, J. Appl. Phys., **49**, 2473, (1978).
6. L.M. Terman, Solid-State Elect., **5**, 285, (1962).
7. L. Hrubein, J. Huran, R. Sandrik, A.P. Kobzev, D.M. Shirokov, Nuc. Instr. and Methods in Phys. Res. B, **85**, 60, (1994).
8. S. Dzioba and R. Rousina, J. Vac. Sci. Technol. B **12**, 433, (1994).
9. W. Puff, M. Boumerzoug, J. Brown, P. Mascher, D. Macdonald, P.J. Simpson and A.G. Balogh, Appl. Phys. A, (1995), in press.

AUTHOR INDEX

- Abdurakhmanov, B.M., 411
 Abernathy, C.R., 485, 497
 Acciarri, M., 913
 Adams, R. Matthew, 533
 Agarwal, Aditya, 71, 291
 Agarwal, Sandeep, 941
 Akasaki, I., 491, 509
 Al-Hemyari, K., 1001
 Allen, L., 579
 Amano, H., 491, 509
 Aroca, G., 823
 Ashok, S., 365
 Ashwin, M.J., 567
 Astafiev, Oleg V., 615
 Avalos, J., 899

 Bae, B.S., 393
 Bagai, R.K., 423
 Balasubramanian, Sathya, 453
 Balogh, Adam G., 977
 Ban, Ibrahim, 737
 Baranov, P.G., 521
 Bathey, B.B., 29
 Beaman, Kevin L., 291
 Becla, P., 47
 Belay, K.B., 201
 Bell II, Ronald E., 647
 Belogorokhov, A.I., 665
 Benamara, M., 863, 869
 Benz, K.W., 77
 Bessolov, Vasily N., 1019
 Besson, J.M., 435
 Bevk, Joze, 857, 887
 Bhat, H.L., 423
 Bilyalov, R.R., 411
 Binetti, S., 913
 Bletskan, Nikolay I., 615
 Block, Thomas R., 783
 Boudreau, M.G., 1007, 1037
 Boumerzoug, M., 1007, 1037
 Brohl, M., 17
 Broser, I., 521
 Brown, E.R., 479
 Brown, J., 1007, 1037
 Brown, R.A., 89, 95
 Brunner, Sebastian, 977
 Bude, J., 857
 Burger, A., 841
 Buyanova, I.A., 135, 881
 Buzynin, Alexander J., 615, 653

 Carlone, Cosmo, 225
 Carlson, N., 579
 Carr, Kevin F., 579
 Chan, K.T., 219
 Chan, M.H., 219
 Chang, James S.C., 231
 Charnyi, L.A., 659, 665

 Chen, C.Y., 875, 959
 Chen, H.K., 153, 189, 195
 Chen, J.C., 153, 189, 195
 Chen, K.T., 841
 Chen, W.M., 135, 881
 Chevallier, J., 435, 459
 Chi, P.H., 875, 959
 Choi, Deuk-Sung, 761
 Choi, H.S., 393
 Choi, K.Y., 393
 Choi, Suk-Ho, 905
 Chou, Y.C., 777
 Christensen, Kim, 71, 737
 Christou, A., 789
 Chu, Peter, 777
 Chung, H., 41
 Cisco, T.C., 777
 Claeys, C., 35
 Clauws, P., 35, 953
 Claverie, A., 677, 863, 869
 Cohen, R.M., 875, 959
 Collart, E.J.H., 115
 Collins, W.E., 841
 Conley, Jr., John F., 377
 Contreras, Miguel A., 803
 Csaszar, Wolfgang, 353
 Cudzinovic, Michael, 767
 Curtis, K., 309

 Danilin, A.B., 659, 665
 Davidson, J.A., 995
 Deng, Xiaojun, 359
 Ding, Chen, 757
 Downey, S.W., 857
 Dudley, M., 41

 Ebling, D.G., 77
 Eckey, L., 521
 Edirisinghe, C., 1007
 Eiche, C., 77
 Elgamel, H., 399
 Endrös, Arthur L., 353, 597
 Engström, O., 371
 Erzgräber, H.B., 141
 Evans, J.H., 629, 995
 Evans, M.J., 341
 Ewvaraye, A.O., 539, 835

 Fahy, M.R., 567
 Fauchet, P.M., 171
 Fedorenko, A.I., 255
 Fengmei, Wu, 225
 Fiederle, M., 77
 Fnaiech, M., 863
 Fujii, Yoshimaro, 731
 Fujikawa, Hisayoshi, 1025
 Fujiyoshi, Katsuhiko, 731
 Furtch, Matthias, 857, 887

Gafiteanu, R., 297
 Gao, X., 213
 Gao, X., 309
 Gaubas, E., 35, 603, 609
 George, M.A., 841
 Gilbert, T.S., 795
 Giles, L.F., 629
 Gillies, D.C., 41
 Ginoudi, A., 459
 Gislason, H.P., 371
 Goldstein, Y., 899
 Gomez, M., 899
 Goorsky, Mark S., 315, 783, 893
 Gorne, G.V., 107
 Gösele, Ulrich M., 279, 297
 Götz, W., 491, 527
 Gräf, D., 17
 Gravestijn, D.J., 115
 Gupta, S.R., 671
 Gurumurthy, Suma, 423

 Haddad, H., 309
 Haga, H., 23
 Hall, Dennis G., 887
 Haller, Eugene E., 509, 547
 Han, Chul-Hi, 129, 761
 Han, M.K., 393
 Hansen, J. Lundsgaard, 285
 Hansson, G.V., 135, 881
 Harris, Jr., J.S., 527
 Hart, L., 567
 Hasebe, Y., 623
 Hattori, T., 623
 Hatzopoulos, Z., 459, 789
 Haugen, H., 1037
 Heiser, T., 585
 Heitz, R., 521
 Hemment, P.L.F., 629
 Henderson, R., 1007
 Henley, W., 405
 Henry, A., 135, 881
 Hettwer, H.-G., 183
 Hieslmair, Henry, 327
 Higgs, V., 989
 Hoffmann, A., 521
 Holmes, S.N., 567
 Holst, J.-Ch., 521
 Hu, Zhihua, 841
 Hu, Zhiyu, 841
 Huang, J.W., 165
 Huang, Xinming, 53
 Huang, Z.C., 153, 189, 195
 Hur, Sung-Hol, 761

 Ianno, N.J., 689
 Ichimura, Masaya, 731
 Ivankov, Andrew F., 1019
 Iwasaki, T., 23
 Izunome, Koji, 53

 Jackman, T.E., 1037
 Jäger, W., 183

 James, R.B., 795
 Jarasunas, K., 59, 603
 Jastrzebski, L., 405
 Jedral, L., 1007
 Jiang, Z., 89
 Jing, Z., 851
 Joerger, W., 77
 Johnson, C.M., 683
 Johnson, N.M., 491
 Johs, B., 689
 Jones, K.S., 635
 Jorio, Anouar, 225
 Joshi, Subhash, 279

 Kagiichi, H., 677
 Kalbe, Hiromasa T., 147
 Kalinushkin, Victor P., 615
 Kalomiro, J., 459
 Kaniava, A., 35, 59, 399, 603, 609
 Karadima, F., 789
 Karimpanakel, S., 405
 Kellert, Forrest G., 231
 Kennedy, B.J., 121
 Kersten, W.J., 115
 Khattak, Chandra P., 767
 Khokhlov, Dmitriy R., 947
 Kim, Choong-Ki, 129, 761
 Kim, Eunja, 1031
 Kim, S.S., 725
 Kim, Y.S., 393
 Kimerling, L.C., 703
 Kimura, Shigeyuki, 53
 King, Oliver, 887
 Kirscht, F.G., 303
 Kissinger, G., 35, 141
 Kitagawa, Hajime, 983
 Kitai, Adrian H., 533
 Kittler, M., 989
 Klose, H., 743
 Koch, F., 743
 Kojima, K., 23
 Konenkova, Elena V., 1019
 Konstantinidis, G., 789
 Kornilios, N., 789
 Kostoulas, Y., 171
 Koutzarov, I., 1007
 Koveshnikov, Sergei V., 71, 291
 Kringhøj, P., 285, 683
 Krisch, K.S., 857
 Krishnamoorthy, V., 635
 Kristjansson, S., 371
 Kuech, T.F., 165
 Kumar, Vikram, 423, 453, 671

 Lagadas, M., 459, 789
 Lagowski, Jacek, 47, 405, 647
 Lambert, U., 17
 Langouche, G., 953
 Laporte, A., 863, 869
 Larsen, A. Nylandsted, 285
 Larson, Jr., D.J., 41
 Lathouwers, E.G.C., 115

- Lavine, J.P., 713
 Lebedev, Mikhail V., 1019
 Lee, El-Hang, 1013
 Lee, Ga-Won, 761
 Lee, H.P., 177
 Lee, Hae Gwon, 1013
 Lee, Ho-Jun, 129
 Lee, Jaemin, 1013
 Lee, Jung-Yeal, 761
 Lee, K.J., 153
 Lee, Yong Hee, 1013
 Lee, Young Hee, 1031
 Lenahan, P.M., 377
 Lescouzères, L., 863, 869
 Li, G.P., 777
 Li, W.M., 875, 959
 Libezny, M., 35
 Lilliental-Weber, Z., 677
 Lin, Tsai-Cheng, 147
 Lindo, S.E., 315
 Lioutas, C.B., 459
 Liu, J., 635
 Liu, Q., 1007
 Liu, X., 83, 207
 Llewellyn, D.L., 201
 Lobad, A.I., 171
 Loghmarti, M., 333, 971
 Lü, J.-Q., 743
 Lucovsky, G., 851
 Luftman, H.S., 857
 Luk'yanov, Albert E., 653

 Machayekhi, B., 435
 MacKenzie, J.D., 497
 Maes, H.E., 953
 Mahajan, S., 29
 Maher, Dennis M., 737
 Mahfoud, K., 333, 971
 Mahnkopf, R., 743
 Maki, B., 479
 Mäkinen, J., 441
 Makino, Takanori, 641
 Many, A., 899
 Marcano, N., 829
 Marshall, C., 579
 Mascher, Peter, 533, 977, 1007, 1037
 Maslovsky, Vladimir M., 65
 Masumura, H., 591
 Matney, K.M., 315
 Matsuda, Koichiro, 429
 Maxim, P., 521
 McColgin, William C., 713
 McHugo, Scott A., 303, 327
 McQuaid, S.A., 441
 Mehrer, H., 183
 Mehta, G.K., 671
 Meier, D.L., 29
 Melngailis, I., 479
 Melton, W., 515
 Meshkinpour, Marjohn, 783
 Mesli, A., 585
 Meyer, B.K., 521

 Mishra, Kamal K., 321
 Missous, M., 441
 Mitchel, W.C., 539, 835
 Mityukhlyayev, V.B., 695
 Mizuno, M., 303
 Mizuta, Masashi, 929
 Mohapatra, Y.N., 941
 Mokhov, E.N., 521
 Molnar, R.J., 479
 Mönch, Winfried, 811
 Monemar, B., 135, 881
 Moore, A., 1007
 Moore, Karen L., 887
 Moore, R.A., 121
 Moreland, John, 249
 Morelhão, S.L., 29
 Morgenstern, G., 141
 Morgenstern, T., 141
 Morita, Etsuro, 641
 Moriya, N., 857
 Muller, J.C., 333, 971
 Mun, Byoung-Hun, 905
 Murphy, Robert, 749

 Nakai, K., 23
 Nakano, M., 591
 Nakashizu, T., 23
 Nam, C.W., 365
 Nashchekina, O.N., 107, 255
 Nejim, A., 629
 Nelson, Art J., 249
 Nemirovski, A.W., 659, 665
 Neugebauer, G.T., 29
 Neugebauer, Jörg, 467
 Newman, R.C., 441, 567
 Ni, W.-X., 135, 881
 Nichols, K.B., 479
 Nickel, N.H., 381
 Nijs, J., 399
 Nishino, T., 263
 Noufi, Rommel, 803
 Nygren, E., 273

 Oberman, D.B., 527
 Ogita, Y., 591
 Ogletree, D.F., 83
 Ohshima, H., 623
 Okumura, Tsugunori, 147, 447
 Osiko, Vyacheslav V., 653
 Ostapenko, Serguei, 405, 647
 Ostendorf, Hans-Christoph, 597
 Öztürk, Mehmet C., 737

 Palm, J., 703
 Paloura, E.C., 459
 Pankove, J.I., 515, 521
 Pao, C.K., 777
 Papavasiliou, C., 789
 Parenteau, Martin, 225
 Park, Hyo-Hoon, 1013
 Park, Min Soo, 1013
 Park, Y., 159

Patterson, George A., 231
 Peaker, A.R., 995
 Pearton, S.J., 485, 497
 Peng, Z.F., 213
 PeyreLavigne, A., 863, 869
 Pinegin, V.I., 255
 Pittal, S., 689
 Pizzini, S., 913
 Poortmans, J., 399
 Prasad, A., 207
 Pritchard, R.E., 441
 Puff, Werner, 977

 Qian, Y.H., 629
 Qiu, C.H., 515, 521
 Queisser, Hans J., 3

 Raghothamachar, B., 41
 Richter, H., 141
 Ridgway, M.C., 201, 683
 Roberts, C., 567
 Rocher, A., 863, 869
 Rogacheva, E.I., 107, 255
 Rose, Doug, 749
 Rosmeulen, M., 399
 Rozgonyi, George A., 71, 291
 Ruckl, A., 183
 Ruda, H.E., 1007

 Sakamoto, Yoshifumi, 429
 Salk, M., 77
 Salmeron, M., 83
 Saraikin, V.V., 659
 Sarabayrouse, G., 863, 869
 Sassa, Koichi, 935
 Sato, D.L., 177
 Savir, E., 899
 Savransky, Semyon D., 965
 Sayah, D., 333
 Schlesinger, T.E., 795
 Schmid, Frederick, 767
 Schöttl, S., 743
 Schwarz, R., 77
 Seifert, W., 989
 Sen, P., 671
 Shama, B.B., 671
 Sharma, R.K., 671
 Shin, Jae-Heon, 1013
 Shinagawa, Tatsuyuki, 447
 Shirafuji, Junji, 429
 Shiraki, Hiroyuki, 935
 Shiryaev, S.Yu., 285
 Shpakovskaya, L.P., 255
 Shul, R.J., 497
 Siffert, P., 333, 971
 Silverman, P.J., 857
 Silvestre, G.C.M., 121
 Simoen, E., 35
 Simons, D.S., 875, 959
 Singh, A., 823, 829
 Sinha, K., 249
 Sinno, T., 95

 Skowronski, M., 159
 Slupinski, T., 83
 Smith, J.S., 207
 Smith, S.R., 539, 835
 Snyder, P.G., 213, 689
 So, S.K., 219
 Sopori, Bhushan L., 359, 579, 749, 767
 Sreedhar, A.K., 423
 Stallinga, P., 207
 Stancampiano, C.V., 713
 Stavola, Michael, 341
 Stefanov, E., 743
 Stesmans, A., 953
 Stolwijk, N.A., 183
 Street, R.A., 491
 Streit, Dwight C., 783
 Sudzius, M., 59
 Sugino, Takashi, 429
 Sundershesu, B., 423
 Sveinbjörnsson, E.Ö., 371
 Swider, W., 677
 Syfosse, G., 435
 Symko, Martha, 767
 Szalkowski, F.J., 177

 Taga, Yasunori, 1025
 Takano, K., 101
 Tan, Teh Y., 279, 297
 Tanaka, Shuji, 983
 Tennant, Andrew, 803
 Terashima, Kazutaka, 53
 Theys, B., 435, 459
 Thompson, Jr., R.H., 635
 Tiwari, U., 671
 Togawa, Shiniji, 53
 Tokuda, Yutaka, 623, 935
 Tong, S.Y., 1037
 Trauwaert, M.-A., 953
 Tsu, Raphael, 757
 Tsumori, Y., 23

 Ucer, K.B., 171
 Uffring, S.J., 341
 Urban, K., 183
 Usami, A., 623
 Usami, Akira, 641, 731

 Vaitkus, J., 59, 603
 Van Bavel, A.-M., 953
 Van de Walle, Chris G., 467, 503
 Vandini, M., 995
 Vanhellemont, J., 35, 399, 953
 Van Scyoc, J.M., 795
 Vartuli, C.B., 485, 497
 Velásquez, L., 823
 Verma, A.K., 207
 Vetterhöffer, J., 417
 Volm, D., 521
 von Bardeleben, H.J., 441
 Voronkov, Vladimir V., 653

 Wagner, J., 567

Wagner, P., 17
Walukiewicz, W., 47, 509
Wang, H.H., 677, 1001
Watkins, G.D., 341
Webb, John, 803
Weber, Eicke, R., 83, 207, 303, 327
Weber, J., 417
Weill, G., 435
Weisz, S.Z., 899
Weitzman, P., 579
Wetzel, C., 509, 521
Whitaker, J.F., 677, 1001
Whitten, J.L., 851
Wichert, Thomas, 237
Wicks, G.W., 171
Wigert, B., 689
Wijaranakula, W., 101, 309, 725
Williams, J.S., 273
Williams, P.M., 341
Williamson, S.L., 1001
Wilson, R.G., 497
Witt, A.G., 47

Wittorf, D., 183
Wojtowicz, Mike, 783
Wong-Leung, J., 273
Woollam, J.A., 689
Wu, C.S., 777
Wu, J., 41

Yamagishi, H., 101
Yang, Bing, 153, 189, 195
Yi, Shi, 225
Yoo, Byueng-Su, 1013
Yoon, H., 893
Yoshida, Hideaki, 641, 731
Youdou, Zheng, 225
Yu, P.W., 213
Yuryev, Vladimir A., 615

Zamouche, A., 585
Zavada, J.M., 497
Zhang, Q.S., 101
Zhang, Y.Q., 213
Zolper, J.C., 485

SUBJECT INDEX

- acceptor state generation, 381
- A-centers, 659
- activation ratio, 623
- adsorption, 905
- AlGaAs, 153
 - deep-level-free, 195
 - DX center, 929
- AlGaN, 509
- alloy fluctuations, 83
- Al-O molecule, 159
- AlSb, 47
- amorphous GaAs, 1013
- annealing, 983
- antisite defects, 207, 423, 567
- As
 - flux, 231
 - implanted GaAs, 677
 - precipitates, 459, 677
 - vacancy, 263
- As₂ and As₄, 231
- As_{Ga} defects, 207, 441
- atomic force microscopy, 17, 841
- Au/GaAs Schottky contact, 829
- barrier height, 811, 823, 829, 835
- binding energy, 225
- bipolar transistors, 743
- blister method, 129
- boron profiling, 857
- capacitance-
 - time (C-t), 737
 - voltage (C-V), 737, 835, 857
- carbon, 547, 913
 - precipitation in Si, 971
- carrier dynamics, 171
- cathodoluminescence, 533
- cavities, 273
- CdTe, 77
- CdZnTe, 41, 841
- charge
 - coupled devices (CCD), 713
 - pumping method, 761
- charged
 - defects, 959
 - traps, 757
- chemistry of point defects, 913
- chemomechanical polishing (CMP), 17
- clustering effect, 1031
- Co in Si, 713
- compensation, 77, 467
- complexes, Au-H, 371
- concentration profiles, 659
- conduction mechanisms, 1025
- conductivity inversion, 653
- consecutive reactions, 983
- constant-capacitance voltage transient spectroscopy (CCVTS), 935
- contactless evaluation, 641
- contamination, 989
- copper, 585
- Cr-B pairs, 647
- critical thickness, 783
- crystal originated
 - defects, 713
 - particles (COP), 17
- Cu(In,Ga)Se₂, 803
- CuInSe₂, 803
- current-voltage (I-V) characteristics, 1025
- Cu_{2-x}Se, 249
- CZ-Si crystal growth, 23
- 2D simulation, 743
- 3d transition-metal impurities, 263
- damage
 - ECR plasma damage, GaAs, 689
 - ion treatment, 653
 - mirror-polishing-induced, 591
 - slicing-induced, 591
 - subsurface, 591
- dark current spectroscopy, 713
- deep levels
 - AlGaAs, 153, 195
 - atomic structure, 159
 - CCDs, 713
 - InGaAs, 165
 - InGaP, 189
 - GaAs, 159
 - GaN, 491
 - hydrogenated, 341, 365
 - LT-GaAs, 147
- defect(s), 3
 - activation, 365, 623
 - As_{Ga}, 207
 - bistability, 929, 935
 - CdS, 695
 - characterization, 509, 615
 - charged, 959
 - clustering, 533
 - control, 703
 - crystal-originated, 725
 - decoration, 995
 - divacancy(-), 953
 - oxygen complex, 953
 - extended, 71, 629
 - flow pattern, 101
 - GaN, 491, 527
 - hydrogen-induced, 365
 - intentional incorporation, 165
 - interfacial, 851
 - LT-GaAs, 441
 - metastable, 851
 - mobility, 65
 - non-equilibrium, 65
 - nonstoichiometric, 255
 - passivation, 195, 371, 623

defects(s) (*continued*)
 plasma-induced, 429, 689
 reaction, 983
 Si/SiO₂, 851
 SnTe, 255
 structural, 327
 structure, 377
 II-VI compounds, 977
 vacancy-type, 359
 vibrational modes, 547
 Zn diffusion, 183
 ZnO, 977
degradation, 777
 and reliability, 743
delta doping, 177, 567
dendritic web silicon, 29
deuterium
 GaAs, 435
 Si, 359
device degradation, 783
dielectric function, 213
diffuse scattering, 315
diffusion(-)
 group III, 875
 hydrogen in
 poly-Si, 393
 Si, 359, 393
 TFTs, 393
 hydrostatic pressure, 435
 InP, 183
 length, 279, 321
 mapping, 597
 segregation equation, 297
 transient, 273
 Zn, 183
dimer, 231
direct wafer bonding, 863
 preamorphized Si, 869
dislocation(s), 59, 579, 749, 783, 989
 loops, 291, 635
 modeling in solar cells, 749
 network(s), 29
 model, 749
 SiGe, 989
disorder, 3
divacancy(-), 953
 oxygen complex, 953
DLTS, 71, 147, 165, 353, 365, 399, 447,
 491, 731, 953, 983, 995
donor(-)
 acceptor pairs, 237
 neutralization, 435
dopant
 activation, 623, 683
 influence of non-stoichiometry, 683
 reactivation, 497
doping, 3
 alkoxide, 159
 carbon, 177
 delta, 177, 567
 InP, 683
 oxygen, 165
DX center, 47, 929, 941, 947
 kinetics, 941
ECR(-)
 CVD, 1037
 etching, GaAs, 689
EL2, 59, 147
 GaAs, 447
 In-AlGaAs, 207, 219
 transient quenching, 59
EL5-EL6 interaction, 935
elastic parameters, 129
electroanalytical metal traces (ELYMAT), 597
electroless contacts, 841
electroluminescence, 803
electron
 beam induced
 current (EBIC), 989
 transformation, 695
 irradiation, 411
 paramagnetic resonance (EPR), 341
 spin resonance (ESR), 377
EP center, H-complexed, 377
exciton, 521
 isoelectronic bound, 887
fall bits, 725
fast diffusing charged defects, 585
Fe-B pairs, 647
Fermi level pinning, 947
 during OMVPE, 875
FeSi₂, 309
first principle calculations, 467, 503
flow pattern defects, generation rate, 101
IV-VI semiconductors, 947
free exciton, 225
GaAs
 EL5 and EL6, 935
 In-doped, 263
 nonstoichiometric, 201
 sulfur passivation, 1019
GaAsP, 83
GaN, 467
 atomic geometry, 503
 deep levels, 491
 electronic structure, 503
 energetics of H, 503
 epitaxial, 479, 521
 hydrostatic pressure, 509
 impurities, 479
 photoconductivity, 515
 photoluminescence, 521
gap states, 811
gate oxide integrity (GOI), 23
Ga vacancy, 959
generation-recombination current, 829
gettering
 backside Al, 279, 297, 327
 C-doped Si, 303
 external, 297
 gold, 297

- gettering (*continued*)
 - internal, 303
 - interstitial Fe, 309
 - ion implantation, 71
 - iron, 321
 - mechanical damage, 315
 - mechanisms, 327
 - P indiffusion, 297, 333
 - phosphorous, 327
 - polycrystalline Si, 321, 327, 333
 - SiGe, 285
 - stability, 303
- gold in Si, 713
- graded buffers, 141
- grain
 - boundaries, 579, 863
 - boundary trap density, 761
- group I and V elements, 237
- grown-in defects, 23
- Hall effect, 527, 983
- heat exchanger method (HEM), 767
- heterojunction bipolar transistors (HBT), 777
- heterostructures
 - AlGaAs/GaAs, 1007
 - Cu₂Se/CdS, 249
 - InGaP/GaAs, 189
 - modulation-doped, 881
 - SiGe/Si, 135, 141, 881, 887
 - sulfur passivation, 1007
- HgI₂, 795
- high(-)
 - electron mobility transistors (HEMT), 783
 - level excitation, 609
 - low junction, 641
 - temperature I-V, 829, 835
- homogeneity, 3
- 6H-SiC, 521, 539, 835
- hydride vapor phase epitaxy, 479
- hydrogen, 547
 - azide, 527
 - implantation, 623
 - in Si
 - defect activation, 365
 - diffusion, 359, 393
 - pathways, 393
 - dislocations, 989
 - electronic properties, 353
 - gold, 371
 - grain boundary, 399
 - H-C complex, 353
 - multicrystalline Si, 399
 - passivation, 341, 359, 411
 - poly-Si, 393
 - PtH₂ complex, 341
 - structural properties, 353
 - transition metal complexes, 341
 - in silicon oxynitride, 1037
 - in III-V
 - AlGaAs alloys, 435
 - acceptor level, 435
 - chalcogens, 417
 - diffusion in GaAs:Si, 435
 - electron traps, 447
 - GaAs, 417, 447
 - GaN, 503
 - InAlN, 497
 - InGaAlN, 497
 - InGaN, 497
 - InP, 429, 453
 - LT-GaAs, 441, 459
 - passivation, 417, 429, 453, 459
 - in II-VI
 - In-doped CdTe, 423
 - passivation, 423
- hydrogenation, 393, 399, 405, 989
- SiGe, 989
- hydrostatic pressure, 435, 509
- image sensors, 713
- impurities
 - capture, 291
 - HgI₂, 795
 - iron, 291
 - vibrational modes, 547
- InAlN, 485
- in-diffusion, 983
- infrared (IR), 547
 - absorption, 567, 603, 665
 - detectors, 41
- InGaAs, HEMT, 783
- InGaP, 189
- in-line monitoring, 703
- insulating properties, 1025
- interatomic potential, 89
- interdiffusion, 875, 959
- interface(-)
 - dipoles, 811
 - direct-bonded Si, 863, 869
 - induced gap states, 811
 - stress, 263
 - traps, 459
- interstitial(s), 635, 959
 - copper, 585
- inversion, conductivity, 653
- ion
 - drift, 585
 - implantation, 291
 - carbon in Si, 737
 - cavities, 273
 - CdS, 695
 - GaAs, 201, 677
 - gettering, 273, 291
 - hydrogen, 623
 - InP, 683
 - isolation, 485
 - lattice strain, 635
 - lifetime, 603, 677
 - low energy, 115
 - MBE, 115

ion (*continued*)
 MeV, 71, 671
 oxygen, 659, 665
 residual damage, 71
 solid phase epitaxy, 201
 structural defects, 71
 substoichiometric, 665
 surface recombination measurement, 641
 III-V nitrides, 485
 treatment, 653
iron in Si, 713, 983
isothermal capacitance transient spectroscopy (ICTS), 429
isotope, 547
kickout reaction, 183
laser
 facets, 1007
 scattering tomography (LST), 35
lattice
 deformation, 671
 properties, 107
leakage current, 795
lifetime
 carrier, 35, 171, 603, 609, 677, 731
 generation, 737
light
 beam induced current (LBIC), 579
 emission, Si, 703
 point defects (LPD), 17
 scattering, 17
 elastic, 615
local vibrational mode (LVM), 341, 417, 547
localization, 547
LT-AlGaAs, 207
LT-GaAs, 147, 213, 441, 677
 outdiffusion, 789
 photodetector, 1001
 point defects, 789
 precipitates, 789
luminescence, 899
magnetic
 circular dichroism of absorption (MCDA), 207
 field induced prolonged changes (MFIPC), 65
material inspection, 615
MBE
 As
 cracking source, 231
 doping, 115
 C doping, 177
 GaAs, 567
 GaN, 527
 gettering, 285
 graphite source, 177
 ion implantation, 115
 LT-GaAs, 219, 459
 metallic contaminants, 285
 Si, 115, 135, 285
 SiGe, 135, 887
 superlattice, 887
 uniformity, 231
membranes, Si, 129
memory devices, 725
MESFETs, LT-GaAs buffer layers, 789
metallic impurities, 767
metal-semiconductor(-) (MS)
 interface, 811, 835, 841
 metal (MSM) photodetector, 1001
metastability, 59, 381, 447, 947
MeV implantation, 671
microgravity, 41
microprecipitates, 971
microstructure, 533
microwave absorption, 35, 603
minority carrier transient spectroscopy (MCTS), 995
misfit dislocations, 129
modulation doping, 881
molecular dynamics simulations, 95
MOS
 capacitors, 737, 857
 structures, 857
MOVPE
 AlGaAs, 153, 195
 carrier gases, 153
 Fermi level pinning, 875
 GaN, 497
 InGaAs, 165
 InGaP, 189
nanoparticles, Si, 757
native defects, 479, 509
negative(-)
 correlation energy, 965
 U defect, 503, 941, 965
 creation and destruction, 965
Ni in Si, 713
nitrogen vacancies, 479
non-contact laser microwave method, 641
non-destructive evaluation, 615
nonstoichiometry, 683
optical
 absorption, 219, 515
 admittance spectroscopy, 539
 detection of magnetic resonance (ODMR), 135
 DLTS, 491
 interconnects, 703
optoelectronics, 1001
order parameters, 1031
oxidation induced stacking faults (OISF), 995
oxide polyhedral precipitates, 309

- oxygen(-), 547
 - implantation, 121
 - in Si, 89
 - chemistry, 913
 - clusters, 89
 - diffusion, 89
 - mass transport, 659
 - precipitation, 35, 303
 - vacancy complex, 665
- passivation
 - amorphous GaAs, 1013
 - Au, 371
 - by Li, 371
 - electron irradiated Si, 411
 - LT-GaAs, 1001
 - surface, 1001, 1013
 - emitting laser, 1013
- persistent photoconductivity, 47, 539, 929, 947
- perturbed angular correlation (PAC), 237
- phase separation, 1031
- photochromic effect, 47
- photoconductivity, 171, 225, 515
- photoionization, 47
- photoluminescence, 35, 141, 177, 453, 509, 527, 893, 899
 - light-induced changes, 905
 - sulfur passivation, 1007
 - time-resolved, 521
- photonic devices, 841
- photoquenching, 147
- photorefractivity, 59
- photothermal deflection spectroscopy (PDS), 219
- PIN photodiodes, 731
- planar solid-liquid interface, 767
- plasma
 - cleaning, 365
 - induced defects, 429
- point defects, 23
 - aggregation, 95
 - interstitial, 875
 - numerical simulation, 101
 - saturation, 101
 - supersaturation, 183
- polycrystalline
 - Si, 381, 405, 411, 761
 - thin films, 803
- poly-Si/SiO₂ interface, 857
- porous silicon, 893, 899, 905
- positive U, 941
- positron annihilation spectroscopy (PAS), 533, 977
- process simulator, 703
- proton implantation
 - CdS, 695
 - ZnO, 977
- pulsed current mode stress, 777
- pyramids, 629
- quality control, 615
- quantum
 - dot diode, 757
 - efficiency, 515
 - wells, 3, 881
- radiation detectors, 795, 841
- radiative recombination, 881
- Raman scattering, 567
- random telegraph signals, 743
- rapid thermal anneal (RTA), 333, 731, 971
- recombination
 - dislocations, 989
 - nonradiative, 135
 - parameters, 603, 609
 - radiative, 881
 - stacking faults, 995
- refresh time degradation, 725
- reliability, HBTs, 777
- residual damage, 315
- resonant tunneling, 757
- reverse bias annealing, 423
- sacrificial oxidation, 629
- scanning
 - defect mapping, 579
 - tunneling microscope (STP), 83
- scattering, diffuse, 893
- Schottky
 - barriers
 - Al/Si/GaInP, 811
 - H-modified, 811
 - metal-6H-SiC, 835
 - metal/Si₃N₄/Si
 - metal/Si₃N₄/Si, 811
 - W-nGaAs, 823
 - diode, 365, 491
- Se doping, 195
- segregation, 77
 - impurities, 273
 - melt, 83
- self-interstitials, 95
- semiconductor technology, 3
- semi-insulating substrates, 539
- sensitivity uniformity, 731
- Si
 - microphotonics, 703
 - nanoparticles, 757
 - photovoltaics, 703
- SiC, 521, 539
 - Ti and V, 539
- SiGe, 141, 1031
- silicon(-)
 - divacancy, 953
 - nitride, ECR, 1007, 1037
 - on-insulator (SOI), 121, 291
 - defect formation, 121
 - oxynitride, 1037
- SIMOX, 629
- SIMS, 459, 749
- SiO₂ thin film, 377, 1037
- Si-SiO₂ interface, 743, 851
- SnTe, 107, 255

SOI, bonded, 731, 863, 869
 solar cells, 29, 279, 411, 597, 749, 767
 dislocations, 749
 hydrogenation, 399
 solubility, donor, 875
 space charge layers, 899
 spectral response, 731
 spectroscopic ellipsometry, 213, 689
 spin-dependent process, 965
 spinodal decomposition, 913
 spin-on-deposition, 333
 spreading resistance (SR), 623
 sputtered contacts, 823
 stacking fault, 121, 629
 bulk, 309
 recombination, 995
 tetrahedra, 629
 stoichiometry, 107
 strain, 635
 fields, 671
 strained layers, 285
 stress relaxation, 141
 stretched exponential, 539
 structural quality, 677
 sulfide solution, alcohol-based, 1019
 sulfur passivation, 1007, 1019
 superlattices, 789, 887
 surface
 defects, 823
 emitting laser, 1013
 passivation, 1013, 1019
 photovoltage (SPV), 405, 647
 recombination velocity, 597, 641
 synchrotron white beam x-ray topography, 41
 tantalum oxide, 1025
 tetramer, 231
 thermal
 anneal, 365
 stress modeling, 29
 thermionic current, 829
 thin film(s), 803
 transistors, (TFT), 393, 761
 threading dislocations, 141
 time(-)
 analyzed transient spectroscopy (TATS), 941
 dependent charge measurements, 77
 transient grating technique, 59
 transition energy, 225
 transmission
 electron microscopy (TEM), 863, 869
 x-ray topography, 29
 trap(s), 377
 assisted tunneling, 743
 electron, 447
 two-color method, 597
 II-VI semiconductors, 77, 237, 977
 type conversion, 381
 ULSI, 703
 ultrafast
 laser spectroscopy, 171
 optical response, 1001
 ultrasound(-)
 stimulated dissociation, 647
 treatment, 405
 UV laser carrier excitation, 591
 vacancies, 17, 95
 cation, 237
 vacancy-
 impurity complex, 65
 type defects, 659, 665
 vibrational mode spectroscopy, 341, 547
 widegap semiconductors, 467, 533
 x-ray
 diffraction
 dislocations, 783
 high-resolution, 635
 SnTe, 255
 triple axis, 315, 893
 fluorescence, 231
 photoemission spectroscopy, 249
 reciprocal space maps, 893
 topography, 671
 Y₂O₃, 1025
 zero phonon intracenter transitions, 263
 ZnS, 533